

9th GRACM

International Congress on
Computational Mechanics

4-6 June 2018, Chania

www.9gracm.tuc.gr/



Editors: Manolis Papadrakakis, National Technical University of Athens
Georgios E. Stavroulakis, Technical University of Crete

Book of Full - length Papers



Greek Association of
Computational Mechanics
<http://gracm.ntua.gr>



Technical
University
of Crete

Technical University of Crete Press, 2018

E-book available on: <http://9gracm.tuc.gr>



9th GRACM International Congress
on Computational Mechanics
4-6 June 2018, Chania, Greece

Book of Full-length Papers

Editors:

Manolis Papadrakakis, National Technical University of Athens

Georgios E. Stavroulakis, Technical University of Crete

Chania, Greece 2018

COMMITTEES

Congress Chairmen

Prof. M. Papadrakakis, National Technical University of Athens
Prof. G. E. Stavroulakis, Technical University of Crete

Organizing Committee – HSTAM Administrative Council

Prof. M. Papadrakakis, National Technical University of Athens, President
Prof. G. E. Stavroulakis, Technical University of Crete, Vice President
Assoc. Prof. V. Papadopoulos, National Technical University of Athens, Secretary
Assoc. Prof. G. Tsiatas, University of Patras, Treasurer
Prof. E. E. Theotokoglou, National Technical University of Athens
Prof. J. T. Katsikadelis, National Technical University of Athens
Prof. A. G. Boudouvis, National Technical University of Athens
Assist. Prof. G. Stefanou, Aristotle University of Thessaloniki
Prof. N. Pelekasis, University of Thessaly

Congress Secretariat

Maria Bakatsaki, M. Sc., Technical University of Crete

Supporting Team

Dr. Aliko Muradova, Preparation of printed material
Dr. Georgios Tairidis, Secretarial assistance and preparation of printed material
Nefeli Manoudaki, Cover-page layout
Dr. Evangelos Liarakos, Secretarial assistance
Dionysios Chatzidakis, Olympia Kalagri, Pantelis Krinakis, Konstantinos Marakakis, Maria Masoura, Demetra Vathi, student assistants

Congress Contact Information

Website: <http://9gracm.tuc.gr>

E-mail: 9gracm@isc.tuc.gr

Institute of Computational Mechanics & Optimization (CoMecO) <http://www.comeco.tuc.gr>

School of Production Engineering & Management of Technical University of Crete



ISBN 978-618-81537-5-2 (e-book)



Technical University of Crete Press, Chania, Greece

PREFACE

The present electronic book is an edited collection of papers presented at the 9th GRACM International Congress on Computational Mechanics, which was held at the Technical University of Crete, Chania, June 4-6, 2018. The congress was organized by the **Greek Association of Computational Mechanics** (GRACM) with the support of the **Institute of Computational Mechanics & Optimization** (CoMecO) of School of Production Engineering & Management of Technical University of Crete.

The volume contains 48 papers, reflecting recent advanced in Computational Mechanics.

The Editors would like to thank all the authors of the papers for submitting a full paper for the present collection, the reviewers of the papers and the members of the Executive Council of GRACM, who served as members of the Scientific Committee.

Thanks are also due to all the people who provided technical and secretarial support to the Congress, especially to Mrs. Maria Bakatsaki from the Technical University of Crete, as well as to the Technical University of Crete Press, which published the present book.

Chania, June 2018

The 9th GRACM Conference co-chairmen

- Manolis Papadrakakis, National Technical University of Athens, GRACM Chairman
- Georgios E. Stavroulakis, Technical University of Crete, GRACM Vice-Chairman

TABLE OF CONTENTS

<i>Dynamic action effect analysis for structural integrity management of very large floating bridges</i>	
Torgeir Moan	1
<i>A performance-based seismic design method for RC/MRFS using modal strength reduction factors</i>	
Edmond Muho, George Papagiannopoulos and Dimitri Beskos	22
<i>Dynamic response of an infinite beam resting on a Winkler foundation to a load moving on its surface with variable speed</i>	
Edmond Muho and Niki Beskou.....	31
<i>Accumulated damage in nonlinear cyclic static and dynamic analysis of reinforced concrete structures through 3D detailed modeling</i>	
Christos Mourlas, George Markou and Manolis Papadrakakis.....	38
<i>Nonlinear local buckling analysis of beams employing a higher order beam theory</i>	
Amalia Argyridi and Evangelos Sapountzakis.....	47
<i>Kdamper concept in seismic isolation of multi storey building structures</i>	
Konstantinos Kapasakalis, Evangelos Sapountzakis and Ioannis Antoniadis.....	56
<i>Numerical and asymptotic solutions of axisymmetric Poiseuille flows of yield stress fluids with pressure-dependent rheological parameters</i>	
Kostas Housiadas, Iasonas Ioannou, Pandelitsa Panaseti and Georgios Georgiou.....	66
<i>Rarefied pulsatile pressure-driven fully-developed gas flow in long circular tubes</i>	
Alexandros Tsimpoukis and Dimitris Valougeorgis.....	76
<i>Aerodynamic shape optimization of diffuser augmented wind turbine blades using asynchronous parallel differential evolution</i>	
Stavros Leloudas, Giorgos Strofylas and Ioannis Nikolos.....	86
<i>Rarefied gas flow analysis over a re-entry space capsule geometry</i>	
Angelos Klothakis, Stavros Leloudas, Georgios Lygidakis and Ioannis Nikolos.....	96
<i>Numerical flow simulation over the M151 combat aircraft model using GALATEA solver</i>	
Dimitrios Inglezakis, Georgios Lygidakis and Ioannis Nikolos.....	106
<i>Multi-objective optimization of a flapping foil system for thrust augmentation in ship propulsion</i>	
Dimitrios Koubogiannis, Ioannis Bonis, Andreas Priovolos and Kostas Belibassakis.....	116
<i>Optimal design of large span structures using the MBN displacement control system</i>	
Themistoklis Nikolaidis, Georgios Stavroulakis and Charalampos Baniotopoulos.....	124
<i>Preliminary analysis method for FRP laminate impact damage size prediction</i>	
Adam Deskiewicz, Ioannis Giannopoulos and Efstathios Theotokoglou.....	134
<i>Dynamic analysis of a ceramic/metal functionally graded thermoelastic layer under ramp-type thermal loading</i>	
Antonios M. Nikolarakis and Efstathios E. Theotokoglou.....	144
<i>Design and structural analysis of wind turbine blades for structural health monitoring consideration</i>	
Meletios Rentoumis, Panagiotis Koutsianitis, Ilias Athanailidis, George Tairidis, G. Tselikos, Nikolaos Bilalis and Georgios E. Stavroulakis	153
<i>Solving engineering optimization problems with an efficient hybrid nature-inspired algorithm</i>	
Alexandros D. Tsipianitis and Yiannis Tsompanakis.....	163
<i>Material optimisation use in steel lattice wind turbine towers</i>	
Nafsika Stavridou, Efthymios Koltsakis and Charalampos Baniotopoulos.....	173
<i>Early warning and hazard analysis system in Republic of Serbia</i>	
Milan Protic and Zoran Bonic.....	181

<i>Smoothing techniques on precipitation time series</i>	
Mladen Milanovic, Milan Gocic, Slavisa Trajkovic and Maja Stanojevic Gocic.....	189
<i>GIS application in floods risk assessment in Leposavic</i>	
Predrag Stanojevic, Jelena Djokic, Bojana Zivkovic and Jelena Rajovic.....	195
<i>Lead particles dispersion modeling in extreme weather conditions from tailing waste in Zvečan</i>	
Jelena Djokic, Nebojša Arsić and Srdjan Jovic.....	201
<i>A new boundary element solution to plates on elastic foundation via Helmholtz's potentials</i>	
Maria Nerantzaki and John Katsikadelis.....	208
<i>A parallel algorithm for the embedded reinforcement mesh generation of large-scale reinforced concrete models</i>	
George Markou.....	211
<i>Finite element analysis of aggregated elongated vaulted structures</i>	
Maria Stavroulaki, Antonis Anousakis and Aikaterini Mesaritaki.....	219
<i>Optimum design of reinforced concrete footings under axial loading using discrete and continuous design variables</i>	
Sinan Melih Nigdeli and Gebrail Bekdaş.....	229
<i>Application of the finite superelement method for the doubly periodic functionally graded solid calculation</i>	
Viacheslav Mokryakov.....	235
<i>Investigation of support conditions between stacked reinforced concrete beams using experimental modal analysis and finite element methods</i>	
Marios Filippoupolitis and Carl Hopkins.....	243
<i>Effects of thermal deformation on the buckling resistance of steel framed members exposed to fire</i>	
Themistoklis Nikolaidis, Evangelia Georgantzia and Charalampos Baniotopoulos.....	248
<i>A fiber approach to the large deflection analysis of beams by BEM</i>	
George Tsiatas, Antonis Siokas and Evangelos Sapountzakis.....	259
<i>The robustness of optimum tuned mass dampers design using transfer function amplitude and JAYA algorithm</i>	
Sinan Melih Nigdeli and Gebrail Bekdaş.....	264
<i>Metaheuristic and frequency domain based optimization of tuned mass dampers and verification of the results on time history analyses</i>	
Sinan Melih Nigdeli, Gebrail Bekdaş and Yusuf Cengiz Toklu.....	274
<i>Non linear homogenization theories with applications to trip steels</i>	
Ioanna Papadioti, Ilias Bellas, Maria - Ioanna Tzini, Peter Christodoulou and Nikolaos Aravas.....	284
<i>Preliminary computational aproach of plasma dynamic evolution produced by low current table-top pinch plasma devices</i>	
Alekos Skoulakis, George Koundourakis, Evaggelos Kaselouris, Ioannis Ftilis, Eugene Clark, Nektarios Vlahakis, Makis Bakarezos, Nektarios Papadogiannis, Vasilis Dimitriou and Michael Tatarakis.....	294
<i>Simulations of laser assisted machining and conventional cutting of AISI H-13 steel</i>	
Evaggelos Kaselouris, Theodoros Papadoulis, Alekos Skoulakis, Andreas Baroutsos, Ioannis Ftilis, Yannis Orphanos, Makis Bakarezos, Nektarios Papadogiannis, Michael Tatarakis and Vasilis Dimitriou.....	304
<i>Estimation of insertion loss of sound barriers via finite element method</i>	
Nikolaos M. Papadakis and Georgios E. Stavroulakis.....	312
<i>The structural integrity of unburied offshore pipelines across active tectonic faults</i>	
Aikaterini Triantafyllaki, Panos Papanastasiou and Dimitrios Loukidis.....	319
<i>Numerical study of offshore natural gas pipelines subjected to submarine landslides</i>	
Dionysios Chatzidakis, Yiannis Tsompanakis and Prodromos N. Psarropoulos.....	328
<i>Effects of the soil-structure-interaction phenomenon on RC structures with pile foundations</i>	
George Markou, Mohammad Alhamaydeh and Dina Saadi.....	338

<i>Numerical simulation of atherosclerotic plaque growth in right coronary arteries</i> Igor Saveljic, N. Filipovic, V. Isailovic, Z. Milosevic, D. Nikolic, M. Nikolic, B. Cirkovic-Andjelkovic, T. Exarchos, D. Fotiadis, G. Pelosi and O. Parodi.....	346
<i>A spectral collocation method for vibration suppression of smart elastic plates</i> Alik Muradova, Georgios Stavroulakis and Georgios Tairidis.....	352
<i>Investigation of the position of the piezoelectric patches on a shunted piezoelectric beam</i> Georgios Tairidis, Panagiotis Koutsianitis, Georgia Foutsitzi, Georgios Stavroulakis, Jean-Francois Deü and Roger Ohayon.....	361
<i>A boundary layer approach for the solution of the general single contact frictional problem in multibody dynamics</i> Sotirios Natsiavas and Elias Paraskevopoulos.....	367
<i>Application of an augmented lagrangian methodology to dynamics of multibody systems with equality constraints</i> Elias Paraskevopoulos, Nikolaos Potosakis and Sotirios Natsiavas.....	377
<i>Seismic response assessment of rigid and flexible rocking frames using simple finite element models</i> Spyridon Diamantopoulos, Kyriakos Koutoulas and Michalis Fragiadakis.....	387
<i>Numerical investigation of the progressive collapse of steel structures due to plan irregularities</i> Amir Homaioon Ebrahimi, Pedro Martinez-Vazquez and Charalampos Baniotopoulos.....	397
<i>Dynamic response of masonry buildings considering the time-dependent soil saturation conditions</i> Alexandros Liratzakis and Yiannis Tsompanakis.....	407
<i>Vibrational features of the traditional percussion instrument bendir using laser holographic interferometry and finite element analysis</i> Makis Bakarezos, Vasilis Dimitriou, Y. Orphanos, I. Sidiras, E. Kaselouris, M. Tatarakis and N. Papadogiannis.....	417
<i>GIS extension tool for visualization of flood risk evaluations</i> Dejan Rančić, Miloš Bogdanović, Uwe Siart and Olivera Pronić Rančić.....	424
Author Index	430

DYNAMIC ACTION EFFECT ANALYSIS FOR STRUCTURAL INTEGRITY MANAGEMENT OF VERY LARGE FLOATING BRIDGES.

T. Moan

Department of Marine Technology
Norwegian University of Science and Technology
Trondheim, NO-47491, Norway

e-mail: tormo@ntnu.no ; web page: <https://www.ntnu.no/ansatte/torgeir.moan>

Keywords: Floating bridges, wave- and wind-induced dynamic response, stochastic analysis, conceptual studies

Abstract. *To improve the efficiency of transport systems across straits, bridges, submerged tunnels and subsea tunnels are introduced to replace ferries. For wide and especially deep straits, floating bridges are attractive. Floating bridges are subjected to permanent, traffic, environmental and accidental loads. The focus herein is on wind, wave and current loads. All these loads and load effects should be properly evaluated for ultimate and other limit state design checks. In this paper a brief overview of relevant concepts, characteristic behaviour and design criteria are given, followed by an outline of the modelling of wind-, wave-, and current-induced loads and their effects. Selected case studies of a possible 4600 m long curved bridge for the crossing of the Bjørnafjord, are presented to illustrate typical features of such bridges. Such bridges have a number of eigenmodes, which might be excited by the environmental loads. The response in the horizontal plane is mainly induced by wind loads, while the vertical response is mainly induced by wave loads. Wave short-crestedness and inhomogeneity are found to have a significant influence on the vertical response. Ocean current loads mainly reduce the dynamic response in the horizontal plan due to the damping effect of the drag forces.*

1 INTRODUCTION

Floating bridges can be traced back to trafficable timber walkways built over an array of boats that were secured together and anchored to the floor of the waterway; known to have been used at least 3000 years ago, according to the review by Wang & Wang [1]. These structures were unlikely to have a significant design lifespan and had to be renewed on a regular basis. The current model of modern floating bridges can be traced to the pontoon bridge design that was implemented in the Hobart Bridge, Australia in 1943, and was a first of its kind in the world. Other early designs were the floating bridges built across the Lake Washington in the Seattle area in 1940 and 1963. Other examples of modern floating bridges include the 1988-m long Hood Canal Bridge built in 1963 (Fig. 1b) ; the Canadian 640-m long Kelowna Floating (concrete) Bridge which was opened to traffic in 1958, the Hawaiian's 457-m long Ford Island Bridge which was completed in 1998. More recent floating bridges built from 1990s include the two Norwegian floating bridges: 845-m long Bergsøysund Floating Bridge built in 1992 near Kristiansund over a fjord depth of 320 m and the 1246-m long Nordhordaland Floating Bridge built in 1994 at Salhus over a 500m deep fjord (see Fig. 2) [2,3].

Later there have been projects involving submerged floating tunnels have been considered as an option for strait crossings, especially wide crossing such as the Gibraltar and Messina straits [4]. In the latter case a submerged tunnel was assessed vs a suspension bridge with a main span of 3700 m. For Høgsfjord in Norway a submerged tunnel was also considered [2].

So far submerged floating tunnels have not been built while immersed tunnels (resting/buried in the seabed) has been used in many places, essentially when the water depth is relatively small.

Currently, the Norwegian Public Roads Administration (NPRA) is assessing replacing ferry transport across 8 fjords by providing bridges, submerged tunnels or subsea rock tunnels on highway E-39 from Trondheim to Kristiansand [3]. The width of the strait crossings is up to 6 kilometers and the water depth is up to 1300 m. Due to the maximum slope of roadways, a subsea tunnel in rock will be very long and expensive (Fig. 3).. Due to the width and depth of the fjords, the free span for bridges with towers on land, will in most cases get excessive span. The current largest free span is about 2 km. Some deliberations on using a 3700 m single span suspension bridge have been made by NPRA [5].

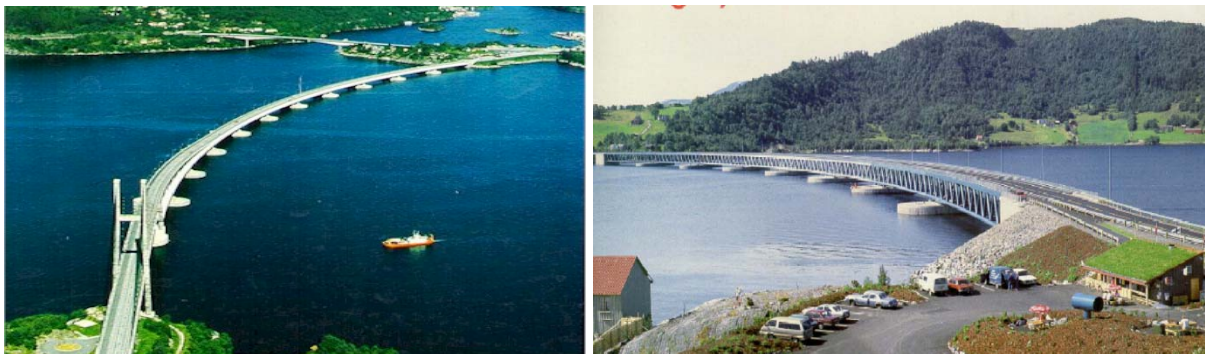
At the moment, the NPRA is considering three possible floating bridge concepts and a submerged tunnel type of concept for strait crossing (Fig. 4).. The floating bridge concepts include

- Curved, End Anchored Floating Bridge combined with a cable stayed high bridge
- Straight, Side Anchored Floating Bridge by mooring system combined with a cable stayed high bridge
- Floating Suspension bridge with two pylons supported by TLPs or spar floating bodies.



a) Floating Xerxes bridge built in 480 B.C. b) Hood Canal bridge in the State of Washington, USA

Fig. 1 Floating bridges from ancient to modern times [1].



a) Nordhordaland bridge

b) Bergsøysund bridge

Fig. 2 Modern floating bridges in Norway.

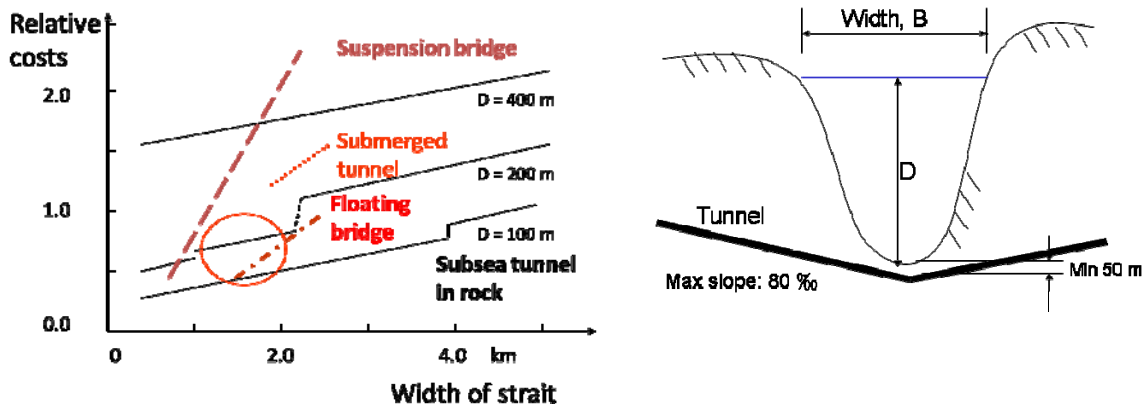
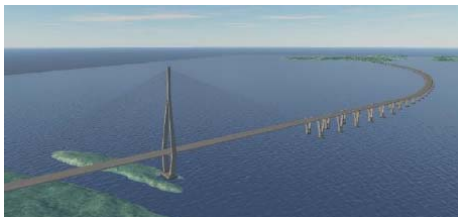


Fig. 3 Indicative relative costs of strait crossing based on tunnel, submerged tunnel and floating bridge or free span suspension bridge for a fiord with a width B and a depth D .

The first concept will be an extension of the existing two floating bridges in Norway; namely the Nordhordaland and Bergsøysund bridges [3]. However, increasing the length introduce additional challenges as discussed below. It is also noted that the bridges are supported on discrete pontoons.

Another issue is that the design should provide passage for ships. This would normally imply that part of the bridge need to be high as indicated for the Nordhordaland bridge in Fig.2a. This feature will be directly accounted for in a floating suspension bridge.



a) Curved, end-anchored bridge



b) A side-anchored straight bridge



c) Suspension bridge with floating pylons (towers)



d) Submerged tunnel based on one or two tubes, with excessive buoyancy, and tethered to the seabed. Alternatively, the bridge can have less larger weight than buoyancy and be supported by pontoons in the surface.

Fig. 4. Floating surface bridge and submerged tunnel concepts.

As an example, the crossing site of Bjørnafjord is approximately 5 km wide, and the fjord at the deepest is 550-600m deep. The bridge was originally conceived to be a side anchored floating bridge with a ship passage in the North under a high bridge placed on fixed foundation and a floating bridge ending in a concrete caisson much in the same philosophy as the Nordhordland bridge [3].

The development of technology for floating bridges has benefitted from transfer of technology from ship and ocean technology and implemented by consideration of the unique serviceability requirements and the target level of safety relevant for bridges. In particular the principles and methods developed for oil and gas platforms and ships as well as for floating airports in the Mega-Float project in Japan during 1995-2000 and the MOB project in USA, especially in the period 1997-2000 [6-9].

The focus herein is on floating surface bridges subjected to wave-, wind and current loads. In areas with significant seismic action can play a role, however, it is noted that floating bridges are compliant and not very sensitive to ground excitation.

In the remaining part of this paper previous research about the global response of floating bridges is first described, followed by a brief summary of the design criteria and characteristic features of the behaviour of floating bridges. Then the methods for modelling environmental conditions, the corresponding loads and load effects. Finally, selected case studies to illustrate the dynamic behaviour of floating bridges, are briefly described.

2 PREVIOUS STUDIES OF THE GLOBAL DYNAMIC RESPONSE OF FLOATING BRIDGES

Floating bridges are subjected to environmental loads, especially due to wind, wave and current. The corresponding load effects are used in connection with appropriate criteria, typically in terms of displacements, motions or resistances, to ensure serviceability and safety [10-13]. Herein, the focus is on the determination of load effects.

Most studies on floating bridges consider pontoon-type bridges, with emphasis on the wave-induced hydro-elastic behaviour. The formulations are based on the theory developed for other stationary floating bodies, e.g. [14, 15]. In early studies Langen and Sigbjørnsson [16] and Hartz [17] investigated numerically the behaviour of floating bridges. Løken et al. [18] conducted numerical and experimental study of a pontoon type floating bridge under long-crested and short-crested waves – relating to the Bergsøysund bridge mentioned above. Numerical results based on potential flow theory presented fairly good agreements with those from the model test. Seif and Inoue [19] proposed a unified method for the analysis of a discrete pontoon floating bridge that takes into account complete hydrodynamic interaction between the pontoons. Fu et al. [20] proposed and applied a time-domain method for hydroelastic analysis of floating bridges based on multi-rigid-body connected by elastic beams. Kvåle and co-workers [21] developed a frequency domain method to account for the hydroelastic responses of pontoon type floating bridges, and applied it to investigate the dynamic behaviour of the Bergsøysund bridge. Kvåle et al. also compared field measurements with numerical predictions of the response of the Bergsøysund bridge, with a focus on determination of natural frequencies and modes based on ambient response. Lie et al. [22] investigated the feasibility of deploying an end-anchored floating bridge in Masfjorden, Norway and compared its dynamic response with a submerged tube bridge concept. Fu et al. [23] studied the effect of inhomogeneous wave conditions. Fredriksen et al. [24] presented dynamic analysis of a side-anchored straight bridge under wave loads, with an emphasis to optimize the design of pontoons to reduce resonance response in the bridge girder. Cheng et al. [25-26] investigated the effects of various hydrodynamic models. Sha et al. [27] did a sensitivity study of a curved bridge under wave and wind loads.

Sun et al. [13] carried out an experimental investigation on the nonlinear hydro-elastic response of a pontoon-type floating bridge under regular wave action.

Compared to wave loads, wind loads and load effects on pontoon-type floating bridges are much less addressed in the literature. For floating suspension bridges account of the joint occurrence of wind and wave loads is crucial, since they are more sensitive to wind loads than the pontoon-type floating bridges. Volkert et al. [29] and Veie and Holtberget [30] assessed alternative bridge concepts for wide strait crossings, including floating suspension bridge alternatives. Fredriksen et al. [31] presented a study of a three span suspension bridge with pylons supported by tension-leg and catenary moored in an early phase feasibility study of a concept applicable for crossing of the Sulafjord. Particular attention was paid to the floating body supporting the pylons.

By using state space representations for frequency dependent wind and wave forces, Xu et al. [32-33] developed a time domain method to simulate the dynamic behaviour of a floating bridges and applied the method to a three-span suspension bridge with two floating pylons. The dynamic behaviour of the bridge is studied considering both first and second order wave excitations as well as mean wind and linear and nonlinear buffeting forces. The importance of nonlinear effects in the modelling is carefully studied to improve the understanding of the dynamic behaviour of this new bridge concept.

3 DESIGN CRITERIA

3.1 General

Floating bridges should in general fulfill sociopolitical criteria that address the aesthetics, environmental sustainability, budgetary and legal constraints. The bridge should satisfy serviceability and safety requirements that should be maintained during the operational life, of say, 100 years, of the bridge, with a minimum of life cycle costs. In the design of floating bridges and submerged tunnels, the following loads must be considered: dead load, hydrostatic pressure (including buoyancy), live load, wind, waves (including swell), earthquakes, temperature change and water current loads, effects of tidal change, effects of seabed movement, effects of movements of bearings, snow load, effects of tsunamis, effects of storm surges, ship waves, seaquake, brake load, effects of drift ice and ice pressure, effects of drifting bodies, and effects of marine growths (corrosion and friction), abnormal loads (such as impact loads due to collision of ships with the floating structure),

Typical criteria for floating bridges are given in e.g. [10-12].

3.2 Serviceability criteria

The purpose of serviceability criteria is to ensure that the structure fulfils its function as specified by the

owner; i.e. the comfort and safety of both drivers and pedestrians. Besides requirements to the width of the roadway, separation of traffic and pedestrians that use the bridge and clearance for ship traffic the bridge should satisfy serviceability requirements to deflections and motions; e.g. [10-12]. For instance, the maximum deflection and rotation of the bridge girder should be less than 1.5 m and 1 deg., respectively for 70 % of the characteristic traffic load. Moreover, the rotation about the bridge axis under 1-year static wind load should be less than 0.5 deg. while the root mean square (rms) value in 1-year storm should be less than 1.5 deg. The rms value of the accelerations in a 1-year storm in any lane should be less than $0.3\text{--}0.5\text{ m/s}^2$, depending on the speed limit. It should be noted that the design specification for the Hood Canal floating bridge had a requirement to the jerk (d^3u/dt^3) [10]. Since floating bridges need to accommodate passing traffic the end connections need provide a smooth transition from the roadway and the bridge under the action of vertical change of position of the bridge due to tidal water level variations and wave actions.

3.3 Safety criteria

Safety requirements ensure that there are no casualties, fatalities, property or environmental damage. Global structural failure, capsizing, sinking, and drifting off-station are failure modes which are taken care of under the safety criteria. Property damage could be acceptable financially, but human loss and environmental damage are permanent effects that are eliminated or minimized under strict design guidelines.

Floating bridges e.g. in Norway should in general be designed for the highest consequence and reliability class (CC3, RC3) [11, 13]. However, particular components might be designed for a lower consequence class (CC2). The design serve life should be 100 years as a minimum. The design should be based on the following principles:

- probability of fatalities should be comparable to accident rate in traffic itself, and less than for voluntary presence on offshore platforms (target P_f for submerged tunnels 1/10 of that of offshore structures)
- storm monitoring and warning will reduce that chance of fatalities due to storm damage
- "uncommon" loads and load combinations, including accidental loads should be accounted for

These principles are implemented by fulfilling ultimate, fatigue and accidental collapse limit states. While Eurocodes [13] refer to these limit states in one group as ULS criteria, the Norwegian bridges follow the offshore standards ISO 19900 and Norsok N-001 principles by considering separate limit states.

This paper focuses on determination of wave, wind and current actions and their effects on floating bridges, especially for serviceability and ultimate limit state (ULS). The latter is based on characteristic values with reference to an annual exceedance of 10^{-2} and characteristic resistances and partial action and material (resistance), generally based on the suite of Eurocodes. However, due the additional uncertainty in action effects relating to wave, wind and current actions, the partial action factor is taken to be 1.6, slightly increased above 1.5 in EN 1990

Very large floating structures such as floating bridges are usually constructed in modules at shore-based facilities and moved in a floating mode to the installation site and then provided with mooring system, which is partly pre-installed.

Owing to the corrosive sea environment, floating structures have to be provided with a good corrosion protection system. Possible degradation due to corrosion or crack growth (fatigue) requires a proper system for inspection, monitoring, maintenance and repair during use to ensure durability.

4 CHARACTERISTIC FEATURES OF THE BEHAVIOUR OF FLOATING BRIDGES

4.1 General

The analysis and design of very large floating structures need to have special consideration when compared to the common size with overall size of 100 m or less.

In floating structures, the static self-weight and pay-loads are carried by buoyancy forces. While floating offshore platforms with an overall size of about 100 m are rigid, very long structures such as floating bridges, are flexible. This implies that a concentrated force cause deformations over a certain characteristic length, λ_c , only, analogous to a beam on an elastic (flexible) foundation.

Floating bridges are subjected to wave and wind actions that exhibit a time variation with a frequency that can cause dynamic effects in the bridges. As shown later, floating bridges have many natural periods that can be excited by random wave and wind loading. Moreover, the characteristic period of the dynamic loading is both smaller and larger than the natural periods and e.g. the characteristic length of waves is much less than the length of the structure.

4.2 Basic characteristics

In the vertical direction low bridges are supported by continuous or preferably discrete pontoons spaced at 100 – 200 m., while a suspension bridge over e.g. a 5 km span might have two pylons with free spans of a length of the order of 1.5 km. The behaviour depends on the relative restoring stiffness due to buoyancy and the bridge girder bending stiffness. Typically the restoring stiffness is relatively small and governs the behaviour of the low bridge, while for the suspension bridge is relatively large and provide limited compliance.

To carry the relatively large horizontal forces due to waves and wind two designs are envisaged. One option is a straight bridge supported by several clusters of catenary mooring lines anchored on the seabed. The alternative is to use a curved bridge that carry the horizontal forces by axial forces due to the “arch effect” and with anchoring of the bridge ends. The pylon/pontoons of a suspension bridge may be anchored by a tension-leg or catenary mooring system. (In Fig. 4c a tension-leg system is indicated). It should be noted that in shallow water the mooring system easily becomes very stiff and virtually prevents the horizontal motion. As a consequence the mooring forces become an order of magnitude larger than in a compliant system. This is because the horizontal wave and dynamic wind forces are balanced by inertia forces in a compliant system.

Where the horizontal size of the structure is larger than the wave length, the resultant horizontal forces will be reduced given that different phases (direction and size) of the wave force will act on various parts of the structure, resulting in smaller forces in the mooring system relative to the total wave force.

4.3 Dynamic features of the response

The dynamic features if the bridge can be conveniently judged based on the natural frequencies and mode shapes in view of the distribution of energy in the action over frequencies, direction and space (phase angle for the action on different parts of the structure, e.g. [34-35].

The dynamic amplification factor, DAF of mode i with a natural frequency of ω_i for an harmonic excitation with frequency, $\bar{\omega}$

$$DAF = \left[(1 - \Omega^2)^2 + (2\zeta\Omega)^2 \right]^{-1/2} \quad (1)$$

where $\Omega = \bar{\omega} / \omega_i$ and ζ is the damping ratio, $\zeta = c/c_{cr}$, where c is the critical damping. Moreover, the phase angle between the excitation and response, ϕ is

$$\phi = \arctg[2\zeta\Omega / (1 - \Omega^2)] \quad (2)$$

Because of the wide range of natural frequencies, excitation frequencies can be both above and below the natural frequencies, implying both an inertia and stiffness dominated system, respectively. In the former case the DAF is less than 1.0 since the inertia forces to some extent balances the excitation forces and reduces the structural response.

It is convenient to express the effect of the spatial distribution of dynamic loading on the system by the generalized dynamic modal loading associated with a given excitation frequency.

$$q_i = \int_0^L q_{ext}(x) \phi_i(x) dx \quad (3)$$

where q_{ext} and q_i are the spatial distribution of loading over a structure of length L at a given excitation frequency and phase angle. Consider as an illustration the hydrodynamic loading (for simplicity assumed to be proportional to the wave elevation) a long-crested wave of length λ acting on a straight bridge with a mode of vibration that have a “wave length” of L_s . If the wave angle of approach, θ is 90 degrees (and the number of “wave lengths” L_s is an equal number), the excitation force becomes zero. If the angle θ is slightly smaller than 90 degrees, i.e. $\cos\theta = \lambda/L_s$, the excitation is completely in phase with the mode and gives a maximum generalized force. If the wave condition is stochastic and short-crested, similar considerations apply but the situation is less transparent. If the bridge is curved the situation becomes more complex since there will be different phase angles of the wave load in different locations of the bridge due to the geometry.

Analogous considerations can be made for the effect of turbulent wind.

5 ENVIRONMENTAL CONDITIONS

5.1 General

In this context only the wind, wave and current loads and their static and dynamic effect is addressed.

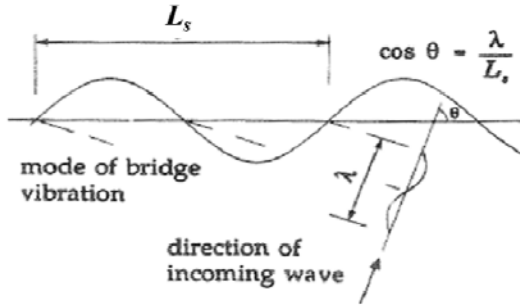


Fig. 5 Illustration of the effect of phase angle in a long-crested wave on the excitation of modes.

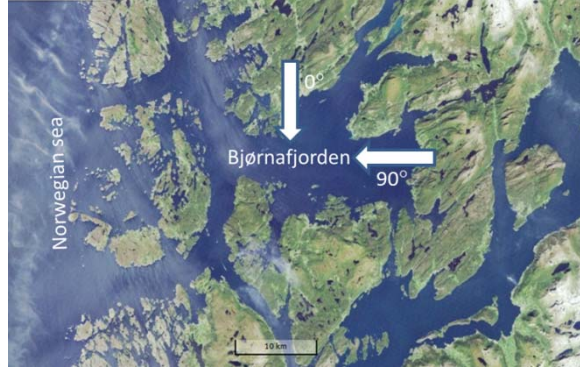


Fig. 6 Topography of a possible site for floating bridge (Bjørnafjorden) and directions of orientation

5.2 Wave and current

The ocean waves at a site generally consists of wind generated sea and swell. Wind-generated waves consist of a large number of wavelets of different heights, periods and directions superimposed on one another. Although regular waves are not found in real seas they can closely model some swell conditions. They also provide the basic components in irregular waves and are commonly used to establish wave conditions for design. Regular waves are characterized by the wave period and height. The kinematics and hydrodynamic pressure within a regular wave are described by the wave potential as described subsequently.

During a suitably short period of time (typically 3 hours) the sea surface elevation, ζ is commonly assumed to be a zero mean, stationary and ergodic Gaussian process, e.g. [14-15]. The Gaussian process is completely specified in terms of the wave spectral density, $S(\omega)$ for long-crested waves. In the time domain the wave elevation may be described by a sum of long-crested waves specified by linear theory, with different amplitudes a_i , frequencies ω_i and phase angles ε_i which are uniformly distributed over $(-\pi, \pi)$.

Wave conditions are typically assumed to be stationary within short-term periods of 3 hours and described by a wave spectrum for the wave amplitudes:

$$S_{\eta}(\omega, \theta) = S(\omega)D(\theta) \quad (4)$$

where $S(\omega)$ is the unidirectional wave spectral density and $D(\theta)$ the directional distribution. The directional distribution for locally wind generated sea is commonly approximated as frequency independent. The wave spectrum is represented by an analytical function; for instance, the simple one-parameter Pierson-Moskowitz spectrum and the $\cos^n \theta$ distribution [36]

$$S(\omega) = 0.0081g^2\omega^{-5} \exp\left(-\frac{3.11}{\omega^4 H_s^2}\right) \quad (5)$$

$$D(\theta) = \frac{\Gamma(n/2 + 1)}{\sqrt{\pi}\Gamma(n/2 + 1/2)} \cos^n(\theta - \theta_p)$$

where θ_p is the mean wave direction. A more general formulation is to let the directional distribution depend on the frequency. Other spectra include the JONSWAP spectrum.

To exemplify the situation consider the East-West oriented Bjørnafjorden in Fig. 6. Fig. 7 gives an indication of the variability of 50 year wind conditions in the fjord due to the local topography. Fig. 7a shows how the ocean wave condition in terms of the significant wave height propagates into a fjord system as determined by software such as Swan and STWave [37-38]. In the East-West oriented Bjørnafjord two possible bridge sites are indicated with red dots. It is seen that the waves at these sites are not affected by waves coming from the ocean. The main waves are generated by wind from North West and East. Other directions are blocked by land masses. The land masses surrounding the crossing site in Bjørnafjorden limit the fetch from less than 5 km to no more than 20 km. As a result, the local wind-generated waves have limited height and period. The significant wave height is 2.4-2.8 m depending on direction and the spectral peak period is in the range of 5-7 s.

A sample time series of the short crested wave surface elevation can be described by:

$$\eta(x, y, t) = \sum_n \sum_m^M \eta_{nm} \cos[k_n(x \cos(\theta'_m) + y \cos(\theta'_m)) - \omega_n t + \varepsilon_{nm}] = \sum_n \sum_m^M \eta_{nm} \eta(x, y, k_n, \theta'_m, \varepsilon_{nm}, t) \quad i \in \{1, 2, \dots, 6\}$$

$$\eta_{nm} = \sqrt{2S_{\eta}(\omega_n, \theta'_m)\Delta\omega\Delta\theta}; \quad \theta'_m = \theta_m - \theta_p \quad (6)$$

In addition to the locally generated wind sea long-crested swell occurs. For instance, because of the local topography, swell can only reach Bjørnafjorden through passages from the North (North) West and from the South West. With wind predominantly from the North, we can expect the North end of the crossing structure to be sheltered by land yielding smaller loads than experienced at the South end of the crossing structure. Also, because the depth of the Bjørnafjord varies considerably, the wave system will be diffracted as it approaches shallower areas. NPRA is conducting a measurement program of the wind, wave and current conditions in several Norwegian fjords. Due to the limited time of the measurement program before design will be carried out, the measurement program essentially is applied to validate hindcast predictions of local wind, wave and current conditions based on meteorological and oceanographic data, [12, 40].

It is noted that the sea state across the strait – along the bridge may be inhomogeneous; i.e. correspond to different spectra. Fig. 7b gives an indication about the wave conditions across the fjord. Moreover, the correlation in different points across the strait might vary [41].

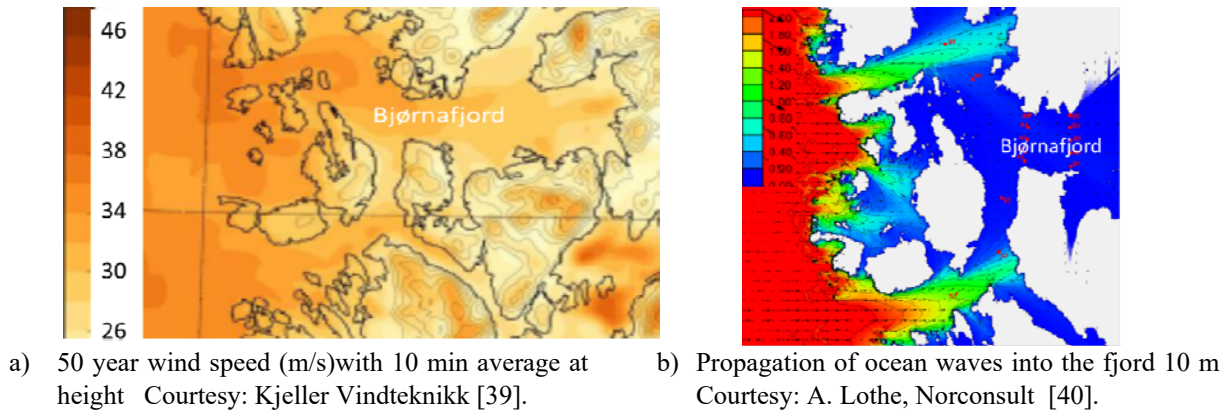


Fig. 7 Macro-environmental conditions in the Bjørnafjord, Norway [38].

The wave elevation at point (x; y) is described by the wave spectrum $S(\omega)$, directional distribution $D(\theta)$, and random phase angle ε_{mn} . When the wave spectrum and directional distribution are given, the wave elevation at point (x; y) can be regarded as a function of significant wave height, H_s and the peak period T_p , the principal wave direction θ_p and random phase angle ε_{mn} . For the floating bridge considered in this study, the wave field is *homogeneous* if these four parameters are identical for all pontoons; otherwise, the wave field is considered *inhomogeneous* [26, 41].

In view of their variability and the dynamic properties of the structure (with natural periods from about 120 s and down to a few seconds), the current velocity is considered constant in time. However its spatial variation is important, especially for submerged tunnels, for which vortex induced vibrations excited by the an asymmetrical current across the fjord may be of interest.

5.3 Wind

The **wind velocity field** is described by three components; with U in the main - along wind direction. Moreover, U_w is split in a mean and turbulent component, \bar{U}_w and u_w , respectively. The mean wind velocity is assumed to typically follow an exponential function

$$\bar{U}_w(h) / \bar{U}_{w-ref} = (h / h_{ref})^\alpha \quad (7)$$

Turbulent velocities u , v and w at two points i and j are described by wind spectra accounting for the coherence. Consider for instance the in-line velocity, u . The spectrum in terms of the frequency f , can be described by the Kaimal spectrum:

$$S_{uu}(\Delta s, f) = S_u(f) \cdot \hat{C}_{o_{uu}}(\Delta s, f)$$

where

$$\frac{f \cdot S_u(f)}{\sigma_u^2} = \frac{A_u \cdot \hat{f}}{(1 + 1.5 \cdot A_u \cdot \hat{f})^{5/3}} \quad \text{and} \quad \hat{f} = \frac{f \cdot \bar{L}_u(z)}{\bar{U}_w} \quad (8a-d)$$

and the normalized co-spectrum is given by

$$\hat{C}_{o_{uu}}(\Delta s, f) = \exp(-c_{us} \frac{f \cdot \Delta s}{\bar{U}_w(z)})$$

Here, Δs is the horizontal or vertical distance between the the points considered. $\bar{L}_u(z)$ is the so-called integral length scale in the x-direction. A_u and c_{us} are coefficients, typically with a value of 6.8 and 10.0 respectively.

Analogous expressions exist for the spectra S_{ww} and S_{uw} ; including the effect of separation between two points normal to the main wind direction. Further details are given in e.g. [11, 42] and in papers [11, 42].

6 MET-OCEAN LOADS

6.1 Wave and current loads

The hydrodynamic modeling of wave loads for the floating bridge has been comprehensively addressed in [21-33], based on the state of art in [14-15]. The pontoons are regarded as large volume structures, their hydrodynamic coefficients, such as added masses, radiation damping, and transfer functions of wave excitation forces, etc., are first estimated based on the potential flow theory. The hydrodynamic interaction between adjacent pontoons are not considered, since the spacing between adjacent pontoons are more than 4 times the typical wave length under 100-year wave condition. The wall effect due to fjord sides on the hydrodynamic coefficients is not considered either. The added masses and radiation damping are then applied as radiation forces in time domain using the convolution technique [43]. Regarding the wave excitation forces, this study accounts for both first order wave loads and second-order difference-frequency wave loads. The second-order wave loads are taken into account by using Newman's approximation, in which only forces in surge and sway and moment in yaw are considered. A more detailed description of the modeling of wave loads for low bridges can e.g. be found in [25-26] and for suspension bridges in [32-33].

The viscous drag forces on the pontoons are incorporated through the Morison's equation by considering only the quadratic viscous drag term. They are caused by the wave kinematics, current velocity and floater velocity. The transverse viscous force per unit length is given by

$$dF_{Drag}^{wa}(t) = \frac{1}{2} \rho_w C_D^{wa} D(u_w + u_c - u_b) |u_w + u_c - u_b| \quad (9)$$

where ρ_w is the water density, u_w is the transverse wave particle velocity, u_b is the local transverse body velocity, u_c is the transverse current velocity, D is the characteristic width of the body, and C_D^{wa} is the quadratic drag coefficient. The drag coefficient used for the pontoons in this study is 1.0 (transverse); 0.4 (longitudinal) and 4.8 (vertical) [36].

6.2 Wind loads

Structures above the MSL are subjected to wind loads under wind conditions. Wind forces may stem from the mean pressure and the fluctuations in the incoming air flow (buffeting forces), vortices shed (vortex shedding) and oscillations of the structure itself (motion induced forces). The corresponding response to the three types of loads are treated separately, because they occur in well separately wind velocity regions, however, without clear borders. At the critical velocities the response increases rapidly and it is assumed that the relevant forced response is determined for conditions outside the critical values.

In the present study, the focus is in the response of low bridges subjected to buffeting forces. For floating suspension bridges motion induced forces are also important in consideration of critical wind velocities with respect to instability phenomena like flutter. The buffeting relative velocity between the wind and structures is accounted for when estimating the wind loads.

The column, tower and cables are mainly subjected to viscous drag forces. The transverse viscous drag forces per unit length due to winds is given by

$$dF_{Drag}^{wi}(t) = \frac{1}{2} \rho_a C_D^{wi} D(U_w - u_b) |U_w - u_b| \quad (10)$$

where ρ_a is the air density, U_w is the transverse wave particle velocity, u_b is the local transverse body velocity, D is the characteristic width of the body and C_D^{wi} is the quadratic drag coefficient. For turbulent winds, the wind velocity can be expressed as a mean part \bar{U}_w and a fluctuating part u_w , i.e. $U_w = \bar{U}_w + u_w$.

The wind load acting on the bridge girder is more complicated than those acting on the column, tower and cables. It usually consists of three parts: the mean force due to mean wind velocity, the buffeting force due to fluctuating wind velocity in the two transverse directions, and the frequency-dependent force induced by girder

motion [42]. In this study, the frequency-dependent aerodynamic forces induced by motion of the structures are neglected. Only the mean force and buffeting force are considered using quasi-steady theory. The instantaneous cross sectional drag and lift forces and moment per unit length are then given by [42].

$$\mathbf{F}_{mean} + \mathbf{F}_{Buff}(t) = \frac{1}{2} \rho_a U_{rel}^2 \begin{bmatrix} \cos \beta & -\sin \beta & 0 \\ \sin \beta & \cos \beta & 0 \\ 0 & 0 & 1 \end{bmatrix} \begin{bmatrix} DC_D^{wi}(\alpha) \\ BC_L^{wi}(\alpha) \\ B^2 C_M^{wi}(\alpha) \end{bmatrix}$$

$$U_{rel}^2 = (U_w + u_w(x, t))^2 + w_w(x, t)^2$$

$$\beta \approx \arctan\left(\frac{w_w(x, t)}{U_w + u_w(x, t)}\right)$$
(11)

where

$$\begin{bmatrix} C_D^{wi}(\alpha) \\ C_L^{wi}(\alpha) \\ C_M^{wi}(\alpha) \end{bmatrix} = \begin{bmatrix} \bar{C}_D + \alpha C'_D \\ \bar{C}_L + \alpha C'_L \\ \bar{C}_M + \alpha C'_M \end{bmatrix}$$

where D is the height of the girder. \bar{C}_D , \bar{C}_L and \bar{C}_M are the mean values of the drag, lift and torsional moment force coefficients (taken at the mean angle of attack), and C'_D , C'_L and C'_M are their derivatives with respect to the fluctuating angle of attack, α , which is equal to the angle between the resultant velocity and the horizontal axis of the cross-section, β for quasi-steady theory [42].

It is normally assumed that the fluctuating wind velocities, u_w and w_w structural velocities are small compared to the mean wind the expression wind velocities the expression can be linearized as follows:

$$U_{rel}^2 \approx U_w^2 + 2U_w u_w(x, t). \quad (12)$$

Besides using the approach (I) indicated above considering airfoil-type aerodynamic loads for the bridge girder, simplified approach (II) by considering only the drag forces on the bridge girder, is envisaged. Cheng et al. [44] show that approach I results in a larger standard deviation in sway and heave motions, bending moments, and especially axial force. The aerodynamic lift force significantly excites the 3rd mode (dominated by horizontal motions) and vertical modes of the floating bridge.

Introduction of the motion-induced aerodynamic loads results in an aerodynamic damping and stiffness in terms of aerodynamic derivatives as established by Scanlan & co-workers [42, 45-46] which is necessary to check the critical velocity of suspension bridge with respect to flutter and other instabilities. These phenomena especially relate to across wind direction and torsion. Xu et al. [47] estimated the critical velocity for a suspension bridge with two floating pylons, both the stability criterion in terms of eigenvalue analysis of the impedance matrix and direct time domain analysis with very good agreement.

7 STRUCTURAL MODELLING AND DYNAMIC EQUATIONS OF MOTION

7.1 Structural modelling

The global model of a long bridge will normally be based on flexible finite elements for the bridge girder, tower and cables; e.g. a beam model. accommodating axial and shear forces, bending and torsional moments for the girder. pontoons are modelled as simple elements with high stiffness or as rigid elements –eccentrically attached to the bridge girder. The pontoons are supported by buoyancy (relatively soft springs).

Given the global response of a substructures(line as section of the girder) local stresses; e.g. for fatigue analysis, is obtained by a detailed shell model.

7.2 General

The equation of motion can e.g. be written as [32-33]:

$$\mathbf{M}_s \ddot{\mathbf{u}}(t) + \mathbf{C}_s \dot{\mathbf{u}}(t) + (\mathbf{K}_s + \mathbf{K}_h) \mathbf{u}(t) = \underbrace{\mathbf{F}_{mean} + \mathbf{F}_{Buff}(t) + \mathbf{F}_{se}(t)}_{\mathbf{F}_{Aero}} + \underbrace{\mathbf{F}_{WA}^{(1)}(t) + \mathbf{F}_{WA}^{(2\pm)}(t) - \mathbf{F}_{Rad}(t)}_{\mathbf{F}_{Hydro}} \quad (13)$$

Here, \mathbf{M}_s , \mathbf{C}_s and \mathbf{K}_s symbolize the still-air mass, damping and stiffness matrix, respectively, \mathbf{u} represents the degrees of freedom of the finite element model. \mathbf{F}_{Aero} represents the wind loads that consist of a time invariant

part \mathbf{F}_{mean} due to the mean wind velocity and a dynamic part \mathbf{F}_{Buff} due to turbulence in the wind field and the self-excited forces \mathbf{F}_{se} generated by the motion of the structure.. \mathbf{F}_{Hydro} represents the wave-induced loads, which consists of the radiation forces \mathbf{F}_{Rad} induced by the motion of the submerged part of the structure and the wave excitation forces. Both first and second order difference and sum frequency wave forces, $\mathbf{F}_{WA}^{(1)}$ and $\mathbf{F}_{WA}^{(2\pm)}$, are considered. \mathbf{K}_h is the hydrostatic restoring stiffness.

When a floating structure oscillates in still water, it radiates waves resulting in oscillating fluid pressures on the surface of the body [15]. The hydrodynamic radiation forces depend on the motion history. To consider the frequency-dependent characteristics, Cummins equation is widely used for time domain simulations of structures interacting with water [43]. It is a vector integro-differential equation which involves convolution terms taking the fluid memory effect into account and has been applied by many researchers, see for instance [48]. It is however very time-consuming to solve the convolution integrals during a dynamic analysis [15, 49-50]. A more efficient approach is to replace the convolution integral with a state-space model [49]. The method was shown to yield the same accuracy as by solving Cummins equation directly but with an order of magnitude faster. A simplified approach is to replace the frequency dependent added mass and damping by constant coefficient, which are chosen at a dominating frequency, for instance, the peak frequency of the wave or the natural frequency of the structural system.

The integrated hydrodynamic pressures give rise to radiation forces, which for a single frequency motion are defined as

$$\mathbf{F}_{Rad} = \mathbf{M}_h(\omega)\ddot{\mathbf{u}} + \mathbf{C}_h(\omega)\dot{\mathbf{u}} \quad (14)$$

where $\mathbf{M}_h(\omega)$ and $\mathbf{C}_h(\omega)$ represents frequency dependent added mass and potential damping matrices. These matrices can be determined by the potential theory transformed into the time domain in terms of a convolution integral [15, 43].

Determination of internal forces in the hull structures is possible in some computer codes for special cases; i.e. when the hydrodynamic loads are determined by Morison formula and the structure is modelled as a frame consisting of beams. In general, determination of internal forces in large volume floating wind turbines requires a finite element model of the hull and a potential theory of hydrodynamic loads that account for radiation and diffraction effects. A general time-domain method for determining internal forces in floating wind turbine support structures is presented and applied for a semi-submersible wind turbine in [51].

Instead of using the second order Eqs of motion, a more efficient formulation by replacing it by a state space formulation involving a set of first order diff. equations; by the fact that the convolution integrals are avoided. The first order wave loads for short-crested waves in the time domain are given by

$$\mathbf{F}_{WA}^{(1)}(x, y, t) = \sum_n^N \sum_m^M \left[\mathbf{H}^{(1)}(\omega_n, \theta_m) \right] \eta_{nm} \cos[k_n(x \cos(\theta_m) + y \sin(\theta_m)) - \omega_n t + \varepsilon_{mn} - \phi_{mn}], \quad i \in \{1, 2, \dots, 6\} \quad (15)$$

$$\phi_{mn} = \tan^{-1} \left(\frac{\text{Im}(\mathbf{H}^{(1)}(\omega_n, \theta_m))}{\text{Re}(\mathbf{H}^{(1)}(\omega_n, \theta_m))} \right)$$

The natural frequencies of the low order modes of the bridge are well below the energy content in the wave spectra such that these modes will not be excited by first order excitation forces. The difference frequency forces can however cause wave excitations in this frequency range. For short crested waves, the difference frequency forces can be written as [52-53],

$$\mathbf{F}_{WA}^{(2-)} = \text{Re} \sum_{l=1}^N \sum_{h=1}^N \sum_{j=1}^N \sum_{k=1}^N \eta_{jl} \eta_{kh} \mathbf{H}^{(2-)}(\omega_j, \omega_k, \theta_l, \theta_h) e^{i(\omega_k - \omega_j)t} e^{i(\varepsilon_{lh} - \varepsilon_{jl})} \quad (16)$$

Here, $\mathbf{H}^{(2-)}$ contains the in-phase and out-of-phase components of the full quadratic transfer function, \mathbf{H}^{ic} and \mathbf{H}^{is} , and represents the forces induced by the interaction of a unit amplitude wave associated with frequency ω_j and direction θ_l and a unit amplitude wave associated with frequency ω_k and direction θ_h . If the direction interaction effects are ignored, i.e., the terms where $\theta_l \neq \theta_h$, the computational effort significantly since far less quadratic transfer functions needs to be obtained. The mean drift force is included in equation above and can be found by putting $\omega_k = \omega_j$: Moreover, if Newman's approximation implying neglecting term outside the diagonal in $\mathbf{H}^{(2-)}$, further reduction in computational efforts are achieved, at the expense of reduced accuracy.

Modelling of the motion induced aerodynamic forces is one of the major challenges in the time domain simulations of the dynamic response since they are dependent on the motion history. One possibility is to use so

called quasi-steady theory where the self-excited forces are modelled using coefficients from static wind tunnel tests. The coefficients in the quasi-steady model are frequency independent, making the model convenient to implement in the time domain. It can however be challenging to model the self-excited forces accurately using quasi-steady theory, which has resulted in a number of suggestions for improvements [54]. The fluid memory effect can be taken into account by transfer functions in the frequency domain, or by convolution integrals in the time domain. The self-excited forces for bridge decks are commonly modelled in frequency domain using flutter derivatives as proposed by Scanlan and coworkers [45-46]. – analogous to hydrodynamic radiation. In time domain simulations of self-excited forces for bridge applications, it is common to start with an empirical expression for the transfer function in the frequency domain or the indicial functions in time domain. The challenge is to fit the various models to the experimental data of the aerodynamic derivatives. Chen et al. [55]. replaced the convolution integrals with a state-space model, to make the numerical simulation more efficient. They conducted flutter and buffeting analysis of a bridge in time domain, but in terms of generalized coordinates. Øiseth, Xu et al. [32, 50] also used a state-space model and introduced the state variables as additional degrees of freedom in each node of a beam element to simulate the fluid memory effect.

8. COMPUTATIONAL STRATEGY FOR LOAD EFFECT ANALYSIS

8.1 General

As mentioned above the wave and wind processes are assumed to be stationary in 3 hours and 10 min periods respectively. Since there is an interaction between the response due to waves and wind, an integrated analysis of wind and wave load effects is in principle desirable, considering simultaneously the two loads in the time domain. However, to do a dynamic analysis involving both waves and wind, would be cumbersome in the time domain analysis with say eighteen 10 min periods in each 3 hours period. A practical approach would be to use a 60 min period for both, with appropriate adjustment of the long-term data to refer to such a characteristic duration. Account of the long-term variability of wave and wind conditions represented by the probability density function of the parameters describing the wave and wind conditions should then refer to 1 hour data samples. To reduce the statistical uncertainty several (e.g. 5-6) samples should be made for each condition.

In the design of floating bridges many load conditions need to be considered to account for the variation in the combined wave, current and wind conditions. Hence, the reference is a so-called long-term analysis, in which the response from all short term conditions which are assumed to be stationary, are combined based on the probability of occurrence of the various short term met-ocean conditions, e.g. [35, 56].

Analyses also need to be carried out for conceptual or detailed design requiring different degree of refinement. A variety of methods – refined and simplified – is hence desirable for dealing with the aerodynamics, hydrodynamics, structural and possible soil mechanics. In general highly efficient methods are required to accomplish analysis in the early design stages when alternative designs need to be assessed. Hence, simplified mechanics models need to be pursued.

The action effects needed for ULS design check is characteristic values corresponding to an annual exceedance probability of 10^{-2} by recognizing the variability of environmental conditions in the long-term period and the short-term periods.

8.2 Short-term analysis

In principle the stochastic dynamic response under wave and wind-induced loads can be determined in the frequency or time domain [34, 35, 42]. Frequency domain approaches are particularly attractive for linear systems or systems that can be linearized with a reasonable accuracy. Moreover, frequency domain methods are very attractive when the mass or damping are frequency dependent. Time domain approaches imply a cumbersome integro-differential equation, as mentioned above, when dealing with frequency properties. On the other hand, linearization of nonlinear features can yield significant uncertainties for extreme values since linearization often is made *sua* to represent the standard deviation in the response.

Xu et al. [32] compared a frequency and time domain approach for a suspension bridge with floating pylons, by first checking that the linear part of the time domain agreed with the frequency domain method. They found that the nonlinearities associated with the geometric stiffness were small while the nonlinear feature of the buffeting wind load had 10 % effect on the girder response.

The basic integrated dynamic analysis is a short term analysis considering the stochastic nature of waves and turbulence of wind. Since some natural frequencies may be as small as 0.01 Hz a long sample may be needed in a time domain analysis to capture the load effects (motions) due to wind and low frequency hydrodynamic loads. On the other hand the time step needs to be small to capture all phenomena – including high frequency features associated with e.g. a mechanical or hydraulic drivetrain.

In the simulation of the load effects in short-term conditions it is important that the sampling time is sufficiently long to limit the statistical uncertainty, especially when determining extreme values. Moreover, when estimating extreme values efforts to use realistic methods to fit the sample and then extrapolate to extreme values. Alternative methods, such as Weibull tail, global maxima and a recently proposed extrapolation method (ACER) based on the mean upcrossing rates, can be used for obtaining the extreme values, see e.g. [35].

In the short-term period the maximum response can be expressed by

$$X_{\max} = x_{\text{mean}} + k \cdot \sigma_x \quad (17)$$

where x_{mean} and σ_x are the mean and standard deviation, respectively, and k is a constant depending on the number of individual maxima in the short term period and the relevant fractile value to be used.

8.3 Long-term analysis

A full long-term analysis (FLTA) is the most accurate approach to determine the effects due to environmental loads, both in terms of extreme load effects for ULS design check and load effect histories (i.e. stress ranges) for FLS design check. Since the full long-term analysis is time consuming simplified methods such as the environmental contour method (ECM) [33, 35, 56-58] and simplified full long-term analysis (SLTA) [59, 33] have been proposed. SLTA is the same as FLTA except that it only include the important environmental conditions and ignore the others that do not contribute much to the long-term results Xu [33] found that the SLTA can predict the long-term extreme load effect as accurately as the FLA with about 10% of the effort.

The ECM is in a way a special SLTA method based on identification of the (single) environmental condition that contribute most to the long-term extreme value. This method has been extensively been used for offshore structures subjected to wave loads and wind turbines subjected to wind and wave loads [35, 56]. These methods are approximate and need to be validated by FLTA, as e.g. illustrated for suspension wind loads on bridges and wave and wind loads on a floating suspension bridge by Xu et al. [33]. Since contour methods use only a single short-term condition to predict the long-term extreme, the short-term extreme value used would normally be a fractile value, larger than the expected maximum in Eq. (17).

Cyclic load histories for fatigue (and possibly wear) design checks normally need to be based on a long term analysis.

The ULS design check is based on checking the nominal stress as compared with the strength, considering yielding and possible buckling effects, in representative locations as illustrated for the bridge girder in Fig. 8. The normal axial stress and shear stress due to axial force and bending moments; and shear forces and torsional moment, respectively, based on beam theory, are considered.

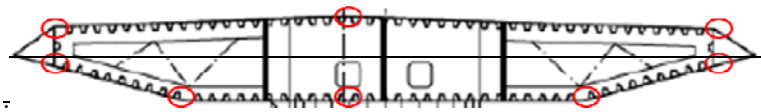


Fig. 8. Typical bridge steel girder cross-section

The focus in this paper is on the global dynamic analysis and not the detailed design check. Given the axial force and bending moments in a cross section the axial stress is determined by beam theory. The shear stress stem from shear forces and St. Venant torsion of the cross section. It is noted that instantaneous extreme values should be considered. Since the maximum cross-sectional resultant forces and moments do not necessarily occur at the same time simplified approaches using combination factors on the different extreme values.

9. CASE STUDIES

9.1 General

In this section a brief account of the comprehensive case studies made of an early floating bridge concept for crossing of the Bjørnafjord [25, 26, 44]. It is anchored at both ends and has a bridge girder curved in the horizontal plane, with a radius of 5000 m and with a total length of approximately 4600 m. Moreover, the bridge girder is a vierendeel beam, consisting of two parallel steel boxes connected by cross-beams. this bridge

concept includes a high bridge part and a floating bridge part. the high bridge is cable-stayed located in the South and is designed for ship navigation. it has a main span of 490 m and a back span of 370 m. a total of 80 cables are used to carry the girder. the floating bridge part is supported by 19 pontoons with a span of 197 m. It can also be divided into a high part and a low part, where the high part is used to smoothly connect the main span. the pontoons are 28 by 68 m and 14.5 high with a draft of 10.5 m. Further details are given in [25].

The first 5 modes with natural periods are 56.7, 31.7 and down to 14.3 s are horizontal modes with some contribution from torsion. The natural periods for the primarily torsional modes are 11.9 and 11.5 s, respectively. Then are 20 vertical modes, some with contribution from torsion, with natural period in the range of 11.5 – 7.5 s, governed by the heave of the pontoons. Modes 17 and 18 have natural periods of 10.6 and 10.5 s, respectively. There are many modes, essentially torsional with natural period in the range of 7 to 3.5 s.

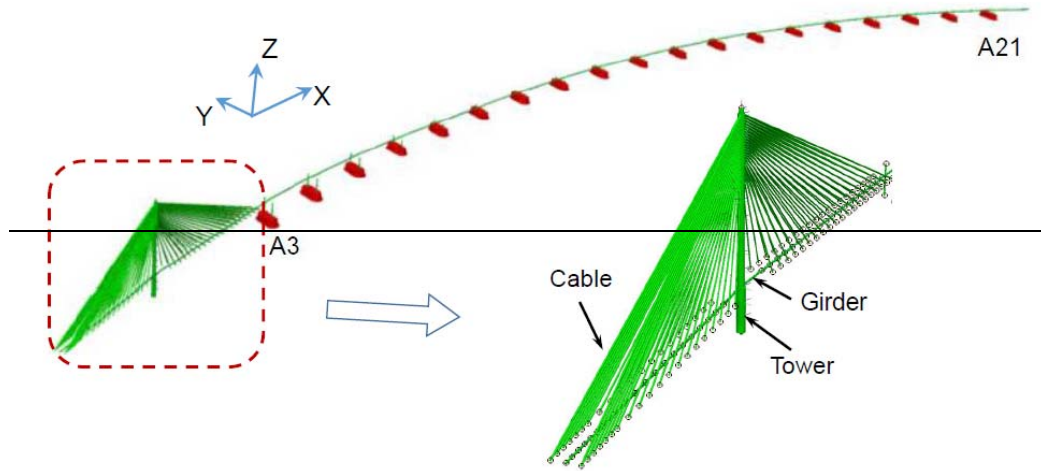


Fig. 9 Curved end-anchored floating bridge concept for the Bjørnafjord

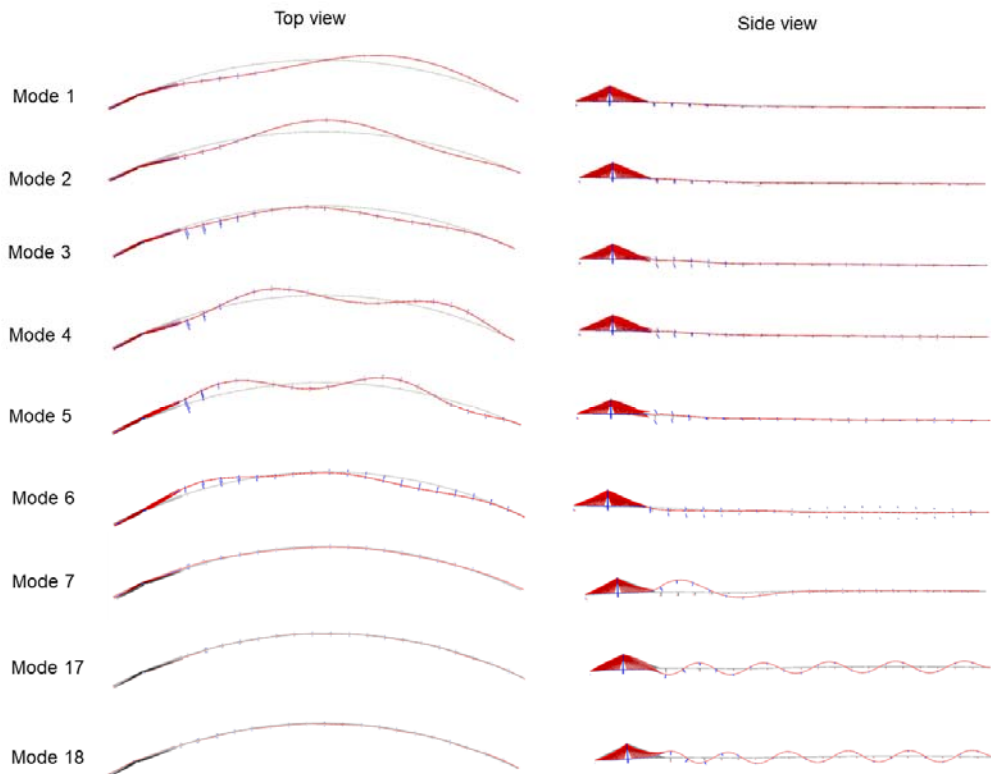


Fig. 10 Normal modes of the bridge.

9.2 Wave-induced response

The standard deviation of the strong axis bending moment, M_z , along the bridge girder is demonstrated in Fig. 11. It is seen that short-crested waves yield larger dynamic response than the long-crested waves for the present direction. By a closer look at the response spectra it is found that the long-crested waves mainly excite the second resonant mode, whereas the short-crested wave excite both the second and third resonant modes.

The static weak axis bending moment in the low bridge due to gravity loads, varies between $+4 \cdot 10^5$ and $-8 \cdot 10^5$ kNm, in the field and at the pontoon support corresponding a continuous beam. The weak axis bending moment M_y is mainly induced by the heave motion of the pontoons, and hence the girder. The standard deviation of the wave induced moment along the girder follows a similar trend as that of heave motion. The M_y is not affected by the second order wave loads, but is strongly influenced by the short-crested waves. For girder nodes between A3 and A14, the M_y of short-crested waves is almost twice of that of long-crested waves. Power spectral analysis also reveals that it is also due to the excited resonant eigen-modes with a period of about 7.8 s.

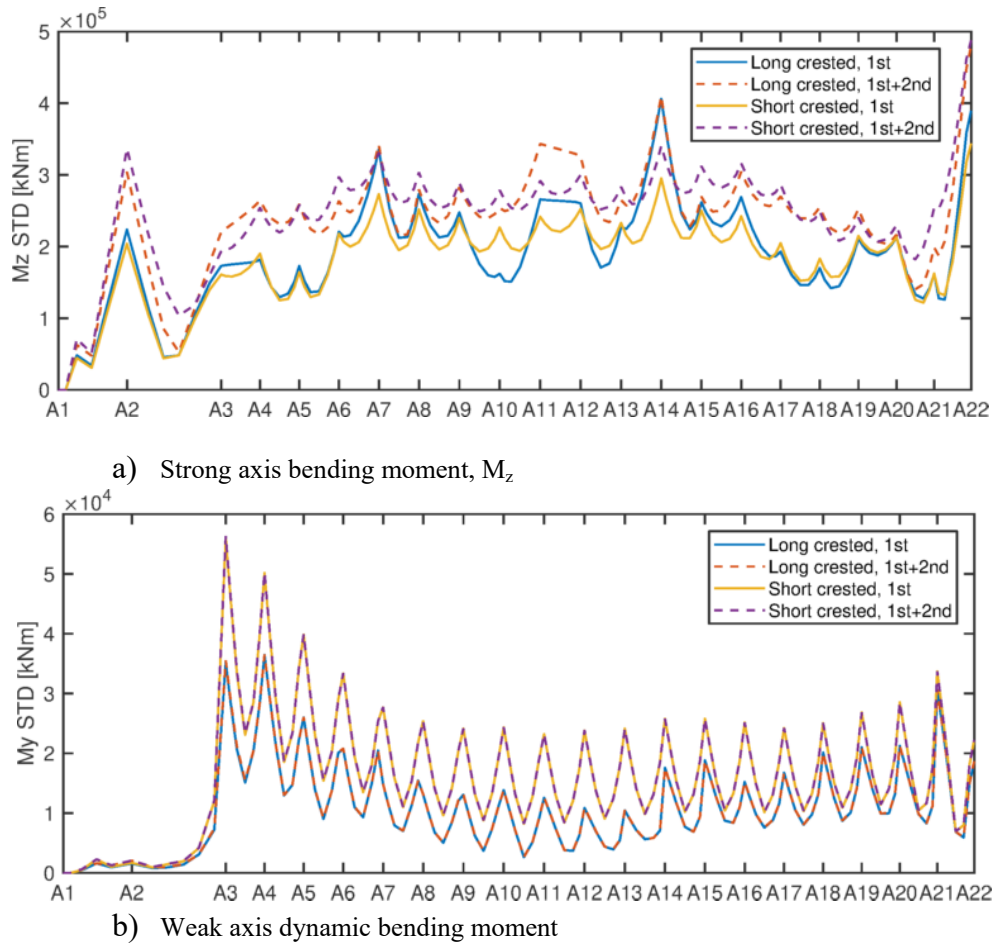


Fig. 11 Standard deviation of the dynamic response under wave loading with a sea state with $H_s = 2.4$ and $T_p = 5.9$ and principal wave direction, $\theta_p = 270$ degrees. Short-crestedness parameter : $n=4$.

9.3 Response in non-homogeneous wave loads

The effect of inhomogeneous waves are investigated by specifying the significant wave height H_s , peak period T_p , principle wave direction θ_p and random seed number for the phase angle to generate the time series of wave elevations at each pontoon. Homogeneous wave conditions are generated by make these parameters identical for each pontoon. The wave conditions considered are specified in Table 1. The effect on the strong axis bending moment is limited, but Fig.11b shows that the weak axis bending moment is significantly influence by the inhomogeneity, especially for the girder between A3 and A10. Examination of the response spectra shows that this is because inhomogeneous wave cases LC2.3 and LC2.4 excite several strong resonant responses with frequency ranging from 0.76 rad/s to 1.12 rad/s.

Table 1. Homogeneous versus inhomogeneous 100 years wave conditions. Pontoons A1 – A21 are numbered from South to North.

Case	Definition of wave conditions
LC2.1 Hom.	$H_s = 2.4$ m, $T_p = 5.9$ s, $\theta_p = 288^\circ$, and identical random phase angles of each wave components
LC2.2 Inhom.	$H_s = 2.4$ m, $T_p = 5.9$ s, $\theta_p = 288^\circ$, and different random phase angles of each wave components
LC2.3 Inhom.	Wave parameters: A3-A6: $H_s=1.6$ m, $\theta_p=315^\circ$; A7-A12: $H_s=2.0$ m, $\theta_p=300^\circ$; A13-A18: $H_s=2.4$ m, $\theta_p=285^\circ$; A19-A21: $H_s=2.0$ m, $\theta_p=270^\circ$. Identical random phase angles..
LC2.4 Inhom.	Wave parameters: A3-A6: $H_s=1.6$ m, $\theta_p=315^\circ$; A7-A12: $H_s=2.0$ m, $\theta_p=300^\circ$; A13-A18: $H_s=2.4$ m, $\theta_p=285^\circ$; A19-A21: $H_s=2.0$ m, $\theta_p=270^\circ$. Different random phase angles..

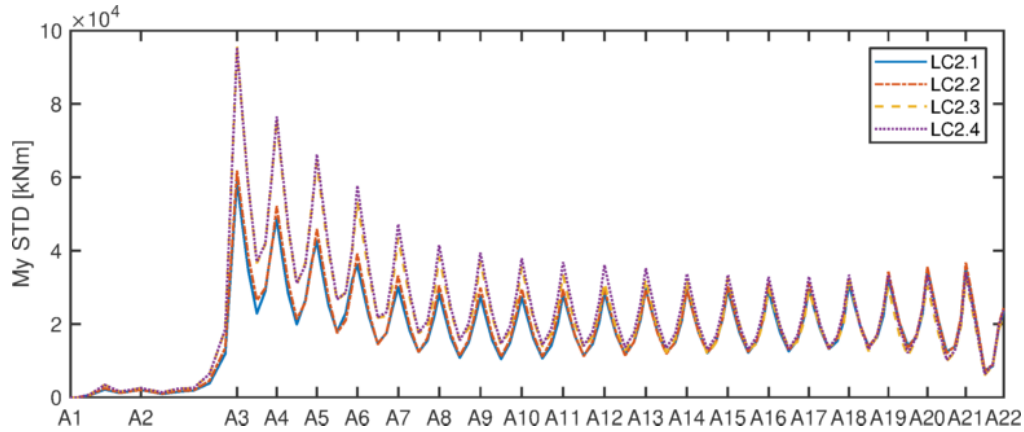


Fig. 12 The standard deviations of the moment about bridge girder weak axis M_y along the bridge girder under 100-year wave condition.

9.4 Response under combined wind, wave and current loads

The effect of combined wave, wind and current was investigated by Cheng et al. [26]. An example of results for dynamic response in terms of the standard deviation are shown in Figures 13 and 14. The plots display the standard deviation in each section and does not necessarily say anything about the simultaneous occurrence of the response. It is seen that the horizontal displacement (not shown), axial force and strong axis bending moment are mainly induced by wind loads while wave excitation dominate the vertical response (heave -not shown, weak axis bending moment) and torsion (not shown). It is noted that the turbulent wind can cause significantly larger low-frequency responses than second order wave excitation. A closer look at the results show that the current and a mean wind reduces the dynamic response due to their damping effects especially on the horizontal motion, axial force and strong axis bending.

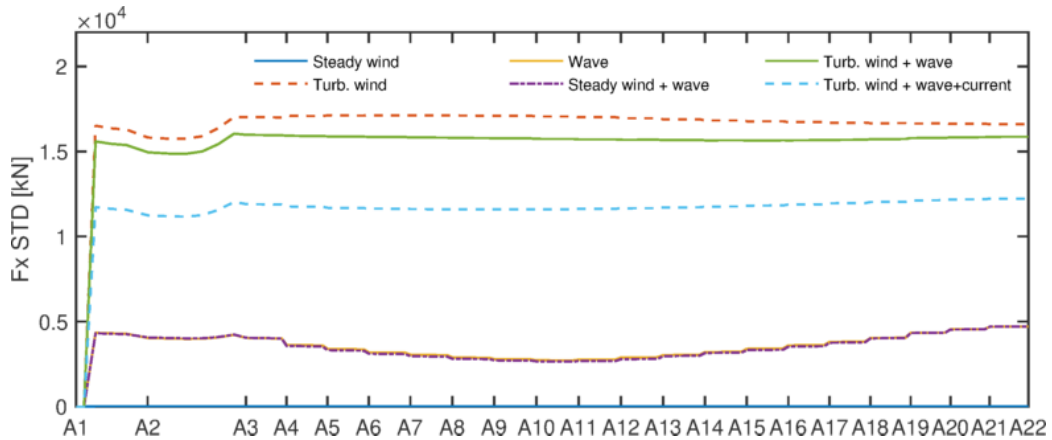


Fig. 13 Axial force in the bridge girder under wave and wind conditions. When waves are included: $H_s = 2.4$ m and $T_p = 5.9$ s. Principal wave direction = 270° . Short-crestedness parameter: $n=4$. When wind is included: $\bar{U}_w = 31$ m/s. $TI = 14\%$.

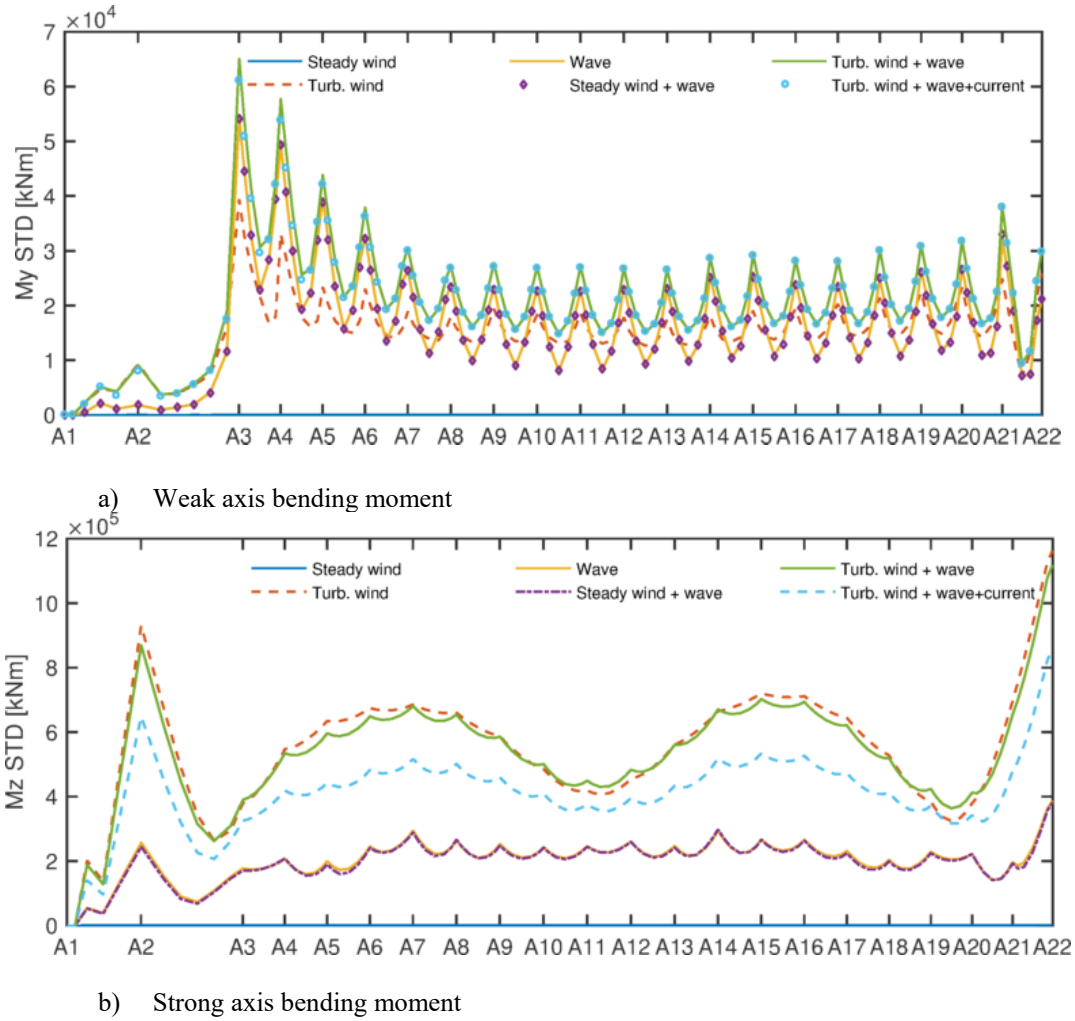


Fig. 14 Bending moments in the bridge girder under wave and wind conditions. When waves are included: $H_s = 2.4$ m and $T_p = 5.9$ s. Principal wave direction = 270° . Short-crestedness parameter: $n = 4$. When wind is included: $\bar{U}_w = 31$ m/s. $TI = 14\%$.

10. CONCLUSIONS

To improve the efficiency of transport systems across straits floating bridges are attractive to replace ferries. Designing a reliable and cost-effective floating bridge for a wide and deep fjord is very challenging because of the complex environmental conditions and the dynamic character of such bridges. First a brief overview of relevant floating bridge concepts as well as relevant serviceability and safety criteria are given, followed by an outline of the modelling of wind-, wave-, and current-induced loads and their effects and the challenges associated with such analyses. A case study of the response in a possible 4600 m long curved bridge for the crossing of the Bjørnafjord, are presented to illustrate the features of such bridges. The considered floating bridge consists of a cable-stayed high bridge part and a pontoon-supported low bridge part. It also has a number of eigen-modes, which might be excited by the environmental loads. The sway motion, axial force and strong axis bending moment of the bridge girder are mainly induced by lift, drag and moment wind loads, while the heave motion, weak axis bending moment and torsional moment are mainly induced by wave loads. The vertical response is significantly influenced by short-crestedness and inhomogeneity in the wave conditions. Current loads mainly reduce the dynamic response of the sway motion, axial force and strong axis bending moment due to the damping effect of the drag forces.

Further work remains regarding collection of environmental data and modelling of the complex environmental conditions in coastal areas, developing simplified ULS design checks considering the variation in time and space of the combined wind-, wave- and current load effects and the inherent uncertainty. A particular challenge is to clarify the possible effect of structural instability (the global second order effect or buckling) of possible slender curved bridges. An uncertainty assessment should be carried out and serve as a reassessment of the inherent safety; i.e. the partial safety factors used in the design of such structures.

ACKNOWLEDGEMENT

I would especially like to acknowledge the cooperation with professors Shixiao Fu, Zhen Gao and Ole Øiseth, dr. Zhengshun Cheng and Mr. Yuwang Xu and the support from the Norwegian Public Road Administration.

REFERENCES

- [1] Wang, C., and Wang, B., (2015). *Large Floating Structures: Technological Advances*. Springer Science+ Business Media Singapore.
- [2] Skorpa, L., Jakobsen, B. and Østlid, H. (2017). Prof. Torgeir Moan and the Record-breaking Fjord Crossings in Norway. Paper OMAE 2917-62659. In *Proc.36th International Conference on Ocean, Offshore and Arctic Engineering, OMAE2017* June 25-30, 2017, ASME. Trondheim, Norway.
- [3] Eidem, M. E., (2017). “Overview of floating bridge projects in Norway”. Paper OMAE2017-62714 In *Proc.36th International Conference on Ocean, Offshore and Arctic Engineering, OMAE2017* June 25-30, 2017, ASME. Trondheim, Norway.
- [4] https://en.wikipedia.org/wiki/Submerged_floating_tunnel
- [5] Isaksen, B. et al. (2013). A 3700 m single span suspension bridge. *Strait Crossing Conf.*, June 13.-19. 2013, Bergen. Proc. published by the Norwegian Public Road Administration.
- [6] TRAM (Technical Research Association of Mega-Float). (2002). Summary of Practical Research on Mega-Float Airport in 2002 (in Japanese).
- [7] Suzuki, H. (2005). Overview of Megafloat: Concept, design criteria, analysis and design. *Marine Structures*, Vol. 18, pp. 111–132.
- [8] Mobile Offshore Base Science and Technology Program (2000). Final Report, Technical Report TR-2125-OCN, Naval Facilities Engineering and Expeditionary Warfare Center, Port Hueneme CA, December 2000.
- [9] Remmers, G., Taylor, R., Palo, P., & Brackett, R. (1999). Mobile offshore base: A Seabasing option. In *Proc. of the 3rd International Workshop on Very Large Floating Structures (VLFS '99)*, Honolulu, Hawaii, September 22–24, 1999.
- [10] Washington State Department of Transportation: Design Criteria for the Hood Canal Floating Bridge (for the reconstructed bridge of 1982) , September 15 1980. Seattle
- [11] Norwegian Public Road Administration. (2017). N400. Handbook for design of bridges, ferry quays and other load carrying structures (in Norwegian).
- [12] Norwegian Public Road Administration (2017). Design Basis Bjørnafjorden Side- and end anchored floating bridges.
- [13] Norwegian Standard (2016). NS-EN 1990:2002+A1:2005+NA:2016 Basis of Design (Norwegian version of EN 1990).
- [14] Newman, J. N., (1977). *Marine Hydrodynamics*. Cambridge: The MIT press.
- [15] Faltinsen, O.M. (1993). *Sea loads on ships and offshore structures*. Cambridge: Cambridge University Press.
- [16] Langen, I., and Sigbjørnsson, R., (1980). “On stochastic dynamics of floating bridges”. *Engineering structures*, Vol. 2(4), pp. 209–216.
- [17] Hartz, B. (1981). “Dynamic response of the hood-canal floating bridge”. In *Second ASCE/EMD Specialty conference on dynamic response of structures*, Atlanta, GA, USA.
- [18] Løken, A. E., Oftedal, R. A., and Aarsnes, J. V. (1990). “Aspects of hydrodynamic loading and responses

in design of floating bridges”. In *Second Symposium on Strait Crossings, Trondheim*, Norway. Proc. published by the Norwegian Public Road Administration.

[19] Seif, M. S., and Inoue, Y., (1998). “Dynamic analysis of floating bridges”. *Marine Structures*, Vol. 11(1), pp. 29 – 46.

[20] Fu, S., Cui, W., Chen, X., and Wang, C. (2005). “Hydroelastic analysis of a nonlinearly connected floating bridge subjected to moving loads”. *Marine Structures*, Vol. 18(1), pp. 85–107.

[21] Kvåle, K. A., Sigbjørnsson, R., and Øiseth, O., (2016). “Modelling the stochastic dynamic behavior of a pontoon bridge: a case study”. *Computers & Structures*, Vol. 165, pp. 123–135.

[22] Lie, H., Fu, S., Fylling, I., Fredriksen, A. G., Bonnemaire, B., and Kjersem, G. L., (2016). “Numerical modelling of floating and submerged bridges subjected to wave, current and wind”. In *Proc. 35th International Conference on Ocean, Offshore and Arctic Engineering, American Society of Mechanical Engineers. OMAE2016*. June 19 – 24, 2016, ASME. Pusan, Korea.

[23] Fu, S., Wei, W., Ou, S., Moan, T., Deng, S., and Lie, H., (2017). “A time-domain method for hydroelastic analysis of floating bridges in inhomogeneous waves”. In *Proc. 36th International Conference on Ocean, Offshore and Arctic Engineering, OMAE2017* June 25-30, 2017, ASME. Trondheim, Norway.

[24] Fredriksen, A.G. et al. (2017) Hydrodynamical Aspects Of Pontoon Optimization for a Side-Anchored Floating Bridge. Paper OMAE2017-62698. *Proc. 36th International Conference on Ocean, Offshore and Arctic Engineering OMAE2017* June 25-30, 2017, ASME. Trondheim, Norway.

[25] Cheng, Z., Gao, Z., and Moan, T. (2017). “Hydrodynamic load modeling and analysis of a floating bridge in homogeneous wave conditions”. *Marine Structures*, Vol. 59, pp 122-141.

[26] Cheng, Z., Gao, Z., and Moan, T., (2017). “Wave load effect analysis of a floating bridge in a fjord considering inhomogeneous wave conditions”. Submitted for possible publication.

[27] Sha, Y., Amdahl, J., Aalberg, A. & Yu, Z. (2018). Numerical investigations of the dynamic response of a floating bridge under environmental loadings. *Ships and Offshore Structures*, DOI: 0.1080/17445302.2018.1426818.

[28] Sun, J., Jiang, P., Sun, Y., Song, C., and Wang, D. (2017). “An experimental investigation on the nonlinear hydroelastic response of a pontoon-type floating bridge under regular wave action”. *Ships and Offshore Structures*, pp. 1–11.

[29] Volkert, O., Bruer, A. and Veie, J. (2013). “How to cross the 7500m wide Boknafjord.” *Strait Crossings. Conf.*, Bergen. Proc. published by the Norwegian Public Road Administration.

[30] Veie, J., and S.H. Holtberget. (2015). “Three span floating suspension bridge crossing the Bjørnafjord.” *Conf. on Multi-Span Large Bridges*. pp. 373-380.

[31] Fredriksen AG, Bonnemaire B, Lie H, Munkeby J, Nesteby A, Buckholm P, et al. (2016). Comparison of Global Response of a 3-Span Floating Suspension Bridge with Different Floater Concepts. In *Proc. 35th International Conference on Ocean, Offshore and Arctic Engineering: American Society of Mechanical Engineers*; V007T06A66-VT06A66.

[32] Xu, Y., Øiseth, O., and Moan, T. (2018). Time domain simulations of wind- and wave-induced load effects on a three-span suspension bridge with two floating pylons. *Marine Structures*. Vol. 58, March 2018, pp. 434-452.

[33] Xu, Y., Øiseth, O., Moan, T. and Næss, A. (2017). Prediction of long-term extreme load effects due to wave and wind for cable supported bridge with floating pylons. Submitted for publication.

[34] Clough, R.W. and Penzien, J. (1975). *Dynamics of Structures*, McGrawHill, New York.

-
- [35] Næss, A. and Moan, T. (2012). *Stochastic Dynamic Analysis of Marine Structures*, Cambridge University Press.
- [36] DNV GL, (2014). Environmental conditions and environmental loads (DNV-RP-C205). Det norske Veritas as, Oslo, Norway.
- [37] <https://csdms.colorado.edu/wiki/Model:STWAVE>
- [38] <https://www.tudelft.nl/en/ceg/about-faculty/departments/hydraulic-engineering/sections/environmental-fluid-mechanics/research/swan/>
- [39] Norwegian Public Road Administration (2016): Bjørnafjorden Hydrodynamics Workshop. June 27-28 2016
- [40] Lothe, A., and Musch, O., (2015). Bjørnafjorden submerged floating tube bridge: sea state simulations. Tech. report, Norconsult AS. Trondheim.
- [41] Cheng, Z., Gao, Z., and Moan, T., (2017). Field Measurements of Inhomogeneous Wave Conditions in Bjørnafjorden. Submitted to the *ASCE Journal of Waterway, Port, Coastal, and Ocean Engineering*
- [42] Strømmen, E., (2010). Theory of bridge aerodynamics. Springer Science & Business Media.
- [43] Cummins, W. E., (1962). The impulse response function and ship motions. Institut für Schiffbau, Universität Hamburg, Hamburg.
- [44] Cheng, Z., Gao, Z., and Moan, T., (2018). “Numerical modelling and dynamic analysis of a floating bridge subjected to wind, wave and current loads”. Submitted for possible publication.
- [45] Scanlan RH, Tomko J. (1971). Air foil and bridge deck flutter derivatives. *Journal of Soil Mechanics & Foundations Div.*
- [46] Scanlan R, Budlong K, Béliveau J. (1974) Indicial aerodynamic functions for bridge decks. *Journal of Sanitary Engineering Division* . Vol.100.
- [47] Xu, Y., Øiseth, O., Næss, A. and Moan, T. (2017) Prediction of long-term extreme load effects due to wind for cable supported bridges using time domain simulations. *Engineering Structures*. Vol. 148, pp. 239-253.
- [48] Kashiwagi M. Transient responses of a VLFS during landing and take-off of an airplane (2004). *Journal of Marine Science and Technology*, Vol. 9, pp. 14-23.
- [49] Taghipour R., Perez T., Moan T. (2008). Hybrid frequency–time domain models for dynamic response analysis of marine structures. *Ocean Engineering*; Vol.35, pp. 685-705.
- [50] Øiseth O., Rönquist A., Sigbjörnsson R. (2010). Simplified prediction of wind-induced response and stability limit of slender long-span suspension bridges, based on modified quasi-steady theory: a case study. *Journal of wind engineering and industrial aerodynamics*, Vol. 98, pp. 730 - 41.
- [51] Luan, C., Gao, Z. and Moan, T. (2017). Development and verification of a time-domain approach for determining forces and moments in structural components of floaters with an application to floating wind turbines. *Marine Structures*. Vol. 51, pp. 87-109.
- [52] Pinkster J. (1988). The influence of directional spreading of waves on mooring forces. OTC-paper No. 5629. *Offshore Technology Conference: Offshore Technology Conference*; Houston.
- [53] Marthinsen T, Winterstein SR.(1992). Second-order load and response statistics for tension-leg platforms. Report RMS-9, Reliability Marine Struc Program, Dept. Civil Engineering, Stanford University.
- [54] Diana G, Rocchi D, Argentini T, Muggiasca S. (2010). Aerodynamic instability of a bridge deck section model: Linear and nonlinear approach to force modeling. *Journal of Wind Engineering and Industrial Aerodynamics* ;Vol. 98:pp. 363-74.

- [55] Chen X, Matsumoto M, Kareem A. (2000). Time Domain Flutter and Buffeting Response Analysis of Bridges. *Journal of Engineering Mechanics* , Vol. 126, pp. 7-16.
- [56] Norwegian Standard. (2017). Norsok N-003 Action and action effects. Standard Norway.Oslo.
- [57] Haver, S., and Winterstein, S. (2009) “Environmental contour lines: A method for estimating long term extremes by a short term analysis”, *Transactions, Society of Naval Architects and Marine Engineers*, Vol. 116, pp. 116–127.
- [58] Winterstein, S., Ude, T., Cornell, C., Bjerager, P., and Haver, S., (1993). Environmental parameters for extreme response: Inverse form with omission factors, In *Proc. of 6th International Conference on Structural Safety and Reliability*, Innsbruck, 1993.
- [59] Videiro, P. M., and Moan, T. (1999). Efficient evaluation of long-term distributions. In *Proc.of the 18th International Conference on Offshore Mechanics and Arctic Engineering*, ASME. .
- [60] Giske, F.-I. Grøtta; Leira, B. J.; Øiseth, O. (2017). Full long-term extreme response analysis of marine structures using inverse FORM. *Probabilistic Engineering Mechanics*;Vol. 50, pp. 1-8.

A PERFORMANCE-BASED SEISMIC DESIGN METHOD FOR RC/MRFs USING MODAL STRENGTH REDUCTION FACTORS

Edmond V. Muho¹, George A. Papagiannopoulos² Dimitri E. Beskos¹

¹State Key Laboratory of Disaster Reduction in Civil Engineering
Tongji University,
Shanghai, CN-200092, China

e-mail: edmondmuho@gmail.com; dimisof@hotmail.com

²Department of Civil Engineering
University of Patras
Patras, GR-26504 Greece e-
mail: gpapagia@upatras.gr

Keywords: Seismic Design, Reinforced Concrete Structures, Force Based Design, Performance Based Design, Modal Strength Reduction Factors, Equivalent Modal Damping Ratios.

Abstract. *A performance-based seismic design method for plane reinforced concrete (R/C) moment-resisting frames (MRF) is proposed. The method is a force-based seismic design one, utilizing not a single strength reduction factor as all modern codes do, but different such factors for each of the first significant modes of the frame. These modal strength reduction factors incorporate dynamic characteristics of the structure, different performance targets and different soil types. Thus, the proposed method can automatically satisfy deformation demands at all performance levels without requiring deformation checks at the end of the design process, as it is the case with code-based design methods. Empirical expressions for those modal strength reduction factors as functions of period, deformation/damage and soil types, which can be used directly in conjunction with the conventional elastic pseudo-acceleration design spectra with 5% damping for seismic design of R/C MRFs, are provided. These expressions have been obtained through extensive parametric studies involving nonlinear dynamic analyses of 38 frames under 100 seismic motions. The method is illustrated by numerical examples which demonstrate its advantages over code-based seismic design methods.*

1 INTRODUCTION

Modern seismic codes like Eurocode 8 [1] employ linear elastic response spectrum analysis in conjunction with the strength reduction (R) or behavior factor (q), which takes into account in a very approximate manner (just constant values depending on structural type) the inelastic behavior of the structure. The deformation check is done at the end of the design process and usually leads to heavier structural sections than those originally selected for satisfaction of strength requirements. This approach of seismic design is known as the force-based design (FBD) because seismic forces are the main parameters.

During the last 20 years or so, a new seismic design philosophy emerged, the performance-based design (PBD), which considers three or four design levels, each one corresponding to a specific seismic intensity and specific performance requirements in terms of deformation and/or damage [2-6].

Two main weaknesses are found in the behavior factor value provided in all modern codes: The first is that it is not fully linked to the dynamic characteristics of the structure. The second one is that it cannot control deformation as required in the performance based design.

In this paper, a performance-based seismic method for reinforced concrete (R/C) moment resisting frames working in the framework of the familiar FBD method is proposed. The main idea is to construct modal strength reduction factors for the first few modes and four performance levels (Immediate Occupancy, Damage Control, Life Safety and Collapse Prevention), which depend on the dynamic characteristics of the structure, the deformation, the damage and the soil type.

2 EQUIVALENT MODAL DAMPING RATIOS AND STRENGTH REDUCTION FACTORS

The transfer function $R(\omega)$, for a viscously damped linear elastic multi - degree - of - freedom building is defined in the frequency domain as the ratio of the roof absolute acceleration $\ddot{U}_r(\omega)$ of the building over the acceleration $\ddot{u}_g(\omega)$ at its base, i.e.,

$$R(\omega) = \frac{\ddot{U}_r(\omega)}{\ddot{u}_g(\omega)} \quad (1)$$

where $\ddot{U}_r(\omega) = \ddot{u}_g(\omega) + \ddot{u}_r(\omega)$, $\ddot{u}_g(\omega)$ and $\ddot{u}_r(\omega)$ are the earthquake motion and roof relative motion, respectively, in the frequency domain, ω is the frequency and overbars denote Fourier transformation. It can be proved [6] that

$$|R_r(\omega = \omega_k)|^2 = 1 + 2 \sum_{j=1}^N \frac{\varphi_{rj} \Gamma_j \omega_k^2 (\omega_j^2 - \omega_k^2)}{(\omega_j^2 - \omega_k^2)^2 + (2\xi_j \omega_j \omega_k)^2} + \sum_{j=1}^N \frac{\varphi_{rj}^2 \Gamma_j^2 \omega_k^4 (\omega_j^2 - \omega_k^2)^2 + 4\xi_j^2 \omega_j^2 \omega_k^2}{[(\omega_j^2 - \omega_k^2)^2 + (2\xi_j \omega_j \omega_k)^2]^2} \quad (2)$$

$$+ 2 \sum_{j \neq m, m > j}^N \frac{\varphi_{rj} \Gamma_j \varphi_{rm} \Gamma_m \omega_k^4 [(\omega_j^2 - \omega_k^2)(\omega_m^2 - \omega_k^2) + 4\xi_j \xi_m \omega_j \omega_m \omega_k^2]}{[(\omega_j^2 - \omega_k^2)^2 + (2\xi_j \omega_j \omega_k)^2][(\omega_m^2 - \omega_k^2)^2 + (2\xi_m \omega_m \omega_k)^2]}$$

where φ_{rj} is the j th modal shape at the top floor r , and ξ_j and Γ_j are the damping ratio and corresponding participation factor at mode j . Furthermore, ω_j and ω_m are natural frequencies corresponding to the eigenvalues problem with $m > j$ and ω_k are resonant frequencies.

The above equation, on the assumption that φ_{rj} , ω_j , Γ_j and $R(\omega_k)$ are known, can be seen as a system of N (number of mode shapes considered) non - linear algebraic equations to be solved for the modal damping ratios ξ_k of the linear structure. The criterion of equivalence of energies is the shape of the $|R(\omega)|$ versus ω curve. When the distorted shape of the non-linear structure with many peaks curve becomes smooth with visible peaks for the first few modes as in Fig. 1.a, at that moment, this curve represents the equivalent linear structure for which Eq. (2) is applicable. However, when the structure is non - linear, that curve has a distorted shape as in Fig. 1.b with no visible peaks, especially for higher modes. More details can be found in [6].

By providing progressively Rayleigh type viscous damping to the structure, one succeeds in obtaining smoother and smoother $|R(\omega)|$ versus ω curves for that structure until for some value of damping the curve becomes completely smooth with clearly visible peaks (Fig. 1.a). At that value of damping the structure is just below its first yield point (first plastic hinge) and hence, the originally non - linear structure has become an equivalent linear for which Eq. (2) for determination of the equivalent damping ratios ξ_k is applicable.

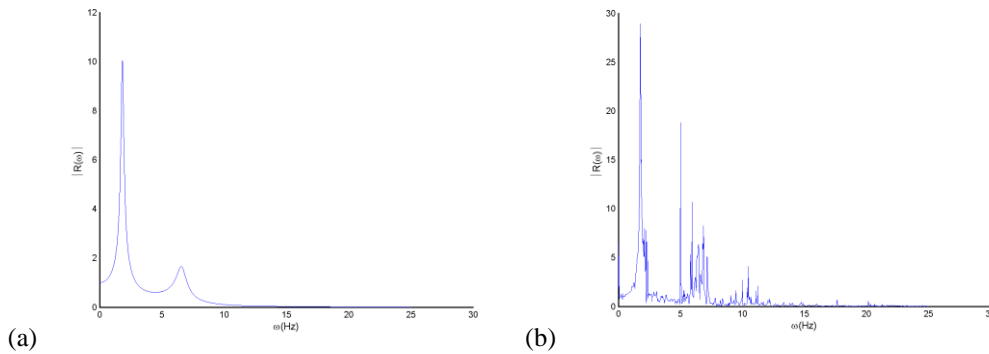


FIGURE 1: Transfer function of (a) a linear and (b) a non-linear structure structure with equivalent damping

Having found the equivalent modal damping ratios ξ_k , the seismic response of the equivalent linear structure can be determined in conjunction with the absolute acceleration response spectra due to the presence of high amounts of damping [6-8].

The modal contribution to the seismic design force is given as $M_k^* S_{a,k}(T_k, \xi_{eq,k})$, where M_k^* is the effective mass. The absolute modal strength reduction factor q_k for the k th mode can be expressed as the ratio of the modal elastic base shear $V_{el,k}$ over the corresponding modal base shear just below the first yield $V_{s,k}$

$$q_k = \frac{V_{el,k}}{V_{s,k}} = \frac{M_k^* S_{a,k}(T_{acc,k}, \xi_{5\%})}{M_k^* S_{a,k}(T_{acc,k}, \xi_{eq,k})} = \frac{S_{a,k}(T_{acc,k}, \xi_{5\%})}{S_{a,k}(T_{acc,k}, \xi_{eq,k})} \quad (3)$$

where ξ_k is the damping ratio, $S_{a,k}(T_k, 5\%)$ the absolute maximum acceleration of the structure with 5% damping, $S_{a,k}(T_{acc,k}, \xi_{eq,k})$ the absolute maximum acceleration of the structure with other than 5% damping and $T_{acc,k}$ is the damped period of the k-th mode computed as $T_{acc,k} = T_k / \sqrt{1 - \xi_k^2}$.

The transition from the absolute modal strength reduction factors q_k into the pseudo-strength reduction factors \bar{q}_k used for the purpose of design is accomplished here by the following procedure. In order to relate $T_{acc,k}$ with T_k at 5% damping and any other damping ratio ξ_{eq} , one defines $S_{a,k}(T_{acc,k}, \xi_{5\%}) = \kappa_1 S_{a,k}(T_k, \xi_{5\%})$ and $S_{a,k}(T_{acc,k}, \xi_{eq,k}) = \kappa_2 S_{a,k}(T_k, \xi_{eq,k})$. Moreover, according to Papagiannopoulos et al. [9], $S_{a,k}(T_k, \xi_{5\%}) = \lambda_1 PS_{a,k}(T_k, \xi_{5\%})$ and $S_{a,k}(T_k, \xi_{eq,k}) = \lambda_2 PS_{a,k}(T_k, \xi_{eq,k})$. Thus, Eq. (3) can be written as

$$\bar{q}_k = \frac{k_2 \lambda_2}{\kappa_1 \lambda_1} q_k \quad (4)$$

3 R/C FRAMES, SEISMIC MOTIONS AND PERFORMANCE LEVELS

3.1 R/C frames considered

A total number of 38 regular R/C MRFs 2 to 20 storeys was designed for this study. The frames are realistically designed and detailed in accordance to EC2 [10] and EC8 [1] for medium ductility class (DCM).

The material properties selected for the design of the R/C frames were C25/30 for concrete and S500 for reinforcing steel. Live loads (Q) were set equal to 2 kN/m^2 . Seismic loads (E) were calculated in accordance to EC8's response spectrum with ground acceleration equal to $a_g = 0.3g$ ($g = 9.81 \text{ m/sec}^2$), soil type B (medium dense sand or stiff clay) and strength reduction factor equal to $q=3.9$. The combinations of loads used for the design were $1.35G+1.5Q$ and $\pm E+G+0.3Q$.

All structural elements for design purposes were modeled with a reduced stiffness of 50% of the gross section ($EI_{eff} = 0.5EI_g$) to account for the cracking effect on concrete members according to EC8 [1]. Beams were designed as T-beams with an effective width equal to $b_{eff} = 1.2 \text{ m}$, the same for all of them. The philosophy of Strong Column - Weak Beam (capacity design) has been followed. All columns have been considered to be fixed to the ground. The complete set of the 38 R/C designed frames with all the pertinent details can be found in [11].

Analyses have been performed using Ruaumoko 2-D software [12]. Every column or beam in bending was modeled as one elastic element with two plastic hinges at its ends [13]. The load-deformation curve of the flexural frame elements is modeled by the Takeda hysteretic model of Fig. 2.a.

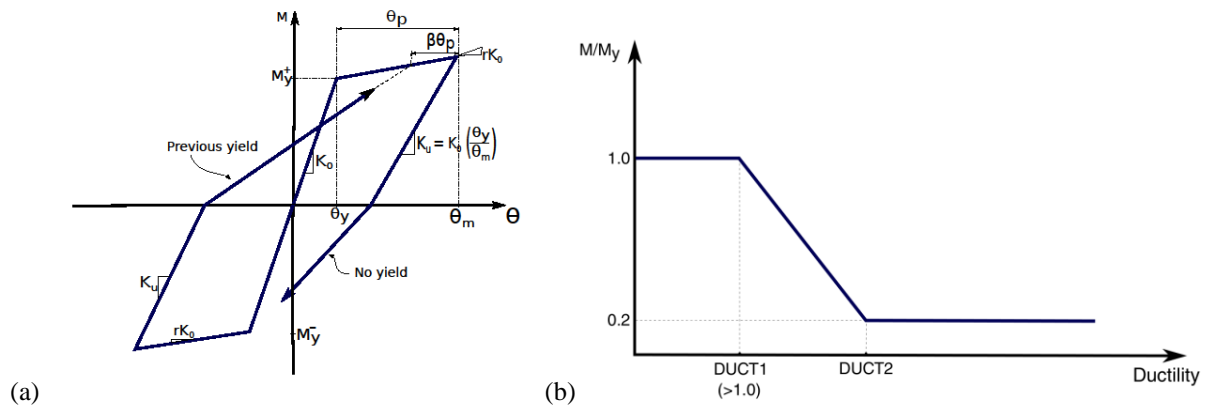


FIGURE 2: (a) Takeda hysteretic rule for moment M (or force F) versus rotation θ (or displacement d) and (b) strength degradation model in terms of ductilities.

A more realistic estimate of the effective elastic stiffness is given by

$$EI_{\text{eff}} = \frac{M_y}{\phi_y} \quad (5)$$

where M_y and ϕ_y are the moment and rotation at first yield. In this study, both the effective stiffness $EI_{\text{eff}} = 0.5EI$ as stipulated by EC8 [1] and the one described by Eq. (5) are employed in the nonlinear analyses. The loss of strength is modeled in the Ruaumoko 2-D software [12] as a function of the maximum ductility as shown in Fig. 2.b.

Ground motions used

In order to perform non-linear IDA, a set of 100 far fault historical earthquake accelerograms recorded worldwide were selected from Pacific Earthquake Engineering Research Center (PEER) ground motion database [14], 25 for each one of the four soil classes A, B, C, D of EC8 [1]. Details about these motions can be found in [11].

Performance levels considered

Usually four structural performance levels are identified: Immediate Occupancy (IO), Damage Control (DC), Life Safety (LS) and Collapse Prevention (CP) [15,16]. According to SEAOC [16] and FEMA 356 [15], for the cases of R/C MRFs, the IDR values corresponding to IO, DC, LS, CP are equal to 0.5% (or 1.0% considering $EI_{\text{eff}} = M_y/\phi_y$), 1.5%, 2.0% (or 2.5%), 4.0%. Moreover, FEMA 356 [15] sets limits for plastic rotations θ_{pl} equal to 0.010, 0.015, 0.020, 0.025 for beams and 0.005, 0.010, 0.015 and 0.020 for columns for IO, DC, LS and CP levels, respectively.

4 MODAL STRENGTH REDUCTION FACTORS

Tables 1 and 2 summarize the expressions for the design modal strength reduction factors \bar{q}_k for two effective stiffness cases ($EI_{\text{eff}} = 0.5EI_g$ and $EI_{\text{eff}} = M_y/\phi_y$), but only for soil class B. The cases pertaining to soil classes A, C and D can be found elsewhere [11]. Figure 3 presents those factors for the two types of member stiffnesses, in a pictorial form for the particular case of soil class B and the first mode.

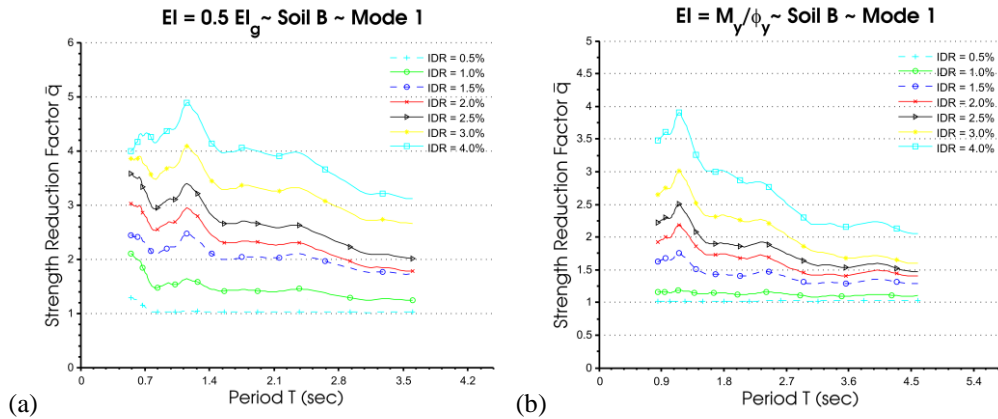


FIGURE 3: Modal strength reduction factors \bar{q}_1 versus period for various IDRs, soil B and two effective stiffnesses: (a) $EI_{\text{eff}} = 0.5EI_g$ and (b) $EI_{\text{eff}} = M_y/\phi_y$

Modal strength reduction factors \bar{q}_k for $EI_{\text{eff}} = 0.5EI_g$ and Soil B			
	\bar{q}_1	\bar{q}_2	\bar{q}_3
IO:	$-0.04T+1.12$	$-0.07T+1.10$	$-0.06T+1.07$
DC:	$-0.20T+2.45$	$1.19T^2-2.98T+3.16$	$-1.06T+1.98$
LS:	$0.46T+3.60$	$1.14T^2+2.47T+3.38$	$17.64T^2+14.44T+0.98$
CP:	$-0.19T^2+0.34T+4.17$	$-1.51T^2+3.21T+2.88$	$-10.91T^2+11.93T+1.18$

Table 1: Modal strength reduction factors \bar{q}_k for design using $EI_{\text{eff}} = 0.5EI_g$ and Soil B

Modal strength reduction factors \bar{q}_k for $EI_{eff} = M_y/\phi_y$ and Soil B			
\bar{q}_1	\bar{q}_2	\bar{q}_3	\bar{q}_4
IO: 1.00	1.00	1.00	1.00
DC: $-0.11T+1.72$	$-0.11T+1.38$	$-0.27T+1.38$	$-0.23T+1.30$
LS: $0.07T^2-0.61T+2.86$	$0.21T^2-0.91T+2.27$	$1.49T^2-2.40T+2.24$	$3.00T^2-3.95T+2.58$
CP: $0.37T^2-2.36T+5.54$	$-1.22T+3.64$	$-10.84T^3-21.55T^2+13.82T+1.37$	$-10.02T^2+10.38T+1.62$

Table 2: Modal strength reduction factors \bar{q}_k for design using $EI_{eff} = M_y/\phi_y$ and Soil B

5 NUMERICAL EXAMPLES

In all cases, the design was accomplished with the aid of the structural software SAP2000 [17] and evaluated through nonlinear time history analysis by the Ruaumoko-2D software [12] employing 36 accelerograms, adjusted to the seismic intensities of the four performance levels.

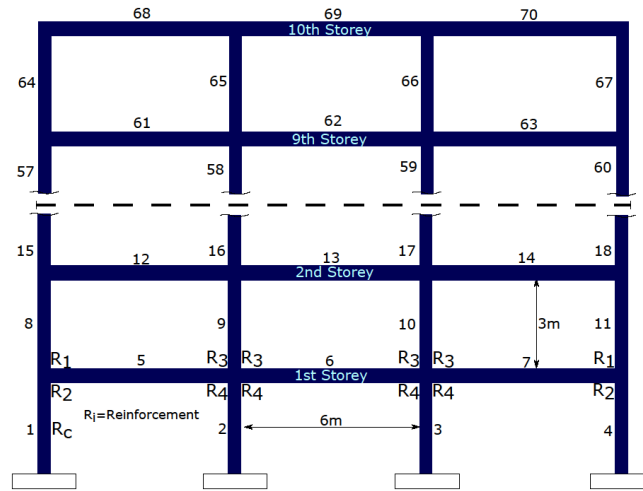


FIGURE 4: Numbering system of the columns, beams and the corresponding reinforcement

Two four-storey frames designed for LS with effective stiffness $EI_{eff} = 0.5EI_g$

A 4 storey RC frame called Frame A was designed following EC2 [10] and EC8 [1] regulations for a peak ground acceleration (PGA) = 0.30g and soil class B. The effective rigidity for all the members was assumed to be $EI_{eff} = 0.5EI_g$. The strength reduction factor was taken equal to $q = 3.9$ [1] and the frame was designed for strength at the life safety (LS) level for the design earthquake and for a maximum deformation of 1% IDR under the frequent earthquake, which here is taken as the design seismic action multiplied by 0.5. Moreover, stability sensitivity coefficient θ , should be less than 0.2 for the design seismic action in order to avoid a second order analysis (P-Δ). The first period was $T_1=1.04$ sec and the final sectional dimensions and reinforcement are shown in the first half of Table 3 with numbering system as in Fig. 4. Symbols used in Fig. 4 and Table 3 and all subsequent ones, are as follows: h is the cross-section height of columns and beams, R is the reinforcement ratio, i.e., the reinforcement area normalized to the cross-sectional area bd , where b is the width and $d=h-4\text{cm}$; the symbol R_c indicates the total reinforcement ratio of columns and R_1, R_2, R_3 and R_4 indicate the reinforcement ratios of each side of the beams following the index of Fig. 4. The reinforcement value coming from the effective slab width in tension is symbolized by a star on R_1 and is equal to $250\text{mm}^2/\text{m}$. In Table 3 only the necessary geometric sizes and reinforcement of the members of the frame are shown. Frames are symmetric, i.e., outer (1,4) and middle (2,3) columns have the same geometry and reinforcement, beams No. 5 and No. 7 also have the same geometry and reinforcement etc.

By increasing gradually the $q=3.90$ until the strength check is just satisfied, one can easily determine that the above dimensions of Table 3 correspond to a strength reduction factor $q=3.00$, which accounts for both strength demand/capacity and deformation (allowable IDR and P-Δ effects) and is smaller than the originally used $q=3.90$, as expected.

A 4 storey RC frame called Frame B was also designed by the proposed seismic design method for the same soil class B and target value of 2.50% IDR, which corresponds to LS level [16]. Final sectional dimensions and reinforcement for the Frame B considering strength demand/capacity satisfaction are shown in the second half of Table 3. For the dimensions of Frame B, the periods of the designed frame were $T_1=1.04$ sec, $T_2=0.33$ sec, $T_3=0.18$

sec and $T_4=0.11$ sec and the corresponding modal strength reduction factors from Table 1 were found to be $\bar{q}_1 = 3.12$, $\bar{q}_2 = 2.69$, $\bar{q}_3 = 3.01$, $\bar{q}_4 = 2.15$. It is interesting to observe that $\bar{q}_1 = 3.12$ is almost the same as the realistic value of $q=3.00$ of Frame A designed by EC8 [1]. Using the elastic design spectrum of EC8 [1] for soil class B, $PGA=0.30g$, $q=1$ and damping $\xi=5\%$, and dividing its ordinates at the values of the initial T_k ($k=1-4$) by the corresponding \bar{q}_k ($k=1-4$), one obtains the four design spectrum values 0.125, 0.340, 0.275 and 0.340 from which a design base shear of 480 kN can be obtained. The so obtained dimensions of Frame B also satisfy deformation requirements and second order effects $P-\Delta$ automatically because they have been obtained by using deformation dependent \bar{q}_k .

Frame A								
Column	h(cm)	$R_c(\%)$	Beam	h(cm)	$R_1^*(\%)$	$R_2(\%)$	$R_3^*(\%)$	$R_4(\%)$
1	40	1.41%	5	40	1.35	1.24	1.40	1.24
2	45	1.23%	6	40	1.40	1.24	1.40	1.24
8	40	1.26%	12	40	1.34	1.18	1.34	1.24
9	45	1.26%	13	40	1.34	1.24	1.34	1.24
15	40	1.26%	19	40	1.03	0.87	1.05	0.94
16	45	1.10%	20	40	1.05	0.94	1.05	0.94
22	35	1.68%	26	40	0.47	0.47	0.58	0.47
23	40	1.26%	27	40	0.58	0.47	0.58	0.47

Frame B								
Column	h(cm)	$R_c(\%)$	Beam	h(cm)	$R_1^*(\%)$	$R_2(\%)$	$R_3^*(\%)$	$R_4(\%)$
1	40	1.41%	5	40	1.45	1.29	1.45	1.34
2	45	1.65%	6	40	1.45	1.34	1.45	1.34
8	40	1.26%	12	40	1.40	1.24	1.41	1.26
9	45	1.42%	13	40	1.41	1.26	1.41	1.26
15	40	1.26%	19	40	1.13	0.99	1.16	1.03
16	45	1.12%	20	40	1.16	1.03	1.16	1.03
22	35	1.68%	26	40	0.47	0.47	0.66	0.58
23	40	1.26%	27	40	0.66	0.58	0.66	0.58

Table 3: Final Sectional dimensions and reinforcement ratios for Frames A and B

The two frames (A and B) are now compared with the aid of non-linear time-history analyses. The results are outlined in Table 4 for comparison purposes. It is observed that, even though the proposed method appears to provide deformation results only slightly better than those coming from EC8[1], it leads to a lighter structure as the design base shear of Frame B is smaller than that of Frame A. Frames A and B are re-analyzed by non-linear dynamic analyses using the secant stiffness to yield, i.e., $EI_{eff} = M_y/\varphi_y$ and the maximum response values are shown in Table 4 in parenthesis. The IDR and beam θ_{pl} values for both Frames A and B are higher than those obtained using $EI_{eff} = 0.5EI_g$ but Frame B, even though it was designed only considering strength demand/capacity, shows a slightly better control of the deformations.

	Frame A	Frame B
$T_1(\text{sec})$	1.04 (1.62)	1.04 (1.59)
Mean./Max. IDR (%)	1.39/1.98 (2.17/3.48)	1.41/1.95 (2.10/3.02)
Mean./Max. Beam θ_{pl}	0.009/0.016 (0.009/0.027)	0.008/0.015 (0.008/0.022)
Mean./Max. Column θ_{pl}	0.007/0.014 (0.004/0.011)	0.007/0.014 (0.004/0.011)
Design Base Shear (kN)	443	480
1 st Yield Base Shear (kN)	550 (570)	598 (607)

Table 4: Response results of dynamic non-linear analyses for Frames A and B with $EI_{eff} = 0.5EI_g$ and in parenthesis with $EI_{eff} = M_y/\varphi_y$

Performance-based design example

Two 4-storey R/C frames called Frame C and Frame D are now designed by the proposed method using the $EI_{eff} = 0.5EI_g$ and $EI_{eff} = M_y/\phi_y$, respectively, the corresponding \bar{q}_k from Tables 1 and 2, soil class B and for four performance levels: immediate occupancy (IO) with IDR = 0.5% (or 1.0% considering $EI_{eff} = M_y/\phi_y$) under the frequently occurred earthquake, damage control (DC) with IDR = 1.5 % under the occasional occurred earthquake, life safety (LS) with IDR = 2.5% under the design basis earthquake and collapse prevention (CP) with IDR = 4.0% under the maximum considered earthquake as proposed by SEAOC [16]. SEAOC [16] proposes to scale the design seismic forces of LS level by 1.50 for CP level, by 0.50 for DC level and by 0.30 for IO level. For each performance level described above use is made of the corresponding modal strength reduction factors.

The proposed method was used to design Frames C and D for the four performance levels separately and from the four resulting designs, the strongest ones were selected. The final design base shears of Frames C and D 523 kN and 565 kN, respectively, correspond to the CP performance level for both Frames. Thus, the CP performance level controls the design for both frames. Table 5 provides final dimensions and reinforcement of Frames C and D.

Frame C								
Column	h(cm)	$R_c(\%)$	Beam	h(cm)	$R_1^*(\%)$	$R_2(\%)$	$R_3^*(\%)$	$R_4(\%)$
1	40	1.76%	5	40	1.53	1.40	1.58	1.43
2	45	1.65%	6	40	1.58	1.43	1.58	1.43
8	40	1.41%	12	40	1.53	1.34	1.53	1.35
9	45	1.65%	13	40	1.53	1.35	1.53	1.35
15	40	1.26%	19	40	1.24	1.06	1.24	1.08
16	45	1.26%	20	40	1.24	1.08	1.24	1.08
22	35	1.88%	26	40	0.47	0.47	0.66	0.58
23	40	1.26%	27	40	0.66	0.58	0.66	0.58

Frame D								
Column	h(cm)	$R_c(\%)$	Beam	h(cm)	$R_1^*(\%)$	$R_2(\%)$	$R_3^*(\%)$	$R_4(\%)$
1	40	2.12%	5	40	1.59	1.45	1.64	1.53
2	45	2.17%	6	40	1.64	1.53	1.64	1.53
8	40	1.43%	12	40	1.58	1.41	1.58	1.43
9	45	1.65%	13	40	1.58	1.43	1.58	1.43
15	40	1.26%	19	40	1.29	1.14	1.29	1.16
16	45	1.38%	20	40	1.29	1.16	1.29	1.16
22	35	1.88%	26	40	0.58	0.47	0.77	0.58
23	40	1.26%	27	40	0.77	0.58	0.77	0.58

Table 5: Final Sectional dimensions and reinforcement ratios for Frames C and D

Frames C and D were analyzed for their deformational response through non-linear dynamic analysis. Results are outlined in Table 6 for both frames C and D. Table 6 provides additionally response results for Frame C, in parenthesis, for the case of the secant stiffness to yield of Eq. (5). It is observed that the maximum IDR values of Frame C for both stiffnesses and for CP, LS and DC levels are below the maximum allowed values of 4.00%, 2.00% and 1.5%, respectively, while for the IO level one (0.48% for $EI_{eff} = 0.5EI_g$) is below and the other (0.64% for $EI_{eff} = M_y/\phi_y$) above the maximum allowable one of 0.50%. The plastic rotations θ_{pl} for both stiffnesses and for IO, DC and LS levels are below the maximum allowed values, while for the CP level are above the maximum allowable one. Considering Frame D, one can see from the second half of Table 6 that all the maximum IDR and θ_{pl} values for all levels are below or slightly above the maximum allowable values for those levels. Considering the mean response values, all of them resulted to be lower than the maximum allowable values.

It is interesting here to evaluate the performance of Frame A, designed by EC8 [1], under the CP level. This is shown in Fig. 11 (b), where in total, 18 beam and 6 column plastic hinges have maximum θ_{pl} values above the limit value for the CP level, with a maximum exceedance equal to 36% and 33%, respectively.

Thus, the proposed seismic design method can be successfully used in the framework of the performance-based design philosophy and provide results of high accuracy. The use of $EI_{eff} = M_y/\phi_y$ and the corresponding \bar{q}_k can provide controlled designs of even higher accuracy.

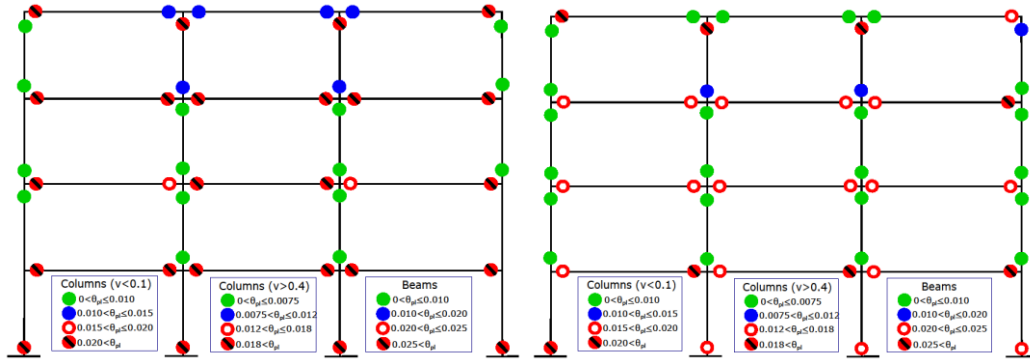


Figure 5. Plastic hinges distribution under CP performance level of (a) Frame D designed with \bar{q}_k for the LS and $EI_{eff} = M_y/\phi_y$ and (b) EC8 Frame A (maximum response from 36 accelerograms)

Frame C				
	IO	DC	LS	CP
Max. IDR (%)	0.49 (0.69)	0.81 (1.14)	1.42 (2.13)	2.10 (2.96)
Max. Beam θ_{pl}	0.000 (0.000)	0.005 (0.004)	0.014 (0.023)	0.027 (0.038)
Max. Column θ_{pl}	0.000 (0.000)	0.002 (0.000)	0.013 (0.012)	0.026 (0.032)
Frame D				
	IO	DC	LS	CP
Max. IDR (%)	0.69	1.14	2.05	2.74
Max. Beam θ_{pl}	0.000	0.000	0.015	0.027
Max. Column θ_{pl}	0.000	0.000	0.015	0.025

Table 6: Deformation Response of Frames C and D designed by the proposed method for 4 performance levels.

6 CONCLUSIONS

On the basis of the preceding developments, the following conclusions can be stated:

- Unlike the conventional code-based approach that considers a single strength reduction factor q value for all modes, the proposed approach with modal strength reduction factors \bar{q}_k offers a more rational alternative. Furthermore, since these factors take into account the dynamic (period T) and deformational (IDR, θ_{pl}) characteristics of the structure, lead to more accurate results than code based methods and without the need of final deformation checks in an iterative way.
- Comparisons of the proposed design method against the EC8 method with the aid of non - linear dynamic analyses on the basis of some characteristic examples, have shown that even though the EC8 method handles well designs at the Life Safety performance level, the proposed method controls more accurately and in a more rational way the deformations than the former method. In addition, the proposed method appears to be more economical than the EC8 method with respect to concrete and reinforcing steel materials.
- The proposed method is a performance - based seismic design, which can consider three to four performance levels depending on the design needs. In addition, the proposed method offers two options concerning the effective member stiffness selection ($EI_{eff} = 0.5EI_g$ or $EI_{eff} = M_y/\phi_y$). Design examples involving four performance levels and two effective member stiffness types have demonstrated the successful applicability of the proposed method.
- The use of modal strength reduction factors \bar{q}_k in conjunction with $EI_{eff} = 0.5EI_g$ gives satisfactory results even though $EI_{eff} = M_y/\phi_y$ leads to more accurate results. The use of $EI_{eff} = M_y/\phi_y$ with the corresponding \bar{q}_k leads to designs with a more controlled performance than those with the use of $EI_{eff} = 0.5EI_g$ and this is achieved with only a slight increase of concrete and steel material

REFERENCES

- [1] EC8, Eurocode 8: Design of structures for earthquake resistance, Part 1: General rules, seismic actions and rules for buildings. European Standard EN 1998-1, Stage 51 Draft, European Committee for Standardization (CEN), Brussels, 2005.
- [2] Y. Bozorgnia and V. V. Bertero, eds., *Earthquake engineering: From engineering seismology to performance - based engineering*. Boca Raton, Florida: CRC Press, 1st ed., Mar. 2004.
- [3] P. Fajfar, "A nonlinear analysis method for performance - based seismic design," *Earthquake Spectra*, vol. 16, no. 3, pp. 573–592, 2000.
- [4] Q. Xue and C.-C. Chen, "Performance-based seismic design of structures: a direct displacement-based approach," *Engineering Structures*, vol. 25, pp. 1803–1813, 2003.
- [5] G. S. Kamaris, G. D. Hatzigeorgiou, and D. E. Beskos, "Direct damage controlled seismic design of plane steel degrading frames," *Bulletin of Earthquake Engineering*, vol. 13, no. 2, pp. 587–612, 2014.
- [6] G. A. Papagiannopoulos and D. E. Beskos, "Towards a seismic design method for plane steel frames using equivalent modal damping ratios," *Soil Dynamics and Earthquake Engineering*, vol. 30, pp. 1106–1118, 2010.
- [7] G. A. Papagiannopoulos and D. E. Beskos, "Modal strength reduction factors for seismic design of plane steel frames," *Earthquakes and Structures*, vol. 2, pp. 65–88, 2011.
- [8] Y. Y. Lin and K. C. Chang, "Study on damping reduction factor for buildings under earthquake ground motions," *Journal of Structural Engineering of ASCE*, vol. 129, pp. 206–214, 2003.
- [9] G. A. Papagiannopoulos, G. D. Hatzigeorgiou, and D. E. Beskos, "Recovery of spectral absolute acceleration and spectral relative velocity from their pseudo-spectral counterparts," *Earthquakes and Structures*, vol. 4, pp. 489–508, 2013.
- [10] EC2, Eurocode 2: Design of concrete structures. Brussels: Part 1.1: General Rules for Buildings, European Standard EN 1992-1-1, European Committee for Standardization (CEN), 2004.
- [11] E. V. Muho, *Seismic design of planar concrete frames using modal strength reduction factors*. University of Patras, Patras, Greece: Ph.D. Thesis, Department of Civil Engineering, 2017 (in Greek).
- [12] A. J. Carr, *Theory and User Guide to Associated Programs*. Christchurch, New Zealand: Ruaumoko Manual. Department of Engineering, University of Canterbury, 2006.
- [13] M. N. Fardis, *Seismic design, assessment and retrofitting of concrete buildings*. Springer, Dordrecht, 2009.
- [14] PEER, "Pacific earthquake engineering research centre, strong ground motion database," 2013.
- [15] FEMA-356, *Prestandard and Commentary for the Seismic Rehabilitation of Buildings*, prepared for the SAC Joint Venture, published by the Federal Emergency Management Agency. Washington, D.C.: American Society of Civil Engineers (ASCE), 2000.
- [16] SEAOC, *Recommended lateral force requirements and commentary*. Sacramento, California: Structural Engineers Association of California, 1999.
- [17] "SAP 2000 Structural Analysis Program, Computers and Structures, Inc., California, USA."

DYNAMIC RESPONSE OF AN INFINITE BEAM RESTING ON A WINKLER FOUNDATION TO A LOAD MOVING ON ITS SURFACE WITH VARIABLE SPEED

Edmond V. Muho¹, Niki D. Beskou²

¹State Key Laboratory of Disaster Reduction in Civil Engineering
Tongji University,
Shanghai, CN-200092, China
e-mail: edmondmuho@gmail.com

²Department of Civil Engineering
University of Patras
Patras, GR-26504 Greece
e-mail: nikidiane@gmail.com

Keywords: Infinite beam, Winkler foundation, Moving load, Variable speed, Laplace transform, Fourier transform.

Abstract. *The problem of the dynamic response of an infinite beam resting on a Winkler foundation to a load moving on its surface with variable speed is solved here analytically/numerically under conditions of plane strain. The beam is linearly elastic with viscous damping and obeys the theory of Bernoulli-Euler. The elastic foundation is characterized by its spring constant and hysteretic damping coefficient. The moving point load has an amplitude harmonically varying with time and moves with constant acceleration or deceleration along the top beam surface. The problem is solved by first applying the Fourier transform with respect to the horizontal coordinate x and the Laplace transform with respect to time t to reduce the governing equation of motion of the beam to an algebraic one, which is solved analytically. The transformed beam deflection solution is inverted numerically after some simplifying analytical manipulations to produce the time domain beam response. Parametric studies are conducted in order to assess the effects of the various parameters on the response of the beam, especially those of acceleration and deceleration. Comparisons with the case of a finite beam are also done in order to assess the effect of the beam length.*

1 INTRODUCTION

The simplest possible model for a rigid pavement under moving vehicle loads is that of an elastic beam or plate on Winkler elastic foundation [1]. The beam or plate can be finite or infinite, thin or thick, with or without viscous damping and the Winkler foundation can consist of vertical and/or horizontal springs and zero or nonzero damping of the viscous or hysteretic type. One can mention here the works of Thompson [2], Achenbach and Sun [3], Sun [4,5], Kim and Roesset [6], Basu and Kameswara Rao [7] and Yu and Yuan [8], dealing with an infinite beam and the one by Lee [9] dealing with a finite beam.

All the existing works utilizing the above models are restricted to the case of loads moving with constant speed. Consideration of constant speed though, does not fully reflect reality, since vehicle loads usually move with speed varying with time.

Very recently, Beskou and Muho [10], were able to study the effect of variable speed on the response of a finite beam on a Winkler foundation to moving loads analytically. The problem was solved in [10] by modal superposition and computation of the resulting Duhamel's integral numerically. This method is applicable only in cases the beam is finite with well-defined boundary conditions at its two ends so as to express its lateral deflection as a superposition of its modal shapes. In cases where the beam is of infinite extent, this method is not applicable. The method of using a moving coordinate system to eliminate the time and reduce the problem to an ordinary differential equation which can be easily solved (e.g., in [2,3,7]), is restricted to the case of loads moving with constant speed.

In the present work, the problem of an infinite beam resting on a Winkler foundation and subjected to a load moving with variable speed on its top surface is solved analytically/numerically by extending the method of Yu and Yuan [8] from the constant speed case to the variable speed case.

The method employs Fourier and Laplace transforms with respect to the horizontal coordinate x and the time t , respectively, to reduce the governing equation of motion of the beam to an algebraic one, which is easily solved analytically. Then the transformed beam deflection solution is inverted numerically after some simplifying

analytical manipulations to produce the time domain beam response. This method is similar to the one employing a double Fourier transform with respect to both x and t described in Kim and Roeset [6] but leads to a much simpler transformed solution than the one of [6]. Thus, the present method requires the numerical evaluation of simpler integrals than in [6] where the double inverse fast Fourier transform is used.

Damping is considered for both the beam and the foundation, while the point load may be constant or varying harmonically with time. Extensive parametric studies are performed to assess the various problem parameters on the response. Comparisons with the case of the finite beam of [10] with very large length are also made in the framework of validation studies.

2 STATEMENT AND SOLUTION OF THE PROBLEM

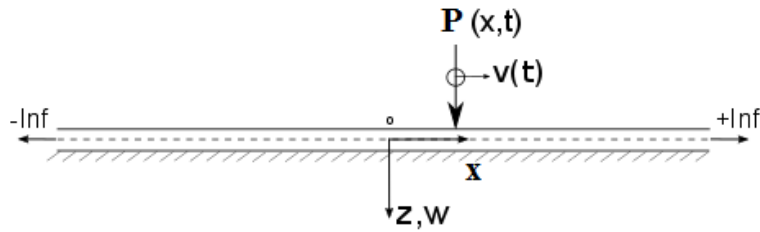


Figure 1. Infinite beam on Winkler foundation with moving load

Consider an infinite Bernoulli-Euler beam resting on a Winkler elastic foundation and subjected to a concentrated load $P(x,t)$ moving on its surface with a variable speed $V(t)$, as shown in Fig. 1. The equation of lateral motion of this beam has the form

$$EI w''''(x, t) + k_f w(x, t) + c \dot{w}(x, t) + m \ddot{w}(x, t) = P(x, t) \quad (1)$$

where $w = w(x, t)$ is the lateral deflection of the beam, EI is the flexural rigidity of the beam, k_f is the foundation spring constant, $c = c_b + c_f$ is the damping coefficient with c_b corresponding to the beam and c_f to the foundation, m is the beam mass per unit length, primes and overdots denote differentiation with respect to the horizontal coordinate x and time t , respectively and $P(x, t)$ is the moving concentrated (point) load. This load can be expressed as

$$P(x, t) = P_o \delta(x - x_o) \quad (2)$$

where P_o is its constant magnitude, δ denotes the Dirac delta function and x_o is expressed in terms of the initial velocity V_o and the constant acceleration (with + sign) or deceleration (with - sign) as

$$x_o = V_o \pm \frac{1}{2} a t^2 \quad (3)$$

Initial conditions are assumed to be zero and w and its derivatives with respect to x tend to zero as x approaches $\pm\infty$.

Following the approach in [8], the Fourier transform with respect to x and the Laplace transform with respect to t are applied on Eq. (1) to reduce this partial differential equation into an algebraic one, which can be easily solved analytically. These two transforms for a function $f(x, t)$ are defined as

$$\bar{f}(\xi, t) = \frac{1}{\sqrt{2\pi}} \int_{-\infty}^{\infty} f(x, t) e^{i\xi x} dx \quad (4)$$

$$\tilde{f}(x, s) = \int_0^{\infty} f(x, t) e^{-st} dt \quad (5)$$

Application of Fourier transform with respect to x on Eq. (1) results in

$$EI \xi^4 \bar{w}(\xi, t) + k_f \bar{w}(\xi, t) + c \bar{w}(\xi, t) + m \bar{w}(\xi, t) = \bar{F}(\xi, t) \quad (6)$$

where,

$$\bar{F}(\xi, t) = P_o \int_{-\infty}^{+\infty} \delta(x - x_0) e^{-i\xi x} dx = P_o e^{-i\xi x_0} \quad (7)$$

Application of Laplace transform with respect to t on Eq. (6) results in

$$EI \xi^4 \tilde{w}(\xi, s) + k_f \tilde{w}(\xi, s) + cs \tilde{w}(\xi, s) + ms^2 \tilde{w}(\xi, s) = \tilde{F}(\xi, s) \quad (8)$$

where, in view of (7),

$$\tilde{F}(\xi, s) = \int_{-\infty}^{+\infty} \bar{F}(\xi, t) e^{-ist} dt = P_o \int_{-\infty}^{+\infty} e^{-i\xi x_0} e^{-ist} dt = P_o \int_{-\infty}^{+\infty} e^{-i(\xi x_0 + st)} dt \quad (9)$$

Equation (8) can be easily solved for the doubly transformed displacement $\tilde{w}(\xi, s)$ reading as

$$\tilde{w}(\xi, s) = \frac{\tilde{F}(\xi, s)}{(EI \xi^4 + k_f + cs + ms^2)} \quad (10)$$

The solution $w(x, t)$ can be obtained from (10) by inversion of the Laplace and Fourier transforms. The inverse Laplace transform of Eq. (10) is

$$L^{-1}[\tilde{w}(\xi, s)] = L^{-1} \left[\frac{\tilde{F}(\xi, s)}{(EI \xi^4 + k_f + cs + ms^2)} \right] \quad (11)$$

Following [8], one can write Eq. (11) as

$$L^{-1}[\tilde{w}(\xi, s)] = \frac{1}{m} \frac{1}{b(\xi)} L^{-1} \left[\tilde{F}(\xi, s) \frac{b(\xi)}{(s + c_m)^2 + b^2(\xi)} \right] \quad (12)$$

where

$$c_m = \frac{c}{2m}, \quad b(\xi) = \sqrt{\frac{EI}{m} \xi^4 + \frac{k_f}{m} - \frac{c^2}{4m^2}} \quad (13)$$

Next, by defining

$$G(s) = \tilde{F}(\xi, s), \quad H(s) = \frac{b(\xi)}{(s + c_m)^2 + b^2(\xi)} \quad (14)$$

and letting $g(t)$, $h(t)$ to represent the inverse Laplace transforms of $G(t)$ and $H(t)$, respectively, one has

$$g(t) = \bar{F}(\xi, t), \quad h(t) = e^{-c_m t} \sin[b(\xi) t] \quad (15)$$

Use of the convolution operation (denoted by $*$) makes possible to write

$$L^{-1}[H(s)G(s)] = g(t) * h(t) = \int_0^t g(s) h(t-s) ds \quad (16)$$

and hence obtain Eq. (12) in the form

$$L^{-1}[\tilde{w}(\xi, s)] = \frac{1}{m} \frac{1}{b(\xi)} \int_0^t g(s) h(t-s) ds \quad (17)$$

Use of Eq. (7) and (15)₂ into Eq. (17) enables one to write it as

$$L^{-1}[\tilde{w}(\xi, s)] = \frac{1}{m} \frac{1}{b(\xi)} \int_0^t P_o e^{-i\xi x_0} e^{-c_m (t-s)} \sin[b(\xi) (t-s)] ds \quad (18)$$

Substitution of x_0 by its expression (3) in Eq. (18) can provide the displacement w in integral form in the time domain as

$$\bar{w}(\xi, t) = P_o \frac{1}{m} \frac{1}{b(\xi)} \int_0^t e^{-i\xi(V_0 s \pm \frac{1}{2} a s^2)} e^{-c_m(t-s)} \sin[b(\xi)(t-s)] ds \quad (19)$$

Taking the inverse Fourier transform of Eq. (19), one can obtain the solution in time and space as

$$w(x, t) = P_o \frac{1}{m} \frac{1}{2\pi} \int_{-\infty}^{+\infty} \frac{1}{b(\xi)} \left\{ \int_0^t e^{-i\xi(V_0 s \pm \frac{1}{2} a s^2)} e^{-c_m(t-s)} \sin[b(\xi)(t-s)] ds \right\} e^{i\xi x} d\xi \quad (20)$$

Finally, by using the relation

$$\frac{1}{2} \int_{-\infty}^{+\infty} e^{i\xi(x-y)} d\xi = \int_0^{\infty} \cos[\xi(x-y)] d\xi \quad (21)$$

the final form of the displacement in space and time domain is obtained in integral forms as

$$w(x, t) = P_o \frac{1}{m} \frac{1}{\pi} \int_0^{\infty} \frac{1}{b(\xi)} \int_0^t e^{-c_m(t-s)} \sin[b(\xi)(t-s)] \cos\left[\xi\left(x - V_0 s \pm \frac{1}{2} a s^2\right)\right] ds d\xi \quad (22)$$

Equation (22) is solved numerically by the Mathematica software [11] by using the Gauss-Kronrod algorithm.

3 VALIDATION STUDY

The method of solution presented in the previous section is validated for the special case of the load moving with constant speed by comparing its results against those of Kim and Roeset [6]. The method of Kim and Roeset [6] employs a double Fourier transform in space and time and determines the response numerically by inverting the transformed solution with the aid of the fast Fourier transform algorithm. The results of Kim and Roeset [6] are based on the following values: $EI = 2.3 \text{ kNm}^2$, $k_f = 68.9 \text{ MPa}$, $m = 48.2 \text{ kg/m}$, different constant velocities ($\alpha = 0 \text{ m/s}^2$, $V_0 = 9.525, 95.25 \text{ and } 114.3 \text{ m/s}$) and distributed load $q = -70 \text{ kN/m}$ over a length $d = 0.15 \text{ m}$. The concentrated load P_o is related to its equivalent distributed load q by the relation

$$P_o = 2q \left(\frac{\sin\left[\frac{d}{2}\xi\right]}{\xi} \right) \quad (23)$$

in the Fourier transformed domain. Thus, Eq. (22) is modified to accommodate the distributed load q and takes the form

$$w(x, t) = \frac{1}{m} \frac{1}{\pi} \int_0^{\infty} \frac{1}{b(\xi)} 2q \left(\frac{\sin\left[\frac{d}{2}\xi\right]}{\xi} \right) \int_0^t e^{-a_c(t-s)} \sin[b(\xi)(t-s)] \cos\left[\xi\left(x - V_0 s \pm \frac{1}{2} a s^2\right)\right] ds d\xi \quad (24)$$

Figure 2 shows the maximum values of the lateral beam displacement w versus distance on either side of the center of load application for three values of constant velocity V_0 and zero damping as obtained by the present method and the one in [6]. The results are identical.

4 PARAMETRIC STUDIES

Using the obtained analytical solution of the previous section, parametric studies are conducted in this section in order to assess the effect of the various parameters of the problem on the response. The data used here are the same as in [10]. Thus, $E = 30 \text{ GPa}$, $h = 0.20 \text{ m}$ and $b = 1.0 \text{ m}$ for the beam, $V_0 = 0, 24, 40 \text{ m/s}$, $\alpha = 0, 6, 12 \text{ m/s}^2$, $k_f = 40, 120 \text{ MPa}$, $c = 500, 1500 \text{ kNs/m}$, $m = 1019 \text{ kg/m}$ and $P_o = 80 \text{ kN}$. Beam deflections w were normalized (denoted by \bar{w}) by dividing them with $mg l^4 / \pi^3 EI$, where l is a beam length taken here to be 50 m .

Table 1 provides the dimensionless maximum infinite beam deflection $\bar{w} \cdot 10^5$ resting on an elastic foundation under a one-axle moving accelerating load for various values of the parameters V_0 , α , k_f and c . For comparison purposes, values of \bar{w} as computed by the method of reference [10] for the case of $l = 50 \text{ m}$ are also presented. As

the length l of the finite beam of [10] increases, the case of the infinite beam considered here can be approximately simulated. Table 2 provides corresponding results for the case of deceleration, while Figs 3 and 4 depict the beam deflection \bar{w} versus the time $\bar{t} = t/[(2/\pi)\sqrt{ml^4/EI}]$ for $c = 500$ kNs/m, various values of V_0 and α and $k_f = 40$ and 120 MPa, respectively.

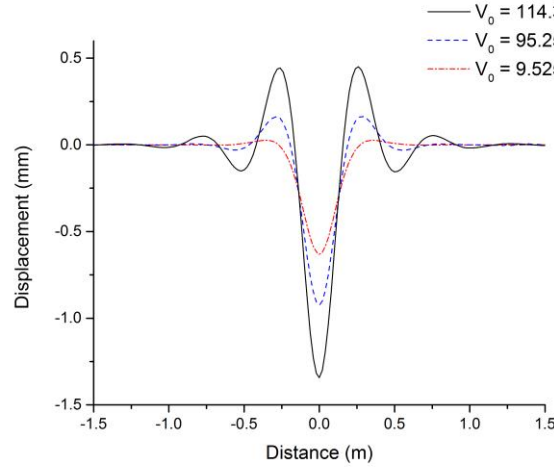


Figure 2. Beam displacement under the load versus distance along the x axis for zero damping

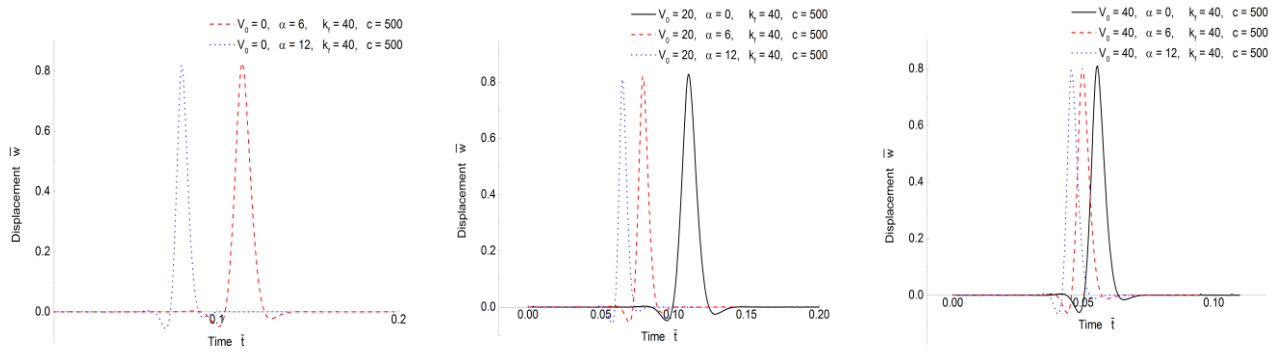


Figure 3. One-Axle modeling: Deflection \bar{w} versus time \bar{t} for various initial velocities V_0 and accelerations α with $k_f = 40$ MPa, $c = 500$ kNs/m and infinite beam length.

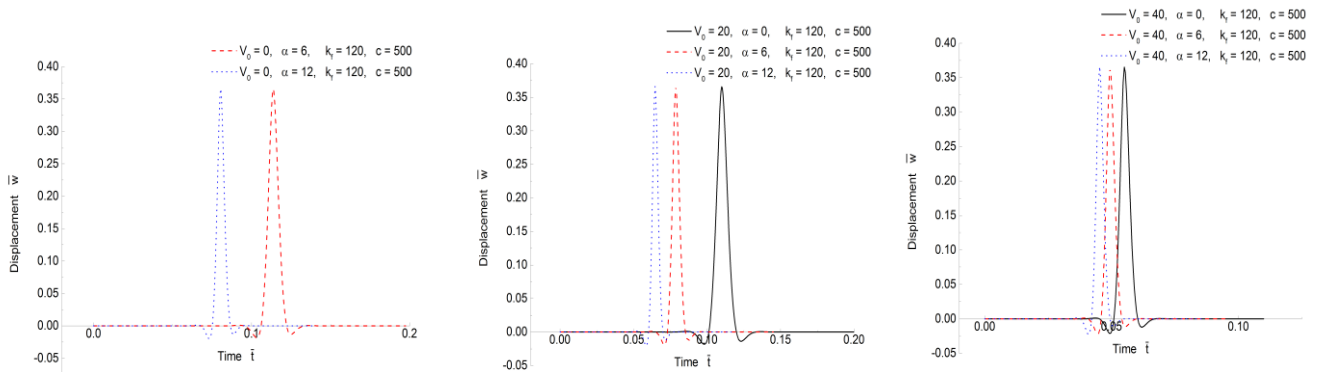


Figure 4. One-Axle modeling: Deflection \bar{w} versus time \bar{t} for various initial velocities V_0 and accelerations α with $k_f = 120$ MPa, $c = 500$ kNs/m and infinite beam length.

Looking at the Tables 1, 2 and Figs 3, 4, one can reach the same conclusions as in [10] and in addition can observe that the response of the finite beam with $l = 50$ m approaches that of the present infinite beam especially for small foundation stiffness and high damping ($k_f = 40$ MPa, $c = 1500$ kNs/m) as well as for high speed and acceleration. In general, deflections of the infinite beam are higher than those of the finite beam, especially for small damping.

V_0 (m/s)	a (m/s ²)	k_f (MPa)	c (kNs/m)	Infinite Beam (1)	Finite Beam $l=50$ m (2)	$[(1)-(2)]/1$ (%)
0	0	-	-	-	-	-
	6	40	500	0.826504	0.772461	6.54%
			1500	0.748733	0.736073	1.69%
		120	500	0.364954	0.313203	14.18%
			1500	0.358306	0.310275	13.41%
	12	40	500	0.818648	0.769446	6.01%
			1500	0.693399	0.703747	-1.49%
		120	500	0.365607	0.313301	14.31%
			1500	0.350829	0.307532	12.34%
20	0	40	500	0.828043	0.771379	6.84%
			1500	0.765709	0.723657	5.49%
		120	500	0.365825	0.31324	14.37%
			1500	0.359809	0.309321	14.03%
	6	40	500	0.819550	0.768431	6.24%
			1500	0.706256	0.693172	1.85%
		120	500	0.366001	0.313331	14.39%
			1500	0.351924	0.306605	12.88%
	12	40	500	0.810274	0.765529	5.52%
			1500	0.660133	0.667097	-1.05%
		120	500	0.366068	0.313404	14.39%
			1500	0.343859	0.303978	11.60%
40	0	40	500	0.810215	0.759587	6.25%
			1500	0.649872	0.622355	4.23%
		120	500	0.365272	0.313583	14.15%
			1500	0.343529	0.298929	12.98%
	6	40	500	0.804898	0.756814	5.97%
			1500	0.614450	0.604659	1.59%
		120	500	0.362642	0.313679	13.50%
			1500	0.338370	0.296573	12.35%
	12	40	500	0.793924	0.754102	5.02%
			1500	0.583276	0.588641	-0.92%
		120	500	0.365961	0.313759	14.26%
			1500	0.330183	0.294285	10.87%

Table 1: Dimensionless maximum deflection $\bar{w} * 10^5$ of an infinite beam on elastic foundation under moving accelerating load for various parameters

5 CONCLUSIONS

On the basis of the previous developments, the following conclusions can be drawn:

1. The dynamic response of an infinite beam resting on a Winkler foundation to a one-axle moving load with acceleration or deceleration has been obtained analytically and parametric studies have been conducted to assess the effects of the various parameters on the beam response.
2. Increasing values of the foundation constant or the viscous damping result in decreasing values of the beam deflection. Increasing values of acceleration and speed result in decreasing values of the beam deflection, while increasing values of deceleration and speed have the opposite effect.
3. The response of the finite beam with a length of 50 m approaches that of the infinite beam, especially for small foundation stiffness and high damping.

V_0 (m/s)	a (m/s ²)	k_f (MPa)	c (kNs/m)	One Axle (1)	Finite Beam $l=50m$ (2)	$[(2)-(1)]/1$ (%)
20	-6	40	500	0.832028	0.774418	6.92%
			1500	0.799478	0.760616	4.86%
		120	500	0.365800	0.313152	14.39%
			1500	0.363572	0.312144	14.15%
	-12	40	500	0.831555	-	-
			1500	0.804197	-	-
		120	500	0.366011	-	-
			1500	0.363311	-	-
40	-6	40	500	0.818187	0.762516	6.80%
			1500	0.692825	0.642180	7.31%
		120	500	0.365432	0.313504	14.21%
			1500	0.350562	0.301334	14.04%
	-12	40	500	0.823309	0.765363	7.04%
			1500	0.720596	0.664572	7.77%
		120	500	0.364849	0.313420	14.10%
			1500	0.355099	0.303884	14.42%

Table 2: Dimensionless maximum midspan deflection $\bar{w} * 10^5$ of infinite beam on elastic foundation under moving decelerating load for various parameters

REFERENCES

- [1] Beskou N.D., Theodorakopoulos D.D., ‘Dynamic effects of moving loads on road pavements: A review’, Soil Dynamics and Earthquake Engineering 2011; 31: 547-567.
- [2] Thompson W.E., ‘Analysis of dynamic behavior of roads subject to longitudinally moving loads’, Highway Research Record 1963; 39: 1-24.
- [3] Achenbach J.D., Sun C.T., ‘Moving load on a flexibly supported Timoshenko beam’, International Journal of Solids and Structures 1965; 1: 353-370.
- [4] Sun L., ‘Dynamic displacement response of beam type structures to moving line loads’, International Journal of Solids and Structures 2001; 38: 8869-8878.
- [5] Sun L., ‘A closed-form solution of beam on viscoelastic subgrade subjected to moving loads’, Computers and Structures 2002; 80: 1-8.
- [6] Kim S.M., Roesset J.M., ‘Dynamic response of a beam on a frequency- independent damped elastic foundation to moving load’, Canadian Journal of Civil Engineering 2003; 30: 460-467.
- [7] Basu D., Kameswara Rao N.S.V., ‘Analytical solutions for Euler-Bernoulli beam on visco-elastic foundation subjected to moving load’, International Journal for Numerical and Analytical Methods in Geomechanics 2013; 37: 945-960.
- [8] Yu H.T., Yuan Y., ‘Analytical solution for an infinite Euler-Bernoulli Beam on a viscoelastic foundation subjected to moving load’, Journal of Engineering Mechanics of ASCE 2014; 140(3): 542-551.
- [9] Lee H.P., ‘Dynamic response of a Timoshenko beam on a Winkler foundation subjected to a moving mass’, Applied Acoustics 1998; 55(3): 203-215.
- [10] Beskou N.D., Muho E.V., ‘Dynamic response of a finite beam resting on a Winkler foundation to a load moving on its surface with variable speed’, Soil Dynamics and Earthquake Engineering, to appear.
- [11] Mathematica, Technical Computing System, Wolfram Co, Champaign, IL, USA 2017.

ACCUMULATED DAMAGE IN NONLINEAR CYCLIC STATIC AND DYNAMIC ANALYSIS OF REINFORCED CONCRETE STRUCTURES THROUGH 3D DETAILED MODELING.

Christos Mourlas¹, George Markou² and Manolis Papadrakakis¹

¹Institute of Structural Analysis & Seismic Research, National Technical University of Athens, 9 Iroon Polytechniou Str., Zografou Campus, GR-15780 Athens, Greece
e-mail: mourlasch@central.ntua.gr , mpapadra@central.ntua.gr

²Catholic University of the Most Holy Conception Concepción, Department of Civil Engineering, Alonso de Ribera 2850, Concepcion, Chile
e-mail: markou@ucsc.cl

Keywords: Nonlinear dynamic analysis; reinforced concrete; finite element method; 3D detailed modeling; damage factor

Abstract. *Accurate nonlinear cyclic static and dynamic analysis of reinforced concrete structures is necessary when trying to capture the behavior of concrete structures during earthquake excitations. The development of an objective and robust 3D constitutive modeling approach that will be able to account for the accumulated material damage during the cyclic loading of concrete structures is of great importance in order to realistically describe the physical failure mechanisms [1]. The proposed method is based on the experimental results and the concrete modelling of Kotsovos and Pavlovic [2] as modified by Markou and Papadrakakis [3]. The objective of this research work is to propose a computationally efficient modeling method that accounts for the accumulated damage developed in both concrete and steel materials during cyclic static and dynamic excitations.*

Two new damage factors are proposed herein that take into account the number of openings and closures of cracks during the nonlinear cyclic analysis, thus provide with the ability to account for the accumulated damage in both steel and concrete materials. Furthermore, a solution strategy that describes the behavior of concrete during the cyclic static and dynamic analysis is also presented.

The proposed numerical method is validated by comparing its numerical response with the corresponding experimental data of a beam-column frame joint and a two-storey reinforced concrete frame, which were tested under cyclic static and dynamic loading conditions, respectively. Based on the numerical findings, the proposed algorithm manages to accurately capture the experimental results, while the simulation of the understudy models was performed with computational robustness and efficiency. This numerical outcome demonstrates the potential of the proposed 3D detailed modeling approach to be implemented for the seismic assessment of full-scale reinforced concrete structures through nonlinear cyclic static and dynamic analysis.

1 INTRODUCTION

During the last decades, many numerical simulations of reinforced concrete (RC) structures under cyclic loading conditions have been proposed. Most models tend to introduce many material parameters that are associated with the nonlinear behavior of concrete structures. They place emphasis on post-peak material characteristics in order to describe phenomena such as ductility, confinement, concrete cracking and crushing of reinforced concrete structures. These models can describe only certain aspects of concrete behavior and their implementation is limited to examples of small practical interest. It is important to formulate a constitutive model which represents accurately the actual mechanical behavior of concrete structures. An efficient and robust algorithm is developed in order to satisfy this cause.

Most models use elastoplastic uniaxial constitutive laws in order to describe the mechanical behavior of concrete. Others use the “equivalent uniaxial strain” concept to combine the uniaxial laws with biaxial or triaxial behavior of concrete. Other approaches propose constitutive models based on biaxial or triaxial failure surfaces. In addition to that, many researchers use the compression field theory to treat the behavior of cracked RC elements subjected to shear. Furthermore, many models combine the plasticity formulations for the behavior of concrete under compression with the fracture energy based smeared crack approaches for the behavior of concrete under tension. Furthermore, many models which are based on damage mechanics are proposed for concrete behavior under monotonic and cyclic loading conditions.

A detailed literature review in regards to the modeling of RC structures under cyclic loading conditions can be found in [3]. Few of these models have been used successfully for 3D dynamic analysis. Spiliopoulos and Lykidis

[4] and Cotsovos [5] used the constitutive model of Kotsovos and Pavlovic [3] integrated in 27-noded hexahedral elements for cyclic and dynamic analysis of RC structures. The latter introduces some restrictions in regards to the number of cracks that are allowed to open in each iteration, in an attempt to obtain convergence during the analysis. Moreover, none of these researchers investigated the computational efficiency of their proposed models, which is deemed crucial when dealing with dynamic nonlinear analyses of RC structures. Recently, Moharrami et al. [6] proposed a 3D constitutive model, which combines the elastoplastic and smeared crack approaches in order to describe the cyclic and dynamic behavior of concrete structures.

The proposed model in this research work, describes the triaxial behavior of concrete by using realistic assumptions without the need of introducing numerous concrete material parameters. The objective of the present paper is the formulation and numerical implementation of an accurate simulation of RC structures subjected to dynamic loading conditions. The uniaxial compressive and tensile strengths, the Young Modulus of elasticity and the Poisson's ratio are the only material parameters, which are needed to be defined for the analysis of concrete. The accuracy, numerical simplicity and the computational efficiency are the most important features in order to show the practical use of any model that can be easily implemented in predicting the nonlinear static and dynamic behavior of RC structures. Therefore, the proposed model adopts the numerical approach which was proposed in [3] (for cyclic loading conditions) thus it is further integrated herein for simulating the dynamic response of RC structures. The concrete model takes into account the effect of crack-closing through the use of a new damage factor. The numerical simulation is based on the proposed model by Markou and Papadrakakis [1], which was an extension of the model presented by Kotsovos and Pavlovic [2]. In order to account for the concrete's accumulated damage and its effect on the behavior of the steel rebars, a second damage factor is introduced for the steel material.

2 CONCRETE MATERIAL CONSTITUTIVE MODEL

The constitutive modelling of concrete has to describe a realistic behavior of concrete under generalized three dimensional states of stress. Therefore, it has to take into account the effect of out of plane small stresses that are usually ignored. The stress-strain relationships are expressed most conveniently by decomposing each state of strain and stress into hydrostatic and deviatoric components, where the proposed model uses two moduli of elasticity (bulk K and shear G) and an equivalent external stress (σ_{id}) in order to describe the constitutive relations as presented by the combined approach [2]. The bulk modulus K and the shear modulus G describe the non-linear σ_0 - $\varepsilon_{0(h)}$ and τ_0 - $\gamma_{0(d)}$ behavior combined with the use of σ_{id} in order to take into account the coupling effect of τ_0 - $\varepsilon_{0(d)}$ (h and d stand for hydrostatic and deviatoric components, respectively). The constitutive relations take the following form:

$$\varepsilon_0 = \varepsilon_{0(h)} + \varepsilon_{0(d)} = (\sigma_0 + \sigma_{id}) / (3K_s) \quad (1)$$

$$\gamma_0 = \gamma_{0(d)} = \tau_0 / (2G_s) \quad (2)$$

where K_s and G_s are the secant forms of bulk and shear moduli, respectively. The secant forms of bulk, shear modulus and σ_{id} are expressed as functions of the current state of stress which derived by regression analysis of the experimental data found in [2].

It is evident that when the deviatoric stress of an uncracked Gauss point of a concrete element, is less than the 50% of the corresponding ultimate strength, then the elastic constitutive matrix is used. Otherwise, the constitutive material matrix is updated using the tangent expressions of bulk and shear modulus [1]. The constitutive material matrix of the uncracked concrete is presented in eq. 3.

$$D = \begin{bmatrix} 2G_t + \mu & \mu & \mu & 0 & 0 & 0 \\ \mu & 2G_t + \mu & \mu & 0 & 0 & 0 \\ \mu & \mu & 2G_t + \mu & 0 & 0 & 0 \\ 0 & 0 & 0 & G_t & 0 & 0 \\ 0 & 0 & 0 & 0 & G_t & 0 \\ 0 & 0 & 0 & 0 & 0 & G_t \end{bmatrix} \quad (3)$$

The strength envelope of concrete is expressed by the value of the ultimate deviatoric stress by using the expressions of Willam and Warkne [7].

$$\tau_{0u} = \frac{2\tau_{0c}(\tau_{0c}^2 - \tau_{0e}^2)\cos\theta + \tau_{0c}(2\tau_{0e} - \tau_{0c})\sqrt{4(\tau_{0c}^2 - \tau_{0e}^2)\cos^2\theta + 5\tau_{0e}^2 - 4\tau_{0c}^2\tau_{0e}^2}}{4(\tau_{0c}^2 - \tau_{0e}^2)\cos^2\theta + (2\tau_{0e} - \tau_{0c})^2} \quad (4)$$

Additionally, the new criterion of crack closing which was introduced in [5], uses the strains that caused the initial formation of the cracks so as to determine whether a crack that starts to close will be eventually closed in a numerical manner as well. The criterion of crack closure takes the following form:

$$\varepsilon_i \leq a \cdot \varepsilon_{cr} \quad (5)$$

where ε_i is the current strain in the i -direction which is normal to the crack plane and ε_{cr} is the strain that caused the crack formation. Parameter a is a reduction factor, which takes the following form:

$$a = 1 - \frac{\varepsilon_{cr}}{\varepsilon_{\max}} = \frac{\varepsilon_{\max} - \varepsilon_{cr}}{\varepsilon_{\max}} \quad (6)$$

The maximum strain ε_{\max} is determined through the iterative Newton-Raphson procedure, whereas, in every internal Newton-Raphson iteration, the strains that are formed along the norm of the crack planes are calculated. Therefore, during an internal iteration when a crack is formed at a Gauss Point, it is assumed that $\varepsilon_{\max} = \varepsilon_{cr}$. Then, in every i iteration (internal or external) the strains ε_i that are formed normal to the crack planes are checked if they are larger than the previously calculated ε_{\max} . If this is the case, then ε_{\max} is set equal to ε_i . For more details in regards to the closing crack criterion can be found in [5]. When the criterion of crack-closure is satisfied at a Gauss Point, which had prior to that only one crack formation, then a part of the stiffness is lost along the previously crack plane which was assumed to form in an orthogonal direction to the maximum principle tensile stress. Therefore the constitutive matrix takes the following form:

$$C' = \begin{bmatrix} a_n \cdot (1 - D_c) \cdot (2G_t + \mu) & a_n \cdot (1 - D_c) \cdot \mu & a_n \cdot (1 - D_c) \cdot \mu & 0 & 0 & 0 \\ a_n \cdot (1 - D_c) \cdot \mu & 2G_t + \mu & \mu & 0 & 0 & 0 \\ a_n \cdot (1 - D_c) \cdot \mu & \mu & 2G_t + \mu & 0 & 0 & 0 \\ 0 & 0 & 0 & a_s \cdot (1 - D_c) \cdot \beta \cdot G_t & 0 & 0 \\ 0 & 0 & 0 & 0 & a_s \cdot (1 - D_c) \cdot \beta \cdot G_t & 0 \\ 0 & 0 & 0 & 0 & 0 & a_s \cdot (1 - D_c) \cdot \beta \cdot G_t \end{bmatrix} \quad (7)$$

where β is a shear retention factor, a_n and a_s are constants with recommended values of 0.25 and 0.125, respectively. The factor, D_c is a proposed damage factor that describes the accumulated energy loss due to the number of times a crack has opened and closed. After a numerical investigation the proposed factor takes the following form:

$$D_c = e^{-\left(1-a\right)/f_{cc}} = e^{-\left(1-\frac{\varepsilon_{cr}}{\varepsilon_{\max}}\right)/f_{cc}} = e^{-\left(\frac{\varepsilon_{cr}}{\varepsilon_{\max}}\right)/f_{cc}} \quad (8)$$

where f_{cc} is the number a crack has closed which is updated in every iteration for every Gauss Point. A schematic representation of Eq. 8 can be seen in the Fig. 1.

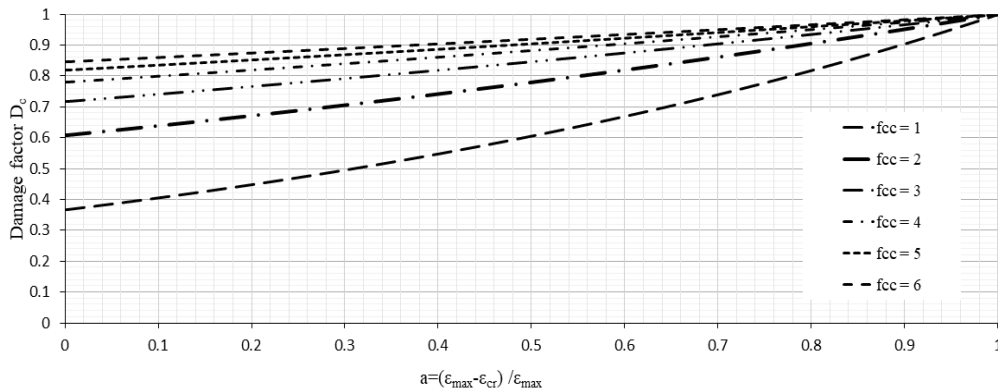


Fig. 1. Schematic representation of the values of the damage factor D Eq. 8 as a function of the parameter a and f_{cc} .

Similarly, the constitutive matrix follows the above procedure in the cases when a crack is closed at a Gauss point, which had previously one, two or three cracks. After the crack closure, the stresses are corrected by using the following expression:

$$\sigma^i = \sigma^{i-1} + C' \cdot \Delta \varepsilon^i \quad (9)$$

Finally, when all the cracks have been closed (uncracked Gauss Point) and the reduction factor aof one of the previous cracks (any of the possibly three cracks) is larger than 0.5, then the constitutive matrix takes the following form:

$$C'' = (1 - D_c) \cdot C \quad (10)$$

The proposed behavior of both cracked and uncracked Gauss points are described in the flow charts presented in Figs. 2 and 3.

Furthermore, a level of damage that is occurred due to the opening of cracks affects the contribution of steel reinforcement to surrounding concrete areas. In this way, a modification of the steel stress-strain relation of Menegotto-Pinto [8] is described. In this way, some pinching characteristics and the loss of bonding between steel reinforcement with the surrounding cracked concrete can indirectly be taken into account by reducing the stiffness contribution of steel reinforcement [9]. The average of all parameters a (Eq. 7) at the 8 Gauss Points within a single hexahedral element can determine the level of damage of the concrete hexahedron as shown in the following expression:

$$D_s = [1 - a_{Element}] \quad (11)$$

where,

$$a_{Element} = \frac{\sum_{i=1}^{ncr} a_i}{ncr}, \text{ ncr is the number of cracked Gauss Points} \quad (12)$$

In the case of unloading, when the structure reaches its initial deformation, a material deterioration of the steel reinforcement is computed based on the following proposed formulae:

$$E_s' = (1 - D_s) E_s \quad (13)$$

The material deterioration is applied when $\sigma_s \cdot \varepsilon_s < 0$, which describes the situations when crack closures and re-openings occur and the pinching phenomena are excessive. The modified material model is illustrated in Fig. 2.

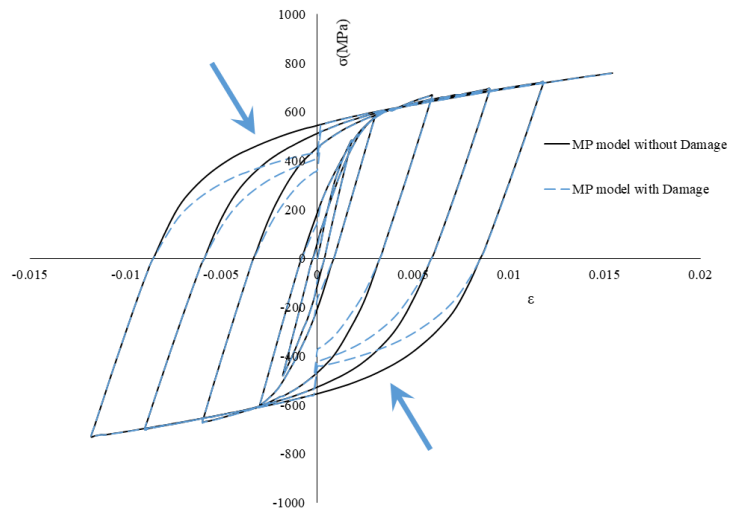


Fig. 2. Menegotto-Pinto steel model by taking into account the accumulated damage due to opening/closure of cracks.

3 NUMERICAL VALIDATION OF THE PROPOSED MODEL UNDER STATIC CYCLIC ANALYSIS.

The beam-column joint shown in Fig. 7, has been analyzed by Kusuhara and Shiohara [10] under static cyclic loading. The uniaxial compressive concrete strength was reported to be equal to $f_c=28.3$ MPa and the yielding stress of the steel reinforcement was 456 MPa for the 13 mm diameter bars in the beam section, while the yielding stress for the 13 mm diameter of the column section was 357 MPa. The Young modulus of elasticity for the longitudinal bar reinforcement was $E_s=176$ GPa. For the stirrup reinforcement, 6 mm in diameter rebars were used with a yielding stress of 326 MPa and a Young modulus of elasticity equal to 151 GPa.

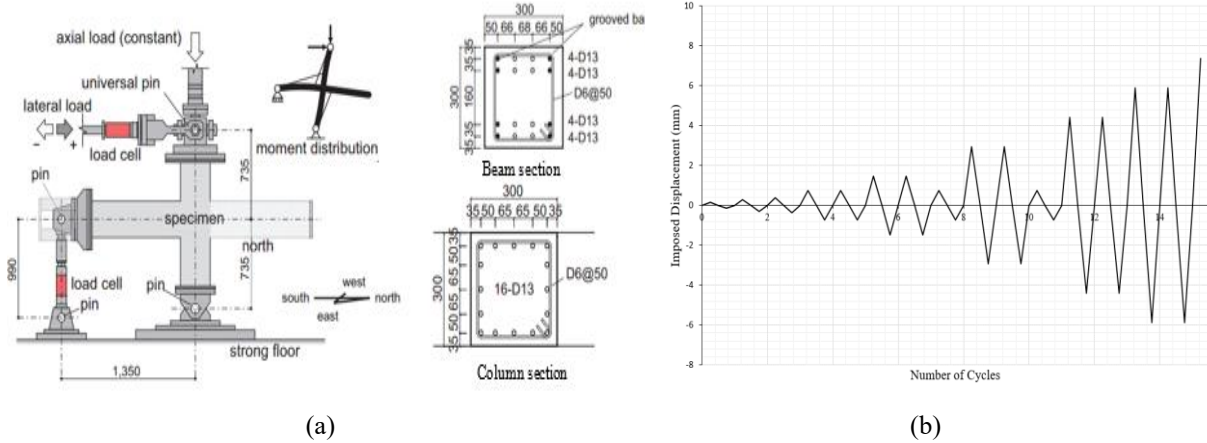


Fig. 3. (a) Geometry and reinforcement details of beam column joint [10] and (b) imposed displacement history of the interior frame joint.

The frame joint was subjected to different cyclic loading sets according to the experimental setup. The loading history that was modeled in this section, is presented in the form of imposed displacements in Fig. 3b, where 15 total displacement cycles can be seen. For the numerical model construction, the concrete domain was discretized with 8-noded hexahedral finite elements and the steel reinforcement was discretized with the beam finite element. A total number of 128 concrete (23cm x 15cm x 15cm) and 888 steel elements were used so as to discretize the entire frame joint, as illustrated in Fig. 4. The beam-column frame joint is supported according to the experimental configuration shown in Fig. 3, where the boundary conditions implemented within the developed model are shown in Fig. 4. As it can be seen in Fig. 4, the displacements were imposed at the top section of the column, while a 216 kN compressive force was also applied at the same section.

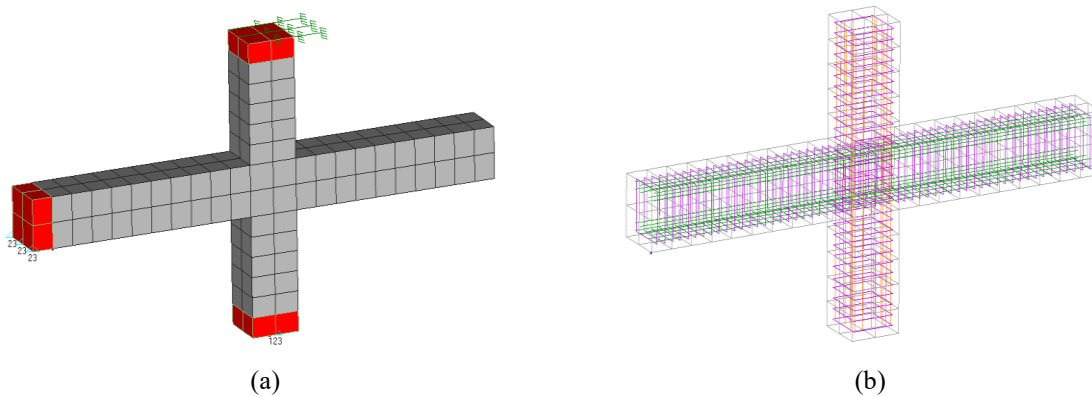


Fig. 4. RC beam-column frame joint. 3D views of the FE mesh of (a) concrete and (b) steel reinforcement elements.

The numerical curves are compared with the corresponding experimental curves in Fig 5. As it can be seen, the numerical results match very well with the experimental ones in terms of stiffness, strength and energy dissipation. Furthermore, Fig. 5 shows that the proposed model manages to capture efficiently the pinching effect in the case where both damage factors are implemented. It must be noted here that, during the analysis the steel rebars did not develop severe yielding but a bond degradation has occurred due to the opening of diagonal cracks

inside the joint according to the experimental results [32]. This observation indicates the importance of accounting the damage within the concrete domain and numerically transferring it to the steel rebar's material response through the proposed damage factor D_s .

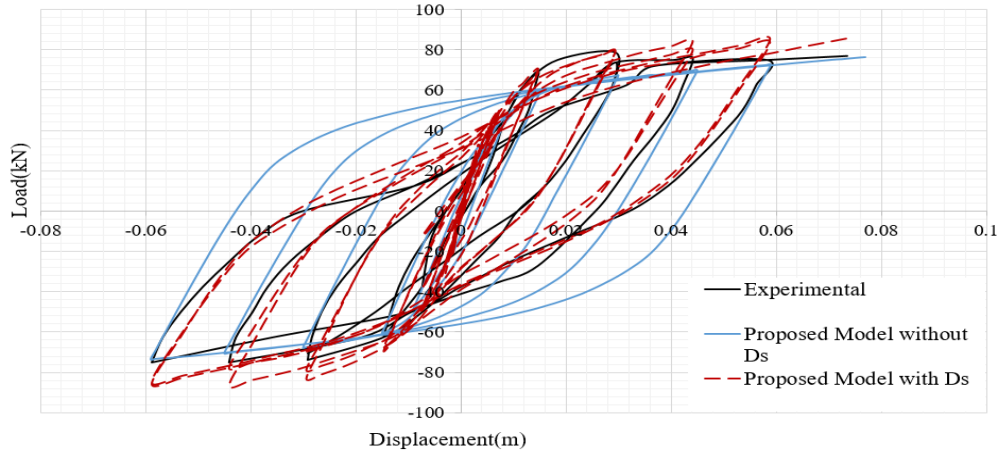


Fig. 2. Beam-Column frame joint. Comparison between numerical and experimental results. Complete force-displacement history.

The required Newton-Raphson internal iterations per load increment are shown in Fig. 6. As it resulted, all the displacement increments required a reasonable number of internal iterations to reach convergence regardless the intense nonlinear behavior of the structure. 77% of the displacement increments require less than 5 internal iterations to converge, while 95% of the displacement increments require less than 10 internal iterations. A total of 173 seconds were required so as to solve 610 displacement increments. This illustrates the computational efficiency of the proposed algorithm and the overall stability of the nonlinear solution procedure.

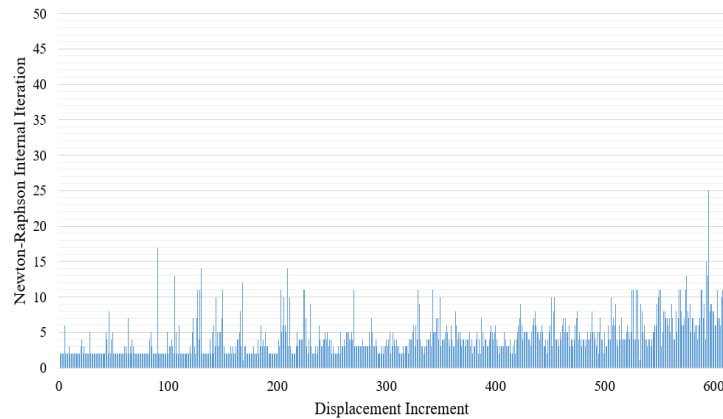


Fig. 6. RC beam-column frame joint. Required Newton-Raphson iteration per displacement increment.

4 NUMERICAL IMPLEMENTATION FOR DYNAMIC ANALYSIS

A two-level RC frames denoted as H30 [11], which was subjected to dynamic loading conditions is investigated in this section. The iterative method uses an energy convergence tolerance criterion set to 10^{-4} , where the nonlinear Newmark integration method was used for the dynamic analysis. The geometric and reinforcement details are shown in Fig. 7a. The uniaxial cylinder compressive strength of concrete (f_c) was 50 MPa. The yielding stress (f_y) of steel reinforcement was 500 MPa and the masses of the frame were 2.87 and 2.62 tons at the lower and upper girders, respectively. The Frame H30 was designed by assuming a ductility of $q = 5$.

The frame was subjected to horizontal motions applied at its base as shown in Fig. 7b. The base motions foresaw of three sinusoidal events that were applied in sequence, as described in [11]. The three accelerograms exhibited a maximum magnitude of approximately one and two times the magnitude of the design ground acceleration of the frame, which was 0.30g.

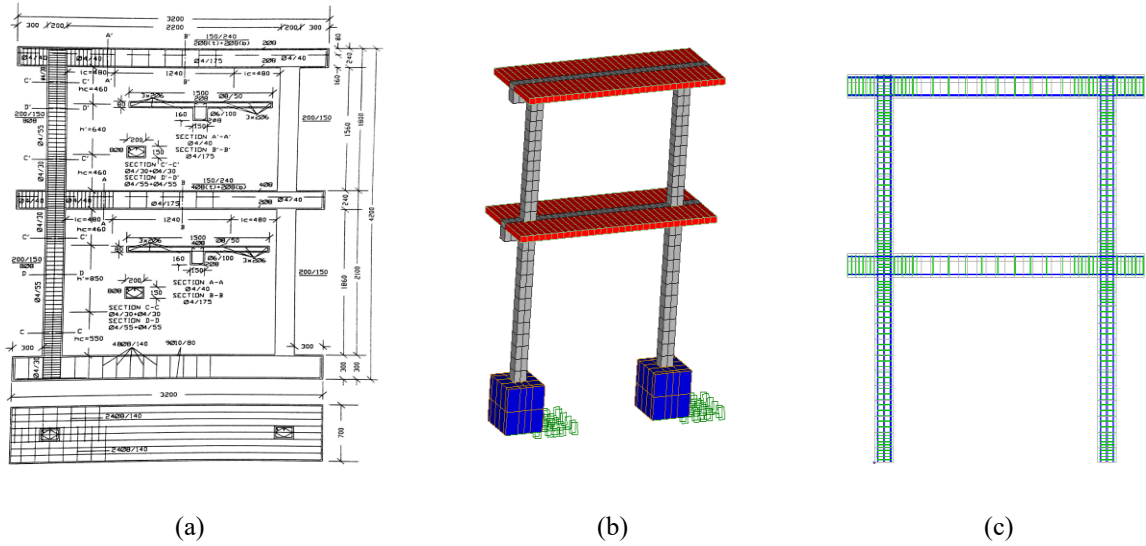


Fig. 3. (a) Geometric and reinforcement details of RC specimen H30, (b) Hexahedral FE mesh and (c) embedded rebar elements.

For the numerical model (H30), a total of 2,384 embedded rebar elements were used, while for the RC slabs, 128 8-noded hexahedral elements were used (red elements). The mass density of the RC slab-elements has been set appropriately in order to take into account the mass of the structure based on the experimental setup [11]. The steel rebars were simulated as embedded beam elements within the hexahedral concrete elements as presented in [12].

The frame developed excessive cracking which occurred at the first dynamic cycles of the dynamic excitation (first 3 s of the experiment, see Fig. 9). This led to significant strength degradations mainly during the third round of dynamic loading ($t > 17$ s) due to the yielding and fracture of the longitudinal reinforcement at the base of the frame, which was also observed during the experiment [11]. The numerically computed displacements of the first and the second floor slabs of the RC frame are compared with the experimental data in Figs. 9 and 10.

The numerical results indicate that the proposed model managed to capture accurately the experimental data during the dynamic tests. During the last dynamic test, the model exhibited a relatively stiffer behavior compared to the experimental data. This can be attributed to severe damages developed at the base which led the specimen practically to fail due to excessive cracking and rebar failures. This explains the remaining deformation that can be noted during the last 5 seconds of the experiment (see Figs. 9 and 10). The numerical model managed to describe the overall behavior of the frame in a satisfactory manner, without any numerical instabilities.

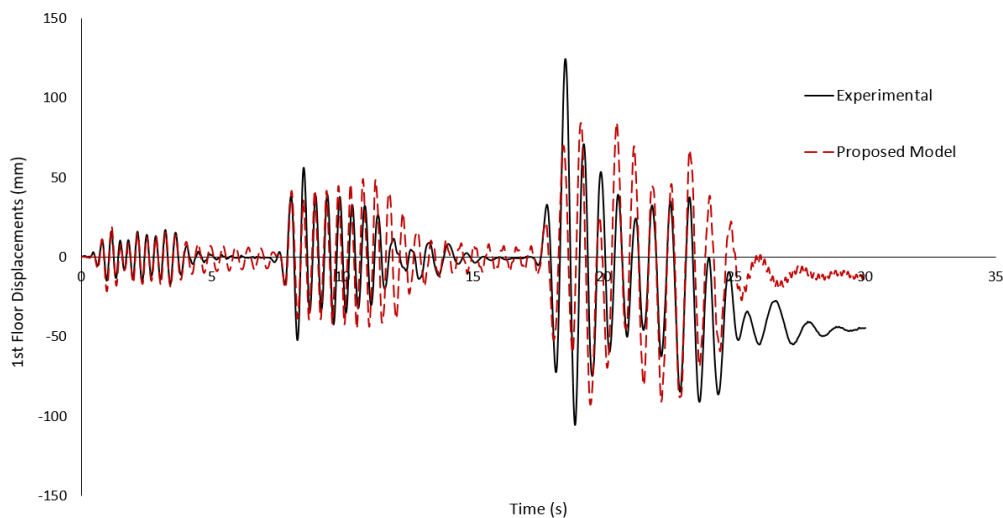


Fig. 4. H30 frame. Comparison between the numerical and experimental results of the 1st level displacement response.

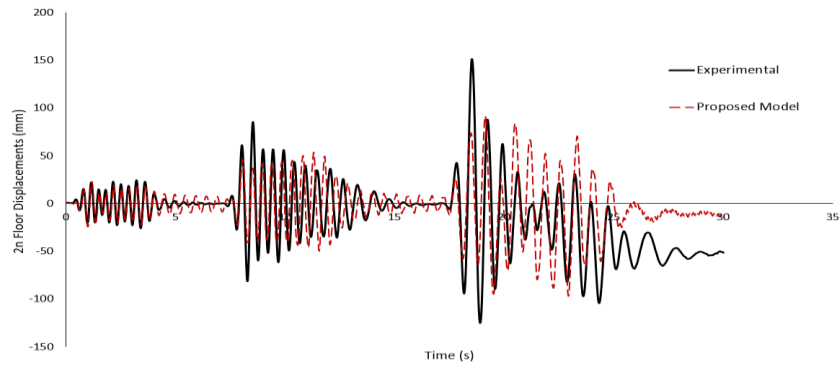


Fig. 10. H30 frame. Comparison between the numerical and experimental results of the 2nd level displacement response.

The required internal iterations, for H30 numerical models, are shown in the Fig 11. As it resulted, the required internal iterations per dynamic step during the solution procedure were limited to an average of 2 to 3, underlining the numerical stability of the proposed method. Based on the numerical findings, a 78% of the dynamic steps required less than 5 internal iterations to achieve convergence. The total required time for solving the nonlinear dynamic problems was 565 s, which refers to the solution of 3,826 dynamic time increment steps.

Finally, Fig. 12 shows the crack patterns that were formed at the end of the dynamic event 3. The numerical crack patterns appear to be a denser than the experiment ones, which is attributed to the smeared crack method. However, there is a good agreement on the distribution, the location and the direction of the cracks predicted by the numerical model.

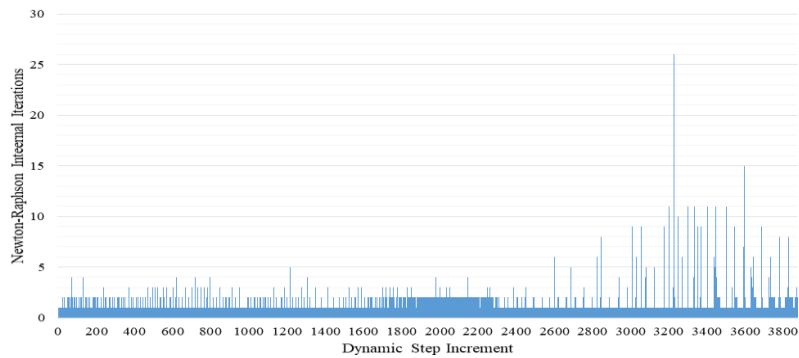


Fig. 11. Required Newton-Raphson internal iterations per dynamic step increment H30.

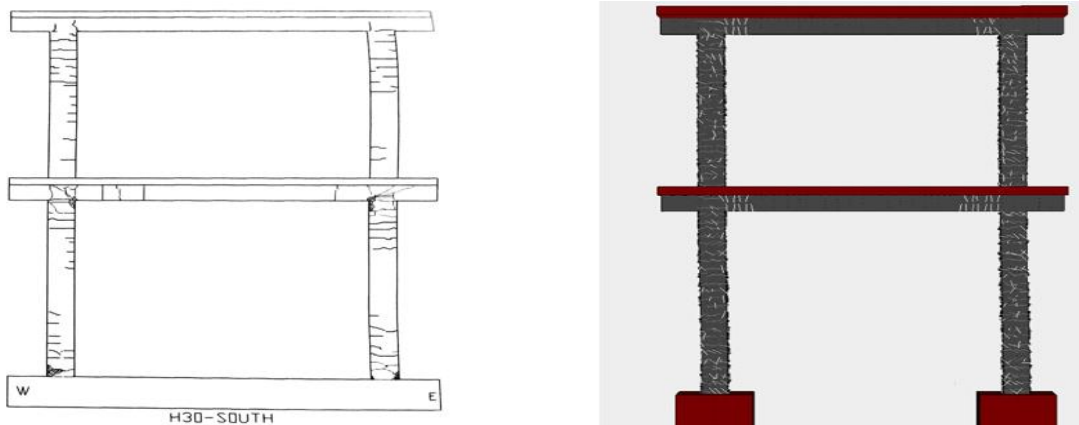


Fig. 12. H30 frame. Comparison of numerical and experimental crack patterns.

5 CONCLUSIONS

In this research work, a 3D detailed finite-element model was proposed for the nonlinear static cyclic and dynamic analysis of RC structures. The concrete material constitutive model describe a realistic behavior of

concrete under generalized three dimensional states of stress and treats cracking with the smeared crack approach. The numerical model has been integrated with a newly proposed concrete damage factor that was constructed by using the characteristics of cracking during the nonlinear static cyclic or dynamic analysis. Furthermore, a damage factor for the steel material that is also directly connected to the number of opening and closing of concrete cracks was introduced.

The proposed model was applied in a beam-column joint specimen, which was subjected to cyclic loading conditions and a two-level RC frame that was subjected to dynamic loading conditions. The numerical study revealed that the steel damage factor was crucial in the case of the static cyclic loading. Furthermore, the proposed concrete damage factor was found to play a controlling role during the dynamic analysis of the frame, while the ability of the proposed modeling approach in predicting the experimental data accurately and efficiently was illustrated. Finally, the numerical ability to capture the 3D cyclic behavior of reinforced concrete structures was presented herein, which is crucial when dealing with large-scale models [13].

ACKNOWLEDGEMENTS

The financial support provided by the European Research Council Advanced Grant “MASTER-Mastering the computational challenges in numerical modeling and optimum design of CNT reinforced composites” (ERC-2011-ADG 20110209) is gratefully acknowledged by the authors. The authors would like to acknowledge M.D. Kotsovos, P.G. Carydis, K. V. Spiliopoulos and G. Ch. Lykidis for providing the experimental data of the analysis of the RC structural members.

References

- [1] Markou, G. and Papadrakakis, M. (2013), “Computationally efficient 3D finite element modeling of RC structures”. *Computers and Structures*; 12(4):443–98.
- [2] Kotsovos, M.D. (2015), “Finite-Element Modelling of Structural Concrete: Short-Term Static and Dynamic Loading Conditions”, CRC Press.
- [3] Mourlas Ch., Papadrakakis M. and Markou G., “A computationally efficient model for the cyclic behavior of reinforced concrete structural members”, *Engineering Structures*. Vol. 141, 97-125, 2017.
- [4] Spiliopoulos, K.V. and Lykidis, G.C. (2006), “An efficient three dimensional solid finite element dynamic analysis of reinforced concrete structures”, *Earthquake Engineering and Structural dynamics*, 35, 137-157.
- [5] Cotsovos M. D., (2013), “Cracking of RC beam/column joints: Implications for the analysis of frame-type structures”, *Engineering Structures*, 52 131-139.
- [6] Moharrami M, Koutromanos I. (2017) “Finite element analysis of damage and failure of reinforced concrete members under earthquake loading”, *Earthquake Engineering & Structural Dynamics*, 1-20.
- [7] Willam K. J. and Warnke E. P., (1974), “Constitutive model for the triaxial behaviour of concrete”, Seminar on concrete structures subjected to triaxial stresses, Instituto Sperimentale Modeli e Strutture, Bergamo, Paper III-1.
- [8] Menegotto, M., and Pinto, P. E. (1973). “Method of analysis for cyclically loaded reinforced concrete plane frames including changes in geometry and non-elastic behavior of elements under combined normal force and bending.” *Proceedings, IABSE Symposium on Resistance and Ultimate Deformability of Structures Acted on by Well Defined Repeated Loads*, Lisbon, Portugal, 15–22.
- [9] Kwak, H.G. and Kim, D.Y. (2004), “Material nonlinear analysis of RC shear walls subject to cyclic loading”, *Engineering Structures*, 26, 1423-1436.
- [10] Shiohara, H. and Kusuhara, F., 2006, *Benchmark Test for Validation of Mathematical Models for Nonlinear and Cyclic Behaviour of R/C Beam–Column Joints*, Department of Architecture, School of Engineering, University of Tokyo.
- [11] Carydis P., (1997), “Shaking table tests of R.C. frames, ECOEST PPREC8”, Report 8, 182.
- [12] Markou, G. and Papadrakakis, M. (2012), “An efficient generation method of embedded reinforcement in hexahedral elements for reinforced concrete simulations”, *Advances in Engineering Software ADES*, 45(1), 175-187.
- [13] Markou G. and Papadrakakis M. (2015), “A Simplified and Efficient Hybrid Finite Element Model (HYMOD) for Non-Linear 3D Simulation of RC Structures”, *Engineering Computations*, Vol. 32 (5), pp. 1477-1524.

NONLINEAR LOCAL BUCKLING ANALYSIS OF BEAMS EMPLOYING A HIGHER ORDER BEAM THEORY

Amalia K. Argyridi¹ and Evangelos J. Sapountzakis²

¹ Institute of Structural Analysis and Antiseismic Research, School of Civil Engineering
National Technical University of Athens, Athens, 15780, Greece
e-mail: a.argyridi@gmail.com

² Institute of Structural Analysis and Antiseismic Research, School of Civil Engineering
National Technical University of Athens, Athens, 15780, Greece
e-mail: cvsapoun@central.ntua.gr, web page: <http://users.ntua.gr/cvsapoun/>

Keywords: Distortion, Warping, In-plane deformation, Out-of-plane deformation, Beam, Postbuckling analysis, Non-linear analysis

Abstract. *In most cases in the analysis of beam-like structures, Euler – Bernoulli beam theory assumptions are adopted, while in the case of non-negligible shear deformation effect, these assumptions are relaxed by using Timoshenko beam theory. However, both theories maintain the assumptions that plane cross-sections remain plane (no out-of-plane deformation) and that their shape does not change after deformation (no in-plane deformation). In order to take into account warping effects in the context of a beam theory, the inclusion of non-uniform warping is necessary, relaxing the assumption of plane cross-section. The shear flow associated with non-uniform warping leads also to in-plane deformation of the cross-section, relaxing the assumption that the cross-section shape does not change after deformation. For this purpose the so-called higher order beam theories have been developed taking into account warping (out-of-plane deformation) and distortional (in-plane deformation) effects. In order to avoid the usage of 2d or 3d theory of elasticity models, in this paper, a beam finite element is employed for the postbuckling analysis of arbitrarily shaped homogeneous beams, taking into account warping and distortional phenomena due to axial shear, flexure and torsion. The beam is subjected to arbitrary axial, transverse and/or torsional concentrated or distributed load, while its edges are restrained by the most general linear boundary conditions. The analysis consists of two stages. In the first stage, where the Boundary Element Method is employed, a cross-sectional analysis is performed based on the so-called sequential equilibrium scheme establishing the possible in-plane (distortion) and out-of-plane (warping) deformation patterns (axial, flexural and torsional modes) of the cross-section. In the second stage, where the Finite Element Method is employed, the extracted deformation patterns are included in the buckling analysis multiplied by respective independent parameters expressing their contribution to the beam deformation. The four rigid body displacements of the cross-section together with the aforementioned independent parameters consist the degrees of freedom of the beam. The non-linear finite element equations are formulated with respect to the aforementioned degrees of freedom. The influence of warping and distortional phenomena in postbuckling analysis is investigated through a numerical example.*

1 INTRODUCTION

In most cases in the analysis of beam-like structures, Euler – Bernoulli beam theory assumptions are adopted, while in the case of non-negligible shear deformation effect, these assumptions are relaxed by using Timoshenko beam theory. However, both theories maintain the assumptions that plane cross-sections remain plane (no out-of-plane deformation) and that their shape does not change after deformation (no in-plane deformation). In order to take into account warping effects in the context of a beam theory, the inclusion of non-uniform warping is necessary, relaxing the assumption of plane cross-section. The shear flow associated with non-uniform warping leads also to in-plane deformation of the cross-section, relaxing the assumption that the cross-section shape does not change after deformation. For this purpose the so-called higher order beam theories have been developed taking into account warping [1] (out-of-plane deformation) and distortional (in-plane deformation) effects [2]. Higher-order beam theories are of increased interest due to their important advantages over refined approaches such as 3-D solid or shell solutions. These advantages are summarized having in mind that beam models a) Require less modelling time, b) Permit isolation of structural phenomena and results' interpretation (rotations, warping parameters, stress resultants etc. are also evaluated in addition to displacements and stress components), c) Facilitate support modeling and external loading application, d) Require significantly less number of DOFs, thus reducing computational time, e) Facilitate parametric analyses without construction of multiple models.

Usually in engineering applications, non-linear analysis, including buckling, is crucial for the evaluation of the actual response of a structure. Thus, in this paper, a beam finite element is employed for the postbuckling analysis [3] of arbitrarily shaped homogeneous beams, taking into account warping and distortional phenomena due to axial, shear, flexure and torsion behavior. The beam is subjected to arbitrary axial, transverse and/or torsional concentrated or distributed load, while its edges are restrained by the most general linear boundary conditions. The analysis consists of two stages. In the first stage, where the Boundary Element Method is employed, a cross-sectional analysis is performed based on the so-called sequential equilibrium scheme establishing the possible in-plane (distortion) and out-of-plane (warping) deformation patterns (axial [4], flexural and torsional modes [5]) of the cross-section. In the second stage, where the Finite Element Method is employed, the extracted deformation patterns are included in the buckling analysis multiplied by respective independent parameters expressing their contribution to the beam deformation. The four rigid body displacements of the cross-section together with the aforementioned independent parameters consist the degrees of freedom of the beam. The non-linear finite element equations are formulated with respect to the aforementioned degrees of freedom. The influence of warping and distortional phenomena in postbuckling analysis is investigated through a numerical example.

The essential features and novel aspects of the proposed formulation, compared with previous ones, are summarized as follows.

- i) A very general beam theory is presented for the non-linear analysis of beams including axial warping and distortional effects, additionally to shear, flexural and torsional ones, following the sequential equilibrium scheme and employing BEM.
- ii) The cross-section can be thin- or thick-walled. The formulation does not stand on the assumption of thin-walled structure.
- iii) It performs non-linear analysis of prismatic members based on a higher-order beam theory, which is of increased interest due to its important advantages over refined approaches such as 3-D solid or shell solutions.
- iv) The influence of Poisson ratio is taken into account in the buckling analysis of beams.
- v) The beam is supported by the most general linear boundary conditions including elastic support or restraint.

2 STATEMENT OF THE PROBLEM

2.1 Displacement components

Let us consider a prismatic beam of length L (Figure 1a), of an arbitrarily shaped cross-section of area A (Figure 1b). The cross-section consists of a homogeneous material, with modulus of elasticity E and poisson ratio ν , occupying the two-dimensional multiply connected region Ω of the y, z plane (Figure 1b) and is bounded by the Γ_j ($j=1,2,...,K$) boundary curves, which are piecewise smooth, i.e. they may have a finite number of corners. In Figure 1 CYZ is the principal bending coordinate system through the cross-section's centroid C , while y_c, z_c are its coordinates with respect to Syz principal shear system of axes through the cross section's shear center S . Finally, it holds that $Y = y - y_c$ and $Z = z - z_c$.

The beam can be supported by the most general linear boundary conditions and is subjected to the combined action of the arbitrarily distributed or concentrated axial loading $p_x(X)$ along X direction, transverse loading $p_y(x)$ and $p_z(x)$ along the y, z directions, respectively, twisting moment $m_x(x)$ along x direction, bending moments $m_y^p(x)$, $m_z^p(x)$ along Y, Z directions, respectively, as well as bending $m_{\phi_y^s}(x)$, $m_{\phi_z^s}(x)$ and primary and secondary torsional $m_{\phi_x^p}(x)$, $m_{\phi_x^s}(x)$ and axial $m_{\phi_u^p}(x)$, $m_{\phi_u^s}(x)$ warping moments, and higher moments $m_{Du}^p(x)$, $m_{Du}^s(x)$, $m_{Dy}^p(x)$, $m_{Dy}^s(x)$, $m_{Dz}^p(x)$, $m_{Dz}^s(x)$, $m_{Dx}^p(x)$, $m_{Dx}^s(x)$ which, in what follows, will be referred to as distortional moments. The displacement field consists of two parts, i.e. the rigid body part and the end effects part (warping and distortional effects). Under the aforementioned loading the displacement field of the beam with respect to the Syz system of axes is given as

$$\begin{aligned} \bar{u}(x, y, z) = & \overbrace{u(x)}^{\text{Rigid Body Motion}} \\ & + \overbrace{\eta_u^p(x)\phi_u^p(y, z) + \bar{\eta}_y^p(x)\phi_y^p(y, z) + \bar{\eta}_z^p(x)\phi_z^p(y, z) + \eta_x^p(x)\phi_x^p(y, z)}^{\text{Primary Warping}} \\ & + \overbrace{\eta_u^s(x)\phi_u^s(y, z) + \eta_y^s(x)\phi_y^s(y, z) + \eta_z^s(x)\phi_z^s(y, z) + \eta_x^s(x)\phi_x^s(y, z)}^{\text{Secondary Warping}} \end{aligned} \quad (1a)$$

$$\begin{aligned}
 \bar{v}(x, y, z) = & \overbrace{v(x) - z \cdot \sin(\theta_x(x)) - y \cdot (1 - \cos(\theta_x(x)))}^{\text{Rigid Body Motion}} \\
 & + \overbrace{z_u^P(x) v_u^P(y, z) + z_Y^P(x) v_Y^P(y, z) + z_Z^P(x) v_Z^P(y, z) + z_x^P(x) v_x^P(y, z)}^{\text{Primary Distortion (component along y axis)}} + \\
 & + \overbrace{z_u^S(x) v_u^S(y, z) + z_Y^S(x) v_Y^S(y, z) + z_Z^S(x) v_Z^S(y, z) + z_x^S(x) v_x^S(y, z)}^{\text{Secondary Distortion (component along y axis)}}
 \end{aligned} \quad (1b)$$

$$\begin{aligned}
 \bar{w}(x, y, z) = & \overbrace{w(x) + y \cdot \sin(\theta_x(x)) - z \cdot (1 - \cos(\theta_x(x)))}^{\text{Rigid Body Motion}} \\
 & + \overbrace{z_u^P(x) w_u^P(y, z) + z_Y^P(x) w_Y^P(y, z) + z_Z^P(x) w_Z^P(y, z) + z_x^P(x) w_x^P(y, z)}^{\text{Primary Distortion (component along z axis)}} \\
 & + \overbrace{z_u^S(x) w_u^S(y, z) + z_Y^S(x) w_Y^S(y, z) + z_Z^S(x) w_Z^S(y, z) + z_x^S(x) w_x^S(y, z)}^{\text{Secondary Distortion (component along z axis)}}
 \end{aligned} \quad (1c)$$

where

$$\phi_Y^P(y, z) = -Z \quad \phi_Z^P(y, z) = -Y \quad (1d,e)$$

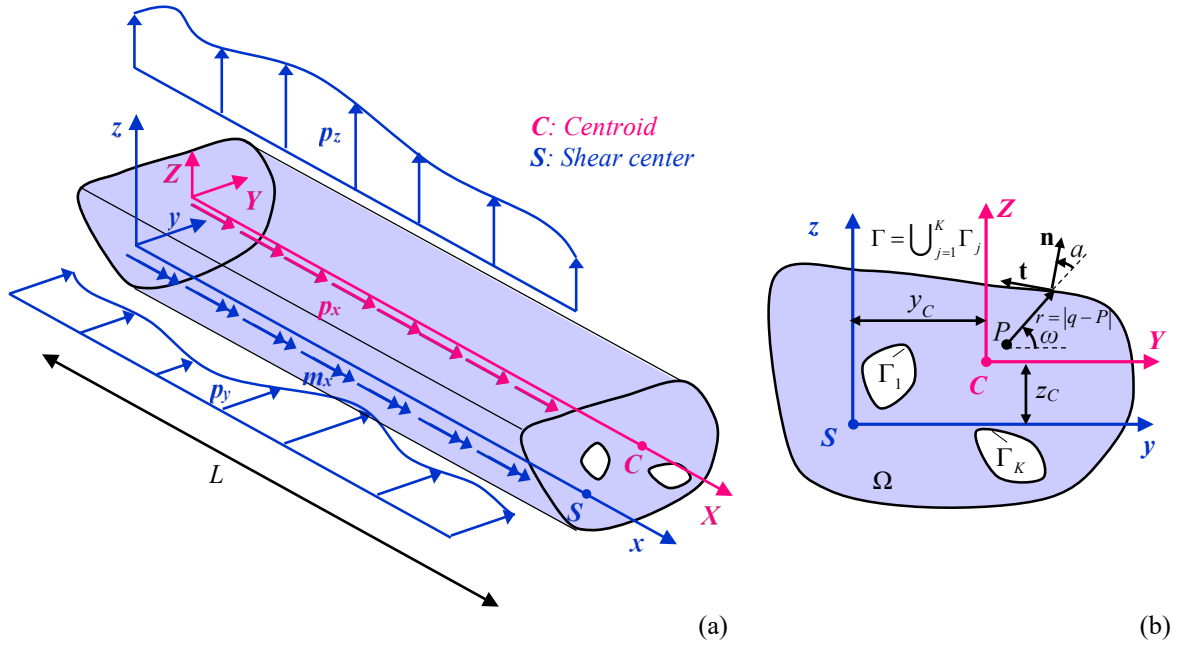


Figure 1: Prismatic beam under loading (a) with a homogeneous cross section of arbitrary shape occupying the two dimensional region Ω (b).

and

$$\bar{\eta}_Y^P = -\eta_Z^P(x) \cdot \sin(\theta_x(x)) + \eta_Y^P(x) \cdot \cos(\theta_x(x)) \quad (1f)$$

$$\bar{\eta}_Z^P = \eta_Z^P(x) \cdot \cos(\theta_x(x)) + \eta_Y^P(x) \cdot \sin(\theta_x(x)) \quad (1g)$$

$$\eta_Y^P = -\theta_Y(x) \quad \eta_Z^P = \theta_Z(x) \quad (1h,i)$$

where $\bar{u}(x, y, z)$, $\bar{v}(x, y, z)$, $\bar{w}(x, y, z)$ are the axial and transverse beam displacement components with respect

to the $Sxyz$ system of axes. Moreover, $u(x)$ denotes the “average” axial displacement of the cross-section, $v(x)$, $w(x)$ are the components of deflection of the center of twist S along y and z axes, respectively, while $\theta_x(x)$ is the angle of twist about the longitudinal axis x . $\eta_i^j(x)$ ($i = u, Y, Z, x$ and $j = P, S$) are the independent warping parameters introduced to describe the nonuniform distribution of primary ($j = P$) or secondary ($j = S$) warping due to axial behavior ($i = u$) or due to bending about Y ($i = Y$) or Z ($i = Z$) axes or due to torsion about x axis ($i = x$). $z_i^j(x)$ ($i = u, Y, Z, x$ and $j = P, S$) are the independent distortional parameters introduced to describe the nonuniform distribution of primary ($j = P$) or secondary ($j = S$) distortion due to axial behavior ($i = u$) or due to bending about Y ($i = Y$) or Z ($i = Z$) axes or due to torsion about x axis ($i = x$). $\eta_Y^P(x)$ and $\eta_Z^P(x)$ are related with the respective bending rotations $\theta_Y(x)$, $\theta_Z(x)$ due to bending about the Y , Z axes, according to Eqs. (1h-i). Despite the fact that $\eta_Y^P(x)$ and $\eta_Z^P(x)$ are basically rigid body rotations, they are referred as primary independent warping parameters, for generality purposes, because they correspond to $z_Y^P(x)$ and $z_Z^P(x)$ which are the primary independent distortional parameters introduced to describe the nonuniform distribution of primary flexural distortion due to bending about the centroidal Y , Z axes, respectively. $\phi_i^j(y, z)$ ($i = u, Y, Z, x$ and $j = P, S$) are the primary ($j = P$) or secondary ($j = S$) warping functions related with axial behavior ($i = u$) or shear due to bending about Y ($i = Y$) or Z ($i = Z$) axes or torsion about x axis ($i = x$). $v_i^j(y, z)$ ($i = u, Y, Z, x$ and $j = P, S$) are the primary ($j = P$) or secondary ($j = S$) components of distortional functions along Y axis related to axial behavior ($i = u$) or shear due to bending about Y ($i = Y$) or Z ($i = Z$) axes or torsion about x axis ($i = x$). $w_i^j(y, z)$ ($i = u, Y, Z, x$ and $j = P, S$) are the primary ($j = P$) or secondary ($j = S$) components of distortional functions along Z axis related to axial behavior ($i = u$) or shear due to bending about Y ($i = Y$) or Z ($i = Z$) axes or torsion about x axis ($i = x$).

According to sequential equilibrium scheme [4,5] in each equilibrium stage four deformation modes are added (one due to axial behavior, two due bending about Y and Z axes and one due to torsion about x axis) each of which includes one warping and one distortional function. Thus, the number of degrees of freedom (dofs) of each node is

$$N_{dofs} = \begin{matrix} \text{Rigid Body} \\ \text{Dofs} \end{matrix} 4 + \begin{matrix} \text{Warping \&} \\ \text{Distortion} \end{matrix} 2 \cdot \left(\begin{matrix} \text{Deformation} \\ \text{Modes} \end{matrix} 4 \cdot N_{stages} \right) \quad (2)$$

where N_{stages} is the number of equilibrium stages which participate in the model. The displacement field that includes up to secondary deformation modes, expressed by Eqs. (1), corresponds to $N_{stages} = 2$ and $N_{dofs} = 20$. If up to tertiary deformations modes are taken into account it will be $N_{stages} = 3$ and $N_{dofs} = 28$ etc. It is worth here noting that the non-linear terms of the displacement field are present in the primary warping part of the axial displacement component $\bar{u}(x, y, z)$ and in the rigid body part of the two transverse displacement components $\bar{v}(x, y, z)$ and $\bar{w}(x, y, z)$. Thus, the additional terms that are added in the displacement field in order to take into account tertiary phenomena or more follow the pattern of secondary terms of the latter displacement components (Eqs. (1a-c)).

2.2 Linear stress components

According to [4] the linear stress components which correspond to Eqs.(1a)-(1c) are

$$\boldsymbol{\sigma}_{6 \times 1}^{lin} = \mathbf{K}_{6 \times 6}^{Material} \cdot \mathbf{D}_{6 \times 2 N_{dofs}}^{lin} \cdot \mathbf{d}_{2 N_{dofs} \times 1}^{tot} \quad (3a)$$

where

$$\mathbf{K}_{6 \times 6}^{Material} = \begin{bmatrix} 2\mu + \lambda & \lambda & \lambda & 0 & 0 & 0 \\ \lambda & 2\mu + \lambda & \lambda & 0 & 0 & 0 \\ \lambda & \lambda & 2\mu + \lambda & 0 & 0 & 0 \\ 0 & 0 & 0 & \mu & 0 & 0 \\ 0 & 0 & 0 & 0 & \mu & 0 \\ 0 & 0 & 0 & 0 & 0 & \mu \end{bmatrix} \quad (3b)$$

$$\mathbf{d}_{2N_{dofs} \times 1}^{tot} = \begin{bmatrix} \mathbf{d}_{N_{dofs} \times 1} \\ \mathbf{d}_{N_{dofs} \times 1}^{,x} \end{bmatrix} \quad (3c)$$

where $\mu = E/(2(1+\nu))$ and $\lambda = \nu E/((1+\nu)(1-2\nu))$ are the shear modulus and the Lamé coefficient of the material, respectively. \mathbf{D}^{lin} is a matrix containing expressions which are functions of the cross-sectional coordinates, the warping functions and the components of distortional functions. $\mathbf{d}^T = [u(x), v(x), w(x), \theta_x(x), \eta_u^p(x), \eta_y^p(x), \eta_z^p(x), \eta_x^s(x), \eta_y^s(x), \eta_z^s(x), \eta_x^s(x), z_u^p(x), z_y^p(x), z_z^p(x), z_x^s(x), z_y^s(x), z_z^s(x), z_x^s(x)]^T$ is the displacement vector. Finally, $(\cdot)_{,i}$ denotes differentiation with respect to i .

2.3 Non-Linear strain components

Substituting Eqs.(1a)-(1c) in the non-linear (Green) strain-displacement relations

$$\varepsilon_{xx} = \frac{\partial \bar{u}}{\partial x} + \frac{1}{2} \left[\left(\frac{\partial \bar{u}}{\partial x} \right)^2 + \left(\frac{\partial \bar{v}}{\partial x} \right)^2 + \left(\frac{\partial \bar{w}}{\partial x} \right)^2 \right] \quad (4a)$$

$$\varepsilon_{yy} = \frac{\partial \bar{v}}{\partial y} + \frac{1}{2} \left[\left(\frac{\partial \bar{u}}{\partial y} \right)^2 + \left(\frac{\partial \bar{v}}{\partial y} \right)^2 + \left(\frac{\partial \bar{w}}{\partial y} \right)^2 \right] \quad (4b)$$

$$\varepsilon_{zz} = \frac{\partial \bar{w}}{\partial z} + \frac{1}{2} \left[\left(\frac{\partial \bar{u}}{\partial z} \right)^2 + \left(\frac{\partial \bar{v}}{\partial z} \right)^2 + \left(\frac{\partial \bar{w}}{\partial z} \right)^2 \right] \quad (4c)$$

$$\gamma_{xy} = \frac{\partial \bar{u}}{\partial y} + \frac{\partial \bar{v}}{\partial x} + \frac{\partial \bar{u}}{\partial y} \frac{\partial \bar{u}}{\partial x} + \frac{\partial \bar{v}}{\partial y} \frac{\partial \bar{v}}{\partial x} + \frac{\partial \bar{w}}{\partial y} \frac{\partial \bar{w}}{\partial x} \quad (4d)$$

$$\gamma_{xz} = \frac{\partial \bar{w}}{\partial x} + \frac{\partial \bar{u}}{\partial z} + \frac{\partial \bar{u}}{\partial z} \frac{\partial \bar{u}}{\partial x} + \frac{\partial \bar{v}}{\partial z} \frac{\partial \bar{v}}{\partial x} + \frac{\partial \bar{w}}{\partial z} \frac{\partial \bar{w}}{\partial x} \quad (4e)$$

$$\gamma_{yz} = \frac{\partial \bar{v}}{\partial z} + \frac{\partial \bar{w}}{\partial y} + \frac{\partial \bar{u}}{\partial y} \frac{\partial \bar{u}}{\partial z} + \frac{\partial \bar{v}}{\partial y} \frac{\partial \bar{v}}{\partial z} + \frac{\partial \bar{w}}{\partial y} \frac{\partial \bar{w}}{\partial z} \quad (4f)$$

($\left(\frac{\partial \bar{u}}{\partial x} \right)^2 \ll \frac{\partial \bar{u}}{\partial x}$, $\left(\frac{\partial \bar{u}}{\partial y} \right)^2 \ll \frac{\partial \bar{v}}{\partial y}$, $\left(\frac{\partial \bar{u}}{\partial z} \right)^2 \ll \frac{\partial \bar{w}}{\partial z}$, $\left(\frac{\partial \bar{u}}{\partial x} \right) \left(\frac{\partial \bar{u}}{\partial y} \right) \ll \frac{\partial \bar{v}}{\partial x} + \frac{\partial \bar{u}}{\partial y}$, $\left(\frac{\partial \bar{u}}{\partial x} \right) \left(\frac{\partial \bar{u}}{\partial z} \right) \ll \frac{\partial \bar{w}}{\partial x} + \frac{\partial \bar{u}}{\partial z}$, $\left(\frac{\partial \bar{u}}{\partial y} \right) \left(\frac{\partial \bar{u}}{\partial z} \right) \ll \frac{\partial \bar{w}}{\partial y} + \frac{\partial \bar{v}}{\partial z}$ i.e. the terms $\left(\frac{\partial \bar{u}}{\partial x} \right)^2$, $\left(\frac{\partial \bar{u}}{\partial y} \right)^2$, $\left(\frac{\partial \bar{u}}{\partial z} \right)^2$, $\left(\frac{\partial \bar{u}}{\partial x} \right) \left(\frac{\partial \bar{u}}{\partial z} \right)$, $\left(\frac{\partial \bar{u}}{\partial x} \right) \left(\frac{\partial \bar{u}}{\partial y} \right)$, and $\left(\frac{\partial \bar{u}}{\partial y} \right) \left(\frac{\partial \bar{u}}{\partial z} \right)$ have been neglected as considered to be small compared with the linear and the rest of the non-linear terms) the non-linear strain resultants are given as

$$\boldsymbol{\varepsilon}_{6 \times 1} = \mathbf{D}_{6 \times N_{Erows}} \cdot \mathbf{E}_{N_{Erows} \times 1} \quad (5)$$

where $\boldsymbol{\varepsilon} = [\varepsilon_{xx} \ \varepsilon_{yy} \ \varepsilon_{yy} \ \varepsilon_{xy} \ \varepsilon_{xz} \ \varepsilon_{yz}]^T$ is the non-linear strain vector which has been written as a product of two matrices. The first matrix ($\mathbf{D} = \mathbf{D}(y, z, \varphi_i^j, v_i^j, w_i^j)$ where $i = u, Y, Z, x$ and $j = P, S$) contains expressions which are functions of the cross-sectional coordinates, the warping functions and the components of distortional functions, while the second matrix ($\mathbf{E} = \mathbf{E}(\mathbf{d}, \mathbf{d}_{,x})$) contains expressions which are functions of the displacements and their derivatives. Finally, N_{Erows} is the number of rows of \mathbf{E} matrix.

2.4 Principle of virtual work

According to principle of virtual work

$$\delta U = \delta W \quad (6)$$

where δU and δW are the virtual work of the internal and external actions of the beam, respectively.

3 VIRTUAL WORK OF THE INTERNAL ACTIONS

The virtual work of the internal actions of beam is given as

$$\delta U = \int_V (\sigma_{xx} \delta \varepsilon_{xx} + \sigma_{yy} \delta \varepsilon_{yy} + \sigma_{zz} \delta \varepsilon_{zz} + \sigma_{xy} \delta \gamma_{xy} + \sigma_{xz} \delta \gamma_{xz} + \sigma_{yz} \delta \gamma_{yz}) dV = \int_V \left(\delta \boldsymbol{\varepsilon}^T \cdot \boldsymbol{\sigma} \right) dV \quad (7)$$

Substituting Eqs. (5) and (3) in Eq. (7) the expression of the virtual work of the non-linear part of the internal actions can be written as

$$\delta U = \int_0^L \delta \mathbf{E}^T \cdot \mathbf{K}^{gc} \cdot \mathbf{d}_{tot} dx = \int_0^L \delta \mathbf{d}_{tot}^T \cdot \left(\frac{\partial \mathbf{E}}{\partial \mathbf{d}_{tot}} \right)^T \cdot \mathbf{K}^{gc} \cdot \mathbf{d}_{tot} dx \quad (8a)$$

where

$$\delta \mathbf{E}^T = \left(\frac{\partial \mathbf{E}}{\partial \mathbf{d}} \cdot \delta \mathbf{d} + \frac{\partial \mathbf{E}}{\partial \mathbf{d}_{,x}} \cdot \delta \mathbf{d}_{,x} \right)^T = \left(\delta \mathbf{d}^T \cdot \left(\frac{\partial \mathbf{E}}{\partial \mathbf{d}} \right)^T + \delta \mathbf{d}_{,x}^T \cdot \left(\frac{\partial \mathbf{E}}{\partial \mathbf{d}_{,x}} \right)^T \right) = \delta \mathbf{d}_{tot}^T \cdot \left(\frac{\partial \mathbf{E}}{\partial \mathbf{d}_{tot}} \right)^T \quad (8b)$$

$$\mathbf{K}^{gc} = \int_{\Omega} \mathbf{D}^T \cdot \mathbf{K}_{Material} \cdot \mathbf{D} d\Omega \quad (8c)$$

\mathbf{K}^{gc} is a matrix that contains the non-linear geometric constants of the cross-section of the beam.

3.1 Virtual work of external actions

According to [4] the virtual work of the external actions of the beam is given as

$$\begin{aligned}
\delta W = & \int_0^L \left(\sum_{j=1}^K \int_{\Gamma_j} \left(\delta \mathbf{d}_{tot}^T \cdot \left(\frac{\partial \mathbf{u}}{\partial \mathbf{d}_{tot}} \right)^T \cdot \mathbf{t}_j \right) ds \right) dx \\
& + \int_{\Omega^0} \left(\delta \mathbf{d}_{tot}^T \Big|_{x=0} \cdot \left(\frac{\partial \mathbf{u}}{\partial \mathbf{d}_{tot}} \right)^T \Big|_{x=0} \cdot \mathbf{t} \Big|_{x=0} \right) d\Omega^0 + \int_{\Omega^L} \left(\delta \mathbf{d}_{tot}^T \Big|_{x=L} \cdot \left(\frac{\partial \mathbf{u}}{\partial \mathbf{d}_{tot}} \right)^T \Big|_{x=L} \cdot \mathbf{t} \Big|_{x=L} \right) d\Omega^L
\end{aligned} \tag{9}$$

where $\mathbf{u}^T = [\bar{u} \ \bar{v} \ \bar{w}]$, $\mathbf{t}^T = [t_x \ t_y \ t_z]$ is the vector applied on the lateral surface of the beam including end cross-sections ($x=0, L$), denoted by Ω^0 and Ω^L .

3.2 Flexural and torsional modes.

The calculation of the $\phi_i^j(y, z)$ ($i = u, Y, Z, x$ and $j = P, S, etc.$) warping functions and $v_i^j(y, z)$ and $w_i^j(y, z)$ ($i = u, Y, Z, x$ and $j = P, S$) components of distortional functions for axial ($i = u$), flexural ($i = Y, Z$) and torsional ($i = x$) modes, which have been employed in section 2.1, are obtained after solving corresponding boundary value problems, formulated exploiting the local equilibrium equations and the corresponding boundary conditions according to the so called sequential equilibrium scheme, as presented in [4] for axial and [5] for flexural and torsional modes, employing the Boundary Element Method. More specifically, in order to compute the involved warping and distortional functions, local equilibrium is sequentially fulfilled by introducing additional warping and distortional functions, so as to equilibrate non-equilibrated stress residuals [5].

4 NUMERICAL SOLUTION

The described problem is numerically solved employing the Finite Element Method (FEM) for the discretization and the incremental solution of Eq. (6).

5 NUMERICAL EXAMPLE AND CONCLUSIONS

In the numerical example, a beam of a standard closed steel profile (HEB500x300x8, $E = 2.1 \cdot 10^8 \text{ kN/m}^2$, $\mu = 8.08 \cdot 10^7 \text{ kN/m}^2$, $\nu = 0.3$) having length 5m is examined. Distortion as well as transverse displacements are prohibited at both ends which are free to warp or move axially. The beam is subjected to uniform axial loads applied at both ends. Thus, in what follows, due to symmetry of geometry and loading, the half beam is modeled. Axial displacement as well as warping is prohibited at the new end of the beam. Let us define as x, y, z the longitudinal axis, the strong axis and the weak axis of the beam, respectively. The origin of the system of axes is at the centroid of the cross section where the load is applied.

The non-linear response is evaluated employing the High Order Beam Theory (HOBT- present study) for varying number of degrees of freedom (N_{dofs}) of each Finite Element (FE) node (25 2-noded Finite Elements-FE) and is compared with the corresponding results obtained by Solid Finite Elements (Solid FEM) [6] (4000 FE). The geometric constants of HOBT were calculated employing 1024 linear discontinuous boundary elements (16 Gauss Points) and 268 domain quadrilateral cells (2x2 Gauss Points). The non-linear analysis is conducted by inducing an initial imperfection which arise from 1st linear buckling mode having a maximum displacement equal to 0.05mm.

In Figure 2 the deformed shape of the beam for Axial Load = 4500KN as calculated employing HOBT for $N_{dofs} = 52$ (Figure 2a) and Solid FEM (Figure 2b) as well as the load-displacement curves of axial displacement at point A (Figure 2c) and transverse displacement along y axis at point B (Figure 2d) as calculated employing HOBT for increasing N_{dofs} and Solid FEM. Point A, which lies on the cross section where the load is applied, is located at $x=0, y=0.15, z=0$ while Point B, where the maximum transverse displacement is developed (see Figures 2a-b), is located at $x=0.2, y=0.15, z=0$. The contour color of Figures 2a and b represents the value of each point's displacement vector.

From the aforementioned results can be concluded that:

- As the number of N_{dofs} increases HOBT (present study) converges with 3d Solid FEM.

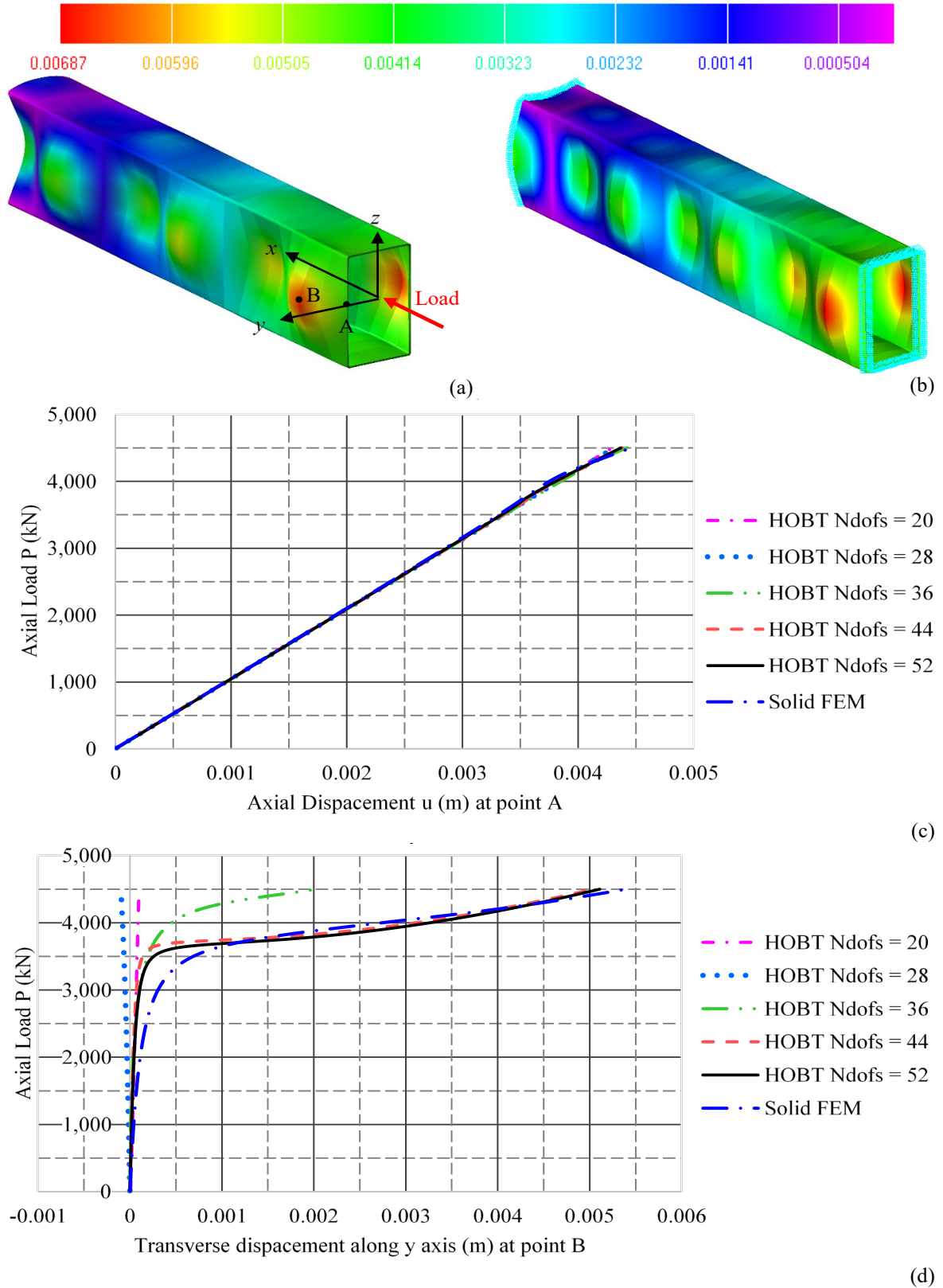


Figure 2: Deformed shape of the beam of the numerical example for Axial Load = 4500kN as calculated employing HOBT for Ndofs = 52 (a) and Solid FEM (b) as well as the load-displacement curves of axial displacement at point A (c) and transverse displacement along y axis at point B (d) as calculated employing HOBT for increasing Ndofs and Solid FEM.

- Distortional phenomenon has great influence in the calculation of the non-linear response of the beam as local buckling dominates.

- HOBt (present study) is able to capture local buckling phenomena with high accuracy which classical beam theories are unable to do.

ACKNOWLEDGEMENTS

The first author would like to express her sincere thanks to “Onassis Foundation”, “Foundation for Education and European Culture” and “A.G. Leventis Foundation” for their support.

REFERENCES

- [1] Reissner, E. (1946), “Analysis of shear lag in box beams by the principle of minimum potential energy”, *Quarterly of Applied Mathematics*, Vol. 4 (3), pp. 268 – 278.
- [2] Schardt, R. (1994b), “Lateral Torsional and Distortional Buckling of Channel- and Hat-Sections”, *Journal of Constructional Steel Research*, 31 (2-3), pp. 243-265.
- [3] Sapountzakis, E.J. and Dourakopoulos, J.A. (2008), “Flexural – Torsional Buckling Analysis of Composite Beams by BEM Including Shear Deformation Effect”, *Mechanics Research Communications*, Vol. 35 (8), pp. 497-516.
- [4] Argyridi, A.K. and Sapountzakis, E.J. (2018), “Higher Order Beam Theory in Local Buckling Analysis of Beams -Application in Standard Steel Profiles”, *Eighth International Conference on THIN-WALLED STRUCTURES – ICTWS 2018*, Lisbon, Portugal, July 24-27.
- [5] Dikaros, I.C. and Sapountzakis, E.J. (2017), “Distortional Analysis of Beams of Arbitrary Cross Section by BEM”, *Journal of Engineering Mechanics*, ASCE, Vol. 143 (10): 04017118, DOI:10.1061/(ASCE)EM.1943-7889.0001340.
- [6] MSC/NASTRAN for Windows, (1999), Finite Element Modelling and Post Processing System, Help System Index, Version 4.0, USA.

KDAMPER CONCEPT IN SEISMIC ISOLATION OF MULTI STOREY BUILDING STRUCTURES

Konstantinos A. Kapasakalis¹, Evangelos I. Sapountzakis² and Ioannis A. Antoniadis³

¹Institute of Structural Analysis and Antiseismic Research
School of Civil Engineering, National Technical University of Athens
Zografou Campus, Athens, GR-157 80, Greece
e-mail: kostskapasakalis@hotmail.com

²Institute of Structural Analysis and Antiseismic Research
School of Civil Engineering, National Technical University of Athens
Zografou Campus, Athens, GR-157 80, Greece
e-mail: cvsapoun@central.ntua.gr, web page: <http://users.ntua.gr/cvsapoun/>

³Mechanical Design and Control Systems Section
Mechanical Engineering Department, National Technical University of Athens
Zografou Campus, Athens, GR-157 80, Greece
e-mail: antogian@central.ntua.gr

Keywords: Seismic Isolation, Negative Stiffness, Building Structures, Transfer Functions, Optimization

Abstract. *The KDamper is a novel passive vibration isolation and damping concept, based essentially on the optimal combination of appropriate stiffness elements, which include a negative stiffness element. The KDamper concept ensures the static stability of the structure, does not require heavy masses and can achieve better dynamic characteristics, compared to the “Quazi Zero Stiffness” (QZS) isolators and the traditional Tuned Mass Damper (TMD). Contrary to the TMD and its variants, the KDamper substitutes the necessary high inertial forces of the added mass by the stiffness force of the negative stiffness element. Among others, this can provide comparative advantages in the very low frequency range. The paper proceeds to a systematic approach for the optimal design and selection of the KDamper parameters, for a multi storey building structure. A dynamic system consisting from a simplified flexible structure model and KDamper devises is considered and its transfer functions are derived. These transfer function are formed for various implementations of the KDamper devises, and are transformed in a parametric form, and an optimization procedure is used to minimize them for appropriate excitation and response points. Finally, an application case of a 3-storey concrete building structure is presented under seismic excitations of broad frequency range.*

1 INTRODUCTION

In response to the damage generated by earthquakes occurring in densely populated areas, the design codes for the design of buildings, bridges and industrial facilities changed with the intention to achieve better seismic performance. In order to mitigate the effects of earthquake shaking on structures, many theories have been developed, with seismic isolation being the most popular approach to earthquake-resistant design, as it is based on the concept of reducing the seismic demand rather than increasing the earthquake resistance capacity of the structure. Contemporary seismic isolation systems for bridge applications provide i) horizontal isolation from the effects of earthquake shaking, by decoupling the bridge deck from bridge substructure during earthquakes, and ii) an energy dissipation mechanism to reduce displacements. In this context, a variety of isolation devises including elastomeric bearings (with and without lead core), frictional/sliding bearings, roller bearings and newly-fabricated hardware incorporating negative stiffness elements for vibration isolation have been developed, with the latter being the most promising.

The concept of negative stiffness elements (or “anti-springs”) has a long history, being first introduced in the pioneering publication of (Molyneaux, 1957), as well as in the milestone developments of (Platus, 1999). The central concept of these approaches is to significantly reduce the stiffness of the isolator and consequently to reduce the natural frequency of the system even at almost zero levels (Carella et al., 2007), being thus called “Quazi Zero Stiffness” (QZS) oscillators. In this way, the transmissibility of the system for all operating frequencies above the natural frequency is reduced, resulting to enhanced vibration isolation. An initial

comprehensive review of such designs can be found in (Ibrahim, 2008).

The negative stiffness behavior is primarily achieved by special mechanical designs involving conventional positive stiffness pre-stressed elastic mechanical elements, such as post-buckled beams, plates, shells and pre-compressed springs, arranged in appropriate geometrical configurations. Some interesting designs are described in (Winterflood et al., 2002), (Virgin et al., 2008). However, alternatively to elastic forces, other forms of physical forces can be used to produce an equivalent negative stiffness effect, such as gravitational (Dyskin and Pasternak, 2012), magnetic (Robertson et al., 2009) or electromagnetic (Zhou and Liu, 2010). Among others, Quazi Zero Stiffness (QZS) oscillators are finding numerous applications in seismic isolation (DeSalvo, 2007), (Iemura and Pradono, 2009), (Sarlis et al., 2012), (Attary et al., 2015).

However, Quazi Zero Stiffness (QZS) oscillators suffer from their fundamental requirement for a drastic reduction of the stiffness of the structure almost to negligible levels, which limits the static load capacity of such structures.

In the same direction, a novel type of oscillator has been proposed (Antoniadis et al., 2015), incorporating a negative stiffness element, which can exhibit extraordinary damping properties, without presenting the drawbacks of the traditional linear oscillator, or of the 'zero-stiffness' designs. This oscillator is designed to present the same overall (static) stiffness as a traditional reference original oscillator. However, it differs both from the original SDOF oscillator, as well as from the known negative stiffness oscillators, by appropriately redistributing the individual stiffness elements and by reallocating the damping. Although the proposed oscillator incorporates a negative stiffness element, it is designed to be both statically and dynamically stable. Once such a system is designed according to the approach proposed in (Antoniadis et al., 2015), it is shown to exhibit an extraordinary damping behaviour. Moreover, a drastic increase of several orders of magnitude has been observed for the damping ratio of the flexural waves propagating within layered periodic structures incorporating such negative stiffness oscillators (Chronopoulos et al., 2015).

In this paper, an initial approach towards the implementation of the KDamper to the seismic isolation of multi storey building structures is considered. The Transfer Functions are formed for the top floor's displacement with a harmonic base excitation, first for the optimum solution of placing 3KDamper and then for 3 additional cases of placing 1 KDamper in all possible positions. The dynamic response of all the test cases is examined before and after the implementation of the KDampers. Finally the new damping ratio of the structure is calculated.

2 OVERVIEW OF THE KDAMPER CONCEPT IN A 3-DOF SYSTEM

Figure 1a presents a 3-DOF system of masses m_1, m_2, m_3 , static stiffness k_1, k_2, k_3 , with the damping ratios ζ_{1-3} common for all the modes of the system. Figure 1b presents the basic layout of the vibration isolation and damping concept to be considered. The first basic requirement of the KDamper is that the overall static stiffness of the system is maintained, as it is stated in Equation 1, where k_{R1-3} and k_{D1-3} represent the stiffness of the conventional springs, k_{N1-3} is the algebraical value of the negative stiffness element and k_{I1-3} stands for the initial static stiffness element of the uncontrolled system.

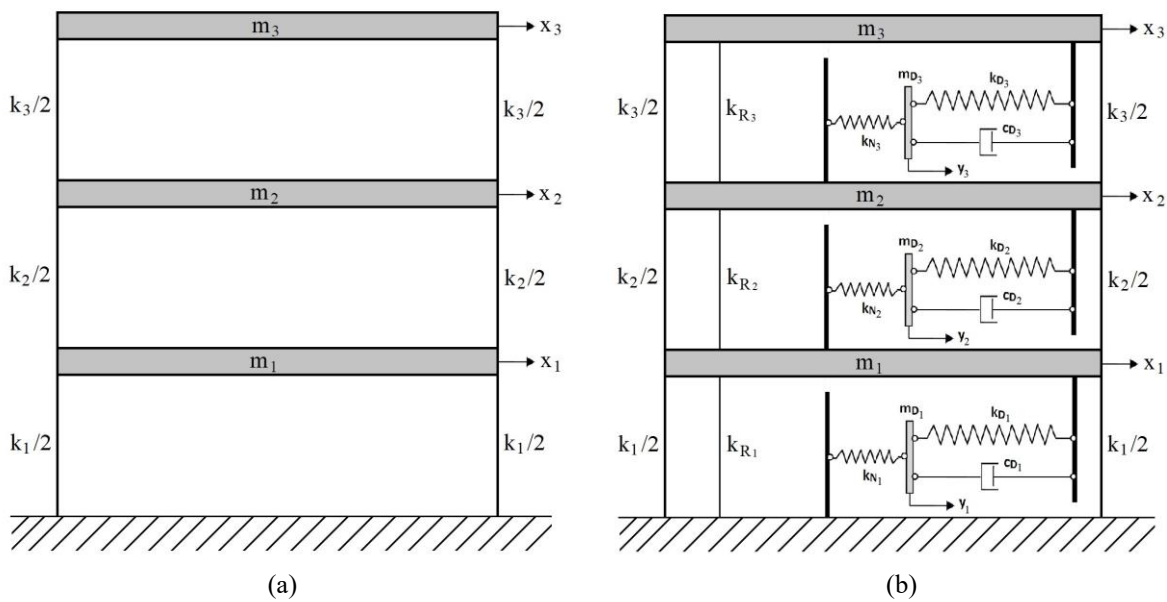


Figure 1. Schematic presentation of a 3-DoF system mounted on a fixed base (a) and (b) schematic presentation of the considered vibration absorption concept

$$k_{Ri} + \frac{k_{Di}k_{Ni}}{k_{Di} + k_{Ni}} = 0, \quad i = 1, 2, 3 \quad (1)$$

In this way, the KDamper can overcome the fundamental disadvantages of the QZS oscillator, which is the reduction of the overall stiffness of the system that simultaneously limits the static loading bearing capacity off the structure.

The resulting equations of motion after the implementation of the 3-KDamper devices, on a 3-DOF system on a fixed base, for an input ground motion x_G are:

$$m_3 \ddot{x}_3 + (k_3 + k_{R3})(x_3 - x_2) + k_{D3}(\dot{x}_3 - \dot{y}_3) + c_{D3}(\dot{x}_3 - \dot{y}_3) = -m_3 \ddot{x}_G \quad (2.1)$$

$$m_{D3} \ddot{y}_3 - k_{D3}(x_3 - y_3) - c_{D3}(\dot{x}_3 - \dot{y}_3) + k_{N3}(y_3 - x_2) = -m_{D3} \ddot{x}_G \quad (2.2)$$

$$m_2 \ddot{x}_2 - (k_3 + k_{R3})(x_3 - x_2) - k_{N3}(y_3 - x_2) + (k_2 + k_{R2})(x_2 - x_1) + k_{D2}(x_2 - y_2) + c_{D2}(\dot{x}_2 - \dot{y}_2) = -m_2 \ddot{x}_G \quad (2.3)$$

$$m_{D2} \ddot{y}_2 - k_{D2}(x_2 - y_2) - c_{D2}(\dot{x}_2 - \dot{y}_2) + k_{N2}(y_2 - x_2) = -m_{D2} \ddot{x}_G \quad (2.4)$$

$$m_1 \ddot{x}_1 - (k_2 + k_{R2})(x_2 - x_1) - k_{N2}(y_2 - y_1) + (k_1 + k_{R1})x_1 + k_{D1}(x_1 - y_1) + c_{D1}(\dot{x}_1 - \dot{y}_1) = -m_1 \ddot{x}_G \quad (2.5)$$

$$m_{D1} \ddot{y}_1 - k_{D1}(x_1 - y_1) - c_{D1}(\dot{x}_1 - \dot{y}_1) + k_{N1}y_1 = -m_{D1} \ddot{x}_G \quad (2.6)$$

Assuming a harmonic ground excitation in the form of:

$$\ddot{x}_G = -\omega^2 X_G e^{j\omega t} \quad (3)$$

And a steady state response of:

$$x_1(t) = X_1 e^{j\omega t}, \quad x_2(t) = X_2 e^{j\omega t}, \quad x_3(t) = X_3 e^{j\omega t} \quad (4.1)$$

$$y_1(t) = Y_1 e^{j\omega t}, \quad y_2(t) = Y_2 e^{j\omega t}, \quad y_3(t) = Y_3 e^{j\omega t} \quad (4.2)$$

Where X_{1-3} and Y_{1-3} denote the complex response amplitudes, the equations of motion (2.1-6) become:

$$[m_3 s^2 + k_3 + k_{R3} + k_{D3} + c_{D3}s]X_3 + [-k_3 - k_{R3}]X_2 + [-k_{D3} - c_{D3}s]Y_3 = m_3 \omega^2 X_G \quad (5.1)$$

$$[m_{D3} s^2 + k_{D3} + c_{D3}s + k_{N3}]Y_3 + [-k_{D3} - c_{D3}s]X_3 + [-k_{N3}]X_2 = m_{D3} \omega^2 X_G \quad (5.2)$$

$$[m_2 s^2 + k_3 + k_{R3} + k_{N3} + k_2 + k_{R2} + k_{D2} + c_{D2}s]X_2 + [-k_2 - k_{R2}]X_1 + [-k_3 - k_{R3}]X_3 + [-k_{N3}]Y_3 + [-k_{D2} - c_{D2}s]Y_2 = m_2 \omega^2 X_G \quad (5.3)$$

$$[m_{D2} s^2 + k_{D2} + c_{D2}s + k_{N2}]Y_2 + [-k_{D2} - c_{D2}s]X_2 + [-k_{N2}]X_1 = m_{D2} \omega^2 X_G \quad (5.4)$$

$$[m_1 s^2 + k_2 + k_{R2} + k_{N2} + k_1 + k_{R1} + k_{D1} + c_{D1}s]X_1 + [-k_2 - k_{R2}]X_2 + [-k_{N2}]Y_2 + [-k_{D1} - c_{D1}s]Y_1 = m_1 \omega^2 X_G \quad (5.5)$$

$$[m_{D1} s^2 + k_{D1} + c_{D1}s + k_{N1}]Y_1 + [-k_{D1} - c_{D1}s]X_1 = m_{D1} \omega^2 X_G \quad (5.6)$$

The damping matrix of the uncontrolled system, $[C_S]_{3 \times 3}$, is not explicitly known but is obtained with the help of Rayleigh's approach using same damping ratio in all modes. Then it is expanded in order to agree with the total Degrees of Freedom of the considered problem. The resulting Transfer Functions of the system for the relative response amplitudes X_3, X_2, X_1, Y_3, Y_2 and Y_1 for a ground motion x_G , are:

$$TF_{Ui} = \frac{[U]_{i,i}}{X_G} = \left[[H]^{-1} \omega^2 \begin{bmatrix} m_3 \\ m_{D3} \\ m_2 \\ m_{D2} \\ m_1 \\ m_{D1} \end{bmatrix} \right]_{(i,1)}, \quad i = 1-6 \quad (6)$$

Where:

$$[U]_{1,6} = [X_3 \quad Y_3 \quad X_2 \quad Y_2 \quad X_1 \quad Y_1]^T \quad (7.1)$$

$$H(1,1) = m_3 s^2 + k_3 + k_{R3} + k_{D3} + c_{D3} s + C_S(1,1) s \quad (7.2)$$

$$H(1,2) = H(2,1) = -k_{D3} - c_{D3} s \quad (7.3)$$

$$H(1,3) = H(3,1) = -k_3 - k_{R3} + C_S(1,2) s \quad (7.4)$$

$$H(2,2) = m_{D3} s^2 + k_{D3} + c_{D3} s + k_{N3} \quad (7.5)$$

$$H(2,3) = H(3,2) = -k_{N3} \quad (7.6)$$

$$H(3,3) = m_2 s^2 + k_3 + k_{R3} + k_{N3} + k_2 + k_{R2} + k_{D2} + c_{D2} s + C_S(2,2) s \quad (7.7)$$

$$H(3,4) = H(4,3) = -k_{D2} - c_{D2} s \quad (7.8)$$

$$H(3,5) = H(5,3) = -k_2 - k_{R2} + C_S(2,3) s \quad (7.9)$$

$$H(4,4) = m_{D2} s^2 + k_{D2} + c_{D2} s + k_{N2} \quad (7.10)$$

$$H(4,5) = H(5,4) = -k_{N2} \quad (7.11)$$

$$H(5,5) = m_1 s^2 + k_2 + k_{R2} + k_{N2} + k_1 + k_{R1} + k_{D1} + c_{D1} s + C_S(3,3) s \quad (7.12)$$

$$H(5,6) = H(6,5) = -k_{D1} - c_{D1} s \quad (7.13)$$

$$H(6,6) = m_{D1} s^2 + k_{D1} + c_{D1} s + k_{N1} \quad (7.14)$$

$$H(1,5) = H(5,1) = C_S(1,3) s \quad (7.15)$$

$$H(1,4) = H(4,1) = 0 \quad (7.16)$$

$$H(1,6) = H(6,1) = 0 \quad (7.17)$$

$$H(2,4-6) = H(4-6,2) = 0 \quad (7.18)$$

$$H(3-4,6) = H(6,3-4) = 0 \quad (7.19)$$

3 IMPLEMENTATION OF THE KDAMPER CONCEPT TO A 3-STOREY CONCRETE BUILDING STRUCTURE

A typical 3-storey concrete building structure as shown in Figure 2 (C20/25, $H_{floor} = 3.5$ m, $g_{tot} = 3.5$ kN/m², $q = 2.5$ kN/m²), is examined. The structure is considered fixed at its base. The seismic excitation are that of JMA (1995) and TABAS, as shown in Figure 3.

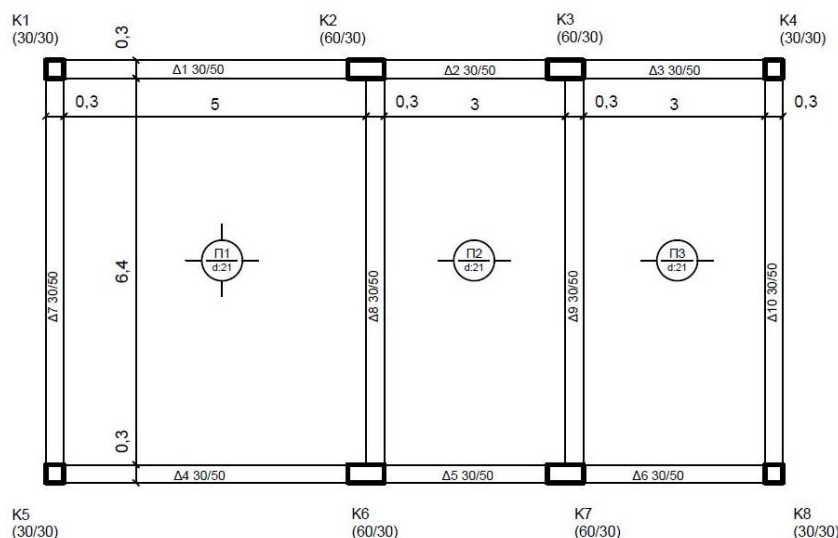


Figure 2. Ground floor plan of a typical floor of the structure

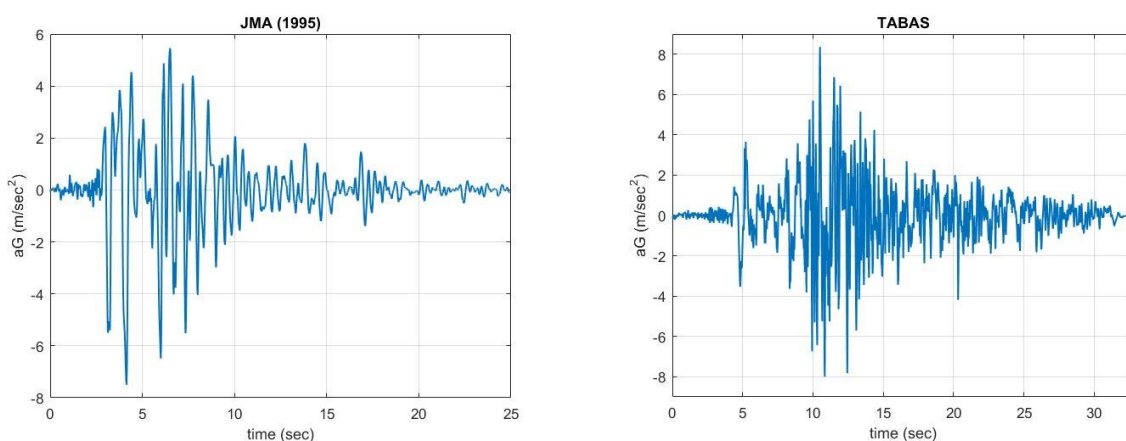


Figure 3. Seismic excitations of JMA (1995) and TABAS

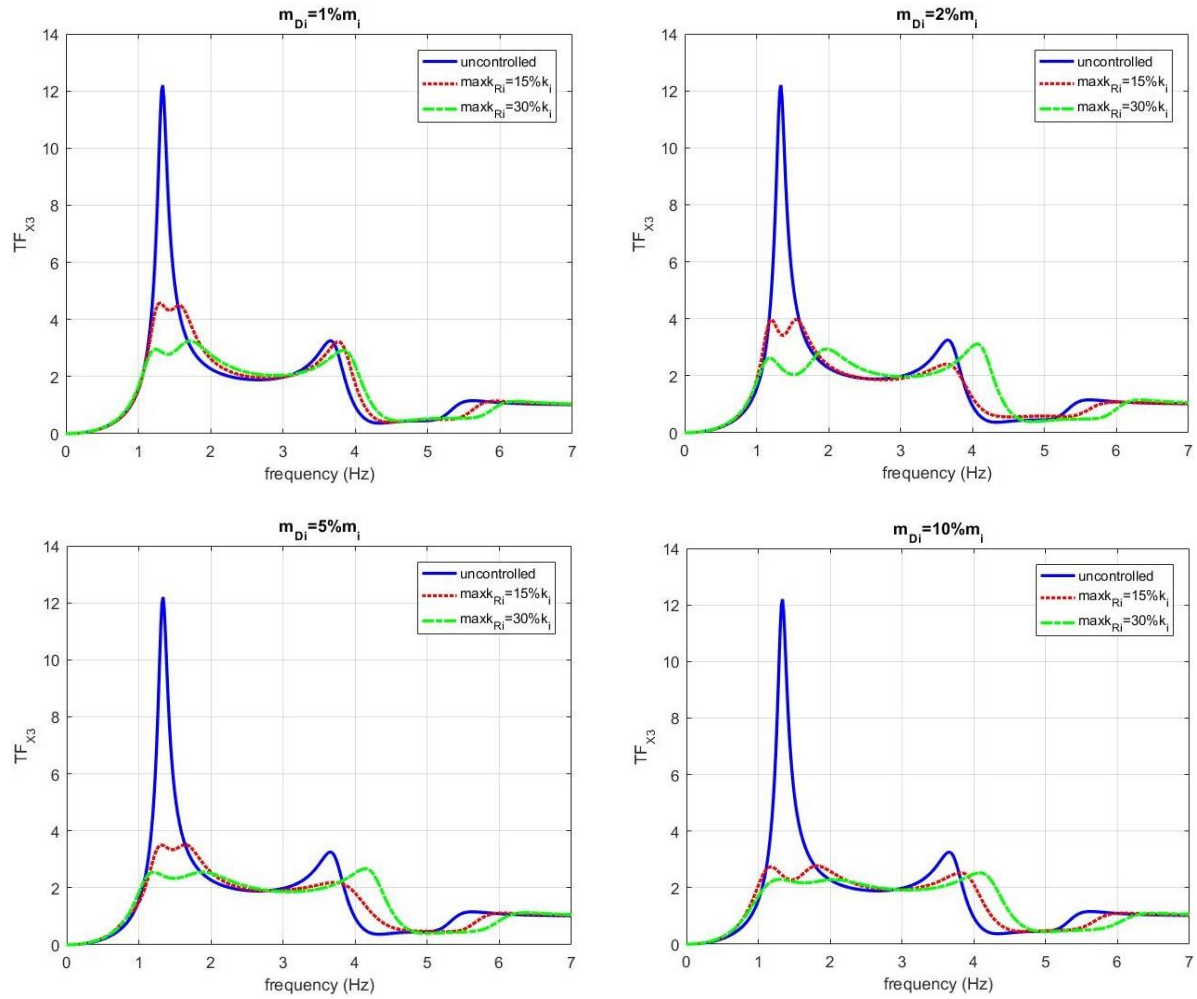
The KDamper devices are placed between each of the 3 floors of the structure as the optimum solution, with the sum of the addition masses of the devices to be equal to the 10% of the total mass of the system, and the stiffness elements and the damping coefficients are determined after optimization. Then in order to evaluate the utility of these devices, each time a KDamper is placed in each floor with the same mass as in the case of the 3 KDampers, to clarify the contribution of each devise to the total reduction of the Transfer Function and the displacement at the top of the structure. The systems parameters are:

Masses	$m_1 = m_2 = m_3 = 10.09 \text{ tn}$
X - stiffness	$k_{1,x} = k_{2,x} = k_{3,x} = 98616.91 \text{ kN / m}$
Y - stiffness	$k_{1,y} = k_{2,y} = k_{3,y} = 32872.3 \text{ kN / m}$

Table 1. System's parameters

3.1 Transfer Functions for the top floor displacement

In Figure 4 are the Transfer Functions for displacement of the 3rd floor, for a harmonic ground motion, by selecting a constant value for the additional equal masses of each of the 3 KDampers 1%, 2%, 5% and 10% respectively. The maximum values for the Transfer Functions are minimized with the proper selection of the dimensional parameters of the 3 KDampers, through optimization with the limitation that the additional stiffness are not more than 15% and 30%, as shown in Figure 4.

Figure 4. Transfer Function for the displacement of the 3rd floor

In Figure 5 are the Transfer Functions for 3 additional cases. This time the initial system is controlled by placing 1 KDamper in the 1st floor, 2nd floor and 3rd floor respectively. The additional mass of the KDamper is constant and equal to 10% of the floors mass and the maximum value of the additional stiffness is not more than 30%. Again the maximum values for the Transfer Functions are minimized with the proper selection of the parameters of the KDamper, through optimization.

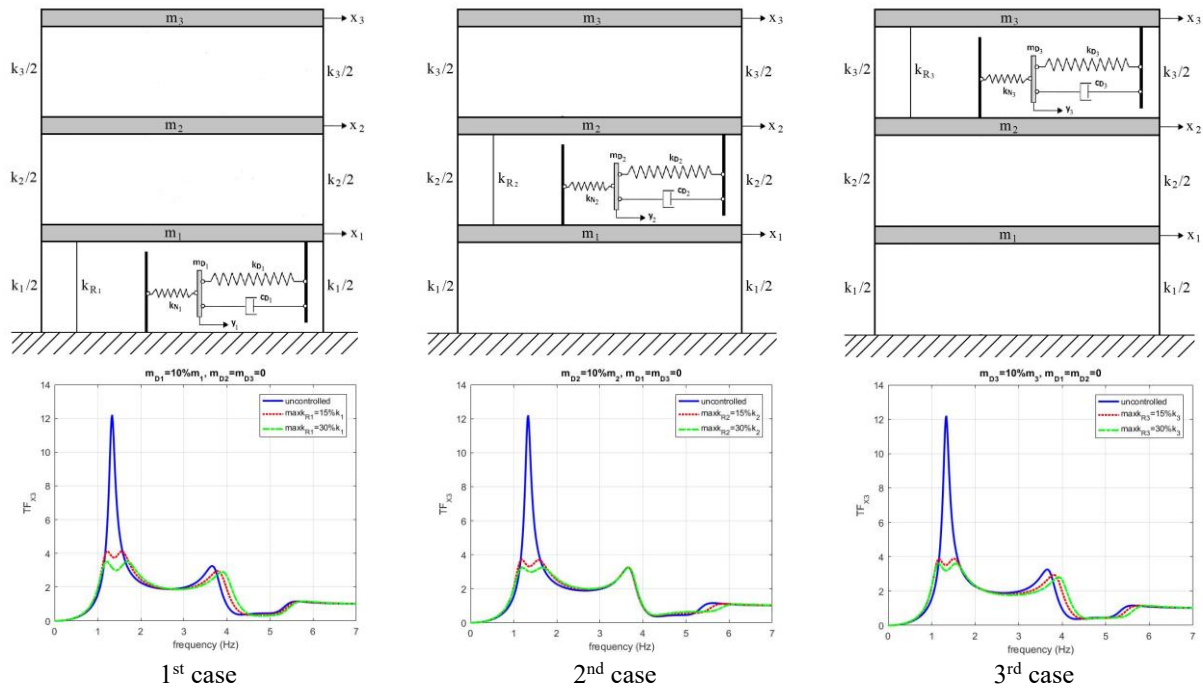


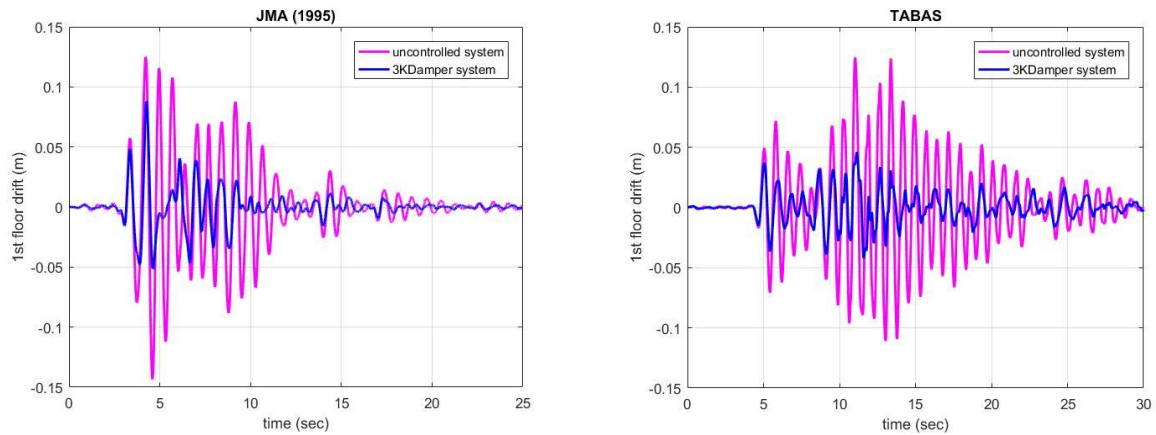
Figure 5. Transfer Function for 3 additional cases of placing 1KDamper instead of 3

3.2 Numerical Results

In Table 2 are the dimensional parameters each of the 3KDampers placed between each floor of the structure, for an additional mass of each device $m_{Di}=10\%m_i$, that are taken through optimization with the limitation that the additional stiffness of the structure is not more than 30%. The system is solved using the Newmark- β with linear acceleration. In Figure 6 the structure's dynamic response is presented in terms of the floor's displacements, for each of the considered excitations, which is the critical factor that determines the stresses of the structure.

#KDamper	k_{Ri} (kN/m)	k_{Di} (kN/m)	k_{Ni} (kN/m)	m_{Di} (tn)	c_{Di} (kNs/m)
KDamber1	9838.0	2827.54	-2196.3	10	83.0
KDamber2	9131.9	4238.14	-2894.7	10	77.8
KDamber3	7748.3	2646.31	-1972.6	10	71.5

Table 2: Dimensional parameters of the case of placing 3KDampers in between each floor



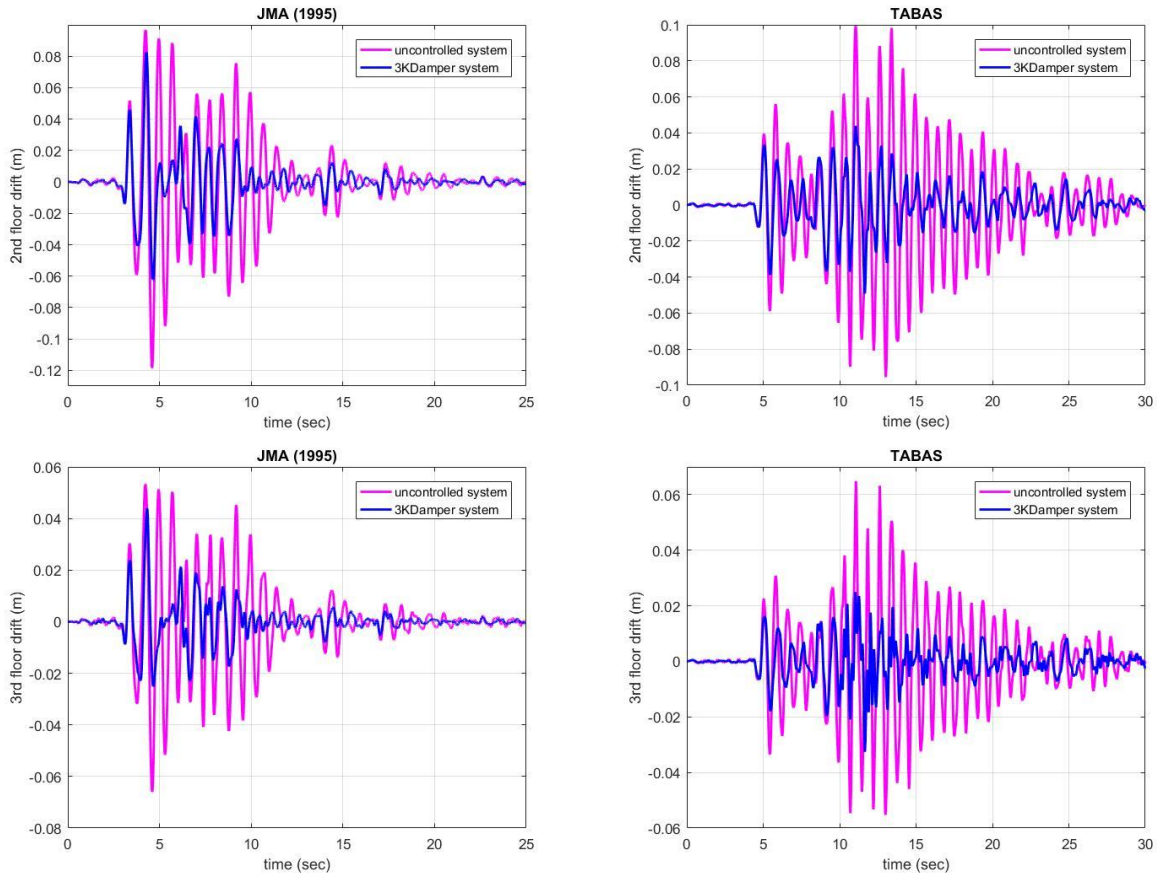


Figure 6. Comparative results between the initial and the isolated system, for the case of placing 3 KDampers between each floor with an additional mass $m_{Di}=10\%m_i$

Excitation	Initial system (m)		3KDamper system (m)		Reduction (%)	Reduction (%)
	JMA (1995)	TABAS	JMA (1995)	TABAS	JMA (1995)	TABAS
1 st floor drift	0.1434	0.1246	0.088	0.0461	38.6	63
2 nd floor drift	0.1186	0.0994	0.0826	0.0492	30.35	50.5
3 rd floor drift	0.066	0.0649	0.044	0.0326	33.33	49.77

Table 3: Dynamic response of the isolated system with 3KDampers

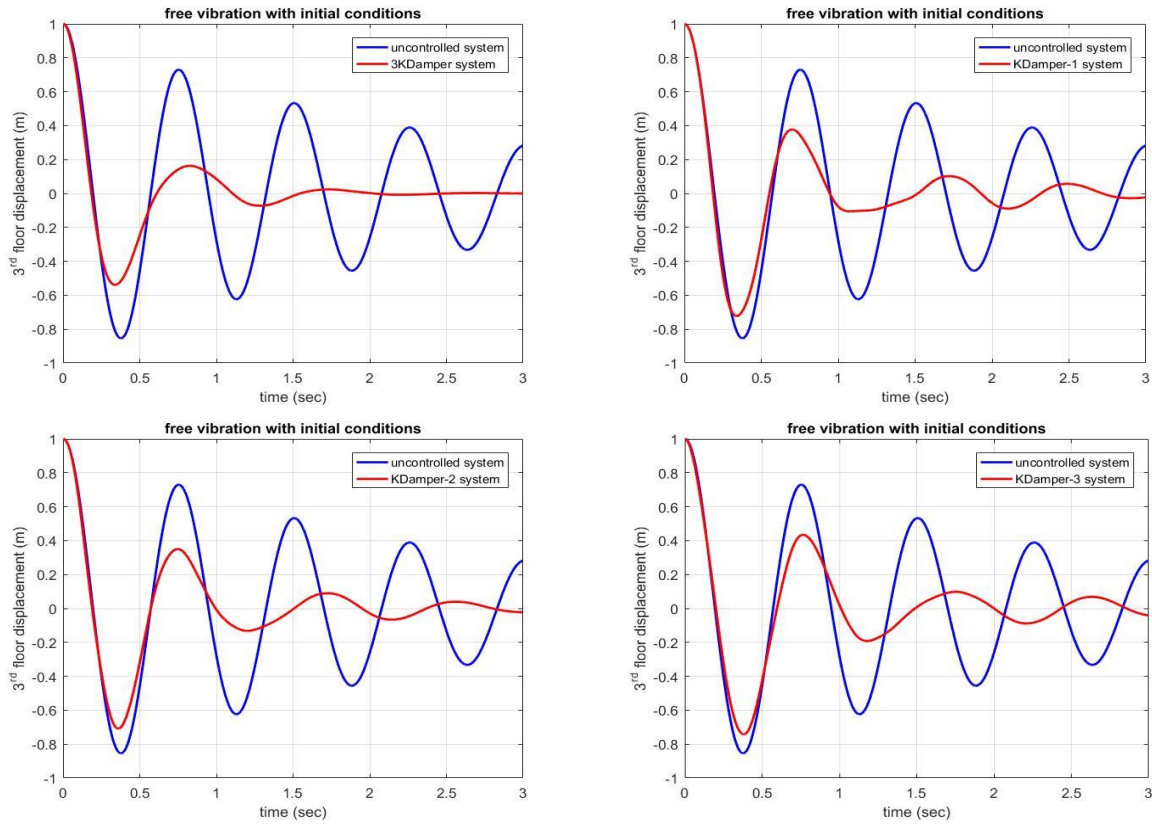
In Table 4 are the results for each of the 3 floor's drifts, for the 3 additional cases of the implementation of 1KDamper instead of 3. For each of the 3 cases the additional mass is equal to 10% of the floor's mass, that the KDamper is placed, and the maximum value that the additional stiffness can have is 30% of the initial stiffness k_i . In the case of KDamper-1, the KDamper is placed between the fixed base and the 1st floor, in the case of KDamper-2, the KDamper is placed between the 1st and 2nd floor and in the last additional case of KDamper-3, the devise is placed between the 3rd and the 2nd floor. Again the rest of the KDamper's parameters are taken through optimization.

Excitation	Initial system (m)		KDamper-1 system (m)		Reduction (%)	Reduction (%)
	JMA (1995)	TABAS	JMA (1995)	TABAS	JMA (1995)	TABAS
1 st floor drift	0.1434	0.1246	0.118	0.0764	17.7	38.68
2 nd floor drift	0.1186	0.0994	0.0801	0.0512	32.46	48.49
3 rd floor drift	0.066	0.0649	0.0446	0.0426	32.42	34.36

	Initial system (m)		KDamper-2 system (m)		Reduction (%)	Reduction (%)
Excitation	JMA (1995)	TABAS	JMA (1995)	TABAS	JMA (1995)	TABAS
1 st floor drift	0.1434	0.1246	0.1064	0.063	25.8	49.44
2 nd floor drift	0.1186	0.0994	0.0948	0.0572	20.07	42.45
3 rd floor drift	0.066	0.0649	0.0437	0.0351	33.79	45.92
	Initial system (m)		KDamper-3 system (m)		Reduction (%)	Reduction (%)
Excitation	JMA (1995)	TABAS	JMA (1995)	TABAS	JMA (1995)	TABAS
1 st floor drift	0.1434	0.1246	0.1098	0.0602	23.43	51.68
2 nd floor drift	0.1186	0.0994	0.0869	0.0548	26.73	44.87
3 rd floor drift	0.066	0.0649	0.0689	0.0543	-4.4	16.33

Table 4: Dynamic response for each of the 3 additional cases of placing 1KDamper

In order to calculate the exact value of the new damping ratio, the isolated system is subjected to a free vibration with initial conditions (Figure 7), that of the first modal eigenform of the uncontrolled system, and is calculated as in Equation 9, and the results are in Table 5.

Figure 7. 3rd floor's displacement for a free vibration with initial conditions

$$\ln \left[\frac{X_3(t)}{X_3(t+T)} \right] = \frac{2\pi\zeta}{\sqrt{1-\zeta^2}} \quad (9)$$

	Uncontrolled system	3KDamper system	KDamper-1 system	KDamper-2 system	KDamper-3 system
Damping ratio (%)	5	27.73	15.34	16.48	13.31

Table 5. New damping ratio of the isolated systems

4 CONCLUSIONS

The KDamper concept can provide a realistic option for seismic isolation of existing concrete building structures. The implementation of the 3KDamper devices as shown, has drastically reduced the dynamic response of the floor's drifts up to 63% and above 30% for the considered excitation, in all the floor's drifts and has improved the damping ratio to 27.73%

Furthermore, the implementation of only 1KDamper device with the same additional mass as an individual KDamper, in the 3KDampers concept, has shown remarkable results in the floor's drifts reaching 50% and in most cases more than 25%, offering high damping properties (around 15%) at the same time. It must be noted that in the last 3 additional cases only 1/3 of the total additional mass of the optimum solution is used.

Finally, the inherent non-linear nature of the negative stiffness force can be exploited to offer further potential advantages of the KDamper concept, such as robustness, broadband response and energy sinks.

5 ACKNOWLEDGMENTS

This research has been co-financed by the Operational Program "Human Resources Development Program, Education and Lifelong Learning" of the Action "Strengthening Human Resources Research Potential via Doctorate Research", of ESPA 2014-2020 with the co-financing of the European Social Fund – ESF and Greek National Funds.

REFERENCES

- [1] Antoniadis I., Chronopoulos D., Spitas V., Koulocheris D. (2015), "Hyper-damping properties of a stable linear oscillator with a negative stiffness element," *Journal of Sound and Vibration*, Vol. 346, pp. 37-52.
- [2] Carella A., Brennan M., Waters T. (2007), "Static analysis of a passive vibration isolator with quasi-zero-stiffness characteristic," *Journal Sound and Vibration*, Vol. 301, pp. 678-689.
- [3] Den Hartog J. P. (1956), *Mechanical Vibrations*, 4th ed., McGraw Hill.
- [4] Elias S., Matsagar V., Datta T. K. (2016), "Effectiveness of distributed tuned mass dampers for multi-mode control of chimney under earthquakes," *Engineering Structures*, Vol. 124.
- [5] Frahm H. (1909), "Device for Damping Vibrations of Bodies," *US patent #989958*.
- [6] Ibrahim R. (2008), "Recent advances in nonlinear passive vibration isolators," *Journal of Sound and Vibration*, Vol. 314, pp. 371–452.
- [7] Kapasakalis K., Sapountzakis E., Antoniadis I. (2017), "Implementation of the KDamper concept to wind turbine towers," *Proceedings of the 6th International Conference on Computational Methods in Structural Dynamics and Earthquake Engineering (COMPDYN)*, Rhodes Island, Greece, 15-17 June.
- [8] Molyneux W. (1957), "Supports for vibration isolation," ARC/CP-322, *Aeronautical Research Council*, Great Britain.
- [9] Platus D. L. (1999), "Negative-stiffness-mechanism vibration isolation systems," *SPIE's International Symposium on Optical Science, Engineering, and Instrumentation*, pp. 98–105.
- [10] Sapountzakis E., Syrimi P., Pantazis I., Antoniadis I. (2017), 'KDamper concept in seismic isolation of bridges with flexible piers,' *Engineering Structures*, Vol. 153, pp. 525-539.
- [11] Syrimi P., Sapountzakis E., Tsiatas G., Antoniadis I. (2017), "Parameter optimization of the KDamper concept in seismic isolation of bridges using harmony search algorithm," *Proceedings of the 6th International Conference on Computational Methods in Structural Dynamics and Earthquake Engineering (COMPDYN)*, Rhodes Island, Greece, 15-17 June.
- [12] Younespour A., Ghaffarzadeh H. (2015), "Structural active vibration control using active mass damper by block pulse functions," *Journal of Vibration and Control*, Vol. 21(14), pp. 2787–2795.

NUMERICAL AND ASYMPTOTIC SOLUTIONS OF AXISYMMETRIC POISEUILLE FLOWS OF YIELD STRESS FLUIDS WITH PRESSURE DEPENDENT RHEOLOGICAL PARAMETERS

Kostas D. Housiadas¹, Pandelitsa Panaseti², Iasonas Ioannou³ and Georgios C. Georgiou⁴

¹Department of Mathematics
University of the Aegean
Karlovasi, GR-832000, Greece
e-mail: housiada@aegean.gr

²Department of Mathematics and Statistics
University of Cyprus, Nicosia, CY-1678, Cyprus
e-mail: pandelitsa@hotmail.com

³Department of Mechanical and Process Engineering (D-MAVT)
ETH Zurich, Leonhardstrasse 21, LEE K, 8092 Zurich, Switzerland
e-mail: iasonasce@gmail.com

⁴Department of Mathematics and Statistics
University of Cyprus, Nicosia, CY-1678, Cyprus
e-mail: georgios@ucy.ac.cy; web page: <http://euclid.mas.ucy.ac.cy/~georgios/>

Keywords: Bingham flow; Poiseuille flow; Lubrication approximation; Pressure-dependent yield stress; Perturbation method; Pseudospectral method.

Abstract. *The lubrication flow of a Bingham plastic in long tubes of varying radius is modeled using the approach proposed by Fusi and Farina (Appl. Math. Comp. 320, 1-15 (2018)). Both the plastic viscosity and the yield stress are assumed to vary linearly with the total pressure. Under the lubrication approximation a final set of two highly non-linear ordinary differential equations with unknowns the total pressure and the shape (radius) of the yield surface are solved by using two different techniques. A pseudospectral numerical method utilizing Chebyshev orthogonal polynomials and an analytical perturbation method with the small parameter being the difference of the two dimensionless parameters which are introduced due to the pressure-dependence of the yield stress and the consistency index of the fluid. In the former, ten spectral coefficients are adequate to fully resolve the pressure and yield-surface profiles down to machine accuracy. In the latter, three terms in the perturbation expansions are found analytically, and then are suitably processed using techniques which accelerate the convergence of series. The agreement between the two techniques is excellent. The implications of the pressure-dependence of the material parameters and the applicability windows of the method are also discussed.*

1 INTRODUCTION

We consider the axisymmetric Poiseuille flow of a Bingham plastic with pressure-dependent rheological parameters. More specifically, we consider the flow in long horizontal tubes of yield-stress materials with pressure-dependent yield stress, $\tau_y^* = \tau_y^*(p^*)$, and plastic viscosity, $\mu^* = \mu^*(p^*)$, where p^* is the pressure. Hence, the constitutive equation can be written in tensorial form as follows:

$$\begin{cases} \dot{\gamma}^* = 0, & \tau^* \leq \tau_y^*(p^*) \\ \tau^* = \left[\frac{\tau_y^*(p^*)}{\dot{\gamma}^*} + \mu^*(p^*) \right] \dot{\gamma}^*, & \tau^* > \tau_y^*(p^*) \end{cases} \quad (1)$$

where τ^* is the viscous extra-stress tensor and $\dot{\gamma}^*$ is the rate-of-deformation tensor, $\dot{\gamma}^* = \nabla^* \mathbf{v}^* + (\nabla^* \mathbf{v}^*)^T$,

\mathbf{v}^* is the velocity vector, and $\dot{\gamma}^* \equiv \sqrt{\text{tr}(\dot{\boldsymbol{\gamma}}^* \cdot \dot{\boldsymbol{\gamma}}^*)/2}$ and $\tau^* \equiv \sqrt{\text{tr}(\boldsymbol{\tau}^* \cdot \boldsymbol{\tau}^*)/2}$ are the magnitudes of $\dot{\boldsymbol{\gamma}}^*$ and $\boldsymbol{\tau}^*$, respectively. Equation (1) is a generalization of the classical Bingham-plastic equation

The axisymmetric Poiseuille flow of a fluid obeying Eq. (1) is of interest in fluid transport in long tubes, where high pressures are required to drive the flow, e.g. in oil-drilling. Hermoso et al. reported experimental data at different pressures and temperatures for the rheological behavior of two oil-based drilling fluids, obeying the Bingham-plastic and the Herschel-Bulkley models [1] and employed the following linear equation [1]

$$\tau_y^*(p^*) = \tau_0^* [1 + \beta^*(p^* - p_0^*)] \quad (2)$$

where τ_0^* denotes the yield stress at a reference pressure p_0^* and β^* is the yield-stress growth coefficient. As for the plastic viscosity, Hermoso et al. (2014) used the Barus-type equation [2], a linearized version of which is

$$\mu^*(p^*) = \mu_0^* [1 + \alpha^*(p^* - p_0^*)] \quad (3)$$

where μ_0^* is the plastic viscosity at the reference pressure and $\alpha^* \geq 0$ is the plastic-viscosity growth coefficient.

Damianou and Georgiou [3] analyzed the plane Poiseuille flow of a Bingham plastic of material parameters obeying Eqs. (2) and (3), such that

$$\begin{aligned} \dot{\boldsymbol{\gamma}}^* &= \mathbf{0}, & \tau^* &\leq \tau_y^*(p^*) \\ \boldsymbol{\tau}^* &= 2 \left[\frac{\tau_0^* [1 + \beta^*(p^* - p_0^*)]}{\dot{\gamma}^*} + \mu_0^* [1 + \alpha^*(p^* - p_0^*)] \right] \dot{\boldsymbol{\gamma}}^*, & \tau^* &> \tau_y^*(p^*) \end{aligned} \quad (4)$$

and reported explicit analytical solutions for the velocity, the pressure, and the width of the central unyielded region, which is constant despite the pressure-dependence of the material parameters. In axisymmetric Poiseuille flow, however, the radius of the unyielded core is not constant in the general case. As pointed out in Ioannou and Georgiou [4], an analytical solution with a cylindrical unyielded region can be derived only when the growth coefficients α^* and β^* are equal, which is indeed a reasonable assumption for certain oil-drilling fluids.

Panaseti et al. [5] extended the lubrication-approximation method of Fusi et al. [6] to model the flow of a Herschel-Bulkley fluid in a symmetric long channel of varying width, under the assumption that both the consistency index and the yield stress vary linearly with pressure. In this method, the unyielded domain is modeled as an evolving non-material volume and by means of an integral formulation for the balance of linear momentum a single integro-differential equation is derived for the pressure. The yield surface and the two velocity components are then calculated from the pressure by means of closed form expressions. The main advantages of this method: (a) the yield surface, i.e. the interface between yielded ($\tau^* > \tau_y^*$) and unyielded ($\tau^* \leq \tau_y^*$) parts of the flow domain, is calculated exactly; and (b) the lubrication-approximation paradox is avoided and the correct shape of the yield surface, unlike other lubrication-approximation approaches [7].

Fusi and Farina [8] extended their method in [6] to time-dependent axisymmetric flows. In this geometry, the zero-order approximation leads to a system formed by an integral equation and an algebraic equation for the yield surface and for the plug velocity, respectively. Fusi and Farina [8] focused on the effects of oscillating walls on the flow. The objective of the present work is to study the steady-state axisymmetric Poiseuille flow of a Bingham plastic with pressure-dependent rheological parameters using the method of Fusi and Farina. We are interested in particular in the general case where the growth coefficients α^* and β^* are not equal and thus the unyielded core may be diverging or diverging depending on the relative values of these two parameters.

2 LUBRICATION APPROXIMATION

We consider the steady-state, pressure-driven flow of an incompressible Bingham plastic obeying constitutive equation (4) in a long tube of length L^* and constant radius R^* , as illustrated in Fig. 1. A uniform pressure p_{in}^* is applied at the inlet of the tube ($z^* = 0$) while the pressure at the exit plane ($z^* = L^*$) is $p_{out}^* < p_{in}^*$, i.e. the imposed pressure difference is $\Delta P^* = p_{in}^* - p_{out}^*$. Without loss of generality, we assume here that p_{out}^* is

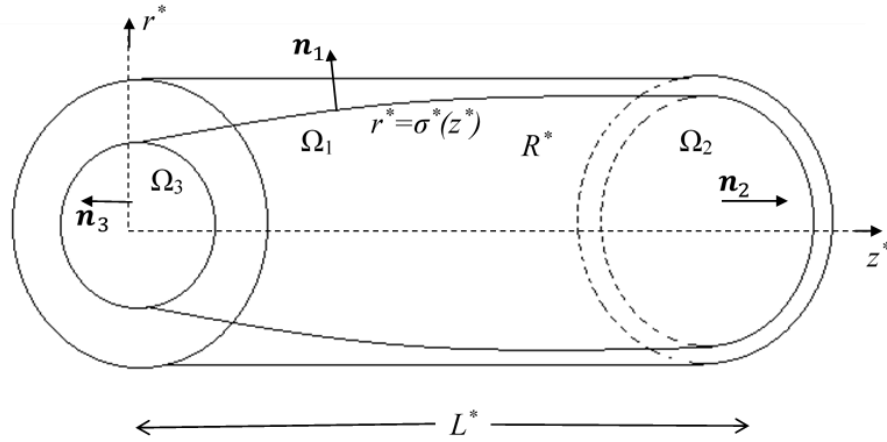


Figure 1. Schematic of the Poiseuille flow configuration showing the unyielded core and the coordinate system

equal to the reference pressure p_0^* that appears in Eq. (4), $p_0^* = p_{out}^*$. Assuming that the azimuthal velocity component is zero ($v_\theta^* = 0$) and the flow is axisymmetric (derivatives with respect to θ^* are zero), the velocity vector in cylindrical coordinates is of the form $\mathbf{v}^* = v_r^*(r^*, z^*)\mathbf{e}_r + v_z^*(r^*, z^*)\mathbf{e}_z$. In the flow of interest (see Fig. 1), the yielded and the unyielded regions are separated by the yield surface $r^* = \sigma^*(z^*)$ for $0 \leq z^* \leq L^*$ where $0 < \sigma^*(z^*) < R^*$. For brevity, we will use the symbols $\sigma_{in}^* \equiv \sigma^*(0)$ and $\sigma_{out}^* \equiv \sigma^*(L^*)$ hereafter.

The main idea in the method of Fusi et al. [5] is the use of the integral balance of linear momentum in the unyielded region $\Omega^* \equiv \{(z^*, r^*, \theta) : z^* \in [0, L^*], r^* \in [0, \sigma^*], \theta \in [0, 2\pi]\}$ which moves in the z -direction as a solid, i.e. at a constant axial velocity v_c^* . Therefore, in Ω^* :

$$v_z^* = v_c^* \quad \text{and} \quad v_r^* = v_\theta^* = 0 \quad \text{for} \quad 0 \leq r^* \leq \sigma^*(z^*) \quad (5)$$

Fusi et al. [5] showed that in the absence of body forces

$$2 \int_0^{L^*} \sigma^* \left[\left\{ -\sigma_z^* (-p^* + \tau_{zz}^*) + \tau_{rz}^* \right\} \right]_{r^* = \sigma^*(z^*)} dz + \sigma_{in}^{*2} p_{in}^* - \sigma_{out}^{*2} p_{out}^* = 0 \quad (6)$$

where $\sigma_z^* \equiv d\sigma^*/dz^*$.

The governing equations are rendered dimensionless by scaling z^* by L^* , r^* and σ^* by R^* , $(p^* - p_o^*)$ by $\tau_0^* L^* / R^*$, v_z^* by $\tau_0^* R^* / \mu_0^*$, v_r^* by $\tau_0^* R^{*2} / (L^* \mu_0^*)$, and the extra-stress components by τ_o^* . With these scales, the continuity equation and the two components of the momentum equation become:

$$\frac{1}{r} \frac{\partial(r v_r)}{\partial r} + \frac{\partial v_z}{\partial z} = 0 \quad (7)$$

$$\varepsilon Re \left(v_r \frac{\partial v_z}{\partial r} + v_z \frac{\partial v_r}{\partial z} \right) = -\frac{\partial p}{\partial z} + \frac{1}{r} \frac{\partial(r \tau_{rz})}{\partial r} + \varepsilon \frac{\partial \tau_{zz}}{\partial z} \quad (8)$$

$$\varepsilon^3 Re \left(v_r \frac{\partial v_r}{\partial r} + v_z \frac{\partial v_r}{\partial z} \right) = -\frac{\partial p}{\partial r} + \varepsilon \frac{\partial \tau_{rr}}{\partial r} + \varepsilon^2 \frac{\partial \tau_{rz}}{\partial z} + \varepsilon \frac{\tau_{rr} - \tau_{\theta\theta}}{r} \quad (9)$$

where

$$\varepsilon \equiv \frac{R^*}{L^*} \quad (10)$$

is the aspect ratio and

$$Re \equiv \frac{\rho^* R^{*2} \tau_0^*}{\mu_0^{*2}} \quad (11)$$

is the Reynolds number. The components of the dimensionless rate-of-deformation tensor are as follows:

$$\dot{\gamma}_{rr} = 2\varepsilon \frac{\partial v_r}{\partial r}, \quad \dot{\gamma}_{rz} = \frac{\partial v_z}{\partial r} + \varepsilon \frac{\partial v_r}{\partial z}, \quad \dot{\gamma}_{zz} = 2\varepsilon \frac{\partial v_z}{\partial z}, \quad \dot{\gamma}_{\theta\theta} = 2\varepsilon \frac{v_r}{r} \quad (12)$$

As for the non-zero components of the stress tensor we get

$$\begin{cases} \dot{\gamma}_{ij} = 0, & \tau \leq 1 + \beta p \\ \tau_{ij} = \left(\frac{1 + \beta p}{\dot{\gamma}} + 1 + \alpha p \right) \dot{\gamma}_{ij}, & \tau > 1 + \beta p, \quad ij = rr, rz, zz, \theta\theta \end{cases} \quad (13)$$

where

$$\alpha \equiv \frac{a^* \tau_o^* L^*}{R^*}, \quad \beta \equiv \frac{\beta^* \tau_o^* L^*}{R^*} \quad (14)$$

are the plastic-viscosity and yield-stress growth parameters,

$$\dot{\gamma} = \sqrt{2\varepsilon^2 \left[\left(\frac{\partial v_r}{\partial r} \right)^2 + \left(\frac{\partial v_z}{\partial z} \right)^2 + \left(\frac{v_r}{r} \right)^2 \right] + \left(\frac{\partial v_z}{\partial r} + \varepsilon \frac{\partial v_r}{\partial z} \right)^2} \quad (15)$$

and

$$\tau = \sqrt{\frac{1}{2} (\tau_{rr}^2 + \tau_{zz}^2 + \tau_{\theta\theta}^2) + \tau_{rz}^2} \quad (16)$$

The above equations hold in the yielded domain $D = \{(z, r, \theta) : 0 < z < 1, \sigma(z) < r < 1, 0 \leq \theta < 2\pi\}$. The dimensionless form of Eq. (6) is

$$2 \int_0^1 \sigma \left[\{-\sigma_z(-p + \varepsilon \tau_{zz}) + \tau_{rz}\} \right]_{r=\sigma(z)} dz + \sigma_{in}^2 p_{in} - \sigma_{out}^2 p_{out} = 0 \quad (17)$$

The system of Eqs. (7)-(9) and (17) is closed by appropriate boundary conditions. At the wall, no-slip and no-penetration conditions are imposed, i.e.

$$v_r = v_z = 0 \quad \text{at } r = 1, 0 \leq z \leq 1 \quad (18)$$

Along the yield surface, the unyielded constant core velocity is imposed:

$$v_r = 0, v_z = v_c \quad \text{at } r = \sigma(z), 0 \leq z \leq 1 \quad (19)$$

and all components of the rate-of-deformation tensor vanish:

$$\dot{\gamma}_{rr} = \dot{\gamma}_{rz} = \dot{\gamma}_{\theta\theta} = \dot{\gamma}_{zz} = 0 \quad \text{at } r = \sigma(z), 0 \leq z \leq 1 \quad (20)$$

Regarding the total pressure, this is zero at the exit of the tube ($z=1$), and equal to the dimensionless pressure difference driving the flow at the tube entrance ($z=0$):

$$p(r,0) = \Delta P, \quad p(r,1) = 0 \quad (21)$$

where $\Delta P \equiv (p_{in}^* - p_{out}^*)R^* / (L^* \tau_0^*)$.

In this work, the zero-order solution is derived and therefore the small parameter ε is set to zero. From the r-momentum equation it is deduced that the pressure depends only on z , i.e. $p = p(z)$, and so do the yield-stress τ_y and the viscosity μ . Integrating the z -momentum equation with respect to r , demanding that $\tau_{rz} = -\tau_y = -(1 + \beta p)$ at the yield surface, and applying the no-slip boundary condition at the wall, we obtain the following expression for the axial velocity component:

$$v_z(r,z) = \frac{p_z}{4(1+\alpha p)}(r^2 - 2\sigma^2 \ln r - 1) - \frac{1+\beta p}{1+\alpha p}(1 - r + \sigma \ln r) \quad (22)$$

Therefore, the constant velocity of the unyielded core is

$$v_c = v_z(\sigma, z) = \frac{p_z}{4(1+\alpha p)}(\sigma^2 - 2\sigma^2 \ln \sigma - 1) - \frac{1+\beta p}{1+\alpha p}(1 - \sigma + \sigma \ln \sigma) \quad (23)$$

As for the radial velocity component, this can be found by integration of the continuity equation with respect to r and applying the no-penetration boundary condition:

$$\begin{aligned} v_r(r,z) = & \frac{1}{16(1+\alpha p)} \left(p_{zz} - \frac{\alpha p_z^2}{1+\alpha p} \right) \frac{1}{r} \left[4\sigma^2 r^2 \ln r + (1-r^2)(1+r^2+2\sigma^2) \right] \\ & + \frac{(\alpha-\beta)}{12(1+\alpha p)^2} \frac{1}{r} \left[3(2-\sigma)(1-r^2) - 4(1-r^3) - 6\sigma r^2 \ln r \right] \end{aligned} \quad (24)$$

For the volumetric flow rate Q it is easily found that

$$Q = \frac{(\sigma-1)^2}{4[1+\sigma^2(2\ln\sigma-1)]} \left\{ (\sigma+1)^2 v_c + \frac{1+\beta p}{3(1+\alpha p)} \left[(1+2\sigma)(1-\sigma^2) + \sigma \ln \sigma (3+2\sigma+\sigma^2) \right] \right\} \quad (25)$$

Equations (23) and (25) constitute a system of two equations, the first of which is algebraic and the second is a first-order ordinary differential equation. The unknowns are the shape of the yield surface $\sigma = \sigma(z)$, the total pressure $p = p(z)$ and constants v_c and Q . Since, the ODE is of first order, only one boundary condition is required. Also, two additional auxiliary conditions are needed due to the presence of v_c and Q in the equations in order to derive a unique solution. Hence, the accompanying auxiliary conditions are:

$$p(0) = \Delta P, \quad p(1) = 0, \quad \int_0^1 \sigma \left(1 + \beta p + \frac{p_z \sigma}{2} \right) dz = 0 \quad (26)$$

The above system of equations is solved using two different methods, an analytical technique and a numerical method, which are presented in the following section.

3 METHODS OF SOLUTION

Before proceeding with the general solution of the system of Eqs. (23), (25) and (26), recall that an analytical solution of the general flow (without the use of the lubrication approximation) exists when the two growth coefficients α and β are equal [4]. This is also the case with the lubrication-approximation solution derived

above. Indeed, for $\beta = a > 0$, we find that the radial velocity vanishes and thus the radius of the unyielded core is constant while $v_z = v_z(r)$. More specifically,

$$\tilde{\sigma} = \frac{2a}{\ln(1+a\Delta P)}, \quad \tilde{v}_c = \frac{(\tilde{\sigma}-1)^2}{2\tilde{\sigma}}, \quad \tilde{Q} = \frac{1}{8\tilde{\sigma}} - \frac{1}{6} + \frac{\tilde{\sigma}^3}{24} \quad (27)$$

while the pressure and the velocity are given by:

$$\tilde{p} = \frac{(1+a\Delta P)^{1-z}-1}{a}, \quad \tilde{v}_z = (r-1)\left(1 - \frac{1+r}{2\tilde{\sigma}}\right), \quad \tilde{v}_r = 0 \quad (28)$$

Let us point out that the above solution is simply the first term of the Taylor expansion of the analytical solution derived by Ioannou and Georgiou [4] in terms of the aspect ratio ε . The critical pressure gradient, ΔP_c , below which no flow occurs can be found from Eq. (27) as the pressure at which $\tilde{\sigma} = 1$:

$$\Delta P_c = \frac{e^{2a}-1}{a} \quad (29)$$

For $\beta = a \rightarrow 0$, the critical pressure difference is $\Delta P_c = 2$. The above special solutions are the base state for the perturbation solution. Moreover, they are useful in testing the numerical method described below.

We solve the system of (23), (25) and (26) using a pseudospectral method with Chebyshev orthogonal polynomials. The method is standard and details can be found in any textbook on spectral methods (see for instance the book of Hesthaven et al. [9]). Briefly, first we map the dimensionless physical domain $[0,1]$ into the computational domain $[-1,1]$ by introducing a new independent variable y as $y = 2z - 1 \Leftrightarrow z = (1+y)/2$. Then, the pressure and the shape of yield surface are represented as:

$$p(y) = \sum_{k=0}^M \hat{p}_k T_k(y), \quad \sigma(y) = \sum_{k=0}^M \hat{\sigma}_k T_k(y) \quad (30)$$

where \hat{p}_k and $\hat{\sigma}_k$ are the spectral coefficients of p and σ , respectively, M is the total number of coefficients, and $T_k(y) \equiv \cos(k \cos^{-1}(y))$ are the Chebyshev polynomials. This representation generates $2M+2$ unknowns which, along with v_c and Q , require $2M+4$ equations. Since the governing equations are strongly non-linear, the computational domain is discretized in $M+1$ nodes and the discretized form of Eq. (23) at all nodes except from the first one, the discretized form of Eq. (25) at all nodes, and the three auxiliary conditions of Eq. (26), provide $2M+4$ algebraic equations. This system of non-linear equations is solved using a Newton iterative scheme with an absolute convergence criterion 10^{-12} . The values of M were chosen in the range between 8 and 14 (depending on the magnitude of the parameters); in all cases both p and σ were resolved down to machine accuracy. Before presenting the results, however, we also describe a perturbation method which allows the derivation of an asymptotic solution of the system of interest.

In order to find an approximate analytical solution of the flow, a perturbation method is employed with the small parameter being the difference between the two growth parameters $\delta \equiv \beta - a$. Then all unknown variables are expanded in standard power series in terms of δ :

$$\chi = \chi_0 + \delta \chi_1 + \delta^2 \chi_2 + \dots \quad \text{as } \delta \rightarrow 0, \quad \text{where } \chi = p, \sigma, v_c, Q \quad (31)$$

The zero-order terms have been already derived above; these are given by Eqs. (27) and (28) for $a = \beta > 0$:

$$p_0 = \tilde{p}, \quad \sigma_0 = \tilde{\sigma}, \quad v_{c0} = \tilde{v}_c, \quad Q_0 = \tilde{Q} \quad (32)$$

Substituting expressions (31) and (32) into Eqs. (23), (25) and (26), expanding all quantities suitably, and collecting all terms of the same powers in δ , results in sequence of perturbation problems. We solve analytically

the equations at $O(\delta)$ and $O(\delta^2)$. Hence, the asymptotic solution for all variables is found in series form with three terms:

$$\chi_{\text{asym}} = \tilde{\chi} + \delta \chi_1 + \delta^2 \chi_2, \quad \chi = p, \sigma, v_c, Q \quad (33)$$

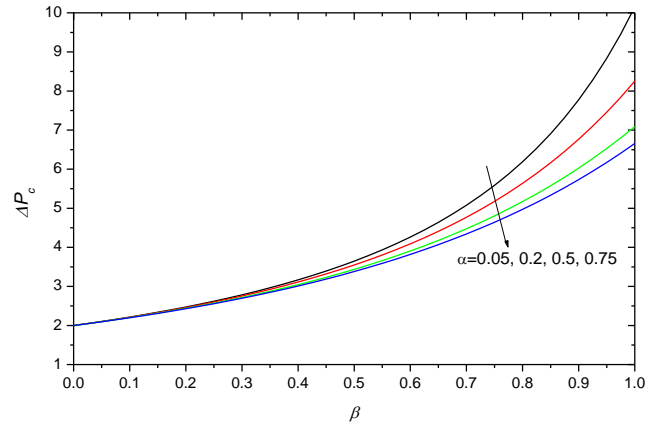
However, the analytical solutions at first and second order in δ are too long to be given here. Thus, expressions (33) are mainly used to check and validate the numerical results. In fact, these approximate solutions can also be processed further using series-convergence acceleration techniques, such as Shanks' non-linear transformation [10].

First, we verified the correctness of the pseudospectral method by comparing the numerical results with the analytical solution given by Eqs. (27) and (28). As a test-case we set $\Delta P = 30$ and $a = \beta = 0.1, 0.15$ and 0.2 . In all cases, the calculated solutions with $M=10$ were accurate up to 10 significant digits. As a second test-case, we set $a = 0.1$, $\beta = 0.15$, and $\Delta P = 30$ to run the pseudospectral code and get the numerical results χ_{num} ; both the pressure and the yield surface were resolved down to machine accuracy using only $M=12$ spectral coefficients. This indicates that for typical values of the dimensionless parameters the maximum accuracy for all variables is achieved with the pseudospectral code.

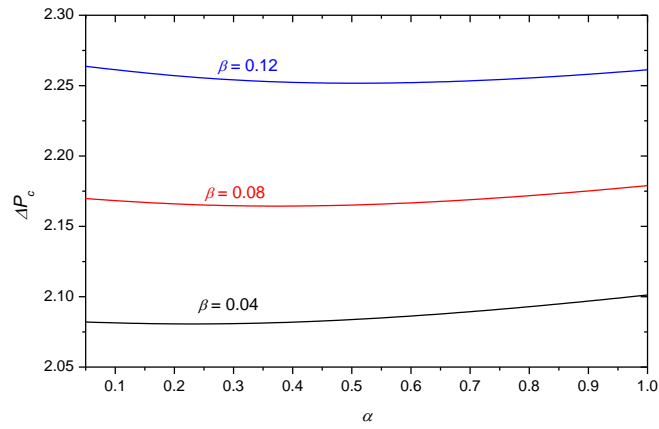
4 RESULTS AND DISCUSSION

In the previous section, the critical pressure difference ΔP_c has been derived analytically for the special case where $a = \beta$. Obtaining an analytical expression of ΔP_c when $a \neq \beta$ is out of the question. This is thus determined either numerically or asymptotically. Representative results are provided in Fig. 2. It should be noted that in the range of the parameters for which the asymptotic series solution is physically admissible, the agreement between the asymptotic and numerical solutions is excellent. Figure 2a shows ΔP_c versus the yield-stress growth parameter β for various values of the plastic-viscosity growth parameter. In Figs. 2b and 2c, ΔP_c is plotted versus a for various values of β . The growth parameters a, β should be considered small, but in order to exaggerate the changes and the effects of the parameters, we also use a, β values as large as unity. We observe that ΔP_c increases monotonically with β for all values of a . This is expected, since the yield stress increases with β (recall that $0 \leq p \leq \Delta P$). If now β is fixed, an increase in a enhances the plastic viscosity of the fluid. Even though intuitively the critical pressure difference for a more viscous fluid is expected to be higher, this is not true at high values of β . For fixed values of β higher than 0.3, ΔP_c decreases with a . The effect of a on ΔP_c is more clearly illustrated seen in Figs. 2b and 2c, where results for low and high values of β are presented. In the former case (Fig. 2b), the dependence of ΔP_c on a is weak and ΔP_c passes through a minimum. At higher values of β the variation of ΔP_c with a becomes more significant and the minimum is shifted farther to the right so that ΔP_c appears to decrease monotonically in the range of interest.

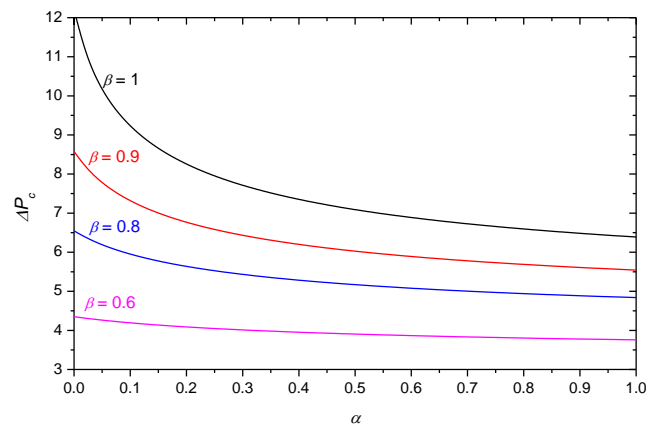
Finally, in Figure 3 we plotted the yield surfaces for various values of the applied pressure difference, starting from $\Delta P \approx \Delta P_c$ (which of course gives a uniform shape of the yield surface $\sigma \approx 1$) and increasing ΔP in order to obtain a yield surface as close as possible to the axis of the symmetry of the tube. First, in Fig. 3a, the results are presented for $a = \beta = 0$ for which $\Delta P_c = 2$; in this case $\sigma = 2 / \Delta P = \text{constant}$. In Fig. 3b, results are shown for $a = 0.2, \beta = 0$, i.e. for a fluid with constant yield stress, for which $\Delta P_c = 2$ too. Since $\beta < a$, the radius of the unyielded core is decreasing downstream. In Fig. 3c, the plastic viscosity is constant, i.e. $a = 0$, while the yield stress varies with the pressure with $\beta = 0.2$; these parameters give $\Delta P_c \approx 2.48$. Since $\beta > a$, the radius of the unyielded core is increasing downstream.



(a)

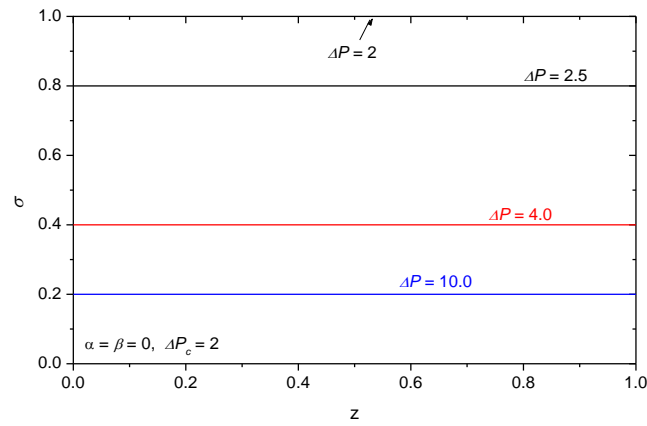


(b)

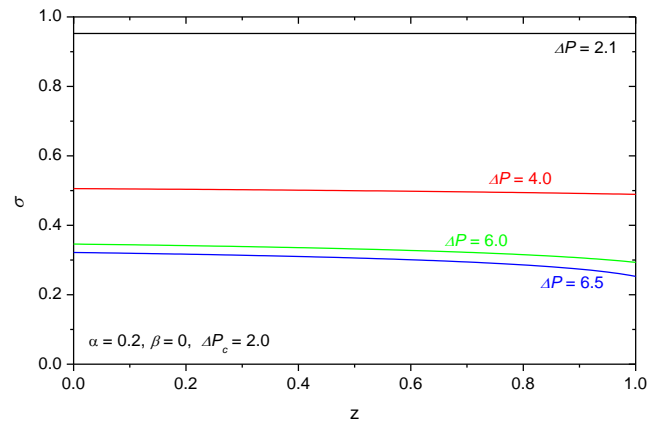


(c)

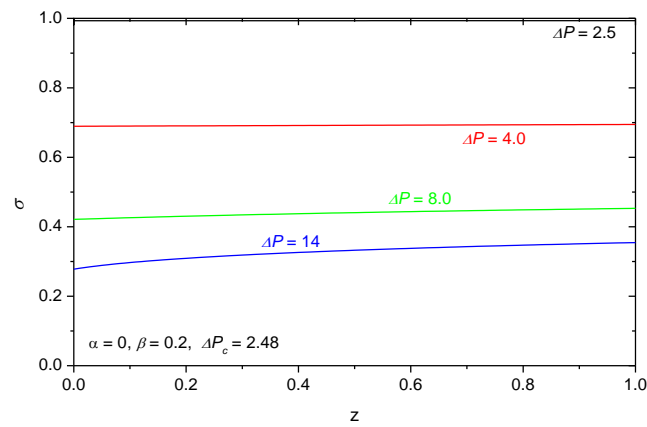
Figure 2. Critical pressure difference for flow to occur: (a) effect of β for various values of α ; (b) effect of α for low values of β ; (c) effect of α for high values of β



(a)



(b)



(c)

Figure 3. The shape of the yield surface for various values of the imposed pressure difference ΔP : (a) $\alpha=\beta=0$; (b) $\alpha=0.2, \beta=0$; (c) $\alpha=0, \beta=0.2$

5 CONCLUSIONS

The axisymmetric Poiseuille flow of a Bingham plastic with pressure dependent rheological parameters has been studied using the lubrication-approximation method of Fusi and Farina (2018), which has the advantage of predicting the correct shape of the yield surface at zero order. Both the plastic viscosity and the yield surface have been assumed to vary linearly with the pressure, thus attaining higher values upstream. The perturbation method leads to explicit expressions for the two velocity components in terms of the radius of the unyielded core $\sigma(z)$ and the pressure distribution $p(z)$. These two variables are calculated by solving a system of a first-order ODE and an algebraic equation. This is solved both numerically using a pseudospectral method and by means of simple perturbation method which allows the derivation of some asymptotic results. It is also solved analytically for the special case where the yield-stress growth parameter β is equal to the plastic-viscosity growth parameter α . The effects of these two parameters on the critical pressure ΔP_c required to drive the flow have been studied. While it increases monotonically with β for any value of α , ΔP_c decreases with the plastic-viscosity growth coefficient α at least initially. When β is low, this reduction is weak and ΔP_c passes through a minimum, and then starts increasing with α ; for higher values of β , ΔP_c appears to decrease monotonically for the wide range of values considered and the initial reduction is more pronounced. It has also been demonstrated that the shape of the central unyielded core depends on the relative values of α and β . This is converging when $\beta < \alpha$, diverging when $\beta > \alpha$, and cylindrical when $\beta = \alpha$.

The method of Fusi and Farina (2018), exploited here in order to tackle steady-state viscoplastic flow in a cylindrical tube, is more general and can be applied to tubes of non-constant radius, e.g. converging or diverging tubes, or tubes with a stenosis, or even with oscillating walls. We are thus planning to extend the present work to flows more relevant to industrial applications.

REFERENCES

- [1] Hermoso, J., Martinez-Boza, F. and Gallegos, C. (2014), "Combined effect of pressure and temperature on the viscous behaviour of all-oil drilling fluids," *Oil & Gas Science and Technology - Rev. IFP energies nouvelles*, Vol. 69, pp. 1283-1296.
- [2] Barus, C. (1893) "Isothermals, isopiestic and isometrics relative to viscosity," *Amer. J. Sci.*, Vol. 45, pp. 87-96.
- [3] Damianou, Y. and Georgiou, G.C. (2017) "On poiseuille flows of a Bingham plastic with pressure-dependent rheological parameters," *J. Non-Newtonian Fluid Mech.*, Vol. 250, pp. 1-7.
- [4] Ioannou, I. and Georgiou, G.C. (2018) "Axisymmetric Poiseuille flow of a Bingham plastic with rheological parameters varying linearly with pressure," *J. non-Newtonian Fluid Mech.*, submitted.
- [5] Panaseti, P., Damianou, Y., Georgiou, G.C. and Housiadas, K.D. (2018) "Pressure-driven flow of a Herschel-Bulkley fluid with pressure-dependent rheological parameters," *Physics of Fluids*, Vol. 30, 030701.
- [6] Fusi, L., Farina, A., Ross, F. and Roscani, S. (2015) "Pressure-driven lubrication flow of a Bingham fluid in a channel: a novel approach," *J. Non-Newtonian Fluid Mech.*, Vol. 221, pp. 66-75.
- [7] Frigarrad, I.A. and Ryan, D.P. (2004) "Flow of a visco-plastic fluid in a channel of slowly varying width," *J. Non-Newtonian Fluid Mech.*, Vol. 123, pp. 67-83.
- [8] Fuis, L. and Farina, A. (2018), "Peristaltic axisymmetric flow of a Bingham plastic," *Appl. Math. Comp.*, Vol. 320, pp. 1-15.
- [9] Hesthaven, J.S. Gottlieb, S. and Gottlieb, D. (2007), *Spectral methods for time-dependent problems*, Cambridge University Press, Cambridge.
- [10] Shanks, D. (1955) "Non-linear transformations of divergent and slowly convergent sequences," *J. Math. and Phys.*, Vol. 34, pp. 1-42.
- [11] Kalogirou, A., Poyiadji, S. and Georgiou, G.C. (2011) "Incompressible Poiseuille flows of Newtonian liquids with pressure-dependent viscosity," *J. Non-Newtonian Fluid Mech.*, Vol. 166, pp. 413-419.
- [12] Housiadas K.D. (2015), "An exact analytical solution for viscoelastic fluids with pressure-dependent viscosity," *J. Non-Newtonian Fluid Mech.*, Vol. 223, pp. 147-156.

RAREFIED PULSATILE PRESSURE-DRIVEN FULLY-DEVELOPED GAS FLOW IN LONG CIRCULAR TUBES

Alexandros Tsimpoukis and Dimitris Valougeorgis

Laboratory of Transport Phenomena, Department of Mechanical Engineering
University of Thessaly
Volos, 38334, Greece

e-mail: atsimpoukis@mie.uth.gr; e-mail: diva@mie.uth.gr

Keywords: Pulsatile flows, Oscillatory flows, Knudsen number, BGK, Richardson effect.

Abstract. *The pulsatile pressure driven fully-developed flow of a rarefied gas through a long circular tube is investigated, based on the time-dependent linear BGK equation, by decomposing the flow into its steady and oscillatory parts. As the oscillation frequency is increased the amplitude of all macroscopic quantities is decreased, while their phase lag with respect to the pressure gradient is increased reaching the limiting value of 90° . As the gas becomes more rarefied higher frequencies are needed to trigger this behavior. The computation of the inertia and viscous forces in terms of the gas rarefaction and oscillation parameters, clarifies when the flow consists of only one oscillating viscous region or of two regions, namely the inviscid piston flow in the core and the oscillating Stokes layer at the wall with the velocity overshooting. The maximum value of the time average oscillatory pumping power is one half of the corresponding steady one.*

1 INTRODUCTION

Time-dependent vacuum gas flows are strongly related to gas distribution systems of fusion reactors, consisting of channels with different lengths and cross sections. The flow in such pipe networks varies from the free molecular regime up to the hydrodynamic limit or in the whole range of the Knudsen number. Depending on the vacuum pumping system, the driving pumps and the operating conditions, phenomena related to oscillatory gas flow may produce enhanced counter flow of gas [1,2]. The detailed investigation of the pulsatile and oscillatory motion of gases in the whole range of the Knudsen number is important to avoid such harmful phenomena and to compute the associated energy losses.

In the hydrodynamic (or viscous) regime, pulsatile and oscillatory pressure-driven fully-developed flows, through channels of various cross sections have received, over the years, considerable attention [3-6]. In the slip, transition and free molecular regimes however, where in addition to the oscillation frequency, the level of gas rarefaction plays a significant role in the flow properties and patterns, the corresponding work in rarefied pulsatile gas flows is very limited. In the slip regime, the oscillatory flow in rectangular channels has been solved in [7], based on the unsteady Stokes equation subject to slip boundary conditions. Of course, continuum-based models are valid provided that both the mean free path and time are much smaller than the characteristic channel size and the pressure gradient oscillation time respectively. Therefore, in the transition and free molecular regimes the flow must be modeled by kinetic theory based on the Boltzmann equation or reliable kinetic model equations [8].

In this framework, very recently, the rarefied oscillatory flow in a cylindrical tube has been simulated, based on the linearized BGK equation, with the assumption of small oscillatory pressure gradient amplitude [9]. Here, the analysis is extended to pulsatile flows in circular tubes and computational results are provided for the flow rate, the wall shear stress and the pumping power as well as for the acting inertia and viscous forces.

2 FLOW CONFIGURATION AND DEFINITION OF MACROSCOPIC QUANTITIES

Consider the time-dependent isothermal flow of a monatomic rarefied gas through an infinite long circular tube of radius R . The flow is caused by a pulsatile pressure gradient that consists of a constant part that does not vary in time and that produces a steady flow forward, plus an oscillatory part, with the oscillation frequency ω , that moves the fluid back and forth and that produces zero net flow over each cycle [9].

The main flow quantities of the pulsatile flow are introduced first in dimensional and then, in dimensionless form. The local pulsatile pressure gradient depends on the flow direction z' and time t' . It may be written as

$$\frac{d\hat{P}_{PUL}(t', z')}{dz'} = \frac{dP_S(z')}{dz'} + \frac{d\hat{P}(z', t')}{dz'} = \frac{dP_S(z')}{dz'} + \frac{dP(z')}{dz'} \cos(\omega t') = \frac{dP_S(z')}{dz'} + \frac{dP(z')}{dz'} \mathbb{R}[\exp(-i\omega t')] \quad (1)$$

where $d\hat{P}_{PUL}/dz'$, dP_S/dz' and $d\hat{P}/dz'$ refer to the pulsatile, steady and oscillatory pressure gradients, $dP(z')/dz'$ is the amplitude of the oscillating pressure gradient, while \mathbb{R} denotes the real part of a complex expression, with $i = \sqrt{-1}$. It is evident that the time average over one period of the pressure gradient of the oscillatory flow is zero, while of the pulsatile flow is different than zero and equal to the steady pressure gradient. Due to the linearity of Eq. (1), the steady and oscillatory parts of the pulsatile fully-developed flow can be solved independently of each other. This is a useful breakdown, because the steady part of the flow has already been solved in [8] and therefore, only the oscillatory part remains for investigation.

The pulsatile pressure gradient generates a gas flow in the z' -direction, which is characterized by its pulsatile velocity and shear stress distributions given by

$$\hat{U}_{PUL}(t', r') = U_S(r') + \hat{U}(t', r') = U_S(r') + \mathbb{R}[U(r') \exp(-i\omega t')] \quad (2)$$

$$\hat{\Pi}_{PUL}(t', r') = \Pi_S(r') + \hat{\Pi}(t', r') = \Pi_S(r') + \mathbb{R}[\Pi(r') \exp(-i\omega t')], \quad (3)$$

respectively. The superscript $\hat{}$ always denotes time-dependent quantities. The complex functions $U(r')$ and $\Pi(r')$ completely determine the oscillatory pressure driven flow. Integrating the velocity over the cross section the mean velocity and wall shear stress are defined:

$$\bar{\hat{U}}_{PUL}(t') = \frac{1}{A'} \iint_{A'} \hat{U}_{PUL}(t', r') dA' = \bar{U}_S + \bar{\hat{U}}(t') = \bar{U}_S + \mathbb{R}[\bar{U} \exp(-i\omega t')] \quad (4)$$

$$\hat{\Pi}_{PUL,W}(t') = \int_{\Gamma'} \hat{\Pi}_{PUL}(t', r') d\Gamma' = \Pi_{S,W} + \hat{\Pi}_W(t') = \Pi_{S,W} + \mathbb{R}[\Pi_W \exp(-i\omega t')] \quad (5)$$

The quantities with the subscript “S” always denote the steady part, while \bar{U} and Π_W are complex and related to the oscillatory part.

Furthermore, the pulsatile mass flow rate is defined as

$$\hat{\dot{M}}_{PUL}(t') = \iint_{A'} \rho(t', z') \hat{U}_{PUL}(t', r') dA' = \dot{M}_S + \dot{\hat{M}}(t') = \dot{M}_S + \mathbb{R}[\dot{M} \exp(-i\omega t')] \quad (6)$$

where \dot{M}_S and $\dot{\hat{M}}(t')$ denote the steady and oscillatory mass flow rates, while the mass density $\rho = \rho(t', z')$ varies in time and in the axial direction (it is constant at each cross section) and it is defined by the equation of state once the operating pressure and temperature are specified.

Next, based on the mean velocity and wall shear stress, the inertia (or acceleration) $\hat{F}'_I(t')$ and viscous $\hat{F}'_V(t')$ forces acting on a fluid volume $A' dz'$ passing through the channel are given by

$$\hat{F}'_{PUL,I}(t') = \rho dz' A' \frac{\partial \bar{\hat{U}}_{PUL}(t')}{\partial t'} = \rho dz' A' \frac{\partial \bar{\hat{U}}(t')}{\partial t'} = \hat{F}'_I(t') \quad (7)$$

and

$$\hat{F}'_{PUL,V}(t') = F'_{S,V} + \hat{F}'_V(t') = dz' \Gamma' (\Pi_{S,W} + \hat{\Pi}_W(t')). \quad (8)$$

As expected the inertia force is related only to the oscillatory part, while the viscous force has both steady and oscillatory parts. At any point in time, the driving pressure force

$$\hat{F}'_{PUL,P}(t') = F'_{S,P} + \hat{F}'_P(t') = A'dP_S + A'd\hat{P}(t') \quad (9)$$

must equal the net sum of the viscous and inertia forces that may add or subtract from each other at different times within the oscillatory cycle. Then, the following steady and oscillatory force balances are formed:

$$\text{Steady: } A'dP_S = dz'\Gamma'\Pi_{S,W} \quad (10)$$

$$\text{Oscillatory: } A'd\hat{P}(t') = \rho dz'A' \frac{\partial \bar{\hat{U}}(t')}{\partial t'} + dz'\Gamma'\hat{\Pi}_W(t') \quad (11)$$

It is noted that due to the fully-developed flow there is no net momentum flux.

Finally, the pumping power needed to drive the pulsatile flow is defined as $\hat{E}'_{PUL}(t') = E'_S + \hat{E}'(t')$, where the steady the oscillatory pumping powers are given by the product of the corresponding acting pressure forces times the mean velocities written as $E'_S = A'dP_S\bar{U}_S$ and

$$\hat{E}'(t') = A'd\hat{P}(t')\bar{U}(t') = A'dP \cos(\omega t') \Re[\bar{U} \exp(-i\omega t')] \quad (12)$$

respectively. Since the oscillatory part $\hat{E}'(t')$ does not produce any net flow forward and since the steady part E'_S is the same as that in steady flow, any power expenditure on the oscillatory part of the flow reduces the efficiency of the flow. It is noted that the integral of the oscillatory pumping power over one cycle is nonzero, hence oscillatory flow requires energy to maintain even the net flow is zero.

The parameters which define the problem in dimensional form include the gas properties, the operating pressure and temperature, the channel geometry and the oscillation frequency. They are significantly reduced by introducing the corresponding quantities in dimensionless form, allowing in parallel, a more detailed flow investigation.

The two dimensionless flow parameters defining the present pulsatile flow are specified [9]. The first one is the gas rarefaction parameter δ and it is given by $\delta = \frac{PR}{\mu\nu}$, where μ is the gas viscosity at some reference temperature T and $\nu = \sqrt{2R_g T}$ is the most probable molecular speed (R_g is the gas constant). The rarefaction parameter is proportional to the inverse Knudsen number. The second one is the frequency parameter θ and it is given by $\theta = \frac{P}{\mu\omega}$, where (P/μ) is the intermolecular collision frequency and ω the oscillation frequency. Hence, small and large values of θ correspond to high and low pressure gradient oscillation respectively. As $\theta \rightarrow \infty$, the oscillatory part of the flow diminishes. When both $\delta \gg 1$ and $\theta \gg 1$, the flow is in the hydrodynamic or slip regimes.

Also, the dimensionless independent space and time variables $r = r'/R$, $z = z'/R$ and $t = t'\omega$, are introduced. The dimensionless area and perimeter of the tube cross section are defined by $A = A'/R^2$ and $\Gamma = \Gamma'/R$ respectively, while $\Gamma/A = 2$. The dimensionless amplitude of the oscillatory pressure gradient is

$$X = \frac{R}{P(z')} \frac{dP(z')}{dz'} = \frac{1}{P(z)} \frac{dP(z)}{dz}, \quad (13)$$

with $X \ll 1$. This assumption is typical in fully-developed flows (also in steady-state setups), in order to permit the linearization of the governing kinetic equation and it is valid for any pressure difference provided that the channel is adequately long [8,9]. For comparison purposes between the oscillatory and steady flow, the amplitude of the oscillatory pressure gradient is taken equal to the steady one ($dP/dz' = dP_S/dz'$). In this way, $X = X_S$, and the peak values of the macroscopic quantities (velocity, flow rate, shear stress, and pumping power) of the oscillatory flow can be compared with the corresponding ones of the steady flow.

All velocities (pulsatile, oscillatory and steady) are non-dimensionalized by the most probable speed ν . More specifically, Eq. (2) is divided by (νX) to yield

$$\hat{u}_{PUL}(t, r) = u_S(r) + \hat{u}(t, r) \quad (14)$$

where $u_S(r)$ is the steady flow velocity and $\hat{u}(t, r)$ is the oscillatory flow velocity, which may be written as

$$\hat{u}(t, r) = \Re[u(r)\exp(-it)] = \Re[u_A(r)\exp(i(u_P(r) - t))] = u_A(r)\cos[t - u_P(r)] \quad (15)$$

In Eq. (15) the subscripts A and P denote the amplitude and the phase of the complex oscillatory velocity $u(r)$. The mean velocities are also non-dimensionalized by the most probable speed ν and the resulting mean steady and oscillatory velocities are denoted by \bar{u}_S and $\bar{\hat{u}}(t)$ respectively.

Next, the dimensionless flow rate is defined by introducing (14) and (15) along with the equation of state $P = \rho\nu^2/2$ into Eq. (6) to obtain $\hat{M}_{PUL}(t') = R^2PX\hat{G}_{PUL}(t)/\nu$, where $\hat{G}_{PUL}(t) = G_S + \hat{G}(t)$. Here, G_S is the well-known steady flow rate [8], $\hat{G}(t)$ is the oscillatory flow rate and they are given by

$$G_S = 4\int_0^1 u_S(r) r dr \quad \text{and} \quad \hat{G}(t) = 4\int_0^1 \hat{u}(t, r) r dr. \quad (16)$$

The oscillatory flow rate $\hat{G}(t)$ may be also written as

$$\hat{G}(t) = \Re[G\exp(-it)] = \Re[G_A\exp(i(G_P - t))] = G_A\cos(G_P - t) \quad (17)$$

where the flow rate G , as well its amplitude G_A and phase G_P , may be computed by integrating accordingly the corresponding velocity quantities. It is readily seen that the dimensionless flow rates may be connected to the dimensionless mean velocities by the following expressions: $G_S = 2\bar{u}_S$ and $\hat{G}(t) = 2\bar{\hat{u}}(t)$.

All stresses (pulsatile, oscillatory and steady) are non-dimensionalized by the reference pressure P . More specifically, Eq. (3) is divided by $(2PX)$ to yield

$$\hat{\tau}_{PUL}(t, r) = \tau_S(r) + \hat{\tau}(t, r) = \tau_S(r) + \tau_A(r)\cos[t - \tau_P(r)], \quad (18)$$

where $\tau_S(r)$ is the steady shear stress and $\hat{\tau}(t, r)$ is the oscillatory shear stress. In Eq. (18) the subscripts A and P denote the amplitude and the phase of the corresponding oscillatory complex shear stresses. The pulsatile wall shear stress is obtained for $r = 1$.

All forces in Eqs. (7-9) are divided by $(PX_P R^2)$ to yield the corresponding dimensionless ones:

$$\hat{F}_{PUL,I}(t) = \hat{F}_I(t) = dzA \frac{\delta}{\theta} \frac{d\hat{G}}{dt} = dzA \frac{\delta}{\theta} G_A \sin(G_P - t) \quad (19)$$

$$\hat{F}_{PUL,V}(t) = F_{S,V} + \hat{F}_V(t) = 2dz\Gamma[\tau_{S,W} + \hat{\tau}_W(t)] = 2dz\Gamma[\tau_{S,W} + \tau_{W,A}\cos(\tau_{W,P} - t)] \quad (20)$$

$$\hat{F}_{PUL,P}(t) = F_{S,P} + \hat{F}_P(t) = Adz(1 + \cos t) \quad (21)$$

The balance equations of the dimensionless steady $F_{S,V} = F_{S,P}$ and oscillatory $\hat{F}_I(t) + \hat{F}_V(t) = \hat{F}_P(t)$ forces are:

$$\text{Steady: } \bar{\tau}_{S,W} = 1/4 \quad (22)$$

$$\text{Oscillatory: } \frac{\delta}{\theta} G_A \sin(G_P - t) + 4\bar{\tau}_{W,A} \cos(\bar{\tau}_{W,P} - t) = \cos t \quad (23)$$

Equation (22) has been also reported in previous works related to steady fully-developed flows [10,11]. Equation

(23) is the corresponding one for oscillatory flow. The first and second terms at the left hand side refer to the inertia and viscous forces respectively, while the right hand side refers to the pressure forces.

Finally, the dimensionless pumping power is derived by dividing Eq. (12) by $(\nu X)(XP)R^2$ to find $\hat{E}_{PUL}(t) = E_S + \hat{E}(t)$, where the steady pumping power is $E_S = AdzG_S / 2$ and the oscillatory one is written as

$$\hat{E}(t) = \frac{1}{2} Adz \cos t G(t) = \frac{1}{2} Adz \cos t \Re \left[G_A \exp(i(G_P - t)) \right] = \frac{1}{2} Adz G_A \cos t \cos(G_P - t) \quad (24)$$

By integrating Eq. (34) over one oscillation cycle, the average pumping power over the cycle is formed as

$$\bar{E} = \frac{1}{2\pi} \int_0^{2\pi} \hat{E}(t) dt = \frac{1}{4} Adz G_A \cos(G_P). \quad (25)$$

In the low frequency regime, where $G_P \rightarrow 0$ and $G_A \simeq G_S$, it is seen that the average oscillatory pumping power is half of the corresponding steady one ($\bar{E} \simeq E_S / 2$).

The prescribed pulsatile flow is solved here in the whole range of δ and θ , which may vary from zero to infinity. The solution is based on the kinetic modeling described in the next section.

3 KINETIC FORMULATION

For arbitrary values of the parameters δ and θ the flow must be simulated based on kinetic theory, where the main unknown is the distribution function $f = f(t', \mathbf{r}', \xi)$, which is a function of time t' , position vector $\mathbf{r}' = (x', y', z')$ and molecular velocity vector $\xi = (\xi_x, \xi_y, \xi_z)$. The unknown distribution obeys the time-dependent nonlinear two-dimensional BGK equation [12]

$$\frac{\partial \tilde{f}}{\partial t'} + \xi_r \frac{\partial \tilde{f}}{\partial r'} - \frac{\xi_\varphi}{r'} \frac{\partial \tilde{f}}{\partial \varphi} + \xi_z \frac{\partial \tilde{f}}{\partial z'} = \frac{P}{\mu} (f^M - \tilde{f}) \quad (26)$$

where (P/μ) is the collision frequency and

$$f^M(t', \mathbf{r}', \xi) = n \left(\frac{m}{2\pi kT} \right)^{3/2} \exp \left[-m(\xi - \hat{U}_{PUL})^2 / (2kT) \right] \quad (27)$$

is the local Maxwellian distribution. Due to the assumption of isothermal fully-developed flow the temperature T is constant and the number density $n = n(z')$ varies only in the z' -direction. Also, the macroscopic velocity has only the z' -component and it is the same with the pulsatile velocity defined in Eq. (2), i.e., $\hat{U}_{PUL} = (0, 0, \hat{U}_{PUL})$. The pulsatile velocity $\hat{U}_{PUL}(t', r')$ and shear stress $\hat{\Pi}_{PUL}(t', r')$ (defined in Eq. (3)) at some position z' in the flow direction may be obtained by the first and second moments of f :

$$\hat{U}_{PUL}(t', r') = \frac{1}{n} \int \xi_z \tilde{f}(t', \mathbf{r}', \xi) d\xi \quad \text{and} \quad \hat{\Pi}_{PUL}(t', r') = m \int \xi_r (\xi_z - \hat{U}_{PUL}) \tilde{f}(t', \mathbf{r}', \xi) d\xi \quad (28)$$

The condition of small local pressure gradient ($X \ll 1$) allows the linearization of Eq. (26) by representing the unknown distribution function as

$$f(t', \mathbf{r}', \xi) = f_0 \left[1 + X \hat{h}_{PUL}(t, r, \mathbf{c}) + Xz \exp(-it) \right], \quad (29)$$

where $\mathbf{c} = \xi/\nu$, $f_0 = \frac{n}{\pi^{3/2}\nu^3} \exp[-c^2]$ is the absolute Maxwellian and $\hat{h}_{PUL}(t, x, y, \mathbf{c})$ is the unknown perturbed distribution function referring to the pulsatile fully-developed flow, which may be decomposed as

$$\hat{h}_{PUL}(t, r, \mathbf{c}) = h_S(r, \mathbf{c}) + \hat{h}(t, r, \mathbf{c}) \quad (30)$$

with $\hat{h}_S(r, \mathbf{c})$ and $\hat{h}(t, r, \mathbf{c})$ referring to the steady and oscillatory parts respectively. Substituting expressions (29) and (30) into Eq. (26) and introducing the dimensionless variables, yields the following two linearized BGK kinetic model equations:

$$c_r \frac{\partial h_S}{\partial r} - \frac{c_\varphi}{r} \frac{\partial h_S}{\partial \varphi} = \delta [2c_z u_S(r) - h_S(r, \mathbf{c})] \quad (31)$$

$$\frac{\delta}{\theta} \frac{\partial \hat{h}}{\partial t} + c_r \frac{\partial \hat{h}}{\partial r} - \frac{c_\varphi}{r} \frac{\partial \hat{h}}{\partial \varphi} + c_z e^{-it} = \delta [2c_z \mathbb{R}\hat{u}(t, r) - \hat{h}(t, r, \mathbf{c})] \quad (32)$$

where $c_r = \zeta \cos \varphi$ and $c_\varphi = \zeta \sin \varphi$. The first one describes the steady fully-developed flow through a circular tube and it is solved in [10]. The second one describes the oscillatory fully-developed flow and it is the one to be solved in the present work. However, since it is also solved in [9], the non-dimensionalization and the linearization are omitted here and only the final kinetic equation is given as

$$\zeta \cos \varphi \frac{\partial Y}{\partial r} - \frac{\zeta \sin \varphi}{r} \frac{\partial Y}{\partial \varphi} + \left(\delta - i \frac{\delta}{\theta} \right) Y = \delta u - \frac{1}{2}. \quad (33)$$

The complex velocity and shear stress are given by the moments of Y as

$$u(r) = \frac{1}{\pi} \int_0^{2\pi} \int_0^\infty Y e^{-\zeta^2} \zeta d\zeta d\varphi \quad \text{and} \quad \tau(r) = \frac{1}{\pi} \int_0^{2\pi} \int_0^\infty (\zeta \cos \varphi) Y e^{-\zeta^2} \zeta d\zeta d\varphi. \quad (34)$$

Turning to the boundary conditions it is noted that purely diffuse scattering is assumed at the wall, i.e., $f^+ = f_w^M$, where the superscript (+) denotes particles departing from the wall and f_w^M is the Maxwellian distribution defined by the wall conditions. Based on the above and following the linearization and projection procedures in [9] it is deduced that the wall boundary ($r = 1$) is given by

$$Y(1, \zeta, \varphi) = 0, \quad \pi/2 < \varphi < 3\pi/2. \quad (35)$$

At the symmetry axis ($r = 0$), molecules are reflected specularly, i.e.,

$$Y(0, \zeta, \varphi) = Y(0, \zeta, \varphi - \pi), \quad 0 < \varphi < \pi/2, \quad 3\pi/2 < \varphi < 2\pi. \quad (36)$$

The kinetic formulation of the oscillatory fully-developed flow setup is properly defined by Eqs. (33-36). The numerical solution is deterministic and it has been extensively applied in steady-state and time-dependent flow configurations with considerable success [8,13,14].

4 RESULTS AND DISCUSSION

In Fig. 1 the oscillatory flow rate $\hat{G}(t) = G_A \cos(t - G_P)$ and the pulsatile one $\hat{G}_{PUL}(t) = G_S + \hat{G}(t)$ are plotted versus time $t \in [0, 2\pi]$ for $\delta = [0.1, 1, 10]$ and $\theta = [0.1, 1, 10]$. The oscillatory flow rate over one cycle, takes both positive and negative values (the fluid is moved forth and back) and the time average flow rate over one cycle is zero (no net flow). The amplitude of the oscillatory flow rate is reduced as θ is decreased and this behavior becomes even stronger as δ is increased (less gas rarefaction). The time evolution of the pulsatile flow rate is obtained by superimposing on the oscillatory flow rate the corresponding steady one, which depends only on δ . Since the steady flow is independent of θ the behavior of the pulsatile flow rate with respect to θ is qualitatively the same with the oscillatory one. Consequently, at large θ (e.g., $\theta = 10$), where the amplitude of the oscillatory flow rate is large, the difference between the amplitude of the pulsatile flow rate and the corresponding steady one is also large. On the contrary, as the oscillatory flow tends to diminish, which is happening as θ is decreased and δ is increased, the pulsatile flow rate gradually tends to the steady one at the corresponding δ . This is particularly evident at $\theta = 0.1$ and $\delta = 10$, where $\hat{G}_{PUL}(t) \approx G_S$. It is also noted that

the pulsatile flow rate takes only positive values, i.e., there is no flow reversal at any time. This observation may be technologically significant in applications where a pulsatile flow is desired, e.g. in order to enhance mixing or heat transfer under rarefied conditions, without however having particles moving opposite to the pumping direction or hot gas transported backwards into colder regions.

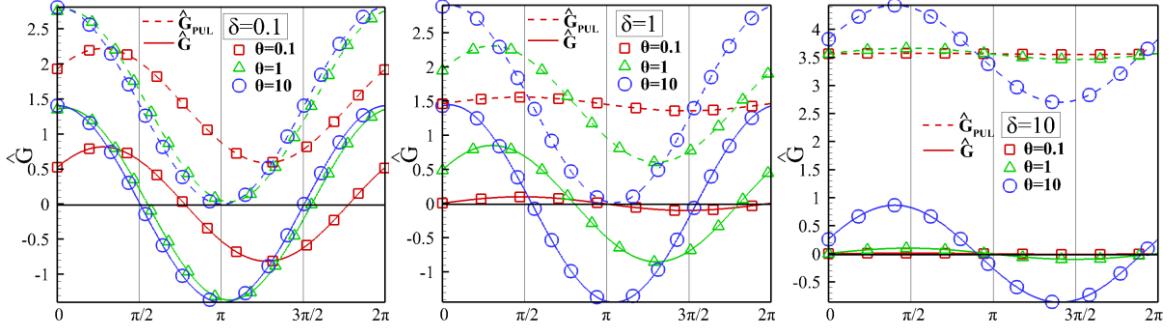


Figure 1: Oscillatory \hat{G} and pulsatile \hat{G}_{PUL} flow rates over one oscillation period for various values of δ and θ .

In Fig. 2, the oscillatory mean wall shear stress amplitude $\tau_{W,A}(\delta, \theta)$ and phase $\tau_{W,P}(\delta, \theta)$ are plotted in terms of δ with $\theta = [0.1, 1, 10, 50, 10^2]$. For very small values of δ the mean wall shear stress amplitude $\tau_{W,A}$ takes the same value as the corresponding steady one $\tau_{S,W} = 0.25$. As δ is increased it is slightly reduced and then, from some δ in the late transition or slip regimes it is rapidly decreased. The value of δ where this rapid decrease of $\tau_{W,A}$ is starting depends on θ and it is increasing as θ is decreasing. Thus, the variation of $\tau_{W,A}$ depends monotonically on δ and does not include the local maxima observed in the variation of G_A that has been reported in [9]. With regard to the phase difference, $\tau_{W,P}$ is always monotonically increased with δ and it is almost independent of the oscillation frequency θ . At very small values of δ it is almost zero, then at moderate values of δ it is rapidly increased and finally, at large values of δ it is asymptotically increased reaching the limiting value of $\pi/2$. The dependency of the oscillatory wall shear stress $\hat{\tau}_W$ on δ and θ is very close to the corresponding one of the flow rate \hat{G} shown in Fig. 1 and therefore, it is omitted here.

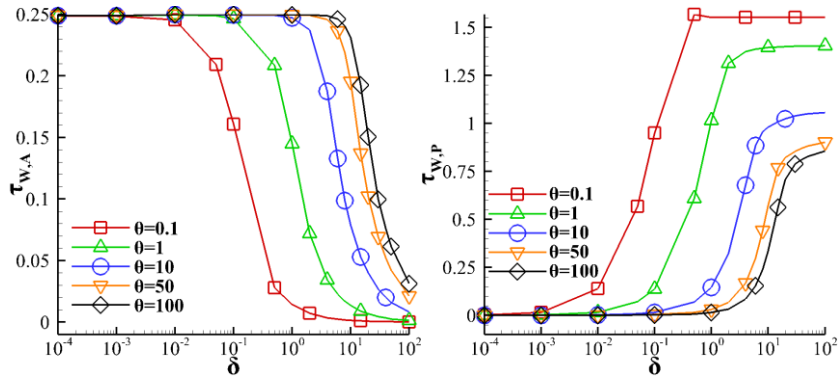


Figure 2: Oscillatory wall shear stress amplitude $\bar{\tau}_{W,A}$ and phase $\bar{\tau}_{W,P}$ in terms of δ for various values of θ .

Next in Fig. 3, the oscillatory pumping power, defined as $\hat{E}/(Adz) = G_A \cos(G_P - t) \cos t / 2$ (see Eq. (24)), is plotted in terms of $t \in [0, 2\pi]$ for $\delta = [0.1, 1, 10]$ and $\theta = [0.1, 1, 10, 10^2]$. The pumping power has two peaks within each oscillatory cycle because it consists of the product of the oscillatory pressure times the oscillatory flow. Its integral over one cycle is not zero in order to drive the oscillatory flow, although the oscillatory net flow is zero. The dependency of the oscillatory pumping power on δ and θ is similar to the one observed for the flow rate, i.e. in general, as θ is decreased (the oscillation frequency is increased) its amplitude is decreased and its phase lag is increased. This behavior becomes more dominant as δ is increased.

As pointed above, even when the flow is reversed, which is occurring at the second half of the oscillation cycle at time $t \in [\pi/2, \pi]$ where the flow rate is negative, the pumping power remains positive. It is seen however, in Fig. 3 that at certain times $t \in [0, 2\pi]$, the oscillatory pumping power may become negative. This is more evident at large δ and small θ and it is occurring because in dense gases and at relatively high frequencies the flow rate is completely out of phase with the pressure gradient (it becomes proportional to a sinusoidal function). Thus, when the pressure gradient becomes negative and the flow is reversed, the sign of the flow rate remains positive for a certain time interval and during this interval the overall pumping power becomes negative. This time interval is increased as θ is decreased. Of course in rarefied gases and/or low frequencies \hat{E} is always positive because the flow rate is in phase with the pressure gradient.

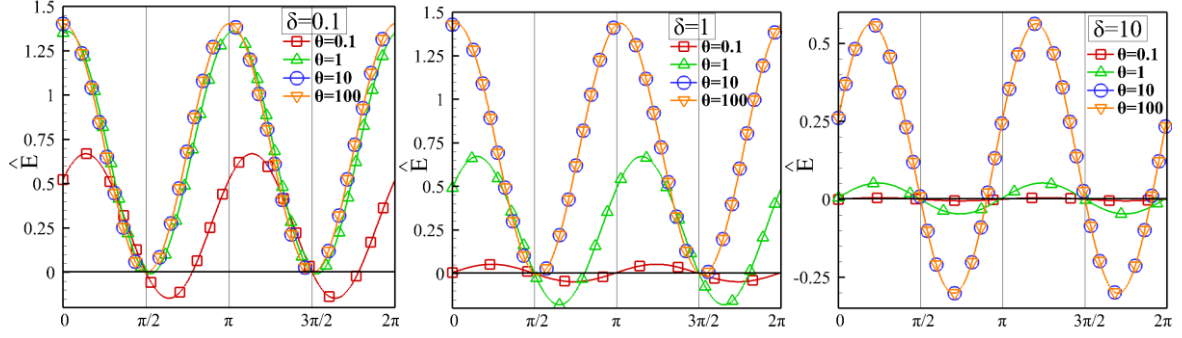


Figure 3: Oscillatory pumping power \hat{E} over one oscillation period for various values of δ and θ (pumping power is divided by Adz).

Finally, in Fig. 4, the oscillatory inertia, \hat{F}_I , viscous \hat{F}_V and pressure \hat{F}_p forces are plotted over one oscillation period $t \in [0, 2\pi]$ for $\delta = [0.1, 1, 10]$ and $\theta = [0.1, 1, 10]$. In all cases the force balance equation (23) is satisfied. The inertia forces refer to the core flow and the viscous forces refer to the Stokes layer. The phase difference between these two forces is always $\pi/2$. In the cases of $(\delta = \theta = 0.1)$, $(\delta = \theta = 1)$ and $(\delta = \theta = 10)$ the viscous and inertia forces lag and lead the corresponding pressure force respectively by a phase angle of $\pi/4$. The amplitudes of the two forces are about the same. Then, in the cases of $(\delta = 10, \theta = 1, 0.1)$ and $(\delta = 1, \theta = 0.1)$, the inertia forces almost coincide with the corresponding pressure forces, while the viscous forces lag the other two forces by almost $\pi/2$ and their amplitudes are close to zero. The flow consists of two regions: the core region oscillating in a plug mode and, adjacent to the wall, the oscillating thin viscous or Stokes layer with the velocity overshooting. In the cases of $(\delta = 1, \theta = 10)$ and $(\delta = 0.1, \theta = 1, 10)$ this behavior is reversed, i.e., the viscous coincide with pressure forces, while the inertia forces lead by almost $\pi/2$ and their amplitudes are close to zero. The flow consists of one oscillating region with no velocity overshooting. This description clarifies the behavior of the inertia and viscous forces in terms of θ and δ .

5 CONCLUDING REMARKS

The pulsatile isothermal fully-developed flow in a circular tube is investigated by decomposing the flow into the steady and oscillatory parts. The steady part is well-known and therefore, the investigation is focused mainly on the oscillatory part, which is numerically solved, based on the time-dependent linear BGK equation, in a wide range of the gas rarefaction parameter δ and the oscillation parameter θ .

Always as θ is decreased (i.e., the oscillation frequency is increased) the amplitude of all macroscopic quantities is decreased and their phase lag with respect to the pressure gradient is increased. Actually, at very small θ the amplitude tends to diminish and the phase lag approaches the limiting value of $\pi/2$. It is important to note however, that as δ is decreased (i.e., the gas becomes more rarefied) higher frequencies are needed to trigger the behavior described above. The amplitude of the oscillatory pressure gradient is taken to be equal with the steady pressure gradient. Having this in mind it is useful to note that the pulsatile flow rate is always positive and therefore, there is no flow reversal. Furthermore, the amplitude of the wall shear stress is increased with θ being always smaller than the corresponding steady ones. In terms of δ the wall shear stress amplitude remains almost constant in the free molecular and transition regimes and then it is rapidly reduced. The phase lag of the wall shear stress is increased as δ is increased.

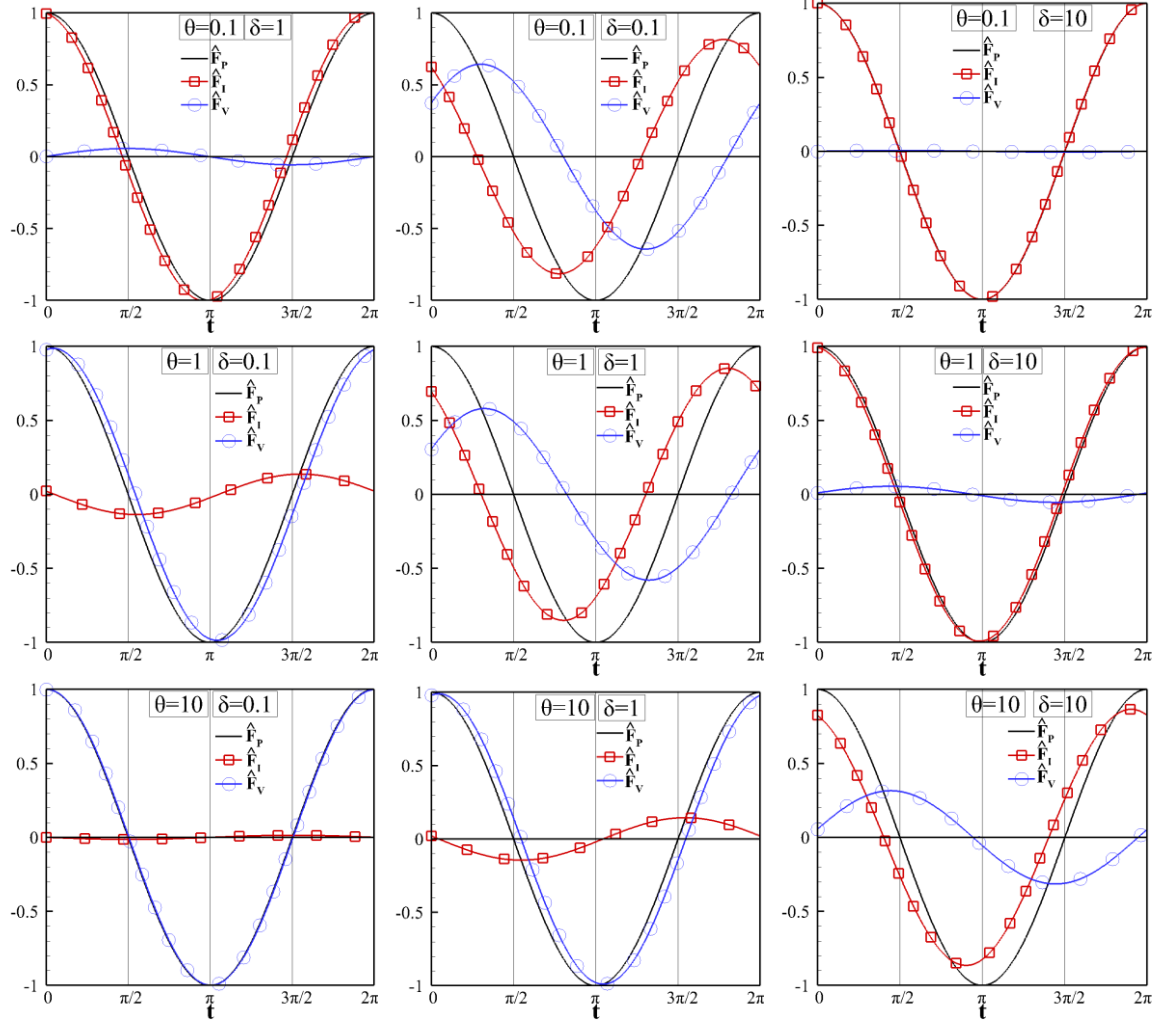


Figure 4: Oscillatory inertia \hat{F}_I , viscous \hat{F}_V and pressure \hat{F}_P forces over one oscillation period for various values of δ and θ (forces are divided by Adz).

The oscillatory pumping power has two peaks within each oscillatory cycle and its integral over one cycle is not zero. The nonzero pumping power is needed to maintain the oscillatory flow, even though the oscillatory net flow is zero and it is increased as the oscillation frequency is reduced. By adding the oscillatory pumping power to the steady one, yields the total power to maintain the pulsatile flow.

Finally, the inertia and viscous forces, having always a phase difference of $\pi/2$, are computed in a wide range of δ and θ . Their amplitudes are about the same when $\delta = \theta$. As δ is increased and θ is decreased the inertia forces dominate causing a core oscillating plug flow with a thin Stokes layer. In the opposite situation (i.e., as δ is decreased and θ is increased) the viscous forces become more important causing a typical viscous oscillatory flow without velocity overshooting.

ACKNOWLEDGEMENTS

This work has been carried out within the framework of the EUROfusion Consortium and has received funding from the Euratom research and training programme 2014-2018 under grant agreement No 633053. The views and opinions expressed herein do not necessarily reflect those of the European Commission.

REFERENCES

1. Vasileiadis, N., Tatsios, G., Misdanitis, S. and Valougeorgis, D. (2016), "Modeling of complex gas distribution systems operating under any vacuum conditions: Simulations of the ITER divertor pumping system", *Fusion Engineering and Design*, Vol. 103, pp. 125-135.
2. Abreu, R. A., Troup, A. P. and Sahm, M. K. (1994), "Causes of anomalous solid formation in the exhaust systems of low-pressure chemical vapor deposition and plasma enhanced chemical vapor deposition semiconductor processes", *Journal of Vacuum Science and technology B*, Vol. 12 (4), pp. 2763-2767.
3. Zamir, M. (2000), *"Physics of Pulsatile Flow"*, Springer-Verlag, New York.
4. Blythman, R., Persoons, T., Jeffers, N., Nolan, K. P. and Murray, D. B. (2017), "Localized dynamics of laminar pulsatile flow in a rectangular channel", *International Journal of Heat and Fluid Flow*, Vol. 66, pp. 8-17.
5. Batikh, A., Caen, R., Colin, S., Baldas, L., Kourta, A. and Boisson, H. C. (2008), "Numerical and experimental study of micro synthetic jets for active flow control", *International Journal of Heat and Technology*, Vol. 26 (1), pp. 139-145.
6. Wang, S., Baldas, L., Colin, S., Kourta, A. and Mazellier, N. (2014), "Numerical and experimental characterization of a micro-oscillator for flow control", Proceedings of the 4th European Conference on Microfluidics, Limerick, Ireland, 10-12 December 2014.
7. Colin, S., Aubert, C. and Caen, R. (1998), "Unsteady gaseous flows in rectangular microchannels: frequency response of one or two pneumatic lines connected in series", *European Journal of Mechanics B/Fluids*, Vol. 17, pp. 79-104.
8. Sharipov, F. (2016), *"Rarefied Gas Dynamics. Fundamentals for Research and Practice"*, Wiley-VCH, New Jersey.
9. Tsimpoukis, A. and Valougeorgis, D. (2018), "Rarefied isothermal gas flow in a long circular tube due to oscillating pressure gradient", *Microfluidics and Nanofluidics*, Vol. 22, 5.
10. Varoutis, S., Lihnaropoulos, J., Mathioulakis, D., Tserepi, A. and Valougeorgis, D. (2008), "Estimation of the Poiseuille number and of the exact hydraulic diameter in rarefied gas flows through channels of various cross sections", *1st European Conference on Microfluidics (mFlu'08)*, Bologna, Italy, 10-12 December 2008.
11. Naris, S. and Valougeorgis, D. (2008), "Rarefied gas flow in a triangular duct based on a boundary fitted lattice", *European Journal of Mechanics B/Fluids*, Vol. 27, pp. 810-822.
12. Bhatnagar, P. L., Gross, E. P. and Krook, M. A. (1954), "A model for collision processes in gases", *Physical Review*, Vol. 94, pp. 511-525.
13. Lihnaropoulos, J. and Valougeorgis, D. (2011), "Unsteady vacuum gas flow in cylindrical tubes", *Fusion Engineering and Design*, Vol. 86, pp. 2139-2142.
14. Buchina, O. and Valougeorgis, D. (2012), "Oscillatory heating in a microchannel at arbitrary oscillation frequency in the whole range of the Knudsen number", *Journal of Physics: Conference Series* 362, 012015.

AERODYNAMIC SHAPE OPTIMIZATION OF DIFFUSER AUGMENTED WIND TURBINE BLADES USING ASYNCHRONOUS PARALLEL DIFFERENTIAL EVOLUTION

Stavros N. Leloudas¹, Giorgos A. Strofylas² and Ioannis K. Nikolos³

^{1,2,3} School of Production Engineering and Management
Technical University of Crete
Chania, GR-73100, Greece

³Contact author, e-mail: jnikolo@dpem.tuc.gr

Keywords: aerodynamic optimization, diffuser augmented wind turbines, rotor blades, asynchronous differential evolution algorithm, parallelization, meta-models.

Abstract. A robust optimization scheme for the aerodynamic design of diffuser augmented wind turbine (DAWT) blades is presented in this study, using an asynchronous, parallel, meta-model assisted differential evolution (DE) algorithm, along with an in-house computational code, that is based on the well-known Blade Element Momentum (BEM) theory and serves as the evaluator. The parallelization of the DE algorithm is performed using the Message Passing Interface (MPI) library functions, while it is realized by means of an asynchronous approach, aiming to maximize the parallel efficiency. Additionally, further acceleration is achieved through the combination of the DE with a Multilayer Perceptron (MLP) and a Radial-Basis Function (RBF) Artificial Neural Networks (ANNs), which serve as surrogate models and work as an ensemble. Direct learning is used for the training of each RBF network and the back-propagation algorithm is applied to determine the synaptic weights of the MLP network, through an iterative supervised training procedure. Finally, the proposed methodology is applied to the design of improved rotor blades for a real-world DAWT application, demonstrating its ability to produce effective blades that enhance significantly the aerodynamic performance of the rotor.

1 INTRODUCTION

In recent years, the wind power sector has become one of the fastest growing industries and the most substantial provider of renewable and sustainable energy [1]. However, the unpredictable nature of the wind and its relatively dilute energy content are significant barriers to the wider application of wind turbines technology, considering that these factors increase the uncertainty on the power output estimations and the cost of energy production. Therefore, in quest of improving the economics of wind energy harvesting, notable efforts have been made to develop efficient wind concentrators, that is, configurations capable of increasing the energy density of the wind and, thus, enhancing the power output of wind turbines [2, 3].

The diffuser augmented wind turbine (DAWT) is considered to be such an innovative wind energy conversion system, that involves the addition of a static diffuser around the rotor, as a means to control the expansion of the wake and create a region of high subatmospheric pressure at the diffuser exit; a phenomenon that eventually results in augmenting the mass flow rate passing through the turbine. Consequently, this promising wind energy harvester has the ability to yield power performance coefficients well in excess of the Betz limit and, thus, extract additional power from the wind compared with a conventional bare wind turbine with the same rotor diameter [4–7]. Besides, the shrouding of the rotor blades also provides lower sensitivity to turbulence and better resistance to fatigue, while reduces the fluctuating blade loads, the tip losses and the emitted noise levels [2].

In this work, a versatile optimization methodology for the efficient design of diffuser augmented wind turbine blades is demonstrated, using a parallel and meta-model assisted Differential Evolution (DE) algorithm, along with an in-house Blade Element Momentum (BEM) code, to serve for the performance analysis of each candidate blade design. The optimization is conducted on a multi-processor platform, while the parallelization is realized by means of an asynchronous approach, applying a Master-Slave model, to overcome the synchronization barrier at the end of each generation, maximize the parallel efficiency and eventually decrease the overall computational time.

2 THE BLADE ELEMENT MOMENTUM (BEM) MODEL

The BEM theory is considered to be the current standard for assessing the rotor performance in turbine design applications, because it is able to obtain remarkably accurate results for a wide range of operating conditions, in a very short period of time [8, 9]. The method relies on the combination of the blade element and one-dimensional momentum theories, in order to estimate the distribution of the axial and tangential velocities over the rotor plane,

which in turn define the local flow conditions and the forces exerted on the blades. However, the classical BEM theory is unable to account for the diffuser's effect on the calculation of the axial and tangential induction factors. For this reason, several studies have been carried out, aiming to modify the momentum part of the classical BEM theory and, thus, make it applicable to the performance analysis of DAWT rotors as well [2, 10–12]. Herein, such an in-house computational BEM code is utilized for the evaluation of each candidate blade design, which has been developed based on the extended BEM model proposed by Rio Vaz et al. [11]. In this section, the main points of the particular model are highlighted, while a detailed description can be found in [11, 13].

Let us consider an elementary control volume, in the shape of an annular streamtube (Figure 1). The thrust dT and torque dM exerted on the examined streamtube can result from the application of the integral momentum and moment of momentum equations on the examined control volume, under the assumption that the rotational velocity upstream of the rotor is equal to zero and denoting as u_θ the rotational velocity in the wake [11]

$$dT = 4\rho\pi r dr a_a(1 - a_a)V_0^2, \quad (1)$$

$$dM = 2\rho a_t V_1 2\omega r^2 dA = 2\pi r^2 \rho V_1 u_\theta dr, \quad (2)$$

where V_0 is the velocity of the wind far upstream, V_1 is the axial component of velocity at the rotor plane, a_a is the axial induction factor, $a_t = u_\theta/(2\omega r)$ is the tangential induction factor and $dA = 2\pi r dr$ is the cross-sectional area of the control volume at the rotor plane.

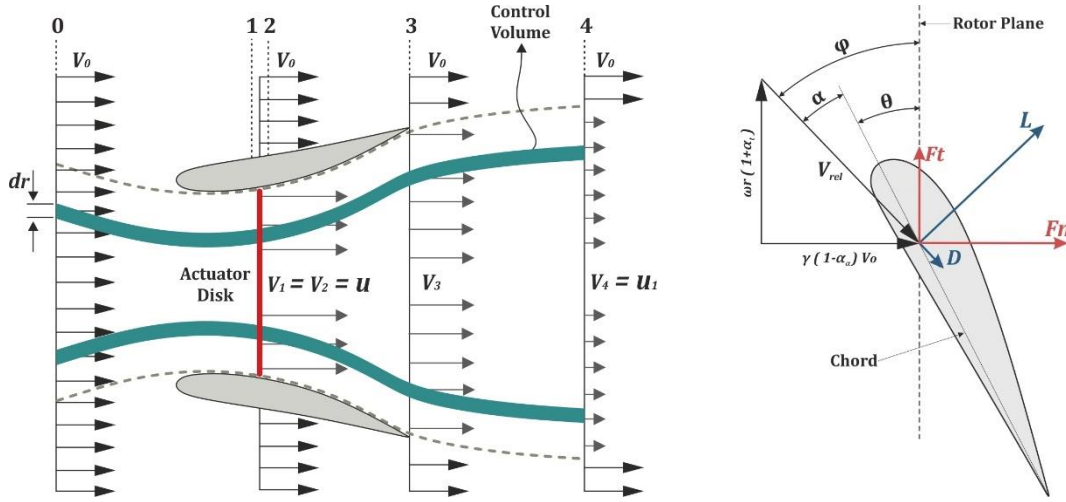


Figure 1. The control volume used for the derivation of the modified 1D momentum theory (left) and the induced velocities on the rotor plane (right).

The power output augmentation achieved by a DAWT is mainly attributed to the high subatmospheric pressure created at the diffuser exit, which results in an increased velocity and mass flow rate at the rotor plane. The velocity speed-up ratio γ for the unloaded diffuser configuration (without the presence of a turbine rotor) is defined as the ratio of the axial velocity of the flow at the rotor plane to the freestream velocity. Thus, the flow velocity at the rotor, is given by

$$V_1 = V_2 = u = \gamma(1 - a_a)V_0, \quad (3)$$

while the speed-up ratio ε for the DAWT configuration, can be expressed as a function of γ as

$$\varepsilon = V_1/V_0 = \gamma(1 - a_a). \quad (4)$$

According to BEM theory, each blade is divided spanwise into N elements of length dr ; it is assumed that each blade element acts independently of the surrounding ones and operates aerodynamically as a 2D airfoil section. The relative velocity V_{rel} seen by a blade section is a combination of the induced axial velocity $\gamma(1 - a_a)V_0$ and the induced tangential velocity $(1 + a_t)\omega r$ at the rotor plane, as illustrated in Figure 1, where θ is the twist angle of the section, i.e. the angle between the chord c and the plane of rotation, and ϕ is the angle between the plane of rotation and the direction of the relative velocity V_{rel} . Therefore, the local angle of attack α is given by

$$\alpha = \phi - \theta. \quad (5)$$

In addition, by observing Figure 1, the expression connecting the local inflow angle ϕ with the axial and tangential

induction factors can be extracted as

$$\varphi = \tan^{-1} \left(\gamma \frac{(1 - a_a)V_o}{(1 + a_t)\omega r} \right). \quad (6)$$

During this analysis, the interest lies only on the forces exerted normal and tangential to the rotor plane. Thus, by projecting the lift and drag forces in these directions, the normal F_n and tangential F_t forces on the examined airfoil section are formed as follows

$$F_n = L \cos(\varphi) + D \sin(\varphi), \quad (7)$$

$$F_t = L \sin(\varphi) - D \cos(\varphi). \quad (8)$$

The normal and tangential forces can be expressed in dimensionless form, by introducing the normal and tangential force coefficients

$$C_n = F_n / (0.5 \rho V_{rel}^2 c), \quad (9)$$

$$C_t = F_t / (0.5 \rho V_{rel}^2 c). \quad (10)$$

The elementary thrust and torque on the annular streamtube swept by the examined blade element, considering that F_n and F_t are forces per length and denoting the number of the rotor's blades as B , are calculated as follows

$$dT = BF_n dr, \quad (11)$$

$$dM = rBF_t dr. \quad (12)$$

So, by taking into consideration equations (13) and (14), which connect the freestream velocity, the relative velocity, the inflow angle, the induction factors and the velocity speed-up ratio for the unloaded diffuser case,

$$V_{rel} \sin(\varphi) = \gamma V_o (1 - a_a), \quad (13)$$

$$V_{rel} \cos(\varphi) = \omega r (1 + a_t), \quad (14)$$

equations (11) and (12) can be rearranged as

$$dT = \frac{1}{2} \rho B \frac{\gamma^2 V_o^2 (1 - a_a)^2}{\sin^2(\varphi)} c C_n dr, \quad (15)$$

$$dM = \frac{1}{2} \rho B \frac{\gamma V_o (1 - a_a) \omega r (1 + a_t)}{\sin(\varphi) \cos(\varphi)} c C_t r dr. \quad (16)$$

Therefore, the expressions providing the axial and tangential induction factors for the case of a DAWT rotor can be obtained by equating equations (1) and (15) for dT , as well as equations (2) and (16) for dM , given that the rotor solidity σ is defined as $\sigma = Bc/(2\pi r)$.

$$a_a = 1 / [(4 \sin^2(\varphi)) / (\gamma^2 \sigma C_n) + 1] \quad (17)$$

$$a_t = 1 / [(4 \sin(\varphi) \cos(\varphi)) / (\sigma C_t) - 1] \quad (18)$$

By observing the expressions providing the axial and tangential induction factors, it is evident that the presence of the diffuser is incorporated within the BEM model, by using only the velocity speed-up ratio γ at the rotor plane of the unloaded diffuser, while the calculation of the induction factors for each blade element can be achieved by following the typical iterative process [14]. Finally, the particular BEM code is further enhanced by the addition of tip/hub losses and Reynolds number correction models, along with the Glauert's correction model with Buhl's modification [15], specially adapted for the analysis of DAWT rotors [13].

3 THE ASYNCHRONOUS DIFFERENTIAL EVOLUTION ALGORITHM

3.1 Basic Features

Evolutionary algorithms (EAs) imitate nature's selection process using a population-based search mechanism, to deal with demanding high-dimensional real-world optimization problems. They are a class of heuristic methods with low sensitivity to local minima treatment and they provide efficient balance between exploitation of the best solutions and exploration of the search space. Additionally, as they combine features of directed and stochastic

search, they are more robust than directed search methods. In this work a Differential Evolution (DE) algorithm is utilized within the proposed optimization framework, which is a versatile parallel stochastic search method, introduced by Storn and Price [16], capable of handling non-differentiable, nonlinear and multimodal cost functions, providing superior convergence performance than other EAs.

Below, a brief description of the basic features of a classic DE algorithm is presented. Given a cost function

$$f(\mathbf{X}) = f(x_1, x_2, \dots, x_n), \quad (19)$$

where \mathbf{X} is a vector (chromosome) that contains the n design variables, the objective of the optimization problem lies on the minimization of this cost function through the adjustment of the values of the design variables, with respect to the prescribed upper and lower bounds for each one of them. Differential Evolution evolves a fixed-size population of N_p chromosomes for a finite number of generations G_{max} . The initialization of the first population is established by randomly assigning values to the parameters within the given boundaries of the design variables.

After the evaluation of each individual's cost function, operators are applied to the population, simulating the according natural processes. Initially, the mutation operator is applied, which generates a new chromosome, based on three randomly selected individuals of the current generation G . The formation of the new parameter vector is realized by adding a weighted difference vector between the two members of the triad to the third one, the so-called "donor". Then, the uniform crossover scheme is applied; the mutant and the chromosome of the current population are subjected to a discrete recombination which produces the final candidate solution.

$$x'_{k,i}{}^{G+1} = \begin{cases} x_{C_{k,i}}^G + F(x_{A_{k,i}}^G - x_{B_{k,i}}^G) & \text{if } (r \leq Cr \text{ or } i = i^*) \\ x_{k,i}^G & \text{otherwise} \end{cases} \quad (20)$$

where $x_{C_{k,i}}^G$ are the elements of the "donor" vector, G is the current generation and i^* is a randomly selected integer within $[1, n]$, chosen once for all members of the population. The random number r is seeded for every gene of each chromosome, whereas the parameters F and Cr control the mutation and crossover operations, respectively. Specifically, the scale factor F controls the diversification rate of the population, while the crossover probability Cr controls the fraction of design values that are inherited from the mutant. Moreover, the design variable, which corresponds to the randomly selected index, i^* , is taken from the mutant to ensure that the trial vector does not duplicate the initial one. Subsequently, each member of the resulting intermediate population is evaluated and competes against its counterpart in the current population; the best fitted individuals are the ones that will form the next generation. The DE selection scheme ensures the survival of the elitists and can be described (for a minimization problem) as follows:

$$\mathbf{X}_k^{G+1} = \begin{cases} \mathbf{X}'_k{}^{G+1} & \text{if } f(\mathbf{X}'_k{}^{G+1}) \leq f(\mathbf{X}_k^G) \\ \mathbf{X}_k^G & \text{otherwise} \end{cases} \quad (21)$$

The process is successively repeated, providing populations with better fitted individuals.

3.2 Surrogate Models

In each DE generation, each trial vector (offspring) must be first evaluated and then compared with its parent, so as to select the better-fitted between them to pass to the next generation. The concept of utilizing surrogate models in this evaluation procedure is to replace the, generally, costly exact evaluations with fast inexact approximations. Each offspring is pre-evaluated, using the available surrogate models, in a fast screening procedure. If an offspring is pre-evaluated and found lower-fitted than its parent, then no further exact evaluation is taking place and the current vector (parent) is transferred to the next generation, while the offspring is abandoned. On the contrary, if the offspring is pre-evaluated as better-fitted than its parent, an exact re-evaluation is performed after the pre-evaluation, along with a second comparison between the two vectors. If the offspring is found again better-fitted than its parent, then the offspring passes to the next generation. Otherwise, its parent will pass to the next generation and the offspring is abandoned.

An additional small percentage (5%-10%) of the candidate solutions are selected with uniform probability to be exactly evaluated, without taking into account their pre-evaluation by the utilized surrogate models, in order to further enhance the robustness of the procedure. Moreover, in the first two generations of the DE, all trial vectors are exactly evaluated, so as to initialize the central data base required for the training and testing of the surrogate models. As it was previously described, only exactly-evaluated candidate solutions have the opportunity to pass to the new generation. Therefore, the current population always comprises individuals that have been selected using exact evaluation. The surrogate models predictions replace exact evaluations only for the less-promising individuals, using the pre-evaluation procedure to quickly reject them, without spending valuable resources. Each evaluated chromosome, along with its resulted fitness, are stored in the central database. The training and testing data sets are selected in each generation from the corresponding database to be used by all available surrogate

models. If NR is the length of the training set and NT is the length of the testing set, the $NR + NT$ best members of the central database are deterministically selected in each generation and, from this set, NR members are randomly selected to be used as the training set, the rest NT being used for testing. In this way, the surrogate models, which are re-trained and re-tested in each generation, evolve with the population and use only the currently most-promising individuals for approximating the cost function.

The utilized surrogate models can be used either independently or as an ensemble. In the first case a single surrogate is used throughout the whole optimization procedure, while in the second case in each generation all surrogates are re-trained and re-tested (using the same training and testing data sets for all surrogates) and then only the best one is used in the pre-evaluation phase of the trial vectors. The selected surrogate (different in each generation) is the one with the lower value of the testing error. In the current work, the DE algorithm is combined with a Multilayer Perceptron (MLP) and a Radial-Basis Function (RBF) Artificial Neural Networks (ANNs), working as an ensemble [17, 18]. The number of hidden units in each one of the two hidden layers of the MLP network is twice the number of the design variables. For the RBF networks the number of centers (M) is set equal to $2/3$ of the number of training data (NR). Direct learning is used for the training of each RBF network, based on a matrix formulation of its governing equations. The presentation of the network with the NR input (training) patterns allows for the formulation of a $(NR \times M)$ matrix, which is inverted through the Gram-Schmidt technique, providing the M values of the connection weights to the single output unit of the network (which are the only adjustable parameters of the RBF network). The back-propagation algorithm is used to determine the synaptic weights of the MLP network, through an iterative supervised training procedure [17, 18]. The main phases of the current optimization procedure are presented as a flow chart in Figure 2.

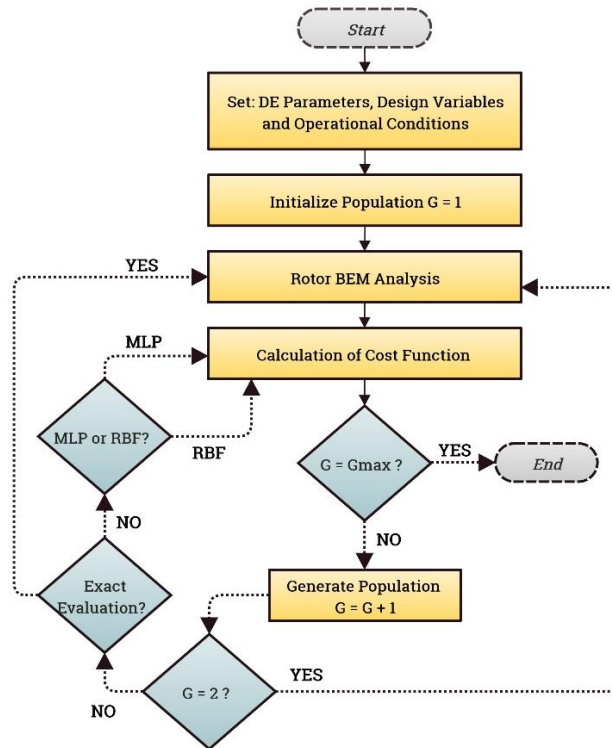


Figure 2. Flowchart with the main phases of the optimization framework.

3.3 Parallel Implementation

The concept behind the developed parallelization strategy is to enable the cooperation of the DE with different simulation software in the form of executables. The required data transfer between the DE and the simulation software is succeeded with appropriate text files, while the communication among the processors and the parallel implementation is achieved using MPI (Message Passing Interface) library functions. The proposed strategy appears to be quite efficient, regardless the use of text files, considering that the computational time of data transfer is negligible compared to the one of the evaluation step. The population members are distributed a priori among the available processors and each processor is in charge for the evaluation of one individual. Next, a unique rank is assigned to each processor, while one of them is identified as the master node that keeps track of the whole procedure. This node performs all the pre-process that is required prior to the beginning of the optimization

procedure, which includes the creation of a working folder for each processor where the executables comprising the evaluation step and their corresponding text files are replicated. Furthermore, the master node distributes all the necessary information concerning the DE algorithm to all other processors, i.e., the number of the design variables, their upper and lower bounds and the control parameters for the DE algorithm. After the completion of the initialization step, the main procedure begins; each processor is generating a random individual within the specified bounds for each gene of the chromosome and evaluates it. Next, the fitness values of the candidate solutions and their corresponding chromosomes are broadcasted to all processors, to update their databases with the new population members. Each processor evolves separately one chromosome, and the new resulting one is stored in its corresponding working folder. All the operations needed (mutation, crossover and selection) for the evolution process, are implemented after the evaluation step of each generation on each node separately for its assigned chromosome. Nevertheless, the auxiliary evaluations of the surrogate models are performed only by the master node for all chromosomes. According to the prescribed procedure, a Boolean array is filled, indicating if the new trial vector is better fitted than its parent and should be exactly evaluated. Subsequently, all selected candidates are exactly evaluated, while, for the rest, the fitness values and trial vectors are explicitly broadcasted by the master node to their corresponding processors for the consistency of the procedure. The optimization process is terminated when a prescribed number of generations is reached.

In the asynchronous implementation of the DE algorithm the generation is not strictly defined and the current population (at each time instant) can comprise individuals belonging to actually different “generations”. Each newly generated trial vector (offspring) can replace its parent (if better fitted) and become a member of the current population just after the completion of its evaluation process, without waiting for the completion of the evaluation phases of the rest members of the auxiliary population. Therefore, individuals evolve independently, without full coordination between generations. As a result, asynchronous update has the clear advantage that the improved solutions can contribute to the evolution immediately, and can speed up the convergence to become faster than the corresponding synchronous update.

4 TWIST AND CHORD OPTIMIZATION OF DAWT BLADES

The previously described optimization methodology was applied for the design of improved rotor blades for the DAWT of Donqui Urban Windmills [19]. The actual diffuser geometry, shown in Figure 3, was designed by the National Aerospace Laboratory (NLR) in the form of a circular *NACA 2207* airfoil, with an exit-area-ratio (i.e., the ratio of the diffuser exit area to the rotor swept area) equal to 1.728 and an exit plane diameter equal to 2 m , while the diffuser is further equipped with a 0.04 m high Gurney flap. The velocity speed-up distribution over the rotor plane for the unloaded diffuser case is shown in Figure 3, as it was measured by van Dorst [20] and numerically approximated by Kesby et al. [12] through CFD simulations. Furthermore, the original blade for the 3-bladed rotor with a diameter equal to 1.5 m was also designed by NLR, utilizing the *NACA 2207* profile along the entire blade span. A 3D representation of the original blade is illustrated in Figure 8.

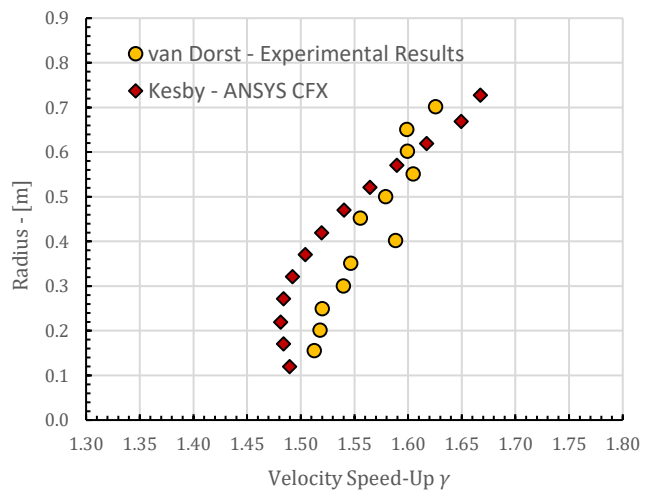
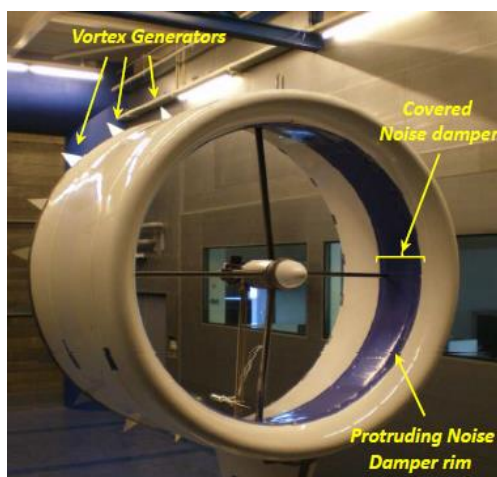


Figure 3. The Donqui Urban Windmills diffuser geometry [19] and the velocity speed-up distribution over the rotor plane, for the unloaded diffuser.

In this study, two distinct blade geometries are produced through a twist and chord optimization procedure, for the 3-bladed rotor of the Donqui Urban Windmills DAWT, as alternatives to the original blade configuration; for

the first optimized blade, denoted as *BD1*, the *NACA 2207* is employed for the entire span (similarly to the original blade), while for the second blade design, denoted as *BD2*, the *RG15* airfoil is proposed, which is a low Reynolds number airfoil with a maximum thickness of 8.92% located at 30.2% of the chord and a maximum camber of 1.8% located at 39.7% of the chord. The lift and drag coefficients for the particular airfoil profiles (inputs to the BEM code) were calculated with XFOIL software [21] at 600,000 Reynolds, which is the diffuser Reynolds number [19]; subsequently, they were extrapolated to the full 360° range of angles of attack, applying the Montgomerie's 360° extrapolation method [22].

4.1 Parameterization, Constraints and Cost Function

The parameterization of the twist and chord distributions is realized by utilizing two 2nd degree B-Spline curves with 5 control points, permitting the movement of each control point only in the y-direction. Therefore, the number of design variables for each one of the encountered optimization cases is 10, corresponding to y coordinates of the B-Spline curves used to represent the twist and chord distributions. As long as the design objective is concerned, it is defined as the maximization of the rotor power output for a range of ambient wind speeds between 5 m/s and 8 m/s, using an increment of 1 m/s. Hence, considering that the current DE algorithm is designed to deal with minimization problems, the objective function is formed as follows

$$f = 1800 - (P_5 + P_6 + P_7 + P_8) \quad (21)$$

where P_k is the aerodynamic power output of the rotor for the operational point corresponding to k m/s.

In this optimization study only explicit constraints are employed, which are formed by the acceptable bounds of the considered design variables. The extraction of the particular ranges was based on a trial and error basis, in order to achieve upper and lower bounds that do not restrict or magnify inefficiently the search space and simultaneously do not permit undesirable twist and chord distributions to be created. Specifically, the bounds for the design variables corresponding to the chord B-Spline curve were set in such a way so the optimal chord distribution to result in a blade geometry as rigid as the current one; while regarding the bounds for the design variables corresponding to the twist B-Spline curve, they were set in such a way so the optimal twist distribution to be as smooth as possible, resulting in a less complicated geometry.

4.2 Optimization Results

The optimization of both blade configurations was carried out on a *DELL™ R815 PowerEdge™* server, with four *AMD Opteron™ 6380* sixteen-core processors at 2.50 GHz (64 cores in total). The population size of the DE was set to 60, while the algorithm was executed for a total of 2000 “generations”. The overall elapsed computation time for the optimization of *BD1* and *BD2* blades was equal to 25.11 and 24.16 minutes respectively.

The twist and chord distributions of the optimized blade designs *BD1* and *BD2*, along with the twist and chord distributions of the original blade are presented through Figures 4 - 6. It is evident that the optimization procedure resulted in blade designs that differ significantly from the original blade, with a much smoother and less complicated twist distribution; a fact that makes them quite attractive from a manufacturing point of view, as simpler geometries are easier to be constructed. As long as the comparison between the twist and chord distribution of *BD1* and *BD2* is concerned, no significant variation is observed, as shown in Figure 6. This is mainly attributed to the similarity between the lift and drag coefficient curves of the *NACA 2207* and *RG15* airfoils. However, since the *RG15* airfoil has a maximum thickness that is 27.4 % larger than the maximum thickness of the *NACA 2207*, the corresponding *BD2* blade is expected to provide better structural features.

The aerodynamic performance of the 3-bladed DAWT rotor under investigation is presented in Figure 7. As it can be observed, the utilization of *BD1* and *BD2*, instead of the original blade geometry, results in a visible improvement of the aerodynamic power output for all the considered operational points. In particular, the *BD1* leads to a mean increase of the aerodynamic power of the rotor of approximately 18.2 %, while the corresponding percentage for *BD2* is 19.4 %. Furthermore, Figure 7 demonstrates the ability of the employed BEM code to approximate the experimental results for the original blade [20] with high accuracy.

At this point, it should be highlighted that the optimization of both *BD1* and *BD2* was conducted by including the correction model proposed by Prandtl to account for the blade tip losses, based on the findings of Phillips [2], who noticed that tip losses exist on DAWT blades as well, despite the relatively close proximity of the blades tips to the diffuser wall; a similar conclusion was also drawn by Kesby et al. [12]. Nevertheless, the inclusion of such a correction model during the BEM analysis of a DAWT rotor may result in an underestimation of the total power output, as the presence of the shroud around the rotor blades produces a noticeable reduction of the particular losses, compared to a bare wind turbine. For this reason, the aerodynamic performance of the examined DAWT rotor for *BD1* and *BD2* optimized blades without the application of a tip losses correction model, is also presented in Figure 7. The 3D drawings of the optimized and original blade designs are presented in Figure 8.

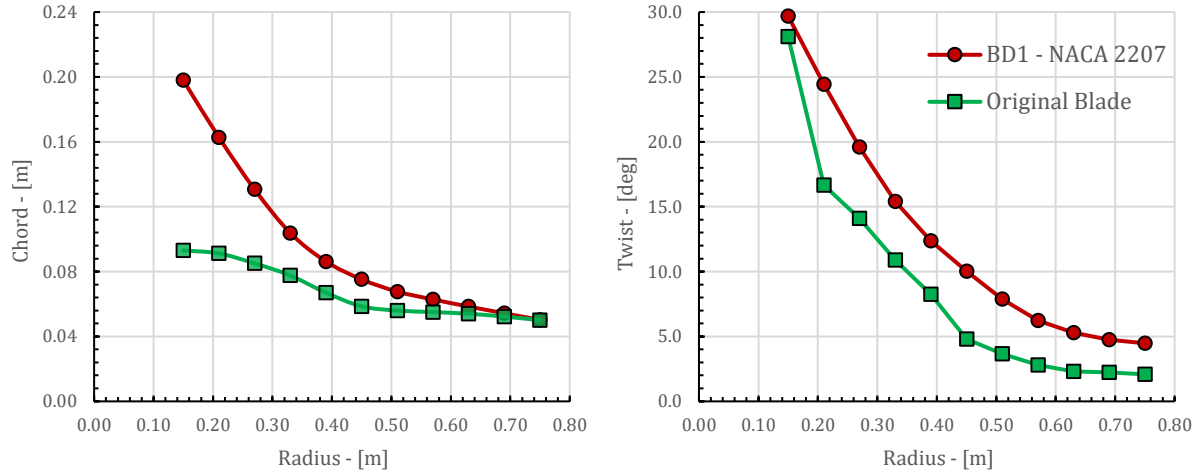


Figure 4. Twist and chord distributions of the optimized blade *BD1*.

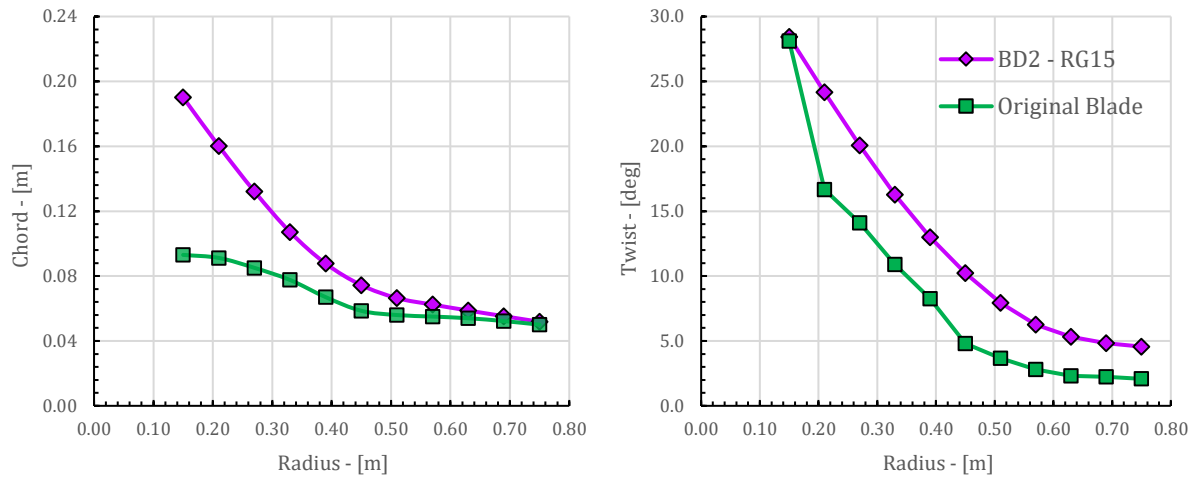


Figure 5. Twist and chord distributions of the optimized blade *BD2*.

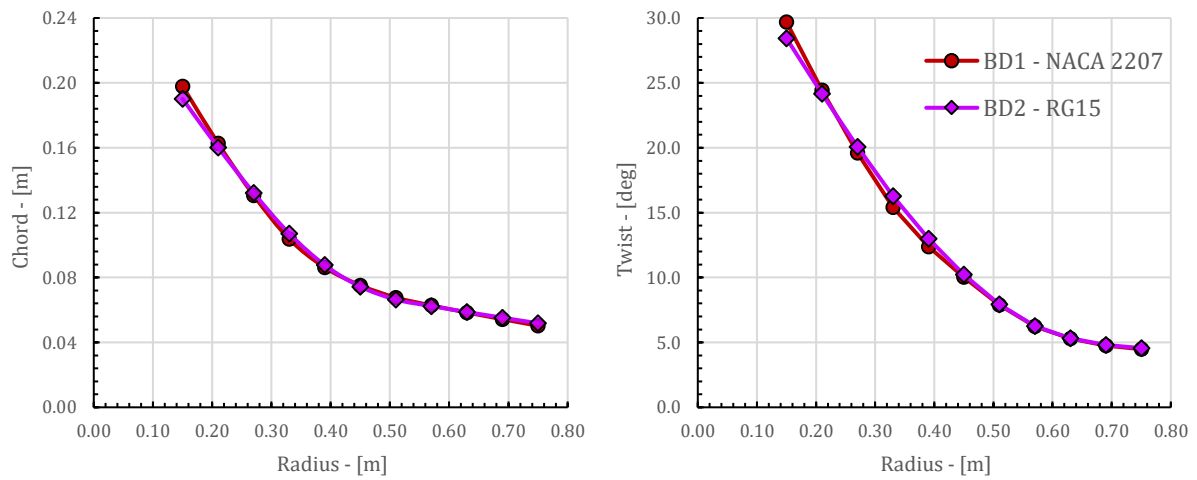


Figure 6. Comparison between the twist and chord distributions of the optimized blades *BD1* and *BD2*.

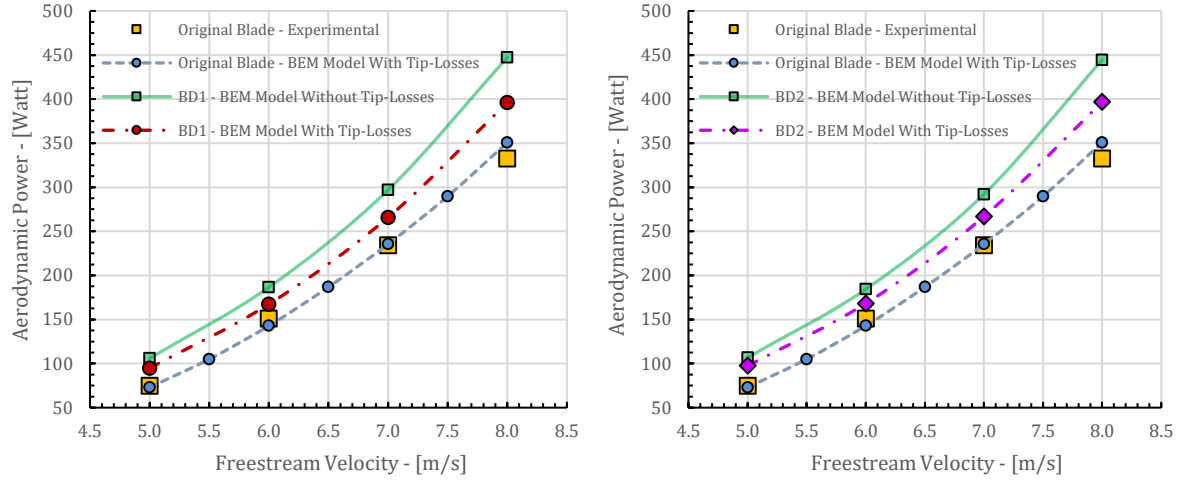


Figure 7. The increased power output of the rotor, utilizing the optimized blade geometries *BD1* and *BD2*.

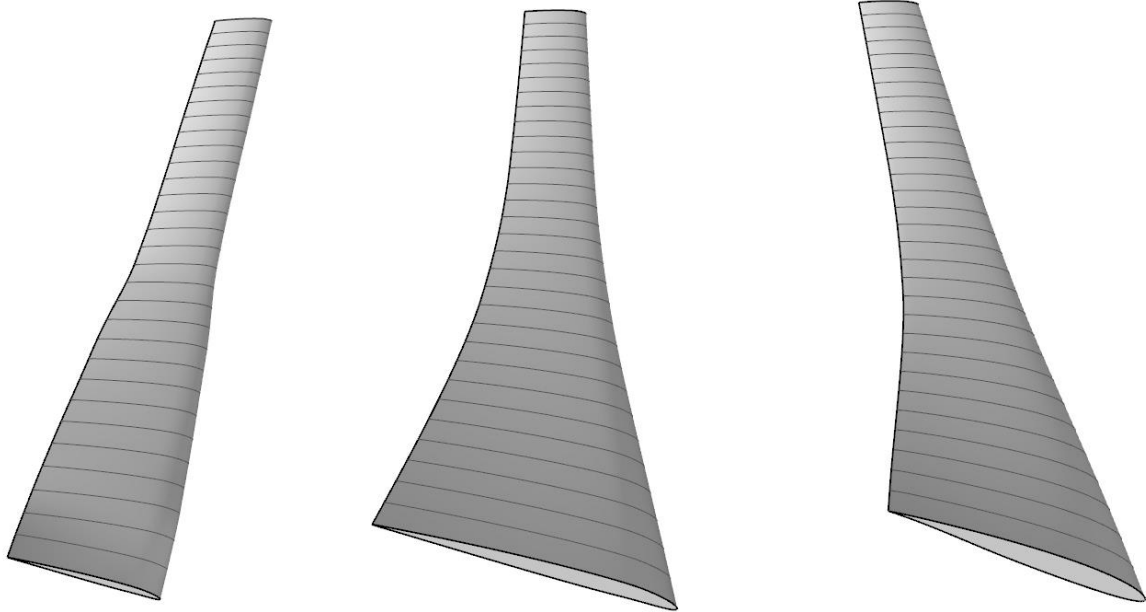


Figure 8. 3D drawings of the original blade (left), optimized blade *BD1* (center) and optimized blade *BD2* (right).

5 CONCLUSIONS

In this work, a robust optimization scheme for the aerodynamic design of DAWT blades was presented, using an asynchronous parallel, meta-model assisted DE algorithm, along with an in-house BEM code, specially tailored for the performance analysis of DAWT rotors. The proposed methodology was applied to the design of improved blades for the rotor of Donqui Urban Windmills DAWT, resulting in two new blade geometries, capable of notably increasing the power output performance of the particular application. The first optimized blade (*BD1*) uses the same airfoil (*NACA 2207*) as the original (reference) blade of the DAWT, while the second optimized blade (*BD2*) uses the *RG15* airfoil. The resulted optimal twist and chord distributions for the two optimized blades are very similar to each other, as a consequence of the common cost function used for both design optimization runs.

ACKNOWLEDGEMENTS

This research has been financially supported by the General Secretariat for Research and Technology (GSRT) and the Hellenic Foundation for Research and Innovation (HFRI) (Scholarship Code: 624).

REFERENCES

- [1] Hjort, S. and Larsen, H. (2015), "Rotor Design for Diffuser Augmented Wind Turbines," *Energies*, Vol. 8, No. 10, pp. 10736–10774.
- [2] Phillips, D. G. (2003), *An Investigation on Diffuser Augmented Wind Turbine Design*, Ph.D. Thesis, University of Auckland.
- [3] Shonhiwa, C. and Makaka, G. (2016), "Concentrator Augmented Wind Turbines: A Review," *Renewable and Sustainable Energy Reviews*, Vol. 59, pp. 1415–1418.
- [4] Lilley, G. M. and Rainbird, W. J. (1956), *A Preliminary Report on the Design and Performance of Ducted Windmills*, The College of Aeronautics, Cranfield University, Report No. 102.
- [5] Igra, O. (1977), "The Shrouded Aerogenerator," *Energy*, Vol. 2, No. 4, pp. 429–439.
- [6] Gilbert, B. L., Oman, R. A. and Foreman, K. M. (1978), "Fluid Dynamics of Diffuser-Augmented Wind Turbines," *Journal of Energy*, Vol. 2, No. 6, pp. 368–374.
- [7] Hansen, M. O. L., Sørensen, N. N. and Flay, R. G. J. (2000), "Effect of Placing a Diffuser around a Wind Turbine," *Wind Energy*, Vol. 3, No. 4, pp. 207–213.
- [8] Refan, M. and Hangan, H. (2012), "Aerodynamic Performance of a Small Horizontal Axis Wind Turbine," *Journal of Solar Energy Engineering*, Vol. 134, No. 2.
- [9] Liu, S. and Janajreh, I. (2012), "Development and Application of an Improved Blade Element Momentum Method Model on Horizontal Axis Wind Turbines," *International Journal of Energy and Environmental Engineering*, Vol. 3, No. 1, p. 30.
- [10] Fletcher, C. A. J. (1981), "Computational Analysis of Diffuser-Augmented Wind Turbines," *Energy Conversion and Management*, Vol. 21, No. 3, pp. 175–183.
- [11] Tavares Dias do Rio Vaz, D. A., Amarante Mesquita, A. L., Pinheiro Vaz, J. R., Cavalcante Blanco, C. J. and Pinho, J. T. (2014), "An Extension of the Blade Element Momentum Method Applied to Diffuser Augmented Wind Turbines," *Energy Conversion and Management*, Vol. 87, pp. 1116–1123.
- [12] Kesby, J. E., Bradney, D. R. and Clausen, P. D. (2016), "Determining Diffuser Augmented Wind Turbine Performance Using a Combined CFD/BEM Method," *Journal of Physics: Conference Series*, Vol. 753, No. 8, p. 082033.
- [13] Leloudas, S. N., Lygidakis, G. N. and Nikolos, I. K. (2017), "Assessment of a Modified Blade Element Momentum Methodology for Diffuser Augmented Wind Turbines," *Proceedings of the ASME 2017 International Mechanical Engineering Congress and Exposition*, Tampa, Florida, USA, November 3–9, 2017, Vol. 7, V007T09A079.
- [14] Hansen, M. O. L. (2007), *Aerodynamics of Wind Turbines*, Earthscan.
- [15] Buhl, M. L. (2005), *A New Empirical Relationship between Thrust Coefficient and Induction Factor for the Turbulent Windmill State*, Technical Report NREL/TP-500-36834, National Renewable Energy Laboratory.
- [16] Storn, R. and Price, K., (1995), "Differential Evolution: A Simple and Efficient Adaptive Scheme for Global Optimization Over Continuous Spaces," *Journal of Global Optimization*, Vol. 23, No. 1.
- [17] Nikolos, I. K. (2011), "Surrogate Modeling in Evolutionary Based Engineering Design Optimization," Tsompanakis, Y. and Topping, B.H.V. (Eds.), *Computational Science, Engineering & Technology Series*, Stirlingshire, UK, pp. 173–203.
- [18] Nikolos, I. K. (2013), "On the Use of Multiple Surrogates within a Differential Evolution Procedure for High-Lift Airfoil Design," *International Journal of Advanced Intelligence Paradigms*, Vol. 5, No. 4, pp. 319–341.
- [19] ten Hoopen, P. D. C. (2009), *An Experimental and Computational Investigation of a Diffuser Augmented Wind Turbine*, M.Sc. Thesis, Faculty of Aerospace Engineering, Delft University of Technology.
- [20] van Dorst, F. A. (2011), *An Improved Rotor Design for Diffuser Augmented Wind Turbine*, M.Sc. Thesis, Faculty of Aerospace Engineering, Delft University of Technology.
- [21] Drela, M. (1989), "XFoil: An Analysis and Design System for Low Reynolds Number Airfoils," *Conference on Low Reynolds Number Airfoil Aerodynamics*, University of Notre Dame.
- [22] Montgomerie, B. (2004), *Methods for Root Effects, Tip Effects and Extending the Angle of Attack Range to +100deg, with Application to Aerodynamics for Blades on Wind Turbines and Propellers*, FOI Swedish Defence Research Agency, Scientific Report FOI-R-1035-SE.

RAREFIED GAS FLOW ANALYSIS OVER A RE-ENTRY SPACE CAPSULE GEOMETRY

Angelos G. Klothakis¹, Stavros N. Leloudas², Georgios N. Lygidakis³ and Ioannis K. Nikolos⁴

^{1,2,3,4}School of Production Engineering and Management
Technical University of Crete
Chania, GR-73100, Greece

e-mail: ¹anklothakis@isc.tuc.gr, ²sleloudas@isc.tuc.gr, ³glygidakis@isc.tuc.gr, ⁴inikolo@dpem.tuc.gr

Keywords: Rarefied gas flow, supersonic flow, re-entry space capsule, node-centered finite-volume, three-dimensional grid.

Abstract. During the past years significant efforts have been applied for the effective and computationally efficient prediction of rarefied gas flows, especially for aerospace applications. Such flows appear to be considerably different from those at the continuum regime, making Navier-Stokes equations to fail against the corresponding phenomena without further modification. In this work, a modified in-house academic CFD (Computational Fluid Dynamics) solver, named Galatea, is presented and assessed. For fluids in slip flow regime, i.e., with Knudsen number greater than 0.01, the no-slip condition is no longer valid on solid wall surfaces, hence, velocity slip and temperature jump boundary conditions have been incorporated to the aforementioned solver. For its assessment rarefied laminar gas flow (inside the slip flow regime) is simulated over a re-entry space capsule geometry, i.e., the blunt portion of a spaceship returning to Earth after a spaceflight. Due to unavailability of corresponding experimental or numerical data, the extracted results are compared with those derived by the parallel open-source kernel SPARTA, which is based on the DSMC (Direct Simulation Monte Carlo) approach. A very satisfactory agreement is succeeded, demonstrating the proposed modified solver's potential to predict effectively such complex flows.

1 INTRODUCTION

During the past decades a considerable effort has been exerted by various researchers to develop methodologies capable to accurately simulate high-velocity rarefied gas flows, e.g., over aerospace geometries [1-3]. Nevertheless, such flows appear to be significantly different compared to those at the continuum regime. As a result, the Navier-Stokes PDEs (Partial Differential Equations), used at macroscale CFD (Computational Fluid Dynamics) solvers, seem to fail when simulating similar phenomena without further adaptations and modifications [1]. In practice the rarefied gas flows are categorized depending on the computed Knudsen number, a classification originally introduced by Schaaf and Chambre [4]; for Knudsen numbers less than 1.0E-2 (continuum regime) the Navier-Stokes PDEs are valid without any additional modification, allowing ordinary CFD solvers to be employed. However, for values between 1.0E-2 and 1.0E-1 (slip flow regime) special treatment of wall boundary conditions is required; velocity slip conditions as well as temperature jump ones have to be applied (as in this work) [1]. If the simulation is coping with Knudsen numbers greater than 1.0E-1 (transition regime and free molecular regime), the rarefaction effects become the sovereign ones necessitating for alternative methodologies, i.e., the DSMC (Direct Simulation Monte Carlo) approach [5] or the numerical solution of the Boltzmann Equation [6].

Although the latter methods can actually be employed throughout all the regimes [1, 6], their implementation at continuum and slip flow regimes calls for excessive computational resources. Thus, Navier-Stokes approaches are usually preferred at those regimes. In particular for the latter regime, regarding actually rarefied gas flows and consequently the implementation of velocity slip and temperature jump conditions, various studies have been conducted during the past years (similarly to this work) examining various geometries, two- or three-dimensional computational fields, structured or unstructured grids, etc. [7-12]. Although the main concept of these conditions was proposed initially by Navier [1], the first corresponding mathematical model was introduced by Maxwell in 1879 [13]. According to this, velocity and temperature of solid wall nodes are defined with the normal to this surface gradients [3]. Since then, it made its way, whereas it was enhanced with various modifications, such as second-order spatial accuracy [14-16] or iterative schemes assuring solution convergence [17].

Despite the development of the aforementioned boundary conditions (slip velocity and temperature jump ones), allowing CFD solvers to extend their applications at slip flow regime, the latter appear to be inadequate to predict flows with larger values of Knudsen number (greater than 1.0E-1) [1]. It is this observation along with the

excessive computational requirements of methodologies depending on the Boltzmann equation that created the need for the development of the DSMC (Direct Simulation Monte Carlo) approach, originally introduced by Bird [5]. Initially, it hadn't been widely accepted by the scientific community, mainly because of its statistical-stochastic nature; thus, its implementation was confined in relatively simple simulations [5]. Gradually, its applications were extended in more complicated engineering problems, demonstrating its capability for accurate flow predictions [18]. Similarly to most of the computational methods, a trade-off relation arises between the desired accuracy and the available computational resources. DSMC approach calls for relatively excessive computational requirements in test cases involving high pressure and large-scale computational fields; a remedy for this drawback was revealed with the advance of the available computer systems and subsequently the capability of parallel processing [18, 19].

In this work the in-house academic CFD solver *Galatea*, which has been recently enhanced to simulate rarefied gas flows inside the slip flow regime (Knudsen number between $1.0E-2$ and $1.0E-1$), is presented in brief and assessed against a re-entry space capsule test case [20, 21]. For rarefied gases the capability of implementing the aforementioned slip velocity and temperature jump boundary conditions [1] on solid wall surfaces has been incorporated. In order to increase the accuracy at the same regions, the second-order accurate slip scheme of Beskok and Karniadakis [14, 15] has been additionally included. It was selected due to its relatively easy implementation on unstructured, tetrahedral or hybrid grids; it can overcome the numerical difficulties, entailed by the evaluation of the second derivative of slip velocity [14]. Furthermore, a normalization scheme [17] has been incorporated to mitigate the excessive oscillations, caused by the slip/jump boundary conditions, especially during the initial steps of the iterative solution procedure. The proposed solver is validated against rarefied laminar gas flow (inside the slip flow regime) over a re-entry space capsule geometry, i.e., the blunt portion of a spaceship returning to Earth after a spaceflight. Due to unavailability of corresponding experimental or numerical data, the obtained results are compared with those extracted by the parallel open-source kernel SPARTA [18], a DSMC-based software [18, 19]. A very good agreement is succeeded, demonstrating the modified proposed solver's potential to predict effectively such demanding flows over complex geometries.

2 THE CFD APPROACH

2.1 The *Galatea* code

The in-house academic CFD code *Galatea* is based on the dimensionless Navier-Stokes PDEs along with a node-centered finite-volume scheme to predict inviscid, viscous laminar, and viscous turbulent flows of compressible fluids on tetrahedral or hybrid unstructured grids (including tetrahedral, prismatic and pyramidal elements) [20, 21]. For turbulence prediction the RANS (Reynolds Averaged Navier-Stokes) approach is implemented along with an appropriate statistical two-equation model, namely the $k-\epsilon$ [22], the $k-\omega$ [23] or the SST (Shear Stress Transport) [24]. An upwind methodology is followed for the computation of the inviscid fluxes, applying the Roe's [25] or the HLLC (Harten-Lax-van Leer-Contact) approximate Riemann solver [26], coupled with a higher-order accurate spatial scheme; the latter is based on the MUSCL (Monotone Upwind Scheme for Conservation Laws) approach along with an appropriate slope limiter, namely the Van Albada-Van Leer, the Minmod, the Barth-Jespersen and the MLP-Venkatakrishnan (Multi-dimensional Limiting Process-Venkatakrishnan) one [20, 21]. For the calculation of the viscous fluxes the required velocity and temperature gradients are evaluated with an element-based (edge-dual volume) or a nodal-averaging method. Time integration and iterative approximation of the final steady-state solution is succeeded with either an explicit scheme, applying a second-order temporal accurate four-stage Runge-Kutta (RK(4)) method, or an implicit one, implementing the Jacobi or the Gauss-Seidel algorithm [20]. To accelerate the solution procedure and reduce the required physical time, appropriate methodologies have been incorporated; an edge-based data structure, a local time-stepping technique, a SPMD (Single Program-Multiple Data) parallelization strategy and an agglomeration multigrid scheme. Further details for the *Galatea* solver can be found in [20] and [21].

2.2 Velocity slip and temperature jump boundary conditions

No-slip conditions on solid wall surfaces appear to fail in the slip flow regime, necessitating for velocity slip and temperature jump ones to be imposed instead [1]. According to this methodology (Maxwell's model), the values of velocity and temperature on wall boundaries are defined with the corresponding normal to the boundary surface gradients [13]. A schematic representation of the aforementioned slip velocity boundary conditions, compared with the no-slip ones, is illustrated in Figure 1. The corresponding model is defined for the dimensionless slip velocity U_s as follows [1, 13, 14]

$$U_s - U_w = \frac{2 - \sigma_u}{\sigma_u} Kn \frac{\partial U_s}{\partial n} + \frac{3}{2\pi} \frac{(\gamma - 1)}{\gamma} \frac{Kn^2 Re}{E_c} \frac{\partial T}{\partial s} \quad (1)$$

where U_w denotes the velocity on the wall surface, Kn the Knudsen number, and $\frac{\partial U_s}{\partial n}$ the transverse velocity gradient, i.e., the derivative of the tangential slip velocity normal to the wall surface (denoted by vector n) [11]. σ_u is the tangential momentum accommodation coefficient (equal to unity in this study) [11, 12, 27]. The second RHS term, which is based on the values of the dimensionless Reynolds (Re) and Eckert (E_c) numbers, the ideal gas constant γ and the tangential to the wall surface derivative of the temperature, represents the slip velocity contribution induced by the thermal creep. It is usually relatively small, because of the second-order in Knudsen number as well as due to the fact that in common engineering problems there is a small temperature change across the wall surfaces; therefore, it is quite common tactic to neglect it (as in this study) [14].

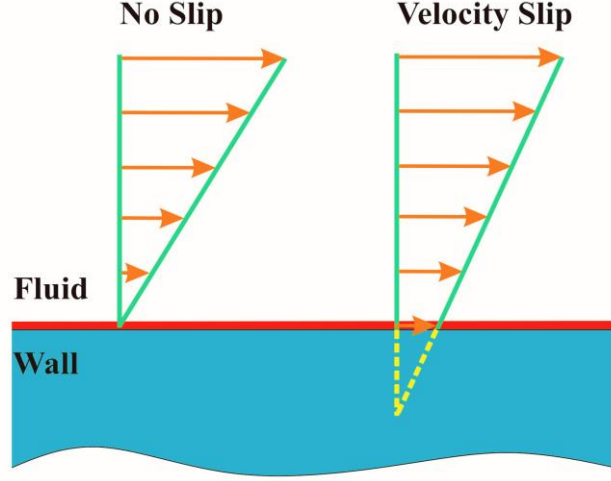


Figure 1. No slip and velocity slip boundary conditions.

Similarly to the velocity slip boundary condition, the temperature jump one is described as follows [14]

$$T_s - T_w = \frac{2 - \sigma_T}{\sigma_T} \frac{2\gamma}{\gamma + 1} \frac{Kn}{Pr} \frac{\partial T}{\partial n} \quad (2)$$

where T_s is the slip temperature, T_w the wall temperature and $\frac{\partial T}{\partial n}$ the derivative of the temperature normal to the wall surface. Pr stands for the dimensionless Prandtl number, whereas σ_T for the thermal or energy accommodation coefficient, depending on the surface quality [14]. The latter is assumed equal to unity in this study [12, 27]. Improved accuracy of the final steady-state solution at the solid wall region is succeeded with the second-order accurate scheme of Beskok and Karniadakis [14]. It appears to overcome the numerical difficulties, entailed by most of the corresponding higher-order schemes, via the reconstruction of the first RHS term of Equation (1) with a Taylor expansion series [16]; not a straightforward procedure when complex three-dimensional geometries are used along with unstructured hybrid grids. Its formulation is defined as

$$U_s - U_w = \frac{2 - \sigma_u}{\sigma_u} \frac{Kn}{(1 - bKn)} \frac{\partial U_s}{\partial n} \quad (3)$$

where b is the slip coefficient, which can be defined either experimentally or via methodologies depending on the Boltzmann equation or the DSMC approach [14]. It was set equal to -1.0 for the simulations encountered in this study [14].

Due to the wall function mode (Dirichlet-type) of the aforementioned boundary conditions, they are susceptible of leading to residual oscillations, especially during the initial iterations, or of leading the solution procedure even to fail. Thus, a normalization scheme was additionally incorporated, to allow for the gradual change of the solid wall nodal velocity and temperature values [17]. It is described as follows [17]

$$U_s^i = \alpha U_s^{i-1} + (1 - \alpha) U_s^i \quad (4)$$

where α is the normalization coefficient, which it is set equal to 0.95 in this study.

3 THE DSMC APPROACH

The DSMC method, a stochastic particle-type methodology, was originally developed by Graeme Bird [5] in

1960. Its implementation is based on the assumption of a large number of particles, the so-called simulator particles, which represent actually the real gas particles, and consequently allow for the simulation of rarefied gas flows [5]. The main idea considers the division of the examined computational field in Cartesian cells to provide the geometric boundaries and volumes, required to sample the macroscopic properties of the flow from the aforementioned simulator particles taking previously into account their movements and collisions [5]. Summarizing, the DSMC iterative algorithm can be decomposed in the four following steps: 1) The particles move to their new positions using a time step. 2) At each computational cell the simulator particles are assigned a new index. 3) The collision pairs are selected and the corresponding intermolecular collisions are performed in a probabilistic manner. 4) The required macroscopic flow properties, such as velocity and temperature, are obtained by averaging temporally (for several time steps) the microscopic properties of the particles in the cells [5]. Figure 2 includes the flow chart of the aforementioned iterative scheme.

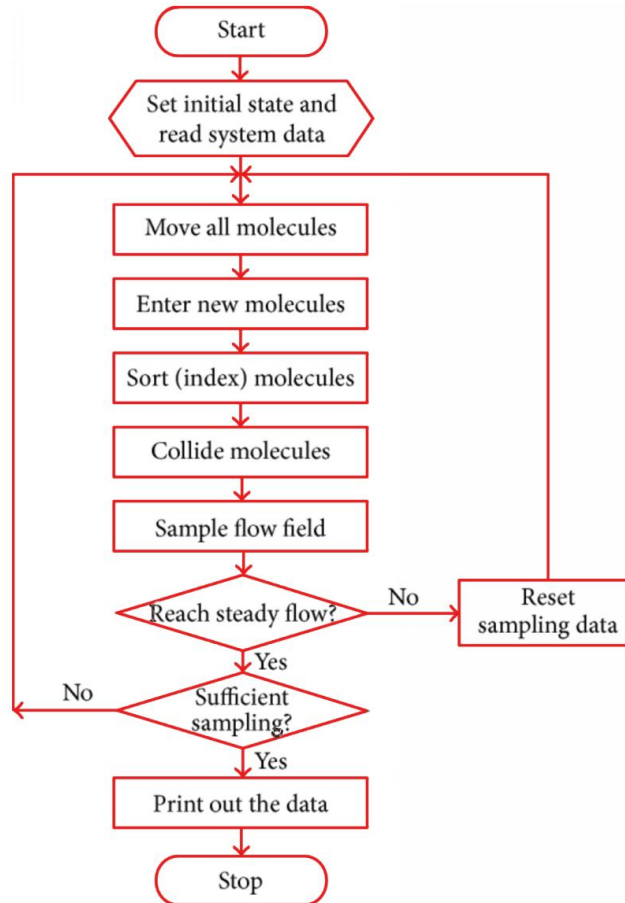


Figure 2. DSMC algorithm flow chart.

Due to the unavailability of experimental or numerical data for the examined space capsule geometry, the results obtained by the modified *Galatea* solver were compared with those, extracted by the parallel open-source DSMC kernel SPARTA [18]. The aforementioned software was developed at Sandia Laboratories approximately in 2014, while it was distributed then as an open source code under the terms of the GPL license. It should be highlighted that, though being very robust and effective, it is a highly demanding software, as it requires a thorough understanding of the DSMC modeling [18, 19].

4 NUMERICAL RESULTS

4.1 The re-entry space capsule geometry

The proposed solver was validated against a re-entry space capsule geometry, i.e., a spherical blunt cone, standing for the blunt portion of a spaceship returning to Earth after a spaceflight. It resembles the REV (Robotic Enhanced Vehicle) of the DART (Delft Aerospace Reentry Test) demonstrator program [28]. This program began at Delft University of Technology approximately in 2001, aiming to study the aerodynamic phenomena appearing

during the re-entry phase of space vehicles. The details of this spherically blunt cone configuration, both in 2D and 3D, are illustrated in Figure 3. The conical forebody has $r_n=345.22$ mm, $L=1546.63$ mm and $R=525$ mm, where r_n is the radius of the spherical nose cap, R the cone's base radius and L the total length of the body. Only the quarter of the aforementioned three-dimensional configuration was modeled, for computational savings [20, 21].

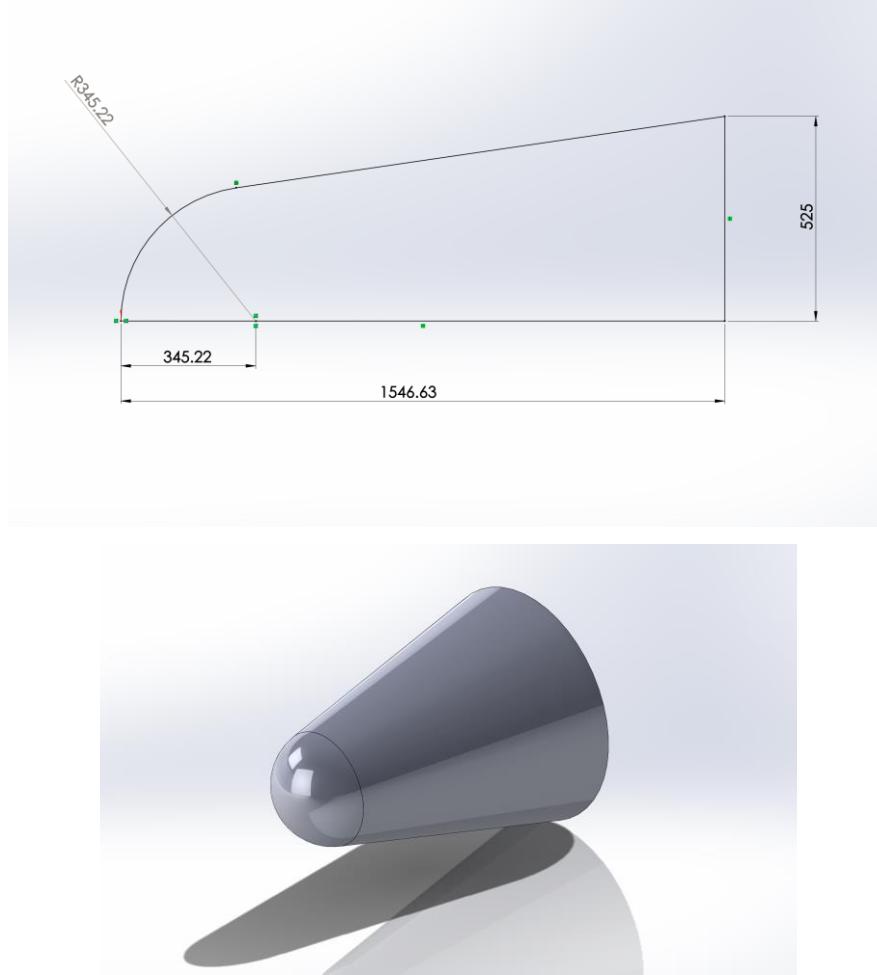


Figure 3. Capsule geometry details in 2D (top) and 3D (bottom).

4.2 Flow data and simulation details

As far as the flow conditions are concerned, the free-stream velocity was assumed to be 850 m/s, whereas the corresponding angle of attack was set equal to 0° . A relatively high Mach number was computed (3.2643), entailing a strong bow shock. Despite this velocity being relatively small comparing to that of such a space capsule during its re-entry phase, it was assumed adequate considering the initial motivation of the study to assess a modified Navier-Stokes solver against a rarefied gas dynamics problem. Finally, the free-stream temperature was set equal to 168.72 K, while this on the capsule surface to 290 K. The background pressure was set to 0.5 Pa, a value corresponding to an altitude of approximately 85 km. The aforementioned flow conditions are summarized in Table 1.

V_∞ (m/s)	850
Re_∞	224.7
Kn_∞ (computed with cone's base radius)	0.0107
ρ_∞ (kg/m ³)	9.986×10^{-6}
T_∞ (K)	168.72
T_w (K)	290

Table 1. Flow conditions.

Considering the aforementioned flow data, a hybrid unstructured grid was generated for the CFD solver, composed of 4,212,308 nodes, 21,032,650 tetrahedra and 1,168,000 prisms. The prismatic layers are located on the solid wall region, i.e., the surface of the space capsule, allowing for the accurate prediction of the corresponding viscous phenomena [20, 21]. Figure 4 depicts the complete computational grid, while Figure 5 focuses on its symmetry/capsule surface. To use this grid with the dimensionless *Galatea* solver, it was re-dimensionalized in order its base's radius to become equal to unity [20]. For the calculation of the inviscid fluxes the Roe's approximate Riemann solver was employed along with a second-order spatial accurate scheme, coupled with the Van Albada-Van Leer slope limiter [20, 25]. The nodal-averaging scheme was applied for the computation of the velocity and temperature gradients, and consequently the viscous fluxes. Time integration and iterative approximation of the final steady-state solution was succeeded with the incorporated second-order accurate in time four-stage Runge-Kutta scheme. The CFL number was set equal to 0.5. To accelerate the iterative procedure the initial grid was divided in eight sub-domains to be processed in parallel [20] (on a workstation with an *AMD FX™ 8350* 8-core processor at *4.00 GHz*). Two coarser resolutions were constructed for each of the aforementioned sub-grids, following the incorporated directional agglomeration strategy, in order the corresponding multigrid scheme to accelerate further the solution process [21].

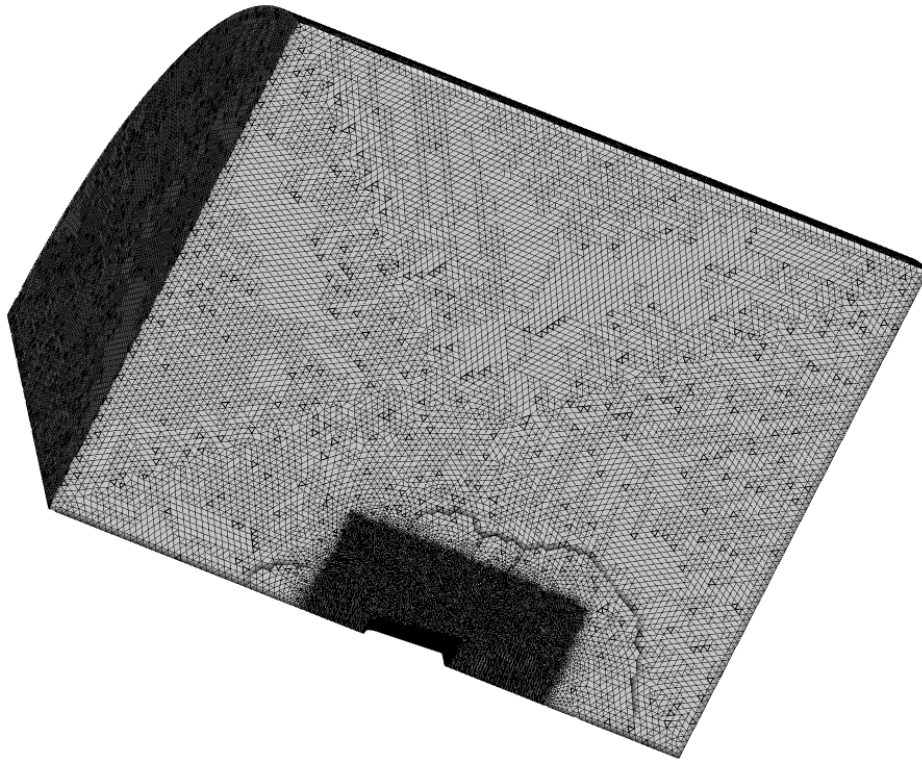


Figure 4. Computational grid, used with the *Galatea* solver.

The results obtained by the modified *Galatea* solver were compared with those extracted by the parallel open-source kernel SPARTA [18, 19]. For its implementation a 2D-axisymmetric computational domain with dimensions 6 m and 2.5 m in x – and r –axis, respectively, was designed. Spatial discretization was succeeded via the division of the aforementioned domain in 10,000,000 cells, by constructing a Cartesian grid with 4000 and 2500 cells in x – and r –axis, respectively. Regarding the corresponding simulation parameters, the number density was set equal to $2.14746 \times 10^{20} \text{ m}^{-3}$, whereas the time step was selected equal to $3 \times 10^{-7} \text{ s}$. The time step was defined so that each particle to need approximately five time steps to cross each cell. The simulation began with a transient period of 100,000 steps, deriving the initial steady-state solution, while at next samples were taken for additional 60,000 time steps, aiming to reduce the statistical scattering error. Considering that DSMC methodology relies strongly on the employed number of particles, several different numbers of them were tested (between 10×10^6 and 86×10^6). From these tests the optimum F_{num} (real particles per simulator particle) of 3×10^{17} was selected, which subsequently produced a total number of 86×10^6 particles for the whole simulation domain. The aforementioned parameters, defining actually the utilized DoFs (Degrees of Freedom), were revealed to derive the desired accuracy, avoiding yet any excessive computational and memory requirements. The whole parameters used with the SPARTA solver are summarized in Table 2. The DSMC run was carried out on a *DELL™ R815 PowerEdge™* server, with four *AMD Opteron™ 6380* 16-core processors at *2.50 GHz* (64 cores in total); 60 cores were used for the run, which required approximately 5 days (wall clock).

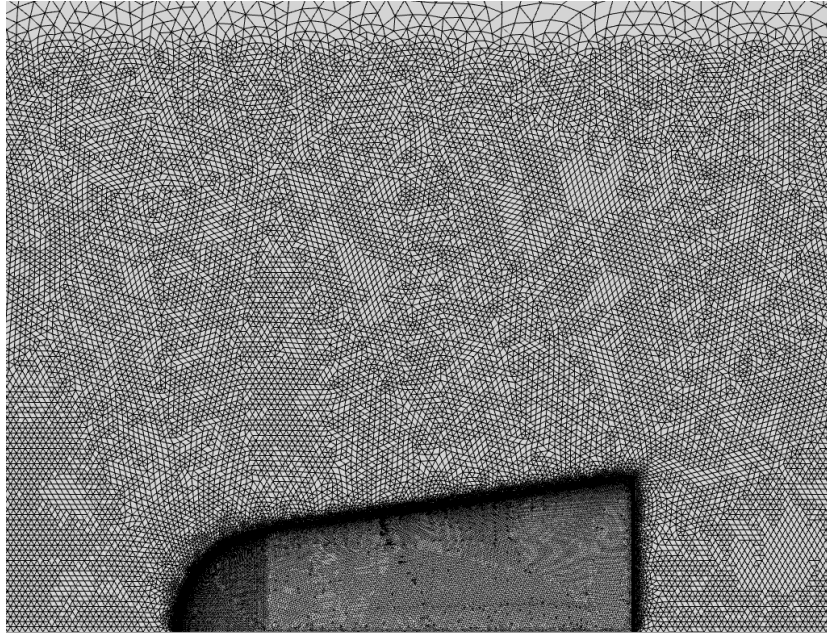
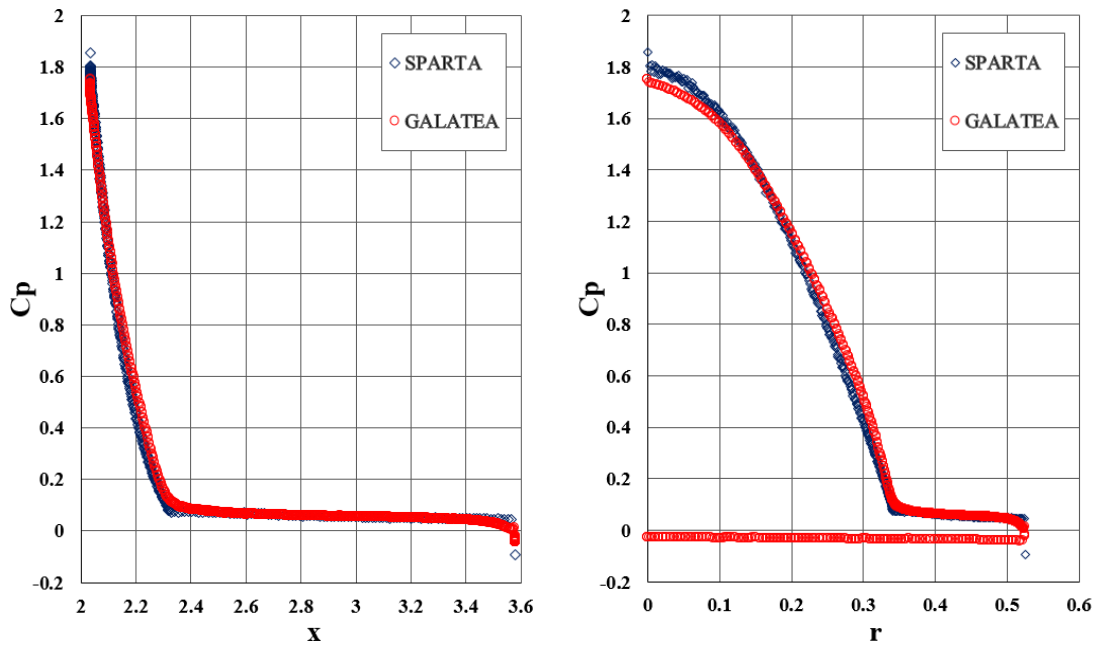


Figure 5. Close-up view of the symmetry/capsule surface of the three-dimensional computational grid.

Number Density (particles/m³)	2.14746×10^{20}
F_{num}	3×10^{17}
Timestep (s)	3×10^{-7}
Transient period	100,000
Sampling period	60,000

Table 2. DSMC simulation parameters.


 Figure 6. Pressure coefficient distribution σ at the capsule surface along the x –axis (left) and the r –axis (right).

4.3 Numerical results and discussion

Figure 6 illustrates the pressure coefficient C_p distributions in x – and r –axis, extracted by both the aforementioned solvers (*Galatea* and *SPARTA*). As one can observe, a very satisfactory comparison is obtained. A slight difference in the front area of the capsule geometry can be identified in Figure 6 (right), regarding C_p

distribution in the r –axis. It stems probably from the strong bow shock in front of the capsule.

In Figure 7 the extracted pressure contours by both solvers are presented. The compared contours appear to be very similar, especially in the bow shock region in front of the capsule. Pressure at the stagnation point was computed approximately equal to 6.8 Pa by both solvers. In Figure 8 the extracted (non-dimensional) velocity contours by both solvers are presented. Figure 9 contains the axial positions where velocity profiles were extracted; the corresponding profiles are depicted in Figure 10, where a very good agreement between the two solvers is observed. A steeper velocity transition at the bow shock region is computed by the SPARTA code, compared to the *Galatea* solver (positions 2, 3 and 4, in Figure 10); this is attributed to the relatively low grid density, used by the *Galatea* solver in the corresponding region (no local grid refinement was applied).

Considering the previously described qualitative and quantitative results, a very satisfactory agreement is clearly identified between the employed solvers, despite the fact that they depend on completely different computational approaches. As a result, the proposed solver's potential to predict effectively such demanding flows is demonstrated.

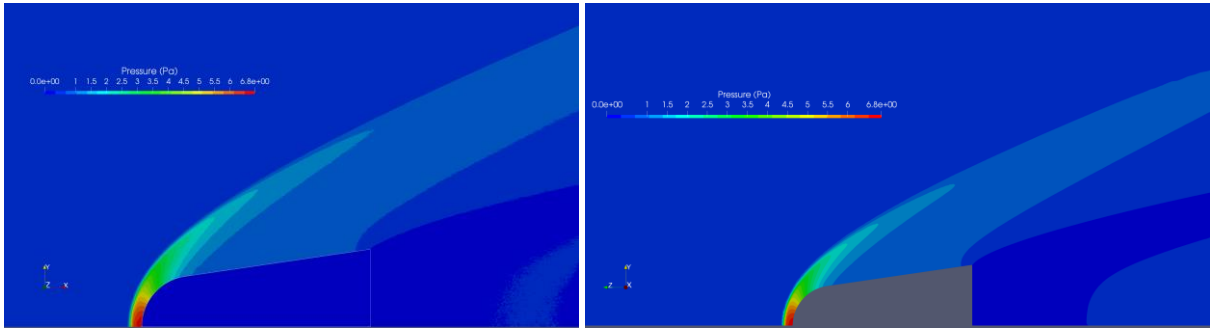


Figure 7. Pressure contours, extracted by the SPARTA software (left) and the *Galatea* solver (right).

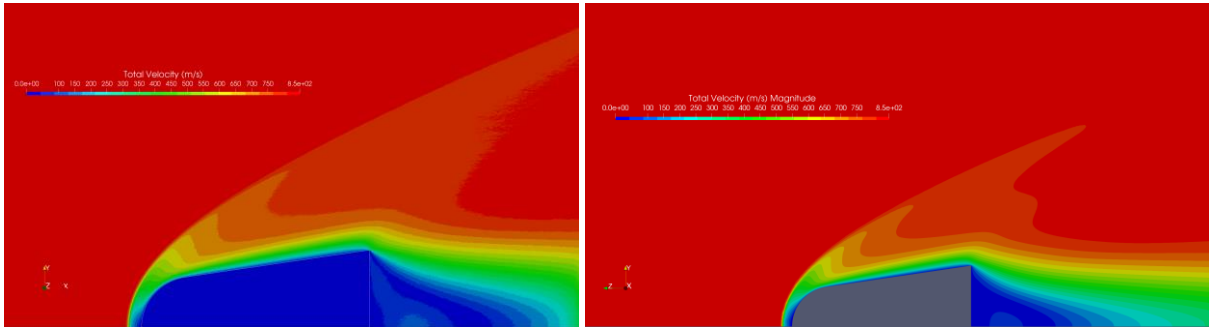


Figure 8. Velocity contours, extracted by the SPARTA software (left) and the *Galatea* solver (right).

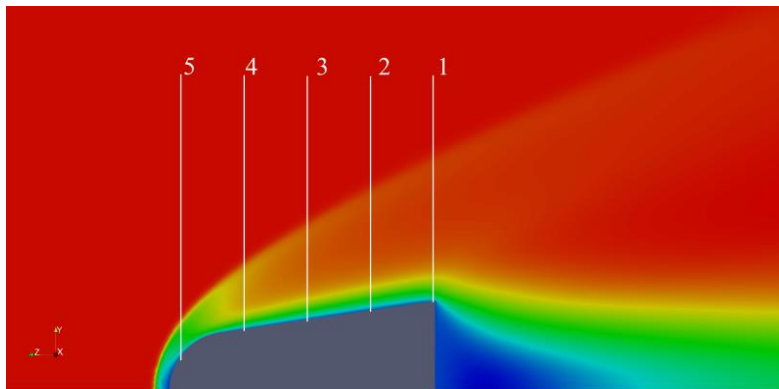


Figure 9. The five axial positions (distance from the cone's base) where velocity profiles were extracted for both solvers (1: $x = 0$ m; 2: $x = 0.355$ m; 3: $x = 0.71$ m; 4: $x = 1.065$ m; 5: $x = 1.42$ m).

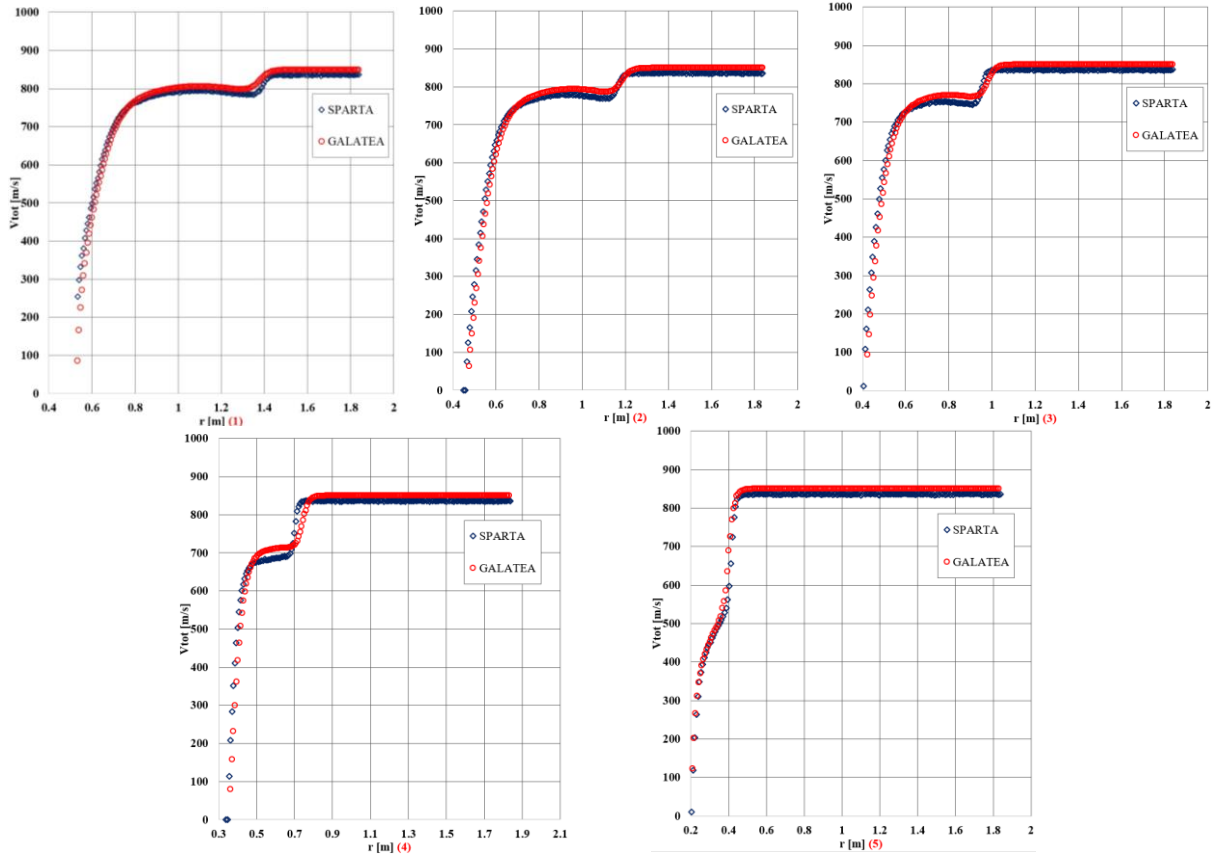


Figure 10. Velocity profiles, extracted for both solvers at the five axial positions of Figure 9.

5 CONCLUSIONS

In this study the in-house academic CFD solver *Galatea*, which has been enhanced to simulate rarefied gas flows inside the slip flow regime (Knudsen number between $1.0E-2$ and $1.0E-1$), was presented in brief and assessed against a re-entry space capsule test case [20, 21]. For rarefied gases the capability of implementing the aforementioned slip velocity and temperature jump boundary conditions [1] on solid wall surfaces has been incorporated. In order to increase the accuracy at the same regions, the second-order accurate slip scheme of Beskok and Karniadakis [14, 15] has been also included. It was selected due to its relatively easy implementation on unstructured, tetrahedral or hybrid grids; it can overcome the numerical difficulties, entailed by the evaluation of the second derivative of slip velocity [14]. Furthermore, a normalization scheme [17] has been incorporated to mitigate the excessive oscillations, caused by the Dirichlet type of the slip/jump boundary conditions, especially during the initial steps of the iterative solution procedure. The proposed solver was validated against rarefied laminar gas flow (inside the slip flow regime) over a re-entry space capsule, i.e., the blunt portion of a spaceship returning to Earth after a spaceflight; it resembles the REV of the DART demonstrator [28]. The obtained results were compared with those extracted by the parallel open-source kernel SPARTA, a DSMC-based software [18, 19]. A very good agreement was succeeded between them, concerning pressure and velocity distributions, as well as velocity profiles, despite the fact that they depend on completely different computational approaches. Ongoing work includes further investigation and validation of the capabilities of the modified CFD code *Galatea*, as well as the incorporation of more sophisticated slip velocity and temperature jump models, such as the Langmuir-Maxwell and Langmuir-Smoluchowski ones [29].

REFERENCES

- [1] Zhang, W.M., Meng, G. and Wei, X. (2012), “A review on slip models for gas microflows,” *Microfluidics and Nanofluidics*, Vol. 13, pp. 845-882.
- [2] Ho, C.M. and Tai, Y.C. (1998), “Micro-electro-mechanical-systems (MEMS) and fluid flows,” *Annual Review of Fluid Mechanics*, Vol. 30, pp. 579-612.
- [3] Gad-el-Hak, M. (1999), “The fluid mechanics of microdevices,” *ASME Journal of Fluids Engineering*, Vol. 121, pp. 5-33.
- [4] Schaaf, S.A. and Chambre, P.L. (1961), *Flows of rarefied gases*, Princeton University Press, Princeton.

- [5] Bird, G.A. (1994), *Molecular gas dynamics and the direct simulation of gas flows*, Clarendon Press, Oxford.
- [6] Evans, B., Morgan, K. and Hassan, Q. (2011), "A discontinuous finite element solution of the Boltzmann kinetic equation in collisionless and BGK forms for macroscopic gas flows," *Applied Mathematical Modelling*, Vol. 35, pp. 996-1015.
- [7] Dongari, N., Sambasivam, R. and Durst, F. (2009), "Extended Navier-Stokes equations and treatments of micro-channel gas flows," *Journal of Fluid Science and Technology*, Vol. 4, pp. 454-467.
- [8] Myong, R.S. (2001), "A computational method for Eu's generalized hydrodynamic equations of rarefied and microscale gas dynamics," *Journal of Computational Physics*, Vol. 168, pp. 47-72.
- [9] Myong, R.S. (2004), "A generalized hydrodynamic computational model for rarefied and microscale diatomic gas flows," *Journal of Computational Physics*, Vol. 195, pp. 655-676.
- [10] Myong, R.S., Reese, J.M., Barber, R.W. and Emerson, D.R. (2005), "Velocity slip in microscale cylindrical Couette flow: The Langmuir model," *Physics of Fluids*, Vol. 17, 087105.
- [11] Madhawa Hettiarachchi, H.D., Golubovic, M., Worek, W.M. and Minkowycz, W.J. (2008), "Three-dimensional laminar slip-flow and heat transfer in a rectangular microchannel with constant wall temperature," *Journal of Heat and Mass Transfer*, Vol. 51, pp. 5088-5096.
- [12] Fan, J., Boyd, I.D., Cai, C.P., Hennighausen, K. and Candler, G.V. (2001), "Computation of rarefied gas flows around a NACA 0012 airfoil," *AIAA Journal*, Vol. 39, pp. 618-625.
- [13] Maxwell, J.C. (1879), "On stresses in rarified gases arising from inequalities of temperature," *Philosophical Transactions of the Royal Society*, Vol. 170, pp. 231-256.
- [14] Beskok, A. and Karniadakis, G.E. (1999), "A model for flows in channels, pipes, and ducts at micro and nano scales," *Microscale Thermophysical Engineering*, Vol. 3, pp. 43-77.
- [15] Karniadakis, G.E. and Beskok, A. (2002), *Micro flows: fundamentals and simulation*, Springer, New York.
- [16] Stevanovic, N.D. and Djordjevic, V.D. (2015), "An exact analytical solution for the second order slip-corrected Reynolds lubrication equation," *FME Transactions*, Vol. 43, pp. 16-20.
- [17] Ferras, W.L., Nobregal, J.M. and Pinho, F.T. (2013), "Implementation of slip boundary conditions in the finite volume method: new techniques," *International Journal for Numerical Methods in Fluids*, Vol. 72, pp. 724-747.
- [18] Gallis, M.A., Torczynski, J.R., Plimpton, S.J., Rader, D.J. and Koehler, T. (2014), "Direct Simulation Monte Carlo: The quest for speed," *Proceedings of the 29th Rarefied Gas Dynamics (RGD) Symposium*, Xi'an, China, July 2014.
- [19] Klothakis, A.G., Nikolos, I.K., Koehler, T.P., Gallis, M.A. and Plimpton, S.J. (2016), "Validation simulations of the DSMC code SPARTA," *Proceedings of the 30th International Symposium on Rarefied Gas Dynamics*, AIP RGD, Victoria, Canada, July 2016.
- [20] Lygidakis, G.N. and Nikolos, I.K. (2015), "Numerical analysis of flow over the NASA Common Research Model using the academic Computational Fluid Dynamics code Galatea," *ASME Journal of Fluids Engineering*, Vol. 137, 071103-1.
- [21] Lygidakis, G.N., Sarakinos, S.S. and Nikolos, I.K. (2016), "Comparison of different agglomeration multigrid schemes for compressible and incompressible flow simulations," *Advances in Engineering Software*, Vol. 101, pp. 77-97.
- [22] Launder, B.E. and Spalding, D.B. (1974), "The numerical computation of turbulent flows," *Computer Methods in Applied Mechanics and Engineering*, Vol. 3, pp. 269-289.
- [23] Saffman, P.G. and Wilcox, D.C. (1974), "Turbulence-model predictions for turbulent boundary layers," *AIAA Journal*, Vol. 12, pp. 541-546.
- [24] Menter, F.R. (1994), "Two-equation eddy viscosity turbulence models for engineering applications," *AIAA Journal*, Vol. 32, pp. 1598-1605.
- [25] Roe, P. (1981), "Approximate Riemann solvers, parameter vectors and difference schemes," *Journal of Computational Physics*, Vol. 43, pp. 357-371.
- [26] Toro, E.F., Spruce, M. and Speares, W. (1994), "Restoration of the contact surface in the HLL Riemann solver," *Shock Waves*, Vol. 4, pp. 25-34.
- [27] Shoja-Seni, A., Roohi, E., Kahrom, M. and Stefanov, S. (2014), "Investigation of aerodynamic characteristics of rarefied flow around NACA0012 airfoil using DSMC and NS solvers," *European Journal of Mechanics B/Fluids*, Vol. 48, pp. 59-74.
- [28] Otten, H.B.A. (2001), "Preliminary computational investigation on aerodynamic phenomena on DELFT aerospace reentry test vehicle," *Proceedings of the 4th Symposium on Aerothermodynamics for Space Applications*, Capua, Italy, October 2001, pp. 207-213.
- [29] Le, N.T.P., White, C., Reese, J.M. and Myong, R.S. (2012), "Langmuir-Maxwell and Langmuir-Smoluchowski boundary conditions for thermal gas flow simulations in hypersonic aerodynamics," *International Journal of Heat and Mass Transfer*, Vol. 55, pp. 5032-5043.

NUMERICAL FLOW SIMULATION OVER THE M151 COMBAT AIRCRAFT MODEL USING GALATEA SOLVER

Dimitrios A. Inglezakis¹, Georgios N. Lygidakis² and Ioannis K. Nikolos³

^{1,2,3}School of Production Engineering and Management
Technical University of Crete
Chania, GR-73100, Greece

e-mail: ¹dinglezakis@isc.tuc.gr, ²glygidakis@isc.tuc.gr, ³jnikolo@dpem.tuc.gr

Keywords: Compressible flow, RANS, node-centered finite-volume method, ARA M151/1, forward swept wings, canards.

Abstract. During the past decades CFD (Computational Fluid Dynamics) has become a rapidly evolving scientific field of engineering, augmented significantly by the corresponding rapid evolution of the available computer systems and the resulting expansion of their capabilities. Therefore, CFD emerged as an indispensable tool of the aerospace manufacturing process and product design, allowing for the prediction of aircraft aerodynamic behavior in a relatively short time period. In this study, such an in-house academic CFD solver, named Galatea, is presented in brief and used for the flow analysis over an uncommon combat aircraft research model with forward swept wings and canards of the Aircraft Research Association (ARA), named M151/1. In particular, a configuration of the M151/1 model with expanded fuselage is examined in two different angles of attack (5.5° , 10°), whereas main attention is directed towards the accurate computation of pressure distribution on the wing and canard surfaces of the aforementioned model. Due to unavailability of experimental data, the extracted results are compared with the corresponding ones derived using the commercial CFD solver ANSYS CFX. A satisfactory agreement is obtained, demonstrating the proposed solver's potential to predict accurately such complex flows.

1 INTRODUCTION

Nowadays, the duration of the design process of a new aircraft has been significantly decreased, comparing to this of the recent past of the twentieth century. This reduction, accompanied by a rapid evolution of aerospace technology, stems partially from the also rapid progress of the CFD (Computational Fluid Dynamics) scientific field, strongly connected to the relevant development of computer technology. The aforementioned advancements additionally supported the cost reduction of the entire production process of a new aircraft. As a result, CFD appears today to be an indispensable tool of the aerospace manufacturing process, which has broadened the potential of achievements in the corresponding scientific domain, whereas the necessity for further research and evolution is indicated.

In this work the in-house academic CFD code, named *Galatea*, is presented in brief and evaluated [1-3]. The proposed solver depends on the Navier-Stokes (RANS, Reynolds-Averaged Navier-Stokes) equations to predict inviscid, viscous laminar or viscous turbulent compressible fluid flows [2, 4]. For turbulence modeling appropriate two-equation models are additionally used [5-7]. Spatial discretization is performed with a node-centered finite-volume scheme on three-dimensional hybrid or tetrahedral unstructured grids [2]. The convective fluxes are computed with either the Roe's approximate Riemann solver [8] or the HLLC (Harten-Lax-van Leer-Contact) [9] one, whereas accuracy improvement is succeeded with a second-order scheme, based on the MUSCL (Monotone Upwind Scheme for Conservation Laws) approach [4] and appropriate slope limiting functions [10-13]. Viscous fluxes are calculated using the velocity components and temperature gradients, evaluated at the interfaces of the median control volumes [2, 4, 14]. Iterative approximation of the final steady-state solution is performed with either an explicit scheme, applying a four-stage Runge-Kutta method, or a point-implicit one employing the Jacobi or the Gauss-Seidel algorithm [2, 4, 15]. To reduce the required computation time, appropriate methodologies have been incorporated, namely, an edge-based data structure, a local time-stepping technique, a SPMD (Single Program-Multiple Data) parallelization strategy and an agglomeration multigrid scheme [3, 16, 17, 18].

In recent history of aerospace industry a wide variety of military aircrafts has been designed and manufactured, whose differences are focused not only on their mission purposes but also on their major geometrical characteristics. Based on long-term research [19-22], Forward Swept Wing (FSW) configuration has been recognized nowadays to enhance fighter aircrafts with significant performance advantages comparing to the Back Swept Wing (BSW) one. Such advantages become more apparent, as well as more promising, when FSW is combined with supercritical airfoils, canards, fly-by-wire system and advanced composite materials [19-22]. More

precisely, its incorporation can improve the following characteristics of such an aircraft: aerodynamic efficiency, maneuverability at high angles of attack, low speed handling, lift-drag ratio, and approach speed [20, 23]. The aforementioned improvements are associated with the spanwise flow from the wingtip to the wing root, which thickens the boundary layer at the latter region and subsequently alleviates the wingtip stalling problem [23]. As a result, the control surfaces remain effective and controllability of the aircraft is retained at the highest incidence angles [24].

FSW configuration was initially introduced in 1931, when aerodynamic data from wind tunnel tests indicated that a 20° FSW was superior of the widely applied BSW one, in terms of the range of active angles of attack [25]. During the World War II (1940), the first FSW aircraft was developed in Germany. It was the Junkers JU-287, a four-engine jet attack aircraft with wings of an approximately 25° forward sweep [23-26]. Throughout the following years (after the end of World War II), various studies were carried out deriving different such experimental models, despite metallic FSWs faced significant structural aeroelastic divergence problems comparing to the BSWs [25, 26]. Therefore, BSWs were preferred at that time for aircrafts designed to fly at the transonic and supersonic region. The aforementioned problem was overpassed two decades later with the advancement and use of composite materials, especially of the laminated ones [24-27], allowing scientific and aviation community to reconsider FSWs. In the 1980s up to 1990s, Grumman Corporation manufactured and tested the X-29, one of the most unusual FSW aircrafts in aviation history; its design, as well as its production and assessment, was the result of a joint NASA, DARPA (Defense Advanced Research Projects Agency) and USAF (US Air Force) program with the aforementioned company [23, 24]. The research interest regarding FSWs was continued. In 1997, Sukhoi Aviation Corporation presented the Su-47 Berkut, a fighter aircraft prototype with forward swept mid-wings, enhancing it with high aspect ratio and consequently with long-range performance capability [24]. Besides the aforementioned aircrafts, a variety of guided weapons, based on FSW concept, has been produced nowadays [23].

In this paper, the flow over a combat aircraft research model with FSWs and canards, named ARA (Aircraft Research Association) M151/1, is numerically predicted with the *Galatea* solver. In particular, an expanded fuselage configuration of the M151/1 model is examined in two different cases; their differences are focused on the angle of attack (5.5°, 10°), the Mach and Reynolds numbers. The methodology, followed for the development of the *Galatea* code, is analyzed in brief, whereas main attention is directed towards the accurate computation of pressure coefficient distributions on the wing and canard surfaces of the model. Due to the unavailability of experimental or numerical data in the open literature, the simulation results are compared with those derived by the widely applied commercial CFD software ANSYS CFX.

2 FLOW MODELING

The *Galatea* solver is based on the density-based Navier-Stokes equations (RANS), which are described in differential form as [2, 4, 28]

$$\frac{\partial \vec{W}}{\partial t} + \frac{\partial \vec{F}_{inv}}{\partial x} + \frac{\partial \vec{G}_{inv}}{\partial y} + \frac{\partial \vec{J}_{inv}}{\partial z} + \frac{\partial \vec{F}_{vis}}{\partial x} + \frac{\partial \vec{G}_{vis}}{\partial y} + \frac{\partial \vec{J}_{vis}}{\partial z} = \vec{S} \quad (1)$$

where \vec{F}_{inv} , \vec{G}_{inv} , \vec{J}_{inv} and \vec{F}_{vis} , \vec{G}_{vis} , \vec{J}_{vis} , the inviscid and viscous fluxes respectively, are defined as follows:

$$\begin{aligned} \vec{F}_{inv} &= \begin{bmatrix} \rho u \\ \rho u^2 + p \\ \rho uv \\ \rho uw \\ (\rho E + p)u \end{bmatrix} \quad \vec{G}_{inv} = \begin{bmatrix} \rho v \\ \rho vu \\ \rho v^2 + p \\ \rho vw \\ (\rho E + p)v \end{bmatrix} \quad \vec{J}_{inv} = \begin{bmatrix} \rho w \\ \rho wu \\ \rho wv \\ \rho w^2 + p \\ (\rho E + p)w \end{bmatrix} \\ \vec{F}_{vis} &= \begin{bmatrix} 0 \\ \tau_{xx} \\ \tau_{xy} \\ \tau_{xz} \\ u\tau_{xx} + v\tau_{xy} + w\tau_{xz} + q_x \end{bmatrix} \quad \vec{G}_{vis} = \begin{bmatrix} 0 \\ \tau_{yx} \\ \tau_{yy} \\ \tau_{yz} \\ u\tau_{yx} + v\tau_{yy} + w\tau_{yz} + q_y \end{bmatrix} \quad \vec{J}_{vis} = \begin{bmatrix} 0 \\ \tau_{zx} \\ \tau_{zy} \\ \tau_{zz} \\ u\tau_{zx} + v\tau_{zy} + w\tau_{zz} + q_z \end{bmatrix} \end{aligned} \quad (2)$$

\vec{W} denotes the conservative variables' vector, whereas \vec{S} the source term, being equal to zero in this study. All the aforementioned terms are based on the dimensionless primitive variables [1, 2, 4, 28, 29]. For the computation of the stress tensors the Boussinesq assumption is employed. Finally, the perfect gas law is used to close the PDEs (Partial Differential Equations) set [1, 2, 28]. For the simulation of turbulent flows, a two-equation model is used; three such alternative models have been incorporated in the solver, namely, the k- ϵ [5], the k- ω [6] and the SST (Shear Stress Transport) one [7]. The aforementioned modeling is performed much in the same way with the flow model.

Both flow and turbulence models' PDEs are discretized using a node-centered finite-volume scheme, coupled with three-dimensional hybrid unstructured grids, composed of tetrahedral, prismatic, and pyramidal elements [2, 4]. The control volume of each node P is constructed by connecting with lines edge mid-points, barycenters of faces, and barycenters of elements that share this node. Figure 1 illustrates the contributions of a tetrahedron and a prism to the control volume of a node P , connected with node Q .

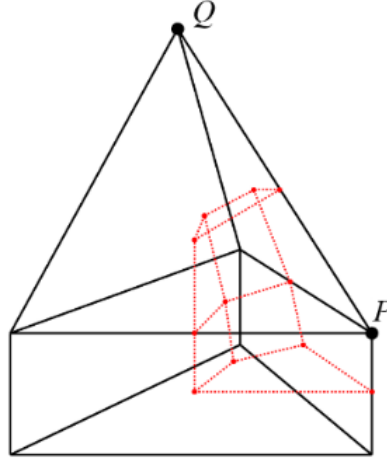


Figure 1. Contributions of a tetrahedral and a prismatic element to the control volume of node P .

The convective fluxes are obtained assuming a one-dimensional Riemann problem along each edge connecting adjacent nodes of the grid (through the corresponding faces of the control volumes) and consequently implementing either the Roe's approximate Riemann solver [8] or the HLLC [9] one [4, 30]. To improve the spatial accuracy, a second-order scheme, based on the MUSCL approach, has been incorporated in the *Galatea* solver. Appropriate (alternative) limiting functions are used, namely the Van Albada-Van-Leer [10], the Min-mod [11], the Barth-Jespersen [12] and the MLP-Venkatakrishnan (Multi-dimensional Limiting Process-Venkatakrishnan) one [13]. For the computation of the diffusive fluxes, the gradients of velocity components and temperature are calculated at the middle of each edge. Two alternative methodologies have been developed for the aforementioned computation, namely an element-based [14] and a nodal-averaging one [4]. As mentioned previously, turbulence modeling is performed similarly to the flow one [2]. Nevertheless, only a first-order accurate scheme is implemented for the computation of the corresponding convective fluxes, assuring stability of the numerical procedure [2]. The final steady-state solution is obtained iteratively with either an explicit scheme, applying a second-order accurate in time four-stage Runge-Kutta method (RK(4)), or a point-implicit one employing the Jacobi or the Gauss-Seidel algorithm [2, 4, 15]. Further details can be found in [2].

Finally, in order to accelerate the solution procedure and reduce the required computation time, appropriate methodologies have been incorporated in the *Galatea* solver, namely, an edge-based data structure, a local time-stepping technique, parallel processing and an agglomeration multigrid scheme [3]. The included SPMD parallelization method depends on the domain decomposition approach and the MPI (Message Passing Interface) communication protocol [3, 18]. The whole procedure begins with the division of the initial mesh into smaller ones using the METIS application [17]. Each sub-grid is assigned to a single processor, whereas an overlapping layer is constructed at the interfaces of adjacent partitions, allowing for the data exchange between them [2, 3]. For the implementation of the incorporated agglomeration multigrid scheme, gradually coarser meshes are generated at each sub-domain by merging (either isotropically or directionally) the neighboring control volumes [3, 16, 31-33]. For the stretched regions of hybrid grids (with prismatic elements) the full-coarsening directional approach is more suitable [3]. The multigrid accelerated solution is obtained with the FAS (Full Approximation Scheme) approach in a V-cycle procedure [3, 16]. Alternatively, a combined FMG-FAS (Full Multigrid-Full Approximation Scheme) strategy can be followed, further improving the efficiency of the proposed solver [3, 4]. Additional details can be found in [3].

3 THE AIRCRAFT RESEARCH MODEL ARA M151/1

The model ARA M151/1, selected for this study, is an experimental fighter aircraft model with forward swept wings and canards; its design details have been reported in [19]. For the purposes of this study, its geometry was defined using the commercial CAD (Computer Aided Design) software CATIA V5, following the design details as analyzed in the aforementioned report. Due to different available configurations of the aircraft model (with expanded and non-expanded fuselage, different canard angles, etc.), its geometry construction was based on three basic structural parts, namely, the fuselage, the wing, and the canard. Each part was constructed separately prior

being combined into the complete structure, whereas only half of the aircraft was modeled for computational savings.

3.1 The fuselage

The fuselage consists of three basic compartments, namely, the main compartment, the air intake and the canopy one. The main fuselage and air intake compartments are defined by simple rectangular sections with rounded corners. The canopy is formed by elliptical sections, whereas it blends into the upper surface of the main fuselage compartment. Two alternative configurations of M151/1 are described in [19], with their differences focused on the rear part of the fuselage, i.e., an expanded and an unexpanded parallel configuration. The former one was selected in this study, with its rear part exhibiting a smooth crosswise expansion at the side wall; its geometry is illustrated in Figure 2.

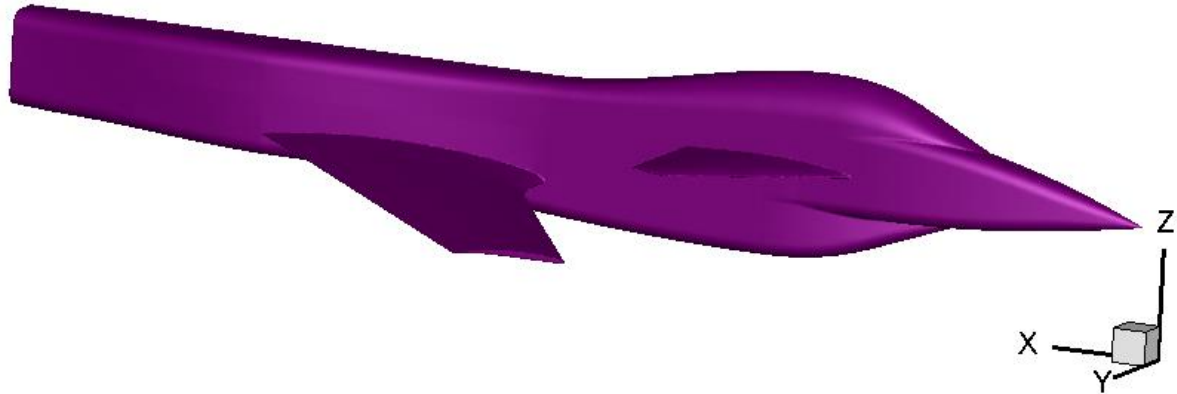


Figure 2. Geometry of the ARA M151/1 expanded fuselage configuration.

As shown in Figure 2, the geometrical characteristics of the near-rectangular sections along the fuselage vary significantly. An alongside compartmental design strategy was implemented for the geometry definition. In particular, the fuselage was divided in thirty sub-compartments (FSs-Fuselage Stations) to be modeled separately. The majority of FSs was located in the front part, due to its higher complexity comparing to the aft one. Although the aforementioned strategy is characterized by relatively high effort and consequently slow implementation, it was preferred because of its resulting accuracy, as well as to avoid any possible compatibility issues between CATIA V5 and ANSYS CFX software.

3.2 The wing

The geometry of the wing, which is described by appropriate mathematical expressions in [19], has a trapezoidal and forward swept shape. It is based on three main airfoils (control stations), linearly connected. Similarly, its leading and trailing edge curves are described in detail by suitable mathematical equations. The wing is low mounted with a negative wing/fuselage setting angle, whereas twist extends throughout it. The leading edge sweep is equal to -30° . The inner wing leading edge remains unswept, entailing structurally sounder means to carry the wing load into the fuselage than a V-junction, usually used with a trapezoidal wing [19]. Table 1 summarizes the basic geometrical data of the M151/1 wing [19].

Wing Area	0.36 m ²
Mean Aerodynamic Chord	0.30 m
Wing Span	1.20 m
Aspect Ratio	4.0
Taper Ratio	0.4

Table 1. Basic geometrical data of the ARA M151/1 wing.

3.3 The canard

The shape of the canard is based on the NACA 64206 airfoil, modified at the tip region; a 4° washout is designed there, i.e., the tip has a 4° nose down in respect to the bodyside chord [19]. Additionally, the leading edge sweep is set equal to 45° in contrast to the unswept trailing edge. The derived taper ratio is computed equal to 0.2. In this study, the canard is rotated by -3° over the crosswise axis of the aircraft model.

4 NUMERICAL RESULTS

4.1 Grid details

Based on the aforementioned geometry, a computational grid, describing the flow domain over the aircraft geometry, was constructed using the commercial mesh generating software ANSYS. It consists of 8,135,315 nodes and 28,799,145 elements (19,115,449 tetrahedra and 9,683,696 prisms). The mesh is characterized by increased density on critical points of the aircraft surface, such as the leading and trailing edge regions of the main wing and the canard, as well as at their junction regions with the fuselage. Moreover, on the aircraft surface forty four prismatic layers were constructed; the first layer height was adjusted to $1.1\text{E-}5$ m, whereas the growth rate was set to 1.115. This highly stretched (prismatic) region is required to adequately resolve the boundary layer phenomena at the solid wall region. Figure 3 (top) illustrates a far view of the utilized numerical grid; a close-up view of the same grid at the symmetry plane is presented in Figure 3 (bottom). In order this grid to be used with the dimensionless *Galatea* solver, it was re-dimensionalized. Thus, its mean aerodynamic chord became equal to unity [2].

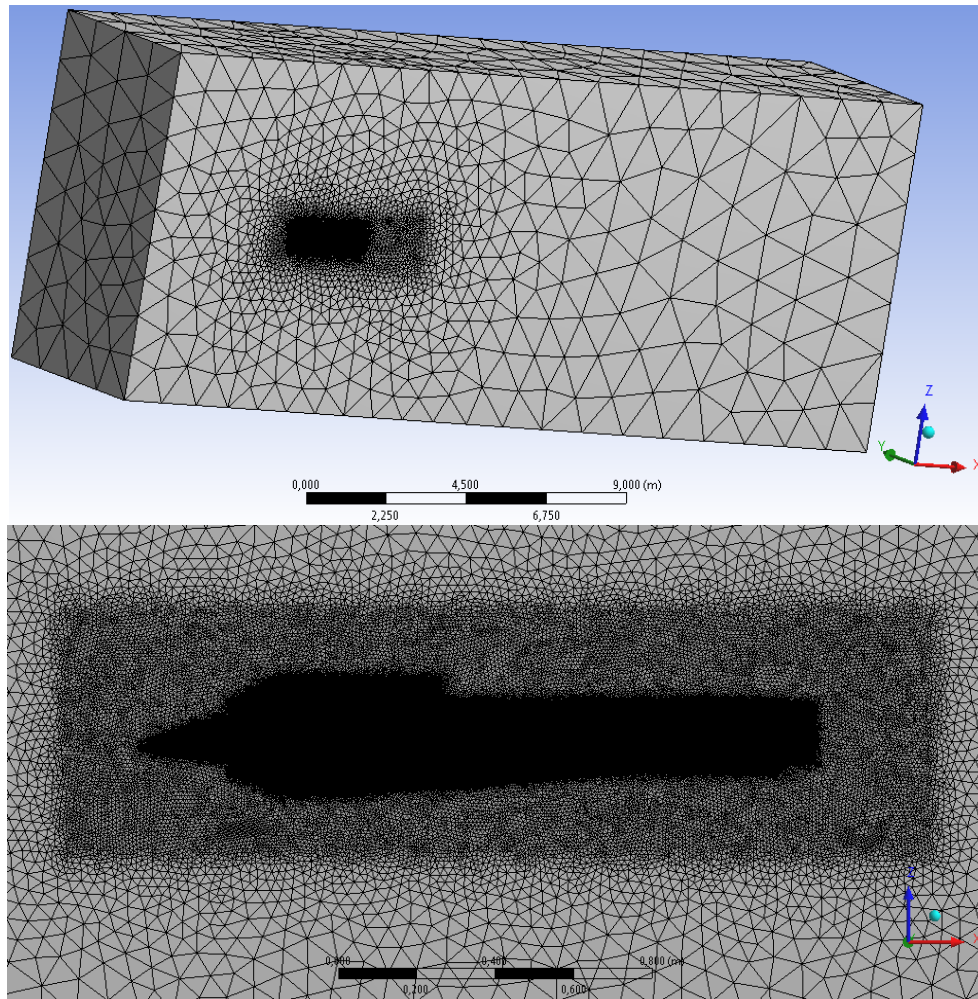


Figure 3. Far view (top) and close-up view at the symmetry plane (bottom) of the utilized grid.

4.2 Flow data

As mentioned in Introduction, two test cases were examined in this study, whose differences are focused on the angle of attack, the Mach and Reynolds numbers. For the first simulation, the angle of attack was set equal to 5.5° , free-stream temperature to 270.535 K and free-stream velocity to 243.28 m/s. The Mach number was calculated equal to 0.7377, while the Reynolds number equal to 5.133.998 (based on mean aerodynamic chord). At the second test case a 10° angle of attack was used, whereas the free-stream velocity and temperature were set equal to 210.9 m/s and 277.85 K, respectively. The Mach and Reynolds numbers were computed equal to 0.6314 and 4.371.948, respectively.

Due to the unavailability of corresponding experimental or numerical data, the extracted results (by the *Galatea*

solver) are compared with those derived by the commercial CFD software ANSYS CFX. For both solvers the same grid was used (in dimensionless form for the *Galatea* solver). Fully turbulent compressible flow was considered, whereas turbulence modeling was obtained for both solvers with the SST model; no transition phenomenon was assumed. In simulations performed with the *Galatea* solver, the Roe's approximate Riemann solver was used, along with a second-order spatial accurate scheme, coupled with the Van Albada-Van Leer limiting function. Time integration and iterative approximation of the final steady-state solution was achieved applying the incorporated second-order accurate in time four-stage Runge–Kutta method (RK(4)), whereas the CFL number was set equal to 0.5. To reduce the required computation time (on a DELL T7500 workstation with two Intel® Xeon®-X5660 six-core processors at 2.8 GHz) the grid was decomposed in eight partitions to be processed in parallel. In addition, two coarser grid resolutions were generated, following the incorporated full-coarsening directional agglomeration mode, in order the developed multigrid scheme to be implemented and consequently further acceleration to be gained.

4.3 Numerical results and discussion

In this section the results, extracted for both aforementioned test cases by *Galatea* and ANSYS CFX solvers are presented and discussed. Figure 4 illustrates the dimensionless pressure contours on the aircraft surface, produced by the *Galatea* solver for the second test case with 10° angle of attack. Figure 5 contains a comparison of the extracted pressure coefficient distributions by both the employed solvers at the canard span-wise section 20%; the left figure refers to 5.5° angle of attack, whereas the right one to 10° . Figures 6 to 8 present the corresponding pressure coefficient distribution comparisons at the main wing span-wise sections 15.88%, 49.53% and 88.79%, respectively. Based on these results, one can observe a satisfactory agreement, despite the fact that the implemented solvers depend on completely different numerical approaches. *Galatea* solver employs a density-based procedure while the CFX solver is based on a pressure-correction methodology. The most noticeable differences, between the pressure coefficient distributions produced by the two solvers, are located at the leading edge regions of the canard and the main wing. Less pronounced differences are observed at the corresponding trailing edge regions. Nevertheless, for the majority of the wing and canard surfaces, the two solvers produced almost identical results for the pressure coefficient. Another pressure coefficient comparison is illustrated in Figure 9 at the symmetry plane on the fuselage of the aircraft model; the results of *Galatea* and ANSYS CFX appear to be almost identical. Finally, Figures 10 and 11 depict the dimensionless pressure contours at the canard span-wise section 57.5% and at the leading edge region of main wing span-wise section 7.47%, respectively, extracted by the *Galatea* solver for the test case with 10° angle of attack. Based on the aforementioned quantitative results, a satisfactory agreement is identified between the two solvers, demonstrating the potential of the proposed one to simulate accurately such demanding flows over complex geometries.

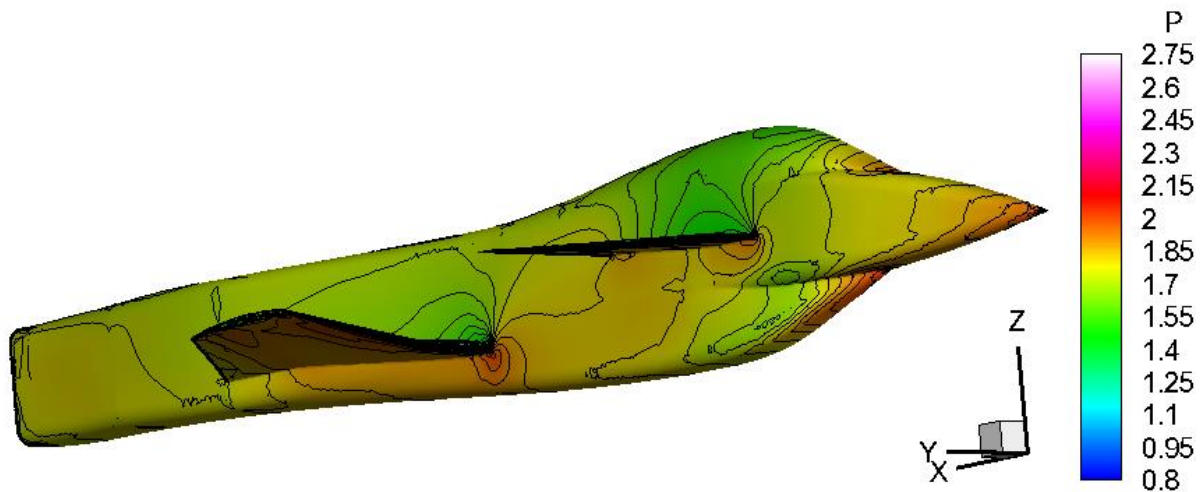


Figure 4. Dimensionless pressure contours on the aircraft surface extracted using the *Galatea* solver for the test case with 10° angle of attack.

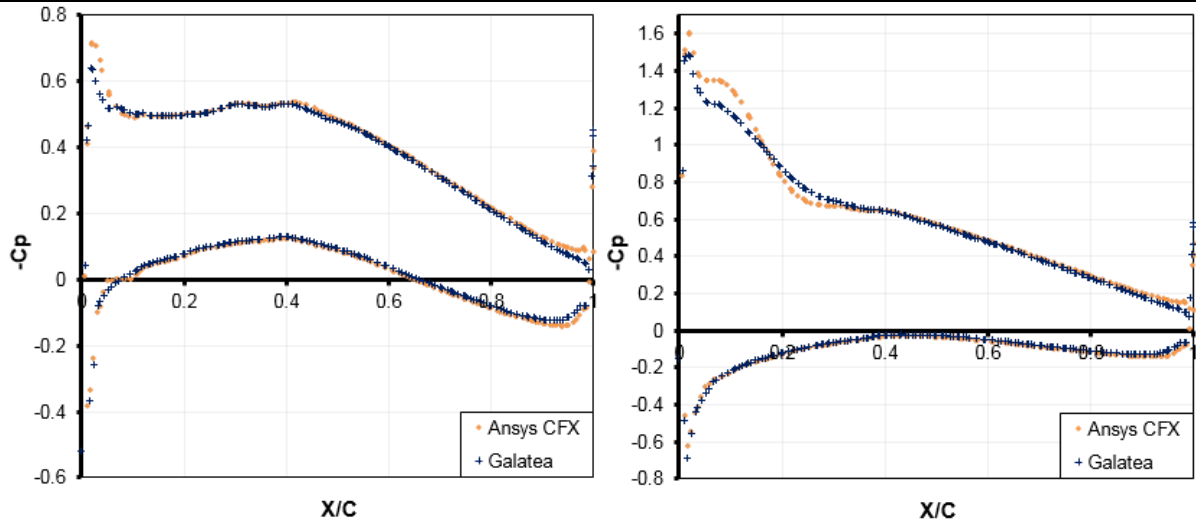


Figure 5. Pressure coefficient distribution at the canard span-wise section 20%: 5.5° angle of attack (left), 10° angle of attack (right).

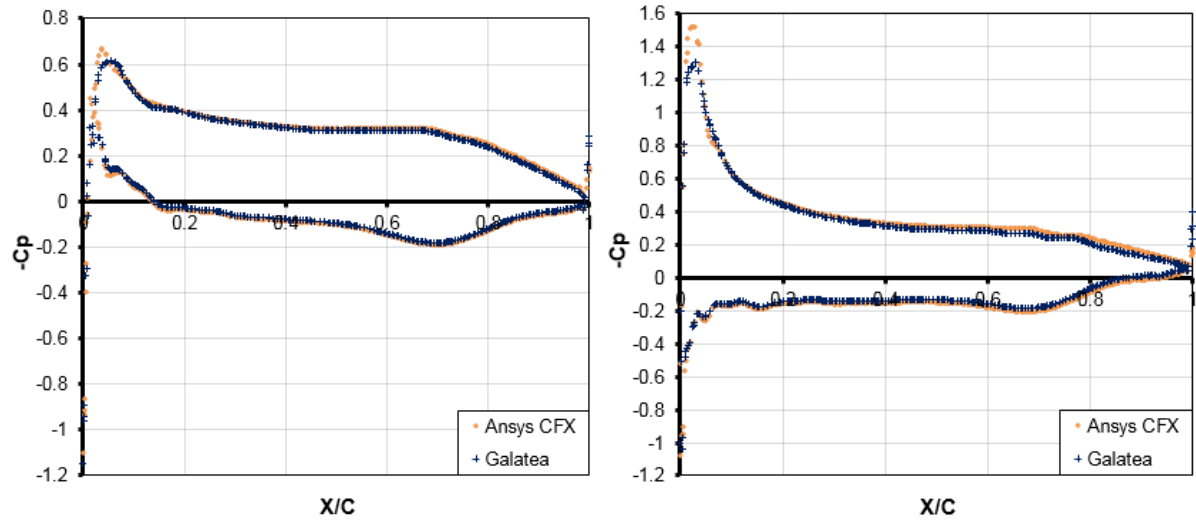


Figure 6. Pressure coefficient distribution at the main wing span-wise section 15.88%: 5.5° angle of attack (left), 10° angle of attack (right).

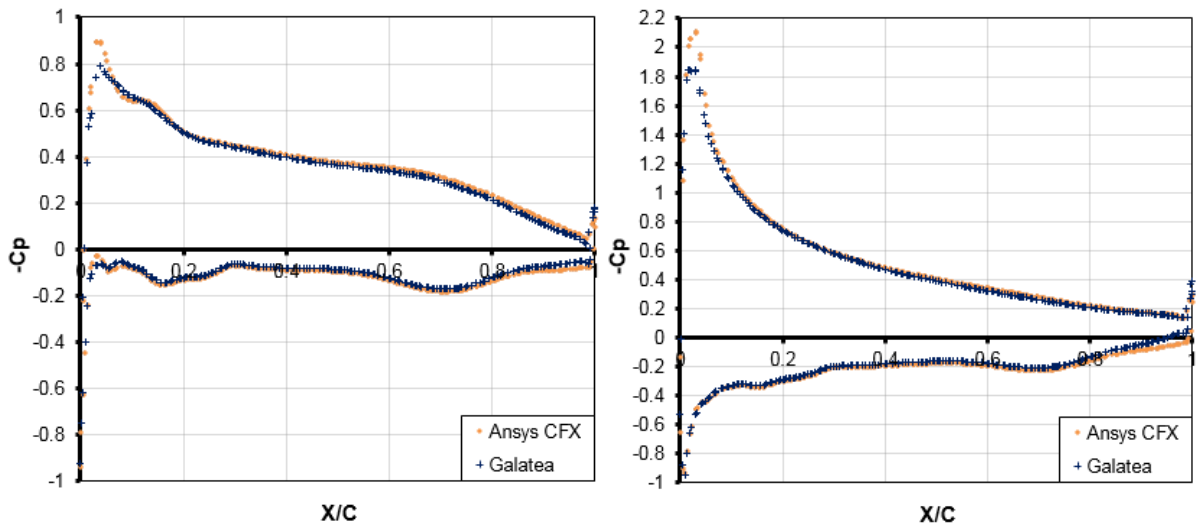


Figure 7. Pressure coefficient distribution at the main wing span-wise section 49.53%: 5.5° angle of attack (left), 10° angle of attack (right).

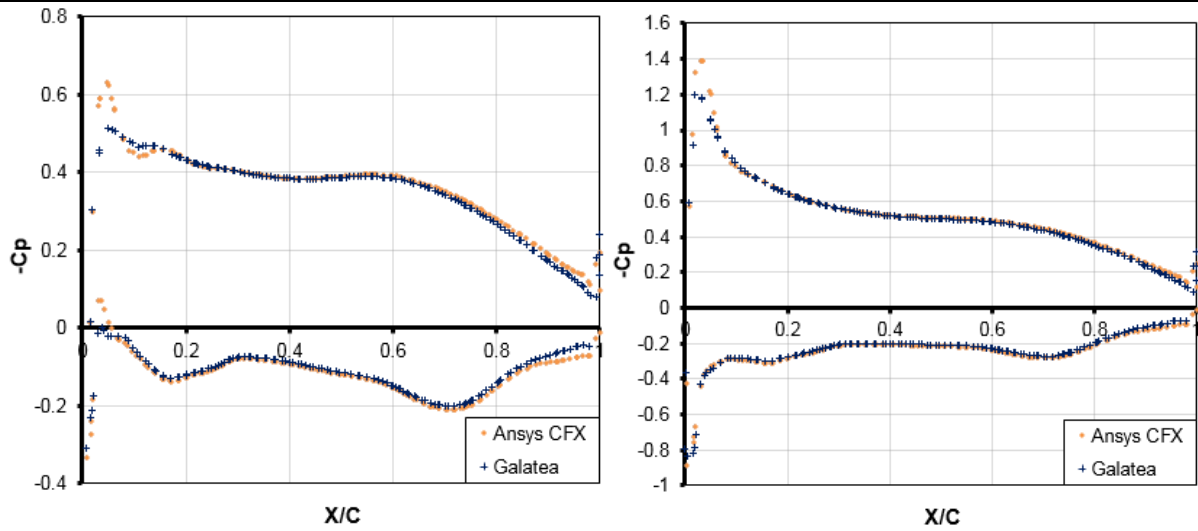


Figure 8. Pressure coefficient distribution at the main wing span-wise section 88.79%: 5.5° angle of attack (left), 10° angle of attack (right).

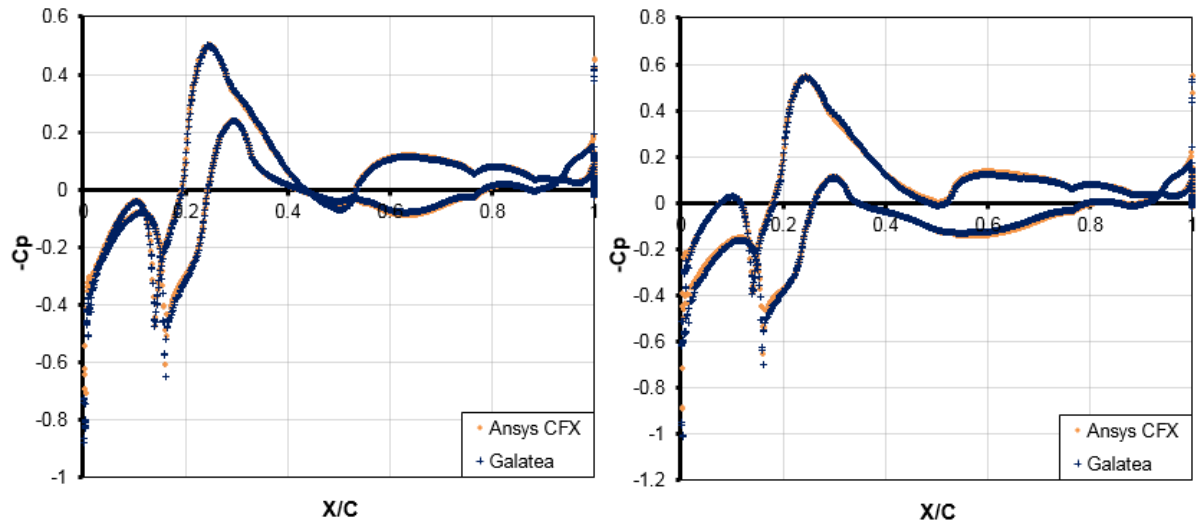


Figure 9. Pressure coefficient distribution at the symmetry plane: 5.5° angle of attack (left), 10° angle of attack (right).

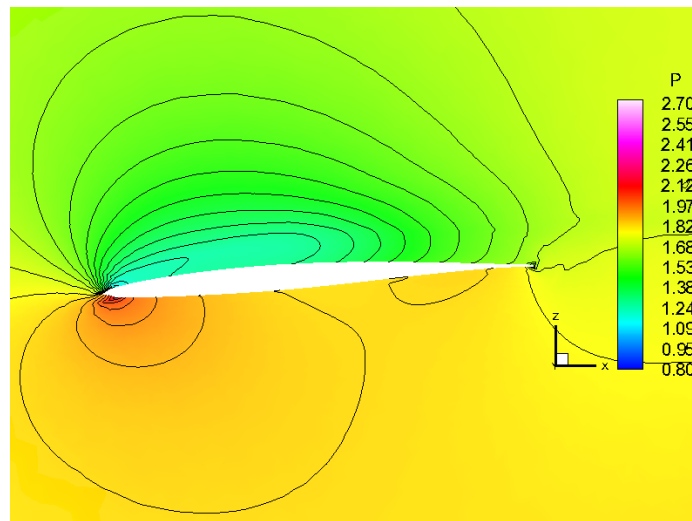


Figure 10. Dimensionless pressure contours at the canard span-wise section 57.5%, extracted by the *Galatea* solver for the test case with 10° angle of attack.

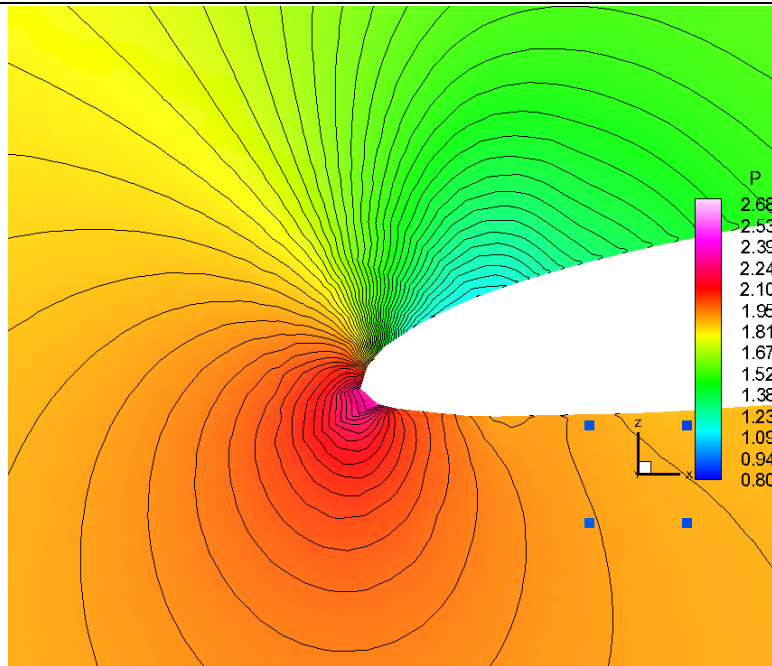


Figure 11. Dimensionless pressure contours at the leading edge of the main wing span-wise section 7.47%, extracted by the *Galatea* solver for the test case with 10° angle of attack.

5 CONCLUSIONS

In this work, the flow over a combat aircraft research model with forward swept wings and canards, ARA M151/1, was numerically simulated using the *Galatea* solver. In particular, the expanded fuselage configuration of the M151/1 model was examined in two different cases; their differences are focused on the angle of attack (5.5° , 10°), the Mach and Reynolds numbers. The methodology followed for the development of the *Galatea* solver was analyzed in brief, whereas main attention was directed towards the computation of pressure distribution on the wing and canard surfaces of the model. Due to the unavailability of any experimental or numerical data, the extracted simulation results were compared with those derived by the widely applied commercial CFD software ANSYS CFX. A satisfactory agreement is obtained, despite the fact that the employed solvers depend on completely different numerical approaches; *Galatea* relies on a density-based procedure while the CFX software is based on a pressure-correction methodology. The presented numerical simulation results revealed the proposed solver's potential to predict effectively such demanding flows over complex geometries in terms of accuracy and geometric flexibility.

REFERENCES

- [1] G.N. Lygidakis and I.K. Nikolos (2014), "Using the DLR-F6 aircraft model for the evaluation of the academic CFD code *Galatea*", *Proceedings of the ASME 2014 International Mechanical Engineering Conference & Exposition, IMECE2014*, Nov. 14-20, Montreal, Quebec, Canada, Paper No. IMECE2014-39756.
- [2] G.N. Lygidakis and I.K. Nikolos (2015), "Numerical analysis of flow over the NASA Common Research Model using the academic Computational Fluid Dynamics code *Galatea*", *ASME Journal of Fluids Engineering*, Vol. 137, 071103-1.
- [3] G.N. Lygidakis, S.S. Sarakinos and I.K. Nikolos (2016), "Comparison of different agglomeration multigrid schemes for compressible and incompressible flow simulations", *Advances in Engineering Software*, Vol. 101, pp. 77-97.
- [4] J. Blazek (2001), *Computational Fluid Dynamics: Principles and Applications*, Elsevier Science, Kidlington.
- [5] B.E. Launder and D.B. Spalding (1974), "The numerical computation of turbulent flows", *Computer Methods in Applied Mechanics and Engineering*, Vol. 3, pp. 269-289.
- [6] P.G. Saffman and D.C. Wilcox (1974), "Turbulence-model predictions for turbulent boundary layers", *AIAA Journal*, Vol. 12, pp. 541-546.
- [7] F.R. Menter (1994), "Two-equation eddy viscosity turbulence models for engineering applications", *AIAA Journal*, Vol. 32, pp. 1598-1605.
- [8] P. Roe (1981), "Approximate Riemann solvers, parameter vectors and difference schemes", *Journal of Computational Physics*, Vol. 43, pp. 357-371.
- [9] E.F. Toro, M. Spruce and W. Speares (1994), "Restoration of the contact surface in the HLL Riemann solver",

- Shock Waves*, Vol. 4, pp. 25-34.
- [10] G.D. Van Albada, B. Van Leer and W.W. Roberts (1982), "A comparative study of computational methods in cosmic gas dynamics", *Astronomy and Astrophysics*, Vol. 108, pp. 46-84.
 - [11] P.K. Sweby (1984), "High resolution schemes using flux limiters for hyperbolic conservation laws", *SIAM Journal on Numerical Analysis*, Vol. 21, pp. 995-1011.
 - [12] T.J. Barth and D.C. Jespersen (1989), "The design and application of upwind schemes on unstructured meshes", *Proceedings of the 27th AIAA Aerospace Sciences Meeting and Exhibit*, Reno, USA, AIAA-89-0366.
 - [13] V. Venkatakrishnan (1995), "Convergence to steady state of the Euler equations on unstructured grids with limiters", *Journal of Computational Physics*, Vol. 118, pp. 120-130.
 - [14] Y. Kallinderis and T. Ahn (2005), "Incompressible Navier-Stokes method with general hybrid meshes", *Journal of Computational Physics*, Vol. 210, pp. 75-108.
 - [15] M.H. Lallemand (1988), *Etude de schemas Runge-Kutta a 4 pas pour la resolution multigrille des equations d'Euler 2D*, Rapport de Recherche, Inria.
 - [16] D.J. Mavriplis (1998), "Multigrid strategies for viscous flow solvers on anisotropic unstructured meshes", *Journal of Computational Physics*, Vol. 145, pp. 141-165.
 - [17] G. Karypis and V. Kumar (1999), "A fast and highly quality multilevel scheme for partitioning irregular graphs", *SIAM, Journal on Scientific Computing*, Vol. 20, pp. 359-392.
 - [18] S. Lanteri (1996), "Parallel solutions of compressible flows using overlapping and nonoverlapping mesh partitioning strategies", *Parallel Computing*, Vol. 22, pp. 943-968.
 - [19] D. Stanniland (1985), "Investigation into the aerodynamic characteristics of a combat aircraft research model fitted with a forward swept wing", *AGARD-AR-303*, Vol. 2, Test Case E8, ARA, Bedford.
 - [20] G. Spacht (1980), "The forward swept wing - a unique design challenge", *AIAA Aircraft Systems Meeting*, Anaheim.
 - [21] C. Bach, R. Jebari, A. Viti, R. Hewson (2017), "Composite stacking sequence optimization for aeroelastically tailored forward-swept wings", *Structural and Multidisciplinary Optimization*, Vol. 55, pp. 105-119.
 - [22] W. Tian, Z. Yang, Y. Gu and Y. Ouyang (2016), "Aeroelastic tailoring of a composite forward swept wing using a novel hybrid pattern search method", *ASCE Journal of Aerospace Engineering*, Vol. 29.
 - [23] L. Juanmian, Z. Shuai and W. Suozhu, (2016), "Numerical study of aerodynamic characteristics of FSW aircraft with different wing positions under supersonic condition", *Chinese Journal of Aeronautics*, Vol. 29, pp. 914-923.
 - [24] E. Vatandas (2007), "Geometrical and positional optimization of the forward swept lift producing surfaces in 3D flow domains", *Aircraft Engineering and Aerospace Technology*, Vol. 79, pp. 635 - 645.
 - [25] E.J. Saltzman and J.W. Hicks (1994), *In-flight lift-drag characteristics for a forward-swept wing aircraft (and comparisons with contemporary aircraft)*, NASA Technical Paper 3414, Edwards, California.
 - [26] T.A. Weisshaar (1980), "Divergence of forward swept composite wings", *AIAA Journal of Aircraft*, Vol. 17, pp. 442-448.
 - [27] W.R. Krüger et al. (2014), "Design and aeroelastic assessment of a forward-swept wing aircraft", *CEAS Aeronautical Journal*, Vol. 5, pp. 419-433.
 - [28] B. Koobus et al. (1996), "Computation of unsteady viscous flows around moving bodies using the k- ϵ turbulence model on unstructured dynamic grids", *Computer Methods in Applied Mechanics and Engineering*, Vol. 190, pp. 1441-1466.
 - [29] K.A. Sørensen, O. Hassan, K. Morgan, N.P. Weatherill (2003), "A multigrid accelerated hybrid unstructured mesh method for 3D compressible turbulent flow", *Computational Mechanics*, Vol. 31, pp. 101-114.
 - [30] T.J. Barth (1992), "Aspects of unstructured grids and finite-volume solvers for the Euler and Navier-Stokes equations", *AGARD-R-787*, pp. 6.1-6.61.
 - [31] G. Carré, L. Fournier, S. Lanteri (2000), "Parallel linear multigrid algorithms for the acceleration of compressible flow calculations", *Computer Methods in Applied Mechanics and Engineering*, Vol. 184, pp. 427-448.
 - [32] H. Nishikawa and B. Diskin (2011), "Development and application of parallel agglomerated multigrid methods for complex geometries", *Proceedings of 20th AIAA Computational Fluid Dynamics Conference*, AIAA 2011-3232.
 - [33] H. Nishikawa et al. (2013), "Recent advances in agglomerated multigrid", *Proceedings of 51st AIAA Aerospace Sciences Meeting*, AIAA 2013-0863.

MULTI-OBJECTIVE OPTIMIZATION OF A FLAPPING FOIL SYSTEM FOR THRUST AUGMENTATION IN SHIP PROPULSION

Dimitrios G. Koubogiannis¹, Ioannis Bonis¹, A. Priovolos² and Kostas Belibassakis²

¹Department of Naval Architecture Engineering
University of West Attica, Greece
e-mails: dkoubog@teiath.gr, ibonis@gmail.com

²School of Naval Architecture & Marine Engineering
National Technical University of Athens, Greece
e-mails: priovolos.antreas@gmail.com, kbel@fluid.mech.ntua.gr

Keywords: Flapping foil, thrust augmentation, multi-objective, boundary element method.

Abstract. *A state-of-the-art application of biomimetics concerns the design of devices for thrust augmentation in ship propulsion. The performance of a flapping foil system that performs a combination of two periodic motions, a heaving and a pitching one with a phase lag between them, has been experimentally studied and numerically simulated in the past. Aiming to develop a control method for dynamically modifying the motion characteristics of the flapping foil for maximum thrust gain in an efficient way, the authors have numerically investigated in the past the effect of the basic motion parameters on the foil performance (thrust production, propulsion efficiency and required power). Parametric studies based on a very fast Boundary Element solver revealed that the corresponding objectives are contradicting. The present paper extends the previous work to the solution of an appropriately defined multi-objective problem, where simultaneous maximization of two objective functions is studied through Pareto-optimality and the results are physically interpreted.*

1 INTRODUCTION

A state-of-the-art application of biomimetics, i.e. the artificial imitation of natural models in order to design more efficient technological systems, concerns the design of devices for propulsion augmentation in ship propulsion. Such devices, inspired by the thunniform swimming mode, have been proposed for marine vehicle and ship thrusters [1], [2]. In [3], the performance of a flapping foil system has been experimentally studied; the foil was moving under the combined action of two periodic (sinusoidal) motions, namely a heaving motion (concerning vertical displacement) and a pitching one (rotation around a point its axis) with a phase lag between them. In [4], the influence of the Strouhal number and the maximum angle of incidence to the performance of such a device were investigated. A similar device has been numerically simulated by the authors by means of a panel method in [5] and an unsteady Navier-Stokes Computational Fluid Dynamics (CFD) solver in [6]. In the latter work, the efficient production of thrust was demonstrated for a fixed Reynolds number based on numerical simulations and the results were compared to the available experimental data [3], [4]. The performance of the foil was further investigated for various maximum angles of attack corresponding to different pitching motions and the need for further improvement from a simulation point of view, in cases where dynamic stall is involved, was highlighted.

The authors, aiming to develop a control methodology for dynamically modifying the motion characteristics of the flapping foil for production of maximum thrust in an efficient way, numerically investigated the effect of the basic motion parameters on thrust production and propulsion efficiency in terms of corresponding performance indices. To this end, parametric studies were performed with respect to amplitude and frequency of the heaving and pitching motions, as well as to phase lag between the two motions [7]. A lower fidelity (compared to the Navier-Stokes solver of [6]) but very fast solver, based on the Boundary Element Method [8] was implemented for the simulations. Alternatively to BEM, in case of thin flapping foils, the Discrete Vortex Method has also very successfully been applied to similar calculations [9]. The accuracy of the results of such a solver are satisfactory, provided that no dynamic stall phenomena (causing massive leading edge flow separation) are involved [5], [8]. The parametric studies in [7] revealed that the above objectives are contradicting. Furthermore, a static single-objective optimization problem was stated and solved in [7] for the values of the motion parameters that maximize the efficiency of the flapping foil system. However, the optimal solution with respect to efficiency yielded very low thrust, dictating that a multi-objective problem has to be solved in order to obtain practical and profitable solutions.

In the light of the above, the present paper extends the previous work to the study of a multi-objective optimization problem for the same flapping foil system. The objectives that are considered herein are the maximization of thrust coefficient (C_t), the maximization of efficiency (η) and the minimization of the power required to achieve the foil motion in terms of the non-dimensional power coefficient (C_p). Pareto-optimality for two of the above objectives is studied and the solutions lying on the Pareto curve are physically interpreted.

2 THE FLAPPING FOIL SYSTEM

2.1 Flapping foil motion

A (symmetric) NACA0012 profile was considered as the hydrofoil in the present study as used also in [3], [4]. The hydrofoil moves forward in an infinite fluid domain at a constant speed U (Figure 1(left)), so in the body-fixed frame of reference the incoming flow is a uniform current parallel to x -axis (Figure 1(right)). In order to operate as a hydrodynamic thruster, the foil undergoes a flapping motion consisting of a vertical heaving motion of the foil and a simultaneous pitching motion at the same frequency. The two motions are described by the formulas

$$y(t) = y_0 \sin(\omega t) \quad (1)$$

$$\theta(t) = \theta_0 \sin(\omega t + \psi) \quad (2)$$

where ω is the angular frequency, y_0 is the heaving amplitude, θ_0 is the pitching amplitude and ψ is the phase lag between them. The instantaneous angle of incidence (Figure 1(right)) is expressed by [3]

$$\alpha(t) = \theta(t) - \tan^{-1}(U^{-1} dy/dt) \quad (3)$$

According to [10], in order to generate positive thrust (i.e. in the negative x -direction) in an efficient manner, the phase lag should take values in the interval $75^\circ < \psi < 105^\circ$. The parameters defining the flapping motion are:

- heave-to-chord ratio y_0/c ,
- Strouhal number $St = y_0 \omega / (\pi U)$ (nondimensional frequency),
- phase lag ψ ,
- pitching amplitude θ_0 (that determines the maximum angle of incidence α_{\max}).

The location of the center of rotation for the pitching motion is another geometric parameter affecting the pitching motion; this is considered herein to be at constant distance $x_R/c = 1/3$ from the foil leading edge. The chord length of the foil ($c=0.1\text{m}$), together with the kinematic viscosity of water ν and the inlet flow velocity U define the flow Reynolds number $Re = Uc/\nu$. The four parameters defined above, i.e. St , ψ , θ_0 and y_0/c are used in the present work as the independent variables to control the performance of the flapping foil system.

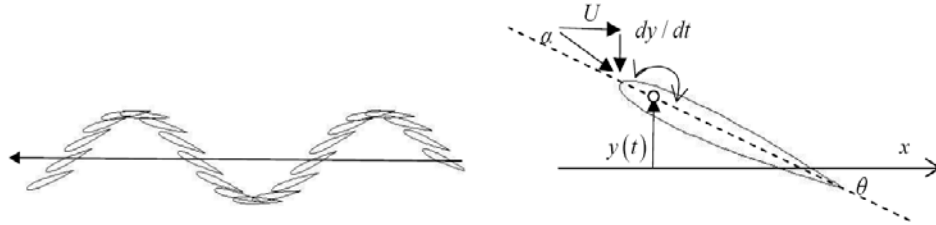


Figure 1. Flapping foil motion (left). Definition of the angle of incidence $\alpha(t)$ (right).

2.2 Flapping foil performance

The performance of the flapping foil system is assessed in terms of thrust production, propulsion efficiency and power required to achieve the flapping motion. In particular, the average thrust coefficient is used to assess thrust production (its maximization is desirable). This coefficient is defined by

$$C_t = \frac{\bar{F}_x}{0.5 \rho c U^2} \quad (4)$$

where the appearing average thrust force \bar{F}_x achieved by the hydrofoil motion (per unit span of the hydrofoil) is calculated during a time interval T , sufficiently greater than the period of the phenomenon ($T \gg 2\pi/\omega$), by the following formula

$$\bar{F}_x = \frac{1}{T} \int_0^T F_x(t) dt \quad (5)$$

The corresponding average mechanical power \bar{P} required for the hydrofoil motions is given by

$$\bar{P} = \frac{1}{T} \left\{ \int_0^T F_y(t) \dot{y}(t) dt + \int_0^T M(t) \dot{\theta}(t) dt \right\} \quad (6)$$

This has to be minimized and is considered in the form of the nondimensional power coefficient

$$C_p = \frac{\bar{P}}{0.5 \rho c U^3} \quad (7)$$

Finally, the efficiency of the propulsion has to be kept maximum. This is calculated by

$$\eta = \frac{C_t}{C_p} = \frac{\bar{F}_x U}{\bar{P}} \quad (8)$$

The three nondimensional coefficients defined above, i.e. C_t , C_p and η are used in the present work to define the objectives related to the required optimum performance of the flapping foil system.

3 THE NUMERICAL SIMULATION TOOL

A numerical tool based on the Discrete Vortex Method (DVM) has been developed to simulate flow around unsteady thin hydrofoils undergoing oscillatory heaving and pitching motions, in case of uniform or gusty incoming flow. Effects associated with foil flexibility have also been modelled. A brief description of this tool with application to flapping thruster systems is provided below, while additional details can be found in [8]. The solution is obtained numerically via a discretization scheme, including a wake model for the trailing edge vorticity, which is created by the unsteadiness of the flow. The strength of the vorticity that is being shed from the trailing edge of the foil is connected to the rate of circulation change around the foil; this is a consequence of Kelvin's theorem concerning circulation conservation around closed paths in the fluid. Having solved for the vortex distribution, pressure is obtained by Bernoulli's theorem, while forces are calculated by integration of pressure on the hydrofoil. In addition, a model to take into account the leading edge suction force has been incorporated; this force has an important effect in case of thin hydrofoils [11]. Furthermore, viscous effects are included by means of an empirical coefficient based on Reynolds number; this coefficient is augmented with extra terms to account for drag increase at higher angles of incidence [11].

The discretization scheme used in the above numerical method is actually based on a boundary integral equation formulation. According to this, a number of panels discretize the chord of the foil; the discrete panels along the foil chord panels according to cosine spacing method, so that panels are accumulated in the leading and trailing edge regions where the most significant hydrodynamic variations are expected according to linear theory. In addition, some more panels discretize the trailing vortex wake. Since the discrete model is assumed to start from rest, the number of wake panels is selected to be equal to the number of time steps and the response is obtained by direct integration. Time is discretized in equal discrete steps Δt . Each of the wake panels has a length of $\Delta w = U \Delta t$. The ratio of wake panel length to that of the foil panel in the trailing edge region is a control parameter tuned for optimum convergence. In a simplified version, the wake panels have the same direction with the free stream velocity which is a consequence of the material conservation of vorticity, as realized approximately by the present wake model. The accuracy of the method has been examined in various test cases, including steady-state problems starting from rest, by increasing the space and time discretization and exhibiting very good convergence characteristics. Some indicative results are provided herein for demonstration purposes.

Figure 2 presents the evolution of the thrust force (in Nt) in time, as predicted numerically by the present DVM-based numerical tool, against corresponding experimental results from [3] for a NACA0012 flapping hydrofoil at $Re=40000$, with $St=0.3$, $y_o/c=0.75$, $\psi=90^\circ$, $\theta_o=23^\circ$. Pitching was realized around a pivot point located at $1/3$ chord length from leading edge ($x_R/c=1/3$). The comparison is satisfactory.

Figure 3 presents further results of the DVM-based tool, compared against experimental results from [4], in the case of the same NACA0012 flapping hydrofoil at $Re=40000$, at large heaving amplitude. Again the pivot point for pitching was located at $x_R/c=1/3$ and phase lag between heaving-pitching motions was $\psi=90^\circ$. The results refer to the performance of the flapping foil thruster in an extended range of motions. To this end, systematic simulations were performed for different values of the Strouhal number, namely 0.20, 0.25, 0.30, 0.35, 0.40, 0.45 and pitch amplitudes ranging from 15° to 50° , resulting in effective angles of attack ranging from 5° to 35° , approximately. Figure 3(left) depicts results concerning the thrust coefficient. Figure 3(right) contains the corresponding thrust plots acquired through the DVM in the parameter range tested by [4] along with iso-efficiency curves. The overall agreement between numerical predictions and experiments is good for moderate to large effective angles of attack up to about 25° and Strouhal numbers up to 0.40, approximately. For large values of incidence angles (upper-left region of Figure 3(left)), the thrust coefficient C_t is underestimated by the DVM for $St>0.3$ with respect to the experimental values. This deviation is attributed to the fact that the NACA0012 section, although symmetric, possesses different hydrodynamic attributes than the flat plate used to model the foil

in the present DVM formulation. The performance of the NACA foil in the experiments worsens significantly for small values of effective angle of incidence as the Strouhal number increases (lower-right region of Figure 2(right)). This is attributed to the degraded angle of incidence time signal, possessing many peaks in a motion period, as has been stated in [4].

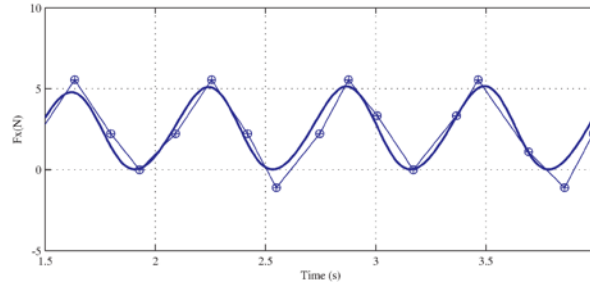


Figure 2. Comparison of the thrust coefficient evolution in time against experimental data for a flapping NACA0012 foil from [3]. Solid lines correspond to values predicted by DVM, while dots refer to the experimental ones ($Re=40000$, $St=0.3$, $y_o/c=0.75$, $\psi=90^\circ$, $\theta_o=23^\circ$, $x_R/c=1/3$).

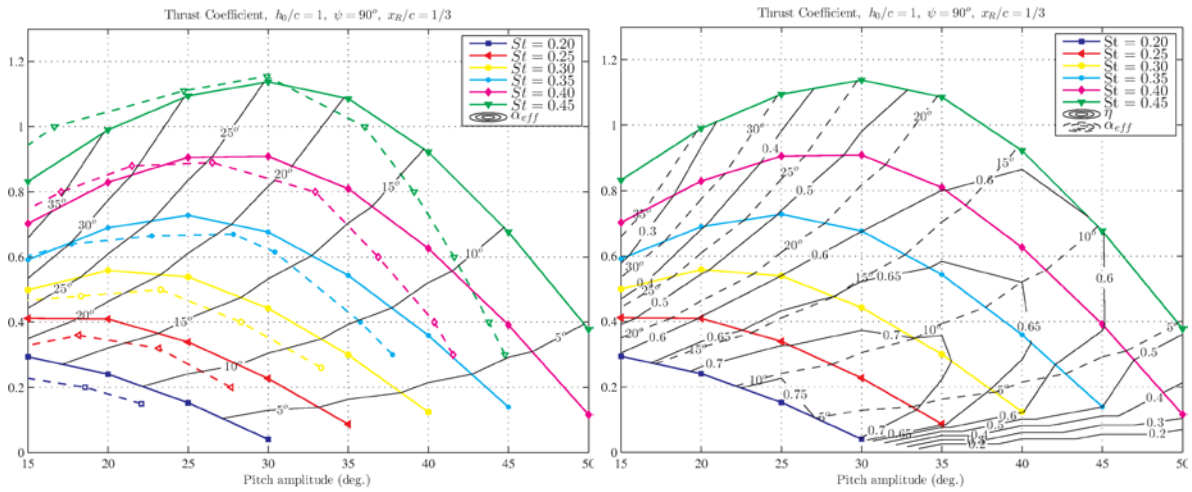


Figure 3. Comparison of thrust coefficient (left) and propulsion efficiency (right) against experimental data for NACA 0012 foil from [4]. Solid lines correspond to the DVM results and dashed lines to the experimental data, respectively. In the examined case $Re=40000$, $y_o/c=1$, $\psi=90^\circ$, $x_R/c=1/3$.

4 THE MULTI-OBJECTIVE PROBLEM

4.1 Problem formulation

The optimal design and operation of the flapping foil system entails the search for the optimal set of values for the independent variables, so as to maximize an appropriately defined objective functions related to its optimum performance sought by the method. As stated in a previous section, the independent variables of the problem are Strouhal number (St), phase lag angle (ψ), pitching amplitude (θ_o) and non-dimensional heaving amplitude as a percentage of foil chord (y_o/c); i.e. the decision variable vector is $\underline{x} = [St \ \psi \ \theta_o \ y_o/c]^T$. On the other hand, the objective functions to be maximized are thrust coefficient C_T and propulsion efficiency η , while minimum power coefficient C_P is desired.

The flapping foil design for maximum efficiency exhibits a very small thrust coefficient. In engineering practice such a design would not be deemed practical and would not be selected. A more balanced solution would normally be selected, which yields a high efficiency and covers some minimal needs of propulsion. This can be expressed as an additional constraint on the thrust coefficient in the optimization problem [7] and it depicts that in reality a multi-objective approach needs to be adopted when designing such a system. Thus in the present work, the Pareto front of the optimal solutions is presented for the flapping foil propulsion system at hand. Since the thrust and power coefficients constitute parallel variables, i.e. one can be expressed as an increasing function of the other, only one of them can be included in the following analysis. Here, the optimization of the thrust coefficient versus the efficiency was considered.

Any of the three objective functions (C_T , η , C_P) is a scalar time-averaged quantity, so its calculation is performed over a period T of the periodic phenomenon. The time-dependent, ordinary differential and algebraic

equations (1)–(3) are the constraints, which hold for every feasible state of the system. Each of these equations can be written in the form $g_i(\underline{x}, t, \underline{z})=0$, where $\underline{z}=[y \ \theta \ \alpha \ U]^T$ is the state variables vector and $i=1,2,3$ is the equation index. Equations (4)–(8) are used to evaluate the system behavior and are time-invariant, as they are calculated for the duration of a period. These equations are solved for the calculation of the objective function using the state variables trajectory that satisfies Equations (1)–(3) and therefore can also be regarded as part of the constraint set. The nonlinear equations g_i can be concatenated in a vector function $G(\underline{x}, t, \underline{z}) \in \mathbb{R}^8$. The multi-objective optimization problem can be formally written as:

$$\max(C_t(x), \eta(x)), \text{ subject to } G(\underline{x})=0 \quad (9)$$

The two optimality criteria ($C_t(x)$, $\eta(x)$) are competitive, in the sense that optimality for one of the two leads to suboptimality for the other. Obtaining a solution which simultaneously optimizes all criteria is not feasible, therefore a satisfactory solution is sought, which is a compromise. The Pareto optimal set is the set of solutions, which are nondominated by any other solution. These solutions are called efficient, non-dominated, Pareto optimal, or objectively equivalent. If one was to traverse the set of Pareto solutions, he would observe that there is a certain amount of sacrifice in one objective, in order to achieve a gain in the other.

The optimization solution adopted a feasible path approach and followed the Nested Analysis and Design paradigm, exploiting the simulator that has been described in the previous sections. A deterministic, gradient-based optimization strategy has been selected here, based on the interior-point method [12]. The Broyden–Fletcher–Goldfarb–Shanno algorithm (BFGS) approximation was employed for the Hessian matrix. The Pareto front is identified using Goal Programming, whereas the two objective functions are assigned weights, which are varied across the front. Deviation variables from the target are introduced and the objective is to minimize the weighted sum of deviation variables, i.e. formally:

$$\min(\gamma), \text{ subject to } F(x)\text{-weight}\gamma \leq \text{goal}, G(x)=0 \quad (10)$$

4.2 Problem data

The initial estimate vector for the independent variables, i.e. the starting point for the optimization solution, is provided in the second column of Table 1, while the corresponding range of variation for each decision variable (optimization domain) is provided in the third column of Table 1. The flow velocity was set to $U=0.4\text{m/s}$, so a fixed Reynolds number of $Re=Uc/v=40000$ was considered in all simulations. The pivot point for the pitching motion was set at $x_R/c=1/3$.

Parameter	Initial estimate	Range of variation
St	0.35	0.15÷0.6
$\psi[^\circ]$	90	45÷135
y_o/c	1	0.0÷1.0
$\theta_o[^\circ]$	35	0÷90

Table 1. Optimization domain and starting point of the control variables for the multi-objective problem.

5 RESULTS AND DISCUSSION

The results concerning the Pareto optimal solutions for the simultaneous maximization of thrust coefficient C_t and propulsion efficiency η are depicted in Figure 4, lying on the so-called Pareto front. In the same diagram, the corresponding power coefficient C_p for each point of the front is also presented. According to Figure 4, the minimum and maximum values of the thrust coefficient are 0.126 and 3.412, respectively, while the corresponding efficiency values are 0.804 and 0.227, i.e. when thrust is maximized efficiency becomes minimum and vice-versa. As mentioned in the previous section, as thrust increases, the required power increases too. To any intermediate thrust solution, between its minimum and maximum values, corresponding intermediate values for efficiency and power are found. Having obtained the Pareto front, the designer is free to select a great thrust in the cost of the increased power or a modest thrust value, achieved with better propulsion efficiency.

Figure 5 presents the variation of the four control variables (St , ψ , y_o/c , θ_o) as the thrust coefficient increases along the Pareto front. In all of these plots, the lower and upper limits of the vertical axis correspond to the range of variation of the corresponding variable. Figure 5(a) depicts the St - C_t plot. According to it, the Strouhal number takes values in almost the whole of its range and attains its maximum allowable value if a maximum thrust value of $C_t > 1.5$ is to be achieved. Due to the fact that $T=2y_o/(USt)$, low thrust along the Pareto front corresponds to low St , i.e. large period of the flapping foil motion, while high thrust corresponds to high St , i.e. low period.

From the ψ - C_t plot presented in Figure 5(b), it can be seen that, although the phase lag ψ is allowed to vary between 45° - 135° , its optimal range of variation for the optimal points is in the narrow band of 80.5° - 110° (according to the literature [3], [4], [10], the value of 90° for ψ is reported for maximum efficiency). The remark here is that, in order to achieve thrust solutions along the Pareto front as much as more efficiently, the phase lag between the two motions has to be slightly increased.

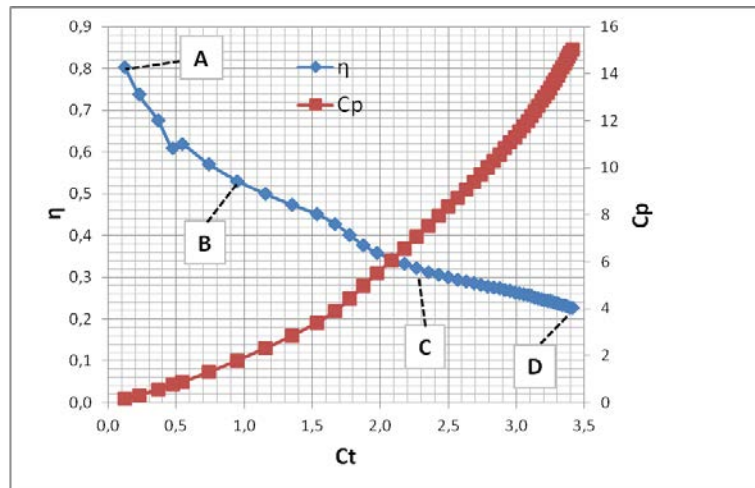


Figure 4. Pareto optimal solution for the simultaneous maximization of thrust coefficient and efficiency, as well as corresponding power coefficient.

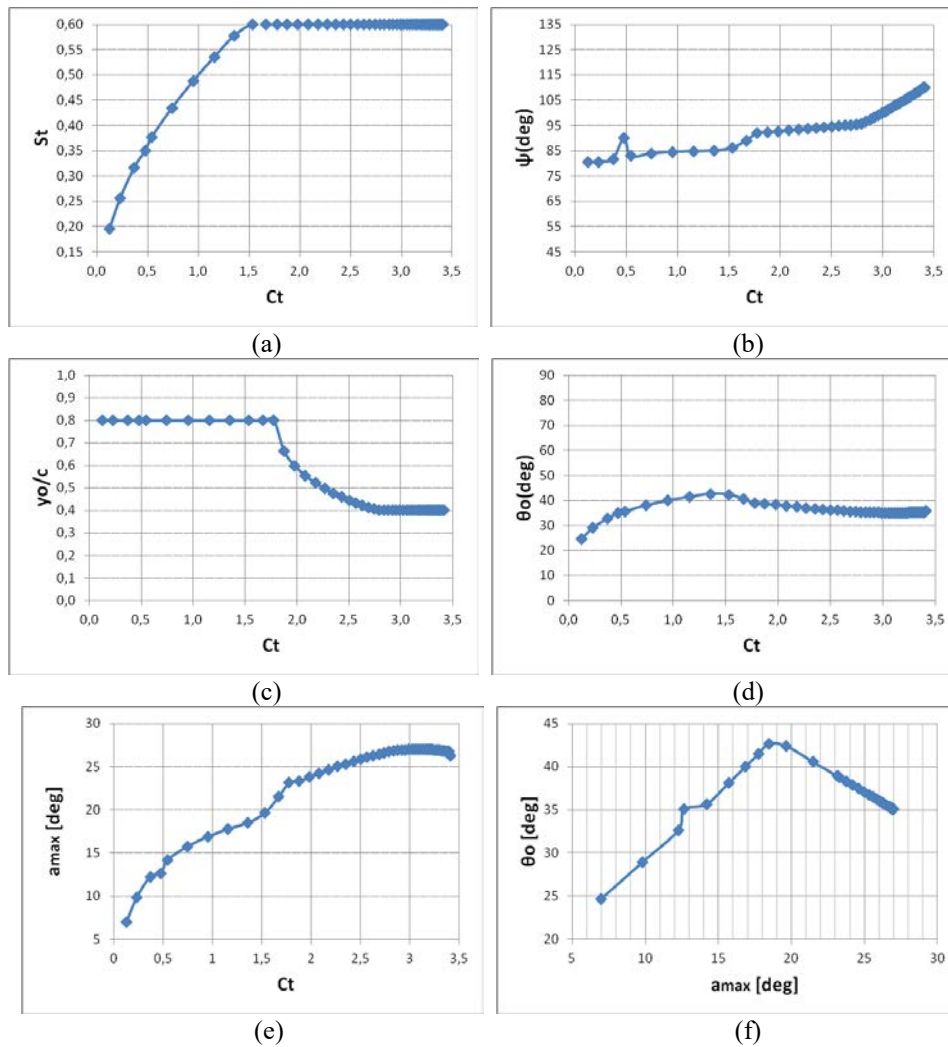


Figure 5. Variation of control variables with thrust coefficient along the Pareto front: (a) Strouhal number, (b) phase lag, (c) heaving amplitude as a percentage of foil chord, (d) pitching amplitude, (e) maximum incidence angle and (f) plot of pitching amplitude against maximum incidence angle.

Figure 5(c) presents the plot of nondimensional heaving amplitude y_0/c with C_t along the Pareto front. Although y_0/c is allowed to vary between 0 and 1, its optimal range of variation is between 0.4 and 0.8.

Furthermore, opposite to what is found for the Strouhal number, y_o/c attains its maximum value of 0.8 for values of thrust in the lower range and drops to 0.4 in order to obtain values $C_T > 1.7$. This means that large heaving amplitude corresponds to low thrust along the Pareto front, while lower (almost half of maximum) values correspond to higher thrust.

Figure 5(d) depicts the variation of pitching amplitude θ_o with C_T along the Pareto front. Although its allowable range of variation is 0° - 90° , the optimal range is in the narrow band of 24.6° - 35.8° . Finally, Figure 5(e) presents the maximum incidence angle α_{\max} for each C_T and Figure 5(f) presents the plot of the pitching amplitude θ_o against the corresponding maximum incidence angle α_{\max} . The remark derived from Figure 5(e) is that high thrust value $C_T > 1.5$ is obtained for maximum incidence angle $\alpha_{\max} > 20^\circ$, corresponding to flow conditions that the accuracy of the DVM solver becomes questionable. Although this is known, no constraint was used for α_{\max} in the formulation and solution of the optimization problem, intentionally, aiming to detect the trends of C_T variation in a broader range of foil motions even, if the solutions are more or less inaccurate in some regions of this range.

In order to physically interpret the different foil motions corresponding to different optimal solutions along the Pareto front, four different solutions were selected on it corresponding to points of increasing thrust, namely A, B, C, D (Figure 4). Point A corresponds to the lowest thrust, while D corresponds to the maximum one. The values of the triad (C_T , η , C_P) for these four points are A(0.126, 0.804, 0.156), B(0.952, 0.531, 1.791), C(2.269, 0.321, 7.057) and D(3.412, 0.227, 15.051).

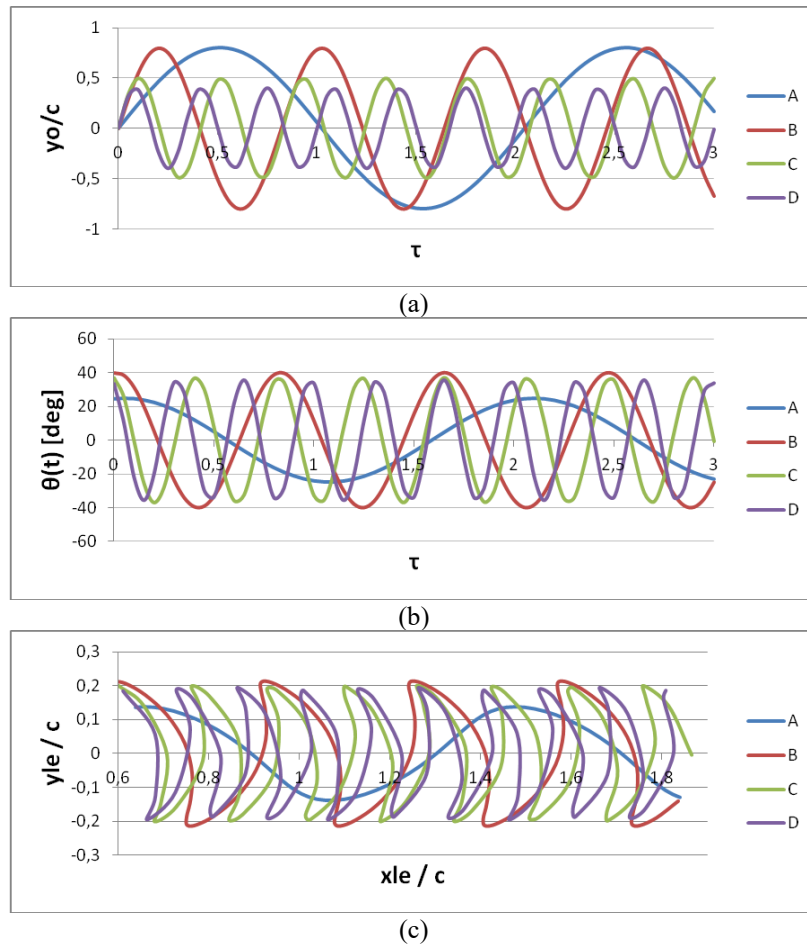


Figure 6. Foil motion for points A, B, C, D along the Pareto curve: (a) heaving motion, (b) pitching motions and (c) leading edge motion in space (moving from the left to the right with velocity U).

Figure 6 presents the different foil motions corresponding to the points A, B, C, D of the Pareto front in Figure 4. In particular Figure 6(a) depicts the evolution of the heaving motion of the foil center in nondimensional time. Heaving of large amplitude and low frequency produces low thrust in an efficient way and with minimum power cost (point A). Moving towards greater thrust values, heaving of large amplitude and higher frequency is required (point B). By performing even higher frequency motion with lower amplitude (faster in time and less extended in space), both thrust and the corresponding effort (power) become greater, while efficiency is reduced (point C). Heaving of the lowest amplitude and the higher frequency leads to maximum thrust but with the lowest efficiency (point D).

Similarly, Figure 6(b) depicts the evolution of pitching angle in time. As shown in Figure 5(d) the amplitude does not significantly vary along the Pareto front. The variation of frequency was explained before (heaving and pitching motions have the same frequency). The remark here is that, in order to achieve higher thrust, i.e. from point A to point D along the Pareto front, the phase lag between the two motions has to be increased.

Finally, Figure 6(c) presents the motion of the foil leading edge in space. It has been considered that the fluid is at rest while the foil moves to the right with velocity U . This figure actually indicates how the flapping foil has to “swim” in the fluid in order to achieve the thrust corresponding to the points A, B, C and D along the Pareto front. Low frequency and low amplitude motions produce low thrust with least effort and best efficiency while, in order to maximize thrust, significant “swimming” effort (i.e. power) is needed, mainly due to the requirement to realize high frequency motions of lower amplitudes and with greater phase lag between them.

6 CONCLUSIONS

A multi-objective problem was formulated and solved for the optimum flapping foil motion that achieves maximum thrust with maximum efficiency. To this end, the foil was considered to undergo combined sinusoidal heaving and pitching motions of the same frequency and a phase lag between them. Pareto optimal solutions were presented and discussed. A low fidelity compared to Navier-Stokes solver, however very fast, was utilized for the numerical simulations. Thrust and propulsion efficiency were proved to be contradicting objectives, while the power required for achieving the desired foil motion is an increasing function of the required thrust.

The results showed that whenever low thrust is required in an efficient way, the foil has to “swim” in the fluid with low frequency-low amplitude motions. In order to maximize thrust against efficiency (however in an optimal way), a significant effort is required to make the foil move with high frequency-lower amplitude and greater phase lag between the two combined motions.

Future research includes the study of the same problem with stochastic-based optimization methods (e.g. genetic algorithms), as well as by utilizing a more advanced simulation tool (Navier-Stokes CFD solver), while the aim in the long-term is to develop a methodology for the dynamic control of the flapping foil motion for maximum thrust.

REFERENCES

- [1] Triantafyllou, M.S., Barrett, D.S., Anderson, J.M., Grosenbaugh, M.A.D., Yue, K.P., Draper, C.S. and Triantafyllou, G.S. (1996), “A New Paradigm of Propulsion and Maneuvering for Marine Vehicles”, *SNAME Transactions*, Vol. 104, pp. 81-100.
- [2] Triantafyllou, M.S., Triantafyllou, G.S. and Yue, D.K.P. (2000), “Hydrodynamics of fishlike swimming”, *Annual Review of Fluid Mechanics*, Vol. 32, pp. 33–53.
- [3] Schouveiler, L., Hover, F.S. and M.S. Triantafyllou, (2005), “Performance of flapping foil propulsion”, *Journal of Fluids and Structures*, Vol. 20, pp. 949-959.
- [4] Read, D.A., Hover, F.S. and Triantafyllou, M.S. (2003), “Forces on oscillating foils for propulsion and maneuvering”, *Journal of Fluids and Structures*, Vol. 17, pp. 163–183.
- [5] Belibassakis K.A. and Politis, G.K. (2013), “Hydrodynamic performance of flapping wings for augmenting ship propulsion in waves”, *Ocean Engineering*, Vol. 72, pp. 227-240.
- [6] Lampropoulos, N., Koubogiannis, D.K. and Belibassakis, K.A. (2016), “Numerical Simulation of Flapping Foil Propulsion”, *11th HSTAM International Congress on Mechanics*, Athens, Greece, 27–30 May 2016.
- [7] Bonis, I., Koubogiannis, D.G., Priovolos, A. and Belibassakis, K. (2017), “Optimization of flapping foil motion in ship propulsion for maximum thrust augmentation”, *2nd International Conference Energy in Transportation 2017 (EinT2017)*, Athens, Greece, October 21 2017.
- [8] Filippas, E.S. and Belibassakis, K.A. (2014), “Hydrodynamic analysis of flapping-foil thrusters operating beneath the free surface and in waves”, *Engineering Analysis with Boundary Elements*, Vol. 41, pp. 47-59.
- [9] Priovolos, A.K., Filippas, E.S. and Belibassakis, K.A. (2017), “Effect of chordwise flexibility on flapping foil thruster performance by Discrete Vortex Method”, *Proceedings of the 17th International Congress of the International Maritime Association of the Mediterranean (IMAM2017)*, Lisbon, Portugal, 9-11 October 2017.
- [10] Anderson, J.M., Streitlien, K., Barret, D.S. and Triantafyllou, M.S. (1998), “Oscillating foils of high propulsive efficiency”, *Journal of Fluid Mechanics*, Vol. 360, pp. 41–72.
- [11] Paraz, F., Schouveiler, L. and Eloy, C. (2016), “Thrust generation by a heaving flexible foil: Resonance, nonlinearities, and optimality”, *Physics of Fluids*, Vol. 26 (Issue 1).
- [12] Byrd, R.H., Gilbert, J.C. and Nocedal, J. (2000) “A Trust Region Method Based on Interior Point Techniques for Nonlinear Programming” *Mathematical Programming*, Vol. 89, No. 1, pp. 149–185.

OPTIMAL DESIGN OF LARGE SPAN STRUCTURES USING THE MBN DISPLACEMENT CONTROL SYSTEM

Themistoklis N. Nikolaidis¹ Georgios V. Stavroulakis² and Charalampos C. Baniotopoulos³

¹Institute of Metal Structures, Department of Civil Engineering, , Faculty of Engineering
Aristotle University of Thessaloniki, 54124 Thessaloniki, Greece
e-mail: thnik@civil.auth.gr ; web page:

http://www.civil.auth.gr/index.php?option=com_contact&task=view&contact_id=191&Itemid

²Institute of Computational Mechanics and Optimization, School of Production Engineering and Management,
Institute of Computational Mechanics and Optimization, Technical University of Crete, University Campus, GR-
73100 Chania, Greece

e-mail: gestavr@dpem.tuc.gr ; web page: <http://users.isc.tuc.gr/~gestavroulakis/>

³School of Engineering, University of Birmingham
B15 2TT Birmingham, United Kingdom

e-mail: c.baniotopoulos@bham.ac.uk; web page: <http://www.birmingham.ac.uk/schools/civil-engineering/people>

Keywords: Optimal prestressing, Displacement minimization problem, Passive control, Large span structures

Abstract. *The structural performance of large span structures with the prestressed control system MBN (type MBN after Michalopoulos, Baniotopoulos, Nikolaidis) corresponding to lines of curved cable nets is herein investigated. This prestressing control system is based on the cable supported beam concept with prestressing control so that the structural behavior of the system is optimized. The novel optimal control system is a prestressing cables mechanism, where permanent loads are relieved by two lines of external curved cables (α) and the moving loads relieved by a passive control system of internal to the deck curved cables (β) that consists of a sequence of highly prestressed segments with significant length, being interconnected by non prestressed segments of small length. The structural system under consideration seems to be appropriate for the design of large span bridges. The passive control design of the system leads to an optimal control problem for structures governed by variational inequalities. The accurate simulation of the complex action of the cables on the structure has been performed by means of the Finite Element Method within an Optimal Prestressing theoretical framework. In this paper a bridge model of span length $L=200,0m$ is proposed and studied as a numerical application of the method.*

1 INTRODUCTION

The structural collaboration between a deck structure and an external prestressed cable is a very advantageous structural system for bridges and large span structures due to the fact that external prestressing can be applied [2], [3], [4], [6]. However, the action of the moving loads causes on the cables large displacements not compatible to the connected deck or structure. In the design of structures with large spans, the significant values of the bending moments at the deck require very heavy members. An effective way to minimize the influence of bending moments to the deck is to apply the MBN (after Michalopoulos, Baniotopoulos, Nikolaidis) passive control system of displacements by the use of external prestressed cables. The proposed displacement control system for large span structures needs two parallel, external lines of flexible cables (see Figure 1). The optimal shape of a prestressing support cable leads to a Form-Finding problem of the structure. The analysis is based on the two-nodes-curved-cable-element, where large displacements and large rotations appear [1]. The upper cable (a'') is actually a group of similar, parallel and loaded cables that support the simply supported concrete plate (deck), which in turn follows the curved shape of the loaded cables. The lower cable (a') is also a group of similar, parallel and loaded external cables following also a curved shape form. The two (upper and lower) cable lines are connected with stanchions of appropriate length between the homologous nodes. The curved shape form of each one of the cable lines depends on the load distribution between the upper and the lower cable. For the meticulous control of the expected displacements due to the moving loads, a system of cable net called cable (β) is also introduced.

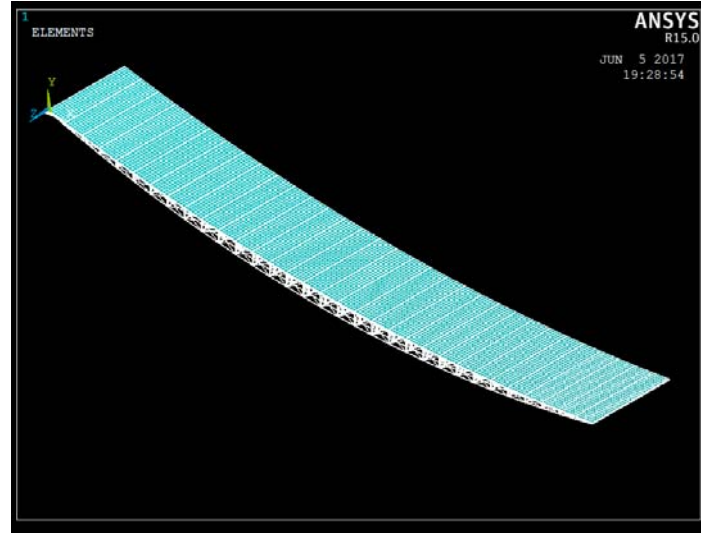


Figure 1. Bridge model including two parallel external lines of prestressed cables

The later have the same length and follows the same curve as the upper cable (a''), but under the permanent loads are inactive, whereas activated only upon the introduction of moving loading on the structure. By this method one is able to obtain the best mechanical properties of the structure by using the deep curve of the lower cable line (a') and at the same time having the low curve form (of the upper cable line (a'')) for the deck which is necessary by the design procedures. The structural system under consideration seems to be appropriate for the design of large span structures and bridges in earthquake prone zones. The accurate simulation of the complex action of the cables on the structure has been performed by means of the Finite Element Method within an Optimal Prestressing theoretical framework. In the present paper, a bridge model of type MBN of open length $L=200\text{m}$ is proposed and studied as a numerical application of the method (see Fig. 1).

2 FORMULATION OF THE PROBLEM

The analysis of the proposed model has been performed by means of the Finite Element Method within an Optimal Prestressing theoretical framework [8]. The equations of equilibrium of the discretized structure, using the stiffness matrix, can be put in the form:

$$[K^*] \cdot \{u\} = \{P\} + [G] \cdot [K_o] \cdot \{e_o\} - [G] \cdot \{S_o\} \quad (1)$$

where $\{e_o\}$ is the initial strain vector and $\{S_o\}$ is the initial stress vector. The unilateral contact effect that possibly appears, due to unilateral contact or no-compression effect on prestressing cables, is described by the inequalities:

$$[A] \cdot \{u\} \leq \{b\} \quad (2)$$

Following a similar notation, the classical support boundary conditions of the structure is put in the general form of equations:

$$[\Gamma] \cdot \{u\} = \{u_0\} \quad (3)$$

where $[\Gamma]$ is a $(p \times n)$ geometric transformation matrix, $\{u_0\}$ is a p – dimensional vector of given boundary displacements and p the number of nodes of the support boundary. The prestressing control action is modeled by means of a sequence of loads. The contribution of the q prestressing forces corresponding to different groups of cables is taken into account under the assumption that each group contributes by introducing the same prestressing force which is added to the loading vector p after an appropriate transformation which is realized by means of an $(n \times q)$ transformation matrix C . Thus, an enlarged loading vector \bar{p} is applied on the structure, where:

$$\{\bar{p}\} = \{p\} + [C] \cdot \{z\} \quad (4)$$

Assuming that displacements and deformation are infinitesimal, the formulated structural analysis problem leads to the following potential energy minimization problem [9]:

$$\min \left\{ \prod \left(\{u\} = \frac{1}{2} \cdot \{u^T\} \cdot [K] \cdot \{u\} - \{P^T\} \cdot \{u\} - \{z^T\} \cdot [C^T] \cdot \{u\} \right) \mid \{u\} \in U_{ad}(z) \right\} \quad (5)$$

where the space of admissible displacements $U_{ad}(z)$ is defined by:

$$U_{ad}(z) = \left\{ \{u\} \in \mathbb{R}^n \mid [A] \cdot \{u\} \leq b, [\Gamma] \cdot \{u\} = \{u_0\} \right\} \quad (6)$$

The solution of problem (4), (5) can be explicitly written as follows:

$$[K] \cdot \{u\} - \{p\} - [C] \cdot \{z\} + [\Gamma^T] \cdot \{u\} + [A^T] \cdot \{\lambda\} = \{0\} \quad (7)$$

$$-[\Gamma] \cdot \{u\} + \{u_0\} = \{0\} \quad (8)$$

$$-[A] \cdot \{u\} + \{b\} + N_{R_+^S(\lambda)} \ni \{0\}. \quad (9)$$

Thus, vector $\{u\}$ corresponds to the discrete nodal reactions at the boundary condition (9), vector $\{\lambda\}$ corresponds to the discrete interface tractions along the unilateral contact interface and the relations (8) are more often written in structural analysis literature in the following complementary system of inequalities:

$$\text{No penetration relation} \quad \{y\} = -[A] \cdot \{u\} + \{b\} \geq 0 \quad (10)$$

$$\text{No tensile tractions} \quad \{\lambda\} \geq \{0\} \quad (11)$$

$$\text{Complementarity} \quad \langle \{\lambda\}, \{y\} \rangle = 0 \quad (12)$$

Relations (7), (8), (9) are the well-known optimality conditions for the quadratic minimization problem (5). Moreover, the problem (7), (8), (9) is also known as the generalized linear complementarity problem. All the aforementioned describe the structural response for variable control vector $\{z\}$ and can be considered as parametric state models for the analysis of the optimal control problem. The prestressed cables require the determination of their suitable form so that the response of the system as a whole is optimized. The two flexible cables connected at the two extreme nodes of the structure exhibit an S-unilateral structural behavior [7] and therefore, are subjected to vertical loads that correspond to cable tension (see Fig. 2). Therefore, the first step is to formulate the general system of equations of each one of the two cables hinged from the two extreme nodes and loaded by a general loading corresponding to a set of vertical nodal forces [2], [9].

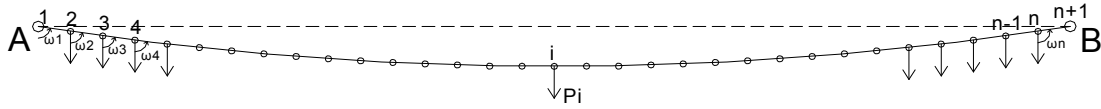


Figure 2. On the form of the cable

This formulation begins by introducing the desired displacement of the cables. Using the equations of each cable, the system (13) is first formulated. The solution of $2n(S_{(u)i}, \omega_{(u)i})$ and $2n(S_{(l)i}, \omega_{(l)i})$ non-linear equation system with $n+1$ cable nodes give the unknown stresses $S_{(u)i}, S_{(l)i}$ and unknown angles $\omega_{(u)i}, \omega_{(l)i}$ (hence also the geometry of cables) before deformation.

$$(1) \quad \begin{cases} \dots\dots\dots \\ S_{0i} \sin \omega_{0i} = S_{0i+1} \sin \omega_{0i+1} \\ S_{0i} \cos \omega_{0i} - S_{0i+1} \cos \omega_{0i+1} = P_{0i+1} \\ \dots\dots\dots \\ \sum_{i=1}^n l_i \sin \omega_{0i} = L_{AB} \\ \sum_{i=1}^n l_i \cos \omega_{0i} = 0 \end{cases} \quad (13)$$

Here ω_{0i} (upper or lower cable) denotes the left-side angle between the vertical axes that passes from the i -th node and the cable (between the nodes i and $i+1$) and S_{0i} (upper or lower cable) is the stress of the

cable at the section l_i . The system (13) mathematically describes, in a general form, the configuration of a cable hinged from its extreme points and loaded by nodal vertical concentrated loads. The previously formulated system (13) can be numerically treated easily by applying suitable commercial software for each one of the two cable lines. The herein proposed model concerns the introduction of a net of cables (β) that acts as an effective passive control system of displacement against the deformations caused by moving loads.

Thus, apart from the cables (a^u) and (a^l), respectively, being the basic cables of suspension, a third set of cables called cables (β), being inactive in the situation of equilibrium under permanent loads is introduced. The latter cables are anchored in the same positions of suspension as the cables (a^u) and are activated as soon as additional moving loads start acting on the deck. The cables (β) have the same length, are parallel and exhibit the same geometry as the cables (a^u) (as they are found in equilibrium under the permanent loads), and therefore, they have equal displacements. Before the selection of the actual cross-section of cable (β) the notion of an "ideal" cross-section of the cable (β^*) is introduced. The cables (a^u) have known cross-section $F^{(a^u)}$, which can be found from the calculation of the stresses due to permanent loads. The cables (β^*) are hinged and anchored in the same positions of the suspension as the cables (a^u). The total cross-section $F^{(a^u)} + F^{(\beta)}$ of the cables, takes over the presented stress as caused by to the moving loads. Hence, due to the form finding the design cable (β^*) undertakes the 90% of moving stresses $S^{mov.}$ and has a cross-section that is analogously multiplied by the already known $F^{(a^u)}$. By analyzing the structure with a finite element program (taking now into account a cross-section $F^{(a^u)} + F^{(\beta^*)}$), if the obtained stresses and displacements are within the allowable limits, the cable (β^*) is replaced by a statically equivalent, real cable (β). The real cable (β) consists of a sequence of prestressed segments with significant length, being interconnected by non prestressed segments of small length. The cables are placed along the central axis of the stiffness plate embedded to a priori constructed channels within the mass of the stiffness plate. The cable (β) has the same geometry with respect to (a^u) and (β^*) and is also hinged and anchored at the same positions of the structure. The real cables (β), as it was reported above, are the statically equivalent cables (β^*). Note that the whole cable (β) exhibits small deformability subjected to the same load with the ideal cable (β^*) and undertaking the same part of stress $S^{mov.}$.

3 DESIGN EXAMPLE OF THE METHOD

As a numerical application of the method a road bridge of length $L=200,0m$ is considered [5]; Starting configuration are the calculated lengths by the system (13) for each one of the two cables (a^u) and (a^l), each one separately hinged by the common ends of suspension A and B (see Fig.3). The formation of the supporting system begins with an arbitrary choice of dead nodal loads $P_i^{perm} = -2370kN$ between the two lines of cables.

By taking into account a 20% of the total nodal load for the lower cable (a^l) and an 80% for the upper cable (a^u), one has $P_i^{perm(u)} = 20\% \cdot (-2370) = -474 kN$ and $P_i^{perm(l)} = 80\% \cdot (-2370) = -1900 kN$. Namely, the two cables system is regulated in such a way such that the permanent loads are distributed by an optimal distribution according to the design procedures (i.e., a desirable value for the cable deflection at the mid-span). Taking into consideration the solution of the cables and in particular the distribution of the permanent nodal loads we determine the corresponding cross-section $F(a^{upper}) = 700cm^2$, $J = 0$, for the upper cable and $F(a^{lower}) = 2000cm^2$, $J = 0$ for the lower cable. Concerning the cable set (β) an idealized cable (β^*) with cross-section $F(\beta^*) = 14000cm^2$ is first taken and the sum of the cross section for the upper cable becomes $F(a^u) + F(\beta^*) = 14700cm^2$. The final form of the supporting system constitutes the initial condition of balance against the deflection of the structure due to the live loading. The cables (β) along with the additional diagonal cables (after the initial condition) are used as passive control system for the suppression of the displacements of the bridge. They lead to very satisfactory results for both the displacements and the stresses.

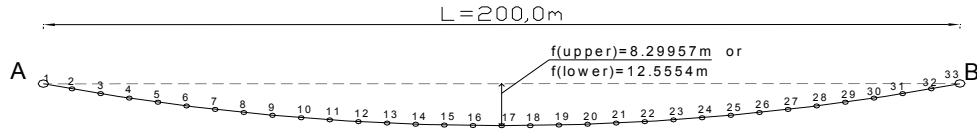


Figure 3. The form of the single cable model

The complete design of the bridge has been based on a three-dimensional finite element (3-D) model using ANSYS computer software. In this analysis, one dimensional elements (bars, cables, stanchions) and surface elements (concrete upper plate) have been used. The loading cases that have been considered in the structural analysis problem are the following:

COMB1: Solution for the initial deck structure where only the cable set $(a^u), (a^l)$ is present. For this loading combination (see Figure 4), the composite structure remained at the initial condition of equilibrium (without displacements for the bridge).

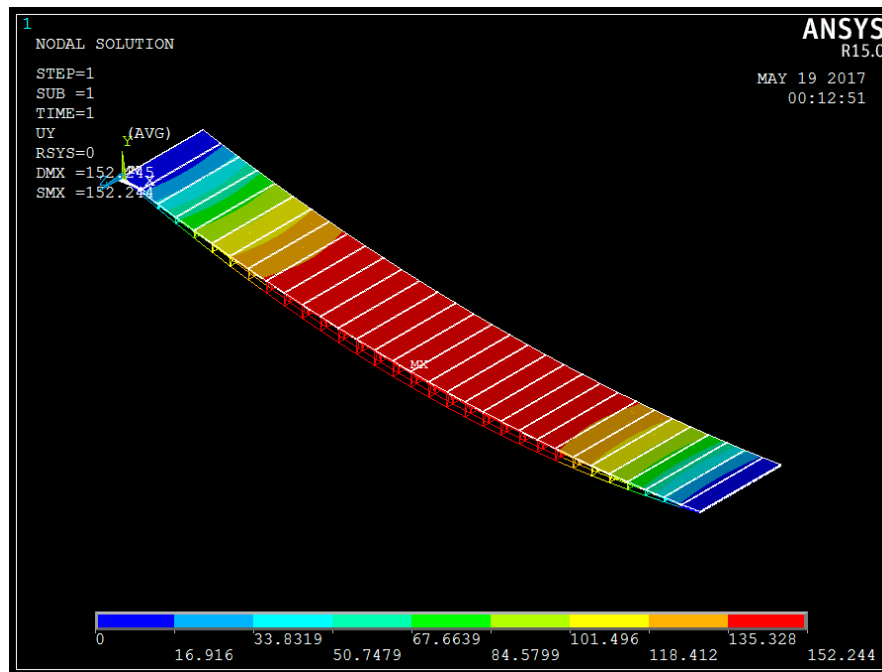


Figure 4. Nodal displacements at S.L.S. on the bridge for (a) the initial condition of equilibrium

COMB2: Load combination including the initial deck structure, the cable set $(a^u), (a^l)$, the additional cables (β) and a distributed live load on the deck. For this loading combination, the maximum deflection at the mid-span becomes decreases (see Figure 5) in comparison with the standard limits of vertical displacements $(L/250)$.

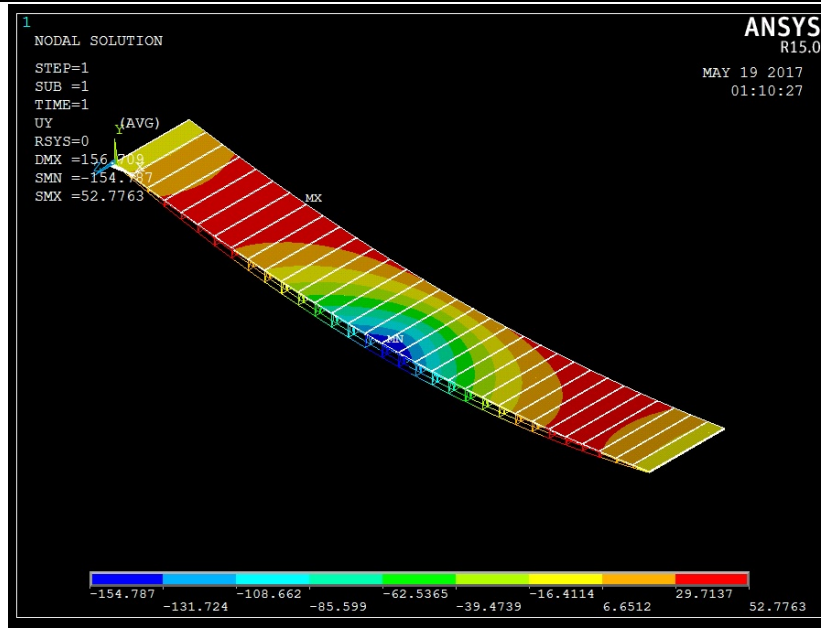


Figure 5. Nodal displacements at S.L.S. on the bridge for the final condition without diagonal cables under traffic loads.

In order to decrease the deformations and increase the stiffness of the structure, diagonal cables (see Figure 6) are added between consecutive nodes of the deck and the cable respectively, as an additional passive control system.

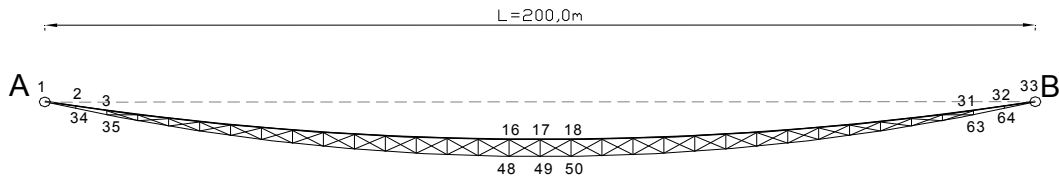


Figure 6. Form of the controlled structure including diagonal cables.

The influence of structural response of the added diagonal cables to the system is showed clearly in Figure 7 especially when the imposed loads act concentrated on the structure. There the maximum deflection at the mid-span is much lower in comparison with a system without diagonal elements and with a satisfactory distribution along the span of the structure. All the solutions for the Serviceability Loading States (SLS) for different imposed loads give satisfactory results in comparison with the respective comfortable limits of $(L/750)$, whereas no extreme deformations and dangerous vibrations arise.

Respectively the results of the solutions for the Ultimate Limit States (ULS) compared with the structural resistance of the members and especially the buckling and stress resistance of the upper composite deck and the stresses limits of the linear and cable elements of the structure. This analysis leads to the appropriate cross-sections of all the elements of the structure according to the design limits.

The maximum stress of the upper cable nets $(a^u) \& (\beta)$ is $S^{(a^u+(\beta))} = 32017kN$ and the cross section of the cable (β) becomes $F(\beta) = 933cm^2$, equal to the 1/15 of the ideal cross section (β^*) of the model.

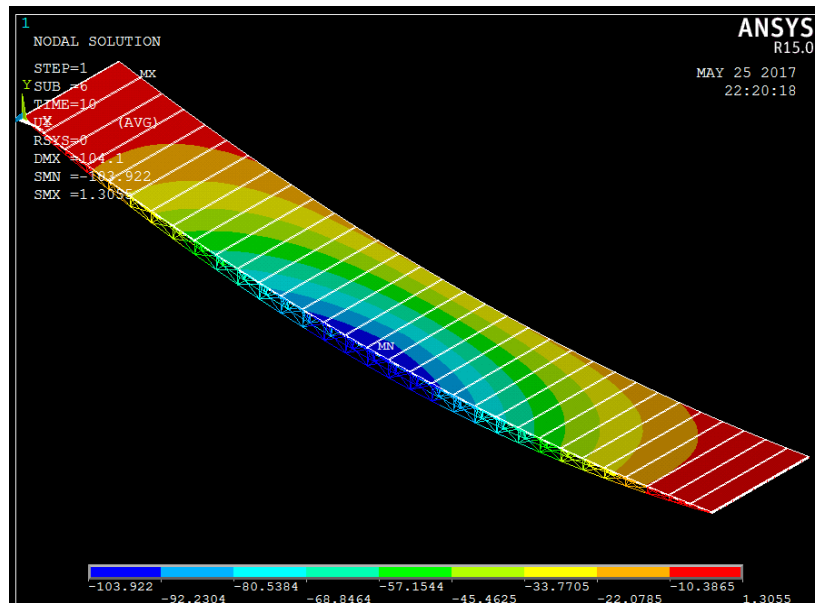


Figure 7. Nodal displacements at S.L.S. on the bridge for the final condition including diagonal cables under traffic loads.

4 DYNAMIC ANALYSIS AND PERFORMANCE

The existence of high pylons leads to additional problems on the foundation, as well as the superstructure of the bridge. In particular, both aerodynamic and seismic loadings may cause dangerous vertical and rotational oscillations. The proposed MBN control system minimizes all the foregoing phenomena as well as the cost of construction. The modal analysis based on the previous described data of the bridge gave the more important mode shapes (see Figures 8 and 9), whereas the response spectrum of the reference seismic action and its solutions under seismic design situation led to satisfactory results. In the case of turbulent wind flow and specifically for an upward loading being a percentage of the main wind load, no significant motion of the structure arises, due to the fact that this loading does not exceed the much bigger self-weight of the bridge deck.

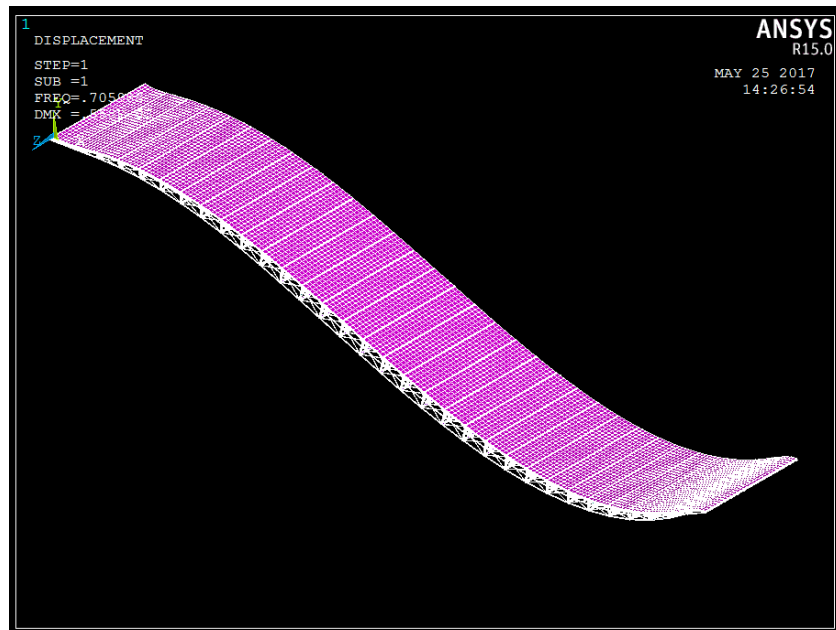
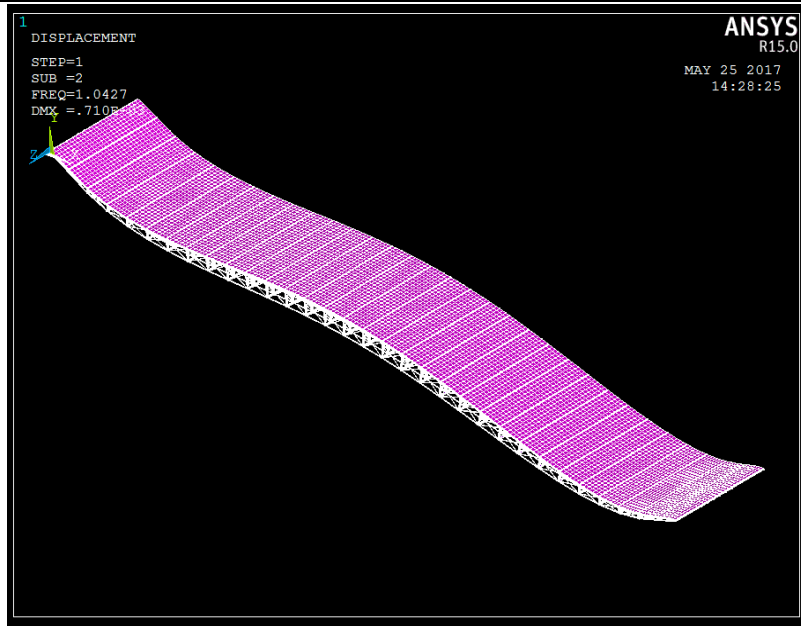
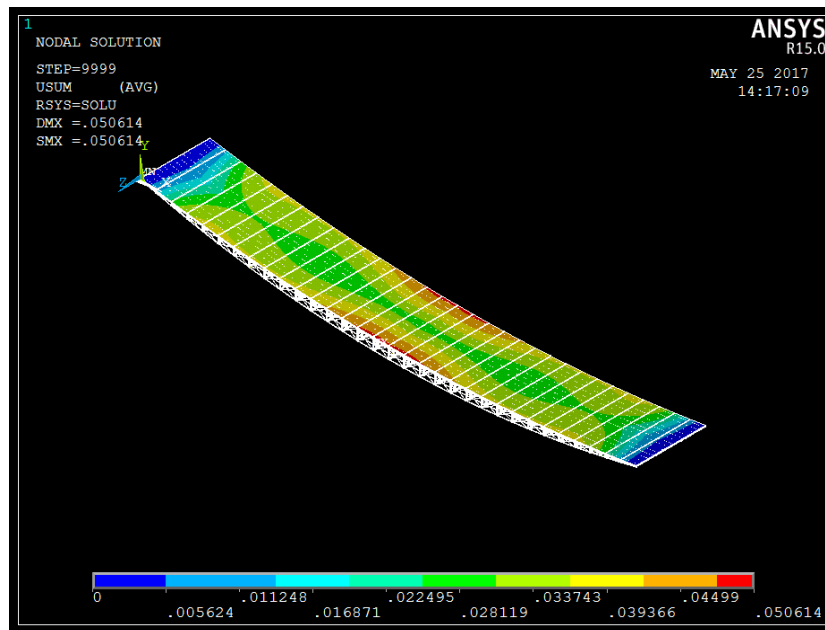


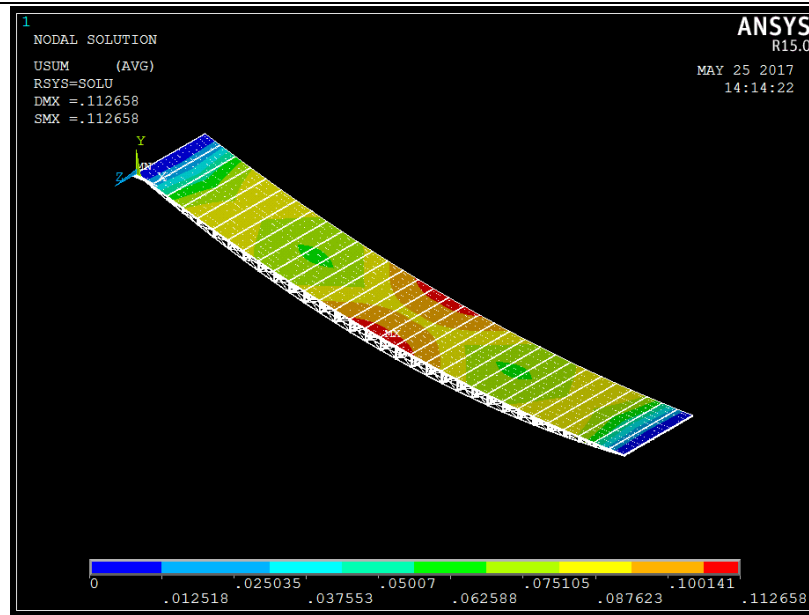
Figure 8. Modal analysis of the bridge for the 1st mode shape

Figure 9. Modal analysis of the bridge for the 2nd mode shape

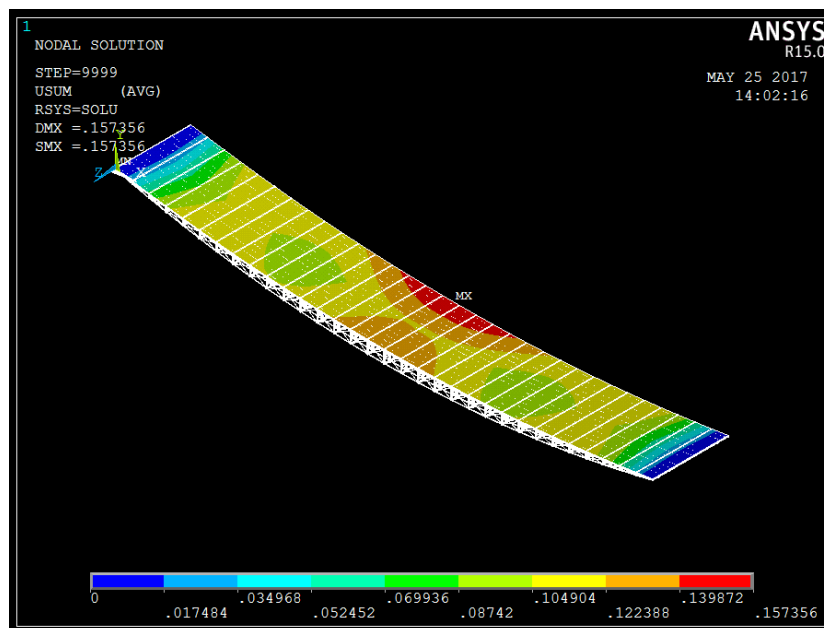
The structural response against earthquake damage has been evaluated satisfactorily using dynamic analysis by the elastic spectrum of the reference earthquake along the x, y and z directions. The behavior factor for this analysis estimated as $q=1$ taking into account elastic response for the bridge system according to Eurocode 8. In this analysis, the seismic performance of the system was excellent taking into account the elastic response spectrum $S_e(T)$ for different design cases about soil types (A to D) and seismic zones (Z1 and Z2) according Eurocode 8 Part 1 (see Figures 10, 11 and 12).

Figure 10. Bridge displacements for the combination of responses $1.0 \cdot E_x + 0.3 \cdot E_y + 0.3 \cdot E_z$

In this analysis E_x is the horizontal seismic response parallel to the longitudinal direction of the bridge, E_y is the horizontal seismic response transverse to the longitudinal direction of the bridge and E_z is the vertical seismic response of the bridge. Although in all cases the structural system of the bridge is influenced only by the prestressing force and the shape form of the cables, so the action on them becomes unilateral for any loading case, which is minor to the weight of the structure.

Figure 11. Bridge displacements for the seismic direction $0.3 \cdot E_x + 0.3 \cdot E_y + 1.0 \cdot E_z$

On the other hand, the two respective ends of the bridge are been connected directly to the ground on small height abutments and therefore both the deck of the bridge and the abutments in any loading case follows the motion of the earth without significant oscillation and damage.

Figure 12. Bridge displacements for the seismic design situation $G + 0.3 \cdot Q + 0.3 \cdot E_x + 0.3 \cdot E_y + 1.0 \cdot E_z$

5 CONCLUSIONS

The displacements control systems that use external prestressed cables, directly neutralize the permanent loads without creating significant bending moments for the structure. Applying an optimal passive control procedure, the value for the necessary prestressing force of the cables depend only on the neutralization of the permanent loads and does not depend on the length of the span of the structure. As passive control system for the bridge displacements a novel design is proposed which uses (β) cables and additional diagonal cables for same cases. This design leads to very satisfactory results for both the displacements and the stresses. This structural system is a very useful one for the design of large span structures in difficult design cases with high environmental and cost problems and especially in countries with high seismic and wind risk. The deck of

the structure is balanced on the curved cables, which act at a seismic action for some directions as safety mechanism for the bridge.

The results at all the loading combinations and especially for the dynamic actions show that the proposed model MBN is suitable for a sustainable structural design. Moreover forms a structure with a high bearing capacity against wind and seismic action, low cost and secure. In any case this cable supported system gives new ideas for the optimal analysis and design of large span structures in the future.

REFERENCES

- [1] Baniotopoulos C.C., Nikolaidis Th., Michalopoulos A. and Stavroulakis G.E. (2013), "Optimization of the structural response of large span structures by the MNB optimal control system" *Proceedings of 10th HSTAM International Congress on Mechanics*, 25-27 May 2013 Chania, Greece, 25-27.
- [2] Janjic D., Pircher M., and Pircher H. (2003). "Optimization of Cable Tensioning in Cable Stayed Bridges", *Journal of Bridge Engineering*, 8(3), pp.131-137.
- [3] Michalopoulos A., Nikolaidis Th., Baniotopoulos C.C. and Stavroulakis G.E. (2005), "Passive Control of Bridges: The Double Cable Net method", *Engineering Structures* Elsevier **27**, (2005), 1835-1842.
- [4] Nikolaidis Th, Michalopoulos A, Stavroulakis G, Baniotopoulos C C (2007), "Bridges with Composite Deck Supported by Prestressed Cables. The MNB Optimal Control System" *Pollack Periodica*, Vol. 2(2), 103-117.
- [5] Nikolaidis, Th., Skarmoutsos G. & Baniotopoulos, C.C., (2017), "Design Optimisation of Long Span Structures by Applying the MBN System using Curved Pretensioned Cables", *Proceedings of the 9th National Conference of Metal Structures*, Larisa, 5-7.10.2017 (in Greek).
- [6] Papanas S., Nikolaidis Th., Baniotopoulos C.C. (2016) "Analysis of Large Span Structures by Applying the MBPN Optimal Control Method", *Proceedings of 11th HSTAM International Congress on Mechanics*, Athens, 27 – 30 May, 2016.
- [7] Panagiotopoulos P D (1975), "A Variational Inequality Approach to the Inelastic Stress Unilateral Analysis of Cable Structures", *Computers & Structures*, 6, pp.133-139.
- [8] Stavroulakis G.E. (1995): "Optimal Prestress of Cracked Unilateral Structures: Finite Element Analysis of an Optimal Control Problem for Variational Inequalities", *Computer Methods in Applied Mechanics and Engineering*, **123**, pp.231-246.
- [9] Wang P.H., Tang T.Y., and Zheng, H.N. (2004). "Analysis of Cable-stayed Bridges During Construction by Cantilever Methods", *Computers & Structures* 82(4), pp.329-346.

PRELIMINARY ANALYSIS METHOD FOR FRP LAMINATE IMPACT DAMAGE SIZE PREDICTION

Adam W Deskiewicz¹, Ioannis K Giannopoulos^{1*}, Efstathios E Theotokoglou²

¹Centre of Excellence for Aeronautics, School of Aerospace, Transport and Manufacturing, Cranfield University,
Cranfield, MK43 0AL, UK

email: deskiewicz.a@gmail.com ; webpage: <https://www.linkedin.com/in/adeskiewicz/>
email: i.giannopoulos@cranfield.ac.uk; webpage: <https://www.cranfield.ac.uk/people/dr-ioannis-giannopoulos-50915>

²Department of Mechanics, Laboratory of Testing and Materials, School of Applied Mathematical and Physical
Sciences, National Technical University of Athens, GR-157 73, Greece

email: stathis@central.ntua.gr; webpage: <http://www.semfe.ntua.gr/el/faculty-members/theotokoglou>

Keywords: Explicit Finite Element Method, composite materials, low velocity impact, BVID

Abstract. *Low velocity impact damage on carbon reinforced polymer laminate composites has been identified as a key threat to airframe structural integrity since it reduces the strength under compressive loading. Airworthiness certification specifications dictate that the airframe structural components up to the full scale subassemblies have to adhere to the strength and fatigue airworthiness requirements imposed whilst being damaged. The study presented herein combines a set of numerical tools for generating an approach to numerically quantify the damage size after low velocity impact on FRP laminates.*

1 INTRODUCTION

Aircraft structures are exposed to damage threats from foreign object impacts in a wide range of conditions. A lot of experimental and numerical analysis research and some analytical works have been devoted to investigating the impact damage on Fiber Reinforced Polymer (FRP) laminates due to the severe consequences it entails on the airframe structural integrity.

Impact damage is categorized in terms of the energy and the subsequent damage size obtained from the event, although impact velocity is also an important factor [1]. The study herein focused on impacts with energies up to 50J, as it is the case when Barely Visible Damage (BVID) is most likely to form. This category encompasses low-velocity impacts such as dropped tools (4-10m/s) as well as intermediate velocity impacts with impactors of relatively small mass, like runway debris (100-150m/s). Metallic airframe structures are subjected to such impacts as well but they tend to absorb the impact kinetic energy by plastic deformation, unlike the mainly elastic behaving until failure CFRP structures, which respond to failure in a subtle manner, hiding the damage extends within the laminated structure from visual inspection on many occasions.

The classic preliminary stage airframe component design procedure mainly addresses and fulfills a number of quasi-static and dynamic loading scenarios in terms of strength and deformation criteria. Not so much attention is paid at this stage to the structural performance degrading environment the structure is to be immersed into. Certain acceptable strength and deformation levels are sought and on some occasions even material fatigue considerations are taken into account during early design. This approach has spawned through the usage of mostly metallic materials for airframes. The performance of structures made of CFRP materials is directly affected by the environment imposing its performance degradation effects by reducing the allowable load carrying levels.

Airworthiness certification specifications require the damaged CFRP structures to attain the acceptable performance levels [2] and this condition has to be proven by test. The airworthiness structural verification testing pyramid [3] commences with tests at the specimen level and proceeds to subcomponent testing until the full scale structure clearance tests. Testing at the specimen level for material characterization is easy and relatively cheap. A great deal of research on impact on composites has been performed based on square, circular or rectangular plates with standardized dimensions aiming at understanding the damage formation and the residual strength decrease especially when under a follow on compression loading. As pointed out by Abrate [4], the results of tests done on samples cannot directly represent the response of the full scale structure. Relevant work has been presented by the U.S. Federal Aviation Administration (FAA) [5] mainly describing the phenomena by parametric formulae curve fitting procedures as resulted from elementary specimen type testing. It

can be stated for the impact damage on CFRP structures, there is a lack of information available on transforming simple plate specimen results into meaningful full scale structural design guidelines.

Numerical simulations with progressive damage modelling capturing the degrading material response onto a complete structural detail can provide with adequate information and level of fidelity. On the other hand they can be quite costly in terms of the resources needed. They are generally employed at a later design phase than the preliminary design stage, mainly for complementary design verification rather than design exploration. An alternative resource of information can come from previously tested similar structural components if access to such data is an option but even if so, these cannot account for a new material or for radically new design details.

The approach suggested within this work, provides with a method to quantify the damage size influencing the structural residual strength from low velocity impacts on FRP structural details, in an effort to optimize a component prior to actually manufacturing and testing. A scaled down numerical analysis methodology is proposed, verified by plate specimen tests, that can be further on used to generating more complicated design details which are practically more difficult to manufacture and test. Results from experimental research on plate specimen along with numerical model results of various design details were used to validate the proposed method presented in this work.

2 EXPERIMENTAL DATA

Experimental data used for validation were obtained from [6], where the damage resistance and CAI strength of IM7/977-3 toughened carbon-epoxy laminates were examined. The data have been used to calibrate and validate the generated numerical models and were employed in the benchmarking against the developed analytical procedure. Samples comprising of 17 lamina layers of 100mm x 150mm dimension were impacted by a 5.81kg impactor according to ASTM D7136 [7], with energies ranging from 8J to 20J. The specimen layup sequence was $[\pm 45, 0, 90, 0, \pm 45, 0, 90, 0, \pm 45, 0, 90, \pm 45]$ s. The lamina properties of the composite used in the experiments are shown in Table 1. Impacted laminates were inspected by nondestructive and destructive inspection techniques and the size of the resulting damage imprints was documented. Some of the analyzed samples (impacted and pristine) underwent quasi-static compression after impact test for determining the CAI strength according to ASTM D7137 [8].

Laminate property	Symbol	Value	Unit
Longitudinal tensile modulus	E_{11}	162	GPa
Transverse tensile modulus	E_{22}	8.19	GPa
In-plane shear modulus	G_{12}	4.96	GPa
In-plane Poisson's ratio	ν_{12}	0.12	--
Mode I critical strain energy release rate	G_{IC}	170	J/m ²
Mode II critical strain energy release rate	G_{IIC}	580	J/m ²
Longitudinal tensile strength	X_T	2110	MPa
Transverse tensile strength	Y_T	64	MPa
Longitudinal compressive strength	X_C	1680	MPa
Transverse compressive strength	Y_C	100	MPa
Shear strength	S	121	MPa
Nominal ply thickness	t_{ply}	0.115	mm
Nominal laminate density		1506	kg/m ³

Table 1 Laminate material properties [6]

3 NUMERICAL MODELLING OF IMPACT

For the numerical simulation of the impact and CAI on FRP laminates, commercial software code LS-DYNA© was used [9, 10]. The aim of the numerical simulations was to generate data on the impact and CAI response of simple plates as well more complex geometries, like slightly curved plates and/or stiffened panel

bays. The numerical results from plate specimen tests have been validated against the results from the experimental study [6] described in the previous section.

3.1 Material modelling

There are many material modelling options available for modeling FRP materials with failure and degradation. In this study, MAT_054/055 was used.

3.2 Laminate modelling

Amongst the various modeling techniques for a composite laminate, the use of solid or shell elements can be chosen depending on the desired simulation fidelity. Factors influencing the final choice are the scale of modelled phenomena, the structure of interest, the desired accuracy and the available computational resources.

Solid elements were used in many previous studies [11, 12] to model composite targets impacted at various velocities where a single element across the thickness was used for each layer. This approach proved to give a very good correlation with experimental results. Moreover, unlike shell elements, that are assumed to be in a plane stress state, solid elements do not neglect the through-the-thickness normal and shear stress tensor components. The main challenges associated with three-dimensional composite models are their very high computational cost as well as laborious FE mesh generation for thin and complex aerospace structures [13]. Composites can be also modelled with the use of shell elements provided that the thickness of the laminate is significantly lower than the remaining dimensions of the structure [14]. Separate plies are then represented by multiple integration points across the shell layer thickness. However, this way of composite modelling does not enable to predict delamination failure since one element accounts for the complete layup across the thickness. Another approach has been described in reference [13] that made it possible to capture the interface failure using 2D elements. The plies forming the laminate are grouped into sub-laminates separated by a cohesive layer or with an appropriate contact definition. This approach has been used in this study as shown in figure 3.

An alternative combining the two aforementioned methods is a thick shell modelling technique. Thick shells have been developed in order to achieve the computational efficiency of 2D shell elements while maintaining the 3D nature of solid elements. A study revealed that this method may bring challenges in terms of solution instability during delamination propagation and the occurrence of severe hour-glassing [14].

A significant amount of comparative analysis and discussion on the subject has been presented in the last decade [13,14,15]. It has been shown that all models are capable of providing a valuable insight into the response of a composite material subjected to low-velocity impact, however, with different levels of accuracy. A very good correlation with the experimental data was obtained with the use of solid and thin shell elements [14]. The latter method was also indicated as giving the most realistic prediction of internal energy and contact force [15]. All researchers agreed, however, that the accuracy of numerical solutions for all methods is strongly dependent on the simulation parameters, such as the element size, contact parameters as well as the number of interfaces.

3.3 Inter-laminar modelling

Since delamination is believed to play the key role in the impact damage size creation and the post-impact behavior of composites under compressive loading, there is a need for a reliable finite element procedure of modelling this phenomenon.

In this study, inter-laminar modelling used the **CONTACT_[...]_TIEBREAK* keyword. When the bonding layer is sufficiently thin to neglect the influence of its mass a contact definition between the bonded layers that has the traction separation laws built in can be used. When the failure criterion is reached the bonding is released and the contact behaves like a normal surface to surface contact.

According to Heimbs et al. [11], tiebreak contacts give less accurate results than the equivalent cohesive layer, due to the change in bending stiffness of the model with increasing number of interfaces and the inability to represent the delamination of each ply constituting the laminate. It is, therefore, suggested that this method should be used for first approximation. However, the results of comparative studies carried out [14, 15] lead to the opposite conclusions. Good accuracy and agreement with experimental results were recorded, proving that 2D shell elements combined with tiebreak contacts are capable of delivering satisfactory levels of accuracy.

3.4 The drop weight impact numerical model set-up

The laminate model has been created with four separate fully integrated shell elements layers comprising eight plies each, shown in figure 1. Shell layers were bonded together with the use of *surface to surface contact* definition, which is the preferred choice in case of limited input data availability and results in reasonable accuracy [12, 13]. The boundary conditions were according to ASTM D7136 [7] experimental set up procedure as shown in figure 2. Initial velocity applied to the ball impacting the plate varied for different simulation cases to

meet the predefined impact energy condition. The mass of the impactor was 5.81kg, which is in agreement with the experimental study performed in [6].

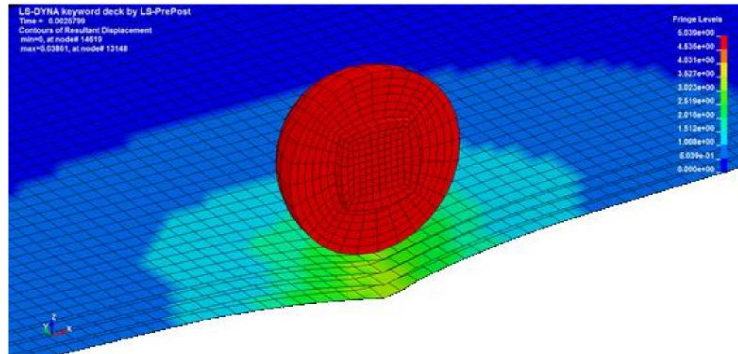


Figure 1 Drop weight impact simulation on a composite laminate modelled by 4 shell element layers representing 17 laminate plies

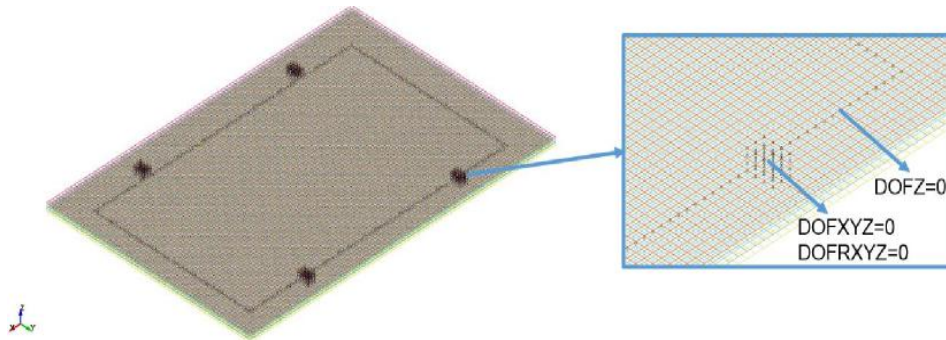


Figure 2 Boundary conditions assumed for the drop weight simulation

3.5 The CAI numerical model set-up

The laminate models used for CAI test simulation was identical to the ones used for the drop weight scenarios but with an artificial damage implemented in the structure. Following the methodology used in experimental studies [12], the impact damage has been represented by releasing contact between two top shell layers in the damage zone as shown in figure 3. Boundary conditions imposed on the model used for simulating the quasi-static compression test as per ASTM D7137 [8] are shown in Figure 4.

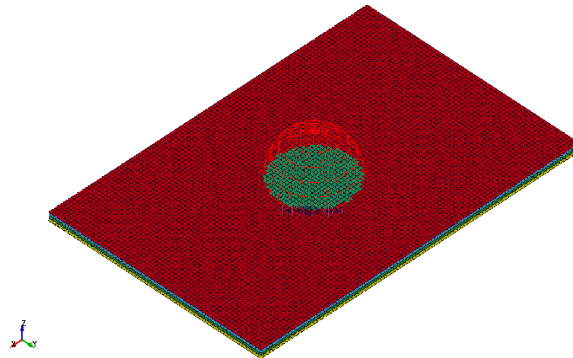


Figure 3 CAI simulations on a composite laminate having removed the inter-laminar bond between the outermost sub-laminate and the rest of the plate

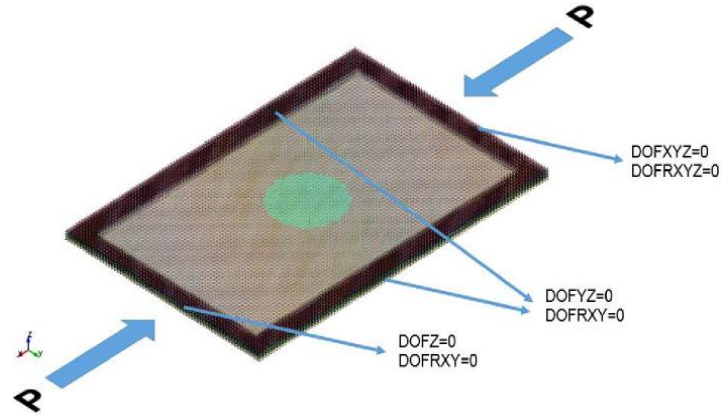


Figure 4 Boundary conditions in CAI test simulation

A simulation of the post-impact residual compressive strength test has been also performed. A sample impacted with the energy of 11.5J and subsequently tested in compression by has been chosen for comparison. The simulation resulted in the CAI strength of 210.6 MPa, which is 12.3% more than the experimental value of 171 MPa. Moreover, the damage pattern observed in the numerical simulation shows an excellent agreement with ASTM D7137 standard [8], as shown in figure 5.



Figure 5 CAI failure mode of the numerical model

3.6 Validation of the numerical models

The numerical model results of impact and CAI strength have been correlated with the results from experimental impact simulations for five representative energy levels [6]. Quantities compared with the experimental data for the impact modelling were the delamination size in terms of width as shown in figure 6 as well as energy absorbed during impact, measured as a difference between the initial and final impactor kinetic energy.

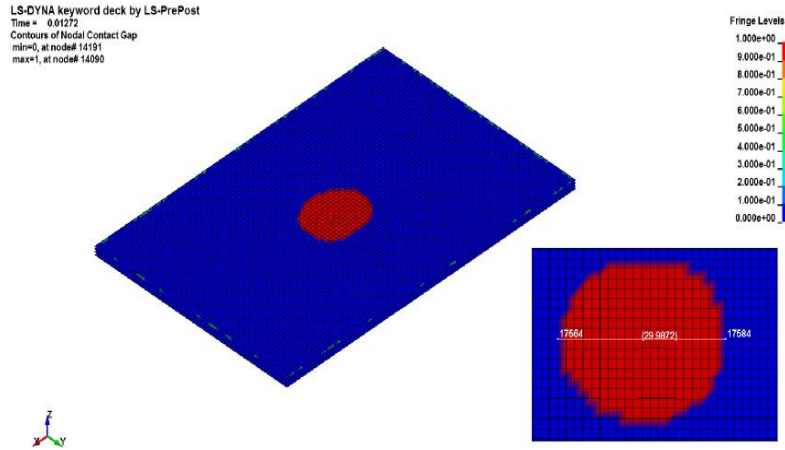


Figure 6 Delamination envelope size on the impacted laminate

In figures 8 and 9 the comparison between the impact and absorbed energy from the experimental survey and the numerical simulations is shown. An interesting observation can be made, suggesting that the numerical model absorbed more energy from the actual experiment under the same impact energy but for the same absorbed energy levels, the delamination sizes are comparable. From the numerical study, a good correlation between the absorbed energy and the peak impact force was found, observation which meant that there was a good correlation between the impact force and the delamination size.

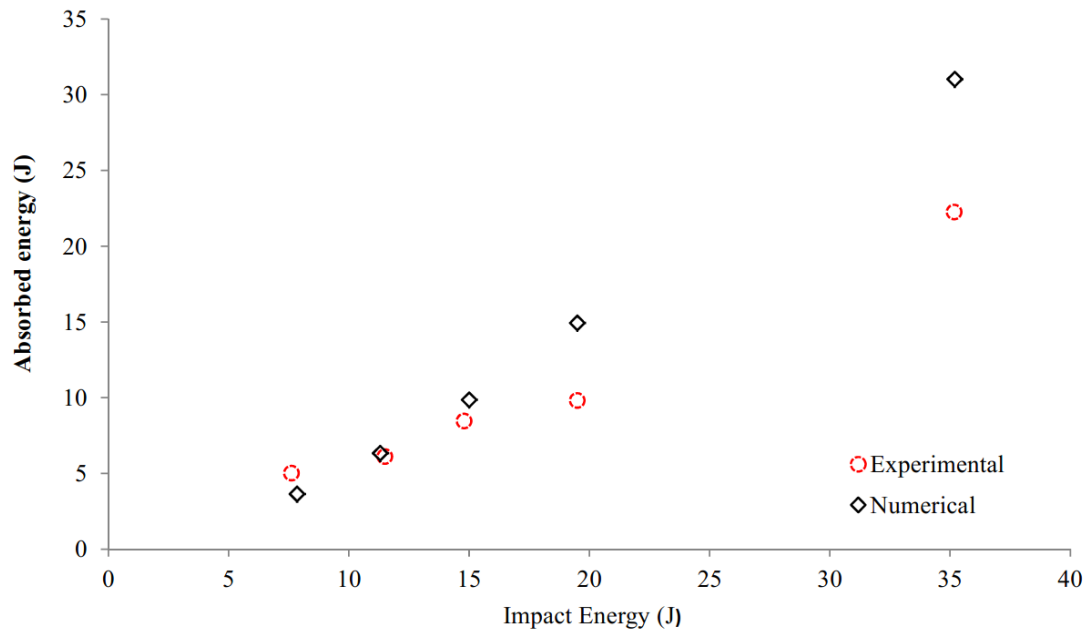


Figure 8: Impact energy versus absorbed energy from the impact

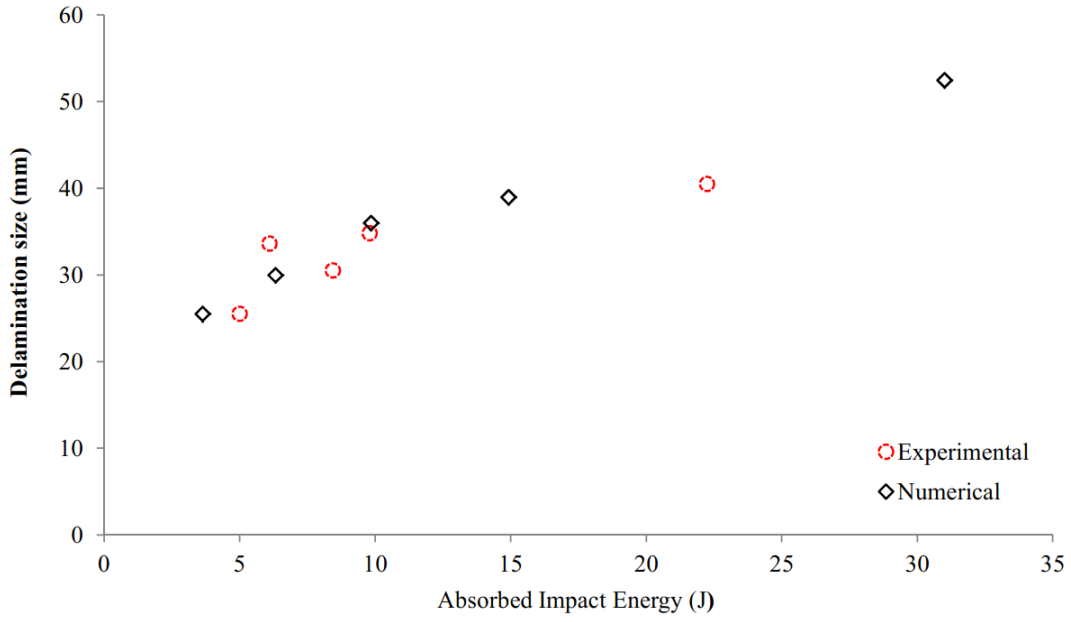


Figure 9: Absorbed energy from the impact versus maximum delamination width

4 ANALYTICAL PREDICTION OF DAMAGE SIZE

A significant amount of work on impact dynamics modeling exists in the literature, the majority of which require numerical tools to be solved [4, 7]. Olsson has provided with closed form analytic solutions based on theoretical models of impact on composite laminates [16].

A research review on composites impact resistance [9, 17, 18] suggested the existence of a direct correlation between the laminate fracture toughness G_{IIc} and the damage extent after impact. Studies carried out [19, 20] led to the conclusion that there is a threshold impact force, below which delamination does not occur. A simple model has been proposed based on quasi-isotropic layups [7].

$$F_{cr} = \pi \sqrt{\frac{8 E_{flex} t^3 G_{IIc}}{9 (1 - \nu^2)}} \quad (1)$$

Where

- F_{cr} Threshold impact force below which delamination does not occur (N),
- E_{flex} Equivalent flexural modulus of the laminate (MPa),
- t Laminate thickness (mm),
- G_{IIc} Fracture toughness under mode II (J/m^2),
- ν Laminate in-plane Poisson's ratio

On the other hand, delamination size can be directly related to the impact and plate parameters according to equation (2) [1], where the nominator in this expression is the Peak Impact Force:

$$D = \frac{V_o \sqrt{M k_b}}{\pi t \bar{\tau}} \quad (2)$$

Where

- D Delamination width of an assumed circular delamination (mm),
- V_o Impactor velocity (mm/s²),
- M impactor mass (kg),
- k_b Equivalent plate stiffness at the impact location if assumed a linear spring (N/mm)
- t Laminate thickness (mm),
- τ Average shear strength (MPa)

Overall, equations (1) and (2) combine in the following expression (3):

$$D = \begin{cases} 0 & \text{if } F_{peak} < \pi \sqrt{\frac{8 E_{flex} t^3 G_{Ilc}}{9 (1 - \nu^2)}} \\ \frac{V_o \sqrt{M k_b}}{\pi t \bar{\tau}} & \text{if } F_{peak} > \pi \sqrt{\frac{8 E_{flex} t^3 G_{Ilc}}{9 (1 - \nu^2)}} \end{cases} \quad (3)$$

On figure 10, the correlation between the experimental, numerical and analytical results is shown.

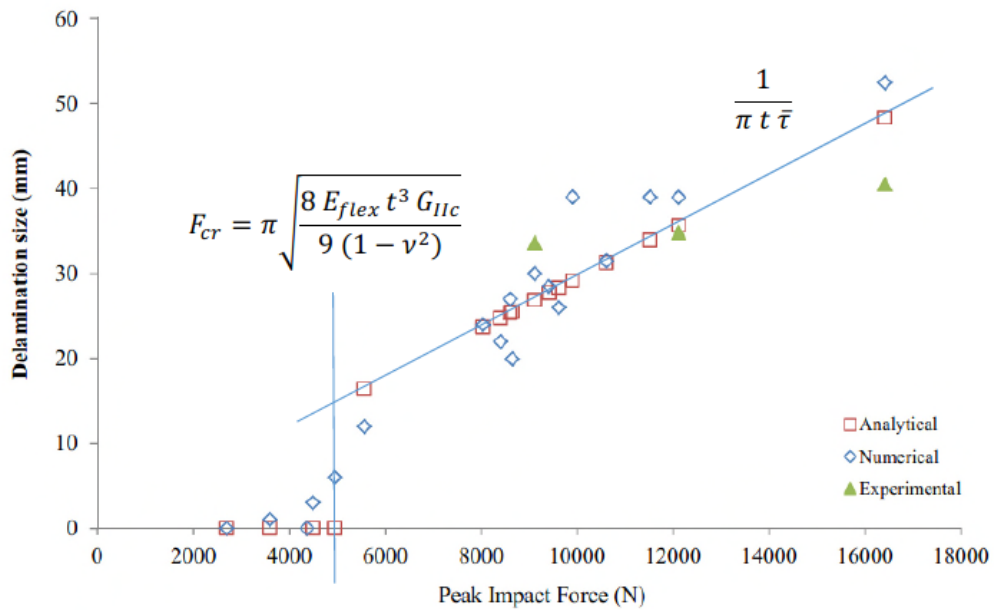


Figure 10: Experimental and numerical results relative to the proposed peak force delamination relation

Equation (3) in essence, relates the impactor velocity and mass with the material properties of the target structure, amongst them being the equivalent plate stiffness of the target at the impact location. The proposition in this work is that in the case the target structure is different than the plate specimens per ASTM D7136, this can be reflected onto the equivalent plate stiffness and hence result on a different damage size according to equation (3). The numerical results on figure 10 are drawn from simple plates, curved plates and bays within stiffened panels.

5 CONCLUSIONS

A semi-analytical methodology was proposed for quantifying the damage size from low velocity impact on FRP laminate airframe design details other than simple plate specimen. The method is suggested for preliminary design analysis prior to component testing. The method has been partially validated via flat plate impact specimen testing and partially through LSDYNA numerical analysis of some more complicated design details. The numerical modeling strategy proposed was in good agreement with the experimental survey.

A proper evaluation of the effects from impact damage can result only after testing the full scale component which would exclude major re-design improvements at that stage. The method can provide with very useful insights to designs benchmarking, design envelope exploration and design optimization.

REFERENCES

- [1] Davies, G., Irving, P. (2015) 'Impact, Post-Impact Strength and Post-Impact Fatigue Behaviour of Polymer Composites', in Irving, P., Soutis, C. (ed.) *Polymer Composites in the Aerospace Industry*, Cambridge: Woodhead Publishing, pp. 216-109
- [2] EASA (2017). Certification specifications and acceptable means of compliance for large aero planes CS10
- [3] EASA (2017). Acceptable means of compliance – composite aircraft structure AMC 20-14.
- [4] Abrate, S. (1994) Impact on Laminated Composites: Recent Advances, *Applied Mechanics Reviews*, 47(11), pp. 517-544
- [5] Federal Aviation Administration (FAA) (1998) Enhanceability Prediction Methodology for Impact Damaged Composite Structures, DOT/FAA/AR-97/79, - National Technical Information Service (NTIS), Virginia
- [6] Krutop, B. N. E. (2007) Effect of Impact Damage and Subsequent Fatigue Damage Development in Carbon Fibre Polymer Composites for Aircraft, MSc Thesis, Cranfield University.
- [7] ASTM International (2015) ASTM D7136/D7136M-15 Standard Test Method for Measuring the Damage Resistance of a Fiber-Reinforced Polymer Matrix Composite to a Drop-Weight Impact Event, West Conshohocken, PA.
- [8] ASTM International (2012) ASTM D7137/D7137M-12 Standard Test Method for Compressive Residual Strength Properties of Damaged Polymer Matrix Composite Plates, West Conshohocken, PA.
- [9] Livemore Software Technology Corporation (LSTC) (2016) Keyword User's Manual, Version 971, Livemore
- [10] Livemore Software Technology Corporation (LSTC) (2017) LS-Dyna Theory Manual, Version 971, Livemore
- [11] Heimbs, S., Heller, S., Middendorf, P. (2008), Simulation of Low Velocity Impact on Composite Plates with Compressive Preload, 7th LS-Dyna Anwenderforum, Bamberg, 15-17 October 2008, DYNAmore GmbH.
- [12] LS-Dyna Aerospace Working Group (AWG) (2016) Modeling Guidelines Document, United States. [13] Esteban, D., Moncayo, J., Wagner, H., Drechsler, K. (2007) Benchmarks for Composite Delamination Using LS-Dyna 971: Low Velocity Impact, 6th LS-Dyna Anwenderforum, Frankenthal, 11-12 October 2007, DYNAmore GmbH.
- [14] Muflahi, S. A., Mohammed, G., Hallett, S. R. (2014) Investigation of Delamination Modelling Capabilities for Thin Composite Structures in LS-DYNA, 13th International LS-Dyna Users Conference, Detroit, June 2014
- [15] Dogan, F., Homayoun, H., Donchev, T., Bhonge, P. S. (2012) Delamination of Impacted Composite Structures by Cohesive Zone Interface Elements and Tiebreak Contact, *Central European Journal of Engineering*, 2(4), pp.612-611
- [16] Olsson, R. (1992) Impact Response of Composite Laminates – A Guide to Closed Form Solutions, FFA TN 1992-18, The Aeronautical Research Institute of Sweden, Sweden
- [17] Irving PE, Cartie DDR. Effect of resin and fibre properties on impact and compression after impact performance of CFRP, *Compos Part A* 2002;18:483-93
- [18] Jih, C. J., Sun, C. T. (1993) Prediction of Delamination in Composite Laminates Subjected to Low Velocity Impact, *Journal of Composite Materials*, 12(7), pp. 684701
- [19] Davies, G. A. O., Robinson, P. (1992) Impactor Mass and Specimen Geometry Effects in Low Velocity Impact of Laminated Composites, *International Journal of Impact Engineering*, 12(2), pp. 189-207
- [20] Schoeppner, G. A., Abrate, S. (2000) Delamination Threshold Loads for Low Velocity Impact on Composite Laminates, *Composites Part A: Applied Science and Manufacturing*, 16(9), pp. 903-915

DYNAMIC ANALYSIS OF A CERAMIC/METAL FUNCTIONALLY GRADED THERMOELASTIC LAYER UNDER RAMP-TYPE THERMAL LOADING

Antonios M. Nikolarakis¹ and Efstathios E. Theotokoglou²

^{1,2}Department of Mechanics – Laboratory of Testing and Materials
School of Applied Mathematical and Physical Sciences
National Technical University of Athens
Zografou Campus 15773, Athens, Greece

¹e-mail: ant_nikola@yahoo.com

² e-mail: stathis@central.ntua.gr

Keywords: Functionally Graded Material, Temperature-Dependency, Coupled Thermoelasticity, Transient Analysis.

Abstract. *In the case of large temperature variations, the thermomechanical properties of a material should be considered as temperature-dependent rather than constants. In the present article the effect of the temperature-dependency of the properties on the thermoelastic response of a ceramic/metal functionally graded layer of finite thickness is investigated. The functionally graded layer is subjected to uniform ramp-type thermal loading at its upper surface and the resulting transient fields of stress and temperature inside the layer are presented, within the theory of linear coupled thermoelasticity. In the above analysis, zirconia is used as the ceramic material and a titanium alloy is used as the metal material. The properties of these materials are assumed to be a cubic function of the temperature. Moreover, the variation of the properties inside the functionally graded layer is considered to be linear. For the numerical analysis the Galerkin finite element method is used, whereas the Newmark method is employed for the time integration of the problem.*

1 INTRODUCTION

Functionally graded materials (FGMs) are advanced materials with continuously varying properties [1]. In the simplest FGMs their properties vary gradually between the properties of two materials. One of the most important applications of FGMs is the thermal protection of metals in high-temperature environments [2]. To be more specific, FGMs made of ceramic and metal constituents are suitable for the protection of metal layers under thermal loads.

In such applications the behavior of a ceramic/metal FGM under severe thermal loading is of major importance. Furthermore, when large temperature variations occur the effect of the temperature on the thermomechanical properties of a material cannot be ignored. Consequently, in the case of large temperature variations the thermomechanical properties of a material should be taken as temperature-dependent [3-4].

In this article we study the dynamic thermoelastic behavior of a ceramic/metal functionally graded layer, where the volume fraction of the metal constituent varies linearly from 0 to 1. In this configuration zirconia (ZrO₂) is used as the ceramic material and a titanium alloy (Ti-6Al-4V) is used as the metal material. The ZrO₂/Ti-6Al-4V functionally graded layer is subjected to uniform ramp-type thermal loading, where the temperature at the upper surface of the layer gradually rises up to a final temperature. The governing equations are derived from the theory of linear coupled thermoelasticity. Moreover, the properties of the materials are considered as temperature-dependent, thus leading to a system of nonlinear differential equations.

The numerical analysis of the aforementioned one-dimensional problem is based on the Galerkin finite element method, while the Newmark method is used for the time integration. The effect of the temperature-dependency of the thermomechanical properties of the materials is discussed. The authors of this contribution have also studied the effect of the temperature-dependency of the properties in the case of a functionally graded ceramic/metal half-space under thermal shock conditions [5].

2 GOVERNING EQUATIONS AND NUMERICAL ANALYSIS

2.1 Effective Properties

Consider an initially undeformed, stress-free and at uniform temperature of $T_0 = 300K$ ceramic-metal functionally graded layer of total thickness L , as shown in Figure 1. The ceramic material is zirconia (ZrO₂) and the metal material is a titanium alloy (Ti-6Al-4V).

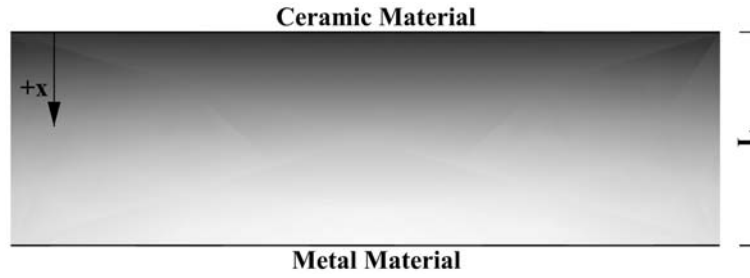


Figure 1. Ceramic/metal functionally graded layer

In this paper, the thermomechanical properties of the materials are considered as temperature-dependent. At high temperatures, the material properties can be expressed as cubic functions of absolute temperature T [6]. Table 1 shows the properties of ZrO_2 and Ti-6Al-4V as functions of absolute temperature T [7,8].

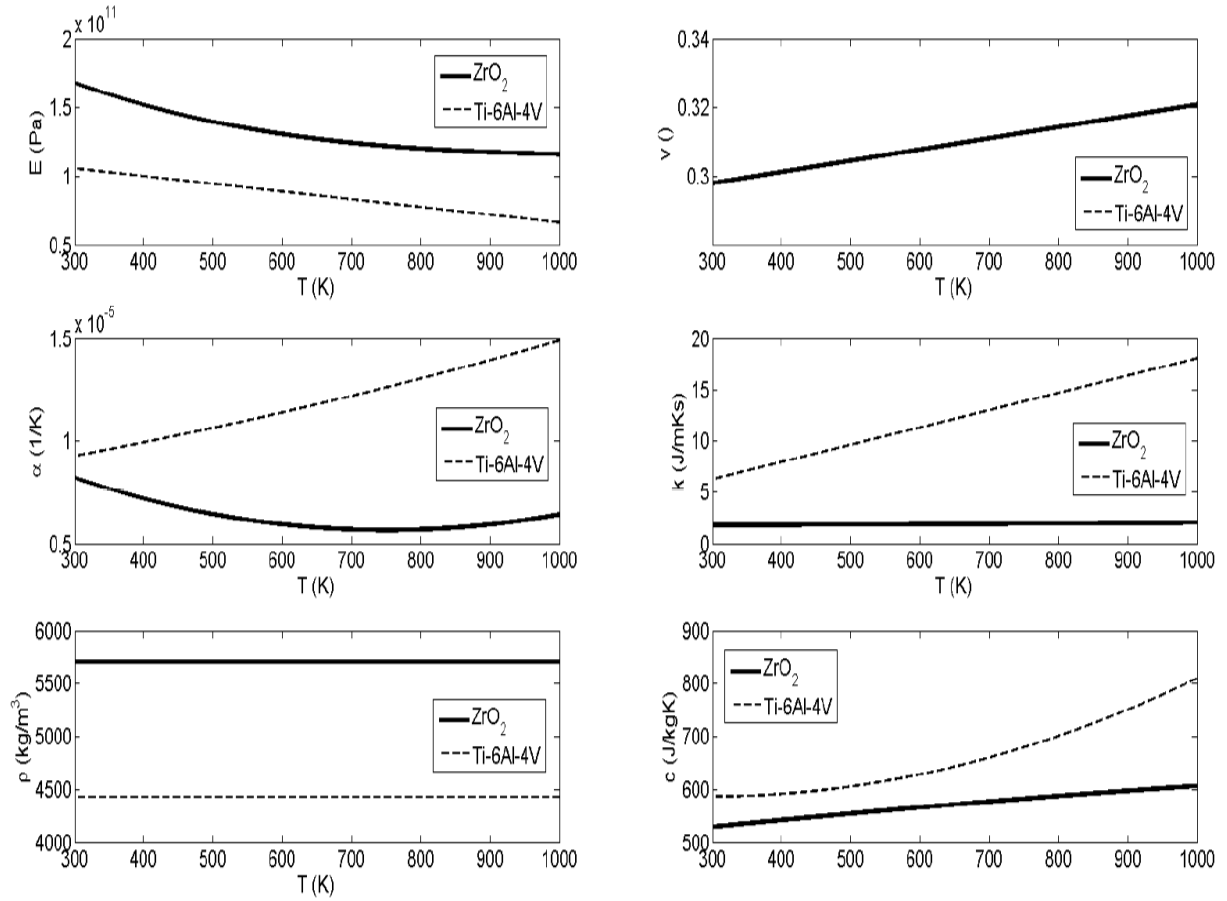
Zirconia (ZrO_2)	
Elasticity Modulus E [Pa]	$244.26596 \cdot 10^9 \cdot (1 - 1.3707 \cdot 10^{-3} T + 1.21393 \cdot 10^{-6} T^2 - 3.681378 \cdot 10^{-10} T^3)$
Poisson Ratio ν []	$0.2882 \cdot (1 + 1.13345 \cdot 10^{-4} T)$
Thermal Expansion Coef. α [1/K]	$12.7657 \cdot 10^{-6} \cdot (1 - 0.00149 \cdot T + 1.0 \cdot 10^{-6} T^2 - 0.6775 \cdot 10^{-11} T^3)$
Thermal Conductivity k [J/mKs]	$1.7 \cdot (1 + 0.0001276 \cdot T + 6.648 \cdot 10^{-8} T^2)$
Density ρ [kg/m ³]	5700
Specific Heat Capacity c [J/kgK]	$487.34279 \cdot (1 + 3.04908 \cdot 10^{-4} T - 6.037232 \cdot 10^{-8} T^2)$

 Table 1: Material properties of ZrO_2 as functions of absolute temperature T [7,8]

Titanium Alloy (Ti-6Al-4V)	
Elasticity Modulus E [Pa]	$122.55676 \cdot 10^9 \cdot (1 - 4.58635 \cdot 10^{-4} T)$
Poisson Ratio ν []	$0.28838235 \cdot (1 + 1.12136 \cdot 10^{-4} T)$
Thermal Expansion Coef. α [1/K]	$7.57876 \cdot 10^{-6} \cdot (1 + 0.00065 \cdot T + 0.31467 \cdot 10^{-6} T^2)$
Thermal Conductivity k [J/mKs]	$1.20947 \cdot (1 + 0.0139375 \cdot T)$
Density ρ [kg/m ³]	4429
Specific Heat Capacity c [J/kgK]	$625.29692 \cdot (1 - 4.2238757 \cdot 10^{-4} T + 7.1786536 \cdot 10^{-7} T^2)$

 Table 2: Material properties of Ti-6Al-4V as functions of absolute temperature T [7,8]

Graphically, the properties of ZrO_2 and Ti-6Al-4V as functions of absolute temperature T are shown in Figure 2. It is concluded that the Poisson ratio ν and the density ρ of the materials can be considered as temperature-independent. On the other hand, as temperature rises the difference between the thermal expansion coefficient α , the thermal conductivity k and the specific heat capacity c of the two materials increases. Finally, the elasticity modulus E is reduced at high temperatures since the materials soften, which could lead to reduced stresses.


 Figure 2. Material properties of ZrO_2 and Ti-6Al-4V as functions of absolute temperature T

The macroscopic effective properties inside the functionally graded layer depend on the volume fraction of the constituents. The volume fraction of the metal constituent V_m inside the FGM layer is supposed to be linear:

$$V_m(x) = \frac{x}{L}, \quad 0 \leq x \leq L \quad (1)$$

where x is the depth inside the layer ($x = 0$ at the upper surface and $x = L$ at the lower surface).

In this paper, the effective material properties in the FGM layer is based on the simple rule of mixture. Therefore, if $P(T)$ is a temperature-dependent material property of the FGM, which has the value $P_c(T)$ in the ceramic material and $P_m(T)$ in the metal material, then the value of $P(T)$ as a function of x is given by:

$$P(x, T) = P_c(T)V_c(x) + P_m(T)V_m(x) = P_c(T)\left(1 - \frac{x}{L}\right) + P_m(T)\frac{x}{L}, \quad 0 \leq x \leq L \quad (2)$$

where V_c is the volume fraction of the ceramic constituent inside the FGM layer.

2.2 The initial-boundary value problem

The ceramic-metal functionally graded layer is initially undeformed, stress-free and has a uniform temperature $T_0 = 300\text{K}$. At time $t = 0$, the temperature of the upper surface starts to increase linearly with regard to time, until the temperature of the upper surface is $T_u = 900\text{K}$. Mechanically, the upper surface is free to deform. On the other hand, the lower surface of the layer has a steady temperature $T_l = 300\text{K}$ and it is mechanically fixed.

Based on the coupled theory of linear thermoelasticity for isotropic materials, the above dynamic one-dimensional problem is described by the following equations [9]:

$$\left\{ \begin{array}{l} \frac{\partial}{\partial x} \left[\lambda(T) + 2\mu(T) \right] \frac{\partial u}{\partial x} - \beta(T) \theta = \rho(T) \frac{\partial^2 u}{\partial t^2} \\ - \left[\rho(T) c(T) \frac{\partial \theta}{\partial t} + T_0 \beta(T) \frac{\partial^2 \theta}{\partial x \partial t} \right] = - \frac{\partial}{\partial x} \left[k(T) \frac{\partial \theta}{\partial x} \right] \end{array} \right\}, \quad \begin{array}{l} 0 \leq x \leq L \\ 0 < t < \infty \end{array} \quad (3)$$

where $u = u(x, t)$ and $\theta = \theta(x, T) = T - T_0$ are the unknown displacement and temperature fields, respectively, $\lambda = \lambda(x, T)$ and $\mu = \mu(x, T)$ are the Lamé constants, $\beta = \beta(x, T)$ is the thermal constant, $\rho = \rho(x, T)$ is the density, $k = k(x, T)$ is the thermal conductivity and $c = c(x, T)$ is the specific heat capacity.

For reasons of normalization we now introduce the following dimensionless variables:

$$\begin{aligned} \tilde{x} &= \frac{1}{l} x, \quad \tilde{t} = \frac{v}{l} t, \quad \tilde{\theta} = \frac{T - T_0}{T_0}, \quad \tilde{u} = \frac{\lambda_m + 2\mu_m}{l \beta_m T_0} u, \quad \tilde{\sigma}_{xx} = \frac{1}{\beta_m T_0} \sigma_{xx} \\ \tilde{c}_E &= \sqrt{\frac{\lambda + 2\mu}{\rho v^2}}, \quad \tilde{c}_K = \sqrt{\frac{k}{\rho c_v l v}}, \quad \tilde{\xi} = \frac{\beta^2 T_0}{\rho c_v (\lambda + 2\mu)} \end{aligned} \quad (4)$$

where l and v are a characteristic length and a characteristic speed respectively, σ_{xx} is the stress field, the index m indicates that the material parameter refers to the metal material at temperature T_0 , \tilde{c}_E is the normalized speed of the elastic dilatational wave and $\tilde{\xi}$ is a dimensionless coupling parameter. The normalized formulation of the aforementioned initial-boundary value problem is given by:

$$\left\{ \begin{array}{l} \frac{\partial}{\partial \tilde{x}} \left[\frac{\lambda(T) + 2\mu(T)}{\lambda_m + 2\mu_m} \frac{\partial \tilde{u}}{\partial \tilde{x}} - \frac{\beta(T)}{\beta_m} \tilde{\theta} \right] = \frac{1}{\tilde{c}_{Em}^2} \frac{\rho(T)}{\rho_m} \tilde{u} \\ - \frac{1}{\tilde{c}_{Km}^2} \left[\frac{\rho(T) c(T)}{\rho_m c_m} \dot{\tilde{\theta}} + \tilde{\xi} \frac{\beta(T)}{\beta_m} \frac{\partial \dot{\tilde{u}}}{\partial \tilde{x}} \right] = - \frac{1}{\tilde{k}_m} \frac{\partial}{\partial \tilde{x}} \left[k(T) \frac{\partial \tilde{\theta}}{\partial \tilde{x}} \right] \end{array} \right\}, \quad \begin{array}{l} 0 \leq \tilde{x} \leq L/l \\ 0 < \tilde{t} < \infty \end{array} \quad (5)$$

with initial-boundary conditions

$$\left\{ \begin{array}{l} \tilde{u}(\tilde{x}, 0) = 0, \quad \dot{\tilde{u}}(\tilde{x}, 0) = 0, \quad \tilde{\theta}(\tilde{x}, 0) = 0, \quad \dot{\tilde{\theta}}(\tilde{x}, 0) = 0 \\ \tilde{\theta}(0, \tilde{t}) = \begin{cases} 2 \frac{\tilde{t}}{\tau}, & 0 \leq \tilde{t} \leq \tau \\ 2, & \tilde{t} > \tau \end{cases}, \quad \tilde{\sigma}_{xx}(0, \tilde{t}) = 0, \quad \tilde{\theta}(L, \tilde{t}) = 0, \quad \tilde{u}(L, \tilde{t}) = 0 \end{array} \right\}$$

where $\tau \geq 0$ is a normalized temporal parameter and a dot above a variable symbolizes partial differentiation with regard to normalized time.

It is mentioned that the stress σ_{xx} and the heat flux q_x are given by:

$$\begin{aligned} \sigma_{xx} &= \beta_m T_0 \left[\frac{\lambda(T) + 2\mu(T)}{\lambda_m + 2\mu_m} \frac{\partial \tilde{u}}{\partial \tilde{x}} - \frac{\beta(T)}{\beta_m} \tilde{\theta} \right] \\ q_x &= \frac{k_m T_0}{l} \left[- \frac{k(T)}{k_m} \frac{\partial \tilde{\theta}}{\partial \tilde{x}} \right] \end{aligned} \quad (6)$$

2.3 Finite element formulation

The initial-boundary value problem (5) is solved numerically via the Galerkin finite element method [10]. Linear Lagrange shape functions are used for both the displacement and the temperature variables. The finite element formulation for the governing equations in the initial-boundary value problem (5) has the following form:

$$\left\{ \begin{aligned} & \frac{h_i}{\xi_{Em}^2 \rho_m} \int_0^1 \rho(T) \mathbf{N}^T \mathbf{N} d\varpi \cdot \ddot{\mathbf{u}} + \frac{1}{h_i (\lambda_m + 2\mu_m)} \int_0^1 [\lambda(T) + 2\mu(T)] (\mathbf{N}')^T \mathbf{N}' d\varpi \cdot \mathbf{u} + \\ & - \frac{1}{\beta_m} \int_0^1 \beta(T) (\mathbf{N}')^T \mathbf{N}' d\varpi \cdot \boldsymbol{\theta} = \mathbf{0} \\ & \frac{\xi_m}{\xi_{Km}^2 \beta_m} \int_0^1 \beta(T) \mathbf{N}^T \mathbf{N}' d\varpi \cdot \dot{\mathbf{u}} + \frac{h_i}{\xi_{Km}^2 \rho_m c_{vm}} \int_0^1 \rho(T) c(T) \mathbf{N}^T \mathbf{N} d\varpi \cdot \dot{\boldsymbol{\theta}} + \frac{1}{h_i k_m} \int_0^1 k(T) (\mathbf{N}')^T \mathbf{N}' d\varpi \cdot \boldsymbol{\theta} = \mathbf{0} \end{aligned} \right\} \quad (7)$$

where $0 \leq \varpi \leq 1$ is the natural coordinate, h_i is the length of element i , $\mathbf{N} = [1 - \varpi \quad \varpi]$ is the vector of the linear Lagrange shape functions, and $\mathbf{u}, \boldsymbol{\theta}$ are the unknown vectors of displacement and temperature respectively. Furthermore, the normalized stress and heat flux are given by:

$$\begin{aligned} \sigma_{xx} &= \frac{1}{\beta_m T_0} \sigma_{xx} = \frac{\lambda(T) + 2\mu(T)}{\lambda_m + 2\mu_m} \frac{\partial u}{\partial x} - \frac{\beta(T)}{\beta_m} \theta \\ q_x &= \frac{l}{k_m T_0} q_x = - \frac{k(T)}{k_m} \frac{\partial \theta}{\partial x} \end{aligned} \quad (8)$$

Assembling the element matrices equations (7) we obtain the global system of nonlinear equations in the matrix form:

$$\begin{bmatrix} \mathbf{M}_{11}(T) & \mathbf{0} \\ \mathbf{0} & \mathbf{0} \end{bmatrix} \ddot{\begin{bmatrix} \mathbf{u} \\ \boldsymbol{\theta} \end{bmatrix}} + \begin{bmatrix} \mathbf{0} & \mathbf{0} \\ \mathbf{C}_{21}(T) & \mathbf{C}_{22}(T) \end{bmatrix} \dot{\begin{bmatrix} \mathbf{u} \\ \boldsymbol{\theta} \end{bmatrix}} + \begin{bmatrix} \mathbf{K}_{11}(T) & \mathbf{K}_{12}(T) \\ \mathbf{0} & \mathbf{K}_{22}(T) \end{bmatrix} \begin{bmatrix} \mathbf{u} \\ \boldsymbol{\theta} \end{bmatrix} = \mathbf{0} \quad (9)$$

The time integration of the matrix equations (9) is done by utilizing the Newmark method [10]. Since equations (9) are nonlinear, the matrices need to be recalculated at each time step. A finite element Matlab code is developed for the numerical analysis of the above problem of linear coupled thermoelasticity with temperature-dependent properties.

3 RESULTS AND DISCUSSION

In this section the numerical results of the initial-boundary value problem (5) are presented. The characteristic length and the characteristic speed are taken as $l = \frac{k_m}{c_{vm} \sqrt{\rho_m (\lambda_m + 2\mu_m)}}$ and $v = c_{Em} = \sqrt{\frac{\lambda_m + 2\mu_m}{\rho_m}}$

respectively. The total thickness of the functionally graded layer is $L = l$, which means that the normalized total thickness is $\bar{L} = L/l = 1$. The resulting transient fields of temperature and stress are studied and the effect of the temperature-dependency of the material properties is discussed. For the numerical analysis, 1000 finite elements and 4000 time steps are used.

Concerning the boundary conditions of the problem, Figure 3 shows the time evolution of the normalized temperature change θ at the upper surface of the layer ($x = 0$) for $\tau = 0$, $\tau = 1/4$, $\tau = 1/2$ and $\tau = 1$. The case $\tau = 0$ corresponds to thermal shock conditions, where the temperature change occurs instantly.

In the case of temperature-dependent properties, the material properties depend on the temperature field and consequently the distribution of the material properties in the FGM layer is different at different times. Figure 4 shows the distribution of the material properties at time $t = 4.00$ for the case of temperature-dependent and temperature-independent properties. This distribution is linear when temperature-independent properties are considered, due to the linear variation of the constituent's volume fraction inside the FGM layer. The graphs shown in Figure 4 are in agreement with the graphs shown in Figure 2: when the temperature-dependency is considered, the modulus of elasticity E and the thermal expansion coefficient α are reduced, while the thermal conductivity k and the specific heat capacity c increase. The results of Figure 4 refer to the value $\tau = 0$.

Subsequently, the transient fields of temperature change θ and stress σ_{xx} are investigated. These fields at time $t = 1.50$ are shown in Figures 5 and 6, respectively, for the cases of temperature-dependent and temperature-independent properties. The values $\tau = 0$ and $\tau = 1$ are considered. From Figure 5 it is concluded that the temperature is slightly increased for temperature-dependent properties, mainly due to the increase of the

thermal conductivity. On the other hand, the value of the temporal parameter τ does not effect the temperature field. On the contrary, from Figure 6 it is deduced that the stresses increase significantly for low values of parameter τ . Moreover, if the temperature-dependency of the material properties is ignored then the stresses are overestimated, since the value of the elasticity modulus of the materials is higher at low temperatures. This result is more obvious when $\tau = 0$.

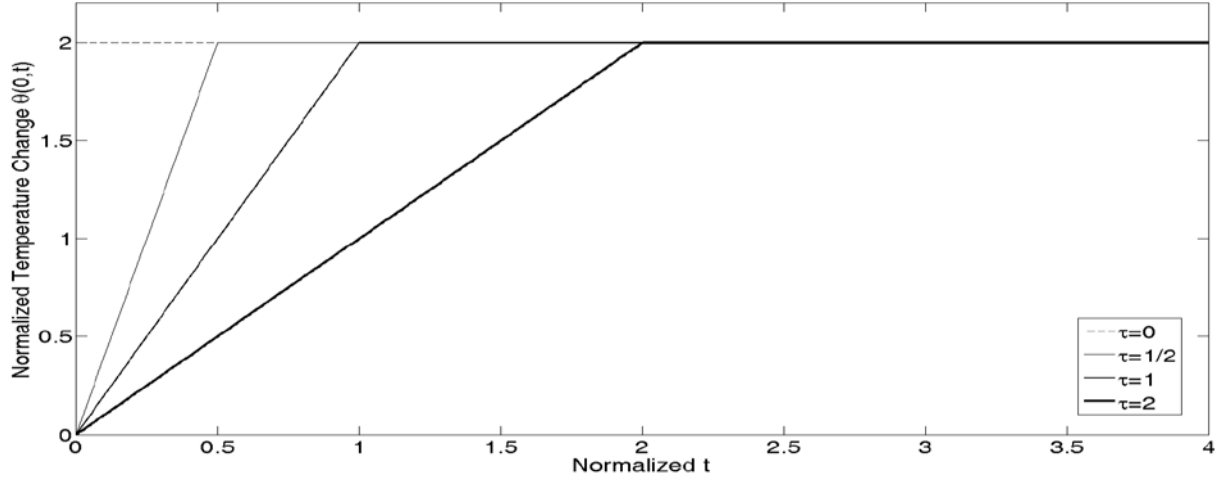


Figure 3. Time evolution of the normalized temperature change θ at $x=0$ for different values of parameter τ

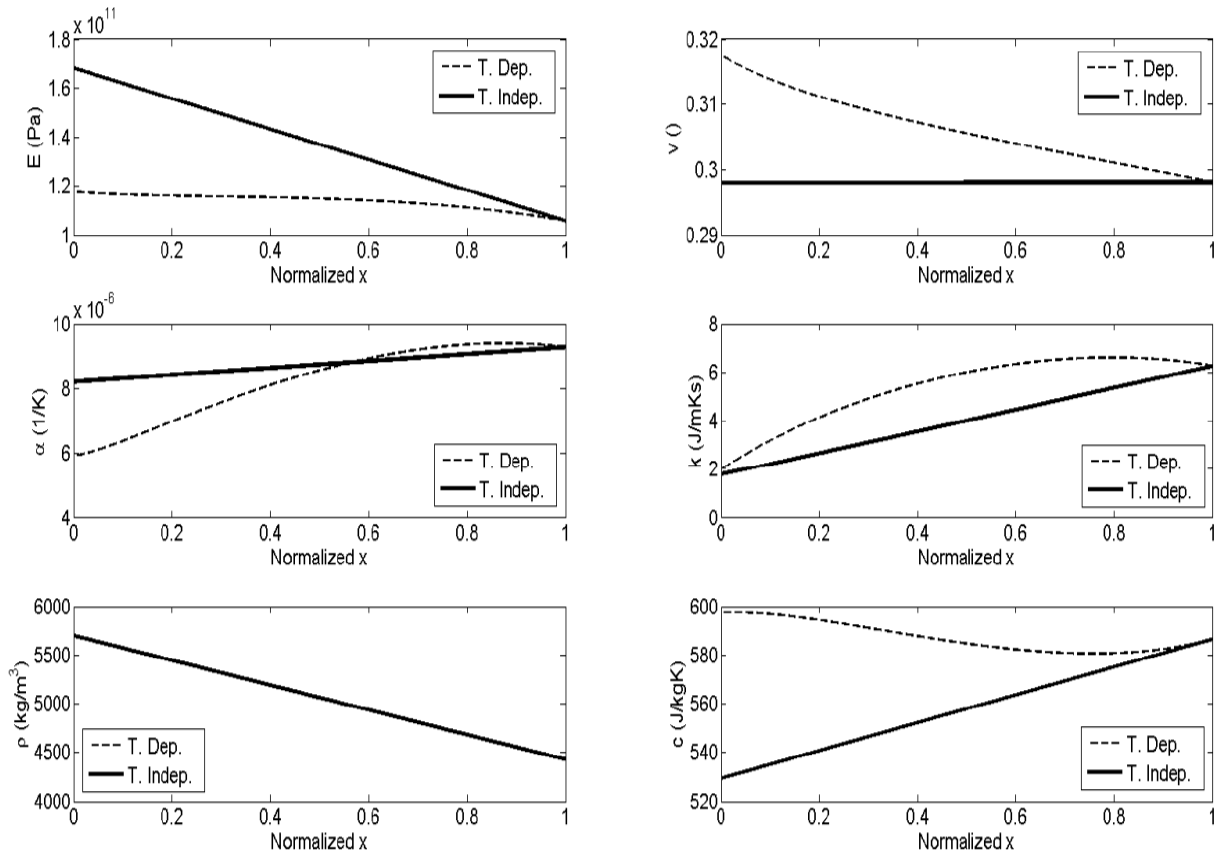


Figure 4. Variation of the material properties in the FGM layer at time $t = 4.00$, for the cases of temperature-dependent and temperature-independent properties ($\tau = 0$)

The above observations are further confirmed by Figures 7 and 8, which show the time evolution of temperature change and stress, respectively, at the middle of the FGM layer, when thermal shock conditions are considered ($\tau = 0$). At Table 3, the maximum values of the normalized displacement \bar{u} , the normalized temperature change $\bar{\theta}$ and the normalized stress $\bar{\sigma}_{xx}$ at position $\bar{x} = 0.50$ are presented for $\tau = 0$, $\tau = 1/4$, $\tau = 1/2$, $\tau = 1$, $\tau = 2$ and $\tau = 4$. The cases of temperature-dependent and temperature-independent material properties are considered. The results of Table 3 indicate that the displacements and the stresses are notably increased as $\tau \rightarrow 0$, while the temperature field is not effected by the parameter τ . On the other hand, the calculated displacements and stresses are overestimated when the temperature-dependency of the properties is not taken into account, while the temperature is slightly reduced. This fact shows that, regarding the displacements and the stresses, the assumption of temperature-independent properties leads to conservative results.

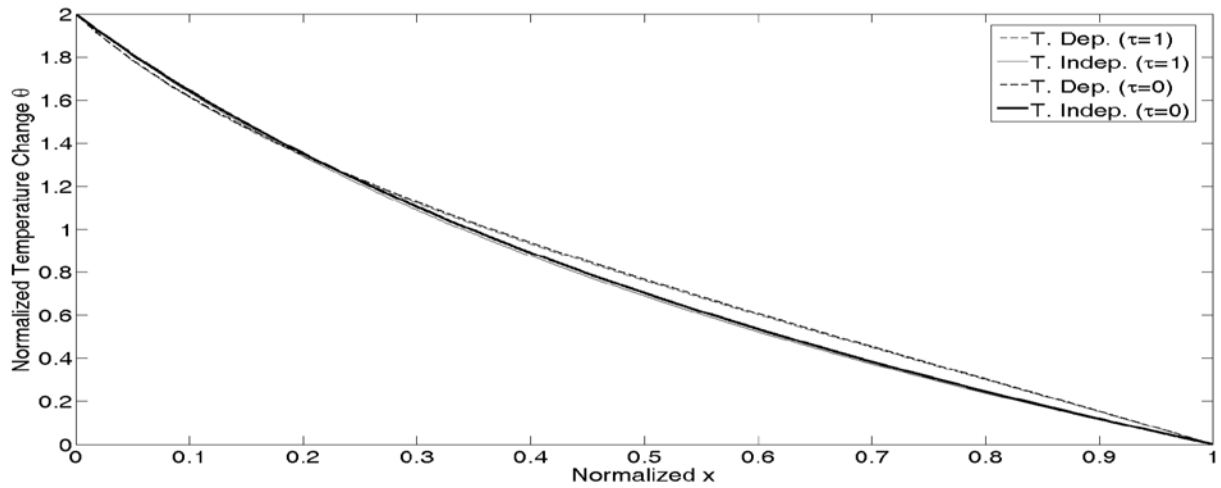


Figure 5. Variation of the normalized temperature change $\bar{\theta}$ in the FGM layer at time $\bar{t} = 1.50$, for the cases of temperature-dependent and temperature-independent properties ($\tau = 0$ or $\tau = 1$)

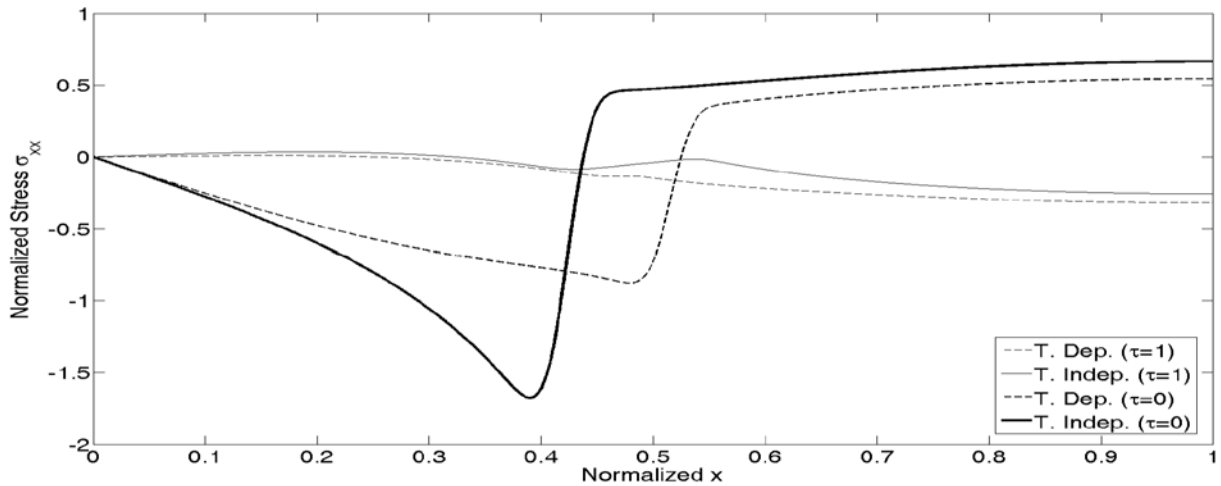


Figure 6. Variation of the normalized stress $\bar{\sigma}_{xx}$ in the FGM layer at time $\bar{t} = 1.50$, for the cases of temperature-dependent and temperature-independent properties ($\tau = 0$ or $\tau = 1$)

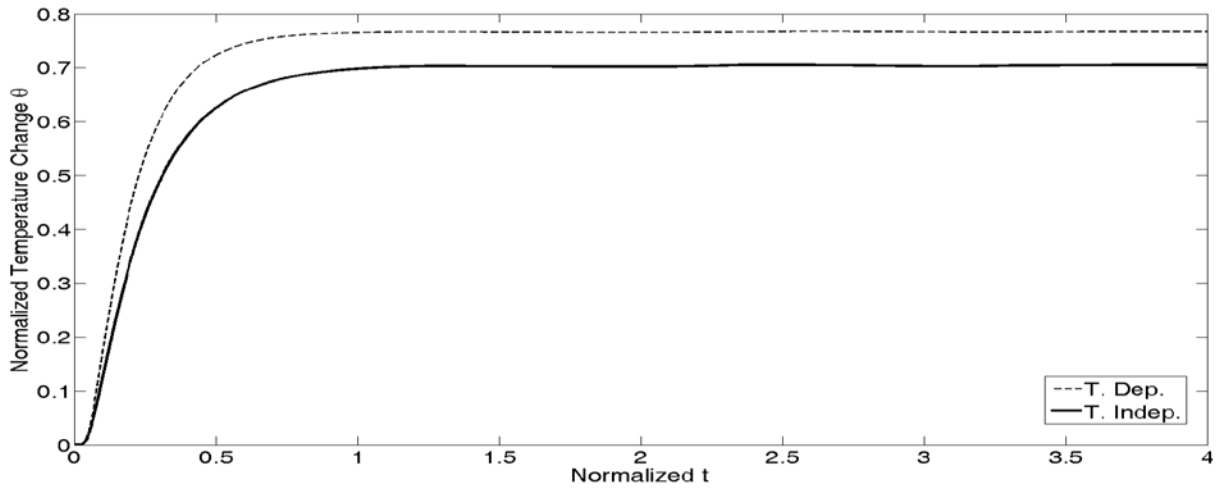


Figure 7. Temporal evolution of the normalized temperature change θ at position $\bar{x} = 0.50$ when $\tau = 0$, for the cases of temperature-dependent and temperature-independent properties

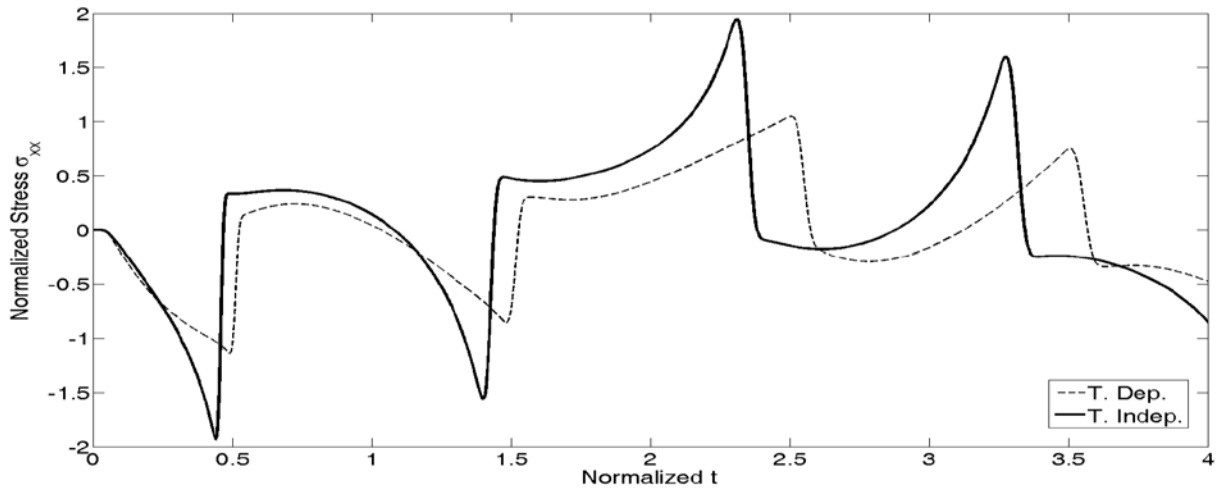


Figure 8. Temporal evolution of the normalized stress σ_{xx} at position $\bar{x} = 0.50$ when $\tau = 0$, for the cases of temperature-dependent and temperature-independent properties

τ		0	1/4	1/2	1	2	4
Temperature Dependent Properties	$\max \bar{u} $	0.48	0.46	0.43	0.39	0.36	0.17
	$\max \bar{\theta}$	0.77	0.77	0.77	0.77	0.77	0.73
	$\max \sigma_{xx}$	1.05	0.95	0.81	0.56	0.31	0.06
Temperature Independent Properties	$\max \bar{u} $	0.55	0.53	0.50	0.44	0.38	0.19
	$\max \bar{\theta}$	0.71	0.71	0.71	0.70	0.70	0.66
	$\max \sigma_{xx}$	1.95	1.40	1.06	0.73	0.47	0.14

Table 3: Maximum values of normalized displacement \bar{u} , normalized temperature change $\bar{\theta}$ and normalized stress σ_{xx} at position $\bar{x} = 0.50$, for the cases of temperature-dependent and temperature-independent properties and for different values of the temporal parameter τ

4 CONCLUSIONS

In this paper the resulting thermal and stress fields inside a ceramic/metal functionally graded layer subjected to ramp-type thermal loading at the upper surface are numerically studied employing the linear coupled thermoelasticity theory. In this study, the temperature-dependency of the material properties is taken into account. The variation of the volume fraction of the metal constituent in the FGM layer is assumed to be linear. A finite element code is developed for the numerical analysis of this nonlinear thermoelastic problem.

A numerical investigation with regard to the temporal parameter τ shows that the displacements and the stresses in the FGM layer increase significantly as the temperature change at the upper surface occurs faster. This is especially notable when $\tau = 0$, which corresponds to thermal shock conditions. On the other hand, the temperature field is not effected by the parameter τ .

Furthermore, when the temperature-dependency of the properties is ignored, the calculated displacements and stresses are overestimated. This points out that the assumption of materials with temperature-independent properties leads to conservative results.

REFERENCES

- [1] Suresh, S. and Mortensen, A. (1998), *Fundamentals of Functionally Graded Materials*, IOM Communications Limited, London, UK.
- [2] Birman, V. and Byrd, L. W. (2007), "Modelling and analysis of functionally graded materials and structures", *ASME Appl. Mech. Rev.*, Vol. 60, pp. 195–216.
- [3] Argho, H. and Eraslan, A. N. (2008), "On the use of temperature-dependent physical properties in thermomechanical calculations for solid and hollow cylinders", *Int. J. Therm. Sci.*, Vol. 47, pp. 136-146.
- [4] Han, J.-C. and Wang, B.-L. (2011), "Thermal shock resistance of ceramics with temperature-dependent material properties at elevated temperature", *Acta Mater.*, Vol. 59, pp. 1373-1382.
- [5] Nikoularakis, A. M. and Theotokoglou, E. E. (2015), "Transient stresses of a functionally graded profile with temperature-dependent materials under thermal shock", *Proceedings of the 8th GRACM International Congress on Computational Mechanics*, Volos, Greece, 12-15 July 2015.
- [6] Touloukian, Y. S. (1967), *Thermophysical properties of high temperature solid materials*, MacMillan, New York, USA.
- [7] Shariyat, M. (2009), "Dynamic thermal buckling of suddenly heated temperature-dependent FGM cylindrical shells, under combined axial compression and external pressure", *Int. J. Solids Struct.*, Vol. 45, pp. 2598-2612.
- [8] Shen, H.-S. and Wang, H. (2015), "Nonlinear bending of FGM cylindrical panels resting on elastic foundations in thermal environments", *Eur. J. Mech. A-Solids*, Vol. 49, pp. 49-59.
- [9] Hetnarski, R. B. and Eslami, M. R. (2009), *Thermal Stresses – Advanced Theory and Applications*, Springer Science+Business Media, Dordrecht, Netherlands.
- [10] Hughes, T. J. R. (1987), *The Finite Element Method, Linear Static and Dynamic Finite Element Analysis*, Prentice Hall, Inc., New Jersey, USA.

DESIGN AND STRUCTURAL ANALYSIS OF WIND TURBINE BLADES FOR STRUCTURAL HEALTH MONITORING CONSIDERATION

¹
Meletios Rentoumis¹, Panagiotis Koutsianitis¹, Ilias Athanailidis¹, Georgios Taridis¹, Georgios Tselikos¹,
Nikolaos Bilalis¹ and Georgios E. Stavroulakis¹

¹School of Production Engineering and Management
Technical University of Crete
Chania, GR-73100, Greece

E-mails: mrentoumis0@gmail.com, panoskout@gmail.com, ilathanailidis@gmail.com,
tairidis@gmail.com, gtselikos@hotmail.com, nbilalis@isc.tuc.gr, gestavr@dpem.tuc.gr;

Web pages: <http://www.comeco.tuc.gr>, <http://www.cadlab.tuc.gr>

Keywords: Wind Turbine Blade, Structural Health Monitoring, Composite Materials, Structural Analysis, CAD.

Abstract. *A large-scale composite wind turbine blade model is designed and analyzed under different loading and damage scenarios to assess structural integrity. The influence of several damage patterns in conjunction with structural failures identification by using dynamic measurements from the structure is studied. A large-scale wind turbine with blade span of approximately 25m is considered. In terms of design approach, the Blade Element Momentum (BEM) theory is promoted. There is a wide range of options in terms of materials and manufacturing techniques utilized in the wind turbine industry. The most common combinations include composite laminates with embedded threaded steel rods in the root section, connecting the blade to the hub through a bolted connection. Polyester, vinyl ester and epoxy resins are common, matched with reinforcing wood, glass, and carbon fibers. Composite epoxy glass, carbon fiber and memory foam are used here. A preliminary analysis for the structural health monitoring is done and several investigations are carried out to calculate the response of the structure under different failure scenarios.*

1 INTRODUCTION

Wind turbines convert the kinetic energy of the wind into mechanical power and then to electricity through a generator. These are large rotating machines whose components, such as blades and blade joints, are subjected to high wind forces and other environmental phenomena that may compromise the integrity of the structure. These forces can limit the productive lifetime of the blades causing them to fail, subjecting the wind turbine to major maintenances. Indisputably, blades are critical components of the wind turbines since they suffer from fatigue due to the dynamic loading posed on them. The composite microstructure of blades enhances this phenomenon.

Within the scope of the current project, a model of a composite large-scale wind turbine blade will be structurally analyzed under different scenarios that will assess the integrity of the build. The main focus of the project will be the study of the influence of several damage patterns, while the blade is in operation, in conjunction with structural failures identification by using dynamic measurements from the structure. In the baseline scenario, a large-scale wind turbine with blade span of approx. 25m, will be taken in consideration. The location of installation is the Mount Panachaiko, Peloponnese, Greece.

In terms of design approach, the Blade Element Momentum (BEM) theory will be fostered. The whole idea behind BEM assumes that the forces acting on the operating wind turbine blades are responsible for the change in axial momentum of the air passing through the swept area of the rotating wind turbine blades [1]. BEM analysis is the combination of results from blade element theory and momentum theory. Blade element theory refers to the analysis of forces at a section of the blade, as a function of blade geometry, in which the blade is split into sections along the length of the blade and each section is analyzed separately. With BEM model, it is also possible to calculate the steady loads and thus also the thrust and power for different settings of wind speed, rotational speed and pitch angle.

The design of the airfoil is the balanced output of two considerations that include: (i) the aerodynamic and (ii) the structural aspect of it. Aerodynamic considerations are the ones dictating the design of the outer shell of the blade while structural considerations are more vital for the design of the inner of the blade [2]. Structurally, the blade is typically hollow, with the outer geometry formed by two separate shells: one on the suction and one on the pressure side. In order to transfer shear loads, one or more structural webs of different geometries are fitted to support and join the two shells together (see Figure 1).

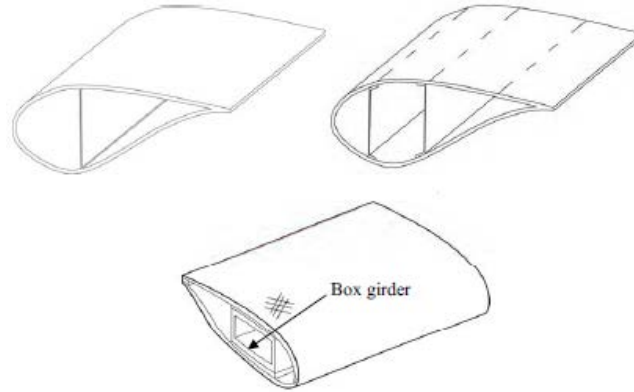


Figure 1 Sketches of various blade design approaches: (a) Single shear web, (b) Double shear web, (c) With load carrying box girder [2].

Nowadays, there is a wide range of materials and manufacturing techniques utilized in the wind turbine industry. The most utilized material combinations used are composite laminates with embedded threaded steel rods in the root section, connecting the blade to the hub in a bolted connection. Polyester, vinyl ester and epoxy resins are common, matched with reinforcing wood, glass, and carbon fibers. A wide range of manufacturing processes are also utilized in blade manufacturing, encompassing: wet lay-up, pre-preg, filament winding, pultrusion, and vacuum infusion (with and without secondary adhesive bonding). More details can be found in [3].

2 PROJECT DEFINITION

2.1 Assumptions Definition

Mount Panachaiko is the most northern mountain of the Peloponnese state area and is occupying the north-central area of Achaia State. To have a better insight of the weather conditions that take place at Mount Panachaiko Mountain we accessed the National's Observatory of Athens Database. The focus was on the annual accumulative results of measurements of the year 2015 since they were unshortened in comparison to 2016 data. Regarding the temperature data, the average max temperature was 11.7°C while the average min temperature was 5.8 °C. The mean temperature during 2015 was 8.5 °C. In the same manner as previously mentioned, the monthly values of wind speed are summarized. The average wind speed has been measured to be 13.5 km/hr (3.75 m/s) while the strongest wind speed of the year recorded was 96.6 km/hr (26.85 m/s). The recorded weather conditions will be taken as reference in the context of calculating the possible values of the operating loads that the wind turbine blade of our design must come through.

2.2 Nominal Loads Definition

The use of computer analysis software such as fluid dynamics (CFD) and finite element (FEA) is now commonplace within the wind turbine industry [4]. Dedicated commercially available software such as LOADS, YawDyn, MOSTAB, GH Bladed, SEACC and AERODYN are utilized to perform calculations based on blade geometry, tip speed and site conditions [5]. To simplify calculations, it has been suggested that a worst case loading condition has to be identified compared to which all other loads may be tolerated [6]. The worst case loading scenario is dependent on blade size and method of control. For small turbines without blade pitching, a 50-year storm condition would be considered as in the limiting case. For larger turbines ($D > 70$ m), loads resulting from the mass of the blade become critical and they should be considered. In practice, several load cases are considered with published methods detailing mathematical analysis for each of the IEC load cases [7]. Modern load analysis of a wind turbine blade would typically consist of a three-dimensional CAD model analyzed using the Finite Element Method [8]. Certification bodies support this method and conclude that there is a range of commercial software available with accurate results [9]. These standards also allow the blade stress condition to be conservatively modeled using classical stress analysis methods. Traditionally, the blade would be modeled as a simple cantilever beam with equivalent point or uniformly distributed loads used to calculate the flap wise and edgewise bending moment. The direct stresses for root sections and bolt inserts would also be calculated.

2.3 Assessment of Structural Health Monitoring (SHM) implementation

Structures, in general, confront damages due to several reasons, such as earthquakes, hurricanes, strong wind loads, extremely high temperatures and impact by birds. This means that a suitably defined system, which will be

able to monitor the structural performance of the whole structure through an automated process, is highly desirable if not necessary. In the particular case of the wind turbines, this need increases dramatically due to the fact that these structures are very often difficultly accessible (e.g. offshore structures). The Structural Health Monitoring (SHM) system is in fact a damage identification procedure, which helps to predict possible damages of the host structure and take available measures where necessary. In the case of wind turbines, a SHM system can prevent significant economic loss and therefore it is very popular. It consists of three main steps, and namely the signal monitoring, the processing, and the interpretation, and it is basically a vibration-based monitoring system. This lies to the fact that vibrations can be used for the detection of hidden or internal damages which are impossible to observe visually [8].

The concept behind vibration-based SHM is that the occurring failures of the structure usually affect the structural characteristics such as stiffness. This means that with dynamic analysis tools, such as modal analysis one can quantify the damage severity of the structure by its eigen-modes or eigen-values. In this project, a wind turbine blade, based on proposed composite materials, will be modeled based on bibliography. Furthermore, the structural reliability will be validated computationally using Finite Element Methods and be compared to the industry standards. To this extent, SHM techniques were utilized in order to detect some of the most common model failure scenarios [9].

The wind turbines' blades are manufactured using composite materials which generally improve the electrical conductance and/or the energy harvesting efficiency. However, composites exhibit anisotropic properties which makes the mechanism behind potential damages and failures complicated. Cracks, delamination of fibers and other failures can be caused even by a minor impact. Finally, composites are influenced by ageing and/or material fatigue. Structural health monitoring combines in-situ sensors with intelligent algorithms for on-line damage detection. This method can achieve high accuracy and reliability for damage detection at the minimum cost [10].

2.4 Material Properties requirements definition

Key trade-off elements involved in wind turbine blade design regard thorough aerodynamic and structural analyses that dictate the shape and geometry, as well as, the materials selected in the manufacturing stage. While the blade geometry varies according to the physical loadings exerted on the structure and drag – efficiency parameters, the process of material selection considers the basic requirements, both physical and chemical, that the structure must meet. According to the international standards, the selection of materials for a wind turbine blade involves several key aspects such as high structural rigidity, resistance to torsion, fatigue & corrosion resistance, a lightweight structure and high temperature tolerance. Composites materials consist of two or more components, which are combined to produce a final product with special properties and characteristics, different from the individual constituents. They are composed of a matrix phase, such as polymer, ceramic or metal and a reinforcing phase that includes materials as carbon, glass, aramid (Kevlar™) and silicon carbide fibers or particulates. The advantages provided by the high-performance fiber – composites are numerous, including the ability to tailor lay-ups for optimum strength and stiffness, improved fatigue life, corrosion resistance and, with good design practice, reduced assembly costs due to fewer parts and fasteners. Furthermore, the specific strength and specific modulus of high strength fiber composites is translated to great weight and materials savings [11]. Common composite systems utilized in wind turbine blade manufacturing include glass and/or carbon fibers as the reinforcement agent and thermosetting polymer matrices, e.g. epoxies, polyester, etc.

Glass fiber composites are the most predominant selection for wind turbine blade applications. There are various glass fiber varieties (density ranging between 2.44-2.72 g/cm³), each exhibiting certain physical properties that answer the needs of a specific type of applications. A typical glass fiber is based on silica (SiO₂), with additions of certain oxides of boron, sodium, calcium, iron and aluminum that produce different types of glass fiber. The content of these oxides in the glass structure affects both its physical and chemical properties and, thus, the different glass fiber types are utilized in various applications depending on the application and the surrounding environment.

The most common type of glass fiber used for wind turbine blades is E-type with fiber diameter of 10-35 μm. In Table 1, the major physical parameters for this type of glass fibers are provided. For applications in wind turbine blade sector that higher rigidity is required H-type of glass fiber can be used. This kind of glass fiber provides stiffness at around 82-86 GPa. Carbon fibers are typically 7-8 μm in diameter. They consist of small crystallites of “turbostatic” graphite, one of the allotropic forms of carbon [12].

The use of sandwich composites (top/bottom skin and core) instead of monolithic laminates for several parts of wind turbine blade that are loaded in compression (e.g. the flange or spar cap), will add additional buckling capacity to the structure by keeping the lightweight design requirement. Their skin part of a sandwich composite in the wind energy industry is comprised of composites of either glass or carbon fibers. For the core selection, there are two general options that include homogeneous or non-homogeneous support structures. The first, as shown in Figure 2 below, is comprised of a solid support structure, such as foam and balsa that relies on the core

material's physical properties. The second core selection can be support structure of a non-solid geometry, such as honeycomb core and corrugated core that best fits the application's needs.

$E=76 \text{ GPa}$
$\rho=2.54 \text{ g/cm}^3$
$\sigma \approx 3.45 \text{ GPa}$
$T_{\max} \approx 550 \text{ }^{\circ}\text{C}$
$\alpha=4.9 \times 10^{-6} \text{ K}^{-1}$

Table 1 Properties of E-type Glass fiber.

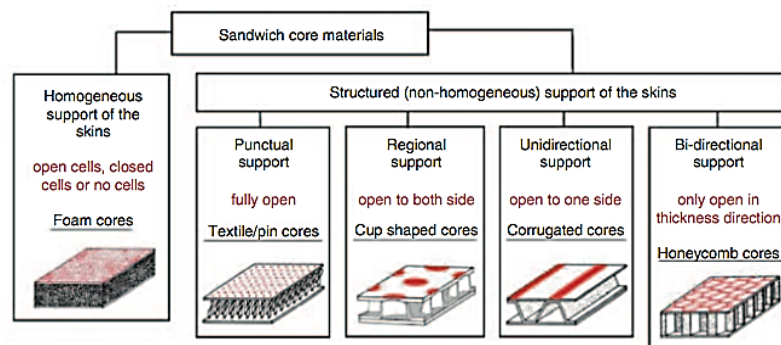


Figure 2 Sandwich core materials and alternatives [12].

A major disadvantage of utilizing sandwich composites compared to monolithic ones is that the former is more prone to delamination and failure due to the presence of large weak interfaces between adjacent materials with very different stiffness and strength properties. This implies that sandwich composites are sensitive to failure by interlaminar shear or through the application of concentrated loads, at joints and points or lines of support, and due to localized effects induced in the vicinity of geometric and material discontinuities. Therefore, severe through-thickness shear and normal stresses are induced.

A way of improving the damage tolerance, as well as, the skin/core interface properties is by developing composite sandwich systems with structural elements in the form of fibers, pins, stitches, or even structural plate elements extending in the through-thickness direction of the sandwich laminate. This kind of strategy, of through-thickness elements, will provide strong and stiff connections between core and the skin laminates, adequate load redistribution in the occurrence of local damage and in-plane stiffness and strength properties at the sandwich composite part.

3 THE WIND TURBINE BLADE DESIGN

Some of the airfoil families utilized for horizontal axis wind turbines (HAWTs) have included the NACA 44XX, NACA 23XXX, NACA 63XXX, and NASA LS series airfoils. All the aforementioned airfoils suffer noticeable performance degradation from roughness effects resulting from leading-edge contamination. It has also been noticed that annual energy losses due to leading-edge roughness are greatest for stall-regulated rotors. The loss is proportional to the reduction in maximum lift coefficient Cl_{\max} along the blade. The airfoil families are classified either as thick or thin. Thick airfoil families with thickness between 16% and 21%, are commonly found in stall-regulated wind turbines. Their utilization indicates that the tip-region airfoils are thick enough to accommodate overspeed-control aerodynamic devices and to reduce the blade weight. On the other hand, airfoil families that are labeled are thin with thickness between 11% and 15%, are more suited to variable-pitch or variable-rpm turbines that use full-span blade pitch. As a general rule, greater thickness is opted for the blade root airfoils to withstand structural and dynamic considerations. The blade-root airfoil thickness falls in the range of 18% to 24%. It has been assessed that thicknesses greater than 26% result to poor performance characteristics. In 1992, an airfoil family (Figure 3) was designed for extra-large blades for turbines rated at 400-1000 kW. This family, which is included in stall-regulated rotors, is composed of the S816, S817, and S818 airfoils. The tip-region airfoil has a Cl_{\max} of 1.1 and a thickness of 16%. The primary outboard airfoil has a Cl_{\max} of 1.2 and a thickness of 21% while the root airfoil has Cl_{\max} of 1.3 and a thickness of 24%.

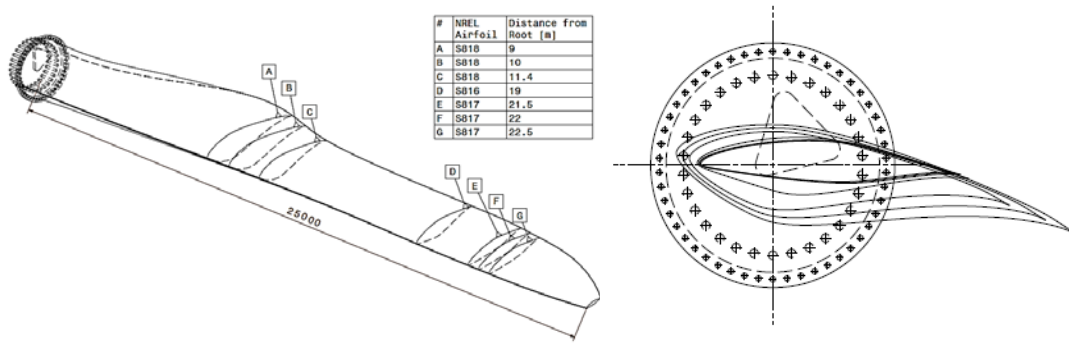


Figure 3 Illustration of airfoils location along the blade span and illustration of different pitch angles of airfoils with reference to the root of the blade.

4 ANALYSES AND APPLICATIONS ON THE BLADE FOR DAMAGE IDENTIFICATION

In this section, the applications which were studied are discussed in detail. At first, some information about the smart composite materials which were chosen for the structure are provided. Then, the details of the analyses which were carried out along with the tools which were used for the identification of two different cracks are given.

4.1 Wind turbine blade materials

The structure has a sandwich form not only concerning the external surfaces, but and the internal spars as well. The thickness of the structure differs from point to point. At the spars, where larger stiffness is needed we assume that more material is necessary, while the external surfaces are thinner, thus less material is used. More specifically, the thickness at the different surfaces vary from 0,035 m to 0,1 m.

More specifically, two different material formulations were considered here. The first one is the so-called “As Is model” which consists of an isotropic elastic PVC foam as the core material of the sandwich, and an Epoxy E-Glass material for the external surfaces. The total mass of the structure in this case is 4.619,63 kg. The second model which is considered here, the so-called “To Be model”, consists of the same PVC foam material for the core of the structure, however, the external material is chosen to be an orthotropic elastic Epoxy Carbon material with enhanced characteristics in terms of electrical conductance, i.e. in terms of sensing ability, which is very useful in these applications. The total mass of the blade in this case is 3.686,39 kg. The characteristics and critical values of the materials which were used, are given in detail below. The isotropic elastic PVC foam, which is used for the core of the blade, is an elastic material of density which equals to 80 kg/m^3 . The detailed material properties of this foam are given in the next table.

Density [kg/m^3]	80
Young's Modulus [Pa]	$1,02 \times 10^8$
Poisson's Ratio	0,3
Bulk Modulus [Pa]	$8,5 \times 10^7$
Shear Modulus [Pa]	$3,9231 \times 10^7$

Table 2 PVC foam material properties.

4.2 Static Analyses

In the present investigation, the blade structure is discretized using quadrilateral finite elements creating a mesh which consists of 22.767 nodes and 19.549 elements. One static analyses for each model, i.e. the As Is model and the To Be model, are carried out.

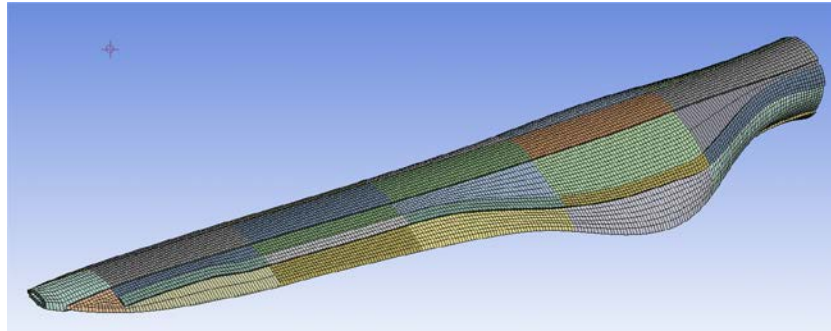


Figure 4 Wind turbine blade mesh

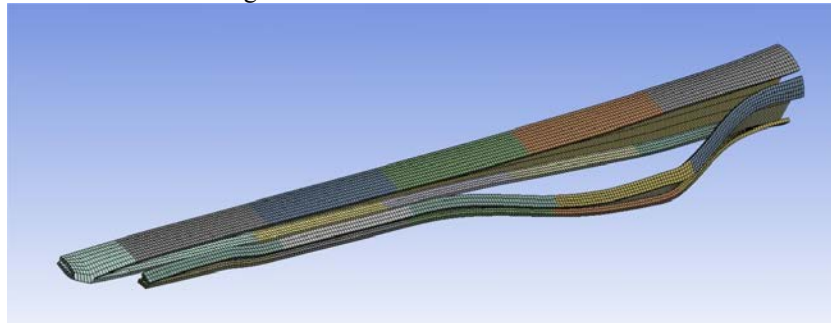


Figure 5 Wind turbine blade's spars mesh

A simple two-point loading at two different points, i.e. at two different sub-surfaces of the lower surface is considered. The loading is applied in a ramp form at the direction of the Z axis and the magnitude of the force at the two sub-surfaces is equal to 1×10^5 N and 4×10^5 N respectively (see Figure 6).

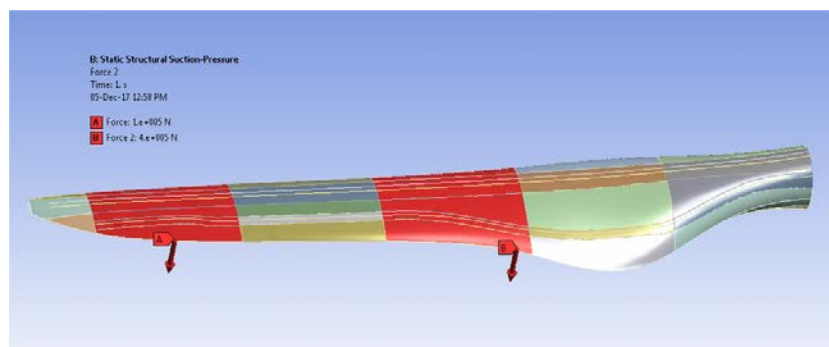


Figure 6 Two-point loading at the suction side of the blade (1st loading scenario).

The results of the analysis for the As Is model, for the five loading scenarios are presented in Figures 7-9 below.

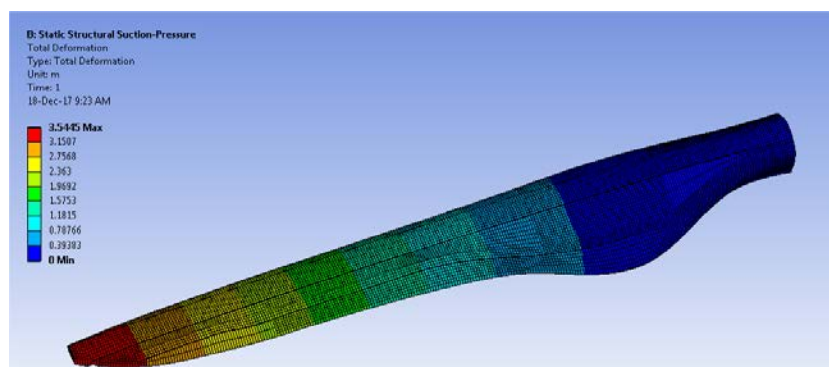


Figure 7 Deformations [m] of the blade from the static analysis of the As Is model for the 1st loading scenario (Two-point loading at the suction side of the blade).

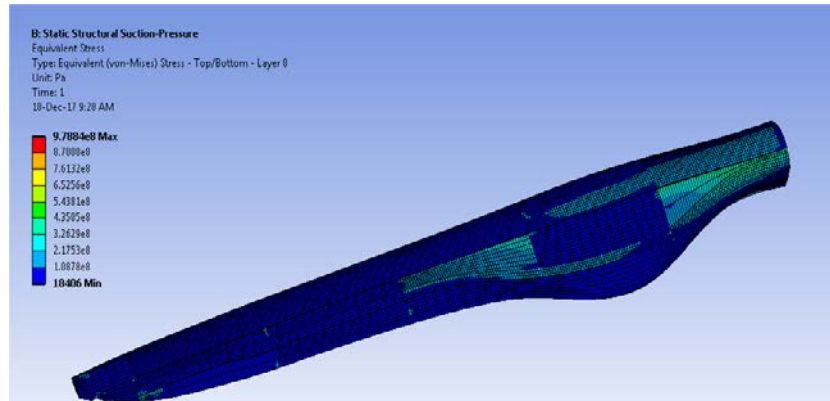


Figure 8 Von-Mises stresses [Pa] of the blade from the static analysis of the As Is model for the 1st loading scenario (Two-point loading at the suction side of the blade).

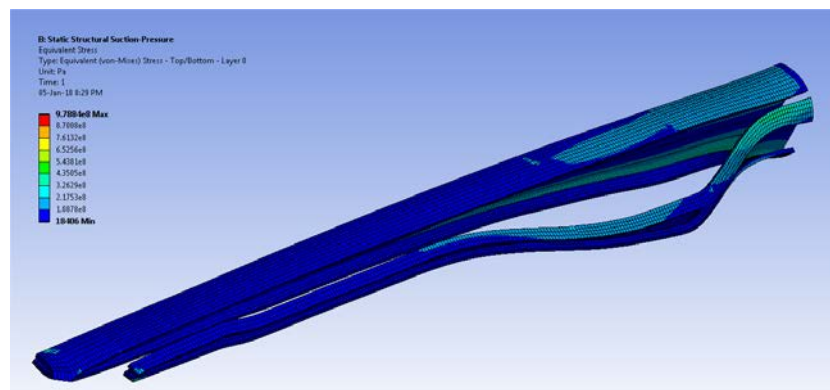


Figure 9 Von-Mises stresses [Pa] of the spars from the static analysis of the As Is model for the 1st loading scenario (Two-point loading at the suction side of the blade).

The results of the analysis for the To Be model, for the five loading scenarios are presented in the Figures 10-12 below. As can be easily seen, the stresses are concentrated at the location of the spar and mainly across its main direction. More specifically, one can observe that the spars receive stresses at the vertical edge of the spar, as well as near the upper and the bottom area near the fixed end respectively. As for the deformations, one can observe that the maximum deformation is 1.79 m, which is clearly lower than the model with the E-glass fibers. As for the Von-Mises stresses, one can clearly observe that they appear mostly at the left side of the blade and in the front corner (exactly at the point where the internal spar ends). This is a critical point for the structure, as many failures may appear there.

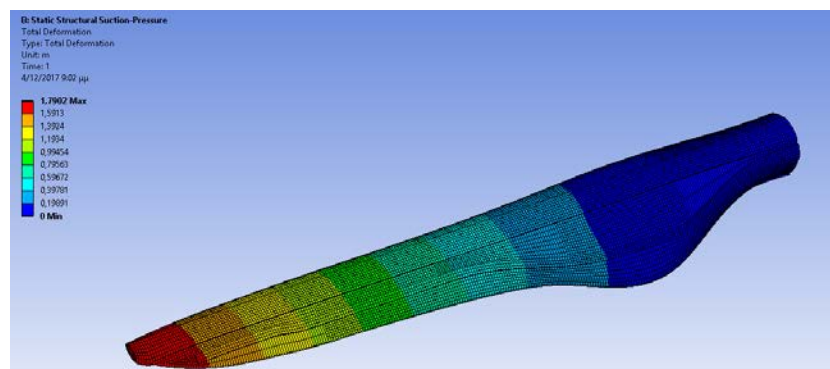


Figure 10 Deformations [m] of the blade from the static analysis of the To Be model for the 2nd loading scenario (Two-point loading at the pressure side of the blade).

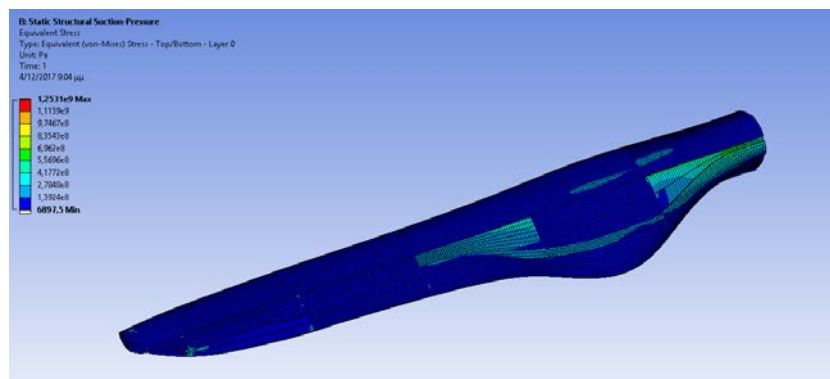


Figure 11 Von-Mises stresses [Pa] of the blade from the static analysis of the To Be model for the 1st loading scenario (Two-point loading at the suction side of the blade).

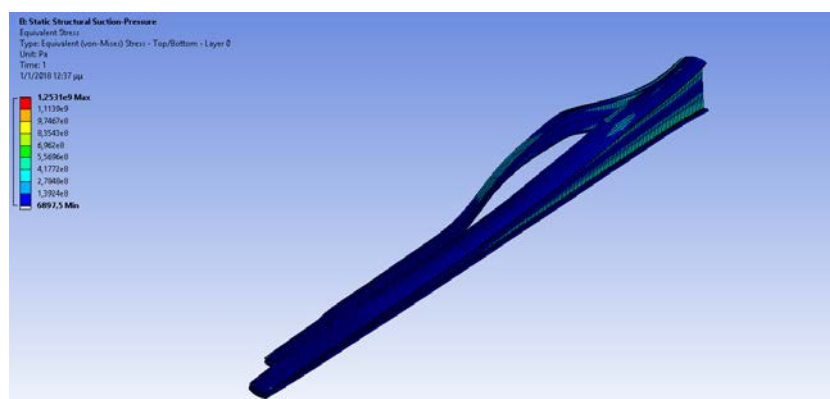


Figure 12 Von-Mises stresses [Pa] of the spar from the static analysis of the To Be model for the 1st loading scenario (Two-point loading at the suction side of the blade).

4.3 Damage identification and SHM

As already discussed previously, modal analysis tools can be very useful for damage identification in smart composite structures. This is due to the alteration of the structural dynamics which is imposed by the damages or the failures. More specifically, the mass and the stiffness of the structure are altered due to the damage, and thus the eigen-frequencies change indicating the existence of the damage.

This means that the first step for the damage identification is the conduction of a complete modal analysis before and after the appearance of the damage (crack) followed by a steady state response analysis. In the present investigation, three different cases are studied; the undamaged model and two models with different cracks, i.e. Crack_1 and Crack_2 as shown in Figure 13) are studied. The specific cracks were selected as two of the most popular damages that maintenance crews come across.

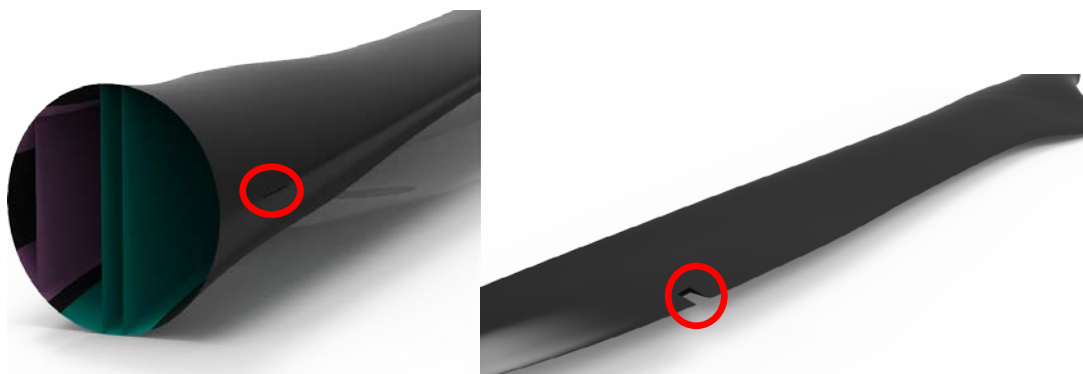


Figure 13 The model with the first and the second crack near the root and the trailing edge respectively

In order to study the behavior of the blade before and after the appearance of the cracks we focus on the first six eigen-modes of the structure for the two formulations, i.e. the As Is (E-Glass) and the To Be (E-Carbon) model. The analysis, which was carried out, was the steady-state response analysis, where a loading of 100 kN was applied to the upper surface and the response of the structure in the frequency domain was taken. The response of the structure in case of a failure or damage can be obtained and studied. In the present investigation three different cases are considered, as described above. The results of the steady-state response for the three cases, i.e. for the healthy model and the models with the two cracks for the As Is formulation are shown in the following diagram.

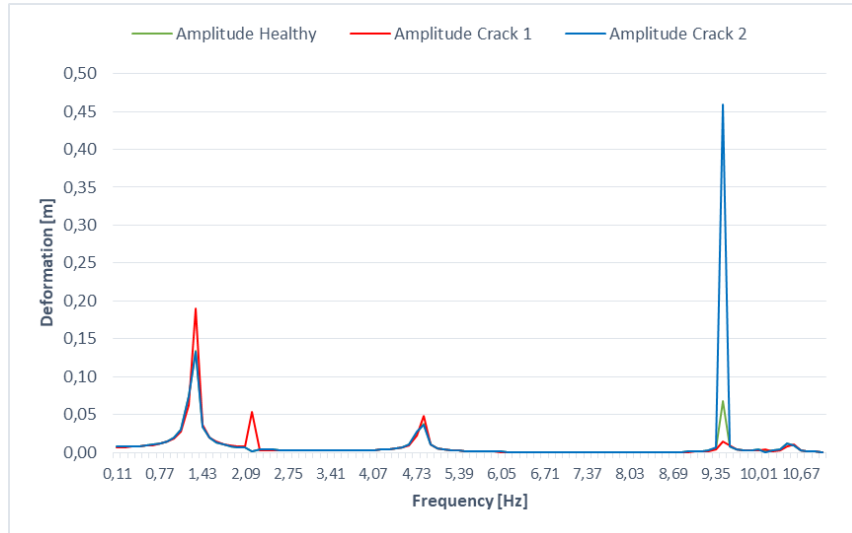


Figure 14 Steady-state response for the three cases (healthy, Crack_1, Crack_2) for the As Is model.

It is shown that the two cracks play significant role to the deformation of the structure. At the first eigen-mode, one can observe that the deformation can be almost doubled for the case with the Crack_1 in comparison with the healthy model, while at the third eigen-mode the case of the Crack_2 has four times higher deformation compared to the healthy case. It is notable that at other modes, i.e. at the fifth, the healthy case presents higher deformation compared to the two damaged cases. The results of the steady-state response for the three cases, i.e. for the healthy model and the models with the two cracks for the To Be formulation are shown below.

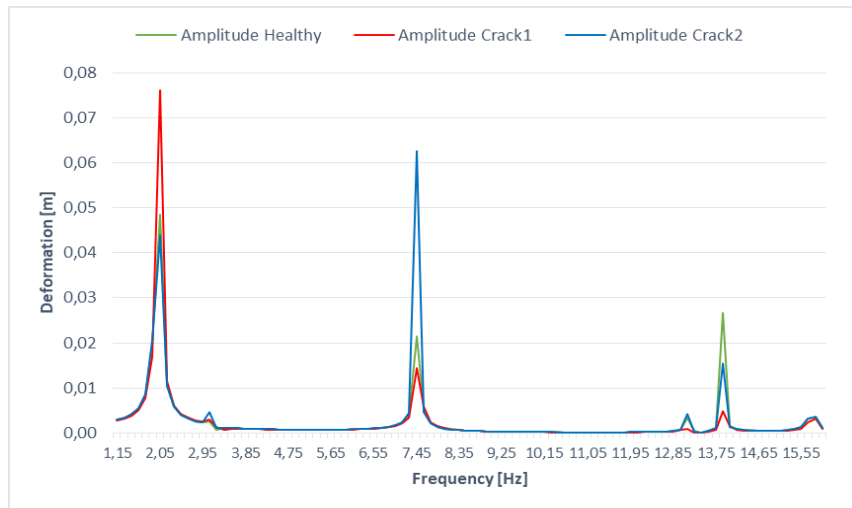


Figure 15 Steady-state response for the three cases (healthy, Crack_1, Crack_2) for the To Be model.

From the diagram above, one can clearly observe that the two cracks influence the deformation of the structure. More specifically, at the first eigen-mode, one can observe that the deformation can be almost doubled for the case with the Crack_1 in comparison with the healthy model, while at the third eigen-mode in the case of the Crack_2 has three times higher deformation compared to the healthy case. Moreover, it is also interesting that at other modes, i.e. at the fifth, the healthy case presents higher deformation compared to the two damaged cases.

5 CONCLUSIONS

According to the design, as well as the static analyses which were carried out, it is clearly shown that the wind turbine blade has very good behavior and durability for the loading scenarios which were carried out for both cases (As is and To be models). The carbon model appears to be efficient in terms of durability, as well as to the displacements (almost 1/3 in contrast to the E-glass model for the same loadings). Moreover, it offers a much lighter structure (nearly 1000 kg less), however the cost increases dramatically.

Based on the static analyses of the present study, a great concentration of stresses near the fixed end of the structure (tip of spar) is observed. According to the literature, this point is more vulnerable compared to others, as damages or failures appear frequently. As for the structural health monitoring of the structure, one can observe that the modification of the structural characteristics of the structure in both cases (As Is and To Be model) brings upon an alteration to the displacement field as shown from the diagrams in the frequency domain, under dynamic loadings. This practically means that in case of use of accelerometers, relative alterations to the frequency diagrams will indicate the existence of damages or failures.

Future work could be the modification of the inner design of the structure using topology optimization tools, for the reduction of the weight and the improvement of the structural behavior, not only for the carbon, but for the E-glass as well, which in turn is much less expensive. Wireless sensors can eliminate wiring and its problems.

Acknowledgments

The project was funded by Technical University of Crete in the context of supporting postgraduate research, 2016-2017.

REFERENCES

- [1] Jonathan Gomez-Leon, Wind Turbine Blade Analysis Using Blade Element Momentum Theory, Faculty of Rensselaer Polytechnic Institute, 2015.
- [2] Mølholt Jensen, Ultimate strength of a large wind turbine blade, Risø National Laboratory for Sustainable Energy & Department of Civil Engineering, Technical University of Denmark, 2008.
- [3] National Research Council, committee on Assessment of research needs for wind turbine rotor materials technology, Energy Engineering Board, Commission on Engineering and Technical Systems, Washington, ISBN: 0-309-58318-7, D.C. 1991.
- [4] Quarton, D.C. The Evolution of Wind Turbine Design Analysis -A Twenty Year Progress Review; Garrad Hassan and Partners Ltd.: Bristol, UK, 1998; pp. 5–24.
- [5] Habali, S.M.; Saleh, I.A. Local design, testing and manufacturing of small mixed airfoil wind turbine blades of glass fiber reinforced plastics Part I: Design of the blade and root. *Energy Convers. Manag.* 2000, 41, 249–280.
- [6] Gasch, R.; Tvele, J. Wind Power Plants; Solarpraxis: Berlin, Germany, 2002.
- [7] Burton, T. Wind Energy Handbook; John Wiley & Sons Ltd.: Chichester, UK, 2011.
- [8] O.M. Bouzid, G.Y. Tian, K. Cumanan, D. Moore, Structural Health Monitoring of Wind Turbine Blades: Acoustic Source Localization Using Wireless Sensor Networks, *Journal of Sensors*, vol. 2015, Article ID 139695, 11 pages, 2015. doi:10.1155/2015/139695.
- [9] A. Ghoshal, M.J. Sundaresan, M.J. Schulz, P.F. Pai, Structural health monitoring techniques for wind turbine blades, *Journal of Wind Engineering and Industrial Aerodynamics*, 85(3), 309–324, 2000.
- [10] H. Li, W. Zhou, J. Xu, Structural Health Monitoring of Wind Turbine Blades, in: *Wind Turbine Control and Monitoring* Eds. N. Luo, Y. Vidal, L. Aho, Springer, 231-265, 2014.
- [11] F.C. Campbell, *Manufacturing Technology for Aerospace Structural Materials*. Elsevier, 2nd edition, 2008.
- [12] D. Hull, T.W. Clyne, *An Introduction to Composite Materials*. Cambridge Solid State Science Series, 2nd edition, 1996.

SOLVING ENGINEERING OPTIMIZATION PROBLEMS WITH AN EFFICIENT HYBRID NATURE-INSPIRED ALGORITHM

Alexandros D. Tsiplanitis¹, Yiannis Tsompanakis^{2*}

¹School of Environmental Engineering
Technical University of Crete
University Campus, GR-73100, Chania, Greece
e-mail: altsipianitis@gmail.com

²School of Environmental Engineering
Technical University of Crete
University Campus, GR-73100, Chania, Greece
e-mail: jt@science.tuc.gr

Keywords: Engineering Optimization, Swarm Intelligence, Metaheuristic Algorithms, Random Search, Hybrid Schemes, Benchmark Problems.

Abstract. Hybrid optimization schemes have been used in many engineering applications over the last decades. In particular, by combining two or more algorithms, the main aim of hybrid optimizers is to alleviate the drawbacks and maximize their efficiency and accuracy of standard approaches. In this manner, a substantial improvement of original algorithms performance is achieved (i.e., achievement of the global optimal solution and/or a faster convergence rate). Hence, to maximize the advantages of basic Cuckoo Search (CS) and Bird Swarm Algorithm (BSA), a hybrid approach, namely CS-BSA is formulated in the present study. More specifically, critical parameters of BSA are introduced into the CS algorithm to improve the convergence towards optimum solution. Four engineering benchmark problems are used to prove the efficiency of the proposed hybrid CS-BSA approach, which is compared with the original CS algorithm and two other popular nature-inspired optimizers: Particle Swarm Optimization (PSO) and Differential Evolution (DE). The obtained results illustrate that the hybrid CS-BSA optimization scheme is superior to the other algorithms regarding the convergence rate and the final solution.

1 INTRODUCTION

Generally, engineering optimization problems are related to the process of achieving the best possible solution with the available resources. A set of design variables and complex functions (objective(s) and constraints) consist the main features of these tasks. In particular, equality or inequality constraints can take the form of simple bounds and/or nonlinear expressions. Usually these functions are highly nonlinear. For this reason, advanced computational tools are used to analyze multiple designs rapidly and accurately. Typically, the mathematical interpretation of a single-objective constrained optimization problem can be described as follows:

$$\begin{aligned} \min F(s) \\ s = \{s_1, s_2, \dots, s_n\}^T \\ l \leq s \leq u, \quad i = 1, 2, \dots, n \\ g_j(s) \geq 0, \quad j = 1, 2, \dots, m \\ h_j(s) = 0, j = m + 1, m + 2, \dots, t \end{aligned} \quad (1)$$

where, s is the vector of design variables, l_i, u_i , refer to the lower and upper bounds of the corresponding design variable, s_i ; $F(s)$ is the objective function to be minimized; $g_j(s)$ and $h_j(s)$ are the constraint functions (equalities and inequalities, respectively).

During the recent years, metaheuristic optimization methods gained popularity compared to mathematical approaches due to their flexibility and gradient-free nature. In addition, these schemes are directly focused on input and output of each problem. Generally, metaheuristic algorithms imitate natural phenomena and biological processes. In other words, they follow the best characteristics observed in nature, thus, they have been proven extremely efficient [1]. They can be categorized into three main classes: evolution-based, physics-based, and swarm-based optimization methods [2, 3]. The more popular evolutionary-based algorithms are: Genetic

Algorithms (GA) [4], Differential Evolution (DE) [5] and Evolution Strategies [6]. On the other hand, the optimization techniques that are included in the physics-based category are: Simulated Annealing (SA) [7], Gravitational Search Algorithm (GSA) [8], etc.

For the purposes of this study the emphasis is given on the last class, namely swarm-based optimizers. The intelligence of swarms, herds or flocks is represented by these techniques. The main feature of swarm-based optimization is related to the collective behavior and the instinct of a group of bird species. Particle Swarm Optimization (PSO) [9], Cuckoo Search (CS) [10], Bat Algorithm (BA) [11], and Bird Swarm Algorithm (BSA) [12], are among the most well-known optimization algorithms that belong to this category.

In general, evolutionary bio-inspired optimization methods present various deficiencies. More specifically, a convergence to the global optimum solution is not guaranteed. On the other hand, many optimization methods converge fast, but they are prone to be trapped in local optima. Additionally, their efficiency mainly depends on the selection of the initial design set and fine tuning of basic parameters.

For this reason, hybrid optimization schemes have been used by combining two or more optimization algorithms. The aim of hybrid optimizers is to alleviate the drawbacks and maximize the advantages of standard schemes. In this manner, the improvement of original algorithms' performance, i.e., the achievement of the global optimal solution and a faster convergence rate can be accomplished.

In this work, a novel hybrid optimization approach that integrates two swarm-based techniques, namely CS and BSA algorithms, is presented. More specifically, critical parameters of BSA are introduced into CS algorithm to enhance its efficiency. For this reason, several modifications are made to the original CS code provided in MATLAB [13, 14]. Subsequently, the results of hybrid CS-BSA algorithm are tested against four popular benchmark examples considering both optimum solution and convergence rate.

The rest of the paper is organized as follows. Section 2 presents the main characteristics of CS algorithm. Analogously, Section 3 illustrates the most important elements of BSA. The structure of hybrid CS-BSA is presented in Section 4. Subsequently, four benchmark examples that have been used in the present investigation are described in Section 5. The comparative results are provided in Section 6. Finally, Section 7 presents the conclusions of this study.

2 CUCKOO SEARCH ALGORITHM

CS is an optimization technique based on the brood parasitism of some cuckoo species and it is enhanced by Levy flights scheme [15]. For the sake of simplicity, three idealized rules will be used as follows [10, 16]:

- Each cuckoo lays one egg at a time and dumps it in a randomly chosen nest.
- The best nests with high-quality eggs will be carried over to the next generation.
- The number of available host nests is fixed, and the egg laid by a cuckoo is discovered by the host bird with a probability $p_a \in (0,1)$. In this case, the host bird can either get rid of the egg or simply abandon the nest and build a completely new nest.

The replacement of a fraction p_a of the n host nests with new nests (i.e., with new random solutions) can be applied as a further approximation [10, 16]. The value of the objective function is proportional to the quality or fitness of a solution in the case of a maximization problem. Regarding the implementation of the algorithm, the simple representation that each egg in a nest represents a solution and that each cuckoo can lay only one egg (thus representing one solution) can be applied. The objective is to use the new and probably better solutions (cuckoos) to replace a not so good solution in the nests. It is obvious that CS algorithm can be extended to more complicated cases, where each nest has multiple eggs that represent a set of solutions. Herein, the simple approach is followed, where each nest is associated to a single egg.

A balanced combination of a local and a global explorative random walk is used by the CS algorithm, and is also controlled by a switching parameter p_a . The local random walk is represented through the following formula [16]:

$$x^{t+1} = x^t + as \otimes H(p_a - \epsilon) \otimes (x_j - x_k) \quad (2)$$

where x_j^t and x_k^t are two different solutions selected randomly by arbitrary permutations, $H(u)$ is a Heaviside function, ϵ is a random number drawn from a uniform distribution, and s is the step size. The entry-wise product of two vectors is represented by \otimes .

In contrast, Levy flights (see Figure 1) are used for the global random walk [16]:

$$x^{t+1} = x^t + aL(s, \lambda) \quad (3)$$

where:

$$L(s, \lambda) = \frac{\lambda \Gamma(\lambda) \sin\left(\frac{\pi\lambda}{2}\right)}{\pi} \frac{1}{s^{1+\lambda}} \quad (4)$$

while $a > 0$ is the step size scaling factor, which should be associated to the scale of each problem at hand. Usually, $a = O(L/10)$, where L is the characteristic scale of the examined problem. In some cases, using $a = O(L/100)$ can be more effective and avoid flying too far. Different a values can also be used for these updating equations, which lead to parameters a_1 and a_2 . For simplicity, these values are set equal, i.e., $a_1 = a_2$.

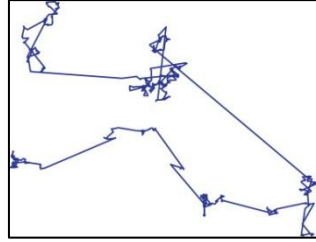


Figure 1. A 2D example of Levy flights [17]

Equation (2) is a stochastic uniform equation related to random walk. Generally, random walk is a Markov chain whose next location depends only on the current state and the transition probability. However, the far field randomization should generate a substantial fraction of the new solutions, and their locations should not be too close to current best solution. This is necessary for the validity of the hypothesis that the system will not be trapped in a local optimum [10, 13].

Considering implementation aspects, two steps are required for the generation of random numbers when implementing Levy flights: the generation of steps which fulfill the chosen Levy distribution and the selection of a random criterion [16]. A uniform distribution drives the generation of a direction, and the generation of steps is a tough part. The so-called Mantegna's algorithm for a symmetric Levy stable distribution is the most efficient way regarding the steps management. In this scheme, the step size s can be evaluated using two Gaussian distributions U and V through the following mathematical formulation [18]:

$$S = \frac{U}{|V|^{1/\lambda}} \quad (5)$$

where:

$$U \sim N(0, \sigma^2), \quad V \sim N(0, 1)$$

while $U \sim (0, \sigma^2)$ means that the samples are drawn from a Gaussian normal distribution with a zero mean and a variance of σ^2 . The variance is obtained as follows:

$$\sigma^2 = \left[\frac{\Gamma(1+\lambda)}{\lambda \Gamma((1+\lambda)/2)} \cdot \frac{\sin(\pi\lambda/2)}{2^{(\lambda-1)/2}} \right]^{1/\lambda} \quad (6)$$

According to Mantegna [18], the random samples which follow the required distribution can be correctly produced by this algorithm.

3 BIRD SWARM ALGORITHM

The BSA algorithm [12] is a bio-inspired optimization algorithm based on the social behavior of bird swarms. More specifically, the behavior of birds can be divided into three main categories: flight behavior, vigilance behavior and foraging behavior. Due to social interactions, the birds can escape from the predators and forage for food. Therefore, in this way they have a high chance of survival. To simplify the aforementioned social behavior of bird swarms, five idealized rules are considered [12]:

- **Rule 1:** The foraging behavior and the vigilance behavior can be switched by each bird. A stochastic

decision models the case whether the bird forages or keeps vigilance.

- **Rule 2:** In the case of keeping vigilance, each bird would try to move towards the centre of the swarm. The interference caused by the competition among the swarm plays the key role to this behavior. The centre of the swarm would be more likely to be occupied by the birds having the higher reserves. In contrast, the birds with the lower reserves would be more likely to lie further from the centre of the swarm.
- **Rule 3:** In the case of foraging behavior, each bird's and swarm's previous best experience regarding food patch is recorded and updated. This experience can also be used for food searching. In addition, social information is shared among the whole swarm.
- **Rule 4:** Birds tend to fly to another site periodically. In this manner, birds' behavior can switch between scrounging and producing. A producer is the bird that contains the highest reserves, while a scrounger is the bird with the lowest reserves, respectively. When birds contain reserves between the lowest and highest level, they would randomly choose whether to be a scrounger or a producer.
- **Rule 5:** Scroungers would randomly follow a producer to search for food, while producers would actively search for food.

3.1 Flight behavior

The threat from possible predators, foraging and any other reasons cause birds to fly to another site, where they would continue to search for food. The species that forage for food are the producers, while other birds, namely scroungers, try to feed from the food reserves that are already gathered by the producers. Thus, Rule 4 separates the producers and the scroungers from the bird swarm. The subsequent equations describe the behavior of the producers and the scroungers, respectively:

$$x_{i,j}^1 = x_{i,j} + randn(0,1) \times x_{i,j} \quad (7)$$

$$x_{i,j}^1 = x_{i,j} + (x_{k,j} - x_{i,j}) \times FL \times rand(0,1) \quad (8)$$

where, $randn(0,1)$ is a Gaussian distributed random number with mean 0 and standard deviation 1, $k \in [1,2,3, \dots, N]$, $k \neq i$; FL ($FL \in [0,2]$) denotes that the scrounger would follow the producer to forage for food.

3.3 Vigilance behavior

With respect to Rule 3, birds would compete to each other when moving to the centre of the swarm. For this reason, each bird would move towards the centre of the swarm indirectly. The formulation of these motions is the following:

$$x_{i,j}^1 = x_{i,j} + A1(mean_j - x_{i,j}) \times rand(0,1) + A2(p_{k,j} - x_{i,j}) \times rand(-1,1) \quad (9)$$

$$A1 = a1 \times \exp\left(-\frac{pFit_i}{sumFit_\varepsilon} \times N\right) \quad (10)$$

$$A2 = a2 \times \exp\left(\left(\frac{pFit_i - pFit_k}{|pFit_k - pFit_i| + \varepsilon}\right) \frac{N \times pFit_k}{sumFit_\varepsilon}\right) \quad (11)$$

where, k ($k \neq i$) is a positive integer, that is randomly chosen between 1 and N , $a1$ and $a2$ are two positive constraints in $[0,2]$, $pFit_i$ is the i th bird's best fitness value and $sumFit$ denotes the sum of the swarms' best fitness value, ε that is used to avoid zero-division error, represents the smallest constant in the computer. Finally, $mean_j$ is the j th element of the average position of the whole swarm.

3.3 Foraging behavior

According to Rule 2, each bird searches for food using its own experience as well as the experience of the whole swarm. The mathematical formulation of this rule is as follows:

$$x_{i,j}^1 = x_{i,j} + (p_{i,j} - x_{i,j}) \times C \times rand(0,1) + (g_j - x_{i,j}) \times S \times rand(0,1) \quad (12)$$

where, $j \in [1, \dots, D]$, $rand(0,1)$ are uniformly distributed numbers in $(0,1)$, C and S are two positive numbers that can be used as cognitive and social accelerated coefficients, $p_{i,j}$ is the best previous position of the i th bird and g_j is the best previous position within the swarm.

4 HYBRID CS-BSA ALGORITHM

The formulation of the hybrid CS-BSA approach will be described in this section. As aforementioned, critical parameters of BSA are introduced into the CS algorithm to improve its convergence towards the global optimum solution. For this reason, the MATLAB platform [14] to implement both algorithms is used, thus, the equations below are transformed into the programming style. More specifically, the first improvement is related to the replacement of the fixed value for the probability of CS ($p_a=0.25$), with the probability of foraging for food of BSA, plus a ratio of the probability divided by the calculation time:

$$p_a = \frac{p_a}{t} + \frac{(rand(time,1) \times 0.2 + 0.8)}{t} \quad (13)$$

where, p_a is the probability of an alien egg to be found by the host bird, and t is the calculation time.

In addition, the second modification of the proposed hybrid optimization technique is related to the replacement of Levy flights scheme of the standard CS algorithm, with the flight behavior of birds as scroungers. Therefore, the mathematical equation introduced into the formulation of the classic CS algorithm is the following:

$$nest(j,:) = nest(j,:) + (pX(person,:) - nest(j,:)) \times FL(j) \times rand(0,1) \quad (14)$$

where, pX is a random initial solution, $person$ is a random integer number, FL ($FL \in [0,2]$) denotes that the scrounger would follow the producer to forage for food, and $nest$ represents the new solution.

Subsequently, the MATLAB code of the hybrid CS-BSA approach is implemented and tested using popular constrained engineering examples to validate its efficiency compared to standard approaches.

5 BENCHMARK PROBLEMS

This section presents the main characteristics of some well-known engineering applications, namely the optimization of: tension/compression spring, speed reducer, pressure vessel and three-bar truss, which have been solved by all types of the well-known optimization techniques (GA, PSO, SA, etc) in many relevant studies. Certainly, more such benchmark examples can be found in the literature, however, only the aforementioned ones are presented herein due to space limitations.

5.1 Tension/compression spring

The minimization of the weight of a tension/compression spring was introduced by Belegundu [19] and Arora [20]. This optimization example is subjected to constraints on minimum deflection, maximum shear stress and geometrical bounds. In addition, three design variables: the length (L), the wire diameter (w), and the mean spring diameter (d) are included in the formulation:

$$\text{Minimize } f(w, d, L) = (L + 2)w^2d$$

subject to:

$$g_1 = 1 - \frac{d^3L}{71785w^4} \leq 0$$

$$g_2 = 1 - \frac{140.45w}{d^2L} \leq 0$$

$$g_3 = \frac{2(w+d)}{3} - 1 \leq 0$$

$$g_4 = \frac{d(4d-w)}{w^3(12566d-w)} + \frac{1}{5108w^2} - 1 \leq 0$$

with the corresponding bounds:

$$0.05 \leq w \leq 2, \quad 0.25 \leq d \leq 1.3, \quad 2 \leq L \leq 15.$$

5.2 Speed reducer

Optimization of a speed reducer is one of the most challenging optimum design problems [21], due to the fact

that seven design variables and eleven constraints are included in the formulation. The objective of this example is the minimization of weight. The constraints are related to the surface stress, the bending stress of gear teeth, the transverse deflections of shafts caused by the transmitted force, and the stresses in shafts. Subsequently, the design variables are: the face width (b), the module of teeth (m), the number of teeth on pinion (z), the length of shafts 1 and 2 between bearing (l_1, l_2), and the shaft diameters 1 and 2 (d_1, d_2). Therefore, the mathematical formulation is:

$$\text{Minimize } f(b, m, z, l_1, l_2, d_1, d_2) = 0.7854bm^2(3.3333z^2 + 14.9334z - 43.0934) - 1.508b(d_1^2 + d_2^2) + 7.477(d_1^3 + d_2^3) + 0.7854(l_1d_1^2 + l_2d_2^2)$$

subject to:

$$g_1 = \frac{27}{bm^2z} - 1 \leq 0$$

$$g_2 = \frac{397.5}{bm^2z^2} - 1 \leq 0$$

$$g_3 = \frac{1.93}{mzl_1^3d_1^4} - 1 \leq 0$$

$$g_4 = \frac{1.93}{mzl_1^3d_2^4} - 1 \leq 0$$

$$g_5 = \frac{\sqrt{\left(\frac{745l_1}{mz}\right)^2 + 16.9 \times 10^6}}{110d_1^3} - 1 \leq 0$$

$$g_6 = \frac{\sqrt{\left(\frac{745l_1}{mz}\right)^2 + 157.5 \times 10^6}}{85d_2^3} - 1 \leq 0$$

$$g_7 = \frac{mz}{40} - 1 \leq 0$$

$$g_8 = \frac{5m}{b} - 1 \leq 0$$

$$g_9 = \frac{b}{12m} - 1 \leq 0$$

$$g_{10} = \frac{1.5d_1 + 1.9}{l_1} - 1 \leq 0$$

$$g_{11} = \frac{1.1d_2 + 1.9}{l_2} - 1 \leq 0$$

The bounds on the design variables are the following:

$$2.6 \leq b \leq 3.6, \quad 0.7 \leq m \leq 0.8, \quad 17 \leq z \leq 28, \quad 7.3 \leq l_1, l_2 \leq 8.3, \quad 2.9 \leq d_1 \leq 3.9, \quad 5 \leq d_2 \leq 5.5.$$

5.3 Pressure vessel

The scope of this problem is the minimization of the total cost (including single 60°C material welding and metal forming costs) of a cylindrical pressure vessel. The design variables are: the thickness (T_s), the thickness of the head (T_h), the inner radius (R) and the length (L) of the cylindrical section of the vessel. Note that thickness design variables can take discrete integer values that are multiples (in the range of 1 to 99) of 0.0625 inch. Therefore, the mathematical formulation of the optimization problem in this case study is as follows [23]:

$$\text{Minimize } f(T_s, T_h, R, L) = 0.6224T_sRL + 1.7781T_hR^2 + 3.1661T_s^2L + 19.84T_h^2L$$

subject to:

$$g_1 = -T_s + 0.0193R \leq 0$$

$$g_2 = -T_h + 0.00954R \leq 0$$

$$g_3 = -\pi R^2 L - \frac{4}{3}\pi R^3 + 1296000 \leq 0$$

$$g_4 = L - 240 \leq 0$$

where: $R \geq 10$ in and $L \leq 200$ in.

5.4 Three-bar truss

Despite its structural simplicity, the optimization of a three-bar truss [22] is a difficult problem due to its complex nonlinear constraints. In particular, the volume of a three-bar truss is to be minimized, subjected to stress constraints for all its members, with two continuous design variables, namely the cross sectional areas: A_1 and A_2 (due to symmetry $A_3=A_1$). The mathematical interpretation of this optimum design engineering application is as follows [23]:

$$\text{Minimize } f(A_1, A_2) = (2\sqrt{2}A_1 + A_2) \times L$$

subject to:

$$g_1 = \frac{\sqrt{2}A_1 + A_2}{\sqrt{2}A_1^2 + 2A_1A_2} - 1 \leq 0$$

$$g_2 = \frac{A_2}{\sqrt{2}A_1^2 + 2A_1A_2} - 1 \leq 0$$

$$g_3 = \frac{1}{A_1 + \sqrt{2}A_2} - 1 \leq 0$$

where:

$$0 \leq A_1, A_2 \leq 1, \quad L = 100\text{cm}.$$

6 RESULTS

The results obtained by applying the different optimizers for the four case studies are briefly presented in this section. In particular, the results for each of the examined benchmark problems of the hybrid CS-BSA are compared with those derived from standard CS, PSO and DE. More specifically, except from the best optimal solutions, the final values of the design variables as well as the violation of the constraints allowable limits are also examined. Additionally, a separate analysis is provided that illustrates the convergence rate towards optimum solution for each optimization algorithm for all benchmark problems.

6.1 Optimization calculations

In Table 1 the optimization results for the tension/compression spring design problem are presented. Evidently, the hybrid CS-BSA algorithm provides the best optimum solution in combination with the fulfillment of constraint variables. It can be noticed that in standard CS and PSO some constraints are violated. In contrast, the DE algorithm produces the same results as the hybrid approach.

	Hybrid CS-BSA	Standard CS	PSO	DE
w	0.05168	0.056585	0.06004	0.0517
d	0.3567	0.48624	0.593084	0.3567
L	11.289	6.4022	4.47318	11.289
g_1	7.976e-9	0.9999 ^a	0.99966 ^a	-2.22e-16
g_2	-5.177e-10	-0.9999	-0.99270	0
g_3	-4.0538	-207.1801	-30.8506	-4.0538
g_4	-0.72773	0.191339 ^a	-0.2675	-0.7273
$f(w,d,L)$	0.012665	0.013081	0.0131022	0.012665

^a Violated sets

Table 1. Optimization results for tension/compression spring problem

Table 2 presents the results for the speed reducer design problem. As aforementioned, this constrained engineering design example is one of the most challenging problems due to the large number of design variables and constraints. Nonetheless, hybrid CS-BSA, CS and DE produced the same results with respect to the optimum

solution. On the other hand, the solution of PSO is slightly different, while a constraint violation is also observed in this case.

	Hybrid CS-BSA	Standard CS	PSO	DE
b	3.5	3.5	3.5325	3.5
m	0.7	0.7	0.7462	0.7
z	17	17	18.89	17
l_1	7.3	7.3	7.5733	7.3
l_2	7.71389	7.71389	8.0837	7.7139
d_1	3.34336	3.34336	3.3796	3.3434
d_2	5.28535	5.28535	5.3878	5.2854
g_1	-0.073915	-0.073915	-0.4026	-0.073915
g_2	-0.198	-0.198	-0.636	-0.198
g_3	-0.49505	-0.49505	-0.654	-0.49505
g_4	-0.9046	-0.9046	-0.9304	-0.9046
g_5	-5.107e-15	-8.312e-9	-0.0287	-4.3415e-9
g_6	-8.4377e-15	-2.5095e-8	-0.0709	-7.9331e-8
g_7	-0.7025	-0.7025	-0.5604	-0.7025
g_8	-4.3299e-15	-2.961e-9	0.0297 ^a	-1.482e-8
g_9	-0.58333	-0.58333	-0.5953	-0.58333
g_{10}	-0.0527333	-0.0527333	-0.0621	-0.0527333
g_{11}	-9.992e-16	3.945e-17	-0.038	-6.6321e-8
$f(b,m,z,l_1,l_2,d_1,d_2)$	2333.4479	2333.4479	2399.248	2333.448

^a Violated sets

Table 2. Optimization results for speed reducer problem

The pressure vessel design problem is the next benchmark test used in this study. According to Table 3, hybrid CS-BSA, standard CS and DE led to the same results, in contrast to PSO algorithm which provides a local optimum. Finally, with respect to the last case study, Table 4 illustrates that all optimization algorithms provide the best optimum design for the three-bar truss, with identical results (except from PSO).

	Hybrid CS-BSA	Standard CS	PSO	DE
T_s	0.7781686	0.7781686	0.842	0.7782
T_h	0.3846492	0.3846492	0.4161	0.3846
R	40.31962	40.31962	43.6443	40.3196
L	200	200	158.3782	200
g_1	0	1.281e-12	0.00033	-3.8858e-15
g_2	2.77556e-16	-2.084e-11	0.00016	-1.5543e-15
g_3	4.6566e-10	-0.0001	0	-2.5145e-8
g_4	-40	-40	-81.6217	-40
$f(T_s,T_h,R,L)$	5885.3328	5885.3328	6002.9301	5885.3328

Table 3. Optimization results for pressure vessel problem

	Hybrid CS-BSA	Standard CS	PSO	DE
A_1	0.78868	0.78868	0.78866	0.7887
A_2	0.40825	0.40825	0.40824	0.4082
g_1	2.22045e-16	1.287e-13	0	0
g_2	-0.267949	-0.267949	-0.2679	-0.267949
g_3	-28.9904	-28.9904	-28.99	-28.9904
$f(A_1, A_2)$	263.8958	263.8958	263.8941	263.8958

Table 4. Optimization results for three-bar truss problem

Hence, concerning the performance of the hybrid CS-BSA towards optimum solution, it can be stated that in most of the examined benchmark problems it is better compared to the standard optimizers, since it combines finding the best optimum solution (i.e., by avoiding to get trapped in local optima), while achieving the best fulfillment of constraints.

6.2 Convergence histories

Figure 2 depicts the convergence histories for all optimizers for every benchmark problem. More specifically, the graphs represent the best objective function value in each optimization cycle as well as the number of iterations needed by the algorithms to reach the optimum solution. It can be observed that in most cases the hybrid CS-BSA algorithm exhibits much faster convergence compared to standard CS, PSO and DE approaches. Thus, it is a strong indication that the hybrid CS-BSA formulation can be considered as a robust and computationally efficient optimizer for complex and challenging engineering problems.

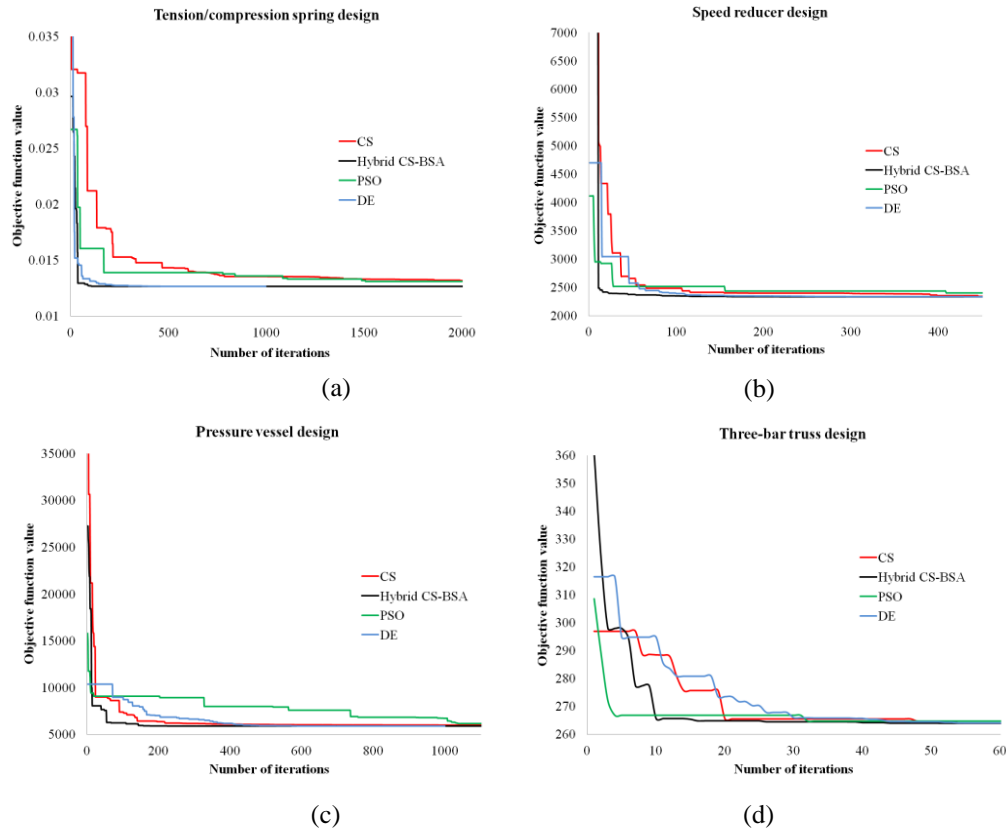


Figure 2. Comparison of optimizers' convergence histories: (a) Tension/compression spring problem; (b) Speed reducer problem; (c) Pressure vessel problem; (d) Three -bar truss problem

7 CONCLUSIONS

In this paper a hybrid CS-BSA optimization algorithm has been proposed. Generally, both optimization techniques are based on nature-inspired, metaheuristic schemes that have been used in various engineering applications. In the presented hybrid scheme, certain critical parameters of the BSA algorithm were introduced into the CS algorithm to improve its convergence rate towards the optimal solution. Four popular engineering benchmark problems were examined in the present investigation to validate the efficiency of the hybrid approach. The optimization results in terms of the optimum solutions and convergence rate for each problem were presented and compared with those obtained using other bio-inspired optimizers (CS, PSO and DE).

The following preliminary conclusions can be derived from this study:

- (a) Hybrid CS-BSA algorithm can be efficiently used in simple as well as complex engineering applications.
- (b) In the majority of the examined benchmark problems the hybrid CS-BSA algorithm achieved faster convergence than the standard CS, PSO and DE optimizers.
- (c) In addition, when the size of the problem is increased (i.e., speed reducer design), the hybrid CS-BSA approach was found to be more efficient.

Certainly, further investigation regarding the effectiveness of the proposed scheme has to be performed, including its application in large-scale real life engineering problems, which is currently under development.

ACKNOWLEDGEMENTS

This research has been generously supported by Bakopouleio Foundation, via a PhD scholarship for the first author. This support is gratefully acknowledged.

REFERENCES

- [1] Yang, X.S. (2011). Review of metaheuristics and generalized evolutionary walk algorithm. *International Journal of Bio-Inspired Computation*, Vol. 3, No. 2, pp. 77-84.
- [2] Blum, C., and Li, X. (2008). Swarm intelligence - Introduction and applications. In Blum, C., and Merkle, D. (eds.) *Swarm intelligence in optimization*, Springer, Berlin, pp. 43-85.
- [3] Biswas, A. Mishra, K., Tiwari, A., and Mishra, A. (2013). Physics-inspired optimization algorithms: a survey. *Journal of Optimization*, Vol. 2013, Article 438152, <http://dx.doi.org/10.1155/2013/438152>.
- [4] Holland, J. (1975). *Adaptation in natural and artificial systems*. Ann Arbor, MI: Univ. of Michigan Press.
- [5] Storn, R., and Price, K. (1997). Differential evolution - a simple and efficient heuristic for global optimization over continuous spaces. *Journal of Global Optimization*, Vol. 11, pp. 341-359.
- [6] Rechenberg, I. (1973). *Evolution strategy: optimization of technical systems by means of biological evolution*. Stuttgart: Fromman-Holzog.
- [7] Kirkpatrick, S., Gelatt, C.D., and Vecchi, M.P. (1983). Optimization by simulated annealing. *Science*, Vol. 220, No 4598, pp. 671-680.
- [8] Rashedi, E., Nezamabadi-pour, H., and Saryazdi, S. (2009). GSA: a gravitational search algorithm. *Information Sciences*, Vol. 179, pp. 2232-2248.
- [9] Eberhart, R.C., and Kennedy, J. (1995). A new optimizer using particle swarm theory. In: *Proceedings of the 6th International Symposium on Micro Machine and Human Science*, pp. 39-43.
- [10] Yang, X.-S. and Deb, S. (2009). Cuckoo search via levy flights. *Proceedings of World Congress on Nature & Biologically Inspired Computing (NaBIC 2009)*. USA: IEEE Publications, pp. 210-214.
- [11] Yang, X.-S., and Gandomi, A.H. (2012). Bat algorithm: a novel approach for global engineering optimization. *Engineering Computations*, Vol. 29, Issue 5, pp. 464-483, <http://doi.org/10.1108/02644401211235834>
- [12] Meng, X.-B., Gao, X.Z., Lu, L., Liu, Y., and Zhang, H. (2015). A new bio-inspired optimization algorithm: bird swarm algorithm. *Journal of Experimental & Theoretical Artificial Intelligence*, Vol. 28, Issue 4, pp. 673-687, DOI: 10.1080/0952813X.2015.1042530
- [13] Yang, X.-S., and Deb, S. (2010). Engineering optimization by cuckoo search. *International Journal of Mathematical Modelling and Numerical Optimisation*, Vol. 1, No. 4, pp. 330-343.
- [14] Mathworks, Inc (2015). *Matlab R2015a*. Natick, M.A.: Mathworks, Inc.
- [15] Pavlyukevich, R.B. (2007). Levy flights, non-local search and simulated annealing. *Journal of Computational Physics*, Vol. 226, pp. 1830-1844.
- [16] Yang, X.-S. (2014). *Nature-inspired optimization algorithms*. 1st Edn. Elsevier, Netherlands.
- [17] Yang, X.-S., and Deb, S. (2013). Multiobjective cuckoo search for design optimization. *Computers and Operations Research*, Vol. 40, Issue 6, pp. 1616-1624.
- [18] Mantegna, R.N. (1994). Fast, accurate algorithm for numerical simulation of levy stable stochastic process. *Physical Review E*, Vol. 49, No 5, pp. 4677-4683.
- [19] Belegundu, A.D. (1982). *A study of mathematical programming methods for structural optimization*. Ph.D Thesis, Department of Civil Environmental Engineering, University of Iowa, USA.
- [20] Arora, J.S. (1989). *Introduction to optimum design*. McGraw-Hill, New York.
- [21] Golinski, J. (1973). An adaptive optimization system applied to machine synthesis. *Mechanism and Machine Synthesis*, Vol. 8, pp. 419-436.
- [22] Nowcki, H. (1974). Optimization in pre-contact ship design. In: Fujita, Y., Lind, K., and Williams, T.J. (eds). *Computer Application in the Automation of Shipyard Operation and Ship Design*, Vol. 2, pp. 327-338, Elsevier, New York.
- [23] Gandomi, A.H., Yang, X.-S., and Alavi, A.H. (2013). Cuckoo search algorithm: a metaheuristic approach to solve structural optimization problems. *Engineering with Computers*, Vol. 29, pp. 17-35, DOI: 10.1007/s00366-011-0241y.

MATERIAL OPTIMISATION USE IN STEEL LATTICE WIND TURBINE TOWERS

Nafsika Stavridou¹, Efthymios Koltsakis² and Charalampos C. Baniotopoulos³

^{1,3}Department of Civil Engineering
University of Birmingham
Edgbaston, B15 2TT, United Kingdom
e-mail: n.stavridou@bham.ac.uk ; c.baniotopoulos@bham.ac.uk ; web page: <http://ccb.civil.auth.gr>

²Department of Civil Engineering
Lulea University of Technology
Porson, 97187, Lulea, Sweden
e-mail: efthymios.koltsakis@ltu.se;

Keywords: steel, lattice wind turbine towers, structural engineering.

Abstract. *Since sustainable energy production has become essential in order to confine the Greenhouse effect consequences, the number of wind farm installation will continue to rise. In addition, since the tower of on-shore wind power generators is about one third of the initial construction cost, there is additional investigation needed to optimize the tower configuration, aiming in eliminating the initial cost and the material used. To this end, and towards taking advantage of the higher energy potential in greater heights, the wind converters' tower concept needs to be configured to be lighter and taller. Getting inspiration from telecommunication masts that are constructed as lattice towers and taking into account certain transportation restrictions of classic tubular wind tower subparts, the solution of lattice wind turbine towers is implemented aiming to achieve greater tower heights. The structural behavior of telecommunication masts has been investigated in the work of Tsitlakidou et al. and Efthymiou et al. , mainly concentrating on towers consisting of standard L shaped cross-sections fabricated in the factory and mounted on site. For wind converters, the scale of the lattice structure capable of supporting the weight and function of the nacelle is way outside the conventional industrial steel profiles. The lattice tower proposed to accommodate the wind converter has a form of a truncated cone with a square cross-section. This type of tower is a statically determinate system, composed of a certain number of discrete structural sub-systems, each with a certain function and applicability. These sub-systems are: the legs, the bracing trusses on the faces, horizontal braces and secondary bracings arranged in the plane of the face bracing trusses and outside (hip braces). All the aforementioned structural sub-systems serve for a particular role in the load transfer mechanism of the lattice tower and since the whole structure is considered a structurally determinate system, the axial stresses of the members can be determined by closed form expressions. The present paper addresses the stability performance of a lattice steel wind turbine tower, examining alternative solutions of bracings. More specifically the tower has the same height of an equivalent tubular one and bears the same loading. An algorithm has been elaborated in Mathematica software that uses an iterative procedure to design the tower members, the need of secondary and hip bracing and evaluates the total material used. The iterative procedures solves the material optimization problem and provides valuable feedback on the effect of secondary bracings on the economy of the material and the tower's structural robustness.*

1 INTRODUCTION

The fossil fuels shortage and the CO₂ that are exacerbating the greenhouse effect have led to the expansion of renewable energy sources use for energy production. To this end, the European Commission has established the European Union Renewable energy directive accepted by all member States, setting a target of 20% final energy consumption produced by renewable sources by 2020 [1]. Wind energy has been proved as one of the most promising renewable energy sources due to its great potential and infinite nature. Hence its evolution the past ten years has been remarkable. Indicatively the power capacity of wind parks installed in Europe has tripled from about 50 GW in 2005 to over 150 GW in 2016 [2]. Since investments on onshore wind structures are becoming bigger in number, there has been a higher demand for minimizing design, material and construction costs. The tower constituting more than 25% of the initial wind turbine cost [3], needs to be investigated and optimized in terms of morphology and material use. In the present work, the structural configuration of onshore wind turbine

towers is investigated and analysed in terms of structural behaviour and material use. The aim of the investigation is to minimize the wind tower initial construction cost by means of limiting the material while maintaining its robustness.

The tower configurations for horizontal axis onshore wind converters are: the tubular steel tower, the lattice tower and the hybrid tower; which combines a truss structure for the lower part and a tubular one for the upper part. The dominant structural configuration is the tubular steel tower due to its robust structural detailing, easier mounting and limited labour required on site. The tubular tower consists of subsequent tubular subparts, manufactured in the factory and mounted on site by means of bolted flanges with the use of pretensioned bolts [4]. The structural detailing optimization of tubular towers has been investigated by Stavridou et al ([5], [6]) aiming to minimize the total material used while preserving the tower's robustness by inserting internal stiffeners at critical points and keeping the tower wall thickness in minimum levels.

There is a constant increase observed in the height of contemporary wind energy structures and their energy production capacity since there is higher energy potential available at greater heights away from the earth's surface. The tubular tower configuration functions as a simple cantilever structure; hence as the tower increases in height there is a parallel increase in the bottom diameter required. Certain transportation limitations (eg. Bridge span at highways etc.) prevent the towers from having greater diameters and longer subparts. In cases where transportation limitations apply, lattice towers appear as an appealing solution for wind turbine towers. These type of structures had been implemented on telecommunication masts and their structural performance has been investigated explicitly by Tsitlakidou et al.[7] and Efthymiou et al.[8]. The implementation of lattice towers on off-shore and on-shore wind turbines has just been investigated the past years by various research groups like: Zwick et al. [9]; Long et al. [10]; Long and Geir [11]; Gencturk et al. [12] and still their optimal design has not yet been studied. Therefore, there is room for development and optimization of such structures. Telecommunication masts are constructed mostly with the use of standard L shaped cross sections fabricated in the factory and mounted on site. The rotor of a wind converter though is of great weight and produces great loads due to the operation of the blades. This fact leads in the case of wind turbine towers, to cross sections that are well outside the range of standard industrial profiles. A lattice tower that is capable of accommodating the nacelle has the form of a truncated cone with a square cross-section. The tower is a statically determinate lattice structure composed of a number of discrete structural sub-systems; the legs, the bracing trusses on the faces, horizontal braces and secondary bracings arranged inside the plane of the face bracing trusses. These structural subsystems have a particular role in the load transfer mechanism that develops inside a lattice tower and since the tower is a statically determinate structure, the axial stresses of the legs and the bracings can be determined by closed form expressions. The present paper investigates the structural performance of a lattice wind turbine tower of a certain height and examines various alternative configurations in order to achieve structural robustness along with minimum tower weight.

2 TOWER OPTIMIZATION CONCEPT

The lattice tower investigated in the present study and is capable of accommodating the nacelle at the top has the form of a truncated cone with a square base. The structure is statically determinate and composes of discrete structural sub-systems; the legs, the bracing trusses on the faces and the horizontal braces as they are presented in Figure 1. Each of the aforesaid structural sub-systems have distinct roles in the load transfer mechanism of the tower, therefore each sub-system is investigated and optimized separately.

The legs transfer the axial load caused by the horizontal shear and top-moment imported to the lattice structure at its top by the nacelle. The face bracing truss undertakes the transfer of the horizontal shear and the horizontal braces take the out-of-plane buckling of the face bracing truss (FBT) elements. Being a structurally determinate system means that the axial stresses of the tower legs and the FBT elements can be determined by closed form expressions.

The problem of the design of a cross section in a certain member calls for the choice of a cylindrical cross-section that will result to a $N_{b,Rd}$ equal to the design axial force N_{Ed} according to Eurocode EN1993-1-1 [13]. The problem of determining the diameter (D) and the thickness (t) of the most economical cross section can be solved by keeping the D/t ratio to the limiting value of Class-III cross sections i.e. $90 \varepsilon^2$ where ε is given by Equation 1.

$$\varepsilon = (235 + f_y)^{0.5} \quad (1)$$

The whole issue of structural optimization of the given problem is treated by developing a specialized script in Mathematica software [14], which finds the diameter of the tubular cross-section that fulfils the buckling resistance and minimizes the tower weight.

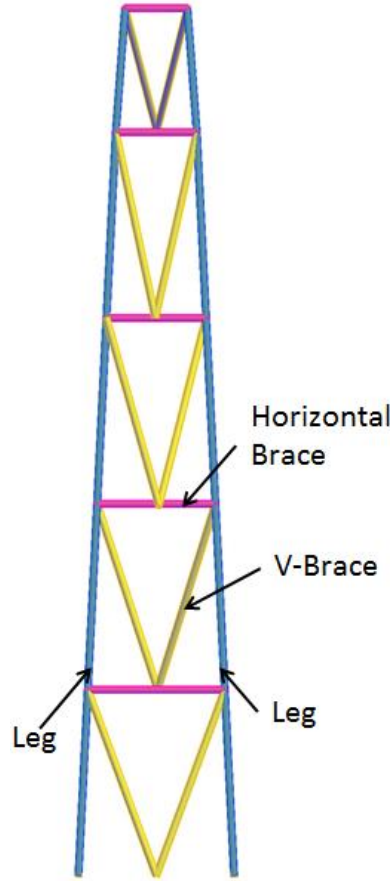


Figure 1. Tower subsystems.

As stated above the different subsystems are optimized separately and certain geometrical parameters have to be taken into consideration for the design of the legs and face bracing trusses (FBTs). The form of the tower is like a truncated cone and among the most popular bracing geometries, the V shaped FBT appears more advantageous since it keeps the total length of the diagonals less than the X brace and the inverted V brace. In order to determine the V brace angle that leads to the minimization of the total FBT weight, a special investigation is being conducted at the beginning of the script. The angle of the V braces that has been proved in all the cases the most favourable was the one of 45 degrees and this angle determines also the buckling length of the tower legs as this length is the length of the segments that the tower is split to by the braces. The normal force that develops in the legs of a tower with a square base is derived from closed form equations and the governing situation for the legs appears when the top shear acts in the direction of the diagonal of the tower. Hence, the axial force is given by Equation 2:

$$N_{45}(z) = \frac{M(z)}{b(z)\sqrt{2}} \times \frac{1}{\cos(\pi/2 - \phi_d)} \quad (2)$$

Where $M(z) = M_{top} + (H - z) \times F_{top}$ is the bending moment of a vertical cantilever acted upon by a moment M_{top} and a horizontal force F_{top} at the tower's top, and $b(z)$ is given by equation 3:

$$b(z) = \frac{B_{top} - B_{base}}{2} \times \frac{z}{H} + B_{base} \quad (3)$$

and ϕ_d is the angle of the leg to the horizontal plane and is given by equation 4:

$$\phi_d = \tan^{-1} \frac{\sqrt{2} \times H}{B_{base} - B_{top}} \quad (4)$$

Using as a reference case the one with constant leg cross-section from bottom to top and therefore constant axial force, there is a characteristic base width given by Equation 5 that keeps the axial force constant.

$$B_{base}^{ch} = B_{top} \frac{M_{top} + H \times F_{top}^H}{M_{top}} \quad (5)$$

Where B_{top} is the top width, M_{top} is the moment at the top of the tower, H is the tower height and F_{top}^H is the horizontal force acting at the top of the tower

Taking all the above into account, the optimization problem of the lattice tower is confined to the search space defined by the two independent variables: B_{top} and μ . The variable μ is a non-dimensional parameter that determines the deviation of the base width from the characteristic and is given by Equation 6.

$$\mu = \frac{B_{base}}{B_{base}^{ch}} \quad (6)$$

The total weight of the tower is determined by the buckling checks described in Eurocode EN1993-1-1 [13]. Working on equation 5 does not guarantee that the result of the design will indeed be of minimal weight as the cross-section of the legs is determined by the buckling checks of Eurocode which is a highly non-linear procedure. In addition the result of the buckling check is up to a point controlled by the buckling length which is controlled by the introduction of secondary braces. Therefore the optimal weight does not come as a result of deriving equation 5, but needs an iterative procedure to take into account and counterbalance the two antagonistic factors that determine the optimal tower design; (a) the parallel increase of the leg axial force along with the reduction of the face bracing weight, when closing the distance between the legs and (b) the parallel reduction of the leg axial force along with the total length and slenderness increase of the V braces, when increasing the distance between the legs

3 RESULTS

As explained in the introduction, the tower subparts are designed and optimized separately. The optimal design of the legs and the braces separately is presented in figure 2 and figure 3 respectively. From all the cases investigated the optimum tower configuration is selected in order to minimize the total material used along with maintaining the tower load bearing capacity. The loads used for the lattice tower design are the same as a real constructed tubular structure of the same height. The total number of lattice tower configuration cases investigated in order to optimize tower weight, are 126. The total weight for the optimal lattice tower solution is 77.47 tn and is given for base width equal to 800mm and μ parameter equal to 0.6.

As the tower is symmetric and the wind load can come from any direction, in each tower subpart the same type of elements are selected to have the same cross-sections. In our case circular hollow cross-sections are used and the optimal tower design is presented in Table 1. It is observed from figure 4 that the tower weight for values of μ equal to 0.8 and lower, the lattice tower is lighter than the tubular one. When μ takes values greater than 0.8 the total tower weight increases radically with the increase of the top width of the tower.

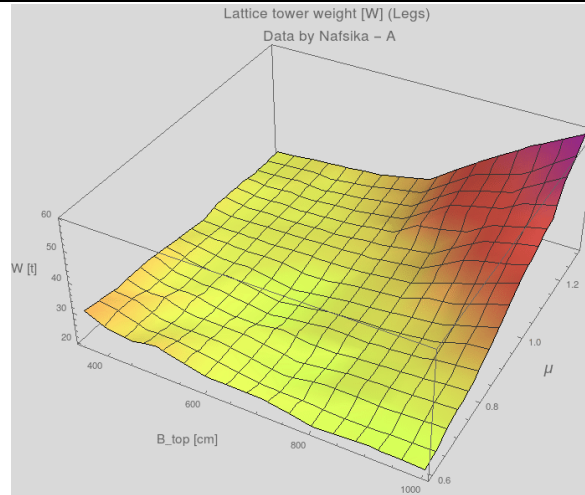


Figure 2. Tower leg weight in comparison to the top tower width and μ .

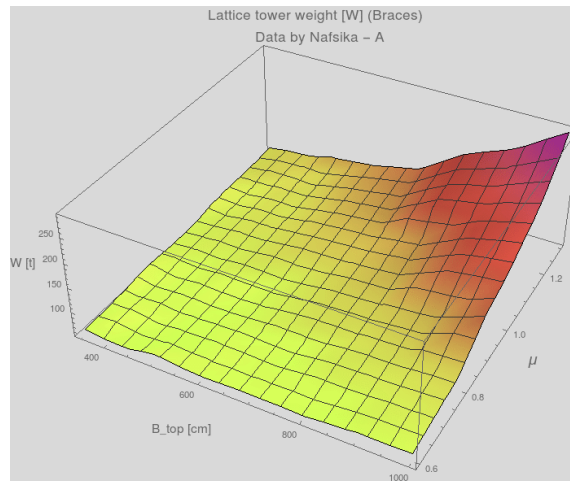


Figure 3. Braces' weight in comparison to the top tower width and μ .

Diameter and thickness of tower cross-sections (mm)					
Legs	P-1	P-2	P-3	P-4	P-5
Diameter	411	371	352	340	286
Thickness	8	8	7	7	5
V-Brace					
Diagonals	P-1	P-2	P-3	P-4	P-5
Diameter	413	385	375	363	253
Thickness	7	7	7	7	5
V-Brace					
Horizontals	P-1	P-2	P-3	P-4	P-5
Diameter	342	282	240	216	214
Thickness	6	5	5	4	4

Table 1 : Example of how to set a table

The tower is almost 30 % of the initial construction cost of a wind turbine. Therefore, the reduction of the material used is of great importance in the economical aspect. When using the lattice solution the total material used is reduced by almost 40 %. Taking also into account the fact that in terms of transportation and in-situ construction, the lattice solution is advantageous in regards to flexibility in transportation and easiness in

mounting, the lattice solution should be taken into consideration for the construction of contemporary wind turbines.

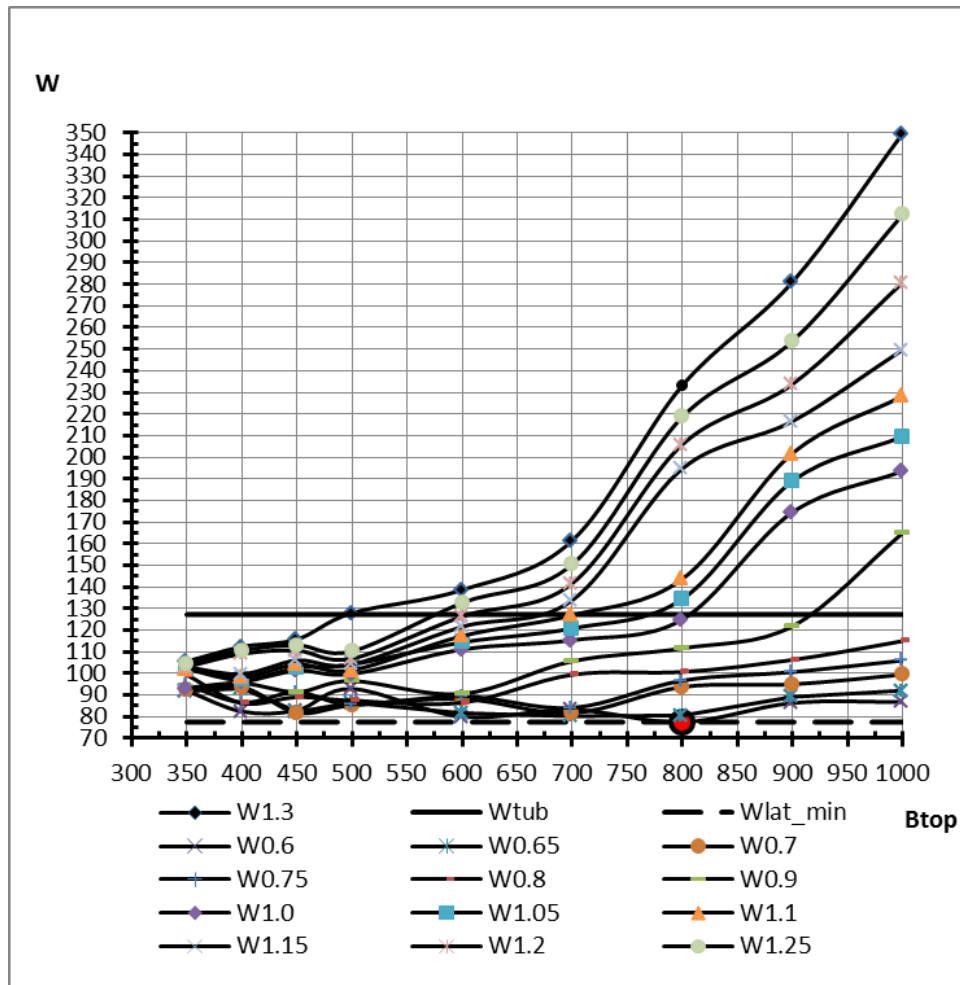


Figure 4 : Total tower weight with regards to top width for given values of μ .

4 CONCLUSIONS

The present study investigates the potential of using lattice wind turbine towers with the prospect of minimizing the total structure weight while preserving its liability and robustness. When constructing taller structures, the minimization of the total material use is of great importance along with the transportation advantages that truss structures exhibit over the tubular ones. Lattice structures when using the appropriate cross-sections for construction of tall structures are proved to be able to sustain great loads with minimum initial material weight. An additional advantage that lattice structures offer is the lower bending moment transferred to the foundation, which facilitates the concrete foundation design and minimizes its construction cost. In the present investigation, a lattice wind turbine of 76.15 meters height has been optimized using a dedicated Mathematica code. The iterative procedure adopted, examines the alternatives of 126 cases and gives back the optimal lattice tower configuration, which minimizes the total tower weight while preserving the structural robustness. The design loads are taken from a real tubular structure and all the alternative lattice solutions are compared in terms of total weight to the tubular one. The optimal lattice tower is 40% lighter than the lattice one, minimizing by almost 15% the total initial construction cost. The advantages that the lattice solution offers in terms of transportation and fabrication, along with the flexibility of its configuration may lead to great and advantageous changes in the configuration concept in wind turbine tower design.

5 ACKNOWLEDGEMENTS



This project has received funding from the European Union's Horizon 2020 research and innovation programme under the Marie Skłodowska-Curie grant agreement No 747921.

REFERENCES

- [1] European Commission. (2017), “Renewable Energy,” EC, Brussels, Belgium, <https://ec.europa.eu/energy/en/topics/renewable-energy> (accessed 07/04/2018).
- [2] Pineda, I., Tandieu, P. (2016), *Wind in Power*, WindEurope, Brussels, Belgium.
- [3] Blanco, M.I. (2009), “The economics of wind energy,” *Renewable and Sustainable Energy Reviews*, Vol. 13(6-7), pp. 1372-1382.
- [4] Lavassas, I., Nikolaidis, G., Zervas, P., Efthymiou, E., Doudoumis, I. N. and Baniotopoulos, C. C. (2003), “Analysis and design of the prototype of a steel 1-MW wind turbine tower,” *Engineering Structures*, Vol. 25, pp. 1097-1106.
- [5] Stavridou, N., Gerasimidis, S., Efthymiou, E. and Baniotopoulos, C. C. (2015), “Investigation of stiffening scheme effectiveness towards buckling stability enhancement in tubular steel wind turbine towers,” *Steel and Composite Structures*, Vol. 19(5), pp. 1115-1144.
- [6] Stavridou, N., Gerasimidis, S., Efthymiou, E. and Baniotopoulos, C. C. (2013), “Modelling of the structural response of wind energy towers stiffened by internal rings,” *Proceedings of the 10th HSTAM International Congress on Mechanics*, Chania, Greece, 25-27 May 2013, pp. 190.
- [7] Tsitlakidou, I., Fanouli, L., Koltsakis, E. and Baniotopoulos C. C. (2005), “Wind and ice design of ground based steel lattice masts,” *Proceedings of the 5th National Conference on Metal Structures*, Xanthi, Greece, pp. 207-214.
- [8] Efthymiou, E., Kaziolas D.N. and Baniotopoulos C. C. (2009), “On the response of steel lattice telecommunication masts under environmental actions and seismic loading,” *Proceedings of the Nordic Steel Construction Conference NSCC2009*, Malmo, Sweden, pp. 375-381.
- [9] Zwick, D., Muskulus, M. and Moe, G. (2012), “Iterative optimization approach for the design of full-height lattice towers for offshore wind turbines,” *Energy Procedia*, Vol. 24, pp. 297-304.
- [10] Long, H. and Moe, G. (2012), “Preliminary design of bottom-fixed lattice offshore wind turbine towers in the fatigue limit state by the frequency domain method,” *Journal of Offshore Mechanics and Arctic Engineering*, Vol. 134(2): 031902.
- [11] Long, H., Moe, G. and Fischer, T. (2012), “Lattice towers for bottom-fixed offshore wind turbines in the ultimate limit state: variation of some geometric parameters,” *Journal of Offshore Mechanics and Arctic Engineering*, Vol. 134(2): 021202.
- [12] Gencturk, B., Attar, A. and Tort, C. (2012), “Optimal design of lattice wind turbine towers,” *Proceedings of the 15th World Conference on Earthquake Engineering*, Lisbon, Portugal, pp. 24-28.
- [13] EN 1993-1-1. (2005), “Eurocode 3: Design of steel structures. Part 1-1: General rules and rules for buildings,” *European Committee for Standardization (CEN)*, Brussels, Belgium.
- [14] Wolfram, S. (1999), “The mathematica,” *Cambridge university press.*, Cambridge, United Kingdom.

EARLY WARNING AND HAZARD ANALYSIS SYSTEM IN REPUBLIC OF SERBIA

Milan P. Protić¹, Zoran D. Bonić²

¹College of Applied Technical Sciences Niš, Serbia, e-mail: protic.milan@ymail.com

²Faculty of Civil Engineering and Architecture, University of Niš, Niš, Serbia, e-mail: zokibon@yahoo.com

Keywords: Landslide, Hazard, Report, Early-warning system.

Abstract. *Landslides are among the most dangerous natural threats to human lives and property, especially in times of dramatic climate change effects on one hand, and urban sprawl and land consumption on the other. Usual landslide triggers are floods and high-yield rainfall, which was the case in the catastrophic cyclone Tamara episode that hit Serbia and surrounding countries in May 2014.*

Landslide reports (in analogue form) greatly underestimated the realistic number of landslides (concentrating more on urgent/acute cases), and was uneven because they were collected by different institutions, depending on the acute needs.

In this respect, it is essential to produce unified large-scale reports of such events and use them for the state-of-the-art hazard analysis and to develop an early-warning system. The actual state of affairs in this field in Serbia is presented in this paper.

1. INTRODUCTION

Landslides comprise an area of land where the process of detachment and displacement of a stone mass across a stable bedding is active. They occur on the slopes and inclines, across a clearly visible area or sliding zone. Landslides belong to the greatest hazards for the population, material property and environment. As the population expands, both in terms of habitation and usage of areas, the risks of the emergence of landslides and considerable damage also increase.



Figure 1. Landslides on the slopes and inclines

The causes for sliding are: additional load of a slope (most often caused by a structure), cutting into a slope (change of slope geometry because of roads construction, or riverbed erosion), change of ground water regime (abrupt drop of ground water table, increase up the slope toe due to the river backwaters, heavy rainfall after a long drought, precipitation of water from sewers, water supply lines, canals...), dynamical impacts in an incoherent soil, clearing of forests on the slopes, freeze-thaw effects, etc..

The global data on the damage and casualties caused by landslide were provided by Lacasse and Nadim (2009.). According to them, there were more than 15 000 casualties caused by landslide in the period 1903-2004, without taking account the cases with less than 10 casualties [4].

The landslides in the territory of the Republic of Serbia are known in more than 70% of the cases and largely investigated. The landslides and rockslides are present in around 25% of the territory of the Republic of Serbia. Around 3.137 of active or potential landslides are known. A part of these landslides presents a hazard for the housing buildings in the populated settlements, while most of them puts the local main roads at risk. They are mostly present in the southeast part of the Pannonian plane and in the Danube riparian area between Belgrade and Smederevo [2].

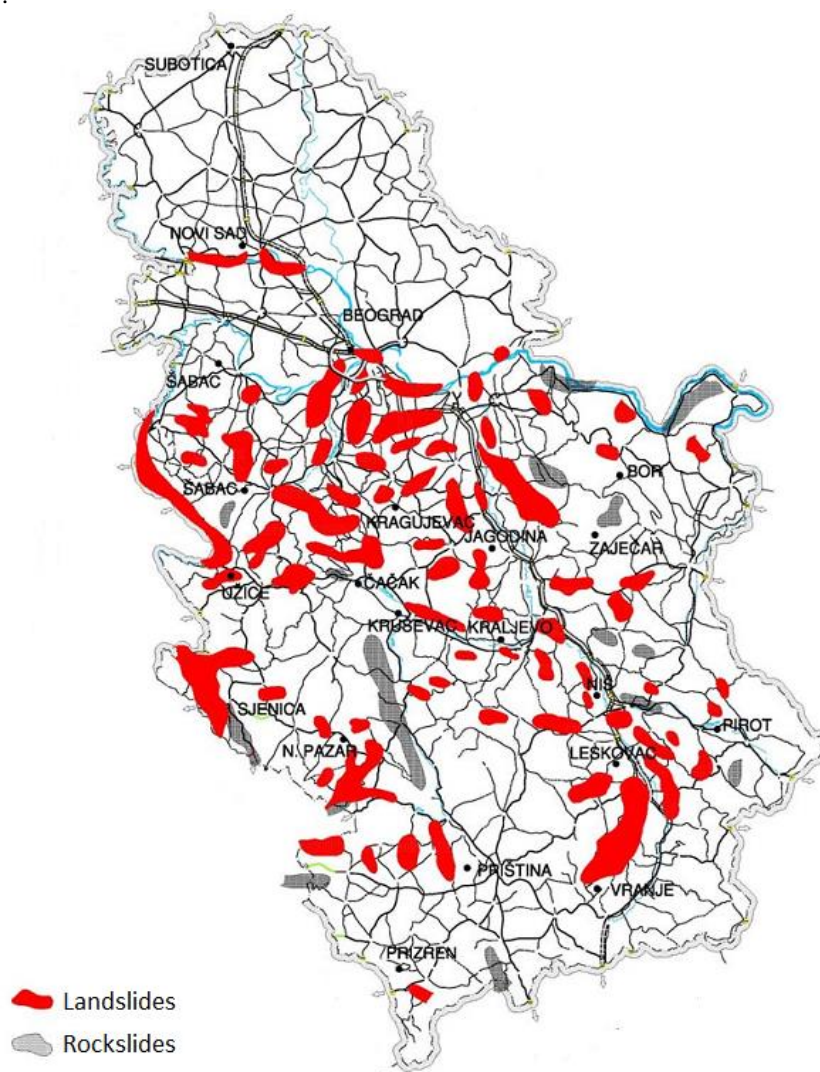


Figure 2. Map of Serbia showing instable areas

For the city of Belgrade and its surrounding area, there is a cadastre of landslides, while for the rest of Serbia, making of the cadastre by several institutions has been underway for number of years, and has not been completed yet.

In order to minimize the risk of human casualties and material damage, it is necessary to have institutions which would react timely and efficiently. This comprises detecting of the signs of sliding, issuing warnings to the population and competent institutions, evacuation and eventually, mitigation of the damage.

The paper analyses efficiency of the operation of the institutions in Serbia in cases of major disasters, and the characteristic example is the Tamara cyclone, which hit Serbia and surrounding countries in 2014.

2. TAMARA CYCLONE AND ITS IMPACTS

In the period from 13th to 18th May 2014 Tamara cyclone hit southeast and central Europe, causing floods and landslides. Serbia and Bosnia and Herzegovina sustained the greatest damage was, with the rainfall exceeding the historical records. Namely, in some localities, the amount of rainfall in three days of May (14th -16th of May) for more than 4 times exceeded the monthly average rainfall.

In the area of western Serbia, the daily amount of rainfall of 15th of May exceeded the normal monthly rainfall of May (RHMS 2014). The maximum rainfall for 48 hours hit Loznica, where the measured value exceeds the once-in-a-thousand-year rainfall, followed by Belgrade and Valjevo where the return period for rainfall was 400 years and Niš with an 80-year return period [3].

Until 20th of May, no less than 62 persons lost their lives. The rainfall set the torrential floods and rockslides into motion, and numerous rivers from the Sava and Morava basins flooded. Over 2000 landslides occurred. According to the official data, over 1.6 million people were affected in Serbia and Bosnia and Herzegovina.

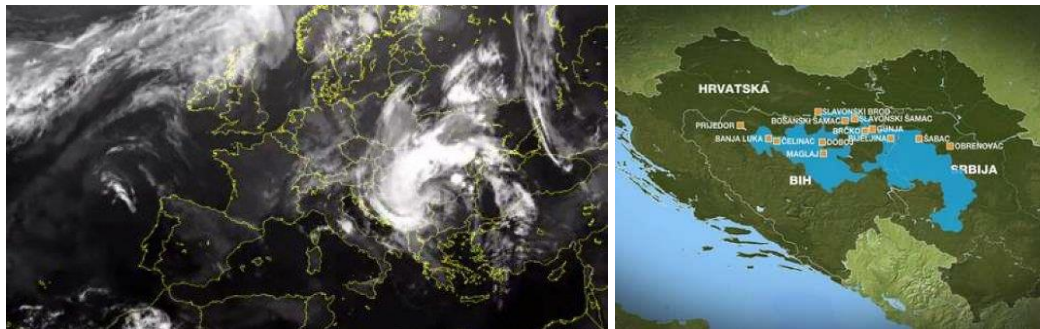


Figure 3. Satellite imagery of Tamara cyclone, and affected areas of Bosnia and Herzegovina and Serbia



Figure 4. Flooded areas in Serbia

Such a large amount of rainfall in the mentioned areas, in addition to floods, torrents and erosions, activated a large number of landslides, and rockslides of various sizes, mechanisms and motion dynamics. The areas most endangered by the landslides can be seen in Figure 5.

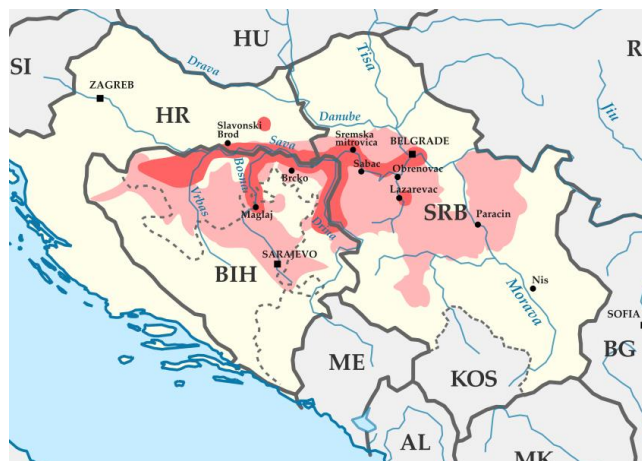


Figure 5. Areas in which landslides occurred

Due to the activated landslides, rockslides and torrential aggradations, a large number of individual and household buildings were demolished, and a number of main and local roads were damaged as well as the bridges on them, and vast agricultural areas were devastated. Many industrial buildings were damaged, too, so the population in the affected area, apart from direct material losses, incurred by the collapse of housing buildings, was additionally affected by losing the jobs. According to some assessments, only the state roads of the 1st and 2nd order sustained damage of over 50 million euro. For the purpose of keeping the roads operational, emergency remedial and prevention measure were undertaken on the state roads. Around 228 landslides and other instabilities on the state road network were fully or partially tackled. A total of 14 landslides and other instabilities on the local road network were repaired.



Figure 6. Landslides caused by Tamara cyclone

3. PREVENTIVE AND REMEDIAL MEASURES FOR LANDSLIDES

For the purpose of remediation of the existing and prevention of potential landslides, the following measures can be undertaken:

- preventive measures,
- emergency remedial measures and
- remedial measures.

The goal of the measures undertaken to deal with the landslides is mitigation of damage which would occur. The remedial measures are procedures bound to minimize the damage and restore the situation into its original condition. However, in order to minimize the damage, it is necessary to implement preventive measures in the most efficient way.

The preventive measures include:

- Mapping of the landslides into the existing maps. In the critical situations, it is necessary to predict what areas would be at the highest risk. There must exist a National Cadastre of landslides, which would be used as a basis for production of prediction maps.

- An Early Warning System. It is a method of geotechnical monitoring used for the assessment of stability of inclines and slopes. It includes various techniques of instrumental observation and monitoring in the real time. The system must be connected to the Emergency situation sector of the local self-governments and at the national level.
- Education and capacity building. Training of the local emergency centers and wider public for reporting and recording of landslides in the territories of local self-governments is a significant step in the organized social action focused on mitigation of natural disaster effects. One of the best ways to inform the population of the importance of a systematic approach to the problems related to the landslides is to present the principle of good and bad practice and provide specific instructions and advice during the training.
- Research of legislative powers. Observation of legal regulations in the area of spatial and town planning, research and remediation of structures and land are the foundations for reducing the hazard of landslides for the population, material and other property, both at the state level and the level of cities and municipalities. For that reason it is important to engage professionals and companies registered for landslide inspection and remediation.

With adequate preventive measures, and with functioning of a global system and data bases, the onset of soil movement would be observed more easily and the system would react in time and warn the competent services. Starting from all this, it is necessary to form a contemporary data base about the processes and phenomena whose existence and effects can indirectly or directly endanger the stability and function of the building in time for the purposes of designing and construction new buildings, and maintenance of the existing structures, especially for the housing buildings and transport infrastructure. The basis should contain: an inventory of (registry) of phenomena, their history of development, maps of “hazards and risks”, data on investigation and success of remediation, quality and quantity assessment of the hazards for an area and structures in it, data on the monitoring during construction and operation, as well as prevention for timely discovery of instability phenomena and timely undertaking of adequate remedial measure [2].

In order to prevent and remedy the described events it is necessary that all the state bodies are well prepared for urgent reaction. Considering that in Serbia, the reaction units in emergency situations in Serbia are the crisis municipal centers, a number of municipalities proclaimed an emergency during Tamara cyclone. However, the lack of a appropriate sliding cadastre and prediction maps of landslide hazard for most of the Serbian territory, or at the level of large territorial units (municipalities/cities), made the operation of emergency centers difficult, when an urgent reaction in the affected areas was necessary. For that reason, a campaign of mapping and recording of landslides was conducted by the most eminent competent institutions dealing with this issue: Geological Institute of Serbia, Transport institute CIP, The Roads Institute, Jaroslav Černi Institute, Minin – geological faculty, etc. Foreign expert teams and groups such as workgroups of the UN, EU and World Bank also took part in the project.

Mapping of the landslides was organized at the level of municipalities and coordinated so that all the municipalities have even criteria and forms for registering of landslides and damage assessment. For every recorded landslide, the following data needed to be entered: exact location, type of phenomenon, dimensions of phenomenon, sketch of the predicted land cross section, motion mechanism, activation date and previous activity status, as well as the relative and quantitative assessment of hazard and damage level. Yet, given that the data on the landslides were collected by various institutions, the reports differed to a great degree, and considering that the field campaign was focused on the most critical locations, many small landslides remained unregistered. In that sense, it was necessary to produce uniform reports on such events and use them for the most contemporary hazard analysis and to develop an early warning system. For that reason, completion of the landslide cadastre in certain municipalities was organized in the framework of the BEWARE project [1].

4. BEWARE PROJECT

Regarding that landslides are a great hazard and that the competences of the governmental bodies and public institutions in the Republic of Serbia are divided, there is need to collect and integrate the data into a single system according to the standards and requirements of the EU, and to make them publicly accessible to mechanical search services. This is a systematic approach to the issue of control and remedy which provides a more quality spatial planning.

For that purpose, in May 2015, conducting of the project “Harmonization of data on landslides and training of local self-governments for their monitoring” under the working title „BEWARE“ (BEyond landslide aWAREness) began.

It is a sub-project of the UNDP initiative for improvement of vitality and readiness for a response to emergency situation in the Republic of Serbia, financed by the Government of Japan, and coordinated through the UNDP Office in the Republic of Serbia for assistance and renovation of the flooded areas and the Ministry of Mining and Energy of the Republic of Serbia [1].

The goals of BEWARE project are:

- Contribution to the methodology of acquiring, processing and production/completion of a data basis of landslides through harmonization and standardization of data; recording of landslides in target municipalities: production of the map of hazards and risks.
- Strengthening of governmental bodies, primarily of the Ministry of Mining and Energy and the Geological institute, for regular landslide monitoring in agreement with the good practice in EU states.
- Production of BEWARE (GIS) web protocol which represents a platform for inspection and reporting of landslides, and accompanying material including the hazard maps.
- Building personnel and material-technical capacities of involved municipalities which can regularly monitor and register landslides in their territories, which is an active participation in completion of the national database of landslides.

The project was realized in 27 target municipalities (according to Figure 7), which were the most affected by the landslides in 2014.

A very important role in terms of sustainability of the project is given to the representatives of local self-governments who are trained for registration of current and future emergence of instability in the territory of their municipalities and cities. For this purpose, appropriate equipment and material was provided and necessary training was conducted.

The equipment of conducting of the Project consisted of one tablet device, one navigation device and a computer with appropriate software. The task of the user – representative of a local self-government is to record the emergence of a landslide by making a field visit, by locating and memorizing the landslide using tablet, and by filling in the accompanying form of the cadastre list and taking photographs of the location.

For the purpose of obtaining as real data on a landslide as possible, it is recommended to visit and record the main scarp and toe of the landslide, and remarkable elements, deformations and ridges, holes and damage on the buildings and infrastructure.



Figure 7. Municipalities in Serbia where BEWARE project was realized

Distribution of registered landslides by municipalities in which the BEWARE project was realized is displayed in Figure 8.

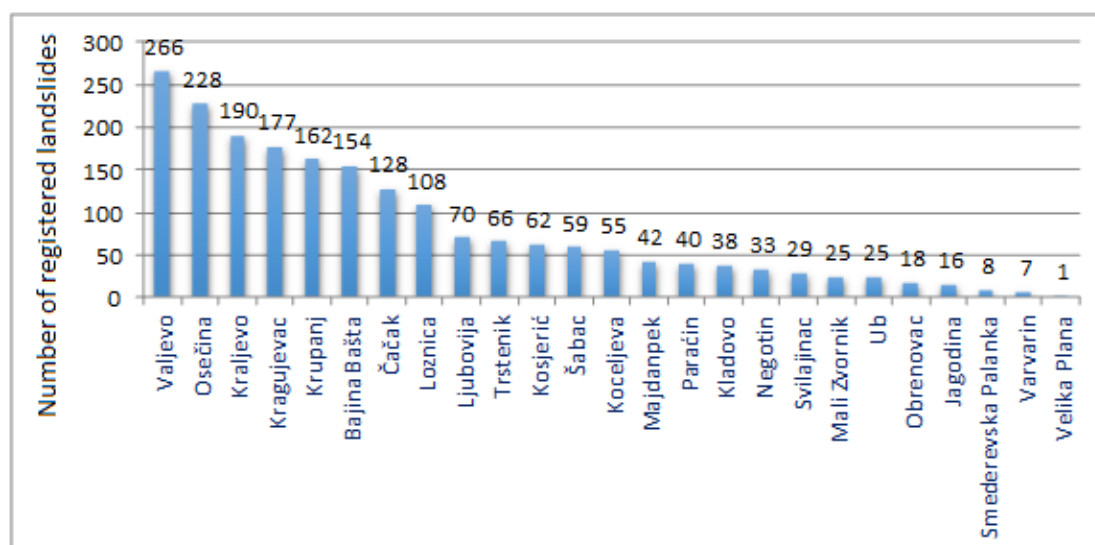


Figure 8. Registered landslides by municipalities in which the BEWARE project was realized

BEWARE project, allows, among other things, formation of a global database which can be continuously completed and updated by the trained personnel from the local self-governments. This provides timely information about the changes which could indicate the onset of danger, so as to react in a proper way and on time.

Further field investigations and analyses are taken over by the appropriate state institutions such as the Geological Institute and other which make the prediction maps of hazards and risks. Hazard comprises probability of emergence of a dangerous event (landslide in this case) with specific characteristics, in a specific time and place. The risk is the measure of expected losses due to the hazard which took place in a specific area during a specific time interval. The expected losses refer to injuries and human casualties and material damage [4].

An example of the hazard map is given for the municipality of Krupanj, which sustained the most damage from landslides from all the mentioned municipalities. The map was made using the AHP method (Analytic Hierarchy Process) and it is displayed in Figure 9.

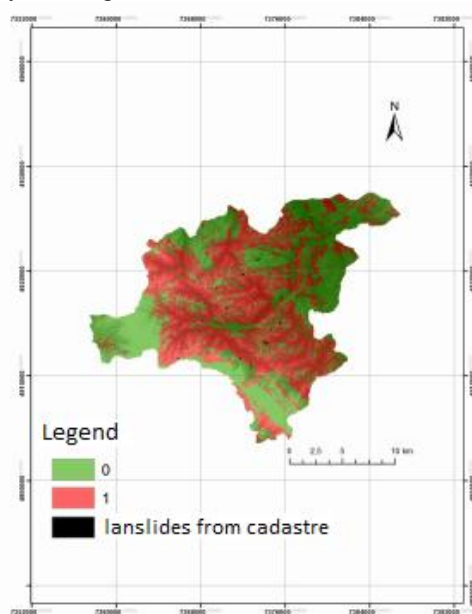


Figure 9. Hazard map for Krupanj municipality

AHP method is a procedure by which several chosen input parameters (digital land model, exposition to sun, energy, relief, slope inclination, distance from the border of units with different hydrogeological function, distance from water courses, vegetative cover and geology) defines the definite land model (susceptibility to sliding). The mentioned factors affect the final model through their severity coefficients (points) whereby all the factors have been normalized (scaled to the same scale, in this case 0-100). Since their impact is simultaneously determined, they demand mutual evaluation, that is, quantification of each individual member in respect to any other. The described AHP method procedure facilitates reduction and control of subjectivity in assessment of input parameters.

5. CONCLUSION

After May of 2014 when Tamara cyclone hit southeast and central Europe and especially Serbia, causing floods and landslides, a need arose to form integrated extensive reports of such events. On their basis, an analysis on a global level could be performed and a system could be developed that would prevent these events and would be capable of issuing a timely working and implementing emergency remedial measures..

Preventive measures comprise permanent activity on recording and monitoring of instabilities. It is necessary to take these location into account when making town plans and designing structures.

It is necessary to adhere to the regulations and whenever possible to avoid instable and potentially instable terrains for building construction, and it is most ration to plant forests on them. It is the most rational preventive approach in management of the land prone to sliding.

6. REFERENCES

- [1] <http://geoliss.mre.gov.rs/beware/>
- [2] Jorić, M., Vujanić, V., Jelisavac, B., (2015), "Klizišta i štete na saobraćajnoj infrastrukturi u Srbiji", *Izgradnja*, Vol. 5-6, pp. 215-225.
- [3] Prohaska,S., Todorović,N., Bartoš Divac, V., Đukić, D., (2015), "Klimatski uslovi koji su prouzrokovali pojavu poplava tokom 2014. godine u Srbiji", *Izgradnja*, vol. 5-6, pp. 169-187.
- [4] Roje-Bonacci, T., (2014), "Klizanje i klizišta", *Hrvatske Vode*, Vol. 22, pp.157-165.
- [5] Vujanić, V., (2007), "Rehabilitacija puteva u uslovima nestabilnih i labilnih terena na prostoru Srbije", *Naučno-stručni skup Rehabilitacija i rekonstrukcija puteva*, Zlatibor, Serbia, 20 – 22 June, 2007.

SMOOTHING TECHNIQUES ON PRECIPITATION TIME SERIES

Mladen Milanovic¹, Milan Gocic², Slavisa Trajkovic³ and Maja Stanojevic Gocic⁴

^{1,2,3} Faculty of Civil Engineering and Architecture
University of Nis

A. Medvedeva 14, 18 000 Nis, Serbia

e-mail: ¹mmsmladen@gmail.com, ²mgocic@yahoo.com, ³slavisa@gaf.ni.ac.rs

⁴ College of Applied Professional Studies
Filipa Filipovica 20, 17000 Vranje, Serbia

e-mail: ⁴majastanojevic30@gmail.com

Keywords: Forecast, smoothing, precipitation, Serbia.

Abstract. *One of important elements in natural hazards analysis is forecast of time series. It is necessary to prepare data before forecasting i.e. to spot and to separate the periodic component of the time series, because periodicity usually has large periods of oscillation, which can bring significant problems in interpreting obtained results. Smoothing technique which is based on removing a random component and uncovering a long-term macro-periodicity can be used for solving this problem.*

This paper analyzes different smoothing techniques for precipitation time series in Serbia for the period 1946–2015. Three smoothing methods were analyzed (moving average method, exponential smoothing and Holt-Winters forecasting model) in order to investigate their applicability in analyzing of precipitation series.

1 INTRODUCTION

A time series can be defined as a sequence of observations indexed by time, ordered in equally spaced intervals. The main aim in the analysis of a time series is to determine the model which would describe the behavior of the observed dynamic system, and to foresee its behavior in the future, based on the behavior in the past and in the present.

Precipitation is one of the main elements of the hydrological cycle, so understanding its behavior can be of great social and economic importance. Precipitation is a highly, spatially and temporally variable climatic parameter at different time scales (inter-annual and intra-annual). Forecasting precipitation may solve some of the complexities of the atmospheric system. The smoothing methods allow an analysis of the basic tendency of the time series, but they also have a wider application in forecasting the future values of the time series.

Many authors have used different smoothing techniques for forecasting time series [10-14]. Ferbar Tratar and Strmčnik in [8] presented short- and long-term heat load forecasting approach for monthly, weekly and daily bases. The comparative analysis for forecasting was conducted between multiple regression and exponential smoothing methods. Results shown that multiple regression was the best forecasting method for daily and weekly short-term heat load forecasting and Holt-Winters method was the best for both long-term and monthly short-term heat load forecasting. In order to evaluate forecast accuracy, simple exponential smoothing method was used on the data of primary production of electricity in Slovakia [11]. Smoothing constant with increments of 0.01 was analyzed. Three forecasting accuracy techniques were used to select the most accurate forecast for one year ahead. Results shown that smoothing constant achieves the best accurate using values 0.26 and 0.29.

In order to determine which smoothing technique is the most applicable to the precipitation time series in Serbia, this paper presents a comparative analysis of three smoothing techniques on the precipitation time series at five meteorological stations on the territory of Serbia for the period 1946–2015.

2 STUDY AREA

The climate in Serbia is temperate continental, with very hot summers and cold short winters. The average air temperature is 10.9 °C. January is the coldest month, while July is the hottest. The average annual precipitation is 896 mm. May and June are the months with the highest level of humidity, and February and October are months with the lowest level of humidity.

The study area in this paper is the territory of Serbia, which is observed through five meteorological stations.

Table 1 gives an overview of the geographical characteristics of the observed stations. The precipitation data from 1946 to 2015, which was used in this paper, had been taken from the meteorological yearbooks issued by the Republic Hydrometeorological Service of Serbia (RHMS).

Station name	Longitude (E)	Latitude (N)	Elevation (m a.s.l.)
Nis	21°54'	43°20'	204
Vranje	21°55'	42°33'	432
Negotin	22°33'	44°14'	42
Novi Sad	19°51'	45°20'	86
Kragujevac	20°56'	44°02'	185

Table 1: Geographical description of the meteorological stations used in this study

Figure 1 shows the annual amount of precipitation for the five observed stations. The highest amount of precipitation was recorded at the Negotin station in 2014 (1237 mm), while the Novi Sad station had the lowest value of precipitation of 287 mm in 2000.

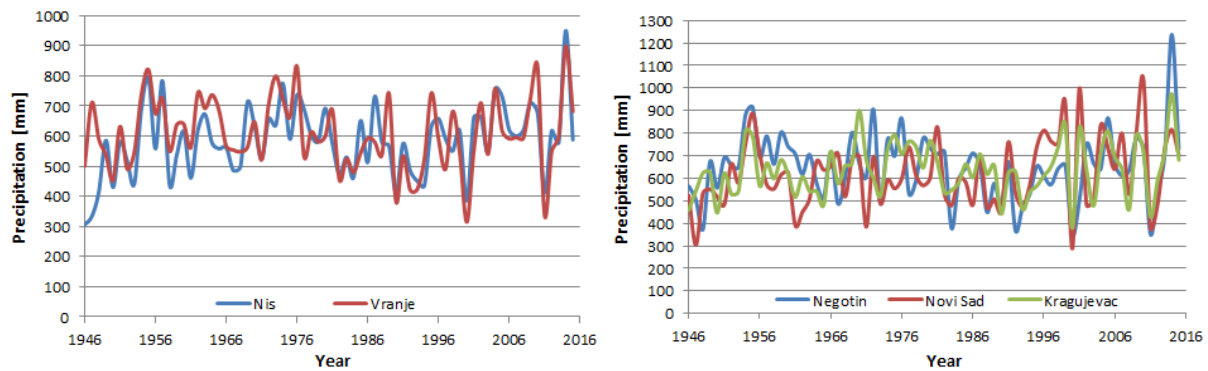


Figure 1. Annual precipitation for meteorological stations

The statistics of the time series for monthly precipitation at five stations during the period 1946-2015 are summarized in Table 2. It can be concluded that the Nis station has the lowest mean value of precipitation (48.69 mm), while Negotin has the greatest one, with 54.03 mm during the observed period of 1946-2015. The skewness values show that there is strong skewness at all the observed time series.

Time series statistics	Nis	Vranje	Negotin	Novi Sad	Kragujevac
Mean	48.69	50.57	54.03	51.64	52.96
Standard deviation	31.52	32.87	40.63	35.91	35.07
Coefficient of variation	64.74 %	64.95 %	75.21 %	69.54 %	66.21 %
Skewness	1.08	1.01	1.45	1.30	1.42

Table 2: Statistics of time series for the observed meteorological stations

3 METHODOLOGY

3.1 Moving Average

The moving average (MA) method is based on calculating the average of the observations, and using that average as the predictor for the next period [1]. According to [2], the moving average method is highly dependent on n , the number of terms selected for constructing the average. The n -period moving average uses the actual value of the last n periods to forecast the next period value. Forecasting is more stable if the method includes a large number of recent actual values, but a small number of recent actual values makes forecasting more responsive. In this method, each value has the same importance in the calculation, regardless of whether it is recent or from a more distant past. The equation for calculation is [7]:

$$F_{t+1} = (Y_t + Y_{t-1} + Y_{t-2} + \dots + Y_{t-n+1}) / n \quad (1)$$

where:

F_{t+1} = the forecast value for the next period,

Y_t = the actual value at period t ,

n = the number of terms in the moving average.

3.2 Simple Exponential Smoothing

The simple exponential smoothing (SES) method was developed by Brown and Holt in the 1950s [3, 4]. A weighted moving average of past data is used as a forecasting basis in this method. The SES gives the greatest weight to more recent observations and lower weight to observations in more distant past [5]. The method is calculated using the equation:

$$F_{t+1} = \alpha Y_t + (1 - \alpha) F_{t-1} \quad (2)$$

where:

F_{t+1} = the new smoothed value or the forecast value,

α = the smoothing constant,

Y_t = the new observation or actual value of the series in period t ,

F_t = the old smoothed value or forecast for period t .

According to [5], the accuracy of this smoothing method depends on the value of α , whose values are between 0 and 1. α serves as the weighing factor, and when α is close to 1, this means that the new forecast will include a substantial adjustment for any error that occurs in the preceding forecast. On the other hand, when α is close to 0, the new forecast is very similar to the old forecast. The SES is the best suited for short-term forecasting, and it is not suitable for long-term forecasting.

3.3 Holt-Winters

The Holt-Winters (HW) method represents a smoothing technique which utilizes simple exponential smoothing to estimate the values of the level, trend and seasonality, which are the three basic components of a time series [6]. There are many variations of the Holt-Winters model, but additive and multiplicative methods are mostly used [8]. When the seasonal variations are roughly constant through the series, the use of the additive method is preferred. The multiplicative method is usually preferred when the seasonal variations are changing proportionally to the level of the series. According to the observed time series, the Holt-Winters additive seasonal technique was used in this paper. The equations for the determining of this method are:

$$L_t = \alpha(Y_t - S_{t-s}) + (1 - \alpha)(L_{t-1} + b_{t-1}) \quad (3)$$

$$b_t = \beta(L_t - L_{t-1}) + (1 - \beta)b_{t-1} \quad (4)$$

$$S_t = \gamma(Y_t - L_t) + (1 - \gamma)S_{t-s} \quad (5)$$

$$F_{t+m} = L_t + b_t m + S_{t-s+m} \quad (6)$$

where:

L_t = smoothed estimate of the level at time t ,

b_t = smoothed estimate of the change in the trend value at time t ,

S_t = smoothed estimate of the appropriate seasonal component at t ,

F_{t+m} = forecast for m period,

α, β, γ = smoothing constants,

m = number of forecast,

Y_t = the new observation or the actual value of the series in period t .

The values of the smoothing constants are between 0 and 1, and they should be set to minimize the discrepancies between the predictions and observed values. Dependence on historical data in the Holt-Winters method is low, and depends on all previous values, with the most weight given to the most recent values. This method is suitable for short-term and for long-term forecasting.

3.4 Measuring Forecasting Error

In order to carry out the comparative analysis of proposed smoothing methods, four statistical tests were used (mean square error – MSE, root mean square error – RMSE, mean absolute percentage error – MAPE, mean absolute error - MAE). MSE represents the measure which is a generally accepted technique for evaluating smoothing methods. This technique is a measure of overall accuracy that gives an indication of the degree of spread of analyzed method. RMSE technique gives information on the short-term performance of the model. MAPE is the most useful measure to compare the accuracy of forecasts since it measures relative performance of methods. According to [9], MAPE is one measure of accuracy commonly used in quantitative methods of forecasting. MAE is also a measure of overall accuracy that gives an indication of the degree of spread, but in case when all errors are assigned equal weights. Equations for calculation of proposed errors are:

$$MSE = \frac{1}{n} \sum_{t=1}^n (Y_t - F_t)^2 \quad (7)$$

$$RMSE = \sqrt{\frac{1}{n} \sum_{t=1}^n (Y_t - F_t)^2} \quad (8)$$

$$MAPE = \frac{1}{n} \sum_{t=1}^n \frac{|Y_t - F_t|}{Y_t} \quad (9)$$

$$MAE = \frac{1}{n} \sum_{t=1}^n |Y_t - F_t| \quad (10)$$

where:

Y_t = the actual value in time period t ,

F_t = the forecast value in time period t ,

n = the number of forecast observations in the estimation period t .

4 RESULTS AND DISCUSSION

The results of the four statistical tests for the analyzed smoothing techniques are shown in Table 3. The table shows that the MA and SES are the best smoothing methods for the precipitation data from the Nis, Vranje, Negotin and Kragujevac stations, and the MA method is especially good for the data from the Novi Sad station.

According to the MSE test, the MA smoothing method has the greatest similarity with the observed precipitation for all the stations. The MAPE shows that the SES method has the greatest similarity with the observed precipitation, and the RMSE and MAE tests show the same results as the MSE. The overall overview of Table 3 shows that the best method (with the best fitting between the smoothed and the original series) for smoothing is the moving average smoothing method.

Station	Statistics	Moving average (MA)	Simple Exponential (SES)	Holt-Winters (HW)
Nis	MSE	946.66	1007.46	1011.74
	RMSE	30.77	31.74	31.81
	MAPE	140.98	135.71	140.20
	MAE	23.77	24.10	24.22
Vranje	MSE	1030.85	1122.58	1128.84
	RMSE	32.11	33.50	33.60
	MAPE	141.45	141.16	144.61

	MAE	25.17	25.91	26.06
Negotin	MSE	1576.80	1678.17	1694.15
	RMSE	39.71	40.97	41.16
	MAPE	233.79	230.91	237.55
	MAE	30.20	30.84	31.06
Novi Sad	MSE	1202.51	1295.74	1372.75
	RMSE	34.68	36.00	37.05
	MAPE	187.94	191.15	192.13
	MAE	26.42	27.16	28.21
Kragujevac	MSE	1175.54	1256.03	1271.06
	RMSE	34.29	35.44	35.65
	MAPE	117.51	116.86	121.36
	MAE	26.24	26.96	27.42

Table 3: Results of statistical tests for three smoothing techniques

5 CONCLUSION

The paper presents the analysis of three smoothing techniques (the moving average, the simple exponential and the Holt-Winters method) on the monthly precipitation data from five meteorological stations in Serbia. The main aim of this analysis is to determine which smoothing technique is the most applicable for the used series.

The analysis of statistical tests at the station level shows that the moving average and simple exponential smoothing methods are the most suitable for use. Statistical tests single out the moving average method as a method with the best fitting of the smoothed and the original precipitation series, while the Holt-Winters method has the worst fitting between the smoothed and the original series.

Further studies will be oriented towards the analysis of robust smoothing techniques, and studies which apply more sophisticated forecasting techniques, such as Box Jenkins and neural networks.

ACKNOWLEDGEMENT

The research presented in the paper is funded by the Ministry of Education, Science and Technological Development of the Republic of Serbia (Grant No. TR 37003) and ERASMUS+ KA2 CBHE project "Development of master curricula for natural disasters risk management in Western Balkan countries (NatRisk)" (Contract number 573806-EPP-1-2016-1-RS-EPPKA2-CBHE-JP).

REFERENCES

- [1] Jarrett, J. (1991) *Business forecasting methods*, Blackwell Publishers, Cambridge.
- [2] Levine, D. M., Berenson, M. L., Stephen, D. (1999) *Statistics for managers using Microsoft Excel*. Prentice-Hall, New Jersey.
- [3] Brown, R. G. (1959) *Statistical Forecasting for Inventory Control*, McGraw-Hill, New York.
- [4] Holt, C. C. (1957) *Forecasting trends and seasonals by exponentially weighted averages*, O.N.R. Memorandum 52/1957, Carnegie Institute of Technology, Pittsburgh.
- [5] Hanke, J. E., Wichern, D. W., Reitsch, A. G. (2001) *Business forecasting*, Prentice-Hall, New Jersey.
- [6] Makridakis, S., Wheelwright, S. C. (1978) *Forecasting: Methods and Applications*, Wiley/Hamilton, New York.
- [7] Mendenhall, W., Sincich, T. (2012) *A Second Course in Statistics: Regression Analysis*, Prentice Hall, New Jersey.
- [8] Ferbar Tratar, Lj., Strmcnik, E. (2016) "The comparison of Holt-Winters method and Multiple regression method: A case study", *Energy*, Vol. 109, pp. 266-276.
- [9] Makridakis, S., Wheelwright, S. C., Hyndman, R. J. (1998) *Forecasting methods and applications*, Wiley, New York.
- [10] Ryu, K., Sanchez, A. (2003) "The Evaluation of Forecasting Methods at an Institutional Foodservice Dining Facility", *Journal of Hospitality Financial Management*, Vol. 11, pp. 27-45.
- [11] Ostertagova, E., Ostertag, O. (2012) "Forecasting Using Simple Exponential Smoothing Method", *Acta Electrotechnica et Informatica*, Vol. 12, pp. 62-66.

- [12] Sudheer, G., Suseelatha, A. (2015) "Short term load forecasting using wavelet transform combined with Holt-Winters and weighted nearest neighbor models", *Electrical Power and Energy Systems*, Vol. 64, pp. 340-346.
- [13] Ferbar Tratar, Lj., Mojskerc, B., Toman, A. (2016) "Demand forecasting with four-parameter exponential smoothing", *International Journal Production Economics*, Vol. 181, pp. 162-173.
- [14] Bermudez, J. D., Corberan-Vallet, A., Vercher, E. (2009) "Forecasting time series with missing data using Holt's model", *Journal of Statistical Planning and Inference*, Vol. 139, pp. 2791-2799.

GIS APPLICATION IN FLOODS RISK ASSESSMENT IN LEPOSAVIC

Stanojevic Predrag¹, Djokic Jelena², Zivkovic Bojana³, Rajovic Jelena⁴

¹Technical College of Applied Sciences, Urosevac (Leposavic), Kosovo*
e-mail: stanojevicpredrag@yahoo.com

²Faculty of Technical Sciences, Kosovska Mitrovica
e-mail: jeladjokic7@gmail.com

³Technical College of Applied Sciences, Urosevac (Leposavic), Kosovo*
e-mail: bojanaz1981@gmail.com

⁴Technical College of Applied Sciences, Urosevac (Leposavic), Kosovo*
e-mail: gvozdena2001@yahoo.com

Keywords: Flood, risk assessment, GIS.

Abstract: *In this paper are presented the risk assessment and mapping of all rivers in Leposavic Municipality that have been flooding or have a potential for flooding of agriculture land, houses, roads, bridges and other objects. For each river, those flooded or potentially flooded surfaces are presented by category of risk (high risk, medium risk and low risk) as well as the causes of the flooding and recommendations for short term and long term activity protection against floods. This risk assessment and mapping shows exact places where they are causing damage and proposes activities that need to be taken to eliminate these damages. By analyzing the locations and vicinity of the human activities, it sets the river priority for intervention. This is enabled by information presented through the Geographical Information System Elements (GIS) of the Water Framework Directive. Although the information presented by GIS depends on the availability of the spatial and field data, it is valuable tool in risk assessment in determining the cumulative sensitivity of the certain region to the floods.*

I. INTRODUCTION

An exceptionally mild winter with hardly any snow has triggered extremely heavy rainfalls during April 2014 and 2015. The rains have caused floods leading to significant infrastructure damage to several communities in Kosovo*. According to the Hydrometeorological Institute April 2014 was the wettest month in recorded history, with 19 days of heavy rainfalls causing flash floods in a number of areas throughout Kosovo*.

As a result of the heavy rainfalls northern Kosovo*, especially the municipalities of Leposavić and Zvečan, was heavily affected by floods. Luckily, the floods did not cause human victims; however, dozens of agricultural plots were affected, thus hindering normal planting process. The infrastructure was seriously damaged, especially bridges and roads. Their state have been significantly worsen during floods.

Scarce technical and financial resources only increased vulnerability of these municipalities. The municipal authorities undertook all efforts to provide assistance to the people in need, to ensure communication and traffic between banks of the Ibar River, and to clean, where possible, riverbeds of the Ibar and its tributaries. Further efforts of the municipalities and international organizations were aimed at restoring the infrastructure and taking measures to protect population and their property from floods in future.

Flood is a recurrent emergency in northern Kosovo*, which takes place almost every year and more or less in the same time of the year. Nevertheless, neither municipal authorities nor landowners seem to have learnt any lessons of preventive behaviour. As an eloquent example, similar breakdown of bridges of the same construction type [1], happened as a result of floods in 2013, 2014 and 2015. Landslide in Zubin Potok, which luckily did not cause any human victims, although triggered by rainfalls, was eventually a result of human miscalculation, poor design and absence of protective measures. It was evaluated that any consequences of floods could have been avoided if basic principles of safe behaviour had not been ignored. Recommendations on flood prevention mainly include necessary measures that should be taken to physically prevent devastating impact of floods. Necessary preventive measures should be taken also at legislative level and in legislation enforcement [2].

In this report are presented all rivers that have been flooded or have a potential that in the future may flood land, houses, roads, bridges and other objects. The soil properties on the river banks are analyzed for their rock composition, as well as for their water contents and hydraulic heads. Each river that flooded surfaces is presented by category of risk (high risk, medium risk and low risk) as well as the causes of the flooding and

recommendations for activities how to eliminate flooding. Rivers are ordered by priority. Priority is based on the damages that can be caused by a possible flooding. There was also introduced the map of anti-erosion activities that need to be taken in the river basins. This is enabled by information presented through the Geographical Information System Elements (GIS) [3] of the Water Framework Directive. Although the information presented by GIS depend on the availability of the spatial and field data, it is valuable tool in risk assessment in determining the cumulative sensitivity of the certain region to the floods [4].

2. STUDY AREA AND METHODOLOGY

Leposavić municipality

The municipality of Leposavić is the northeast municipality in Kosovo. It covers an area of approximately 750 km² and includes Leposavić town and 72 villages. According to the municipal administration the total population is estimated at 18 900 persons. The whole territory of Leposavić municipality is predominantly mountainous, with most of the settlements lying along the Ibar River and its tributaries in the valley and on the lower slopes.

The economy of Leposavić municipality is mainly based on agriculture and small trade businesses. There is no reliable data on the number of registered businesses and number of people employed in private sector. The terrain data are imported from WebGIS in a form of SRTM Digital Terrain Files, N42E020.hgt and N43E020.hgt with horizontal datum WGS84 and presented in Fig.1 a) and b)

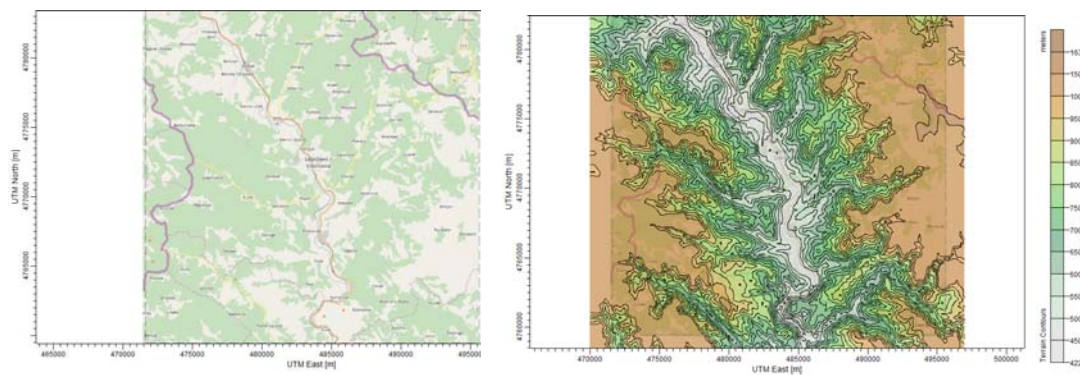


Fig.1. Leposavic Municipality area a) UTM location, b) Terrain data

GIS is the most complete information system for modeling, analyzing spatial data and displaying community vulnerability. When we identify hazard locations with critical infrastructure, processed GIS Models can be useful for determination of event impact and necessary mitigation requirement. Preparedness is important when disastrous event occurs. On analysis of risk and hazards is beneficial in Emergency management program.

Disaster and emergency management in situational awareness is essential thing. GIS techniques plays vital role to provide location information of the event, that is, where is the event happened and what happening exactly in real time. Also by linking people, processes spatial information situational awareness established. GIS map interface important in handling emergency condition.

To achievement of preparedness, gathering of information and its advance data storing is important. In GIS, integration of information from other sources is possible. GIS solution is a standards-based. Accurate cataloging of GIS data provide useful information during emergency conditions.

GIS provides right information in the phases of disaster management:

- Preparedness and planning of disasters
- Forecasting and early warning of disastrous event
- For relief management, rescue operations

GIS database with various themes is helpful to disaster managers in decision making process when catastrophic event occur.

The following information were taken from GIS database:

1. Different satellite images OS for GIS data creation and preparation of hydro geomorphologic map, slope map, terrain map, and DEM generation in GIS for disaster planning in Leposavic Municipality area.
2. Macro and micro level maps used for identifying vulnerability and threat conditions.
3. Identification of safe locations and zones for rehabilitation

4. Road and location maps used for finding alternate routes, shelters and locations
5. Planning of evacuation and operation
6. Management of Rehabilitation and post-disaster reconstruction.

3 RESULTS AND DISCUSSION

3.1. Hydrology data

For the purpose of this study there were a lot of data obtained in the location in consultation with residents of the district, with the responsible persons in the respective municipalities, in different maps, different studies and researches. Leposavić municipality is characterized with a very developed river network. Ibar river is the main river of the municipality. This river passes in the middle of the municipality and divides it nearly into to equal parts. All rivers that belong to this municipality discharge into Ibar river. So, they are branches of this river. All branches of this river have torrential characteristics, which mean that the imbalance between minimal and maximal quantity of water is big. These rivers are dangerous in the time when precipitations are big and last for a short time. Therefore, residents are not prepared and the damages are big, in humans, objects and agricultural lands. The information on rivers and the catchments are enabled by information presented through GIS, and presented in Table 1. and Fig.2.

Table 1. Rivers in the research area of Leposavic and their catchment areas

River Name	Length	Discharge Elevation	Highest Elevation	Slope	Kategory	ID1	Geometry_S K	Catchment_Area_Km
Vucanska r.	18534.589 m	458	1270	4.4%	Secondary River	19	1blw:	28.8
Josanicka r.	17594.882 m	447	1145	4%	Secondary River	21	1blw:	57.1
Trebicka r.	7439.812 m	435	880	6.0%	Secondary River	23	1blw:/	11.2
Trifunski p.	3035.226 m	425	780	11.8%	Secondary River	25	1blw;;f	3.9
Kremenjack i p.	2307.715 m	428	825	17.3%	Secondary River	26	1blw:	6.3
Lesanska r.	4051.466 m	432	900	11.7%	Secondary River	27	1blw:0	6.8
Ostracki p.	5201.819 m	430	930	9.6%	Secondary River	28	1blw:	5.8
Zigoljski p.	4803.892 m	431	1030	12.5%	Secondary River	29	1blw:0	4.1
Bistricka reka	12595.535 m	427	1440	8.0%	Secondary River	30	1blw:	31.4
Dobravska r.	14785.241 m	448	1480	6.9%	Secondary River	42	1blw:>	28.4
Tvrđjanska r.	16577.017 m	440	1320	5.3%	Secondary River	44	1blw:>	41.7

Based on the obtained data the hydrology situation in Leposavic is presented in Fig.2.

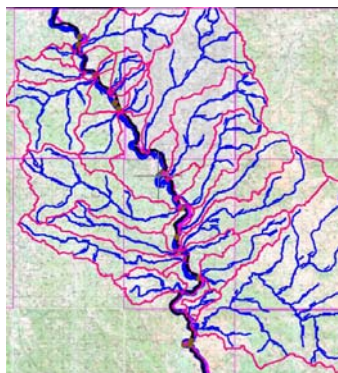


Fig.2. River Ibar Catchment in Leposavić Municipality

In the territory of Leposavić municipality there are eight rivers of which flood or have the potential for flooding of land and buildings, as shown in the Table 1. However, in this paper there will be presented just two of them, Cerajska river and Socanicka river, influencing the total River Ibar Catchment, as presented in Fig. 5.

River Cerajska reka, in the segment from the bridge in Kosovska Mitrovica-Leposavic road to discharge into Ibar and 200m above the bridge, very often floods lands and the road to Monastery. The road floods in length of 25m. Floods happen because people that live nearby have reduced the transversal profile of the river, by planting trees in the riverbed and by filling it with soil and by throwing rubbish in the riverbed. The risk assessment is presented in Fig.3.

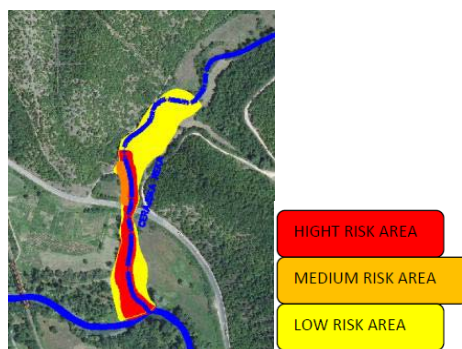


Fig.3. Risk assessment of the Cerajska Reka

In the region of Socanicka river, Floods happen because during the rainfall the river brings a lot of alluvium from the upper basin. This alluvium is deposited in the flat part of the river and creates a natural “dam” and the river comes out of its bed forming new route and floods lands. Another reason is also reduction of transversal profile because people are trying to protect their fields from floods, so they plant trees near the river and also throw rubbish in the river.

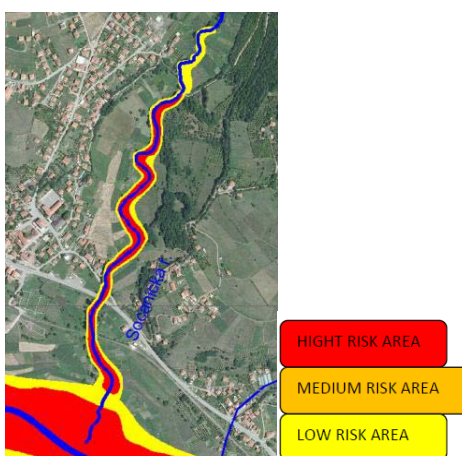


Fig. 4. Risk assessment of Socanicka river

These rivers are examples of the on-site situations along the river Ibar Catchment. The source and mechanism of flooding in a the river Ibar basin is different at different times in the year and in a different segments, depending on the terrain. Therefore different flood management responses may be required in different river basin segments or at different times of the year. This region is facing mainly to flush flooding in upland areas. These floods pose great challenges to the national meteorological services, the emergency services and local communities, in the area of flood forecasting, warning, emergency preparedness and response.

The recently published result of the Fourth Assessment Report under the Intergovernmental Panel on Climate Change (IPCC) indicates that Europe is likely to see more flash floods in future.

Flash floods are particularly hazardous to life and property because **i)** typically they develop in steep upland areas and reach their peak within a matter of hours, so there is limited time for warning, mitigation and evacuation **ii)** being in upland areas, the river channel gradients are steeper than normal and the river corridor is narrow, so the velocity and the depth of the flow are high, meaning they have high destructive potential. The risk assessment of the Ibar river basin segment in Leposavic municipality is presented in Fig.5. As shown in the fig.5. the endangered area is mainly agricultural, with roads and bridges along the river.

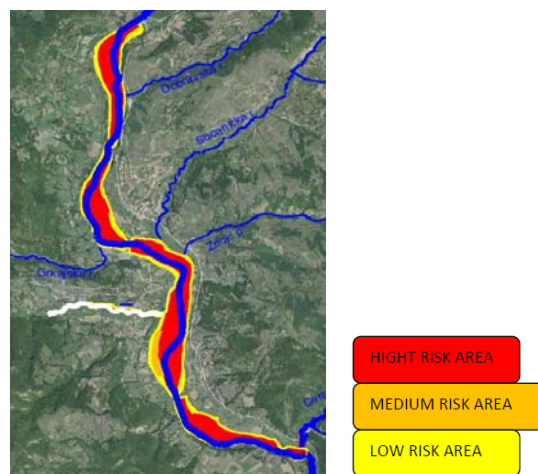


Fig.5. Risk assessment of the Ibar river basin segment in Leposavic municipality

High	1124061 m ²	agriculture land, Bridges, Roads
Low	1512430m ²	agriculture land,Bridges, Roads
Medium	27562m ²	agriculture land, Roads

4. CONCLUSIONS

In order to mitigate the causes of flooding the following measures should be taken:

1. Technical-construction Measures
 - Placing of concrete or stone thresholds in certain places along the river or its branches;
2. Technical flood-way measures
 - Checking for the possibility of building a catchment (small reservoir) which could be used for other purposes (drinking water, recreation, electricity production, irrigation, etc.) ;
3. Technical –forestry measures
 - Stopping of cutting trees in the entire river basin and planting new seedlings;
4. Educational and propaganda measures
 - Awareness of residents through lectures at schools, promotion of documentary films, books and printing of different brochures;
 - Prohibition of disposal of garbage in the river bed;
 - Maintenance of the river basin and surrounding environment.

The aforementioned activities are mainly related to defense planning from erosion that has been a major flood factor of the river in the above mentioned segment

REFERENCES

- [1] J. Đokić, N. Arsić, S. Jović, P. Stanojević, DESK STUDY ON ASSESSMENT AND RECOMMENDATIONS IN INFRASTRUCTURE REHABILITATION IN POST DISASTER PERIOD, International Scientific conference: IMPACT OF CHANGES IN OPERATIONAL ENVIRONMENT on preparation and execution (design) of operations, POKO 2017, The Military Academy, University of defence in Belgrade Serbia, The Military Academy, University of defence in Belgrade, Serbia, pp. 641 - 651, 978-86-335-0582-6, Belgrade, Serbia.

- [2] J Đokić, Vucina Jankovic, Jelisaveta Marjanović, INSTITUTIONAL AND LEGAL OBSTACLES IN PERFORMING NATURAL DISASTER RISK MANAGEMENT IN THE NORTH OF KOSOVO AND METOHIJA, Safety for the future 2017, Proceedings, Regional Association for Security and Crisis Management S4 GLOSEC Global security doo, pp. 256 - 265, 978-86-80698-07-6, Obrenovac, 2017.
- [3] Burrough, P.A. and McDonnell, R.A., (1998) principles of Geographical Information Systems. Oxford University Press, Oxford, 327 pp.
- [4] Bonacci, O. (2008) Water related risk management, Vodoprivreda 40,UDK: 626/628:33, 167-174.

LEAD PARTICLES DISPERSION MODELING IN EXTREME WEATHER CONDITIONS FROM TAILING WASTE IN ZVEČAN

Jelena V. Dokić¹, Nebojša B. Arsić¹ and Srđan V. Jović¹

¹Faculty of Technical Sciences

University of Priština in Kosovska Mitrovica

Kosovska Mitrovica, 38220, Serbia

e-mail: jelena.djokic@pr.ac.rs ; web page: <http://xn--j1aebtj.xn--90a3ac/>

Keywords: Wind rose, lead particles, air pollution simulation.

Abstract. "Gornje polje" tailing waste deposit is situated close to the river Ibar, between Kosovska Mitrovica and Zvečan municipalities. The tailing waste was deposited since 1930. It occupies the surface of 50 ha with 12,000,000 m³ of waste.. The tailing waste is dry, oxidized and mostly solid. In order to estimate environmental risk, several studies were done. Based on the chemical composition it was concluded that the main risk originates from lead based particles. In the climatic conditions on site during summer and winter periods (wind rate 3.3) lead particles concentrations in the air were measured, and compared with the concentration range calculated by using SCREENview, Screening Air Dispersion Model. Contamination with lead bearing particles exceeding maximum limits was 2 km. Lead containing material was initially investigated by using multiple instrumental techniques, Scanning Electron Microscopy, X-Ray Diffraction and Granulometric testing, in order to determine diameter, shape and mineralogy of particles being dispersed by the wind. Emission rate of the particles was measured in the laboratory, where the initial values for modelling were tested. In the situation of extreme weather, the reports have recorded the maximum wind velocity of more than 10m/s, for three days in a row, so that value for the wind speed was inserted into simulation. Air Dispersion model AERMOD has shown that in that case, the range of pollution exceeding maximum limits will cover the area of 11 km in diameter, and it will be directed to the south, endangering large populated area.

1. INTRODUCTION

Air pollution by fine solid particles from mining, ore processing and metallurgy waste deposits are evident in all regions where mining and metallurgy are in operation. The WHO guidelines provide interim targets for countries that still have very high levels of air pollution to encourage the gradual reduction of emissions [1]. In the Environment and Security Initiative Project: Mining in South East Europe [2], it was concluded that almost the full range of warning signals for environmentally damaging incidents of large scale consequence are present in the region. These include large (historical) milling and metallurgy plants with significant slag deposits, mountainous terrain; abandoned sites with little or no closure or control; lack of ongoing physical and/or biochemical monitoring of operational and/or abandoned sites; lack of ongoing maintenance, both proactive and reactive.

Mining activities were very intensive in the Northern part of Kosovo in the last century. Since these activities were done by open pit exploitation, lead and Zinc ore was removed from the mine and crushed and transported to milling and beneficiating plants for concentrating the ore, and smelting, and refining. In Trepca, beneficiating was done by floatation method. Firstly, the lead and zinc ores milled which entails a crushing, grinding and filtration process in order to achieve uniform particles. Flotation is the use of a chemical reagent to make the minerals adhere to air bubbles. Lead and Zinc metal compounds are separated from the fine-grained ore with the help of a flotation process, where water, sulphur dioxide (SO₂), calcium hydroxide (Ca(OH)₂), copper sulphate pentahydrate, zinc sulfate, coal tar, sodium or calcium cyanide and an organic compound is added as agents, in order to promote flotation. The result is of the process is concentrating the minerals from the ore. The extraction and beneficiation of metals produce significant amounts of waste and byproducts, such as tailing waste. The tailing wastes in Trepca are dry, and there are no dams, but they are opened and exposed to erosion [3]. The flotation landfill at Gornje Polje (Fig. 1.) is located on the Ibar River bank, in the area between Kosovska Mitrovica and Zvečan town. In this landfill, flotation tailings from the Zvečan processing plant had been deposited here since operations started in 1930 and continued until it was closed in 1983. Galena, sphalerite, pyrite, arsenopyrite and pyrrhotite constitute the primary ore mineral assemblage that was processed in .

Commonly skarn minerals (ilvaite, hedenbergite, garnet) precede sulfide mineralization. The major gangue minerals are carbonates with variable cation composition (calcite, kuthnorite, rodochrosite, siderite) and quartz [4]. It covers a surface of approximately 500,000 m² and there lies deposits of around 12 million cubic meters of tailings. In the northern part of the landfill, tailings from the lead smelter have been disposed of for a long period of time, therefore the landfill has been created in form of a cone. Deposited flotation tailing is in general oxidized and solid [5].



Fig.1. Location of the Gornje Polje Research Area

The oldest tailing waste deposit in Trepca is Gornje polje, and being located inside a processing plant and in a close vicinity to the residential are, a lot of attention is put on its environmental impact. Different reports were made on the projects initiated by international organization, about the proposed activities for solving the environmental problems, and in those reports the tailing waste deposit Gornje polje was described to be some 50 ha large surface area with 12,000,000 tones of waste materials [6,7]. The published studies on this tailing [8-11] are analyzing the environmental impact of the Trepca's tailings, by analyzing the top soil, waters and air surrounding the locations. The Gornje Polje tailing waste deposit is a resource to manage and a threat to control. By its location on the river bank, and constant risk from flooding and low level of slope stability, it presents an environmental disaster risk. On the other hand, by its heavy metal content, and occurrences of the rare metals, it can be treated as source of valuable components. In order to determine the level of environmental risk, in the changing climatic conditions, some proper materials characterization was conducted, and imported into simulation of the Natech situation where the extreme weather conditions were simulated.

2. METHODS AND MATERIALS

As a large deposit with non-homogenous structure that was changing over time with equipment and technology advancing, its precise composition could not be determined before. A homogenous sample was formed by taking a portion of the deposit originating from different ages of the deposit.

2.1. Chemical analysis

The chemical composition is determined by using x-Ray fluorescence (ARL86480). For the chemical analysis of the samples also the following techniques are used: Ca and Mg concentrations are analyzed by using Volumetry-EDTA, Si is analyzed by Gravimetry, HCL digestion, Al, Na, K, Pb, Zn, Cd, Cu, Sb by AAS, equipment AAnalyst 300, Perkin-Elmer. Volumetry method by oxi-reduction is used for Fe analysis.

2.2 Microscopy and Mineralogy

SEM investigation was carried out on Scanning Electron Microscopy instrument from JEOL (JSM6460), with Energy Dispersive Spectrometer, EDS by Oxford Instruments. XRD (X-Ray Diffractometry) analysis was used for mineralogical investigation. Samples were investigated using diffractometer Philips PW 1710 under following conditions: radiation from copper anticatode with $\text{CuK}\alpha = 1.54178 \text{ \AA}$ and graphite monochromator, working voltage $U=40 \text{ kV}$, current strength $I=30 \text{ mA}$. Samples were investigated in the range of $5 - 70^\circ 2\theta$ (with step of 0.02° and time 0.5 s).

2.3 Dusting experiment

A fan type ABE-3,5 apparatus was employed for measuring dust loading (mg/m^2) in the laboratory, using a flow of $3600 \text{ m}^3/\text{h}$ and a vacuum of 200 Pa for airflow simulation, with a gravimetric sampler of the respiratory dust. The sample was set in a shallow metal plate, along with the measuring scale for the residual solid particles on the filter paper and a digital anemometer (DA-4000). The measurements were performed with the material set in the airflow direction from the fan and before the apparatus for polluted air vacuuming. The wind velocity was changed by the distance between the fan and the metal plate for each sample. The measurements were performed in wind velocities of 5, 7 and 10 m/s . A wind velocity larger than 10 m/s is outside the interval of wind velocities occurring in this region. The humidity in the laboratory was within the interval of 37–53 % and the dust concentration was 0 %.

2.4. Modeling and Simulation

The meteorological data for the wind speed, wind directions and frequency distribution were taken from the nearest meteorological station, 4 km from the site. The data was analyzed using the program Wind Rose Plot for Meteorological Data, Version 7.0. The obtained results are imported into the AIRxxx together with the PM10 properties, terrain data, receptors grid and impact area for modeling and simulation.

3. RESULTS AND DISCUSSION

The material characterization has shown that the waste is small grained, toxic mineral mixture.

3.1 Chemical composition

Chemical composition of the waste is presented in the Table 1.

Element	Pb	As	Zn	Cu	Ni	Fe	Mn	Cr	Rb	Sr	Zr
mg/kg	2736	3867	1848	177.3	115.78	117786	8241.41	366.8	72.1	120.5	109.1

Table 1. Chemical composition of the tailing waste deposit Gornje Polje

3.2. Mineralogy and grain size

The scanning results for Veliko Rudare have pointed out that lead is found in different forms. By the results presented in Table 2. most of the iron is in a form of pyrite, it can be seen that most of the sulfur was compounded with iron., so lead, zinc, silver and antimony are largely in a form of oxides and sulfates, or carbonates, as the carbon content is not analyzed by SEM-EDS. Arsenic is coupled by either Iron and/or lead. The grains are shown in the Fig.2. Small grain particles, PM2.5 of lead and ferro-sulfates, and arsenic ferro sulfates are spread on the quartz and carbonate base.

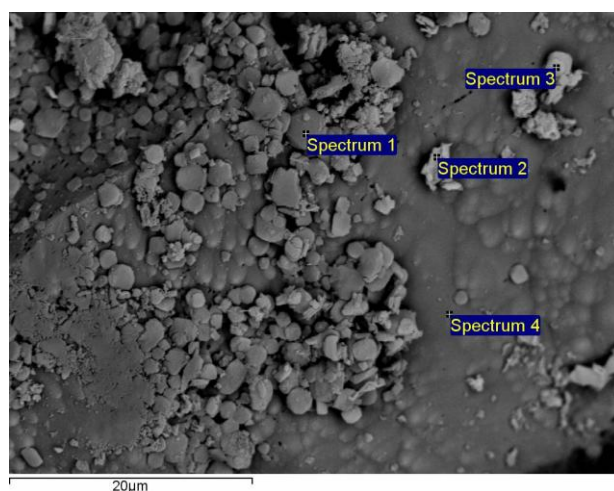


Fig. 2. Scanning Electron Microscopy of the tailing waste sample.

Table 2. The composition of the surface of the sample Gornje Polje

Spectrum	In stats.	O	Al	Si	S	Ca	Fe	Zn	As	Ag	Cd	Sb	Hg	Pb	Total
Spectrum 1	Yes	57.21	0.10	3.23	8.57	4.70	22.00	0.00	1.51	0.00	0.00	0.00	0.00	2.69	100.00
Spectrum 2	Yes	57.05	0.33	5.66	3.06	8.01	23.57	0.00	2.15	0.17	0.00	0.00	0.00	0.00	100.00
Spectrum 3	Yes	57.18	0.16	5.54	6.30	7.55	22.45	0.00	0.00	0.00	0.00	0.00	0.00	0.81	100.00
Spectrum 4	Yes	26.46	0.25	6.24	1.30	21.95	43.79	0.00	0.00	0.00	0.00	0.00	0.00	0.00	100.00

3.3 Meteorological data

As the measurements were performed at a relatively small distance and under the actual climate conditions for the defined period, it was necessary to define the approximate dusting under different climatic conditions. The initial conditions such as dust under laboratory conditions, waste characteristics, deposit dimensions and surrounding relief were inputted into the software Screenview and the obtained diagram showed reasonable agreement with the measured values. The calculated results are presented in Fig. 3.

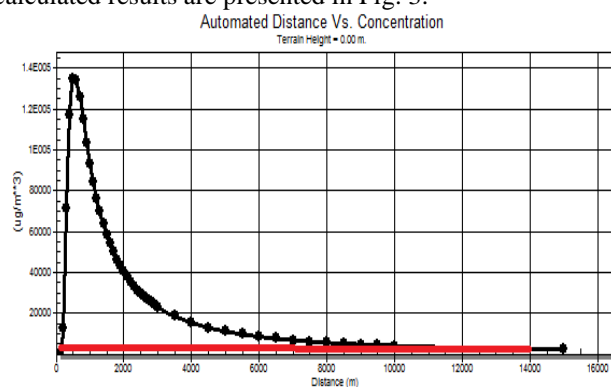


Figure 3. Calculated particles dispersion

By analyzing the data for wind speeds, directions and frequencies, it can be concluded that the winds have changed their frequencies over the last 20 years. In 1999, the weather was mostly stable, and just 7.0 % of the winds had a speed of more than 3.6 m/s. Southern winds were the strongest and northeastern winds were the most frequent, *i.e.*, 20 % of the winds came from this direction. Just 1 % of the winds were stronger than 8.8 m/s. In 2010, 21.1 % was in the wind class 3.6–5.7 m/s, and 2.8 % of the winds had a wind speed of more than 5.7 m/s. Southern winds were the most frequent, but southwestern winds also increased in frequency and speed. This is usually the case in the summer, when strong hot winds blow from the Mediterranean area, with hot and dry weather (Fig.4)

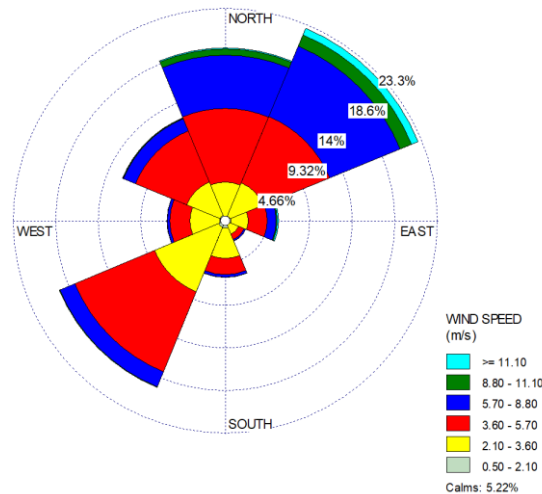


Fig.4. Wind Rose used for simulation

In extreme weather conditions, the wind speed larger than 10 m/s is expected, and there are no data on pollution in these climatic conditions. The potentially unstable weather was taken into consideration for modelling and simulation. The distance of 5000 m from the source of pollution was set for discrete distance calculations. Simulation was done by using Gaussian Plume Air Dispersion Model AERMOD. AERMOD incorporates, with a new simple approach, current concepts about flow and dispersion in complex terrain. In this case the plume is modeled and impacting and following the terrain. The first terrain layer for the research area is presented in Fig. 5.

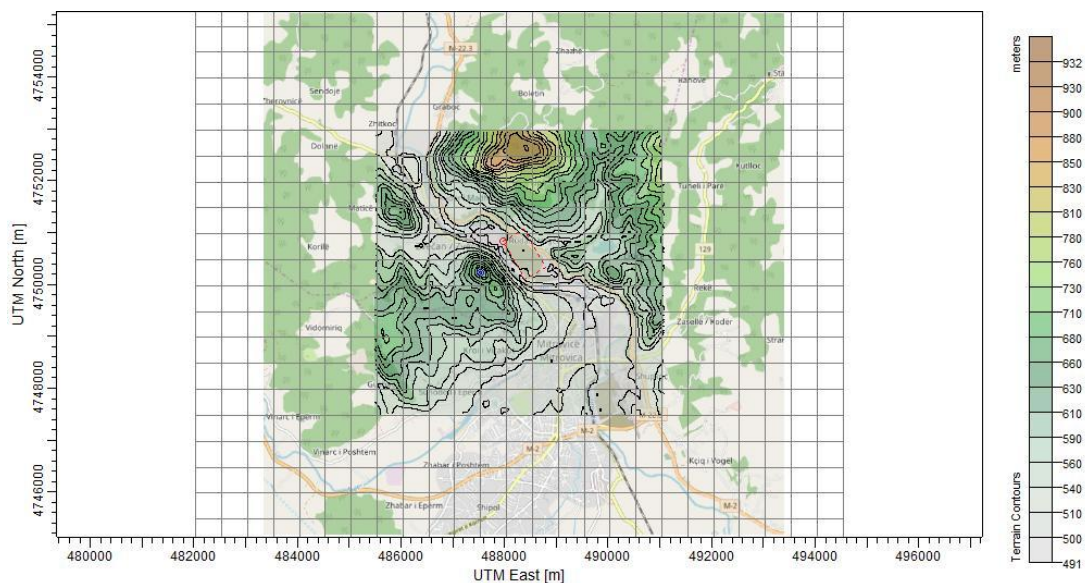


Fig.5. The terrain information on Gornje Polje

Surface characteristics in the form of albedo, surface roughness and Bowen ratio, plus standard meteorological observations (wind speed, wind direction, temperature, and cloud cover), are input to AERMET. AERMET then calculates the PBL parameters: friction velocity (u^*), Monin-Obukhov length (L), convective velocity scale (w^*), temperature scale (θ^*), mixing height (z_i), and surface heat flux (H). These parameters are then passed to the INTERFACE (which is within AERMOD) where similarity expressions (in conjunction with measurements) are used to calculate vertical profiles of wind speed (u), lateral and vertical turbulent fluctuations (v , w), temperature gradient (d/dz), potential temperature (θ), and the horizontal Lagrangian time scale (TL_y).

After the calculation the air dispersion model is presented in Fig.6. Red line shows the impact zone, and the pollution data are more than 20 times higher than allowed concentrations

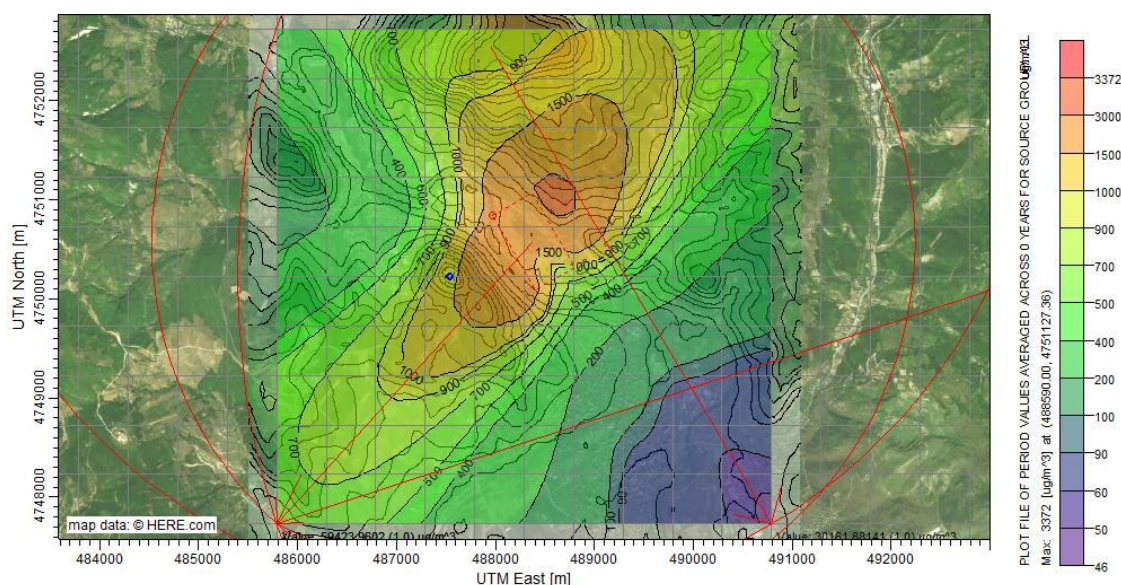
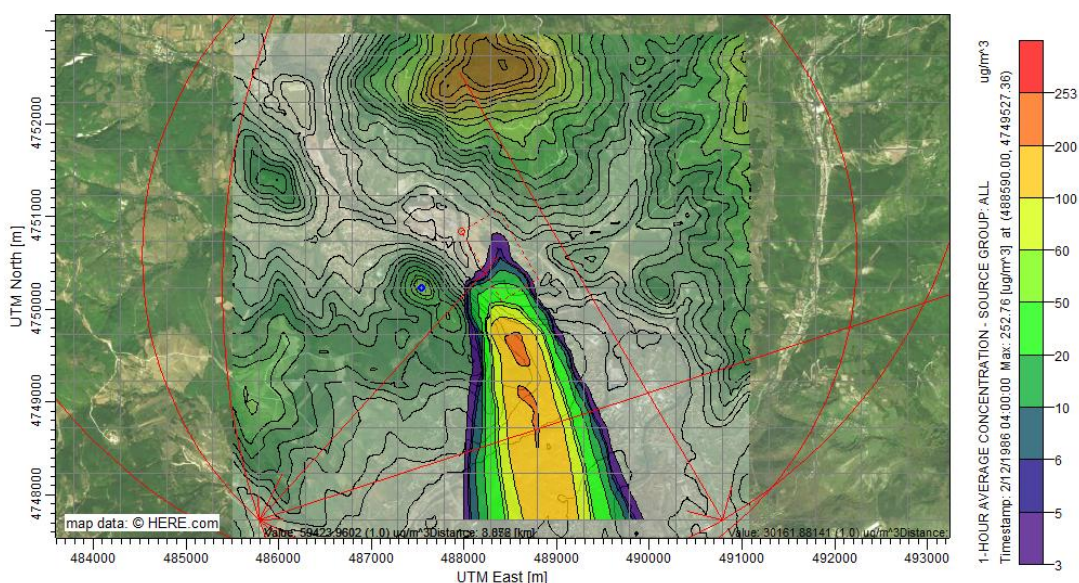


Fig.6. Calculated PM10 concentrations in wind speed 11.1 m/s

In order to observe separate situations and the difference in dispersion in stable and extreme weather, the simulation with daily average data was presented in Fig.7.



4. CONCLUSIONS

The tailing waste deposit from lead and zinc ore processing was proven to have a great environmental impact, due to its form, fine grains of PM₁₀, and TSP. Under stable weather conditions, the dusting is scattered by up to 1400–2000 m around the waste deposit. With climate change, *i.e.*, decreased relative humidity and the frequency of strong winds (3.6–5.7 m/s) reaching 21.9 %, with 1 % of the winds attaining a speed interval 8.8 m/s to 11.1 m/s the impact range was wider, and more intense. Thus, a larger area, up to 5 km in diameter, is endangered but because of the topography of the area and surrounding hills, the area is not larger.

REFERENCES

- [1] WHO Air quality and health, Fact sheet No. 313 (2008)
- [2] Philip Peck (2004), Desk-assessment study for the Environment and Security Initiative Project UNEP Regional Office for Europe & UNEP Division of Technology, Industry and Economics
- [3] S. Frese, R. Klitgaard, E. Kock Pedersen , Environmental Management in Kosovo, Heavy Metal emission from Trepca, TekSam, Institut for Miljo, Teknologij og Samfund, 2004
- [4] Strmić Palinkaš, S., Palinkaš, L., Lüders, V., Molnar, F., P-T-X conditions of mineralizing fluids from Pb-Zn-Ag hydrothermal-metasomatic deposit Stari Trg, Trepča, Kosovo, Architecture of collisional orogens / Franz Neubauer (ur.).Salzburg, 2007. pp. 71-72
- [5] Tošović, R.; Dašić, P.; Ristović, I. Sustainable Use of Metallic Mineral Resources of Serbia from An Environmental Perspective. *Environmental Engineering and Management Journal* **2016**, Volume 15, pp. 2075-2084.
- [6] F.Riesbeck, Trepca Tailings and Trepca Mines – environmental problems an overview of solutions , International Conference Report, Taking Action Together: Industrial Waste Management for Trepca Enterprise, UNDP, Mitrovica, 19–20 September 2011,pp.10
- [7] Milentijević, G., Spalević, Ž., Bjelajac, Ž., Djokić, J., Nedeljković, B. Impact Analysis of Mining Company 'Trepca' to the Contamination of the River Ibar Water, National Vs. European Law Regulations. *Metalurgia international* **2013**, Volume 18, pp. 283-288.
- [8] Milentijević, G., Nedeljković, B., Lekić, M., Nikić, Z., Ristović I., Djokić, J. Application of a Method for Intelligent Multi-Criteria Analysis of the Environmental Impact of Tailing Ponds in Northern Kosovo and Metohija. *Energies* **2016**, Volume 9 (11), pp. 935-952, DOI: 10.3390/en9110935.
- [9] Đokić J., **Milentijević G.**, Nedeljković B.: Exploring Possibilities for Tailing Waste Deposit Management Mitrovica Innovations Scientific International Conference – MISIC 2015: The Role of Business in Sustainable Development in the Western Balkans, 15-16 September, Pristina and Mitrovica, pp. 185-192, 2015
- [10]Nannoni F, Protano G, Riccobono F (2011) Fractionation and geochemical mobility of heavy elements in soils of a mining area in Northern Kosovo. *Geoderma* 161:63–73. doi:[10.1016/j.geoderma.2010.12.008](https://doi.org/10.1016/j.geoderma.2010.12.008)
- [11]Borgna L, Di Lella LA, Nannoni F, Pisani A, Pizzetti E, Protano G, Riccobono F, Rossi S (2009) The high contents of lead in soils of Northern Kosovo. *J Geochem Explor* 101:137–146. doi:[10.1016/j.gexplo.2008.05.001](https://doi.org/10.1016/j.gexplo.2008.05.001)
- [12]Barać, N., Škrivanj, S., Bukumirić, Z. et al. *Environ Sci Pollut Res* (2016) 23: 9000. <https://doi.org/10.1007/s11356-016-6142-2>

A NEW BOUNDARY ELEMENT SOLUTION TO PLATES ON ELASTIC FOUNDATION VIA HELMHOLTZ'S POTENTIALS

Maria S. Nerantzaki¹ and John T. Katsikadelis²

School of Civil Engineering
National Technical University
Athens, GR-17753, Greece

¹e-mail: majori@central.ntua.gr

²e-mail: jkats@central.ntua.gr, web page: <http://users.ntua.gr/jkats>

Keywords: Boundary Element Method; Plate on elastic foundation; Helmholtz' potentials representation.

Abstract. A new pure boundary element method is presented for the analysis of plates resting on elastic foundation described by the Winkler and Pasternak model. The solution is sought as the sum of the homogeneous and particular solution. The homogeneous solution is represented as a sum of two Helmholtz's potentials, which are expressed by their integral representation. The integral representations of the Helmholtz's potentials together with the boundary conditions provide the necessary boundary equations for the establishment of the unknown boundary quantities. Then the solution of the plate at any point is obtained from its integral representation, which is used as a mathematical formula. The example problems demonstrate the effectiveness and accuracy of the developed method.

1. THE PLATE ON ELASTIC FOUNDATION AND THE SOLUTION PROCEDURE

The response of the plate resting on an elastic foundation is governed by the equation [1-4]

$$D\nabla^4 w - G\nabla^2 w + kw = f(x, y), \quad x, y \in \Omega \quad (1)$$

$w(x, y)$ is the deflection surface, $f(x, y)$ the transverse load, and G, k the subgrade parameters ($G \neq 0, k \neq 0$ Pasternak, $G = 0, k \neq 0$ Winkler elastic foundation).

The BEM for the solution of (1) has been obtained using the fundamental of (1) [1-3]. This approach, besides the analytical difficulties in establishing the fundamental solution and the pertinent boundary integral equations, leads to boundary integral equations, whose numerical solution requires special care. The AEM has also been developed for plates on elastic foundation using the simple known fundamental solution of the biharmonic (plate) equation, alleviating the BEM from establishing the fundamental solution of the governing equation [4].

In This investigation, the solution is sought as the sum of the homogeneous solution w_0 and a particular solution w_p

$$w = w_0 + w_p \quad (2a)$$

$$D\nabla^4 w_0 - G\nabla^2 w_0 + kw_0 = 0 \quad (2b)$$

$$D\nabla^4 w_p - G\nabla^2 w_p + kw_p = f(x, y) \quad (2c)$$

If ρ_1, ρ_2 are the squares of the roots of the characteristic polynomial $D\rho^4 + G\rho^2 + k = 0$, then we can write Eq. (2b) as

$$D\nabla^4 w_0 + kw_0 = D(\nabla^2 - \rho_2)(\nabla^2 - \rho_1)w_0 = 0 \quad (3)$$

The key to developing solution procedure is the following statement:

Statement:

If $\phi(x, y)$ and $\psi(x, y)$ are the solutions of the Helmholtz's equations

$$(\nabla^2 - \rho_1)\varphi = 0 \quad \text{and} \quad (\nabla^2 - \rho_2)\psi = 0 \quad (4a,b)$$

then the function

$$w_0(x, y) = \varphi(x, y) + \psi(x, y) \quad (5)$$

gives the general solution of Eq. (3).

Apparently, this statement is readily proved by direct substitution of $w_0(x, y)$ from Eq. (5) into Eq. (3).

The particular solution $w_p(x, y)$ is evaluated analytically using a simple method developed by Katsikadelis [5].

The two Helmholtz's potentials $\phi(x, y)$ and $\psi(x, y)$ are expressed by their integral representation in terms of their boundary values and their normal derivatives [6]

$$\varepsilon_1 \phi = \int_{\Gamma} (v_1 \phi_{,n} - \phi v_{1,n}) ds, \quad \varepsilon_2 \psi = \int_{\Gamma} (v_2 \psi_{,n} - \psi v_{2,n}) ds \quad (6a,b)$$

where v_1 and v_2 are the fundamental solution of Eqs. (4a,b) [7], and $\varepsilon_1, \varepsilon_2$ the free term coefficients.

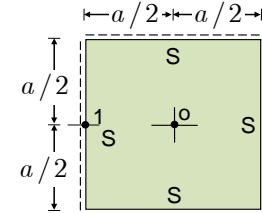
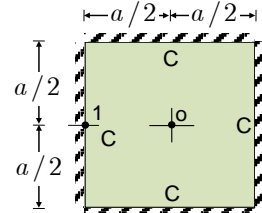
The plate is subjected to boundary conditions

$$\text{Clamped edge: } w = 0, \quad w_n = 0 \quad (7a)$$

$$\text{Simply supported edge: } w = 0, \quad M_n = -D[\nabla^2 w + (\nu - 1)(w_{ss} + \kappa w_n)] = 0 \quad (7b)$$

For free edges special care is required depending on subgrade model [8].

Table 1 Deflections and stress resultants in plates on elastic foundation for $\lambda = k / D = 0, 1, 100$ under a uniform load q . Upper value: Computed; Lower value: Available from literature [10].

Plate geometry and BCs	$w^0 / (f_0 a^4 / D)$	$M_n^1 / (q a^2)$	$M_x^0 / (q a^2)$
	0.00406		0.0476
	0.00402		0.0473
	0.00319		0.0369
	0.00406		0.0479
	0.00405		0.0477
	0.00321		0.0370
	0.00127	-0.0514	0.0229
	0.00127	-0.0508	0.0231
	0.00119	-0.0486	0.0209
	0.00126	-0.0513	0.0231

The boundary conditions together with the boundary integral equations (6a,b) provide a set of four boundary equations, which are solved numerically to give the boundary values of the Helmholtz potentials and their normal derivatives, i.e., $\phi, \phi_{,n}, \psi, \psi_{,n}$. Then the Helmholtz potentials are computed at any point from their integral representations (7a,b), which are used as mathematical formulae. Subsequently, these values are employed in Eq. (5) to compute $w_0(x, y)$ and then the plate solution $w(x, y)$ from Eq. (2a). All types of plate boundary conditions are treated. Example plate problems are presented, which demonstrate the effectiveness and accuracy of the proposed method. Table 1 shows results obtained by this method for a square plate with different boundary conditions.

2. CONCLUSIONS

The search for a solution via Helmholtz's potentials, motivated from the Almansi representation of the biharmonic equation [9] paves the path to develop a pure BEM solution to the general poly-harmonic equation

$$a_n \nabla^{2n} w + a_{n-1} \nabla^{2(n-1)} w + \dots + a_1 \nabla^2 w + a_0 w = f(x, y) \quad (8)$$

Eq (8) describes the response of several physical systems, such as microplates, poly-harmonic subgrade reaction models for plates on an elastic foundation e.g., Levinson-Bharatha [4]. The solution of such problems will be the subject of forthcoming publications.

REFERENCES

- [1] Katsikadelis, J.T. (1982). *The Analysis of Plates on Elastic Foundation by the Boundary Integral Equation Method*", Dissertation in partial fulfilment for the Degree of Doctor of Philosophy (PhD) in Applied Mechanics at the Polytechnic University of New York, New York.
- [2] Katsikadelis J.T. and Armenakas A.E. (1984). Analysis of Clamped Plates on Elastic Foundation by the Boundary Integral Equation Method. *Journal of Applied Mechanics, Transactions ASME*, 51, pp. 547-580.
- [3] Katsikadelis J.T. and Kallivokas L. (1986). Clamped Plates on Pasternak-type Elastic Foundation by the Boundary Element Method. *Journal of Applied Mechanics, Transactions ASME*, 53 (4), pp. 909-917.
- [4] Katsikadelis, J.T. (2014). *The Boundary Element Method for Plate Analysis*, Academic Press, Elsevier, UK.
- [5] Katsikadelis J.T. (2018). *Analytical Evaluation of Particular Solutions of Partial Differential Equations* (to be published).
- [6] Katsikadelis, J. T. (2016), *Boundary Elements for Engineers and Scientists*, Academic Press, Elsevier, Oxford, UK.
- [7] Paulsen K.D., Lynch D.R., Liu W. (1992). Conjugate Direction Methods For Helmholtz Problems With Complex-Value Wavenumbers. *International Journal For Numerical Methods In Engineering*, 35, Pp. 601-622.
- [8] Katsikadelis J.T. and Kallivokas L.F.(1988). Plates on Biparametric Elastic Foundation by BDIE method. *ASCE Journal of Engineering Mechanics*, 114, (5), pp.847-875.
- [9] Nerantzaki M.S. and Katsikadelis J.T. (2016). A New Boundary Element Solution Of The Plate Problem Based On Almansi Representation Of The Biharmonic Equation. 119th HSTAM International Congress on Mechanics, 27-30 May, Athens.
- [10] Timoshenko, S., and Woinowsky-Krieger, S., 1959. *Theory of Plates and Shells*, 2nd ed., McGraw-Hill Book Company, New York.

A PARALLEL ALGORITHM FOR THE EMBEDDED REINFORCEMENT MESH GENERATION OF LARGE-SCALE REINFORCED CONCRETE MODELS

George Markou

Department of Civil Engineering
Universidad Católica de la Santísima Concepción
Concepción, Alonso de Ribera 2850, Chile
e-mail: markou@ucsc.cl

Keywords: Parallel Algorithms, Embedded Reinforcement, Mesh Generation, Large-Scale Models.

Abstract. Modeling of large-scale reinforced concrete structures under monotonic and cyclic analysis requires significant computational demand given that models can incorporate hundreds of thousands of embedded rebars. In order to discretize and simulate any reinforced concrete structure by the 3D detailed modeling approach, the embedded mesh has to be generated prior to the analysis, a procedure that is controlled by the hexahedral mesh that is used to discretize the concrete domain. Numerically managing the computational demands that rise from the embedded mesh generation procedure can be challenging and time-consuming, especially in the case where the numerical models foresee the use of more than half a million of embedded rebars. Parallel processing and the use of a simple but efficient algorithmic implementation are presented in this research work. The use of OpenMP API for Shared Memory Parallelization specifications is adopted herein so as to integrate the proposed embedded mesh generation algorithm with the ability to use multiple cores during the search and creation of embedded rebars within large-scale hexahedral meshes. In order to investigate the performance of the proposed algorithm, a reinforced concrete model of a Reactor Building was constructed that foresees the use of 181,076 concrete hexahedrons and 2,703,400 embedded rebar elements.

1 INTRODUCTION

The accurate assessment of reinforced concrete (RC) structures through the use of 3D detailed modeling (under monotonic and cyclic loading [1-3]), foresees the discretization of the concrete domain through the isoparametric hexahedral element (8-, -20 or 27-noded) that treats crack openings by deploying the smeared crack approach and models the reinforcement mesh by discretizing it with the embedded rod or beam finite elements. In order to allocate the embedded rebar elements that are found within each hexahedral element, a search procedure is performed to allocate the intersection of the macro-elements [4] with the hexahedral mesh (see Fig. 1), while the nodes of the embedded bar macro-elements are also checked whether they are located within a hexahedral element or lie on one of its surfaces. This procedure can be time consuming when the analysis foresees the solution of a large-scale model [4] that consists hundreds of thousands of embedded rebar elements.

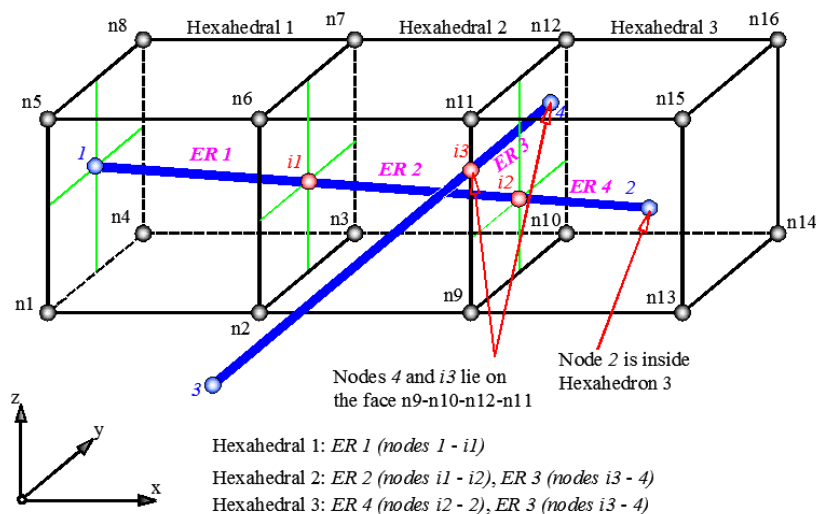


Figure 1 Embedded rebar macro-elements inside hexahedral finite elements [4].

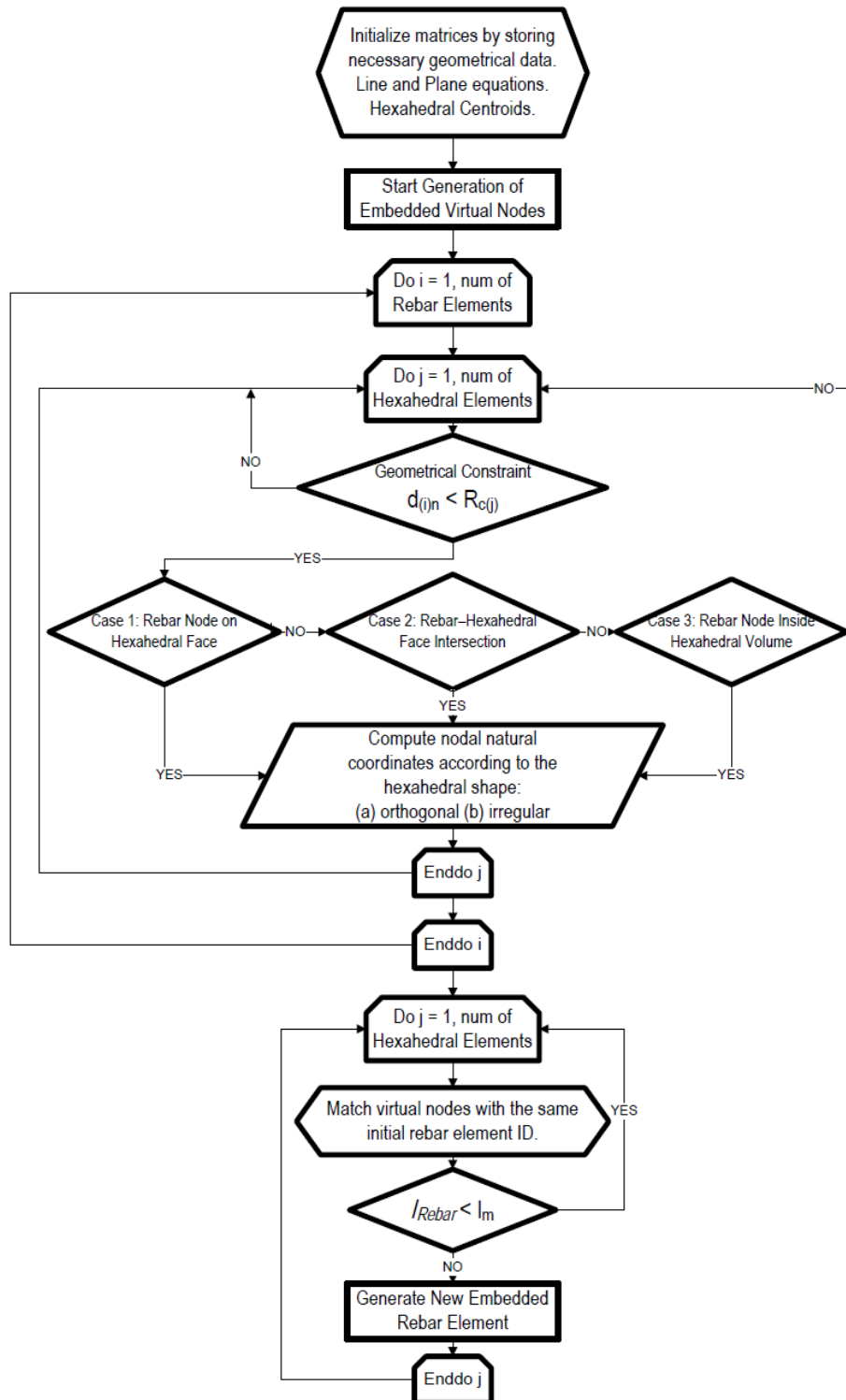


Figure 2. Flow chart of the updated embedded rebar element mesh generation method. [4]

As it was presented in [4], the numerical method for allocating and generating the embedded rebars inside hexahedral elements was proposed by Barzegar and Maddipudi [5], which was an extension of the work of Elwi and Hruday [6]. Their proposed mesh generation method [5] has the advantage of allowing arbitrary positioning of the rebars inside the concrete elements and a free geometry for each hexahedral element. The method was found to be hindered with additional computational demand [4] when dealing with a large number of rebars, given that the iterative solution procedure that was required during the search of intersection points was computationally demanding. The computational performance of this procedure was optimized by Markou [4], through the introduction of a geometric constraint (see Fig. 2) that was used to decrease unnecessary searches of intersection points between elements that were found in faraway parts of the mesh. Additionally, the method was also integrated with an algorithm that was able to determine whether a hexahedral element was symmetric, where the natural

coordinates of a virtual node were computed explicitly. This approach further increased the computational efficiency of the embedded rebar mesh generation procedure that was computationally efficient in handling meshes up to half a million embedded rebars.

Nevertheless, the required computational time for generating the embedded rebar elements of a double deck RC bridge model required 6 hours as it was reported in [4], which constitutes a significant computational time duration. It is evident that, taking into advantage the ability of parallel processing is the next step to take so as to decrease the computational cost of the embedded rebar mesh generation procedure, thus be able to numerically handle even larger models that will consist billions of rebars. The objective of this research work, is to investigate the parallelization of the algorithm proposed in [4], by using the OpenMP API [7] for shared memory parallelization specifications. The performance of the proposed algorithm was numerically investigated through the use of a large-scale RC structure that foresaw the generation of 2,703,400 embedded rebar elements.

2 EMBEDDED MESH GENERATION ALGORITHM

Generating the embedded rebar mesh of any 3D detailed model requires the use of a pre-processing software to construct the hexahedral mesh and the embedded macro-elements (EMEs). For the needs of this research, Femap [8] commercial software is used to perform the mesh construction of the under study RC structure, which is then analyzed through the use of the research software Reconan FEA [9] that was recently integrated with the parallel embedded rebar mesh generation algorithm. Fig. 2 shows the serial algorithm that was proposed in [4], where the search of embedded rebar elements is performed by applying the geometric constraint approach and the short embedded rebar filter that was also first introduced in [4]. As it can be seen in Fig. 2, for each EME the hexahedral elements of the model are checked whether they have any intersections with the under study EME, given that the hexahedrons satisfy the corresponding geometrical constraint. The algorithmic structure of the embedded mesh generation procedure, as described in Fig. 2, offers the advantage of parallelizing the entire procedure without the need of applying any special parallel solution approaches. The next section will discuss the parallelization features of the proposed algorithm.

3 PARALLEL ALGORITHM

3.1 OpenMP

As it was stated in [7], the OpenMP API specification provides a model for parallel programming that is portable across shared memory architectures. One of the main advantages of OpenMP is that numerous vendors support it, where different compilers can be used to build parallel applications. In addition to that, the use of OpenMP extends to different programming languages such as C, C++ and Fortran, while the specifications provide support for sharing and privatizing data [7]. Microsoft Visual Studio 2010 and later versions, support OpenMP, where the latest compilers integrated within the studio software have the option of activating and deactivating the ability of generating parallel code by using the OpenMP specifications. Additionally, the procedure of developing parallel algorithms with OpenMP is considered to be less demanding in comparison to other solutions such as MPI.

When programming any parallel solution algorithm, the ability of debugging the under development code is not feasible thus the use of commands that are easy to implement and control during the programming procedure is of great importance in achieving an error free product with high performance characteristics and high scalability. For this reason OpenMP introduced commands that can automatically parallelize “do” (Fortran) or “for” (C, C++) loops, without the need of using a large number of additional command lines. Furthermore, the use of the parallel sections construct is available and it was also found in this work to be the most effective OpenMP command when parallelizing a double “do” loop. Therefore, for the needs of this research work, the sections construct (see Fig. 3) was adopted for distributing the computational load to the selected cores.

```

Subroutine SectionConstructExample
  Implicit None
  !$OMP Parallel Sections
    !$OMP Section ! Sec 1
      Call DoWork_1
    !$OMP Section ! Sec 2
      Call DoWork_2
      .
      .
    !$OMP Section ! Sec i
      Call DoWork_i
  !$OMP End Parallel Sections
End Subroutine SectionConstructExample

```

Figure 3. OpenMP parallel section construct in Fortran language.

3.2 Proposed Parallel Algorithm

As it was stated in the previous section, the serial algorithm found in Fig. 2 was restructured so as to be able to be solved in a parallel manner. In achieving this objective, the first step foresaw the allocation of the algorithmic parts that involved the main computational demand of the mesh generation procedure. Based on a numerical investigation, it was found that the double “do” loop was the algorithmic procedure that required most of the computational time during the mesh generation procedure, as shown in Fig. 2. The second step in developing the parallel algorithm was to develop the mechanism through which the computational load was to be distributed to the cores, where it was chosen to directly divide the number of EMEs into equal in number subdomains. Therefore, the EMEs were allocated during the preparatory stage of the proposed algorithm that foresaw the computation of their total number and then based on their ID numbering, they were accordingly divided into subdomains.

It is important to note here that, the length of each EME determines the number of hexahedral elements that will be intersected thus controls the number of calculations and the corresponding computational demand required during the mesh generation procedure. The computational demand that immerses in each search loop was found to be proportional to the length of the EMEs and the corresponding sizes of the hexahedral finite elements. In this research work, the construction of the subdomains did not account for this factor, which will be a subject of future investigation. Fig. 4 shows the flowchart of the proposed parallel algorithm that was numerically investigated for the needs of this research work.

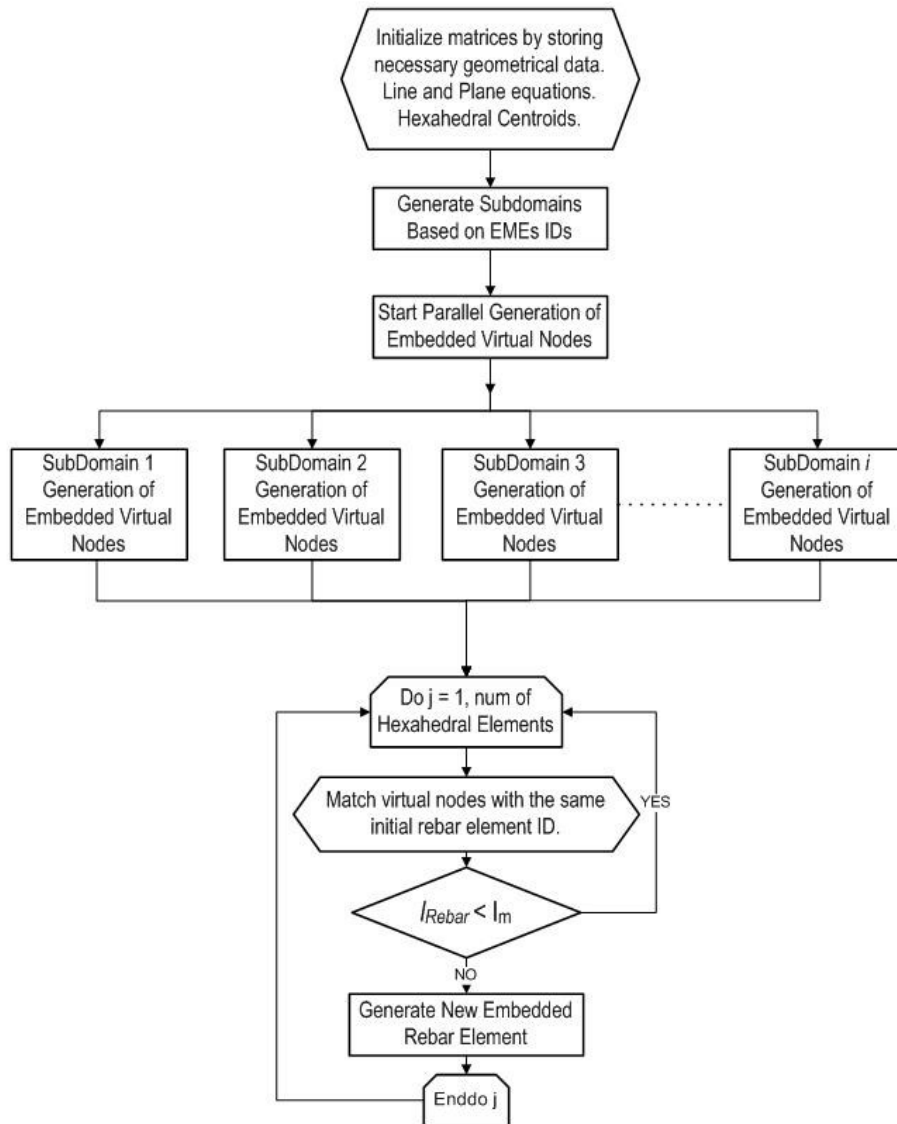


Figure 4. Flow chart of the proposed parallel embedded rebar mesh generation procedure.

4 NUMERICAL RESULTS AND DISCUSSION

So as to investigate the numerical performance of the proposed algorithm, a RC reactor building was used to be discretized and analyzed by using the under study algorithmic parallel implementation. In section 4.1 the

model's mesh that was used to assess the numerical performance of the proposed algorithm is presented, while the preliminary computational investigation that was performed when engaging the proposed parallel embedded rebar mesh generation algorithm for generating the mesh of the under study building, are presented in section 4.2.

4.1 Reinforced Concrete Model

Fig. 5 shows the 3D view the hexahedral mesh of a NUSCALE reactor building that has a total length of 75.25 m and a width of 30 m. The maximum height of the RC structure is 39.55 m, where the 8-noded hexahedral isoparametric finite element was used to discretize the framing system of the building. The 177,504 EMEs that were used during the embedded rebar mesh generation procedure can be seen in Fig. 6, while the details of the constructed mesh can be depicted in Table 1. In order to decrease the mesh construction procedure, the option of using very long EMEs was adopted herein. The longest EMEs are found in the raft slab, the exterior walls and along the roof slab (see Fig. 6).

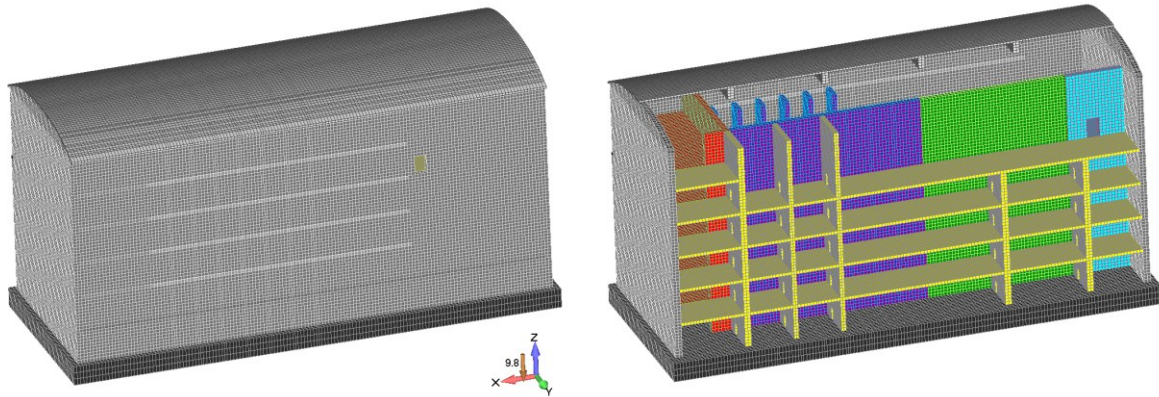


Figure 5 Reactor Building. Hexahedral elements finite element mesh.

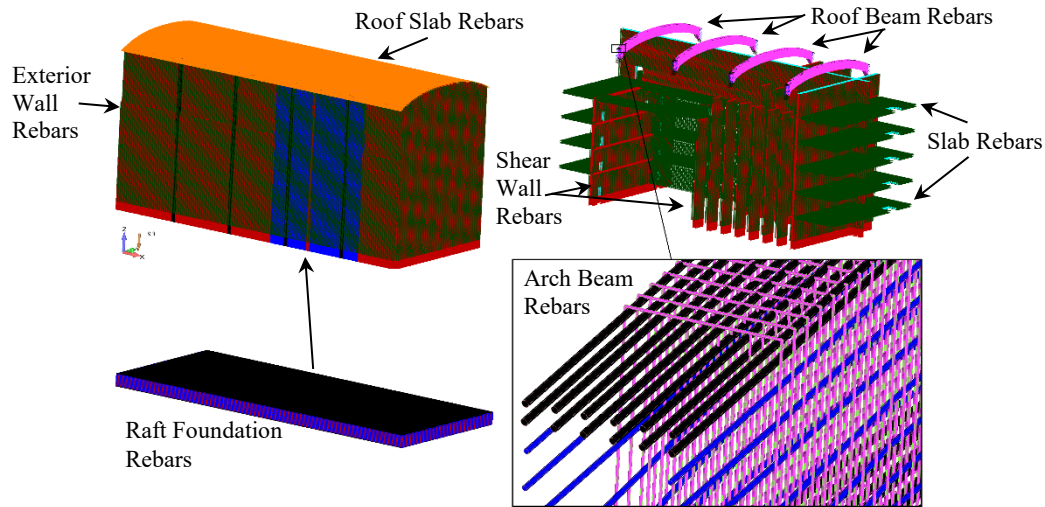


Figure 6 Reactor Building. Embedded rod elements finite element mesh.

Num. of Hexa Elements	Num. of Embedded Macro-Elements	Num. of Hexa Nodes	Num. of Generated Embedded Rebar Elem.	Num. of Short Embedded Rebar Elem.
181,076	177,504	271,226	2,703,400	3,392

Table 1 Finite element mesh details.

4.2 Algorithmic Performance

In order to investigate the algorithmic performance of the proposed parallel embedded rebar mesh generation algorithm, a standard 8-core CPU system was used, while the embedded rebar mesh generation was performed by using different numbers of cores per run. It must be noted here that, the Intel(R) Xeon processor that was used herein had a 3.70 GHz computing power per core. Fig. 7 shows the graph that derived from the 8 analyses that were performed in order to test the scalability of the proposed parallel algorithm. All 8 analyses were performed twice in order to reassure that the recorded computational times were objective and that the software was not affected by any other applications that were running simultaneously at the background. In addition to that, the

CPU that was used to perform the analyses was dedicated to this project and only the minimum required applications were running during the parametric investigation.

As it can be observed in Fig. 7 and Table 2, the required computational time decreases proportionally to the number of cores increase, where the scalability of the problem is found to be optimum for the cases of 2, 3 and 4 cores. This is attributed to the fact that the embedded mesh generation procedure foresees for each EME search to be independent thus no time is spent in order to perform reduction procedures or computations that need to use the same matrices or connectivity arrays (minimal communication demands). Moreover, Reconan FEA uses the latest Fortran attributes that allow for the use of the derived data type which is similar to C structures and has some similarities with C++ classes. Therefore, the data management does not require any additional treatment when the embedded mesh generation procedure was converted to parallel, whereas each core receives the variables and data that refer to the at hand subdomain with minimum communication demands. The overall performance of the proposed parallel algorithm demonstrated a maximum scalability when using up to 4 cores, while the performance of the code exhibited a lower scalability ratio when 5, 6, 7 and 8 cores were used (see Table 2).

This numerical finding was attributed to the fact that the EMEs were constructed by using various lengths that varied between 0.7 and 75 meters long (based on the geometry of the RC structural members). Therefore, when the mesh was divided into subdomains of equal in number EMEs, their length was not accounted as a controlling factor during the subdivision procedure. Consequently, some subdomains incorporated EMEs that require a significantly larger number of calculations in comparison to others, affecting the overall scalability of the proposed algorithm, especially when 5 subdomains were used to divide the EMEs. This created a notable load imbalance ratio, regardless the fact that there was no significant communication volume during the analysis that would have added further computational demand during the parallel solution procedure. Nevertheless, the CPU parallel efficiency of the proposed algorithm was found to be satisfactory (see Table 2). It is significant to note at this point that, the last loop of the proposed algorithm (Fig. 4) is performed in a serial manner, where its computational time is also accounted within the provided computational time durations depicted in Table 2. Therefore, the computational time that is required to perform the serial part of the mesh generation procedure is not affected when more than one core is used, thus the computed average CPU parallel efficiency is negatively affected by this adopted algorithmic approach. This numerical issue will be further optimized and presented in an updated version of the proposed parallel algorithm.

In addition to the above discussed load imbalance issue, a direct solution is to use a constant EME length throughout the mesh that will ensure similar computational demands for all virtual node searches, thus achieve an optimum scalability. Nonetheless, this mesh construction approach would create a restraint to the mesh development stage, thus a more general solution is deemed proper that would account for the length of each EME. By considering each EME's length as a weight factor and by using it to determine the optimal subdomain division during the preparatory stage of the parallel algorithm (see Fig. 4) in achieving a minimum imbalance ratio, would provide with a comprehensive solution to the load imbalance ratio issue. This is currently a subject of future research work.

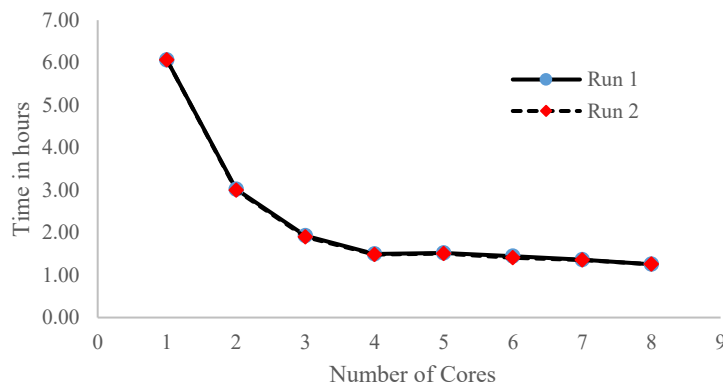


Figure 7 Computational time vs number of cores.

Based on the data provided in Table 2, it can be noted that the required average computational time for generating 2,703,400 embedded rebar elements (and discard 3,392 short embedded rebar elements) was 6.065 hours when using the serial code, while the corresponding time was decreased to 1.25 hours when 8 cores were deployed (60.4% CPU parallel efficiency). This illustrates the ability of the proposed parallel algorithm to significantly decrease the computational time, even in the case where the subdomains were not optimally constructed so as to ensure an even computational load distribution, thus achieving a high CPU parallel efficiency. It is noteworthy to state here that, the under study model presented in this research work is currently the largest model found in the international literature in terms of the number of generated embedded rebar elements. Regardless the significantly large number of embedded rebar elements, the proposed parallel algorithm was found to be able to handle this numerically intensive task in a computationally efficient manner, providing with a

satisfactory CPU parallel efficiency. Finally, the deformed shape of the embedded rebar elements and the von Mises strain contour of part of the roof's hexahedral mesh are shown in Fig. 8, as they resulted from a static numerical analysis for the self-weight of the structure.

Num. of Cores	Comp. Time Run 1 (h)	Comp. Time Run 2 (h)	Average CPU Parallel Efficiency (%)
1	6.07	6.06	Reference
2	3.02	3.00	100.8
3	1.93	1.90	105.6
4	1.50	1.48	101.7
5	1.52	1.50	80.3
6	1.44	1.41	70.9
7	1.36	1.35	63.8
8	1.25	1.25	60.4

Table 2 Computational time for generating the embedded rebar mesh for different number of cores.

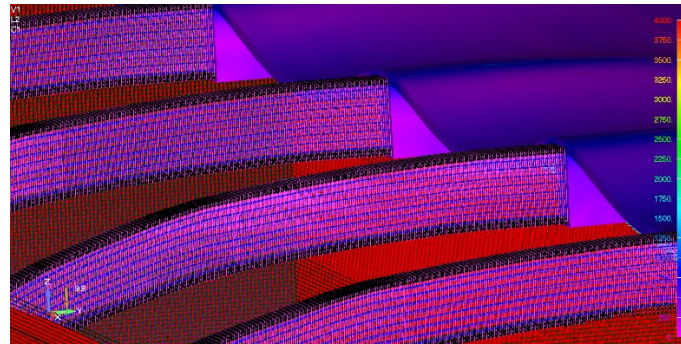


Figure 8 Deformed shape and solid von Mises stress contour of the roof.

5 CONCLUSIONS

A simple and efficient parallel algorithm was proposed for the embedded rebar mesh generation of large-scale RC models that use hexahedral isoparametric finite elements to discretize the concrete domain and model the steel reinforcement as embedded rebar elements. The proposed parallel algorithm used the OpenMP specifications so as to distribute the computational work to the cores based on a proposed parallel algorithm presented herein. The computational performance of the proposed parallel algorithm was investigated by performing parallel analyses that foresaw the use of 2 to 8 cores during different parallel analyses. Based on the numerical findings it was concluded that the proposed parallel algorithm was able to decrease the computational time with a satisfactory CPU parallel efficiency when dealing with a mesh that incorporated more than 2.7 million embedded rebars. Furthermore, it was found that the various EME lengths found in the initial RC mesh affected the scalability of the developed algorithm. Having subdomains that consisted very long EMEs in comparison to other subdomains that had the same number of EMEs but with shorter lengths, a load imbalance ratio immersed that affected the CPU parallel performance of the proposed algorithm. Nevertheless, the overall scalability of the proposed first version parallel embedded rebar mesh generation algorithm was found to be satisfactory.

A future objective of this research work is to investigate the development of a weight factor that will control the subdomain decomposition thus ensure a balanced computational load distribution according to each EME length. In addition to that, the solution of larger in size problems will be performed by using more cores in order to investigate the scalability of the propose algorithm when engaging more than 8 cores. Finally, the use of MPI will also be a subject of research in an attempt to compare the overall performance of the mesh generation procedure in parallel computing environments with shared memory.

REFERENCES

- [1] Markou G., Papadrakakis M. (2013), “Computationally efficient 3D finite element modeling of RC structures”. *Computers and Structures*, 12(4):443–98.
- [2] Markou, G., Mourlas, Ch. and Papadrakakis, M. (2017), “Cyclic Nonlinear Analysis of Large-Scale Finite Element Meshes Through the Use of Hybrid Modeling (HYMOD)”, *International Journal of Mechanics*, 11(2017), pp. 218-225.
- [3] Mourlas Ch., Papadrakakis M. and Markou G. (2017), “A computationally efficient model for the cyclic behavior of reinforced concrete structural members”, *Engineering Structures*, 141:97-125.
- [4] Markou G. (2015), “Computational Performance of an Embedded Reinforcement Mesh Generation Method for Large-Scale RC Simulations”, *International Journal of Computational Methods*, 12(3): 1550019-1:48.
- [5] Barzegar F. and Maddipudi S., (1994), “Generating reinforcement in FE modeling of concrete structures”, *Journal of Structural Engineering*, 120, pp.1656 –1662.
- [6] Elwi A.E. and Hrudey T.M., (1989), “Finite element model for curved embedded reinforcement”, *Journal of Engineering Mechanics*, 115:740 –754.
- [7] OpenMP Application Program Interface Examples, Version 4.0.0, OpenMP Architecture Review Board, November 2013.
- [8] Femap, Siemens Product Lifecycle Management Software Inc., 2017.
- [9] ReConAn - Finite Element Analysis Software; v1.00, Institute of Structural Analysis and Seismic Research; National Technical University of Athens, 2010.

FINITE ELEMENT ANALYSIS OF AGGREGATED ELONGATED VAULTED STRUCTURES

Maria E. Stavroulaki¹, Antonis Anousakis¹ and Aikaterini Mesaritaki¹

¹School of Architecture
Technical University of Crete
Chania, GR-73100, Greece

e-mail: mstavr@mred.tuc.gr; anousakis_ant@hotmail.com; aikaterinimes@gmail.com ; web page:
<https://www.arch.tuc.gr/en/staff/faculty-staff/faculty/stavroulaki-maria>

Keywords: finite elements, masonry, structural dynamics, vaulted structures, aggregated buildings

Abstract. *Analysis of historical aggregated masonry buildings is important to understand the way the structure behaves and to understand the cause and significance of the cracks, if they are visible. Only with a good comprehension of both aspects can the engineer or architect take decisions about the techniques of conservation which could be used. In parallel, the absence of data about the adjacent buildings, raises a lot of queries in the simulation. Many methods for the analysis of masonry structures and especially the vaults have been developed.*

The aim of this research is the static and dynamic analysis of the existing state (taking into account the structural pathology like cracks, weak material areas) of part of a monastic share studied by the finite element method in order to document the causes of its deterioration. There are two elongated vaulted spaces where the transverse wall has collapsed and there is a visible crack in the one vault. Different finite element models were analyzed for the simulation of each vaulted structure separated or connected, in order to study the dynamic behaviour of these buildings in continuity and to investigate the influence of boundary conditions to the dynamic behaviour.

1 INTRODUCTION

Aggregated buildings represent an important and typical peculiarity in many old town centers. They consist of buildings in continuity with common walls in between them, which lead to a structural dynamic behaviour as a group. The same structural system appears in old monastic and agricultural or arsenal complexes. The experience of earthquakes which affected old town centers with masonry aggregated buildings creates the need to analyze the behaviour of these systems, taking into account the specific geometric characteristic, structural materials and boundary conditions. Their dynamic response relates with the stiffness of each building separately as well as the stiffness of the overall complex.

Different approaches have been used to investigation of masonry building compounds which were affected by L'Aquila earthquake and, more recently, the Emilia-Romagna one which demonstrated that aggregated buildings generally show a group behaviour which improves seismic performances of the component structural units, also when they are made of low quality masonry [1-2].

From a work about the seismic vulnerability assessment of an old stone masonry building aggregate it was concluded that building aggregates result as a middle term scale class of buildings whose optimal assessment should embrace numerical analysis for a more detailed investigation, always depending on the objective of the project in hands. Numerical analysis shall be used as a complement of indirect techniques assessment, for a more detailed examination of the structure and its behaviour when subjected to a seismic action, contributing for the designing of more adequate and efficient retrofitting interventions [3].

Two main factors influenced the seismic response of historical masonry buildings: the constructive techniques of recent interventions and the state of conservation. Also the state of preservation played an important role particularly referring to damage caused to contiguous buildings; in fact, in many cases, buildings adjacent to abandoned constructions have been damaged due to the lack of the stabilizing contribution of neighboring cells [4].

From the study of complex historical buildings like the Palazzo La Sapienza in Pisa it was concluded that the analysis must be executed considering the construction not a single unit but a "structural aggregate", made up of different parts interconnected to each other in various ways and using different techniques since such complexities and structural heterogeneity usually result in widely disparate responses of different parts of the building to external actions, with widespread cracking phenomena and possible structural problems and failures

[5].

In order to simulate the three dimensional effects of the vault, the stabilization role of the spandrels and the existing condition, including the permanent deformations, an accurate geometry of the vault is necessary for the estimation of the structural strength and dynamic behaviour [6].

The goal of the present study is the analysis, using the finite elements method (FEM), of the behaviour of the north-east part of a monastery complex in dynamic loading. Different finite element models were analyzed in order to simulate each vaulted structure separated or connected, in order to study the dynamic behaviour of these buildings in continuity and to investigate the influence of boundary conditions to the dynamic behaviour. The absence of symmetry of the construction, due to differences of the transverse walls, the differences to stiffness of the longitudinal walls and the different boundary conditions, led to necessity of three dimensional modeling of the structure. Because the study takes place at the macro level, it was assumed that the masonry walls are composed of homogeneous and isotropic continuum material with elastic-plastic behaviour in compression and low strength in tension. For this purpose, the study is structured in the following four sections: architectural documentation, analysis of the FEM model of the north vaulted part as an isolated entity in a theoretical model, study of the FEM model of the same volume combined with neighbor parallel vaults as they exist in reality and finally conclusions related to the comparison of the previous FEM models.

2. DESCRIPTION OF STRUCTURE

2.1 Geometry – Pathology

The studied building belongs to the Monastery of Ayia Triada Tsagarolon in the area of Akrotiri of Chania municipality. The building complex is located in the village of Sternes in the local area of Prinodasos. The first historical reference about the monastic share, goes up to the second decade of the 17th century and therefore it can be considered as a historical monument of the Venetian occupation period in Crete. At the same period there are also references to a small church dedicated to St. Dimitrios in the northwest side of the same property (Fig. 1) [7-10].



Figure 1. Map of Akrotiri region where the monastic share of Ayia Triada Monastery is indicated (orthophoto). The studied volume of the building complex is marked with red color.

The building complex consists of two separate adjacent building volumes in L-shape formation encompassing two internal yards. The two separate building volumes are surrounded by an external wall which is a common feature of Monasteries in Crete. The total constructed area of the monastic share including the small church reaches up to approximately 710,6m², due to ruminant conservation status of several parts. The northeastern part, which is documented, has rectangular shape, general dimensions: 9.20m x 14m and total area of approximately 126.85 m² because of the collapse of the eastern facade. The main entrance is located in the southern part and leads to an internal yard through which the main building is accessible and is surrounded by three ground floor building volumes. (Fig. 2). This study focuses on the north volume of the building complex which is split into two smaller longitudinal vaulted rooms. The southern part of the volume is an arcade with a view to the internal yard and allows the access to the north and east chambers. The northern part of the volume is also accessible by the external north enclosure of the building complex and has two windows facing the arcade. The north part of the building complex is selected because of its longitudinal vaulted geometry. It is studied separately in two cases: in the first one, the room [D] is studied as an isolated geometry and in the second one the same room is studied in contact with spaces [E] (an arcade of similar geometry) and space [F], (a smaller corridor

also vaulted). The room [D] is an elongated vaulted space with internal dimensions 14.65m x 3.9m with two windows and a door on its south masonry and one door on its northern masonry (Fig. 3).

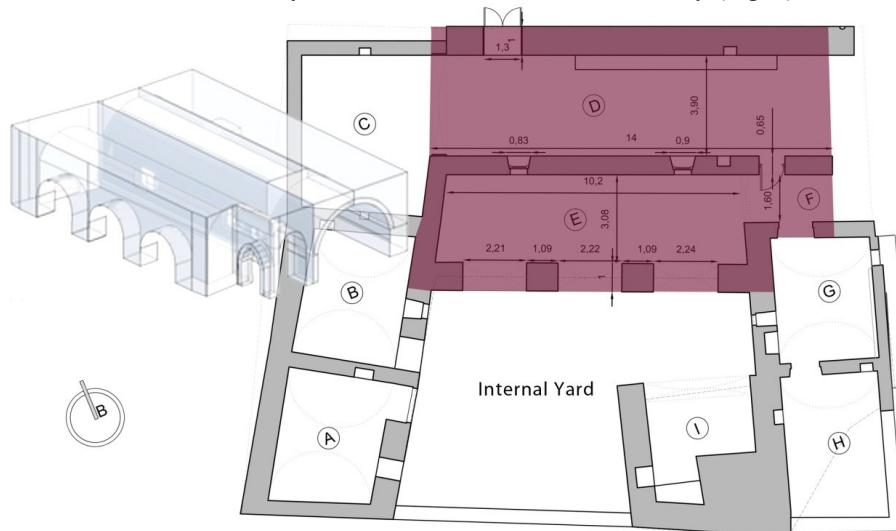


Figure 2. Floor-plan of eastern volume of the building complex where the studied volume is indicated with red color and presented in 3d model in the left part of the figure.

The longitudinal external masonry that bares the vaults has a width of 1m while the width of the internal wall among the two spaces is 0.65m. Every room of the building complex is vaulted and has a covering of cement mortar without reinforcement (Fig. 4). The vertical baring masonry is constructed by rubble stone masonry, consisting of rough shaped bioclastic limestones of medium and small size. The carved stones of the vaults have similar dimensions. The bounding mortar is made of clay and small aggregates of limestone. The width of the vault is approximately 30-35cm and the width of its cement covering mortar, ranges between 5 and 10cm.



Figure 3. Internal view of the chamber [E] with the pillars (left). External view of the northeast corner of the chamber [D] and the collapsed façade (right).



Figure 4. External view of the north masonry of [D] and the developed tree (left). Internal layer of eastern collapsed façade and cement mortar covering (middle). Alteration of stone surface of the pillars of [E] chamber and material loss (right).

The eastern transverse façade has partially collapsed: it is entirely collapsed in the part in front of the rooms [D] and [F] while only the internal half of a three-layered masonry is preserved in front of rooms [G] and [H]. From the remaining foundation masonry, it is estimated that the initial wall width was 0.90m (Fig. 3). In the upper side of the northeast corner of the [D] room, a native (fig) tree is developed inside the masonry, causing severe disruption and local detachment of the masonry (Fig. 4). The three rooms [D-E-F] have small crackings at the covering cement mortar and the [D] room has a centrally located 3m long crack of small range, starting from

the eastern side where the front wall has collapsed. The intense humidity inside the building, has been measured during a time period of one week in March 2017, between 82,9 – 96,9 %. Humidity has caused severe disintegration of the bounding mortar at the areas where the coating is not preserved, as well as biological colonization on the surfaces of the stones. The areas' environmental conditions combined with intense wind flows inside the room (E), have caused alteration in the stones of the arcade pillars such as differential erosion, detachment and partly material loss (Fig. 4).

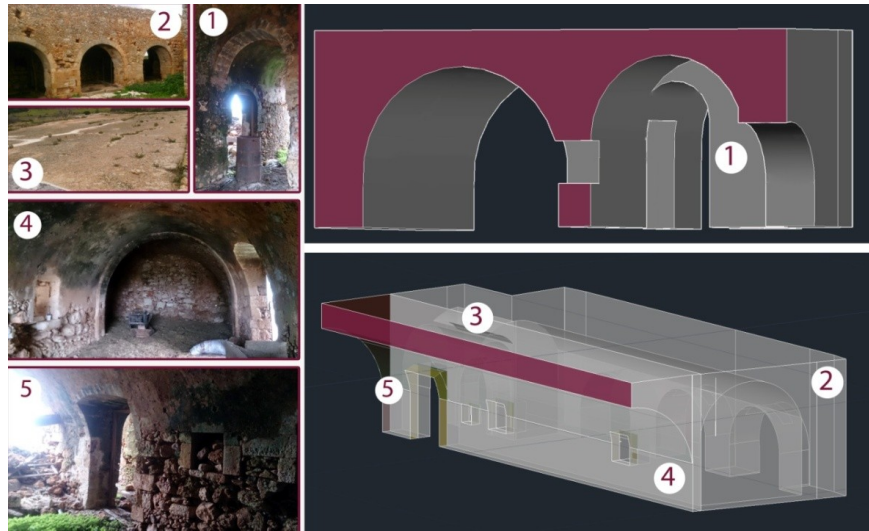


Figure 5 . Axonometric 3d section views of the studied volume, with picture references

3. FINITE ELEMENT ANALYSIS

3.1 Mechanical properties of the masonry

In terms of mechanical properties, masonry is considered to be a material that is strong in compression with acceptable shear strengths but weak in tensile forces. Several equations to determine the mechanical properties of masonry have been formulated. In this work however, the European Regulation (EC6) guidelines have been adopted. Based on the national Annex of EC6, the value of compressive strength of the masonry is: $f_{wc} = K f_{bc}^{0,65} f_{mc}^{0,30}$ (MPa), where K is the coefficient that depends on the type of the masonry with standard values ranging from 0.40 to 0.60, f_{bc} is the compressive strength of the stone and f_{mc} is the compressive strength of the bounding mortar.

The tensile strength of the masonry is significantly lower than its compressive strength. Therefore, the regulations consider the tensile strength negligible. However, in the case of horizontally loaded wall (earthquake, wind) a bending tensile strength of the masonry is defined. A common way to determine the value of the shear strength of an unreinforced masonry (f_{vk}) is either by testing or by using experimental data related to the cohesion (f_{vko}) (EN1052-3, 4) or by the proposed values of the EC6 Regulation.

In the present study, the compressive strength of the stone is considered of a value of 60 Mpa in the analysis, while the compressive strength of the mortar equal to 2 Mpa. Therefore the typical strength of the masonry is $f_{wc} = 14.4$ MPa. The adopted values of the design strengths are provided by the following expression based on the characteristics values: $f_d = f_k / \gamma_m$, where $\gamma_m = 2.7 \times 2/3 = 1.8$, the security coefficient. In summary the selected mechanical properties are shown in Table 1.

Considering the current preservation status of the masonry some areas of the models were assumed with lower strengths.

Material	Young's modulus E (GPa)	Yield stress (MPa)	Compressive strength, f_{cd} (MPa)	Tensile strength, f_{td} (MPa)	Shear strength, f_{vd} (MPa)	Poisson ratio ν	Mass Density $\rho(t/m^3)$
M1	8	8	8	0.4	0.5	0.25	1.8

Table 1: Mechanical properties of masonry

3.2 Description of the computational models

Unilateral contact effects arise in masonry structures due to the absence of mortar or its low quality and many of the damages like cracks can be described by loss of contact, sliding or, rarely, compressive yield of masonry. Consequently, in this research nonlinear finite element models based on the principles of non-smooth mechanics

were adopted to represent the mechanical performance of the structure. Unilateral contact law governs the behaviour in the normal direction of the interface, indicating that no tension forces can be transmitted in that direction. The behaviour in the tangential direction takes into account that sliding may or may not occur.

At every point of an interface the basic unilateral contact mechanism can be described by the following set of relations: the no-penetration inequality, the no-tension inequality and a complementarity either-or relation, which indicates that either, separation with zero contact force or compressive contact force with zero gap appear. For a discretized structure, the previous relations are written for every point of a unilateral boundary or interface by using appropriate vectors. The arising nonsmooth structural analysis problem has the form of a nonlinear complementarity problem. More details can be found, among others, in [11-13].

The behaviour in the tangential direction is ruled by the Coulomb friction model that exhibits a similar either-or, variable structure, unilateral behaviour: no-slip is enforced, if the frictional force is within limits, and slip with constant friction force is allowed at the limits. As with the contact problem, a complementarity problem also arises for friction.

The one-sided (unilateral) behaviour, due to contact, and the stick-slip mechanism of friction transforms the usual variational equality formulation of the mechanical problem into a variational inequality [11]. In this study, for the enforcement of the contact constraints, the penalty method has been chosen. The friction problem can, in principle, be approached by a similar method. Finally, the coupled problem has been solved by the Newton Raphson incremental iterative procedure.

3.3 Finite element models for analysis

The sub-section of the structure as mentioned above, communicates laterally with adjacent spaces and therefore some movement engagements are applied on the contact area at the directions of the lateral support. The value of stiffness provided from this support is not known in advance. The goal of the present study is to test the main vault of space (D) in two extreme scenarios: one with total rigid support and the second one with no support, and then compare the results with the existing geometry in the present status. For the evaluation of the mechanical behaviour of the core an appropriate FEM for simulation of monumental constructions was used, of special geometry, stiffness and mechanical behaviour that cannot be stimulated with simplified models, according to the existing research [14-16].

During the analysis three models (M1-M2-M3) have been studied to observe the different results that arise from each one of the different side commitments. For the simulation of the model the architectural particularities are accurately designed and also the current pathology of masonry elements is considered as well as the vector and the mechanical material properties. The crack was modeled with unilateral contact along specific interface which was assumed at the place where the main crack exists, assuming that across these interface separation and friction effects are considered.

The M1 and M2 models consist of 8 nodal and 5 nodal solid elements with 3 degrees of freedom at each node. The finite element mesh results from the attempt to achieve the appropriate simulation of the model. The M3 model, which presents the overall form of the buildings, was analyzed in the appropriate software for the FEM analysis (Marc-Mentat) as an isolated volume using the default parameters for the meshing procedure.

The vaulted geometry and the current vector pathology lead to specific modelling requirements including a technique for bounding the individual parts of the masonry. The models were divided in individual bodies, with the ability of being separately deformed. The interaction between the attached bodies is determined by the boundary conditions, imposed on each one of them. Thus for the parts of the masonry, where no important cracking is observed, the boundary condition is set as “glued” state. In this setting the discrete elements are in constant contact with each other and consequently, relative velocity cannot be developed between them. Similarly, the surface of the main vault of [D] where there is a 3m long crack, is simulated with different bodies in contact with each other, where the friction is possible (friction coefficient = 0.9). In this case the considered boundary condition is set at “touching” state. The decay tense is defined at 400 KPa. The same friction coefficients were defined for every model and as a safety margin a friction stress limit 1 MPa was imposed. In the next paragraphs, a detailed description of the different model cases follows (Fig. 6):

Case1 : The models M1 and M2 consist of 2647 three dimensional solid finite elements. In several areas of the vault (especially in the lower parts of its baring structure), a material property of a percentage 75% of the initial strength of the rest of the masonry, is defined, due to the damage caused by the descending moisture and the decaying of the bounding mortar. The material loss has been simulated in several parts of the masonry by the removal of finite elements. The difference between the models M1 and M2 is the following: the first one indicates the present conservation status, while the second one refers to a possible future situation in which, the vault is completely disorganized into two parts following the existing crack along the full length of the structure.

Case2 : In the model M3, four separate deformable bodies were used for the analysis. The same boundary conditions and parameters of the masonry pathology of the previous case were used, in order to have comparable analysis results with the other models. Several parameters were tested before the final selection of the finite

elements' mesh properties, to ensure the best possible accuracy of the simulation results of the real structure.

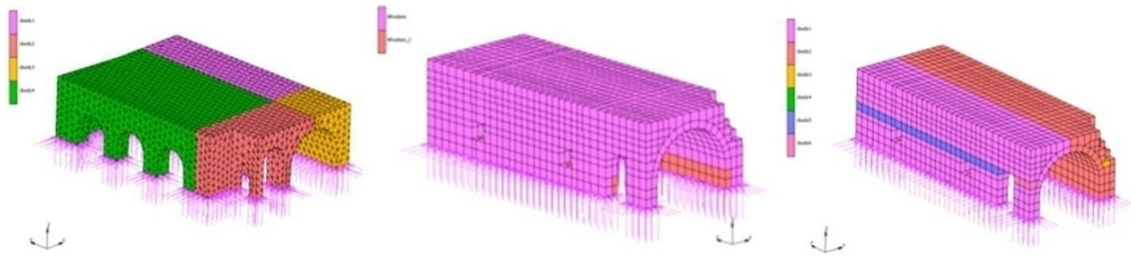


Figure 6 . Axonometric views of the finite elements model (M3 – M1 – M2)

The material properties of the masonry are considered homogeneous and isotropic. The generalized Mohr-Coulomb Parabolic model, that was developed by Drucker and Prager, is used for the masonry, the material properties of which are characterized by elastic-plastic behaviour based on a yield surface that is exposed in hydrostatic stress dependence. Such behaviour is observed in a wide variety of soil and rock-soil materials. As far as the boundary conditions are concerned, the whole structure supports its gravity loads, vertical loads on the top and the nodes of the base are considered to be fixed with the ground since no signs of slip or movement phenomena exist in the structure (zero displacements on the three axes).

3.4 Non-linear analysis of the structure

For the evaluation of the structural behaviour under seismic excitations, the accelerograms of three seismic events were selected and applied to the models, in the nonlinear dynamic analysis. In order to display any failure of the vector, the nonlinear law of fracture (damage) was used. In terms of this law, the nonlinear law of stress-strain for both tensile and compressive behaviour was adopted, according to previously mentioned information.

The characteristics of earthquakes and the accelerograms that were selected are given in Table 2. In terms of the analysis, seismic excitation was applied in two directions (x, y) of the structure, considering that in the vertical direction the vibration is not significant for this structure. In x direction (vertical to the long side of the walls) the 100% of the ground motion was considered and a 30% of the ground motion was applied in y direction (parallel to the masonry axis).

a/a	Earthquake	Earthquake magnitude	Peak ground acceleration (g)
1	Aegio, Greece, 1995	6.40	0.54
2	Irpinia, Italy, 1980	6.69	0.29
3	Kobe, Japan, 1995	6.90	0.80

Table 2: Characteristics of seismic events

Additionally, the criterion of the failure maximum stress (MSC) was used, to indicate the areas of failure in the analysis. It is based on the calculation of nine failure indices F at each integration point. The nine failure indices are given by:

$$F_i = \left(\frac{S_i}{f_{td}} \right) \text{ if } S_i > 0, i = x, y, z \quad (1)$$

$$F_j = \left(\frac{S_j}{f_{cd}} \right) \text{ if } S_j < 0, j = x, y, z \quad (2)$$

$$F_{ij} = \left(\frac{S_{ij}}{f_{sn}} \right), i \neq j, i, j = x, y, z \quad (3)$$

Where:

f_{td}, f_{cd} are the maximum allowable stresses in tension and compression.

S_i are the stresses in tension, in x, y and z direction

S_j are the stresses in compression, in x, y and z direction

S_{ij} are the shear stresses in the 3 planes xy, yz and xz

f_{sn} is the maximum allowable shear stress.

From the comparison of the two analyzed models for the Aegio earthquake, it is apparent that the distribution of stresses and areas of expected failure varies according to the different restriction settings of the theoretical models in comparison with the real geometry of the structure. During the analysis of the M1 model, at the partial step 693, the maximum stress ranges from -2.10MPa compressive to 3.25MPa tensile (Fig. 7). During the step 354 of the analysis, (Fig. 8) all the models are compared with the limit in stress values, that are developed in the

M1 model with no lateral restriction. In the case of absence of lateral restriction, the developed values are significantly lower than in the case of full restriction. The main regions where the stress values increase are located in the area of the crack along the vault - the lower baring area of the masonry and around the openings.

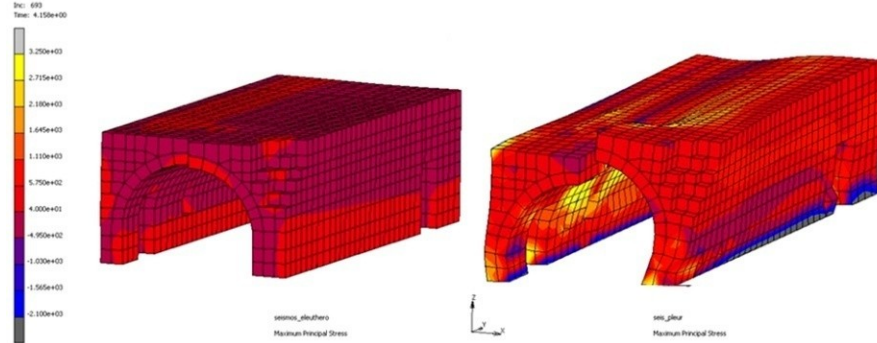


Figure 7 . Axonometric north-east views of maximum principal stress at the 693 step of the analysis as a free model (left) and with lateral restriction (right).

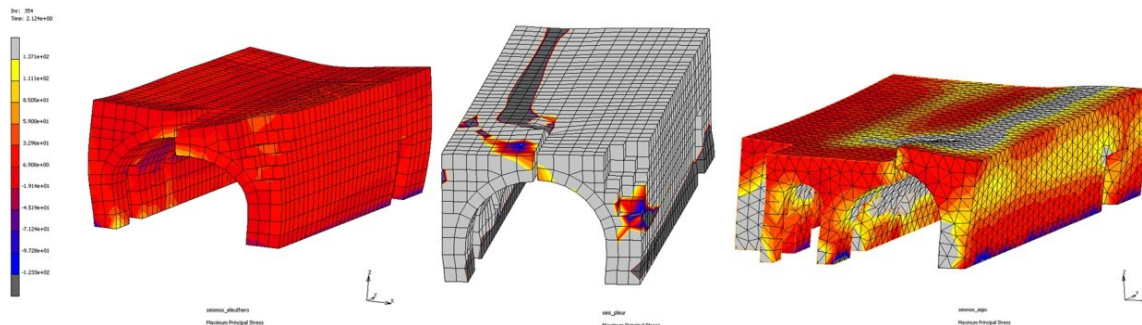


Figure 8 . The maximum principal stress at the 354 step of the analysis as a free model (left), with lateral restriction (middle) and as the existing geometry, for the Aegio earthquake (right).

At the partial step 331 of the Aegio earthquake analysis, failures due to the excess of the tensile stresses along the z (vertical) axis are observed in the case of the lack of lateral bonding in the areas around the openings and in the inner part of the masonry of the vault (failure index 3 with a maximum ratio of 7 and values higher the 1 is shown in Figure 9). Additionally, in the case of rigid engagement, failures are observed at higher ratio values, which extend to the external longitudinal wall of the masonry, but also in the area of the crack, where strong detachment tendency of the vault is observed.

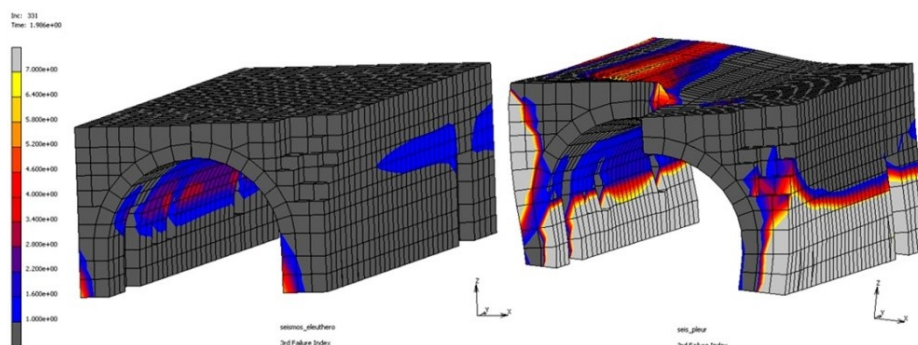


Figure 9 . Axonometric north-east view of the 3rd failure index at the 331 step of the analysis of the [D] vault, as a free model (left) and with lateral restriction (right).

By setting a scale from 0-1 (non failure) at the Failure index 6 and 3 (as defined in Marc Mentat software settings) in partial steps 372 and 356 of the analysis, in the case of full side engagement, exceeded values are developed, and as a result failures are observed in almost the entire structure (Fig. 10-11). Unlikely the previous results of the model with no lateral restrictions (M1), the model M3 seems to reach the failure values, without exceeding them, at the lower area and the openings, while exceeding the limit value (value greater than one) in the area of the crack, indicating a tendency of its further opening. The restriction of the apex of the vault tends to maintain the southern part of the baring masonry, in a state of restraint of its movement, at and at the same time it

affects the distorted behaviour of the entire structure and contributes to the development of higher tension values resulting to further expansion of the crack.

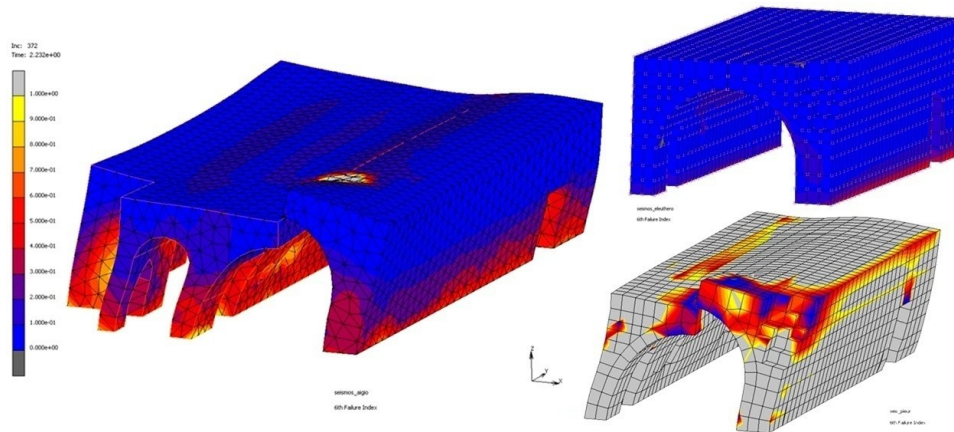


Figure 10 . The 6th failure index at the 372 step of the analysis of the [D] vault, as the geometry exists (left), as a free model with no lateral restrictions (up-right) and with lateral restriction (bottom- right), studied for the Aegio earthquake.

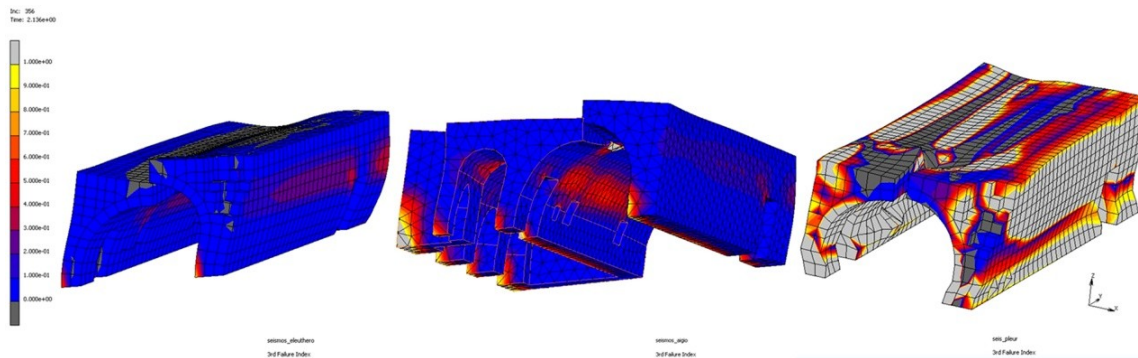


Figure 11 . The 3rd failure index at the 356 step of the analysis of the [D] vault, as a free model (left), the existing geometry studied for the Aegio earthquake (middle) and with lateral restriction (right).

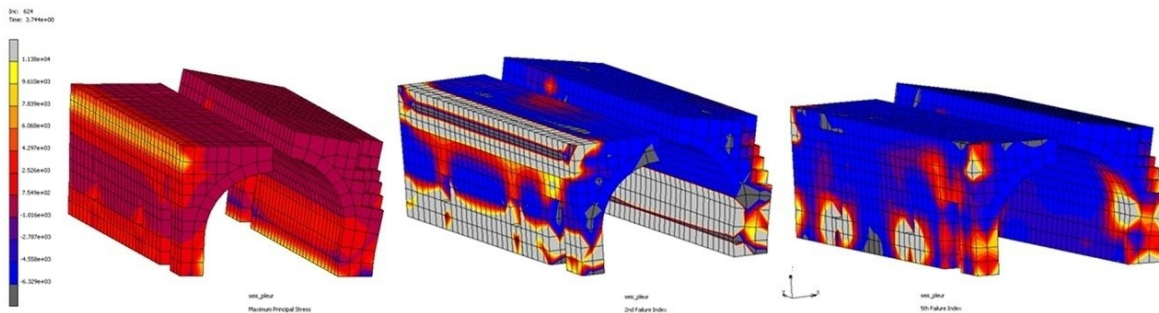


Figure 12 . Axonometric south-east view of the [D] vault at the 624 step of the analysis with lateral restriction: maximum principal stress (left), the 2nd failure index (middle) and the 5th failure index (right).

In the case study of full expansion of the vault crack where the two main parts of the masonry remain in contact only by friction forces (model M2), the existence of the lateral fully rigid support will result in a further increase of the intensive values both in the restrictment area but also in the region of the base of the south side. After the detachment, the south side will behave as a potential “cantilever beam”. The maximum stress values at the step 624 of the analysis, as well as the failure indexes 2 and 5, where the values exceed the limit value of 1.0 and failures are expected, are shown in the Figure 12.

Finally, during the analysis of imposed seismic base excitation of the Kobe earthquake in steps 146 and 148 of the analysis, it is concluded that failure indexes 2 and 5 show the exceeded values of failure in a large part of M1, as opposed to M3 where the exceeded values are observed locally at the area of crack (the failure index 2 is shown in Figure 13). From the first steps of the analysis, it is obvious that the M1 model with the strong Kobe earthquake imposed, reaches the ductile area over a large part of its volume, while in the model M3 the existence

of plastic deformations is limited locally to the crack area and particularly at the structural elements that have not been detached yet.

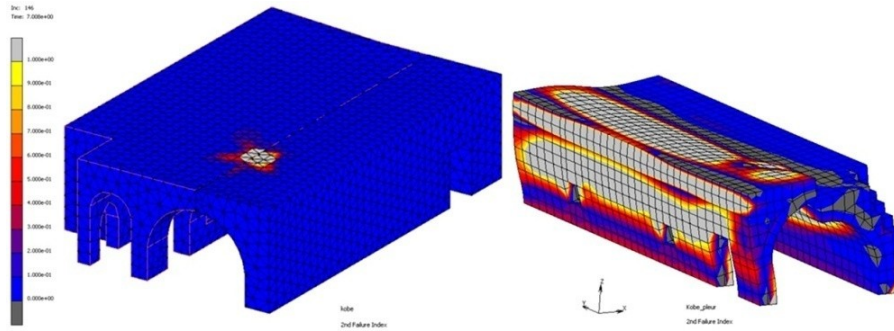


Figure 13. The 2nd failure index of the whole structure (left) and with lateral restriction (right) at the 146 step of the analysis studied for the Kobe earthquake.

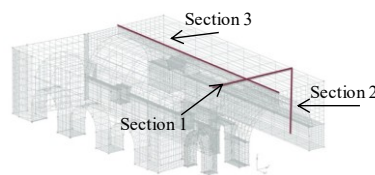


Figure 14. Sections for the displacements presentation.

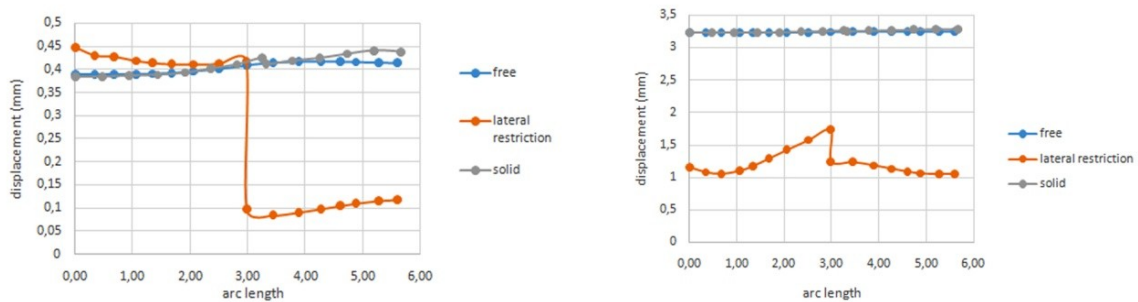


Figure 15. Displacement U at Section 1 for Increments 137 and 145.

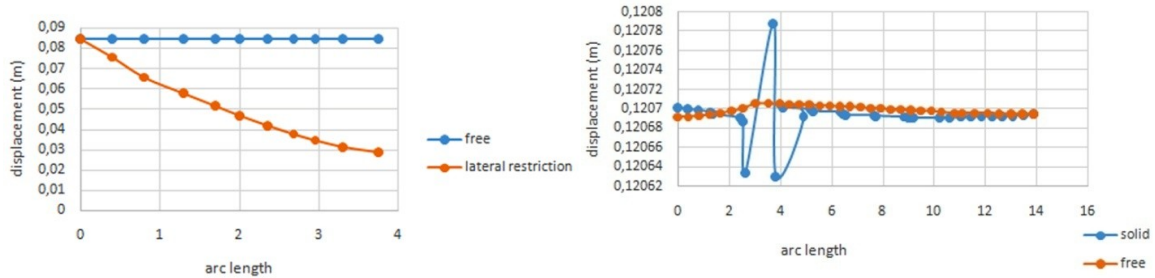


Figure 16. Displacement U at Section 2 for the increment 155 and at section 3 for the increment 202.

Diagrams of the displacements have been created at indicative section views for the Kobe earthquake (Fig. 14-16). These models seem to have different initial displacements of certain nodes in some analysis steps because different modes of oscillation occur due to the seismic simulation. However, more important is the relative movement of the start and end nodes. It is obvious that the sharp increase or decrease of the displacements in the area of the crack opening is shown by the characteristic "step" in the diagrams. The influence of the crack on the model and the existence or not of lateral side restriction is more evident at this phase.

4 CONCLUSIONS

The goal of the present study was the finite element analysis of aggregated elongated vaulted structure in order to study the dynamic behaviour of these buildings in continuity and to investigate the influence of boundary conditions which are considered to the finite element model. Different models of the north-east part of a

monastery complex were used in order to simulate each vaulted structure as a free model with or without lateral restriction and the existing geometry. In parallel the existing failures like a main crack was considered to the models which were analyzed for different earthquakes.

From the preceding analysis, it was concluded that the dynamic behaviour of the structure differs significantly between the two case studies, one with lateral restriction and a second with the real geometry of the building. The distribution of the stress values and the areas of exceedance of the allowed values are located in different positions in these two cases. Furthermore, for the same forced dynamic parameters, the developed stresses vary widely in the matter of values, where low numbers are observed in the case of the free model, intense values in case of the lateral restriction and between these two the case of the real geometry of the building is located. Therefore, every model that is being studied for the FEM analysis should simulate with the best possible accuracy, the real geometry and conservation status of the building, including also the accurate documentation of the neighbor volumes, in order to avoid over sizing phenomena and mistaken positions of the interventions, during the design of the restoration methods. The research continue to the estimation of the stiffness of neighbor structures and the way of modeling since in many cases there is no access to neighboring structures and real conditions mapping.

REFERENCES

- [1] Formisano, A. (2016), "Theoretical and Numerical Seismic Analysis of Masonry Building Aggregates: Case Studies in San Pio Delle Camere (L'Aquila, Italy)", *Journal of Earthquake Engineering*, Vol.0 pp. 1–19.
- [2] Formisano, A., Florio, G., Landolfo, R., Mazzolani, F.M. (2015), "Numerical calibration of an easy method for seismic behavior assessment on large scale of masonry building aggregates", *Advances in Engineering Software*, Elsevier, Vol. 80, pp. 116–138.
- [3] Maio, R., Vicente, R., Formisano, A., Varum, H. (2015), "Seismic vulnerability of building aggregates through hybrid and indirect assessment techniques", *Bull Earthquake Eng*, Springer, Vol. 13, pp. 2995–3014.
- [4] Carocci, C. F. (2012), "Small centres damaged by 2009 L'Aquila earthquake: on site analyses of historical masonry aggregates", *Bull Earthquake Eng*, Springer, Vol. 10, pp. 45–71.
- [5] Caprili, S., Mangini, F. and Salvatore, W. (2015), "Numerical modelling, analysis and retrofit of the historical masonry building "LA SAPIENZA"", *Proceedings of the 5th ECCOMAS Thematic Conference on Computational Methods in Structural Dynamics and Earthquake Engineering (COMPdyn201)*, Greece, 25–27 May 2015.
- [6] Stavroulaki, M.E. and Tsinarakis, T. (2011), "Finite element analysis of masonry barrel vaults", *Proceedings of the 7th GRACM International Congress on Computational Mechanics*, Athens, 30 June – 2 July 2011
- [7] Andrianakis, M. (1994), *Holy Stavropigiac Monastery of Ayia Triada Tsagarolon*, Archaeological guide, Chania.
- [8] Fatourou – Isihaki, K., (1983), "The Cretan Renaissance and the Italian standards of its Architecture", *Ariadni*, Vol. 1, pp. 103-138.
- [9] Papadopetrakis, G. (1966), "History of the Holy Monastery of Ayia Triada, called Tsagarolon until 1862", *Cretan Chronicles*, Vol.20, pp. 17-162.
- [10] Psilakis, N. (1986), *The Cretan Monasteries*, Publications of Bank of Crete, Athens.
- [11] Mistakidis, E.S., Stavroulakis, G.E. (1998), *Nonconvex optimization in mechanics, Smooth and nonsmooth algorithms, heuristics and engineering applications*, Kluwer Academic Publishers, Dordrecht.
- [12] Stavroulaki, M.E., Stavroulakis, G.E. (2002), "Unilateral contact applications using FEM software", *Intern. Journal of Applied Mathematics and Computer Sciences, Special Issue on 'Mathematical Modeling and Numerical Analysis in Solid Mechanics'*, Vol. 12(1), pp. 101-111.
- [13] Stavroulaki, M.E., Stavroulakis, G.E. (2002), "Unilateral frictional contact nonlinearities in aseismic design and restoration of heritage structures", *International Conference on Nonsmooth/Nonconvex Mechanics, with Applications in Engineering*, Thessaloniki, Greece, July 5-6, pp. 209-216.
- [14] Spyarakos, C.C. (1995), *Finite Element Modeling in Engineering Practice*, Algor Publishing Division, Pittsburgh, PA.
- [15] Lourenco, P.B. (2002), "Computations on historic masonry structures", *Prog Struct Engin Material*, Vol. 4, pp. 301-319.
- [16] Leftheris, B.P., Stavroulaki, M.E., Sapounaki, A.K., Stavroulakis, G.E. (2006), *Computational mechanics for heritage structures*. WIT Press, Southampton (UK).

OPTIMUM DESIGN OF REINFORCED CONCRETE FOOTINGS UNDER AXIAL LOADING USING DISCRETE AND CONTINUOUS DESIGN VARIABLES

Sinan Melih Nigdeli¹ and Gebrail Bekdas¹

¹Department of Civil Engineering
Istanbul University
Istanbul, TR-34320, Turkey

e-mail: melihnig@istanbul.edu.tr, bekdas@istanbul.edu.tr

Keywords: RC footing, Optimization, Metaheuristic Algorithms, Flower Pollination Algorithm (FPA), Teaching Learning based Optimization (TLBO), Jaya Algorithm (JA).

Abstract. *In this study, the optimum design of reinforced concrete (RC) footings is investigated by using discrete and continuous variables. The optimization methodology employs metaheuristic algorithms in development of candidate solutions. The problem was evaluated by using Flower Pollination Algorithm (FPA), Teaching Learning based Optimization (TLBO), Jaya Algorithm (JA) and a hybrid algorithm (JA1SP). The optimization objective is the total material cost of the RC footing. The design variables include the dimension variables and the reinforcement design. For discrete variables, all algorithms have the same efficiency, but JA1SP is more effective than the others on finding the minimum cost of the design.*

1 INTRODUCTION

Reinforced concrete (RC) spread footings are an important component of the structures which direct the structural loads to the ground. The optimum design of RC spread footings has been investigated in several studies, but the design of other RC member is generally developed more than spread footings. The main idea of the RC spread footings optimization studies is to find a low-cost design.

Wang and Kulhawy investigated the optimum design of foundations considering the ultimate limit state, serviceability limit state and economics [1]. Wang proposed a reliability-based economic design optimization of RC spread foundations [2]. Zhang et al. proposed an indirect method for reliability-based optimization of geotechnical systems such as spread footings and retaining walls [3]. A modified particle swarm optimization was employed by Khajehzadeh et al. in order to find designs of RC spread footings and retaining walls [4]. A gravitational search is used in the methodology optimizing shallow foundations by Khajehzadeh et al. [5].

In the present study, three new generation metaheuristic algorithms such as Flower Pollination Algorithm (FPA), Teaching Learning based Optimization (TLBO), Jaya Algorithm (JA) are presented. Also, a hybrid algorithm (JA1SP) combining the JA and the student phase of TLBO is proposed. The performance of the algorithms was tested on the cost optimization problem of RC footings by considering discrete and continuous design variables.

2 METHODOLOGY

The optimum sizing and reinforcement design of reinforced concrete (RC) footings is investigated by using several metaheuristic algorithms. The design methodology contains two state limits such as geotechnical and structural ones as design constraints and the codes of American Concrete Institute (ACI318) [6] are considered. The metaheuristic algorithms such as Flower Pollination Algorithm (FPA) [7], Teaching Learning based Optimization (TLBO) [8], Jaya Algorithm (JA) [9] and a hybrid algorithm (JA1SP) are employed.

JA1SP uses the single phase of JA and student phase of TLBO by considering a probability to choose a phase. In JA1SP, a single phase is employed in an iteration according to the defined probability like the switch probability in FPA.

The total material cost of RC footing is the design objective ($f(x)$) and it is penalized with a big value (10^6 \$) if the constraints provided by ACI-318 [6] are violated. The design variables of the RC footing is shown as Figure 1. In Figure 1, X_1 - X_3 are dimensional design variables while X_4 and X_5 are the sizes of reinforcement bars and X_6 and X_7 are the distances between bars. The flowchart of the methodology is shown in Figure 2.

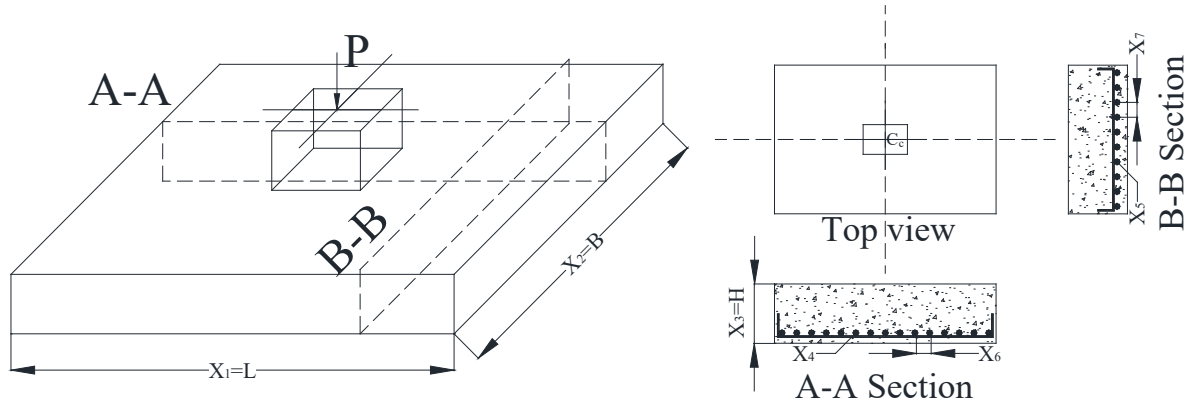


Figure 1. The optimization problem with design variables.

2.1. The Jaya algorithm

Jaya algorithm (JA) is a metaheuristic algorithm which is developed by Rao after the success of algorithm-specific parameter-less algorithm called TLBO. Jaya algorithm is much easier than TLBO since a single phase is employed. In the single phase, the best and the worst solutions are used to generate solutions of the next iteration. The principle of the JA is to converge to the best solution while divergence to the worst solution is provided. Thus, the best solution is found and it is victorious. For that reason, the Sanskrit word; Jaya meaning victory is chosen as the name of the algorithm.

Jaya algorithm is a parameter-free algorithm and it does not contain randomly chosen factors like teaching factor (TF) in TLBO. Only the population is a user defined control parameter. Differently from teaching factor, two random values (r_1 and r_2) are used as seen in Eq. (1) for an example with n population and m maximum iterations. The random values are linear distribution between 0 and 1.

$$x_i^{t+1} = x_i^t + r_1(x_{best} - |x_i^t|) - r_2(x_{worst} - |x_i^t|) \quad i = 1 \text{ to } n \text{ and } t = 1 \text{ to } m \quad (1)$$

x is the set of design variables and the subscripts, i represents the i^{th} candidate solution, best represent the current best solution with the best objective function ($f(x)$) and the worst represents the current worst solution with the worst objective function. The upper scripts show the iteration number and the initial values are used if $t=0$.

The population number seems as an important parameter for JA. If it is less than 3, for example 2; one of the two solution will be best while the other one is the worst solution. In that case, the updated solution will be the best or the worst one and only a single part (+ or -) of the Eq. (1) will work to find the optimum solution. For that reason, the population number may be effective on convergence of the algorithm and preventing to entrapping to a local solution.

2.2. Teaching learning based optimization

TLBO inspired from the education process of a classroom uses two phases which are used in order. The global phase called teacher phase is formulated as Eq.(2).

$$x_i^{t+1} = x_i^t + r_1(x_{best}^t - TF x_{mean}^t) \quad (2)$$

The best solution represents the teacher which may change in every iteration and it is the candidate solutions with the best knowledge in the class. Teaching Factor (TF) is a random integer number which can be 1 or 2. The mean of all candidate solutions is x_{mean} for t^{th} iteration.

The local optimization of TLBO is done in student phase where two random candidate solutions (j and k) are used as seen in Eq. (3).

$$x_i^{t+1} = \begin{cases} x_i^t + r_1(x_j^t - x_k^t) & \text{if } j^{th} \text{ solution is better than } k^{th} \text{ solution} \\ x_i^t + r_1(x_k^t - x_j^t) & \text{if } k^{th} \text{ solution is better than } j^{th} \text{ solution} \end{cases} \quad (3)$$

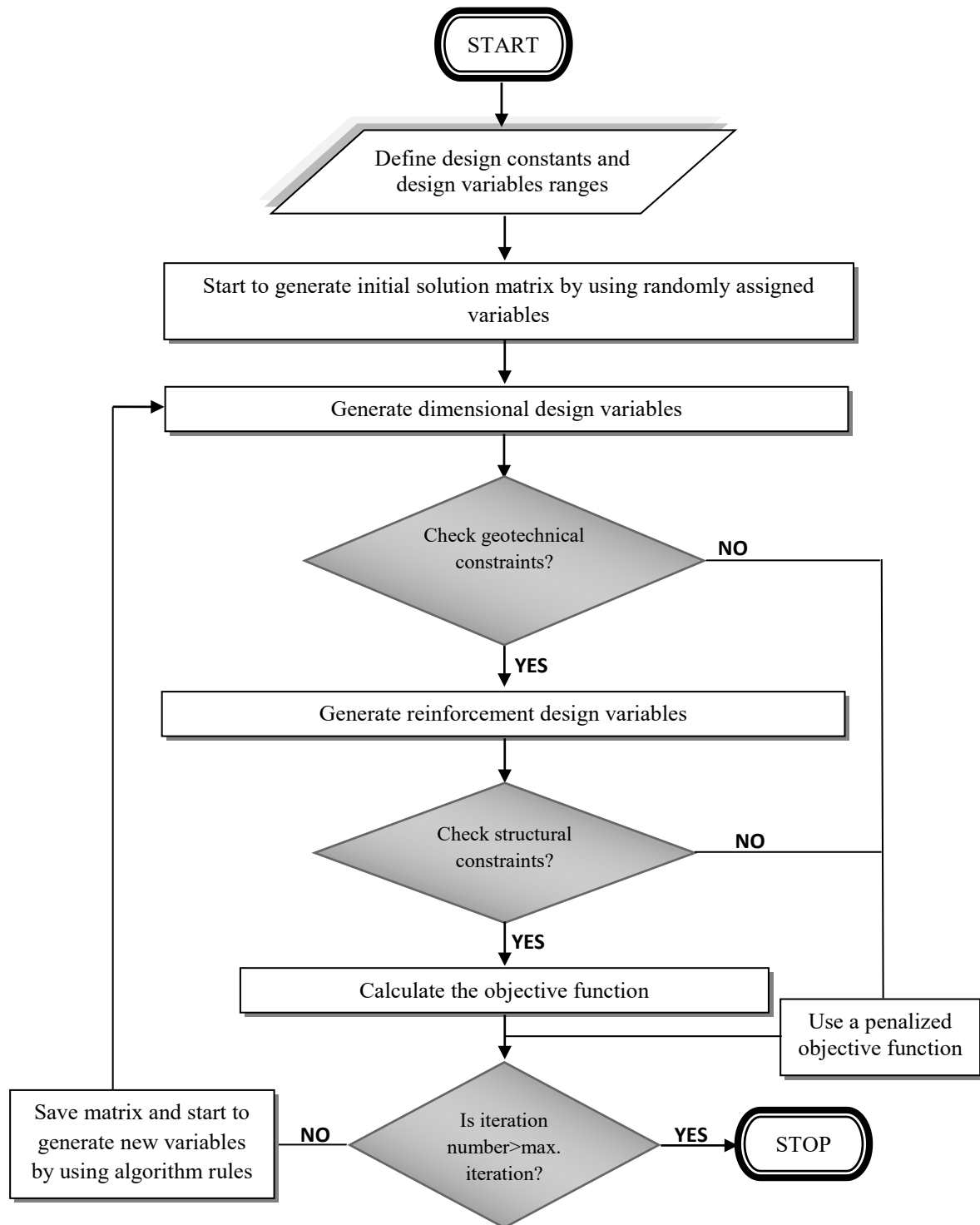


Figure 2. The optimization flowchart.

2.3. Flower Pollination Algorithm

The flower pollination algorithm (FPA) developed by Yang uses the rules of reproduction of flowering plants via pollination. The main rule is the flower constancy and it is the tendency of pollinators to specific flower types. Global and local pollinations use the analogy of biotic (or cross) and abiotic (or self) pollinations, respectively. The formulation for global and local pollinations are given in Eq. (4) and Eq. (5), respectively and the control between the two types is done with a switch probability (p).

$$x_i^{t+1} = x_i^t + L_1(x_{best}^t - x_i^t) \quad (4)$$

$$x_i^{t+1} = x_i^t + L_1(x_j^t - x_k^t) \quad (5)$$

3 NUMERICAL EXAMPLE

The design constants and ranges of the design variables with the numerical values are given as Table 1. The dimension design variables were selected as discrete and continuous in the numerical example. The design variables about reinforcement bars are always taken as discrete since constant sizes can be found in the market and placement of bars can be only done in fixed dimensions.

In the optimization, the population number is 50 and the switch probability was taken as 0.5. The optimum results are presented in Table 2 for 30 independent run of the optimization process. Also, the number required analyses to reach the optimum values are also listed in Table 2.

Definition	Symbol	Unit	Value
Yield strength of steel	f_y	MPa	420
Compressive strength of concrete	f'_c	MPa	25
Concrete cover	c_c	mm	100
Max. aggregate diameter	D_{max}	mm	16
Elasticity modulus of steel	E_s	GPa	200
Specific gravity of steel	γ_s	t/m ³	7.86
Specific gravity of concrete	γ_c	kN/m ³	23.5
Cost of concrete per m ³	C_c	\$/m ³	40
Cost of steel per ton	C_s	\$/t	400
Internal friction angle of soil	ϕ'	°	35
Unit weight of base soil	γ_B	kN/m ³	18.5
Poisson ratio of soil	ν	-	0.3
Modulus of elasticity of soil	E	MPa	50
Maximum allowable settlement	δ	mm	25
Factor of safety	FS	-	3.0
Minimum footing thickness	h_{min}	m	0.25
Column breadth in two direction	b/h	mm/mm	500/500
Dead axial loading	P_G	kN	750
Live axial loading	P_Q	kN	500
Range of width of footing	B	m	2.0-5.0
Range of length of footing	L	m	2.0-5.0
Range of height of footing	H	m	0.25-1.0
Range of diameter of reinforcement bars of two direction	ϕ	mm	16-24
Range of distance between reinforcement bars	s	mm	5 ϕ -250

Table 1. Design constants and ranges of design variables.

	Case for discrete variables				Case for continuous variables			
	FPA	TLBO	JA	JA1SP	FPA	TLBO	JA	JA1SP
L (X ₁) (m)	1.65	1.65	1.65	1.65	1.46	1.68	1.68	1.68
B (X ₂) (m)	1.65	1.65	1.65	1.65	1.46	1.68	1.68	1.68
H (X ₃) (m)	0.85	0.85	0.85	0.85	1.14	0.80	0.80	0.80
ϕ_x (X ₄) (mm)	16	16	16	16	16	16	16	16
S _x (X ₆) (mm)	250	250	250	250	250	250	250	250
ϕ_y (X ₅) (mm)	16	16	16	16	16	16	16	16
S _y (X ₇) (mm)	250	250	250	250	250	250	250	250
Best Cost (\$)	104.92	104.92	104.92	104.92	107.73	103.02	103.22	103.00
Average Cost (\$)	105.80	104.92	104.92	104.92	108.03	103.04	105.00	103.00
Standard Deviation (\$)	1.845	4.8×10^{-14}	7.2×10^{-14}	2.6×10^{-14}	0.12	0.03	0.37	1.4×10^{-14}
Analyses number to each the optimum result	2961	84	67	63	1267	2783	1284	400

Table 2. The optimum results.

In discrete design variables, the dimension variables are the multiples of 0.05 m. The reinforcement sizes are always odd numbers for both cases. The distance between the bars are the multiples of 50 mm. For the discrete case using discrete variables, all algorithms are effective to find the best solutions which have 104.9 \$ material cost. The major difference in this case is the average cost and standard deviation values of FPA. FPA using a Lévy distribution is the worst one comparing to other algorithms such as TLBO, JA and JA1SP. JA1SP is a little better comparing to other ones, but the it is not a significant advantage.

For continuous design variables, more iterations are needed to find the best optimum values. The optimization was done for 1 million maximum analyses. In the case using continuous variables, the best optimum results are different for the algorithms. FPA fails to find an optimum value, because the best result is more expensive than the optimum values for discrete variables. Also, the classical form of JA cannot find an effective solution for continuous variables. These algorithms trap to local optimum values. TLBO is effective on optimization, but JA1SP is better in average cost, standard deviation and number of analyses.

4. CONCLUSION

Since the possible sets of combinations of design variables are less in discrete optimization, all algorithms are effective on finding the same results with a little computational effort and robustness (except FPA). The discrete case is a feasible solution in practice, but the essential comparison and performance evaluation can be done for continuous variables.

All algorithms cannot find the best optimum solution. FPA and the classical form of JA trap to local optimums which lead to an expensive cost than the discrete case. The number of needed analyses is also more than the discrete variable case. In continuous optimization, the developed hybrid algorithm (JA1SP) has a significant contribution in finding the best result immediately and robustly. The student phase of TLBO is an effective formulation to produce possible design variables in the optimization problem.

REFERENCES

- [1]. Wang, Y., & Kulhawy, F. H. (2008). Economic design optimization of foundations. *Journal of Geotechnical and Geoenvironmental Engineering*, 134(8), 1097-1105.
- [2]. Wang, Y. (2009). Reliability-based economic design optimization of spread foundations. *Journal of geotechnical and geoenvironmental engineering*, 135(7), 954-959.
- [3]. Zhang, J., Zhang, L. M., & Tang, W. H. (2011). Reliability-based optimization of geotechnical systems. *Journal of geotechnical and geoenvironmental engineering*.
- [4]. Khajehzadeh, M., Taha, M. R., El-Shafie, A., & Eslami, M. (2011). Modified particle swarm optimization for optimum design of spread footing and retaining wall. *Journal of Zhejiang University SCIENCE A*, 12(6), 415-427.
- [5]. Khajehzadeh, M., Taha, M. R., El-shafie, A., & Eslami, M. (2012). Optimization of Shallow Foundation Using Gravitational Search Algorithm. *Journal of Applied Engineering and Technology*, 4(9), 1124-1130.
- [6]. American Concrete Institute (2008). Building code requirements for structural concrete (ACI 318-08) and commentary.
- [7]. Yang, X.-S. (2012). Flower pollination algorithm for global optimization. In *unconventional computation and natural computation*, 240-249.
- [8]. Rao, R. V., Savsani, V. J. and Vakharia, D. P. (2011). Teachinglearning-based optimization: a novel method for constrained mechanical design optimization problems. *Computer-Aided Design*, 43(3), 303-315.
- [9]. Rao, R. (2016). Jaya: A simple and new optimization algorithm for solving constrained and unconstrained optimization problems. *International Journal of Industrial Engineering Computations*, 7(1), 19-34.

APPLICATION OF THE FINITE SUPERELEMENT METHOD FOR THE DOUBLY PERIODIC FUNCTIONALLY GRADED SOLID CALCULATION

Viacheslav V. Mokryakov

Laboratory of Mechanics of Strength and Fracture of Materials and Structures,
A.Yu. Ishlinsky Institute for Problems in Mechanics RAS, 119526, Moscow, Russia
email: vmokryakov@mail.ru; web page: <http://www.ipmnet.ru>

Keywords: finite superelement, Bernstein polynomials, elasticity, functionally graded material, doubly periodic medium.

Abstract. *The well-known finite element method is not effective in case of continuously heterogeneous media, such as functionally graded solids. But single finite superelement [1] can represent an inhomogeneous region, dependently of superelement's basis power.*

In the paper, a numerical model of a functionally graded elastic medium by the finite superelement method is constructed. The superelement is developed by meshless method [2] and based on Bernstein polynomials [3]. A number of problems of the theory of elasticity are considered: doubly periodic media are constructed from one or two types of characteristic regions under external loadings.

The first heterogeneous region is a central distributed inclusion; the second one is a central damaged area. Several doubly periodic combinations of these regions were considered. Stress-strain states are obtained.

Introduction

In the numerical calculation of problems of the theory of elasticity about periodic structures, the widely used finite element method (FEM) is ineffective. Since the characteristic element of the medium is an inhomogeneity, the required number of elements and the calculation time can be unacceptable.

The article [4] considers a model of a finite superelement (finite element improvement) that allows describing a continuously-inhomogeneous elastic medium, for example, a functionally graded material. Several examples of functionally graded media were examined. In particular, samples with the central damage and with the central distributed inclusion were considered.

In this paper, we present doubly-periodic media constructed from these superelements. The stress-strain states are considered at uniform tension.

Statement of problem

In the first part, three superelements **a**, **b**, **c** are considered, describing three elastic regions of a square shape of the same size. The first region is homogeneous. The second and third ones contain distributed heterogeneities of different types. Their mechanical characteristics are considered.

In the second part, two doubly-periodic media are considered, which are composed, respectively, of superelements **b** and **c**. The behavior of these media under conditions of uniform effective strain (linear strain is 0.1%) is considered; the distributions of the first principal stress and the von Mises stress are calculated.

In the third part, we consider three doubly-periodic media containing pairs of superelements \mathbf{a} and \mathbf{b} , \mathbf{a} and \mathbf{c} , \mathbf{b} and \mathbf{c} , respectively. The behavior of these media under conditions of uniform effective strain is considered too, and the stress distributions are calculated.

Superelement \mathbf{a} (homogeneous)

The superelement \mathbf{a} describes the square region of a homogeneous elastic medium. It is analogous to an ordinary finite element, except for a functional basis: like for other superelements, its basis functions are Bernstein polynomials. For the calculation, mechanical characteristics corresponding to epoxy resin elastic moduli are selected [5]: Young's modulus is $E_e = 3.48$ GPa; shear modulus is $G_e = 1.27$ GPa (hence the Poisson's ratio is $\nu_e = 0.5(E_e/G_e) - 1 \approx 0.37$).

Superelement \mathbf{b} (distributed inclusion)

The superelement \mathbf{b} contains a distributed inclusion: quartz particles ($E_q = 72.6$ GPa, $G_q = 31$ GPa [6]) were added to the epoxy resin so that the volume fraction of particles gradually changed from 0% at the boundary of the region to 50% in the center.

The rule of a mixture [7] allows approximately to estimate the effective elastic moduli:

$$\begin{aligned} \frac{1}{E_{\text{mix}}} &= \frac{(1-\Delta_q)}{E_e} + \frac{\Delta_q}{E_q} = \frac{1}{E_e} + \Delta_q \left(\frac{1}{E_q} - \frac{1}{E_e} \right); \\ \frac{1}{G_{\text{mix}}} &= \frac{(1-\Delta_q)}{G_e} + \frac{\Delta_q}{G_q} = \frac{1}{G_e} + \Delta_q \left(\frac{1}{G_q} - \frac{1}{G_e} \right) \end{aligned} \quad (1)$$

For $\Delta_q = 50\%$ we get $E_{\text{mix}} \approx 6.64$ GPa, $G_{\text{mix}} \approx 2.44$ GPa.

The Young's modulus and the shear modulus of this region are shown in Fig.1.

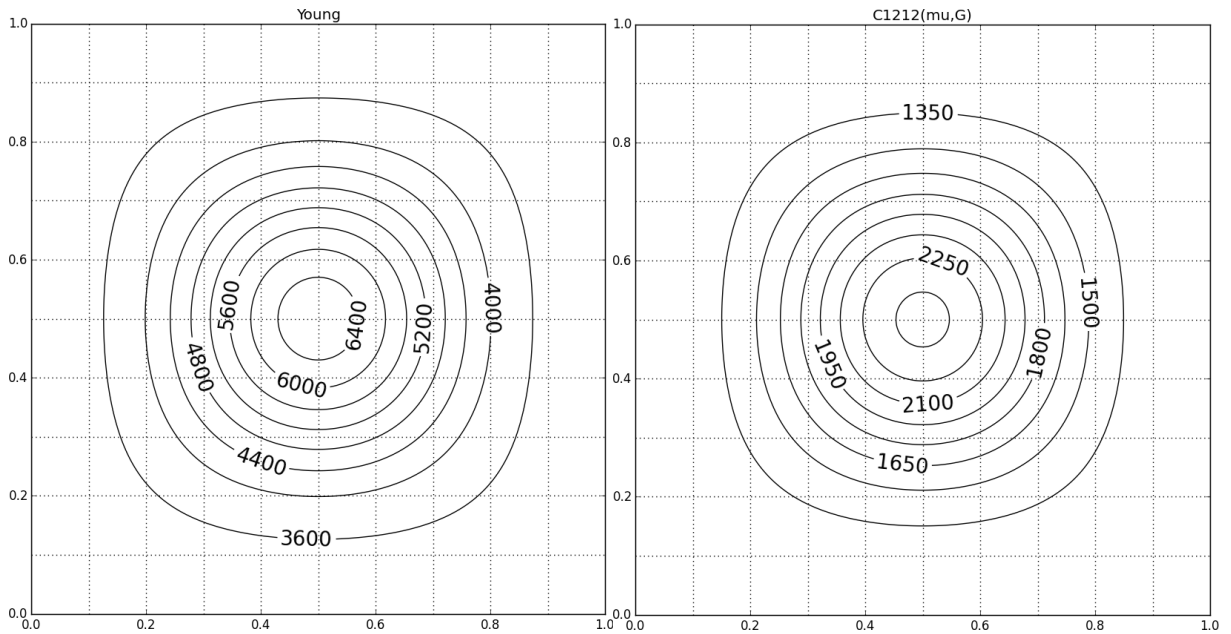


Figure 1. The Young's modulus E [MPa] and the shear modulus G [MPa] of the superelement \mathbf{b} .

Superelement c (damage region)

The last considered superelement c contains the central region of damage. Similar regions occur, for example, in the process of steel casting (central porosity [8], fig. 2). The values of the elastic moduli E and G are halved in the center of the superelement (it is assumed that the Poisson's ratio is constant). Distributions of the elastic moduli of the superelement c are shown in Fig. 3.

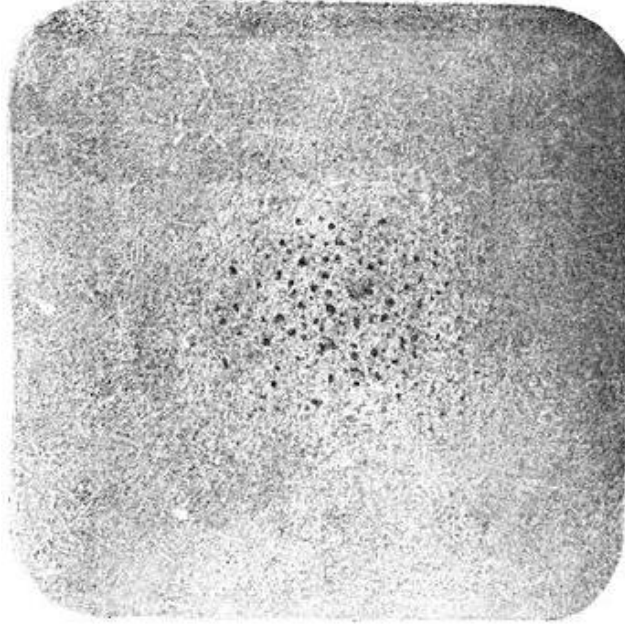


Figure 2. The central porosity at the cut of the ingot of steel.

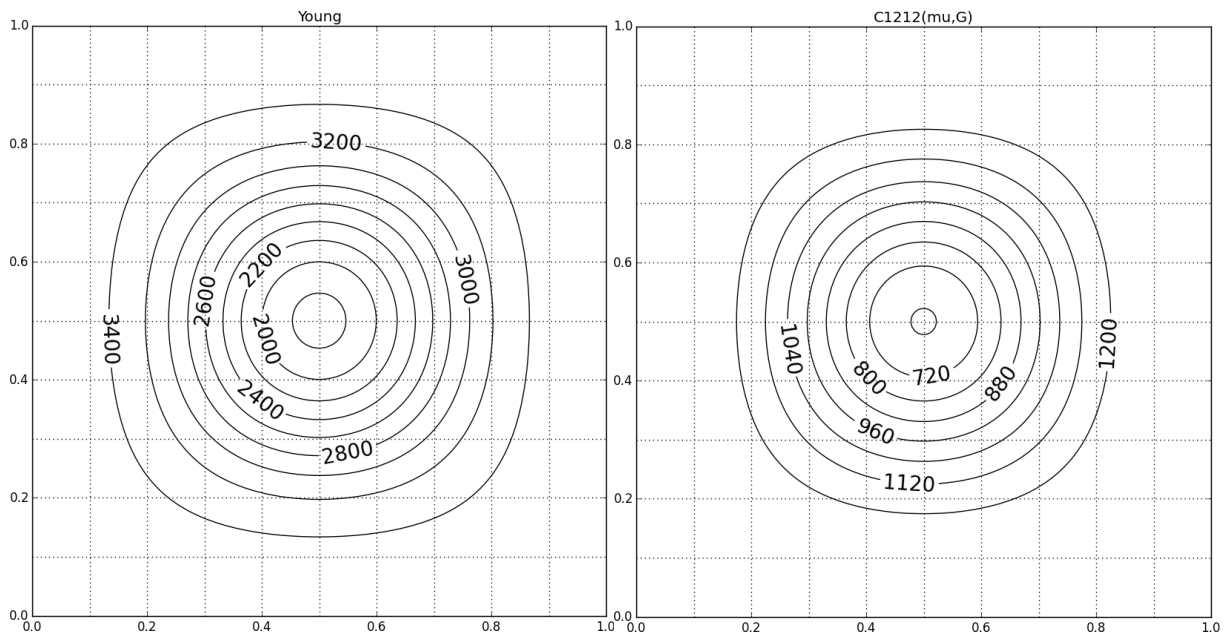


Figure 3. The Young's modulus E [MPa] and the shear modulus G [MPa] of the superelement c .

Doubly-periodic problem with one type of superelements

An infinite doubly-periodic medium is considered, its cell is a superelement of the type b or c , under conditions of uniform effective strain.

The following boundary conditions are set for calculating the stress-strain state. The angular displacements are set so that the conditions of uniform effective strain are realized (linear strain is 0.1%). Displacements on opposite faces are equal, taking into account the cell size change. Loads on opposite faces have got opposite signs. Fig. 4 presents the calculated distribution of the first principal stress σ_{\max} and the von Mises stress σ_M to superelement **b**, fig. 5 presents the same fields for superelement **c**.

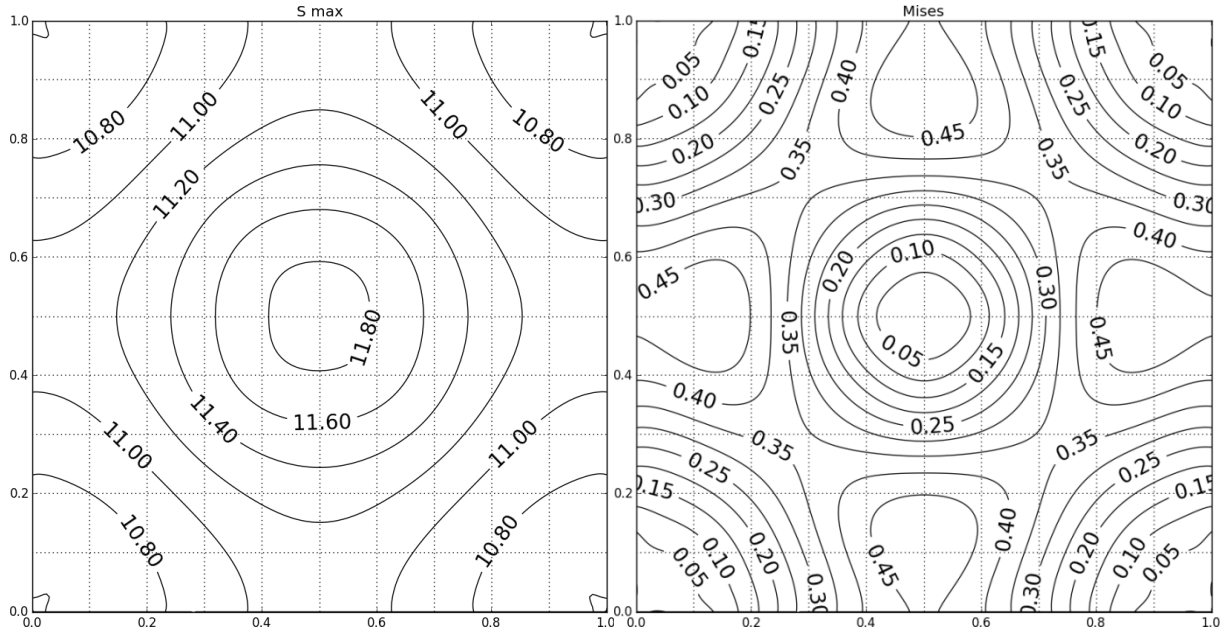


Figure 4. The first principal stress σ_{\max} [MPa] and von Mises stress σ_M [MPa]
(doubly periodic media containing superelements **b**).

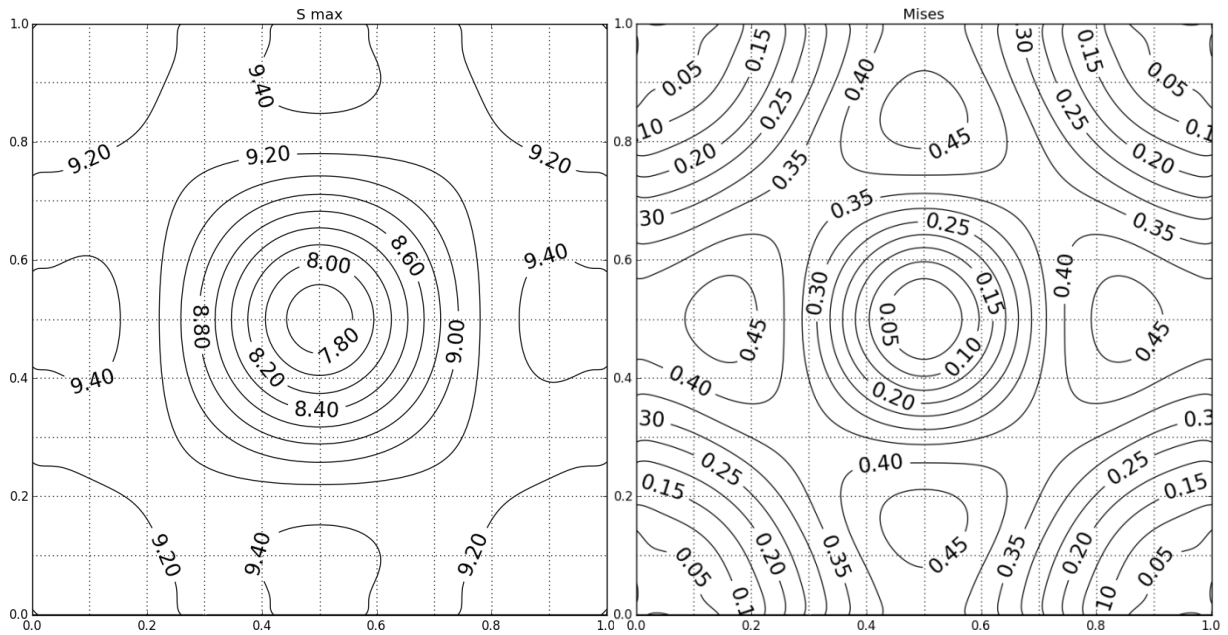


Figure 5. The first principal stress σ_{\max} [MPa] and von Mises stress σ_M [MPa]
(doubly periodic media containing superelements **c**)

Doubly-periodic problem with two types of superelements

An infinite doubly-periodic medium containing two types of superelements ($[a, b]$, $[a, c]$ or $[b, c]$) is considered. Superelements in the medium are staggered. The elastic moduli are shown in fig. 6, 8, 10. To calculate the stress-strain state, the boundary conditions are set as follows. The angular displacements are also set so that the conditions of the uniform effective strain are realized (linear strain is 0.1%).

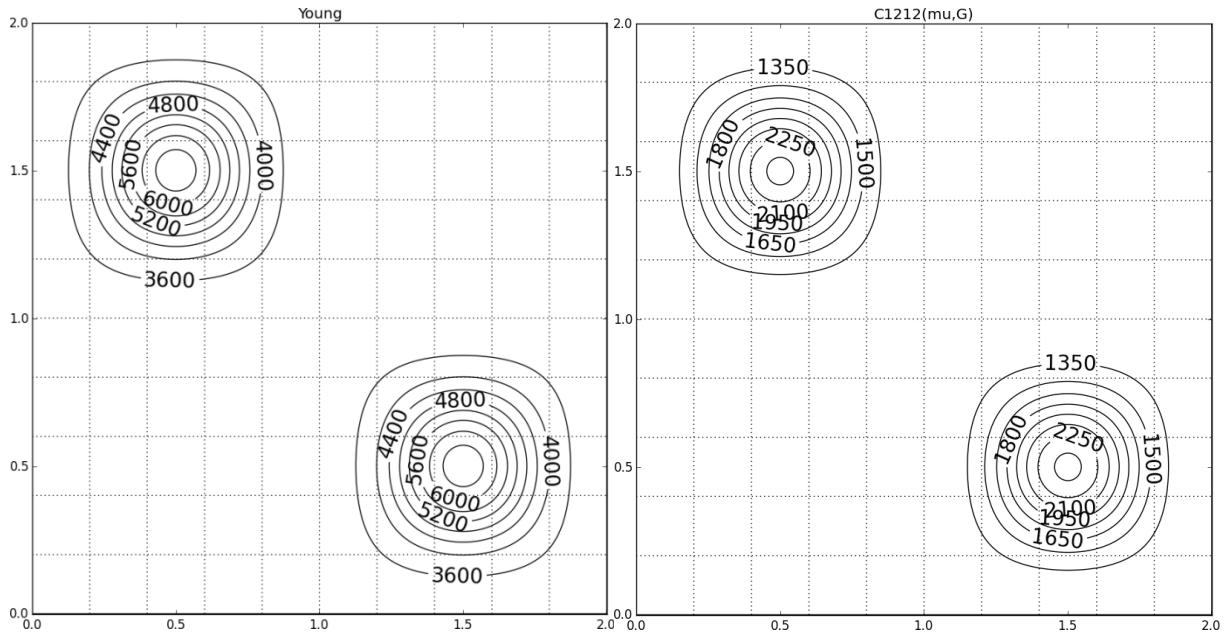


Figure 6. The Young's modulus E [MPa] and the shear modulus G [MPa] (doubly periodic media containing superelements a and b in staggered).

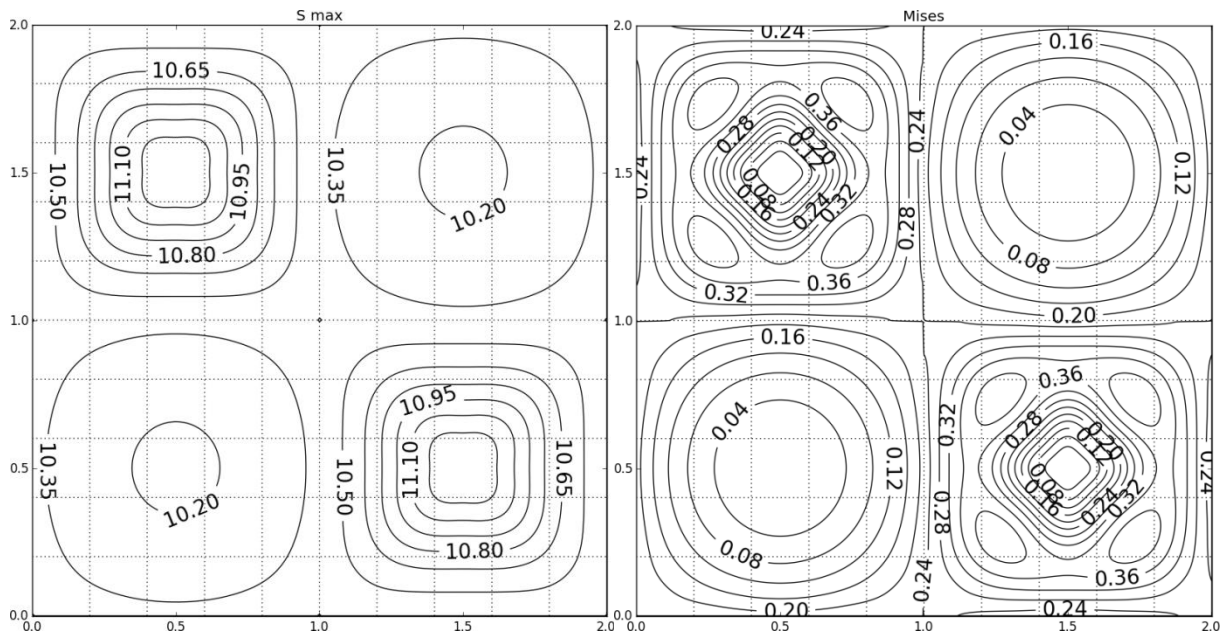


Figure 7. The first principal stress [MPa] and von Mises stress [MPa] (doubly periodic media containing superelements a and b in staggered).

Displacements on one face of one superelement must be equal to the displacements on the opposite face of another superelement. The loads on one face of one superelement must be opposite in sign to the loads on the opposite face of another superelement. The calculated distributions of the first principal stress σ_{\max} and the von Mises stress σ_M of the two-element media are presented in fig. 7, 9, 11.

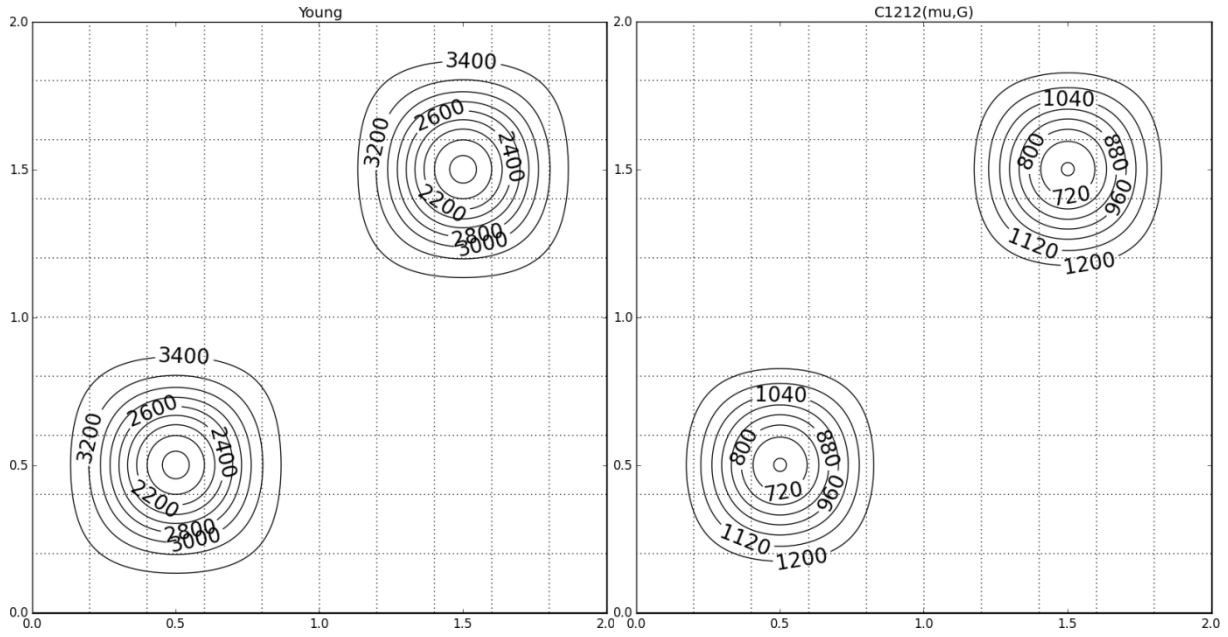


Figure 8. The Young's modulus E [MPa] and the shear modulus G [MPa] (doubly periodic media containing superelements a and c in staggered).

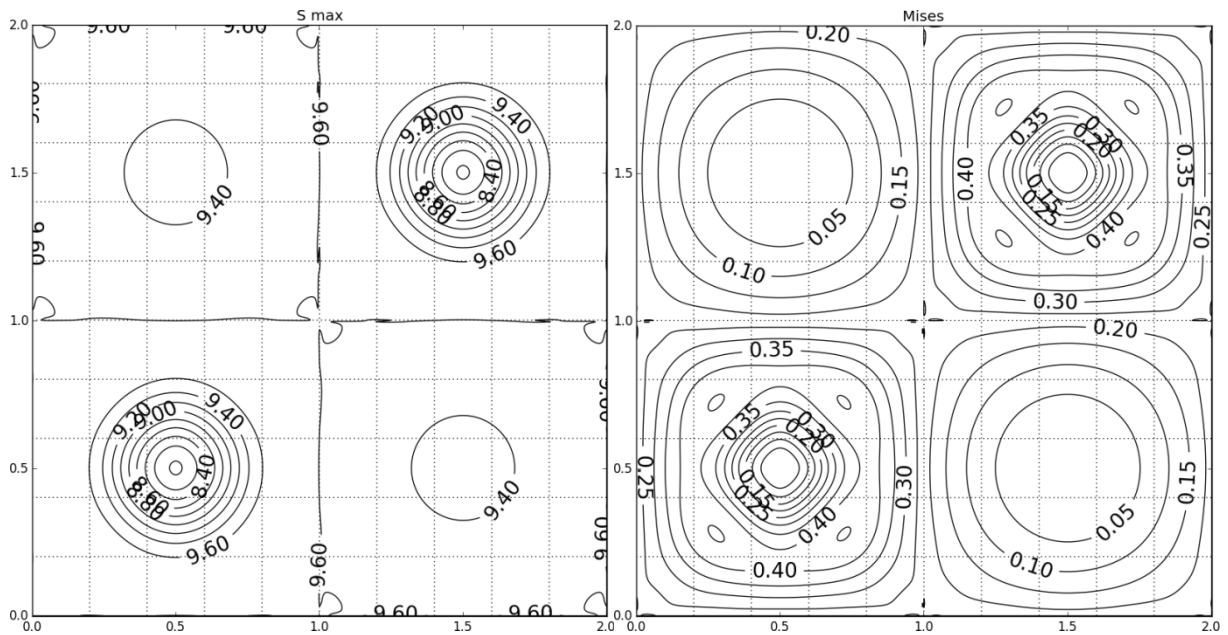


Figure 9. The first principal stress [MPa] and von Mises stress [MPa] (doubly periodic media containing superelements a and c in staggered).

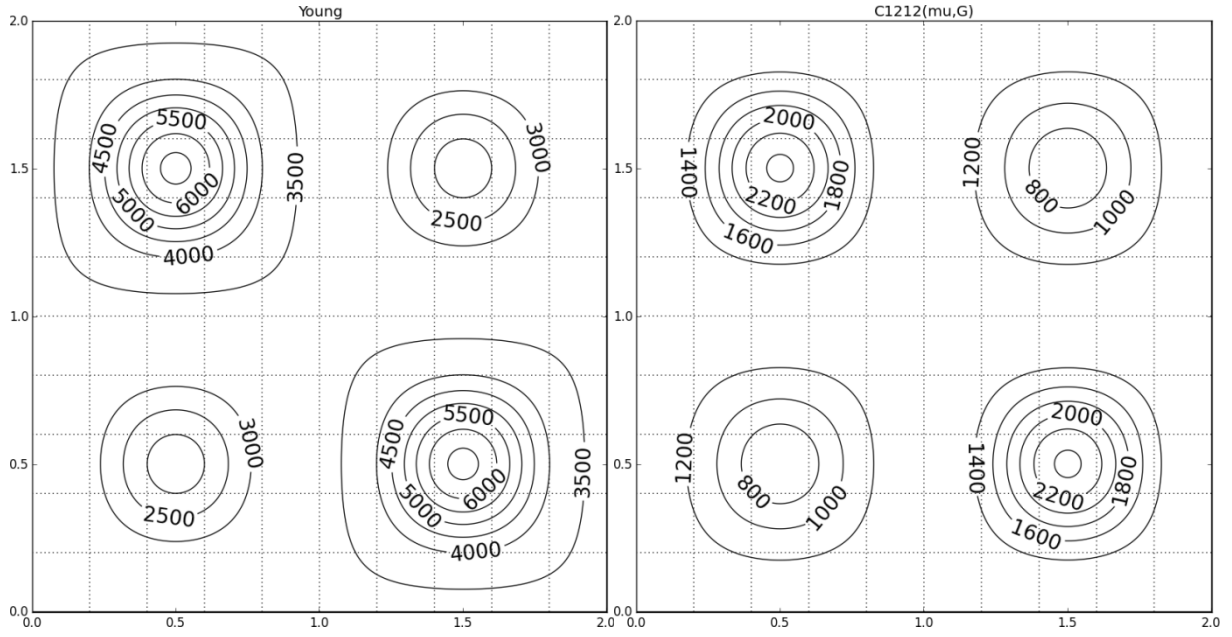


Figure 10. The Young's modulus E [MPa] and the shear modulus G [MPa] (doubly periodic media containing superelements b and c in staggered).

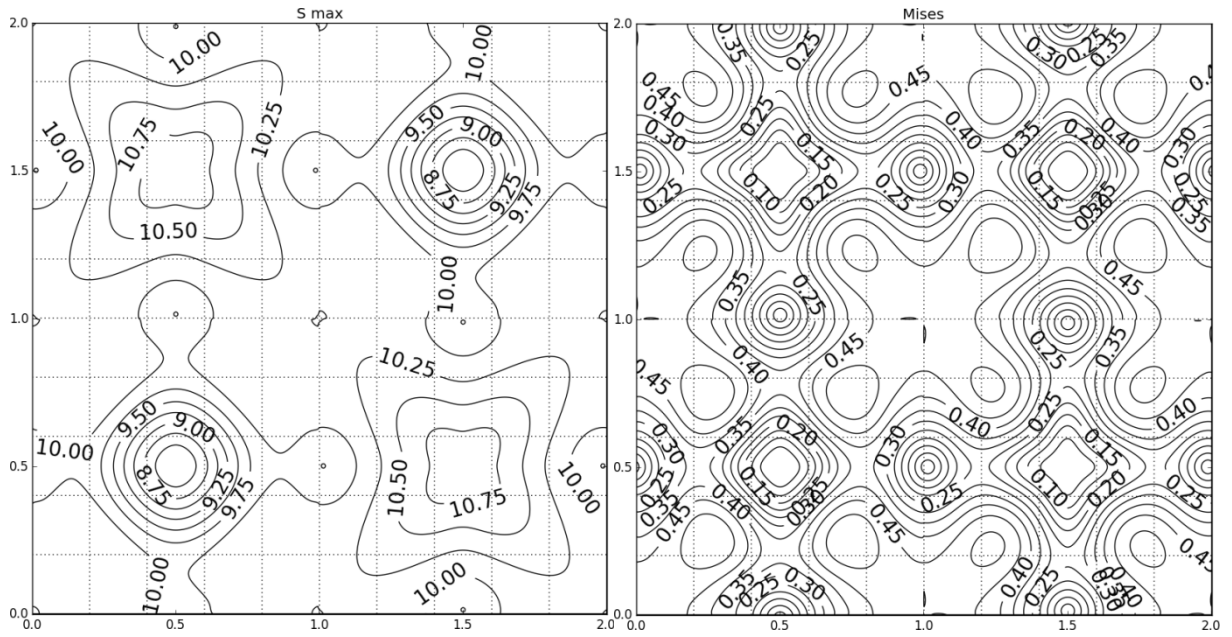


Figure 11. The first principal stress [MPa] and von Mises stress [MPa] (doubly periodic media containing superelements b and c in staggered).

Conclusion

A superelement solving the plane elasticity problem for a heterogeneous square region is considered. The distributions of the elastic moduli are described by the Bernstein polynomial. The boundary conditions (in terms of displacements or loads) must also be described by polynomial functions. A numerical algorithm for solving the assigned problem is developed. A computer program has also been developed that implements the proposed algorithm.

A number of elasticity problems were solved using the proposed method. The constructed superelements describe a homogeneous medium, a medium with a central distributed inclusion, a medium with a central region of damage. With their help, a series of doubly-periodic media was constructed; their stress-strain states under conditions of uniform effective strain were calculated.

The developed program can be used to simulate porous and other inhomogeneous media. The proposed numerical algorithm allows, if necessary, to modify the composition of the basic functions. The additional functions increase the accuracy and efficiency of calculating the stress-strain state taking into account the features of the given inhomogeneous medium.

Acknowledgements

The work is supported by the Federal Agency of Scientific Organizations State Assignment (Theme No. AAAA-A17-117021310386-3). Part of the considered tasks was calculated with the support of the Russian Foundation for Basic Research (Project № 17-01-00526).

References

- [1] Galanin, M. and Savenkov, E. (2002), "Fedorenko finite superelement method as special Galerkin approximation", *Mathematical Modelling and Analysis*, Vol. 7, N. 1, pp. 41-50.
- [2] Chen, Y., Lee, J.D., and Eskandarian, A. (2006), *Meshless Methods in Solids Mechanics*, Springer Science+Business Media, Inc., New York.
- [3] Lorenz, G.G. (1986), *Bernstein Polynomials*, 2nd edn. Chelsea Publishing Company, New York.
- [4] Mokryakov, V.V. (2018), "Numerical simulation of functionally graded plane elastic medium by finite superelement method", *AIP Conference Proceedings*, Vol. 1922, pp. 030004-1 - 030004-10.
- [5] Lubin G., ed. (1982), *Handbook of Composites*, Van Nostrand Reinhold Company Inc., New York.
- [6] Huntington H.B. (1958), *The elastic constants of crystals*, Solid State Physics, V. 7, p. 213-351.
- [7] Fujii T., Zako M. (1982), *Fracture mechanics of composite materials*, Mir, Moscow.
- [8] GOST 10243-75. (1985), *Steel, Method of test and estimation of the macrostructure*, Publishing house of standards, Moscow.

INVESTIGATION OF SUPPORT CONDITIONS BETWEEN STACKED REINFORCED CONCRETE BEAMS USING EXPERIMENTAL MODAL ANALYSIS AND FINITE ELEMENT METHODS

Marios Filippoupolitis¹ and Carl Hopkins²

¹Institute for Risk and Uncertainty
University of Liverpool
Liverpool, L69 7ZF, UK

e-mail: m.filippoupolitis@liverpool.ac.uk ;
web page: <http://www.liru-cdt.org/>

²Acoustics Research Unit
University of Liverpool
Liverpool, L69 7ZN, UK

e-mail: carl.hopkins@liverpool.ac.uk

web page: <https://www.liverpool.ac.uk/architecture/research/acoustics-research-unit/>

Keywords: Beam junctions, Finite element method, Experimental modal analysis, Contact stiffness

Abstract. *The prediction of vibration transmission in collapsed and fragmented reinforced-concrete buildings has the potential to inform decisions about the possibility to detect human survivors trapped in buildings after earthquakes by using structure-borne sound propagation. This paper focuses on the investigation of the support conditions between two stacked reinforced concrete beams using experimental modal analysis and finite element methods. Finite element models were developed in Abaqus of three different junctions of two beam with surface-to-surface support conditions between the beams. These were validated against the results of experimental modal analysis, in terms of eigenfrequencies and modeshapes. It is shown that the contact between the two beams in each junction is elastic and that on average the value of the contact stiffness is independent of the shape of the junction.*

1 INTRODUCTION

Earthquakes have the highest rate of mortality among all the natural disasters. From 1970 to 2009, 36% of fatalities that have occurred due to natural disasters are due to earthquakes [1]. When victims are trapped inside a collapsed building, the challenge is to detect and locate survivors within a period of time that will allow them to be rescued. The prediction of vibration transmission in collapsed and fragmented reinforced-concrete buildings has the potential to inform decisions about the possibility to detect trapped human survivors by using structure-borne sound propagation. This research forms part of a funded project concerning an approach to search for human survivors using structure-borne sound propagation in collapsed and fragmented structures through the development, validation and use of theoretical models.

Previous research indicated that the support condition between two reinforced concrete beams stacked on top of each other (i.e. without bonding material) is elastic and could be approximated in FEM using the normal contact stiffness [2]. The aim of this paper is to investigate the dependency of the normal contact stiffness on the shape of the junction and estimate its value using experimentally validated finite element models of three junctions of two beams with surface-to-surface support conditions. Experimental modal analysis is carried out in each junction and the results are used to model update the value of the contact stiffness in the frequency range between 700 and 3200 Hz.

2 EXPERIMENTAL WORK

2.1 Test specimens

The experimental samples consist of two reinforced concrete beams (C25/30, S500) with the same dimensions (2.4 m length, 0.2 m width and 0.3 m depth). Beams 1 and 2 are reinforced with four and eight longitudinal steel bars of 16 mm diameter, respectively. The transverse reinforcement of both beams consists of 8 mm diameter stirrups placed at 200 mm centres along the beams.

2.2 Test setups

In test setup 1 (see Fig.2), square-section aluminum bars (25x25mm) supported beam 1 at each end to approximate simply supported conditions. Next, three beam junctions were formed after placing beam 2 on top of beam 1 (see Fig. 1 and Fig. 2). In setups 2 and 3, the angle between the beams is equal to 90° but the beams are in contact at a different position along the length. In setup 4 the two beams are at an angle of 41° .

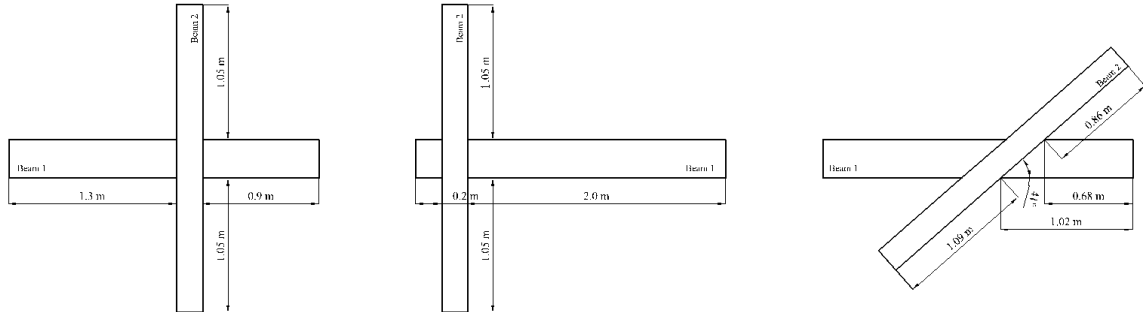


Figure 1. Test setups - (from left to right) Setup 2, Setup 3 and Setup 4

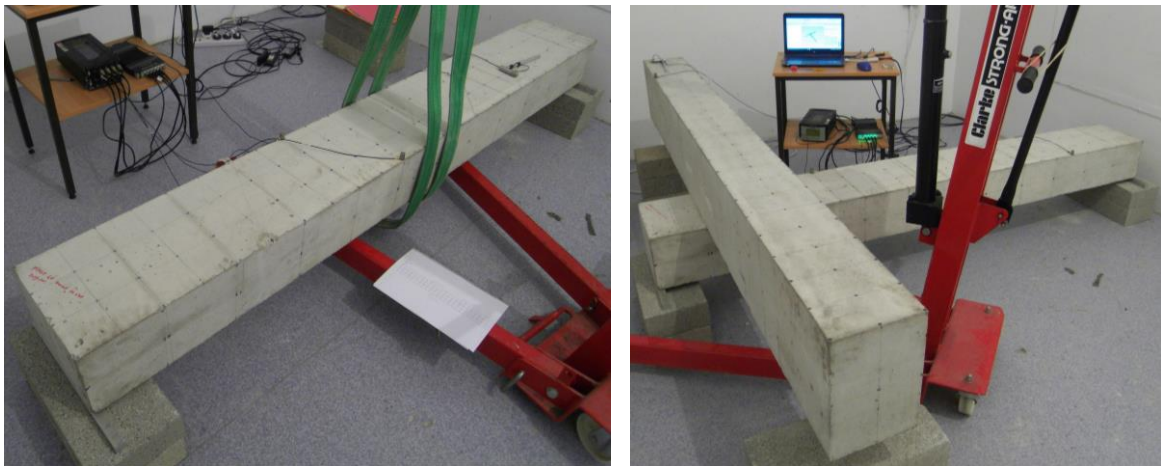


Figure 2. (Left) Test setup 1 showing the transducers and the aluminium sections that approximate the simply support condition for the beam 1, (Right) Test setup 3 showing the test equipment and the junction formed by beams 1 and 2

2.3 Experimental modal analysis

Experimental modal analysis was carried out to identify the eigenfrequencies and mode shapes of the four setups. The beams were excited using an impact hammer (Brüel & Kjær Type 8200) and the out-of-plane response was measured using three accelerometers (Brüel & Kjær Type 4371). Brüel & Kjær Pulse Reflex software was used for signal processing and modal analysis. During the modal testing, the accelerometers remained at fixed positions whilst the impact hammer was moved along the excitation points.

3 FINITE ELEMENT MODELLING

FEM models of the four setups were developed in Abaqus v6.14 [3] and eigenfrequency analysis was carried out to identify their dynamic characteristics (eigenfrequencies and modeshapes). Solid element C3D20R (20 nodes) and the beam element B32 (3 nodes) were selected from the element library of Abaqus to model the concrete and steel bars respectively. The mesh density provides at least six elements per wavelength in structural and vibroacoustic problems [4]. Table 1 shows the physical and mechanical properties of the materials used in the models. More information regarding the estimation of the material properties can be found in [5].

Material	Density, ρ [kg/m ³]		Young's modulus, E [N/m ²]	Poisson's ratio, ν [-]
Concrete	Beam 1	2328.7	36875E06	0.2
	Beam 2	2245.2	32475E06	
Steel	7800		200E09	0.3

Table 1: Material properties.

The linear spring element, SPRING1 was selected from the Abaqus element library to approximate the elastic support provided by the square-section aluminium bars to the lower beam, beam 1. After model updating against the fundamental eigenfrequency of setup 1, the stiffness of the springs was estimated to be 4.1E05 N/m.

The contact between the two beams was modelled using the general contact algorithm of Abaqus/Standard and was defined to have either only elastic normal behaviour (FEM model 1) or both elastic normal and rough tangential behaviour (FEM model 2). The latter was implemented assuming an infinite friction coefficient such that the common nodes of the contact area moved together in the horizontal plane. For every mode pair in setups 2, 3 and 4, the value of the normal contact stiffness was optimized through model updating to give the closest agreement between measured and FEM eigenfrequencies.

4 RESULTS

4.1 Normal contact stiffness

Table 2 shows the mean normal contact stiffness resulted from the model updating of FEM models 1 and 2. The mean normal contact stiffness in Table 2 was used in the FEM models for each setup. The inclusion of rough tangential behaviour in FEM model 2 results in a value that is, on average, 2.7 times lower than the normal contact stiffness of FEM model 1. This is likely to be due to the absence of the in-plane stiffness component in FEM model 1. Table 2 indicates that the mean normal contact stiffness is not dependent on the shape of the junction as similar values of contact stiffness were estimated for two and three setups with FEM models 1 and 2 respectively, after model updating. The next sections allow an assessment of FEM models 1 and 2 against the experimental modal analysis results.

FEM model	Setup	Mode pairs used in the model updating	Contact area, A [m ²]	Mean contact stiffness, $K_{c,mean}$ [N/m]
1	2	22	0.06	4.45E+08
	3	22	0.06	7.56E+08
	4	23	0.09	7.54E+08
2	2	25	0.06	2.44E+08
	3	23	0.06	2.04E+08
	4	24	0.09	2.66E+08

Table 2 Mean normal contact stiffness of Setups 2, 3 and 4 for FEM models 1 and 2.

4.2 Eigenfrequencies

Figure 3 compares FEM models 1 and 2 against the experimental modal analysis results for setups 2, 3 and 4, in terms of eigenfrequencies.

Both FEM models show close agreement with the experimental eigenfrequencies with differences less than 5% for the majority of the mode pairs in the frequency range from 700 to 3200Hz. However, FEM model 2 predicted a greater number of mode pairs than FEM model 1 as indicated in Table 2 and Fig.3. It is also shown that the three setups have similar eigenfrequencies. The reason for this is expected to be that the global eigenfrequencies of Setups 2, 3 and 4 will be partly determined by the eigenfrequencies of the individual isolated beams, and these beams are the same in the three setups.

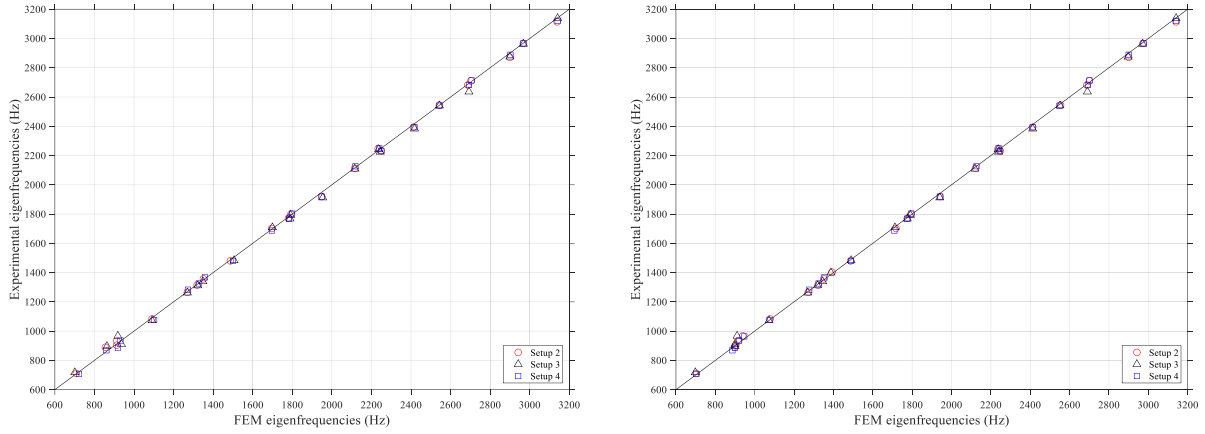


Figure 3. Comparison of FEM models against experimental eigenfrequencies for setup 2, 3 and 4. (Left) FEM model 1, (Right) FEM model 2.

4.3 Mode shapes

Figures 4, 5 and 6 compare FEM and experimental results for setups 2, 3 and 4 respectively in terms of mode shapes using the Modal Assurance Criterion (MAC) [6]. Note that only bending and torsional modes were included in the validation procedure of the FEM models.

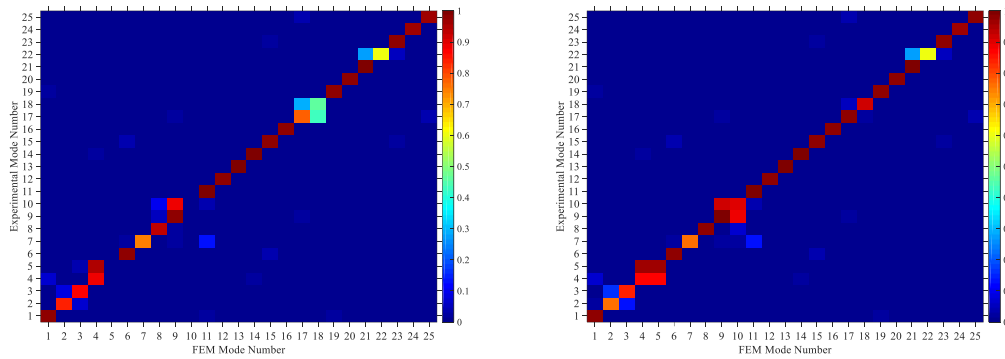


Figure 4. Setup 2 - (Left) MAC values for FEM model 1, (Right) MAC values for FEM model 2

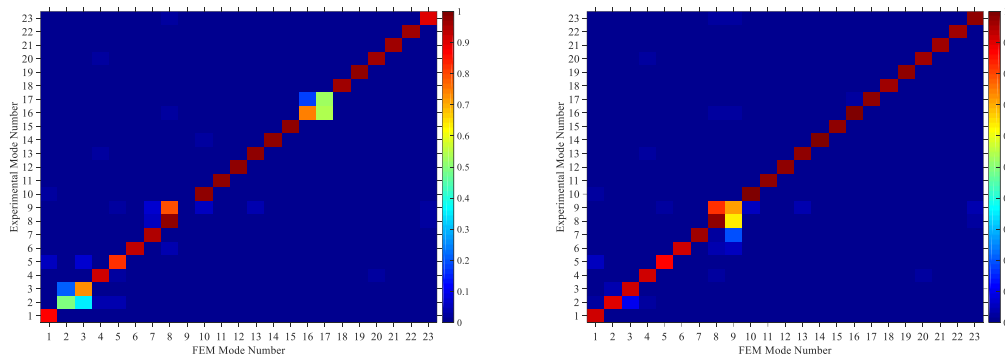


Figure 5. Setup 3 - (Left) MAC values for FEM model 1, (Right) MAC values for FEM model 2

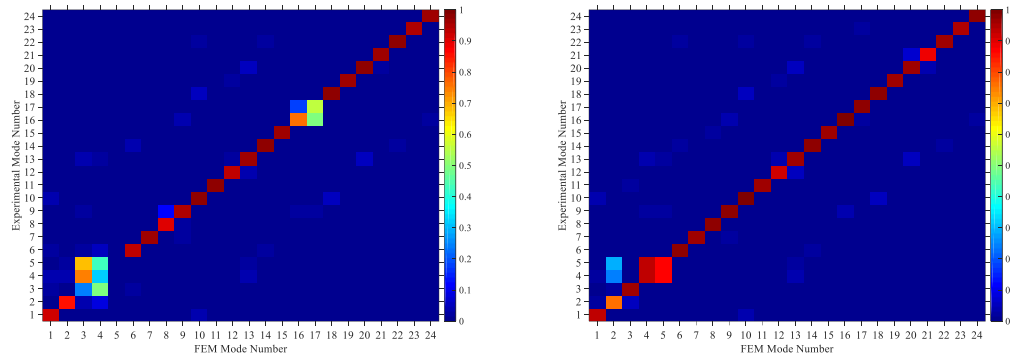


Figure 6. Setup 4 - (Left) MAC values for FEM model 1, (Right) MAC values for FEM model 2.

For FEM model 1, close agreement was achieved for the majority of mode pairs above the first five global modes (i.e. between 1000 and 3200 Hz); MAC values were greater than 0.8 for 19, 18 and 19 of the mode pairs for setups 2, 3 and 4 respectively. For the first five global modes (i.e. below 1000 Hz), there is less agreement for setups 3 and 4 with the exception of the first two modes which have MAC values greater than 0.8. For FEM model 2, close agreement with MAC values greater than 0.8 was achieved for the majority of mode pairs.

The results of this validation indicate that both FEM models reasonably describe the dynamic behaviour of a beam junction formed by two reinforced concrete beams stacked on each other in the frequency range. However, the FEM model with the rough tangential behaviour (FEM model 2) is more appropriate for modelling the first five modes.

5 CONCLUSIONS

Experimental modal analysis was carried out to determine the dynamic characteristics (eigenfrequencies and mode shapes) of three beam junctions that consisted of two beams stacked on top of each other. It was found that the shape of the junction (relative position and angle of the beams) did not significantly affect the eigenfrequencies.

Two FEM models were used: FEM model 1 with elastic normal behaviour and FEM model 2 with elastic normal and rough tangential behaviour. Model updating resulted in normal contact stiffness values which had a factor of 2.7 between FEM models 1 and 2 and were not strongly dependent on the shape of the junction. Both FEM models achieved close agreement with the measurements in terms of eigenfrequencies. In addition, the mode shapes from both FEM models were in close agreement with experimental modal analysis for the majority of modes but only FEM model 2 which incorporated rough tangential behaviour gave close agreement for the first five modes.

ACKNOWLEDGEMENTS

The authors are grateful for the funding provided by the EPSRC and ESRC Centre for Doctoral Training in Quantification Management of Risk & Uncertainty in Complex Systems and Environments at the University of Liverpool.

REFERENCES

- [1] Bobrowsky, P. T. Ed., (2013) *Encyclopedia of Natural Hazards*, Springer Netherlands.
- [2] Filippoupolitis, M., Hopkins, C. and Au, S. K. (2017), "Vibration transmission between stacked reinforced concrete beams using monte carlo simulations with finite element methods," *Proceedings of the 24th International Congress on Sound and Vibration (ICSV24)*, London, UK, 23-27 July 2017
- [3] Hibbitt, D., Karlsson, B. and Sorensen, P. (2014), *Abaqus 6.14 Documentation and User Manual*, Dessault Systemes Simulia Corp, Providence, Rhode Island
- [4] Atalla, N. and Sgard, F. (2015), *Finite Element and Boundary Methods on Structural Acoustics and Vibration*, CRC Press, Taylor & Francis Group, Boca Raton
- [5] Filippoupolitis, M., Hopkins, C. and Au, S. K. (2016), "Experimentally validated finite element models of two reinforced concrete beams subjected to surface-to-surface contact condition," *Proceedings of the 45th International Congress and Exposition of Noise Control Engineering (InterNoise 2016)*, Hamburg, Germany, 21-24 August 2016
- [6] Ewins, D. J. (2000), *Modal Testing*, Research Studies Ltd, Hertfordshire

EFFECTS OF THERMAL DEFORMATION ON THE BUCKLING RESISTANCE OF STEEL FRAMED MEMBERS EXPOSED TO FIRE

Themistoklis N. Nikolaidis¹ Evangelia V. Georgantzia² and Charalampos C. Baniotopoulos³

¹Institute of Metal Structures, Department of Civil Engineering, Faculty of Engineering
Aristotle University of Thessaloniki, 54124 Thessaloniki, Greece
e-mail: thnik@civil.auth.gr ; web page:

http://www.civil.auth.gr/index.php?option=com_contact&task=view&contact_id=191&Itemid

²Institute of Metal Structures, Dept. of Civil Engineering, Faculty of Engineering
Aristotle University of Thessaloniki, Thessaloniki, GR-54124, Greece
e-mail: egeorgantzia@gmail.com; web page: <https://gr.linkedin.com/in/EvangeliaGeorgantzia>

³School of Engineering, University of Birmingham
B15 2TT Birmingham, United Kingdom
e-mail: c.baniotopoulos@bham.ac.uk; web page: <http://www.birmingham.ac.uk/schools/civil-engineering/people>

Keywords: Fire design, Transient analysis, Coupled-field analysis, Thermal deviation, Load bearing capacity

Abstract. *The accidental situation of fire in steel members lead to changes their physical and mechanical properties when temperature is significantly increasing during time. According to Eurocode 3, the critical load of a steel member at uniform temperature increase is defined by using a reduction factor to the load bearing capacity properties. The effect of the thermal deformation resulting from thermal gradients across the cross-section due to different insulating condition at each side could change the bearing capacity of the steel member. In order to determine the influence of this thermal deviation to the critical design load of a steel member an advanced calculation scheme is herein proposed. This scheme combines a transient thermal analysis of the steel section exposed to fire with a coupled field structural analysis of the respective critical steel member including different thermal load action across the cross-section. In the present paper a steel column in a certain fire compartment of a building is studied. The overall analysis of both models has been made by the ANSYS computer software.*

1 INTRODUCTION

In the accidental situation of fire in steel buildings elevated temperatures product significant effects and reduction on both strength and strain resistance of the steel members. So the linear elastic response of the steel members becomes distinctly nonlinear and at the same time the temperature induced thermal elongations changes its buckling behavior. This change has a strong and interesting influence on the local and global stability behavior of the steel framed members. According to Eurocode 3, the critical load of a steel member at uniform temperature increase is defined by using a reduction factor to the load bearing capacity properties. The effect of the thermal deformation resulting from thermal gradients across the cross-section due to different insulating condition at each side changes the reduction on the strength and strain resistance as well as its buckling behavior. Taking into account that temperature changes in the materials lead to changes in their properties and in particular, in strength characteristics, a fact that becomes obvious when temperature is significantly increase, the only possibility to obtain a passive control of steel section strength in fire is to protect it from thermal expansion by an appropriately chosen insulating material or combination of materials applied to the envelope. In order to determine the influence of this thermal deviation to the critical design load [3], [4], [5], [9], of a steel member an advanced calculation scheme is used. This scheme combines a transient thermal analysis of the steel section at elevated temperatures with a coupled field nonlinear structural analysis of the respective critical steel member element including different thermal load action across the cross-section.

According to Eurocode 1 - Part 1-2, §3.3.2, the temperature - time curve determines the temperature distribution due to fire as a function of time. By this analysis is checked the performance of steel-framed elements due to standard fire curve defined in Eurocode 1 - Part 1-2 as well as due to the fire curve of an advanced FDS (Fire Dynamic Simulator), using a software simulation

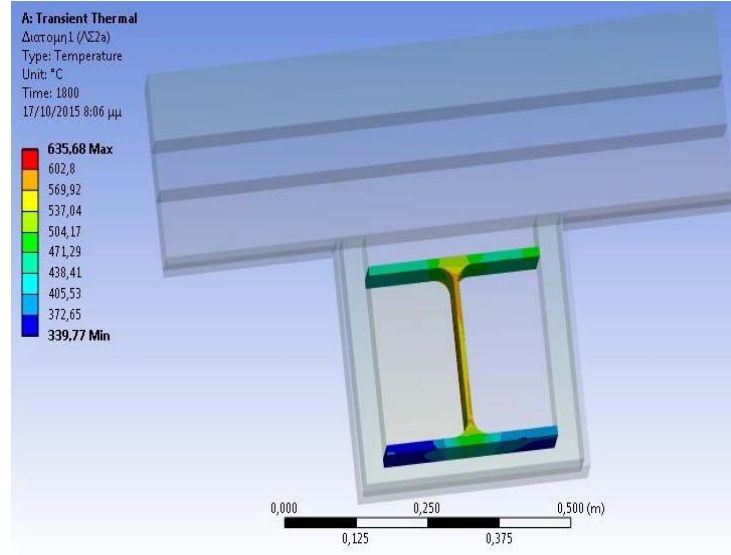


Figure 1. Temperature distribution on a fire insulating steel cross section of a column in a transient thermal FEM model.

2 THE HEAT TRANSFER SIMULATION PROBLEM IN FIRE CONDITIONS

2.1 The heat transfer problem

The transfer of flow heat from a high temperature object, called “heating”, to a lower temperature object changes the internal energy of both systems. A convenient definition of temperature is that it is a measure of the average translational kinetic energy associated with the disordered microscopic molecular motion into the body. Considering all net energy transfers to the system of a steel body as positive and all the net energy transfers from the system as negative, the conversation of energy can be described by the following form known as the first law of thermodynamics in quasistatic conditions:

$$dU = \delta Q - P \cdot dV \quad (1)$$

in this form dU denotes the change in internal energy of a body, δQ denotes the infinitesimal amount of heat energy supplied to the system from its surroundings and $P \cdot dV = W$ the work done on the system, whereas P is the pressure change and dV is the volume change of the body. Moreover the term δQ express the amount of energy added or removed to a body by conduction of heat or by thermal radiation.

In the case of a steel element the system body is in contact equilibrium with several other systems including separate connections with subsystems through walls that are permeable to the transfer of internal energy as heat. Under these conditions the first law of thermodynamics can be described in terms of externally defined thermodynamic variables:

$$dU_0 = \delta Q - P \cdot dV - \sum dU_i (i = 1, \dots, m) \quad (2)$$

Where dU_0 denotes the change of internal energy of the system, and dU_i the change of internal energy of the i th of the m surrounding subsystems that are in open contact with the system, due to transfer between the system and that i th surrounding subsystem. Moreover δQ denotes the infinitesimal amount of internal energy transferred as heat from the heat sources of the surroundings to the system, and $W = P \cdot dV$ denotes the work transferred from the system to the surrounding subsystems that are in adiabatic connection with it. In general the heat transfer from the fire to the surrounding bodies can occur with conduction, convection and radiation or a combination of these three mechanisms.

The first mechanism of heat transfer by means of molecular agitation within a body without any motion of the body as a whole is called conduction. If one end of a steel element or one side of the cross section of the steel element is at a higher temperature, then energy will be transferred toward the colder end or sides because the higher speed particles will collide with the slower ones with the net transfer of energy to the slower ones. For heat transfer between plane surfaces, (a body and an insulation envelope), the rate of conduction, internal energy

rate per time Q/t , could be estimated by the form:

$$Q/t = \kappa \cdot A \cdot (T_{hot} - T_{cold}) / d \quad (3)$$

where κ is the coefficient of thermal conductivity of the envelope, A is the area through which heat transfer takes place, T is the temperature and d is the thickness of the envelope.

The second mechanism of heat transfer is convection and is a linear function of the fire temperature. Convection above a hot surface occurs because hot air expands, becomes less dense and rises.

The third mechanism of heat transfer is radiation caused by the emission of electromagnetic waves which carry energy away from the emitting body. The governing radiation problem from hot objects can be expressed by the form:

$$Q = e \cdot \sigma \cdot A \cdot (T^4 - T_c^4) \quad (4)$$

where Q in the net radiated energy, A is the radiating area, σ is a constant, e is the emissivity coefficient, T is the temperature of radiator and T_c is the temperature of surroundings.

A large number of scientists and engineers have been done theoretical and experimental research works on the influence of a wide range of different parameters on both the cross-sectional capacity and the buckling strength of centrically and eccentrically loaded steel columns at elevated temperatures. The analysis of the influence of the cross-sectional capacity on the overall load-carrying behavior of a column at elevated temperatures uses different steel sections with different cross-sectional slenderness ratios. In addition, the influence of high temperature thermal creep of steel on the ultimate load was investigated.

Almeida et al. [1] made a thermo-structural analysis of an open section cold-formed steel beam in contact with a concrete slab and a masonry wall in fire situation. This type of beam is used in residential buildings for low-income families in Brazil. Brazilian Standards allow the use of steel with no thermal protection in the case of buildings with a total area under 750 m².

The typical static structural continua problem in thermal conditions described by the following form, always contain a body load term:

$$\int_V \sigma^T \cdot \delta \cdot dV = \int_V \alpha \cdot E \cdot \Delta T dV + \int_\delta F \cdot w dS \quad (5)$$

Thermal loads may be considered body loads. Body temperatures are converted to structural body loads via the coefficient of thermal expansion, α (units: Temperature⁻¹), where $\alpha \cdot \Delta T$ is the Thermal strain and $\alpha \cdot E \cdot \Delta T$ is the Thermal stress. In an element, the discrete form of the thermal condition becomes:

$$\int_{V^e} N^e \cdot \alpha \cdot E \cdot \Delta T dV^e \quad (6)$$

It is thus characterized by a load vector obtained by integrating every element with a temperature other than the reference temperature. This load vector is then added to the global applied load vector. Thus ΔT is the difference between the temperature of the body and the reference temperature at which the coefficient of thermal expansion was measured.

2.2 The fire simulation problem

In the field of engineering Computational Fluid Dynamics is widely used to precisely predict the behaviors of fluid phenomena. This study proposes a series of data conversion techniques and a real-time processing framework to develop a fire training simulator on the basis of a precise Computational Fluid Dynamics simulation that is capable of calculating various invisible physical quantities such as toxic gases and heat as well as visible factors such as smoke and flame. It's also proposed a real-time simulator framework that include a series of data handling processes such as data structure conversion, space partitioning/search, memory management, three-dimensional volume rendering, and training evaluation for the secured large-volume data. This fire simulator can undertake simple firefighting activities. The functions and real-time performance of the simulator were experimentally measured to verify the applicability of the problem.

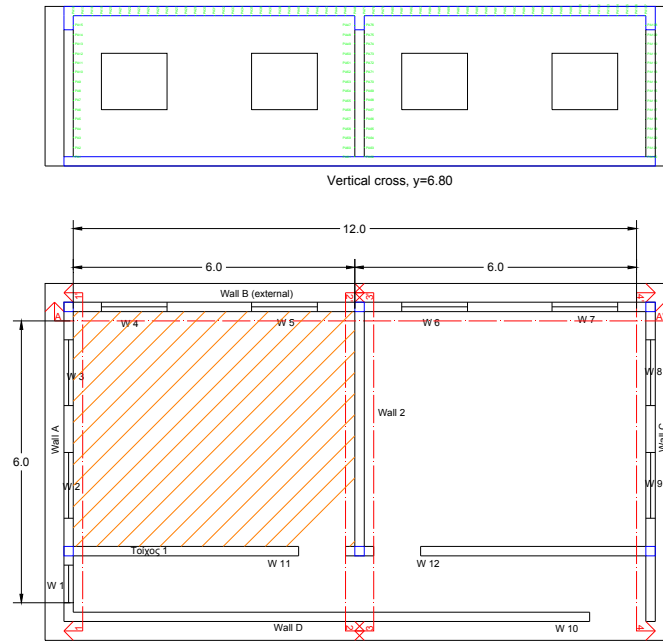


Figure 2. Typical fire compartment plan in a steel-framed building.

According to Eurocode 1 - Part 1-2, §3.3.2, the temperature - time curve determines the temperature distribution due to fire as a function of time. By this analysis is checked the performance of steel-framed elements due to standard fire curve defined in Eurocode 1 - Part 1-2 as well as due to the fire curve of an advanced FDS (Fire Dynamic Simulator), using a software simulation. This fire simulation software for a certain fire compartment is a computational fluid mechanics program which forms a fluid flow model driven by fire. The computational model solves numerically a form of Navier-Stokes equations for low flow speeds [6], [7]. The fire model is obtained by the numerical solution of the partial differential equations giving, in all points of a compartment, the thermodynamical and aerodynamical variables. The thermal flow guidance is supplemented with data from smoke emissions and heat transfer due to the fire. The approximation involves the filtering out of acoustic waves while allowing for large-variations in temperature and density in which the dissipative terms are computed directly.

In order to implement a reliable fire simulation model is necessary to establish a common and representative fire compartment (see Fig. 2) with dimensions of 12X5 meters of typical building model with residential use. This is a representative case of a compartment in a residential building where the selected room includes one side common with the external shell and thus corresponds to the resolution of an internal non-heated room [2], [8].

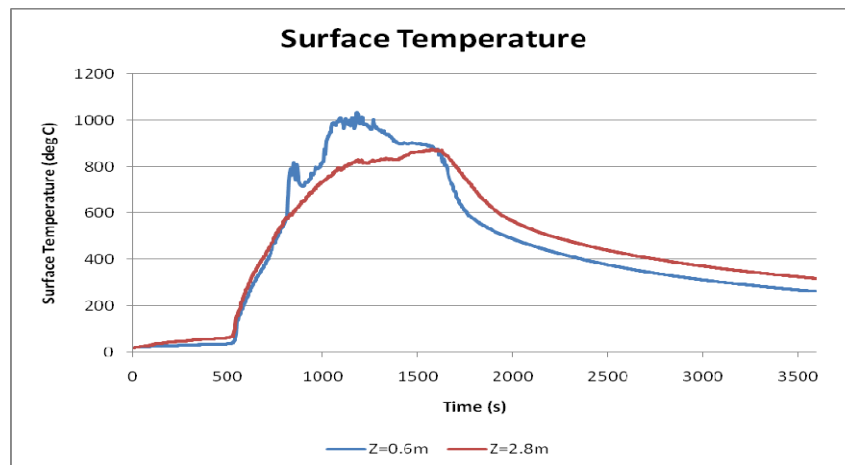


Figure 3. Temperature-time fire distribution curves due to FDS simulation to the top and to the bottom of the fire compartment.

The performance analysis of curves according to the two fire models used here is different, but both are additively representative. The obtained results of the fire models combine the temperature distribution (vertical axis) versus time (horizontal axis) with values in $^{\circ}C$ and sec respectively to the top and the bottom of the fire compartment (see Fig. 3).

3. FIRE PROTECTION CRITERIA FOR STEEL-FRAMED MEMBERS

3.1 Passive fire protection and sustainability

Taking into account that temperature changes in the materials lead to changes in their properties and in particular, in strength characteristics, a fact that becomes obvious when temperature is significantly increase, the only possibility to obtain a passive control of steel section strength in fire is to protect it from thermal expansion by an appropriately chosen insulating material or combination of materials applied to the envelope (bricks, coatings etc.). More specifically, the passive fire protection of the building envelope configurations take into account the category of structural members, the type of the insulation materials, the varying thickness of insulation, the position of insulation, and the type/thickness of the assumed coatings. In addition, it is important during a fire event any passive protection system taken into account in the design of the envelope be adequately maintained.

The sustainability indicators of a steel-framed structure exposed to fire can be grouped under three elements of sustainable development. The first indicator relates the safety and the resistance of the structure, the second relates the impact to the society and finally the third relates the passive fire protection design to the environmental protection including life-cycle aspects of used materials. The impact of the first indicator is mainly influenced by two different levels of reliability, 1) life safety and no-collapse requirement and 2) fire resistance of steel-framed structure and damage limitation. No-collapse requirement impact means that the structural performance is evaluated to avoid local or global failure and collapse. On the other hand fire resistance impact means that the structural resistance is taken into account damage limitation requirements. This is an evaluation in respect to the limitation of use and the costs that would be disproportionately high in comparison with the costs of the structure itself.

3.2 Critical temperatures of steel elements exposed to fire

For the purposes of Eurocodes, fire resistance is the ability of a structure to fulfill its required function for a specified load level, for a specified fire exposure and for a specified period of time. For a given (thermal due to fire) load level, the temperature at which failure is expected to occur in a structural steel element characterized as the critical temperature where an effective yield strength $f_{y,\theta}$ is truncated to provide a yield plateau. The relationship between the effective yield strength $f_{y,\theta}$ to the yield strength of the structural steel f_y and also of the slope of the linear elastic range $E_{a,\theta}$ to the modulus of elasticity of the structural steel element for normal temperature design E_a is expressed by the reduction factors $k_{y,\theta}$ and $k_{E,\theta}$ respectively at elevated temperatures according to Eurocode 3.1. In the range $20^{\circ}C \leq \theta_a \leq 400^{\circ}C$ of elevated temperatures, the value of the reduction factor of the effective yield strength is constant $k_{y,\theta} = 1,0$ and at the same time the effect of the reduction factor for the slope of the linear elastic range is not significant $1,0 \leq k_{E,\theta} \leq 0,7$. Therefore, a first secure limit to evaluate the fire resistance of the steel element is the time from the beginning of exposure to fire to a single compartment of the building, when the temperature on the steel element reaches $\theta_a = 400^{\circ}C$. During this period of time the structural resistance of the steel-framed structure is still safe taking into account an analysis of structure in accidental design situations. A second limit under consideration is the time from the beginning of exposure to fire when the temperature on the steel element reaches $\theta_a = 600^{\circ}C$. At this time the reduction factor of the effective yield strength is decreased continuously to the value of $k_{y,\theta} = 0,47$ and therefore, the effective yield strength $f_{y,\theta}$ decreased to a 50% of the initial yield strength of the structural steel element f_y . Then the reduction factor for the slope of the linear elastic range takes a much lower value, $k_{E,\theta} = 0,31$ and the buckling resistance of the cross-section decreases. In order to quantify the impact of the performance of the steel-framed elements in terms of temperature and time, two temperature limits could be taken into account. The first limit is that of $\theta_o^1 = 400^{\circ}C$, where under the time in thermal exposure of this limit both structural safety and resistance

with damage limitation are considered, and the second one is that of $\theta_o^2 = 600^\circ\text{C}$, where over the time in thermal exposure of this limit the structural failure and collapse is possible, respectively.

4 FINITE ELEMENT ANALYSIS OF THE HEAT TRANSFER PROBLEM

The fire curve of Eurocode EN1991-1-2 and advances fire dynamic simulation (FDS) curve are used here to investigate the heat transfer on external shell and especially to investigate the effect of increasing the temperature of the connected with the shell steel element.

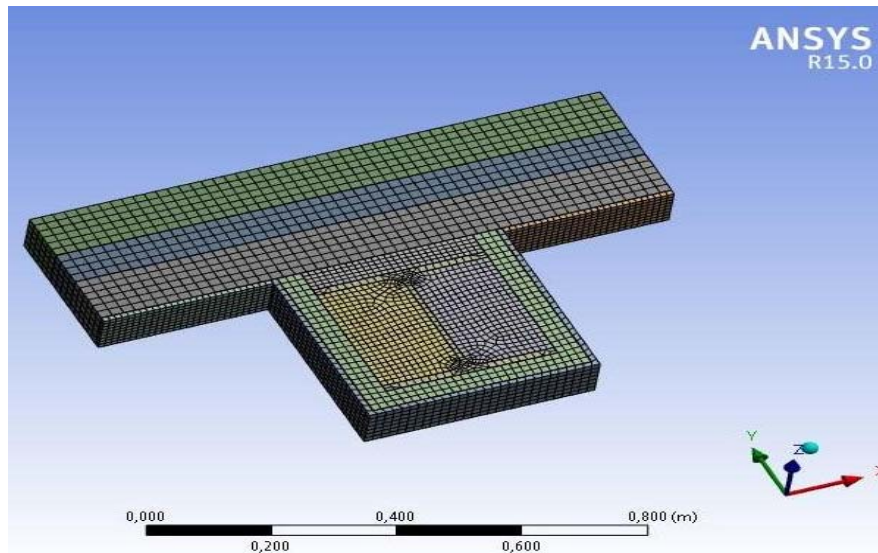


Figure 4. 3-D FEM model of a steel member (column), in connection with a typical layered envelope.

Therefore, a certain part of a characteristic detail including shell in connection with a steel element and insulation fire and thermal layers is discretized and analyzed. This analysis can be done by the development of a 3D Finite Element Model (see Fig. 4) with ANSYS computer program under a thermal solution scheme. Because of performing nonlinear transient structural analysis material and geometrical nonlinearities were considered, such as metal plasticity shown in Figure 5, as well as the variation of the stress-strain diagrams with temperature, according to Eurocode prescriptions. The variation of the resistance reducer with the time of fire exposure was also evaluated.

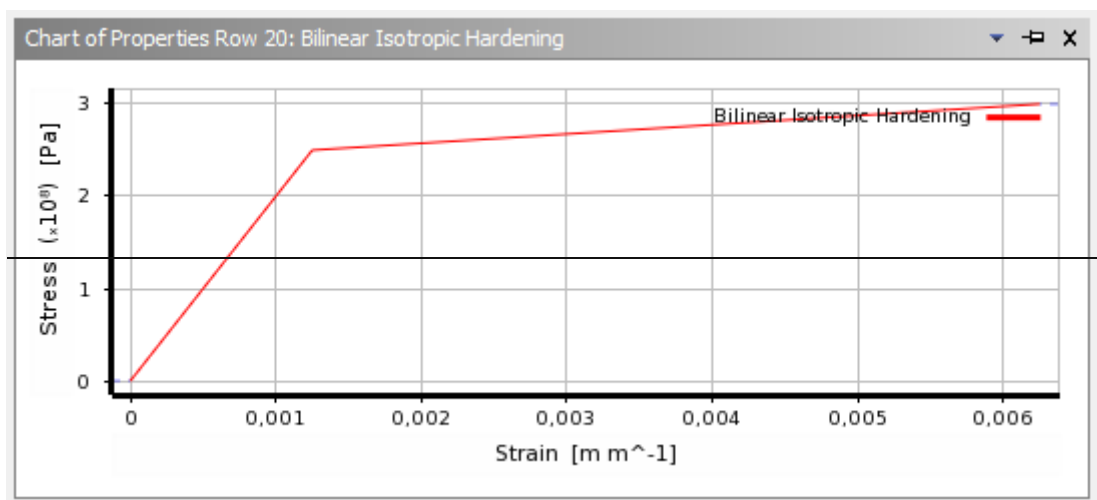


Figure 5. Bilinear Isotropic Hardening

For the first step of transient analysis, it is assumed that the column's cross-section has an initial temperature of 22°C . The temperature distribution is uniform at column's cross-section and its values have been given in

30steps (totally 3600sec.). Because of the simple shape of the model and low level of complexity we chose a hard mesh in order to produce more accurate results. Also, we had to take into account that Young's Modulus changes while the temperature increasing as shown in Figure 6.

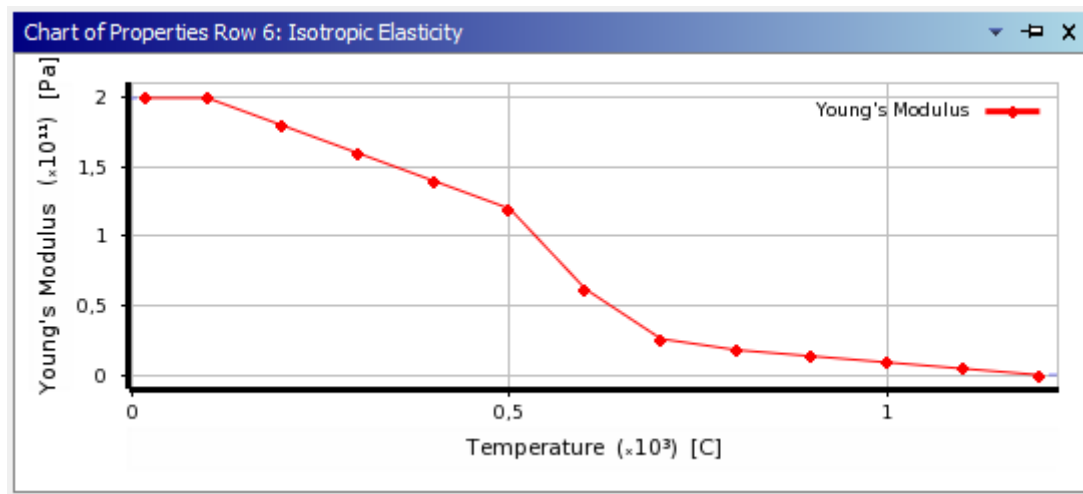


Figure 6. Isotropic Elasticity

The input data in this multi-layer model include all the thermodynamic characteristics and properties of the materials. The geometry of each layer (envelope walls, insulation materials etc.) is made under a solid model simulation where the connection between separated layers is simulated by complex non-linear contact elements that specified all the conditions of connections between neighboring layers. Moreover, the thermal solution uses here as initial inputs the temperatures-time curve such as the curves described above. The analysis is parametric and easily can be change thickness of any layer the kind of materials and the configuration of the shell, even the fire protection layer of the steel element (see Fig. 7).

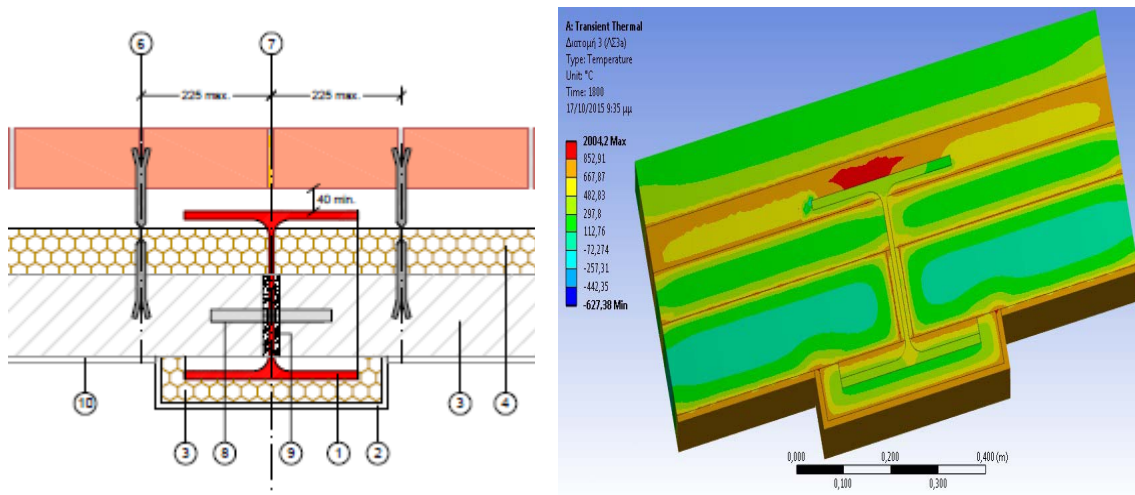


Figure 7. Critical temperature distribution due to fire on a complex structural detail configuration using thermal transient FEM analysis.

The temperature distribution on the shell layers at each time step are the expected results of this analysis. The evaluation of the results using the two limits of time for the fire resistance can be used to obtain the optimal site of the steel element. Whilst can be evaluate all those construction materials that are efficient under fire condition taking into account simultaneously their thermophysical, hydrothermal and environmental properties. By this analysis is obtained the distribution of the temperature and the heat transfer through the components of the shell and the influence of temperature to the steel elements (see Fig. 8). Results were delivered through tabulated data and are summarized in the following tables and figures.

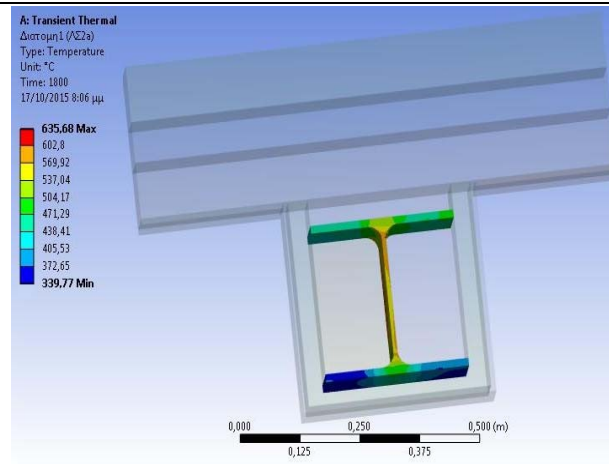


Figure 8. Temperature distribution of a complex FEM model on the steel member (column).

For example using a similar to the previously described FEM model for a building detail of the list, the thermal solution shows that the steel reaches a temperature of 400°C in the first 120 sec after the fire exposure and of 600°C to 1310 sec. The typical fire protection here is a rockwool layer and works effectively decreasing the temperature distribution on the steel element in comparison with the input temperature distribution of the fire simulation in the fire compartment (see Fig. 9).

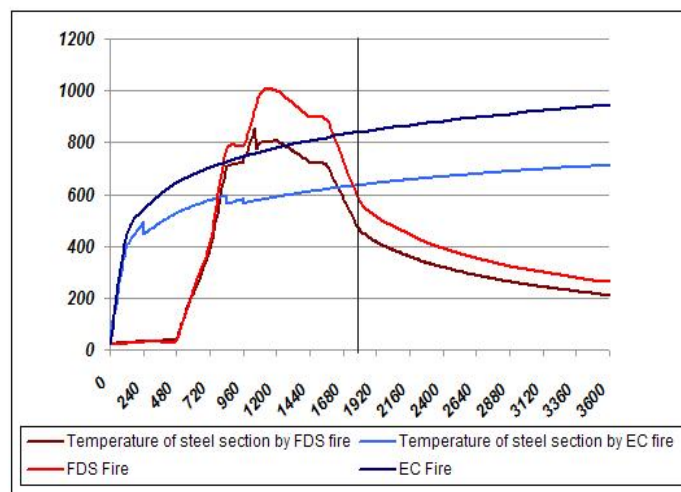


Figure 9. Temperature distribution on a steel element of a structural detail using FDS fire simulation versus EC fire.

4 FINITE ELEMENT ANALYSIS OF THE STATIC STRUCTURAL PROBLEM IN FIRE CONDITIONS

Nonlinear buckling analysis before and after fire conditions as well as transient structural analysis with thermal load has been done in a steel column of HEA450 section with height $h=3.45\text{m}$. First, the load was applied on the top of the column representing both axial and bending moment loads with the temperature field obtained from the transient thermal analysis. The first case under consideration in respect with the foregoing transient thermal analyses in that the steel member was not insulated against fire and the second case is that the steel member protected against fire by a thick layer of stonewool (5cm). As thermal load inserted the output of the transient thermal's respective analysis which became by the above-mentioned ones. The steel column exposed to 3600sec heat transfer which was constant along the column's height while simultaneously insinuating by gravity loads on top. The steel column has remote displacements in top (fixed 3 rotations and 2 displacements along the longitudinal axis and the strong axis) and bottom (fixed only 3 displacements and all rotations are free). Because of performing nonlinear transient structural analysis we should take into account a non linear stress-strain relationship, such as metal plasticity shown in figures 5 and 6.

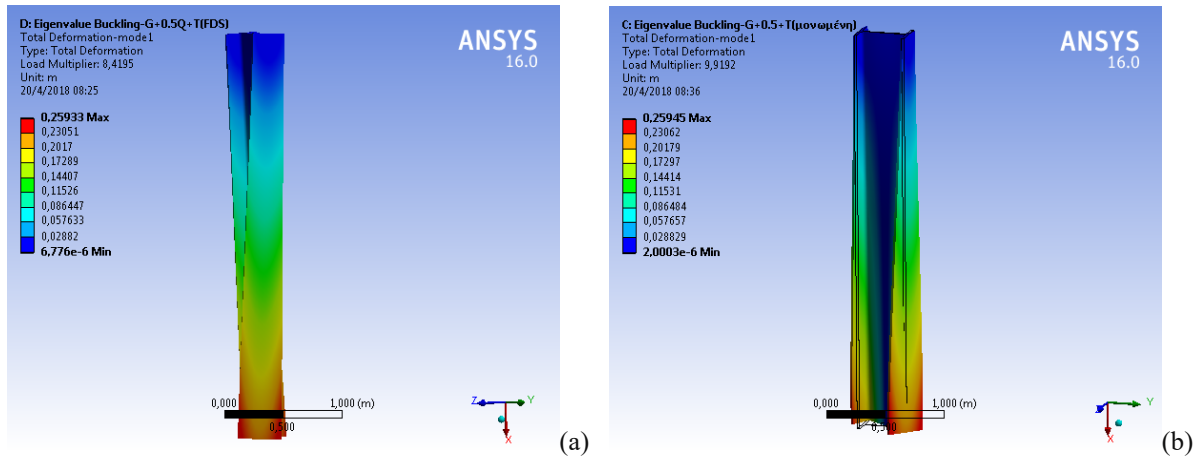


Figure 10. Eigenvalue nonlinear buckling analysis (Mode-1) including initial deformations of a steel column for (a) non fire insulated member and (b) for fire insulated member.

In this parametric study, a number of application cases were compared about their nonlinear buckling behavior, such as the influence of a fire-insulated column or not (see Fig. 10). Corresponding analysis was made to compare the developing deformations in the column for frequent design situations with the eigenvalue modes of that of accidental-fire design situations (see Fig. 11).

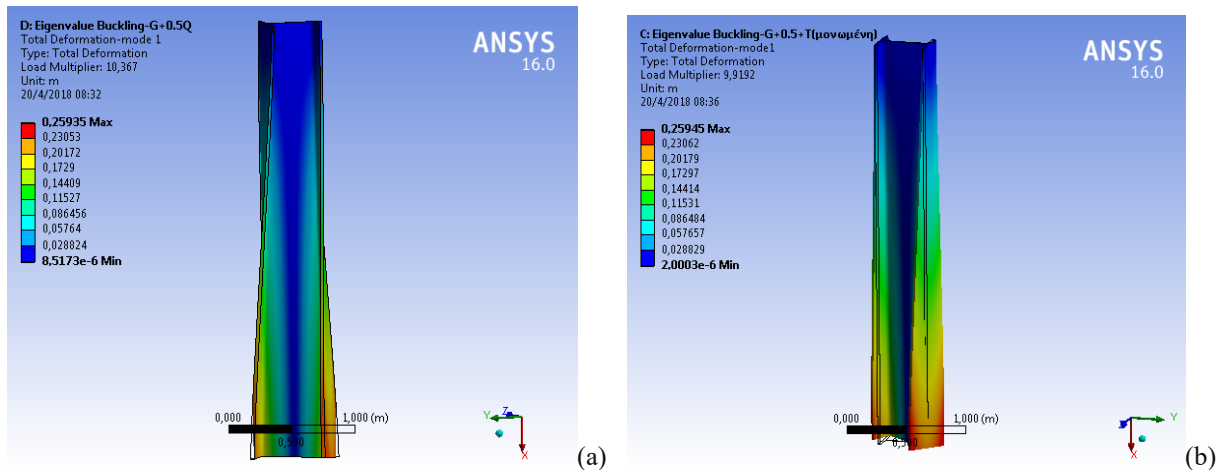


Figure 11. Eigenvalue nonlinear buckling analysis (Mode-1) of a steel column under (a) frequent design situations and (b) after fire design situations.

Several transient nonlinear structural analyses numerical tests with fire load was taken by inserting the temperature to time curve of EC fire or FDS fire. Because of the change in the modulus of elasticity at each solving step of this non-linear analysis, no valuation can be obtained at the field of stresses in the cross section of the column. Therefore critical parameter is the deformation of the steel member. This analysis includes in a first step an estimation of the deformations development on the column in frequent design situations. In a second step this analysis estimates the deformations development on the column in fire design situations. This last deformation image looks to be similar to that of an image of a real steel column after fire (see Fig. 12).

On the other hand the comparison between the deformations development on the column for the two design situations under consideration is very interesting. In the range $20^{\circ}C \leq \theta_a \leq 400^{\circ}C$ of elevated temperatures on the steel member, the value of the reduction factor of the effective yield strength is constant and at the same time the effect of the reduction factor for the slope of the linear elastic range is not significant.

In the range $400^{\circ}C < \theta_a \leq 600^{\circ}C$ of elevated temperatures on the steel member, the value of the reduction factor of the effective yield strength decreases and at the same time the effect of the reduction factor for the slope of the linear elastic range decreases too. The difference in the range of displacements across and along the steel column showed clearly in Figure 13.

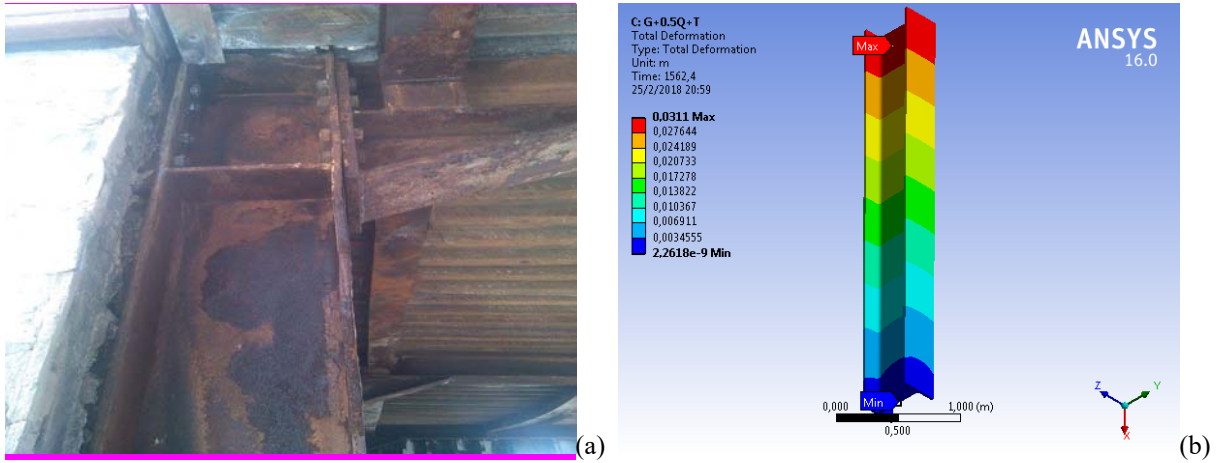


Figure 12. Comparison of the total deformation on a steel column of (a) real damaged steel member after fire and of (b) FEM model under nonlinear transient structural analysis after fire.

The buckling behavior as well as the ultimate resistance of a steel member under frequent design situations is strongly affected by increasing temperature after fire and especially when the temperature on the steel member overcome the limit of $\theta_o^2 = 600^\circ C$.

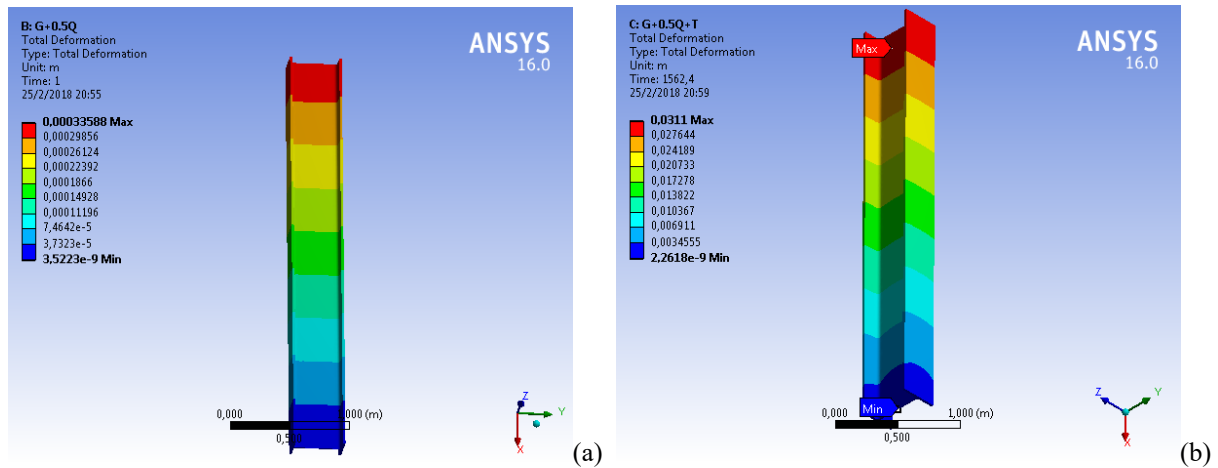


Figure 13. Comparison of the total deformation on a steel FEM column model under nonlinear transient structural analysis on (a) frequent design situations and on (b) fire design situations.

5 CONCLUSIONS

The design of steel-framed buildings with fire insulation layer as a part of the shell brick cladding is a practical, viable and efficient construction technique.

Taking into consideration a critical evaluation of the structural details it is estimated that the case where the steel element is placed on the interior side of the shell includes several design advantages and could be designed to be optimal.

In the range $20^\circ C \leq \theta_a \leq 400^\circ C$ of elevated temperatures on the steel member, the value of the reduction factor of the effective yield strength is constant and at the same time the effect of the reduction factor for the slope of the linear elastic range is not significant. Therefore, a first secure limit to evaluate the fire resistance of the steel element is the time from the beginning of exposure to fire to a single compartment of the building, when the temperature on the steel member reaches $\theta_a = 400^\circ C$.

In the range $400^\circ C < \theta_a \leq 600^\circ C$ of elevated temperatures on the steel member, the value of the reduction factor of the effective yield strength decreases and at the same time the effect of the reduction factor for the slope of the linear elastic range decreases too. The total difference to the developed displacements under structural static loads including thermal fire loads in this range don't overlaps known safety standards. But in

any case the question about the possibility to reuse this building after fire becomes critical because of the post-buckling behavior of the column including initial deformations.

The buckling behavior as well as the ultimate resistance of a steel member under frequent design situations is strongly affected by increasing temperature after fire and especially when the temperature on the steel member overcome the limit of $\theta_o^2 = 600^\circ C$.

Finally, the results of this study can be used for the estimation of the maximum load capacity of a structural steel member in fire conditions and of the buckling behavior of it after fire event.

REFERENCES

- [1] Almeida S.J.C. Rigobello R., Neto J.M., Silva V.P. (2010), "Thermo-Structural Analysis of an Open Section Cold-Formed Steel Beam in Contact with a Concrete Slab and a Masonry Wall in Fire Situation" *Journal of Structural Fire Engineering*, v.1-1, 2010, pp.29-41.
- [2] Bezas M., Nikolaidis, Th., Baniotopoulos C.C., (2017), "Fire protection and sustainability of structural steel buildings with double-shell brickwork cladding", *Proceeding of SBE16, Sustainable Synergies from Buildings to the Urban Scale*, 17-19 Oct. 2016, Thessaloniki, Greece", PROENV391212, Procedia Environmental Sciences, Science Direct, Elsevier, pp.298-305.
- [3] Chen, W.F. and Lui, E.M. (1985), "Columns with end restraint and bending in load and resistance design factor", *Engineering Journal / American Institute of Steel Construction*, pp.105-132.
- [4] Goode M.G. (2004), "Fire Protection of Structural Steel in High-Rise Buildings", *NIST GCR 04-872, Building and Fire Research Laboratory*, Maryland, USA, July 2004.
- [5] Guo Q. , Shi, K., Jia, Z., Jeffers, A.E. (2013). "Probabilistic Evaluation of Structural Fire Resistance," *Fire technology*, 49(3), pp.793-811.
- [6] McGrattan K, Hostikka S, Floyd J, Baum H, Rehm R, (2007), Fire Dynamics Simulator (Version 5), Technical Reference Guide, *National Institute of Standards and Technology NIST*, Special publication 1018-5.
- [7] Moohyun C, Soonhung H, Jaikyung L, Byungil C (2012), "A virtual reality based fire training simulator integrated with fire dynamic data", *Fire Safety Journal*, ELSEVIER Vol.50, 2012, pp. 12-24.
- [8] Nikolaidis, Th., Tsalikis C., Baniotopoulos C.C. (2014), Investigation of the Structural Response of a steel framed member in fire, *Proceedings of the 8th National Conference of Metal Structures*, Tripoli, (in Greek).
- [9] Zhang C., Li G. Q., Wang Y. C., (2014), "Probabilistic Analysis of steel columns protected by intumescent coatings subjected to natural fires", *Structural Safety* 50 (2014) pp.16-26.

A FIBER APPROACH TO THE LARGE DEFLECTION ANALYSIS OF BEAMS BY BEM

George C. Tsiatas¹, Antonis G. Siokas², and Evangelos J. Sapountzakis³

¹Department of Mathematics
University of Patras
Rio, GR-26504, Greece

e-mail: gtsiatas@math.upatras.gr; web page: <http://www.math.upatras.gr/~gtsiatas/>

²School of Civil Engineering
National Technical University of Athens
Zografou Campus, GR-15773, Athens, Greece
e-mail: antonissiokas@gmail.com

³School of Civil Engineering
National Technical University of Athens
Zografou Campus, GR-15773, Athens, Greece
e-mail: cvsapoun@central.ntua.gr; web page: <http://users.ntua.gr/cvsapoun/>

Keywords: Nonlinear analysis, Boundary Elements, Beam.

Abstract- *The aim of this paper is to present a new fiber approach methodology to the large deflection analysis of initially straight Euler-Bernoulli beams by the Boundary Element Method (BEM). The beam undergoes large displacements with small strains and moderate rotations (intermediate nonlinear theory) under general boundary conditions which may be nonlinear. The formulation of the problem is in terms of the displacements whereas the two governing equations are coupled and nonlinear. Their solution is achieved by employing the Analog Equation Method (AEM) together with an iterative numerical process, using both longitudinal and section discretization. In order to validate the reliability and effectiveness of the proposed methodology, a representative example is studied and the obtained results are compared with those available in the literature.*

1 INTRODUCTION

The historical research shows that beam elements have found applications in the process of structural modelling and analysis in a wide range of engineering disciplines, from civil (e.g. buildings, bridges) to mechanical (e.g. shafts, wind turbine rotors, nuclear reactor components) to aeronautical and aerospace (e.g. aircraft wings, spacecraft parts) [1], to name a few. For this reason, considerable research has been devoted towards accurately capturing the structural linear and nonlinear behavior of beams under static or dynamic loads. Generally, two common sources of nonlinearity may arise in the response of structural elements: material and geometrical [2]. Closed form solutions cannot be obtained when general boundary conditions are considered; therefore, recourse to numerical solutions is inevitable [3]. The most widely used numerical methods in Computational Mechanics are the Finite Difference Method (FDM), the Finite Element Method (FEM) and the Boundary Element Method (BEM) [4, 5].

To the problem at hand, the FEM has been employed by several researchers for the nonlinear analysis of beams with a constant cross-section having both geometrical and material nonlinearities. More specifically, Mondkar and Powell [6], applying the principle of virtual displacements, developed a general formulation of the incremental equations of motion for structures undergoing large displacement-finite strain deformation. Bathe and Bolourchi [7] presented an updated Lagrangian and a total Lagrangian formulation of a three-dimensional beam element for large displacement and large rotation analysis. Cai et al. [8] presented a simple finite element method, based on a Von Karman type nonlinear theory of deformation, for geometrically nonlinear large rotation analyses of space frames consisting of members of arbitrary cross-section.

Furthermore, the BEM has also been employed for the linear and nonlinear analysis of beams. Its first application dates back to the work of Banerjee and Butterfield [9], who developed the BEM for the one-dimensional problem and applied it to the analysis of the Bernoulli-Euler beam under static loads. Providakis and Beskos [10] applied the BEM

to the dynamic problem of Bernoulli-Euler beams. The Analog Equation Method (AEM), a BEM-based method, has been presented by Katsikadelis and Tsiatas for the nonlinear static [3] and dynamic [11] flexural analysis of beams of cross-sections with variable stiffness taking into account the axial deformation also.

In this paper, a fiber approach to the large deflection analysis of initially straight Euler-Bernoulli beams by the Boundary Element Method (BEM) is presented. The beam undergoes large displacements with small strains and moderate rotations (intermediate nonlinear theory) under the most general boundary conditions. The problem is formulated in terms of the displacements whereas the two resulting governing equations are coupled and nonlinear. The solution of the system is achieved by employing the Analog Equation Method (AEM) together with an iterative numerical process, using both longitudinal and section discretization. In order to validate the reliability and effectiveness of the proposed methodology, a representative example is studied and the obtained results are compared with those available in the literature.

2 STATEMENT OF THE PROBLEM

Consider an initially straight beam of length l having variable axial stiffness EA and bending stiffness EI . The x axis coincides with the neutral axis of the beam, which is bent in its plane of symmetry xz under the combined action of the distributed loads $p_x = p_x(x)$ and $p_z = p_z(x)$ in the x and z direction, respectively [3].

2.1 Governing Equations of the Problem and Boundary Conditions

In the context of the classical Euler-Bernoulli beam theory, by applying the principle of total minimum potential energy, for the stable equilibrium and the fundamental lemma of the calculus of variations, the governing equilibrium differential equations of the beam are obtained as

$$N_{,x} = -p_x(x), \quad (1)$$

$$Q_{,x} + (Nw_{,x})_{,x} = -p_z(x), \quad (2)$$

$$M_{,x} - Q = 0, \quad (3)$$

which after the elimination of Q , using eqn (3), take the following form

$$N_{,x} = -p_x(x), \quad (4)$$

$$M_{,xx} + (Nw_{,x})_{,x} = -p_z(x). \quad (5)$$

In general case of linearly elastic material, the stress-strain relation is known. Hence, analytical integration can be performed and the stress resultants in terms of displacements are written as [3]

$$N = EA \left[u_{,x} + \frac{1}{2} (w_{,x})^2 \right], \quad M = -EIw_{,xx}. \quad (6), (7)$$

Substituting eqs (6), and (7) into eqs (4) and (5), the governing equations in terms of displacements become

$$\left[EA \left(u_{,x} + \frac{1}{2} w_{,x}^2 \right) \right]_{,x} = -p_x(x), \quad (8)$$

$$-(EIw_{,xx})_{,xx} + \left[EA \left(u_{,x} + \frac{1}{2} w_{,x}^2 \right) w_{,x} \right]_{,x} = -p_z(x). \quad (9)$$

The general boundary conditions of the problem are written as

$$a_1 u(0) + a_2 N(0) = a_3, \quad \bar{a}_1 u(l) + \bar{a}_2 N(l) = \bar{a}_3, \quad (10), (11)$$

$$\beta_1 w(0) + \beta_2 Q^*(0) = \beta_3, \quad \bar{\beta}_1 w(l) + \bar{\beta}_2 Q^*(l) = \bar{\beta}_3, \quad (12), (13)$$

$$\gamma_1 w_{,x}(0) + \gamma_2 M(0) = \gamma_3, \quad \bar{\gamma}_1 w_{,x}(l) + \bar{\gamma}_2 M(l) = \bar{\gamma}_3, \quad (14), (15)$$

where $\alpha_\kappa, \bar{\alpha}_\kappa, \beta_\kappa, \bar{\beta}_\kappa, \gamma_\kappa, \bar{\gamma}_\kappa$ ($\kappa = 1, 2, 3$) are given constants, and $Q^* = Q + Nw_{,x}$. Equations (10)-(15) describe the most general boundary conditions of the problem and can include elastic support of the beam.

However, when the distribution of the normal stresses on the cross section is not a priori known or the stress-strain relation may not even be explicitly described by a mathematical function but by a set of experimental data, the fiber approach should be employed to obtain the stress resultants.

2.2 The fiber/layer approach

According to the fiber approach a number of monitoring cross-sections can be defined, which coincide with the discretized nodal points as well as the two beam ends. Each cross-section is decomposed into a number of fibers, i.e. triangular or quadrilateral cells. On each cell representative points are defined and the strain is expressed as a function of the nodal displacement values. Further, the stresses on each point can be computed and the stress resultants can be obtained by an appropriate integration scheme. In the case of doubly-symmetric cross-sections and without restricting the generality a layered model is adopted as shown in Fig. 1.

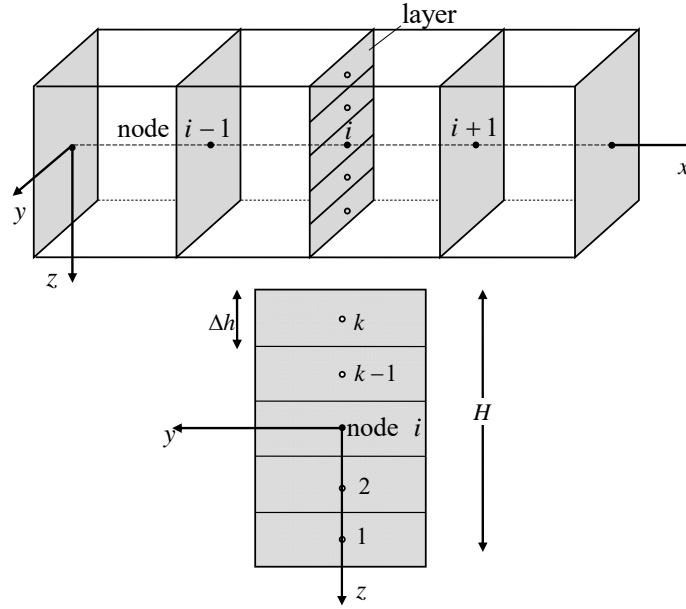


Figure 1. Discretization of the beam into monitoring cross-sections and cross-section layers

Each cross-section is divided into an odd number of layers with the same height Δh . If k is the total number of layers then the center of the beam's cross-section is located at the middle of the $(k+1)/2$ layer. The z coordinate of the center of the i -th layer is expressed as

$$z_i = \left(\frac{k+1}{2} - i \right) \Delta h. \quad (16)$$

The axial force N_i and bending moment M_i for each layer are computed as

$$N_i = S_{xx}^i \Delta A_i, \quad M_i = S_{xx}^i z_i \Delta A_i, \quad (17), (18)$$

where S_{xx}^i , ΔA_i are the stress component at the center of each layer and the area of each layer respectively. As a result, the stress resultants can be approximated as

$$N = \sum_{i=0}^k S_{xx}^i \Delta A, \quad M = \sum_{i=0}^k S_{xx}^i z_i \Delta A_i. \quad (19), (20)$$

The nonlinear system of the governing differential equations in terms of the stress resultants, described by eqns (4) and (5), is solved iteratively employing the AEM in the context of fiber approach. According to the AEM, the two coupled nonlinear differential equations are replaced by two uncoupled linear ones pertaining to the axial and transverse deformation of a substitute beam with unit axial and bending stiffness, respectively, under fictitious load

distributions [3]. At each step of the iterative procedure, an initial guess is made for the fictitious loads and the displacements and their derivatives are computed at any cross-section of the beam using the respective integral representations. Subsequently, the stress resultants are evaluated for each layer using eqs (17), (18) and for the whole cross-section by applying eqs (19), (20). In the end, the governing equations (4) and (5) are checked for equilibrium. If the equilibrium is satisfied, the process is terminated. Otherwise, the fictitious load distributions are updated and the procedure starts over again.

3 NUMERICAL EXAMPLE

In order to exemplify the efficiency and accuracy of the proposed methodology, a uniform beam fixed at its both ends has been analyzed. The beam has a rectangular cross section $b \times h$ with length $l = 0.508\text{ m}$, and is subjected to a concentrated force at its midspan. Mondkar and Powell [6] and Katsikadelis and Tsiatas [3] have also studied this problem employing a FEM and a BEM formulation, respectively. The results are obtained for $N = 51$ nodal points and $k = 19$ layers. The load P_z versus deflection w curve at the center of the beam is shown in Fig. 2. The nonlinear response is in excellent agreement with both FEM [6] and BEM [3] solutions. Moreover, the profiles of the deflection and the axial displacement for $P_z = 3.11\text{ kN}$ are shown in Fig. 3 and Fig. 4, respectively, as compared with those presented in [3].

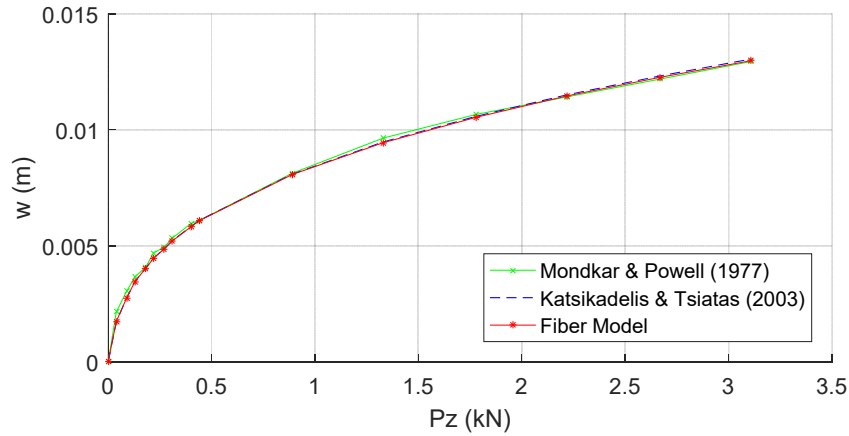


Figure 2. Load versus deflection at the center of the beam

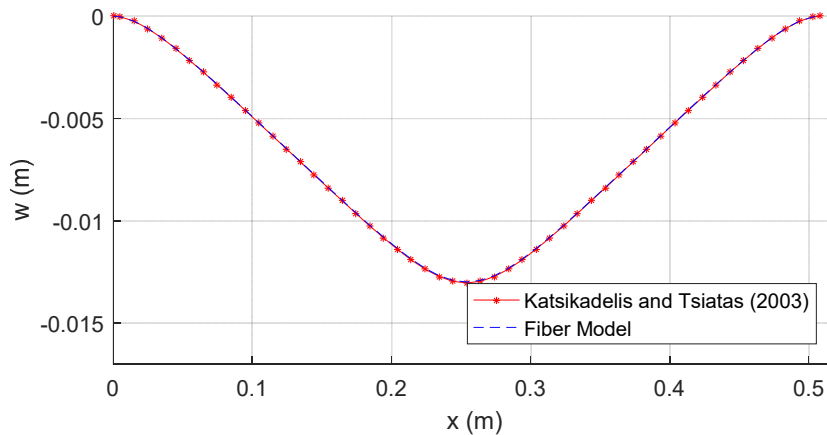


Figure 3. Profile of the deflection

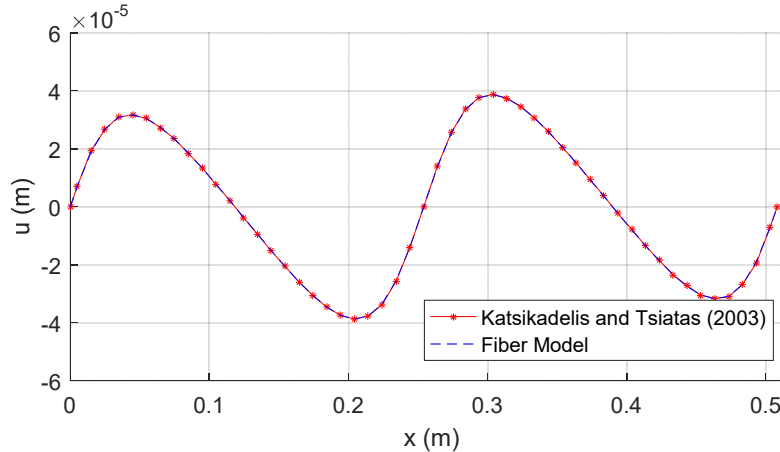


Figure 4. Profile of the axial displacement

4 CONCLUSIONS

In this paper, a fiber approach to the large deflection analysis of beams has been presented. The governing equations are derived through a variational approach, and their solution was achieved by employing the AEM together with an iterative numerical process, using both longitudinal and section discretization. From the presented analysis and the numerical results the following main conclusions can be drawn: (a) The numerical solution is efficient, exhibits stability and a small number of constant elements and layers are adequate to obtain accurate results for the displacements and the stress resultants; (b) The fiber approach has proven to be very competent and in conjunction with the AEM can solve difficult nonlinear coupled problems; (c) The solution of the nonlinear bending problem of beams with material and geometrical nonlinearity can be considered as a future application of the fiber approach methodology.

REFERENCES

- [1] Hodges, D.H. (2006), *Nonlinear composite beam theory*, Progress in Astronautics and Aeronautics, Vol.213, AIAA.
- [2] Reddy, J.N. (2005), *An introduction to Nonlinear Finite Element Analysis*, Oxford University Press.
- [3] Katsikadelis, J.T., Tsiatas, G.C. (2003), "Large deflection analysis of beams with variable stiffness", *Acta Mechanica*, Vol. 164, pp. 1-13.
- [4] Becker, A.A. (1992), *The Boundary Element Method in Engineering: A Complete Course*, Mc Graw-Hill, New York.
- [5] Banerjee, P.K., Butterfield R. (1981), *Boundary Element Methods in Engineering Science*, Mc Graw-Hill, London.
- [6] Mondkar, D.P., Powell, G.H. (1977), "Finite element analysis of nonlinear static and dynamic response", *International Journal for Numerical Methods in Engineering*, Vol. 11, pp. 499-520.
- [7] Bathe, K.J., Bolourchi, S. (1979), "Large displacement analysis of three-dimensional beam structures", *International Journal for Numerical Methods in Engineering*, Vol. 14, pp. 961-986.
- [8] Cai, Y., Paik, J.K., Atluri, S.N. (2009), "Large deformation analyses of space-frame structures, with members of arbitrary cross-section, using explicit tangent stiffness matrices, based on a Von Karman type nonlinear theory in rotated reference frames", *CMES, Computer Modeling in Engineering and Sciences*, Vol. 53, pp. 117-145.
- [9] Banerjee, P.K. (1994), *The Boundary Element Methods in Engineering*, Mc Graw-Hill, London.
- [10] Providakis, C.P., Beskos D.E. (1986), "Dynamic analysis of beams by the boundary element methods", *Computers and Structures*, Vol. 22, pp. 957-964.
- [11] Katsikadelis, J.T., Tsiatas, G.C. (2004), "Nonlinear dynamic analysis of beams with variable stiffness", *Journal of Sound and Vibration*, Vol. 270, pp. 847-863.

THE ROBUSTNESS OF OPTIMUM TUNED MASS DAMPERS DESIGN USING TRANSFER FUNCTION AMPLITUDE AND JAYA ALGORITHM

Sinan Melih Nigdeli¹ and Gebrail Bekdas¹

¹Department of Civil Engineering

Istanbul University

Istanbul, TR-34320, Turkey

e-mail: melihnig@istanbul.edu.tr, bekdas@istanbul.edu.tr

Keywords: Tuned mass damper, Robustness, Transfer function.

Abstract. *The optimization of tuned mass dampers for structures is a stochastic problem because of existing of damping. In that case, heuristic algorithms are useful tools in that field for an objective function in frequency or time domain. In the present study, the robustness of optimum tuned mass damper (TMD) results obtained by the transfer function response minimization are verified. The numerical examples involve two shear buildings which are 10-story and 40-story structural models. According to the results, the optimum TMD is robust against the change of the mass or stiffness of the structure by $\pm 50\%$ difference.*

1 INTRODUCTION

By adding mechanical components or motor driven systems, civil structures can be passively or actively controlled in order to reduce distributing and dangerous vibrations resulting from several sources like earthquakes, winds, traffic and human steps. The structural control systems have been included to several structures, but several drawbacks prevent the often use of these systems. These drawbacks are generally related with economy based problems, but safety issues like stability problems can also play a great role. In that case, the performance of these systems is depended to perfect tuning of design variables of implemented system according to the super-structure behavior and response. For that reason, optimization is a must in order to increase the influence and benefit of control systems.

Tuned mass dampers (TMDs) are vibration absorber devices consisting of a mass attached to the main system by using stiffness members and dampers. The primitive form of the device without damping was invented and patented by Frahm [1]. Without damping, it is not possible to use the device on structures excited by vibrations with random frequency content. The damped and current idea of TMD was proposed by Ormondroyd and Den Hartog [2]. The design variables in the optimum tuning of TMDs are mass (m_d), stiffness (k_d) and damping coefficients (c_d). In the documented methods, the ratio of frequencies of TMD and superstructure (f_{opt}), and the damping ratio of TMD (ξ_{opt}) have been proposed with close form expressions in terms of mass ratio of TMD and superstructure (μ) ([3, 4]). These expressions are for single degree of freedom systems, but the optimum values can be found by using a single vibration mode for multiple degree of freedom system. Also, Sadek et. al. [5] proposed formulations by including inherent damping of superstructure according to numerical analyses. The best tuning technique is to use numerical algorithm by considering all vibration modes of structures. Generally, heuristic based algorithms have been employed in the optimum tuning. Genetic algorithm (GA) is an evolutionary heuristic algorithm have been employed by Hadi and Arfiadi [6] for optimum stiffness and damping of TMD. Marano et al. [7] included the mass of TMD as a design variable by using an optimization methodology employing GA. GA based optimization methods have been also proposed for control of torsional irregularity by using TMDs ([8, 9]). Pourzeynali et al. [10] optimized active tuned mass dampers (ATMDs) by using GA and fuzzy logic. Another heuristic algorithms proposed for TMDs are particle swarm optimization ([11,12]), bionic algorithm ([13]), harmony search algorithm ([14-16]), ant colony ([17]), artificial bee colony ([18]), shuffled complex evaluation ([19]), flower pollination algorithm ([20]), teaching learning based optimization ([21]) and bat algorithm ([14]).

In this study, the robustness of the optimum TMD parameters were evaluated by changing the mass and the stiffness of the structure by up to $\pm 50\%$ differences.

2 THE METHOD AND OPTIMIZATION

In the present study, shear building models are investigated for an optimum TMD on the top of the structure. The equation of motion of the shear building with a TMD (Figure 1) is formulated as Eq. (1) domain.

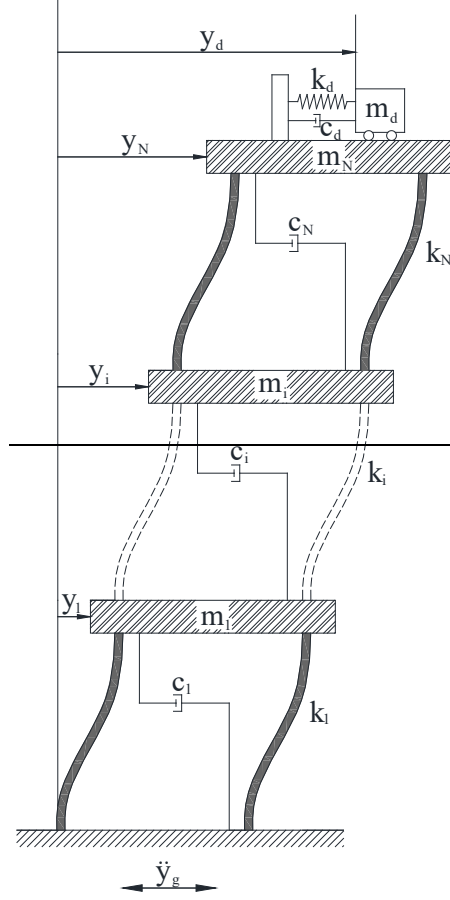


Figure 1. The shear building model with a TMD

$$\mathbf{M}\ddot{\mathbf{y}}(t) + \mathbf{C}\dot{\mathbf{y}}(t) + \mathbf{K}\mathbf{y}(t) = -\mathbf{M}\{\mathbf{1}\}\ddot{y}_g(t) \quad (1)$$

\mathbf{M} , \mathbf{C} and \mathbf{K} (Eqs. 2-4) represent the mass, damping and stiffness matrix of shear building, respectively. $\mathbf{y}(t)$ is the response of the structure against the ground acceleration ($\ddot{y}_g(t)$) in time domain. The dot (.) on the response represents the derivation of response with respect to time and $\ddot{\mathbf{y}}(t)$, $\dot{\mathbf{y}}(t)$ and $\mathbf{y}(t)$ are the symbolic representations of acceleration, velocity and displacement vectors of the structure, respectively. The displacement vector contains all the values of stories ($y_i(t)$ for $i=1, 2, 3, \dots, N$ if N is the number stories) and TMD ($y_d(t)$) as seen in Eq. (5).

$$\mathbf{M} = \text{diag}[m_1 \ m_2 \ \dots \ m_N \ m_d] \quad (2)$$

$$\mathbf{C} = \begin{bmatrix} (c_1 + c_2) & -c_2 & & & & \\ -c_2 & (c_2 + c_3) & -c_3 & & & \\ & \cdot & \cdot & & & \\ & \cdot & \cdot & \cdot & & \\ & & \cdot & \cdot & \cdot & \\ & & & \cdot & \cdot & \\ & & & & -c_N & (c_N + c_d) & -c_d \\ & & & & & -c_d & c_d \end{bmatrix} \quad (3)$$

$$K = \begin{bmatrix} (k_1 + k_2) & -k_2 & & & & \\ -k_2 & (k_2 + k_3) & -k_3 & & & \\ & \cdot & \cdot & & & \\ & \cdot & \cdot & \cdot & & \\ & & \cdot & \cdot & \cdot & \\ & & & -k_N & (k_N + k_d) & -k_d \\ & & & & -k_d & k_d \end{bmatrix} \quad (4)$$

$$y(t) = \begin{Bmatrix} y_1(t) \\ y_1(t) \\ \vdots \\ y_N(t) \\ y_d(t) \end{Bmatrix} \quad (5)$$

In the matrices, m , c and k represent mass, damping and stiffness coefficient. The subscripts represent the story number or TMD for d . In that case, the TMD properties are m_d , c_d and k_d .

The transfer function is the ratio of Laplace transformations of a structural response (acceleration in the present study) to the external excitation. The acceleration transfer function ($TF(\omega)$) as a function of frequency (ω) is shown as Eq. (6). The $TF(\omega)$ vector contains the function for all stories (TF_1, TF_2, \dots, TF_N) and TMD (TF_d).

$$TF(\omega) = \begin{bmatrix} TF_1(\omega) \\ TF_2(\omega) \\ \vdots \\ TF_N(\omega) \\ TF_d(\omega) \end{bmatrix} = \left[-M\omega^2 + C\omega j + K \right]^{-1} M\omega^2 \mathbf{1} \quad (6)$$

The objective of the methodology is to find the design variables (x_i) minimizing the amplitude of the acceleration transfer function of the top story. The function $f_i(x_i)$ is formulated in Eq. (7) for i^{th} candidate solution.

$$f_i(x_i) = 20 \log_{10} |\max(TF_N(\omega))| \quad (7)$$

The transfer function is unitless and contains real and imaginary parts. By taking the absolute value of transfer function, the amplitude is obtained. Then, base-10 logarithm of the amplitude is multiplied with 20 and decibel (dB) value of transfer function is found. The design variables are mass (m_d), period (T_d) and damping ratio (ξ_d) of TMD as seen in Eq. (8).

$$x_i = \begin{Bmatrix} m_{di} \\ T_{di} \\ \xi_{di} \end{Bmatrix} \text{ for } i = 1, 2, \dots, n \quad (8)$$

The period (T_d) and damping ratio (ξ_d) of TMD are the functions of the properties of TMD shown in Figure 1 and the equations are given as Eq. (9) and Eq. (10).

$$T_d = 2\pi \sqrt{\frac{m_d}{k_d}} \quad (9)$$

$$\xi_d = \frac{c_d}{2m_d \sqrt{\frac{k_d}{m_d}}} \quad (10)$$

The optimum design variables can be found by using metaheuristic methods. In the present study, Jaya algorithm [22] developed by Rao was employed. JA is a single phase algorithm and it has no user-defined parameters. The aim of the algorithm is to generate possible design variables by using the existing worst and best solutions to minimize the objective function.

3 NUMERICAL EXAMPLE

The numerical examples involve two shear buildings which are 10-story and 40-story structural models.

The 10-story shear building have the same story parameters (m_i , k_i and c_i for the i^{th} story) and the story parameters presented in Table 1 are taken from Singh et al. [23].

Story	m_i (t)	k_i (MN/m)	c_i (MN/s/m)
1	360	650	6.2
2	360	650	6.2
3	360	650	6.2
4	360	650	6.2
5	360	650	6.2
6	360	650	6.2
7	360	650	6.2
8	360	650	6.2
9	360	650	6.2
10	360	650	6.2

Table 1 : Properties of shear buildings

The first natural frequency of the 10-story structure is 1 Hz. The maximum acceleration transfer function amplitude of 10-story structure at 1 Hz is 26.2091 dB for the case without TMD. The optimum TMD parameters are $m_d=360\text{t}$, $T_d=1.10864\text{s}$ and $\xi_d=0.2596$ (25.969%) for the 10-story shear building. By using the optimum TMD parameters, the minimum objective function (f_{\min}) defined as the maximum amplitude of acceleration transfer function is reduced to 11.3316 dB. The percentage of the reduction is 56.76% for the optimum TMD parameters found by using JA.

The plot of the acceleration transfer function of the top story of 10-story structure is shown as Fig. 2 with the comparison of the structure without TMD. As seen in the plot, the optimum TMD has also a minor effect on the second peak in frequency of the second mode.

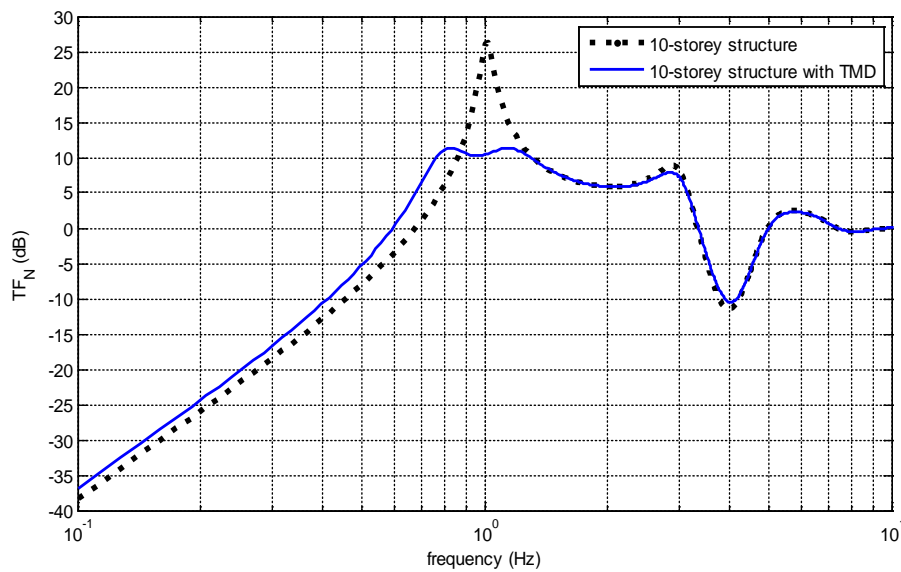


Figure 2. TF_N plot for 10-story structure

The optimum results were also tested for a big structure with 40 stories. The properties taken from Liu et al. [24] are given as seen in Table 2. The optimum TMD parameters were found for two cases of maximum mass ratio. In Case 1 and 2, the maximum allowable mass ratio of the TMD is 10% and 2%, respectively. The optimum results are presented in Table 3.

Story	m_i (t)	k_i (MN/m)	c_i (MNs/m)
1	980	2130.00	42.60
2	980	2100.97	42.02
3	980	2071.95	41.44
4	980	2042.92	40.86
5	980	2013.90	40.28
6	980	1984.87	39.70
7	980	1955.85	39.12
8	980	1926.82	38.54
9	980	1897.79	37.96
10	980	1868.77	37.38
11	980	1839.74	36.79
12	980	1810.72	36.21
13	980	1781.69	35.63
14	980	1752.67	35.05
15	980	1723.64	34.47
16	980	1694.62	33.89
17	980	1665.59	33.31
18	980	1636.56	32.73
19	980	1607.54	32.15
20	980	1578.51	31.57
21	980	1549.49	30.99
22	980	1520.46	30.41
23	980	1491.44	29.83
24	980	1462.41	29.25
25	980	1433.38	28.67
26	980	1404.36	28.09
27	980	1375.33	27.51
28	980	1346.31	26.93
29	980	1317.28	26.35
30	980	1288.26	25.77
31	980	1259.23	25.18
32	980	1230.21	24.60
33	980	1201.18	24.02
34	980	1172.15	23.44
35	980	1143.13	22.86
36	980	1114.10	22.28
37	980	1085.08	21.70
38	980	1056.05	21.12
39	980	1027.03	20.54
40	980	998.00	19.96

Table 2 : The story parameters of 40-story structure

Case 1	m_d (t)	3920	Case 2	m_d (t)	784
	T_d (s)	4.358596		T_d (s)	3.949575
	ξ_d	0.281294		ξ_d	0.131671
	f_{best}	11.72735		f_{best}	17.32852
	f_{ave}	11.72735		f_{ave}	17.32852
	σ	0		σ	3.65E-15
	c_{best}	1375		c_{best}	1300

Table 3 : Optimum results of 40-story structure

In Case 1, the optimum mass of TMD is bigger than the mass of a story of the structure. In that case, Case 2 will be more realistic than Case 1 in practical application. The maximum amplitude seen for 0.25 Hz (4s period) is 26.68dB for the structure without TMD. The maximum amplitude is reduced to 11.7273dB and 17.3285dB for Case 1 and Case 2, respectively. The frequency plot for the top story acceleration transfer function is seen in Fig. 3.

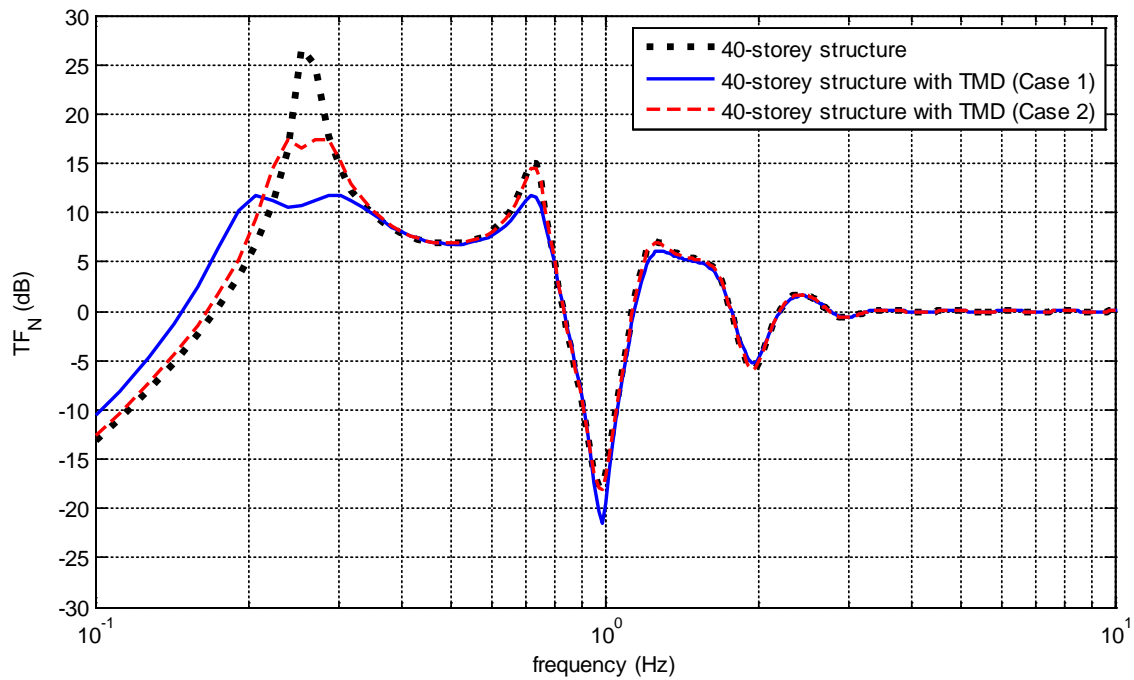


Fig. 3. TFN plot for 40-story structure

Case 1 is also effective on the maximum responses the second and third natural frequency of the structure as seen in the plot. Case 2 is only effective at the first natural frequency, but it is an economical and feasible application.

4 THE ROBUSTNESS OF THE OPTIMUM TMD AGAINST SENSIBILITY OF STRUCTURAL PARAMETERS

In this section, the robustness of TMD is evaluated by changing the mass and stiffness of the structure. The change of these parameters may change the critical natural frequency and the optimum TMD may be detuned. Thus, the sensibility limit of structural parameters is investigated.

Mass of the structures are not a constant value because of the existing of live-loads. Also, the stiffness of the stories may be different because of non-linear factors and several assumptions. The change of both values will affect the natural frequency of the structure, but the sensibility of mass and stiffness are both investigated.

In the study, the mass or stiffness (rigidity) were changed by $\pm 50\%$. The maximum possible change is taken as high in order to see if the optimum TMD is detuned or not. As seen from the results, a negative effect is only seen for the 40-story structure with an optimum TMD obtained by using the mass range of Case 2.

4.1 The robustness of the optimum TMD for 10-story structure

In Table 4, the maximum amplitudes of top story acceleration transfer function values are presented for 10-story structure with -50%, -30%, -10%, 0% (predicted value), +10%, +30% and +50% change of the mass of all stories of structure. As seen from the results, the optimum TMD is effective in all mass cases.

Mass	-50%	-30%	-10%	0%	+10%	+30%	+50%
f (dB) without TMD	23.4078	24.8671	25.9573	26.2091	26.6195	27.4263	28.1421
f (dB) with TMD	12.2668	12.1125	11.6199	11.3316	12.8959	15.7767	18.2759

Table 4. Performance evaluation of optimum TMD for mass uncertainty of 10-story structure

The shifting of the place of the peak amplitude of 10-story structure without TMD can be clearly seen in TF_N plot given as Fig. 4. The straight lines shows the values of the TMD controlled structure, while the uncontrolled structure is shown with dotted line. The optimum TMD reduces all peak amplitudes effectively. Also, the TMD is robust against the change of the stiffness values of the structure. The maximum results are given as Table 5 and TF_N plot is given as Fig. 5 for rigidity uncertainty.

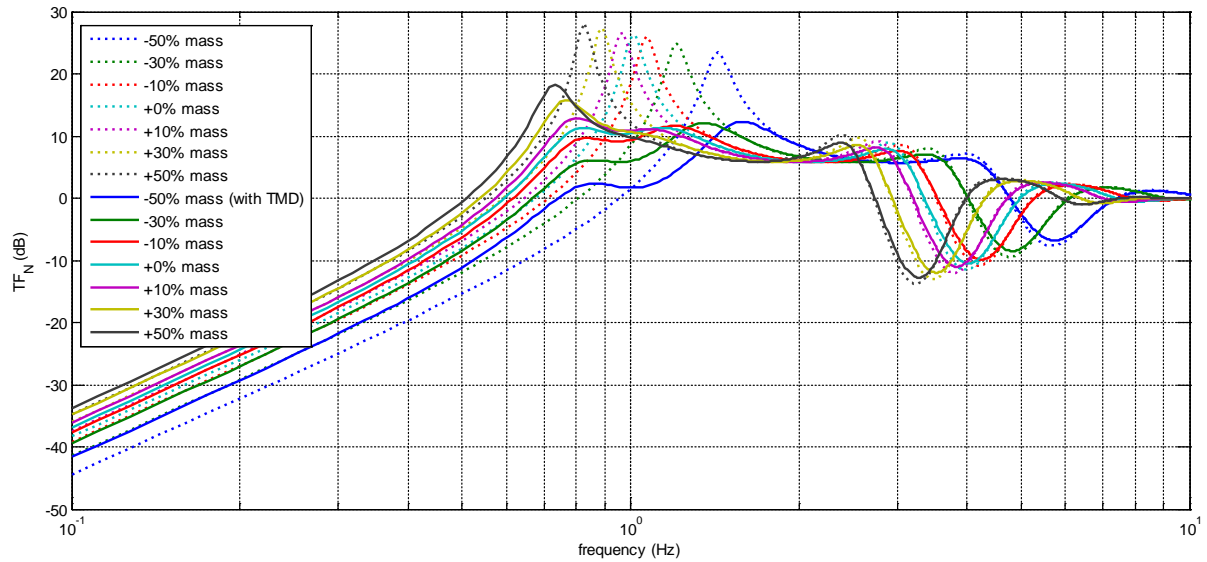
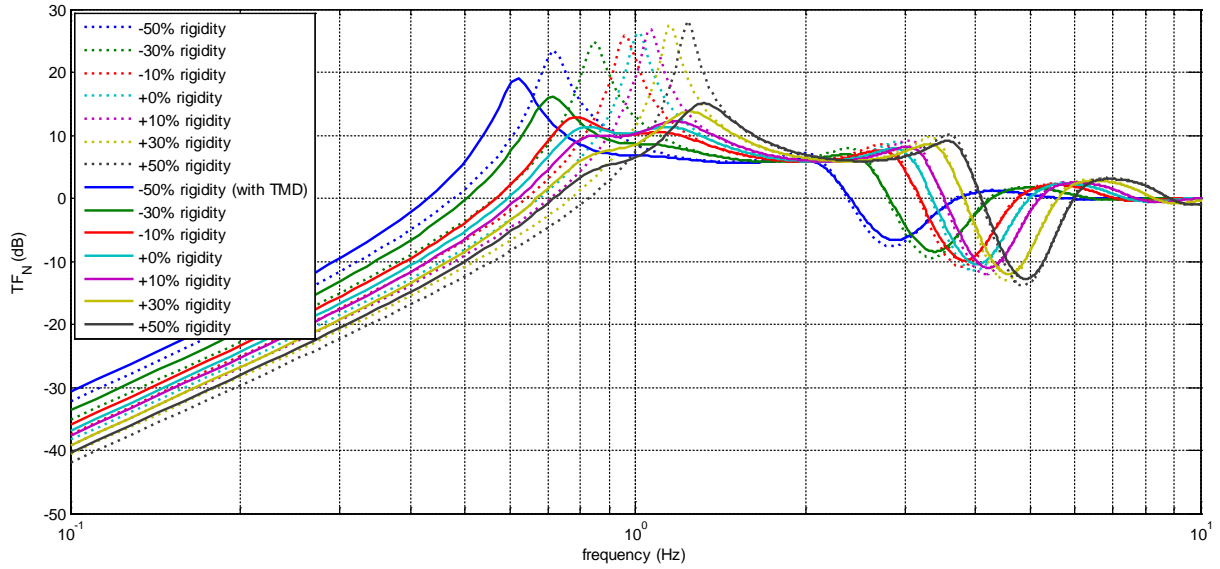


Fig. 4. TF_N plot of 10-story structure for mass uncertainty

Rigidity	-50%	-30%	-10%	0%	+10%	+30%	+50%
f (dB) without TMD	23.4078	24.8157	25.8414	26.2091	26.7032	27.3025	28.1421
f (dB) with TMD	18.9435	16.0250	12.8140	11.3316	12.1856	13.7254	15.0625

Table 5. Performance evaluation of optimum TMD for rigidity uncertainty of 10-story structure

Fig. 5. TF_N plot of 10-story structure for rigidity uncertainty

4.2 The robustness of the optimum TMD for 40-story structure

The robustness evaluation of 40-story structure is more important than the 10-story structure since Case 2 has a small mass comparing to the total mass of the structure. In Table 6, the maximum amplitudes are presented for 40-story structure without TMD and with TMD (Case 1 and 2) for mass uncertainty. Also, the values for rigidity uncertainty can be seen in Table 7.

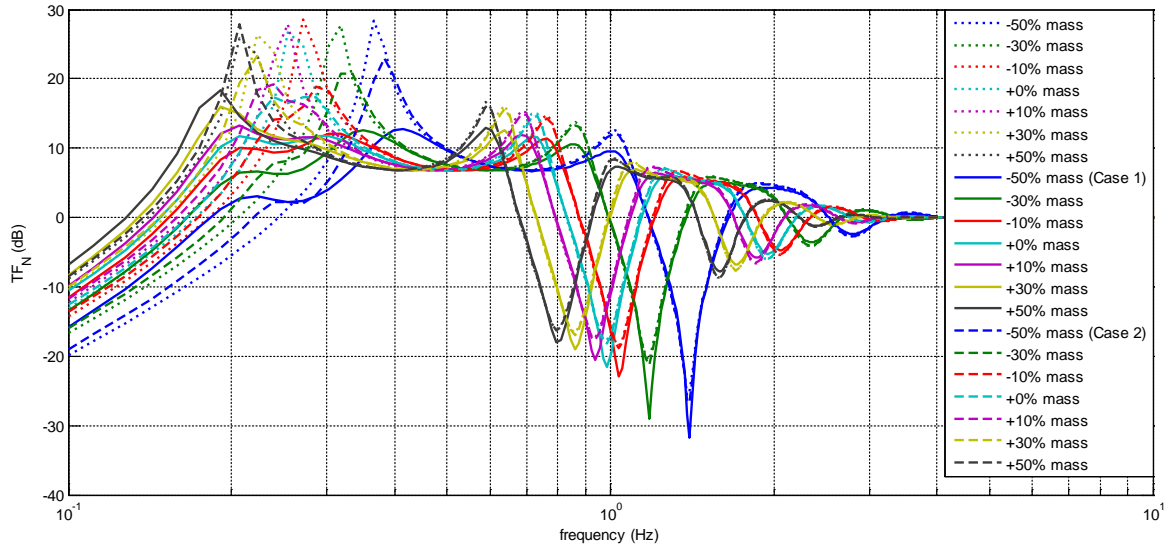
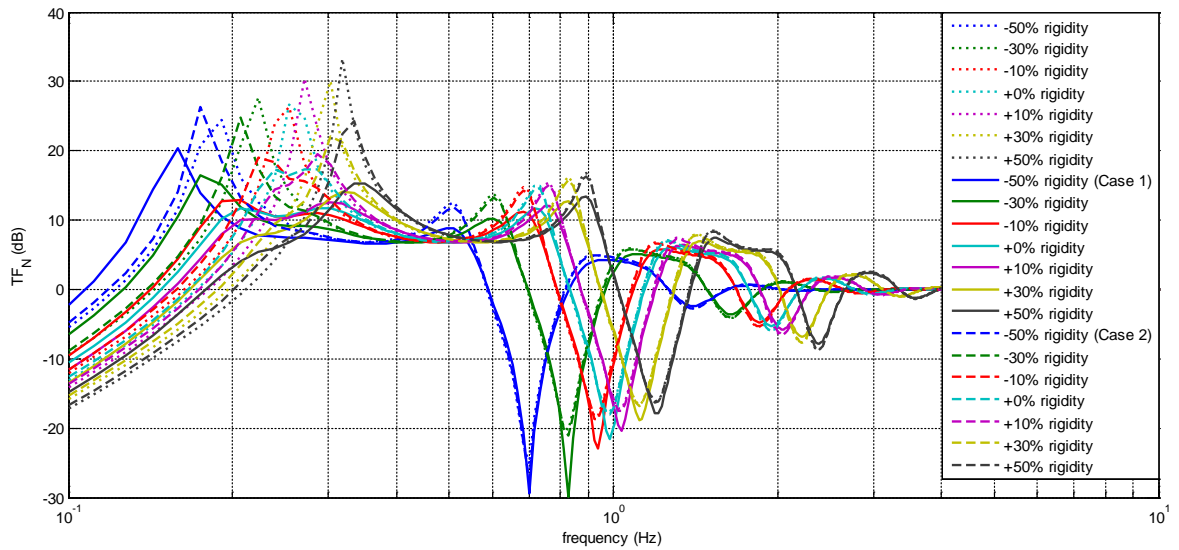
Mass	-50%	-30%	-10%	0%	+10%	+30%	+50%
f (dB) without TMD	28.4611	27.6896	28.5573	26.6753	27.8215	26.3671	25.8331
f (dB) (Case 1)	12.7946	12.5759	11.9943	11.7274	13.2204	16.0236	18.3351
f (dB) (Case 2)	22.9611	20.7366	18.8666	17.3286	19.1971	23.3579	27.9158

Table 6. Performance evaluation of optimum TMD for mass uncertainty of 40-story structure

Rigidity	-50%	-30%	-10%	0%	+10%	+30%	+50%
f (dB) without TMD	24.4572	27.6896	26.3926	26.6753	30.4101	29.9931	33.3609
f (dB) (Case 1)	20.4031	16.3936	12.9145	11.7274	12.6067	14.0525	15.2406
f (dB) (Case 2)	26.3568	24.7697	19.0215	17.3286	19.5956	22.0111	24.2516

Table 7. Performance evaluation of optimum TMD for rigidity uncertainty of 40-story structure

As seen from the results, the optimum TMD using the ranges of Case 1 is always robust, but the robustness limit is 50% for Case 2. +50% mass change and -50% rigidity change are the cases where the effectiveness of TMD is lost for Case 2. The plots of TF_N are given as Fig. 6 and Fig. 7 for mass and rigidity uncertainty, respectively.

Fig. 6. TF_N plot of 40-story structure for mass uncertaintyFig. 7. TF_N plot of 40-story structure for rigidity uncertainty

5 DISCUSSION AND CONCLUSION

The detuning of mass damper is an important problem because of the uncertainty of the main-structure properties. The optimum TMD is robust against the change of the mass or stiffness of the structure by $\pm 50\%$ difference. Only, the second case of 40-story structure is not robust when the 50% uncertainty is possible. This situation is resulted from small mass of TMD comparing to the total mass of 40-story structure. Whereas, Case 2 may be more practical TMD comparing to Case 1.

REFERENCES

- [1]. Frahm H. Device for damping of bodies. U.S. Patent No: 989,958, 1911.
- [2]. Ormondroyd J, Den Hartog JP. The theory of dynamic vibration absorber. T ASME 50:922, 1928.
- [3]. Den Hartog, J.P. (1947), *Mechanical Vibrations*, McGraw-Hill, New York.
- [4]. Warburton, G.B. (1982), Optimum absorber parameters for various combinations of response and excitation parameters, *Earthquake Engineering and Structural Dynamics*, 10, 381-401.
- [5]. Sadek, F., Mohraz, B., Taylor, A.W. and Chung, R.M. (1997), A method of estimating the parameters of tuned mass dampers for seismic applications, *Earthquake Engineering and Structural Dynamics*, 26, 617-635.
- [6]. Hadi, M.N.S. and Arfiadi, Y. (1998), Optimum design of absorber for MDOF structures, *Journal of Structural Engineering-ASCE*, 124, 1272-1280.
- [7]. Marano, G.C., Greco, R. and Chiaia, B. (2010), A comparison between different optimization criteria for tuned mass dampers design, *Journal of Sound and Vibration*, 329, 4880-4890.
- [8]. Singh, M.P., Singh, S. and Moreschi, L.M. (2002), Tuned mass dampers for response control of torsional buildings, *Earthquake Engineering and Structural Dynamics*, 31, 749-769.
- [9]. Desu, N.B., Deb, S.K., Dutta, A. (2006), Coupled tuned mass dampers for control of coupled vibrations in asymmetric buildings, *Struct. Control Hlth.*, 13, 897-916.
- [10]. Pourzeynali, S., Lavasani, H.H., Modarayi, A.H. (2007), Active control of high rise building structures using fuzzy logic and genetic algorithms, *Eng. Struct.*, 29, 346-357.
- [11]. Leung, A.Y.T., Zhang, H., Cheng, C.C. and Lee, Y.Y. (2008), Particle swarm optimization of TMD by non-stationary base excitation during earthquake, *Earthquake Engineering and Structural Dynamics*, 37, 1223-1246.
- [12]. Leung, A.Y.T. and Zhang, H. (2009), Particle swarm optimization of tuned mass dampers, *Engineering Structures*, 31, 715-728.
- [13]. Steinbuch, R. (2011), Bionic optimisation of the earthquake resistance of high buildings by tuned mass dampers, *Journal of Bionic Engineering*, 8, 335-344.
- [14]. Bekdaş, G. and Nigdeli, S.M. (2017), Metaheuristic based optimization of tuned mass dampers under earthquake excitation by considering soil-structure interaction, *Soil Dynamics and Earthquake Engineering*, 92, 443-461.
- [15]. Nigdeli, S.M. and Bekdaş, G. (2017), Optimum tuned mass damper design in frequency domain for structures, *KSCE Journal of Civil Engineering*, 21(3), 912-922.
- [16]. Zhang, H. Y. and Zhang, L. J. (2017). Tuned mass damper system of high-rise intake towers optimized by improved harmony search algorithm. *Engineering Structures*, 138, 270-282.
- [17]. Farshidianfar, A., Soheili, S. (2013), Ant colony optimization of tuned mass dampers for earthquake oscillations of high-rise structures including soil-structure interaction, *Soil Dyn. Earthquake Eng.*, 51, 14-22.
- [18]. Farshidianfar, A., Soheili, S. (2013), ABC optimization of TMD parameters for tall buildings with soil structure interaction, *Interact. Multiscale Mech.*, 6, 339-356.
- [19]. Farshidianfar, A., Soheili, S. (2013), Optimization of TMD parameters for Earthquake Vibrations of Tall Buildings Including Soil Structure Interaction, *Int. J. Optim. Civ. Eng.*, 3, 409-429.
- [20]. Nigdeli SM, Bekdaş G, Yang X-S (2017), Optimum Tuning of Mass Dampers by Using a Hybrid Method Using Harmony Search and Flower Pollination Algorithm. In: *Harmony Search Algorithm. Advances in Intelligent Systems and Computing*, vol 514, Del Ser J. (eds) Springer, pp. 222-231.
- [21]. Nigdeli SM, Bekdaş G. (2015), Teaching-Learning-Based Optimization for Estimating Tuned Mass Damper Parameters. 3rd International Conference on Optimization Techniques in Engineering (OTENG '15), 7-9 November 2015, Rome, Italy
- [22]. Rao, R. (2016). Jaya: A simple and new optimization algorithm for solving constrained and unconstrained optimization problems. *International Journal of Industrial Engineering Computations*, 7(1), 19-34.
- [23]. Singh, M.P., Matheu, E.E, Suarez, L.E. (1997), Active and semi-active control of structures under seismic excitation, *Earthq. Eng. Struct. D.*, 26, 193-213.
- [24]. Liu, M.Y., Chiang, W.L., Hwang, J.H., Chu, C.R. (2008), "Wind-induced vibration of high-rise building with tuned mass damper including soil-structure interaction", *J. Wind Eng. Ind. Aerodyn.*, 96, 1092-1102.

METAHEURISTIC AND FREQUENCY DOMAIN BASED OPTIMIZATION OF TUNED MASS DAMPERS AND VERIFICATION OF THE RESULTS ON TIME HISTORY ANALYSES

Sinan Melih Nigdeli¹, Gebrail Bekdaş¹ and Yusuf Cengiz Toklu²

¹Department of Civil Engineering
Istanbul University
Istanbul, TR-34320, Turkey

e-mail: melihnig@istanbul.edu.tr, bekdas@istanbul.edu.tr

²Department of Civil Engineering
Okan University
Istanbul, TR-34359, Turkey
e-mail: cengiztoklu@gmail.com

Keywords: Tuned mass damper, Jaya algorithm, Transfer function.

Abstract. *The optimization of tuned mass dampers for structures is a stochastic problem because of existing of damping. In that case, heuristic algorithms are useful tools in that field for an objective function in frequency or time domain. In the present study, the transfer function response of structures are minimized by using TMDs optimized by the developed methodology employing the newly developed Jaya algorithm which is a recently proposed simple but powerful algorithm. The numerical experiments on methodology are presented by using a 10 story structure and a 40 story structure with comparison of other algorithms such as harmony search, flower pollination algorithm, teaching learning based optimization and a new version of Jaya algorithm combined with Lévy flights. The main purpose of TMD is to damp vibrations by reducing the maximum displacement and providing a rapid steady-state response. For that reason, the optimum results were tested by using several groups of earthquake data.*

1 INTRODUCTION

Tuned mass dampers (TMDs) are vibration absorber devices which are used to absorb the vibration of mechanical systems including civil structures. The initial form of Frahm [1] was without damping and Ormondroyd and Den Hartog [2] proposed damping for vibrations with random frequency. For the optimization of design variables of TMD parameters such as mass (m_d), stiffness (k_d) and damping coefficients (c_d), the formulation of the ratio of frequencies of TMD and superstructure (f_{opt}) and the damping ratio of TMD (ξ_{opt}) have been proposed according to the mass ratio of TMD and superstructure (μ) [3-5]. These expressions were derived for single degree of freedom systems. In order to consider all vibration modes, heuristic based algorithms have been employed [6-10]. In this study, the newly developed Jaya algorithm is employed for the TMD optimization problem in order to minimize the amplitude of the acceleration transfer function which is a control factor of frequency domain analyses of the structure. The classical form of the Jaya algorithm (JA) [11] was used and two newly developed variants of the Jaya algorithm are also employed in the proposed methodology. The results were also compared with other metaheuristics including harmony search (HS) [12], teaching learning based optimization (TLBO) [13] and flower pollination algorithm (FPA) [14]. The performances of the optimum TMDs were also tested for time-history analyses.

2 THE METHOD AND OPTIMIZATION

The objective of the problem is to find the design variables which are mass (m_d), period (T_d) and damping ratio (ξ_d) minimizing the amplitude of the acceleration transfer function of the top story (f) formulated as Eq. (1). The absolute value of transfer function of the top story ($TF_N(\omega)$) is taken to find the amplitude and is obtained. The base-10 logarithm of the amplitude multiplied with 20 is taken to find the value in decibel (dB).

In optimization processes using metaheuristic methods, the operation starts with generating an initial solution matrix. This matrix contains randomly assigned design variables and these design variables are updated by using algorithm specific rules and considering the solution of the objective function.

$$f = 20\text{Log}_{10}|\max(TF_N(\omega))| \quad (1)$$

Jaya algorithm (JA) is a recently developed metaheuristic algorithm and it has no algorithm-specific parameter

like TLBO, but JA use a single phase in an iteration. In the formulation of JA, two random values (r_1 and r_2) are used as seen in Eq. (2) for n population and m maximum iterations (t). x is the set of design variables and the subscripts; i , best and worst represent the i^{th} candidate solution, the current best solution and the worst current solution, respectively.

$$x_i^{t+1} = x_i^t + r_1(x_{best} - |x_i^t|) - r_2(x_{worst} - |x_i^t|) \quad i = 1 \text{ to } n \text{ and } t = 1 \text{ to } m \quad (2)$$

2.1. The Jaya algorithm with Lévy flight (JALF)

The usage of random variables with linear distribution may lead to convergence to local optimum results. Thus, the random numbers with linear distribution are changed with Lévy flight distributions (L1 and L2) as seen in Eq. (3) and a global optimization phase is generated.

$$x_i^{t+1} = x_i^t + L_1(x_{best} - |x_i^t|) - L_2(x_{worst} - |x_i^t|) \quad i = 1 \text{ to } n \text{ and } t = 1 \text{ to } m \quad (3)$$

2.2. Two phase Jaya algorithm (2PJA)

The global optimization formulation given as Eq. (3) may negatively influence the convergence of the algorithm. Thus, a two phase JA like TLBO is proposed using a global phase according to Eq. (3) and a local phase according to the classical form of JA defined in Eq. (2). These two phases are consequently done as same as TLBO. Thus, it is not necessary to use a control parameter to choose the type of the optimization.

3 NUMERICAL EXAMPLE

The numerical examples involve two shear buildings which are 10-story and 40-story structural models. The results of JA, JALF and JA2P are compared with HS, FPA and TLBO. The population number for the algorithms are chosen as 25. The HMCR and switch probability are 0.5, while PAR is 0.2 for the numerical examples. The mass of the TMD is limited in order to prevent the extreme increase of the axial loads of the structure. Also, the other design variables are searched in a solution range in order to find optimum results easily. The mass of the TMD (m_d) must be less than 10% of the total mass of the structures. The lower bound for m_d is 1%. The period of the TMD (T_d) is between 0.8 and 1.2 times of the critical period of the structure. The damping ratio is between 1% and 30%. The total mass of the 40-story structure may be too much, for that reason, the maximum mass ratio is taken as 2% for a second case.

3.1. The optimum results for 10-story structure

The 10-story shear building have the same story parameters (mass; $m_i=360$ t, stiffness; $k_i=650$ MN/m and damping coefficients; $c_i=6.2$ MNs/m) [15]. As seen in Table 2, the algorithm such as FPA, TLBO, JA, JALF and 2PJA are effective to find the optimum result. The optimum TMD parameters are $m_d=360$ t, $T_d=1.10864$ s and $\xi_d=0.2596$ (25.969%) for the 10-story shear building. Also, the average values (f_{ave}) of 20 runs of these algorithms are the same except the minor changes of TLBO and JALF. In that case, the standard deviation (σ) values are 0 or nearly 0. The number of variable evaluations needed to reach the optimum results is shown with c_{best} . This value is the lowest for FPA. As seen from computational effort, the Lévy flight distribution has a negative effect on the convergence of the JA. The c_{best} value for 2PJA is nearly double of JA while JALF needs the most computational effort. It is clearly seen that the classical JA and FPA outperform the other algorithms in means of computational effort.

	HS	FPA	TLBO	JA	JALF	2PJA
m_d (t)	360	360	360	360	360	360
T_d (s)	1.109193	1.108639	1.108639	1.108639	1.108639	1.108639
ξ_d	0.262109	0.25969	0.25969	0.25969	0.25969	0.25969
f_{best}	11.33419	11.33157	11.33157	11.33157	11.33157	11.33157
f_{ave}	11.33295	11.33157	11.33157	11.33157	11.33157	11.33157
σ	0.000321	0	3.62E-13	0	2.50E-11	0
c_{best}	7006	950	5750	1575	8125	2925

Table 2 : The optimum result of 10-story structure

3.2. The optimum results for 40-story structure

The proposed methodology was also tested for a big structure with 40 stories. The properties taken from Lui et al. [16] and all story parameters are different (mass; $m_i=980$ t, stiffness; k_i =linearly change between 2130-998 MN/m and damping coefficients; c_i = linearly change between 42.6-19.96 MNs/m).

As mentioned before, the optimum TMD parameters were found for two cases of maximum mass ratio. In Case 1 and 2, the maximum allowable mass ratio of the TMD is 10% and 2%, respectively. The optimum values for 40-story structure is presented in Table 2. JA is the fastest algorithm in finding the optimum results of the TMD parameters of the 40-story structure.

		HS	FPA	TLBO	JA	JALF	2PJA
Case 1	m_d (t)	3920	3920	3920	3920	3920	3920
	T_d (s)	4.35918	4.358596	4.358596	4.358596	4.358596	4.358596
	ξ_d	0.281695	0.281294	0.281294	0.281294	0.281294	0.281294
	f_{best}	11.72978	11.72735	11.72735	11.72735	11.72735	11.72735
	f_{ave}	11.72975	11.72866	11.72735	11.72735	11.72998	11.72998
	σ	0.000472	0.002619	0	0	0.003605	0.003605
	c_{best}	44349	1725	5150	1375	2425	1525
Case 2	m_d (t)	784	784	784	784	784	784
	T_d (s)	3.94892	3.949575	3.949575	3.949575	3.949575	3.949575
	ξ_d	0.131255	0.131671	0.131671	0.131671	0.131671	0.131671
	f_{best}	17.33442	17.32852	17.32852	17.32852	17.32852	17.32852
	f_{ave}	17.33572	17.32852	17.32852	17.32852	17.32852	17.32852
	σ	0.002938	3.65E-15	3.65E-15	3.65E-15	3.65E-15	3.65E-15
	c_{best}	43186	1450	4800	1300	3525	1750

Table 2 : Optimum result of 40-story structure

Earthquake No.	Earthquake Name	Recording Station	Year	Magnitude	FN Component	FP Component
1	Northridge	Beverly Hills - Mulhol	1994	6,7	NORTHR/MUL009	NORTHR/MUL279
2	Northridge	Canyon Country-WLC	1994	6,7	NORTHR/LOS000	NORTHR/LOS270
3	Duzce, Turkey	Bolu	1999	7,1	DUZCE/BOL000	DUZCE/BOL090
4	Hector Mine	Hector	1999	7,1	HECTOR/HEC000	HECTOR/HEC090
5	Imperial Valley	Delta	1979	6,5	IMPVALL/H-DLT262	IMPVALL/H-DLT352
6	Imperial Valley	El Centro Array #11	1979	6,5	IMPVALL/H-E11140	IMPVALL/H-E11230
7	Kobe, Japan	Nishi-Akashi	1995	6,9	KOBE/NIS000	KOBE/NIS090
8	Kobe, Japan	Shin-Osaka	1995	6,9	KOBE/SHI000	KOBE/SHI090
9	Kocaeli, Turkey	Duzce	1999	7,5	KOCAELI/DZC180	KOCAELI/DZC270
10	Kocaeli, Turkey	Arcelik	1999	7,5	KOCAELI/ARC000	KOCAELI/ARC090
11	Landers	Yermo Fire Station	1992	7,3	LANDERS/YER270	LANDERS/YER360
12	Landers	Coolwater	1992	7,3	LANDERS/CLW-LN	LANDERS/CLW-TR
13	Loma Prieta	Capitola	1989	6,9	LOMAP/CAP000	LOMAP/CAP090
14	Loma Prieta	Gilroy Array #3	1989	6,9	LOMAP/G03000	LOMAP/G03090
15	Manjil, Iran	Abbar	1990	7,4	MANJIL/ABBAR--L	MANJIL/ABBAR--T
16	Superstition Hills	El Centro Imp. Co.	1987	6,5	SUPERST/B-ICC000	SUPERST/B-ICC090
17	Superstition Hills	Poe Road (temp)	1987	6,5	SUPERST/B-POE270	SUPERST/B-POE360
18	Cape Mendocino	Rio Dell Overpass	1992	7,0	CAPEMEND/RIO270	CAPEMEND/RIO360
19	Chi-Chi, Taiwan	CHY101	1999	7,6	CHICHI/CHY101-E	CHICHI/CHY101-N
20	Chi-Chi, Taiwan	TCU045	1999	7,6	CHICHI/TCU045-E	CHICHI/TCU045-N
21	San Fernando	LA - Hollywood Stor	1971	6,6	SFERN/PEL090	SFERN/PEL180
22	Friuli, Italy	Tolmezzo	1976	6,5	FRIULI/A-TMZ000	FRIULI/A-TMZ270

Table 5. Far-field ground motions (FEMA, 2009)

3.3. The performance of optimum TMDs on benchmark earthquakes

It is clearly seen that the optimum TMDs are effective in the reduction of the acceleration transfer function at the points where the peak amplitude is seen. The main purpose of TMD is to damp vibrations by reducing the maximum displacement and providing a rapid steady-state response. For that reason, the optimum results were

tested by using several groups of earthquake data. These data are found in FEMA P-695: Quantification of Building Seismic Performance Factors (FEMA, 2009). The earthquake records in Table 5 represent the far-field ground motions.

The optimum TMD parameters were also tested under the near-field ground motions including (Table 6) or not including (Table 7) significant impulsive pulses. The Tables 5-7 contain the information of the records including earthquake name, recording station, year, magnitude, fault normal (FN) and fault parallel (FP) components.

Earthquake No.	Earthquake Name	Recording Station	Year	Magnitude	FN Component	FP Component
1	Imperial Valley-06	El Centro Array #6	1979	6.5	Impvall/H-E06_233	Impvall/H-E06_323
2	Imperial Valley-06	El Centro Array #7	1979	6.5	Impvall/H-E07_233	Impvall/H-E07_323
3	Irpina, Italy-01	Sturmo	1980	6.9	Italy/A-Stu_223	Italy/A-Stu_313
4	Superstition Hills-02	Parachute Test Site	1987	6.5	Superst/B-Pts_037	Superst/B-Pts_127
5	Loma Prieta	Saratoga - Aloha	1989	6.9	Lomap/Stg_038	Lomap/Stg_128
6	Erzikan, Turkey	Erzikan	1992	6.7	Erzikan/Erz_032	Erzikan/Erz_122
7	Cape Mendocino	Petrolia	1992	7.0	Capemend/Pet_260	Capemend/Pet_350
8	Landers	Lucerne 01 Rinaldi	1992	7.3	Landers/Lcn_239	Landers/Lcn_329
9	Northridge-01	Receiving Sta	1994	6.7	Northr/Rrs_032	Northr/Rrs_122
10	Northridge-01	01 Sylmar - Olive View	1994	6.7	Northr/Syl_032	Northr/Syl_122
11	Kocaeli, Turkey	Izmit	1999	7.5	Kocaeli/Izt_180	Kocaeli/Izt_270
12	Chi-Chi, Taiwan	TCU065	1999	7.6	Chichi/Tcu065_272	Chichi/Tcu065_002
13	Chi-Chi, Taiwan	TCU102	1999	7.6	Chichi/Tcu102_278	Chichi/Tcu102_008
14	Duzce, Turkey	Duzce	1999	7.1	Duzce/Dzc_172	Duzce/Dzc_262

Table 6. Near-field ground motions with pulses (FEMA, 2009)

Earthquake No.	Earthquake Name	Recording Station	Year	Magnitude	FN Component	FP Component
1	Gazli, Ussr	Karakyr	1976	6.8	Gazli/Gaz_177	Gazli/Gaz_267
2	Imperial Valley-06	El Centro Array #7	1979	6.5	Impvall/H-Ber_233	Impvall/H-Ber_323
3	Imperial Valley-06	Sturmo	1979	6.5	Impvall/H-Chi_233	Impvall/H-Chi_323
4	Nahanni, Canada	Site 1	1985	6.8	Nahanni/S1_070	Nahanni/S1_160
5	Nahanni, Canada	Site 2	1985	6.8	Nahanni/S2_070	Nahanni/S2_160
6	Loma Prieta	Bran	1989	6.9	Lomap/Brn_038	Lomap/Brn_128
7	Loma Prieta	Corralitos	1989	6.9	Lomap/Clis_038	Lomap/Clis_128
8	Cape Mendocino	Cape Mendocino	1992	7.0	Capemend/Cpm_260	Capemend/Cpm_350
9	Northridge-01	La - Sepulveda Va	1994	6.7	Northr/0637_032	Northr/0637_122
10	Northridge-01	Northridge - Saticoy	1994	6.7	Northr/Stc_032	Northr/Stc_122
11	Kocaeli, Turkey	Yarimca	1999	7.5	Kocaeli/Ypt_180	Kocaeli/Ypt_270
12	Chi-Chi, Taiwan	Tcu067	1999	7.6	Chichi/Tcu067_285	Chichi/Tcu067_015
13	Chi-Chi, Taiwan	Tcu084	1999	7.6	Chichi/Tcu084_271	Chichi/Tcu084_001
14	Denali, Alaska	Taps Pump Sta. #10	2002	7.9	Denali/Ps10_199	Denali/Ps10_289

Table 7. Near-field ground motions without pulses (FEMA, 2009)

3.3.1 The results for 10-story structure

The structural responses obtained from the 10-story structure without and with TMD are presented in Tables 8, 9 and 10 for far-field records, the near-field records with pulses and without pulses, respectively. The maximum values given in the Tables 8-10 are the top story displacement (y_{10}) and the total acceleration of the top story ($\ddot{y}_{10} + \ddot{y}_g$). The FP component (DUZCE/BOL090) of Bolu record of the 1999 Düzce earthquake is the most critical excitation for the 10-story structure. The maximum displacement for the 10th story is 0.4101m and the optimum TMD is effective to reduce it to 0.2622 with 36.06% performance.

Earthquake	Component	$\ddot{y}_{10} + \ddot{y}_g$			
		Without TMD	With TMD	Without TMD	With TMD
1	FN	0.3693	0.2382	15.8042	8.2525
	FP	0.3110	0.2713	12.9883	9.5841
2	FN	0.1326	0.1086	6.3276	5.0632
	FP	0.2236	0.1461	9.2066	6.4152
3	FN	0.2590	0.1569	12.7887	7.6020
	FP	0.4101	0.2622	19.2864	12.0021
4	FN	0.1118	0.1070	5.0418	4.2105
	FP	0.1317	0.1391	5.4565	4.4950
5	FN	0.1110	0.0652	5.3268	3.2047
	FP	0.1894	0.1082	7.8952	4.2661
6	FN	0.0765	0.0670	4.5812	3.7041
	FP	0.0705	0.0888	4.3957	4.4892
7	FN	0.1112	0.0999	5.9113	5.6091
	FP	0.1013	0.0882	5.1205	5.2906
8	FN	0.1045	0.1310	4.9963	5.3914
	FP	0.0764	0.0806	3.2676	3.0263
9	FN	0.1548	0.1150	8.4409	6.3647
	FP	0.2235	0.1903	9.8120	7.7423
10	FN	0.0407	0.0280	2.0715	1.6708
	FP	0.0396	0.0373	1.9932	1.2496
11	FN	0.1797	0.1371	7.4196	5.1637
	FP	0.1139	0.0815	4.9984	3.0643
12	FN	0.0834	0.0636	6.0349	3.5787
	FP	0.1369	0.1390	6.1439	5.7271
13	FN	0.1467	0.1539	8.9522	6.9083
	FP	0.0949	0.0950	5.0056	5.5921
14	FN	0.1139	0.0724	6.6829	6.0693
	FP	0.1223	0.1293	6.0778	5.5444
15	FN	0.1236	0.0919	6.0631	4.9267
	FP	0.1847	0.1375	9.9501	6.9884
16	FN	0.0848	0.1501	5.5291	5.7908
	FP	0.0837	0.0815	3.3533	3.4759
17	FN	0.1151	0.0925	5.1103	4.4676
	FP	0.1375	0.0811	6.2135	4.8139
18	FN	0.1829	0.1426	8.5183	7.0506
	FP	0.1398	0.0946	7.7027	6.1423
19	FN	0.1608	0.1088	7.6721	5.2595
	FP	0.3547	0.1922	13.8343	8.5836
20	FN	0.1085	0.0704	6.6454	4.9365
	FP	0.1514	0.1169	7.1653	6.2917
21	FN	0.0851	0.0639	4.5123	3.1191
	FP	0.0614	0.0314	2.8126	1.5212
22	FN	0.0847	0.0606	5.3753	3.9533
	FP	0.1013	0.0756	5.2738	4.6214

Table 8. The responses of 10-story structure under far-field records

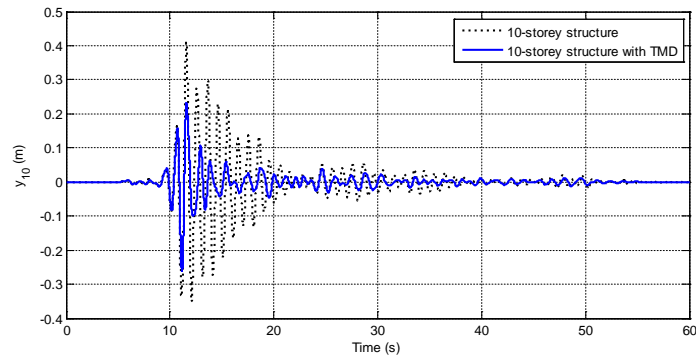


Fig. 4. Top story displacement of the 10-story structure (DUZCE/BOL090)

The time-history plot for this excitation is also drawn in Fig. 4. The reduction of the maximum point and the effectiveness of the TMD on the damping of the vibrations are clearly seen. Also, the maximum top story acceleration is reduced to 12.0121m/s^2 from 19.2864m/s^2 for the same excitation. The maximum top story displacement under near-field records with pulses is 0.6457m and it is reduced to 0.5052m by using the optimum TMD (21.76% reduction). The critical excitation, which is the FN component (Northhr/Rrs-032) of 01 Rinaldi Receiving Sta. station of the 1994 Northridge earthquake, was used to obtain the top-story displacement time-history plot given as Fig. 5.

Earthquake	Component	$\ddot{y}_{10} + \ddot{y}_g$			
		y_{10}			
		Without TMD	With TMD	Without TMD	With TMD
1	FN	0.2159	0.1281	9.4237	5.3776
	FP	0.1509	0.1503	6.6648	5.8373
2	FN	0.2254	0.1712	9.5061	7.4246
	FP	0.2302	0.2110	9.5597	8.2970
3	FN	0.1045	0.1033	4.6150	3.5535
	FP	0.1546	0.1196	6.9255	4.2733
4	FN	0.3562	0.2679	13.5591	8.8910
	FP	0.1702	0.1438	7.3747	6.3768
5	FN	0.1538	0.1424	7.0769	5.8079
	FP	0.1281	0.0758	7.1845	4.6857
6	FN	0.1957	0.1820	11.1409	8.1833
	FP	0.2837	0.2301	11.7546	8.7199
7	FN	0.2135	0.1744	11.3048	9.3217
	FP	0.3367	0.2761	15.4409	12.0723
8	FN	0.1372	0.1889	6.3171	6.8368
	FP	0.1086	0.0696	5.1209	3.8508
9	FN	0.6457	0.5052	27.7301	17.4081
	FP	0.2700	0.2159	13.4820	9.2885
10	FN	0.2137	0.2090	9.2710	7.3446
	FP	0.2716	0.2935	14.8096	13.4099
11	FN	0.1105	0.0746	5.8749	2.8830
	FP	0.1141	0.0528	5.0043	1.9691
12	FN	0.4373	0.2742	18.2119	12.2201
	FP	0.4048	0.2349	17.9800	9.6555
13	FN	0.1912	0.1823	8.0242	5.8896
	FP	0.2293	0.1285	8.9202	4.4755
14	FN	0.1925	0.1176	8.0411	6.1547
	FP	0.2878	0.1706	11.5440	7.4123

Table 9. The responses of 10-story structure under near-field records with pulses

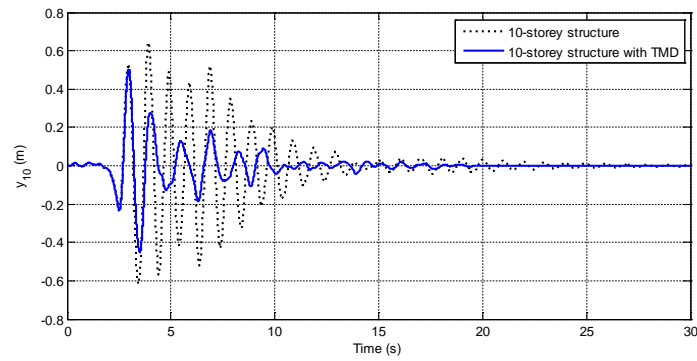


Fig. 5. Top story displacement of the 10-story structure (Northhr/Rrs-032)

Earthquake	Component	$\ddot{y}_{10} + \ddot{y}_g$			
		y_{10}			
		Without TMD	With TMD	Without TMD	With TMD
1	FN	0.2725	0.1793	11.0867	6.8370
	FP	0.1759	0.1165	8.7232	5.6536
2	FN	0.1551	0.1137	8.0885	6.3350
	FP	0.1668	0.1680	9.7206	9.3497
3	FN	0.0997	0.0703	3.9616	2.8200
	FP	0.1684	0.0945	6.1314	3.9323
4	FN	0.1485	0.1238	9.5579	7.9522
	FP	0.1907	0.0944	8.4289	5.5497
5	FN	0.0437	0.0456	2.8066	2.7346
	FP	0.0972	0.0776	4.6745	3.7971
6	FN	0.2075	0.1445	11.2136	7.9960
	FP	0.1304	0.1282	7.0685	6.6956
7	FN	0.1323	0.1198	9.9175	7.6878
	FP	0.1981	0.1421	9.3531	6.7038
8	FN	0.2499	0.2030	18.7204	15.8961
	FP	0.1048	0.1061	7.0698	6.4187
9	FN	0.3936	0.3095	17.5241	12.7042
	FP	0.2374	0.1441	11.7440	10.8559
10	FN	0.1150	0.1138	5.9471	4.6714
	FP	0.3162	0.2385	13.9212	9.1484
11	FN	0.1307	0.1059	6.0181	4.1239
	FP	0.1228	0.1198	5.9340	4.6953
12	FN	0.3129	0.2043	12.9713	8.0932
	FP	0.2153	0.1699	9.5389	5.8795
13	FN	0.9920	0.5311	41.4756	20.8102
	FP	0.3063	0.1698	15.0598	7.6624
14	FN	0.3218	0.2761	11.7795	8.5293
	FP	0.1886	0.1509	7.7362	4.7067

Table 10. The responses of 10-story structure under near-field records without pulses

The critical excitation of near-field records without pulses is FN component (Chichi/Tcu084-271) of Tcu084 record of 1999 Chi-Chi earthquake for the 10-story structure. As seen from the top-story displacement plot given in Fig. 6, the optimum TMD is effective in reducing of the peak value by 20.07% (from 0.9920m to 0.5311m).

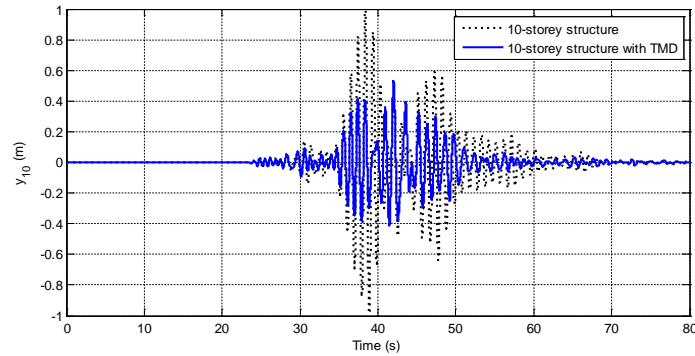


Fig. 6. Top story displacement of the 10-story structure (Chichi/Tcu084-271)

3.3.2 The results for 40-story structure

In the time domain, the maximum responses for 40-story structure are presented in Tables 11-13. In these tables, the maximum results are given for both cases of maximum mass ratio.

Earthquake	Component	y_{10}			$\ddot{y}_{10} + \ddot{y}_g$		
		Without TMD	Case 1	Case 2	Without TMD	Case 1	Case 2
1	FN	0.2922	0.2850	0.2769	4.8623	4.7520	4.8420
	FP	0.2727	0.2233	0.2648	4.9423	5.5232	4.8834
2	FN	0.3287	0.2948	0.3210	3.3403	5.0772	3.2797
	FP	0.3486	0.2793	0.3291	3.1108	4.7877	3.0670
3	FN	0.4901	0.3382	0.4052	3.6592	8.0792	3.5815
	FP	0.2931	0.2347	0.2985	6.2482	6.7095	6.1251
4	FN	0.2378	0.2209	0.2160	2.0845	2.7074	2.0568
	FP	0.3234	0.2984	0.3022	3.0633	3.8086	3.0129
5	FN	0.5701	0.3705	0.3490	1.8986	3.2737	1.7188
	FP	0.4188	0.3296	0.3689	2.8242	3.5652	2.6286
6	FN	0.4795	0.3464	0.4319	2.2561	4.4601	2.1070
	FP	0.3469	0.2961	0.3254	2.4169	4.6619	2.3542
7	FN	0.2543	0.2088	0.2305	2.5383	6.2970	2.5014
	FP	0.2403	0.2396	0.2122	2.2089	5.8867	2.1374
8	FN	0.3128	0.2279	0.2910	3.1928	3.4189	3.0974
	FP	0.1981	0.1469	0.1832	1.9873	2.9447	1.9651
9	FN	1.4433	0.7533	1.0769	4.8147	4.0122	3.9386
	FP	0.5285	0.3417	0.4180	3.9598	5.0122	3.9028
10	FN	0.1658	0.1390	0.1601	0.8272	1.6813	0.8409
	FP	0.4850	0.5374	0.4486	1.5452	1.6854	1.4830
11	FN	0.4879	0.5153	0.4809	3.4140	3.6909	3.4239
	FP	0.4117	0.3764	0.4138	2.1439	2.2846	2.2017
12	FN	0.2436	0.2131	0.2367	1.7939	2.8637	1.8231
	FP	0.2219	0.2454	0.2386	4.3720	5.0739	4.2680
13	FN	0.1943	0.1670	0.1957	3.9979	5.5859	3.9189
	FP	0.1924	0.1266	0.1527	2.6245	4.9397	2.6643
14	FN	0.2853	0.2253	0.2514	2.0954	6.0325	2.0191
	FP	0.4002	0.3758	0.3963	2.8984	5.4905	2.8606
15	FN	0.5659	0.3977	0.5061	3.4267	6.1291	3.2162
	FP	0.5621	0.4635	0.5536	2.6492	6.6539	2.6272
16	FN	0.7282	0.2935	0.3850	3.5269	3.6304	3.5055
	FP	0.4586	0.3432	0.3600	1.9760	3.2566	1.9468
17	FN	0.3750	0.2234	0.2624	2.8304	4.9268	2.7687
	FP	0.4061	0.3018	0.3248	2.3584	3.7651	1.8918
18	FN	0.2185	0.2147	0.2212	3.4061	4.3505	3.3848
	FP	0.2076	0.1580	0.1982	2.5629	4.9132	2.5141
19	FN	1.6377	1.0625	1.2877	5.0558	4.1746	4.1287
	FP	1.9278	1.6892	1.7826	6.1731	4.5408	5.3554
20	FN	0.2429	0.2974	0.2406	2.6781	5.0635	2.6104
	FP	0.2295	0.1410	0.1490	2.9085	5.0203	2.8554
21	FN	0.5883	0.3387	0.4751	2.4535	2.6689	2.3626
	FP	0.2370	0.1686	0.2077	0.9904	1.7330	0.8970
22	FN	0.1024	0.0867	0.0917	1.3802	3.5177	1.3512
	FP	0.1448	0.1085	0.1332	2.2727	3.6330	2.2450

Table 11. The responses of 40-story structure under far-field records

Earthquake	Component	y_{10}			$\ddot{y}_{10} + \ddot{y}_g$		
		Without TMD	Case 1	Case 2	Without TMD	Case 1	Case 2
1	FN	0.9555	0.8055	0.9165	4.3428	4.4556	4.1246
	FP	2.2888	1.5169	2.0299	6.8914	6.7629	6.0929
2	FN	0.6599	0.5527	0.5456	3.4359	4.2673	3.4530
	FP	1.7659	1.2614	1.4549	6.2306	8.8257	6.1116
3	FN	0.4391	0.2740	0.3896	2.4019	3.5059	2.3471
	FP	1.0167	0.8291	0.9613	3.7016	4.4648	3.5401
4	FN	1.1657	1.1077	1.1677	7.6609	8.9766	7.5722
	FP	0.8347	0.4181	0.5809	4.0297	4.4268	4.0058
5	FN	0.3623	0.3246	0.3532	3.0572	5.6333	2.9996
	FP	0.7790	0.6418	0.7443	3.0652	3.8672	2.8766
6	FN	0.8675	0.5804	0.7257	4.5306	6.0259	4.4733
	FP	0.7798	0.7134	0.7649	6.4902	7.1655	6.3749
7	FN	0.3352	0.2914	0.3121	4.1974	7.4609	4.1180
	FP	0.7505	0.6846	0.7344	6.4979	9.9769	6.3617
8	FN	1.9216	1.4268	1.6975	6.8344	10.9192	6.5257
	FP	0.5554	0.3752	0.4861	2.3450	7.8364	2.1513
9	FN	0.8639	0.6846	0.7921	11.6282	9.9869	11.5128
	FP	0.6187	0.5221	0.5758	5.1647	6.9083	5.0746
10	FN	0.6237	0.4558	0.5736	5.0746	6.9267	4.8771
	FP	0.9390	0.7677	0.8926	7.0513	9.1464	6.9089
11	FN	0.5183	0.3610	0.4722	2.3327	3.0393	2.2875
	FP	0.4472	0.2514	0.3094	1.4601	2.2604	1.4277
12	FN	3.1361	2.0005	2.3028	12.1423	7.6718	8.6289
	FP	1.1577	0.9672	1.0853	6.7557	7.9618	6.4150
13	FN	1.2386	1.2029	1.2214	6.1225	5.9385	5.1657
	FP	1.1097	1.1599	1.0408	4.1691	4.0931	3.1410
14	FN	1.4232	0.8479	0.8584	3.9849	3.9349	3.8082
	FP	1.2290	1.0120	1.1217	5.5273	5.6801	5.2564

Table 12. The responses of 40-story structure under near-field records with pulses

Earthquake	Component	y_{10}			$\ddot{y}_{10} + \ddot{y}_g$		
		Without TMD	Case 1	Case 2	Without TMD	Case 1	Case 2
1	FN	1.2436	0.7617	1.0809	5.9727	8.5253	5.3713
	FP	1.0734	0.7335	0.8328	5.0065	9.0017	4.6325
2	FN	0.3417	0.2807	0.3242	3.3732	8.3351	3.2609
	FP	0.2496	0.2587	0.2150	3.8054	8.9856	3.8781
3	FN	0.2163	0.2012	0.2310	2.1930	3.6929	2.1407
	FP	0.4396	0.2224	0.3066	2.6648	2.8891	2.6714
4	FN	0.4329	0.2336	0.3209	2.7785	9.7955	2.4568
	FP	0.5405	0.3151	0.3910	2.4301	10.4285	2.3156
5	FN	0.1445	0.1249	0.1400	1.5664	4.7302	1.5489
	FP	0.1456	0.1286	0.1420	2.1042	3.8375	2.0714
6	FN	0.3740	0.2523	0.3354	3.9188	5.8252	3.7466
	FP	0.1864	0.1655	0.1824	3.3813	5.6537	3.3437
7	FN	0.2390	0.1728	0.2222	3.4209	6.2938	3.3707
	FP	0.3442	0.2244	0.2941	4.6077	6.4762	4.5045
8	FN	1.0199	0.7391	0.8844	5.7668	14.3103	5.6493
	FP	0.3606	0.3127	0.3409	2.7603	10.7399	2.7214
9	FN	0.3659	0.2609	0.3373	7.4937	10.3620	7.4208
	FP	0.6782	0.4640	0.5951	4.8309	12.2230	4.4784
10	FN	0.3083	0.2383	0.2536	3.5648	3.7057	3.4094
	FP	0.6040	0.4731	0.5051	4.6685	7.1175	4.6441
11	FN	1.9469	1.2295	1.5422	6.8494	5.7939	5.3973
	FP	1.5798	1.0581	1.2584	6.5296	5.9817	5.7488
12	FN	0.7826	0.7768	0.7425	4.7846	5.7389	4.7023
	FP	1.1129	0.5987	0.6873	4.0426	5.3779	3.9305
13	FN	1.0034	0.8266	0.8666	10.7592	14.6794	11.3775
	FP	0.6722	0.4286	0.5607	4.0907	4.4096	4.0988
14	FN	1.2876	1.1295	1.2428	6.3268	5.7601	6.0415
	FP	1.1516	0.7893	0.9258	4.4826	3.7376	3.8755

Table 13. The responses of 40-story structure under near-field records without pulses

In far-field records, the FP component (Chichi/Chy101-N) of CHY101 record of 1999 Chi-Chi earthquake is the critical one for the 40-story structure and the optimum TMD is effective to reduce the maximum displacement of 40th story from 1.9278m to 1.6892m for Case 1 and 1.7826m for Case2. The response is plotted in Fig. 7 and the effectiveness of the optimum TMD on obtaining a rapid steady-state response is clearly seen and it is distinct in Case 1 which have a big optimum mass.

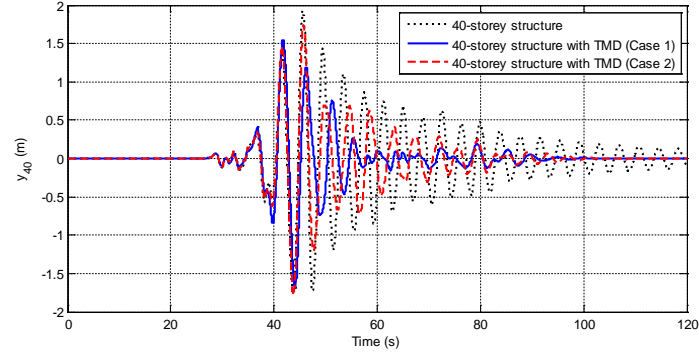


Fig. 7. Top story displacement of the 40-story structure (Chichi/Chy101-N)

The history plot given in Fig.8 is the displacement of the 40th story of the structure under the FN component (Chichi/Tcu065-272) of Tcu065 record of 1999 Chi-Chi earthquake and it is the critical one of the near-field records with pulses. The optimum TMD provides 36.21% reduction in Case 1 and 26.59% reduction in Case 2. The maximum top story displacement of 40-story structure is 1.9469m for near-field records without pulses. This value belongs to the analyses under the FN component (Kocaeli/Ypt-180) of Yarımca record of the 1999 Kocaeli earthquake and it is plotted in Fig. 9. The maximum displacement which is 1.9469m, is reduced to 1.2295m and 1.5422m for Cases 1 and 2, respectively.

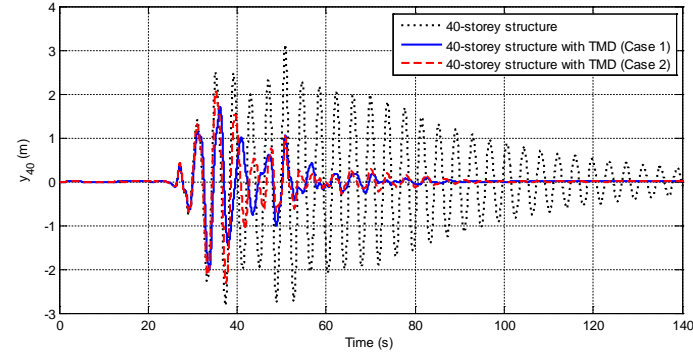


Fig. 8. Top story displacement of the 40-story structure (Chichi/Tcu065-272)

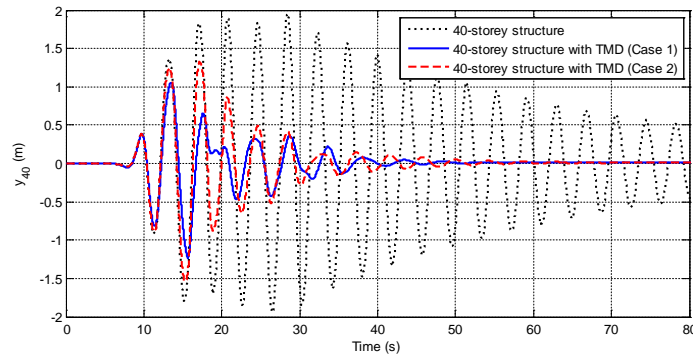


Fig. 9. Top story displacement of the 40-story structure (Kocaeli/Ypt-180)

4 DISCUSSION AND CONCLUSION

All algorithms are effective in finding the optimum TMD parameters minimizing the maximum amplitude of the top story acceleration transfer function. The main factor of the comparison of the algorithms are the required computational effort which is the best for FPA and the classical JA. The variant of JA presented in this study is not effective on finding reduction of required number of evaluations. On the contrary, the variants such as JALF and JA2P are worse than the classical JA. For the 40-story structure, JA is better than FPA in computational effort.

In the numerical examples, the optimum TMD is effective to reduce the objective function value by 56.76% for 10-story structure, while the optimum TMD has a minor effect on the peak value corresponding to the second

mode of the structure. Similarly, the optimum TMD is effective on the values of second and third mode for the 40-story structure, but the case with a small TMD mass upper limit (Case 2) has only minor effects. For Case 1 of 40-story structure, the reduction percentage of the objective function is 56.04%. In Case 2, which is a practical case because of a small mass, is also resulted with a significant reduction of objective function (35.05%).

The essential purposes of TMDs are to damp vibrations and reduce the maximum responses of the structure. For that reason, the validation of optimum TMD parameters is needed by using benchmark earthquake records. The benchmark earthquake records are chosen according to several grouped historical records presented in FEMA P-695. According to the results, the optimum TMD is effective on the benchmark earthquakes which are recorded far or near of the fault rupture. Especially, the performance of obtaining a steady-state response by damping of vibrations is significant for the critical excitations which have the maximum effects on the example structures.

The optimum TMD is both effective in the reduction of maximum top story displacements and total accelerations for both structures with 10 and 40 stories. The optimum TMD is effective to reduce the maximum top story displacement by 36.06% and 20.07% for the critical excitations for far-field and near field records, respectively. The reduction of maximum top story displacements of 40-story structure with TMD optimized with Case 1 are 12.38% and 35.82 for far-field and near field records, respectively. These percentages are respectively reduced to 7.53% and 20.79 in Case 2 for far-field and near field critical excitations.

As the final conclusion, the metaheuristic based methods are effective in optimizing TMDs and the newly developed JA is one of the best algorithms because of simplification of using a single phase without algorithm-specific parameters and randomly chosen parameters like Teaching Factor in TLBO. For the numerical examples, the problem of trapping to a local optimum is not seen for the single phase JA using linear random distribution. For that reason, the variants presented in the study (JALF and JA2P) is not necessary. These variants only extend the computational time for the optimization process.

REFERENCES

- [1]. Frahm H. Device for damping of bodies. U.S. Patent No: 989,958, 1911.
- [2]. Ormondroyd J, Den Hartog JP. The theory of dynamic vibration absorber. *T ASME* 50:922, 1928.
- [3]. Den Hartog, J.P. (1947), *Mechanical Vibrations*, McGraw-Hill, New York.
- [4]. Warburton, G.B. (1982), Optimum absorber parameters for various combinations of response and excitation parameters, *Earthquake Engineering and Structural Dynamics*, 10, 381-401.
- [5]. Sadek, F., Mohraz, B., Taylor, A.W. and Chung, R.M. (1997), A method of estimating the parameters of tuned mass dampers for seismic applications, *Earthquake Engineering and Structural Dynamics*, 26, 617-635.
- [6]. Hadi, M.N.S. and Arfiadi, Y. (1998), Optimum design of absorber for MDOF structures, *Journal of Structural Engineering-ASCE*, 124, 1272-1280.
- [7]. Leung, A.Y.T., Zhang, H., Cheng, C.C. and Lee, Y.Y. (2008), Particle swarm optimization of TMD by non-stationary base excitation during earthquake, *Earthquake Engineering and Structural Dynamics*, 37, 1223-1246.
- [8]. Leung, A.Y.T. and Zhang, H. (2009), Particle swarm optimization of tuned mass dampers, *Engineering Structures*, 31, 715-728.
- [9]. Bekdaş, G. and Nigdeli, S.M. (2017), Metaheuristic based optimization of tuned mass dampers under earthquake excitation by considering soil-structure interaction, *Soil Dynamics and Earthquake Engineering*, 92, 443-461.
- [10]. Nigdeli, S.M. and Bekdaş, G. (2017), Optimum tuned mass damper design in frequency domain for structures, *KSCE Journal of Civil Engineering*, 21(3), 912-922.
- [11]. Rao, R. (2016). Jaya: A simple and new optimization algorithm for solving constrained and unconstrained optimization problems. *International Journal of Industrial Engineering Computations*, 7(1), 19-34.
- [12]. Geem, Z.W., Kim, J.H. and Loganathan, G.V. (2001), A new heuristic optimization algorithm: harmony search, *Simul.*, 76, 6068.
- [13]. Rao, R. V., Savsani, V. J. and Vakharia, D. P. (2011). Teaching learning-based optimization: a novel method for constrained mechanical design optimization problems. *Computer-Aided Design*, 43(3), 303-315.
- [14]. Yang, X.-S. (2012), Flower pollination algorithm for global optimization. In *unconventional computation and natural computation*, 240-249.
- [15]. Singh, M.P., Matheu, E.E., Suarez, L.E. (1997), Active and semi-active control of structures under seismic excitation, *Earthq. Eng. Struct. D.*, 26, 193-213.
- [16]. Liu, M.Y., Chiang, W.L., Hwang, J.H., Chu, C.R. (2008), "Wind-induced vibration of high-rise building with tuned mass damper including soil-structure interaction", *J. Wind Eng. Ind. Aerodyn.*, 96, 1092-1102.
- [17]. FEMA P-695, Quantification of Building Seismic Performance Factors, Federal Emergency Management Agency, Washington DC, 2009.

NON-LINEAR HOMOGENIZATION THEORIES WITH APPLICATIONS TO TRIP STEELS

I. Papadioti¹, I. Bellas¹, M.-I.T. Tzini¹, P.I. Christodoulou¹ and N. Aravas^{1,2}

¹Department of Mechanical Engineering
University of Thessaly

Volos, GR-38334, Greece

e-mail: papadioti@uth.gr, iliabellias@gmail.com, margiannatz@gmail.com, pchristod@uth.gr,
aravas@uth.gr

²International Institute for Carbon Neutral Energy Research (WPI-I2CNER)

Kyushu University

Fukuoka 819-0395, Japan

Keywords: Homogenization; Elasto-plasticity; Composite materials; Finite strains; TRIP steels.

Abstract. A general constitutive model for N -phase isotropic, incompressible, rate-independent elasto-plastic composite materials at finite strains is developed. The formulation is based on the non-linear homogenization variational (or modified secant) method which makes use of a linear comparison composite (LCC) material to estimate the effective flow stress of the non-linear composite material. The homogenization approach leads to an algebraic optimization problem, which for a two-phase material ($N = 2$) is solved analytically, whereas for $N \geq 3$ the solution is obtained numerically. The model is validated by periodic three-dimensional unit cell calculations comprising a large number of spherical inclusions distributed randomly in a matrix phase. The homogenization technique provides accurate estimates not only for the effective flow stress but also for the average strains in the constituent phases. These estimates form the basis for the development of an approximate analytical model for the elastoplastic behavior of a composite with hardening phases. The predictions of the model are in excellent agreement with the results of detailed unit cell finite element calculations of a composite with hardening phases for different types of loadings, including uniaxial tension and finite shear. The homogenization theory is also used to develop a constitutive model for the mechanical behavior of **TRIP** (**TR**ansformation **I**nduced **P**lasticity) steels. TRIP steels are essentially composite materials with evolving volume fractions of the constituent phases. The calibration of the model is based on uniaxial tension tests on TRIP steels. The constitutive model is used for the calculation of “Forming Limit Diagrams” (FLDs) for sheets made of TRIP steels; it is found that the TRIP phenomenon increases the strain at which local necking results from a gradual localization of the strains at an initial thickness imperfection in the sheet.

1 INTRODUCTION

An analytical and numerical methodology for estimation of the effective response of N -phase isotropic elasto-plastic metallic composites is developed. Special attention is given to particulate microstructures, i.e., composite materials with a distinct matrix phase and an isotropic distribution of spherical particles. The particles are assumed to be stiffer than the matrix, which is the case in most metallic materials of interest, such as TRIP steels. Such materials, usually contain second-phase particles (e.g., intermetallics, carbon particles) or just second and third phase variants (e.g., retained austenite, bainite, martensitic phases). In addition, these phases/particles tend to reinforce the yield strength of the composite while they usually have different strength and hardening behavior than the host matrix phase.

In the literature of non-linear homogenization there exists a large number of studies for two-phase composite materials. Nonetheless, very few studies exist in the context of three- or N -phase composites. In view of this, the present work uses the non-linear variational homogenization method of Ponte Castañeda [1], which makes use of a linear comparison composite (LCC) material, to estimate the effective response of a N -phase non-linear composite material. Simple analytical expressions are given for the effective yield stress of a two-phase composite (see also Ponte Castañeda and deBotton [2]) while a simple semi-analytical expression (requiring the solution of a constrained optimization problem for $N-1$ scalar quantities) is given for the N -phase composite. Additional analytical expressions are also provided for the phase concentration tensors and average strains in each phase in terms of the aforementioned optimized scalar quantities.

2 THE HOMOGENIZATION METHOD

We consider a composite material made of N isotropic, incompressible viscoplastic phases. The phases are distributed randomly and isotropically. The constitutive equations of each phase is of the form:

$$\mathbf{D} = \frac{\partial U}{\partial \boldsymbol{\sigma}} = \dot{\boldsymbol{\varepsilon}} \mathbf{N}, \quad U(\sigma_e) = \frac{\sigma_0 \dot{\varepsilon}_0}{n+1} \left(\frac{\sigma_e}{\sigma_0} \right)^{n+1}, \quad \text{with} \quad \dot{\boldsymbol{\varepsilon}} = \dot{\varepsilon}_0 \left(\frac{\boldsymbol{\sigma}_e}{\sigma_0} \right), \quad \mathbf{N} = \frac{\partial \sigma_e}{\partial \boldsymbol{\sigma}} = \frac{3}{2\sigma_e} \mathbf{s}, \quad (1)$$

where \mathbf{D} is the deformation rate, $\boldsymbol{\sigma}$ the stress tensor, $p = \sigma_{kk}/3$ the hydrostatic stress, $\mathbf{s} = \boldsymbol{\sigma} - p\boldsymbol{\delta}$ the stress deviator, $\boldsymbol{\delta}$ being the second-order identity tensor, $\sigma_e = \sqrt{\frac{3}{2}\mathbf{s}:\mathbf{s}}$ the von Mises equivalent stress, σ_0 is a reference stress, $\dot{\varepsilon}_0$ a reference strain rate, n the creep exponent ($1 \leq n \leq \infty$), \mathbf{N} is a second order tensor that defines the direction of \mathbf{D} and $\dot{\boldsymbol{\varepsilon}} = \sqrt{\frac{2}{3}\mathbf{D}:\mathbf{D}}$ is the equivalent plastic strain rate that defines the magnitude of \mathbf{D} .

The constitutive equation of the isotropic non-linear composite is written in terms of the effective viscoplastic stress potential $\tilde{U}(\boldsymbol{\sigma})$ so that

$$\mathbf{D} = \frac{\partial \tilde{U}}{\partial \boldsymbol{\sigma}}, \quad (2)$$

where $\boldsymbol{\sigma}$ and \mathbf{D} are respectively the macroscopic stress and deformation rate in the composite. An estimate for \tilde{U} is obtained by using the variational methodology of Ponte Castañeda ([1], [3]):

$$\tilde{U}(\sigma_e) = \sup_{\mu^{(r)} \geq 0} \left\{ \frac{\sigma_e^2}{6\tilde{\mu}(\mu^{(r)})} - \sup_{\sigma_e^{(r)} \geq 0} \sum_{r=1}^N c^{(r)} \left[\frac{(\sigma_e^{(r)})^2}{6\mu^{(r)}} - U^{(r)} \left(\frac{\sigma_e^{(r)}}{\mu^{(r)}} \right) \right] \right\}, \quad (3)$$

where $\tilde{\mu}$ is the effective viscosity of the “linear comparison composite” (LCC). One way to estimate $\tilde{\mu}$ is to use the well-known Hashin-Shtrikman relationship for particulate composites [4].

An approximation for the deformation rate field in the non-linear composite may be obtained from the deformation rate field in the LCC evaluated at the optimal comparison moduli $\hat{\mu}^{(r)}$ defined by the optimization problem in (3). In particular, the average deformation rate field in the phases $\mathbf{D}^{(r)}$ may be determined from the macroscopic deformation rate \mathbf{D} in terms of a “strain concentration tensor” $\mathbf{A}^{(r)}$

$$\mathbf{D}^{(r)} = \mathbf{A}^{(r)} : \mathbf{D}, \quad (4)$$

where

$$\mathbf{D}^{(r)} = \mathbf{A}^{(r)} : \mathbf{D} = a^{(r)} \mathbf{D}, \quad a^{(r)} = \frac{1}{3\mu_0 + 2\hat{\mu}^{(r)}} \left(\sum_{s=1}^N \frac{c^{(s)}}{3\mu_0 + 2\hat{\mu}^{(s)}} \right)^{-1}, \quad (5)$$

$c^{(r)}$ are the volume fractions of the phases and μ_0 a reference viscosity. Details of the derivation are given in Papadioti *et al.* [5].

2.1 Perfectly Plastic Phases

We consider the case of perfectly plastic phases ($n^{(r)} \rightarrow \infty$). The optimization in (3) as ($n^{(r)} \rightarrow \infty$) is carried out in three steps. In the first step, we consider the optimization over $\sigma_e^{(r)}$. All creep exponents are set equal in the second step, i.e., we set $n^{(1)} = n^{(2)} = \dots = n^{(N)} \equiv n$. In the final third step we consider the limit $n^{(r)} \rightarrow \infty$. Details of the derivation are given in Papadioti *et al.* [5].

The resulting effective potential $\tilde{U}(\sigma_e)$ defines the effective flow stress $\tilde{\sigma}_0$ of the composite:

$$\tilde{\sigma}_0 = \sqrt{\inf_{\substack{y^{(1)}=1, y^{(r)} \geq 0 \\ r=2, \dots, N}} \frac{H_\infty(y^{(r)})}{F(y^{(r)})}}, \quad (6)$$

$$H_\infty(y^{(r)}) = \sum_{r=1}^N c^{(r)} (\sigma_0^{(r)})^2 y^{(r)}, \quad F(y^{(r)}) = \left(\sum_{r=1}^N \frac{c^{(r)} y^{(r)}}{3y^{(r)} + 2y_0} \right) \left(\sum_{s=1}^N \frac{c^{(s)}}{3y^{(s)} + 2y_0} \right)^{-1},$$

where $y^{(r)} = \mu^{(1)} / \mu^{(r)}$ and $y_0 = \mu^{(1)} / \mu_0$.

Calculation of the effective yield stress $\tilde{\sigma}_0$ requires the solution of the constrained optimization problem in (6) for the values of $y^{(r)}$, which define in turn the appropriate values of the viscosities $\mu^{(r)}$. In the special case of a two-phase composite ($N = 2$) the solution of the optimization problem can be found analytically as described in Section 2.2. The solution of more general cases ($N \geq 3$) is obtained by using the methodology of Kaufman *et al.* [6] and the CONMAX software for the solution of the optimization problem in (6).

The strain concentration values $a^{(r)}$ defined in (5) can be written in the form

$$a^{(r)} = \frac{\hat{y}^{(r)}}{3\hat{y}^{(r)} + 2y_0} \left(\sum_{s=1}^N \frac{c^{(s)} \hat{y}^{(s)}}{3\hat{y}^{(s)} + 2y_0} \right)^{-1}, \quad (7)$$

where $\hat{y}^{(r)}$ are the optimal values of $y^{(r)}$ resulting from the optimization in (6).

2.2 The two-phase perfectly plastic composite – An analytic estimate for the effective flow stress and the strain concentration factors

We consider an isotropic two-phase composite ($N = 2$, $c^{(1)} + c^{(2)} = 1$). Each phase is perfectly plastic with flow stress $\sigma_0^{(1)}$ and $\sigma_0^{(2)}$. The estimate for $\tilde{\sigma}_0$ depends on the chosen value of the reference viscosity μ_0 . Results for various choices of μ_0 are reported in Papadioti [7]. Here we present in some detail the formulation based on a Hashin-Strikman lower bound with $\mu_0 = \mu^{(1)}$ ($y_0 = 1$); this particular choice of μ_0 shows the best agreement with detailed unit cell finite element calculations.

For $\mu_0 = \mu^{(1)}$, the ratio H_∞ / F in (6) takes the value

$$\frac{H_\infty(y^{(2)})}{F(y^{(2)})} = (\sigma_0^{(1)})^2 (c^{(1)} + c^{(2)} r^2 y^{(2)}) \frac{2 + 3c^{(2)} + 3c^{(1)} y^{(2)}}{2c^{(1)} + (3 + 2c^{(2)}) y^{(2)}}, \quad r = \frac{\sigma_0^{(2)}}{\sigma_0^{(1)}} > 1. \quad (8)$$

The optimum value of $\hat{y}^{(2)}$ to be used in (6) is calculated by using the condition

$$\frac{\partial}{\partial y^{(2)}} \left(\frac{H_\infty}{F} \right) = 0 \quad (9)$$

together with the constraint $y^{(2)} \geq 0$. After some lengthy, but straightforward, calculations we find the resulting optimal value $\hat{y}^{(2)}$ to be

$$\hat{y}^{(2)} = \begin{cases} \frac{1}{3 + 2c^{(2)}} \left[-2c^{(1)} + \frac{5}{\sqrt{3}} \sqrt{\left(3 + 2c^{(2)}\right) \frac{1}{2} - 2c^{(2)}} \right] & \text{if } 1 \leq r \leq r_{\text{cr}} \quad (c^{(2)} \leq c_{\text{cr}}^{(2)}), \\ 0 & \text{if } r \geq r_{\text{cr}} \quad (c^{(2)} \geq c_{\text{cr}}^{(2)}), \end{cases} \quad (10)$$

where

$$r_{cr} = \frac{5}{\sqrt{4 + 6c^{(2)}}} \quad \text{and} \quad c_{cr}^{(2)} = \frac{1}{6} \left[\left(\frac{5}{r} \right)^2 - 4 \right]. \quad (11)$$

According to (10), for a given particle concentration $c^{(2)}$, when the contrast ratio $r = \sigma_0^{(2)} / \sigma_0^{(1)}$ is larger than a value r_{cr} , the comparison material for phase 2 is rigid ($\hat{y}^{(2)} = 0$).

The corresponding estimate for the effective flow stress resulting from (6) is

$$\frac{\tilde{\sigma}_0}{\sigma_0^{(1)}} = \begin{cases} \frac{1}{3 + 2c^{(2)}} \left[5c^{(2)}r + c^{(1)}\sqrt{9 + 6c^{(2)}(1 - r^2)} \right] & \text{if } 1 \leq r \leq r_{cr} \quad (c^{(2)} \leq c_{cr}^{(2)}), \\ \frac{1}{2}\sqrt{4 + 6c^{(2)}} & \text{if } r_{cr} \leq r \quad (c_{cr}^{(2)} \leq c^{(2)}). \end{cases} \quad (12)$$

The strain concentration values $a^{(r)}$ given in (7) can be written in the form

$$a^{(1)} = \frac{1}{(2y_0 + 3)\mathcal{D}}, \quad a^{(2)} = \frac{\hat{y}^{(2)}}{(2y_0 + 3\hat{y}^{(2)})\mathcal{D}}, \quad \mathcal{D} = \frac{c^{(1)}}{2y_0 + 3} + \frac{c^{(2)}\hat{y}^{(2)}}{2y_0 + 3\hat{y}^{(2)}} \quad (13)$$

and $\hat{y}^{(2)}$ is defined in (10).

3 UNIT CELL FINITE ELEMENT CALCULATIONS AND ASSESSMENT OF THE MODEL

In this section we present the results of unit cell finite element calculations for a composite material made up of a statistically isotropic random distribution of isotropic, linearly-elastic perfectly-plastic spherical inclusions embedded in a continuous, isotropic, linearly-elastic perfectly-plastic matrix. The elastic Young modulus used in the finite element calculations for all phases is three orders of magnitude higher than the highest yield stress involved; this minimizes the effects of elasticity and the results are very close to those of rigid-perfectly-plastic materials.

We study numerically two- and three-phase composites. The matrix is labelled as phase 1 and the reinforcing particles are spherical and have higher flow stresses ($\sigma_0^{(i)} > \sigma_0^{(1)}$, $i > 1$). The periodic unit cell is a cube with edge size L and is constructed using the method presented by Segurado and Llorca [8] and extended to polydisperse inclusion distributions by Lopez-Pamies *et al.* [9]. The virtual microstructure contains a dispersion of a sufficiently large number of non-overlapping spheres of uniform (monodisperse) or different (polydisperse) size. The inclusions are randomly located within the cell and are generated using the Random Sequential Adsorption Algorithm (RSA) [10].

3.1 The effective yield stress

We determine numerically the effective yield stress by solving the problem of a unit cell loaded in uniaxial tension. Figure 1a shows the variation of the calculated effective flow stress from the unit cell finite element calculations with the contrast ratio $r = \sigma_0^{(2)} / \sigma_0^{(1)}$ for various volume fractions, together with the predictions (6) of the homogenization model, based on the Hashin-Shtrikman lower bound ($\mu_0 = \mu^{(1)}$). For that data shown in Fig. 1a, the maximum difference between the predictions (6) and the results of the unit cell finite element calculations is 3%. It is also interesting to mention that an increase of the flow stress $\sigma_0^{(2)}$ in the inclusions beyond (approximately) two times the flow stress of the matrix ($2\sigma_0^{(1)}$) does not change the effective flow stress of the composite for all volume fractions considered here. Figure 1b shows the variation of $\tilde{\sigma}_0 / \sigma_0^{(1)}$ of a three-phase composite for different values of the volume fraction $c^{(3)}$ as determined from the unit cell finite element calculations and the predictions (6) of the homogenization model. The material data are typical for a TRIP steel with a ferritic matrix (phase 1) containing retained austenite (phase 2), which transforms gradually to martensite

(phase 3) as the TRIP steel deforms plastically.

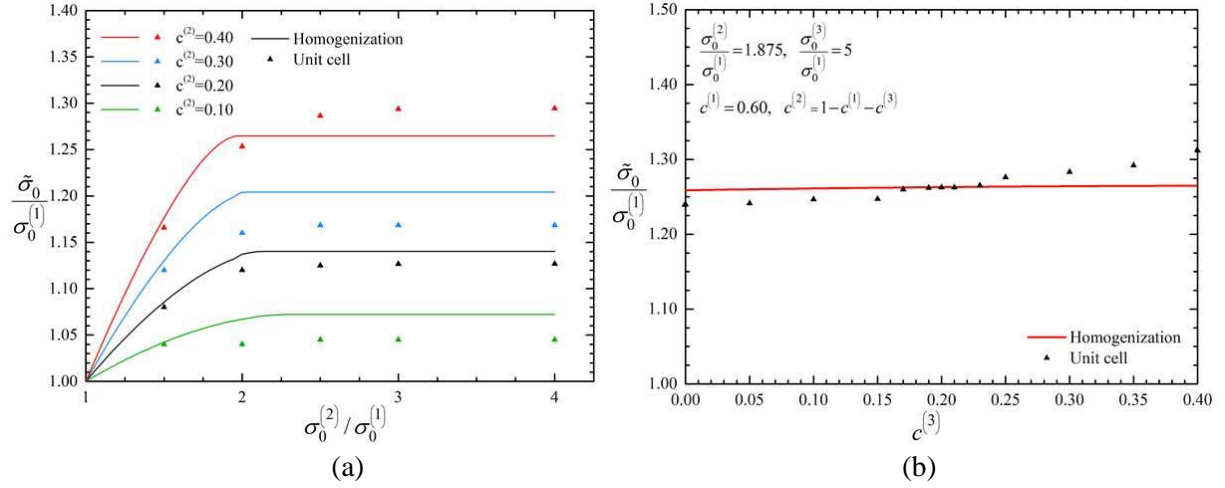


Figure 1. Variation of normalized effective flow stress $\tilde{\sigma}_0 / \sigma_0^{(1)}$ (a) of a two-phase composite for various volume fractions (b) of a three-phase composite for different values of the volume fraction $c^{(3)}$.

3.2 The strain concentration tensors

The unit cell finite element calculations discussed above were used also to determine the strain concentration factors defined in (7). Figure 2a shows the variation of the strain concentration factors $a^{(r)}$ in a two-phase composite with the contrast ratio $r = \sigma_0^{(2)} / \sigma_0^{(1)}$ for $c^{(2)} = 0.30$ as determined from the unit cell finite element calculations and the homogenization theory. An important observation in the context of this figure is that at a contrast ratio of $r \approx 2$, a sharp transition is observed where the particles start behaving as being rigid, i.e., the average strain in the particle is almost zero. This is validated by both the model and the numerical results. A similar plot for a three-phase composite is shown in Fig. 2b. The predictions of homogenization theory agree well with the results of the unit cell finite element calculations.

3.3 On the possible dependence of the effective flow stress on J_3

Suquet and Ponte Castañeda [11],[12] studied the effective mechanical behavior of weakly inhomogeneous composites and showed that, for the case of incompressible “power-law” phases, the effective potential of the composite may depend, to second order, on the third invariant of the applied strain.

We carry out detailed unit cell finite element calculations in order to check for a possible dependence of the effective yield stress $\tilde{\sigma}_0$ on the third invariant J_3 of the stress deviator \mathbf{s} ($J_3 = \det \mathbf{s} = -(2/27)\sigma_e^3 \sin 3\theta$, where θ is the “Lode angle”). Angle θ takes values in the range $-30^\circ \leq \theta \leq 30^\circ$, where, to within a given hydrostatic stress, $\theta = -30^\circ$ corresponds to uniaxial tension, $\theta = 0^\circ$ to pure shear, and $\theta = 30^\circ$ to uniaxial compression.

Figure 3 illustrates the variation of the normalized effective flow stress $\tilde{\sigma}_0 / \sigma_0^{(1)}$ as determined from unit cell finite element calculations, with Lode angle θ for particle volume fractions $c^{(2)} = 0.10, 0.20$ and 0.40 . It is shown that the effective flow stress of the composite is essentially independent of the third stress invariant J_3 which is in agreement with earlier results by Idiart [13] in the case of rigid particles.

4 HARDENING PHASES

In this section we present an approximate method for the prediction of the incremental elastoplastic behavior of macroscopically isotropic composites made of N isotropic, rate-independent, elastic-plastic hardening phases. Let the flow stresses $\sigma_y^{(i)}$ of each phase be known functions of the corresponding equivalent plastic strains $\bar{\epsilon}^{(i)}$ ($i = 1, 2, \dots, N$).

It should be noted that the elastic and plastic response of the homogenized composite are treated independently, and combined later to obtain the full elastic-plastic response. The composite is assumed to behave as “incrementally perfectly plastic” with a flow stress $\tilde{\sigma}_0$, which is updated at every increment. The value of $\tilde{\sigma}_0$

is calculated by the solution of the corresponding optimization problem (6) using the $\sigma_0^{(i)}$ values at each increment. The solution of the optimization problem (6) defines also the optimal values $\hat{y}^{(i)}$, which determine the corresponding strain concentration factors $a^{(i)}$ in (7) for the increment. Details on the numerical integration of constitutive equations are given in Papadioti [7].

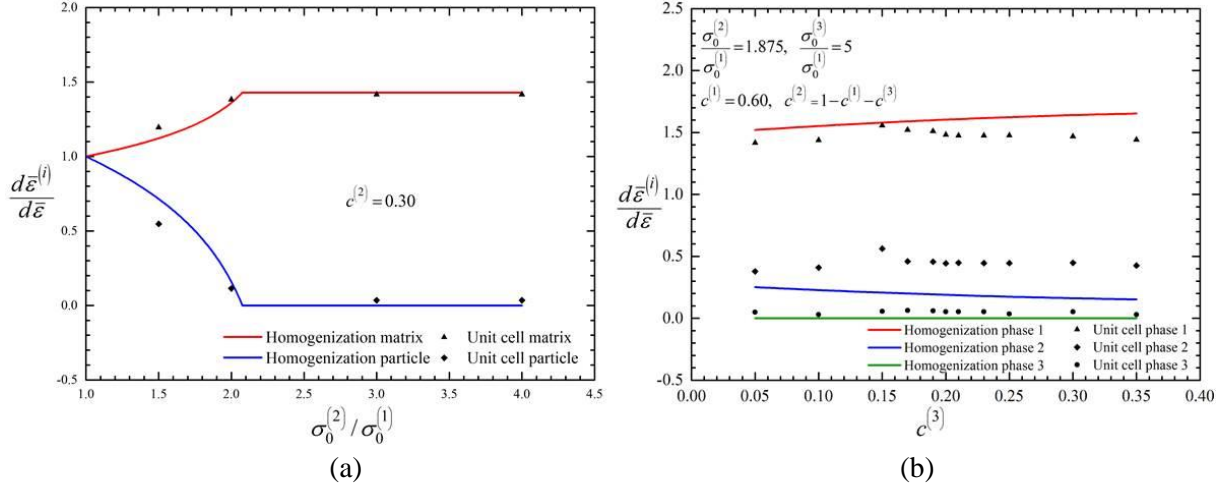


Figure 2. Strain concentration factors $a^{(r)}$ (a) for a two-phase composite and (b) for a three-phase composite.

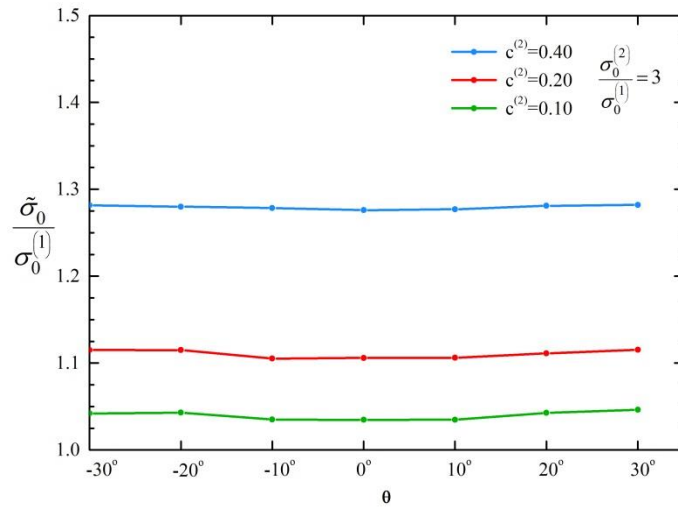


Figure 3. Variation of effective normalized flow stress $\tilde{\sigma}_0 / \sigma_0^{(1)}$ with Lode angle θ for particle volume fractions of 10, 20 and 40%. The results show almost no dependence on J_3 .

4.1 Unit cell calculations and assessment of the model with hardening phases

In this section we present the results of unit cell finite element calculations for a composite material made up of a statistically isotropic random distribution of isotropic, linearly-elastic hardening-plastic spherical inclusions embedded in a continuous, isotropic, linearly-elastic hardening-plastic matrix. All analyses were carried out incrementally and accounted for geometry changes due to deformation (finite strain solutions).

In all cases analyzed, the matrix material is identified as “phase 1” and the flow stress $\sigma_y^{(i)}$ of “phase i ” is a function of the corresponding equivalent plastic strain $\bar{\epsilon}^{(i)}$:

$$\sigma_y^{(i)}(\bar{\epsilon}^{(i)}) = \sigma_0^{(i)} \left(1 + \frac{\bar{\epsilon}^{(i)}}{\epsilon_0} \right)^{\frac{1}{\eta^{(i)}}}, \quad \epsilon_0 = 0.005, \quad (14)$$

where $\sigma_0^{(i)}$ is the yield stress of phase i , E is the elastic Young's modulus, and the hardening exponents $\eta^{(i)}$ take values in the region $1 \leq \eta^{(i)} \leq \infty$, with the limiting case $\eta^{(i)} = \infty$ corresponding to perfect plasticity. The values $E = 917\sigma_0^{(1)}$ and $\nu = 0.3$ for Young's modulus E and Poisson ratio ν are used in the calculations.

In addition, one-element finite element calculations were carried out, in which the element is subjected to the same deformation gradient as the unit cell and the corresponding uniform stress state in the element is calculated for the homogenized material. In particular, we consider a three-phase composite with

$$\frac{\sigma_0^{(2)}}{\sigma_0^{(1)}} = 1.875, \quad \frac{\sigma_0^{(3)}}{\sigma_0^{(1)}} = 5, \quad \eta^{(1)} = 5, \quad \eta^{(2)} = 3, \quad \eta^{(3)} = 2.5. \quad (15)$$

The problems of uniaxial tension and finite shear deformation are solved. Figure 4 shows the deformed unit cells for uniaxial tension at $\lambda = 1.20$ and finite shear $\gamma = 0.20$ and Figure 5 shows the stress-strain curves in uniaxial tension and finite shear, for a three-phase composite with composition $c^{(1)} = 0.60$, $c^{(2)} = 0.25$, and $c^{(3)} = 0.15$. The predictions of the homogenization model agree well with the results of the unit cell finite element calculations. The model is capable of predicting sufficiently well both the initial yield strength of the three-phase composite as well the hardening evolution as a function of the applied strains both in uniaxial tension and shear loading.

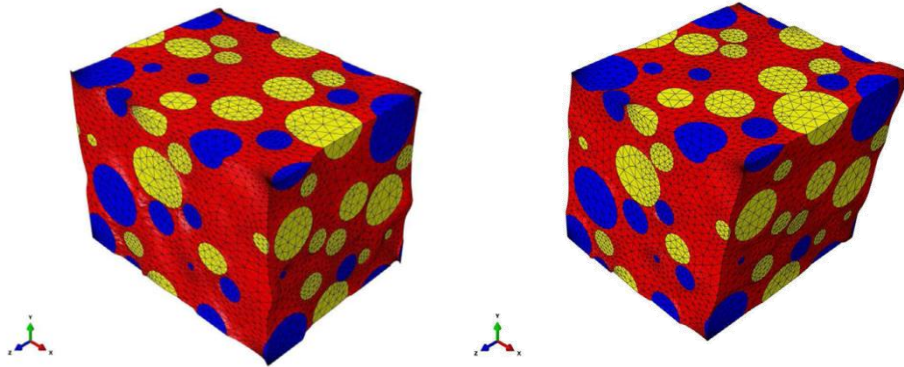


Figure 4. Deformed configurations of unit cells of the three-phase composite in uniaxial tension and simple shear.

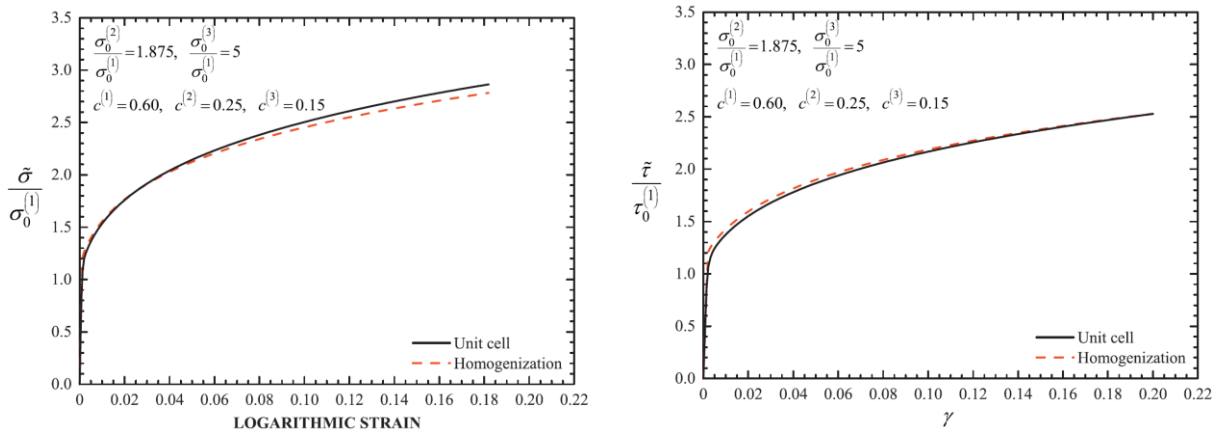


Figure 5 Stress-strain curves of the three-phase composite in uniaxial tension and simple shear.

5 APPLICATIONS TO TRIP STEELS

The homogenization techniques for non-linear composites, described in the previous sections, are used to

determine the effective properties and overall behavior of TRIP steels. We consider four-phase TRIP steels that consist of a ferritic matrix with dispersed bainite and austenite, which transforms gradually into martensite as the material deforms plastically. The following labels are used for the constituent phases: (1) for ferrite, (2) for bainite, (3) or (a) for austenite and (4) or (m) for martensite. The constitutive equations are developed for the case of finite geometry changes.

An important aspect of the martensitic transformation is the strain softening which occurs due to the strain associated with the transformation process. This strain softening is accounted for by introducing in the constitutive model an additional deformation rate that is proportional to the rate of increase of the volume fraction of martensite. The total deformation rate can be split into elastic, plastic and transformation parts:

$$\mathbf{D} = \mathbf{D}^e + \mathbf{D}^p + \mathbf{D}^{TRIP}. \quad (16)$$

Details on the constitutive formulation and the numerical integration of the resulting elastoplastic constitutive equations are given in Papadioti [7]. The model is then implemented into the ABAQUS. The calibration of the model is based on experimental data of uniaxial tension tests on TRIP. The constitutive model is also used to calculate “forming limit diagrams” for sheets made of TRIP steels. Calculations are also conducted for a non-transforming steel for comparison purposes.

5.1 Forming Limit Diagrams

In this section, the constitutive model developed for the four-phase TRIP steel is used to calculate “forming limit diagrams” for sheets made of TRIP steels. Forming limit diagrams show the maximum deformation to which a sheet metal can be subjected before the material fails. In the present work, we concentrate on the formation of instabilities in a narrow straight band in metal sheets deformed under plane stress conditions. The predictions of the analytical model are compared to experimental data from the same TRIP steel which was used for the calibration. For comparison purposes, a separate set of calculations is conducted for a non-transforming TRIP steel with same initial values of the volume fractions of the phases.

We consider a sheet made of TRIP steel that is deformed uniformly on its plane in a way that the in-plane principal strain increments increase proportionally. We study the possibility of the formation of an instability in the form of a narrow straight band and construct the corresponding “forming limit diagram”.

We follow the approach of Marciniak and Kuzynski [14], known as the “M-K” model, in which the sheet is assumed to contain a small initial inhomogeneity and necking results from a gradual localization of the strains at the inhomogeneity. The inhomogeneity is in the form of straight narrow band (neck) of reduced thickness $H^b < H$. Both inside and outside the band a state of uniform plane stress is assumed, and the analysis consists in determining the uniform state of deformation inside the band that is consistent kinematically and statically with the prescribed uniform state outside the band. Given the initial sheet thickness inside and outside the band and the imposed uniform deformation history outside the band, the equations of equilibrium are solved incrementally to obtain the deformation history inside the band. Localization is said to occur when the ratio of some scalar measure of the amount of incremental straining inside the band to the corresponding value outside the band becomes unbounded.

The initial volume fractions of the four phases in the TRIP steel are assumed to be $c^{(1)} = 0.50$, $c^{(2)} = 0.38$, $c^{(a)} = 0.103$ and $c^{(m)} = 0.017$. The curves $\sigma_y^{(r)}$, $r = 1, 4$ that define the variation of the flow stress of the phases are (in MPa):

$$\begin{aligned} \sigma_y^{(1)} &= 260 \left(1 + \frac{\bar{\varepsilon}}{0.0042} \right)^{\frac{1}{4.25}}, & \sigma_y^{(a)} &= 550 \left(1 + \frac{\bar{\varepsilon}}{0.1} \right)^{\frac{1}{4.2}}, \\ \sigma_y^{(2)} &= 825 \left(1 + \frac{\bar{\varepsilon}}{0.0104} \right)^{\frac{1}{10.36}}, & \sigma_y^{(m)} &= 1132 \left(1 + \frac{\bar{\varepsilon}}{0.0004} \right)^{\frac{1}{16.65}}. \end{aligned} \quad (17)$$

Figure 6 illustrates forming limit curves obtained for imposed proportional straining ρ for two different values of the initial thickness imperfection, namely $H^b/H = 0.999$ and $H^b/H = 0.99$ and for the case without imperfection i.e. $H^b/H = 1$. The three solid curves correspond to the TRIP steel, whereas the dashed curves are for the non-transforming steel. As we can see, the TRIP effect increases the necking localization strains. This result was also presented by Papatriantafillou *et al.* [15], who used a rate dependent constitutive model for TRIP steels (as opposed to the rate independent model used here). In details, for no imperfection and $\rho = 0$ (plane

strain), the critical strain ε_{11}^{cr} increases from 0.19228 for the non-transforming steel to 0.21203 for the TRIP steel; the corresponding values of ε_{11}^{cr} for $H^b/H = 0.999$ and $\rho = 0$ are 0.17369 for the non-transforming steel and 0.19395 for the TRIP steel and for $H^b/H = 0.99$ and $\rho = 0$ are 0.13775 for the non-transforming steel and 0.15869 for the TRIP steel.

The model predictions are also compared to available experimental data. The experimental data refer to the same TRIP steel which was used for the calibration of the model. Details on the experiments are given in Papatriantafillou et al. [15]. The model predictions fit the experimental data reasonably well.

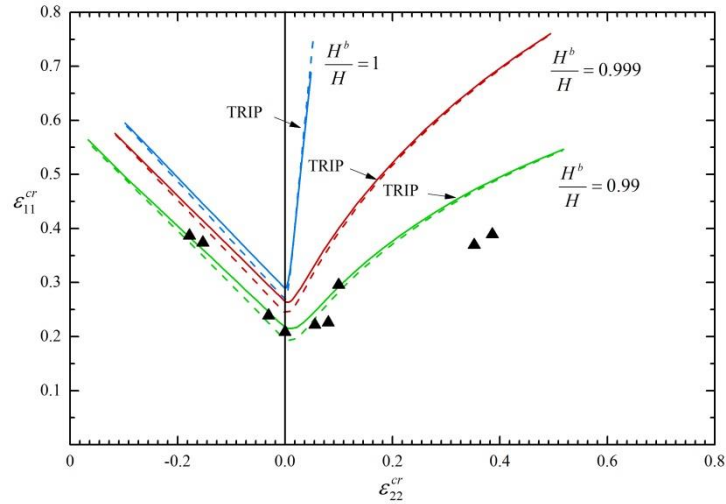


Figure 6 Forming limit curves for two different values of initial thickness inhomogeneities $H^b/H = 0.999$ and $H^b/H = 0.99$. The solid lines correspond to the TRIP steel, whereas the dashed lines are for a non-transforming steel. The dark triangles are experimental data.

6 ACKNOWLEDGEMENTS

This work was carried out in the framework of “TRIP steels: Simulation and experimental study of heat treatment and mechanical behavior” project. This research is implemented through the Operational Program "Human Resources Development, Education and Lifelong Learning" and is co-financed by the European Union (European Social Fund) and Greek national funds. The authors would like also to acknowledge the help of late Prof. A. Stamatis of University of Thessaly on the solution of the optimization problem. Use of the FORTRAN code CONMAX (<http://www.netlib.org/opt/conmax.f>) is gratefully acknowledged.

REFERENCES

- [1] Ponte Castañeda P. (1991), “The effective mechanical properties of non-linear isotropic composites”, *J. Mech. Phys. Solids* Vol. 39, pp. 45-71.
- [2] Ponte Castañeda P. and deBotton G. (1992), “On the homogenized yield strength of two-phase composites”, *Proc. R. Soc. Lond. A* Vol. 438, pp. 419-431.
- [3] Ponte Castañeda P. (1992), “New variational principles in plasticity and their application to composite materials”, *J. Mech. Phys. Solids* Vol. 40, pp. 1757-1788.
- [4] Willis J.R. (1982), “Elasticity theory of composites” In: Hopkins H.G., Sewell M.J. (Eds.), *Mechanics of Solids, The Rodney Hill 60th Anniversary Volume*. Pergamon Press, pp. 653-686.
- [5] Papadioti I., Danas K. and N. Aravas N. (2016), “A methodology for the estimation of the effective yield function of isotropic composites”, *Int. J. Solids Struct.* Vol. 87, pp. 120-138.
- [6] Kaufman E.H., Jr., Leeming D.J. and Taylor G.D. (1995), “An ODE-based approach to non-linearly constrained minimax problems”, *Numerical Algorithms* Vol. 9, pp. 25-37.
- [7] Papadioti I. (2016), “Non-linear Homogenization Theories with Applications to TRIP Steels. Ph.D. Thesis. University of Thessaly, Greece.
- [8] Segurado J. and Llorca J. (2002), “A numerical approximation to the elastic properties of sphere-reinforced composites”, *J. Mech. Phys. Solids*, Vol. 50, pp. 2107-2121.
- [9] Lopez-Pamies O., Goudarzi T. and Danas K. (2013), “The non-linear elastic response of suspensions of rigid inclusions in rubber. II. A simple explicit approximation for finite-concentration suspensions”, *J. Mech. Phys. Solids* Vol. 61, 19-37.
- [10] Rintoul M.D. and Torquato S. (1997), “Reconstruction of the structure of dispersions”, *J. Colloid Inter. Sci.* Vol. 186, pp. 467-476.
- [11] Suquet P. and Castañeda P. (1993), “Small-contrast perturbation expansions for the effective properties of non-linear composites”, *C. R. Acad. Sci. Paris (Série II)* Vol. 317, pp. 1515-1522.
- [12] Ponte Castañeda P. and Suquet P. (1995), “On the effective mechanical behavior of weakly inhomogeneous non-linear materials”, *Eur. J. Mech. A/Solids* Vol. 14, pp. 205-236.
- [13] Idiart M. (2008), “Modeling the macroscopic behavior of two-phase non-linear composites by in finite rank laminates”, *J. Mech. Phys. Solids* Vol. 56, pp. 2599-2617.
- [14] Marciniak Z. and Kuczynski K. (1967), “Limit strains in the process of stretch forming sheet metal”, *Int. J. Mech. Sciences* Vol. 9, pp. 609–620.
- [15] Papatriantafillou I., Agoras M., Aravas N. and Haidemenopoulos G. (2006), “Constitutive modeling and finite element methods for TRIP steels”, *Comp. Methods Appl. Mech. Eng.* Vol. 195, pp. 5094–5114.

PRELIMINARY COMPUTATIONAL STUDY OF PLASMA DYNAMIC EVOLUTION PRODUCED BY LOW CURRENT TABLE-TOP PINCH PLASMA DEVICES

Alekos Skoulakis^{1,2}, Giorgos Koundourakis^{1,3}, Evaggelos Kaselouris^{1,2}, Ioannis Ftilis^{1,2}, Efthimios Bakarezos^{1,4}, E.L. Clark^{1,2}, Nektarios Vlahakis^{1,3}, Nektarios A. Papadogiannis^{1,4}, Vasilis Dimitriou^{1,5}
and Michael Tatarakis^{1,2}

¹Centre for Plasma Physics and Lasers
School of Applied Sciences, TEI of Crete
Chania, GR-73133, Rethymnon, GR-74100, Greece
web page: <http://www.cppl.teicrete.gr>

²Department of Electronic Engineering
Chania, GR-73133, Greece

e-mails: skoulakis@chania.teicrete.gr, vkas@chania.teicrete.gr, ftilis@staff.teicrete.gr,
e.clark@chania.teicrete.gr, m.tatarakis@chania.teicrete.gr

³Department of Astrophysics, Astronomy and Mechanics, Faculty of Physics, Kapodistrian University of Athens,
15784 Zografos, Athens, Greece

e-mails: g.koundourakis@chania.teicrete.gr, vlahakis@phys.uoa.gr

⁴Department of Music Technology & Acoustics Engineering
Rethymnon, GR-74133, Greece

e-mails: bakarezos@staff.teicrete.gr, npapadogiannis@staff.teicrete.gr

⁵Department of Natural Resources and Environmental Engineering
Chania, GR-73133, Greece

e-mails: dimvasi@chania.teicrete.gr

Keywords: Magneto Hydro Dynamics - MHD, Plasma physics, Plasma pinch devices, Radiation transport.

Abstract. Pulsed power generators like Z- and X- Pinch devices produce hot and dense plasma. This type of plasma attracts the research interest due to the important emerging applications covering a wide range of disciplines like high energy density physics–HEDP, inertial confinement fusion, laboratory astrophysics and point projection radiography. In order to study such a multiphysics problem, the development of advanced computational models and simulation schemes is required, to offer insights to the experimental results. In our preliminary computational study, the astrophysical magnetohydrodynamics-MHD code PLUTO is partially modified to simulate the dynamics of plasma evolution. New algorithms for the PLUTO modules that extend the code applicability to laboratory plasmas are developed and tested, summarized to the: i. modified PVTE Equation of state-EOS using tabulated data by SESAME Database ii. electric resistivity according to the Spitzer formulation iii. radiative losses from an optically thin plasma using FLYCHK code tabulated data iv. modified radiation transfer model updated to include metal materials v. determination of plasma density, where effective ionization charge state, tabulated values by the FLYCHK code. These PLUTO modifications provide the ability of studying the formation of minidiodes, constrictions and also micro explosions of the hot points, on Z- type loads.

1 INTRODUCTION

Pulsed power plasma generators, Z-pinch, X-pinch or multi-wire configurations, offer a unique plasma environment for the investigation of plasma characteristics and specifically the plasma instabilities generation, plasma jet formation and their dynamic behavior. This is a research topic of continuous interest due to the important emerging applications which cover a wide range of disciplines. Pulsed power generators deliver a few tens of kA on the Z- or X- wire loads within some nanoseconds and produce hot and dense plasma, offering research capabilities for point projection X-ray radiography, high energy density plasma dynamics and astrophysical plasma jets. One of the major limitations of the pulsed powered produced plasmas, is the development of instabilities, such as the well investigated over the years Magneto-Hydro-Dynamic (MHD) and Rayleigh–Taylor (RT) instabilities. The initialization of the instabilities and their growth rate are of significant research interest, especially when are correlated to the initial physical parameters of the target load [1-3], the

phase changes of the target from solid to melting, vaporization and finally plasma, or the so called “cold start” in the simulations.

The study of plasma generation and evolution is a complex multiphysics problem. That kind of problems demand the development of advanced computational models and simulation schemes to provide insights to the experiments. In this computational study, the originally astrophysical MHD code PLUTO [4,5], is partially modified to simulate the dynamics of laboratory plasmas. The open source code of PLUTO is modular built using C and C++ offering a flexible programming environment. In this environment: i. the PVTE (Pressure-Volume-Temperature-Energy) Equations of state – EOS are modified using tabulated data by SESAME Database [6] ii. the electrical resistivity has been updated according to the formulation of Spitzer (1962) iii. the radiative losses are taken into account from an optically thin plasma using tabulated data by the help of the FLYCHK code [7] iv. the modified radiation transfer model is updated to include metal materials v. plasma density is determined using the effective ionization charge state, by the help of tabulated values that FLYCHK code provides. These five new approaches are adopted to simulate the material models of the problem: the Z-load wire of tungsten and the surrounding low mass density region of air (vacuum). The modeling of the interface region is based on four approximations and two different PLUTO solvers are used for the simulation resulting to eight simulation cases. The simulations are repeated with the Temperature of vacuum constrained. The comparisons of the simulations to experimental results provide insights for the influence of the developed physical quantities such as density, magnetic field and energy.

2 PLUTO MHD CODE – ALGORITHMIC MODIFICATIONS

PLUTO a finite volume/finite difference, shock-capturing code designed to integrate a system of conservation laws of the form:

$$\frac{\partial \mathbf{U}}{\partial t} = -\nabla \cdot \mathbf{T}(\mathbf{U}) + \mathbf{S}(\mathbf{U}) \quad (1)$$

where \mathbf{U} represents a set of conservative quantities, $\mathbf{T}(\mathbf{U})$ is the flux tensor and $\mathbf{S}(\mathbf{U})$ defines the source terms. An equivalent set of primitive variables \mathbf{V} is more conveniently used for assigning initial and boundary conditions.

The sets of conservative and primitive variables \mathbf{U} and \mathbf{V} are given by

$$\mathbf{U} = (\rho, \mathbf{m}, E, \mathbf{B})^T, \quad \mathbf{V} = (\rho, \mathbf{u}, p, \mathbf{B})^T \quad (2)$$

where, ρ is the material density, \mathbf{m} is the momentum density, with $\mathbf{m} = \rho \mathbf{u}$, E is the total energy density, \mathbf{B} is the magnetic field and a factor of $1/\sqrt{4\pi}$ has been absorbed, p is the thermal pressure and \mathbf{u} the bulk velocity. Resistivity, thermal conductivity, viscosity and other dissipative effects can be enabled through the appropriate switches. The MHD module deals with the Equations of classical ideal or resistive MHD. The resistive MHD module is used and is modified to follow the transport of radiation as presented in the following Equations:

$$\frac{\partial \rho}{\partial t} + \nabla \cdot (\rho \mathbf{u}) = 0 \quad (3)$$

$$\frac{\partial (\mathbf{m})}{\partial t} + \nabla \cdot \left[\mathbf{m} \mathbf{u} + \left(p + \frac{1}{2} B^2 \right) \mathbf{I} - \mathbf{B} \mathbf{B} \right] = \rho \mathbf{a}_{rad} \quad (4)$$

$$\frac{\partial E}{\partial t} + \nabla \cdot \left[\left(E + p + \frac{1}{2} B^2 \right) \mathbf{u} + (\mathbf{u} \cdot \mathbf{B}) \mathbf{B} \right] = -\nabla \cdot [(\mathbf{n} \cdot \mathbf{J}) \times \mathbf{B}] + \rho \mathbf{u} \cdot \mathbf{a}_{rad} \quad (5)$$

$$\frac{\partial \mathbf{B}}{\partial t} + \nabla \cdot (\mathbf{u} \mathbf{B} - \mathbf{B} \mathbf{u}) = -\nabla \times (\mathbf{n} \cdot \mathbf{J}) \quad (6)$$

where \mathbf{a}_{rad} the acceleration from the radiation pressure that is defined in Equation 11 by the help of radiative flux \mathbf{F} . The system of the Equations 3-6 is defined by the set of Equations given in Equation 7:

$$\begin{aligned} E &= \frac{1}{2} \rho u^2 + \rho e + \frac{1}{2} B^2 \\ \mathbf{J} &\equiv \nabla \times \mathbf{B} \\ n &= \left(\frac{c}{4\pi} \right)^2 n_r, \quad n \equiv \text{diag}(n_{x1}, n_{x2}, n_{x3}) \end{aligned} \quad (7)$$

where E is the total energy density, e is the specific internal energy, \mathbf{J} the current density, n is the diffusivity having a diagonal form and being expressed as a function of the resistive tensor n_r (subscripts denote the three coordinate directions).

Spitzer's conductivity formula:

$$\sigma = \frac{8.7 \times 10^{13} \text{Te}^{1.5}}{Z_{\text{eff}} \ln \Lambda} \quad (8)$$

is used for the determination of n_r and T_e (eV) is the electron temperature and Z_{eff} is the effective ionization charge state and $\ln \Lambda$ is the Coulomb's logarithm.

The evolution of the radiation energy density E_{rad} is given by the following Equation [8]:

$$\frac{\partial E_{\text{rad}}}{\partial t} + \nabla \cdot \mathbf{F} = k_P \rho c (a_R T^4 - E_{\text{rad}}) \quad (9)$$

where E_{rad} is the radiation energy density, k_P is the Planck mean opacity, a_R is the radiation constant and T the gas temperature. The radiative flux is denoted by \mathbf{F} and is a function of λ , the flux limiter and k_R , the Rosseland mean opacity. The flux limiter used is based on the work of Kley [8]. Equation 9 is solved with the corresponding heating-cooling term in the internal energy of the fluid, given by Equation 10:

$$\frac{\partial \rho e}{\partial t} = -k_P \rho c (a_R T^4 - E_{\text{rad}}) \quad (10)$$

The determination of \mathbf{F} may let as define \mathbf{a}_{rad} as:

$$\mathbf{a}_{\text{rad}} = \frac{k_R}{c} \mathbf{F} \quad (11)$$

The above system of Equations is closed by the PVTE EOS that is calculated via curvilinear mapping of the thermal pressure table data $p = p(\rho, T)$ and of the internal energy density table data $\rho e = \rho e(\rho, T)$. These logarithmic curves are tabulated data of the SESAME EOS [6]. These data have a range of 10^{-4} to 10^4 gr/cm³ approximately for the density and for lower density values an extrapolation algorithm is used.

Time-dependent optically thin radiative losses are taken into account by:

$$\frac{\partial(\rho e)}{\partial t} = -\Lambda(\rho, T) N_e N_i \quad (12)$$

where $\Lambda(T, \rho)$ is the radiative cooling coefficient that is calculated by tabulated data from the FLYCHK code, with $N_i = \rho m_i^{-1}$ the ion density, m_i the ion mass and for the determination of the electron plasma density it holds that:

$$N_e = Z_{\text{eff}}(\rho, T) N_i \quad (13)$$

where Z_{eff} is the effective ionization charge state that is calculated through tabulated data from the FLYCHK code.

The Rosseland and Planck mean opacities are implemented for the dry air in the code from the tabular data of TOPS Opacities webpage [9,10]. The two opacities for the tungsten are calculated using an exponential fit as presented at Equation 14, with T in keV [11].

$$k_P = 646.4 \frac{\rho^{0.199}}{T^{1.225}}, \quad k_R = 244.12 \frac{\rho^{0.005}}{T^{1.119}} \quad (14)$$

All of the physical quantities are in CGS units.

3 MHD MATERIAL MODELING

The PLUTO MHD code is able to model the solution domain consisted of different materials by the help of user defined functions. In this study the existence of two materials in the solution domain is modeled by four approximations: i. approximation *mat*, where the solution domain consists of the tungsten material. ii.

approximation *vac*, where two individual material regions of tungsten and vacuum are considered. The materials surface interface is defined by the six orders lower value ρ_{lim} of density compared to the density of the solid tungsten. iii and iv. approximations *lin* and *exp* are implemented. A new density threshold $\rho_{vac} = \rho_{lim}/2$ in conjunction with ρ_{lim} is used to create three regions for the connection of the pure vacuum, Region I, with the dense tungsten, Region III and the Region II is their transition region. In approximation *lin*, the linear mixing function Q for the pressure, internal energy, temperature and radiative cooling coefficient is defined by:

$$Q = f_w 10^{\log Q(w)} + (1-f_w) 10^{\log Q(air)} \quad (15)$$

where $\log Q(w)$ and $\log Q(air)$ are the logarithmic data from the SESAME tables for tungsten and air respectively and f_w is a weighted function. Likewise, for the forth approximation *exp*, an exponential function is used:

$$Q = 10^{f_w \log Q(w) + (1-f_w) \log Q(air)} \quad (16)$$

The weighted function for the approximations iii. *lin* and iv. *exp*, is expressed as:

$$f_w = \begin{cases} \text{Region ID} & \text{Range} & \text{lin or exp} \\ I & \rho \leq \rho_{vac} & 0 \\ II & \rho_{vac} \leq \rho \leq \rho_{lim} & (\rho - \rho_{vac}) / (\rho_{lim} - \rho_{vac}) \\ III & \rho_{lim} \leq \rho & 1 \end{cases} \quad (17)$$

The effective ionization charge state, is calculated by linear interpolation using the weighted function of Equation 17.

4 COMPUTATIONAL RESULTS

The physical Z-pinch experiment, studied in this work, has a load of a single cylindrical tungsten wire with a diameter of 5 μm . Based on the quarter symmetry of the model only the first quarter of the domain is modeled, and the 3D solution domain has the size of 5000 x 5000 x 80 μm . The numerical results are presented on the XY plane cross section of the model at the midpoint of the wire and are spatially focused on the region of interest having a size of 200 x 200 μm . Symmetric boundary conditions are used on the symmetry planes while outflow is set for the outer XZ and YZ boundary planes and periodic for the top and bottom XY planes of the domain [4]. The size of the solution domain was determined by sensitivity analysis. In relation to the solution time of the model these dimensions prevent the reflections of the shock waves on the XZ and YZ outer boundaries.

The initial distributions of material density ρ , thermal pressure p , the magnitude of the magnetic field B_{mag} , temperature T (eV), the electron density Ne and radiation energy density E_{rad} . The material density and thermal pressure have a Gaussian spatial distribution profile, in order to provide a smooth transition from the core of the wire to the rest of the domain. The amplitudes and widths of these Gaussian distributions are selected in accordance to the experimental observations and represent the physical conditions at the initial timesteps of the plasma generation. As may be observed in Figure 1, the maximum value of the material density approaches the value of 0.53 gr/cm^3 , being 40 times smaller than tungsten's solid density and asymptotically approaches the value of ρ_{vac} . The maximum value of thermal pressure approaches the value of $1.7 \times 10^6 \text{ dyn}/\text{cm}^2$ and asymptotically approaches the pressure of the chamber of the experiment. The temperature distribution is related to the physical quantities of the EOS follows the distribution of pressure and density, while at the coronal plasma a thermal shock wave is observed and is in accordance to the experimental findings. The temperature at the core of the wire approaches the melting temperature of tungsten and asymptotically approximates the environmental temperature. The component of the magnetic field that is taken into account is the azimuthal one and is computed based on the assumption of existence of current density only on the Z direction and the skin effect is also included. The magnetic field increases proportionally to the radial distance to a maximum value. For a radius of 20 μm , where the core and coronal plasma meet, the magnetic field decreases and expands to the domain following the 1/radius law. The temporal evolution of the magnetic field follows the form of the current with a peak of 160 kA and a rise time (10%–90%) of 65 ns [12]. The radiation energy density is computed using the Stefan–Boltzmann law (black-body radiation). It may be observed that the radiation energy density follows the distribution of temperature. The electron density occurs from the contributions of the physical quantities of the EOS and the effective ionization charge state following a shifted Gaussian distribution having a maximum value where core and coronal plasma meet. In the sub-figure of electron density, the discretization of the finite volume scheme is presented, having a size of 700 x 700 x 8 cells for the solution domain with a unit length of 10 μm for all axes.

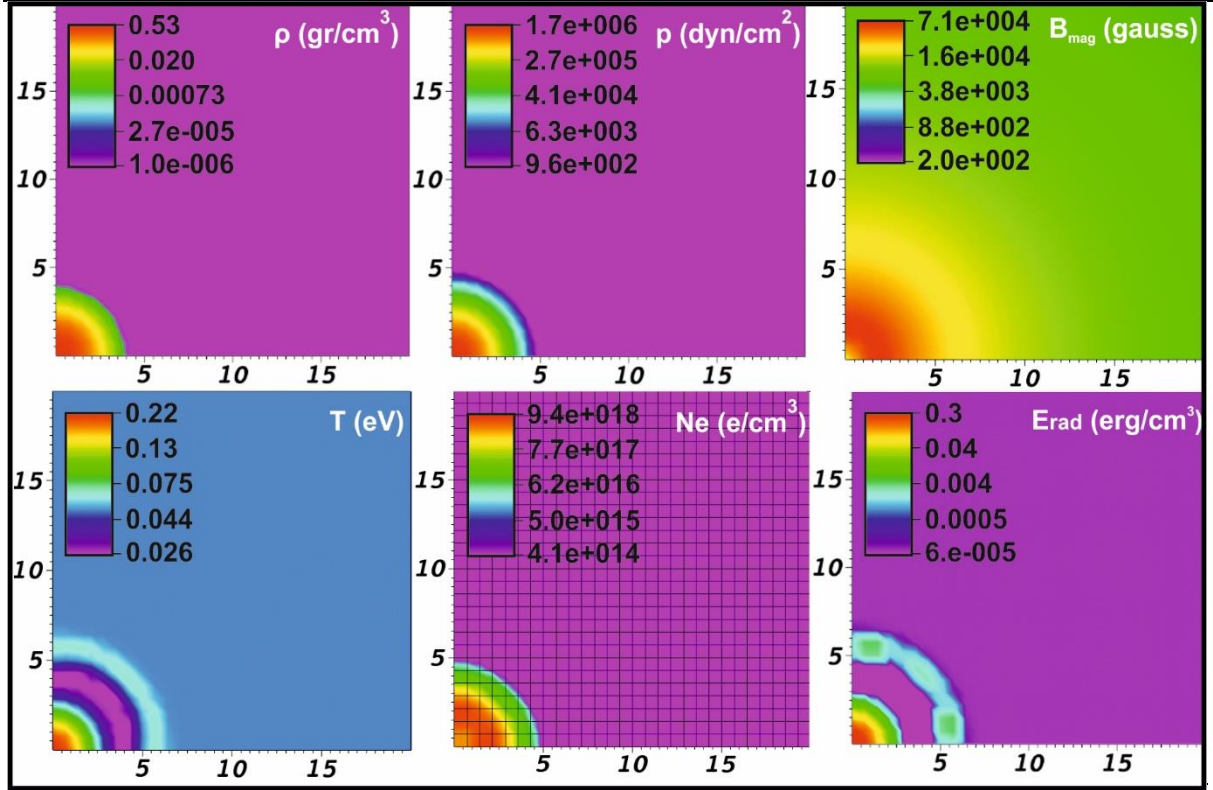


Figure 1. Initial distributions of: material density ρ , thermal pressure p , magnitude of magnetic field B_{mag} , temperature T (eV), electron density N_e and radiation energy density E_{rad} over XY plane cross section

Two different Riemann solvers [4,5] are tested, the **Hllc** solver and the **TvdIf** solver for the flux computation. The prevention of the diffusion of the magnetic field in the vacuum region is obtained by preserving the resistivity value at a high level. This is achieved by setting the vacuum temperature at a constant low value, e.g. 50 meV for this study and for densities having values lower than the ρ_{lim} . Therefore, the approximations **lin**, **exp**, **mat**, **vac** solved by two solvers and constant **const temp** or varying **var temp**, vacuum temperature, result to 16 different test cases. With regard to the expected results the cylindrical symmetry of the model should prescribe a correspondent evolution of the physical phenomena without any azimuthal variations. In Figures 2-4 three representative physical quantities of the electron density, the magnetic field and the temperature, respectively, are selected to demonstrate the performance of the 16 model cases for a problem temporal time of $t=22$ ns. Two test cases, the **vac** approximation with constant vacuum temperature and the **mat** approximation with varying vacuum temperature and for the Hllc solver had an early termination time at 17 and 21 ns respectively.

In Figure 2, for the majority of the investigated test cases, the computed electron density is in very good agreement with the experimental results measured in [12] where the corona plasma expands to a radius of $65 \mu m$ for an electron density of about $3 \times 10^{18} cm^{-3}$ in 22 ns from the current start. In more particular, the majority of the investigated test cases present slight deviations from the ideal cylindrical symmetry, while large deviations are presented for the **exp** and **mat** approximations using the Hllc solver and for varying vacuum temperature. For all the approximations with constant temperature a shock wave appears in the corona regime.

In Figure 3, for all the test cases, the diffusion of the magnetic field is apparent since the maximum value of the magnetic field is located in a radius of $80 \pm 20 \mu m$, in relation to the initial radius. The form of the diffusion of the magnetic field is not realistic for the approximations **lin** and **vac** using the two solvers and for varying temperature. The **exp** approximation using the Hllc solver and for varying vacuum temperature presents azimuthal variations in the magnetic field.

In Figure 4, the test cases with constant vacuum temperature provide a more realistic approximation of the temperature distribution. A temperature range of 1-20 eV is apparent in the corona regime, while the core temperature increases to about 0.9 eV.

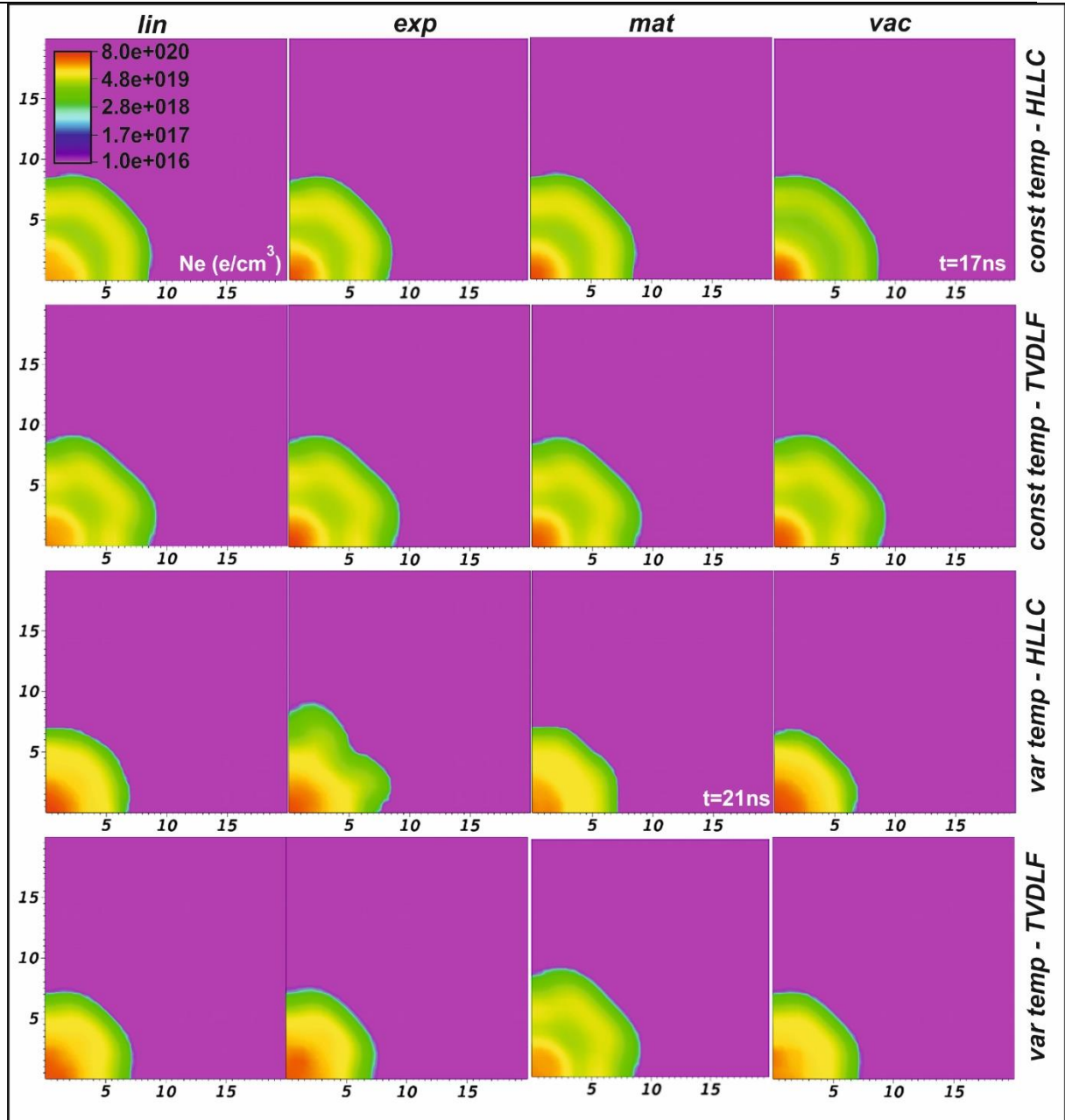


Figure 2. Electron density for the 16 different test cases

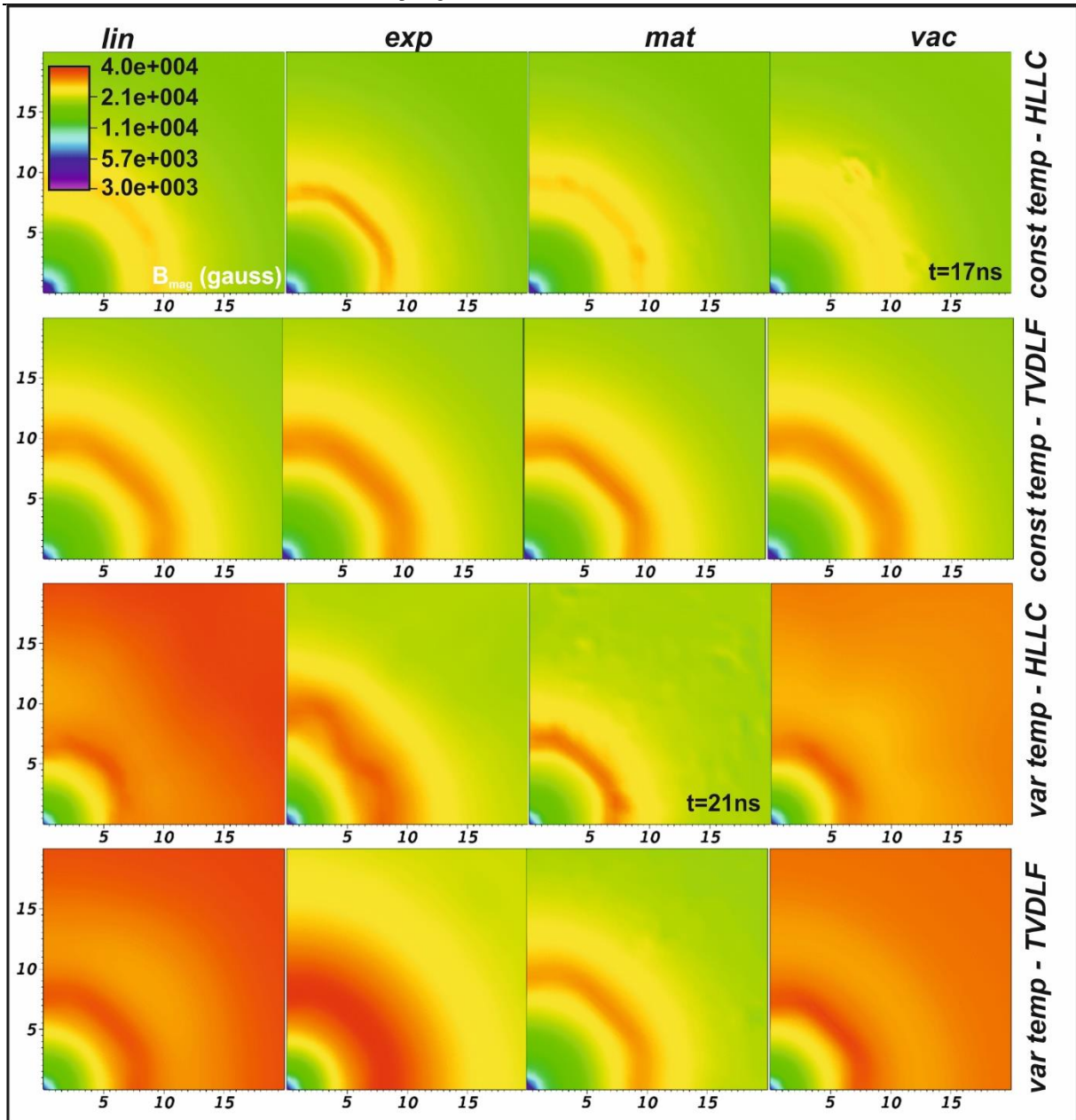


Figure 3. Magnitude of magnetic field for the 16 different test cases

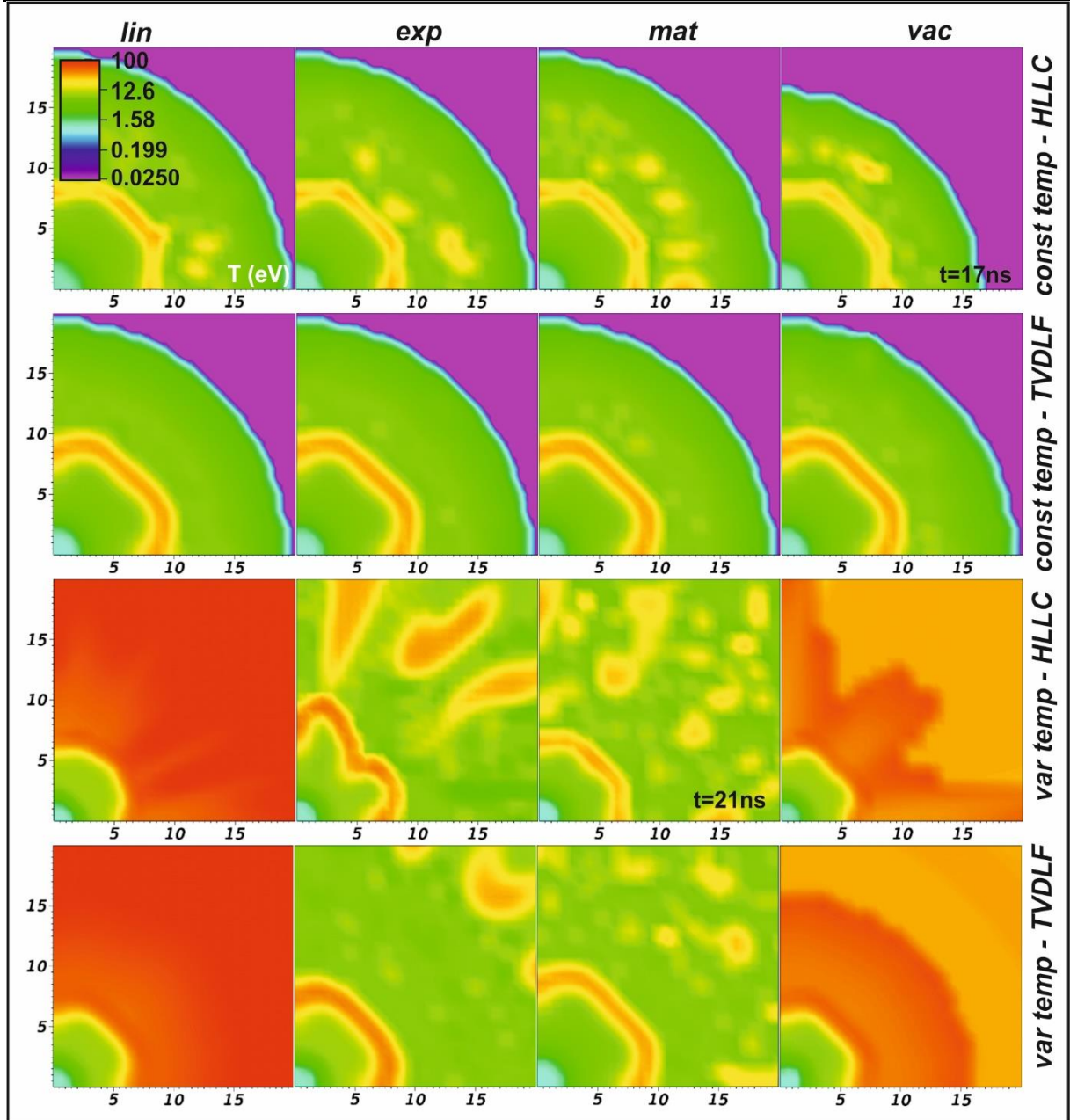


Figure 4. Temperature distribution for the 16 test cases

In Figure 5 is presented the influence of the radiation transport model on the plasma evolution for a representative test case. Results of electron density, thermal pressure, plasma temperature, material density and radiation energy density are depicted for the *lin* approximation using the Tvdlf solver and for constant temperature of the vacuum. It is observed that the radiation transport terms remove energy from the plasma and provide better expansion and cooling results. The model with no radiation presents: i. deviations from the cylindrical symmetry for both electron and material density, ii. the expansion of the thermal pressure is very large and iii. the plasma temperature of ~ 200 eV is not physical in the corona regime. The core and corona expansion for the model with radiation is located in a radius of $30 \mu\text{m}$ and $75 \mu\text{m}$ respectively. Furthermore, regarding the energy radiation density, the maximum value appears near the outer limit of the corona region.

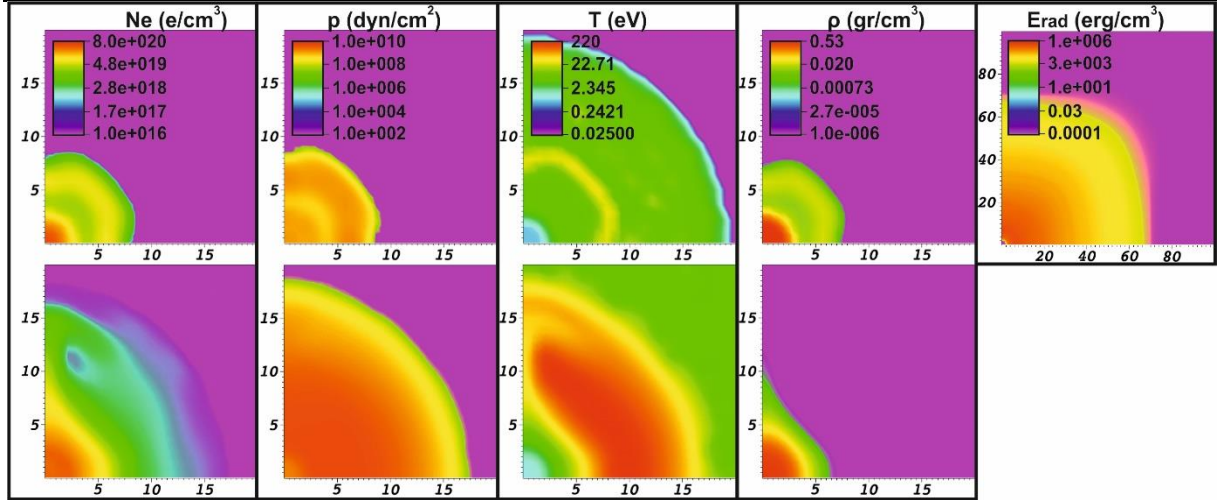


Figure 5. Influence of the radiation transport model. The results including the radiation transport are depicted on the top row.

5 CONCLUSIONS

The inclusion of the radiation transport is very crucial so that the computed quantities of electron density, pressure and temperature are consistent with literature values. The majority of the investigated test cases simulate the plasma expansion with small variations from the experimental reference measurements. Regarding the necessary preservation of the expected cylindrical shape of the computed physical quantities, qualitative results are obtained using the approximations with constant vacuum temperature. Tvdlf solver provides smoother but more diffusive results. For further extension of the present study the effects of thermal conductivity and viscosity will also be taken into account in order to approximate with more accuracy the real physical problem.

ACKNOWLEDGEMENTS

We acknowledge support of this work by the project “ELI - LASERLAB Europe Synergy, HiPER & IPERION-CH.gr” (MIS 5002735) which is implemented under the Action “Reinforcement of the Research and Innovation Infrastructure”, funded by the Operational Programme “Competitiveness, Entrepreneurship and Innovation” (NSRF 2014-2020) and co-financed by Greece and the European Union (European Regional Development Fund). The authors also acknowledge the ‘ARIS’ National HPC Infrastructure of the Greek Research and Technology Network (GRNET), project PluPS-2.

REFERENCES

- [1] Kaselouris, E., Dimitriou, V., Ftilis, I., Skoulakis, A., Koundourakis, G., Clark, E.L., Chatzakis, J., Bakarezos, M., Nikolos, I.K., Papadogiannis, N. A. and Tatarakis M. (2017), “The influence of the solid to plasma phase transition on the generation of plasma instabilities”, *Nature Communications*, Vol 8, pp. 1713.
- [2] Kaselouris, E., Dimitriou, V., Ftilis, I., Skoulakis, A., Koundourakis, G., Clark, E.L., Chatzakis, J., Bakarezos, M., Nikolos, I.K., Papadogiannis, N. A. and M. Tatarakis (2018), “Preliminary investigation on the use of low current pulsed power Z-pinch plasma devices for the study of early stage plasma instabilities”, *Plasma Physics and Controlled Fusion*, Vol 60 pp. 014031.
- [3] Kaselouris, E., Ftilis, I., Skoulakis, A., Koundourakis, G., Dimitriou, V., Bakarezos, E., Clark, E.L., Papadogiannis, N.A. and Tatarakis, M. “Plasma instabilities: the influence on plasma instabilities during the solid-plasma phase transition”, 27th Symposium on Plasma Physics and Technology, Prague, Czech, 20-23, June 2016.
- [4] Mignone, A. et al. (2007), “PLUTO: A Numerical Code for Computational Astrophysics”, *The Astrophysical Journal Supplement Series*, Vol. 170, Issue 1, pp. 228-242.
- [5] <http://plutocode.ph.unito.it/>.
- [6] Kashiwa, B. A. The MGGB Equation-of-State for Multifield Applications: A Numerical Recipe for Analytic Expression of Sesame EOS Data, LA-1442 Issued: September 2010. <http://www.doe.gov/bridge>.
- [7] Tungsten Charge State Distribution by FLYCHK NLTE Kinetics Calculation at NIST by International Atomic Energy Agency- Atomic Molecular Data Services provided by the Nuclear Data Section.
- [8] Kolb, S.M., Stute, M. Kley, W. and A. Mignone (2013), “Radiation hydrodynamics integrated in the PLUTO code”, *Astronomy and Astrophysics*, Vol. 559, pp. A80.

- [9] Magee Jr., N. H., Abdallah Jr., J., Clark, R.E.H. et al. (1995), "Atomic Structure Calculations and New Los Alamos Astrophysical Opacities", *Astronomical Society of the Pacific Conference Series (Astrophysical Applications of Powerful New Databases*, S. J. Adelman and W. L. Wiese eds.) Vol. 78, pp. 51.
- [10] <http://aphysics2.lanl.gov/cgi-bin/opacrun/tops.pl>.
- [11] Tsakiris, G.D., Eidmann, K. (1987), "An approximate method for calculating Planck and Rosseland mean opacities in hot, dense plasmas", *Journal of Quantitative Spectroscopy and Radiative Transfer*, Vol. 38, pp. 353-368.
- [12] Ruiz-Camacho, J. et al. (1999), "Z-pinch discharges in aluminum and tungsten wires", *Physics of Plasmas*, Vol. 6, pp. 2579-2587.

SIMULATIONS OF LASER ASSISTED MACHINING AND CONVENTIONAL CUTTING OF AISI H-13 STEEL

Evangelos Kaselouris^{1,2}, Theodoros Papadoulis^{1,3}, Alekos Skoulakis^{1,2}, Andreas Baroutsos^{1,3}, Ioannis Fitis^{1,2}, Yannis Orphanos^{1,4}, Efthimios Bakarezos^{1,4}, Nektarios A. Papadogiannis^{1,4}, Michael Tatarakis^{1,2} and Vasilis Dimitriou^{1,3}

¹Centre for Plasma Physics and Lasers
School of Applied Sciences, TEI of Crete
Chania, GR-73133, Rethymnon, GR-74100, Greece

web page: <http://www.cppl.teicrete.gr>

²Department of Electronic Engineering
Chania, GR-73133, Greece

e-mails: vkas@chania.teicrete.gr, skoulakis@chania.teicrete.gr, fitis@staff.teicrete.gr,
m.tatarakis@chania.teicrete.gr

³Department of Natural Resources and Environmental Engineering
Chania, GR-73133, Greece

e-mails: papadoulis@staff.teicrete.gr, abarouts@staff.teicrete.gr, dimvasi@chania.teicrete.gr

⁴Department of Music Technology & Acoustics Engineering
Rethymnon, GR-74133, Greece

e-mails: bakarezos@staff.teicrete.gr, yorphanos@staff.teicrete.gr, npapadogiannis@staff.teicrete.gr

Keywords: Laser assisted machining - LAM, Laser preheating, Finite Element Method, Metal Cutting.

Abstract. *Laser-assisted machining- LAM is a method capable of increasing the machinability of hard-to-cut materials, by decreasing the values of the cutting forces and extending the tool life. During LAM, the workpiece is heated directly by a laser beam ahead of the cutting tool, that leads to the yield strength and hardness reduction of the workpiece material. LAM method combines all the classic cut parameters, such as cutting speed, feed rate, depth of cut with the laser parameters, like the laser power, the spot radius and the beam profile. The current research focuses on the finite element simulation of the machinability of AISI H-13 steel parts, with conventional and laser-assisted machining. Thermal-structural numerical modeling and simulations of the conventional orthogonal cutting of AISI H-13 steel and laser-assisted orthogonal cutting are performed. Parametric simulations are carried out for constant laser beam diameter and laser heat flux. These two machining methods are compared according to the obtained numerical results for the cutting forces, temperature distributions, plastic strains and Von Mises stresses and valuable conclusions are drawn for the contribution of the aforementioned parameters to the models' dynamic behavior.*

1 INTRODUCTION

One of the most common industrial manufacturing process is metal cutting. It is a complex contact process where parameters such as: the geometry of the cutting tool (angles and tip radius), the material properties for the workpiece and the tool, the friction conditions, the cutting velocity, the feed rate and the depth of cut determine the conventional machining process [1]. Nowadays for hard-to-cut materials Laser-assisted machining-LAM is an advanced promising hybrid method capable of increasing the machinability of the material by decreasing the values of the cutting forces.

LAM uses the laser beam as a heat source to ensure sufficient local heating of the workpiece at a certain distance from the cutting tool, while the conventional cutting occurs. The principle of the process is the reduction of the cutting forces during material machining via increasing the temperature to the point where the strength of the material is reduced. The reduction of the material yield strength through the localized heating, without melting or sublimation, leads to: reduced cutting forces and tool wear, improved surface finish and higher material removal rate [2-4]. Thanks to the rapid development of laser technology, LAM has emerged as a major viable industrial choice for cutting.

A major feature of the LAM process is the number of parameters that must be controlled during the cutting operation. In addition to the aforementioned conventional cutting parameters there are the laser parameters such as the laser power, the wavelength and the diameter of the laser spot and also interaction parameters such as the position of the laser beam relative to the tool and the incidence angle of the laser beam in relation to the workpiece

[2-4]. One can understand that the correct selection of all the cutting parameters, synthesizes a multi-parametric system that requires the use of computational methods and simulations to facilitate the application of both LAM and conventional experimental machining processes.

The application of numerical simulations, able to guide the experimental machining processes, can improve significantly the machinability and the final quality of the workpiece. Explicit numerical FEM, finite element method, is commonly applied to metal machining. It is based on the Lagrangian approach, where the FE mesh is attached to the workpiece and both deform. Moreover, the Lagrangian formulation has the advantage to model the evolution of the chip from the incipient stage to a steady form [5]. The chip formation occurs through the plastic deformation of the elements based on erosion criteria and the chip shape is developed as a function of the physical deformation process, machining parameters and material properties.

The current research focuses on the finite element simulation of the machinability of AISI H-13 steel parts, with conventional and laser-assisted machining. Thermal-structural numerical simulations of the conventional and laser-assisted orthogonal cutting of AISI H-13 steel are performed, while the conventional cutting simulations were recently validated with experimental literature results [1]. The cutting tool is modeled as a rigid FEM body that incrementally penetrates the flexible deformable workpiece. The laser beam is modeled as a Gaussian moving heat source. The dynamic elastoplastic behavior of the workpiece material is investigated by taking into account the Johnson-Cook constitutive strength material model. Parametric simulations are carried out for constant laser beam diameter and laser heat flux. These two machining methods are compared according to the obtained numerical results for the cutting forces, temperature distributions, plastic strains and Von Mises stresses. The influence of the laser assistance is discussed, and valuable conclusions are drawn for the contribution and effectiveness of the aforementioned parameters to the models' dynamic behavior.

2 FINITE ELEMENT MODELING

LS-DYNA FEM software [6] is used to model the conventional and LAM turning process of AISI H13 steel and investigate the effects of different laser parameters on the machining forces, temperature distributions, plastic strains and Von Mises stresses. 3D transient thermal-structural simulations are performed. Moreover, the workpiece is defined as a deformable body and the tool is modeled as a rigid body, while the laser beam is modeled as a Gaussian moving heat source.

2.1 Governing equations

The 3D transient heat conduction equation for the thermal problem is given by:

$$\rho c_p \left(\frac{\partial T}{\partial t} + V_x \frac{\partial T}{\partial x} \right) = \frac{\partial}{\partial x} \left(k \frac{\partial T}{\partial x} \right) + \frac{\partial}{\partial y} \left(k \frac{\partial T}{\partial y} \right) + \frac{\partial}{\partial z} \left(k \frac{\partial T}{\partial z} \right) + \dot{Q} \quad (1)$$

where ρ , c_p , V_x , k , and \dot{Q} are the density, specific heat, laser scanning speed along the x-direction, thermal conductivity, and the rate of volumetric heat generation respectively.

The mechanical equation of momentum is given by:

$$\rho \frac{\partial v_i}{\partial t} = \nabla \sigma_{ij} + \rho b_i \quad (2)$$

where v_i is the material velocity, $\sigma_{i,j}$ is the stress tensor and b_i is the body force.

2.2 Modeling of laser heat source

The Gaussian distribution of the $q(r)$ absorbed laser heat flux or laser power intensity is given by [7]:

$$q(x, z) = \frac{2P_{tot}}{\pi r_b^2} e^{-\left(\frac{2((x-tV_x)^2 + z^2)}{r_b^2} \right)} \quad (3)$$

where P_{tot} is the total absorbed power and r_b is the laser beam radius. It also holds that:

$$P_{tot} = \eta P_{inc} \quad (4)$$

where P_{inc} is the incident laser power, η is the average absorptivity of the workpiece material and t is the time.

The laser heat flux is applied to the top surface of the workpiece. The boundary condition on the top laser irradiated surface takes into account the heat flux, convection and radiation and it holds:

$$-k \frac{\partial T}{\partial y} = q(x, z) - h(T - T_0) - \sigma \varepsilon (T^4 - T_0^4) \quad (5)$$

where h is the convective heat transfer coefficient, T_0 is the ambient temperature, σ is the Stefan–Boltzmann constant ($5.67 \cdot 10^{-8} \text{W/m}^2\text{K}^4$) and ε is emmisivity. Heat flux is considered to be normal to the laser irradiated surface, while the motion of the laser beam is considered along the X-direction.

2.3 Modeling of orthogonal cutting

The cutting insert has a rake angle of -5° , a clearance angle of 5° and a fillet of 0.02 mm radius, while the workpiece dimensions are 3.0 x 0.5 x 0.5 mm. The cutting rigid tool is modeled with approximately 35,000 hexahedron solid elements and the workpiece with approximately 115,000 solid elements. The tool is placed to a vertical distance, denoted as f -feed from the top surface of the workpiece, according to the depth-of-cut that is defined at each simulation. The mesh of the cutting tool and workpiece are shown in Figure 1.

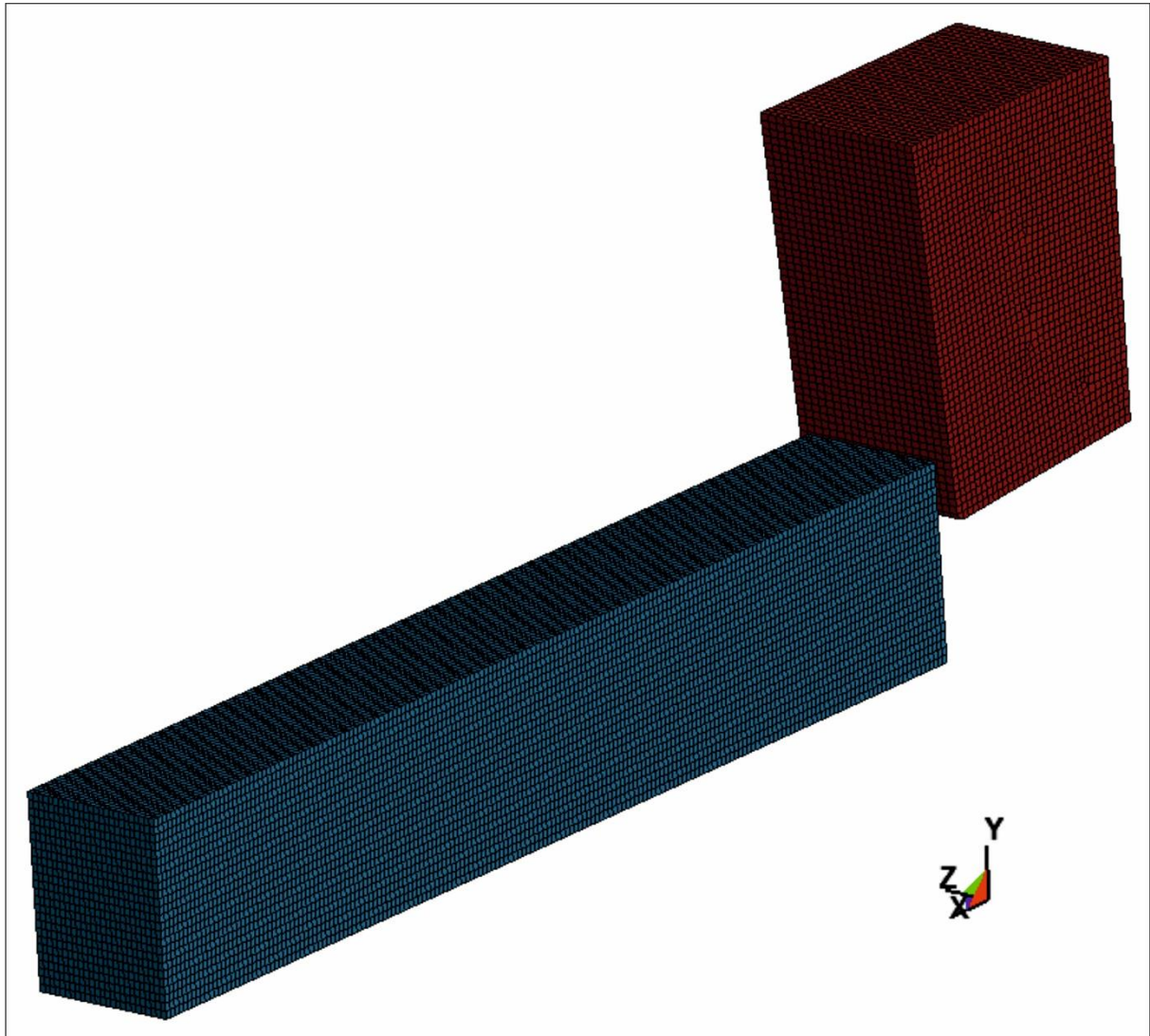


Figure 1. Mesh of the orthogonal cutting

For the determination of the optimal mesh size, given the provided dimensions of the solution domain, a mesh sensitivity analysis is carried out. In addition, for the elimination of the possibility of mesh distortions and hourglass nonphysical, zero-energy modes of deformation, an effective algorithm is used for the FE models. This is achieved by the Hourglass control, where viscosity is added to hexahedral solid elements that use reduced integration. Moreover, the FEM approximation obeys to a failure criterion, developed for use with Lagrangian solid hexahedral elements, that allows element erosion (element deletion) and therefore for the workpiece-tool interaction an eroding node to surface contact algorithm is used, that allows the contact surface to be updated as

exterior elements are deleted [6].

Regarding the initial and boundary conditions, the motion of the tool is imposed along the X-direction. All translations and rotations of the bottom and the left side of the workpiece are fully constrained and Z translations at its front and back side are also constrained. The ambient temperature is assumed to be 20 °C.

2.4 Material models

The adoption of a suitable material-constitutive model for the workpiece is critical for the accuracy of metal cutting simulations. The material model selected in our study is the Johnson-Cook (J-C), a purely empirical one that takes into account the effect of plastic strain, strain rate and temperature. The flow stress is expressed as:

$$\sigma_y = (A + B\varepsilon^n)(1 + C\ln \frac{\dot{\varepsilon}}{\dot{\varepsilon}_0})(1 - \frac{T-T_r}{T_m-T_r})^m \quad (6)$$

where ε is the equivalent plastic strain, $\dot{\varepsilon}/\dot{\varepsilon}_0$ is the dimensionless plastic strain rate, $\dot{\varepsilon}_0=1s^{-1}$ is a reference strain rate used to normalize the strain rate, A is the yield stress, B is the hardening constant, C is the strain rate sensitivity, n is the hardening exponent, m is the thermal softening exponent, T_m is the melting temperature of the workpiece and T_r the room temperature. The material constants A, B, C, n, m are determined from experimental results [8].

The J-C material model includes also a fracture model that takes into account the nucleation, growth and coalescence of voids in a ductile material at high strain rates. It defines the equivalent plastic strain at the onset of damage as:

$$\varepsilon_f = \left(\left[D_1 + D_2 \exp D_3 \frac{p}{\sigma_{VM}} \right] \left[1 + D_4 \ln \frac{\dot{\varepsilon}}{\dot{\varepsilon}_0} \right] \left[1 + D_5 \frac{T-T_r}{T_m-T_r} \right] \right) \quad (7)$$

where D_1, D_2, D_3, D_4 and D_5 are the failure parameters and σ_{VM} the Von Mises stress [8]. The material fracture occurs when the damage parameter D reaches the value of 1:

$$D = \sum \frac{\Delta \varepsilon}{\varepsilon_f} \quad (8)$$

3 RESULTS

The physical properties of the AISI H-13 steel workpiece and the polycrystalline cubic boron nitride (PCBN) tool, chosen for our test cases, are listed in Table 1 for room temperature. The J-C material model and failure parameters of the workpiece are listed in Table 2. Moreover, temperature-dependent of thermal conductivity, specific heat and thermal expansion are taken into account for the workpiece [9].

Property	Workpiece	Tool
Density [kg/m ³]	7800	3399
Elastic modulus [GPa]	211	652
Poisson's ratio [-]	0.28	0.128
Specific heat [J/kg K]	560	960
Thermal conductivity [W/m K]	37	100
Thermal expansion [10 ⁻⁶ C]	10.4	-
Melting Point [K]	1700	-

Table 1: Mechanical and physical properties of AISI H-13 and PCBN [1] in room temperature

Material model Parameters	A [MPa]	B [MPa]	n [-]	C [-]	m [-]
Values	674.8	239.2	0.28	0.027	1.3
Failure Parameters	D1 [-]	D2 [-]	D3 [-]	D4 [-]	D5 [-]
Values	-0.8	2.1	-0.5	0.0002	2.7

Table 2: Johnson-Cook material model and failure parameters of AISI H-13 [1]

Furthermore, a mean value of absorptivity $\eta=0.5$ and a mean value of emmisivity $\varepsilon=0.4$ are considered based on the work of Singh et al [7]. For the convectonal heat transfer to the surrounding air, a heat transfer coefficient of $h=5$ W/m²K is also considered [7]. The same laser scanning speed and cutting speed of 150 m/min and a feed rate of 0.15 mm/rev are considered for the simulations of the developed models, while the tool is placed 1 mm away from the laser spot. Moreover, the Coulomb static and dynamic friction coefficients for the tool-workpiece

interaction are set to 0.3 [1]. Models with the same cutting speed and feed rate values were previously validated with experimental literature data [1].

3.1 Effects of constant laser heat flux

For a large number of materials a significant reduction in the tensile strength or hardness occurs between 500 and 600 °C. The cutting tool must operate in the zone where the temperature remains higher than this value [10]. Furthermore, the distance between the tool and the laser spot must be sufficient to prevent degradation of the tool due to the high temperature, therefore as aforementioned this distance is selected to be 1 mm in this study.

In order to investigate the influence of the constant laser heat flux via varying the laser power and beam radius such that the ratio of P_{tot}/r_b^2 remains stable, a parametric analysis is carried out. In Table 3 are presented the laser different parameters and the maximum computed temperature, which is always higher than 600 °C in order to achieve a significant reduction of the material tensile strength.

Heat flux (kW/mm ²)	Laser power (W)	Laser beam diameter (μm)	Maximum Temperature (°C)
2	62.8	200	630
2	98.2	250	750
2	141.4	300	850

Table 3: Laser parameters and maximum computed temperature

In Figure 2 are presented the results of the parametric analysis for constant laser heat flux. The results of cutting and thrust forces for the LAM models are compared to the conventional corresponding ones.

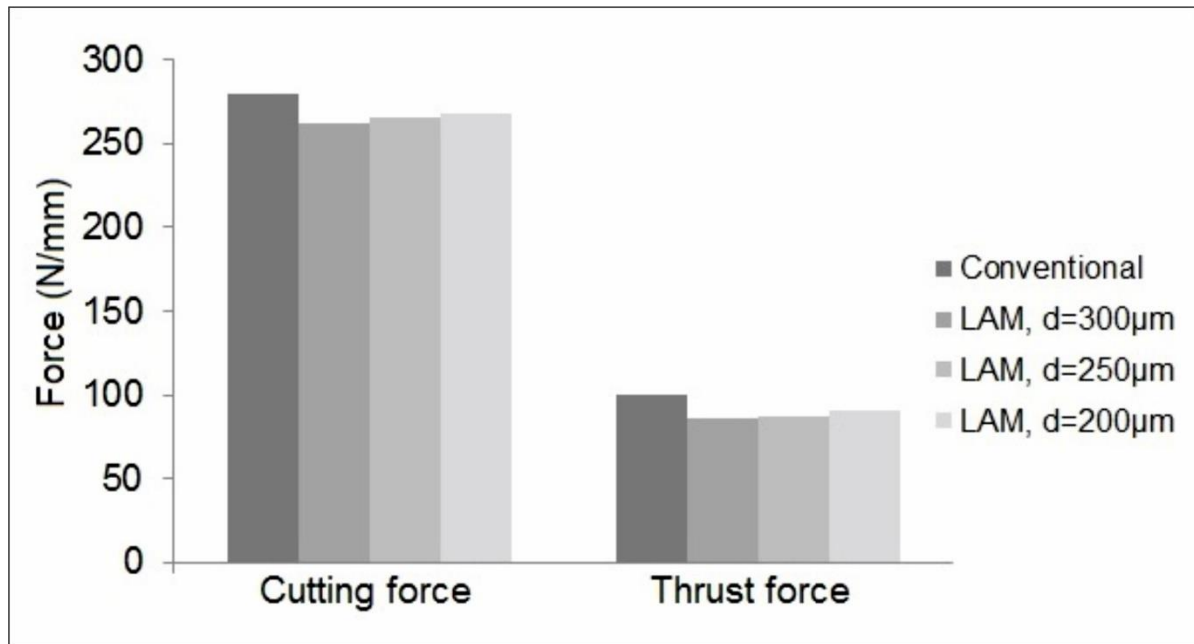


Figure 2. Effect of the constant laser flux on the forces results and comparison with conventional cutting

Regarding the forces for the LAM model with beam diameter 300 μm, a maximum reduction of about 6.2% for the cutting force and 14.3% for the thrust force is observed in relation to conventional machining forces.

3.2 Effects of constant laser beam diameter

In order to investigate the influence of the constant laser beam diameter d via varying the laser power and hence the laser heat flux, a parametric analysis is carried out. In Table 4 are presented the laser different parameters and the maximum computed temperature, which is always higher than 600 °C in order to achieve a significant reduction of the material tensile strength.

Heat flux (kW/mm ²)	Laser power (W)	Laser beam diameter (μm)	Maximum Temperature (°C)
2	98.2	250	750
2.22	109.0	250	830
2.44	119.8	250	900

Table 4: Laser parameters and maximum computed temperature

In Figure 3 are presented the results of the parametric analysis for constant laser beam diameter. The results of cutting and thrust forces for the LAM models are compared to the conventional corresponding ones.

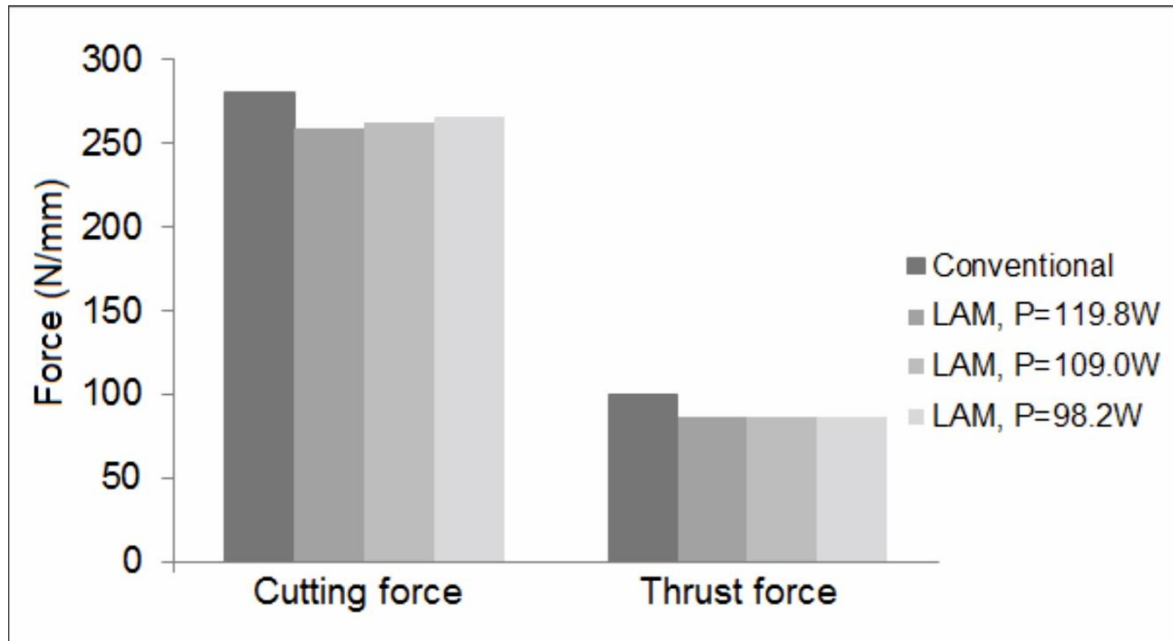


Figure 3. Effect of the constant laser beam radius on the forces results and comparison with conventional cutting

Regarding the forces for the LAM model with laser power 119.8 W, a maximum reduction of about 7.7% for the cutting force and 14% for the thrust force is observed in relation to conventional machining forces.

3.3 Temperature, Von Mises and plastic strain distribution

In Figure 4 are presented representative simulation results for the conventional cutting model and for the two LAM models where the lower cutting forces are computed, for 0.4 ms after the cutting tool initiation. In Figure 4(A)-(C) are presented the temperature, Von Mises stress and plastic strain distribution for the model of Conventional cutting, respectively. In Figure 4(D)-(F) are presented the temperature, Von Mises stress and plastic strain distribution for the LAM model with laser beam diameter 250 μm and laser power 119.8 W, respectively and in Figure 4(G)-(I) the temperature, Von Mises stress and plastic strain distribution for the LAM model with laser heat flux 2 kW/mm² and laser beam diameter 300 μm, respectively.

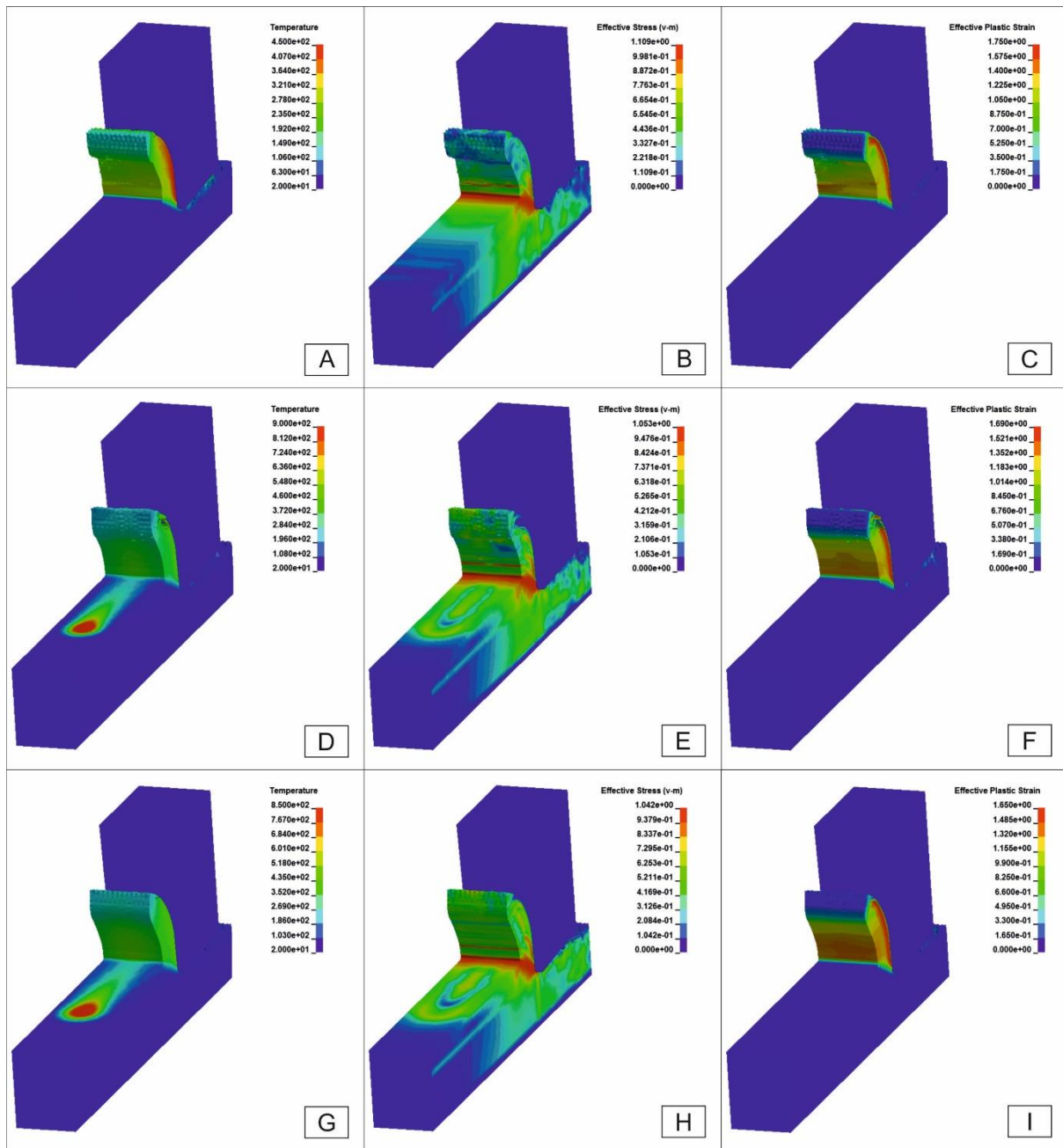


Figure 4. Temperature, Von Mises stress and plastic strain distribution for model i) of Conventional cutting from (A)-(C) ii) of LAM for laser beam diameter 250 μm and laser power 119.8 W from (D)-(F), iii) of LAM for laser heat flux 2 kW/mm^2 and laser beam diameter 300 μm from (G)-(I)

For the LAM model with laser heat flux 2 kW/mm^2 and laser beam diameter 300 μm the maximum developed Von Mises stresses and the plastic strains are about 6% lower than the corresponding ones due to conventional cutting. For the LAM model with laser beam diameter 250 μm and laser power 119.8 W, compared to conventional cutting, this reduction is approximately 5%.

4 CONCLUSIONS

In this preliminary study for the simulation of Laser Assisted Machining – LAM, a validated FEM model for the conventional cutting of the AISI H13 steel is updated to include the assistance of a laser to the cutting process. A parametric analysis is carried out regarding the effects of constant laser heat flux and constant laser beam diameter on the cutting and thrust forces, stresses and strains and valuable conclusions are drawn. For future development these LAM simulation results will be compared to experimental measurements regarding forces, temperature and stress distributions, while difficult-to-cut materials such as Ti6AL4V will be tested. The reduction

of the yield strength of the material through the localized heating by the laser beam, leads to reduced cutting forces and higher material removal rates while tool life is increased.

ACKNOWLEDGEMENTS

We acknowledge support of this work by the project “ELI - LASERLAB Europe Synergy, HiPER & IPERION-CH.gr” (MIS 5002735) which is implemented under the Action “Reinforcement of the Research and Innovation Infrastructure”, funded by the Operational Programme "Competitiveness, Entrepreneurship and Innovation" (NSRF 2014-2020) and co-financed by Greece and the European Union (European Regional Development Fund).

REFERENCES

- [1] Kaselouris, E., Papadoulis, T., Variantza, E., Baroutsos, A. and Dimitriou, V. (2017), “A study of explicit numerical simulations in orthogonal metal cutting”, *Solid State Phenomena*, Vol. 261, 339-346.
- [2] Kim, K.-S. (2011), “A Review on Research and Development of Laser Assisted Turning”, *International Journal of Precision Engineering Manufacturing*, Vol. 12, pp. 753-759.
- [3] Venkatesan, K. (2014), “A Review on conventional and laser assisted machining of aluminium based metal matrix composites”, *Engineering Review*, Vol. 34, pp. 75-84.
- [4] Punugupati, G. (2016), “Laser assisted machining: a state of art review”, *IOP Conf. Series: Materials Science and Engineering*, Vol. 149, 012014.
- [5] Mamalis, A.G., Kunderák, J., Markopoulos, A. and Manolacos, D.E. (2008), “On the finite element modelling of high speed hard turning”, *International Journal of Advanced Manufacturing Technology*, Vol. 38, pp. 441-446.
- [6] Hallquist, J.O. (2006), *LS-DYNA Theory Manual*, Livermore Software Technology Corporation, California.
- [7] Singh, R., Alberts, M.J. and Melkote, S.N. (2008), “Characterization and prediction of the heat-affected zone in a laser-assisted mechanical micromachining process”, *International Journal of Machine Tools & Manufacture*, Vol. 48, pp. 994–1004.
- [8] Johnson, G.R. Cook, W.H. (1985), “Fracture characteristics of three metals subjected to various strains, strain rates, temperatures and pressures”, *Engineering Fracture Mechanics*, Vol. 21, pp. 31-48.
- [9] Afazov, S. M., Ratchev S. M. and Segal, J. (2012), “Prediction and experimental validation of micro-milling cutting forces of AISI H13 steel at hardness between 35 and 60 HRC”, *International Journal of Advanced Manufacturing Technology*, Vol. 62, pp. 887–899.
- [10] Germain, G., Dal Santo, P., Lebrun, J.L. (2011), “Comprehension of chip formation in laser assisted machining”, *International Journal of Machine Tools & Manufacture*, Vol. 51, pp. 230-238.

ESTIMATION OF INSERTION LOSS OF SOUND BARRIERS VIA FINITE ELEMENT METHOD

Nikolaos M. Papadakis^{1,2}, Georgios E. Stavroulakis²

¹Department of Music Technology and Acoustics,
Technological Educational Institute of Crete,
Rethymno, GR-74100, Greece

e-mail: nikpapadakis@isc.tuc.gr ; web page: <https://www.teicrete.gr/mta/>

²Department of Production Engineering and Management,
Technical University of Crete,
Chania, GR-73100, Greece

e-mail: gestavr@dpem.tuc.gr ; web page: <http://www.comeco.tuc.gr/>

Keywords: Sound barriers, insertion loss, finite element method.

Abstract. *The insertion loss of a sound barrier was calculated via Finite Element Method (FEM) and compared with Ray Tracing techniques. FEM was used to model the Helmholtz equation with a sound source and diffraction effects of a sound barrier in the frequency domain. For mesh creation the rule of thumb $\lambda/h=5$ was applied where λ and h respectively denote wavelength of upper limit frequency and the maximum nodal distance. The open pressure acoustic domain was modeled with the use of a Perfectly Matched Layer. Two models were created: for the first one the sound pressure at the receiver point was calculated with the presence of a sound barrier and for the second one without a sound barrier for the same source position. Results compared with Kurze-Anderson and Tatge equations indicate that there is a difference less than 1 dB and less than 0.3 dB respectively for all frequencies calculated. Implications of the findings suggest that FEM can be used effectively for the modeling of insertion loss of sound barriers.*

1 INTRODUCTION

Sound barriers are an important aspect of fighting noise pollution caused by major infrastructure projects such as roads and railways. Accurate modeling of the acoustic behavior of barriers can lead to effective designs which in turn can improve the living conditions of populations in areas with excessive sound levels. The main phenomenon characterizing the acoustic performance of a sound barrier is diffraction, while absorption and transmission are also important. The performance of a sound barrier is measured by insertion loss which is defined as the difference in sound level at a receiver location with and without the presence of a noise barrier, assuming no change in the sound level of the source.

Ray tracing techniques have been used to establish the acoustic performance of a barrier and still remain the basis of most of the practical methods for calculating barrier performance. Originally, the theory of diffraction was developed for optics, and was later applied in the field of acoustics. Simple analytic expressions were proposed for the calculation of insertion loss due to diffraction of sound rays around a barrier emanating from a point source in the case of a semi-infinite plane screen in a free field [1-4]. This analysis takes into account oblique sound incidence at the barrier and also includes the transition region from the bright zone to the shadow zone behind the barrier. A review of commonly used analytical and empirical formulae for predicting sound diffracted by a thin screen can be found in Li [5]. In the case of a finite length sound barrier, an analytical solution for the insertion loss was proposed by Lam [6].

Numerical methods have been applied in many fields of acoustics. Most numerical studies modeling the acoustic behavior of sound barriers have focused on Boundary Element Method (BEM) [7, 8] while also Finite Difference Method have been applied [9]. FEM is a powerful numerical technique that can be utilized for the modeling of wave phenomena and can simultaneously incorporate effects of diffraction, absorption and transmission both in frequency and time domain. In the literature there are not many studies on the utilization of FEM [10, 11] for the modeling of sound barriers. Scope of this study is the calculation of insertion loss of sound barriers via FEM and comparison of the results with Ray Tracing techniques.

In this study FEM was used to model the Helmholtz equation with a sound source and the effects of diffraction of a sound barrier in the frequency domain. Appropriate mesh creation was applied and the open pressure acoustic domain was modeled with the use of a Perfectly Matched Layer. Insertion loss was calculated and compared for the same source and receiver positions for FEM and Ray Tracing techniques. Results indicate that there is a good agreement between FEM and Ray Tracing techniques.

To the best of our knowledge there is no similar research in the literature regarding the calculation of insertion loss of a sound barrier via FEM. Implications of the findings suggest that FEM can be used effectively for the modeling of insertion loss of sound barriers. Application of the method can be extended in 3d space to predict the behavior of sound barriers with various shapes and also with a profile which absorbs or disperses sound. Optimization and active noise control can also be utilized with the use of FEM.

Section 2 introduces the setup of the FEM calculations while the section 3 presents the calculations via Ray Tracing methods. Results and discussion section follows. Finally, in Section 6, concluding remarks are presented.

2 FINITE ELEMENT METHOD SETUP

In this study the FEM was used to model the Helmholtz equation with a sound source and the effects of diffraction of a sound barrier in the frequency domain. Two models were created: for the first one the sound pressure at the receiver point was calculated with the presence of a sound barrier and for the second one without a sound barrier for the same source position. Insertion loss was calculated as the difference in sound level at receiver location with and without the presence of a noise barrier. The point source and receiver positions in relation to the sound barrier are presented in Fig.1.

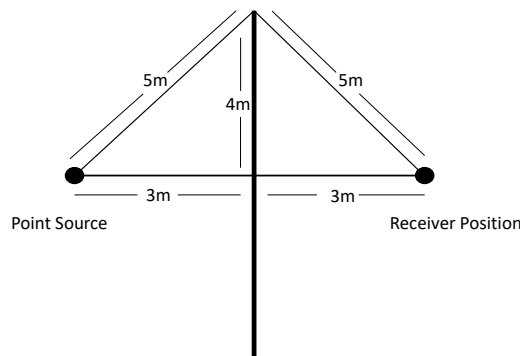


Figure 1. Source and Receiver positions

For mesh creation the rule of thumb $\lambda/h=5$ was applied where λ and h respectively denote wavelength of upper limit frequency and the maximum nodal distance. Five elements per wavelength are typical [12] for acoustic modeling in the frequency domain, while different considerations apply for modeling in the time domain [13]. The mesh created is presented in Fig.2.

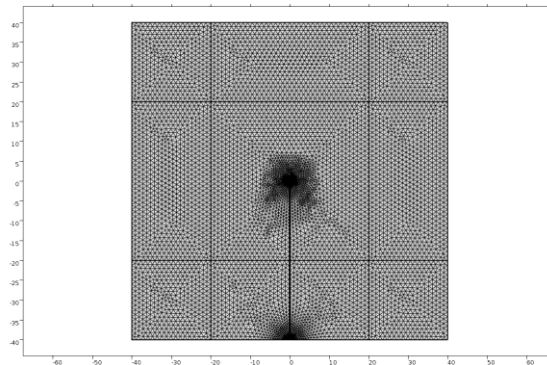


Figure 2. Mesh for FEM model with sound barrier

The open pressure acoustic domain was modeled with the use of a Perfectly Matched Layer (PML). The PML is an approximation methodology originally developed by Jean- Pierre Berenger [14] for use with Finite Difference method for electromagnetic modeling calculations. It was later developed for acoustic waves [15] and applied in the field of acoustics. The key property of a PML that distinguishes it from an ordinary absorbing material is that it is designed so that waves incident upon the PML from a non-PML medium do not reflect at the interface. The FEM model with the PML is presented in Fig.3.

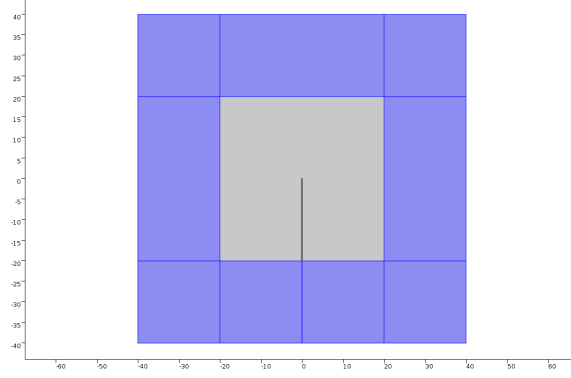


Figure 3. FEM model with sound barrier and Perfectly Matched Layer (Blue color)

3 RAY TRACING TECHNIQUES

By origin, the theory of diffraction was developed in the field of optics. It was later applied in acoustics and for sound barriers. By applying Kirchhoff's diffraction theory [16], which embodies the basic idea of the Huygens-Fresnel principle, to the semi-infinite screen, the sound attenuation by the screen after some approximations can be calculated. It is desirable, for most cases of practical noise control, that the diffraction problems are treated by a simplified and approximate method. Simple analytic expressions are proposed for the calculation of the excess attenuation due to diffraction around a barrier of sound rays emanating from a point source.

If we assume that the sound is emitted by a point source and the barrier can be considered to be thin and infinitely long, then the insertion loss can be calculated by the following equation proposed by Kurze-Anderson [2]:

$$IL = 20 \log \frac{\sqrt{2\pi N}}{\tanh(\sqrt{2\pi N})} + 5dB \quad (1)$$

N is the Freshnel number which is given by $2(D-R)/\lambda$. R is the length of the travel path for the diffracted acoustic ray, D is the length of the travel path for the incident ray when there is no obstacle, and λ is the wavelength in meters.

A similar equation is provided by Tatge [3] for $N > -0.1$:

$$IL = 10 \cdot \log(3 + 20N) \quad (2)$$

4 RESULTS - DISCUSSION

The insertion loss between the results obtained with the FEM and Ray Tracing techniques was assessed. Acoustic pressures and sound pressures were calculated from 20Hz to 60Hz. In Fig.4 and Fig.5 the acoustic pressure is presented for the frequencies of 20Hz and 60Hz respectively with and without the presence of a sound barrier. The effect of diffraction is evident. Fig.6 presents the sound pressures with a sound barrier for the frequencies of 20Hz and 60Hz.

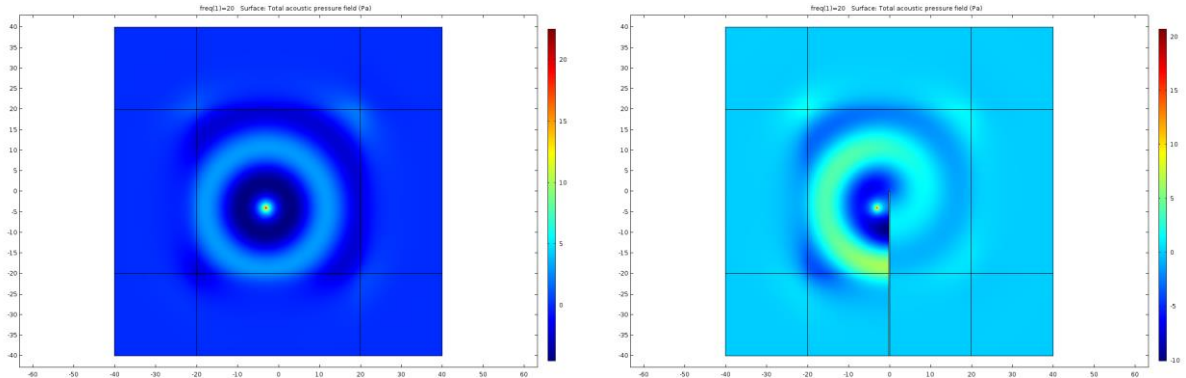


Figure 4. Acoustic pressure without (left) and with (right) a sound barrier (20 Hz)

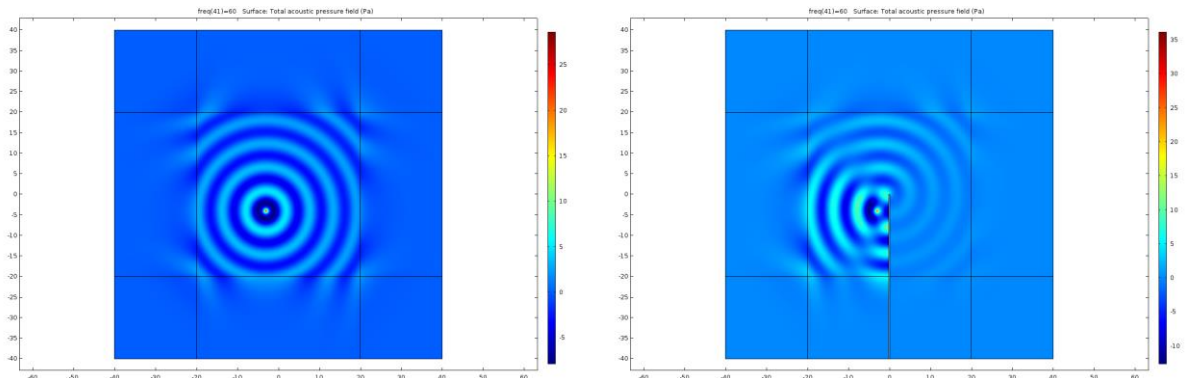


Figure 5. Acoustic pressure without (left) and with (right) a sound barrier (60 Hz)

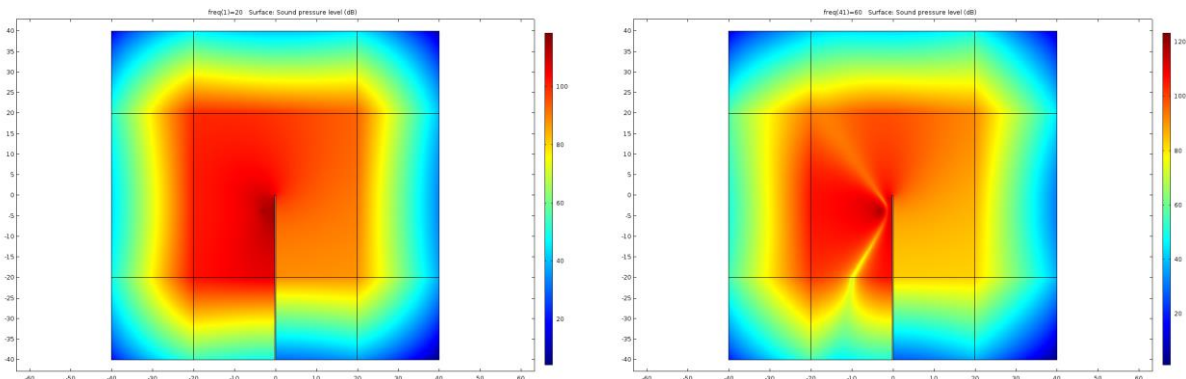


Figure 6. Sound pressure with a sound barrier for 20 Hz (left) and for 60 Hz (right)

Insertion loss for the FEM method was calculated as the difference in sound pressure level at a receiver location with and without the presence of a noise barrier. Results compared with Kurze-Anderson and Tatge equations indicate that there is a difference less than 1 dB and less than 0.3 dB respectively for all frequencies calculated as can be seen in Fig.7.

The results are encouraging and support the idea of the applicability of FEM for the calculation of insertion loss of sound barriers. The results of the Ray Tracing methods are consistent with experimental results [1] which indicate that FEM results could also be consistent with experimental results.

Given that our findings are based on a single source and receiver position, the results from our analyses should be treated with caution. Future research will concentrate in the acoustic behavior of sound barriers in

multiple positions inside and outside the shadow zone of a sound barrier.

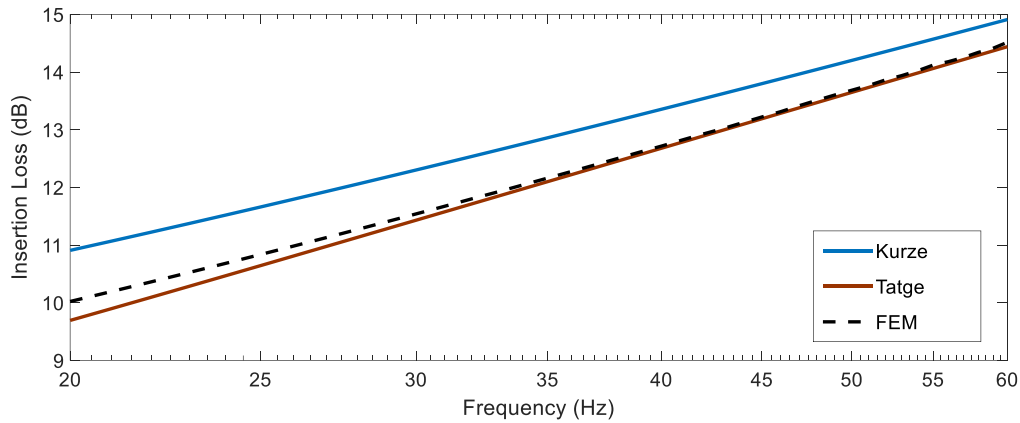


Figure 7. Comparison of Insertion Loss between FEM and Ray Tracing techniques

Another important finding was the importance of correct implementation of PML. Fig. 8 presents an incorrect implementation of the PML that was applied in the beginning of the study. The sound barrier does not extend inside the PML as in the correct implementation presented in Fig.3. Fig.9 depicts the acoustic pressure for the frequency of 60 Hz. It can be seen that diffraction occurs inside the PML in the lower edge of the sound barrier. A direct comparison between Fig.9 and Fig.5 (right) depicts the difference in the acoustic pressure because of the implementation of PML. Fig.10 presents the difference in the calculation of insertion loss with and without the correct implementation of PML. The deviation of insertion loss is due to wave interference from acoustic waves from the lower edge of the sound barrier.

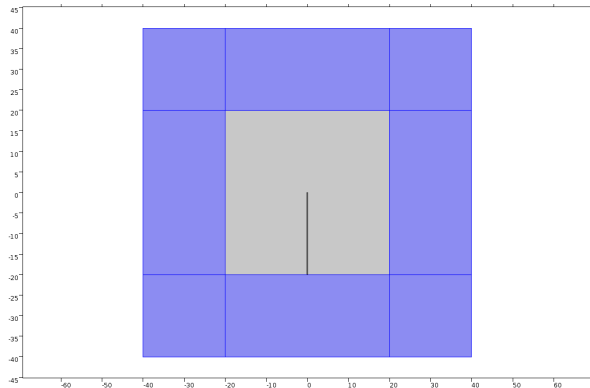


Figure 8. Incorrect implementation of PML

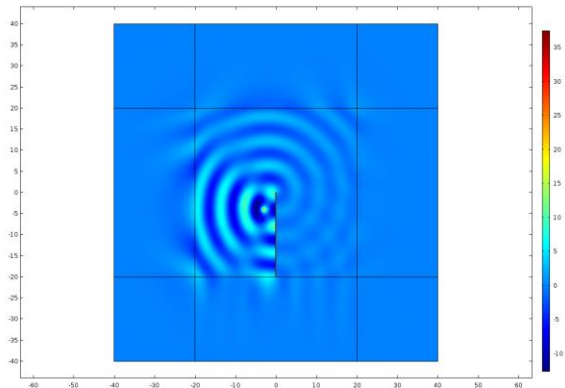


Figure 9. Effects of incorrect implementation of PML on acoustic pressure (60 Hz)

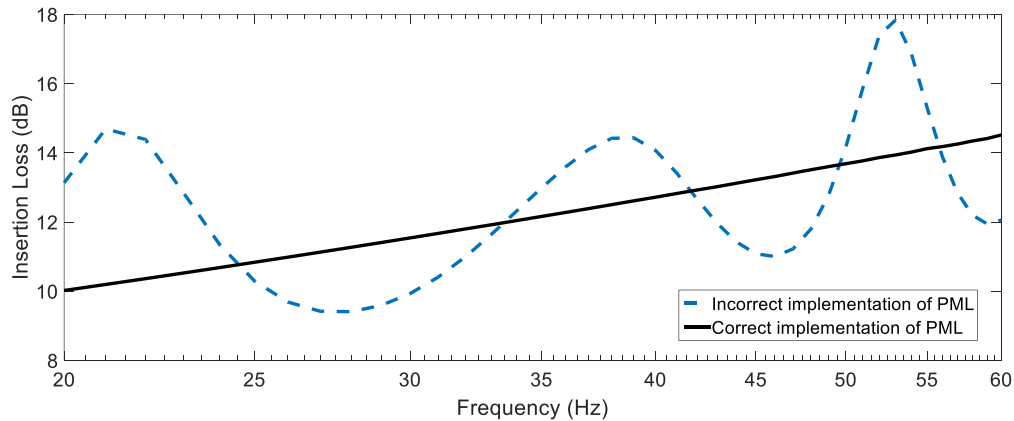


Figure 1. Comparison of Insertion Loss with and without correct implementation of PML

As mentioned in the literature review Ray Tracing techniques are the established methods that are applied in practical applications for predicting the acoustic behavior of sound barriers. However, there are certain drawbacks associated with the use of these techniques. The wave nature of sound is neglected and therefore wave phenomena such as standing waves and wave interference cannot be calculated directly. The basic advantage of a wave based methods such as FEM are that all wave phenomena are included in the theoretical background and thus can be predicted with correct implementation of the method.

We believe that the application of FEM in the field of sound barriers will assist researchers to design and implement new and better designs. The advantages of FEM far outweigh the disadvantages which are mainly computational cost and the long duration for calculation of the results. With the rapid progress of computer technology FEM will become even more applicable for conducting acoustical investigations and carrying out design processes even in the 3d domain. FEM is the computational basis of many computer-assisted design and modeling programs, hence the integration of sound barrier design and modeling can be easily implemented, reduce application cost and spread the usage.

5 CONCLUSION

The accuracy and applicability of FEM have been investigated for the calculation of insertion loss of sound barriers. Results obtained with FEM and Ray Tracing techniques were assessed and the findings support the idea that FEM can be used effectively for accurate modeling of insertion loss. Insights for the correct implementations of PML for sound barriers were also presented.

In our view this study constitutes an excellent step toward further utilization of FEM for the accurate modeling of sound barriers. We have obtained accurate results demonstrating that FEM is a viable alternative to the established methods that are applied in practical applications for predicting the acoustic behavior of sound barriers without certain drawbacks. In the light of our findings, we believe that our analysis may assist researchers to design and implement new and better designs.

Since the present study has only investigated the application of FEM for the calculation of insertion loss of sound barriers in 2d domain we believe our work could be a starting point for further research in a variety of areas. In terms of directions for future work, FEM could be applied for the prediction of the behavior of sound barriers with various shapes and with a profile which absorbs or disperses sound. A fruitful area for further work could be the implementation of optimization and active noise control which can also be modeled with the use of FEM. Finally there is abundant room for further progress in the applicability of FEM for determining the acoustic behavior of sound barriers in 3d space which could lead to effective designs and also custom made designs for specific cases.

REFERENCES

- [1] Maekawa, Z. (1968), "Noise reduction by screens", *Applied acoustics*, Vol. 1(3), pp. 157-173.
- [2] Kurze, U., Anderson, G., (1971), "Sound attenuation by barriers", *Applied Acoustics*, Vol. 4(1), pp. 35-53.
- [3] Tatge, R., (1973), "Barrier-wall attenuation with a finite-sized source", *The Journal of the Acoustical Society of America*, Vol. 53(5), pp. 1317-1319.
- [4] Menounou, P., (2001), "A correction to Maekawa's curve for the insertion loss behind barriers", *The Journal of the Acoustical Society of America*, Vol. 110(4), pp. 1828-1838.
- [5] Li, K., Wong, H., (2005), "A review of commonly used analytical and empirical formulae for predicting sound diffracted by a thin screen", *Applied Acoustics*, Vol. 66(1), pp. 45-76.
- [6] Lam, Y., (1994), "Using Maekawa's chart to calculate finite length barrier insertion loss", *Applied Acoustics*, Vol. 42(1), pp. 29-40.
- [7] Godinho, L., António, J., Tadeu, A., (2001), "3D sound scattering by rigid barriers in the vicinity of tall buildings", *Applied Acoustics*, Vol. 62(11), pp. 1229-1248.
- [8] Monazzam, M., Lam, Y., (2005), "Performance of profiled single noise barriers covered with quadratic residue diffusers", *Applied Acoustics*, Vol. 66(6): p. 709-730.
- [9] Sakamoto, S., Seimiya, T., Tachibana, H., (2002), "Visualization of sound reflection and diffraction using finite difference time domain method", *Acoustical Science and Technology*, Vol. 23(1), pp. 34-39.
- [10] Reiter, P., Wehr, R., Ziegelwanger, H., (2017), "Simulation and measurement of noise barrier sound-reflection properties", *Applied Acoustics*, Vol. 123, pp. 133-142.
- [11] Dae, B., El Nagggar, H., (2017), "3D finite element analysis of composite noise barrier constructed of polyurethane products", *Frontiers of Structural and Civil Engineering*, Vol. 11(1), pp. 100-110.
- [12] Ihlenburg, F., (2006), *Finite element analysis of acoustic scattering*, Springer Science & Business Media.
- [13] Papadakis, N.M., Stavroulakis, G.E., (2018), "Effect of Mesh Size for Modeling Impulse Responses of Acoustic Spaces via Finite Element Method in the Time Domain", *Euronoise 2018*, Heraclion, Crete, 27-31 May.
- [14] Berenger, J.P., (1994), "A perfectly matched layer for the absorption of electromagnetic waves", *Journal of computational physics*, Vol. 114(2), pp. 185-200.
- [15] Liu, Q.H., Tao, J., (1997), "The perfectly matched layer for acoustic waves in absorptive media", *The Journal of the Acoustical Society of America*, Vol. 102(4), pp. 2072-2082.
- [16] Born, M., Wolf, E., (1980), *Principles of optics*, Pergamon, New York.

THE STRUCTURAL INTEGRITY OF UNBURIED OFFSHORE PIPELINES ACROSS ACTIVE TECTONIC FAULTS

Aikaterini E. Triantafyllaki¹, Panos Papanastasiou² and Dimitrios Loukidis³

¹ PhD Candidate

Department of Civil and Environmental Engineering
University of Cyprus
Nicosia, 1678, Cyprus
e-mail: triantafyllaki.aikaterini@ucy.ac.cy

²Professor

Department of Civil and Environmental Engineering
University of Cyprus
Nicosia, 1678, Cyprus
e-mail: panospap@ucy.ac.cy

³Assistant Professor

Department of Civil and Environmental Engineering
University of Cyprus
Nicosia, 1678, Cyprus
e-mail: loukidis@ucy.ac.cy

Keywords: Subsea pipelines, Structural integrity, Fault crossing, Finite-element modelling

Abstract: *This preliminary study addresses the mechanical behavior of unburied steel pipelines crossing active tectonic normal-slip faults. The investigation aims to determine the stresses developed on the steel pipes at fault crossings based on parametric numerical simulation of the nonlinear response of a 3D simplified model. The study is based on finite element analysis that takes into account large strains and displacements and inelastic material behavior. Steel pipes with diameter to thickness ratio and material grade typical for oil and gas pipelines are considered. The analysis is conducted through an incremental application of fault displacement and determines strains developed on the tension and compression sides in the pipe. Appropriate performance criteria of the steel pipeline are defined and monitored throughout the analysis. The results from the present study can be used for the development of performance-based design methodologies for unburied steel pipelines.*

1. INTRODUCTION

There is a steadily growing dependence of the global energy demand on natural gas which is reflected in numbers: one quarter of the total energy demand in the US and Europe is currently satisfied by natural gas delivery [1] while it is projected that by 2040 nearly one quarter of the global electricity will be generated by natural gas [2]. The increasing demand for energy in European countries will require the safe transfer of hydrocarbons from East Mediterranean in the following decades.

Due to the need to transport hydrocarbons from offshore oil & gas fields to onshore treating and export facilities and country markets, offshore pipelines are crossing wide areas with geomorphological and geological conditions that may present a variety of geohazards such as active seismic faults, earthquake-induced liquefaction or slope instability regions. Geohazards impose substantial ground deformations to the pipelines and potentially threaten their integrity. Permanent ground-induced actions due to earthquakes are applied on the pipeline in a quasi-static manner, and are not necessarily associated with severe seismic shaking, but may cause serious plastic deformation to the pipeline, leading to pipe wall fracture and loss of containment [3]. Potential damages and disruptions of a subsea pipeline caused by geohazards may affect the service life and lead to significant financial losses due to service interruptions, explosions and environmental contamination. In the past, extensive damages to pipelines due to surface faulting have been observed during earthquakes, which revealed the fact that the strain demand on pipes crossing active faults can be quite extreme [4].

In Eastern Mediterranean, which is an area characterized by intense seismicity, the risk is high and may lead to pipeline damages or failures, unless appropriate pipeline route is selected based on seismic design. After a literature review, it is concluded that the experience in seismic design of offshore pipelines is rather limited due to the fact that most pipelines are crossing non-seismic or low seismicity regions (e.g. North Sea, West Australia, Gulf of Mexico etc.) and have been constructed without taking into account the seismic hazards. Moreover, there is a lack of sufficient standards and norms worldwide for offshore pipelines crossing active seismic faults. In particular, ISO (2004) and API (2009) do not include specific guidelines for seismic design of offshore pipelines.

In the offshore standard DNV (2012), it is mentioned that additional geohazard studies are required where there is an area with significant historic seismic events or increased geological activity. On the other hand, there are simplistic provisions in the seismic design standards or norms regarding onshore pipelines.

In East Mediterranean there are large areas with active submarine seismicity, faults and tectonic movements that cause large permanent ground displacements. These mechanisms load the pipelines with additional stresses that may cause rupture or buckling resulting in loss of structural integrity. More specifically, the damage mechanisms that may hit the pipeline system include: crossing of the subduction zone and surface faulting, slope instability and settlements, and lateral movements due to soil liquefaction. Surface faulting is an important consideration for pipelines and a major hazard in East Mediterranean, which is characterized by an active subduction zone constituting the boundary between the African and Eurasian tectonic plates.

The evaluation of pipeline response to faulting requires numerical analyses that account for non-linear soil and pipeline behaviour. In this study, 3D nonlinear numerical analysis of a soil-pipe system is carried out using the finite element method. The response of the nonlinear soil-pipe interaction to incrementally applied fault displacements is calculated and the structural behavior of continuous unburied steel pipeline crossing normal-slip fault is examined.

2. STEEL PIPELINES AT FAULT CROSSINGS

Fault crossing is one of the major hazards to offshore pipelines, whether buried or unburied. Numerous investigations have been carried out for different types of ground movements. The pipeline's ability to deform in the plastic range under tension helps prevent rupture at fault crossings. If compression of the pipeline in a fault crossing is unavoidable, the compressive strain should be limited to within the local buckling criteria [5]. The type of faulting and the estimate of soil displacements are the main factors for designing pipelines to resist permanent ground deformation at fault crossings.

Fig.1 shows schematically the different types of surface faulting. The strike-slip fault is associated with horizontal movement of the blocks, whereas normal and reverse faulting is associated with downward and upward block movements.

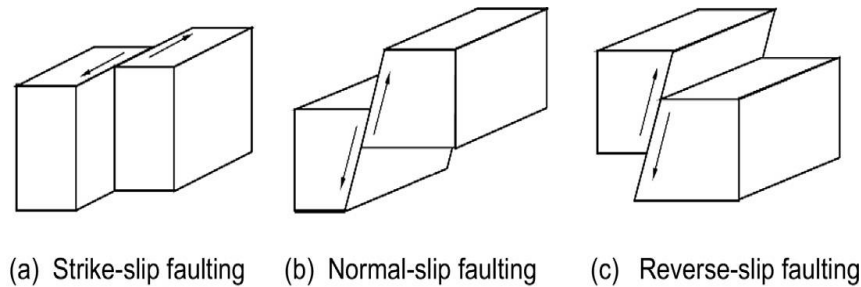


Fig. 1. Classification of surface fault movement [5]

The fault displacement can be estimated using empirical formulas, such as those proposed by Wells and Coppersmith [6]. The median estimate of maximum co-seismic total displacement at the seabed, D (in meters) is given by the expression:

$$D = 10^{a+bM} \quad (1)$$

where M is the earthquake moment magnitude and a and b are fitting coefficients that depend on the fault type. Indicative values of fault-induced ground displacement for two earthquake magnitudes (6.0 and 7.0) are given by Kershenbaum et al. [7]. The fault movements are given as input into the FEA model as a static displacement, as these deformations are considered to be quasi-static, which means that any inertial effects due to rupture propagation in the bedrock may be ignored.

Ground fault type	Coefficients:		Ground displacement D (m) for :	
	a	b	M=6	M=7
Strike-slip	-6.32	0.90	0.120	0.955
Normal slip	-4.45	0.63	0.214	0.912
Longitudinal component			0.152	0.647
Vertical component			0.152	0.647
Reverse-slip	-0.74	0.08	0.550	0.661
Longitudinal component			0.390	0.469
Vertical component			0.390	0.469

Table 1. Indicative values of fault displacement D for major earthquakes [7]

Two seminal analytical methods were proposed under certain assumptions for the fault crossing analysis of pipelines by Newmark and Hall [8] and Kennedy et al. [9]. Kennedy et al. extended the ideas of Newmark and Hall and incorporated improvements in the method for evaluating the maximum axial strain, considering the effects of lateral interaction and the influence of large axial strains on the pipe's bending stiffness. Liu and O'Rourke [10] reported that the Kennedy et al. model for strike slip faulting, which results in axial tension, provides the best match to finite element results, based on an independent comparison of the available analytical approaches.

The axial strains induced to the pipeline at active fault crossing may become fairly large and lead to rupture due to tension or buckling. The nonlinear behaviour of the pipeline steel, the soil-pipe interaction and the second order effects induced by large deformations, make the analyses complicated and demanding. A finite element analysis (FEA) is the most general and versatile tool that allows for a rigorous solution and accurate determination of pipeline stresses and strains at various locations along the pipeline route with a wide range of parameters [5].

3. NUMERICAL MODELING

The structural response of a steel pipeline under normal faulting for earthquake moment magnitude $M=6$ and $M=7$ (Table 1) is examined numerically using the general-purpose finite element program ABAQUS [11]. The nonlinear material behaviour of the steel pipeline and soil, the interaction between them, as well as the distortion of the pipeline are modelled in a rigorous manner and the pipeline performance criteria are evaluated with a high-level of accuracy.

The model that is considered herein is a typical offshore high pressure pipeline with an external diameter (d) of 0.61 m (24 in). Analyses are performed for two different wall thicknesses values, 0.025m ($d/t=24$) and 0.015m ($d/t=41$). The total length of the modelled pipe is 60m, intersecting a fault in the middle of its length. The pipeline model is made of steel API-X70 type, which corresponds to European pipes marked L485. The nonlinear behaviour of the steel pipeline is described by the Ramberg-Osgood model. The yield stress of the steel is equal to 485 MPa and the Young's modulus 210 GPa. Moreover, the parameter of the hardening exponent n is assumed to be equal to 5. The mechanical behaviour of the soil material is described through an elastic-perfectly plastic Mohr-Coulomb material. The unburied pipeline is laying on a clay seabed soil behaving under undrained conditions, with cohesion (undrained shear strength) $c=60$ kPa, friction angle $\phi=0^\circ$, dilation angle $\psi=0^\circ$, Young's modulus $E=25$ MPa and Poisson's ratio $\nu=0.5$. The FE model length is 60m, the width 10m and the depth 5m in order to minimize any boundary effects (Fig. 2).

The unburied pipeline is slightly embedded in the soil prism (Fig. 2b). Pipeline embedment is calculated equal to 0.21 m (34% of d) regarding Verley and Lund method [12]. For the modelling of the cylindrical pipeline segment, the four-node reduced-integration shell elements (type S4R) are employed, while for the soil the eight-node reduced-integration "brick" elements (type C3D8R) are used. The pipeline and the soil interact through a frictional surface-to-surface contact, with the pipe being the slave surface and the upper surface of the soil being the master surface. For the interaction properties between the surfaces the penalty friction contact is assumed. The behaviour in the normal direction is set to allow separation with zero resistance.

The Coulomb friction model is the classic and simplest method to describe the pipe-soil interaction along the soil surface [5]. The friction coefficient which is a material constant related to the soil properties and pipe roughness and in situ conditions, and as such it is not easy to quantify precisely. In this study, different values of the friction coefficient μ will be examined in order to investigate the effect of this parameter to the numerical results.

The numerical analysis consists of two steps, the gravity loading is applied first and then a static analysis step imposes the fault movement at the boundaries of half of the model, using a displacement-controlled scheme, which increases linearly the applied fault displacement D . The fault plane divides the bottom boundary in two parts of equal size. In non-moving half of the model, the bottom boundary is fixed in all directions. In the other half, an incremental fault displacement parallel to the assumed fault plane is gradually applied to the bottom boundary and the vertical boundary perpendicular to the fault axis [13]. The nodes of the rest of the lateral boundaries of the soil prism are fixed in the normal direction. Regarding the boundary conditions of the pipeline, two cases are considered. In both cases, the end nodes of the pipeline are set to be fixed along the axial direction in the non-moving block. In the moving block, the end nodes of the pipeline are released in all directions in the first case, and in the second case the end nodes of the pipeline are set follow the applied movement of the block in the z -direction (axial).

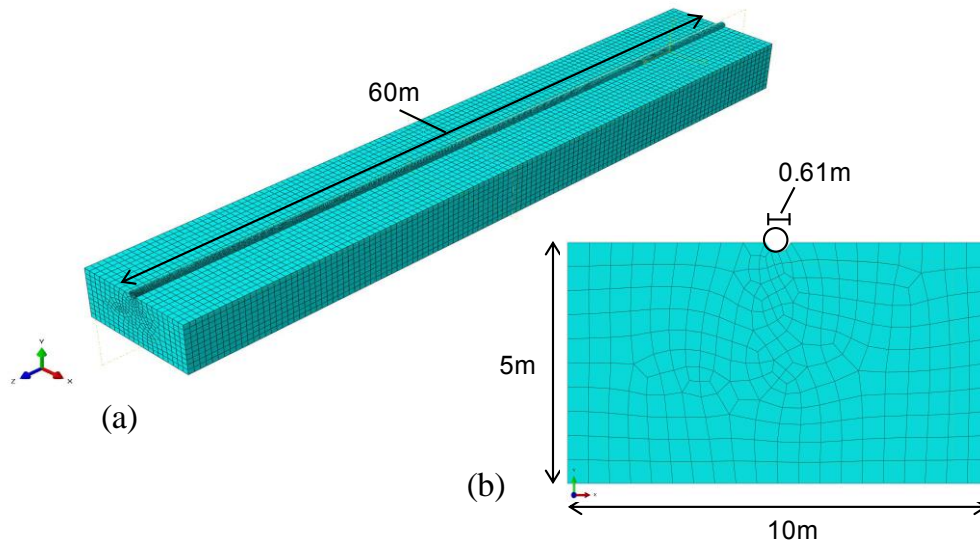


Fig. 2. Finite element mesh a) 3D view b) vertical cross-section.

The angle β between the fault plane and the horizontal plane is assumed to be equal to 60° .

4. NUMERICAL RESULTS

In order to examine the influence of key parameters to the distress of pipelines subjected to fault rupture, a numerical parametric is conducted. The main parameters that are examined are the

- Magnitude of fault displacement D (0.214 m for $M=6$ and $D=0.912$ m for $M=7$)
- Friction coefficient μ between steel pipeline and the soil (0.1, 0.2, 0.3, 0.8, 3.0)
- Pipe wall thickness t (1.5cm and 2.5cm)

Case a (free end)

In this case, the end nodes of the pipeline on the block that the fault displacement is applied are released in all directions. Fig. 3 shows the (exaggerated) deformed shape of the pipeline-soil system after the application of fault displacement for an earthquake of magnitude $M=6$. Figs. 4 and 5 show the von Mises stress for $M=6$ and $M=7$, respectively. Stresses in Fig. 4 are lower (12.6% of the steel yield strength) than those in Fig. 5 (23.4% of the steel yield strength), as expected, since the applied fault displacement is smaller.

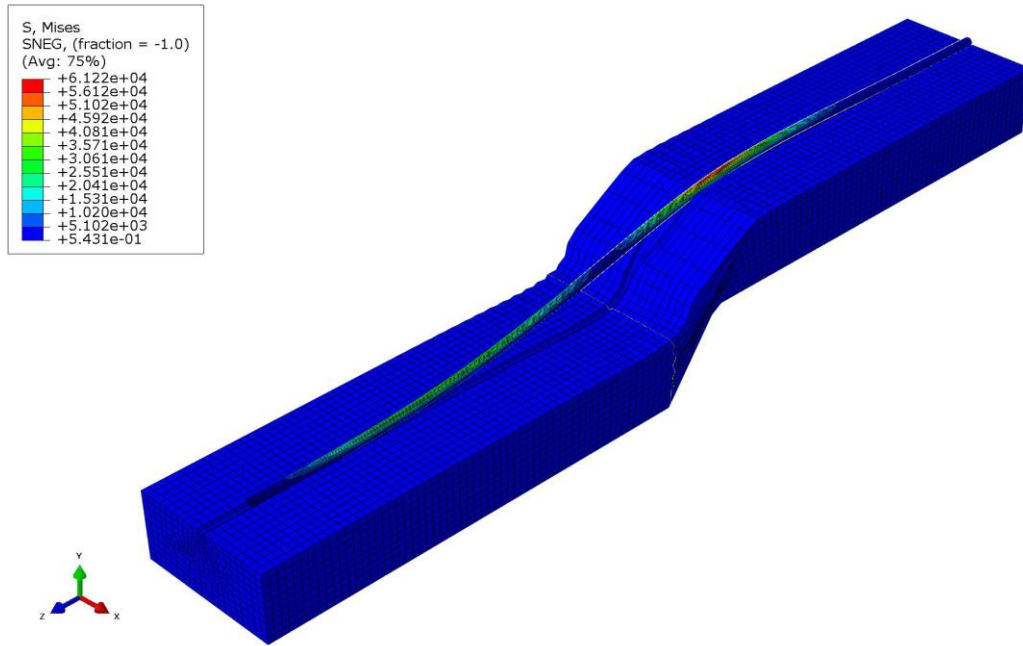


Fig. 3. Deformation of the pipeline-soil system after fault displacement; contours depict the von Mises stress.

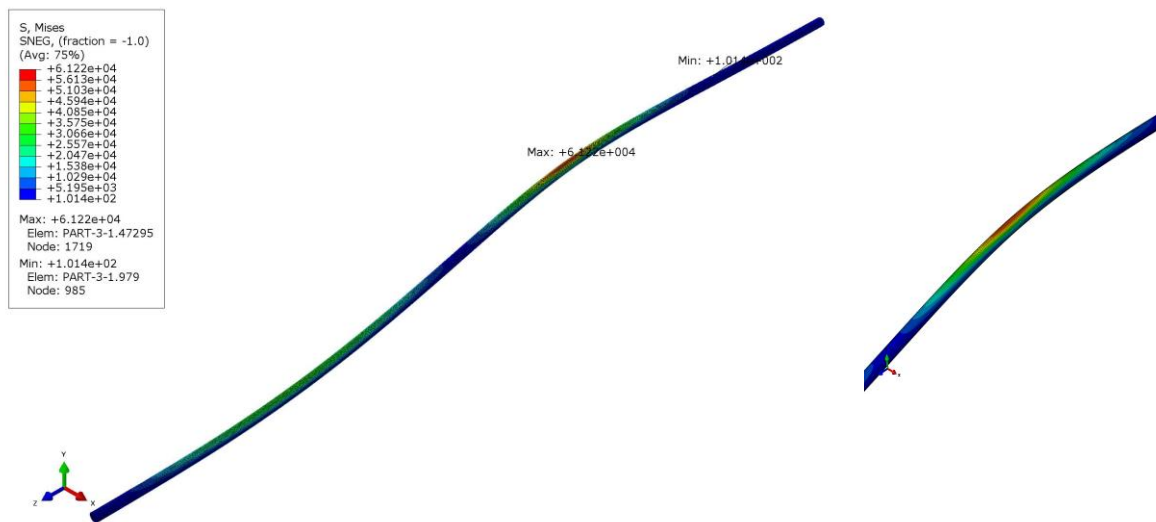


Fig. 4. Von Mises stress for pipe deformation for M=6.

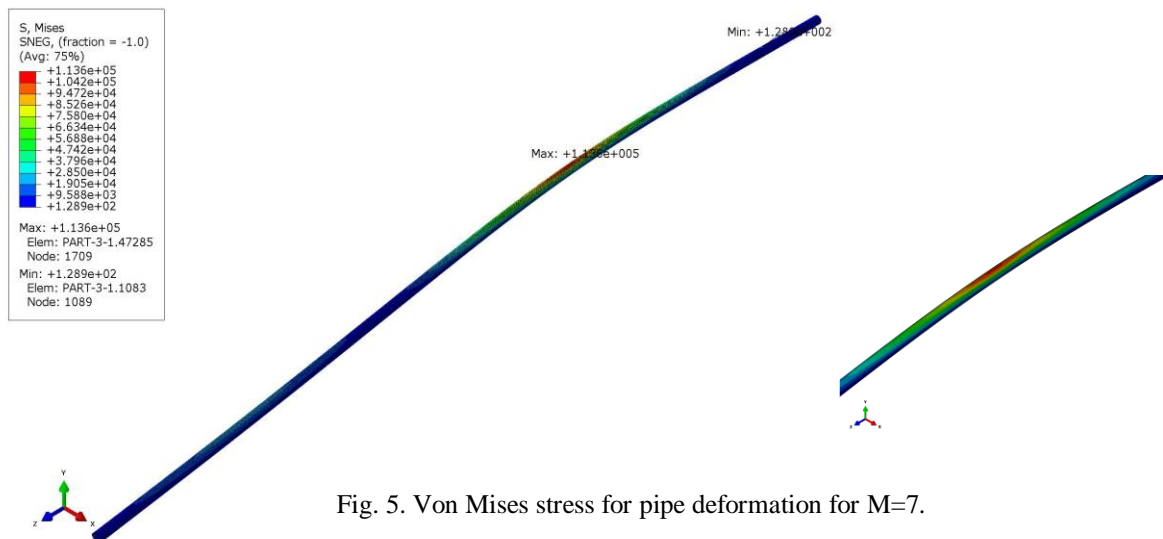


Fig. 5. Von Mises stress for pipe deformation for M=7.

A series of analyses are conducted to assess the effect of the friction coefficient μ for each case of earthquake moment magnitude, $M=6$ & 7 . The value of the friction coefficient has a rather small effect (differences lower than 11%) on the numerical results (Fig. 6), with the von Mises stresses in pipeline for each earthquake moment magnitude remaining lower than the yield stress of the X70 pipeline, which is 485 MPa. That leads to the conjecture that the case of normal fault does not produce a significant amplification of the stresses.

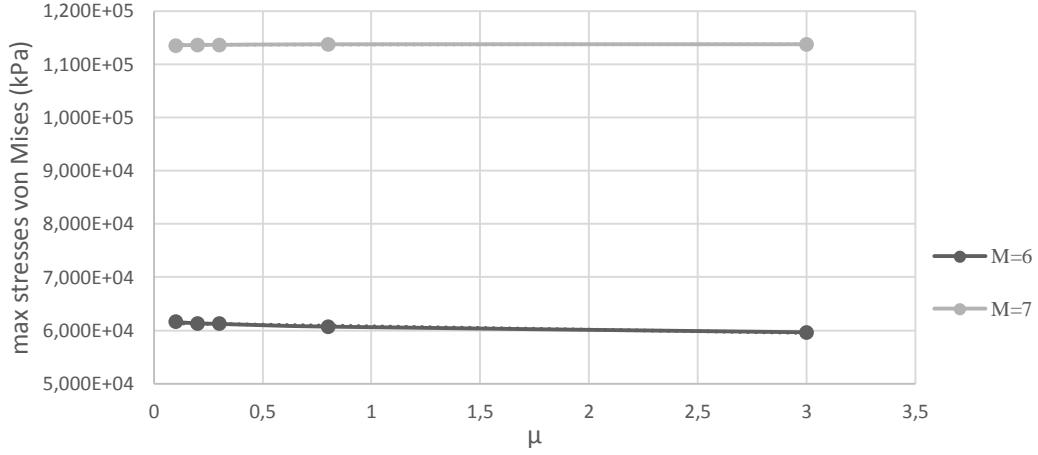


Fig. 6. Maximum von Mises stresses in pipeline for different values of μ .

Two pipe thicknesses are investigated for the high strength steel pipe properties X70, namely 0.025 m ($d/t=24$) and 0.015 m ($d/t=41$) were chosen to examine each case for earthquake moment magnitudes ($M=6$ & 7). The friction coefficient is set equal to $\mu=0.3$. Higher stresses are developed in the pipeline with a high d/t making them more vulnerable than the pipelines with a low d/t (Fig.7). Furthermore, for the high d/t ratio, deformations and distortion of the pipeline starts at smaller fault movements.

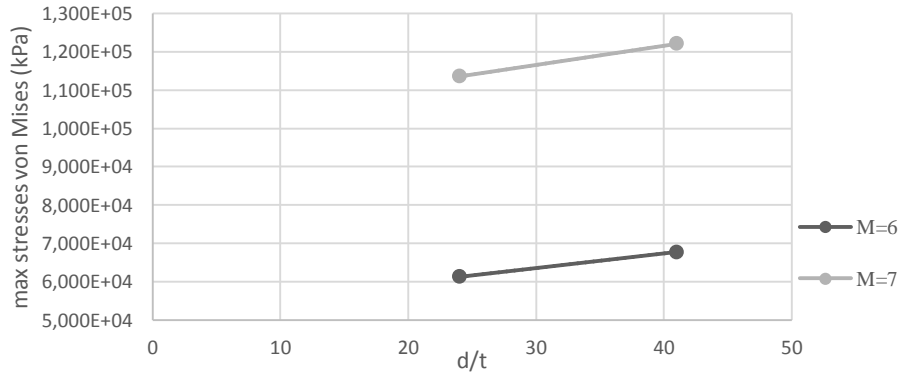


Fig. 7. Maximum von Mises stresses in pipeline for two different d/t ratios

Case b (fixed end)

In case b, the end nodes of the pipeline follow the movement of the moving block in z-direction whereas on the other end the nodes are fixed. Fig. 8 shows the deformed model of pipeline-soil system. Figs. 9 and 10 show the von Mises stress in the pipeline after a fault displacement generated by an earthquake of magnitude $M=6$ and $M=7$, respectively. Stresses in Fig. 9 are almost 50% lower (74.2% the steel yield stress) than in Fig. 10 since the applied fault displacement is smaller. However, unlike case a, the von Mises stress for $M=7$ exceeds the yield strength of the X70 steel of 485 MPa (126.9% of the steel yield stress). Hence, case b suggests that normal faulting can produce a significant amplification of the pipeline stress.

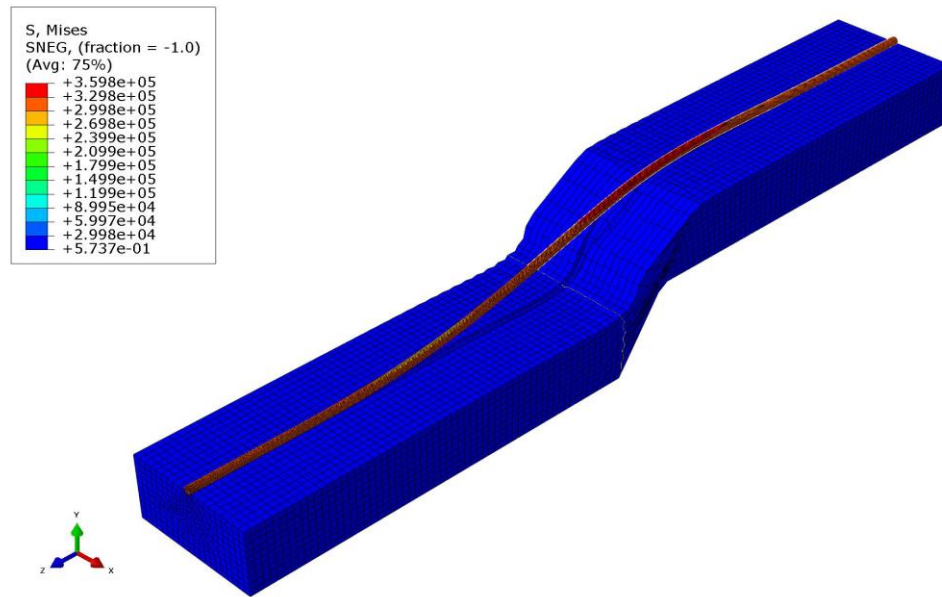


Fig. 8. Deformation of the pipeline-soil system after application of fault displacement; finite element results depict the von Mises stress

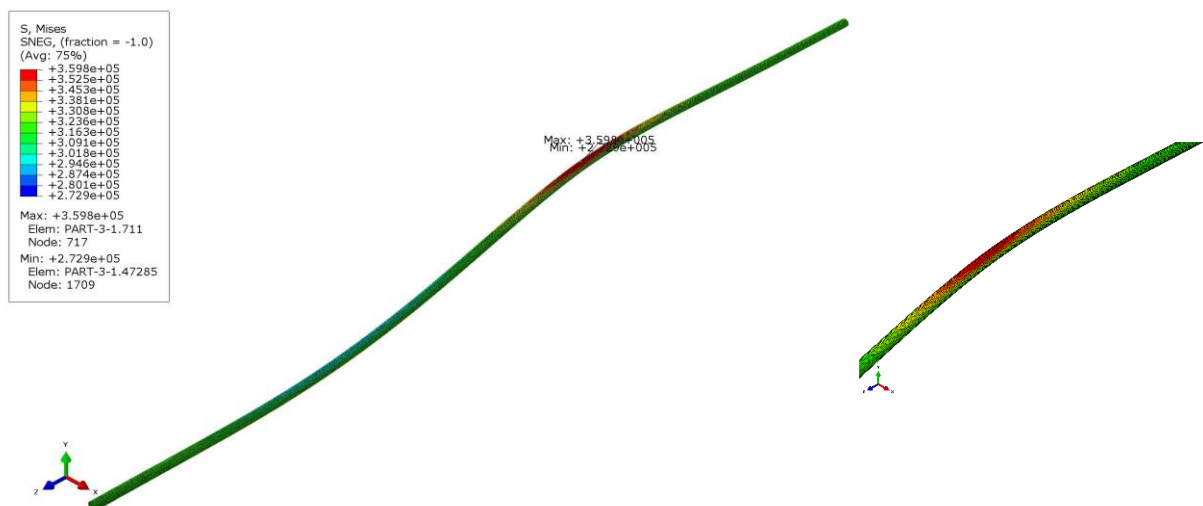


Fig.9. Determined von Mises stress pipe deformation for M=6.

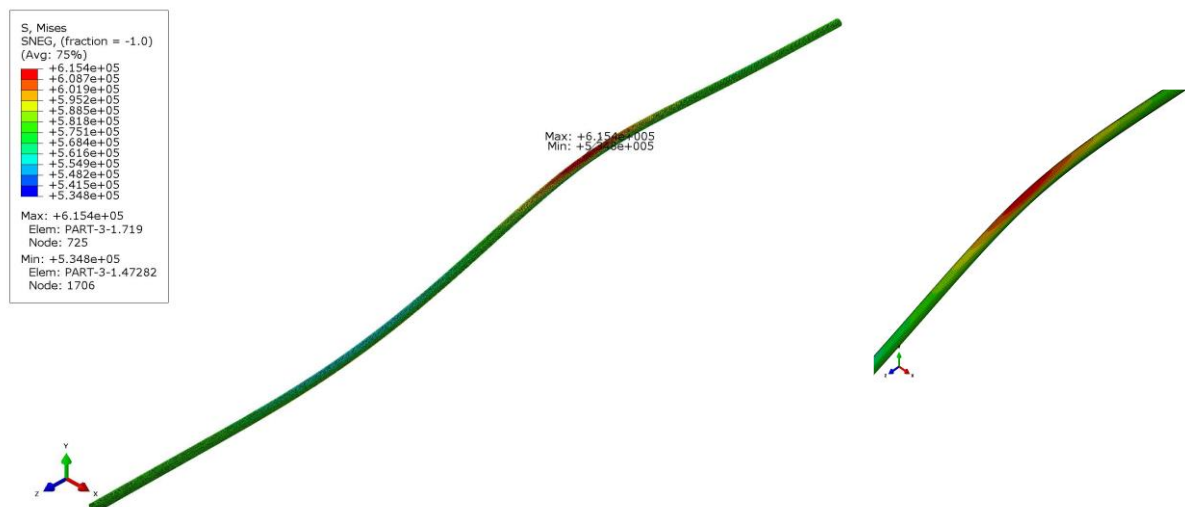


Fig. 10. Determined von Mises stress pipe deformation for M=7.

Similarly to case a, the parameter μ has a negligible effect on the numerical results (Fig. 11).

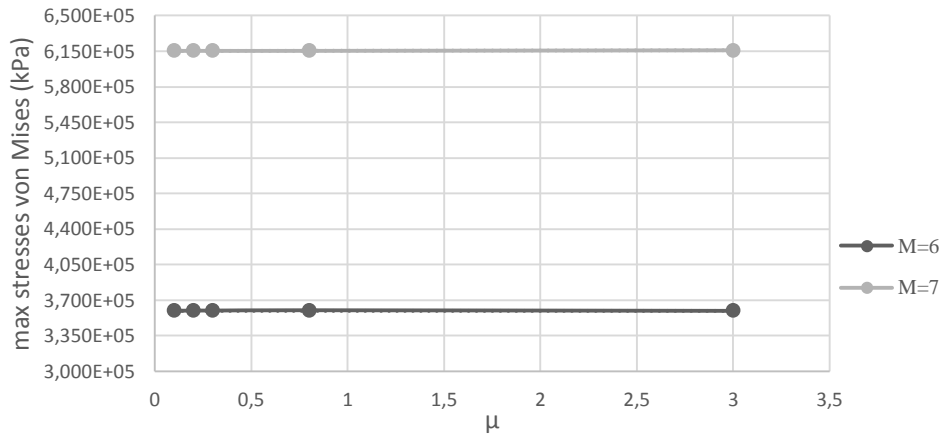


Fig. 11. Maximum stresses von Mises in pipeline for different values of friction coefficient μ .

Again, two thicknesses 0.025 m ($d/t=24$) and 0.015 m ($d/t=41$) are examined for each case of earthquake moment magnitude $M=6$ and 7. The friction coefficient between the surface of the steel pipeline and the soil surface is maintained equal to $\mu=0.3$. Fig. 12 shows the maximum von Mises stress in pipeline for the two different d/t ratios. The results, for the boundary condition of case b, show that the pipeline thickness does not have any influence on the developed von Mises stress. It has to be pointed out that in this study the initial (before fault rupture) pipeline stresses due to the difference in internal and external pressures are ignored.

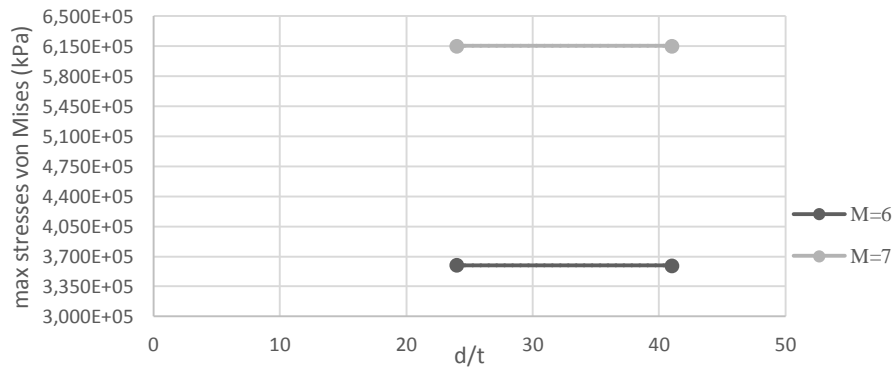


Fig. 12. Maximum von Mises stress in pipeline for two different pipe diameter to thickness ratios.

5. CONCLUSIONS

The development of advanced numerical methods over the last decades and their application to geotechnical engineering problems, such as the soil-pipeline interaction, provide offshore engineers with an extremely powerful analysis tools. Using an advanced finite element simulation tool, the stress and deformation response of unburied steel pipelines crossing normal faults with a dip angle of 60° was examined. A detailed 3D nonlinear static pipe-soil interaction model, which takes into account the inelastic soil and pipeline material behaviour, was used. The pipeline material behaviour is assumed to be independent of the slip rate and the temperature, and the internal and external pipe pressures are currently ignored. The main objective of this study is the investigation of the combined effects of the earthquake moment magnitude, the friction coefficient between steel pipe and soil, and the pipe-wall thickness. The following preliminary conclusions can be made:

- The applied boundary condition at the pipeline end that lies in the moving block can affect significantly the obtained results. Two extreme cases have been examined (fully free and fully fixed end) and the real conditions of the pipeline are expected to lie between these two bounds.
- A strong influence of the pipeline diameter-to-thickness ratio d/t was found for the case of a free moving pipeline boundary.
- Variation of the friction coefficient μ value has a small to negligible effect on the numerical results in both cases.

- Higher stresses develop with increasing fault movement, but these remain far below the yield stress of the high strength steel in the case of a free moving pipeline boundary. However, in the case of a fixed boundary for an earthquake of magnitude $M=7$, the stresses overcome the yield stress of the steel pipeline. This leads to the conclusion that a proper boundary condition for the pipeline needs further investigation.

ACNOWLEDGEMENTS

This research is supported by the Petroleum Engineering Program of the University of Cyprus.

REFERENCES

- [1] Regulation (EU) No 994/2010 of the European Parliament and of the Council of 20 October 2010 concerning measures to safeguard security of gas supply and repealing Council Directive 2004/67/EC. Off J Eur. Union 2010: pp. 1–22.
- [2] International Energy Agency. World energy outlook 2015.
- [3] Vazouras, P., Karamanos, S. A. & Dakoulas, P. (2012), “Mechanical behaviour of buried steel pipes crossing active strike-slip faults.” *Soil Dynamics and Earthquake Engineering*, 41, 164-180. doi:10.1016/j.soildyn.2012.05.012
- [4] Takada, S., Hassani, N., & Fukuda, K. (2001), “A new proposal for simplified design of buried steel pipes crossing active faults.” *Earthquake Engineering & Structural Dynamics*, 30(8), 1243-1257. doi:10.1002/eqe.62
- [5] Bai Q., Bai Y. (2014). *Subsea Pipeline Design, Analysis, and Installation*. Elsevier Inc.
- [6] Wells D. L. and Coppersmith K.J. (1994), “New empirical relationships among magnitude, rupture length, rupture width, rupture area, and surface displacement.” *Bulletin of the Seismological Society of America*, 84(4), 974-1002, 1994.
- [7] Kershenbaum, N., Mebarkia, S. & Choi, H. (2000), “Behaviour of marine pipelines under seismic faults.” *Ocean Engineering*, 27(5), 473-487. doi:10.1016/s0029-8018(98)00079-1
- [8] Newmark N. M., Hall W.J. (1975), “Pipeline Design to Resist Large Fault Displacement.” *Proceedings of the 1975 U.S. National Conference on Earthquake Engineering*. Ann Arbor. Michigan. pp. 416-425
- [9] Kennedy R.P., Chow A.W. & Williamson R.A. (1977), “Fault movement effects on buried oil pipelines.” *Journal of the Transportation Engineering Division*. ASCE, 1977. vol. 103, pp. 617-33
- [10] Liu X., O'Rourke M.J. (1999), “Response of buried pipelines subject to earthquake effects.” *Multidisciplinary Centre for Earthquake Engineering Research*. Monograph No. (1999), p. 3
- [11] ABAQUS. Users' Manual. Simulia, Providence, RI, USA. 2016
- [12] Verley R R, Lund KM. (1995), “A soil resistance model for pipelines placed on clay soils.” *In Proceedings of OMAE '95*, vol. 5. Pipeline Technology, Copenhagen. 1995
- [13] Loukidis, D., Bouckovalas, G. D. & Papadimitriou, A. G. (2009), “Analysis of fault rupture propagation through uniform soil cover.” *Soil Dynamics and Earthquake Engineering*, 29(11-12), 1389-1404. doi:10.1016/j.soildyn.2009.04.003

NUMERICAL STUDY OF OFFSHORE NATURAL GAS PIPELINES SUBJECTED TO SUBMARINE LANDSLIDES

Dionysios Chatzidakis¹, Yiannis Tsompanakis^{2*} and Prodromos N. Psarropoulos³

¹School of Environmental Engineering
Technical University of Crete
Chania, GR-73100, Greece
e-mail: chatzidakis_d@hotmail.com

²School of Environmental Engineering
Technical University of Crete
Chania, GR-73100, Greece
e-mail: jt@science.tuc.gr

³School of Rural and Surveying Engineering
National Technical University of Athens
Athens, GR-15780, Greece
e-mail: prod@central.ntua.gr

Keywords: Numerical Simulations, Offshore Pipelines, Geohazards, Submarine Landslides, Kinematic Distress, Mitigation Measures.

Abstract. *Natural gas is undoubtedly one of the main energy sources of our era with increasing demand and continuous exploitation of new onshore and offshore deposits. The transportation of natural gas to the urban and industrial centers is frequently accomplished via large-scale pipeline networks. These networks often consist of offshore parts, placed on the seabed in big depths, extending for hundreds of kilometers. Such pipelines are very important infrastructures, since any possible damage may cause serious problems and devastating consequences on the environment and the economy. Geohazards, such as strong ground motion, active faults, offshore landslides and debris flows, tsunamis, etc, consist the most crucial threats that an offshore pipeline has to overcome. The purpose of this work is to study numerically, utilizing the finite element method and realistic data from the offshore part of the Trans Adriatic Pipeline (TAP), the kinematic distress of offshore natural gas pipelines due to submarine landslides. Firstly, numerical models are developed and compared with available analytical and numerical solutions. Subsequently, the use of efficient mitigation measures, such as anchor points, in different positions along the pipeline route is examined in order to reduce its vulnerability in an optimal techno-economical manner.*

1 INTRODUCTION

Hydrocarbons, such as oil and natural gas, have been used as an energy source since the first industrial revolution in the 19th century and to date thousands of kilometers of onshore and offshore pipelines have been constructed for their transfer. The fact that onshore pipelines have been constructed several decades earlier than offshore pipelines, has prompt several researchers to investigate their response under geohazards and other hazards, which has led to national and international standards and guidelines for their efficient design. For instance, American Lifeline Alliance (ALA), Eurocode 8, and ISO 19900–19906 are the outcome of this research. On the other hand, offshore pipelines are far from that level, since there is no similar experience yet and deep water soil conditions are highly adverse and difficult to determine.

Offshore pipelines may extend for hundreds of kilometers, from shallow to deep water. While shallow water pipelines are usually buried, deep water pipelines are often placed directly on the seabed. This makes them more vulnerable to geohazards that a buried pipeline may easily overcome, such as soil liquefaction, offshore landslides and debris flows. In the wider South-Eastern region of Europe there is an increasing activity regarding offshore pipelines with several large-scale projects being constructed or planned, such as Blue Stream, Turkish Stream and East Med projects. Trans Adriatic Pipeline (TAP) is an under construction project of a 878 km long pipeline connecting Greece, Albania and Italy. The offshore part of the pipeline is 105 km, reaching the depth of 820 m in the Adriatic Sea. According to the TAP project [1, 2], the deep water offshore part of the pipeline is considered for depths greater than 200 m, where the pipeline is directly laid on the seabed.

The investigation of offshore pipelines under kinematic distress due to geohazards can be separated into three parts: the pipe-soil interaction determination, the impact force assessment and the pipeline response assessment utilizing experimental, analytical and numerical models. The international recommended practice guidelines DNV GL [3] (Det Norske Veritas – Germanischer Lloyd) consist a first attempt to summarize the gained experience by introducing a coherent proposal of pipe-soil interaction modeling for various soil conditions, such as fine or coarse grained soils, drained or undrained response, etc. Other noteworthy works are the studies by Bruton et al. [4] and White and Cheuk [5], which investigate the axial and lateral pipe-soil interaction based on experimental results, while Randolph et al. [6] and Wang and Yang [7] deal with the axial pipe-soil interaction.

Considering the impact force assessment, Zakeri et al. [8, 9]-taking into account experimental data- derived analytical expressions for calculating the drag force on offshore pipelines depending on parameters such as soil conditions, slope and intersection angles, etc. Subsequently, Randolph & White [10] and Liu et al. [11] improved initial flaws of the analytical formulas taking into account additional parameters.

The investigation of kinematic distress due to geohazards necessitates the accurate response assessment of pipelines through experimental, analytical and numerical models. Nonetheless, only a limited number of numerical and analytical approaches can be found in the recent literature. Parker et al. [12] presented an analytical model that investigates the case of landslide impact vertical to the pipeline axis. Subsequently, Randolph et al. [13] and Yuan et al. [14] presented both analytical and numerical models for the same problem.

The objective of the current work is to investigate numerically the kinematic distress of the deepest offshore part of TAP pipeline subjected to lateral landslide impact. The pipeline and soil properties used are realistic as they are derived from the TAP project description and geotechnical survey [1, 2]. The pipe-soil interaction simulation is considered according to the DNV GL [3] using the soil properties of the investigated area. Firstly, the proposed numerical model is compared with the results of the aforementioned analytical and numerical models. Subsequently, various landslide widths and forces are applied, while the use of anchor points in different positions along the pipeline route is examined in order to reduce the vulnerability of the pipeline.

2 PROBLEM AND MODEL DEFINITION

Geohazards like offshore landslides and debris flows are frequent phenomena on the seabed, even for small slope angles (e.g., 1° - 5°), due to the presence of fine-grained saturated soils. Earthquakes or underwater currents are the two main causes that can trigger such phenomena. The numerical simulation of a deepwater offshore pipeline subjected to a lateral landslide and based on realistic data is described in the sequence.

2.1 Problem description

Figure 1 depicts the investigated case of a surface laid pipeline under lateral loading due to a landslide or a debris flow. It is noted that common practice suggests offshore pipelines when crossing a landslide prone area should be placed either vertical or parallel to the anticipated soil movement. The pipeline is considered to be straight and “free” along both sides adjacent to the landslide area, i.e., no anchors, wellheads, or curvatures. Additionally, the seabed is considered to have constant bottom depth and soil characteristics along the investigated area.

The above situation is not an idealization, but it can represent real conditions, as it will be discussed in the sequence. The upper and side view of the selected case are illustrated in Figure 1, in which F_L is the lateral and F_A the axial pipe-soil interaction forces per unit length, while the vertical pipe-soil interaction is not taken into account. Q_L is the lateral load due to the kinematic distress, which is parallel to the seabed bottom. The pipeline is considered to be embedded on the seabed in a depth, z , due to its own weight and the laying process. The slope angle, ϕ , is considered to be almost zero, thus, the vertical force, V , is equal to the pipe weight.

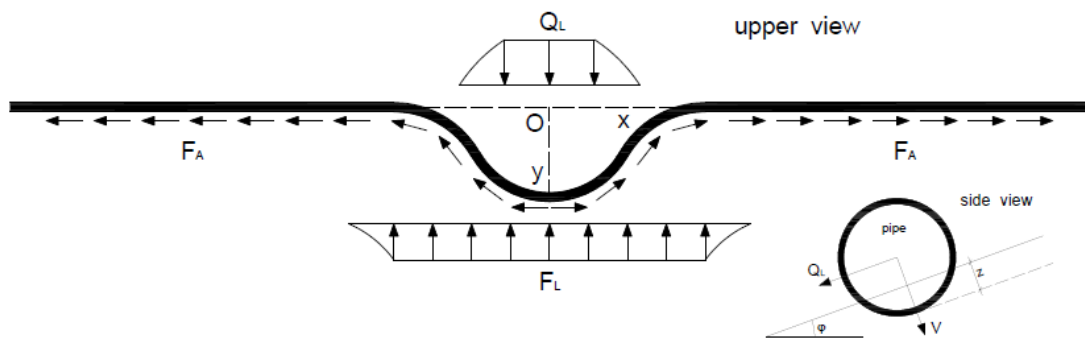


Figure 1. Upper and side view of the pipeline configuration

2.2 Soil and pipeline characteristics

In order to examine a realistic case, the deepest part of the Trans Adriatic Pipeline (TAP) is selected. As illustrated in Figure 2, the pipeline crosses an area of several kilometers on a straight line in the middle of the Adriatic Sea. The seabed terrain is flat (inclination $\phi \approx 0.1^\circ$), with constant bottom depth about 800 m, and the seabed consists of a 6 m depth soft clay layer. According to TAP report [1], the characteristic soil parameter values for the aforementioned part are the unit weight, $\gamma = 14.5 \text{ kN/m}^3$, the internal soil friction angle, $\phi = 25^\circ$ and the undrained shear strength, $s_u = 1 + 1.17 z \text{ (kPa)}$, for $0.0 < z < 6.0 \text{ m}$, where z is the soil depth.



Figure 2. The examined offshore area of the Trans Adriatic Pipeline [2]

The above soil parameter values were used in order to calculate the lateral and axial soil resistance forces according to DNV GL [3]. It is worth mentioning that DNV GL recommendations idealize the axial resistance using both tri-linear and bi-linear models and the lateral soil resistance using always a tri-linear model, as depicted in Figure 3. Axial reaction depends on the level of drainage, while lateral reaction takes under consideration the embedment of the pipeline. As shown in Figure 3, F_A is the axial soil resistance force per unit length, F_L is the lateral resistance force per unit length, while x and y denote the axial and lateral relative displacements. Subscripts “brk”, “res” and “mob” correspond to breakout, residual and mobilization resistance forces and displacements, respectively. Only the tri-linear formulation for both axial and lateral directions is examined herein. The soil resistance forces and corresponding displacements, as calculated using DNV GL [3], are depicted in Table 1.

The pipeline characteristics were taken from TAP report [2] for the deep water part of the pipeline, i.e., over 200 m depth. The pipeline has an outer diameter, $D = 945 \text{ mm}$, a wall thickness, $t = 37 \text{ mm}$ and the steel grade is API 5L X65 (Young’s modulus, $E = 210 \text{ GPa}$, Poisson’s ratio, $\nu = 0.3$, yield strength $f_y = 448 \text{ MPa}$, ultimate strength $f_u = 531 \text{ MPa}$ and maximum elongation 18%). The pipeline has a protection of an anti-corrosive coating of polyethylene with a thickness of $t_{\text{coating}} = 3 \text{ mm}$. The internal pressure of the pipe is 7.5 MPa and the external pressure is approximately 8 MPa due to the 800 m sea depth.

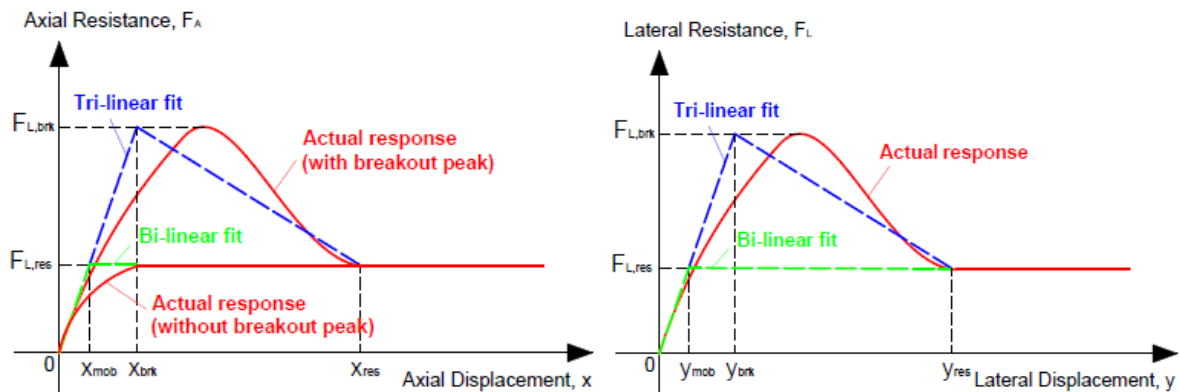


Figure 3. Axial (left) and lateral (right) pipe-soil interaction idealization

Force (kN/m)	Displacement (mm)
$F_{A,brk} = 0.8$	$x_{brk} = 5$
$F_{A,res} = 0.75$	$x_{res} = 30$
$F_{L,brk} = 1.7$	$y_{brk} = 93$
$F_{L,res} = 0.8$	$y_{res} = 1427$

Table 1. Soil resistance forces and corresponding displacements

2.3 Numerical model configuration

The problem is modeled numerically utilizing the finite element method (FEM), using ABAQUS software [15]. Taking into consideration that the problem is symmetrical and plane, half of the pipeline in 2-D conditions is simulated, as shown in Figure 4, in order to reduce the computational cost. The left end of the model corresponds to the middle of the landslide and an x-symmetrical boundary condition is implemented (fixed in XX' direction, fixed rotation and free movement in YY' direction), while the right end of the pipe is fixed. The drag force due to the landslide is considered uniform along the landslide length B. The pipeline finite element length is equal to 0.5 m along the whole length of the pipeline for small models, i.e., up to 3 - 4 km long. For bigger models, a gradually increasing element length, from 0.5 m to 4 m, was implemented along the expansion length of the pipeline, L_{exp} , in order to minimize the computational cost. Both axial and lateral resistances are taken into account in all three parts, while vertical soil resistance is neglected everywhere.

The pipeline is modeled with Timoshenko beam elements, utilizing the pipeline element PIPE21 of ABAQUS [15]. As shown in Figure 5, these elements have one integration point on the axial direction and four along the cross section. This pipeline configuration enables the implementation of both internal and external pressures in order to represent the gas and hydrostatic pressure, respectively. Considering the soil resistance, pipe-soil interaction elements (PSI24) were used to represent both lateral and axial soil resistances. These are four-noded plain elements with two nodes attached to the pipe and two representing the far field conditions, which are considered as fixed in this study. The direction of both axial and lateral reaction forces is adjusted according to the pipeline movement. Large displacements, nonlinear plastic strains and geometrical nonlinear response are taken into account in a computationally efficient manner.

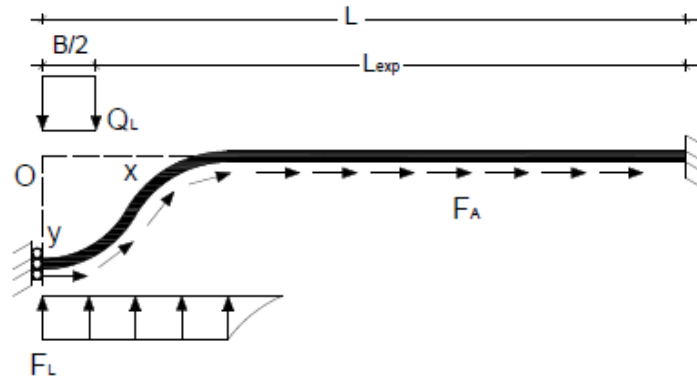


Figure 4. Numerical model configuration

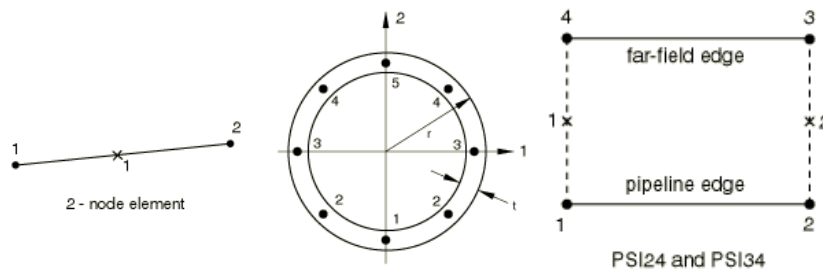


Figure 5. PIPE21 element (left) and PSI24 element (right) with their integration points [15]

3 VALIDATION AND COMPARISON

In order to validate the numerical methodology developed herein, its results are compared with those obtained from the analytical approaches of Randolph et al. [13] and Yuan et al. [14] and also with the numerical results of the later study. In both analytical approaches the landslide impact is simulated as a linear drag force, while the pipeline non-linear response is not taken into account and the elastic beam theory of Euler-Bernoulli is adopted for the simulation of the pipeline. In addition, it is noted that axial friction is neglected in both models in the segments where the lateral soil resistance is non-zero and has a constant value thereafter. Regarding the differences between the two studies, Randolph et al. [13] consider a rigid-plastic model for the lateral soil resistance, which results in constant lateral soil resistance until the lateral displacement of the pipe is almost zero. On the other hand, Yuan et al. [14] consider that the lateral soil resistance exhibits an elastic-plastic bi-linear behavior. Moreover, Randolph et al. [13] assume the axial tension constant until the zero lateral displacement point, while Yuan et al. [14] consider the horizontal component of the axial tension constant, which takes into account the effect of lateral soil resistance. Finally, the model of Randolph et al. [13] has a discontinuity in the bending moment at the zero lateral displacement point, while this is not the case for the model of Yuan et al. [14].

The numerical approach of Yuan et al. [14] is based on a vector form intrinsic finite-element method (VFIFE) implementation, introduced by Ting et al. [16]. The pipeline is discretized into a series of nodes and elements, with the mass of the pipeline concentrated on the nodes. The pipeline movement is discretized into a small time steps with small deformations and constant material properties and pipe dimensions in each step.

Initially, in order to compare the results of the proposed numerical approach with the aforementioned analytical and numerical models, the pipeline properties and loading conditions of Yuan et al. [14] models were implemented. More specifically, the values of pipeline outer diameter and thickness were taken equal to, $D = 600$ mm and $t = 25$ mm, respectively. The drag force was considered equal to $Q_L = 6$ kN/m along a landslide width of $B = 120$ m. The maximum lateral and axial soil resistance forces were considered equal to $p_0 = 3$ kN/m and $f_0 = 0.5$ kNm, respectively. Finally, the elastic modulus and the Poisson's ratio were taken equal to $E = 210$ GPa and $\nu = 0.3$, respectively. It is noted that the proposed model was examined for six different element lengths, from 0.25 m to 4 m, with small differences among them regarding both lateral displacement and axial force. The element length of 0.5 m was chosen in order to maximize the accuracy of the computations.

Figures 6 and 7 illustrate the normalized pipeline displacements and the normalized axial forces obtained by the analytical approaches of Randolph et al. [13] and Yuan et al. [14], the numerical approach of the later study and the proposed numerical model. As shown in Figure 6, all models have similar response considering both the maximum pipeline displacement and the displacement pattern along the pipeline. However, the analytical model of Yuan et al. [14] presents a slightly higher lateral displacement and the analytical model of Randolph et al. [13] presents considerable response differences along the pipeline route.

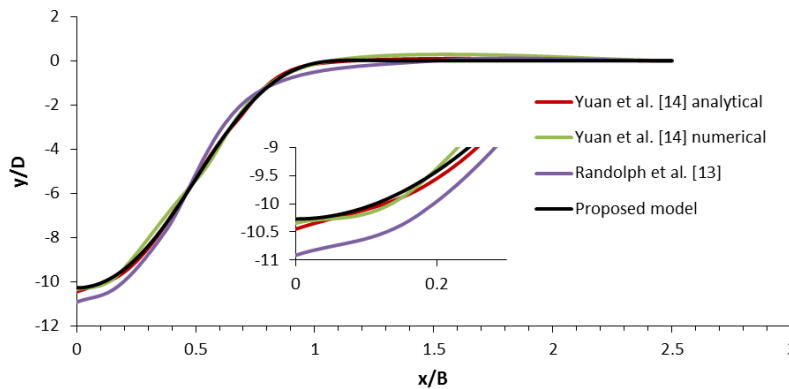


Figure 6. Comparison of normalized pipeline displacements

Considering the axial tension shown in Figure 7, the two numerical models present similar response after the landslide area ($x/B > 0.5$), while they have significant discrepancies within the landslide region. The proposed model presents maximum axial tension in the middle of the pipe and decreases thereafter, while the numerical model of Yuan et al. [14] presents maximum axial tension at distance $x/B = 0.17$. The discrepancies are justified due to the fact that the proposed model takes into consideration geometrical nonlinearities. Yuan et al. [14] analytical approach underestimates the axial tension in the landslide area, while it overestimates the axial tension in the remaining part of the pipeline. Furthermore, the maximum axial tension point is located approximately at the end of the landslide ($x/B = 0.5$) in contrast to the numerical models. This is observed because the axial soil resistance is omitted. In the analytical model of Randolph et al. [13] the axial tension remains constant along the

pipeline up to a distance of $x/B = 1$ and is significantly smaller compared to the other three approaches. This is attributed to the fact that the axial soil resistance is not taken into account and the axial tension is considered constant.

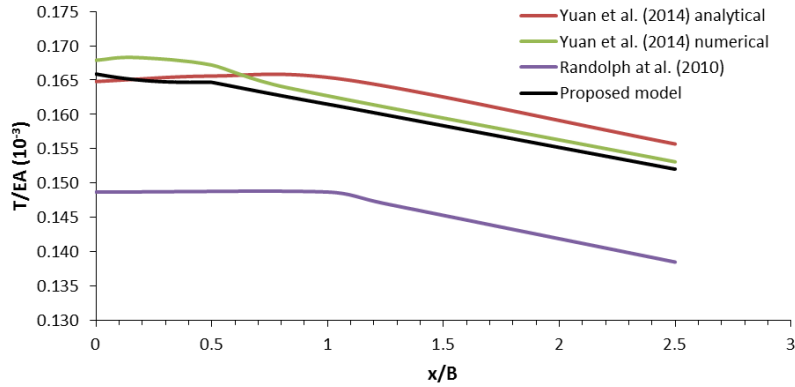


Figure 7. Comparison of normalized pipeline axial forces

4 PARAMETRIC STUDY

After the verification of the numerical approach, a detailed parametric investigation has been conducted in order to investigate the influence of different landslide forces and landslide lengths on the pipeline response. As aforementioned, the pipeline and soil characteristics used in this parametric study are taken from the TAP project, as described in details in Section 2. Due to space limitations, indicative results and discussions are presented in the sequence.

4.1 Landslide drag force

Considering the landslide force influence, four different drag forces were implemented: $Q_L = 5, 10, 20$ and 20 kN/m. The landslide length for all the above cases is constant and equal to $B = 300$ m. As illustrated in Figure 8, larger drag force results in larger lateral normalized displacements, y/D , while a longer part of the pipe is moving laterally. The maximum absolute lateral movement of the pipe in every case is 38.13, 88.31, 187.83 and 287.41 m for 5, 10, 20 and 30 kN/m drag force, respectively. It is noted that, the values of 5 and 10 kN/m correspond to more realistic scenarios, while the higher values of 20 and 30 kN/m are less probable to occur.

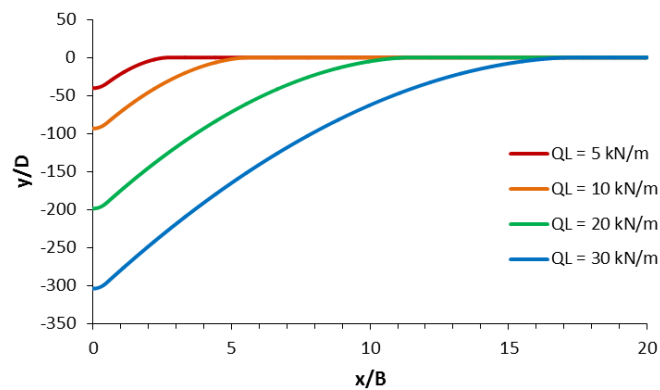


Figure 8. Comparison of normalized pipeline displacements for different drag forces

Natural gas pipelines are usually constructed using industrial steel material with definite response, failure mode, etc. Therefore, common practice for determining the pipeline failure is through strain limits, due to the fact that strain can be directly measured by setting, e.g., strain gauges at the critical areas. As shown in Figure 8, the pipe is expected to develop axial and bending strains. Therefore, the axial strain, ϵ_{11} , on both the upstream and downstream points, according to the landslide direction, was calculated and defined hereafter as ‘top’ and ‘bottom’ strains, respectively (see Figure 9).

As shown in Figure 10, the bottom line strains receive maximum values near the middle of the pipe ($x/B = 0$) and minimum after the landslide area ($x/B = 0.5$), while the top line strains display the reverse pattern. It is noted that, in Figure 10, only tensile strains are noticed, so only tensile plastic failure is expected. Both bottom and top axial strains receive the same values at distance where the second curvature occurs in Figure 8. This distance increases as the drag force increases. After the above point, axial strains have a constantly decreasing value.

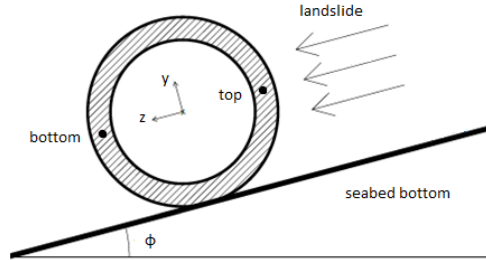


Figure 9. Pipeline cross section points for axial strain calculations

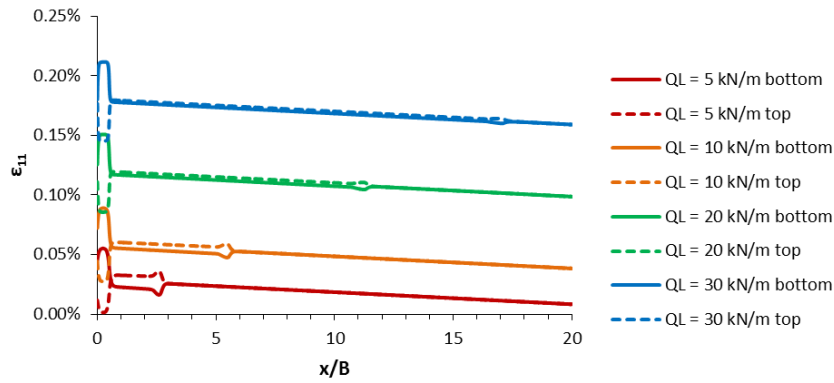


Figure 10. Comparison of axial strains for different drag forces

4.2 Landslide width

Considering the impact of landslide width, five different widths were used: $B = 100, 200, 300, 400$ and 500 m. The landslide drag force for all the above cases is constant and equal to $Q_L = 10$ kN/m. As illustrated in the left part of Figure 11, larger landslide width results in larger lateral displacements, y , while a longer part of the pipeline is moving laterally. The absolute maximum lateral movement of the pipeline is large in every case, and more specifically $21.87, 53.45, 88.31, 126.28$ and 164.9 m for $100, 200, 300, 400$ and 500 m landslide width, respectively. However, as illustrated in the right part of Figure 10, it is noticed that the part of the pipeline that moves laterally is constant when normalized to the landslide width, B , and has a value of $x/B \approx 5$ m. The normalized displacement, y/D , is increasing with the landslide width.

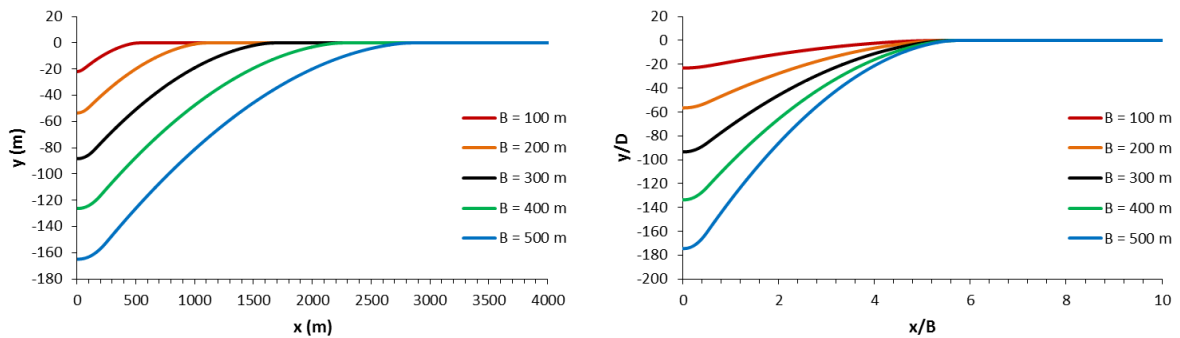


Figure 11. Comparison of absolute pipeline displacements and length (left) and normalized pipeline displacements and length (right) for different landslide widths

In Figure 12, the bottom and top line strain of the pipe cross section for the different landslide widths are

depicted. Bottom line strains present maximum values near the middle of the pipe ($x/B = 0$) and minimum after the landslide area ($x/B = 0.5$), while the top line strains display the reverse pattern. Both bottom and top axial strains present the same values at a normalized distance of $x/B \approx 5$ m, which is in agreement with the lateral movement pattern of Figure 11. In contrast to the findings of the investigation related to drag force, compressive strains occur within the landslide area for the case of a landslide width equal to $B = 100$ m at the top line of the cross section. Therefore, the part of the pipeline within the landslide region is vulnerable to the occurrence of critical local buckling phenomena.

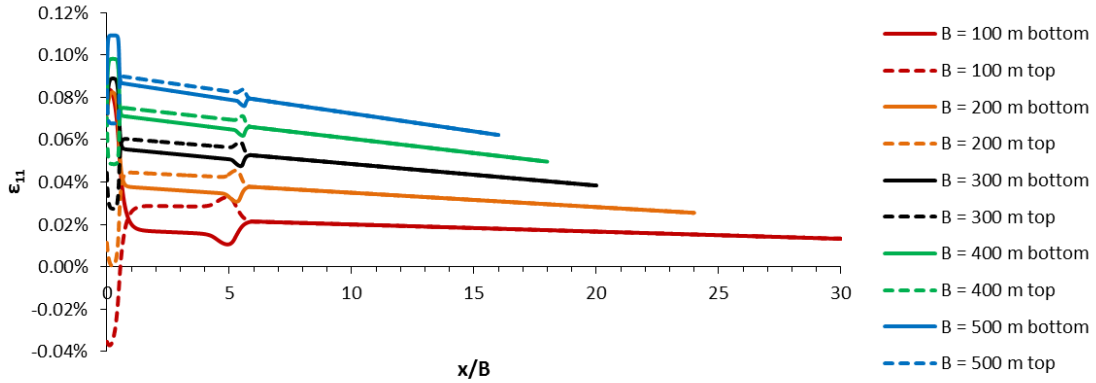


Figure 12. Comparison of axial strains for different landslide widths

5 IMPLEMENTATION OF MITIGATION MEASURES

Offshore pipelines are technical works of high importance, constructed in an adverse environment with various hazards and uncertainties. Offshore landslides can occur even for slope angles equal to $0.5 - 1^\circ$, while debris flows can intersect with an offshore pipeline even at a flat terrain, as a result of a nearby landslide or soil liquefaction. So far the relevant studies considered the response of offshore pipelines to be within the elastic region [12-14]. Consequently, the critical strain limit considered herein is the presence of plastic strains anywhere along the pipeline. The pipeline and soil characteristics used in this parametric study are taken from the offshore section of TAP pipeline, as described in details in Section 2.

A common, economical and relatively easily applicable mitigation measure for offshore pipelines is the construction of anchor points along their route. In this work, the isolation of the pipeline inside a critical landslide area, through the installation of two anchor points on both sides of the critical area is investigated. The landslide or debris flow direction is considered to be vertical to the pipeline axis (Figure 1). The numerical model used is the one presented in Section 2 and Figure 4, for various expansion lengths, L_{exp} , and landslide widths, B . The minimum and maximum expansion lengths used for the parametric study are presented in Table 2, in which L is the total length of the model, as shown in Figure 4. The minimum expansion length for all cases was chosen as $L/B = 2$, since it is not easy to specify the exact ends of the landslide region, while the anchor point was chosen to be always outside the landslide region.

Landslide width B (m)	Expansion length, L_{exp} (m)		min L/B	max L/B
	min	max		
100	150	2950	2	30
200	300	4700	2	24
300	450	5850	2	20
400	600	7000	2	18
500	750	7750	2	16

Table 2. Parametric study for the anchor point implementation

The results are depicted in Figure 13, in which $Q_{L,cr}$ is the critical lateral load when plasticity occurs and L/B the normalized total length. The dashed black line corresponds to the break point change, i.e., the critical ratio of L/B for which plasticity inside the landslide occurs for all the examined cases. More specifically, plasticity occurs at a distance $x = 21.5, 52.5, 103, 156$ and 207 m from the middle of the landslide for the respective landslide widths $B = 100, 200, 300, 400$ and 500 m. For smaller L/B ratios, plasticity occurs at the anchor point, while for bigger ratios plasticity occurs within the landslide region. In all cases examined, the critical load

follows a bi-linear response with constant increase as the expansion length increases until the break point change and thereafter the critical load increases with a smaller ratio. As expected, the critical load decreases as the landslide width increases. However, smaller landslide widths (i.e., between $B = 100$ and 200 m) present greater decrease than bigger landslide widths (i.e., between $B = 400$ and 500 m). Moreover, the break point change line seems to reveal a linear correlation between the critical load and the L/B ratio that plasticity begins to occur within the landslide area. It is also noted that when plasticity occurs the total strain is approximately 0.2% for all cases and failure modes. Finally, it is mentioned that, except from the cases in which the anchor points were placed very close to the landslide area, failure occurs for extreme drag forces values, i.e., higher than 20 kN/m.

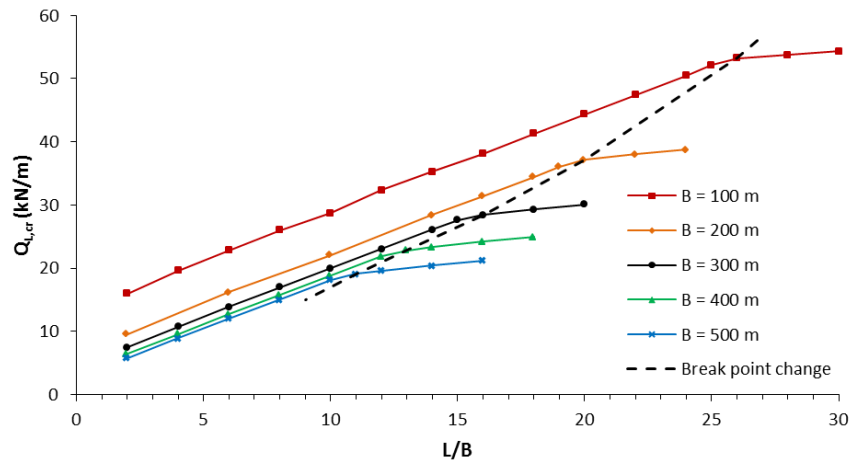


Figure 13. Critical load and break point change for different expansion lengths and landslide widths

5 CONCLUSIONS

The aim of the current work is to investigate the response of offshore pipelines subjected to lateral landslides. For this purpose, realistic data from Trans Adriatic Pipeline (TAP) are used together with the international recommended practice guidelines DNV GL. A computationally efficient numerical model has been developed and compared with available numerical and analytical approaches. Additionally, a parametric investigation of various loading conditions and mitigation measures was conducted.

The main conclusions can be summarized as follows:

- The fact that different numerical and analytical approaches result in similar pipeline response is promising. The discrepancies between the numerical models are attributed to the fact that the proposed model takes into account geometrical nonlinearities.
- Regarding the pipeline lateral displacement, the parametric study indicates that larger drag force and landslide width result in greater displacements.
- With reference to the part of the pipeline that moves laterally, the parametric study indicates that larger drag force and landslide width result in longer part of the pipeline to be exposed to lateral movement. However, for constant drag force and increasing landslide width, the laterally dislocated part of the pipeline with respect to the landslide width is constant.
- Regarding the axial strains, it is concluded that bottom and top line strains display the exact reverse pattern. Nonetheless, in almost every case only tensile strain occurs, which is considered beneficial since the thin pipeline is much more vulnerable to compressive strains. Compressive strains appear only for small landslide widths; hence, it is recommended to avoid regions with potential small landslide widths.
- Failure occurs within the landslide area, unless anchor points are installed on both sides adjacent to the landslide zone. In this case, failure happens at the anchor points, which is beneficial for monitoring and maintenance, since failure within the landslide area is subjected to several uncertainties.
- In the examined cases, when the anchor points are placed quite far from the landslide zone, failure occurs for rather extreme drag force values.
- There is a linear correlation between the critical drag force and the location of the anchor points. Furthermore, the distance that mitigation measures cease to influence the pipeline failure seems to have a linear correlation with the critical drag force and the landslide width.

Certainly, the validation of the numerical models with real pipe response or experimental results would be extremely useful, but currently not possible due to lack of relevant data. Further parametric investigation of the

examined problem is required. Other parameters, such as the bottom slope angles, internal and external pressures, pipeline material properties, and cross section geometries, as well as non-symmetrical configurations should be investigated. Furthermore, DNV GL guidelines should be implemented on a variety of soils (sands, clays, silts, organic soils, etc) so that a more realistic representation could be obtained considering the variation of soil response. Finally, the use of alternative mitigation measures and cases of non-symmetrical configurations should also be studied for the worst case scenarios, in order to ensure the safety and functionality of offshore pipelines in such adverse conditions.

REFERENCES

- [1] TAP (2013a), *Trans Adriatic Pipeline Appendix 11: Geotechnical Report - Shallow Geotechnical Survey - Part A Soil Parameters for Design*, ESIA, Italy.
- [2] TAP (2013b), *Trans Adriatic Pipeline Section 4 - Project Description*, ESIA, Albania.
- [3] DNV GL (2017), *Pipe-soil interaction for submarine pipelines*, Recommended Practice, DNVGL-RP-F114.
- [4] Bruton D.A.S., White D.J., Carr M. and Cheuk J.C.Y. (2008), "Pipe-soil interaction during lateral buckling and pipeline walking - The safebuck jip", *Proceedings of the Offshore Technology Conference*, Houston, USA, 5-8 May 2008.
- [5] White D.J. and Cheuk C.Y. (2008), "Modelling the soil resistance on seabed pipelines during large cycles of lateral movement", *Marine Structures*, Vol. 21, pp. 59-79.
- [6] Randolph M.F., White D. and Yan Y. (2012), "Modelling the axial soil resistance on deep-water pipelines", *Geotechnique*, Vol. 62, No. 9, pp. 837-846.
- [7] Wang J. and Yang Z. (2016), "Axial friction response of full-scale pipes in soft clays", *Applied Ocean Research*, Vol. 59, pp. 10-23.
- [8] Zakeri A., Hoeg K. and Nadim F. (2008), "Submarine debris flow impact on pipelines-Part I: Experimental investigation", *Coastal Engineering*, Vol. 55, No. 12, pp. 1209-1218.
- [9] Zakeri A., Hoeg K., Nadim F. (2009), "Submarine debris flow impact on pipelines-Part II: Numerical Analysis", *Coastal Engineering*, Vol. 56, No. 1, pp. 1-10.
- [10] Randolph M.F. and White D.J. (2012), "Interaction forces between pipelines and submarine slides – A geotechnical viewpoint", *Ocean Engineering*, Vol. 48, pp. 32-37.
- [11] Liu J., Tian J. and Yi P. (2015), "Impact forces of submarine landslides on offshore pipelines", *Ocean Engineering*, Vol. 95, pp. 116-127.
- [12] Parker E.J., Traverso C., Moore R., Evans T. and Usher N. (2008), "Evaluation of landslide impact on deepwater submarine pipelines", *Proceedings of the Offshore Technology Conference*, Houston, USA, 5-8 May 2008.
- [13] Randolph M.F., Seo D. and White, D.J. (2010), "Parametric solutions for slide impact on pipelines", *Journal of Geotechnical and Geoenvironmental Engineering*, Vol. 136, No 7, pp. 940-949.
- [14] Yuan F., Li L., Guo Z. and Wang L. (2014), "Landslide impact on submarine pipelines: Analytical and numerical analysis", *Journal of Engineering Mechanics*, Vol. 141, No. 2, pp. 28-37.
- [15] ABAQUS (2014), *ABAQUS/Analysis user's manual-Version 6.14*, Simulia Corp., Providence, RI, USA.
- [16] Ting E.C., Shih C. and Wang Y.K. (2004), "Fundamentals of a vector form intrinsic finite element: Part I. Basic procedure and a plane frame element", *Journal of Mechanics*, Vol. 20, No. 2, pp. 113-122.

EFFECTS OF THE SOIL-STRUCTURE-INTERACTION PHENOMENON ON RC STRUCTURES WITH PILE FOUNDATIONS

George Markou¹, Mohammad AlHamaydeh² and Dina Saadi³

¹Department of Civil Engineering
Universidad Católica de la Santísima Concepción
Concepción, Alonso de Ribera 2850, Chile
e-mail: markou@ucsc.cl

^{2,3}Department of Civil Engineering
American University of Sharjah
P.O. Box 26666, Sharjah, United Arab Emirates

²e-mail: malhamaydeh@aus.edu ³email: g00037041@aus.edu

Keywords: Soil-Structure-Interaction, FEA, Reinforced Concrete, Pile Foundation, Cyclic Loading.

Abstract. *The Soil-Structure Interaction (SSI) has a significant effect on the overall structural behavior of reinforced concrete buildings, especially under cyclic loading conditions. Considering the SSI effects within experimental setups comprise cumbersome procedures that are usually very difficult to control and monitor. Furthermore, when the foundation type of the structure foresees the use of pilecaps connected to piles, accounting for the SSI effect becomes further complicated to investigate. Consequently, most SSI experiments involve very simple geometry configurations for specimens under monotonic loading conditions. The need for developing new numerical methods that will enable realistic capturing of this phenomenon, is deemed to be of great importance. This research work aims to study the SSI effect for the case of a 6-storey building with a pile foundation undergoing cyclic loads. The numerical model foresees the study of the main shear wall of the structure that is connected to six reinforced concrete slabs and is resting on a pilecap that is connected to three piles found within a soil class E, according to ASCE7-10. By using the hexahedral isoparametric finite element, the structure is discretized in 3D, where the adopted concrete material model is integrated with the smeared crack approach and the steel bars are modelled by using embedded rebar elements. Both soil and concrete foundation are discretized with hexahedral elements, while monotonic and cyclic analyses are performed in order to study the mechanical behavior of the fixed-base structure and the corresponding SSI counterpart structure that is founded on the flexible soil.*

1 INTRODUCTION

The Soil Structure Interaction (SSI) phenomenon can be of great importance when assessing the capacity of a structure founded on a soil with low mechanical properties [1]. The flexible soil combined with large superstructure loads can cause the foundation system to deform substantially, posing significant effects on the overall structural response. The effect of the SSI on the overall mechanical behavior of structures can vary based on the adopted foundation type [2]. The local stress and strain are redistributed when the foundation is free to deform, affecting the response of the structure. This is of great importance, especially when a reinforced concrete (RC) framing system is designed to undertake seismic excitations which generate high lateral forces.

Accounting for SSI effects may be necessary when the dynamic response of a structure, its foundation and its soil collectively contribute to the overall seismic response [3]. Researchers face major difficulties in conducting experimental tests to understand the complicated SSI mechanisms, which develop during seismic excitation. As a result, the majority of experimental tests in existing literature are limited to simple specimens under monotonic loading. The study of the SSI mechanisms is further complicated by the complexity of their geotechnical aspects and prediction of soil mechanical behavior.

Modeling the SSI phenomenon through numerical models has been frequently implemented by researchers over the last two decades [1-10]. It is worth noting that the commercial software used to perform SSI analysis have evolved substantially over the years [11-17]. The main challenges associated with nonlinear finite element modeling of full-scale structures founded on soil are attributed to computational inefficiency. The need to account for material nonlinearities of both soil and concrete domains adds further complications. Therefore, modeling the soil domain through springs is the most popular simulation approach given its numerical simplicity. Nevertheless, this approach is found to be impractical and inaccurate when dealing with foundations that have complicated

geometries (i.e. pile foundation). Thus, capturing complicated SSI mechanisms that develop due to the 3D deformation of the foundation system is not feasible through this numerical method. Hence, the use of hexahedral elements was proposed to discretize the soil and concrete mediums [1, 2]. This FE method helps in achieving an accurate representation of the structural system as well as the soil.

When the structure and soil are discretized with 8-noded hexahedral elements, an exact representation of the geometry is achieved [1]. Furthermore, performing static pushover analysis to study the SSI effect in terms of capacity, deformation, energy dissipation and damage can be investigated at a material level. The 3D modeling approach allows for special considerations at the concrete-soil interface, which also affects the overall mechanical response of the SSI system. A previously published work [1] examined the structure with an isolated foundation resting on class E soil, based on ASCE7-10 [18]. The structure was tested under monotonic and cyclic loading, at which the effect of the SSI on the structural response was studied. The same approach is adopted herein, to investigate the mechanical response of a structure supported by deep foundation consisting of three piles. The effects of the SSI phenomenon will be examined and presented through this numerical investigation.

The SSI effects play a paramount role in seismic response, especially for nonlinear dynamic analysis and inelastic response assessment where realistic damage estimates are needed for RC structures of various types. All reported findings in such research investigations [19-31] are expected to require re-assessments.

2 NUMERICAL MODEL

2.1 Material Models

The 3D detailed discretization that was adopted in this work follows the concept proposed in “Nonlinear FEA of Soil-Structure-Interaction Effects on RC Shear Wall Structures” [1], which demonstrated the use of 8-noded hexahedral finite elements to discretize the structure and the soil domains. The steel reinforcement was modeled by the embedded rebar element. In addition, the model used in this research work demonstrates the use of springs positioned at the pile cap-soil interfaces, to simulate the phenomenon of soil detachment when the interface undergoes tension. Furthermore, the interface of the piles and the soil is modeled through hexahedral elements that were numerically calibrated to account for the friction stresses, but not transfer tension to the soil domain. The pile-soil interface elements are modeled to resist a maximum shear stress after a certain allowable settlement, which was taken as 0.6% of the pile diameter to comply with conditions for numerical analysis described in section 3.

The concrete material model, which is integrated within the 8-noded hexahedral elements is based on the proposed algorithmic implementation presented in [2]. The model is based on the concrete material model proposed by Mourlas et al. [32], which was integrated with a flexible crack closure criterion. The criterion was found to induce numerical stability for problems that tackle nonlinear analysis of RC structures under ultimate limit state cyclic loading conditions [32]. To capture the numerical effects of cracking during monotonic and cyclic analyses, the smeared crack approach is adopted [33]. When a crack opens at a given Gauss point (shown in Fig. 1), the constitutive material matrix is modified accordingly to account for the material's damage [32].

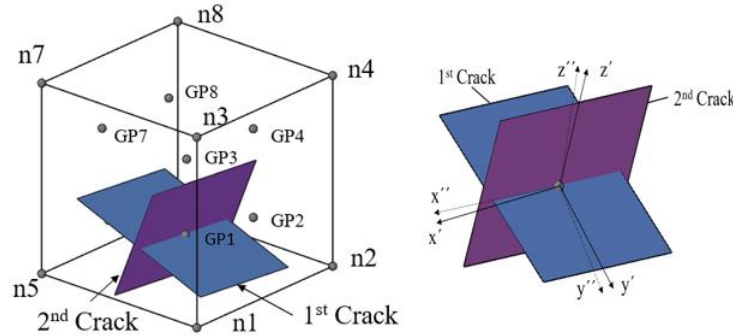


Fig. 1: Local axes for the case of two cracks at a specific Gauss point. [32]

According to the concrete model adopted in this numerical investigation, when the 3D stresses at a given Gauss point exceed the concrete's strength envelope, a crack occurs along the plane perpendicular to the maximum principal tensile stress. The concrete's strength envelope is computed by Eq. 1, which is based on the Willam and Warkne [34] formulae.

$$\tau_{0u} = \frac{2\tau_{0c}(\tau_{0c}^2 - \tau_{0e}^2)\cos\theta + \tau_{0c}(2\tau_{0e} - \tau_{0c})\sqrt{4(\tau_{0c}^2 - \tau_{0e}^2)\cos^2\theta + 5\tau_{0e}^2 - 4\tau_{0c}^2\tau_{0e}^2}}{4(\tau_{0c}^2 - \tau_{0e}^2)\cos^2\theta + (2\tau_{0e} - \tau_{0c})^2} \quad (1)$$

where, θ defines the rotational variable of the deviatory stress orientation on the octahedral plane. The terms τ_{0e} ($\theta=0^\circ$) and τ_{0c} ($\theta=60^\circ$) correspond to the states of $\sigma_1=\sigma_2>\sigma_3$ and $\sigma_1>\sigma_2=\sigma_3$, respectively.

The Menegotto Pinto [35] steel model incorporating the Bauschinger effect (shown in Fig. 2) is used to model

the embedded rebar elements within the concrete hexahedral mesh in the steel model adopted in this paper.

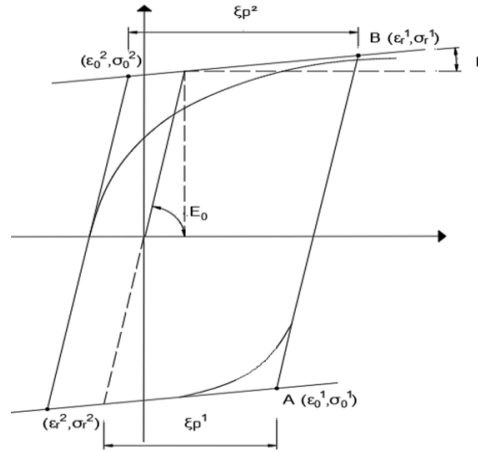


Fig. 2: Menegotto – Pinto steel model. [35]

The stress-strain corresponding to the steel model is presented below:

$$\sigma^* = b\varepsilon^* + \frac{(1-b)\varepsilon^*}{(1+\varepsilon^{*R})^{1/R}} \quad (2)$$

where,

$$\varepsilon^* = (\varepsilon - \varepsilon_r) / (\varepsilon_0 - \varepsilon_r), \quad \sigma^* = (\sigma - \sigma_r) / (\sigma_0 - \sigma_r) \quad \text{and} \quad R = R_0 - a_1 \xi / (\alpha_2 + \xi)$$

It must be noted that the SSI model, which uses the 8-noded hexahedral elements to discretize the soil domain, is integrated with a von Mises material model. This material model helps in capturing the nonlinear behavior of the soil domain in the case where the ultimate compressive strength of its material is exceeded.

2.2 Finite Element Model

The investigation of a 6-storey RC building was performed in this work through two finite element models; the first was the fixed-base (FX) model (illustrated in Fig. 3a) and the second involved discretizing the soil domain with hexahedral elements to account for the SSI effect (illustrated in Fig. 3b). The foundation type that was designed and discretized accordingly consisted of three piles with a diameter of 1.2m connected to a pile cap of size 2.5x9.5x1.6m. The 24m tall shear wall had a section of 400x4500cm and was reinforced based on the design presented in [19-22]. Furthermore, the foundation system was designed based on the ACI 318 provisions [36] and the resulting reinforcement was modeled in 3D as shown in Fig. 4.

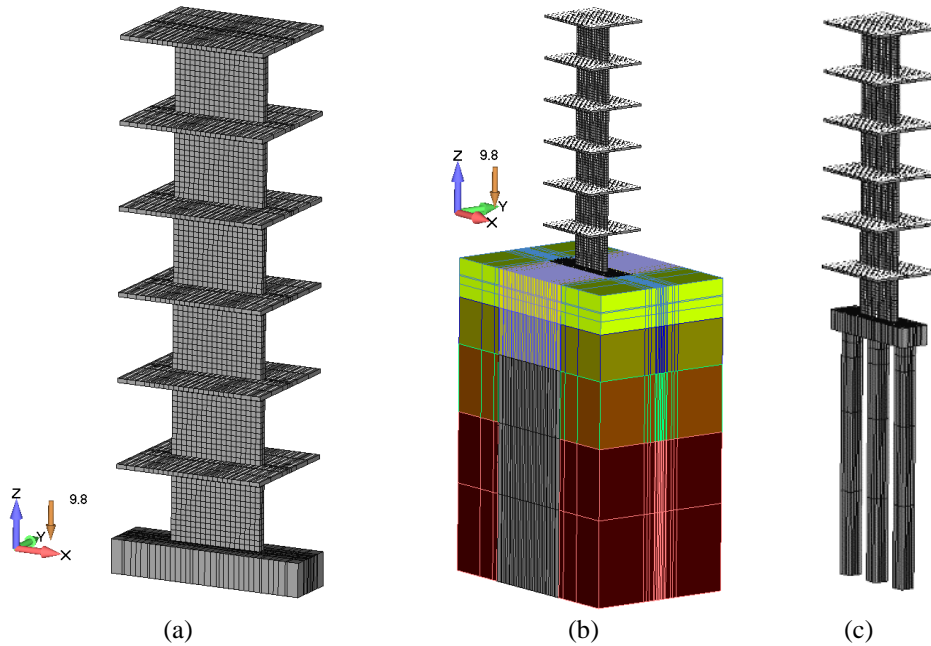


Fig. 3: Hexahedral finite element mesh of the (a) fixed-base and (b) SSI models. (c) SSI model's hexahedral

mesh without the soil elements.

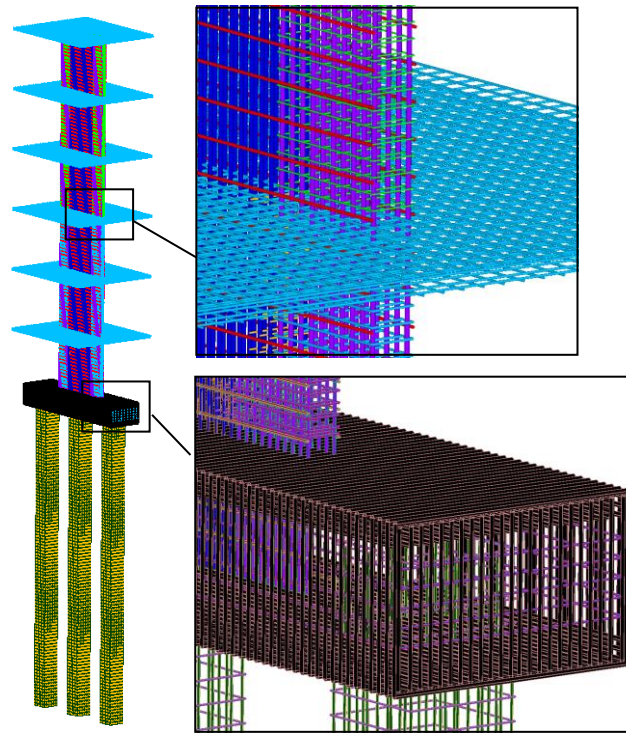


Fig. 4: Embedded rebar finite element mesh of the SSI model.

Model	Num. of Concrete Hexa Elements	Num. of Soil Hexa Elements	Num. of Steel Embedded Rebar Elements
FX	4,824	-	56,803
SSI	5,400	5,228	62,405

Table 1: Mesh details

Soil Parameter	E	ν	q_u
Value	65.7 MPa	0.3	964 kPa

Table 2: Soil Properties (Class E)

It is noteworthy to state here that the tributary areas of the six slabs connected to the discretized shear wall were also included in the numerical model. This modelling approach was applied to optimize the number of computations and the execution time of the heavy computational demand imposed by the numerical analysis of a full-scale structure.

Table 1 shows the number of hexahedral elements and embedded rebar elements used to construct the two aforementioned 3D models. It may be observed that the SSI model consists of a larger number of finite elements, given that the pile foundation and the soil domain are discretized and included within the 3D model. The material properties used to define the soil domain, which are characteristic of an ASCE7-10 Class E soil [18], are summarized in Table 2. The soil domain within the SSI mesh was divided into four different layers, with a total depth of 30m (shown in Fig. 3b). The soil material properties were modified based on the depth of each layer. Thus, the deeper the soil layer, the larger the Young modulus and the larger the corresponding uniaxial compressive strength. Furthermore, each pile had a total length of 20m and the concrete material exhibited an ultimate uniaxial compressive strength of 38 MPa. The steel rebars had a yielding stress of 420 MPa.

The tributary areas of the slabs, which have a thickness of 20cm, are based on the design of the 6-storey RC building presented in previously published work [19-22]. The slabs were subjected to dead loads and live loads are consistent with previously published work. The slab edges were restrained in order to capture the mechanical behaviour of a continuous slab, which is expected to develop bending moments and shear. Therefore, the edges were assumed to displace along the x-axis (the direction of the imposed displacements) but not displace along the z-axis. Finally, the displacement-control nonlinear analysis performed in this work demonstrates the application of imposed displacements at the nodes located at the perimeter of each slab.

3 NUMERICAL RESULTS AND DISCUSSION

Pushover analysis was performed in order to compare the mechanical response of the structure with and without SSI considerations. The analysis was implemented to numerically assess the mechanical behavior of the two models under static push over analysis. The horizontal monotonic displacements at each slab were computed based on Eq. 3.

$$\delta_{floor} = (x/L)^k \quad (3)$$

where, x is the ground to slab height, L is the total height of the structure and k is a constant, which was set to be equal to 1.2, based on the parametric investigation performed in [1].

3.1 Push-Over Analysis

Fig. 5 shows the base shear force vs horizontal displacement curves obtained numerically through quasi-static push-over analysis. As observed, the SSI model derived a more flexible behavior in comparison to the FX model. This may be attributed to the flexible behavior of the foundation system, which undertakes the superstructure loads as shown in Fig. 6. Based on the numerical findings, it is evident that the deformation of the soil and the foundation system (comprised of the pile cap and piles) affects the overall mechanical behavior of the structure, which was found to be more flexible by 52% in terms of initial stiffness. The stiffness decrease is attributed to the relatively flexible soil and the fact that the soil-pile interface elements reach their friction capacity at an early stage of the analysis. Thus, the piles are mainly transferring the vertical superstructure loads to the soil through the head bearing mechanism. Additionally, the corresponding ultimate base shear of the SSI model was found to be 29.58% smaller compared to the FX model as depicted in Fig. 5. This decrease is attributed to the flexibility induced by the soil domain, which deforms accordingly as the imposed displacements increase.

It is also evident that, the SSI model derived a different nonlinear mechanical behavior when the imposed displacements were larger than 150 mm. When the imposed horizontal deformation was 150 mm, the FX model exhibited a sudden drop in terms of capacity, attributed to the longitudinal reinforcement yielding and concrete cracking, a mechanical phenomenon that was noted in a lower degree in the corresponding SSI model. As it was found from the numerical investigation, the fixed-base assumption within the FX model forced the shear wall to develop higher deformations at the ground floor level, where the rebar yielding occurred due to the large bending moment developed at the base of the structure. Furthermore, as it can be seen in Fig. 5, the corresponding capacity drop shifted significantly when the SSI effect is accounted for. This is once more attributed to the overall flexible behavior of the pile foundation when compared to the mechanical behavior of the fixed-base assumption that does not allow any deformation to occur at the foundation level. It must be noted at this point that, the numerical results from the parametric investigation that foresee the analysis of the structure under cyclic loads was also performed but will be presented in a future publication.

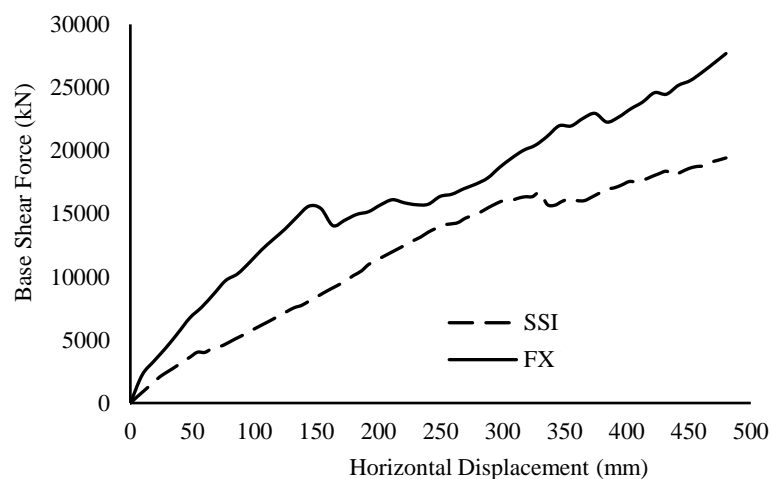


Fig. 5: Base shear force vs horizontal displacement curves from push-over analysis.

3.2 Pile Foundation Mechanical Response

Fig. 6 shows the deformed shape and the corresponding strain contour of the pile cap and the three piles resulting from the push over analysis. The two deformed shapes given in this figure correspond to the results obtained for the displacement increments corresponding to a 12mm and 60mm horizontal displacement at the roof slab, respectively. To emphasize the deformed shapes, a deformation scale factor of 500x was used. Thus, it can be easily observed that the pile cap develops a shear deformation due to the large bending moment developed at

the base of the RC shear wall. The piles were found to develop a bending deformation since the pile cap displaces along the x-axis (direction of the imposed displacements), forcing the pile heads to displace horizontally as well.

The complexity of the under study problem is evident in the complicated 3D deformed shapes, which incorporate several SSI resistance mechanisms. Therefore, even for cases of simple loading such as the push-over, delivering a realistic representation of the behavior of SSI systems requires advanced numerical tools. This also explains why the simplistic spring model approach cannot be used in this type of analysis without compromising numerical accuracy.

In addition to the above findings, the numerical investigation also revealed that the damages due to strain concentration agreed with the findings in [1]. According to the numerical analysis presented in this paper, the ground floor shear wall exhibited increased cracks in the FX model, whereas the SSI model exhibited lower strain concentration due to the foundation's ability to deform. Moreover, the upper floors of the SSI model were found to generate larger deformations due to the flexibility of the soil, which causes redistribution of the internal stresses and in return alters the structure's deformed shape.

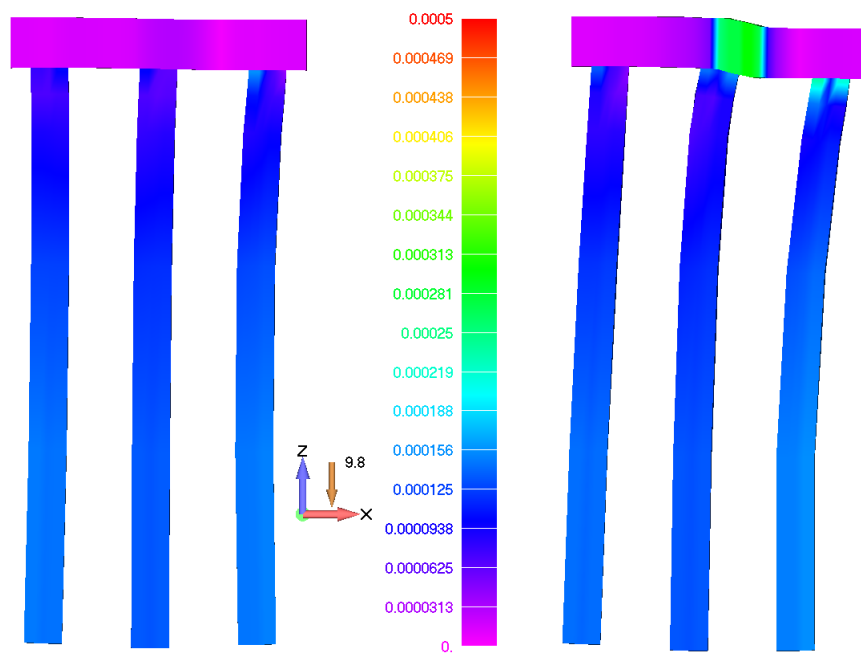


Fig. 6: Deformed shape and von Mises strain contour of the pile foundation for a horizontal roof displacement of (Left) $\delta = 12$ mm and (Right) $\delta = 60$ mm. Deformation scale factor: 500x.

4 CONCLUSIONS

In this work, the SSI effect was numerically investigated by studying a 6-storey RC structure resting on a pile foundation system. The pile foundation was supported by a soil of class E as per the ASCE 7-10 provisions. The superstructure was modeled with 8-noded hexahedral elements, which analyze cracks through the smeared crack approach. The reinforcement bars were modeled as embedded rebar elements. The soil domain was also discretized with 8-noded isoparametric hexahedral elements. Special considerations were accommodated for modeling the friction and potential soil detachments at the concrete-soil interfaces. The SSI effect was modeled and studied numerically, and the obtained results were compared to those of an equivalent fixed base model.

Upon successful completion of the parametric investigation presented in section 3.1 (Push-Over Analysis), it was concluded that the SSI model demonstrated a more flexible behavior. The ability of the foundation system to deform causes the soil to develop settlements proportional to the superstructure loads. Based on the numerical findings, the SSI model's initial stiffness decreased by 52%. In addition, the computed maximum base shear was 29.58% smaller than that obtained from the equivalent FX model. Furthermore, in the SSI system, the shear wall was found to behave in a more flexible manner, yielding lower strain concentrations at the ground floor. Moreover, the deformed shape of the foundation system confirmed the shortcomings of the simplistic spring model in representing the SSI mechanisms.

The research presented in this paper is part of a future project to extend the obtained numerical results to further cases of structures with various geometries and reinforcement arrangements. The objective of this project would be to investigate the relationship between superstructure characteristics and the extent to which the SSI effects influence overall structural response, e.g. stress/strain concentration regions, excessive cracking, etc.

REFERENCES

- [1] AlHamaydeh, M., Markou, G. and Saadi D., “Nonlinear FEA of Soil-Structure-Interaction Effects on RC Shear Wall Structures”, *6th International Conference on Computational Methods in Structural Dynamics and Earthquake Engineering*, 15-17 June 2017, Rhodes Island, Greece.
- [2] Markou, G., Sabouni, R., Suleiman, F. and El-Chouli, R. (2015), “Full-Scale Modeling of the Soil-Structure Interaction Problem Through the use of Hybrid Models (HYMOD)”, *International Journal of Current Engineering and Technology*, Vol. 5(2), pp. 885-892.
- [3] H. Torabi and M. T. Rayhani (2014), “Three dimensional Finite Element modeling of seismic soil–structure interaction in soft soil”, *Comput. Geotech.*, Vol. 60, pp. 9–19.
- [4] Tabatabaiefar, S. H. R., Fatahi, B. and Samali, B. (2013), “Seismic Behavior of Building Frames Considering Dynamic Soil-Structure Interaction”, *International Journal in Geomechanics*, Vol. 13, no. 4, pp. 409–420.
- [5] Güllü, H. and Pala, M. (2014), “On the resonance effect by dynamic soil-structure interaction: A revelation study,” *National Hazards*, Vol. 72(2), pp. 827–847.
- [6] Ghandil, M. and Behnamfar, F. (2015), “The near-field method for dynamic analysis of structures on soft soils including inelastic soil-structure interaction,” *Soil Dynamics in Earthquake Engineering*, Vol. 75, pp. 1–17.
- [7] Agalianos, A., Psychari, A., Vassiliou, M. F., Stojadinovic, B. and Anastasopoulos, I. (2017), “Comparative Assessment of Two Rocking Isolation Techniques for a Motorway Overpass Bridge”, *Front. Built Environ.*, Vol. 3(8), pp. 1–19.
- [8] Drosos, V., Georgarakos, T., Loli, M., Anastasopoulos, I., Zarzouras, O., Gazetas, G. and Asce, M. (2012), “Soil-Foundation-Structure Interaction with Mobilization of Bearing Capacity : Experimental Study on Sand”, *Journal of Geotechnical and Geoenvironmental Engineering*, Vol. 138(11), pp. 1369–1386.
- [9] Krishnamoorthy, A. and Anita, S. (2016) “Soil–structure interaction analysis of a FPS-isolated structure using finite element model”, *Structures*, Vol. 5, pp. 44–57.
- [10] Mitropoulou, C. C., Kostopanagiotis, C., Kopanos, M., Ioakim, D. and Lagaros, N. D. (2016), “Influence of soil–structure interaction on fragility assessment of building structures”, *Structures*, Vol. 6, pp. 85–98, 2016.
- [11] Itasca International Inc. (2017), *FLAC, Fast Lagrangian Analysis of Continua, is numerical modeling software for advanced geotechnical analysis of soil, rock, groundwater, and ground support in two dimensions*, Minneapolis, 2017.
- [12] GeoMotions LLC (2009), *SHAKE2000, A Computer Program for Equivalent-Linear Site Response Analysis*.
- [13] CSI (2015), *SAP2000 Manual*, Berkeley, California, United States.
- [14] ABAQUS Inc. (2016), *Abaqus FEA*, Dassault Systemes.
- [15] Schellenberg; T. Yang; and E. Kohama (2015), *OpenSees Navigator ver. 2.5.5*, Pacific Earthquake Engineering Research Center (PEER), Berkeley; California; USA.
- [16] Computers & Structures Inc. (2015), *ETABS, Integrated Analysis, Design, and Drafting of Building Systems*, Berkeley, California, United States.
- [17] ReConAn (2010), *Finite Element Analysis Software v1.00*, Institute of Structural Analysis and Seismic Research, National Technical University of Athens.
- [18] American Society of Civil Engineers (2010), *Minimum Design Loads for Buildings and Other Structures*, ASCE 7-10.
- [19] M. AlHamaydeh, N. Aly, and K. Galal, “Effect of Diverse Seismic Hazard Estimates on Design and Performance of RC Shear Wall Buildings in Dubai, UAE,” in *The 2015 World Congress on Advances in Structural Engineering and Mechanics (ASEM15)*, August 25-29, 2015.
- [20] N. Aly, M. AlHamaydeh, and K. Galal, “Quantification of the Impact of Detailing on the Performance and Cost of RC Shear Wall Buildings in Regions with High Uncertainty in Seismicity Hazards,” *Journal of Earthquake Engineering*, vol. In Press, 2018.
- [21] M. AlHamaydeh, N. Aly, and K. Galal, “Seismic Response and Life-Cycle Cost of Reinforced Concrete Special Structural Wall Buildings in Dubai, UAE,” *Structural Concrete*, pp. 1–12, 2017.
- [22] M. AlHamaydeh, N. Aly, and K. Galal, “Impact of Seismicity on Performance and Cost of RC Shear Wall Buildings in Dubai, United Arab Emirates,” *ASCE, Journal of Performance of Constructed Facilities*, no. DOI: 10.1061/(ASCE)CF.1943-5509.0001079, 2017.
- [23] M. AlHamaydeh and G. Al-Shamsi, “Development of Analytical Fragility Curves for Representative Buildings in Dubai, United Arab Emirates,” in *The International Conference on Earthquake Engineering; Skopje Earthquake - 50 Years of European Earthquake Engineering (SE-50EEE)*, May 29-31, 2013
- [24] M. AlHamaydeh, K. Galal, and S. Yehia, “Impact of Lateral Force-Resisting System and Design/Construction Practices on Seismic Performance and Cost of Tall Buildings in Dubai, UAE,” *Earthquake Engineering and Engineering Vibration*, vol. 12, no. 3, pp. 385–397, 2013
- [25] M. AlHamaydeh, S. Yehia, N. Aly, A. Douba, and L. Hamzeh, “Design Alternatives for Lateral Force-Resisting Systems of Tall Buildings in Dubai, UAE,” *International Journal of Civil and Environmental Engineering*, vol. 6, pp. 185–188, 2012

- [26] M. AlHamaydeh, S. Abdullah, A. Hamid, and A. Mustapha, "Seismic design factors for RC special moment resisting frames in Dubai, UAE," *Earthquake Engineering and Engineering Vibration*, vol. 10, no. 4, pp. 495–506, 2011.
- [27] M. AlHamaydeh, J. Abdalla, S. Abdalla, A. Al-Rahmani, and A. Mostafa, "Inelastic Seismic Demands For Reinforced Concrete Frames In Dubai," in *The 14th European Earthquake Engineering Conference (14EEEE)*, Aug. 30-Sept. 3, 2010.
- [28] M. Al Satari, *Estimation of Seismic Response Demands for R/C Framed Structures: An Insight Into The Nonlinear Seismic Behavior*. VDM Verlag, Saarbrücken, Germany, 2008.
- [29] M. Al Satari and J. Anderson, "Nonlinearity Effects on the Seismic Behavior of RC Framed Structures," in *The 76th SEAOC Annual Convention*, September 26-29, 2007.
- [30] M. Al Satari and J. Anderson, "Estimating Inelastic Seismic Demands by Elastic Analysis for Reinforced Concrete (RC) Framed Structures," in *The 75th SEAOC Annual Convention*, September 13-16, 2006, pp. 153–167.
- [31] M. H. Al Satari, "Estimation of Seismic Response Demands for RC Framed Structures," University of Southern California, 2005.
- [32] Mourlas, Ch., Papadrakakis, M. and Markou, G. (2017), "A computationally efficient model for the cyclic behavior of reinforced concrete structural members", *Engineering Structures*, Vol. 141, 97-125.
- [33] Gonzalez-Vidoso F., Kotsovos M.D. and Pavlovic M.N. (1991), "A three-dimensional nonlinear finite-element model for structural concrete. Part 1: main features and objectivity study; and Part 2: generality study", *Proceedings of the Institution of Civil Engineers*, Part 2, Research and Theory, Vol. 91, pp. 517-544.
- [34] Willam K. J. and Warnke E. P., (1974), "Constitutive model for the triaxial behaviour of concrete", *Seminar on concrete structures subjected to triaxial stresses*, Instituto Sperimentale Modeli e Strutture, Bergamo, Paper III-1.
- [35] Menegotto, M., and Pinto, P. E. (1973). "Method of analysis for cyclically loaded reinforced concrete plane frames including changes in geometry and non-elastic behavior of elements under combined normal force and bending." *Proceedings, IABSE Symposium on Resistance and Ultimate Deformability of Structures Acted on by Well Defined Repeated Loads*, Lisbon, Portugal, 15–22.
- [36] ACI Committee, *Building Code Requirements for Structural Concrete*, (ACI 318M-11), 2011.

NUMERICAL SIMULATION OF ATHEROSCLEROTIC PLAQUE GROWTH IN RIGHT CORONARY ARTERIES

Igor Saveljic^{1,2}, Velibor Isailovic^{1,2}, Zarko Milosevic^{1,2}, Dalibor Nikolic^{1,2}, Milica Nikolic^{1,2}, Bojana Cirkovic-Andjelkovic^{1,2}, Exarchos Themis³, Dimitris Fotiadis³, Gualtiero Pelosi⁴, Oberdan Parodi⁴
and Nenad Filipovic^{1,2}

¹Faculty of engineering, University of Kragujevac, Kragujevac, Serbia

²Bioengineering Research and Development Center, Kragujevac, Serbia

³University of Ioannina, Ioannina, Greece

⁴National Research Council Pisa, Italy

E-mail: isaveljic@kg.ac.rs

Keywords: Computational Fluid Dynamics, Coronary Artery, Plaque Concentration, Wall Shear Stress.

Abstract. Atherosclerosis is a leading cause of mortality in the all developed countries. This disease begins with endothelial dysfunction, which favors lipid and cell elements crossing inside blood vessel wall. Interaction between the blood and the plaque can lead to plaque rupture. An important hemodynamic parameter in interaction between fluid and vessel wall is the wall shear stress (WSS), which is the mechanical force imposed on the endothelium by the flowing blood. The objective of this study is to examine influence of wall shear stress on the atherosclerosis development. Using computational fluid dynamics (CFD) in right coronary arteries, previously obtained using DICOM images, numerical simulation was performed. Also, plaque concentration in the arterial wall was calculated. The three-dimensional blood flow was described using Navier–Stokes equation and the continuity equation. Mass transfer within the blood lumen and through the arterial wall is coupled with the blood flow and is modeled by a convection–diffusion equation. Kedem–Katchalsky equations were used for transports the low-density lipoproteins (LDL) in the lumen and throw the vessel tissue. The inflammatory process is modeled using three additional reaction–diffusion partial differential equations. The results for plaque concentration for the right coronary arteries are presented in this paper.

1 INTRODUCTION

Atherosclerosis is a disorder in the function of the membrane (endothelium) of the first layer of the blood vessel that leads to accumulation of lipids in the intima layer of the blood vessel. Atherosclerosis starts with endothelial dysfunction and after that comes to accumulations of lipid, cholesterol, calcium and cell elements inside blood vessel wall (fig 1). Many studies confirmed different risk factor which contributes development of the atherosclerosis; the most common are higher blood pressure, increased blood sugar values, age, cigarette consumption, etc. Great contribution to atherosclerosis development gives mechanical quantities such as low shear stress areas which lead to dysfunction of the first layer of the vessel wall [1].

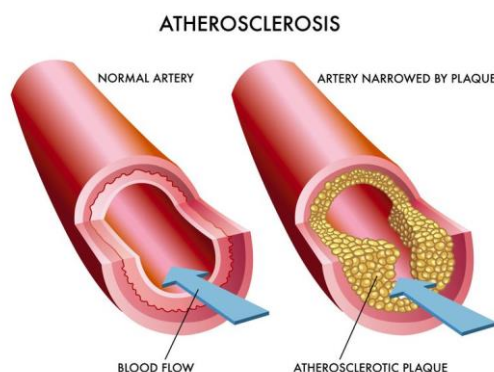


Figure 1. Normal and partially blocked blood vessels

The purpose of this paper was to determine hemodynamic parameters such as mass flow and wall shear stress

with computational fluid dynamics in the right coronary artery using patient-specific data obtained from computed tomography. Also, plaque concentration in the arterial wall was calculated. Finite element method, used in this work, is for many years the dominant numerical methods for solving fields of physical quantities. Many researchers have studied influence of the wall shear stress on the development of plaque progression, determining the relationship between the location of the plaque and the value of the wall shear stress [2], [3].

Two time periods were analyzed: baseline (0 months) and follow-up (after 8 months). Plaque progression was performed using numerical approach. Mass transport of low density lipoprotein through the arterial wall was firstly described. Fluid motion in the lumen domain is described with Navier–Stokes equations, the fluid filtration with the Darcy law, while the Kedem–Katchalsky equations used for the solute flow between the lumen domain, endothelium and the first layer of the vessel wall–intima.

2 MATERIALS AND METHODS

2.1 Computer model

The fundamental equations for the low density lipoprotein transport through the lumen and solid domain and for plaque development are given within this section. Navier–Stokes equation eqn (1), and continuity equation eqn (2) of incompressible fluid was used for 3D blood flow:

$$-\mu \nabla^2 u_l + \rho (u_l \cdot \nabla) u_l + \nabla p_l = 0 \quad (1)$$

$$\nabla u_l = 0 \quad (2)$$

where u_l is blood velocity, p_l is pressure, μ is blood dynamic viscosity and ρ is density [4], [5]. Darcy's Law for Newtonian fluids was used to model mass transfer across the wall of the blood vessel:

$$u_w - \nabla \left(\frac{k}{\mu_p} p_w \right) = 0 \quad (3)$$

$$\nabla u_w = 0 \quad (4)$$

where u_w is transmural velocity, k is the Darcian permeability coefficient of the arterial wall, p_w pressure in the vessel wall and μ_p is viscosity of blood plasma. Mass transfer in the lumen domain was modeled using convective diffusion equations eqn (5):

$$\nabla \cdot (-D_l \nabla c_l + c_l u_l) = 0 \quad (5)$$

where D_l is diffusion coefficient of the lumen while the c_l represents blood concentration. Convective diffusion reactive equations eqn (6) were used for modeling mass transfer in the wall which was related to transmural flow:

$$\nabla \cdot (-D_w \nabla c_w + K c_w u_w) = r_w c_w \quad (6)$$

where D_w is diffusive coefficient of solution in the wall, c_w is solute concentration, K is solute lag coefficient and r_w is consumption rate constant.

Low density lipoprotein transport in the lumen of the vessel was coupled with Kedem-Katchalsky equations eqn (7), eqn (8):

$$J_v = L_p (\Delta p - \sigma_d \Delta \pi) \quad (7)$$

$$J_s = P \Delta c + (1 - \sigma_f) J_v \bar{c} \quad (8)$$

where L_p is the hydraulic conductivity of the endothelium, Δp is the pressure drop across the endothelium, $\Delta \pi$ is the oncotic pressure difference across the endothelium, Δc is the solute concentration difference across the endothelium, σ_d is the osmotic reflection coefficient, σ_f is the solvent reflection coefficient, P is the solute endothelial permeability, and \bar{c} is the mean endothelial concentration [6], [7].

Three additional partial differential equations were used for solving the inflammatory process [8], [9]:

$$\begin{aligned}\partial_t O_x &= d_2 \Delta O_x - k_1 O_x \cdot M \\ \partial_t M + \text{div}(v_w M) &= d_1 \Delta M - k_1 O_x \cdot M + S / (1 - S) \\ \partial_t S &= d_3 \Delta S - \lambda S + k_1 O_x \cdot M + \gamma (O_x - O_x^{thr})\end{aligned}\quad (9)$$

where O_x represent oxidized lipoprotein transport or c_w – the solute concentration in the wall, M is concentration in the intima of macrophages, S is concentration in the intima of cytokines, d_1 , d_2 , d_3 are the corresponding diffusion coefficients, λ and γ are degradation and lipoprotein transport oxidized detection coefficients, and v_w is the inflammatory velocity of plaque growth.

2.2 Boundary conditions

Computer finite element model used here for performing simulations were generated using medical images (CT). There are 516 DICOM images for this model.

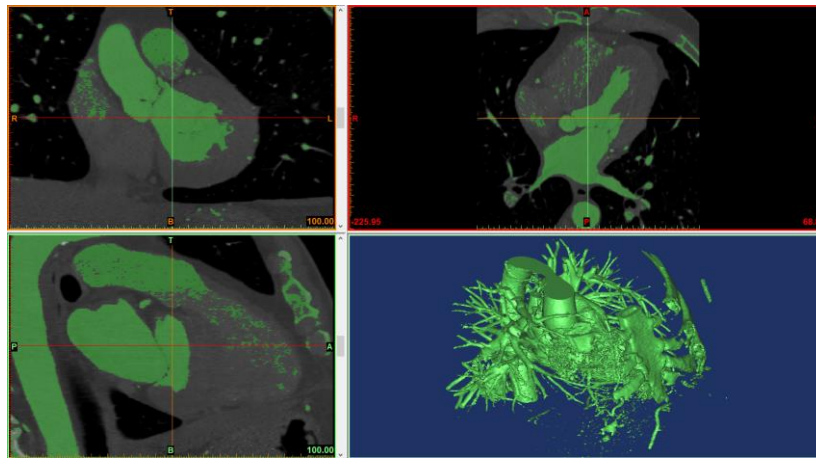


Figure 2. Application of segmentation algorithm and representation of 3D model

Figure 2 represents the process of obtaining a three-dimensional model using an automatic segmentation algorithm within the Materialize Mimics 10.01 software. Blood flow through the right coronary artery (RCA) was simulated using PAK solver [10]. Blood was considered as a Newtonian fluid with a dynamic viscosity of $\mu=0.00365$ Pas and incompressible with a density of $\rho=1050$ kg/m³. Pulsatile coronary inlet velocity waveform was used (fig 3). A three-dimensional mesh consists of 230687 nodes and 184236 elements.

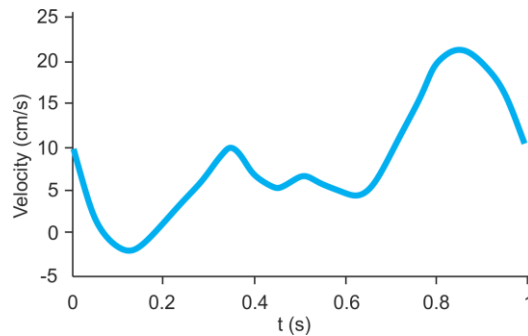


Figure 3. Pulsatile coronary inlet velocity waveform [11]

3 RESULTS

A three-dimensional simulation of blood flow through lumen and plaque progression in vessel wall was simulated. The bio molecular parameters such as LDL, HDL and triglycerides are used for the computer simulation (tab 1).

Patient No.	LDL		HDL		Triglycerides	
	baseline	follow-up	baseline	follow-up	baseline	follow-up
#01	16	96.4	46	40	182	113
#02	107	104.6	59	55	178	157
#03	164	164	74	75	110	108

Table 1. The bio molecular parameters and adhesion molecules

Patient #01 is 67 years old male, which of cardiovascular risks has past smoking and dyslipidemia. From the current therapy receives the Statins. Statins, also known as HMG-CoA reductase inhibitors, are a class of lipid-lowering medications. Statins have been found to reduce cardiovascular disease (CVD) and mortality in those who are at high risk of cardiovascular disease. The evidence is strong that statins are effective for treating CVD in the early stages of the disease (secondary prevention) and in those at elevated risk but without CVD (primary prevention). Figure 4 shows results of shear stress distribution and plaque concentration for patient #01.

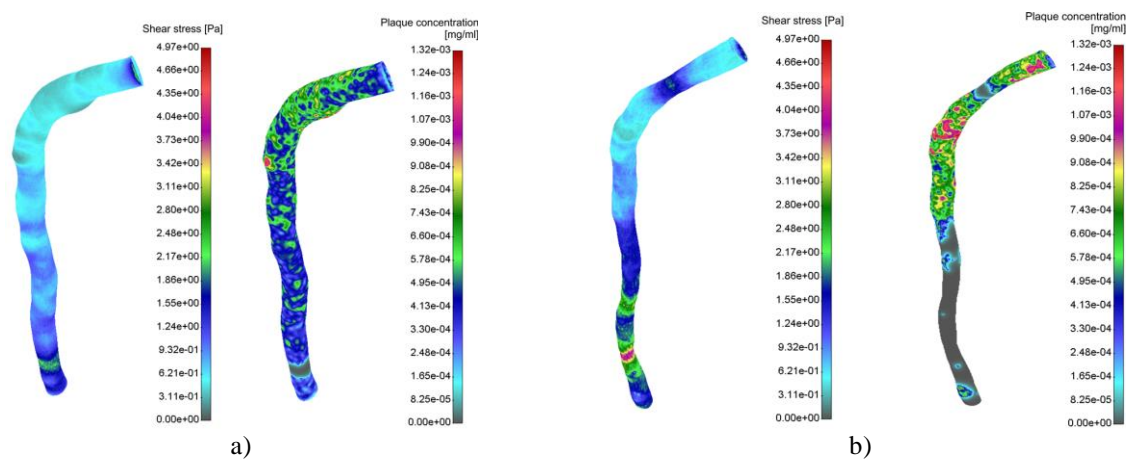


Figure 4. Shear stress distribution and plaque concentration for patient #01: a) baseline, b) follow up

At a length of 5 to 11 mm, from the inlet of the coronary artery, a low values of wall shear stress was observed. Average values range from 0.32 to 0.43 Pa, measured at cross sections, at a distance of 0.5 mm. Also, at 21.1 mm from the inlet of the artery, a low value of the wall shear stress was noticed. Low shear stress values are associated with increased plaque concentration, as shown in the fig 4a (right; red color). The highest values of plaque concentration in these zones are 1.32e-03 mg/ml. The second time moment, follow up (fig 4b), shows higher values of wall shear stress in the observed zone, and higher plaque concentration values that indicating there has been further plaque progression.

Patient #02 is 69 years old female, which of cardiovascular risks has hypertension. From the current therapy receives the ACE-Inhibitors and Aspirin. An angiotensin-converting enzyme inhibitor (ACE inhibitor) is a pharmaceutical drug used primarily for the treatment of hypertension (elevated blood pressure) and congestive heart failure. This group of drugs causes relaxation of blood vessels as well as a decrease in the volume of blood, which leads to lower blood pressure and reduced demand from the heart. Aspirin, also known as acetylsalicylic acid (ASA), is a nonsteroidal anti-inflammatory drug (NSAID) and works similar to other NSAIDs but also suppresses the normal functioning of platelets. Results of shear stress distribution and plaque concentration for patient #02 are shown on fig 5.

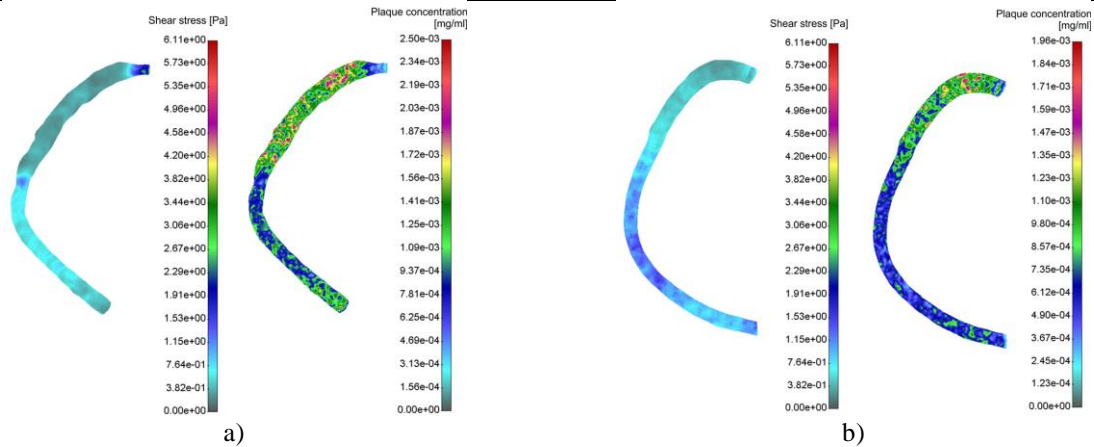


Figure 5. Shear stress distribution and plaque concentration for patient #02: a) baseline, b) follow-up

As can be seen from Figure 5, at the inlet of the coronary artery, from 5 mm to 37 mm, there is a low values of wall shear stress. Average values range from 0.21 to 0.27 Pa, measured at cross sections, at a distance of 0.5 mm. At the same time, on the mentioned part of the coronary artery, an increased plaque concentration with a maximum value of 2.5×10^{-3} mg/ml was observed. The second time moment, follow-up (fig 5b), shows lower values of wall shear stress in the observed zone, and lower plaque concentration values indicating that the applied therapy gave results.

Patient #03 is 47 years old male, which of cardiovascular risks has dyslipidemia. From the current therapy receives the Aspirin. Results of shear stress distribution and plaque concentration for patient #03 are shown on fig 6.

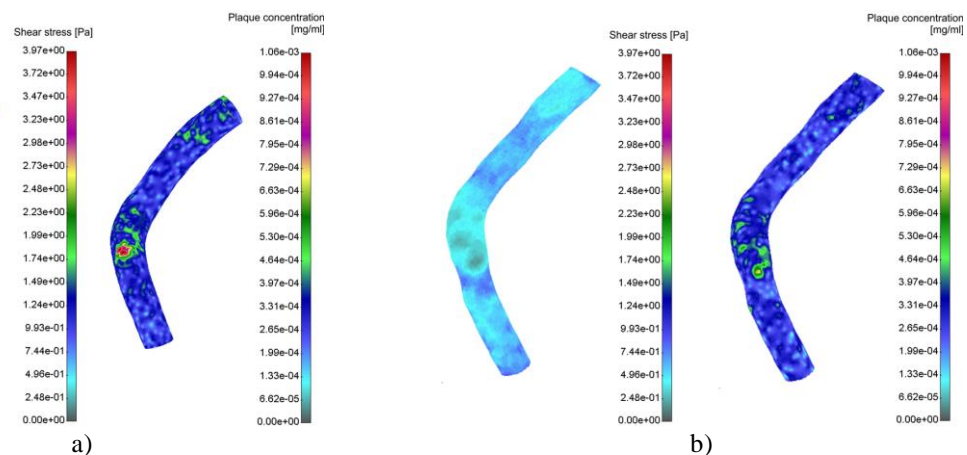


Figure 6. Shear stress distribution and plaque concentration for patient #03: a) baseline, b) follow up

At 19mm, viewed from above, from the artery entrance, a low value of wall shear stress and a potentially site of plaque concentration was observed. The mean value is 0.22 Pa. At the observed site of the artery, the concentration of plaque of 1.06×10^{-3} mg/ml was measured. Observing another time moment, follow up, it can be noticed that there is a mild drop in wall shear stress value and plaque concentrations at that location. So, it can be concluded that there has been stabilization and prevention of further progression of the disease.

4 CONCLUSIONS

Cardiovascular disease is responsible for an increasing number of mortality in all developed countries. Great attention is focused on studying this disease in order to reduce the mortality rate. In this study three-dimensional simulations were investigated in order to determine hemodynamic parameter such as wall shear stress with computational fluid dynamics in the coronary artery using patient-specific data from computed tomography. Also, plaque concentration in the arterial wall was calculated. Two time moments were observed: baseline (0 months) and follow-up 1 (after 8 months). The results of the performed analyzes have shown that sites with lower shear stress values were correlated with the sites of plaque accumulation measurements.

By knowing bio-molecular parameters such as LDL, HDL and triglycerides, it is possible to predict the sites of plaque occurrence as well as concentration in certain places of the artery using computer simulation.

ACKNOWLEDGMENTS

This study was funded by the grants from the Serbian Ministry of Education, Science and Technological Development III41007, ON174028 and EC HORIZON2020 689068 SMARTool project.

REFERENCES

- [1] Filipovic, N., Rosic, M., Tanaskovic, I., Milosevic, Z., D Nikolic, Zdravkovic, N, Peulic, A., Kojic, M., Fotiadis, D., Parodi, O. (2011), “ARTreat project: Three-dimensional Numerical Simulation of Plaque Formation and Development in the Arteries,” *Information Technology in BioMedicine*, Vol. 16, pp. 272-278.
- [2] Caro, C.G., Fitz-Gerald, J.M., Schroter, R.C. (1971), “Atheroma and arterial wall shear observation, correlation and proposal of a shear-dependent mass transfer Mechanism for Atherogenesis,” *Proc Roy Soc*, Vol. 177, pp. 109–159.
- [3] Giannogolou, G.D., Soulis, J.V., Farmakis, T.M., Farmakis, D.M., Louridas, G.E. (2002), “Haemodynamic factors and the important role of local low static pressure in coronary wall thickening,” *International journal of Cardiology*, Vol. 86, pp. 27–40.
- [4] Filipovic, N., Kojic, M., Ivanovic, M., Stojanovic, B., Otasevic, L., Rankovic, V. (2006), *MedCFD, Specialized CFD software for simulation of blood flow through arteries*, University of Kragujevac, Serbia.
- [5] Kojic, M., Filipovic, N., Stojanovic, B., Kojic, N. (2008), *Computer Modeling in Bioengineering: Theoretical Background, Examples and Software*, John Wiley and Sons, Chichester, England.
- [6] Kedem, O., Katchalsky, A. (1961), “A physical interpretation of the phenomenological coefficients of membrane permeability,” *J General Physiol*, Vol. 45, pp. 143–79.
- [7] Kedem, O., Katchalsky, A. (1958), “Thermodynamic analysis of the permeability of biological membranes to non-electrolytes,” *Biochim Biophys*, Vol. 27, pp. 229–46.
- [8] Calvez, V., Ebde, A., N. Meunier, A. Raoult, “Mathematical modelling of the atherosclerotic plaque formation”, *ESAIM Proceedings*, 28, 2008, pp. 1-12.
- [9] Boynard, M., Calvez, V., Hamraoui, A., Meunier, N., Raoult, A. (2009), “Mathematical modelling of earliest stage of atherosclerosis,” *COMPdyn 2009 – SEECM 2009*, 22 - 24 June 2009, Island of Rhodes, Greece.
- [11] Kojic, M., Filipovic, N., Stojanovic, B., Kojic, N. (2008), *Computer Modeling in Bioengineering – Theoretical Background, Examples and Software*, John Wiley and Sons, England.
- [12] Johnston, B.M., Johnston, P.R., Corney, S., Kilpatrick, D. (2005), “Non-Newtonian blood flow in human right coronary arteries: Transient simulations,” *J Biomech.*, Vol. 39, pp. 1116–1128.

A SPECTRAL COLLOCATION METHOD FOR VIBRATION SUPPRESSION OF SMART ELASTIC PLATES

Aliki D. Muradova¹, Georgios E. Stavroulakis² and Georgios K. Tairidis³

School of Production Engineering and Management
Technical University of Crete
Chania, GR-73100, Greece

e-mail: ¹aliki@mred.tuc.gr, ²gestavr@dpem.tuc.gr, ³tairidis@gmail.com

web page: ^{1,2,3}<http://www.comeco.tuc.gr/Personnel.html>

Keywords: Smart Plate Model, Fourier Expansions, Collocation Method, Fuzzy Control, Computational Algorithm.

Abstract. *A dynamic control model for vibration suppression of a smart elastic plate with piezoelectric materials is considered. The plate is subjected to external transversal disturbances and generalized control forces, produced by the electromechanical coupling effects. Various boundary conditions are considered. A spectral collocation method is proposed in order to spatially discretize the model. Mamdani type fuzzy inference system is used in order to compose the controller. The external loading and control forces are located at the discrete collocation points on the plate domain. Numerical results are presented.*

1 INTRODUCTION

Classical mathematical theories of control work well on linear systems. However, their effectiveness depends on many restrictions. On the other hand nonlinear controllers, based on fuzzy logic with built in smart computational methods can give a good description of a behaviour of nonlinear structures and provide a nonlinear feedback.

An active vibration control of smart elastic plates has been considered by many authors. Different methods have been proposed [4, 6, 10, 11, 12, 16, 18] etc. The control systems are classified on three groups, control systems with Mamdani fuzzy controllers, control systems with Takagi-Sugeno fuzzy controllers, and adaptive and predictive control systems.

Here a vibration suppression of a smart piezoelectric plate is performed by the algorithm, based on spatial discretization by means of a spectral collocation method. The obtained system of ordinary differential equations is solved with the use of Newmark method [14] and an application Mamdani type fuzzy inference system. The collocation method gives possibilities to locate control forces at discrete points of the plate. Usually, for solving partial differential equations spline and Chebyshev collocation methods are developed (e.g., [5, 15]). In the paper [5] a pseudo-spectral Chebyshev-collocation technique for solving the nonlinear problem for a plate is applied. Here we propose an effective combination of spectral and collocation methods which possess a high accuracy order at collocation points, convenient and the same time simple in applications to control problems. The proposed numerical algorithm is intended for a control of Fourier coefficients in the Fourier double series expansions for the solution. After computing the coefficients we can easily calculate the displacement, velocity and Airy's function at each point of the plate.

Active fuzzy control is a suitable tool for the systematic development of nonlinear control strategies and can be fine-tuned if no experience exists in the behaviour of considered body (structure) or if one designs more complicated control schemes. In some cases the fine tuning of fuzzy parameters can be optimized by using optimization methods ([7, 8, 13, 19] etc.).

The present paper is organized as follows. Section 2 focuses on the formulation of the mechanical models, along with the set up of the initial and of the boundary conditions. In Section 3 the model is spatially discretized with the use of the collocation method, while in Section 4 Newmark- β is considered for solving the system of equations. In the following two Sections 5 and 6 are given the piezoelectric constitutive equations and the details of the fuzzy controller respectively. Finally, numerical results are given in Section 7 and the main conclusions are reported in Section 8.

2 FORMULATION OF THE PROBLEM

A mathematical model describing vibrations of an isotropic, homogeneous elastic plate with piezoelectric

materials in the presence of active control, and allowance for the rotational inertia of the plate elements and viscous damping, is written as

$$L(w) \equiv \rho h w_{tt} - \rho \frac{h^3}{12} \Delta w_{tt} + h c w_t + D \Delta^2 w = [Q] + [Z], \quad (1)$$

in the linear case (Kirchhoff's plate small deformations, e.g. [1, 17]).

And in general for the nonlinear case (von Kármán's plate model for large deflections ([1, 2, 3] etc.)

$$L_1(w, \psi) \equiv L(w) - h[w, \psi] = [Q] + [Z], \quad (2)$$

$$L_2(w, \psi) \equiv \Delta^2 \psi - \frac{E}{2}[w, w] = 0, \quad (t, x, y) \in \Omega, \quad (3)$$

where the following notations are used:

- $[w, \psi] = \partial_{11} w \partial_{22} \psi + \partial_{11} \psi \partial_{22} w - 2 \partial_{12} w \partial_{12} \psi$ (Monge-Ampère's form).
- w is the deflection (displacement) of the plate.
- $\psi(t, x, y)$ is the Airy stress potential describing internal stresses, which appear due to the deformation of the plate.
- $\Omega = (0, T] \times G$, where T is the final time and $G = (0, l_1) \times (0, l_2)$ is the shape of the plate (l_1 and l_2 are the lengths of the sides of the plate).
- ρ is the density of the material.
- h is the thickness of the plate.
- c is the viscous damping coefficient.
- D is the flexural rigidity of the plate.
- $[Q]$ are the external transversal loading forces.
- $[Z]$ are the control forces.

For the collocation method it is required that $w, \psi \in C^2(0, T; C^2(G)) \cup C(0, T; C^4(G))$. Regarding the loading forces we consider $[Q]$ as a function of (t, x, y) or as a discrete function only of t , defined at some collocation points of the plate. The suppression of vibrations is done through the control of the Fourier coefficients. We consider a time-discrete type of control force $[Z]$, located at some discrete-collocation points of the plate, which may be different from the points where external forces are applied.

For the displacement and velocity at the initial time we assume

$$w(0, x, y) = u(x, y), \quad w_t(0, x, y) = v(x, y) \text{ in } G,$$

where the functions $u, v \in C(G)$.

Regarding the boundary conditions we consider simply supported, partially and totally clamped plates (see [9]).

3 DISCRETIZATION WITH THE USE OF THE COLLOCATION METHOD

An approximate analytical solution of (2), (3) in the form of partial sums of double Fourier's series with the time-dependent coefficients ([9, 10, 11]) reads

$$W_N(t, x, y) = \sum_{i,j=1}^N w_N^{ij}(t) \omega_{ij}(x, y), \quad W_{t,N}(t, x, y) = \sum_{i,j=1}^N w_{t,N}^{ij}(t) \omega_{ij}(x, y), \quad (4)$$

$$\Psi_N(t, x, y) = \sum_{i,j=1}^N \psi_N^{ij}(t) \varphi_{ij}(x, y), \quad (t > 0), \quad (5)$$

where the global basis functions $\omega_{ij}, \varphi_{ij}$ are chosen to match the boundary conditions. For the initial conditions we have

$$W_N(0, x, y) = u_N(x, y) = \sum_{i,j=1}^N w_N^{ij}(0) \omega_{ij}(x, y), \quad (6)$$

$$W_{t,N}(0, x, y) = v_N(x, y) = \sum_{i,j=1}^N w_{t,N}^{ij}(0) \sigma_{ij}(x, y), \quad (7)$$

where φ_{ij} and σ_{ij} are the bases. It is assumed $\varphi_{ij} = \sigma_{ij} = \omega_{ij}$.

Let us now consider the collocation points (x_m, y_n) , $\{(x_m, y_n), 0 < x_m < l_1, 0 < y_n < l_2, m, n = 1, 2, \dots, N\}$ on the spatial domain G for the equation (1) and for the system (2), (3). Suppose, that $[Q]$ is the function of time defined at some or all collocation points. Similarly, let the control forces $[Z]$ be put at some collocation points, which may coincide with the points of application of the loading pressure. We find the solution of (2), (3) in the form (4), (5) when W_N and Ψ_N satisfy the equations (2), (3) at the collocation points, i.e.

$$L_1(W_N, \Psi_N)|_{(x=x_m, y=y_n)} \equiv L(W_N)|_{(x=x_m, y=y_n)} - h[W_N, \Psi_N]|_{(x=x_m, y=y_n)} \quad (8)$$

$$= [Q]|_{(x=x_m, y=y_n)} + [Z]|_{(x=x_m, y=y_n)},$$

$$L_2(W_N, \Psi_N)|_{(x=x_m, y=y_n)} = 0, \quad m, n = 1, 2, \dots, N. \quad (9)$$

Supposing that control forces are located at every or some collocation points, from (8) and (9) we obtain a system of nonlinear ordinary differential equations of motion with respect to w_N^{mn} and ψ_N^{mn}

$$(\mathbf{M}\ddot{\mathbf{w}}_N)_{mn} + (\mathbf{C}\dot{\mathbf{w}}_N)_{mn} + (\mathbf{K}_1\mathbf{w}_N)_{mn} = (\mathbf{A}_{1,N}(\mathbf{w}_N, \Psi_N))_{mn} + q_{mn} + \mathbf{z}_{mn}, \quad (\mathbf{K}_2\Psi_N)_{mn} = \mathbf{A}_{2,N}(\mathbf{w}_N, \mathbf{w}_N)_{mn}$$

or

$$(\mathbf{M}\ddot{\mathbf{w}}_N)_{mn} + (\mathbf{C}\dot{\mathbf{w}}_N)_{mn} + (\mathbf{K}_1\mathbf{w}_N)_{mn} = (\mathbf{A}_{1,N}(\mathbf{w}_N, \mathbf{K}_2^{-1}\mathbf{A}_{2,N}(\mathbf{w}_N, \mathbf{w}_N)))_{mn} + q_{mn} + \mathbf{z}_{mn}, \quad (10)$$

where

$$(\mathbf{M}\ddot{\mathbf{w}}_N)_{mn} = \sum_{i,j=1}^N w_{tt}^{ij}(t) \left(\rho h - \rho \frac{h^3}{12} \Delta \right) \omega_{ij}(x_m, y_n),$$

$$(\mathbf{C}\dot{\mathbf{w}}_N)_{mn} = hc \sum_{i,j=1}^N w_t^{ij}(t) \omega_{ij}(x_m, y_n),$$

$$(\mathbf{K}_1\mathbf{w}_N)_{mn} = D \sum_{i,j=1}^N \Delta^2 w^{ij}(t) \omega_{ij}(x_m, y_n),$$

$$(\mathbf{K}_2\Psi_N)_{mn} = \sum_{i,j=1}^N \Delta^2 \psi^{ij}(t) \varphi_{ij}(x_m, y_n),$$

$$\mathbf{A}_{1,N}(\mathbf{w}_N, \Psi_N) = h(\mathbf{A}_N(\mathbf{w}_N, \Psi_N))_{mn},$$

$$\mathbf{A}_{2,N}(\mathbf{w}_N, \Psi_N) = \frac{E}{2}(\mathbf{A}_N(\mathbf{w}_N, \Psi_N))_{mn},$$

$$(\mathbf{A}_N(\mathbf{w}_N, \Psi_N))_{mn} = \sum_{i,j=1}^N \sum_{k,l=1}^N w^{ij}(t) w^{kl}(t) (\partial_{11} \omega_{ij}(x_m, y_n) \partial_{22} \varphi_{kl}(x_m, y_n) + \varphi_{ij}(x_m, y_n) \partial_{22} \omega_{kl}(x_m, y_n) - 2 \partial_{12} \omega_{ij}(x_m, y_n) \partial_{12} \varphi_{kl}(x_m, y_n)).$$

Obviously, for the linear model (1) the nonlinear part in the right-hand side of (10), $\mathbf{A}_{1,N}(\mathbf{w}_N, \mathbf{K}_2^{-1}\mathbf{A}_{2,N}(\mathbf{w}_N, \mathbf{w}_N))$ does not present. Furthermore, q_{mn} are the values of the time-discrete forces at some collocation points (x_m, y_n) , $m, n = N_1, N_1 + 1, \dots, N_2$ and \mathbf{z}_{mn} are the values of the control forces at some collocation points (x_m, y_n) , $m, n = M_1, M_1 + 1, \dots, M_2$. The collocation points where the external loading forces are applied are called loading points and the points where we put/locate the control are called control points. In case $N_1 \equiv M_1 \leq N$ and $N_2 \equiv M_2 \leq N$ the loading points coincide with the control points. Obviously, we can also deal with free collocation points, where the external and control forces are absent. At these points the values of the external and control forces are supposed to be zero.

The advantage of the collocation method over the Galerkin's projections is that we do not need to take the inner products, and we can consider external loading disturbances at the discrete points and locate the control forces of (all or some) collocation points in the proper way. Inversely, the collocation points can be considered at the best positions for the control, i.e. the collocation points are chosen in order to provide optimal suppressions of vibrations of the plate.

However, the collocation method may be not so accurate in the area domain between the collocation points, and the obtained mass, damping and stiffness matrices are not so sparse as in case of Galerkin's projections.

For the initial conditions from (6), (7) we have

$$\sum_{i,j=1}^N w_N^{ij}(0) \omega_{ij}(x_m, y_n) = u_N(x_m, y_n), \quad \sum_{i,j=1}^N w_{t,N}^{ij}(0) \omega_{ij}(x_m, y_n) = v_N(x_m, y_n), \quad m, n = 1, 2, \dots, N.$$

4 NEWMARK-- β FORMULAS FOR THE SYSTEM (10)

For solving the system of equations (10) the Newmark- β method, [14] is applied. According to the method the following formulas for the displacement, velocity and acceleration hold

$$\mathbf{w}_k = \mathbf{g}_{k,0} + \beta \Delta t^2 \ddot{\mathbf{w}}_{k+1}, \quad ^1$$

$$\dot{\mathbf{w}}_k = \mathbf{g}_{k,1} + \gamma \Delta t \ddot{\mathbf{w}}_{k+1},$$

where

$$\mathbf{g}_{k,0} = \mathbf{w}_k + \Delta t \dot{\mathbf{w}}_k + \Delta t^2 (0.5 - \beta) \ddot{\mathbf{w}}_{k+1}, \quad \mathbf{g}_{k,1} = \mathbf{w}_k + \Delta t (1 - \gamma) \dot{\mathbf{w}}_{k+1},$$

$$\mathbf{w}_k = \mathbf{w}(t_k), \quad t_k = k\Delta t, \quad k = 0, 1, \dots, K_T, \quad \Delta t = \frac{T}{K_T}.$$

Here and below the index N is omitted for the convenience.

For the integration constants we take $\beta = 0.25$, $\gamma = 0.5$ that corresponds to the case of unconditionally stable constant average acceleration method.

5 PIEZOELECTRIC EQUATIONS

For the application of the fuzzy control mechanism, piezoelectric elements which provide the smart behavior are considered across the structure. The formulation of the piezoelectric equations takes into account some assumptions. For example, the mechanical and the electrical forces are balanced at a certain time, due to the existence of vibrations and thus, the piezoelectric equations can be decoupled. Moreover, the temperature variation is neglected. Under these assumptions, the linear piezoelectric equations of the coupling between the elastic and the electric field can be written in matrix form as

$$\{D\} = [e]\{\varepsilon\} + [\xi]\{E\}$$

$$\{\sigma\} = [c]\{\varepsilon\} - [e]^T\{E\}$$

where $\{D\}$ is the electric displacement, $[e]$ is the piezoelectric stress, $\{\varepsilon\}$ is the strain, $[\xi]$ is the dielectric constant, $\{E\}$ is the electric field, $\{\sigma\}$ is the stress and $[c]$ is the plane-stress ([20]).

In the case where the piezoelectric patch acts as a sensor, the sensor equation can be derived from the equation of the electro-elastic relation of a piezoelectric material which reads

$$D_z = \tilde{\varepsilon}_{31} \varepsilon_x + \tilde{\xi}_{33} E_z$$

Note that only strains produced by the host structure, act on the piezoelectric patch, thus the output charge from the sensor is given by

$$q(t) = \frac{1}{2} \left\{ \left(\int_{S_{ef}} D_z dS \right)_{z=h/2} + \left(\int_{S_{ef}} D_z dS \right)_{z=h/2+h_p} \right\}$$

where S_{ef} is the effective surface electrode of the patch. The effective surface electrode of the patch is the portion of the patch that is covered by electrodes on both sides. The electric charge generated due to the external mechanical disturbance will be detected only if the charge is collected through the effective surface electrode. In this work, it is assumed that the entire piezoelectric patch serves as effective surface electrode. According to the direct piezoelectric phenomenon and taking into account that no electric field applied to the sensor layer, we get

$$q(t) = \int_{S_{ef}} \tilde{\varepsilon}_{31} \varepsilon_x dS = \int_{S_{ef}} \tilde{\varepsilon}_{31} \left(\frac{h+h_p}{2} \right) \frac{\partial \psi}{\partial x} dS$$

The current on the surface of the patch can be calculated by differentiating the charge with respect to time.

$$i(t) = \frac{dq(t)}{dt}$$

The current is converted into voltage output by

$$V(t) = G_s i(t)$$

where G_s is the gain of the current amplifier.

6 COMPUTATIONAL PROCEDURE WITH THE USE OF FUZZY INFERENCE CONTROLLER

Similarly with the techniques, described in [10, 11] a nonlinear fuzzy controller is constructed by using the Fuzzy Toolbox of MatLab. The Mamdani-type FIS with two inputs and one output is used. Giving "mappings" of input variables into membership functions and truth values, the controller makes decisions for what action to take based on a set of "rules". The system receives as inputs the coefficient w^{ij} for the displacement and velocity w_t^{ij} , and gives as output the control force z at a given point of the structure. The controller system uses 15 rules. All rules have weight equal to 1 and use the AND-type logical operator. The rules are presented in Table 1.

Vel\Disp	FarUp	CloseUp	Equil	CloseDn	FarDn
Up	Max	Med+	Low+	Null	Low-
Null	Med+	Low+	Null	Low-	Med-
Down	Low+	Null	Low-	Med-	Min

Table 1. The fuzzy inference rules (e.g. if the displacement is "FarUp" and the velocity is "UP" then the control force is "Max").

Triangular and trapezoidal shape membership functions have been chosen both for the inputs and for the output. The implication method has been set to minimum (min), while the aggregation method has been set to maximum (max). The defuzzified output value has been created by using the MOM (Mean of Maximum) defuzzification method.

We start from a prediction of deflection of the plate and calculate the range of expected displacements and velocities, which can be done from practical calculations, and evaluation of the external loading forces, we design the FIS. We construct the control rules, state the membership functions (fuzzy sets) for input and output, and tune the parameters.

7 NUMERICAL RESULTS

In this section we present numerical results for solving (1) with the simply supported boundary conditions. A dynamic, sinusoidal periodic loading is used, $Q(t, x, y) = \sin \omega t$, $\omega = 5\pi$, $q_{11}(t) = Q(t, x_1, y_1)$, $q_{13}(t) = Q(t, x_1, y_3)$, $q_{31}(t) = Q(t, x_3, y_1)$, $q_{33}(t) = Q(t, x_3, y_3)$, and $q_{mn} = 0$ at the other collocation points. The collocation points are defined as $x_m = mh_1$, $y_n = nh_2$, $m, n = 1, 2, \dots, N$, $h_1 = l_1/(N+1)$, $h_2 = l_2/(N+1)$. The purpose of the fuzzy controller is to reduce the oscillation. The collocated controller takes as input the displacement and the velocity at discrete points of the plate and gives back the control forces to be applied at the same point. The physical parameters take the following values: $l_1 = l_2 = 1$, $E = 2$, $h = 0.5$, $\rho = 1000$, $c = 0$, $D = 1$. The computations have been done with $T = 50$, $N = 3$ and $K = 500$. On Figures 1, 2 and 3 the membership functions for the inputs (displacement and velocity) and output (control) are shown.

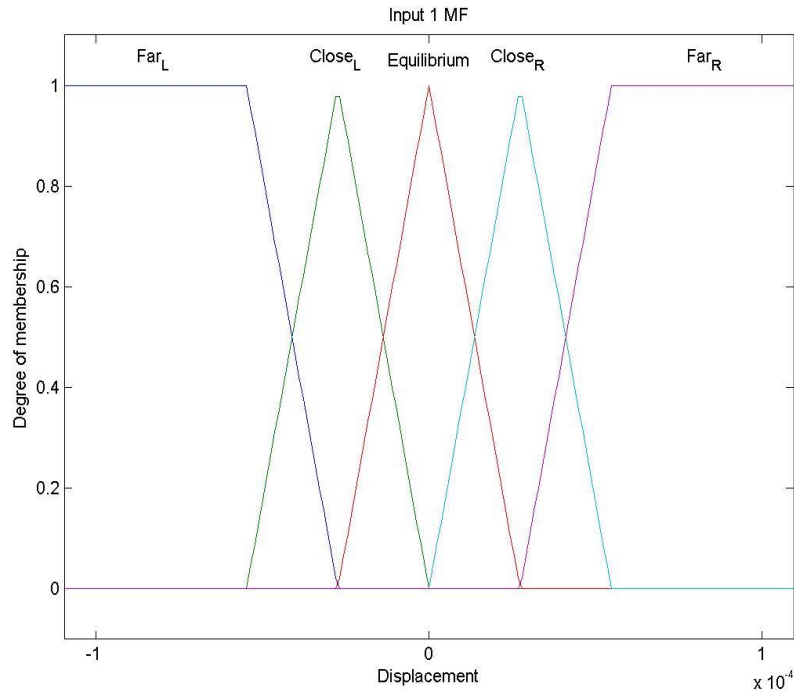


Figure 1. Membership functions for the input (displacement) of the fuzzy inference system.

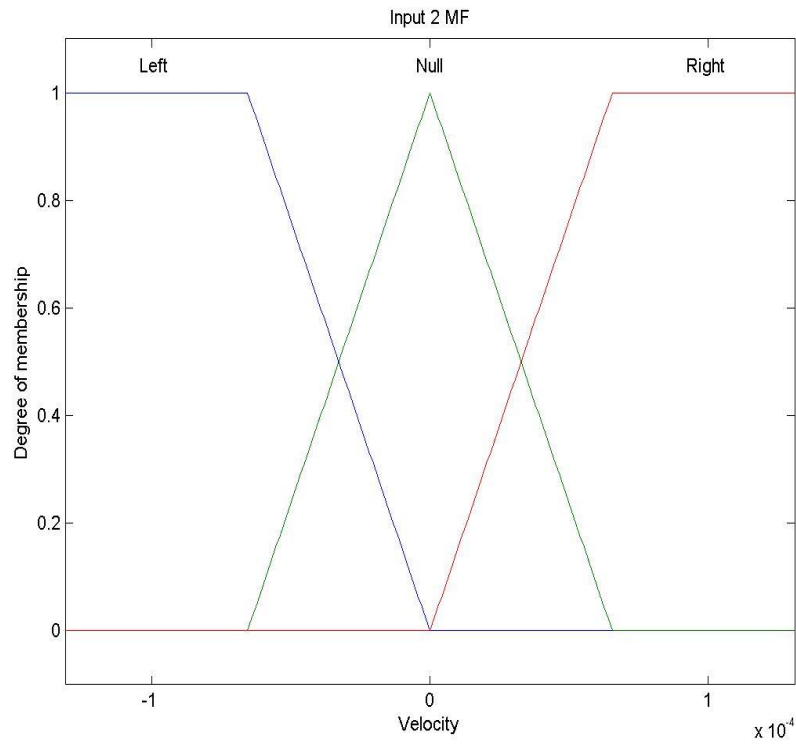


Figure 2. Membership functions for the input (velocity) of the fuzzy inference system.

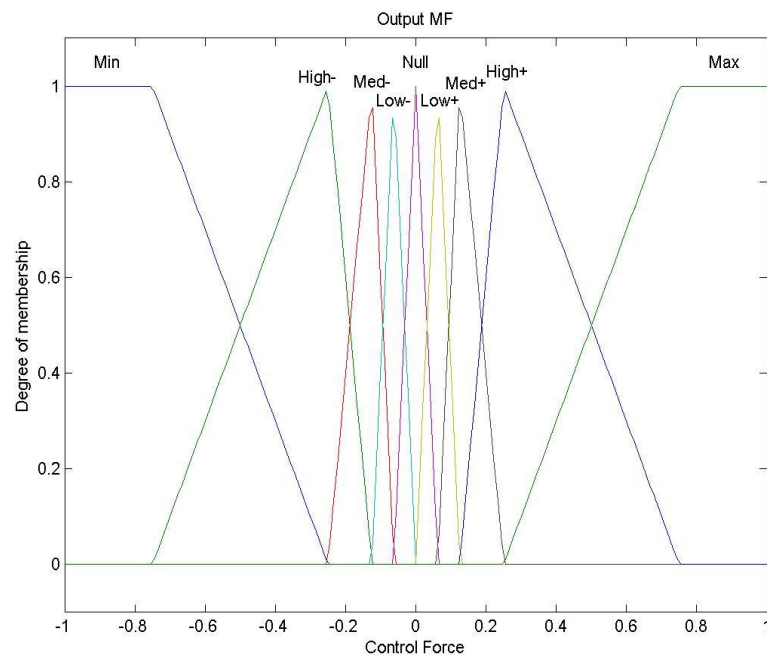


Figure 3. Membership functions for the output (control) of the fuzzy inference system.

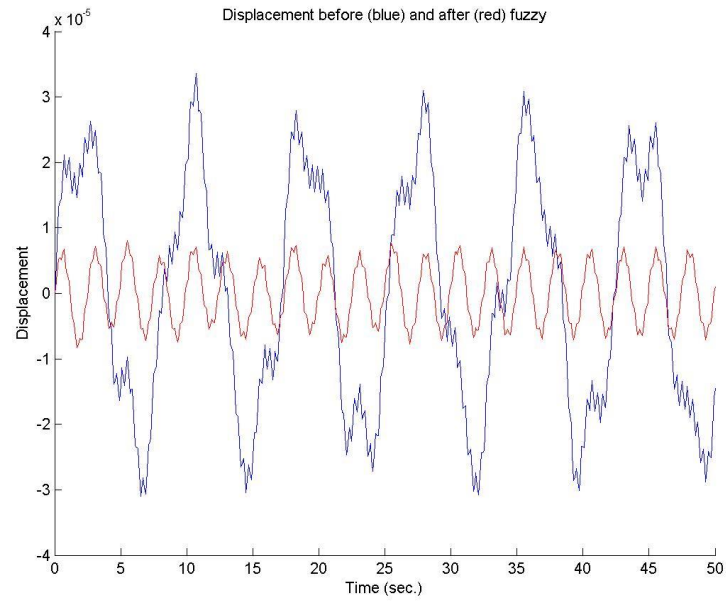


Figure 4. Displacement at the collocation point (x_1, y_1) of the plate before and after the fuzzy.

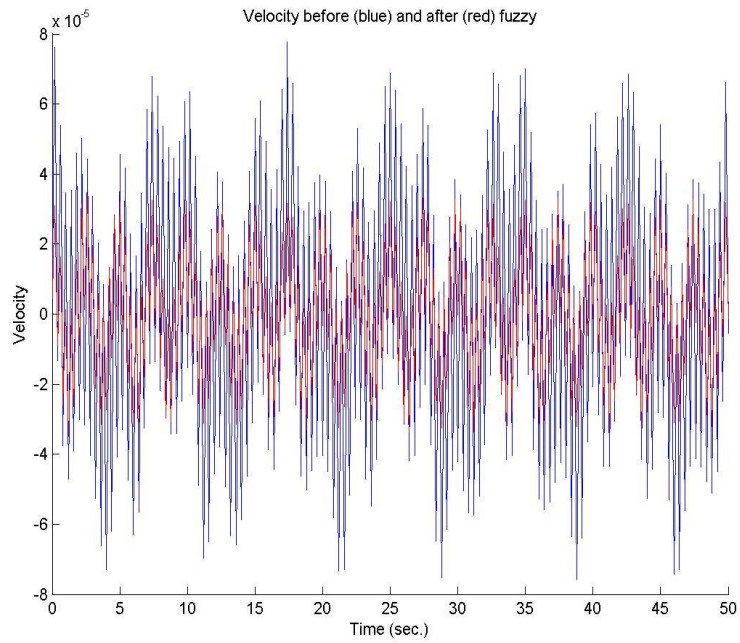


Figure 5. Velocity at the collocation point (x_1, y_1) of the plate before and after the fuzzy.

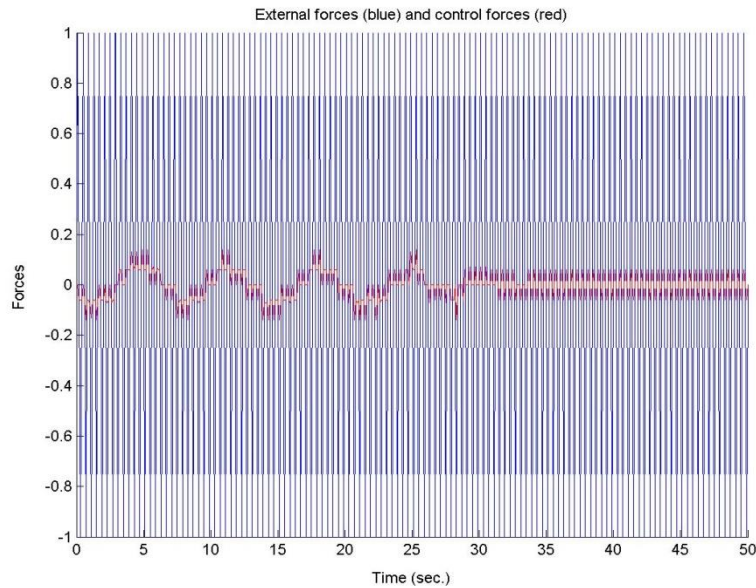


Figure 6. External forces and control forces after the fuzzy at the collocation point (x_1, y_1) of the plate.

The obtained results, the displacement and velocity are show in Figures 3, 4. The external loading and control forces after using the fuzzy inference controller are plotted in Figures 5, 6.

8 CONCLUSIONS

A vibration suppression of an elastic plate with the use of a spectral-collocation method and a fuzzy inference controller has been presented. First, the mechanical model has been spatially discretized and then the obtained system has been solved by means of the Newmark method. On each time step of the simulation the discrete values of control have been included in the system of ordinary differential equations. A numerical example has been illustrated.

REFERENCES

- [1] Ciarlet Ph. G. (1997), *Mathematical Elasticity, v. II: Theory of Plates*, Elsevier, Amsterdam.
- [2] Ciarlet P. and Rabier P. (1980), *Les equations de von Kármán*, Springer-Verlag, Berlin, Heidelberg, New York.
- [3] Duvaut G. and Lions J. L. (1972), *Les inequations en mecaniques et en physiques*, Dunod.
- [4] Fisco N.R. and Adeli H., (2011), "Smart structures: Part II, Hybrid control systems and control strategies", *Scientia Iranica*, Vol. 18(3), pp. 285-295.
- [5] Kirby R. M., Yosibash Z. (2004), "Solution of von Kármán dynamic non-linear plate equatons using a pseudo spectral method", *Comp. Meth. Appl. Mech. Eng.*, Vol. 193, pp. 575-599.
- [6] Korkmaz S. (2011), "A review of active structural control: challenges for engineering informatics", *Comput. and Struct.*, 89, 2113–2132.
- [7] Lu Q., Peng Zh., Chu F., and Huang J., (2003), "Design of fuzzy controller for smart structures using genetic algorithms", *Smart Mater. Struct.*, Vol. 12(6), pp. 979-986.
- [8] Koutsianitis P., Tairidis G. K., Drosopoulos G. A., Foutsitzi G. A. and Stavroulakis G. E. (2017), "Effectiveness of optimized fuzzy controllers on partially delaminated piezocomposites", *Acta Mechanica*, Vol. 228(4), pp. 1373-1392.
- [9] Muradova A. D. (2015), "A time spectral method for solving the nonlinear dynamic equations of a rectangular elastic plate", *J. Eng. Math.*, Vol. 92, pp. 83–101.
- [10] Muradova A. D. and Stavroulakis G. E., (2013), "Fuzzy vibration control of a smart plate", *Int. J. Comput. Meth. in Eng. Sci. Mech*, Vol. 14, pp. 212–220.
- [11] Muradova A. D. and Stavroulakis G. E. (2015), "Hybrid control of vibrations of smart von Kármán plate", *Acta Mechanica*, Vol. 226, pp. 3463–3475.
- [12] Muradova A. D., Tairidis G. K. and Stavroulakis G. E. (2018), "Fuzzy vibration suppression of a smart elastic plate using graphical computing environment", *Soft Computing in Civil Engineering*, Vol. 2(1), pp. 1-17.
- [13] Muradova A. D., Tairidis G. K., Stavroulakis G. E. (2017), "Adaptive Neuro-Fuzzy Vibration Control of a Smart Plate", *Numerical Algebra, Control and Optimization*, AIMS (Amer. Ins. Math. Sci.), @AIM Sciences,

- Vol. 7(3), pp. 251-271.
- [14] Newmark N. M. (1959), "A Method of Computation for Structural Dynamics", *ASCE J. of the Eng. Mech. Division*, Vol. 85, N. EM3.
- [15] Schiesser W. E. (2017), *Spline Collocation Methods for Partial Differential Equation*, Wiley.
- [16] Shirazi A. H. N., Owji H. R. and Rafeeyan M. (2011), "Active vibration control of an FGM rectangular plate using fuzzy logic controllers. *Procedia Engineering*", Vol. 14, pp. 3019–3026.
- [17] Reddy J. N. (2007), *Theory and Analysis of Elastic Plates and Shells*, CRC Press, Taylor & Francis.
- [18] Tavakolpour A. R., Mailah M., Darus I. Z. M. and Tokhi O. (2010), "Selflearning active vibration control of a flexible plate structure with piezoelectric actuator", *Simul. Model. Prac. and Theory*, Vol. 18, pp. 516–532.
- [19] Tairidis G. K. Foutsitzi G., Koutsianitis P. and Stavroulakis G.E. (2016), "Fine tuning of a fuzzy controller for vibration suppression of smart plates using genetic algorithms", *Advances in Engineering Software*, Vol. 101, pp. 123–135.
- [20] Reddy, J.N. (2004). *Mechanics of Laminated Composite Plates and Shells, Theory and Analysis* (2nd edition). CRC Press, Boca Raton, FL.

INVESTIGATION OF THE POSITION OF THE PIEZOELECTRIC PATCHES ON A SHUNTED PIEZOELECTRIC BEAM

Georgios K. Tairidis ^{1,3}, Panagiotis Koutsianitis ¹, Georgia Foutsitzi ², Georgios E. Stavroulakis ¹,
Jean-Francois Deü ³ and Roger Ohayon ³

¹ School of Production Engineering and Management
Technical University of Crete, Chania, GR-73100, Greece

² Department of Computer Engineering
Technological Educational Institution of Epirus, Preveza, GR-48100, Greece

³ Structural Mechanics and Coupled Systems Laboratory
Conservatoire National des Arts et Métiers, Paris, FR-75003, France

e-mails: tairidis@gmail.com, panoskout@gmail.com, gfoutsitzi@teiep.gr, gestavr@dpem.tuc.gr,
jeanfrancois.deu@cnam.fr, roger.ohayon@cnam.fr

web pages: <http://www.comeco.tuc.gr>, <http://www.lmssc.cnam.fr>

Keywords: Smart Structures, Piezocomposites, Shunt Circuits

Abstract. *Shunt piezoelectric systems are very popular in structural damping applications. The main characteristic of such systems is that they can absorb vibrations and destroy the kinetic energy, by consuming it in an electric circuit which consists of resistors, inductors and capacitors. The aim of the present paper is to investigate the optimal placement of the piezoelectric patches on a shunted piezoelectric beam which consists of an elastic part and a pair of piezoelectric elements which are connected to the shunt circuits. The investigation is carried out using the tools of modal analysis for the evaluation of the different positions of the patches.*

1 INTRODUCTION

Smart structures with embedded sensors, actuators, or even control systems have the ability to respond and/or suppress excitations which, in turn, are caused by external and/or unknown reasons. Various smart materials such as piezoelectrics, piezoceramics, electrostrictive materials, magnetostrictive materials, etc. can be used to provide flexible structures with smart characteristics. It is noteworthy that the combination of both functions, i.e. sensing and actuation, is possible, due to the nature of the piezoelectric effect. Thus, an increasing interest in passive control of vibrations by shunted piezoelectric transducers with electrical impedances is observed during the last years. Shunt damping, which is implemented through the adequate placement of piezoelectric patches is a widely used method for the vibration suppression of smart flexible structures [1], [2]. In addition, in the case of a smart controlled structure with some, even small, energy demands, energy harvesting can be added to a structure with shunt circuits in order to provide the small amount of energy which is required for the controller.

The shunt piezoelectric systems are capable of suppressing mechanical vibrations and/or noise of smart composite flexible structures, which can be critical for several applications, e.g. on wind energy turbine systems. Thus, the optimization of such systems, e.g. in the direction of the optimal placement of piezoelectric patches can be very helpful.

2 THE BEAM MODEL

For the investigations of the present paper, a smart piezoelectric beam with shunt characteristics is considered as seen in figure 1. One can observe that the beam is divided in three areas. The area 2 is the position of the piezoelectric patch, while the other two areas of the beam consist only of the elastic part of the structure. Note that area 2 can be discretized by several elements, for example in our application with 5 finite elements. The form and the layout of the piezoelectric elements, depends on the desired result in terms of vibration suppression, as well as the structural geometry and/or the involved materials [3]. Similar models can be used in various applications including, among others, the design of smart piezocomposite structures [4], [5], in structural control as can be found in review articles [6], [7] or energy harvesting applications as considered, among others, in [8], [9], [10].

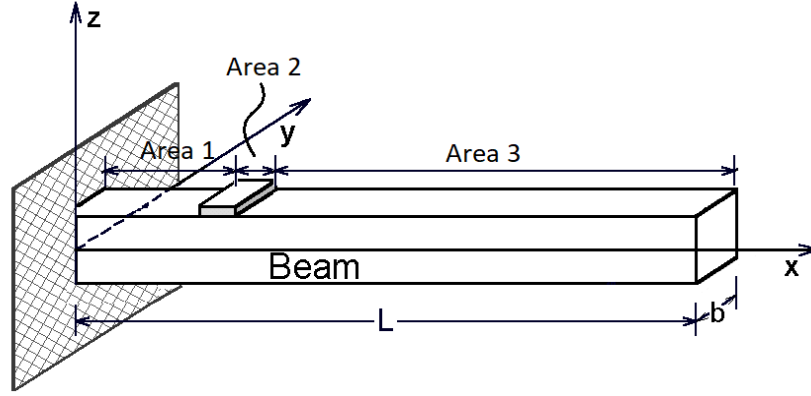


Figure 1: A smart beam model

2.1 Equations of motion for the beam and calculation of system response

The equations of motion for the beam with surface bonded piezoelectric patches, are derived by the Hamilton's principle:

$$\int_0^T (\delta T - \delta U + \delta W) dt = 0 \quad (1)$$

The total strain energy U and the kinetic energy T are calculated using the expressions:

$$U = \frac{1}{2} \int_0^L \int_A [\sigma_x \varepsilon_x + \tau_{xz} \gamma_{xz} - E_z D_z] dA dx, \quad T = \frac{1}{2} \int_0^L \int_A \rho [\dot{u}_x^2 + \dot{u}_z^2] dA dx \quad (2)$$

where dA is the area of cross-section of the beam.

If the only loading consists of moments induced by piezoelectric actuators and since the structure has no bending-twisting couple, then δW is given as:

$$\delta W = b \int_0^L M^A \delta \left(\frac{\partial \psi}{\partial x} \right) dx \quad (3)$$

where M^A is the moment per unit length induced by the actuator and expressed as:

$$M^A = \int_{-h/2-h_A}^{-h/2} z \sigma_x^A dz = \int_{-h/2-h_A}^{-h/2} z Q_{11} d_{31} E_z^A dz \quad (4)$$

and

$$E_z^A = \frac{V_A}{h_A} \quad (5)$$

where V_A is the applied voltage across the direction of the thickness of the piezoelectric patch and h_A is the thickness of the piezoelectric transducer.

The calculation of the eigen modes is necessary in order to find the system's response. The eigen frequencies ω_i and eigen vector Φ_i depend only on the mechanical properties of the system and can be found by calculating the N eigen values of the following problem:

$$K_m - \omega^2 M_m \Phi = 0 \quad (6)$$

The displacement field can be described as:

$$U(t) = \sum_{i=1}^N \Phi_i q_i(t) \quad (7)$$

2.2 The shunt circuits

With the term passive shunt circuit, one implies the connection of an electric impedance (e.g. a resistance, an inductance, etc.) to a piezoelectric element which in turn is attached to a smart composite structure, with basic

aim of the technique the vibration suppression of the host structure at several frequencies. The connection of a shunt system with impedance equals to $Z(\omega)$ to a piezoelectric patch leads to a relation between the voltage V and the charge q which has as follows:

$$V = -Z(\omega)q \quad (8)$$

A system based on shunt circuits can be modeled using only the pure mechanical systems and analogous electric systems. The optimum values of the electric components can be derived from the minimization of the controlled displacement fields. The amount of the maximum current which flows within the system can be used in the design of the electric components of the system. More information on shunt piezoelectric systems can be found in [1], [2], [11].

3 NUMERICAL INVESTIGATION

In the present investigation, the optimum position of the piezoelectric patch for shunt damping is sought. For this reason, the piezoelectric patch was placed at different positions of the beam and namely at elements 2-6, 12-16, 22-26 and 32-36, occupying five finite elements each time.

Firstly, the case of placement at the elements 2-6, i.e. near the fixed end of the structure is considered. The system response for the first four eigen frequencies is shown in the following figures. With blue color is denoted the initial system and with red color is shown a suitably defined resonant shunt system. From the results one can observe that this position is excellent, as satisfactory suppression is achieved for each one from the first four modes.

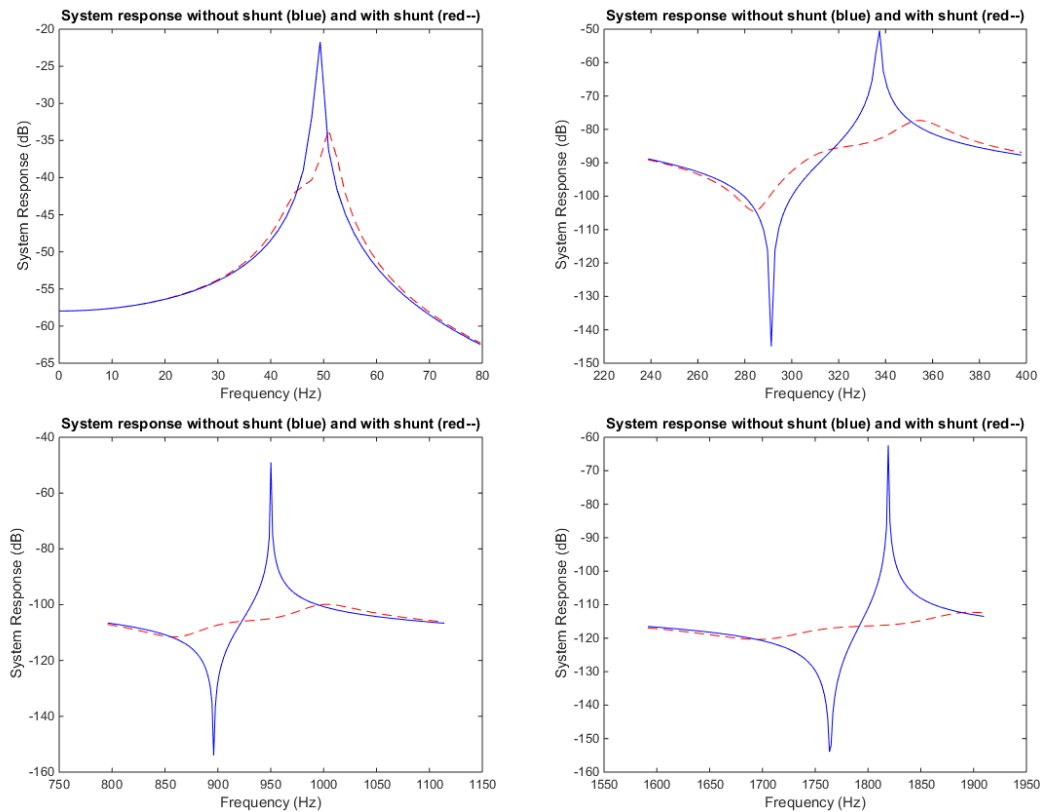


Figure 2: The response in the area of the first four eigen frequencies of the structure when piezoelectric patch is placed at elements 2-6

During the second test, the piezoelectric patch was placed on the finite elements 12-16. The results, which are shown in figure 3 below, indicate that the suppression is not adequate for the examined modes.

When the piezoelectric patch is placed on the elements 22-26, it is obvious from the system response that the reduction is less compared to the previous cases. One may have expected this, as this area is near a vibration bond. The results of this test are shown in figure 4.

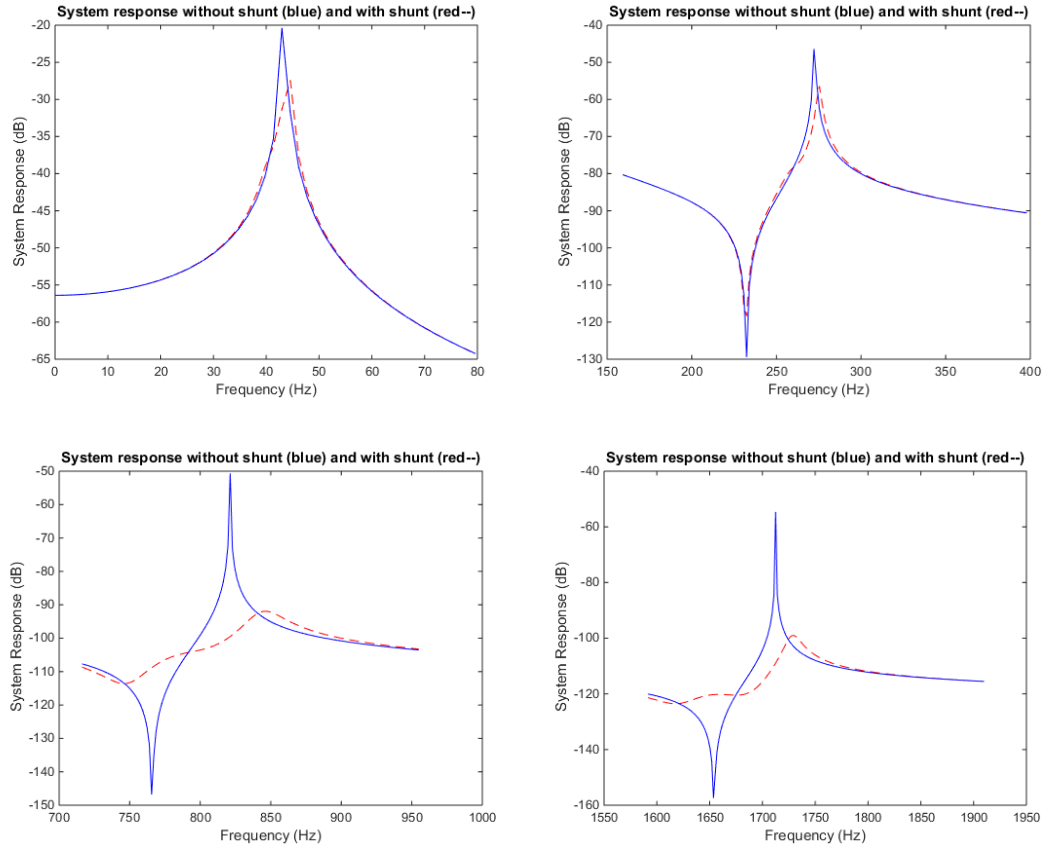


Figure 3: The response for the first four eigen frequencies when piezoelectric patch is placed at elements 12-16

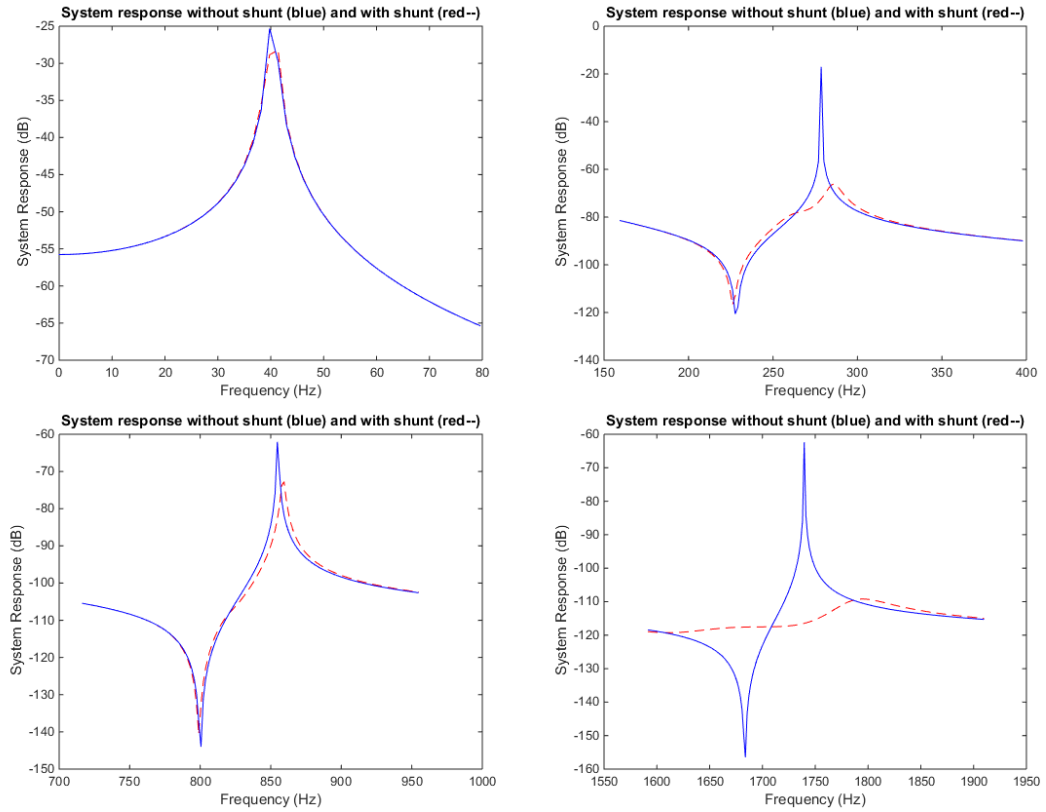


Figure 4: The response for the first four eigen frequencies of the structure when piezoelectric patch is placed at elements 22-26

Finally, the piezoelectric element was placed near the free end, on elements 32-36. In this case one can observe that the system is not working for the first eigen mode. This result was rather expected, as it is known from dynamics that near this area there is no information about this mode. The results are shown schematically in the figure 5 below.

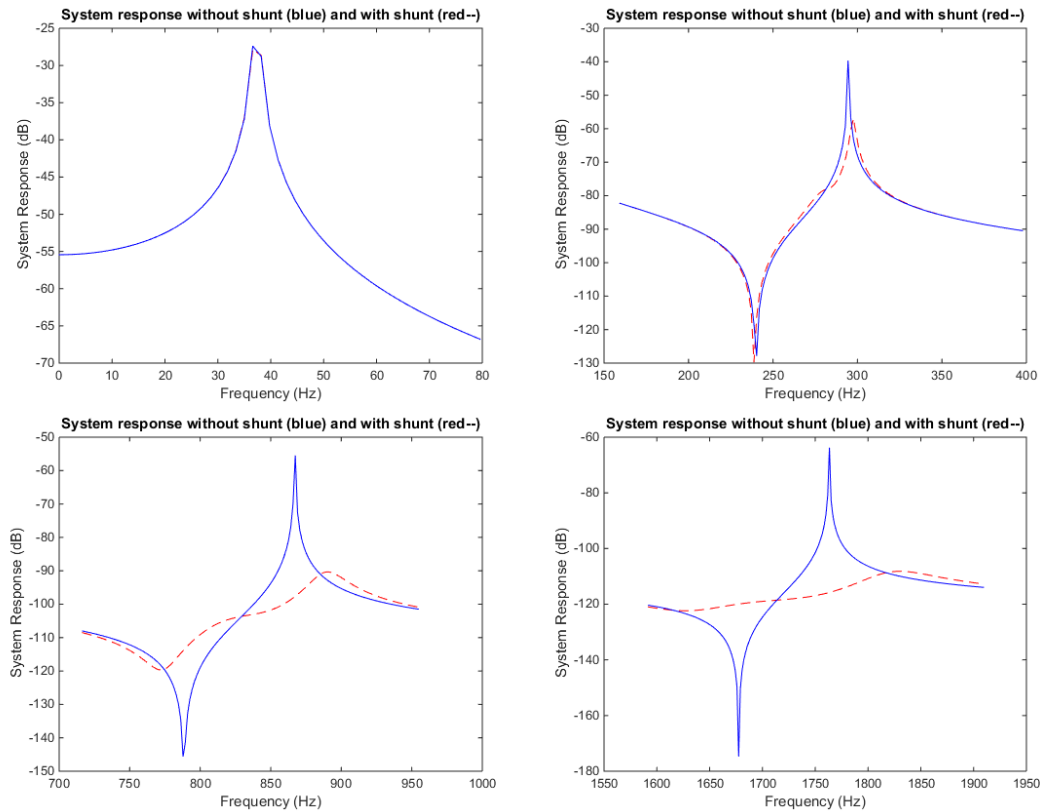


Figure 5: The response in the area of the first four eigen frequencies when the patch is placed at elements 32-36

From the above results, one can conclude that the best position for the piezoelectric element is near the fixed end, i.e. at the finite elements 2-6.

4 CONCLUSIONS

Shunt piezoelectric systems have the ability to add the necessary damping to smart structures in order to overtake vibrations which are due to external causes. It is known that the more the piezoelectric material in one smart structure, the more the coupling, as the total stiffness is affected. However, if the modification of the values of inductance and/or the resistance is possible, then a single patch, or a symmetrically placed pair of patches is sufficient in order to obtain the desired properties. In the present paper, several different positions of the piezoelectric patch on a smart beam were investigated. The selection of the possible positions was based on intuition. The results have shown that the best position of the patch is near the fixed end, as the system can suppress more modes. To extend this work, one may consider using a global optimization method, e.g. a genetic algorithm, which may provide better results.

ACKNOWLEDGMENTS

The work of Georgios Tairidis has been supported by a postdoctoral research grant through the “IKY fellowship of excellence for postgraduate studies in Greece – Siemens programme”.

Georgios Tairidis also gratefully acknowledges the French Embassy in Greece and the French Government for the funding of his visit to the Structural Mechanics and Coupled Systems Laboratory of the institute Conservatoire national des arts et métiers through a fellowship of the program “Séjours scientifiques de haut niveau” for new researchers, as well as Professor Jean-Francois Deü and Professor Roger Ohayon of Conservatoire national des arts et métiers for their precious assistance and cooperation.

REFERENCES

- [1] Deü, J.-F., Larbi, W., Ohayon, R. and Sampaio, R. (2014), "Piezoelectric Shunt Vibration Damping of Structural-Acoustic Systems: Finite Element Formulation and Reduced-Order Model," *J. Vib. Acoust.*, Vol. 136, p. 031007 (8 pages).
- [2] Larbi, W., Deü, J.-F., and Ohayon, R. (2016), "Finite element reduced order model for noise and vibration reduction of double sandwich panels using shunted piezoelectric patches," *Applied Acoustics*, Vol. 108, pp. 40-49.
- [3] Thomas, O., Deü, J.-F., and Ducarne, J. (2009), "Vibrations of an elastic structure with shunted piezoelectric patches: efficient finite element formulation and electromechanical coupling coefficients," *Int. J. Numer. Meth. Engng*, vol. 80, pp. 235-268.
- [4] Hadjigeorgiou, E. P., Stavroulakis, G. E. and Massalas, C. V. (2006), "Shape control and damage identification of beams using piezoelectric actuation and genetic optimization," *Int J Eng Sci*, vol. 44, pp. 409-421.
- [5] Stavroulakis, G.E., Foutsitzi, G., Hadjigeorgiou, V., Marinova, D.G. and Baniotopoulos, C.C. (2005), "Design and Robust Optimal Control of Smart Beams with Application on Vibrations Suppression," *Adv Eng Software*, vol. 36, pp. 806-813.
- [6] Irschik, H. (2002) "A review of static and dynamic shape control of structures using piezoelectric actuation," *Eng Struct*, Vol. 24, pp. 5-11.
- [7] Song, G., Sethi, V. and Li, H. N. (2006), "Vibration control of civil structures using piezoceramic smart materials: A review," *Eng Struct*, Vol. 28, pp. 1513-1524.
- [8] Priya, S. and Inman, D. J. (2009), *Energy harvesting technologies*, Springer, Berlin.
- [9] Tairidis, G. K., Foutsitzi, G. A., Koutsianitis, P. and Stavroulakis, G. E. (2015) "Energy Harvesting using Piezoelectric Materials on Smart Composite Structures," *Proceedings of the fifteenth international conference on civil, structural and environmental engineering computing*, Prague, Czech Republic, 1-4 September 2015, Civil-Comp Press, Stirlingshire, UK, Paper 238, 2015. doi:10.4203/ccp.108.238
- [10] Tairidis, G. K., Marakakis, K., Koutsianitis, P., Foutsitzi, G., Stavroulakis, G.E., Deü, J.-F., and Ohayon, R. (2018) "Energy harvesting system for the power supply of a shunt piezoelectric system developed for vibration suppression," *Proceedings of the international conference on wind energy harvesting*, Catanzaro Lido, Italy, 21-23 March 2018, Vol. I, pp. 223-227.
- [11] Ducarne, J., Thomas, O. and Deü, J.-F. (2012), "Placement and dimension optimization of shunted piezoelectric patches for vibration reduction," *Journal of Sound and Vibration*, Vol. 331, pp. 3286-3303.

A BOUNDARY LAYER APPROACH FOR THE SOLUTION OF THE GENERAL SINGLE CONTACT FRICTIONAL PROBLEM IN MULTIBODY DYNAMICS

Sotirios Natsiavas¹ and Elias Paraskevopoulos¹

¹Department of Mechanical Engineering
Aristotle University
Thessaloniki, GR-54124, Greece
e-mail: natsiava@auth.gr

Keywords: Analytical dynamics, Unilateral constraint, Manifold with boundary, Frictional contact.

Abstract. *This study presents a new formulation of the dynamics of systems involving a single frictional contact. An analytical dynamics framework is employed, together with some fundamental tools of differential geometry. This provides a foundation for applying Newton's law of motion to systems possessing configuration manifolds with boundary. It is shown that the contact phase takes place inside a thin boundary layer, where the dominant dynamics is described by a set of three ordinary differential equations. The study includes a selected set of examples, with emphasis put on investigating phenomena arising during central or eccentric collision of bodies.*

1 INTRODUCTION

Dynamics of systems possessing mechanical components that come in contact during their motion is a classical subject of Mechanics (e.g., [1-6]). This is due to both its large practical significance and the challenging theoretical issues arising in the effort to predict and understand the various phenomena observed and related to contact events. Previous studies have demonstrated that friction effects are responsible for the appearance of a plethora of new phenomena during contact. Based on the type of approach adopted, these studies can roughly be divided in two general categories. In the first category, the contact event is assumed to take place in an instantaneous manner. This leads to the appearance of a discontinuity in the velocities, accompanied by unbounded contact forces in order to avoid interpenetration. This, in turn, leads to the necessity of employing techniques of the so-called Nonsmooth Mechanics (e.g., [1-5]). In essence, these approaches lead to prediction of the post-impact velocities through an algebraic process, making use of the pre-impact velocities and appropriate restitution coefficients. On the other hand, the second category of previous studies on systems with unilateral constraints is based on the Darboux-Keller approach (e.g., [6-10]). Their common characteristic is that they consider the normal impulse as an independent time-like variable and lead to a set of equations of motion during the contact phase in the form of ordinary differential equations (ODEs).

The present study is a continuation of earlier work of the authors [11,12] and applies to a class of constrained mechanical systems, involving a single contact event with friction. The approach taken is novel compared to previous studies on the subject. In particular, the analysis applied is carried out within the classical framework of analytical dynamics and can handle systems with general properties, including rigid and deformable bodies. The formulation is based on a proper application of Newton's law of motion during the contact phase. The final outcome is a completely continuous formulation, in contrast to the approaches based on non-smooth techniques. This is achieved through the use of some key ideas and concepts of b-geometry, which provide a natural and strong setting for studying mechanical systems subject to a unilateral constraint [13]. After defining the boundary of the configuration manifold and determining the essential geometric properties needed for the application of the law of motion inside a thin layer starting at this boundary, it is shown that the dominant dynamics during a single frictional collision is described by a set of three coupled ODEs. These equations describe action in a three dimensional distribution of the configuration manifold, which is related directly to the action in the physical space, where the contact event examined takes place. Using time as an independent variable presents an advantage over the Darboux-Keller approaches, since it provides a valuable time scale for investigating the part of the motion inside the boundary layer. Moreover, the general spirit of the new approach is completely different. Instead of modeling the contact with stiff springs, which demands to give up the rigidity assumption in case of a rigid body contact, application of the theory for a manifold with boundary reveals that the associated contact action is modeled by a large change in the inertia properties [13], in combination with the appearance of a strong repulsive force. More specifically, the components of the metric and the connection employed along the normal to its boundary vary in a quite rapid fashion in the vicinity of the boundary in the configuration space. This

causes a fast deceleration of the figurative particle modeling the motion of the mechanical system in the configuration manifold, as it approaches the boundary. Also, once this particle enters the boundary layer, it is pushed away from it by a strong repulsive force, which is exerted on it until its exit from the boundary [12].

In the second part of this study, the attention is shifted on applying the new analysis to investigating collision of a particle with a rigid wall and continues with examination of central and eccentric collisions of solid bodies. The more accurate modeling provides a strong basis and leads to a better understanding of the phenomena involved. Finally, the analysis is presented in a way that permits its extension to more complex problems, involving situations with multiple contacts [14].

The organization of this paper is as follows. First, the general theoretical setting is presented in the following section. Then, the essential geometric properties are presented in Section 3. This information is employed in Section 4, where the equations governing the motion during the contact phase are derived. Next, several characteristic examples are examined in Section 5. Finally, the new findings are briefly summarized in Section 6.

2 MANIFOLDS WITH BOUNDARY AND MECHANICAL SYSTEMS WITH CONTACT

This study is a continuation of recent work of the authors on the dynamics of mechanical systems subject to unilateral constraints [12]. The new ingredient is that the contact involves frictional effects. Adopting the general framework of Analytical Dynamics, the spatial configuration of the system is described by a finite set of generalized coordinates, $q = (q^1, \dots, q^n)$, selected to be minimal. These are related to a fictitious point p , moving as a function of time t on an n -dimensional manifold M , the configuration manifold of the unconstrained system [15]. Then, the presence of a contact event is signaled by an inequality condition

$$\rho(p) \geq 0, \quad (1)$$

assuring no interpenetration. The equality in this condition defines a hypersurface in M and the motion of point p occurs on one side of this hypersurface only. In this way, the function ρ acts as a boundary defining function on manifold M and gives rise to a new manifold

$$X = \{p \in M : \rho(p) \geq 0\},$$

with dimension n [13]. This manifold possesses a boundary ∂X and an interior $X^\circ = X \setminus \partial X$. Then, the new manifold is represented by the disjoint union

$$X = X^\circ \amalg \partial X,$$

while the motion of the class of systems examined is represented by a curve on the constrained manifold X . The tangent vector to such a curve at a point p belongs to an n -dimensional vector space $T_p X$, the tangent space at p . Therefore, if $\mathfrak{B}_e = \{\underline{e}_1 \dots \underline{e}_n\}$ is a basis of $T_p X$, then any of its elements can be put in the form

$$\underline{u} = u^I \underline{e}_I = u^1 \underline{e}_1 + u^i \underline{e}_i,$$

with the summation conventions

$$u^I \underline{e}_I = \sum_{I=1}^n u^I \underline{e}_I \quad \text{and} \quad u^i \underline{e}_i = \sum_{i=2}^n u^i \underline{e}_i,$$

so that a capital Latin index ranges from 1 to n and a lower case Latin index runs from 2 to n .

The tangent space at each point of X is accompanied by a cotangent space, denoted by $T_p^* X$. In fact, to each vector \underline{u} of $T_p X$ there corresponds a covector \underline{u}^* of $T_p^* X$. In dynamics, it is convenient to establish this correspondence by using the following dual product

$$\underline{u}^*(\underline{w}) = \langle \underline{u}, \underline{w} \rangle, \quad \forall \underline{w} \in T_p X, \quad (2)$$

where $\langle \cdot, \cdot \rangle$ represents the inner product of the vector space $T_p X$. In this way, for any basis \mathfrak{B}_e of $T_p X$, a dual basis $\mathfrak{B}_e^* = \{\underline{e}^1 \dots \underline{e}^n\}$ can be obtained for $T_p^* X$, by employing the conditions $\underline{e}^I(\underline{e}_J) = \delta_J^I$, where $I, J = 1, \dots, n$ and the symbol in the right hand side denotes a Kronecker's delta [15]. Finally, definition of the vector spaces $T_p X$ and $T_p^* X$ at each point of manifold X is essential in creating two other spaces, by

$$TX = \coprod_{p \in X} T_p X \quad \text{and} \quad T^*X = \coprod_{p \in X} T_p^* X,$$

known as the tangent and cotangent vector bundles over X , respectively [16].

If $V(X)$ denotes the space of all smooth vector fields on X , the integration of its elements to obtain the corresponding flows is not closed on X . To fix this problem, the theory of manifolds with boundary, or b-manifolds [13], is employed. In particular, these vector fields are elements of the space

$$V_b(X) \equiv \{V \in V(X) : V \text{ is tangent to } \partial X\}.$$

This means that if the local coordinates $x = (x^1, \dots, x^n)$ are introduced at a point p of the boundary ∂X , so that $\rho = x^1 \geq 0$, then any element of a vector field belonging to $V_b(X)$ can be put in the form

$${}^b\underline{v} = \alpha x^1 \underline{g}_1 + a^i \underline{g}_i, \quad (3)$$

over a holonomic basis $\mathfrak{B}_g = \{\underline{g}_1, \underline{g}_2, \dots, \underline{g}_n\}$, where $\underline{g}_i \equiv \partial/\partial x^i$ are tangent vectors to the coordinate lines starting at p [15]. Therefore, the special set ${}^b\mathfrak{B}_g = \{x^1 \underline{g}_1, \underline{g}_2, \dots, \underline{g}_n\}$ forms a basis for $V_b(X)$ at each point near the boundary. The first element of this set vanishes at points on the boundary, but it can be shown that there exists a new vector bundle over X , denoted by bTX , where the component vector space ${}^bT_p X$ is n -dimensional even at points of the boundary ∂X [13]. A companion b-cotangent bundle ${}^bT^*X$ can also be defined in a similar manner. Then, at a point p of ∂X , a typical element of ${}^bT^*X$ can be expressed in the form

$${}^b\underline{v}^* = \beta \frac{dx^1}{x^1} + b_i dx^i, \quad (4)$$

with $dx^i \equiv g^i$. This demonstrates that the set ${}^b\mathfrak{B}_g^* = \{dx^1/x^1, dx^2, \dots, dx^n\}$ represents a basis of ${}^bT_p^*X$ near the boundary. Finally, both the b-tangent bundle bTX and the b-cotangent bundle ${}^bT^*X$ coincide with the ordinary bundles TX and T^*X , respectively, away from the boundary (for more details, see [13] and [12]).

3 ESSENTIAL GEOMETRIC PROPERTIES OF A MANIFOLD WITH BOUNDARY

In determining the geometric properties of manifold X , it is convenient to employ two special bases in ${}^bT_p X$. The first corresponds to a local x -coordinate system, as defined in the previous section, while the second is related to the original q -coordinate system, denoted by $\mathfrak{B}_e = \{\underline{e}_1 \dots \underline{e}_n\}$ and $\mathfrak{B}_{e'} = \{\underline{e}'_1 \dots \underline{e}'_n\}$, respectively. Then, any element of ${}^bT_p X$ can be expressed in the following two alternative forms

$${}^b\underline{v} = \dot{x}^I \underline{e}_I = \dot{q}^{I'} \underline{e}'_{I'}.$$

By considering the corresponding transformation between \mathfrak{B}_e and $\mathfrak{B}_{e'}$, expressed in the form

$$\underline{e}_{I'} = A_{I'}^I \underline{e}_I \quad \text{or} \quad \underline{e}_I = B_I^{I'} \underline{e}'_{I'}, \quad (5)$$

for $I, I' = 1, \dots, n$ [15], the components of a b-vector in those bases are related by

$$\dot{x}^I = A_{I'}^I \dot{q}^{I'} \quad \text{and} \quad \dot{q}^{I'} = B_I^{I'} \dot{x}^I, \quad (6)$$

where matrix $A = [A_{I'}^I]$ is the inverse of matrix $B = [B_I^{I'}]$.

Within this setting, the components of the b-metric tensor can now be obtained. This tensor has components $\bar{g}_{IJ} = \bar{g}_{JI} = \langle \underline{e}_I, \underline{e}_J \rangle$ with respect to a basis of the x -coordinate system. This metric is virtually unaffected by the presence of the boundary at points away from the boundary ∂X , i.e.,

$$\bar{g}_{IJ} = g_{IJ} \quad \text{over } X^o, \quad (7)$$

with $G = [g_{IJ}]$. Near the boundary, the b-metric is affected in a significant way [13]. In particular, one can always find a special x -coordinate system, where the metric matrix can be put in the block diagonal form

$$\bar{G} = [\bar{g}_{IJ}] = \begin{bmatrix} \bar{g}_{11} & \underline{0}^T \\ \underline{0} & \bar{G}_r \end{bmatrix}, \quad (8)$$

with

$$\bar{g}_{IJ} = g_{IJ} + \hat{g}_{IJ}. \quad (9)$$

The term \hat{g}_{IJ} is solely due to the presence of the boundary and appears in the explicit form

$$\hat{g}_{11} = \bar{g}_{11}/(x^1)^2 \quad \text{and} \quad \hat{g}_{i1} = \hat{g}_{1i} = \hat{g}_{ij} = 0. \quad (10)$$

By employing the basis transformation expressed by Eq. (5), the metric components in the x -coordinate system can be related to the components of the metric with respect to the q -coordinate system [15], through

$$g_{IJ} = B_I^{I'} B_J^{J'} g_{I'J'} \quad \text{and} \quad g_{I'J'} = A_{I'}^I A_{J'}^J g_{IJ}. \quad (11)$$

Then, using Eq. (9), it is easily obtained that near the boundary

$$\bar{g}_{I'J'} = g_{I'J'} + \hat{g}_{I'J'}, \quad (12)$$

which is similar in form to Eq. (9). Moreover, taking into account Eq. (10), the last term is obtained through

$$\hat{g}_{I'J'} = A_{I'}^1 A_{J'}^1 \hat{g}_{11}.$$

Clearly, only the first line of matrix $A = [A_{I'}^I]$ needs to be specified for determining $\hat{g}_{IJ'}$, which is evaluated by

$$A_{I'}^I = \xi^I(\underline{e}_{I'}) = \langle \nabla \rho, \underline{e}_{I'} \rangle, \quad (13)$$

so that the gradient vector $\nabla \rho$ is normal to the boundary hypersurface defined by $\rho(q) = 0$.

Next, in analogy to Eq. (9), the b-affinities are also decomposed in the form

$$\bar{\Lambda}_{IJ}^K = \Lambda_{IJ}^K + A_{IJ}^K, \quad (14)$$

with respect to a basis of the x -coordinate system. The terms Λ_{IJ}^K coincide with the affinities of the ordinary vector bundle TX , defined over the extension manifold M , while A_{IJ}^K are terms arising from the presence of the boundary. The latter terms are negligible away from ∂X , so that

$$\bar{\Lambda}_{IJ}^K = \Lambda_{IJ}^K \quad \text{over } X^\circ. \quad (15)$$

Moreover, the correction terms A_{IJ}^K in Eq. (14) are in fact components of a tensor [12]. Also,

$$\bar{\Lambda}_{I'J'}^{K'} = \Lambda_{I'J'}^{K'} + A_{I'J'}^{K'}, \quad (16)$$

which has a similar structure to Eq. (14). It can be shown that the component A_{11}^1 has the following form

$$A_{11}^1 = \bar{\Lambda}_{11}^1 - \Lambda_{11}^1 \approx \bar{\Lambda}_{11}^1 = -1/x^1. \quad (17)$$

This term contributes to all the b-affinities of the q -coordinate system through

$$A_{I'J'}^{K'} = A_{I'}^1 A_{J'}^1 B_1^{K'} A_{11}^1,$$

which involves only terms of the form $A_{I'}^1$ and $B_1^{K'}$ [12]. The first of them are determined by Eq. (13). In addition, using Eqs (5) and (11) together with the identity $g^{IJ'} g_{J'K'} = \delta_{K'}^{I'}$, it can be shown that

$$B_1^{I'} = g^{IJ'} A_{J'}^J g_{JI}.$$

Therefore,

$$B_1^{I'} = g^{IJ'} A_{J'}^1 g_{11},$$

which implies that $B_1^{I'}$ can be evaluated by knowledge of the known components $A_{I'}^1$ only. Moreover, the affinities Λ_{IJ}^K are transformed back to the basis of the q -coordinate system by

$$\Lambda_{I'J'}^{K'} = A_{I'}^I A_{J'}^J B_K^{K'} \Lambda_{IJ}^K + B_K^{K'} A_{J',I'}^K.$$

4 EQUATIONS OF MOTION FOR THE PROBLEM OF SINGLE CONTACT WITH FRICTION

The true path of the figurative particle representing the motion on the configuration manifold is determined by application of Newton's law [11,16]. On a manifold without boundary, this law is expressed in the form

$$\nabla_{\underline{v}} \underline{p}^* = \underline{f}^*, \quad (18)$$

where ∇ represents an affine connection on the manifold, so that the left hand represents the covariant differential of the generalized momentum \underline{p}^* along a path on the manifold with tangent vector \underline{v} [17], so that

$$\nabla_{\underline{v}} \underline{p}^* = (\dot{p}_I - \Lambda_{JI}^L p_L v^J) \underline{e}^I,$$

with components of the generalized momentum given by

$$p_I = g_{IJ} v^J. \quad (19)$$

In addition, \underline{f}^* represents the generalized applied forces. On manifold X , this law appears in the form

$${}^b \nabla_{\underline{v}} \bar{\underline{p}}^* = \bar{\underline{f}}^*, \quad (20)$$

since the appropriate quantities live in the b-tangent space ${}^b T_p X$ and the b-cotangent space ${}^b T_p^* X$, respectively.

According to the material presented in the previous section, both the metric components and the affinities involved in Newton's law are affected in a significant manner by the presence of the boundary. However, this occurs only within a layer starting at the boundary ∂X of X , with a relatively small width b , introduced by the unilateral constraint examined. On the other hand, it is clear that the laws of motion expressed by Eqs (18) and (20) are identical within the interior X° of manifold X . This picture is illustrated by Fig. 1. First, in Fig. 1a is depicted the original configuration manifold M , including the constrained configuration manifold X , which results by imposing condition (1). Then, in Fig. 1b is shown a magnified picture of the boundary layer area surrounding the neighborhood of a point p on ∂X . Apart from the special x -coordinate system, originating at

p and having axis x^1 normal to the boundary, two curves (γ_α and γ_β) belonging to the special b-vector field $V_b(X)$, passing tangentially through point p with a different curvature, are also shown.

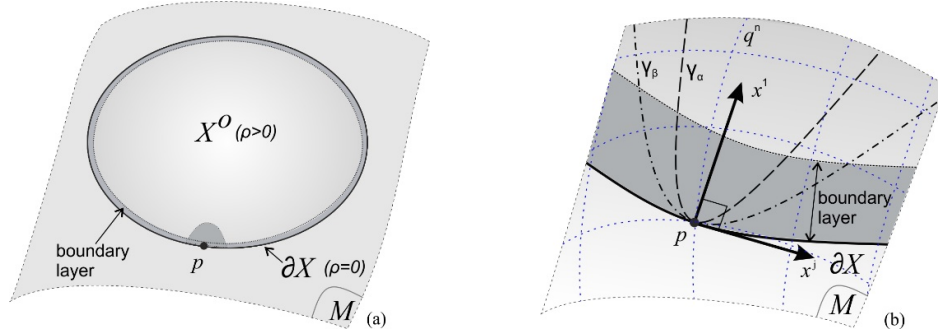


Figure 1. (a) Original configuration manifold M and constrained manifold X , for a system subject to a unilateral constraint. (b) Magnification around a boundary point p .

The focus of the present study is now shifted to the interior of the boundary layer. As a first step, this necessitates an appropriate scaling of the terms involved in the equations of motion [18]. This task is most conveniently performed in a local x -coordinate system. Then, using the above analysis and keeping only the dominant terms, it can be shown that for points near the boundary Eq. (20) is replaced by

$$\hat{p}_1 - \bar{\Lambda}_{11}^1 \hat{p}_1 v^1 - \hat{f}_1 = 0. \quad (21)$$

and

$$\dot{p}_i - \Lambda_{ji}^i p_i v^j - \bar{f}_i = 0, \quad (22)$$

for $i = 2, \dots, n$. For a frictionless contact, all terms in the last equation are $O(1)$, while those in Eq. (21) are $O(1/x^1)$. For this reason, the repulsive forcing arising within the boundary layer is chosen by the expression

$$\hat{f}_1(x^1, \dot{x}^1) = \left[\frac{k_1}{x^1} - \frac{c_1 \dot{x}^1}{(x^1)^2} \right] \hat{s}(x^1; a, b). \quad (23)$$

The first term in the right side models the effect of a force generated by a gravity type potential. It represents a strong force pushing the figurative point away from the boundary. On the other hand, the second term is associated with the dissipation of energy taking place during the motion within the boundary layer. Since this force must vanish in the outer region, a smooth function $\hat{s}(x^1; a, b)$ is also included in Eq. (23) in order to guarantee a smooth transition of the boundary force from the inner to the outer region of the boundary layer [12].

The generality of the geometric approach employed makes possible the consideration of contact events arising from the interaction between any combination of particles, rigid bodies and deformable bodies. In accordance to the general setting of Analytical Mechanics, the behavior of these bodies in the physical space, denoted by E^3 , is determined and analyzed in the configuration space X of the mechanical system examined. Apart from determining the corresponding geometric properties, this requires a set up of mappings between the physical space and the configuration space. For instance, starting from the kinematics, the relative velocity \underline{V} at the contact point of the two bodies that come in touch in the physical space is related to the generalized velocities through a general linear mapping

$$\underline{V} = D \underline{\dot{q}}. \quad (24)$$

The column vectors $\underline{V} = V^\alpha \underline{n}_\alpha$ and $\underline{\dot{q}} = \dot{q}^{I'} \underline{e}_{I'}$, with $\alpha = 1, 2, 3$ and $I' = 1, \dots, n$, are expressed with respect to the bases $\{\underline{n}_1 \ \underline{n}_2 \ \underline{n}_3\}$ and $\{\underline{e}_{1'} \ \dots \ \underline{e}_{n'}\}$ in the tangent space of the physical and the configuration manifold, respectively. This implies that the dual mapping between the corresponding momenta (covectors) is expressed by

$$\underline{p}^* = \underline{P}^* D, \quad (25)$$

where \underline{p}^* and \underline{P}^* are row vectors in the cotangent space of the configuration manifold and the physical space.

If $\chi^\alpha = \chi^\alpha(q^{I'})$ are the coordinates of a point in the physical space with respect to that special coordinate system, the differential of the boundary defining function in the configuration space can be evaluated from

$$d\rho = \frac{\partial \rho}{\partial q} = \frac{\partial \hat{\rho}}{\partial \underline{\chi}} D \Rightarrow d\rho = d\hat{\rho} D, \quad (26)$$

with $\hat{\rho} = \rho(\chi(q))$ and $D = \partial \underline{\chi} / \partial q$. Consequently, if $\{\underline{n}^1 \ \underline{n}^2 \ \underline{n}^3\}$ is a special basis of the cotangent physical space, selected so that the representative of the base covector \underline{n}^1 , as defined by Eq. (2), is normal to the local plane of contact, Eq. (26) in conjunction with Eq. (25), yields

$$\underline{e}^1 = \underline{n}^1 D. \quad (27)$$

Based on this, a new basis $\mathfrak{B}_{e^*}^* = \{\underline{e}^{1'} \ \dots \ \underline{e}^{n'}\}$ is constructed in the cotangent space ${}^b T_p^* X$, defined by

$$\underline{e}^{I'} = A_{I'}^{I''} \underline{e}^{I''} = \begin{cases} \underline{n}^{I''} D, & I'' = 1, 2, 3 \\ \delta_{I'}^{I''} \underline{e}^{I''}, & I'' = 4, \dots, n \end{cases} \quad (28)$$

Consequently, in order to create a basis for the x -coordinate system, these components a partial Gram-Schmidt orthogonalization scheme is applied in the form

$$\underline{e}^J = \underline{e}^{J'} - \gamma_J^{I'} \underline{e}^{I'} \text{ for } I = I' = 1, \dots, n \text{ and } J = 1, 2, 3, \quad (29)$$

with

$$\langle \underline{e}^I, \underline{e}^J \rangle = 0 \text{ for } I \text{ or } J = 1, 2, 3 \text{ and } I \neq J.$$

In this way, combination of Eqs (28) and (29) yields the first three basis vectors in the form

$$\underline{e}^J = \underline{\eta}^J D \text{ for } J = 1, 2, 3,$$

with

$$\underline{\eta}^1 = \underline{n}^1, \quad \underline{\eta}^2 = \underline{n}^2 - \gamma_1^{2'} \underline{n}^1 \text{ and } \underline{\eta}^3 = \underline{n}^3 - \gamma_2^{3'} \underline{n}^2 + (\gamma_2^{3'} \gamma_1^{2'} - \gamma_1^{3'}) \underline{n}^1.$$

Next, the components of the generalized force in the configuration space is evaluated in the form

$$\hat{f}_1 = F_1 + \gamma_1^{2'} F_2 + \gamma_1^{3'} F_3, \quad \hat{f}_2 = F_2 + \gamma_2^{3'} F_3 \text{ and } \hat{f}_3 = F_3. \quad (30)$$

The relation between the normal component F_1 and the two tangential components F_2 and F_3 of the contact force \underline{F} is established through an appropriate constitutive law, describing the friction action. For instance, the Amontons-Coulomb law is the most frequently adopted law for calculations in the physical space [2-6].

Based on the above, it becomes obvious that the presence of friction causes two important effects in the formulation established so far in the configuration space. First, taking into account Eq. (30), it appears that the forcing terms \hat{f}_2 and \hat{f}_3 should be comparable to \hat{f}_1 , which means that they should all be of the same order, $O(1/x^1)$, so that the friction can cause tangible effects. Therefore, since the terms $\Lambda_{ji}^\ell p_\ell v^j$ and $\dot{g}_{ij} v^j$ of Eq. (22) remain $O(1)$ even inside the boundary layer, the only possible way to balance the aforementioned forcing terms is to assume that the terms \dot{v}^2 and \dot{v}^3 , representing a velocity change, vary rapidly, i.e., they are $O(1/x^1)$ within the boundary layer. This implies that the first two relations in Eq. (22) separate from the rest (i.e., those with $i = 4, \dots, n$) and appear in the form

$$g_{22} \dot{v}^2 - \hat{f}_2 = 0 \text{ and } g_{33} \dot{v}^3 - \hat{f}_3 = 0, \quad (31)$$

where the forcing terms \hat{f}_2 and \hat{f}_3 are determined by Eq. (30). Moreover, friction affects the amplitude of the forcing in the normal direction. Specifically, the equation of motion along the normal direction to the manifold boundary is expressed by Eq. (21), again, but now with \hat{f}_1 given by Eq. (30), where $F_1(\chi^1, \dot{\chi}^1)$ appears in a form similar to that in Eq. (23), with x^1 and \dot{x}^1 replaced by χ^1 and $\dot{\chi}^1$, respectively, while F_2 and F_3 are determined by the friction law employed.

Finally, if a holonomic set of coordinates is employed, represented by the quantity $\underline{q} = (q^1 \ \dots \ q^n)^T$, Eqs (21) and (31) give rise to a set of equations of motion, which can be put in the matrix form

$$M(\underline{q}) \ddot{\underline{q}} + \underline{h}(\underline{q}, \dot{\underline{q}}, t) = \underline{0}, \quad (32)$$

even during the contact phase. This form is coincident with the second order ODE form obtained by classical formulations for systems with no constraints. If non-holonomic coordinates are also involved, then the set of equations of motion is expressed in terms of a set of quasi-velocities in place of $\dot{\underline{q}}$ [15].

5 EXAMPLES

In the first example, dynamics of a single particle colliding with a rigid wall is examined, while the second example refers to impact between a rigid body and a half-space.

5.1 Collision of a particle with a rigid wall

A single particle with mass m hits a rigid wall. During free motion, its position is determined by three Cartesian coordinates χ^1 , χ^2 and χ^3 in the physical space E^3 . If the q -coordinates are identical to them, the original configuration space is $M = \mathbb{R}^3$. Then, if these coordinates are selected so that the wall is at $\chi^1 = 0$,

$$\rho(q) = q^1.$$

Based on Eq. (26), this implies that $D = I_3$, where I_3 is the 3×3 identity matrix, while Eq. (13) yields

$$A^1 = (1 \ 0 \ 0) = \eta^1.$$

Also, the x -coordinate system can be chosen to coincide with the q -coordinate system. Therefore,

$$G = [g_{IJ}] = mI_3 \quad \text{and} \quad \Lambda_{IJ}^K = 0, \quad (I, J, K = 1, 2, 3).$$

Next, a selected set of numerical results is presented. First, in Fig. 2a is shown the history of the normal force \hat{f}_1 exerted from the boundary to the particle. The results illustrate the effect of the boundary force parameter k , for $c = 0$. The time is normalized by the total duration of the contact phase, t_f . The results of Fig. 2a indicate that the distribution of the normal force \hat{f}_1 is symmetric with respect to the line $t = t_f/2$. Also, this force reaches a plateau around the middle of the contact phase for relatively small values of k . This symmetry is broken by the presence of the boundary force dissipation parameter c , as shown in Fig. 2b, for $k = 10$. In fact, a gradual increase in the value of this parameter causes a reduction in the time interval where this force is impulsive.

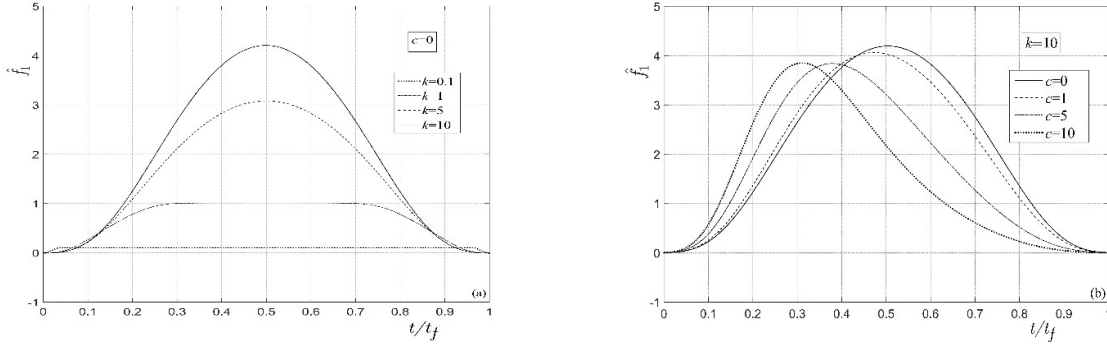


Figure 2: History of the boundary generated normal force \hat{f}_1 on the particle: (a) effect of parameter k , for $c = 0$; (b) effect of parameter c , for $k = 10$.

Likewise, to demonstrate the effects of the friction coefficient μ , in Fig. 3 is presented the history of the tangential velocity of the particle for several values of μ and $c = 0$. Specifically, the results in Fig. 3a and 3b were obtained for $k = 1$ and $k = 10$, respectively. In both cases, sufficiently small values of μ lead to conditions of gross slip, while larger values lead to slip-stick. Moreover, an increase in k favors the development of gross slip. A similar effect is also caused by increasing the magnitude of the dissipation parameter c .

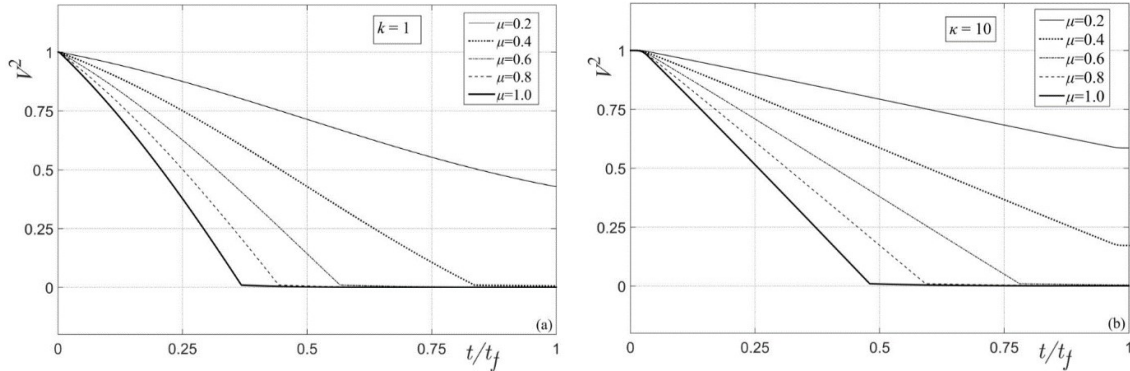


Figure 3. History of the tangential velocity of the particle for several values of the friction coefficient μ and $c = 0$: (a) $k = 1$ and (b) $k = 10$.

5.2 Collision of a rigid body with a rough half-space

In the second example, dynamics of a rigid body colliding with a plane rigid wall in the presence of friction is studied. In general, the configuration space of a free rigid body is represented by a six dimensional product space $M \equiv \mathbb{R}^3 \times M(3)$ [19]. The position of the body with respect to an inertial Cartesian reference frame \mathbb{F} in the physical space E^3 is represented by a point on manifold M with generalized coordinates $\underline{q}(t)$ split in two parts, \underline{q}_C and \underline{q}_R . The former specifies the position of the center of mass C of the body, while the latter describes the orientation of the body in the physical space. Consequently, the velocity vector is also split in the form $\underline{v}(t) = (\underline{v}_C^T \quad \underline{v}_R^T)^T$, where $\underline{v}_C = \dot{\underline{q}}_C(t)$ and the rotational part is expressed in terms of quasi-coordinates \underline{g} , with

$$\underline{v}_R = \dot{\underline{g}} \equiv (\Omega^1 \quad \Omega^2 \quad \Omega^3)^T \quad \text{and} \quad \dot{\underline{g}} = T(\underline{q}_R) \dot{\underline{q}}_R,$$

where $T(\underline{q}_R)$ is the tangent operator at \underline{q}_R [20]. Then, based on the kinetic energy of the body, the metric on space M can be selected in the following block diagonal form

$$G_q = [g_{IJ}] = \begin{bmatrix} mI_3 & 0 \\ 0 & J_C \end{bmatrix},$$

where m is the mass and J_C is the mass moment of inertia matrix of the body with respect to an orthonormal frame fixed in the body, with origin at its center of mass C. Moreover, the only non-zero affinities $\Lambda_{IJ'}^{K'}$ are

$$\Lambda_{5'6'}^{4'} = -\Lambda_{6'5'}^{4'} = \Lambda_{6'4'}^{5'} = -\Lambda_{4'6'}^{5'} = \Lambda_{3'5'}^{6'} = -\Lambda_{5'3'}^{6'} = 1.$$

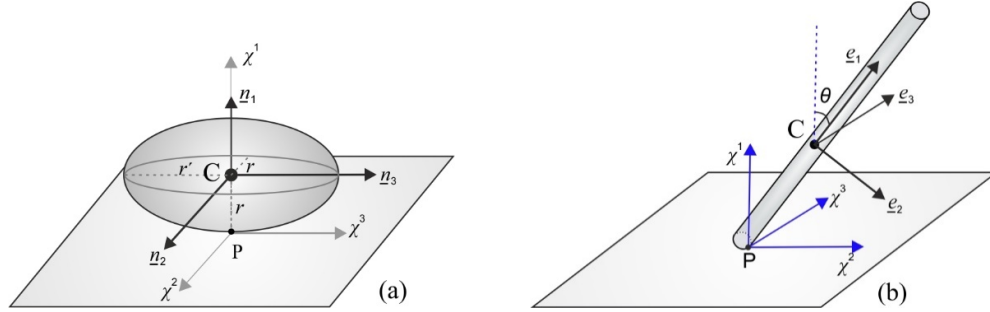


Figure 4. (a) A spheroid and (b) a bar, hitting a rough half-space.

5.2.1 Collision of a rigid spheroid with a rigid half-space

First, consider a homogeneous rigid spheroid (i.e., an ellipsoid of revolution), with mass m and radii r , r and r' , aligned with the axes of a Cartesian coordinate system in the physical space when hitting a rigid wall, as shown in Fig. 4a. The contact point P lies on the intersection of its circular equator with the χ^1 -axis.

The set of results presented in Fig. 5a are hodographs obtained for $k = 10$, $c = 0$ and three values of the ratio J_{11}/J_{33} , corresponding to an oblate spheroid, a sphere and a prolate spheroid. In all cases, the spheroid hits the ground with an initial normal velocity $V^1(0) = -1$ and zero angular velocity with respect to the wall. Also, the initial components of the velocities in the plane of the wall are $V^2(0) = 1$ and $V^3(0) = 1$, as indicated by the coordinates of point A. For relatively small values of μ , the spheroid undergoes gross slip. For instance, points B, C and D on the three hodographs examined indicate the end of the contact phase for $\mu = 0.1$. Also, the hodographs selected end up at point (0,0) for the limiting values $\mu = 0.18$, 0.20 and 0.28, corresponding to $J_{11}/J_{33} = 8/5$, 1 and $2/5$, respectively. Then, a final stick state is reached for larger values of μ . Clearly, the sliding direction varies during the motion for the case of the oblate or prolate spheroid. In the case of a sphere, where $J_{11}/J_{33} = 1$, the hodograph is an isocline [8,9].

Finally, in Fig. 5b are presented the histories of the two tangential components of the velocity of the contact point for $J_{11}/J_{33} = 2/5$ and two characteristic values of μ . First, results are shown for $\mu = 0.16$, which is smaller than the critical value leading to final stick. Clearly, this leads to conditions of gross slip. Similar results are also presented for $\mu = 0.20$, which is a bit larger than the critical value. The results verify that the contact event finishes now with a stick phase.

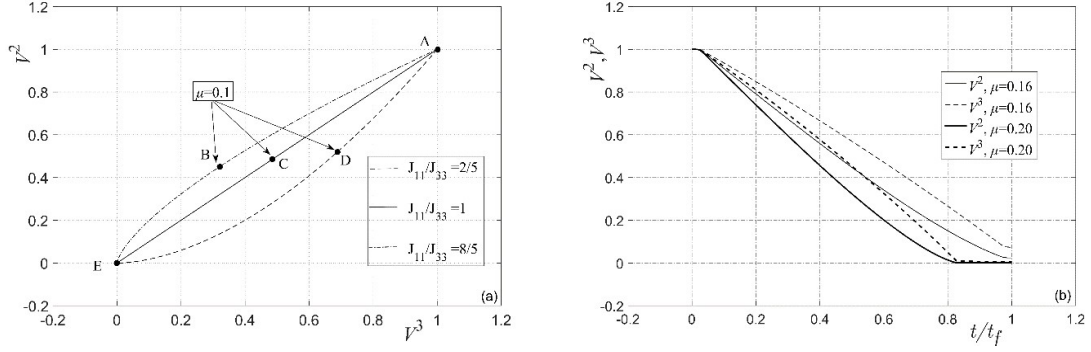


Figure 5. Collision of a spheroid with a plane: (a) hodographs starting at $(V^2, V^3) = (1, 1)$; (b) tangential velocity components of the contact point for $J_{11}/J_{33} = 2/5$ and $\mu = 0.16$ or 0.20 .

5.2.2 Oblique collision of a rigid rod with a rigid half-space

The last set of results refers to collision of a homogeneous rigid cylinder with mass m , length 2ℓ and radius r with a rough half-space, as shown in Fig. 4b. The longitudinal axis of the cylinder lies in the plane $O\chi^1\chi^2$ and makes an angle θ with the axis $O\chi^1$. First, in Fig. 6a are presented hodographs, originating from the same point of the plane (V^2, V^3) , for $k = 10$, $c = 0$ and several values of μ . The value of angle θ is selected to be equal to 1.10 rad, so that two critical friction parameter values are determined as $\bar{\mu} = 0.7499$ and $\mu_* = 0.5721$ [6,9]. For $\mu < \mu_*$, conditions of gross slip are observed, while the shape of the hodographs demonstrate that the sliding direction varies continuously during the motion. At the critical value $\mu = \mu_*$, the hodograph becomes an almost straight line (isocline). In addition, following a temporary stick, the sliding direction changes but remains constant and parallel to the χ^2 -axis throughout the subsequent motion. For $\mu_* < \mu < \bar{\mu}$, the tangential velocity becomes zero at some instance but continuous slipping immediately afterwards. Finally, for $\mu > \bar{\mu}$, once the stick state appears it persists until the end of the contact phase. Finally, in Fig. 6b are presented hodographs obtained for three different values of parameter k . The results verify that as the value of k is increased gradually, leads to the appearance of an isocline on plane (V^2, V^3) .

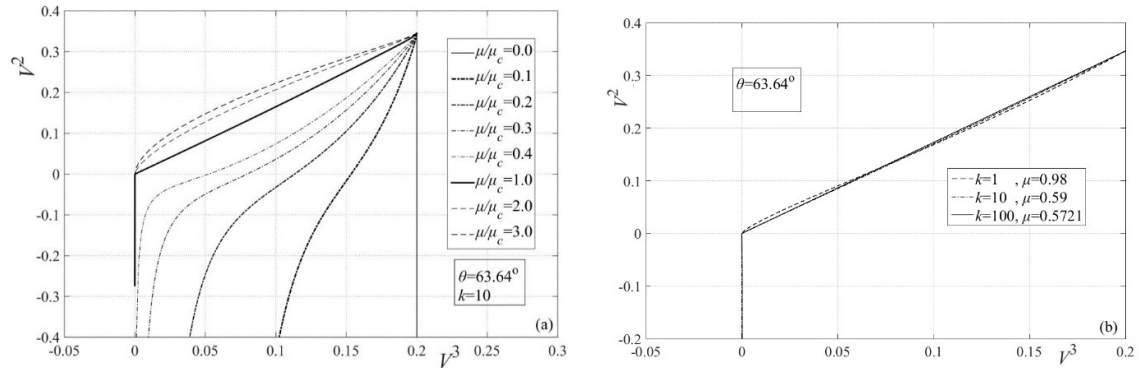


Figure 6. Hodographs for collision of a bar with a rough half-space, for different values of: (a) μ and (b) k .

6 SYNOPSIS AND EXTENSIONS

In the first part of this study, an analysis was presented on the dynamics of general single point frictional collision between two mechanical bodies. This analysis was performed within the framework of analytical dynamics, by employing some key concepts of differential geometry. First, a boundary was constructed for the original configuration manifold by using the condition of no impenetrability. Then, the essential geometric properties of the constrained manifold were determined. This provided the foundation for applying Newton's law of motion and led to an elegant geometric picture. Specifically, the motion during the contact phase was found to be governed by a set of three ODEs, when expressed in a special coordinate system in the close vicinity of the

configuration boundary, having one axis normal to the boundary and the remaining axes tangent to the boundary. The inertia of the figurative particle representing the motion of the system was found to increase rapidly as it approaches the boundary along this axis. At the same time, a strong repulsive force arises pushing this particle away from the boundary. In addition, friction was found to activate action along two special tangential directions only, determined by a mapping with the physical space. Finally, the equations of motion in the original coordinate system were simply obtained by a proper projection of these three ODEs. In the second part, the study focused on investigating several phenomena arising during frictional contact, by using selected examples.

The new formulation was developed in a systematic way, which provides a firm basis for attacking more challenging problems, like those involving multiple contacts. For this, there already exists a sound theoretical background, based on the theory of manifolds with corners [21,22]. In addition, the enhanced understanding provided by the geometric interpretation of the collision phenomenon studied is expected to lead to development of more accurate and efficient numerical techniques for determining the dynamics of the class of systems examined. This is closely related to development and application of suitable contact detection methods and will also help in developing more effective and robust optimization and control algorithms.

REFERENCES

- [1] Moreau, J.J., Panagiotopoulos, P.D. (1988), *Nonsmooth Mechanics and Applications*, CISM Courses and Lectures, Vol. 302, Springer-Verlag, Wien.
- [2] Pfeiffer, F., Glocker, Ch. (1996), *Multibody Dynamics with Unilateral Contacts*, J. Wiley & Sons, New York.
- [3] Glocker, Ch. (2001), *Set-Valued Force Laws*, Dynamics of Non-Smooth Systems, Springer, Berlin.
- [4] Leine, R.I., Nijmeijer, H. (2013), *Dynamics and Bifurcations of Non-Smooth Mechanical Systems*, Springer-Verlag, Berlin.
- [5] Brogliato, B. (2016), *Nonsmooth Mechanics: Models, Dynamics and Control*, Springer-Verlag, 3 ed., London.
- [6] Stronge, W.J. (2000), *Impact Mechanics*, Cambridge University Press, 2000, Cambridge, UK.
- [7] Keller, J.B. (1986), "Impact with friction," *ASME J. Appl. Mech.*, Vol. 53, pp. 1–4.
- [8] Battle, J.A., Condomines, A.B. (1991), "Rough collisions in multibody systems," *Mech. Mach. Theory*, Vol. 26, pp. 565–577.
- [9] Zhen, Z., Liu, C. (2007), "The analysis and simulation for three-dimensional impact with friction," *Multibody Syst. Dyn.*, Vol. 18, pp. 511-530.
- [10] Stronge, W.J. (2013), "Smooth dynamics of oblique impact with friction," *Int. J. Impact Eng.*, Vol. 51, pp. 36–49.
- [11] Paraskevopoulos, E., Natsiavas, S. (2013), "On application of Newton's law to mechanical systems with motion constraints," *Nonlinear Dyn.*, Vol. 72, pp. 455-475.
- [12] Paraskevopoulos, E., Natsiavas, S. (2017), "A geometric solution to the general single contact frictionless problem by combining concepts of analytical dynamics and b-calculus," *Int. J. Non-Linear Mech.*, Vol. 95, pp. 117-131.
- [13] Melrose, R.B. (1993), *The Atiyah-Patodi-Singer Index Theorem*, Research Notes in Mathematics, Vol. 4, A.K. Peters Ltd., Wellesley, MA.
- [14] Nguyen, N.S., Brogliato, B. (2014), *Multiple Impacts in Dissipative Granular Chains*, Lecture Notes in Applied and Computational Mechanics, Vol. 72, Springer, Berlin.
- [15] Papastavridis, J.G. (1999), *Tensor Calculus and Analytical Dynamics*, CRC Press, Boca Raton.
- [16] Bloch, A.M. (2003), *Nonholonomic Mechanics and Control*, Springer-Verlag New York Inc., New York.
- [17] Natsiavas, S., Paraskevopoulos, E. (2015), "A set of ordinary differential equations of motion for constrained mechanical systems," *Nonlinear Dyn.*, Vol. 79, pp. 1911-1938.
- [18] Kevorkian, J., Cole, J.D. (1985), *Perturbation Methods in Applied Mathematics*, 2nd ed., Springer-Verlag, New York.
- [19] Paraskevopoulos, E., Natsiavas, S. (2013), "A new look into the kinematics and dynamics of finite rigid body rotations using Lie group theory," *Int. J. Solids Struct.*, Vol. 50, pp. 57-72.
- [20] Geradin, M., Cardona, A. (2001), *Flexible Multibody Dynamics: A Finite Element Approach*, John Wiley & Sons, New York.
- [21] Melrose, R.B. (1992), "Calculus of conormal distributions on manifolds with corners," *Int. Math. Res. Not. IMRN*, pp.51–61.
- [22] Joyce, D. (2016), "A generalization of manifolds with corners," *Advances Math.*, Vol. 299, pp. 760–862.

APPLICATION OF AN AUGMENTED LAGRANGIAN METHODOLOGY TO DYNAMICS OF MULTIBODY SYSTEMS WITH EQUALITY CONSTRAINTS

Elias Paraskevopoulos¹, Nikolaos Potosakis¹ and Sotirios Natsiavas¹

¹ Department of Mechanical Engineering
Aristotle University
Thessaloniki, GR-54124, Greece
e-mail: natsiava@auth.gr

Keywords: Multibody systems, Equality motion constraints, Three field weak form, Augmented Lagrangian.

Abstract. *Some new theoretical and numerical results are presented for a class of multibody systems subjected to equality motion constraints. The formulation is based on a new set of equations of motion, represented by a system of second order ordinary differential equations. First, after introducing an appropriate set of penalty terms, these equations are put in an augmented Lagrangian form. Also, the position, velocity and momentum type quantities are assumed to be independent, leading to a three field set of equations. This set is then used for producing a new time integration scheme. The validity and efficiency of this scheme is verified by applying it to example systems.*

1 INTRODUCTION

Research on the dynamics of mechanical systems subject to motion constraints is a traditional and favorable topic among researchers with different backgrounds (e.g., [1-4]). This is in part due to the fact that this area of Analytical Mechanics is still challenging and several theoretical aspects related to it remain unexplored and are amenable to improvement. Another driving factor is that a better understanding of the fundamentals in this area provides a stronger foundation and offers substantial help in the efforts to solve difficult engineering problems by deriving and employing new, more advanced, accurate and robust numerical techniques [5,6]. This in turn leads to useful design gains in many areas, including mechanisms, robotics, machinery, biomechanics, automotive and aerospace structures.

Typically, the equations of motion for this class of systems are derived and cast in the form of a set of differential-algebraic equations (DAEs) of high index. However, both the theoretical and the numerical treatment of DAEs is a delicate and difficult task [7]. For this reason, many attempts have been performed in the past in an effort to cure the problems related to a DAE modeling. Over the years, it has become apparent that many of the theoretical questions in the area of Analytical Dynamics can be answered in an illustrative and complete way by employing fundamental concepts of differential geometry [8,9]. Based on this observation, the main objective of this work is to use such concepts in order to provide a better theoretical foundation and to develop an appropriate numerical scheme for treating a class of constrained mechanical systems.

The new approach assigns appropriate inertia, damping and stiffness properties to the constraints. As a result, the equations of motion are second order ordinary differential equations (ODEs) in both the generalized coordinates and the Lagrange multipliers, related to the constraint action [10,11]. This, in turn, leads to elimination of the singularities associated with DAE or penalty formulations. As a consequence, there is no need to introduce artificial parameters for scaling and stabilization. In addition, the geometrical properties of the original manifold are kept unchanged by the additional constraints. This preserves the properties of the special curves of the manifold employed in the numerical discretization and leads to major advantages compared to previous work in the field of computational Multibody Dynamics [5,6]. By introducing appropriate penalty terms, these equations are first put in a convenient Augmented Lagrangian form. Moreover, the position, velocity and momentum type quantities are assumed to be independent, forming a three field set of equations [12,13]. In particular, the weak velocities and the strong time derivatives of all the coordinates involved in the formulation are related through a new set of Lagrange multipliers, which represent momentum type variables. Next, the formulation developed is employed as a basis for producing a suitable time integration scheme for the class of systems examined. The validity and efficiency of this scheme was tested and illustrated by applying it to a number of characteristic example mechanical systems. Among other things, the results obtained verify that the scheme developed passes successfully all the tests related to a special set of challenging benchmark problems, chosen by the multibody dynamics community [14]. In addition, the same scheme was also applied successfully to a number of large scale industrial applications.

The organization of this paper is as follows. First, the set of equations of motion governing the dynamics of an unconstrained discrete mechanical system is presented briefly in the following section. Then, similar equations arising in the presence of bilateral constraints are also presented in the third section. These equations are easily put in an Augmented Lagrangian form, by just adding suitable penalty terms. Based on this form, a temporal discretization scheme was developed and numerical results were obtained for several mechanical examples. Some characteristic numerical results are presented in the fourth section.

2 APPLICATION OF NEWTON'S LAW TO SYSTEMS WITH NO MOTION CONSTRAINTS

This work examines a class of mechanical systems whose position is determined by a finite number of generalized coordinates $q = (q^1, \dots, q^n)$, at any time instance $t \in [1, 9]$. The motion of such a system can be represented by the motion of a fictitious point, say p , along a curve $\gamma = \gamma(t)$ in an n -dimensional manifold M , the configuration space of the system. Moreover, the tangent vector $\underline{v} = d\gamma/dt$ to this curve belongs to an n -dimensional vector space, the tangent space of the manifold at p , denoted by $T_p M$ [4]. By construction, for any point p of M , a coordinate map ϕ can be defined by $q = \phi(p)$, acting from a neighborhood of p on M to the Euclidean space \mathbb{R}^n . Then, by adopting the usual summation convention on repeated indices, each tangent vector at point p , representing a generalized velocity, can be expressed in the form

$$\underline{v}(t) = v^i(t) \underline{e}_i, \quad (1)$$

where $\mathfrak{B}_e = \{\underline{e}_1 \dots \underline{e}_n\}$ is a basis for space $T_p M$. Likewise, one can define the dual space to $T_p M$, denoted by $T_p^* M$, with elements known as covectors. In dynamics, a covector represents a generalized momentum. Also, the correspondence between a covector \underline{u}^* and a vector \underline{u} is established through the dual product

$$\underline{u}^*(\underline{w}) \equiv \langle \underline{u}, \underline{w} \rangle, \quad \forall \underline{w} \in T_p M, \quad (2)$$

where $\langle \cdot, \cdot \rangle$ denotes the inner product of vector space $T_p M$ [8]. In this way, to each basis $\{\underline{e}_i\}$ (with $i = 1, \dots, n$) of $T_p M$, a dual basis $\{\underline{e}^i\}$ can be established for $T_p^* M$ by employing the condition $\underline{e}^i(\underline{e}_j) = \delta_j^i$. Then, determination of the true path of motion on a manifold is based on application of Newton's second law in the form

$$\nabla_{\underline{v}} \underline{p}_M^* = \underline{f}_M^*, \quad (3)$$

where \underline{v} is the tangent vector of the natural trajectory $\gamma(t)$, while $\underline{f}_M^* = f_i \underline{e}^i$ represents the applied force [1,9]. Then, if $\underline{v} = v^i \underline{e}_i$ and $\underline{p}_M^* = p_i \underline{e}^i$, application of Eq. (2) leads to

$$p_i = g_{ij} v^j, \quad (4)$$

where the quantities $g_{ij} = \langle \underline{e}_i, \underline{e}_j \rangle$ represent the components of the metric tensor at point p . These quantities are selected to coincide with the elements of the mass matrix of the system, defined through the kinetic energy. Finally, the covariant differential of the covector field $\underline{p}_M^*(t)$ on M along a vector \underline{v} of $T_p M$ is evaluated by

$$\nabla_{\underline{v}} \underline{p}_M^*(t) = (\dot{p}_i - \Lambda_{ji}^m p_m v^j) \underline{e}^i. \quad (5)$$

where ∇ is the affine connection of the manifold. The components Λ_{ij}^k of the connection ∇ in the basis of $T_p M$ are known as affinities [2,9].

Through the definition of a class of special covectors (called Newton covectors, see [11]) by

$$\underline{h}_M^* \equiv \nabla_{\underline{v}} \underline{p}_M^* - \underline{f}_M^* \quad (6)$$

the equations of motion (3) at any point on a configuration manifold M can be put in the form

$$\underline{h}_M^* = \underline{0}. \quad (7)$$

Therefore, when there exist no motion constraints, it should be true that

$$\underline{h}_M^*(\underline{w}) = 0 \Rightarrow \int_{t_1}^{t_2} \underline{h}_M^*(\underline{w}) dt = 0, \quad \forall \underline{w} \in T_p M \quad (8)$$

along a natural trajectory on the manifold and within any time interval $[t_1, t_2]$. Manipulation of the last integral requires application of integration by parts of the covariant derivative appearing in Eq. (6). This is achieved by employing the identity

$$\nabla_{\underline{v}}(\underline{p}_M^*(\underline{w})) = (\nabla_{\underline{v}}\underline{p}_M^*)(\underline{w}) + \underline{p}_M^*(\nabla_{\underline{v}}\underline{w}),$$

which can be interpreted as a Leibniz rule on differentiation. Then, the following expression is obtained

$$\int_{t_1}^{t_2} [\nabla_{\underline{v}}(\underline{p}_M^*(\underline{w})) - \underline{p}_M^*(\nabla_{\underline{v}}\underline{w}) - \underline{f}_M^*(\underline{w})] dt = 0,$$

which, after an integration by parts of the first term inside the integral, becomes

$$[\underline{p}_M^*(\underline{w})]_{t_1}^{t_2} - \int_{t_1}^{t_2} [\underline{p}_M^*(\nabla_{\underline{v}}\underline{w}) + \underline{f}_M^*(\underline{w})] dt = 0. \quad (9)$$

This equation represents the so called weak form of the equations of motion [15]. In essence, it constitutes an alternative way to determine the true history of the coordinates (i.e., position) and velocities of a mechanical system satisfying the law of motion, as expressed by Eq. (3) originally.

Further manipulation of the weak form given by Eq. (9) involves differentiation along the vectors \underline{v} and \underline{w} . This requires the construction of two smooth vector fields on M . The first of these can be constructed by considering the tangent vector \underline{v} at each point of the natural trajectory $\gamma(t)$. The second vector field can then be created by introducing another vector \underline{w} of the tangent space at each point of the same trajectory, which can be arbitrary. Therefore, a variation of any scalar function f is defined as the derivative of f along vector \underline{w} , by

$$\delta f \equiv \underline{w}(f) = f_{,i} w^i.$$

Then, $w^i = \delta q^i$ for holonomic coordinates. Moreover, after defining the objective function

$$\mathcal{F}_M = \frac{1}{2} \|\underline{h}_M^*\|^2, \quad (10)$$

it is straightforward to show that

$$\delta \mathcal{F}_M = \underline{h}_M^*(\underline{w}) = 0, \quad \forall \underline{w} \in T_p M,$$

which leads to Eq. (8).

3 A NUMERICAL SCHEME FOR SYSTEMS WITH BILATERAL CONSTRAINTS

Next, consider systems subject to an additional set of k scleronomic constraints, which can be put in the form

$$\psi(q, \underline{v}) \equiv A(q) \underline{v} = \underline{0}, \quad (11)$$

where \underline{v} is a vector in $T_p M$ and $A = [a_i^R]$ is a known $k \times n$ matrix. In the special case where a constraint is holonomic, its equation can be integrated and written in the algebraic form

$$\phi^R(q) = 0. \quad (12)$$

Based on the above, the equations of motion of the class of systems examined can now be cast in the form

$$\underline{h}^* \equiv \underline{h}_M^* - \underline{h}_C^* = \underline{0} \quad (13)$$

on the original manifold M [11], with

$$\underline{h}_M^* = h_i \underline{e}^i = [(g_{ij} v^j)^\cdot - \Lambda_{\ell i}^m g_{mj} v^j v^\ell - f_i] \underline{e}^i \quad \text{and} \quad \underline{h}_C^* = \sum_{R=1}^k h_R a_i^R \underline{e}^i, \quad (14)$$

where

$$h_R = (\bar{m}_{RR} \dot{\lambda}^R)^\cdot + \bar{c}_{RR} \dot{\lambda}^R + \bar{k}_{RR} \lambda^R - \bar{f}_R. \quad (15)$$

In the last relation, the convention on repeated indices does not apply to index R . Moreover, the coefficients

$$\bar{m}_{RR} = c_R^i g_{ij} c_R^j, \quad \bar{c}_{RR} = -c_R^i \frac{\partial f_i}{\partial v^j}(q, \underline{v}, t) c_R^j, \quad \bar{k}_{RR} = -c_R^i f_{i,j}(q, \underline{v}, t) c_R^j, \quad \bar{f}_R = c_R^i f_i(q, \underline{v}, t) \quad (16)$$

represent an equivalent mass, damping, stiffness and forcing quantity, respectively, obtained through a projection along a special direction \underline{c}_R on $T_p M$ [11]. Specifically, the components of the n -vector \underline{c}_R are selected to satisfy

$$a_i^R c_R^i = 1. \quad (17)$$

If generalized (true) coordinates are used, which means that $v^i = \dot{q}^i$, Eq. (13) represents a set of n second order coupled ODEs in the $n+k$ unknowns q^i and λ^R . The additional information needed for a complete mathematical formulation is obtained by incorporating the k equations of the constraints. In particular, for each holonomic or

non-holonomic constraint, a second order ODE is obtained, with form

$$\mathbf{g}_R \equiv (\bar{\mathbf{m}}_{RR} \dot{\phi}^R)^* + \bar{\mathbf{c}}_{RR} \dot{\phi}^R + \bar{\mathbf{k}}_{RR} \phi^R = 0 \quad \text{or} \quad \mathbf{g}_R \equiv (\bar{\mathbf{m}}_{RR} \dot{\psi}^R)^* + \bar{\mathbf{c}}_{RR} \dot{\psi}^R = 0, \quad (18)$$

respectively.

Next, in analogy to Eq. (10) and taking into account the motion constraints, define the function

$$\mathcal{F}_A = \frac{1}{2} \|\underline{h}^*\|^2 - \frac{1}{2} \|\underline{h}_\rho^*\|^2, \quad (19)$$

which is augmented by the norm of the covector

$$\underline{h}_\rho^* = \sum_{R=1}^k \rho_R \mathbf{g}_R \mathbf{a}_i^R \underline{\mathbf{e}}^i, \quad (20)$$

including the penalty factors ρ_R . Then, it is easy to show that the above definitions lead to

$$\delta \mathcal{F}_A = (\underline{h}^* - \underline{h}_\rho^*)(\underline{w}) = 0, \quad \forall \underline{w} \in T_p M,$$

and eventually to

$$\int_{t_1}^{t_2} (\underline{h}_M^* - \underline{h}_C^*)(\underline{w}) dt + \int_{t_1}^{t_2} \underline{h}_\rho^*(\underline{w}) dt = 0, \quad \forall \underline{w} \in T_p M. \quad (21)$$

The last form is also complemented by the following terms

$$\int_{t_1}^{t_2} \mathbf{g}_R \delta \lambda^R dt = 0, \quad (22)$$

for each motion constraint and arbitrary multipliers $\delta \lambda^R$.

In a weak formulation, it is advantageous to consider the position, velocity and momentum variables as independent [15]. For this, a new velocity field $\hat{\mathbf{v}}$ is introduced on manifold M , which should eventually be forced to become identical to the true velocity field \mathbf{v} through the action of an arbitrary covector with components $\delta \hat{p}_i$. A similar action can be taken for the velocity components $\mu^R \equiv \dot{\lambda}^R$, by introducing another vector field with components $\hat{\mu}^R$ and a new set of multipliers, $\delta \hat{\pi}_R$. Likewise, one can relate the variations in the strong time derivatives \dot{v}^i and $\dot{\mu}^R$ of the position type variables to those of the weak velocities, \hat{v}^i and $\hat{\mu}^R$, through two new sets of Lagrange multipliers, denoted by \hat{p}_i and $\hat{\pi}_R$, respectively. To achieve these tasks, the weak form expressed by Eqs (21) and (22) should be augmented by the terms

$$\int_{t_1}^{t_2} [\hat{p}_i (\delta \hat{v}^i - \delta v^i) + \delta \hat{p}_i (\hat{v}^i - v^i)] dt \quad \text{and} \quad \int_{t_1}^{t_2} [\hat{\pi}_R (\delta \hat{\mu}^R - \delta \mu^R) + \delta \hat{\pi}_R (\hat{\mu}^R - \mu^R)] dt. \quad (23)$$

Finally, by adding up all these terms and performing appropriate mathematical operations, including the usual integration by parts step, it yields eventually the following three field set of equations

$$\begin{aligned} & (p_i - \sum_{R=1}^k a_i^R \bar{\mathbf{m}}_{RR} \bar{\mu}^R) w^i \Big|_{t_1}^{t_2} + \sum_{R=1}^k \bar{\mathbf{m}}_{RR} \dot{\phi}^R \delta \lambda^R \Big|_{t_1}^{t_2} + \int_{t_1}^{t_2} [\delta \hat{p}_i (\hat{v}^i - v^i) + \sum_{R=1}^k \delta \hat{\pi}_R (\hat{\mu}^R - \mu^R)] dt \\ & + \int_{t_1}^{t_2} [(-p_i + \sum_{R=1}^k a_i^R \bar{\mathbf{m}}_{RR} \bar{\mu}^R + \hat{p}_i) \delta \hat{v}^i + \sum_{R=1}^k (\hat{\pi}_R - \bar{\mathbf{m}}_{RR} \dot{\phi}^R) \delta \hat{\mu}^R] dt - \int_{t_1}^{t_2} (\hat{p}_i \delta v^i + \sum_{R=1}^k \hat{\pi}_R \delta \mu^R) dt \\ & + \int_{t_1}^{t_2} \{f_i + \sum_{R=1}^k [(\bar{\mathbf{c}}_{RR} \bar{\mu}^R + \bar{\mathbf{k}}_{RR} \bar{\lambda}^R - \bar{f}_R) a_i^R - \bar{\mathbf{m}}_{RR} \mu^R \frac{Da_i^R}{Dt}]\} w^i dt + \sum_{R=1}^k \int_{t_1}^{t_2} (\bar{\mathbf{c}}_{RR} \dot{\phi}^R + \bar{\mathbf{k}}_{RR} \phi^R) \delta \lambda^R dt = 0, \end{aligned} \quad (24)$$

where the variations w^i , $\delta \lambda^R$, $\delta \hat{v}^i$, $\delta \hat{\mu}^R$, $\delta \hat{p}_i$ and $\delta \hat{\pi}_R$ are independent for all $i = 1, \dots, n$ and $R = 1, \dots, k$, while

$$\frac{Da_i^R}{Dt} = \dot{a}_i^R - \Lambda_{ji}^R a_i^R \hat{v}^j, \quad \bar{\mu}^R = \hat{\mu}^R + \rho_R \dot{\phi}^R \quad \text{and} \quad \bar{\lambda}^R = \hat{\lambda}^R + \rho_R \phi^R.$$

Equation (24) is the final weak form obtained for the class of constrained mechanical systems examined. This form is convenient for performing an appropriate numerical discretization, leading to improvements over existing numerical schemes based on advanced analytical tools. For the purposes of the present work, this form was also put within the framework of an augmented Lagrangian formulation [16-18]. More specifically, this method is appropriate for performing a geometrically exact discretization. In brief, after assuming consistent polynomial expansions, a set of nonlinear algebraic equations is obtained for the unknowns of the problem, which consist of q^i , λ^R , \hat{v}^i , $\hat{\mu}^R$, \hat{p}_i and $\hat{\pi}_R$. This set is solved by a block-type iterative technique within each time step, according to the following scheme. First, assume that the values of all the unknowns but \hat{v}^i are fixed. After solving for the new values of the velocities \hat{v}^i the subsystem resulting by the terms in the weak form multiplied by δq^i (for holonomic coordinates) and $\delta \lambda^R$, an appropriate augmentation is performed leading to the new values of $\hat{\mu}^R$.

Then, the values of the coordinate variables q^i and λ^R are determined through a direct update, resulting by the terms of the weak form multiplied by $\delta \hat{p}_i$ and $\delta \hat{\pi}_R$. Finally, the updated values of the momentum variables \hat{p}_i and $\hat{\pi}_R$ can be obtained by using the subsystem resulting by the terms of the weak form multiplied by $\delta \hat{v}^i$ and $\delta \hat{\mu}^R$. This scheme leads to a full exploration of the major advantages of the theoretical method applied, in a quite natural manner. It is especially useful when the configuration space of the system possesses group properties [19,20]. The success of this formulation was demonstrated by the accurate solution obtained for a number of challenging problems. Some characteristic results are presented next for several typical examples. The first ones have a relatively simple geometry and are of academic interest, while the last example was taken from an industrial application.

4 NUMERICAL RESULTS

4.1 Plane Pendulum

The first set of numerical results refers to a planar pendulum, composed of a particle with mass $m = 1\text{kg}$, attached to one end of a massless rigid rod with length $L = 1\text{m}$. The other end of the rod is connected to the ground through a revolute joint so that the system motion is limited in the x-y plane. This system is released from rest, from an initial position, shown in Fig. 1a. Consequently, it undergoes large amplitude oscillations, due to the action of gravity along the negative Y direction.

In Figs 1b-1d are presented and compared numerical results obtained by the new solver (labeled by LMD) with results obtained from a state of the art code, employing a BDF solver [21]. In both cases, an effort was made to keep the same time step and accuracy level in the numerical calculations. In particular, an accuracy level of 0.01 was required in all runs, using either code.

First, in Fig. 1b is shown the mechanical energy of the system as a function of time, assuming a zero potential energy at the position shown in Fig. 1a. Clearly, the commercial code exhibits a gradual and substantial mechanical energy loss. This is probably related to the high level of artificial damping induced in the BDF scheme employed. The consequences of this effect are demonstrated in Figs 1c and 1d, presenting the time history of the vertical component of the displacement of the particle at the beginning and at a later time interval of the oscillation. The results indicate a drift and a reduction in the amplitude of oscillation obtained by the BDF method. It is important to note that a similar behavior with [21] was also observed by employing another state of the art code in multibody dynamics, which uses also a BDF scheme [22].

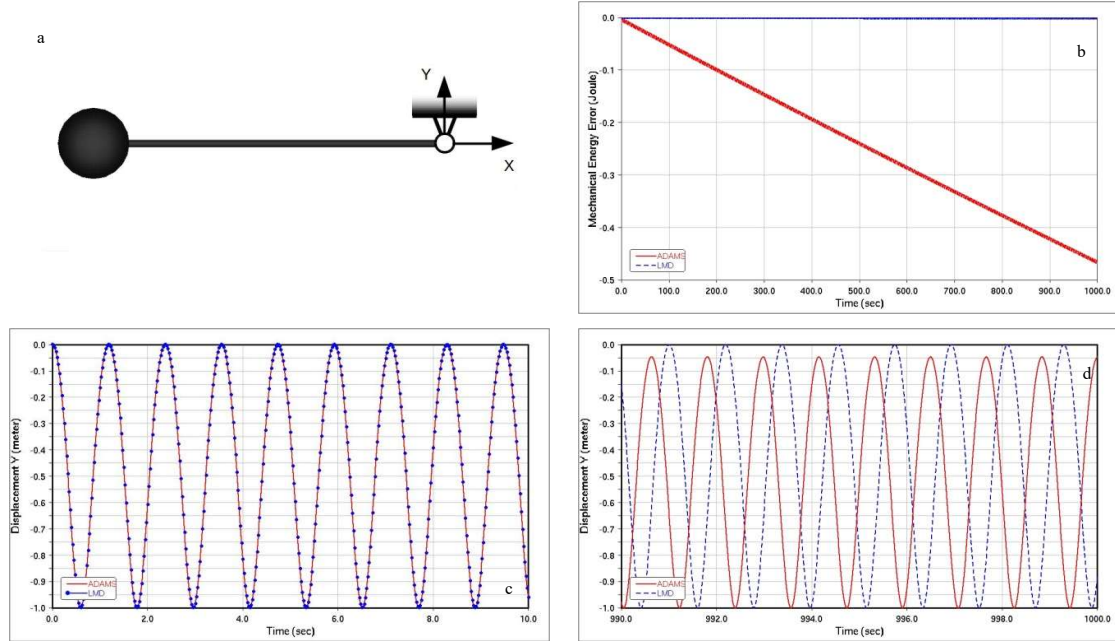


Figure 1. Numerical results for a planar pendulum: (a) mechanical model, (b) mechanical energy error, (c)/(d) history of the particle vertical displacement.

The good performance of the new code is due to the fact that the new set of equations of motion employed

includes suitable terms, avoiding a growth in the constraint violation error in an automatic manner. For instance, in Fig. 2a are shown results obtained by the new code, by taking into account the critical term \bar{m}_{RR} , evaluated by Eq. (16), or setting it to a different value in the calculations, i.e., $\bar{m}_{RR}/10$, $\bar{m}_{RR}/100$ or 0. As it is obvious from Eqs (14) and (15), this term assures the presence of the constraint inertia term $\ddot{\lambda}^R$ in the equations of motion. Obviously, an incorrect choice or elimination of this term leads to a dramatic reduction of the time step, causing a sudden termination of the numerical calculations. In all cases, the initial penalty values were chosen to be equal to 100. In Fig. 2b are shown the changes in the values of the penalty factors leading to convergence in the case with $\bar{m}_{RR}/10$. Obviously, the penalty factors change with time and are different for each constraint. For the correct value of \bar{m}_{RR} , the step size was found to remain constant in all cases examined for the specific example, as shown in Fig. 2c. Likewise, the penalty values were also kept constant, as is shown in Fig. 2d, while the violation of the constraint was also limited to very low levels, as indicated by the results of Fig. 2e. Finally, Fig. 2f shows results for three cases, corresponding to $\bar{m}_{RR}/10$, where the penalty factors are kept constant. For the larger penalty value the correct solution is obtained without a reduction in the time step. For the intermediate penalty value a solution is reached, after an order of magnitude reduction of the time step. The smallest penalty value leads to a drastic reduction of the time step and termination of the solution process. These results are expected to worsen in more complicated examples, where the values of the \bar{m}_{RR} are not constant.

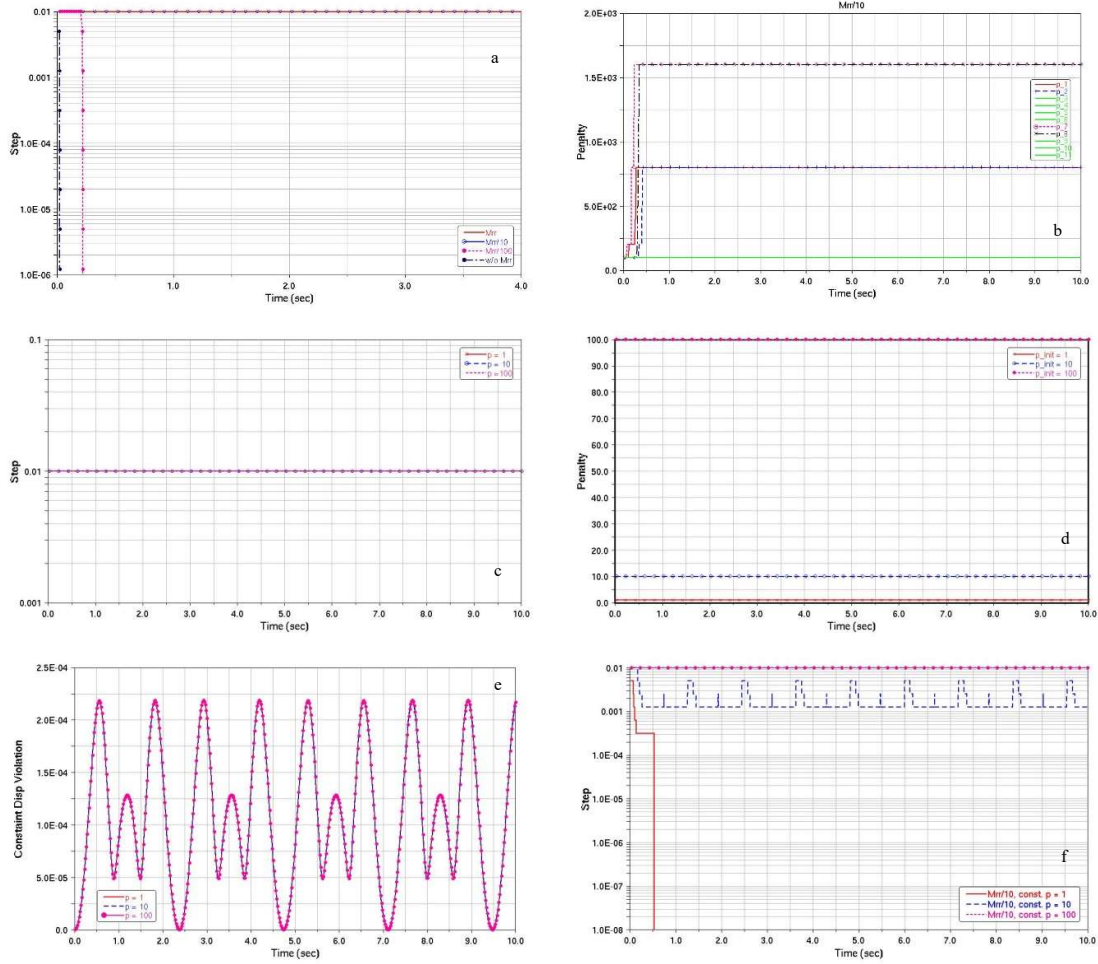


Figure 2. Numerical results for a planar pendulum: (a) time step as a function of time for different fraction values of \bar{m}_{RR} (all initial penalty values are equal to 100), (b) changes in the values of the penalty factors leading to convergence in case with $\bar{m}_{RR}/10$, (c) step size for the correct value of \bar{m}_{RR} , (d) penalty values for the correct value of \bar{m}_{RR} , (e) violation of the constraint for the correct value of \bar{m}_{RR} , (f) step size for constant penalty factors and $\bar{m}_{RR}/10$.

4.2 Double Four Bar Mechanism

Next, in Fig. 3 are compared results obtained by applying the new method with similar results obtained for a typical benchmark problem [14]. In brief, the double four bar mechanism examined is a representative of a multibody system passing from a singular configuration. All the rods have equal length and uniformly distributed mass. Specifically, when the bars reach the horizontal position, the number of degrees of freedom increases instantaneously from one to three. In the set of calculations presented next, the mechanism starts from rest from the position shown in Fig. 3a and executes oscillations due to the action of gravity along the $-y$ direction. Again, the results of the new method are labeled by LMD.

First, the results of Fig. 3b verify the closeness of the results obtained by the two methods, within the time interval considered. However, the results presented in Fig. 3c demonstrate a difference in the error in the mechanical energy (taking as a reference configuration the one shown in Fig. 3a). The new method predicts a constant value close to zero, which is the exact value. In addition, the results shown in Figs 3d, 3e and 3f show three different types of failure in the response obtained by using the same BDF solver as in the previous example [21]. More specifically, the simulation stops suddenly (Fig. 3d), the solver finds a wrong solution (Fig. 3e) or it predicts a breaking of the connections leading to a disassembling of its members (Fig. 3f), as the mechanism passes from the singular position.

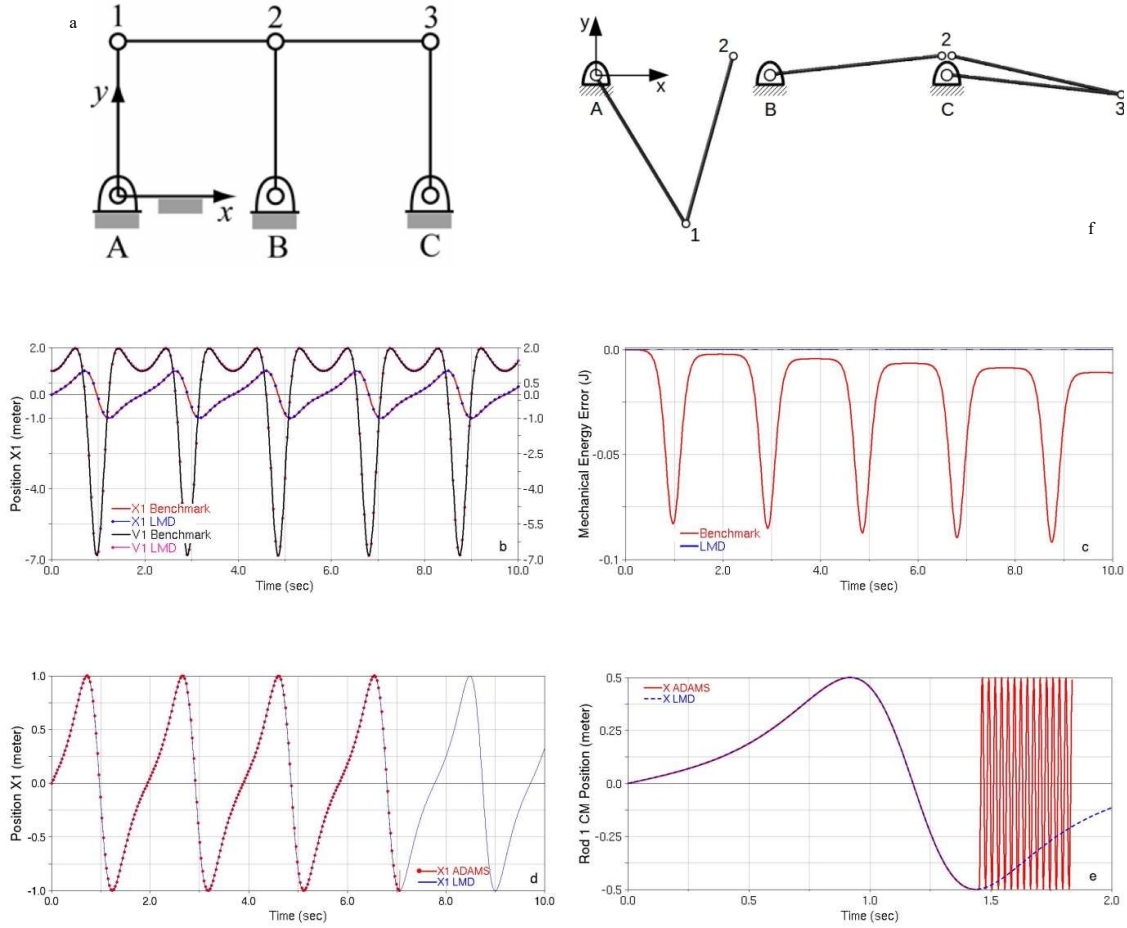


Figure 3. Numerical results for a double four bar mechanism: (a) mechanical model, (b) history of position and velocity of point P_1 of the mechanism, (c) mechanical energy error, ADAMS results (using a BDF method) where (d) simulation stops, (e) solver finds a wrong solution and (f) the mechanism breaks.

4.3 Rectangular Bricard Mechanism

The next set of results refers to a six-bar rectangular Bricard mechanism, shown in Fig. 4a. All the rods are connected with revolute joints, have equal length and uniformly distributed mass. Again, this system moves due to gravity acting along the negative y -axis. The mechanism examined represents a mechanical system which is

redundantly constrained throughout its motion and, due to this property, it also belongs to a special set of benchmark problems [14].

First, in Fig. 4b are shown the time histories of the x , y and z coordinates of point P_2 , while in Fig. 4c is depicted the mechanical energy of the system. Finally, in Figs 4d and 4e are presented the corresponding histories of the constraint violations in the position and velocity levels during the same time interval, represented by the norm of the array of the constraints at each level.

Direct comparison of the results in Fig. 4 illustrates that the present method is accurate and passes successfully the benchmark tests. It also presents an improved numerical performance. For instance, the mechanical energy computed by the present method remains virtually constant (Fig. 4c). In addition, the errors in both the displacement and velocity constraint violations are bounded and stay at the same level, throughout the time interval examined (Figs 4d and 4e).

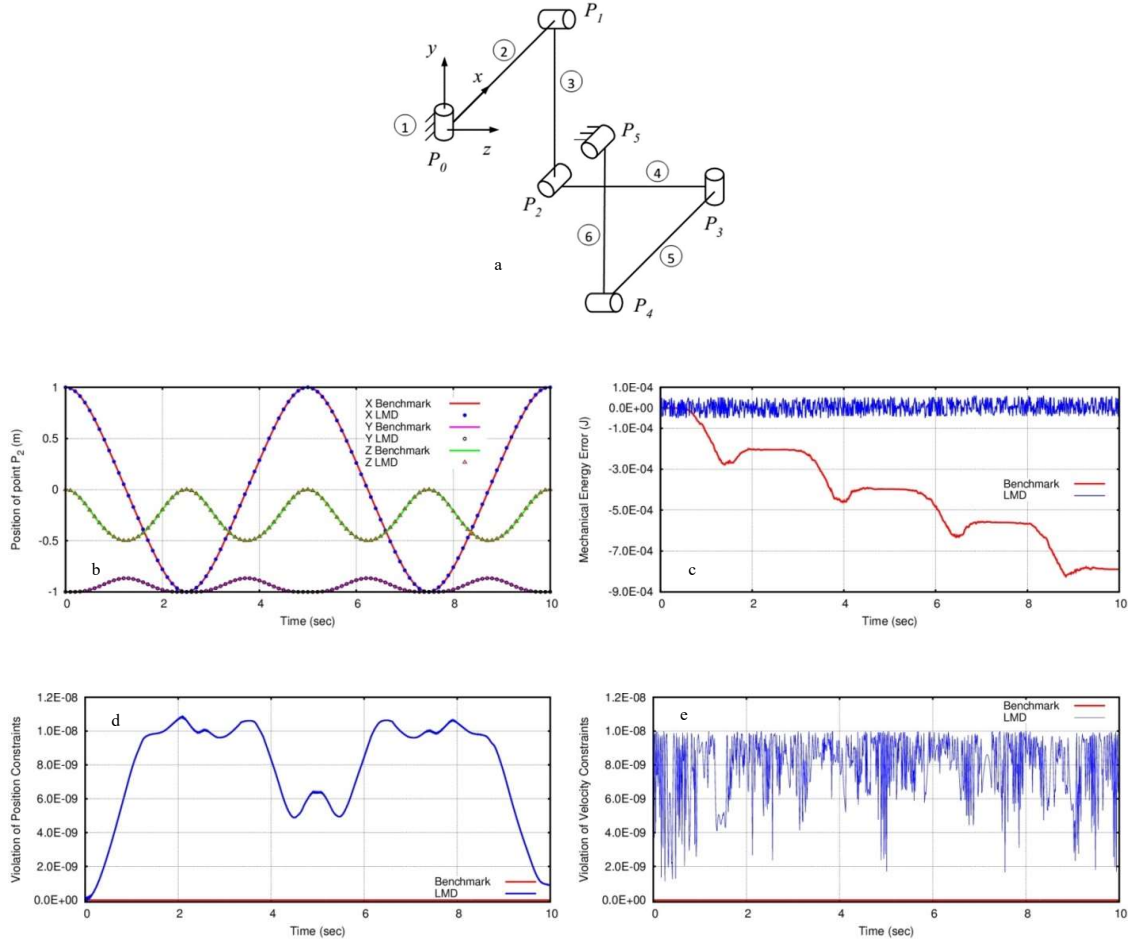


Figure 4. (a) Mechanical model of a Bricard mechanism, (b) history of the x , y and z coordinates of point P_2 , (c) mechanical energy, (d) violation of position and (e) violation of velocity constraints.

4.4 Complex Model of a Ground Vehicle

In the last example, a quite complex model of a ground vehicle is examined, shown in Fig. 5a. This model is composed of a basic powertrain system, a complex steering system, together with involved front and rear suspension systems with jounce and rebound bumpers. Also, the tires were modeled using the well-known Pacejka tire model [23]. In total, the model consists of 53 rigid bodies, interconnected with 49 kinematical constraints, 29 bushings, 9 spring-damper systems and 9 action-reaction force elements. As a consequence, the total number of degrees of freedom of the final model is 134. In the examples examined, the vehicle is subjected to two classical road handling tests. For this, an appropriate driving torque and steering angle is applied at the car's differential and wheel during the motion, as shown in Figs 5b and 5c. In the first test, the vehicle is running over a straight

path with a constant longitudinal velocity $V_x \approx -60 \text{ Km/h}$ before it starts performing a typical double lane change (DLC). In Figs 5d and 5f are presented selected results obtained for tire forces and velocity components by applying the new numerical method (labeled by LMD). Moreover, these results are compared with results obtained for the same model by two state of the art numerical codes [21,22]. These codes set up the equations of motion and solve them numerically as a system of DAEs. In the second test, a swept steering maneuver is performed. Typical results for tire forces and velocity components are shown and compared in Figs 5e and 5g. The difference between the results obtained by the new method and one of the codes [22] is most probably due to differences in the tire models employed.

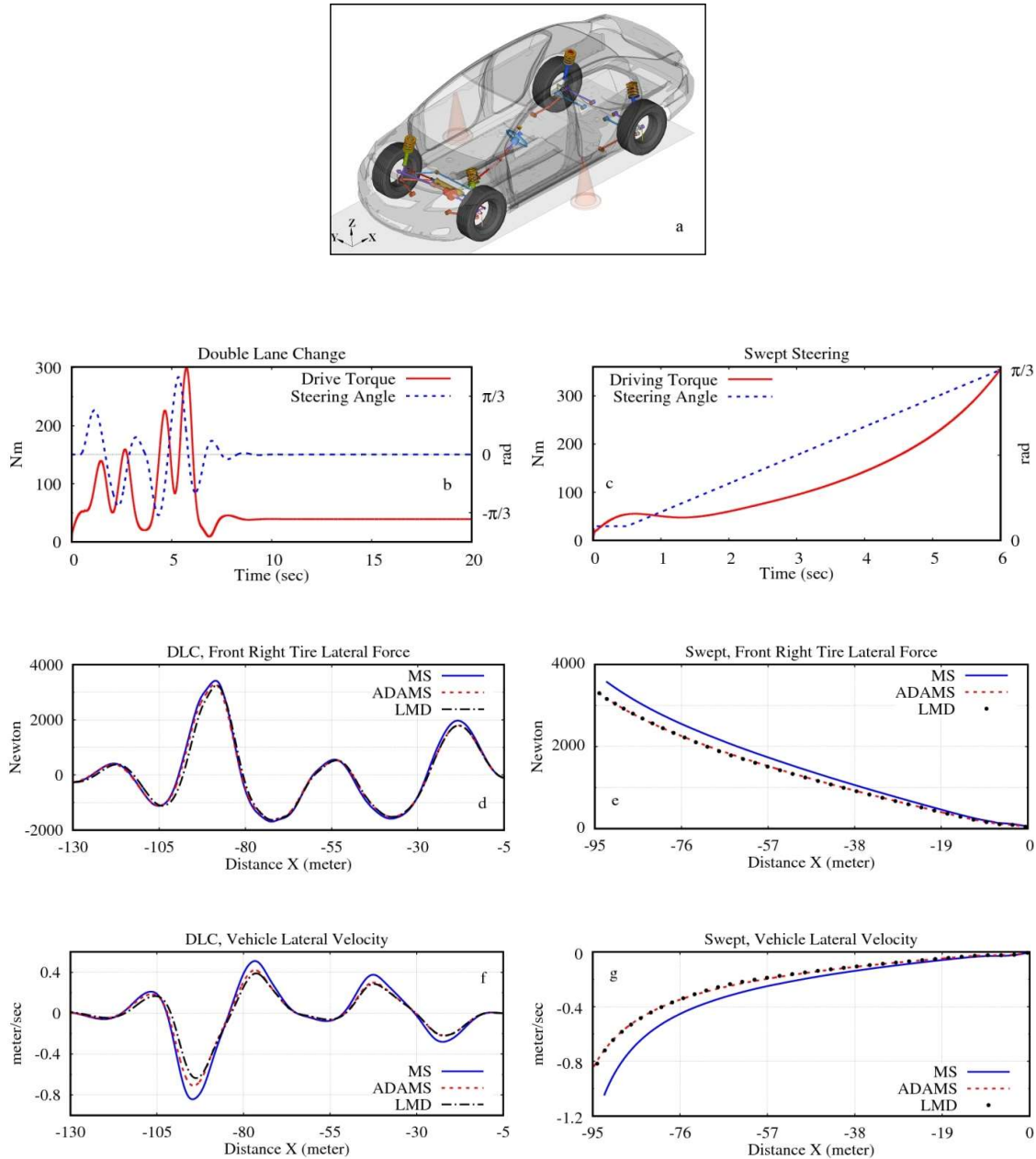


Figure 5. Numerical results for a car model: (a) vehicle model, (b)/(c) driving torque and steering angle input curves, (d)/(f) front right tire lateral force and vehicle lateral velocity for the DLC analysis, (e)/(g) front right tire lateral force and vehicle lateral velocity for the swept test analysis.

REFERENCES

- [1] Greenwood, D.T. (1988), *Principles of Dynamics*, Prentice-Hall Inc., Englewood Cliffs, New Jersey.
- [2] Murray, R.M., Li, Z., Sastry, S.S. (1994), *A Mathematical Introduction to Robot Manipulation*, CRC Press, Boca Raton, Florida.
- [3] Geradin M., Cardona A. (2001), *Flexible Multibody Dynamic*, John Wiley & Sons, New York.
- [4] Bloch, A.M. (2003), *Nonholonomic Mechanics and Control*, Springer-Verlag, New York.
- [5] Shabana, A.A. (2005), *Dynamics of Multibody Systems*, third ed. Cambridge University Press, New York.
- [6] Bauchau, O.A. (2011), *Flexible Multibody Dynamics*, Springer Science+Business Media, London.
- [7] Brennan, K.E., Campbell, S.L., Petzhold, L.R. (1989), *Numerical Solution of Initial-Value Problems in Differential-Algebraic Equations*, North-Holland, New York.
- [8] Marsden, J.E., Ratiu, T.S. (1999), *Introduction to Mechanics and Symmetry*, second ed. Springer Science+Business Media Inc., New York.
- [9] Papastavridis, J.G. (1999), *Tensor Calculus and Analytical Dynamics*, CRC Press, Boca Raton.
- [10] Paraskevopoulos, E., Natsiavas, S. (2013), "On application of Newton's law to mechanical systems with motion constraints," *Nonlinear Dyn.*, Vol. 72, pp. 455-475.
- [11] Natsiavas, S. and Paraskevopoulos, E. (2015), "A set of ordinary differential equations of motion for constrained mechanical systems," *Nonlinear Dyn.*, Vol. 79, pp. 1911-1938.
- [12] Rektorys, K. (1977), *Variational Methods in Mathematics, Science and Engineering*, D. Reidel Publishing Company, Dordrecht.
- [13] Ženišek, A. (1990), *Nonlinear Elliptic and Evolution Problems and their Finite Element Approximations*, Academic Press, London.
- [14] IFToMM T.C. for Multibody Dynamics, Library of Computational Benchmark Problems, <http://www.iftomm-multibody.org/benchmark>
- [15] Paraskevopoulos, E., Natsiavas, S. (2015), "Weak formulation and first order form of the equations of motion for a class of constrained mechanical systems," *Int. J. Non-linear Mech.*, Vol. 77, pp. 208-222.
- [16] Nocedal, J., Wright S.J. (1999), *Numerical Optimization*, Springer Series in Operations Research, New York.
- [17] Bayo, E., Ledesma, R. (1996), "Augmented Lagrangian and mass-orthogonal projection methods for constrained multibody dynamics," *Nonlinear Dyn.*, Vol. 9, pp. 113-130.
- [18] Blajer, W. (2002), "Augmented Lagrangian formulation: geometrical interpretation and application to systems with singularities and redundancy," *Multibody Syst. Dyn.*, Vol. 8, pp. 141-159.
- [19] Bröls, O., Cardona, A., Arnold, M. (2012), "Lie group generalized- α time integration of constrained flexible multibody systems," *Mech. Mach. Theory*, Vol. 48, pp. 121-137.
- [20] Paraskevopoulos, E., Natsiavas, S. (2013), "A new look into the kinematics and dynamics of finite rigid body rotations using Lie group theory," *Int. J. Solids Struct.*, Vol. 50, pp. 57-72.
- [21] MSC ADAMS 2016, *User Guide*, MSC Software Corporation, California, USA.
- [22] MotionSolve v14.0, *User Guide*, Altair Engineering Inc., Irvine, California, USA.
- [23] Pacejka, H.B. (2012), *Tyre and Vehicle Dynamics*, third ed. Butterworth-Heinemann.

SEISMIC RESPONSE ASSESSMENT OF RIGID AND FLEXIBLE ROCKING FRAMES USING SIMPLE FINITE ELEMENT MODELS

S. Diamantopoulos¹, K. Koutoulas² and M. Fragiadakis³

¹School of Civil Engineering, National Technical University of Athens,
Iroon Polytechniou, GR-15780, Zografou, Athens, Greece
e-mail: sdiamadop@central.ntua.gr

²School of Civil Engineering, National Technical University of Athens,
Iroon Polytechniou, GR-15780, Zografou, Athens, Greece
e-mail: koutoulasbs18@gmail.com

³School of Civil Engineering, National Technical University of Athens,
Iroon Polytechniou, GR-15780, Zografou, Athens, Greece
e-mail: mfrag@mail.ntua.gr; web page: <http://users.ntua.gr/mfrag/>

Keywords: Rocking Frame, Rocking Bridge, Finite Element Modelling, Non-linear Response History Analysis, Earthquake Engineering.

Abstract. *The paper examines the seismic response of rocking frames with both rigid and flexible columns using simplified Finite Element modeling. Rocking frames are found in both ancient and modern structures. In ancient structures free-standing columns are capped with a freely supported rigid beam (architrave) forming a rocking frame. Today rocking frames are becoming popular in various systems, especially bridges, due to their remarkable resistance to earthquakes despite the apparent lack of a lateral load carrying mechanism. Makris and his coworkers have shown that the seismic behavior of rocking frames can be modeled as an equivalent rocking block for frames with rigid structural members. In this work, initially we solve the rocking frame as an equivalent block with the aid of a simple single-degree-of-freedom rocking oscillator which neglects sliding and uplift. We show that the rocking frame can be modeled using beam elements connected with rotational springs with their base and their deck/epistyle. The springs have a negative stiffness moment-rotation relationship. A second, detailed modeling, using beam elements is also presented. We show that modeling with beam finite elements allows to solve rocking frames which are either rigid or flexible. FEM modeling also offers stable solutions for rocking frames with vertically restrained columns with an elastic tendon that passes through its centerline. The proposed solution scheme can be easily implement in Finite Element codes which are widely available and engineers are comfortable with, offering accurate results and avoiding complicated and specifically-tailored analytical solutions.*

1 INTRODUCTION

The rocking response of a solitary rigid block that rests on a rigid base has been studied for more than a century following the work of Milne [1]. As a result, the idea of allowing columns to uplift and then pivot during a seismic excitation is not new [2] and can be found in a large number of ancient monuments (e.g. free-standing columns that support free-standing epistyles) that have survived strong earthquakes over many centuries thanks to their rocking behavior. This observation has led bridge engineers on a “damage avoidance design” [3] of modern structures allowing the columns to some partial/controlled rocking motion. Such examples are the Rangitikei Railway Bridge and the Deadman’s Point Bridge at Cromwell in New Zealand [4,5]. Rocking provides a form of seismic isolation, while self-centering systems eliminate the residual displacements and reduce transient deformations and damage in the columns [6].

In 1963 Housner [7] proposed the equation of motion of a solitary free-standing column which was the basis for many following studies on the rigid block problem. Following observations on the dynamics of the free-standing block, many researchers, including Makris and Vassiliou [8], DeJong and Dimitrakopoulos [9] and Dimitrakopoulos and Giouvanidis [2] more extended the problem to the rocking response and the stability assessment of the planar rocking frame. Throughout their studies they expressed the equation of motion of a simple frame using principles of analytical dynamics. Moreover, the rocking problem of blocks was extended to blocks with post-tensioned tendons [10] and more recently with vertical restrainers [11,12] which are useful for the modeling of precast bridges.

Our interest on the seismic response of rocking frames is motivated by the need to have simplified Finite

Element models, equivalent simple solutions and robust algorithms for both simple and more complicated frame structures. Such tools provide credible models for designing new rocking bridges and in general offer solutions that can be easily computed in widely available open-source [13] or commercially available software [14]. Initially, we simulate a rocking frame with an equivalent oscillator [15] that has either an equivalent size parameter R , or an equivalent moment of inertia I_o , both obtained modifying the equation of motion of the rocking frame. Subsequently, we examine a simplified approach using beam-column elements for the rigid rocking columns and the deck. The columns and the deck are connected with zero-length, non-linear rotational springs. We also show that flexibility complicates further the dynamic response of a solitary block (e.g. [16, 17, 18]) or of the rocking frame with flexible columns. Finally, we study the dynamic response of a frame with pre-stressed elastic rocking columns. In all analyses, energy is dissipated introducing an “event-based” damping scheme [15]. The accuracy and the robustness of the proposed modeling is demonstrated using both far-fault and pulse-like ground motion records [19].

2 THEORETICAL BACKGROUND

We consider the free-standing rectangular rigid block with height $2h$ and width $2b$ shown in Figure 1a. We assume that the coefficient of friction between the block and the rigid base is always infinite and prevents sliding. The seismic response of a block with size parameter $R = \sqrt{b^2 + h^2}$ and slenderness $\alpha = \tan^{-1}(b/h)$, subjected to a horizontal seismic excitation $\ddot{u}_g(t)$ is given by the equation of motion:

$$\ddot{\theta}(t) = -p^2 \left(\sin[\alpha \operatorname{sgn}(\theta(t)) - \theta(t)] + \frac{\ddot{u}_g(t)}{g} \cos[\alpha \operatorname{sgn}(\theta(t)) - \theta(t)] \right) \quad (1)$$

The block will start rocking around the pivot point O (or O'), only when the ground acceleration exceeds a threshold value, i.e. when $\ddot{u}_g = g \tan \alpha$. Furthermore, $p^2 = 3g/4R$ is the frequency parameter of the block while another significant parameter is the moment of inertia I_o . For rectangular blocks it is given by the expression $I_o = (4/3)mR^2$.

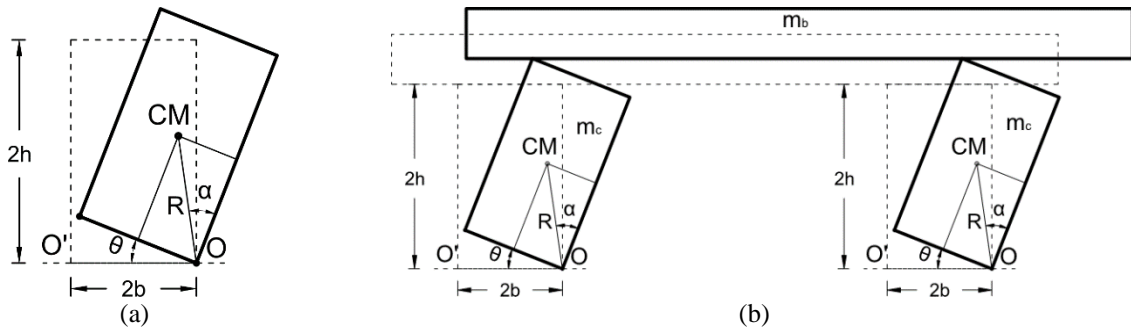


Figure 1. (a) rocking block. (b) rocking frame.

The frame of Figure 1b is another rocking system that consists of two free standing rocking columns and a rigid beam. The parameter that affects the seismic response of the rocking frame is $\gamma = m_b/2m_c$, the ratio of the mass of the deck/epistyle, m_b , over the mass of the two rocking columns, m_c . Similarly to the equation of motion of a free standing block (Eq. 1), Makris and Vassiliou [8] have shown that the equation of motion of a rocking frame can be written in a compact form:

$$\ddot{\theta}(t) = -\frac{1+2\gamma}{1+3\gamma} p^2 \left(\sin[\alpha \operatorname{sgn}(\theta(t)) - \theta(t)] + \frac{\ddot{u}_g(t)}{g} \cos[\alpha \operatorname{sgn}(\theta(t)) - \theta(t)] \right) \quad (2)$$

The frame's equation (Eq. 2) is similar to that of the rigid block (Eq. 1), if the latter is multiplied with $(1+2\gamma)/(1+3\gamma)$. We can thus solve Eq. 2, assuming an equivalent rigid block with $\hat{p} = p\sqrt{(1+2\gamma)/(1+3\gamma)}$, the same slenderness $\alpha = \tan^{-1}(b/h)$ with that of the rocking block, while the minimum uplift acceleration is again equal to $g \tan \alpha$. Furthermore, the rigid block and the plane rocking frame dissipate energy when an impact occurs and the rotation $\theta(t)$ alternates sign. According to Makris and Vassiliou [8] and taking into account Housner's [7]

coefficient of restitution for a rocking block, $\eta = \sqrt{r} = 1 - 1.5\sin^2\alpha$, the angular velocity after the impact is \sqrt{r} times the velocity before the impact. It is proved that the ratio of kinetic energy before and after the impact of a rocking frame is a function of the slenderness α and the mass ratio γ [2, 8] and simplifies to:

$$r_{frame} = \left(\frac{\dot{\theta}_2}{\dot{\theta}_1} \right)^2 = \left(\frac{1 - \frac{3}{2}\sin^2\alpha + 3\gamma\cos 2\alpha}{1 + 3\gamma} \right)^2 \quad (3)$$

3 MODELING THE ROCKING FRAME AS AN EQUIVALENT ROCKING BLOCK

We present an equivalent simple single-degree-of-freedom oscillator using beam-column elements that is able to accurately model the seismic response of a rocking frame. More specifically, we first propose two formulations that are based on solving the rocking frame as an equivalent rocking block [8]. Using the models, first proposed by Diamantopoulos and Fragiadakis [15], we can simulate a solitary rocking block with an equivalent oscillator using a beam-column element and a non-linear rotational spring (Figure 2a). The oscillator of Figure 2a has height h , width b , size parameter R , frequency parameter p , slenderness α , mass m_c and rotational moment of inertia equal to $I_A = (1/3)m_c R^2 + m_c b^2$. The non-linear moment-rotation relationship of the spring is shown in Figure 2b and is given by the expression $M(\theta) = m_c g R \sin(\alpha \operatorname{sgn}\theta - \theta)$. Since this modeling can accurately solve the rigid block problem, it can be also applied for solving the rocking frame as an equivalent block provided that either a block with modified size parameter \hat{R} or modified moment of inertia I' is adopted.

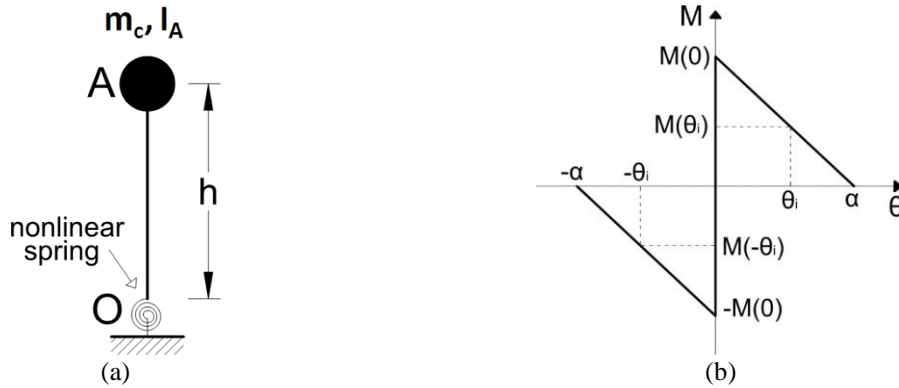


Figure 2. (a) The equivalent oscillator of a rocking block, (b) moment-rotation relationship of the single-degree-of-freedom oscillator.

3.1 Equivalent rocking block with modified size parameter \hat{R}

As shown by Makris and Vassiliou [8], the rocking frame of Figure 1b can be solved as an equivalent rocking block with frequency parameter $\hat{p} = p\sqrt{(1+2\gamma)/(1+3\gamma)}$, size parameter $\hat{R} = (1+3\gamma)/(1+2\gamma)R$ and, therefore, rotational moment of inertia with respect to point O equal to $\hat{I}_O = (4/3)m_c \hat{R}^2$. The equation of motion (Eq. 2) of a rocking frame can be rewritten as follows [8]:

$$\hat{I}_O \ddot{\theta}(t) + m_c g \hat{R} \sin[\alpha \operatorname{sgn}(\theta(t)) - \theta(t)] = -m_c \ddot{u}_g(t) \hat{R} \cos[\alpha \operatorname{sgn}(\theta(t)) - \theta(t)] \quad (4)$$

The above equation is similar to Eq. 1 and that proves that a rocking frame can be solved as a rocking block with modified characteristics. Extending the equivalent block concept, we can solve the rocking frame with an equivalent SDOF oscillator (Figure 2a) assuming that the block has dimensions $\hat{h} = \hat{R}\cos\alpha$, $\hat{b} = \hat{R}\sin\alpha$ and slenderness α . For the SDOF oscillator we assume that the rotational moment of inertia with respect to point A is $\hat{I}_A = (1/3)m_c \hat{R}^2 + m_c \hat{b}^2$.

Furthermore, the moment-rotation relationship (Figure 2b) of the rotational spring describes the self-centering capacity of the frame and is $M(\theta) = m_c g \hat{R} \sin(\alpha \operatorname{sgn}\theta - \theta)$. This expression indicates that the rocking motion will start when the overturning moment is equal to the maximum restoring moment $M_0 = m_c g \hat{R} \sin\alpha$. Furthermore, we introduce an event-based form of damping. Energy is dissipated at every impact

and is function of the coefficient of restitution $\eta_{frame} = \sqrt{r_{frame}}$. As originally proposed in reference [15] we are introducing damping, in all the models proposed, by pausing the analysis when an impact is detected and setting the post-impact angular velocity equal to the product of the pre-impact velocity of every degree of freedom with the restitution factor η_{frame} .

3.2 Equivalent rocking block with modified moment of inertia I'

Instead of modifying the size parameter R we can use an equivalent oscillator with modified rotational moment of inertia I_A . The equation of motion (Eq. 2) of a rocking frame can be written as [8]:

$$\frac{1+3\gamma}{1+2\gamma} I_o \ddot{\theta}(t) + m_c g R \sin[\alpha \operatorname{sgn}(\theta(t)) - \theta(t)] = -m_c \ddot{u}_g(t) R \cos[\alpha \operatorname{sgn}(\theta(t)) - \theta(t)] \quad (5)$$

Instead of assuming an equivalent size parameter, we may assume an equivalent moment of inertia equal to I'_A , while the remaining of the model is kept the same, i.e. the equivalent block has frequency parameter p , size R , height h , width b , slenderness α . From the above equation, the equivalent rotational moment of inertia with respect to the pivot point is described by the following equation:

$$I_o' = \frac{1+3\gamma}{1+2\gamma} I_o \Leftrightarrow I_o' = \frac{4}{3} m_c R^2 + \frac{4}{3} \frac{\gamma}{2\gamma+1} m_c R^2 \quad (6)$$

Having calculated the rotational moment of inertia with respect to the pivot point, its value with respect to the center of mass A will be equal to: $I'_A = (1/3)m_c R^2 + m_c b^2 + (4/3)[\gamma/(2\gamma+1)]m_c R^2$. Moreover, the block will again have mass m_c and its M - θ relationship is obtained from the properties of the rocking columns consisted. Table 1 summarizes the properties of the proposed SDOF oscillators for the seismic response assessment of a rigid block and a rocking frame when considered as an equivalent block.

Table1: Properties of the SDOF oscillators.

Rigid block [15]	h	b	R	α	m_c	M_0	$M(\theta)$	I_o	I_A
Rigid frame (modified R)	\hat{h}	\hat{b}	\hat{R}	α	m_c	$m_c g \hat{R} \sin \alpha$	$m_c g \hat{R} \sin(\alpha \operatorname{sgn} \theta - \theta)$	\hat{I}_o	\hat{I}_A
Rigid frame (modified I_A)	h	b	R	α	m_c	$m_c g R \sin \alpha$	$m_c g R \sin(\alpha \operatorname{sgn} \theta - \theta)$	I_o'	I_A'

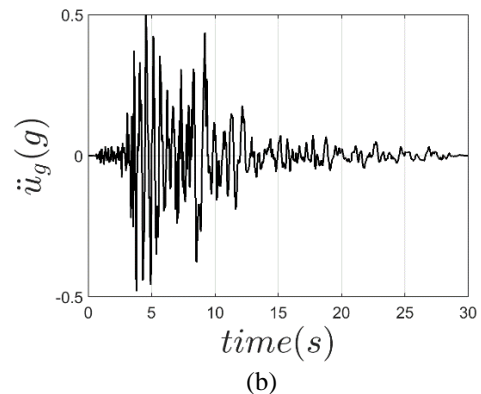
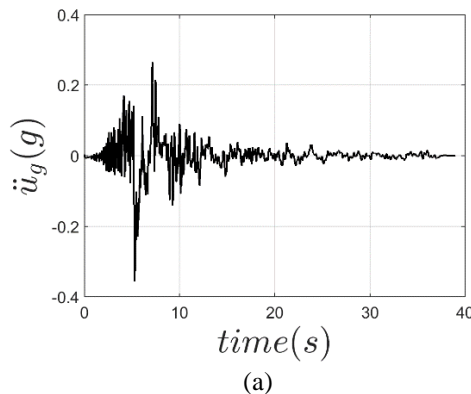


Figure 3. (a) near-fault excitation (Imperial Valley (1999), Aeropuerto Mexicali), and (b) far-fault excitation (Northridge (1994) earthquake MUL279 component).

3.3 Validation

We consider a near-fault and a far-fault ground motion record, both shown in Figure 3, with $PGA=0.36g$ and

PGA=0.52g, respectively. In Figure 4 and Figure 5 we show the seismic response of two rocking frames. The first rocking frame system corresponds to an ancient monument and has properties: $2h=5m$, $2b=0.75m$, $\gamma=1$, while the second frame has the dimensional of a contemporary rocking bridge and properties $2h=8.4m$, $2b=1.4m$, $\gamma=5$. For both frames, the slenderness values were selected as typical values of columns that are not stocky, since Housner's [7] rocking energy dissipation is not valid in this case. Furthermore, note that in bridges the mass ratio γ is usually larger than 4 while in the case of monuments this ratio is much lower, e.g. $\gamma=1$. According to Figure 4 and Figure 5, perfect agreement is observed for both frames with rigid rocking columns, either using the modified size parameter \hat{R} , or the modified moment of inertia I' model.

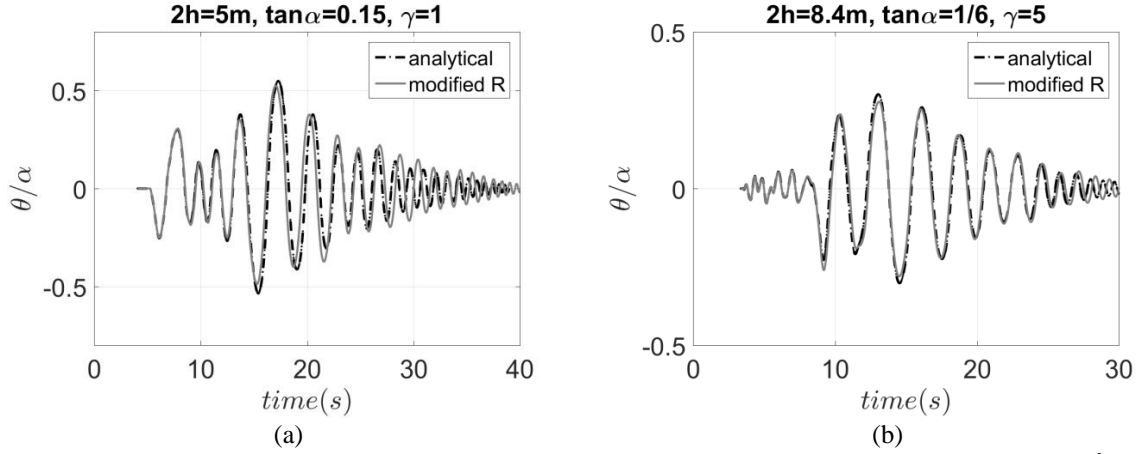


Figure 4. Rocking response history of two rocking frames, modeled with the modified size parameter \hat{R} model, when subjected to the seismic excitations of Figure 3.

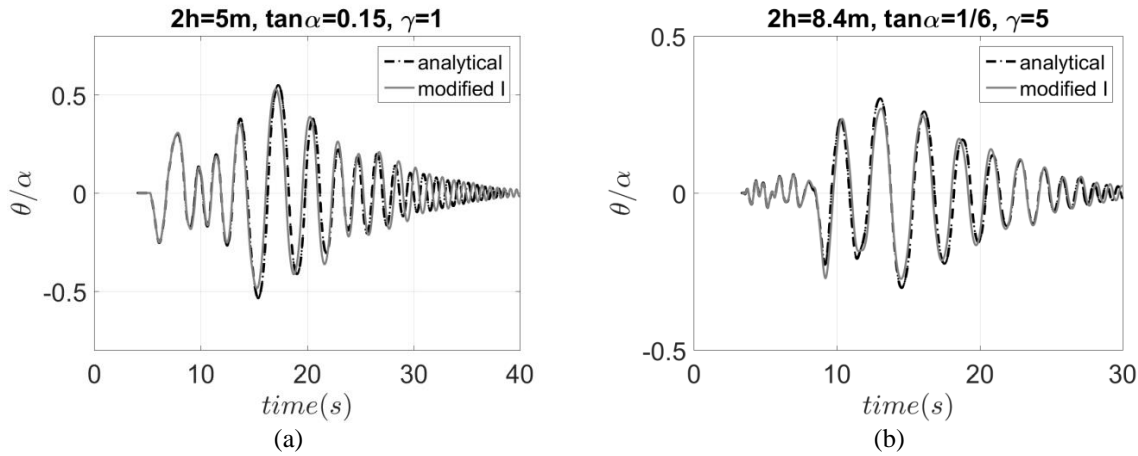


Figure 5. Rocking response history of two rocking frames, modeled with the modified moment of inertia I' model, when subjected to the seismic excitations of Figure 3.

4 DETAILED MODELLING OF THE ROCKING FRAME WITH BEAM ELEMENTS

Instead of equivalent blocks, rocking frames can be modeled with more detailed models, as shown in Figure 6. We assume that the mass of the rectangular rocking columns, m_c , is concentrated at their center of gravity and that the mass of the deck/architrave, m_b , is lumped at its two ends denoted D_1 and D_2 in Figure 6. The nonlinear springs at the base and the top of the columns fully describe the rocking of the system under the condition that there is no sliding. Moreover, if the deck's mass is lumped at the pivot point of the top of the columns and its distance from the pivot point of the base is $2R$ we assume that the rotational moment of inertia at the center of gravity of each column is $I_{c1} = I_{c2} = (1/3)m_c R^2 + m_c b^2 + (m_b/2)(2b)^2$. The rotational moment of inertia with respect to the point O (or O') is $I_o = (4/3)(3\gamma + 1)m_c R^2$. The M- θ relationship of each of the four similar springs is obtained from the restoring moment, assuming that it is equally distributed at the bottom and the top of

$$M(\theta) = \frac{1}{2} m_c g R \sin(\alpha \operatorname{sgn} \theta - \theta) + \frac{1}{2} (m_b / 2) g (2R) \sin(\alpha \operatorname{sgn} \theta - \theta) \quad (7)$$

Furthermore, assuming that the initial uplift of the columns is not negligible and that the mass ratio is $\gamma = m_b/2m_c$, the restoring moment of each spring is obtained from Eq. 7 setting $\theta=0$ and therefore $M_0 = (1/2)(2\gamma + 1)m_c g R \sin \alpha$. Figure 7 and Figure 8 compare the response history between the analytical solution using the Eq. 2 and the proposed “detailed” model when subjected to the ground motions of Figure 3. Excellent agreement is obtained for all cases shown.

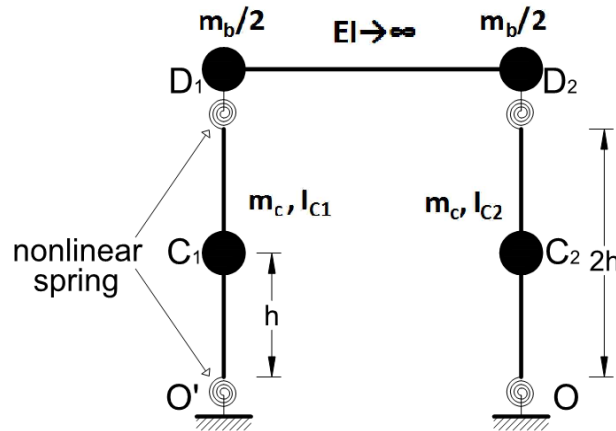


Figure 6. “Detailed” modeling of a rocking frame with rigid columns.

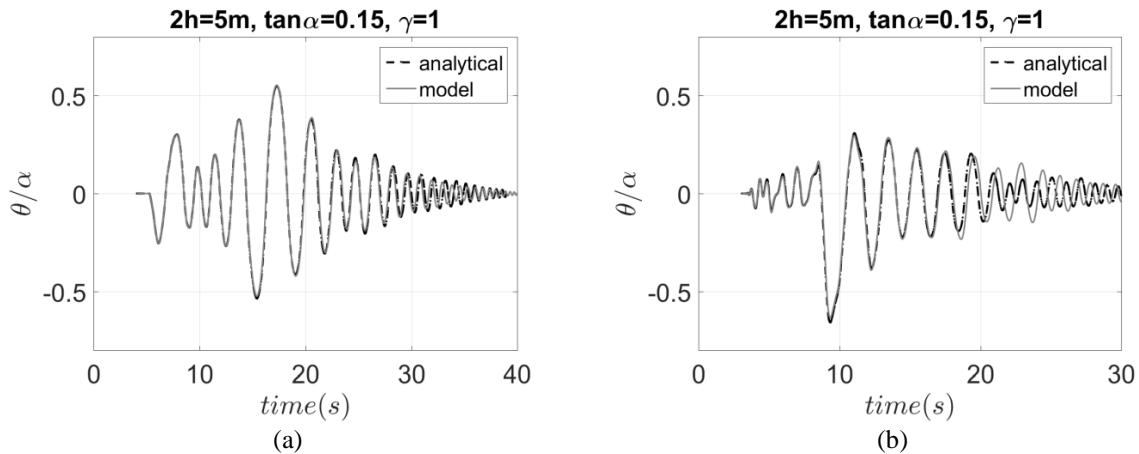


Figure 7. Comparison of the response history of a rocking frame with $2h=5\text{m}$, $2b=0.75\text{m}$, $\gamma=1$ (rocking columns and an architrave).

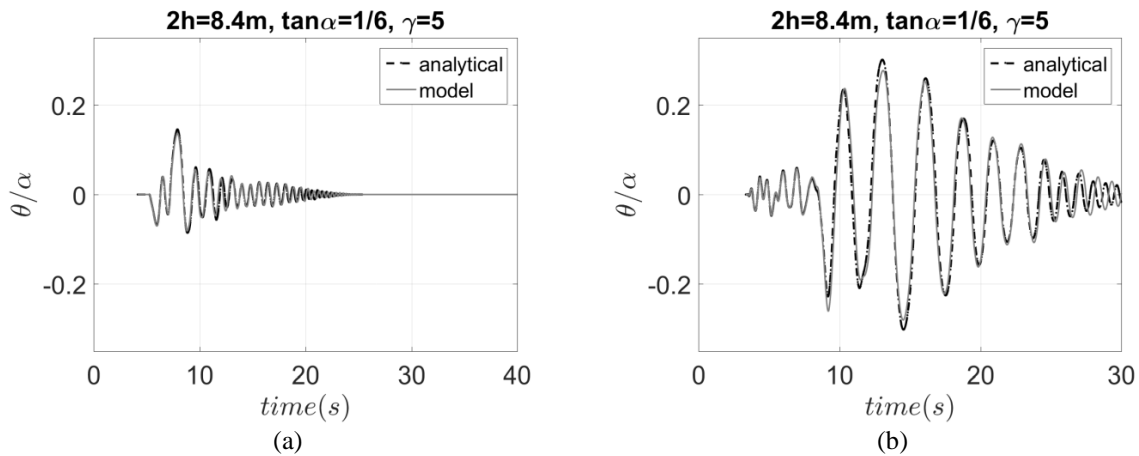


Figure 8. Comparison of the response history of a rocking frame with $2h=8.4\text{m}$, $2b=1.4\text{m}$, $\gamma=5$ (rocking bridge).

5 PRESTRESSED AND FLEXIBLE ROCKING FRAMES

The detailed model of section 4 can be easily extended to the case of a rocking frame with restrained columns, if the M - θ relationship of each spring is appropriately modified. The equivalent equation of motion of a rocking frame with vertical restrainers (Eq. 8) has been already demonstrated by Makris and Vassiliou [11] and is:

$$\ddot{\theta}(t) = -\frac{1+2\gamma}{1+3\gamma} p^2 \left[\sin(\alpha \operatorname{sgn} \theta(t) - \theta(t)) + \frac{\ddot{u}_g}{g} \cos(\alpha \operatorname{sgn} \theta(t) - \theta(t)) \right] - \frac{2}{1+3\gamma} p^2 \sin \alpha \sin \theta(t) \left(\frac{EA}{m_c g} \tan \alpha + \frac{P_o}{m_c g} \frac{1}{\sqrt{2-2\cos \theta(t)}} \right) \quad (8)$$

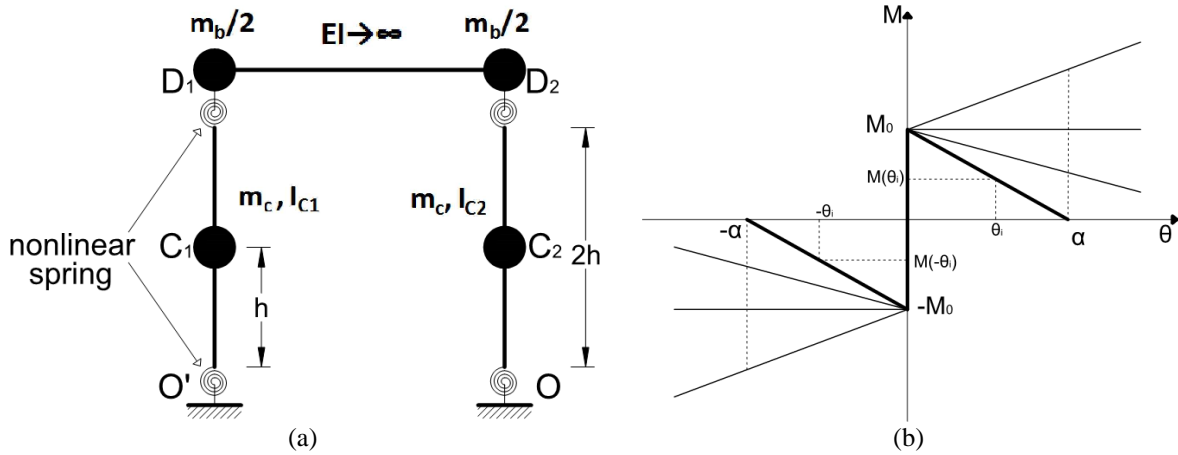


Figure 9. (a) “Detailed” modeling of a rocking frame with rigid pre-stressed columns. (b) The moment-rotation (M - θ) relationship of each spring of the simplified approach for modeling rigid pre-stressed rocking frames.

According to Eq. (8), the minimum acceleration necessary for the initial uplift is $\ddot{u}_g = g \tan \alpha [1 + 2/(2\gamma + 1)] P_0/m_c g$. We used the detailed model that presented previously and we considered that the rotational moment of inertia of each column is $I_{c1} = I_{c2} = (1/3)m_c R^2 + m_c b^2 + (m_b/2)(2b)^2$, equal to a rocking frame without tendons. The M - θ relationship (Figure 9b) describes the self-centering restoring moment and modifies the equation of motion of the rocking frame. In the case of restrained blocks, the restoring moment $M(\theta)$ is function of the tendon's elasticity EA and the initial pre-stressing force P_o . The influence of the tendons to the restoring moment of each spring of a frame is described by the Eq. 9, while at $\theta=0$ the moment is equal to $M_0 = (1/2)(2\gamma + 1)m_c g R \sin \alpha + P_o R \sin \alpha$.

$$M(\theta) = \frac{1}{2} \left[m_c g R \sin(\alpha \operatorname{sgn} \theta - \theta) + \frac{m_b}{2} g (2R) \sin(\alpha \operatorname{sgn} \theta - \theta) \right] + R \sin \alpha \left[\sin \theta \tan \alpha (EA) + P_o \frac{\sin \theta}{\sqrt{2-2\cos \theta}} \right] \quad (9)$$

From Figure 9b and Eq. 9, it is clear that the restoring moment $M(\theta)$ may be stiffening or softening, depending on the stiffness EA of the restrainers. Therefore, manipulating Eq. 9, we determine that the minimum tendon's stiffness necessary for positive stiffness of the moment-rotation M - θ relationship of Figure 9b is:

$$\frac{EA}{m_c g} \geq \frac{\left(\gamma + \frac{1}{2} \right) + \frac{P_o}{m_c g} \left(1 - \frac{\sin \alpha}{\sqrt{2-2\cos \alpha}} \right)}{\sin \alpha \tan \alpha} \quad (10)$$

The proposed model is verified for a typical rocking bridge ($2h=8.4m$, $\tan\alpha=1/6$, $\gamma=5$) subjected to a ground motion record for negative ($EA/m_cg=80$), zero ($EA/m_cg=200.8$) and positive ($EA/m_cg=250$) stiffness of the springs moment-rotation relationship assuming $P_o/m_cg=0.5$. As shown in Figure 10, perfect agreement is obtained for all three EA/m_cg cases for the frame considered solving it either analytically (Eq. 8) with the appropriate ODE23s solver [14] or using the proposed modeling.

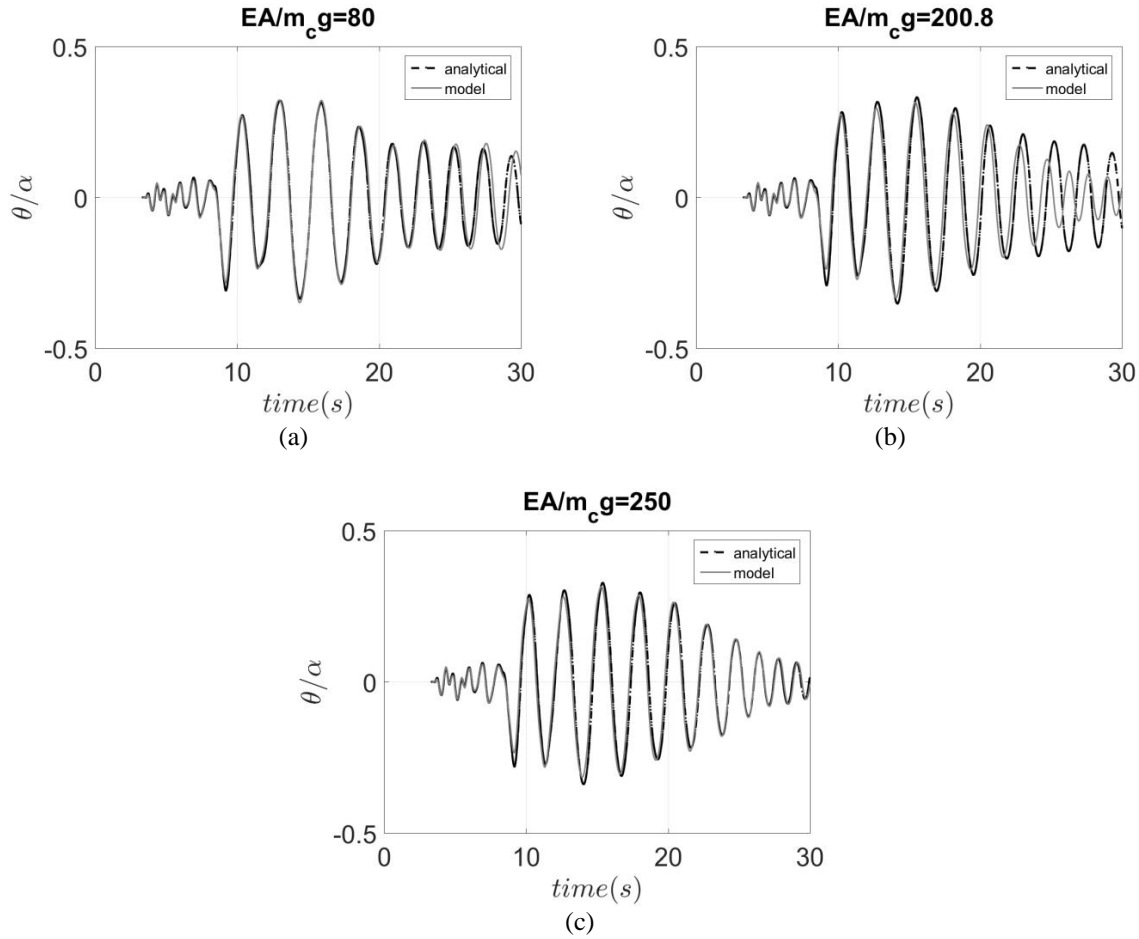


Figure 10. Comparison of the response obtained for the semi analytical solution of the equation of motion of pre-stressed rocking columns and the proposed modeling subjected to Northridge (1994) earthquake for (a) negative, (b) zero and (c) positive stiffness of the springs, respectively.

The detailed modeling with beam elements can be also applied to rocking frames with flexible columns. Especially for frames with slender columns, the response may be sensitive to the bending flexibility EI of the columns. The model assumes that the column's mass is distributed along its height, as shown in Figure 11, while the rotational moment of inertia of each column is equal to the moment of inertia of a linear elastic cantilever column with height $h = R\cos\alpha$ and with a pivot point at its base, i.e. $I_o = (4/3)m_c R^2 \cos^2\alpha$. Since the model's moment of inertia differs from the moment of inertia of a block, we distribute the additional rotational inertia $\Delta I_o = (4/3)m_c R^2 \sin^2\alpha + (m_b/2)(2b)^2 = (1 + 3\gamma)(4/3)m_c R^2 \sin^2\alpha$ among the rotational degrees of freedom of the nodes, thus adding rotational mass equal to $\Delta I_o/(n - 1)$ to the rotational degree of freedom of each node (n is the number of nodes). The moment-rotation relationship of each spring is described by Eq. 7 and its stiffness is always negative.

We assume a frame with two symmetric columns with $2h=15m$ and $2b=1.5m$ and mass ratio $\gamma=5$ (Figure 12). Initially, we solve the problem considering rigid columns and subsequently a flexible frame with concrete columns and properties i.e. $E=30GPa$ and $\rho=2.5Mg/m^3$. For the problem at hand the flexibility is important, while clearly there are cases of seismic excitations (e.g. Figure 12) where the assumption of rigid columns may not be on the safe side.

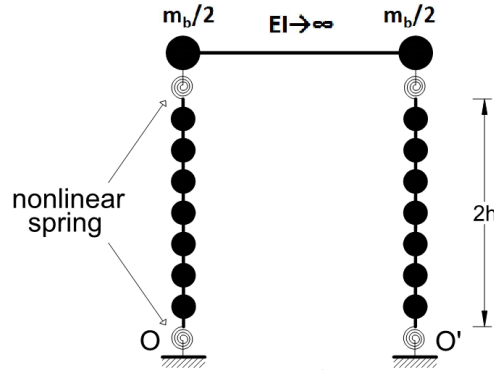


Figure 11. Modeling rocking frames with flexible columns.

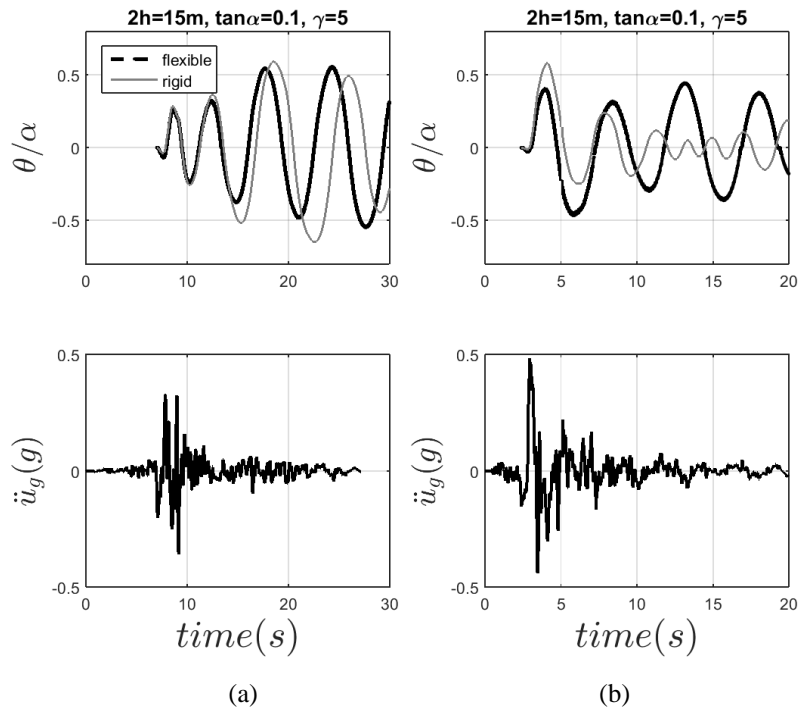


Figure 12. Seismic response comparison of a slender rocking column either considering as rigid or flexible with $E=30\text{GPa}$ and $\rho=2.5\text{Mg/m}^3$ under (a) a far-fault seismic excitation (Kocaeli (1999)/DZC270 component, Turkey earthquake) and (b) a near-fault ground motion record (Whittier Narrows (1987) LB-Orange Ave).

6 CONCLUSIONS

The paper investigates the rocking response and the seismic stability of rocking frames under natural ground motion records. More specifically, we discuss the use of Finite Element modeling for assessing the response of this complicated, nonlinear problem. The remarkable resistance of rocking frames, apparent from the stability of ancient monuments has been also verified in our study. We first examined two equivalent models that assume that the rocking frame problem can be solved as an equivalent rocking block with modified parameters. Furthermore, we propose a simplified model with beam-column elements that describe the rocking bodies and rotational-springs, whose moment-rotation relationship describes the capacity of the structure. We extend the proposed modeling concept to the case of frames with flexible columns and we also examine frames with pre-stressed columns. The last two extensions aim to bridge engineers and such models are easily implemented in a structural analysis software offering robust and accurate solutions to more complicated rocking problems.

ACKNOWLEDGEMENTS

The financial support provided by the European Research Council Advanced Grant “MASTER Mastering the computational challenges in numerical modeling and optimum design of CNT reinforced composites” (ERC-2011-ADG 20110209) is gratefully acknowledged.

REFERENCES

- [1] Milne J. (1885), "Seismic experiments", *Transactions of the Seismological Society of Japan*, Vol 8. pp. 1-82.
- [2] Dimitrakopoulos E.G., Giouvanidis A.I. (2015), "Seismic response analysis of the planar rocking frame", *Journal of Engineering Mechanics*, 141(7).
- [3] Mander J.B., Cheng C.-T. (1997), "Seismic resistance of bridge piers based on damage avoidance design", *Technical Rep., National Center for Earthquake Engineering Research, State Univ. of New York, Buffalo, New York*.
- [4] Priestley M.N., Seible F., Calvi G.M. (1996). *Seismic design and retrofit of bridges*, Wiley, New York.
- [5] Skinner R., Tyler R., Heine A., Robinson W. (1980), "Hysteretic dampers for the protection of structures from earthquakes", *Bull. N. Z. Natl. Soc. Earthquake Eng.*, Vol. 13(1), pp. 22-36.
- [6] Giouvanidis A.I., Dimitrakopoulos E.G., DeJong M.J. (2015), "Seismic response of rocking bridge bents with parameterized flag-shaped hysteretic behavior", *Proceedings of the Tenth Pacific Conference on Earthquake Engineering Building an Earthquake-Resilient Pacific*, Sydney, Australia, 6-8 November 2015.
- [7] Housner H.H. (1963), "The behavior of inverted pendulum structures during earthquakes", *Bulletin of the Seismological Society of America*, Vol. 53, pp. 404-417.
- [8] Makris N., Vassiliou M.F. (2013), "Planar rocking response and stability analysis of an array of free-standing columns capped with a freely supported rigid beam", *Earthquake Engineering and Structural Dynamics*, Vol. 42, pp. 431-449.
- [9] DeJong M.J., Dimitrakopoulos E.G. (2014), "Dynamically equivalent rocking structures", *Earthquake Engineering and Structural Dynamics*, Vol. 43(10), pp. 1543-1563.
- [10] Barthes C., Hube M, and Stojadinovic, B. (2010), "Dynamics of a post-tensioned rocking block", *Proceedings of the 9th U.S. National and 10th Canadian Conference on Earthquake Engineering*, Toronto, Canada, 25-29 July 2010.
- [11] Makris N., Vassiliou, M.F. (2014), "Dynamics of the Rocking Frame with Vertical Restrainers", *Journal of Structural Engineering*, 04014245.
- [12] Giouvanidis A.I., Dimitrakopoulos E.G. (2016), "The role of the prestressed tendons on the seismic performance of hybrid rocking bridge bents", *ECCOMAS Congress 2016 VII European Congress on Computational Methods in Applied Sciences and Engineering*, Crete Island, Greece, 5-10 June 2016, pp. 4983-4996.
- [13] OpenSEES (Open System for Earthquake Engineering Simulations). opensees.berkeley.edu
- [14] Matlab Version 2015b. The Language of Technical Computing.
- [15] Diamantopoulos S., Fragiadakis M. (2017), "Simple models for the seismic response of rigid or flexible blocks", *6th ECCOMAS Thematic Conference on Computational Methods in Structural Dynamics and Earthquake Engineering*, Rhodes Island, Greece, 15-17 June 2017, pp. 3027-3044.
- [16] Psycharis I.N., (1983), "Dynamics of flexible systems with partial lift-off", *Earthquake Engineering and Structural Dynamics*, Vol. 11(4), pp. 501-521.
- [17] Acikgoz S., DeJong M.J. (2012), "The interaction of elasticity and rocking in flexible structures allowed to uplift", *Earthquake Engineering and Structural Dynamics*, Vol. 41(15), pp. 2177-2194.
- [18] Vassiliou M.F., Mackie K.R., Stojadinovic B. (2016), "A finite element model for seismic response analysis of deformable rocking frames", *Earthquake Engineering and Structural Dynamics*, Vol. 46(3), pp. 447-466.
- [19] Psycharis I.N., Fragiadakis M., Stefanou I. (2013), "Seismic reliability assessment of classical columns subjected to near-fault ground motions", *Earthquake Engineering and Structural Dynamics*, Vol. 42, pp. 2061-2079.
- [20] Dimitrakopoulos E.G., DeJong M.J., Giouvanidis A.I. (2013), "Seismic assessment of rocking bridge bents using an equivalent rocking block", *2013 World Congress on Advances in Structural Engineering and Mechanics (Session T4I-I)*, Korea Federation of Science and Technology Societies, International Association of Structural Engineering & Mechanics (IASSEM), Korea National Tourism Corporation, Jeju Convention & Visitors Bureau, Jeju, Korea.
- [21] Vassiliou M.F., Mackie K.R., Stojadinovic B. (2014), "Dynamic response analysis of solitary flexible rocking bodies: modeling and behavior under pulse-like ground excitation", *Earthquake Engineering and Structural Dynamics*, Vol. 43(10), pp. 1463-1481.

NUMERICAL INVESTIGATION OF THE PROGRESSIVE COLLAPSE OF STEEL STRUCTURES DUE TO PLAN IRREGULARITIES

Amir Homaioon Ebrahimi¹, Pedro Martinez-Vazquez¹, and Charalampos C.Baniotopoulos¹

¹School of Engineering, University of Birmingham, Edgbaston, Birmingham, B15 2TT, United Kingdom

e-mail: homaioon.ebrahimi@yahoo.com

Keywords: progressive collapse, irregularity in plans, steel structures, non-linear dynamic analysis, non-linear static analysis.

Abstract. *Three buildings of different height, regular and irregular as per their plan layout, are designed according to AISC [1] and ASCE7 [2]. These structures were considered to be located in regions with different seismic activity with the purpose of observing their dynamic response under seven load-column-removal scenarios by using non-linear static and dynamic analyses. Non-linear dynamic analyses examine the effect of columns removal on adjacent columns, including node-displacement configurations whilst non-linear static analyses focus on the push-over curve and yield load factor. The results indicate that irregular structures designed in site class C seismic zone do collapse in most of the column removal scenarios. It is also demonstrated that higher level of redundancy showed by the 5-storey with respect to the 2-storey building plays an important role in the prediction of progressive collapse. The collected data lead to various reflections related to regular and irregular building performance under seismic load and the importance of prioritising redundancy and robustness in the context of ultimate limit strength design approaches.*

1 INTRODUCTION

Over the past years, the incidence of blast load in and around buildings and the subsequent progressive collapse have accounted for significant human casualties and structural damage (American Society of Civil Engineers[ASCE]) [3]. Risks and unusual loads potentially causing failure include plane crash, incorrect design or construction, gas explosion, fire, occasional overload, vehicle impact and explosions (National Institute of Standard and Technology[NIST]) [4]. Yet, as the risk relating to such occurrences is not high, buildings are not designed to resist the unusual overload, and neither is the influence of such loads on structures thoroughly examined; thus, structures remain vulnerable to different degrees of damage. Nonetheless, measures exist to mitigate effect of progressive collapse. Such measures are proposed by Facilities Criteria (UFC) and the General Services Administration (GSA) [5,6], both of which address the Alternative Path Method (APM), which remains the most widely practiced measure in fighting progressive collapse.

The proper parameterisation of the procedure is, nevertheless, still being examined. Powel [7], for instance, made a comparison of linear static, non-linear static and non-linear dynamic analyses, finding that using a load factor of 2 in static analyses, we can produce significantly conservative results. Ruth, Marchand, and Williamson [8], likewise, analysed 2D and 3D steel frames so as to demonstrate that a load factor of 2 in non-linear static analyses could be conservative. A factor of ~1.5 was then found to be more accurate in capturing dynamic impact obtained from quasi-static analyses, and a load factor of 2 was found to be more suitable for high-ductility structures, on condition that the materials' behaviour is not elastic-perfectly plastic and that the materials harden over a wide range of strains after yielding. Thus, the authors of the present study recommended using load factors of 2 and 1.5 for ductile structures and others, respectively.

The last decades have also seen wide research into the assessment of the sensitivity, or the lack thereof, to local damage. Gerasimidis and Baniotopoulos [9], studied the disproportionate collapse in steel moment frames and made a comparison of the APM with a numerical approximation, which was based upon β -Newmark and linear Hilbert-Hughes-Taylor procedures. Gerasimidis, Bisbos, and Baniotopoulos [10], reported a parametric study, in which irregular steel frames subject to vertical geometric irregularity had been examined; meanwhile, Gerasimidis, Bisbos, and Baniotopoulos [11], considered structural sensitivity to local damage and introduced the idea of partial damage to structural elements.

Khandelwal, El-Tawil, and Sadek [12], studied the lateral stability of structures by analysing the progressive collapse of steel-braced frames designed seismically, using explicit transient dynamic simulations. In this study,

the APM on previously designed 10-storey prototype buildings was used, which demonstrated that concentrically braced frames are far more susceptible to progressive collapse than are their eccentrically braced counterparts. Chen, Peng, Ma, and He [13], studied the effectiveness of horizontal bracing on a steel moment resisting frame, and found that rotation angles and displacements in the model with bracings were nowhere as large as those in the absence of bracing. Kim and Park [14], investigated the progressive collapse-resisting capacity of special truss moment frames in various arbitrary column-removal scenarios. Structures designed according to the AISC seismic provision, it was noted, collapsed, upon the sudden removal of a column, as a result of plastic hinge formation at highly stressed regions. Gerasimidis and Baniotopoulos [15], too, investigated the effect of different strengthening techniques to mitigate progressive collapse in 2D steel moment frames, while Gerasimidis, Deodatis, Kontoroupi, and Ettouney [16], in accordance with the APM, analysed the progressive collapse of a tall steel frame upon the removal of a corner column. Homaioon Ebrahimi, Martinez-Vazquez, and Baniotopoulos [17], investigated the effect of plan irregularities on the progressive collapse of four steel structures located in regions with different seismic activity, and when comparing regular and irregular structures designed in site class E seismic zone, the demand force to capacity ratio (D/C) of the columns in the irregular structures is on average between 1.5 and 2 times that of the regular ones. In addition, Homaioon Ebrahimi, Martinez-Vazquez, and Baniotopoulos [18], analysed the effect of plan irregularities on the progressive collapse of braced and un-braced steel structures located in regions with different seismic activity. The present paper builds on previous research and focus on the impact of three buildings of different height, regular and irregular as per their plan layout, and structural stability evaluated at two distinct seismic regions, C and E, which creates risk scenarios that have not received adequate attention from scholars. Consequently, the spread of damage induced by various column-removal scenarios on three building regular and irregular prototypes is examined and discussed throughout.

2 MODEL STRUCTURES

Three 2, 3 and 5-storey steel structures with regular and irregular plan were selected for the present investigation. Intermediate Steel Moment Frames were pre-designed with ETABS software according to the AISC (2010) and ASCE (2010) to study progressive collapse scenarios in structures. Each of the 6 structures has 3 m height and 6 bays of 4 m wide each, and plan of structures for regular and irregular buildings shown in Figure 1. All structures are assumed to be located in site class C and E seismic zones. The buildings were loaded with 192 kg/m² and 520 kg/m² dead- and live-load respectively. Further details of the six structures are provided in Table 1 whilst sections of structural members for the regular and irregular structures are given in Tables 2,3,4, and 5 respectively.

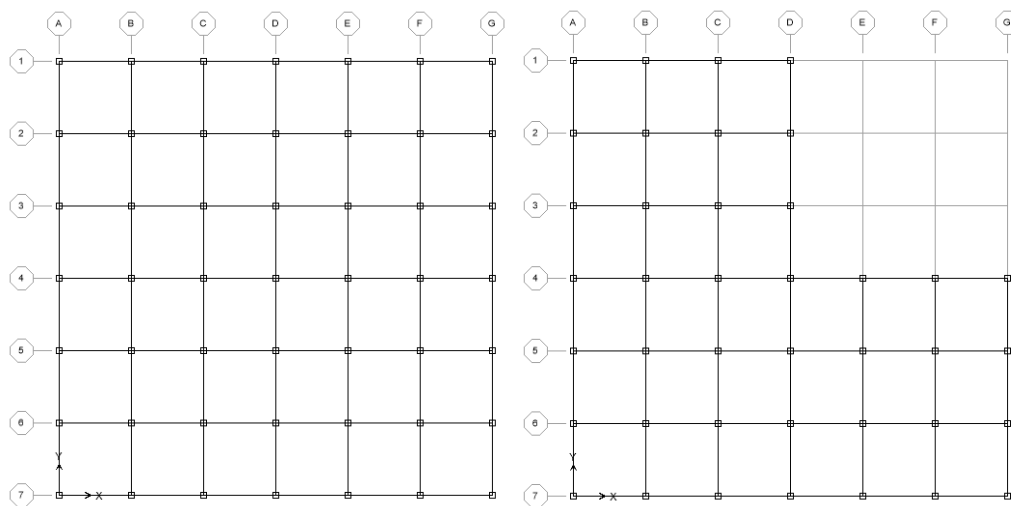


Figure 1: Regular and irregular structures plan

Structure	Seismic zone	Type of Soil	Regularity	Number
Structure 1	C	very dense soil and soft rock	Irregular	2,3,5
Structure 2	E	soft clay soil	Irregular	2,3,5
Structure 3	C	very dense soil and soft rock	Regular	2,3,5
Structure 4	E	soft clay soil	Regular	2,3,5

Table 1. Analysis model structures

		Regular-Seismic region C		Regular-Seismic region E		Irregular-Seismic region C		Irregular-Seismic region E	
		1 st	2 nd	1 st	2 nd	1 st	2 nd	1 st	2 nd
Column (Box)	b	200,180	180	200,180	180	200,180	180	200	180
	t	10,8	8	10	8	12,10	8	12,10	10
Beam	b _f	150	140	150	140	150	140	150	150
	t _f	8	8	8	8	8	8	8	8
	b _w	250	250	250	250	250	250	250	250
	t _w	8	6	8	6	8	6	8	8

Table 2. Detail of sections used in 2- story structures

		Regular-Seismic region C			Regular-Seismic region E			Irregular-Seismic region C			Irregular-Seismic region E		
		1 st	2 nd	3 rd	1 st	2 nd	3 rd	1 st	2 nd	3 rd	1 st	2 nd	3 rd
Column (Box)	b	200	180	180	200	180	180	200	200	180	200	200	200
	t	12, 10	8	8	12,10	10	8	12	10	8	15,12	12	10
Beam	b _f	150	140	140	150	140	140	150	150	140	150	150	150
	t _f	8	8	8	10,8	8	8	8	8	8	12,10	8	8
	b	250	250	250	250	250	250	250	250	250	250	250	250
	t	8	6	6	8	6	6	8	8	6	8	8	8

Table 3. Detail of sections used in 3- story structures

				Regular-Seismic region C					Regular-Seismic region E		
		1 st	2 nd	3 rd	4 th	5 rd	1 st	2 nd	3 rd	4 th	5 rd
Column (Box)	b	200	200	200	200	200	200	200	200	200	200
	t	12,10	10	10	10	10	15,12,10	15,10	12,10	10	10
Beam	b _f	150	150	150	150	150	150	150	150	150	150
	t _f	8	8	8	8	8	12,10	12,10	10,8	8	8
	b _w	250	250	250	250	250	250	250	250	250	250
	t _w	8	8	8	8	8	8	8	8	8	8

Table 4. Detail of sections used in 5- story structures

				Irregular-Seismic region C					Irregular-Seismic region E		
		1 st	2 nd	3 rd	4 th	5 rd	1 st	2 nd	3 rd	4 th	5 rd
Column (Box)	b	200	200	200	200	200	200	200	200	200	200
	t	12	10	10	10	10	20,15	15	12	10	10
Beam	b _f	150	150	150	150	150	150	150	150	150	150
	t _f	8	8	8	8	8	15,12,10	15,12,10	12,10,8	8	8
	b _w	250	250	250	250	250	250	250	250	250	250
	t _w	8	8	8	8	8	8	8	8	8	8

Table 5. Detail of sections used in 5- story structures

3 NUMERICAL MODELING

The 3D model structures were numerically analysed with OpenSees software. Non-linear analyses were run considering a simple bi-linear material model with post-yield stiffness of 2% of the initial stiffness. Non-linear beam-column elements were used for modelling the cross-sectional areas as precisely as possible. The plastification over element length and cross-sections were also considered, whereas large displacements effects were also accounted for by the employment of the co-rotational transformation of the geometric stiffness matrix. The dynamic behaviour caused by sudden column removal was not a factor in the load reversal because, in structures subjected to earthquake loads, using a complicated hysteretic model is unnecessary. The fraction of damping was assumed to be 5% which is usually the case for structures with large deformations.

4 ANALYSIS METHOD FOR PROGRESSIVE COLLAPSE

Following the GSA (2013) guidelines, load combinations including 120% of dead load plus 50% of the total live load were gradually applied within a time frame of 5 s. Then, and in order to account for non-linear dynamic effects, the load was maintained steady for the following 2 s. After the 7 s sequence, when gravity load effects are considered to be fully transferred to the structure, a pre-selected column was suddenly removed from the model and the structural response was examined.

In parallel, non-linear static analyses were performed, following the GSA (2003, 2013) recommendation for using a dynamic amplification factor of ~2. That, in order to reflect a ratio of 2 between the load that is applied to the spans that are adjacent to the removed column with respect to that applied on other spans. In this case, vertical loading is applied by following a step-wise increase until the maximum amplified loads are attained or the structure collapses. This vertical pushover analysis procedure, which is often called the 'pushdown analysis method', accounts for non-linear effects which approximate the non-linear dynamic response whilst providing a reliable estimation of the elastic and failure limits of the subject structure.

Derived from the non-linear static analyses, the effective imposed load plotted against the node displacement of the removed column indicates the capacity of a structure against progressive collapse. If the load value is divided by the standard gravity load, the vertical axes of the pushdown capacity curve are converted into dimensionless load factors, as in Eqn. (1). This standardises the load ratio and makes it easier to establish generic observations. The load factor calculated in this way have thus been used herein as a criterion for assessing structural collapse. Namely, if the load factor corresponding to the displacement causing material yield is higher than 1, the structure can withstand the removal of a column, otherwise the structure will collapse.

$$\text{Load Factor} = \frac{\text{Load}}{\text{Nominal gravity load}} \quad (1)$$

5 ANALYSIS RESULTS

As outlined above, in this investigation, the potential collapse of the structures listed in Table 1 is studied under the scenarios set out in Table 6 and Figure 2. In all cases, the column removed correspond those located in the ground floor, as that induced the most critical conditions concerning structural stability. Additionally, a range of column-removal scenarios have been identified in order to induce meaningful configurations of potential failure. In each of these scenarios, a column is suddenly removed and the response of the structure is examined through non-linear dynamic and static analyses, as described above. The columns selected for removal are shown in Figure 3.

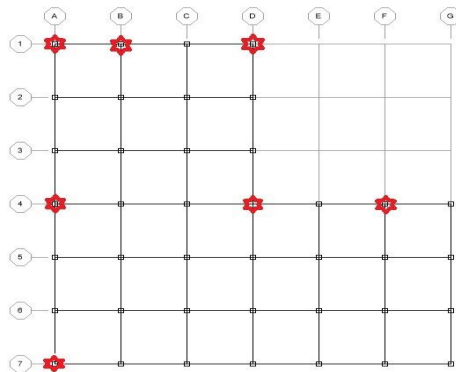


Figure 2: Location of the columns removed for each of the six structures

Number	Location of removal column			Scenario notation
	Storey	Frame	Pier	
1	1	1	A	S1F1PA
2	1	1	B	S1F1PB
3	1	1	D	S1F1PD
4	1	4	A	S1F4PA
5	1	4	D	S1F4PD
6	1	4	F	S1F4PF
7	1	7	A	S1F7PA

Table 6. Column-removal scenarios for each of the six structures.

5.1 Nonlinear static analysis results

5.1.1 Two-storey moment-resisting frame steel structure results

Considering the six regular and irregular structures analysed in this study using nonlinear static analysis. In Fig. 3, a comparison has been conducted between load factors in different column removal scenarios for 2-storey structure.

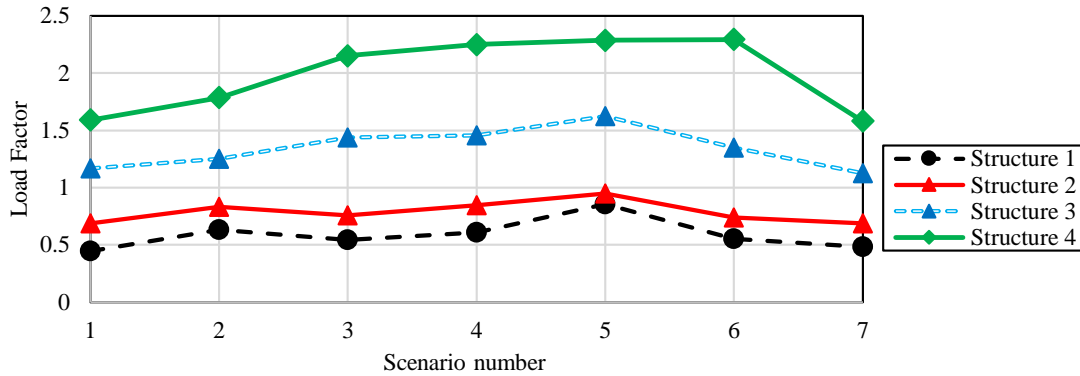


Figure 3: Load factors for all the structures and scenarios in 2-storey

Considering Fig. 3, it may be understood that under all column removal states, the two irregular structures (1 and 2) are not able to bear the force imposed by column removal in two C and E seismic regions, respectively. The most critical state is related to a state when the corner columns on “A” axis are removed. Under various column removal scenarios, both regular structures (3 and 4) managed to bear the load imposed to adjacent columns.

5.1.2 Three-storey moment-resisting frame steel structure results

In Fig. 4, the load factor for regular and irregular structures in 3-storey structure has been shown. As it may be seen, like 2-storey, also here removal of corner column represents maximum damages and minimum structural endurance against progressive collapse are resulted.

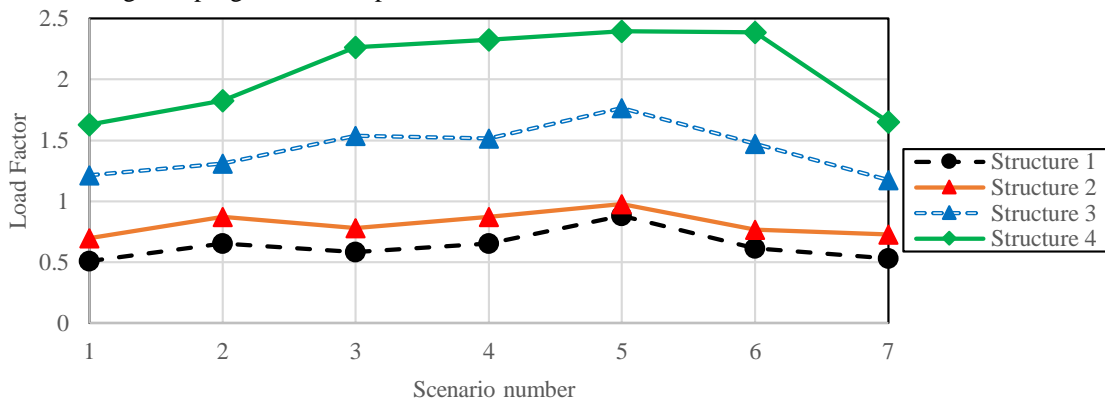


Figure 4: Load factors for all the structures and scenarios in 3-storey

Both regular structures (3 & 4) managed to resist against progressive collapse under various column removal scenarios. Also in these structures, corner (S1F1PA) and internal (S1F4PD) columns removal imposes maximum and minimum damages to the structures, respectively. On the other hand, it is seen that upon increasing structure height from 2 to 3 stories, the structure capacity against progressive collapse also increases. Comparing the load factor in 2- and 3-storey structures with similar status the same issue may be instated. The load factor in structure 1 with scenario 3 is equal to 0.545, while for 3-storey the same is equal to 0.581. In other words, a rough increase of 7% has been observed in the structure capacity.

5.1.3 Five-storey moment-resisting frame steel structure results

Considering Fig. 5, as expected, by increasing the height, and in case of removing S1F4PD Column, the structure may bear the load caused by vertical loading at the removed column. This issue has been expressed using a 1.18 load factor for Structure 2 situated in E seismic region. However, still irregular Structure 1 may not bear the force caused by vertical loading at the removed column and force distribution amongst its adjacent members.

A comparison between the 5-storey structure with those 2- and 3-storey ones demonstrates that under all states the capacity and load factor have increased upon increasing the structure height and developing more stiffness along the structure height.

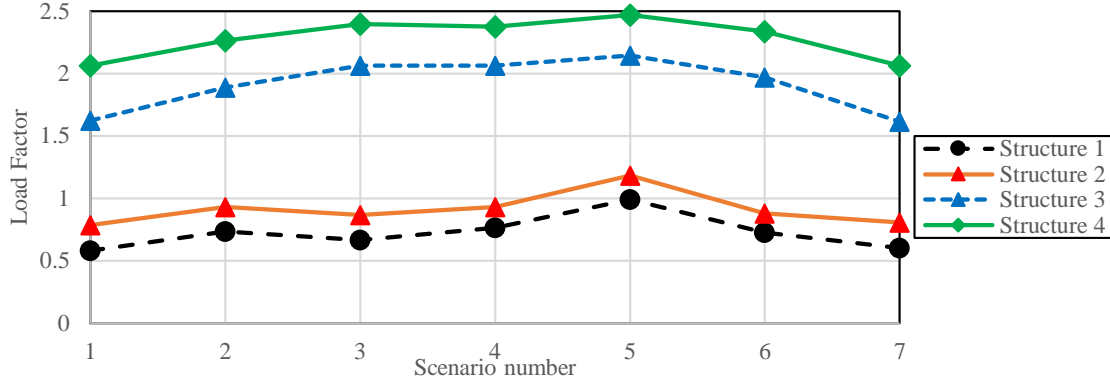


Figure 5: Load factors for all the structures and scenarios in 5-storey

In Fig. 6, the load factor changes in terms of height have been given for all structures (1 through 4). Regarding forces in height ratio changes it may have expressed that the relation between force and height for regular structures is almost linear, while the same is nonlinear for irregular ones.

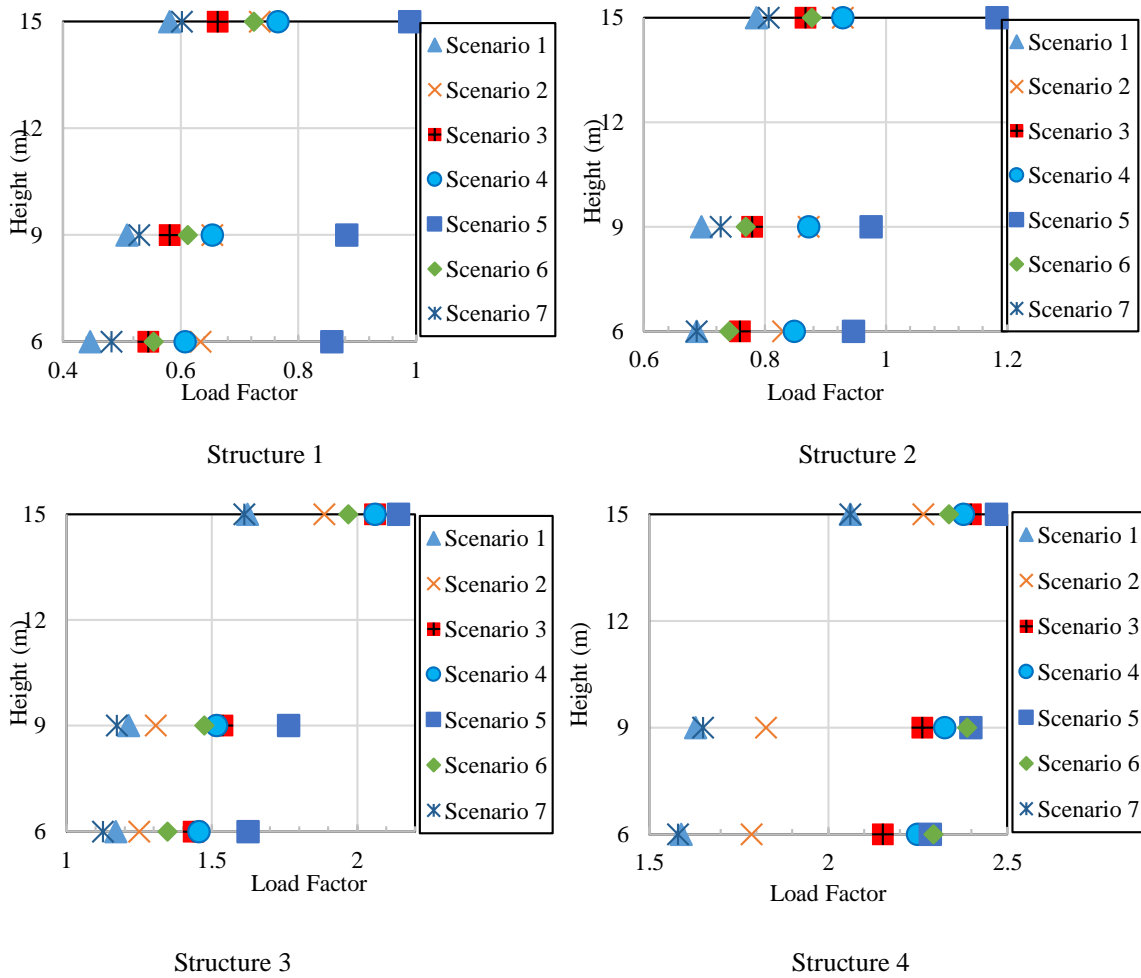


Figure 6: Yield load factors vs. Height for all the structures and scenarios

5.2 Nonlinear dynamic analysis results

Non-linear dynamic analyses were used to calculate the peak displacement of the node above a removed column. Figure 7, 8 and 9 shows the results obtained for scenarios 1 and 3 across all structures, respectively. As it can be

inferred from the results, node displacements in structures 1 and 2 represent structural collapse of the region around the removed column. In contrast, the node displacement remains constant after 7 s from the removal in all structures 3 and 4 for scenarios 3 which reveals a robust structural performance following the potential failure of the target column.

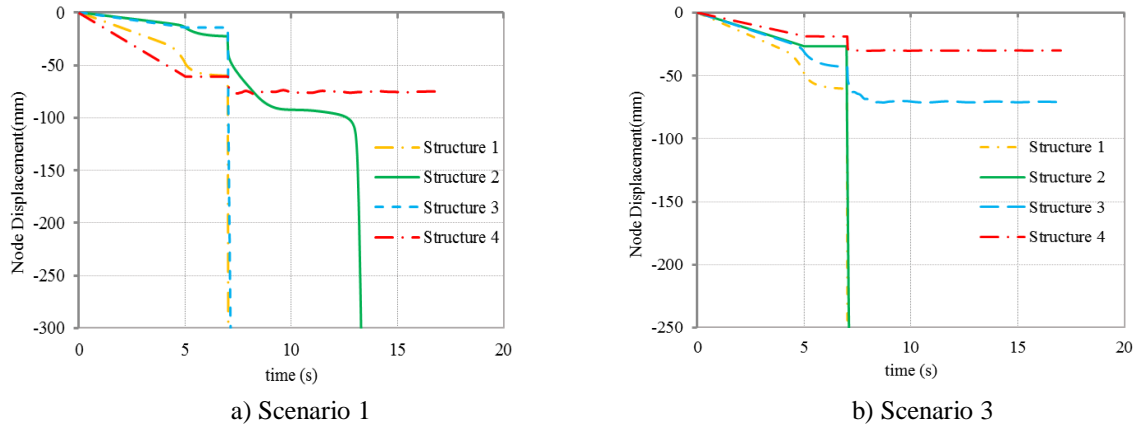


Figure 7: Vertical displacement of removal point of 2-storey structures, a) Scenario 1, b) Scenario 3

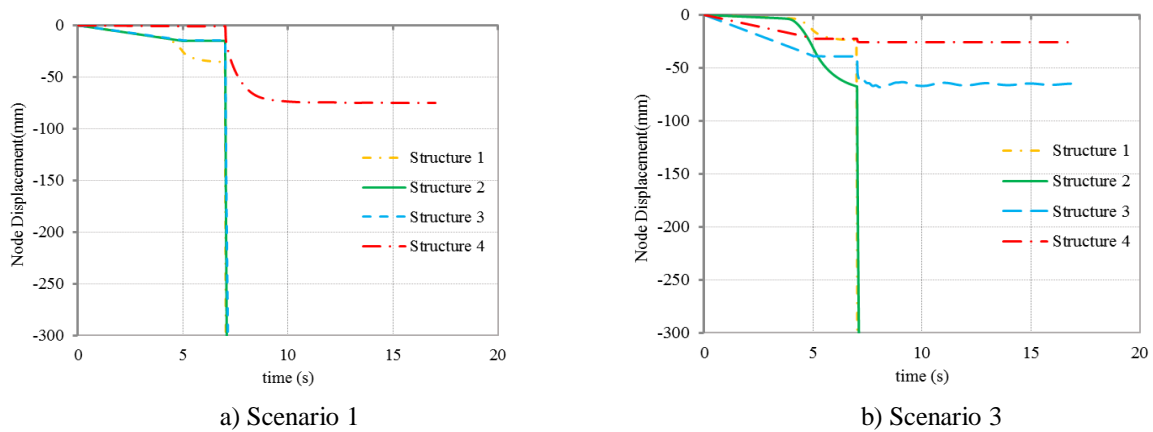


Figure 8: Vertical displacement of removal point of 3-storey structures, a) Scenario 1, b) Scenario 3

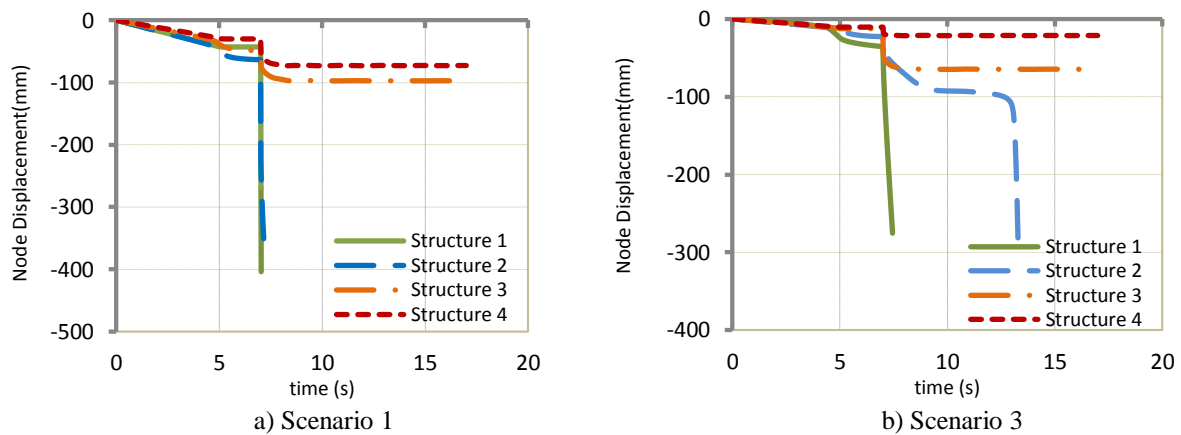


Figure 9: Vertical displacement of removal point of 5-storey structures, a) Scenario 1, b) Scenario 3

Another key aspect for assessing structural performance under progressive collapse is the force taken by columns that are adjacent to the removed column. In Figure 10 the demand to capacity (D/C) ratio of the columns adjacent to the corner columns in scenario 1 across all the structures is given. It can be seen in this figure that the D/C ratio associated to adjacent columns is around 1 in scenario 1 related to structures 3 and 4. This suggests that columns adjacent to the target-removal one may not be exposed to total damage as alternative load paths do not seem to directly redistribute to those spans.

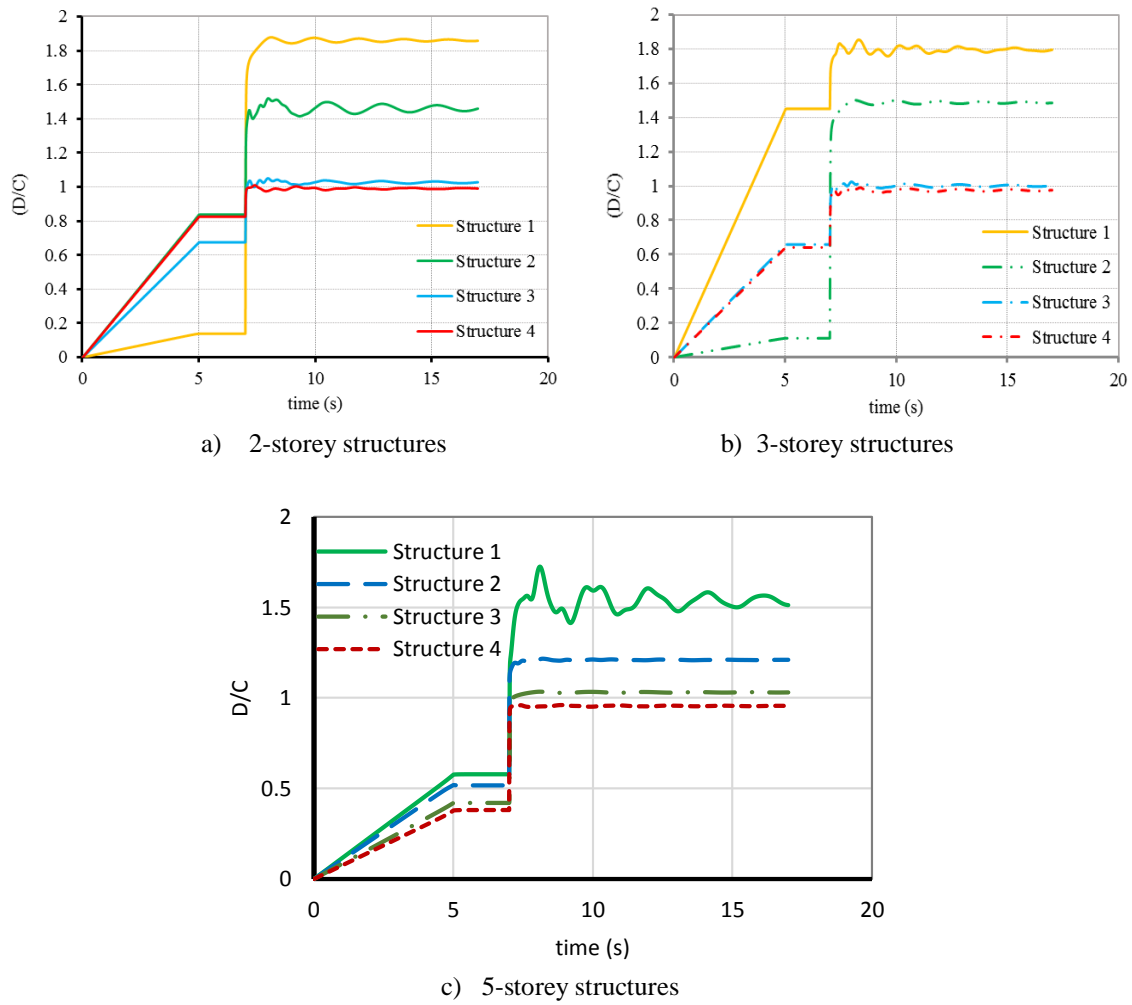


Figure 10: The demand force to capacity ratio (D/C) of the adjacent columns in Scenario 1
a) 2-storey structures, b) 3-storey structures, c) 5-storey structures

According to the structures 3 and 4 in five storey structures exhibit D/C of 0.6 and 0.73 for scenario 3, respectively. Therefore, these columns are not exposed to collapse under that column-removal scenario, but they would be damaged if belonging to structures 1, 2 and also in these structures the required force for both adjacent columns in the progressive collapse analysis is between 1.2 and 1.8 times the column capacity, which indicates that these columns would have been damaged after the collapse of the target column.

On the other hand, it can be seen the D/C ratio associated to adjacent columns for both two and three storey structures is greater than 1 in scenario 3 related to structures 1, 2, and 3 which indicates that these columns would have been damaged after the collapse of the target column. In Table 7, 8, and 9 node displacement and maximum D/C ratio of adjacent columns is given for all the scenarios and structures.

Scenario	Structure 1		Structure 2		Structure 3		Structure 4	
	Node Displacement	D/C	Node Displacement	D/C	Node Displacement	D/C	Node Displacement	D/C
S1F1PA	Fail	1.89	Fail	1.55	Fail	1.16	78	1.01
S1F1PB	Fail	1.42	Fail	1.12	64	0.79	27	0.66
S1F1PD	Fail	1.75	Fail	1.32	71.1	1.82	30	0.72
S1F4PA	Fail	1.33	97	1.09	63.4	0.78	27.1	0.67
S1F4PD	Fail	1.2	95.5	1.07	64.2	0.79	27	0.66
S1F4PF	Fail	1.47	Fail	1.15	71	0.82	28	0.67
S1F7PA	Fail	1.87	Fail	1.52	Fail	1.16	78	1.01

Table 7: Node displacement and maximum D/C ratio of adjacent columns for 2-storey structures

Scenario	Structure 1		Structure 2		Structure 3		Structure 4	
	Node Displacement (mm)	D/C	Node Displacement (mm)	D/C	Node Displacement (mm)	D/C	Node Displacement (mm)	D/C
S1F1PA	Fail	1.85	Fail	1.51	Fail	1.13	75	0.99
S1F1PB	Fail	1.36	95	1.07	62	0.77	24.1	0.62
S1F1PD	Fail	1.68	Fail	1.29	68.2	1.79	26	0.68
S1F4PA	Fail	1.27	93	1.04	61.5	0.77	24.2	0.61
S1F4PD	Fail	1.16	92	1.03	61	0.75	24	0.57
S1F4PF	Fail	1.41	96.5	1.09	68	0.77	25	0.63
S1F7PA	Fail	1.8	Fail	1.45	Fail	1.14	75	0.99

Table 8: Node displacement and maximum D/C ratio of adjacent columns for 3-storey structures

Scenario	Structure 1		Structure 2		Structure 3		Structure 4	
	Node Displacement (mm)	D/C	Node Displacement (mm)	D/C	Node Displacement (mm)	D/C	Node Displacement (mm)	D/C
S1F1PA	Fail	1.77	Fail	1.44	Fail	1.06	42.4	0.96
S1F1PB	Fail	1.29	86	0.92	64.61	0.68	21.4	0.48
S1F1PD	Fail	1.5	Fail	1.23	Fail	1.06	42.4	0.96
S1F4PA	Fail	1.15	84.9	0.87	76.3	0.61	16.3	0.41
S1F4PD	91	1.05	84	0.83	65.7	0.52	14.1	0.39
S1F4PF	Fail	1.31	87.8	0.94	57.6	0.62	18.2	0.42
S1F7PA	Fail	1.67	Fail	1.38	Fail	1.03	40.1	0.91

Table 9: Node displacement and maximum D/C ratio of adjacent columns for 5-storey structures

6 CONCLUSION

In this study, three 2, 3 and 5-storey irregular and regular steel structures with moment-resisting frame were designed in site class C and E according to the AISC (2010) and ASCE7 (2010). The effect of plan irregularities and type of seismic regionalisation on progressive collapse have been analysed under various column removal scenarios. The results of the analyses reveal that in cases where the structural plans were similar, the structure designed in a region in site class E seismic risk has less collapse potential. Moreover, the potential for progressive collapse was identified to be higher for buildings with plan irregularities and or in site class C. It was also seen that the displacement of the node above the removed column and the D/C ratio of the columns adjacent to the one removed could provide a fair indication of the risk of overall collapse of structures.

The results showed that upon increasing structure height from 2 to 3 stories, the structure capacity against progressive collapse also increases. Comparing the yield load factor in two 2- and 3-storey structures with similar status the same issue may be instated. The yield load factor in structure 1 with scenario 3 was equal to 0.545, whilst for 3-storey the same was equal to 0.581. In other words, a rough increase of 7% has been observed in the structure capacity. Generally, a comparison between the 5-storey structure with those 2- and 3-storey ones demonstrated that under all states the capacity and yield load factor have increased upon increasing the structure height.

7 REFERENCES

- [1] AISC (2010) Manual of steel construction, American Institute of Steel Construction, Chicago, [IL, USA](#).
- [2] ASCE 7 (2010) Minimum design loads for buildings and other structures, American Society of Civil Engineers, Reston, VA, [USA](#).
- [3] ASCE 7-05 (2005), *Minimum Design Loads for Buildings and Other Structures*, American Society of Civil Engineers, Reston, VA, [USA](#).

- [4] National Institute of Standard and Technology (NIST) (2007), *Best practices for reducing the potential for progressive collapse in buildings*, NISTIR 7396, Technology administration, U.S. Department of Commerce.
- [5] GSA (2013), *Alternate Path Analysis and Design Guidelines for Progressive Collapse Resistance*, General Services Administration, Washington, DC, [USA](#).
- [6] Unified Facilities Criteria (UFC) (2009), *Design of buildings to resist progressive collapse*, Department of Defense, Washington DC, USA.
- [7] Powel, G. (2005), Progressive collapse: case studies using nonlinear analysis, Proc. Of Metropolis and Beyond-Structures Congress. Reston, VA: ASCE.
- [8] Ruth, P., Marchand, K.A. & Williamson, EB. (2006), Static equivalency in progressive collapse alternate path analysis: reducing conservatism while retaining structural integrity, *Journal of Performance of Constructed Facilities*, 20(4), 349–64.
- [9] Gerasimidis, S. & Baniotopoulos, C.C. (2011), Steel Moment Frames Column Loss Analysis: The Influence of Time Step Size, *Journal of constructional steel research*, 67, 557-564.
- [10] Gerasimidis, S., Bisbos, C. & Baniotopoulos, C.C. (2012), Vertical Geometric Irregularity Assessment of Steel Frames on Robustness and Disproportionate Collapse, *Journal of constructional steel research*, 74, 76-89.
- [11] Gerasimidis, S., Bisbos, C. & Baniotopoulos, C.C. (2013), A computational model for full or partial damage of single or multiple adjacent columns in disproportionate collapse analysis via linear programming, *Structure and Infrastructure Engineering*, 10(5), 1-14.
- [12] Khandelwal, K., El-Tawil, S. & Sadek, F. (2009), Progressive collapse analysis of seismically designed steel braced frames, *Journal of Constructional Steel Research*, 65, 699–708.
- [13] Chen, J., Peng, W., Ma, R. & He., M. (2012), Strengthening of horizontal bracing on progressive collapse resistance of multistory steel moment frame, [Journal of Performance of Constructed Facilities](#), 26(5), 720–4.
- [14] Kim, J. & Park, J. (2014), Design of Special Truss Moment Frames Considering Progressive Collapse, *International Journal of Steel Structures*, 14(2), 331-43.
- [15] Gerasimidis, S. & Baniotopoulos, C.C. (2015), Progressive Collapse Mitigation of 2D Steel Moment Frames- Assessment of the Effect of Different Strengthening Schemes, *Stahlbau*, 84 (5), 324-331.
- [16] Gerasimidis, S., Deodatis, G., Kontoroupi, T. & Ettouney, M. (2015), Loss-of-stability induced progressive collapse modes in 3D steel moment frames, *Structure and Infrastructure Engineering*, 11(3), 334-44.
- [17] Homaioon Ebrahimi, A., Martinez-Vazquez, P. & Baniotopoulos C.C. (2017) Numerical studies on the effect of plan irregularities in the progressive collapse of steel structures. *Structure and Infrastructure Engineering*, 13: (12):1576-1583
- [18] Homaioon Ebrahimi, A., Martinez-Vazquez, P. & Baniotopoulos C.C. (2017) *Progressive collapse of braced irregular steel structures located in regions with different seismic activity*. UKACM Conference, University of Birmingham.

DYNAMIC RESPONSE OF MASONRY BUILDINGS CONSIDERING THE TIME-DEPENDENT SOIL SATURATION CONDITIONS

Alexandros Liratzakis¹, Yiannis Tsompanakis^{2*}

¹School of Environmental Engineering
Technical University of Crete
Chania, GR-73100, Greece
e-mail: alyratzak@isc.tuc.gr

²School of Environmental Engineering
Technical University of Crete
Chania, GR-73100, Greece
e-mail: jt@science.tuc.gr

Keywords: Masonry Buildings, Seismic Hazard, Soil-Structure Interaction, Soil Saturation, Incremental Dynamic Analysis, Limit States, Rehabilitation Measures.

Abstract. *The main aim of this work is to investigate the seismic vulnerability of traditional masonry buildings, taking into account the impact of dynamic soil-structure interaction (SSI). More specifically, the dynamic response of a typical unreinforced masonry (URM) building constructed over a silty sand layer is examined. The main novelty of the present study is that it considers time-varying soil mechanical properties, i.e., depending on the soil saturation level, which usually varies with time. In addition, a new structural assessment approach, which aims to accurately assess the performance levels (Limit States) of historic buildings and monuments after performing certain seismic rehabilitation measures has been applied. Under this perspective, a quite simple and efficient -in terms of time, cost and effectiveness- intervention was considered, in which blocks of expanded polystyrene (EPS) geofoam are placed at the perimeter of the foundation of the URM building in order to improve its dynamic response and reduce its seismic vulnerability under the examined circumstances. Subsequently, the calculation of building's nominal life is performed in a realistic manner by taking into account the annual changes in the soil saturation level.*

1 INTRODUCTION

Modern regulations for the evaluation of existing structures [1-3] are based on performance-based assessment, which aims to implement a number of limit states in relation to predetermined seismic actions scenarios [4]. On the other hand, the challenge of balancing safety versus maintenance of the architectural and artistic features of historic structures remains a crucial issue to address, usually on a case-by-case basis. There is a lack of a unified approach for the assessment of seismic risk of monuments and historic structures. Ensuring the monumental buildings' integrity in long terms is an issue that needs further attention and improvements. The most important difficulty, in creating a holistic methodology for assessing the seismic hazard of cultural heritage structures, is the limitations that are imposed on structural interventions. The constraints on the implementation of interventions in cultural heritage buildings are arising from the internationally accepted guidelines and the conceptual differences compared to design of new structures [5]. The best retrofitting practice in monumental structures is considered the application of reversible interventions in order to limit their vulnerability in a less intrusive manner.

Performance through Limited Duration Rehabilitation Interventions (LDRI) is a new methodology, which aims to assess the seismic risk of monumental structures [6, 7]. This methodology attempts to provide a framework that quantifies the "safe" duration (i.e., the nominal life) of an intervention that upgrades structural integrity in a specified manner. The nominal life of an intervention is defined as the period for which this action ensures that the structure fulfills selected performance level(s) for a certain seismic scenario (e.g., probability of exceedance 10% and 20% in 50 years, respectively for Significant Damage and Damage Limitation Levels).

A typical two-storey URM building, recently presented by the authors [8], was selected as a case study to perform the LDRI methodology, introducing also a new retrofitting scheme as it will be presented in the sequence. In the previous work [8], the impact of silty sand soil saturation level on the dynamic response of a typical masonry building was presented. Additionally, a slight retrofitting scheme was also examined, in which reinforced concrete (RC) friezes were placed at the floor levels and wooden lintels were replaced with RC lintels. The results indicated that the examined building presented higher drifts when the structure was constructed on relatively dry soil, while the slight strengthening with RC elements substantially improved its response and also reduced the impact of saturation conditions.

As an extension, the present study proposes the application of a new mitigation method capable of also improving the dynamic structural response, depending on the soil saturation level. More specifically, a layer of expanded polystyrene (EPS) geofoam is placed between the surrounding silty sand layer and the external side at the perimeter of building's foundation, acting as a compressible "shield". EPS blocks are commonly used as a lightweight filling material in many civil engineering applications, e.g., embankments, retaining walls, pipelines, ground vibration isolations, etc. This simple, economic and fast intervention, which does not cause any structural or functional disturbance, aims to isolate the structure from ground shaking and absorb most of the seismic energy. In addition, this paper attempts to determine the nominal life of the URM building after this slight intervention considering either constant or annually varying soil saturation conditions.

2 THEORETICAL BACKGROUND

2.1 Performance-based design/assessment

As already mentioned, modern seismic design norms/guidelines for the seismic design of new structures and for the assessment of interventions in existing buildings have included state-of-the-art methodologies for assessing the structural response based on performance-based assessment for certain limit states (design levels).

2.1.1. Greek Code for Structural Interventions

The Greek norm for structural interventions for existing reinforced concrete structures (Greek Code for Structural Interventions (CSI) [9]) has adopted two seismic hazard levels:

- Seismic excitation with exceedance probability 50% in 50 years.
- Seismic excitation with exceedance probability 10% in 50 years.

In addition, CSI defines three performance levels, namely: Damage Limitation, Significant Damage, and Near Collapse, for structures with a conventional lifetime of $T_L=50$ years.

Accepting that the cultural heritage structures belong to importance classes III and IV, CSI defines three performance levels:

- A1: Limited damage for seismic excitation with exceedance probability 10% in 50 years.
- A2: Limited damage for seismic excitation with exceedance probability 50% in 50 years.
- B1: Important damage for seismic excitation with exceedance probability 10% in 50 years.

It is noteworthy that CSI does not consider the performance level "Near Collapse" as acceptable for important monumental structures.

Greek Earthquake Planning and Protection Organization (EPPO) has more recently released a draft regulation: Code for the Assessment and Interventions of Masonry Structures (CASIM) aiming to establish criteria for the assessment of the bearing capacity of existing masonry structures [10], and a draft with specialized guidelines for monuments [11]. In general, CASIM follows the same principles and performance levels as CSI.

2.1.2. Eurocode EC8

Eurocode 8 -Part 1 [12] and Part 3 [2]- follows similar principles as CSI, while it provides an additional seismic hazard level:

- Seismic excitation with exceedance probability 20% in 50 years.
- Seismic excitation with exceedance probability 50% in 50 years.
- Seismic excitation with exceedance probability 10% in 50 years.

The target performance level results from the combination of acceptable damage level and seismic risk scenario, as well as the importance class of the structure.

It has to be noted that EC8 does not refer with specific guidelines for the cases of high historical or artistic value monumental structures [7]. However, its principles can be followed for structural assessment and retrofitting in such cases as well.

2.1.3. FEMA 349

According to US guidelines FEMA 349, the following four performance levels are defined for masonry structures [4]:

- Slight Damage State.
- Moderate Damage State.
- Extensive Damage State.
- Complete Collapse.

Similarly, to EC8, FEMA 349 adopts three seismic hazard levels [4]:

- Seismic excitation with exceedance probability of 50% in 50 years.

- Seismic excitation with exceedance probability of 10% in 50 years.
- Seismic excitation with exceedance probability of 2% in 50 years.

In addition, FEMA 349 [4] proposes limit drift values for each performance level. The proposed values in Table 1 change according to the construction materials and the norm under which the structure was designed. Note that for historic structures, the limit values of the URM buildings correspond to design level "Low-Code".

Performance Level	Average Inter-Story Drift Ratio					
	Capacity Curve Control Points		Structural Damage State Thresholds			
			(Fragility Medians)			
	Yield	Plastic	Slight	Moderate	Extensive	Complete
Special High - Code	0.0057	0.1371	0.005	0.015	0.05	0.125
High – Code	0.0038	0.0913	0.004	0.012	0.04	0.1
Moderate – Code	0.0029	0.0514	0.004	0.0099	0.0306	0.75
Low – Code	0.0019	0.0343	0.004	0.0099	0.0306	0.75
Pre – Code	0.0019	0.0343	0.0032	0.0079	0.0245	0.06

Table 1 : Structural Damage State thresholds per Performance Level [4]

2.2 Limited Duration Rehabilitation Interventions

Improvement of dynamic structural response by applying the so-called “Limited Duration Rehabilitation Interventions” (LDRI) [6, 7] aims to implement mitigation measures for a specified period and for a predefined limit state, after which a re-assessment of the building must be performed and depending on the results to revise the mitigation measures. According to this conceptual methodology, the time for which the operation ensures a predetermined performance level is defined as the nominal life of an intervention (T_{Δ}).

This methodology uses the following Equations for each of the three seismic hazard zones in Greece (Z_1 , Z_2 , Z_3) for the calculation of the return period (T_{RL}) with respect to reference peak ground acceleration (a_{gR}):

$$\log a_{gR} \approx 0.277 \log T_{RL} + 1.579 \quad (1)$$

$$\log a_{gR} \approx 0.264 \log T_{RL} + 1.739 \quad (2)$$

$$\log a_{gR} \approx 0.240 \log T_{RL} + 2.015 \quad (3)$$

The code-imposed acceleration values a_{gRL} for of the three Greek seismic hazard zones are 0.16g, 0.24g and 0.36g, respectively [13]. The return period T_{RL} related to the corresponding a_{gR} is calculated using the proper attenuation relationship among (1) - (3), for which a 20% reduction, i.e., $a_{gR} = 0.8a_{gRL}$, is also considered [7].

Adopting a Poissonian distribution for the occurrence of seismic events, T_{Δ} is related to the return period T_{RL} and to the probability of occurrence P_R as follows:

$$T_{RL} = - \frac{T_{\Delta}}{\ln(1 - P_R)} \quad (4)$$

If the seismic action is defined in terms of the reference peak ground acceleration a_{gR} , the value of the importance factor γ_I multiplying the reference seismic action to achieve the same probability of exceedance in T_{Δ} years as in the $T_{\Delta R}$ years for which the reference seismic action is defined, can be computed by:

$$\gamma_I = \left(\frac{T_{\Delta R}}{T_{\Delta}} \right)^{-1/k} \quad (5)$$

where exponential parameter k is in the order of 3 [12] and relates nominal life of the examined intervention with the importance class [7].

3 CASE STUDY

Details for the examined URM building can be found in [8, 14], herein due to space limitations only a brief description is given. The mechanical characteristics of masonry walls were calculated according to EC6 [15], while the parabolic Drucker-Prager yield criterion [16] was used for the description of the inelastic behavior of the masonry walls. The structure is constructed on unsaturated silty sand, the mechanical properties of which with respect to the degree of saturation are taken from the study of Byun et al. [17]. Regarding the inelastic behavior of the soil, the Cam-Clay yield criterion according to the Critical State theory for unsaturated soils was used [18].

Numerical analyses were performed utilizing general purpose finite element software MSC Marc [19]. For the dynamic nonlinear analyses, the multiple-stripe dynamic analysis (MSDA) procedure was repeated for eight different soil saturation conditions (8%, 12%, 16%, 20%, 32%, 54%, 63% and 80%) and ten seismic intensity levels [8]. The twenty seismic records (Table 2) which have been used in this study were selected from PEER database [20] and were scaled utilizing EC8 [12] guidelines as implemented in ISSARS software [21].

No	Region	Station name	Magnitude	Epicentral distance (km)	PGA (g)
1	Imperial Valley	Bonds Corner	6.53	6.2	0.686
2		El Centro Array #5		27.8	0.448
3		El Centro Array #7		27.64	0.42
4		El Centro Array #8		28.09	0.538
5	Mammoth Lakes	Convict Creek	6.06	1.43	0.419
6	Coalinga	Pleasant Valley P.P	6.36	9.98	0.571
7	N. Palm Springs	North Palm Springs	6.06	10.57	0.59
8		Whitewater Trout Farm		4.24	0.602
9	Chalfant Valley	Zack Brothers	6.19	14.33	0.425
10	Loma Prieta	Capitola	6.93	9.78	0.48
11		Gilroy Array #3		31.4	0.462
12	Cape Mendocino	Rio Dell Overpass	7.01	22.64	0.424
13	Big Bear	Big Bear Lake - Civic	6.46	10.15	0.503
14	Northridge	Beverly Hills	6.69	13.39	0.459
15		Canyon Country		26.49	0.436
16		LA Obregon Park		39.39	0.467
17		Newhall - Fire Sta		20.27	0.698
18		Pardee – SCE		25.65	0.505
19		Rinaldi Receiving		10.91	0.634
20		S. Monica City Hall		22.45	0.591

Table 2 : Characteristics of the ground motion records

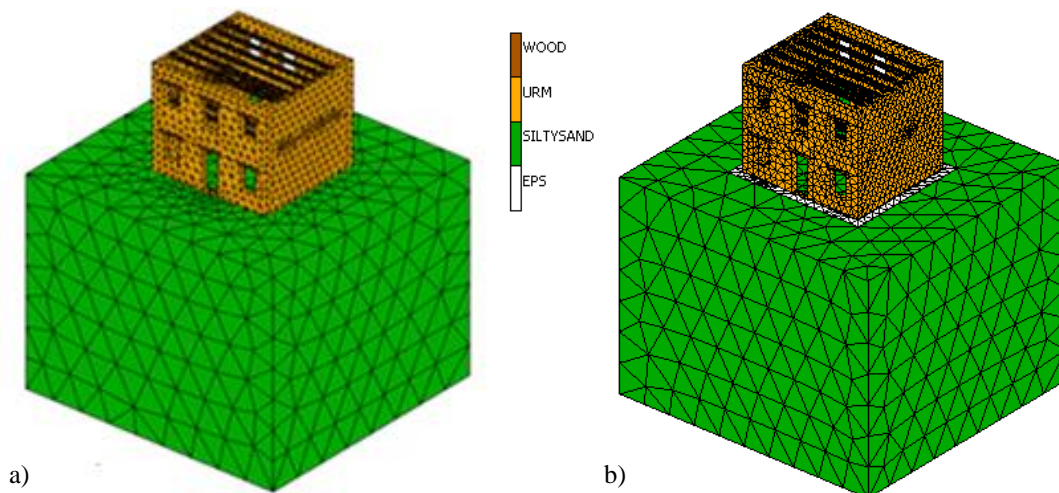


Figure 1. a) Model in its initial state; b) Retrofitted model with EPS geofoam

As a continuation of the previous study [8], the original building was slightly retrofitted with EPS blocks, with height equal to 1m and width 0.50m (Figure 1), which are placed at the exterior of the foundation, aiming to improve the seismic response of the building and to minimize the impact of soil saturation conditions. This cost-effective intervention can enhance the dynamic behavior of the building, as this EPS layer acts as a damper (due to its high compressibility), absorbing most of the dynamic distress, thus, protecting the structure, especially for lower S_r (<32%) values. This is evident by examining Figure 2, which depicts the total drift MSDA curves for the retrofitted building, by comparing median curves of initial and retrofitted models, i.e., bold continuous vs. dashed curves, respectively.

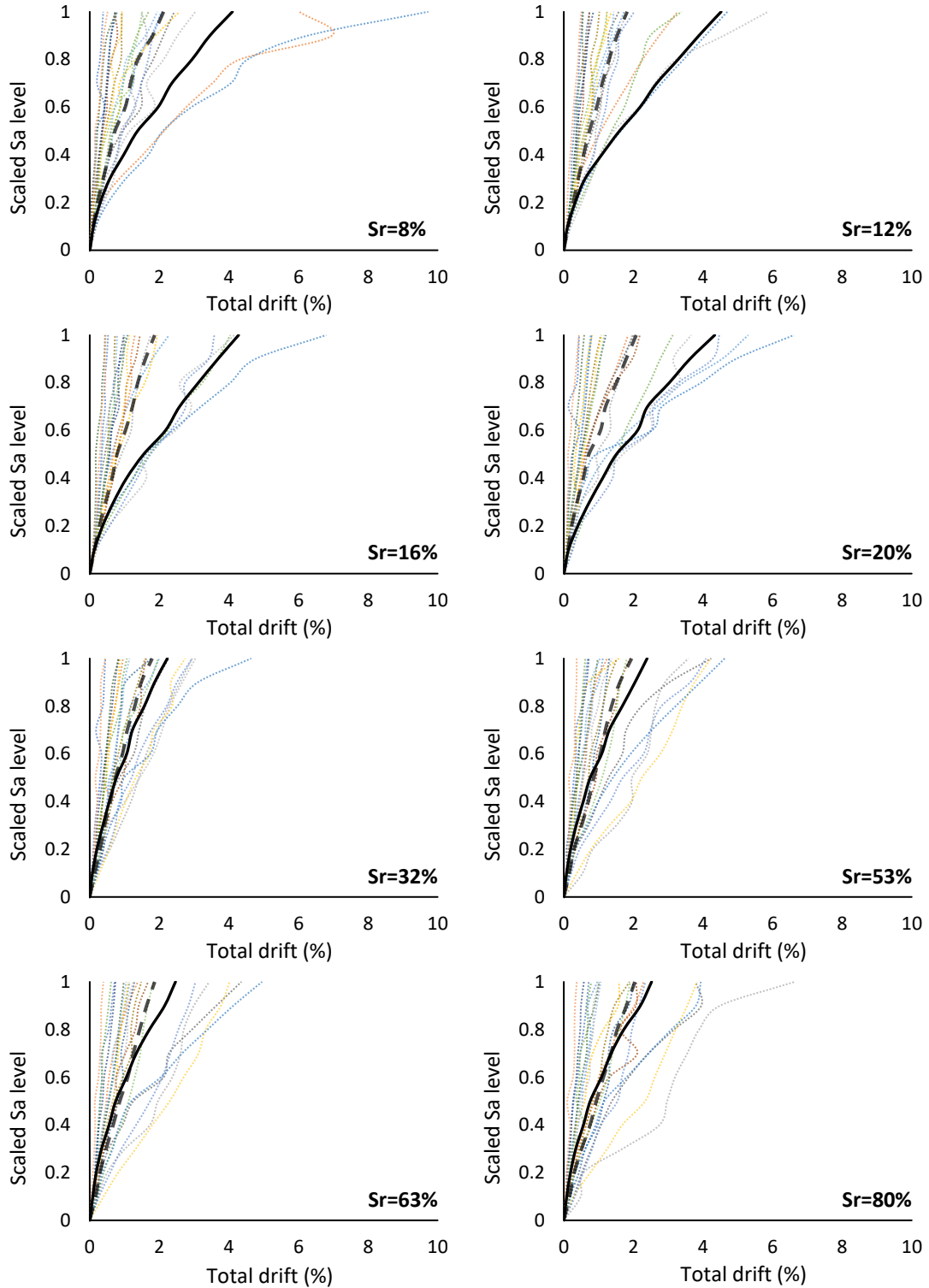


Figure 2. Total drift MSDA curves for the retrofitted building model, while bold dashed curves correspond to median values, while the bold continuous curves present median values for the initial building

4 BUILDING'S NOMINAL LIFE FOR CONSTANT SOIL SATURATION LEVEL

As aforementioned, the MSDA curves of the retrofitted model were used to assess its performance following the LDRI principles. For this purpose, two performance levels: Slight and Moderate Damage States, as defined in FEMA 356 [1] were used. Accordingly, the values for URM buildings and Performance level "Low-Code" were taken from Table 1. Firstly, the calculation of the nominal life was performed considering that the building is based on soil with constant saturation level, i.e., not varying with time. Figure 3 depicts the average dynamic resistance

curve and the limits (vertical lines) of the two performance levels for the examined building for eight different saturation conditions ($S_r = 8\%, 12\%, 16\%, 20\%, 32\%, 54\%, 63\%$ and 80%).

In the comparative plot of Figure 3, there is a clear trend that the selected retrofitting intervention in most cases leads to a substantial improvement of the structural response. However, it has to be noticed that during the first scaling steps the MSDA curves of the original and the retrofitted building are identical. In other words, for low seismic intensity levels the soil saturation conditions do not play a crucial role. Furthermore, for higher saturation levels ($S_r > 32\%$) the response of the structure is not improved in the first steps of record scaling. On the other hand, for higher seismic intensity levels, in all cases the application of this retrofitting scheme drastically improves the response of the structure, depending on the saturation level. In particular, the improvement of the response of the retrofitted structure is even more pronounced at lower saturation levels.

In addition, the results of the original building seem to be grouped, i.e., to have slight variations for low ($S_r = 8\%$ to 20%) and high ($S_r = 32\%$ to 80%) saturation levels. This is due to the variation of soil stiffness for these soil conditions, since according to the experimental data [17], the impact of saturation level substantially affects the basic mechanical parameters of the soil in this specific manner. In contrast, the application of EPS geofoam at foundation level alleviates this scattering and groups the curves in a more uniform way irrespective of the saturation conditions.

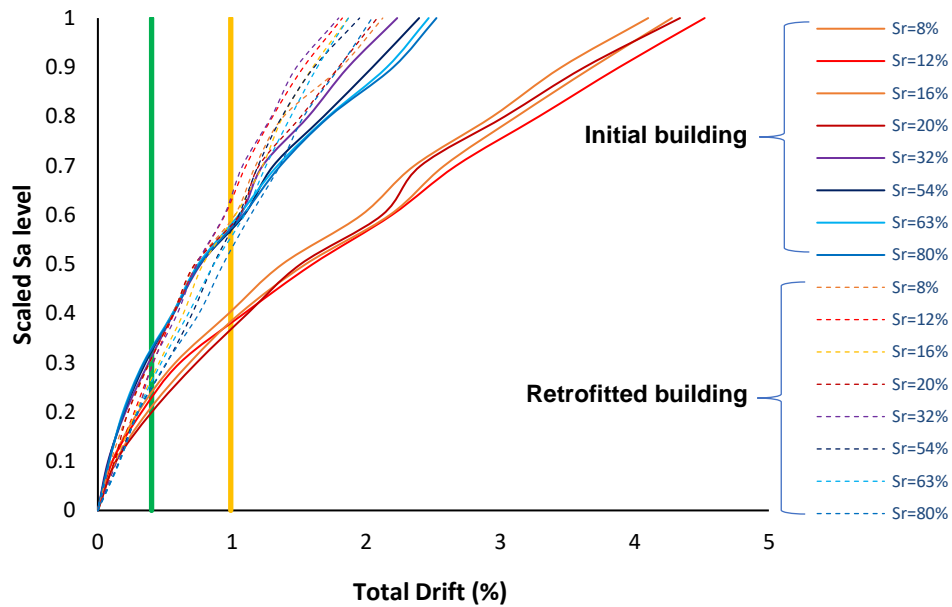


Figure 3. Comparison of initial and retrofitted model's IDA curves.

Regarding the calculations of nominal life of the retrofitted and initial models utilizing LDRI approach, it is assumed that the building is located at seismic zone Z2, thus, T_{RL} return period is calculated via Equation (2). The nominal life for all examined models is calculated using Equation (4) and the results are presented in Table 3. As a consequence of the building's response variation according to the degree of saturation, the nominal life of the structure varies considerably depending on the soil conditions.

The response of the initial building has proven to be directly dependent on the degree of soil saturation. More specifically, it was observed that the increase of soil saturation ($S_r > 32\%$) contributes to the increase of the building's nominal life. When the building is founded on soil with a $S_r < 32\%$, the nominal life of the building varies from 7 to 14 years for A2 design level and from 11 to 16 years for B1 design level. Conversely, when the building is founded on soil with higher S_r , the nominal life increases significantly, reaching between 39 and 48 years for A2 design level and from 58 to 62 years for B1 design level. The nominal life of the original building is extremely small for low soil saturation levels. Moreover, the nominal life varies considerably depending on the degree of subsoil saturation. In particular, the nominal life is altered between 9 and 49 years for A2 design level and from 11 to 62 years for B1 design level. Therefore, it is obvious that a reliable prediction of the initial building's nominal life is not a straightforward task.

Since the scattering of the initial structure's nominal life is quite high, retrofitting of the structure was deemed necessary from this viewpoint as well. Nonetheless, even after the selected retrofitting with EPS blocks at the foundation, the nominal life of the structure varies depending on the degree of soil saturation. However, the variation is obviously less compared to the structure in its initial state. As it is presented in Table 3, when the building is founded on soil with $S_r < 32\%$, the nominal life of the building is significant higher than the original building for both A2 and B1 performance levels. On the other hand, when the building is founded on soil with a

$S_r > 32\%$, a decrease of the nominal life is observed, especially for the lower (i.e., A2) performance level.

Design Level	A2		B1	
Soil Saturation	Original Building	EPS Retrofitted Building	Original Building	EPS Retrofitted Building
$S_r=8\%$	14	38	16	67
$S_r=12\%$	12	30	12	84
$S_r=16\%$	9	22	13	65
$S_r=20\%$	7	38	11	63
$S_r=32\%$	39	30	61	88
$S_r=54\%$	44	16	58	58
$S_r=63\%$	48	19	62	53
$S_r=80\%$	46	16	59	44

Table 3 : Nominal Life (in years) for each model for A2 and B1 design levels.

5 BUILDING'S NOMINAL LIFE FOR VARRYING SOIL SATURATION LEVEL

In the preceding section, the calculation of nominal life performed separately for each soil saturation level. In other words, it was assumed that the degree of soil saturation remains constant. In reality, the degree of saturation varies within each year, i.e., usually it is higher in winter than in summer months. Thus, the response of the building is different, which should be considered in the calculation of building's nominal life.

The accurate calculation of the nominal life as a function of the soil saturation variation requires data representing the annual change of S_r . Unfortunately, there are no accurate related measurements (which strongly depend on the location and the climate), thus, an assumption is made that the annual change of S_r follows a sinusoidal curve and the degree of saturation takes values between the two extreme values of the selected S_r bounds, namely 8% and 80%. The minimum and maximum values correspond to the summer and winter months, as shown in Figure 4. Based on this simplifying assumption, it is considered that during a year the change in the soil saturation level is given by:

$$S_r = 44 + 36 \cos \frac{\pi T}{6} \quad (6)$$

where: T denotes month's number (January=1, February=2,..., December=12).

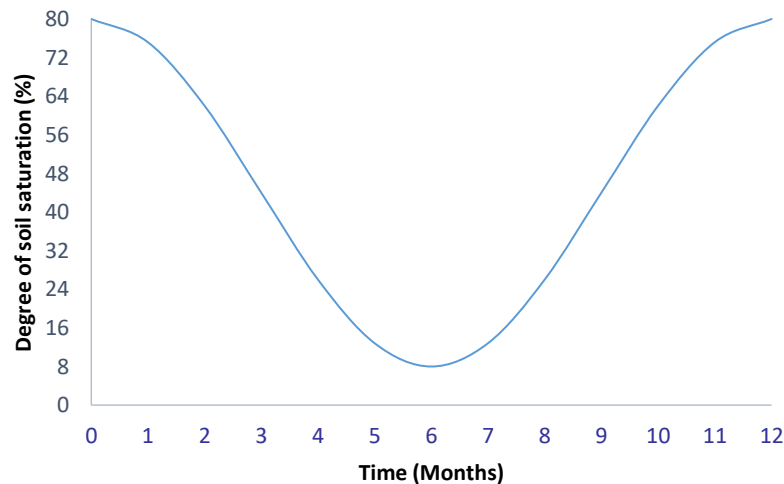


Figure 4. Change of soil saturation level during one year.

The change of peak ground acceleration to achieve A2 and B1 performance levels as a function of S_r are shown in Figure 5a for the initial and the retrofitted buildings. The curves for the two models were constructed based on a_{gR} values according to the MSDA curves shown in Figure 3. Firstly, the degree of saturation for each month was calculated according to Equation (6). Subsequently, the peak ground acceleration for each month was calculated

by linear interpolation and the results are displayed in Figure 5b.

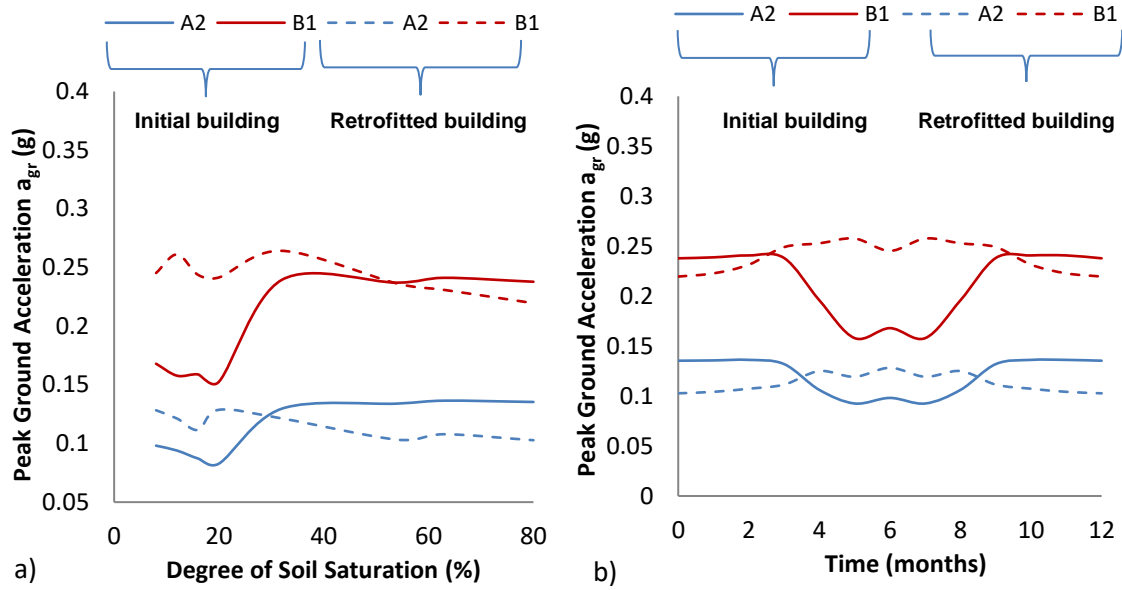


Figure 5. a) Change of peak ground acceleration for various saturation levels; b) Peak ground acceleration's annual variation

Month	S_r (%)	Initial Building				EPS Retrofitted Building			
		Design level A2		Design level B1		Design level A2		Design level B1	
		$T_{\Delta r}$ (years)	P_a (%) in 11 years	$T_{\Delta r}$ (years)	P_a (%) in 13 years	$T_{\Delta r}$ (years)	P_a (%) in 16 years	$T_{\Delta r}$ (years)	P_a (%) in 44 years
1	75.2	46	15.14	60	2.25	17	47.71	46	9.55
2	62	47	14.94	62	2.19	19	43.98	53	8.31
3	44	42	16.65	60	2.28	22	39.50	70	6.37
4	26	18	34.01	28	4.71	34	27.77	75	6.03
5	12.8	11	50.00	13	10.00	29	32.20	80	5.62
6	8	14	42.87	16	8.28	38	25.56	67	6.73
7	12.8	11	50.00	13	10.00	29	32.20	80	5.62
8	26	18	34.01	28	4.71	34	27.77	75	6.03
9	44	42	16.65	60	2.28	22	39.50	70	6.37
10	62	47	14.94	62	2.19	19	43.98	53	8.31
11	75.2	46	15.14	60	2.25	17	47.71	46	9.55
12	80	46	15.26	59	2.29	16	50.00	44	10.00

Table 4 : T_{Δ} and P_a calculations per month for each design level

Table 4 presents on a monthly basis the values of the degree of saturation and peak ground acceleration. Considering that each month a_{gr} remains constant all years throughout the life of the structure, the relevant nominal life ($T_{\Delta r}$) is determined. Under this perspective, twelve different nominal lives are obtained (one per month) and the most critical equivalent nominal life ($T_{\Delta cr}$) is defined. For instance, initial building's critical equivalent nominal life is presented at fifth and seventh month when the building is founded on soil with $S_r=12.8\%$. The critical equivalent nominal life is equal to 11 and 13 years for performance levels A2 and B1, respectively. On the other hand, when the building is slightly retrofitted, $T_{\Delta cr}$ is calculated for the twelfth month (December), when the building is founded on soil with 80% degree of saturation. The retrofitted model's critical equivalent nominal life is equal to 16 and 44 years, for performance levels A2 and B1, respectively.

Subsequently, the probability (P_a) to exceed the drift limits of the chosen performance levels is determined within the specific $T_{\Delta cr}$ for all months (e.g., $T_{\Delta cr}=11$ years for A2 performance level for the initial building, as shown in the 4th column of Table 4). The average probability during $T_{\Delta cr}$ and the final nominal life of the initial

and the retrofitted buildings for performance levels A2 and B1 are calculated (considering that the probability of an earthquake during the year is the same for all months) using the following formula:

$$T_{\Delta} = \frac{P_a T_{\Delta cr}}{P_{av}} \quad (6)$$

Model	Design Level	P_a	$T_{\Delta cr}$	P_{av}	T_{Δ}
Original Building	A2	50	11	26.63	20
	B1	10	13	4.45	29
EPS Retrofitted Building	A2	50	16	38.16	21
	B1	10	44	7.37	60

Table 5 : Calculation of final nominal life (in years)

According to the results of the adopted procedure, by taking into account in a realistic manner the annual changes in the soil saturation level the nominal life is increased when retrofitting the foundation with EPS blocks. As it is presented in Table 5, the nominal life notably increases from 29 to 60 years for performance level B1 when the building is slightly retrofitted with EPS geofoam. In contrast, the nominal life for design level A2 is only slightly increased from 20 to 21 years. In any case, since the nominal life is increased for the more crucial design level B1, the use of EPS blocks improves the overall behavior of the building.

6 CONCLUSIONS

The main aim of this work is to investigate the seismic vulnerability of masonry buildings taking into account the impact of dynamic soil-structure interaction (SSI). More specifically, this paper examines the dynamic response of a typical unreinforced masonry (URM) building constructed over a silty sand layer. The main novelty of the present study is that it considers time-varying soil mechanical properties, since they are taken as dependant on the soil saturation level, which changes annually (in a cyclic manner during the four seasons).

The dynamic response of the coupled model (URM building and its foundation layer) is numerically examined via repeated incremental dynamic analyses, considering the impact of SSI along with the nonlinear behavior of the soil and the structure. A suite of twenty input motions -recorded in similar soil conditions- was selected to obtain a reliable assessment of the dispersion of engineering demand parameters of the examined masonry building, while eight different saturation levels were considered, covering a wide range of soil conditions to elaborately investigate the problem at hand.

In addition, a new structural assessment approach, the so-called “Performance through Limited Duration Rehabilitation Interventions” [6, 7], which aims to identify the performance levels of historic buildings after performing certain seismic rehabilitation measures was applied. This methodology attempts to provide a framework that quantifies the “safe” duration (i.e., nominal life) of an intervention that upgrades the structural integrity in a specified manner. The nominal life of an intervention is defined as the period for which this action ensures that the structure fulfills selected performance level(s) for a certain probability of exceedance.

Under this perspective, a simple and efficient -in terms of time, cost and effectiveness due to its minimum functional and structural disturbance- intervention with EPS blocks at the exterior of the URM building foundation was applied in order to improve its dynamic response and reduce its vulnerability under the examined circumstances. Firstly, the nominal life of each coupled structural model (initial and retrofitted) with constant soil saturation conditions is calculated. Subsequently, the calculation of nominal life is performed in a more realistic manner, by taking into account the annual changes in the soil saturation level. This light intervention scheme increased the nominal life of the building and limited the scattering of the results due to varying soil saturation conditions, especially for B1 performance level. Certainly, alternative retrofitting approaches, either as single or combined schemes, e.g. by applying EPS blocks at the foundation together with RC structural elements, should be investigated in order to examine their effectiveness in similar soil conditions. Additionally, a more accurate representation of the variation of soil saturation for specific local climate conditions would consist a further improvement of the process.

REFERENCES

- [1] FEMA 356, (2000). *Prestandard and commentary for the seismic rehabilitation of buildings*. Federal Emergency Management Agency, Washington, DC, USA.
- [2] EC8-3 (2004). *Design of structures for earthquake resistance Part 3: Assessment and retrofitting of buildings*.

- European Committee for Standardization, Brussels, Belgium.
- [3] ASCE, (2007). *Seismic rehabilitation of existing buildings*. ASCE/SEI Standard 41-06. American Society of Civil Engineers, Reston, Virginia, USA.
- [4] FEMA 349, (2000). *Action plan for performance based seismic design*. Federal Emergency Management Agency, Washington, DC, USA.
- [5] Lagomarsino, S., Modaressi, H., Pitilakis, K., Bosjlikov, V., Calderini, C., D'Ayala, D., Benouar, D., and Cattari, S. (2010). PERPETUATE Project: the proposal of a performance-based approach to earthquake protection of cultural heritage. *Advanced Materials Research*, Vols. 133-134: 1119- 1124, doi:10.4028/www.scientific.net/AMR.133-134.1119
- [6] Spyrakos C.C. (2015). Seismic risk of historic structures and monuments: a need for a unified policy. 5th ECCOMAS Thematic Conference on Computational Methods in Structural Dynamics and Earthquake Engineering (COMPDYN 2015), Crete Island, Greece.
- [7] Spyrakos, C.C. (2018). Bridging performance based seismic design with restricted interventions on cultural heritage structures. *Engineering Structures*, April 2018, DOI: 10.1016/j.engstruct.2018.01.022.
- [8] Liratzakis, A., and Tsompanakis, Y. (2018), Impact of soil saturation level on the dynamic response of masonry buildings. *Frontiers in Built Environment - Earthquake Engineering*, April 2018, Vol. 4, Article 24, doi: 10.3389/fbuil.2018.00024.
- [9] CSI, (2012). *Code of Structural Interventions*. Final harmonized text, English temporary version V1. Harmonization Team of Code of Interventions to Eurocodes. Earthquake Planning Protection Organization (EPPO). Athens, Greece.
- [10] CASIM, (2014). Draft code for the assessment and structural interventions on masonry structures, Earthquake Planning Protection Organization (EPPO) and European Centre on Prevention and Forecasting of Earthquakes (ECPFE). Athens, Greece. (in Greek)
- [11] EPPO, (2011). Draft Framework regulatory document for structural interventions and seismic protection of monuments. Earthquake Planning Protection Organization (EPPO) and European Centre on Prevention and Forecasting of Earthquakes (ECPFE). Athens, Greece. (in Greek)
- [12] EC8-1 (2004). Design of structures for earthquake resistance Part 1: General rules, seismic actions and rules for buildings. European Committee for Standardization, Brussels, Belgium.
- [13] ELOT, (2005). Greek National Annex to Eurocode 8: Design of structures for earthquake resistance - Part 1: General rules, seismic actions and rules for buildings. Hellenic Organization for Standardization, Athens, Greece. (in Greek)
- [14] Liratzakis, A., (2016). Impact of soil saturation level on structural assessment and retrofitting of masonry buildings via incremental dynamic non-linear analysis, MSc. Thesis, School of Architectural Engineering, Technical University of Crete, Greece (in Greek).
- [15] EC6 (2005). Eurocode 6: design of masonry structures - Part 1-1: general rules for reinforced and unreinforced masonry structures, European Committee for Standardization, Brussels, Belgium.
- [16] Stavroulaki M., and Liarakos E.V. (2008). Parametric finite element analysis of masonry structures using different constitutive models, 6th GRACM International Congress on Computational Mechanics, Thessaloniki, Greece.
- [17] Byun, Y.H., Lee, J.S., Cho, S.H., and Yoon, H.K. (2013), Evaluation of void ratio and elastic modulus of unsaturated soil using elastic waves. *Proceedings of the 18th International Conference on Soil Mechanics and Geotechnical Engineering*, Paris, France
- [18] Casini, F., Vassallo, R., Mancuso, C., and Desideri, A. (2008). Application to a compacted soil of a Cam Clay model extended to unsaturated conditions, *Proceedings of the 1st European Conference of Unsaturated Soils (E-Unsat 2008)*, Durham, United Kingdom, pp. 609-615, doi: 10.1201/9780203884430.CH82.
- [19] Marc, (2014). Marc 2014.2 software documentation, MSC Software Corporation, Newport Beach, California, USA.
- [20] PEER, (2015). PEER NGA-West2 ground motion database, Pacific Earthquake Engineering Research Center, University of California, Berkeley, CA, USA, available at: <http://ngawest2.berkeley.edu/>.
- [21] Katsanos E.I., and Sextos A.G. (2013). ISSARS: An integrated software environment for structure-specific earthquake ground motion selection. *Advances in Engineering Software*, Vol. 58, pp. 70-85, <http://dx.doi.org/10.1016/j.advengsoft.2013.01.003>.

VIBRATIONAL FEATURES OF THE TRADITIONAL PERCUSSION INSTRUMENT BENDIR USING LASER HOLOGRAPHIC INTERFEROMETRY AND FINITE ELEMENT ANALYSIS METHODS

Makis Bakarezos^{1,2}, Vasilis Dimitriou^{1,3}, Yannis Orphanos^{1,2}, Ioannis Sidiras², Evaggelos Kaselouris^{1,4},
Michael Tatarakis^{1,4} and Nektarios A. Papadogiannis^{1,2}

¹Centre for Plasma Physics and Lasers
School of Applied Sciences, TEI of Crete
Chania, GR-73133, Rethymnon, GR-74100, Greece
web page: <http://www.cppl.teicrete.gr>

²Department of Music Technology & Acoustics Engineering
Rethymnon, GR-74133, Greece
e-mails: bakarezos@staff.teicrete.gr, yorphanos@staff.teicrete.gr, johnironf2vs@hotmail.com,
npapadogiannis@staff.teicrete.gr

³Department of Natural Resources and Environmental Engineering
Chania, GR-73133, Greece
e-mail: dimvasi@chania.teicrete.gr

⁴Department of Electronic Engineering
Chania, GR-73133, Greece
e-mails: vkas@chania.teicrete.gr, m.tatarakis@chania.teicrete.gr

Keywords: Electronic Speckle Pattern Interferometry – ESPI, Modal analysis, Applied acoustics, Finite Element Method - FEM, Thermomechanical simulations

Abstract. *The vibrational characteristics of the traditional percussion music instrument Bendir are studied in this paper. Time-averaged laser Electronic Speckle Pattern Interferometry – ESPI is experimentally performed on the Bendir for the determination of its eigenmodes and respective eigenfrequencies. A structural finite element - FE model is developed and validated by experiments. The eigenmodes of the FE model and the respective eigenfrequencies are also numerically identified by the modal finite element analysis performed. Furthermore, the initial physical and mechanical parameters of this percussion instrument are modified. The membrane of Bendir is being pre-stressed and its temperature is controllably increased. The effects of these changes to the eigenmodes and eigenfrequencies of the instruments are again experimentally measured. The FE model is appropriately updated in order to include the characteristics of the real physical problem. The new eigenmode simulation results are compared to the experimental results and are found to be in a very good agreement. This combination of FEM with the ESPI is providing a new methodology able to certify and clarify the manufacturing and performance of percussion instruments.*

1 INTRODUCTION

The percussion instruments are the oldest musical instruments and their acoustic properties are extensively studied worldwide [1], but it is a fact that only a few and non-systematic studies have been performed for the traditional percussion instruments in Southeastern Mediterranean region. These percussion instruments mainly consist of a cylindrical frame on which a membrane, of an animal skin or of a plastic film, is stretched. The normal ways of oscillating this membrane play an important role to the characteristics of the finally broadcasted sound from the instrument.

In this paper, we study experimentally the characteristic eigenfrequencies and the corresponding modes of the membrane of Bendir, a percussion instrument that originates from North Africa. The structural dimensions of Bendir that is analyzed in this paper may vary, but the most common values of the diameter of this cylindrical instrument are in the range of 35 to 45 centimeters. It is commonly manufactured by the assembling of a cylindrical wooden frame to the natural leather or synthetic membrane and during play it is held in a vertical position and is supported by the thumb of the left hand in special holes on its frame [2]. The instrument was examined using a 532nm Nd:YAG laser source in a specially developed Electronic Speckle Pattern Interferometry (ESPI) setup [3]. Important mechanical characteristics of the instrument, like the winding tensions and the membranes material properties, that affect its acoustic behavior, are modified and their influence on the modes is monitored and recorded. The experimental results are compared to numerical results based on a Finite Element Analysis (FEA) performed for the instrument Computer Aided Design (CAD) model.

2 THE PHYSICAL MODEL

In order to study the vibrating properties of Bendir, we mainly focus on the circular membrane of the instrument. A membrane may vibrate by an infinite number of ways, depending on the shape of the membrane at an initial time and the transverse velocity of its points. The resulting vibrations are given by the solutions of the two-dimensional wave equation with Dirichlet boundary conditions. These boundary conditions represent the constraints provided by the circular ring frame of the instrument where the membrane is assembled and tuned. Regarding the analysis of the membranes, simple or complex vibrations may be decomposed into a series of the normal modes of the membrane. Since Bendir's membrane has a circular geometry we may use polar coordinates (r, θ, t) to write the governing wave equation of the physical problem in the form of equation 1:

$$\frac{\partial^2 u}{\partial t^2} = c^2 \left(\frac{\partial^2 u}{\partial r^2} + \frac{1}{r} \frac{\partial u}{\partial r} + \frac{1}{r^2} \frac{\partial^2 u}{\partial \theta^2} \right), \quad 0 \leq r < r_0, -0 \leq \theta \leq 2\pi \quad (1)$$

where r_0 is the radius of the membrane. We assume a solution in separated variables, $u(r, \theta, t) = R(r) \Theta(\theta) e^{j\omega t}$ and from the wave equation we get a differential equation of the form:

$$\frac{d^2 R}{dr^2} + \frac{dR}{dr} + \left(\frac{\omega}{c^2} - \frac{m^2}{r^2} \right) R = 0 \quad (2)$$

By substituting $y = R$ και $x = kr = \omega r / c$ equation 2 results to equation 3:

$$\frac{d^2 y}{dx^2} + \frac{1}{x} \frac{dy}{dx} + \left(1 - \frac{m^2}{x^2} \right) y = 0 \quad (3)$$

that is a Bessel's equation having a solution of the form:

$$R(r) = J_m(k_{mn} r), \quad m=0, 1, \dots \text{ and } n=1, 2, \dots \quad (4)$$

where $k_{mn} = \frac{\alpha_{mn}}{r_0}$, α_{mn} is the n^{th} positive root of J_m . The resulting equation of the displacements of the circular membrane has the final form presented in equation 5:

$$u_{mn}(r, \theta, t) = J_m(k_{mn} r) (A \cos m\theta + B \sin m\theta) e^{j\omega t}, \quad m=0, 1, \dots \text{ and } n=1, 2, \dots \quad (5)$$

The n^{th} root of $J_m(k_{mn} r)$ provides the frequency of the vibration $f(m, n)$ with m nodal diameters and n nodal circles [4].

The cylindrical frame of Bendir may be vibrated in two ways, according to the vibrations produced by the membrane. When the point of excitation of membrane is far from the center and close to the frame, the frame is angularly stressed and bending forces dependent on $\sim \cos n\phi$ are broadcasting sounds. In the case of the excitation of the circular center of the membrane the produced displacement is of the form of $\cos(knz + \beta) \cos m\phi$, with z, ϕ , being the axial and the angular coordinates, respectively.

The air cavity of the instrument has a significant effect on the sound and the tone of the instrument. A basic precondition for generating sound is the vibrations that arise due to the elasticity of the enclosed air at this cavity. In the case where a membrane is placed on the support frame, the resonance frequency can be calculated either as a Helmholtz resonator or as an open-closed tube system. An important parameter affecting the produced sound and its tone from the instrument is the temperature. The temperature may affect the properties of the materials of the instrument, if it changes in high ranges and basically for the materials that have high thermal conductivity and expansion property values. Moreover, the temperature changes influence the density of the air and the speed of sound in the material.

3 EXPERIMENTAL SET-UP AND MEASUREMENTS

In our Bendir study a natural organic membrane of cow leather is investigated. The frame of the instrument has a diameter of 45 centimeters. The ESPI experimental set-up that is used is presented in Figure 1.

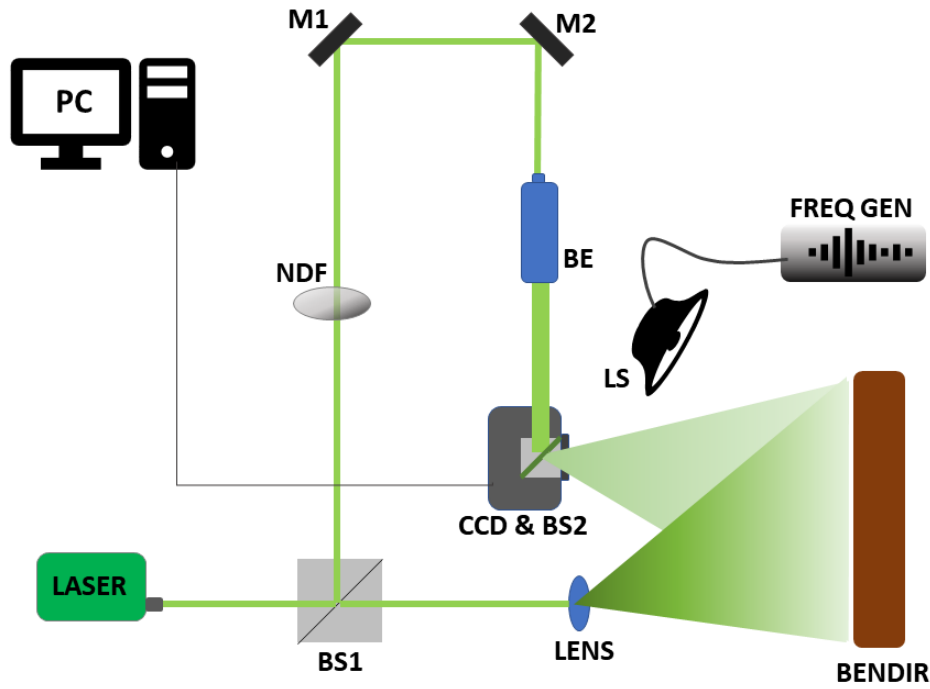


Figure 1. ESPI experimental setup. BS – Beam splitters, NDF – Variable Neutral Density Filter, M – Mirrors, BE – Beam Expander, CCD – CCD Camera, FREQ GEN – Frequency Generator and LS – Loudspeaker.

The experimental setup consists of an Nd:YAG solid state CW laser source with a wavelength of $\lambda=532\text{nm}$ and maximum power of 150 mW [2,3]. The laser beam is divided by means of the first Beam splitter (BS1) into bendir lighting beam and a reference beam in 80:20 percentage respectively. The bendir lighting part is expanded through a negative lens ($f=-50\text{mm}$). The reference beam passes through a Variable Neutral Density Filter (NDF) in order to compensate the intensity of the reflected to the camera bendir illumination. The beam passes through mirrors (M1 & M2) and is further directed to pass through a Beam Expander (BE) which expands the beam 20 times to fulfill the area of the 2/3" CCD sensor. The CCD camera, Basler A102f offers a 1392 x 1040 effective pixel count with $6.45 \times 6.45 \mu\text{m}$ pixel size and it is specially amended to fit a 50:50 beam splitter. The reflected light from the bendir is collected by means of an objective lens attached to the camera. Both beams (bendir reflection and reference beam) are combined to the CCD sensor to produce the speckle interferogram which is then recorded to the computer (PC) using a firewire connection and an in house developed recording software.



Figure 2. ESPI experimental setup image.

A Genelec - 8030apm speaker, connected to a special frequency generator and to an oscilloscope, is used for the excitation of the instrument. The frequency ranges from 50 to 2100 Hz and the amplitude of the excitation voltage to 2.5V due to the speaker specifications. The speaker is placed at a distance of 1 m far from the instrument, in order to avoid the near field of the speaker and to achieve the smallest irradiation angle. The instrument is supported on a base of Sorbothane material that isolates the vibrations transferred from the support, and in a way that represents the support of the organ player during the execution. The audio transmission spectrum was determined through recordings based on a special protocol [3], at the specially designed room of the digital recording studio of the Department of Music Engineering Technology & Acoustics of TEI of Crete. For the study of the dependence of vibrational characteristics to small temperature changes, a controlled heating system that consists of a heating lamp and a custom digital thermometer was used [2].

4 FEM MODELING

The Finite Element Method – FEM has been extensively used for the study and the vibration analysis of percussion instruments [5-8]. The free vibration analysis procedure is very similar to performing a linear static analysis. The solution domain is defined by the CAD geometry of the solid, surface or line body that is studied and the material properties are assigned to each part of the geometry. Young's Modulus, Poisson's Ratio, and Density are required. If the CAD geometry is an assembly that consists of more than one parts, then the contact regions of the parts must be identified. The inclusion of supports is the final step before solving the computational modal problem.

For a free vibration analysis, the natural circular frequencies ω_i and mode shapes φ_i are calculated from equation:

$$([K] - \omega_i^2[M])\{\varphi_i\} = 0 \quad (6)$$

It is assumed that the stiffness matrix $[K]$ and the mass matrix $[M]$ are constant, and the materials retain their elastic behavior during the study. Moreover, the small deflection theory is used, without the presence of nonlinearities, external forces or damping. The resulting mode shapes $\{\varphi\}$ are relative values, not absolute. The stress state of structural body under static loading affects its natural frequencies. This prestressing in acoustics is associated with the static loads applied when e.g. a music instrument is tuned. In the case that prestress effects are considered when a free vibration analysis is performed, equation 6 has to be updated in order to include the stress stiffness matrix $[S]$ and results to equation (7).

$$([K + S] - \omega_i^2[M])\{\varphi_i\} = 0 \quad (7)$$

The numerical identification of the stress stiffness matrix is based on the solution of a linear static model where constant loads are applied on the solution domain of the structure. The linear static analysis is based on the solution of equation (8) that provides the resulting stresses $[\sigma_0]$ that gives $[S]$:

$$[K]\{x_0\} = \{F\} \quad (8)$$

For the modeling and simulation of Bendir, a CAD model is initially developed, representing the geometric characteristics of Bendir. The circular domain of the membrane is assembled to a cylindrical wooden frame to support uniformly its edges, having a bonded contact with it. An elastic ring is also modeled for the tuning. The constraints and loads of the model will be further applied to this frame for the performance of the static and modal analysis.

5 EXPERIMENTAL AND SIMULATION RESULTS

The ESPI experiments in the bendir with cow leather were first performed with a low tensioned membrane (low tuning). The ESPI experimental process described in section 3 provided the experimental results presented in Figure 3. Having these experimental mode shapes and their correspondent frequency as a reference, the developed FEM model is used to approximate them. An initial free vibration analysis is performed on the assembly of the membrane with the cylindrical frame support and the first eigenmode of the model is identified at a very low frequency, as expected. The thickness of the leather used at the model is 0.13 mm, while bibliographic values were assigned to the density, the modulus of elasticity and the Poisson ratio that is 850 kg/m³, 7×10⁸ Pa and 0.45 respectively.

Considering that in the real problem of the percussion instrument the membrane is already pre-stressed, even at low tuning, pressure is applied to the inner surface of the elastic ring of the cylindrical supporting frame in the FEM model, in order to approximate the real supporting and loading conditions of the Bendir. The assembled geometry is fixed at the bottom edges of the frame and for this approximation, elastic material properties are

assigned to it. The linear static model is set and solved to provide the structural results and basically the stress stiffness matrix $[S]$ needed for the pre-stressed modal analysis. The static analysis results are given as an input for the modal analysis. After the identification of the first computed mode shape at a frequency close to 100 Hz, as measured by the experiment, the computational model may further provide the number of the eigenmodes needed at their correspondent eigenfrequencies. The comparison of the experimental to the simulation results, for a pressure load of 40 kPa is presented in Figure 3.

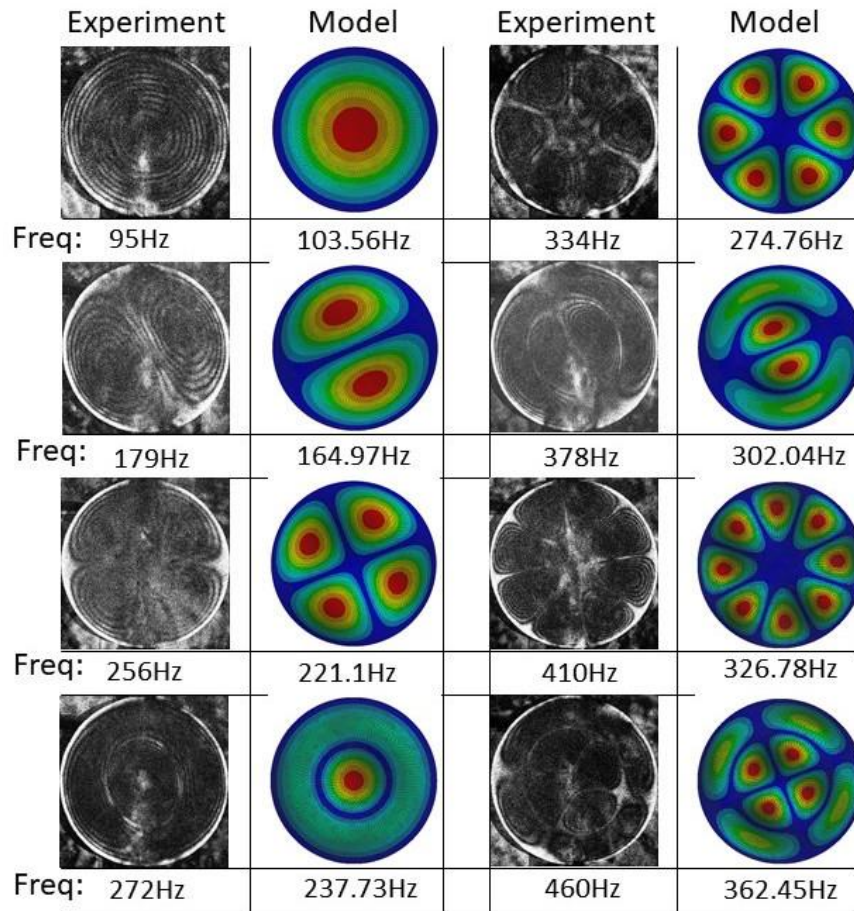


Figure 3. Experimental results using ESPI and simulated results for the bendir in low tension pressure (low tuning).

After the first set of ESPI measurements, the instrument is further medium and then highly tuned. The uniform pressure load is further raised to 70 and 100 kPa to simulate the intermediate and finally the high tuning, respectively. In Figure 4 and 5 are presented the results for medium and high tuning, respectively, where a satisfactory agreement between experiment and simulation is observed regarding the eigenmodes and the eigenfrequencies that they appear.

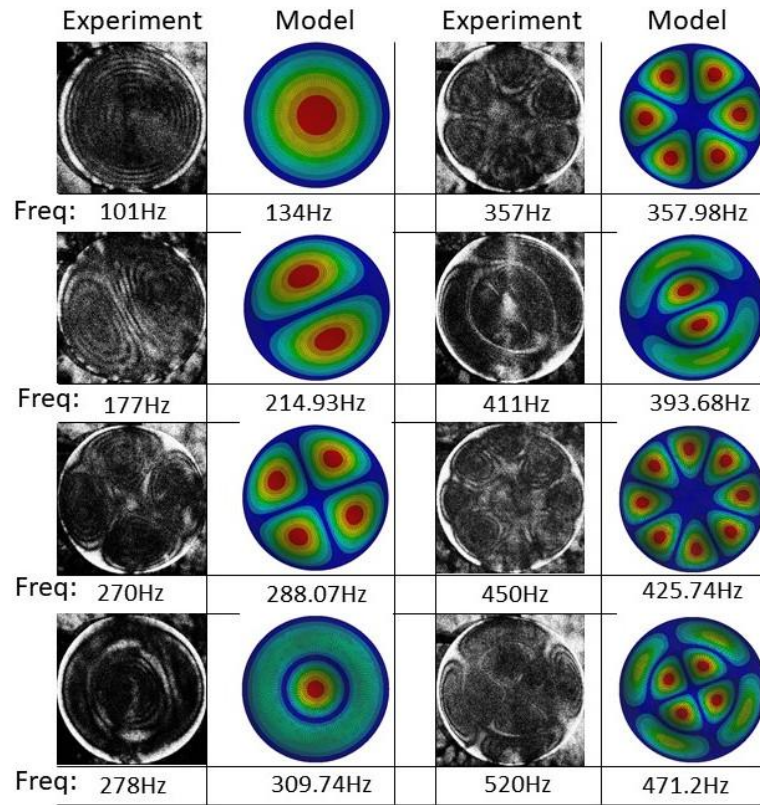


Figure 4. Experimental results using ESPI and simulated results for the bendir in medium tension pressure (medium tuning).

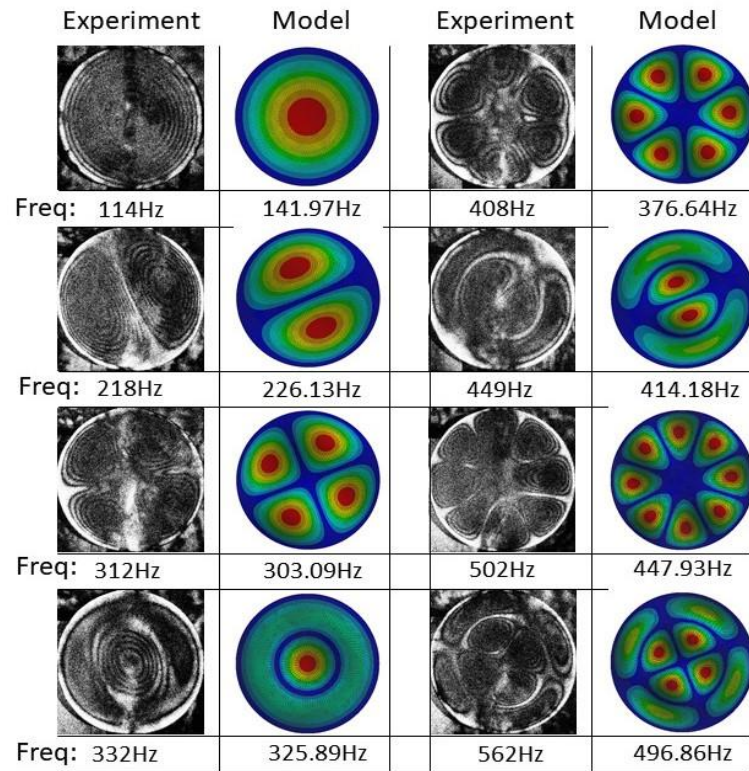


Figure 5. Experimental results using ESPI and simulated results for the bendir in high tension pressure (high tuning).

6 CONCLUSIONS

The vibrational characteristics of the traditional percussion music instrument Bendir are studied using a time-average ESPI experimental method. The instrument is studied in different conditions, e.g. regarding its tuning as a result of the tension applied to it. Analysis of the experimental results allowed for the determination of its eigenmodes and respective eigenfrequencies. A structural FE model is initially developed based on the actual parameters of the experiments and is validated by the experimental results, in terms of the eigenmodes and the respective eigenfrequencies of the instrument that are also numerically identified by the modal finite element analysis performed. The experimental and numerical results are in satisfactory agreement, thus the combination of these provides a solid methodology able to certify and clarify the manufacturing and performance of percussion instruments.

ACKNOWLEDGEMENTS

We acknowledge support of this work by the project “ELI - LASERLAB Europe Synergy, HiPER & IPERION-CH.gr” (MIS 5002735) which is implemented under the Action “Reinforcement of the Research and Innovation Infrastructure”, funded by the Operational Programme “Competitiveness, Entrepreneurship and Innovation” (NSRF 2014-2020) and co-financed by Greece and the European Union (European Regional Development Fund).

REFERENCES

- [1] Rossing, T. D. (2000), *Science of Percussion Instruments*, World Scientific, Series in Popular Science, Singapore.
- [2] Sidiras, I. (2013), “A study of the vibrational characteristics of traditional percussion instruments using experimental laser symbolometry techniques”, Diploma Thesis, Dept. of Music Engineering Technology & Acoustics, School of Applied Sciences, TEI of Crete.
- [3] Bakarezos, M., Vathis, V., Brezas, S., Orphanos, Y. and Papadogiannis, N.A., (2012), “Acoustics of the Chelys - An ancient Greek tortoise-shell lyre”, *Applied Acoustics*, Vol. 73, pp. 478-483.
- [4] Asmar, N.H., (2005), *Partial differential equations with Fourier series and boundary value problems*, Upper Saddle River, N.J.: Pearson Prentice Hall. p. 198.
- [5] Kokkinakis, E. (2013), “Simulation of the vibrational characteristics of a percussion instrument”, Diploma Thesis, Dept. of Music Engineering Technology & Acoustics, School of Applied Sciences, TEI of Crete.
- [6] Worland, R., (2010), “Normal modes of a musical drumhead under non-uniform tension”, *Journal of the Acoustical Society of America*, Vol. 127, pp. 525-533.
- [7] Rossing, T.D., Yoo, J., Morrison, A. (2004), “Acoustics of percussion instruments: An update”, *Acoustical Science and Technology*, Vol. 25, pp. 406-412.
- [8] Bedri, R., Al-Nais M.O. (2005), “Prestressed modal analysis using finite element package ANSYS”, *Lecture Notes in Computer Science*, Vol. 3401, pp. 171-178.

GIS EXTENSION TOOL FOR VISUALIZATION OF FLOOD RISK EVALUATIONS

Dejan Rančić¹, Miloš Bogdanović¹, Uwe Siart² and Olivera Pronić Rančić¹

¹Faculty of Electronic Engineering
University of Niš
Niš, 18000, Serbia

e-mail: dejan.rancic@elfak.ni.ac.rs, milos.bogdanovic@elfak.ni.ac.rs, olivera.pronic@elfak.ni.ac.rs

² Department of Electrical and Computer Engineering
Technical University of Munich
Munich, Germany
e-mail: uwe.siart@tum.de

Keywords: GIS, visualization, flood, estimation, spatial analysis

Abstract. *This paper presents a proposal of a Geo-Information System (GIS) extension tool capable of performing flood prediction and visualization. The GIS tool we present is custom developed and capable of providing support for diverse data types, data conversion, visualization and analysis. Also, we present flood prediction algorithm implemented within this tool. This algorithm is based on the usage of ground-level precipitation data generated by analyzing the attenuation of microwave signals of cellular networks. For a selected area covered with microwave links, our algorithm calculates overall rainfall amount, combines it with digital elevation model of the observed area and performs flood fill algorithm starting from the point with lowest altitude. As output, this tool visualizes geographic area potentially endangered by estimated rainfall.*

1 INTRODUCTION

We are witnessing intense climate change worldwide. As a result, world is in a constant demand for mechanisms capable of predicting destructive disasters resulting from climate change. The overall noble goal is to prevent fatalities and prevent any kind of damage, as much as possible. Flooding is one of the destructive disasters with increased intensity in the past decade [1, 2, 3, 4, 5]. Although floods are more likely to happen in areas surrounding river basins, they can also appear in larger regions due to increased intense precipitation [13, 14]. Various studies coming from different parts of the world indicate there is increased flood risk. For example, study presented in [6] examines 28-year span and reports over 3,000 floods, 3 billion endangered persons and enormous financial loss. Authors of [14, 15] report 0.8 billion people will be exposed to a 1-in-100-years river flood disasters. Also, study presented in [17], as well as [16], indicates increased economic activities on coastal plains resulting from socioeconomic growth. Due to this, coastal floods are expected to endanger 40 million people and may cause \$3 trillion damage.

Floods can be of different types and scales. Thus, different strategies, models and data source should be combined to estimate flood risks and impacts. This gives us a variety in the architecture and implementation of flood prediction systems. For example, the type of landscape itself can result in a number of different flooding behaviors [18]. Since the number of factors influencing flood risk estimation is significant, a part of implementations of flood risks estimation and visualization systems authors decide to use advantages offered by Geo-Information Systems (GIS). As stated in [24], "A geographic information system (GIS) is a special type of computer-based information system tailored to store, process and manipulate geospatial data". Aside from being capable of analyzing geospatial data, GIS is a very powerful tool when it comes to visualizing the results of a geospatial data analysis. GIS solutions offer mature and stable architecture that can be easily upgraded for various purposes, and flood prediction and visualization is one of them. In this paper, we present a GIS extension tool capable of using rainfall information to perform visualization and simulation of flood risks.

The usage of GIS tool for these purposes is a proposal on top of existing previous research in this field of science. Previously, research community has successfully used rainfall data as a mean for detecting possible flooding. The approach we embed into our solution uses numerical processes for precipitation detection on the basis of the received signal level (RSL) of commercial microwave links. Numerical methods that we rely on are a form of a preprocessing phase since they implement complex calculations that may require a lot of time. Thus, implementation of these methods can expose some limitations for real-time information systems. One possible substitute for numerical methods would be to use machine learning methods for precipitation detection based on

the received signal level of microwave links. The usage of machine learning methods would significantly increase the efficiency of the information system since they have the ability to reduce the time required to process the data obtained at the link. Either way, the output is a precipitation data estimation which can be combined with soil and elevation models for predicting flood risks. Since DEM and raster images naturally belong to GIS solutions, it is our opinion that the combining process and the final estimation should be delegated to GIS extension tool.

2 RELATED WORK

The intensity and frequency of flood incidents and other natural disasters has risen permanently worldwide over the past decades. Since, flood incidents significantly affects environment, causing extensive damage, this led to the development of many flood estimation and alerting systems.

Accurate simulation of flooding and estimation of flood risks is often based on rainfall data, although this approach is not a novelty in research community. In order to accomplish precise flooding estimation, information systems should be capable of using complex models (like one-dimensional Saint-Venant equation) in real-time. Expected output should be accompanied with spatial information [7], [8]. Since the proposed models are numerically very extensive, they can hardly be used in near real-time information systems. Therefore, many less complex computational models have been proposed [9], [10], [11], resulting eventually in development of several global flood alerting and weather forecasting systems.

GloFAS is the global system provides information regarding flood alerts. GloFAS uses global forecast and ERA-Interim precipitation dataset as inputs and HTESSEL and Lisflood for flood forecasting. HTESSEL computes the land surface response to atmospheric forcing and estimates the surface water and energy fluxes and the temporal evolution of soil temperature, moisture content and snowpack conditions. Lisflood is a GIS-based spatially distributed hydrological model, which includes a one-dimensional channel routing model.

The most popular system for extreme weather forecasting and alerting in Europe is Meteoalarm. It uses information from meteorological services from European countries and calculates four risk levels for corresponding countries and regions. System SCHAPI coordinates flood forecasting in France. The forecast is based on observation collected from 500 real time rain gauges, 24 meteorological radars and 1500 real time water level stations, soil properties and various types of hydrological models.

The usage of GIS provides reliable platforms for the development of flood forecasting systems worldwide. GIS can also be integrated with remote sensing techniques for early warning systems [19]. Nowadays, there are a significant number of flood forecasting and warning solutions using GIS components for visualization and decision-making support. For instance, in [20], GIS is used for flood prediction in Malaysia. It is shown that combination of hydrological models and water balance model in GIS is very suitable as a tool to obtain preliminary flood possibility information.

The usage of GIS with the aim to develop decision support system for flood prediction and monitoring is presented in [21]. This solution, based on integration of GIS and hydrological modeling with additional bridge sensors and users' observation, provides water level prediction for the next 24 to 48 hours. The results are displayed via dynamic web pages. The water level prediction is overlaid with maps of the transportation networks, property boundaries, municipal infrastructure and water depth contour lines. Authors of [21] claim they can provide good flood prediction and strong support to the public evacuation in the case of flooding. GIS-based forecasting and early warning system is proposed in [22]. This system provides near-real time access to all available hydrometeorological data in the Amur River basin of Russia (data from weather and gaging stations, data from hydrological forecasts, and, satellite data) and supports timely decision-making for flood risk reduction. Another mobile GIS based flood warning and information system is described in [23].

3 FLOOD PREDICTION VISUALIZATION PROCESS

Nowadays, there is a vast amount of technical equipment installed into fields and open spaces that can be used for measuring rainfall. The reasons for deploying various kinds of equipment are different commercial activities. Since this equipment already has a different commercial purpose, its side effects can be used as a cheap sources of ground level rainfall measurements. For example, the attenuation of microwave signals of cellular networks has already proven to be a reliable source for determining and acquiring quantified spatial and temporal distributions of ground-level precipitation [12]. Microwave links form a network capable of covering large areas. They provide acceptable spatial and temporal resolution and can be used as sensor substitute for the areas not covered by other types of meteorological sensors.

If the flooding estimation process uses rainfall as its basic input, it is necessary to perform rainfall prediction. Rainfall rate is in most cases acquired from ground level gauges specially installed for these purposes. In order to perform estimations of the rainfall across the area that is assessed, this type of input is the best choice. However, this approach has its commercial disadvantages that cannot be omitted. Gauging stations have to cover the hover area and have to be regularly maintained and monitored. These activities can prove to be rather expensive. Further, there has to a centralized data collection point in a form of a internet-accessible service capable of

gathering measurements in order to provide accurate estimations of the possible flooding danger.

Instead of rain gauges, we consider microwave links to be a reliable and acceptable source for determining rainfall rate. Such approach has already been developed and initial algorithms relating to the attenuation rate of cellular network signals to rainfall intensity along signal lines were previously provided as a result of the “Regional Precipitation Observation by Cellular Network Microwave Attenuation and Application to Water Resources Management” (PROCEMA) project [12]. In this project, rain detection and rainfall rate estimation was performed due to the fact that commercial cell stations can provide signal attenuation data in near real time. Thus, it was possible to calculate rainfall rate for a line in area between two mobile cell stations whose signal attenuation is measured. Although much cheaper, approach based on microwave link usage does not have the ability to cover exact locations that are most appropriate for rainfall measuring. Approaches based on gauges usage provide very precise rainfall in distinct locations. The approach we used on the other hand provides increased coverage of the observed area and can provide rainfall rates along the lines between pairs of stations.

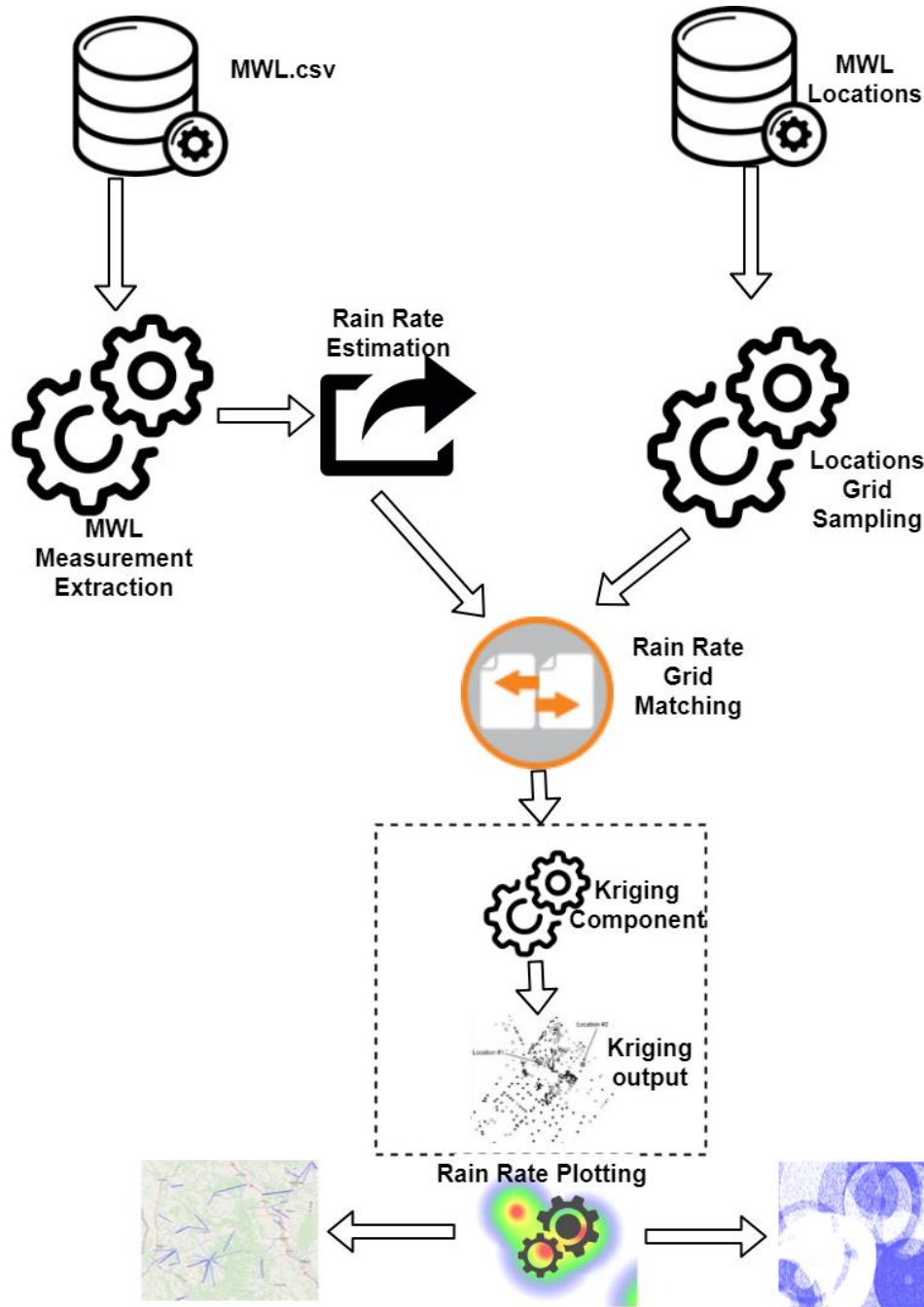


Figure 1. Rainfall prediction

The first goal of our research while developing GIS extension tool was to estimate if microwave link attenuation data within Serbia can be used for rainfall estimation, once the data is provided by the Serbian telecom operators. In order to do so, we have used ground level rainfall rate data are obtained in North Western Bavaria in Germany. This data was to be combined with already existing Digital Elevation Model (DEM) data and GIS flood estimation modules developed for Serbia. In order to make initial research proof of concept, we had to simulate cell stations in Serbia but in a proper way so that the data coming from Germany can be coupled with imaginary stations. We achieved this by translating locations of base stations from Germany to cover the area in Serbia and treating translated base stations from Germany as imaginary ones in Serbia. Once translation was performed, the overall rainfall prediction process, shown in Figure 1, was conducted.

In order to be able to calculate ground level precipitation for the whole observed area, it is necessary to perform spatial interpolation of the available data. The first step in this process is sampling distinct points along the lines of microwave links. Microwave link line length varies between each two base station. Therefore, it was necessary to choose sampling that will produce a number of points along lines according to line length. We have chosen equal distance sampling which generates a dot along the sampled line on each kilometer of the link length. If we have chosen to sample using predefined constant number of dots along lines, shorter lines would be having higher influence on the spatial interpolation because of the higher points density.

Once all link lines have been sampled and a set of points is generated, it is necessary to perform spatial interpolation of the whole area starting from the generated scattered set of points. For these purposes, we have developed a separate module named Kriging module. Kriging module uses *kriging.js* library, a JavaScript library that is capable of calculating the spatially interpolated model from a distinct set of spatial locations with rainfall rate values. As its name says, this module acquires scattered set of points and performs kriging - an advanced geostatistical procedure. As output, this procedure generates surface consisting of estimated precipitation points. Generated surface covers the whole space under analysis and represents kriging model. Once it is generated, kriging model is used to gather precipitation value for each point in the observed area.

Kriging model is used for two more purposes during the process. Precipitation estimation heatmap is generated out of the kriging model and visualized within the GIS tool. Since each point within kriging model is georeferenced, heatmap is visualized at the location of the area being observed and represents the expected precipitation levels. Most important, it is also possible to calculate the volume of the rainfall for the given timeframe on the given area.

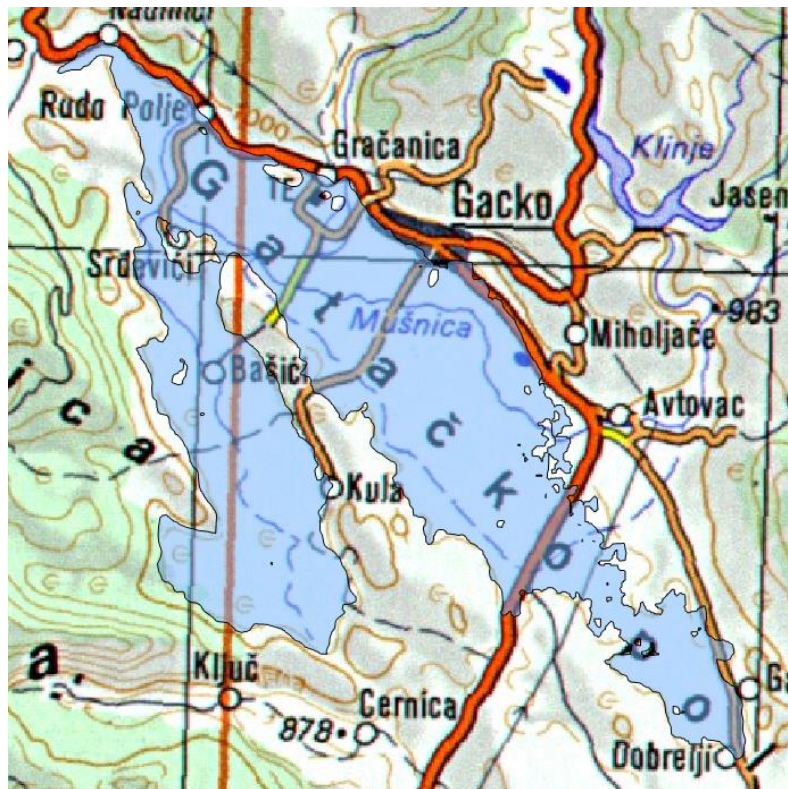


Figure 2. Example of flood prediction output

Calculate volume of the rainfall is the core of flood prediction visualization process. Visualization is performed within the extension GIS tool which is a part of our GIS-based technical platform. Our GIS platform is a custom developed GIS solution designed to provide support for diverse data types, data conversion, visualization and analysis. It incorporates open source libraries for a part of functionalities and has custom developed functionalities of its own. We have added GIS extension tool for visualization of flood risk estimation as a plug-in module to this platform. The extension tool needs overall rainfall amount for flood analysis to be possible. This information is obtained from Kriging module and the process continues using DEM model of the observed area. DEM model is used to determine the point with lowest elevation in observed area.

In this usage scenario, we have chosen an area with no river basins so we expect all rainfall to interflow towards the point with lowest altitude. Therefore, GIS extension tool will use this point as a starting point for flood estimation visualization. Starting from the point with lowest elevation, GIS extension tool performs flood fill algorithm. Our tool simulates flooding in iterations. Each iteration increases the reached water level at the point with lowest elevation. The rest of the area is filled according to chosen algorithm. Once an iteration is finished, GIS tool calculates the amount of water used for filling the area so far. This value is compared to the total amount of rainfall estimated by kriging algorithm. Once the two values become the same, filling algorithm is over and GIS tool visualizes the area expected to be flooded. An example of area expected to be flooded is shown in Figure 2.

4 CONCLUSION AND FUTURE WORK

A GIS extension tool capable of using rainfall information to perform visualization and simulation of flood risks is presented in this paper. The solution is based on the usage of rainfall prediction performed in multiple subsequent steps. Quantified ground-level precipitation can be obtained based on the measured signal level on the existing commercial microwave links. GIS solution uses this data for precipitation prediction through spatial interpolation methods. Estimated total amount of rainfall is further used for flood fill algorithm which starts at the lowest elevation point of the area of interest.

In the future research, the proposed system will be upgraded by including the impact of soil structure upon predicted total amount of rainfall. Also, we plan to investigate appropriateness of the presented methodology in cases of river basins intersecting the area of interest. The comparison of the interpolated values obtained by the system to actual measurements in the areas covered with real time rain gauges will also be done.

5 ACKNOWLEDGMENT

This work was funded by the bilateral Serbian-German project "Flood Prediction and Alerting System" supported by the DAAD foundation and Serbian Ministry of Education, Science and Technological Development.

REFERENCES

- [1] Gruntfest, E. and Handmer, J. (Eds.): *Coping with Flash Floods*, NATO Science Series, Vol. 77, Springer Verlag Science, Dordrecht, the Netherlands, 243 pp., 2001.
- [2] Barredo, J. I.: Normalised flood losses in Europe: 1970–2006, *Nat. Hazards Earth Syst. Sci.*, 9, 97–104, doi:10.5194/nhess-9-97-2009, 2009.
- [3] Hallegatte, S., Green, C., Nicholls, R. J., and Corfee-Morlot, J.: Future flood losses in major coastal cities, *Nat. Clim. Change*, 3, 802–806, 2013.
- [4] Sampson, C. C., Smith, A. M., Bates, P. D., Neal, J. C., Alfieri, L., and Freer, J. E.: A high-resolution global flood hazard model, *Water Resour. Res.*, 51, 7358–7381, 2015.
- [5] Yang, T.H., Hwang, G.D., Tsai, C.C., Ho, J.Y., Using rainfall threshold and ensemble precipitation forecasts to issue and improve urban inundation alerts, *Hydrology and Earth System Sciences*, Volume 20, Issue 12, 2016, pp.4731-4745
- [6] Mues, L., Heckley, C., Reis, A., Taylor, H.: *Estimating Floodplain Populations and Assessing Flood Risk and Flood Mitigation in Puerto Rico*, Bachelor of Science Project, Faculty of Worcester Polytechnic Institute, available online: https://web.wpi.edu/Pubs/E-project/Available/E-project-050411-133623/unrestricted/Estimating_Floodplain_Populations_and_Assessing_Flood_Risk_and_Flood_Mitigation_in_Puerto_Rico.pdf
- [7] Nguyen, P., Thorstensen, A., Sorooshian, S., Hsu, K., and AghaKouchak, A.: Flood forecasting and inundation mapping using HiResFlood-UCI and near-real-time satellite precipitation data: the 2008 Iowa flood, *J. Hydrometeorol.*, 16, 1171–1183, 2015.
- [8] Huthoff, F., Remo, J. W. F., and Pinter, N.: Improving flood preparedness using hydrodynamic levee-breach and inundation modelling: middle Mississippi River, USA, *J. Flood Risk Manage.*, 8, 2–18, 2015.

- [9] Posner, A. J. and Georgakakos, K. P.: Soil moisture and precipitation thresholds for real-time landslide prediction in El Salvador, *Landslides*, 12, 1179–1196, 2015.
- [10] Lin, G., Lin, H., and Chou, Y.: Development of a real-time regionalinundation forecasting model for the inundation warning system, *J. Hydroinform.*, 15, 1391–1407, 2013.
- [11] Shao, Q., Weatherley, D., Huang, L., and Baumgartl, T.: RunCA: a cellular automata model for simulating surface runoff at different scales, *J. Hydrol.*, 529, 816–829, 2015.
- [12] Hipp, S., Siart, U., Chwala, C., Eibert, T., Kunstmann, H., 2011. Dynamic modelling of atmospheric microwave transmission for precipitation quantification using mie scattering. *Antennas and Propagation (EUCAP), Proceedings of the 5th European Conference*, pp. 3380–3383.
- [13] IPCC: Climate Change 2014: Impacts, Adaptation, and Vulnerability. Part A: Global and Sectoral Aspects, in: Contribution of Working Group II to the Fifth Assessment Report of the Intergovernmental Panel on Climate Change, edited by: Field, C. B., Barros, V. R., Dokken, D. J., Mach, K. J., Mastrandrea, M. D., Bilir, T. E., Chatterjee, M., Ebi, K. L., Estrada, Y. O., Genova, R. C., Girma, B., Kissel, E. S., Levy, A. N., MacCracken, S., Mastrandrea, P. R., and White, L. L., Cambridge University Press, Cambridge, UK and New York, NY, USA, 1132 pp., 2014
- [14] Winsemius, H. C., Aerts, J. C. J. H., van Beek, L. P. H., Bierkens, M. F. P., Bouwman, A., Jongman, B., Kwadijk, J. C. J., Ligtoet, W., Lucas, P. L., van Vuuren, D. P., and Ward, P. J.: Global drivers of future river flood risk, *Nat. Clim. Change*, 6, 381–385, doi:10.1038/nclimate2893, 2016
- [15] Jongman, B., Ward, P. J., and Aerts, J. C. J. H.: Global exposure to river and coastal flooding: Long term trendsandchanges, *Global Environ. Change*, 22, 823–835, doi:10.1016/j.gloenvcha.2012.07.004, 2012
- [16] Kundzewicz, Z. W., Kanae, S., Seneviratne, S. I., Handmer, J., Nicholls, N., Peduzzi, P., Mechler, R., Bouwer, L. M., Arnell, N., Mach, K., Muir-Wood, R., Brakenridge, G. R., Kron, W., Benito, G., Honda, Y., Takahashi, K., and Sherstyukov, B.: Flood risk and climate change: global and regional perspectives, *Hydrolog. Sci. J.*, 59, 1–28, doi:10.1080/02626667.2013.857411, 2013
- [17] Hanson, S., Nicholls, R., Ranger, N., Hallegatte, S., Corfee-Morlot, J., Herweijer, C., and Chateau, J.: A global ranking of portcities with high exposure to climate extremes, *Climatic Change*, 104, 89–111, doi:10.1007/s10584-010-9977-4, 2011
- [18] Plate, E.J., 2009. Classification of hydrological models for flood management. *Hydrology and Earth System Sciences*, 13, 1939–1951. doi:10.5194/hess-13-1939-2009.
- [19] Sharif, H., Hashmi, M.A., “Use of Remote Sensing and GIS in flood forecasting and early warning system for Indus basin,” in *Proc. of the International Conference on Advances in Space Technologies*, pp.21-24, 2006, viewed on 23 Oct 2011, <http://ieeexplore.ieee.org/stamp/stamp.jsp?arnumber=04106401>
- [20] Farah Ahmad, Masiri Kaamin, Siti Nooraiin Mohd Razali, Suhaila Sahat, " Geographical information system (GIS) application for flood prediction at Sungai Sembrong ", In *Proc. of The 8th International Conference on Awareness Science and Technology (iCAST 2017)*, November 08-10, 2017, Taichung, Taiwan, doi: 10.1063/1.5005404
- [21] Mioc, D., Nickerson, B., Anton, F., Fraser, D., McGillivray, E., Morton, A., Tang, P., Arp, J.P. and Liang, G., Web-GIS application for flood prediction and monitoring, *International Conference on Flood Recovery Innovation and Response*, London, WIT Transactions on Ecology and the Environment (ISBN: 978-1-84564-132-0), WIT Press, pp. 145-154, 2008.
- [22] Frolov, A.V., Asmus, V.V., Borshch, S.V. et al. Russ. Meteorol. Hydrol. (2016) GIS-Amur system of flood monitoring, forecasting, and early warning, 41: 157. <https://doi.org/10.3103/S1068373916030018>
- [23] Zipf, A. and Leiner, R., 2004. A mobile GIS based flood warning and information system. In: 2nd Symposium on Location Based Services and TeleCartography, 28–29 January, Vienna, Austria
- [24] M.F. Worboys, (1995) GIS: A Computing Perspective. Taylor and Francis, London.

AUTHOR INDEX

- Alhamaydeh Mohammad, 338
 Anousakis Antonis, 219
 Antoniadis Ioannis, 56
 Aravas Nikolaos, 284
 Argyridi Amalia, 47
 Arsić Nebojša, 201
 Athanailidis Ilias, 153
 Bakarezos Efthymios, 294, 304
 Baniotopoulos Charalampos, 124, 173, 248, 397
 Baroutsos Andreas, 304
 Bekdaş Gebrail, 229, 264, 274
 Belibassakis Kostas, 116
 Bellas Ilias, 284
 Beskos Dimitri, 22
 Beskou Niki, 31
 Bilalis Nikolaos, 153
 Bogdanović Miloš, 424
 Bonic Zoran, 181
 Bonis Ioannis, 116
 Chatzidakis Dionysios, 328
 Christodoulou Peter, 284
 Cirkovic-Andjelkovic Bojana, 346
 Clark Eugene, 294
 Deskiewicz Adam, 134
 Deü Jean-Francois, 361
 Diamantopoulos Spyridon, 387
 Dimitriou Vasilis, 294, 304, 417
 Djokic Jelena, 195, 201
 Ebrahimi Amir Homaioon, 397
 Exarchos Themis, 346
 Filipovic Nenad, 346
 Filippoupolitis Marios, 243
 Fitis Ioannis, 294, 304
 Fotiadis Dimitris, 346
 Foutsitzi Georgia, 361
 Fragiadakis Michalis, 387
 Georgantzia Evangelia, 248
 Georgiou Georgios, 66
 Giannopoulos Ioannis, 134
 Gocic Milan, 189
 Hopkins Carl, 243
 Housiadas Kostas, 66
 Inglezakis Dimitrios, 106
 Ioannou Iasonas, 66
 Isailovic Velibor, 346
 Jovic Srdjan, 201
 Kapasakalis Konstantinos, 56
 Kaselouris Evaggelos, 294, 304, 417
 Katsikadelis, John, 208
 Klothakis Angelos, 96
 Koltsakis Efthymios, 173
 Koubogiannis Dimitrios, 116
 Koundourakis George, 294
 Koutoulas Kyriakos, 387
 Koutsianitis Panagiotis, 153, 361
 Leloudas Stavros, 86, 96
 Liratzakis Alexandros, 407
 Loukidis Dimitrios, 319
 Lygidakis Georgios, 96, 106
 Markou George, 38, 211, 338
 Martinez-Vazquez Pedro, 397
 Mesaritaki Aikaterini, 219
 Milanovic Mladen, 189
 Milosevic Zarko, 346
 Moan Torgeir, 1
 Mokryakov Viacheslav, 235
 Mourlas Christos, 38
 Muho Edmond, 22, 31
 Muradova Alik, 352
 Natsiavas Sotirios, 367, 377
 Nerantzaki Maria, 208
 Nigdeli Sinan Melih, 229, 264, 274
 Nikolaidis Themistoklis, 124, 248
 Nikolarakis Antonios, 144
 Nikolic Dalibor, 346
 Nikolic Milica, 346
 Nikolos Ioannis, 86, 96, 106
 Ohayon Roger, 361
 Orphanos Yannis, 304, 417
 Panaseti Pandelitsa, 66
 Papadakis Nikolaos, 312
 Papadioti, Ioanna, 284
 Papadogiannis Nektarios, 294, 304, 417
 Papadoulis Theodoros, 304
 Papadrakakis Manolis, 38
 Papagiannopoulos George, 22
 Papanastasiou Panos, 319
 Paraskevopoulos Elias, 367, 377
 Parodi Oberdan, 346
 Pelosi Gualtiero, 346
 Potosakis Nikolaos, 377
 Priovolos Andreas, 116
 Pronić Rančić Olivera, 424
 Protic Milan, 181
 Psarropoulos Prodromos, 328
 Rajovic Jelena, 195
 Rančić Dejan, 424
 Rentoumis Meletios, 153
 Saadi Dina, 338
 Sapountzakis Evangelos, 47, 56, 259

Saveljic, Igor, 346
 Siart Uwe, 424
 Sidiras Ioannis, 417
 Siokas Antonis, 259
 Skoulakis Alekos, 294, 304
 Stanojevic Predrag, 195
 Stanojevic Gocic Maja, 189
 Stavridou Nafsika, 173
 Stavroulaki Maria, 219
 Stavroulakis E. Georgios, 124, 153, 312, 352, 361
 Strofylas, Giorgos, 86
 Tairidis Georgios, 153, 352, 361
 Tatarakis Michael, 294, 304, 417
 Theotokoglou Efstathios, 134, 144
 Toklu Yusuf Cengiz, 274
 Trajkovic Slavisa, 189
 Triantafyllaki Aikaterini, 319
 Tselikos Georgios, 153
 Tsiatas George, 259
 Tsimpoukis Alexandros, 76
 Tsipianitis Alexandros 163
 Tsompanakis Yiannis, 163, 328, 407
 Tzini Maria-Ioanna, 284
 Valougeorgis Dimitris, 76
 Vlahakis Nektarios, 294
 Zivkovic Bojana, 195

Previous Congresses organized by the GRACM

1st GRACM, 1992, Athens

2nd GRACM, 1996, Chania

3rd GRACM, 1999, Volos

4th GRACM, 2002, Patras

5th GRACM, 2005, Limassol

6th GRACM, 2008, Thessaloniki

7th GRACM, 2011, Athens

8th GRACM, 2015, Volos



Greek Association of
Computational Mechanics
<http://gracm.ntua.gr>



Technical
University
of Crete

ISBN 978-618-81537-5-2



9 786188 153752 >

ISBN 978-618-81537-5-2



ΕΚΔΟΣΕΙΣ
ΠΟΛΥΤΕΧΝΕΙΟΥ
ΚΡΗΤΗΣ

Technical University of Crete Press, 2018